Medical Radiology · Diagnostic Imaging
Series Editors: H.-U. Kauczor · P. M. Parizel · W. C. G. Peh

Rosemarie Forstner
Teresa Margarida Cunha
Bernd Hamm *Editors*

MRI and CT of the Female Pelvis

Second Edition

Springer

Medical Radiology

Diagnostic Imaging

Series Editors

Hans-Ulrich Kauczor
Paul M. Parizel
Wilfred C. G. Peh

For further volumes:
http://www.springer.com/series/4534

Rosemarie Forstner
Teresa Margarida Cunha • Bernd Hamm
Editors

MRI and CT of the Female Pelvis

Second Edition

Springer

Editors
Rosemarie Forstner
Paracelsus Medical University
Salzburg
Austria

Teresa Margarida Cunha
Serviço de Radiologia
Instituto Português de Oncologia de
Lisboa Francisco Gentil
Lisbon
Portugal

Bernd Hamm
Charité Universitätsmedizin
Humboldt University of Berlin
Berlin
Germany

ISSN 0942-5373 ISSN 2197-4187 (electronic)
Medical Radiology
ISBN 978-3-319-42573-3 ISBN 978-3-319-42575-7 (eBook)
https://doi.org/10.1007/978-3-319-42575-7

Library of Congress Control Number: 2018946651

This Springer imprint is published by the registered company Springer Nature Switzerland AG
The registered company address is: Gewerbestrasse 11, 6330 Cham, Switzerland

Contents

Contributors

Sebastiano Barbieri Department of Diagnostic, Interventional and Pediatric Radiology, Inselspital, University of Bern, Bern, Switzerland

Ernst Beinder Departments of Obstetrics and Radiology, Kantonsspital Baden AG, Baden, Switzerland

Federico Collettini Klinik für Radiologie (Campus Virchow-Klinikum), Charité—Universitätsmedizin Berlin, Berlin, Germany

Teresa Margarida Cunha Serviço de Radiologia, Instituto Português de Oncologia de Lisboa Francisco Gentil, Lisboa, Portugal

Amy Davis Department of Radiology, Epsom and St Helier University Hospitals NHS Trust, London, UK

João Lopes Dias Centro Hospitalar de Lisboa Central, Lisbon, Portugal

Hospital Lusíadas de Lisboa, Lisbon, Portugal

B. Fedida Sorbonne Universités, UPMC Univ Paris 06, IUC, Paris, France

Department of Radiology, AP-HP, Hôpital Tenon, Paris, France

Rosemarie Forstner Salzburger Landeskliniken, Paracelsus Medical University, Salzburg, Austria

Universitätsinsitut für Radiologie Landeskliniken Salzburg, Paracelsus Medical University, Salzburg, Austria

Helga Fritsch Division of Clinical and Functional Anatomy, Department of Anatomy, Histology and Embryology, Medical University of Innsbruck, Innsbruck, Austria

Bernd Hamm Institut für Radiologie (Campus Mitte), Klinik für Radiologie (Campus Virchow-Klinikum), Klinik und Hochschulambulanz für Radiologie (Campus Benjamin Franklin), Charité—Universitätsmedizin Berlin, Berlin, Germany

Kirsi H. Härmä Department of Diagnostic, Interventional and Pediatric Radiology, Inselspital, University of Bern, Bern, Switzerland

Gertraud Heinz-Peer Department of Medical and Interventional Radiology, University Hospital St. Pölten, St. Pölten, Austria

Martin Heubner Department of Gynaecology and Obstetrics, Kantonsspital Baden AG, Baden, Switzerland

Mariana Horta Serviço de Radiologia, Instituto Português de Oncologia de Lisboa Francisco Gentil, Lisboa, Portugal

E. Kermarrec Department of Radiology, AP-HP, Hôpital Tenon, Paris, France

Karen Kinkel Institut de Radiologie, Clinique des Grangettes, Geneva, Switzerland

Thomas J. Kröncke Klinik für Diagnostische und Interventionelle, Radiologie und Neuroradiologie, Klinikum Augsburg, Augsburg, Germany

Rahel A. Kubik-Huch Institute of Radiology, Kantonsspital Baden AG, Baden, Switzerland

Andreas Lienemann Radiologie Mühleninsel, Landshut, Germany

Rita Lucas Hospital dos Lusíadas de Lisboa, Lisbon, Portugal

Gabriele Masselli Radiology Dea Department, Umberto I Hospital, Sapienza University, Rome, Italy

Gligor Milosevic Institute of Radiology, Kantonsspital Baden AG, Baden, Switzerland

Andrea Rockall Department of Radiology, The Royal Marsden Hospital, NHS Foundation Trust, London, UK

Justus Roos Institute of Radiology, Luzerner Kantonsspital, Luzern, Switzerland

Leonhard Schäffer Departments of Obstetrics and Radiology, Kantonsspital Baden AG, Baden, Switzerland

Alexander Schlattau Salzburger Landeskliniken, Paracelsus Medical University, Salzburg, Austria

Vera Schreiter Department of Radiology, Charité—Universitätsmedizin Berlin, Berlin, Germany

Harriet C. Thoeny Department of Diagnostic, Interventional and Pediatric Radiology, Inselspital, University of Bern, Bern, Switzerland

I. Thomassin-Naggara Sorbonne Universités, UPMC Univ Paris 06, IUC, Paris, France

INSERM, UMR970, Equipe 2, Imagerie de l'angiogenèse, Paris, France

Department of Radiology, AP-HP, Hôpital Tenon, Paris, France

Service de Radiologie, Hôpital Tenon, Paris, France

Athina C. Tsili Department of Clinical Radiology, Medical School, University of Ioannina, University Campus, Ioannina, Greece

Clinical Anatomy of the Female Pelvis

Helga Fritsch

Contents

Abstract

The pelvic floor constitutes the caudal border of the human's visceral cavity. It is characterized by a complex morphology because different functional systems join here. A clear understanding of the pelvic anatomy is crucial for the diagnosis of female pelvic diseases, for female pelvic surgery, as well as for fundamental mechanisms of urogenital dysfunction and treatment.

1 Introduction

The pelvic floor constitutes the caudal border of the human's visceral cavity. It is characterized by a complex morphology because different functional systems join here. A clear understanding of the pelvic anatomy is crucial for the diagnosis of female pelvic diseases, for female pelvic surgery, as well as for fundamental mechanisms of urogenital dysfunction and treatment.

Modern imaging techniques are used for the diagnosis of pelvic floor or sphincter disorders. Furthermore, they are employed to determine the extent of pelvic diseases and the staging of pelvic tumors. In order to be able to recognize the structures seen on CT and MRI as well as on dynamic MRI, a detailed knowledge of the relationship of the anatomical entities within the pelvic anatomy is required.

The *Terminologia Anatomica* (Federative Committee on Anatomical Terminology 1998)

This chapter is dedicated to my friend Harald Hötzinger who was an excellent radiologist and a good coworker.

H. Fritsch, M.D.
Division of Clinical and Functional Anatomy,
Department of Anatomy, Histology and Embryology,
Medical University of Innsbruck,
Müllerstrasse 59, 6020 Innsbruck, Austria
e-mail: rektorat@i-med.ac.at

Med Radiol Diagn Imaging (2017)
DOI 10.1007/174_2017_52, © Springer International Publishing AG
Published Online: 16 May 2017

contains a mixture of old and new terms describing the different structures of the pelvis. Throughout this chapter the actual anatomical terms are used and compared with clinical terms. Furthermore, they are defined and illustrated (see Table 1).

2 Morphological and Clinical Subdivision of the Female Pelvis

The anatomy of the female pelvis and perineum shows a lack of conceptual clarity. These regions are best understood when they are clearly described and subdivided according to functional and clinical requirements: The actual clinical subdivision discerns an anterior, a middle, and a posterior compartment. Whereas an anterior and posterior compartment may be found in the male as well as in the female, a middle compartment can only be found in the latter. The term "compartment" is routinely used by radiologists and all surgeons operating on the pelvic floor. This term is not identical with the term "space." According to former literature a lot of spaces are supposed to be arranged in the region of the pelvis: retrorectal, pararectal, rectoprostatic, rectovaginal, retropubic, paravesical, etc. (Lierse 1984; Pernkopf 1941; Waldeyer 1899). From the point of view of the surgeon, "spaces" are empty (Richter and Frick 1985). They are only filled with loose connective tissue and neither contain large vessels nor nerves. Some years ago, we already proposed dropping the term "space" and speaking of compartments instead, taking into account that a compartment may be filled by different tissue components (Fritsch 1994).

Within the following chapter we first present the posterior compartment and then the anterior one. This is in accordance with the viewpoint of the radiologists and with the course of the vessels and nerves. An "extra" middle compartment that is characteristic for the female is presented in detail at the end of this chapter.

What is our common knowledge about the borders of the different pelvic compartments and what do we know about their content?

2.1 Posterior Compartment

The borders of the posterior compartment are the skeletal elements of the sacrum and the coccyx dorsally. They are completed by the anococcygeal body (see Table 1) dorsocaudally and by the components of the levator ani muscle laterally and caudally (Fig. 1a). The rectovaginal fascia constitutes an incomplete border ventrocranially. The ventrocaudal border is composed of the perineal body (see Table 1). The only organ of the posterior compartment is the anorectum (see Table 1) (Fig. 1a, b).

2.2 Anterior Compartment

The borders of the anterior compartment are the pubic symphysis ventrally, the components of the levator ani muscle laterally (Fig. 1b), and the perineal membrane (see Table 1) caudally. There is no distinct border between the anterior and middle compartment in the female. The contents of the anterior compartment are bladder and urethra (Fig. 1b).

2.3 Middle Compartment

The borders are the components of the levator ani muscle laterally and the perineal body caudally (Fig. 1b). No distinct borders can be described ventrally, whereas the rectovaginal fascia/septum constitutes the dorsal border. The middle compartment contains the female genital organs that are arranged in a more or less coronal plane. In more detail the ovaries, uterine tubes, uterus, and vagina are situated in this compartment (Fig. 1a).

2.4 Perineal Body

The perineal body is part of the perineum. It is situated between the genital organs and the anus and may be considered as a central or meeting point because a number of different structures join here.

Table 1 Box of terms and definitions

Term	Figure	Terminologia Anatomica (TA)		Clinical term	Definition	Renaming (according to our results)	Existence
		English	Latin				
1. Anococcygeal body	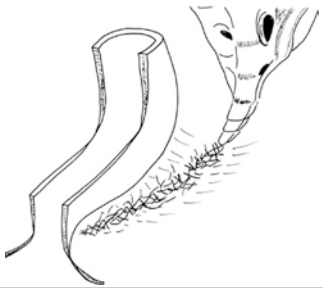	Anococcygeal body; anococcygeal ligament	Corpus anococcygeum; corpus anococcygeum	–	TA: The term corpus, rather than ligamentum, is used in TA because it is a stratified nonligamentous structure in which fleshy muscle attachments underlie a tendon	Not necessary	+
2. Perineal body	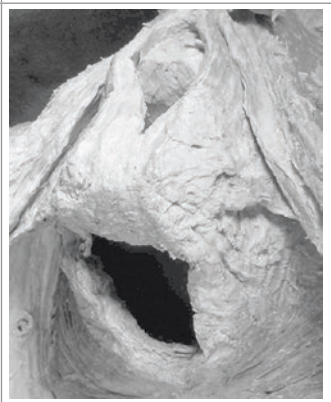	Perineal body	Corpus perineale; centrum perinei	–	TA: The perineal body is fibromuscular rather than tendinous and quite unlike the centrum tendineum of the diaphragm Our option: The perineal body itself is tendinous; nevertheless it cannot be compared with the flat centrum tendineum of the diaphragm	Though tendinous, not necessary	+

(continued)

Table 1 (continued)

Term	Figure	Terminologia Anatomica (TA)		Clinical term	Definition	Renaming (according to our results)	Existence
		English	Latin				
3. Perineal membrane		Perineal membrane	Membrana perinea	–	Dense connective tissue between external urethral sphincter (and transverse perineal muscle in male) and pubic bone	Not necessary	+
4. Anorectum	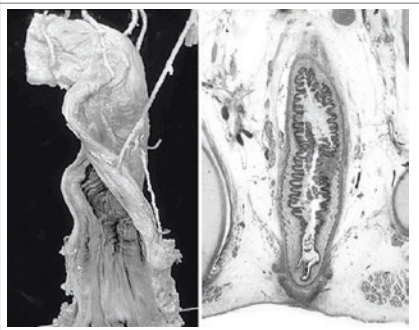	Rectum and anal canal	Rectum et canalis analis	Ano rectum	Our option: The clinical term includes both, the rectum and the anal canal, not taking into account that they are of different origin	Necessary to pick up in TA	+

5. Presacral (sub) compartment	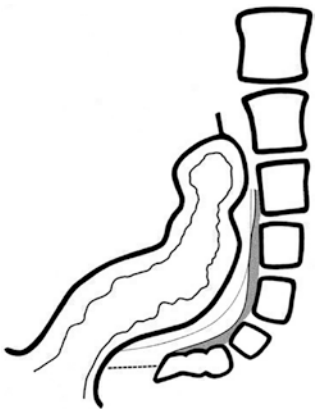	–	–	–	Our option: Small space between presacral fascia and sacral and coccygeal vertebrae containing vessels	Necessary to pick up in TA	+
6. Presacral fascia		Presacral fascia	Fascia presacralis	Waldeyer's fascia (?)	Caudal part of the parietal pelvic fascia		+
7. Perirectal compartment	 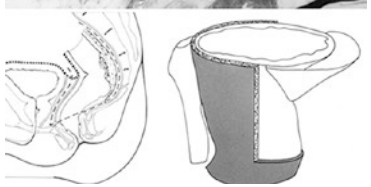	–	–	Mesorectum	Our option: Compartment filled by the rectal adventitia including nerves, vessels, lymph nodes	Necessary to pick up in TA	+

(continued)

Table 1 (continued)

Term	Figure	Terminologia Anatomica (TA)		Clinical term	Definition	Renaming (according to our results)	Existence
		English	Latin				
8. Rectal fascia or "Grenzlamelle"	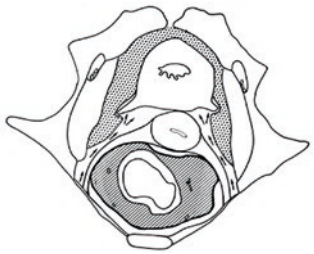	–	–	Waldeyer's fascia (?)	Our option: Outer connective tissue lamella of the rectal adventitia, bordering the perirectal compartment	Necessary to pick up in TA	+
9. Inferior hypogastric plexus	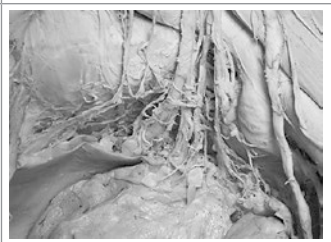	Inferior hypogastric plexus; pelvic plexus	Plexus hypogastricus inferior; plexus pelvicus	Pelvic plexus	Autonomic nerve plexus within the rectouterine or recto-vesical fold	Exclusively into the old and clinical term: pelvic plexus	+
10. Uterosacral ligament	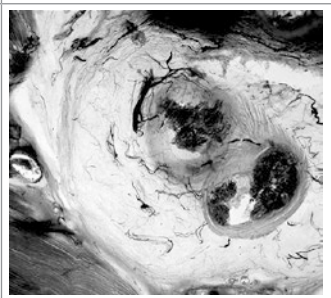	Uterosacral ligament or rectouterine ligament	Li. rectouterinum	–	Dense connective tissue running from the edges of the cervix uteri to the region of the sacrospinous ligament, then ascending and joining the pelvic parietal fascia	Exclusively into the uterosacral ligament	+

11. Rectovaginal fascia	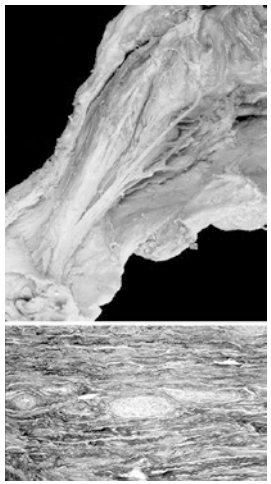	Rectovaginal fascia; rectovaginal septum (female)	Fascia rectovaginalis; septum rectovaginale	–	Our option: Plate of dense connective tissue, smooth muscle cells and nerves, locally arranged between rectum and vagina	Exclusively into the term rectovaginal/ rectogenital septum	+
12. Anal sphincter complex	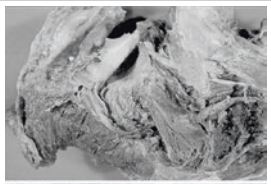	–	–	–	Includes all muscle layers of the anal canal: internal (smooth) sphincter, longitudinal (smooth) muscle, external (striated) sphincter	Necessary to pick up in TA	+
13. Pubovesical ligament	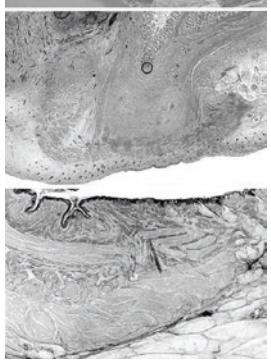	Medial pubovesical ligament, pubovesicalis, lateral pubovesical ligament	Lig. mediale pubovesicale, m. pubovesicalis, lig. Laterale pubovesicalis	–	Most confusing structure! Our option: there is only one structure running from the pubic bone to the vesical neck. It mainly consists of smooth muscle cells intermingled with strands of dense connective tissue	Exclusively into the term pubovesical muscle	+

(continued)

Table 1 (continued)

Term	Figure	Terminologia Anatomica (TA)		Clinical term	Definition	Renaming (according to our results)	Existence
		English	Latin				
14. Levator ani muscle	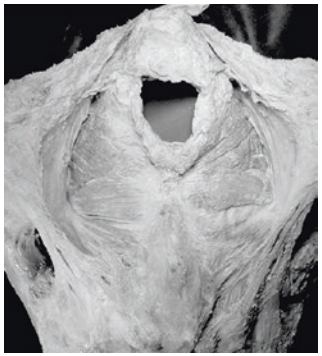	Levator ani	M. levator ani	–	Muscle that constitutes the main part of the pelvic diaphragm and is composed of the Mm. pubococcygeus, iliococcygeus, and puborectalis of each side		+
15. Tendinous arch of the pelvic fascia	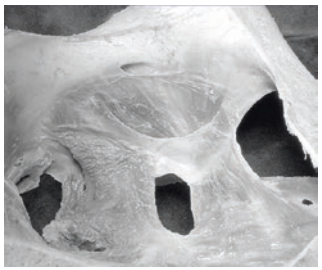	Tendinous arch of the pelvic fascia	Arcus tendineus fasciae pelvis	–	Our option: This structure originates from the pubic bone laterally, it is connected with the superior fascia of the pelvic diaphragm "white line" laterally and with the pubovesical ligament medially. It may falsely be called Lig. laterale puboprostaticum or Lig. laterale pubovesicale		+

16. Paravisceral fat pad		–	–	–	Our option: Fat pad at the lateral side of the bladder that develops in situ. Functionally necessary for the movements of bladder	Necessary to pick up in TA	+
17. Broad ligament	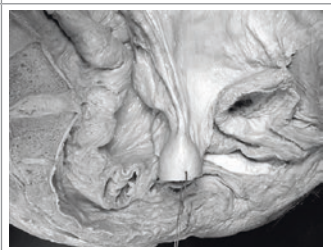	Broad ligament of the uterus	Lig. latum uteri	–	Peritoneal fold between the uterus and the lateral wall of the pelvis		+
18. Rectouterine fold	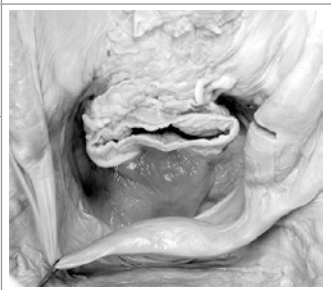	Rectouterine fold	Plica rectouterina	–	Peritoneal fold passing from the cervix uteri on each side of the rectum to the posterior pelvic wall		+
19. Rectouterine pouch		Rectouterine pouch	Excavatio rectouterina	Space of Douglas	Deep peritoneal pouch situated between the rectouterine folds of each side		+

(continued)

Table 1 (continued)

Term	Figure	Terminologia Anatomica (TA)		Clinical term	Definition	Renaming (according to our results)	Existence
		English	Latin				
20. Vesico-uterine fold	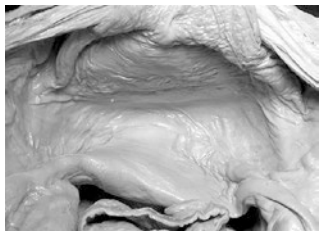	Vesico-uterine fold	Plica vesicouterina	–	Peritoneal fold between bladder and uterus on each side		+
21. Vesico-uterine pouch		Vesico-uterine pouch	Excavatio vesicouterina	–	Slight peritoneal pouch between the vesicouterine folds of each side		+
22. Transverse cervical ligament or cardinal ligament	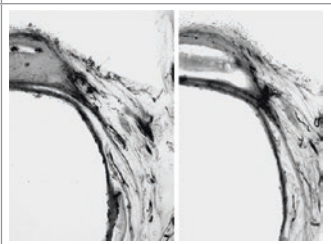	Transverse cervical ligament, cardinal ligament	Lig. transversum cervicis, lig. Cardinale	Cardinal ligament	Connective tissue structures that should extend from the side of the cervix to the lateral pelvic wall Our option: The cardinal ligament does not exist	Necessary to omit	0
23. Mesosalpinx	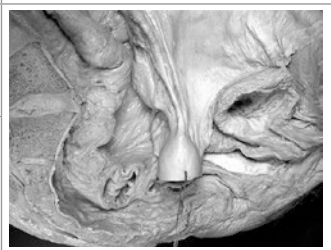	Mesosalpinx	Mesosalpinx	Identical	Double fold of peritoneum at the upper margin of the broad ligament		+
24. Mesovarium		Mesovarium	Mesovarium	Identical	Double fold of peritoneum attached at the dorsal portion of the broad ligament		+
25. Mesometrium	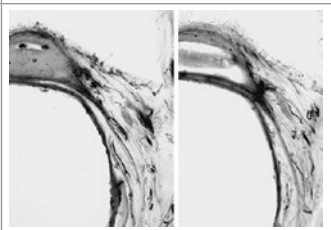	Mesometrium	Mesometrium	–	So-called meso of the uterus, greatest portion of broad ligament	According to Höckel is morphogenetic unit of cervix and proximal vagina. Necessary to redefine	+

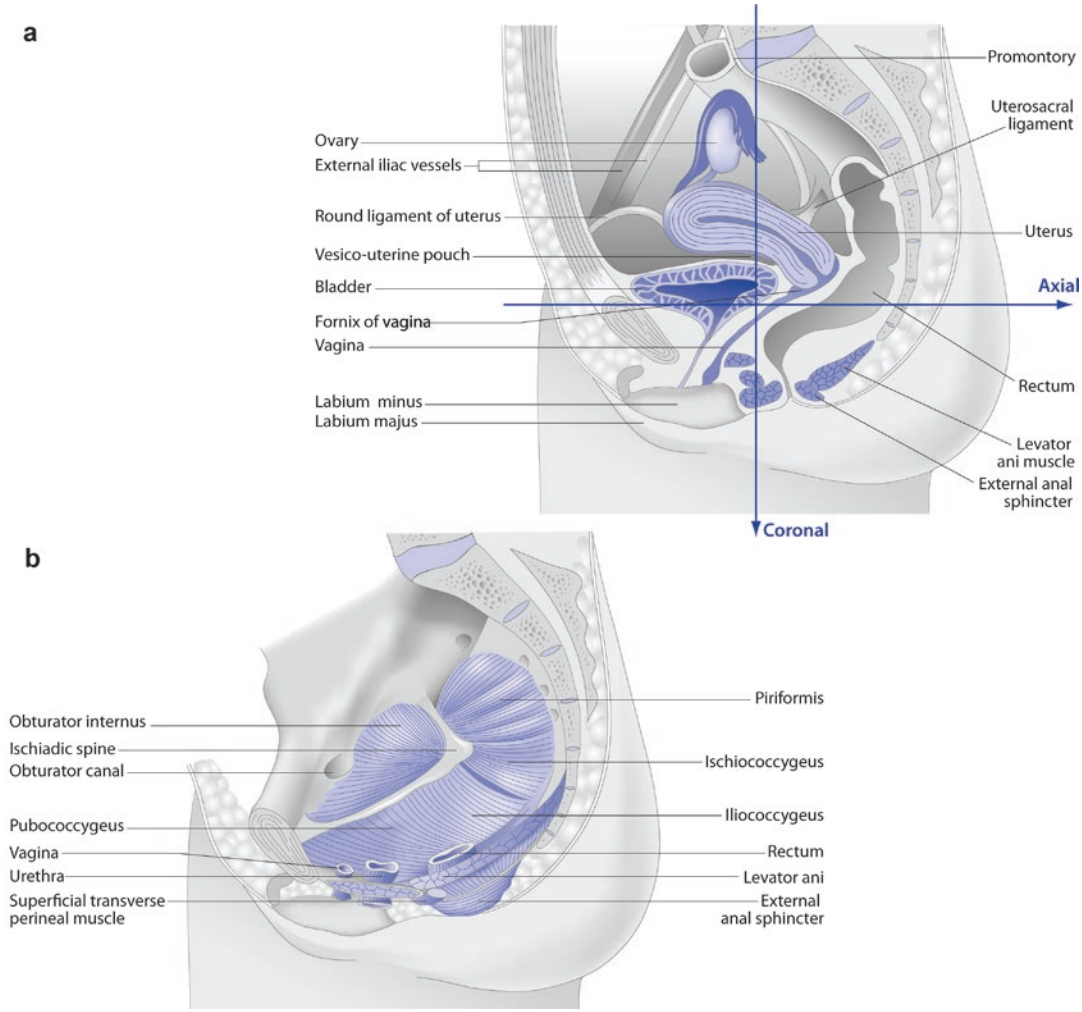

Fig. 1 (**a**) Female pelvic organs in a sagittal view. (**b**) Muscles of the pelvic floor

3 Compartments

3.1 Posterior Compartment

3.1.1 Connective Tissue Structures

In macroscopic dissection of embalmed cadavers it is nearly impossible to distinguish subcompartments within the connective tissue of the posterior compartment. Our comparative study of adult and fetal pelves shows that two subcompartments can be distinguished within the posterior compartment:

A small presacral subcompartment (see Table 1) is situated in front of the sacrum and coccyx. It is bordered by the caudal segments of the vertebral column dorsally and ventrolaterally, and it is clearly demarcated by the pelvic parietal fascia (see Table 1) (Fig. 2), which is called presacral fascia (see Table 1) at this position. In fetuses, the presacral subcompartment contains loose connective tissue, but it is predominated by large presacral veins.

The major part of the posterior pelvic compartment is filled by the anorectum and its accompanying tissues, constituting the perirectal subcompartment (see Table 1). This perirectal tissue is identical with the rectal adventitial tissue (Fritsch 1990; Fritsch et al. 2004) (see

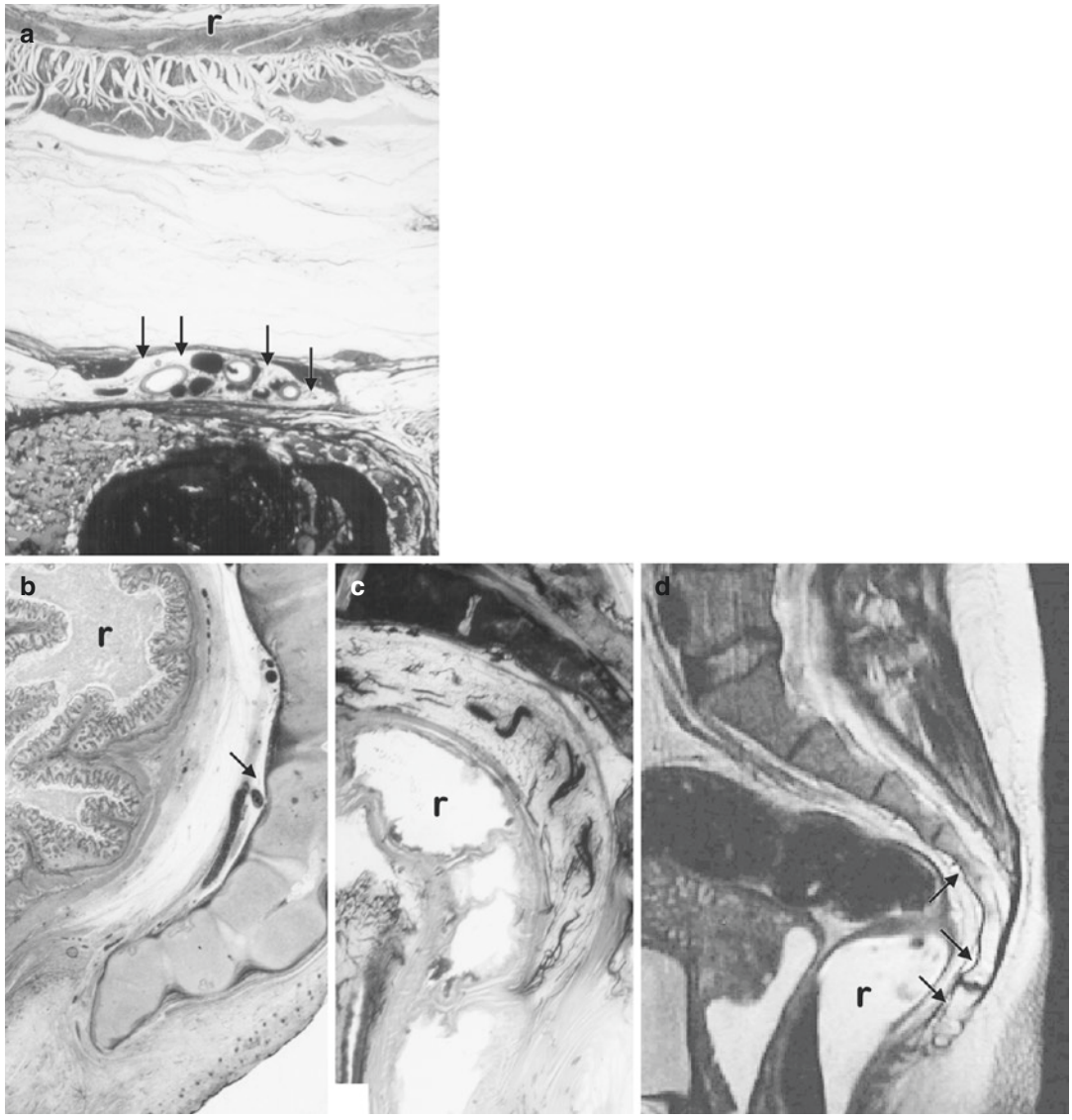

Fig. 2 Presacral space (*arrows*). (**a**) Axial section (500 µm) of an adult. ×4. (**b**) Sagittal section (400 µm) of a 24-week-old female fetus. ×9. (**c**) Sagittal section (5 mm) of an adult female. ×0.45. (**d**) Midsagittal MR image of an adult female. *r* rectum

Table 1), which develops along the superior rectal vessels. In the adult, it mainly consists of adipose tissue subdivided by several connective tissue septa (Fig. 3a, b). Within this perirectal tissue the supplying structures of the rectum are enclosed: the superior rectal vessels, stems and branches, branches of the variable medial rectal vessels, rectal nerves and rectal lymphatics, vessels, and nerves. The localization of these lymphatic nodes is strikingly different from that of the other lymph nodes of the posterior compartment that are situated laterally in the neighborhood of the iliac vessels (Nobis 1988; Stelzner 1998).

The rectal adventitia develops from a layer of condensed mesenchymal tissue, which—later on—forms a dense connective tissue in fetuses (Fig. 3c). In the newborn child it is remodeled by small fat lobules occurring between the connective tissue lamellae. The outer lamella covers the

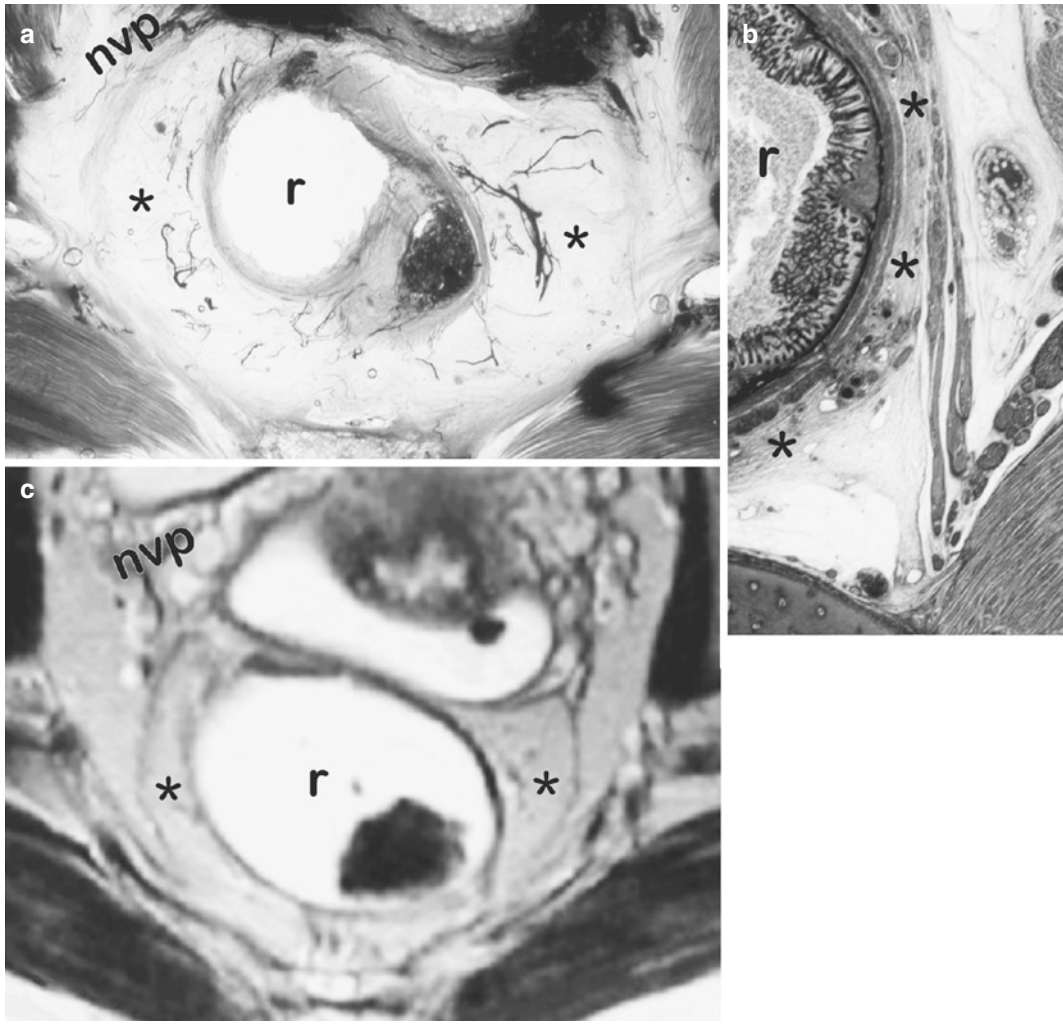

Fig. 3 Perirectal tissue (*asterisks*). (**a**) Axial section (5 mm) of an adult female. ×0.45. (**b**) Axial MR image of an adult female. (**c**) Axial section (400 μm) of a 24-week old female fetus. ×5. *nvp* nerve vessel plate, *r* rectum

perirectal subcompartment and is called "rectal fascia" (Fritsch 1990; Fritsch et al. 1996) or "Grenzlamelle" (Stelzner 1989, 1998) (see Table 1). It constitutes the morphological border of the perirectal subcompartment. The craniocaudal extent of the perirectal subcompartment depends on the branching pattern of the superior rectal vessels; thus the perirectal compartment is broad laterally and dorsally and it is often rather thin ventrally where it is only composed of some connective tissue lamellae. As can be seen in sagittal sections the extent of the perirectal subcompartment decreases in size in a craniocaudal direction (Fig. 2c).

What is situated outside the rectal fascia and therefore outside the perirectal subcompartment? Dorsally, the presacral subcompartment is loosely attached to the perirectal compartment (see above). Laterally the supplying structures (autonomic nerves and branches of the iliac vessels) of the urogenital organs constitute a nerve-vessel plate (Fig. 3c). The latter is accompanied by connective tissue and fills the remaining space between the perirectal compartment and the lateral pelvic wall. In the female, the nerves of the inferior hypogastric plexus (see Table 1) are attached to the uterosacral ligament (see Table 1) that is directly situated between the rectal fascia

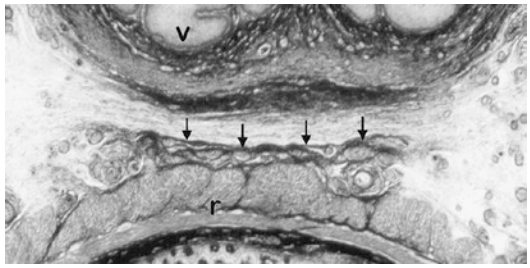

Fig. 4 Rectovaginal fascia (*arrows*). Axial section (400 μm) of a 24-week-old female fetus. ×28. *v* vagina, *r* rectum

and the inferior hypogastric plexus (Fig. 3a, c) (Fritsch 1992).

The ventral border of the perirectal compartment represents the border between posterior and middle compartment. It differs in a craniocaudal direction, i.e., to the peritoneum of the rectouterine pouch at a level with the cervix uteri and the fornix vaginae and to the posterior wall of the vagina more caudally. As we have recently shown (Aigner et al. 2004; Fritsch et al. 2004; Ludwikowski et al. 2002) a two-layered rectovaginal fascia/septum (see Table 1) develops in the female and is identical to the male's rectoprostatic fascia/septum or Denonvilliers' fascia (Tobin and Benjamin 1945). At a level with the anorectal flexure, additional bundles of longitudinal smooth muscles are situated at the anterior rectal wall forming the muscular portion of the rectovaginal fascia ventrally (Fig. 4). The smooth muscle bundles are accompanied by nerves, some of them crossing the midline, and they are connected to the smooth muscle layer of the rectal wall. Caudally these additional smooth muscle bundles are attached to the connective tissue of the perineal body (Fig. 4).

3.1.2 Muscles

Within the posterior pelvic compartment all components of the levator ani muscle are to be found: the pubococcygeus muscles and the iliococcygeus muscles constitute an irregular plate and insert into the coccyx where they overlap each other in a staggered arrangement (Fig. 5). The inferior component, the puborectalis muscles, does not insert into any skeletal structure. Behind the rectal wall the fiber bundles of each puborectalis muscle crisscross, thus constituting a muscular sling around the anorectal flexure (Fig. 6). In the craniocaudal direction the pubococcygeus muscle and the puborectalis muscle are more or less continuous. In sectional anatomy they can be differentiated by the different directions of their fiber bundles, those of the pubococcygeus taking a slightly descending course, and those of the puborectalis exclusively situated in the horizontal plane. The different components of the levator ani muscle can already be distinguished in early fetal life (Fritsch and Fröhlich 1994). Sexual differences found in the levator ani muscle of the adult are already marked in late fetal life: the levator ani constitutes a thick and well-developed muscle in the male fetus whereas it is thinner and already intermingled with connective tissue in the female fetus (Fig. 6b). This is particularly true of its puborectalis portion.

The puborectalis muscle is continuous with the external anal sphincter caudally (Fig. 7). The macroscopic distinction between both muscles is provided by the anococcygeal body. The puborectalis has no skeletal attachment dorsally, but the deep portion of the sphincter ani externus is indirectly fastened to the coccyx by the anococcygeal body.

The sphincter ani externus is the outer part of the anal sphincter complex (see Table 1). The other components are the smooth internal sphincter and the longitudinal muscle layer of the anorectum; the latter is interposed between the sphincters. Whereas macroscopically the external anal sphincter presents itself as a continuous sheet covering the anal canal (Fig. 8a), it can be subdivided into a deep, anorectal portion and a superficial, subcutaneous portion in sectional anatomy (see Fig. 8b). This deep portion is a clearly demarcated layer of circularly arranged striated muscle fibers; the superficial portion is characterized by an intermingling of the striated muscle fibers with the smooth longitudinal muscle (also called "intersphincteric

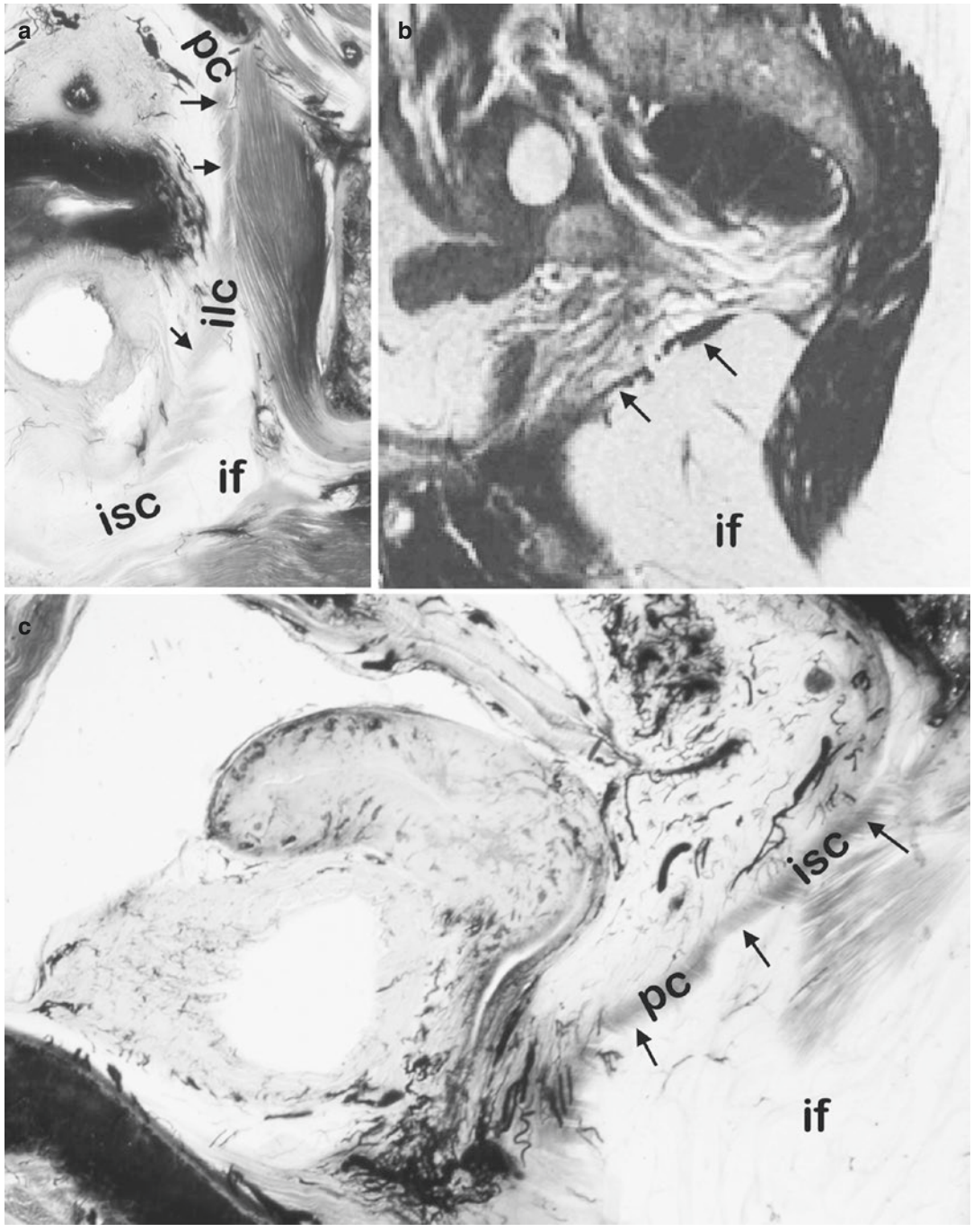

Fig. 5 Levator ani muscle (*arrows*). (**a**) Axial section (5 mm) of an adult female. ×0.6. (**b**) Parasagittal MR image of an adult female. (**c**) Sagittal section (5 mm) of an adult female. ×1.0. *isc* ischiococcygeal muscle, *if* ischioanal fossa, *ilc* iliococcygeal muscle, *pc* pubococcygeal muscle

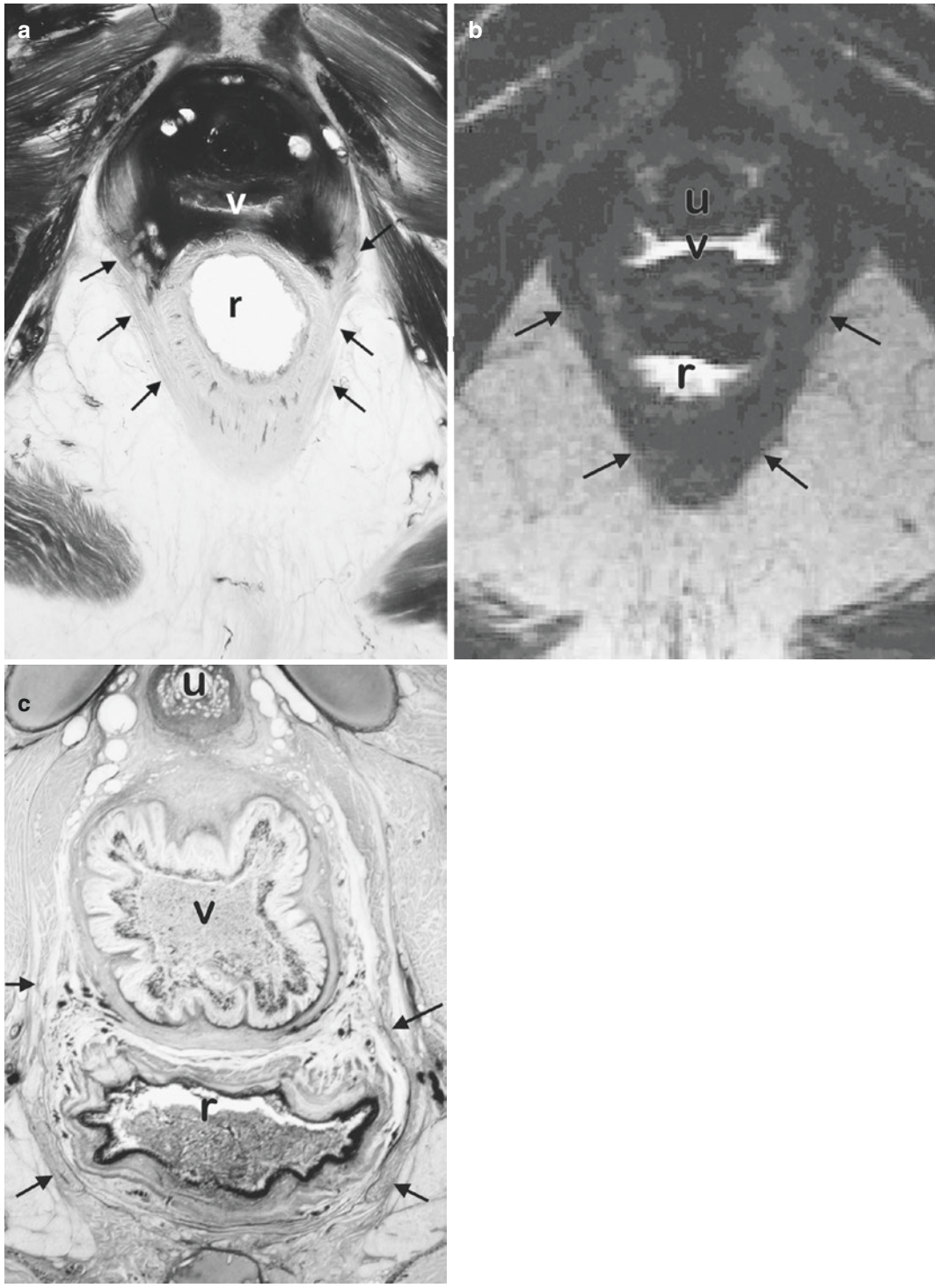

Fig. 6 Puborectalis muscle (*arrows*). (**a**) Axial section (5 mm) of an adult female. ×0.8. (**b**) Axial MR image of an adult female. (**c**) Axial section (400 μm) of a female newborn specimen. ×4. *u* urethra, *v* vagina, *r* rectum

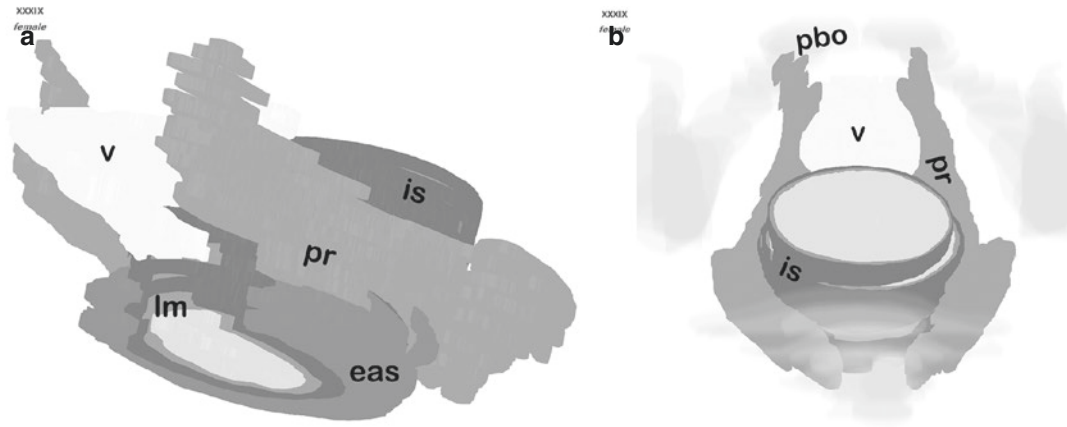

Fig. 7 Computer-assisted reconstructions of a female fetus. (**a**) Oblique ventrolateral view. (**b**) Descending dorsoventral view. *v* vagina, *lm* longitudinal muscular layer, *pr* puborectalis muscle, *eas* external anal sphincter, *is* internal sphincter, *pbo* pubic bone

space"). The form of the external anal sphincter can be best studied in three-dimensional reconstructions of histological or anatomical orthogonal sections (Fritsch et al. 2002): At an anorectal level above the perineum where the external anal sphincter is continuous with the puborectalis muscle dorsally (Fig. 8c), it is missing in the midline ventrally, but it is thickened ventrolaterally where it becomes part of the anterior compartment in males and the middle compartment in females. At a level of the perineum the external anal sphincter is complete ventrally (see Fig. 15a), but it turns inwards and forms a muscular continuum with the smooth internal sphincter and the longitudinal muscle dorsally. As can be seen from the fetal sections, sexual differences in the anal sphincter complex are already present prenatally: the sphincter complex as a whole is thicker in the male than in the female, and the anterior portion, however, is thick in the female and thinner and more elongated in the male.

3.1.3 Reinterpreted Anatomy and Clinical Relevance

The posterior compartment is predominated by the rectum and its surrounding connective tissue. The morphological demarcation of this compartment is formed by the rectal fascia. In CT the rectal fascia may be discriminated as a slightly hyperdense sheath (Grabbe et al. 1982; WEW and Tucker 1986) and in MRI it is visible as a thin, hypointense structure. It is important for the diagnosis and staging of rectal tumor (Beets-Tan et al. 2001; Brown et al. 2003; Heald 1995). According to our results the macroscopic borders of the perirectal compartment are clearly demarcated in the adult female where the sacrouterine ligaments constitute the lateral borders and where the posterior border is marked by the pelvic parietal fascia. The perirectal adipose tissue constitutes functional fat that adapts to the different filling volumes of the rectum and constitutes a gliding sheath for the movements of that organ. In contrast to prior literature (Pernkopf 1941; Richter 1998) we did not find any ligament or even ligamentous structures binding the rectum to the lateral pelvic wall. Thus, there is neither a "rectal stalk" nor a dense "paraproctium."

The most common surgically correctable cause of fecal incontinence in woman is childbirth with injury of the sphincter. External sphincter injuries occur in 6–30% of women (Sultan et al. 1993). It should be differentiated between complete or incomplete sphincter disruptions. Our morphological investigation (Fritsch et al. 2002) supports the fact that the external anal sphincter is not a totally circular muscle. We have thoroughly described the parts of the sphincter complex, in order to help the pelvic radiologists and surgeons to identify these structures and, if possible, to reconstruct them in a meticulous way.

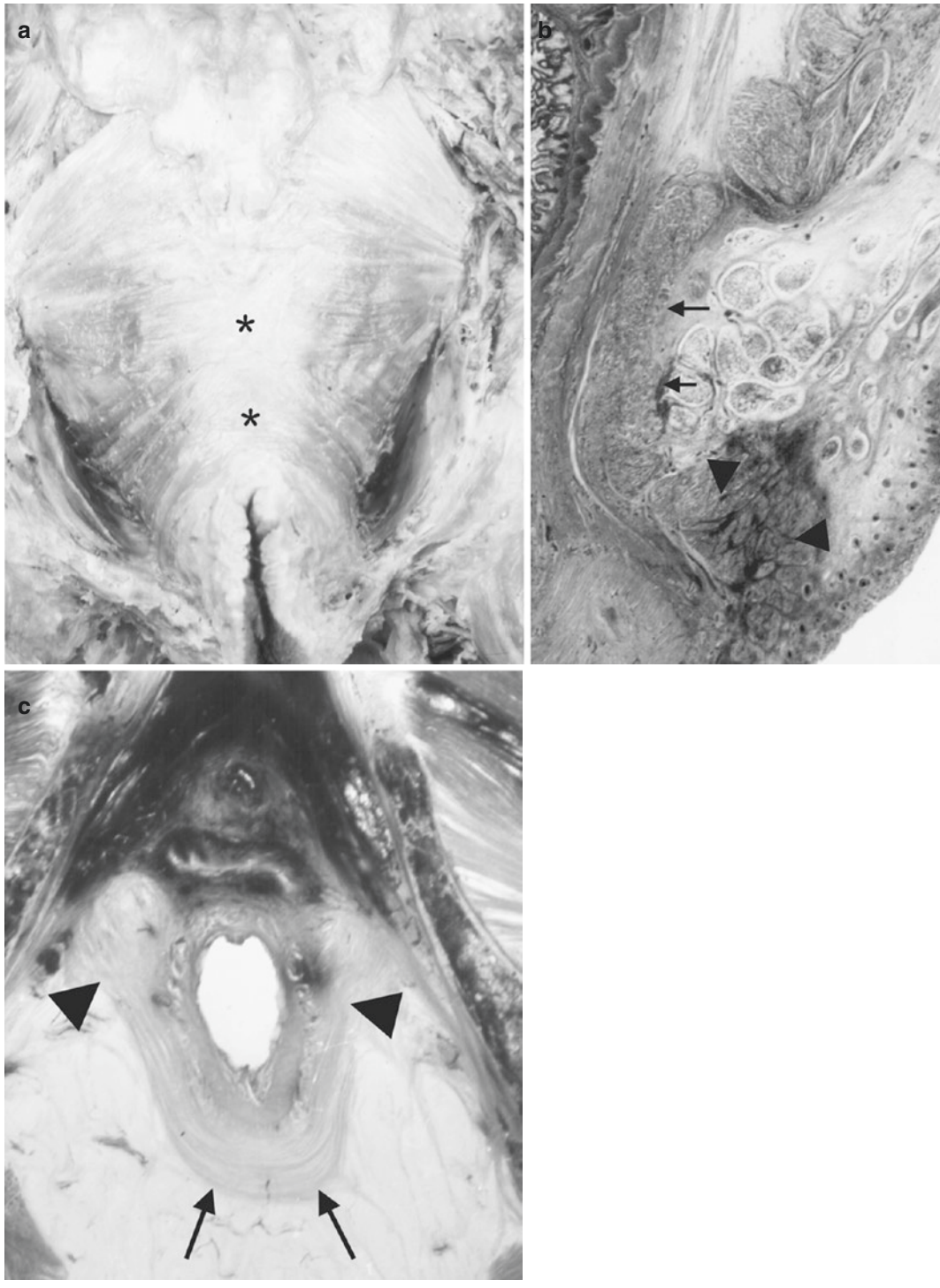

Fig. 8 Anal sphincter complex. (**a**) Macroscopic preparation of an adult female with anococcygeal body (*asterisks*). (**b**) Sagittal section (500 μm) of a 20-week-old female fetus with deep (*arrows*) and superficial (*arrowheads*) portion. ×10. (**c**) Axial section (5 mm) of an adult female, fusion of the external sphincter (*arrow*) and the puborectalis (*arrowhead*). ×0.6

Rectoceles are hernial protrusions of the anterior rectal wall and the posterior vaginal wall into the vagina and/or throughout the vaginal introitus. The size of the rectocele does not correlate with symptoms and it is often diagnosed in a population without symptoms. Trauma or obstetrical injuries weaken the rectovaginal fascia/septum. Rectoceles occur with laxity of the connective tissue in advancing years, multiparity, poor bowel habits, perineal relaxation, and increased intra-abdominal pressure in constipation (Khubchandani et al. 1983; Zbar et al. 2003). In the successful repair of a rectocele the rectovaginal fascia/septum seems to be the key structure (Cundiff et al. 1998; Richardson 1993).

3.1.4 Important Vessels, Nerves, and Lymphatics of the Posterior Compartment

- Superior rectal artery
- Rectal nerves
- Rectal lymph nodes
- Inferior hypogastric plexus
- Superior hypogastric plexus
- Common iliac artery
- Internal iliac artery

(Veins have a corresponding course)

3.2 Anterior Compartment

3.2.1 Connective Tissue Structures

When dissecting along the lateral and ventral wall in embalmed cadavers, it is easy to isolate the bladder including the embedding tissues and all the adjacent structures. During dissection, no lateral stalks are found that might be responsible for the fixation of the bladder or the urethra. Ventrally a cord can be identified. It takes an ascending course from the pubic bone to the neck of the bladder and it is usually called the pubovesical ligament (see Table 1) (Fig. 9a). It is

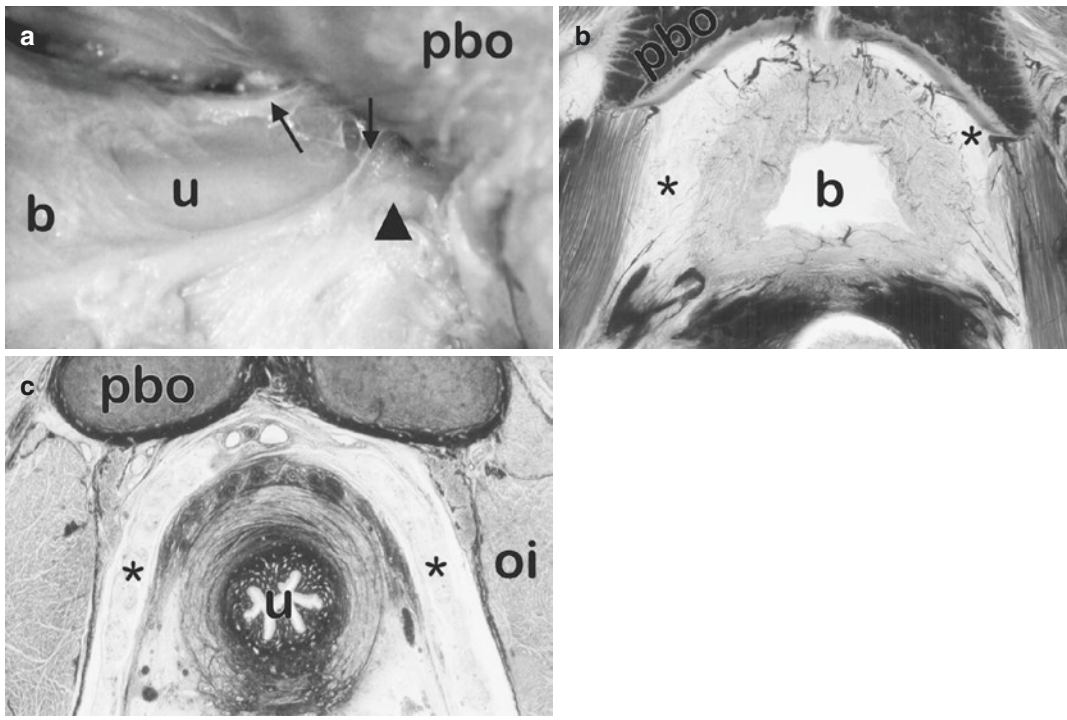

Fig. 9 Anterior compartment. (**a**) Macroscopic preparation of a 23-week-old female fetus with the pubovesical ligament (*arrow*) and the tendinous arch (*arrowhead*). ×9. (**b**) In an axial section (5 mm) of an adult female with the paravisceral fat pad (*asterisks*). ×. (**c**) Axial section (400 μm) of a 24-week-old female fetus with the developing paravisceral fat pad (*asterisks*). ×8. *b* bladder, *u* urethra, *pbo* pubic bone, *oi* obturator internus muscle

connected to the tendinous arch of the pelvic fascia (see Table 1). Together, both structures incompletely subdivide the retropubic region into a prevesical subcompartment and a preurethral subcompartment. From the comparative sectional study of fetal and adult pelves we learned the detailed composition of the connective tissue structures within the anterior compartment.

With the exception of its neck and its posterior wall the bladder is covered by adipose tissue (Fig. 9b). The latter constitutes a semicircular pad that fills the gap between the lateral pelvic wall and the ventral and lateral wall of the bladder. The fat pad is not subdivided by ligaments or any other dense connective tissue septa, but sometimes may be crossed by variable branches from the obturator vessels. It develops in situ (Fig. 9c) from a large paravisceral fat pad (see Table 1) in human fetuses (Fritsch and Kühnel 1992) and neither contains large vessels, nerves, nor lymphatics. The latter derive from the internal iliac vessels and join the dorsolateral edge of the bladder. Their branches, which are always accompanied by a sheath of dense connective tissue, embrace the bladder and urethra. Thus nerves, vessels, and lymphatics are directly situated at the lateral and dorsal wall of the bladder and medially to the fat pad. Ventrocranially, both fat pads join in the midline. Their dorsal edge nearly abuts at the perirectal compartment and their caudal border abuts the levator ani laterally and the pubovesical or puboprostatic ligament ventrally. Thus they are not part of the preurethral subcompartment that is filled by connective tissue accompanying the deep dorsal vessels of the clitoris.

Within the anterior compartment two structures are found that are composed of dense connective tissue: the tendinous arch of the pelvic fascia that originates from the pubic bone and that is connected to the pelvic parietal fascia covering the levator ani muscle on its visceral side (superior fascia of the pelvic diaphragm; see Table 1) and the semicircular fibrous sheath that covers the ventral and lateral wall of the bladder and the urethra. As the sheath is strong ventrally it can be considered as an incomplete ventral vesical or urethral fascia. Whereas the ventral vesical fascia has absolutely no fixation to the lateral pelvic wall, at a level of the urogenital hiatus the ventral urethral fascia, but not the urethra (Ludwikowski et al. 2001), is attached to the fascia of the levator ani muscle laterally (Fig. 10a). Thus, within the hiatus a fibrous bridge connects the fasciae of the levator ani muscles of both sides. To summarize: the fibrous structures of the anterior compartment build up a hammocklike (DeLancey 1994) construction for bladder and urethra. These findings can most clearly be shown in fetuses and are matching but not so evident in the adult. It is important to know that there is absolutely no kind of a lateral bony fixation for bladder or urethra. In a dorsocranial direction, the ventral fascia of bladder and urethra is continuous with the connective tissue sheath of the internal iliac vessels. Ventrally, the hammocklike construction is indirectly fixed to the pubic bone by means of the tendinous arch and by the so-called pubovesical ligament (Fig. 10b–d). The latter is composed of cholinergic innervated smooth muscle cells (Wilson et al. 1983) and is connected to the vesical neck cranially (see above).

An additional fibrous structure can be found to close the hiatus ventrally: a plate of dense connective tissue fills the space between pubic bone and urethral sphincter, thus constituting the perineal membrane (Fig. 11a).

3.2.2 Muscles

The striated muscles of the anterior compartment are the ventral parts of the levator ani muscle (see Table 1), i.e., the pubococcygeus and puborectalis muscle of each side. As they are covered by the superior fascia of the pelvic diaphragm, they are clearly separated by the adjacent organs (Fig. 10a, d and Fig. 11a) and the external urethral sphincter. As has been reported previously (Ludwikowski et al. 2001), this muscle is horseshoe- or omega-shaped during fetal development and incompletely covers the urethra (Fig. 11). The dorsal ends of this muscle are connected by a plate of dense connective tissue that is small in the female where it is firmly attached to the ventral wall of the vagina (Figs. 10d, 11a). Whereas most of the fibers of the external urethral sphincter

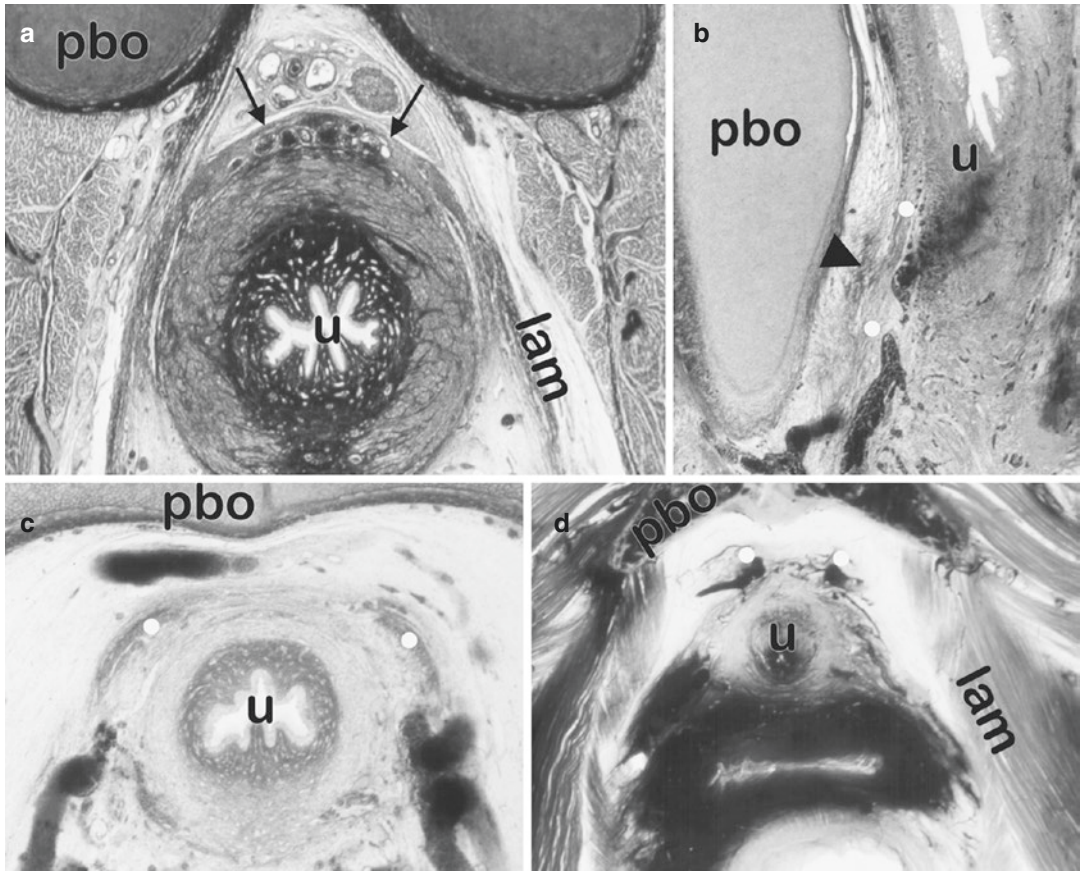

Fig. 10 Anterior compartment and the so-called ligaments of the urethra. (**a**) Axial section (400 μm) of a 24-week-old female fetus with the semicircular urethral sheath (*arrows*). ×12. (**b**) Sagittal section (500 μm) of a 13- to 14-week-old female fetus with the pubovesical ligament (*white spots*) and the origin of the tendinous arch (*arrowhead*). ×25. (**c**) Axial section (400 μm) of a 17-week-old female fetus with the pubovesical ligaments (*white spots*). ×12. (**d**) Axial section (5 mm) of an adult female with the pubovesical ligaments (*white spots*). ×7.5. *pbo* pubic bone, *u* urethra, *lam* levator ani muscle

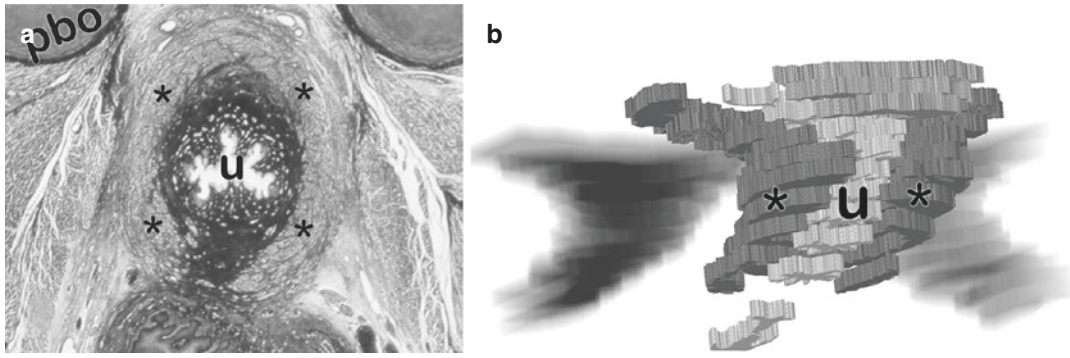

Fig. 11 External urethral sphincter (*asterisks*). (**a**) Axial section (400 μm) of a 24-week-old female fetus, embedded in the transverse perineal membrane. ×9. (**b**) Computer-assisted three-dimensional reconstruction of a female fetus. *Pbo* pubic bone, *u* urethra

run semicircular, the most caudal fibers nearly run in a transverse plane. This portion predominates in the male and therefore has been considered as the male's deep transverse perineal muscle. However, it does not exist in the female (Oelrich 1983).

As has been described above, smooth muscles are found outside the walls of the urogenital organs constituting parts of the pubovesical ligament in front of the ventral wall of the urethra.

3.2.3 Reinterpreted Anatomy and Clinical Relevance

The extent of the fat pad described here is identical to the anterior portion of the paravisceral space as reported by Gasparri and Brizzi (Gasparri and Brizzi 1961). It is obvious that the main function of the semicircular, paravisceral fat pad is to constitute a gliding pad for the bladder (Kux and Fritsch 2000). The fat pad accompanies the bladder whenever moving.

Dorschner et al. (Dorschner et al. 2001) pointed out the fact that the smooth muscle bundles of the pubovesical ligaments are continuous with longitudinal muscle fibers of the neck of the bladder that they call dilatator urethrae. Maybe again there is a similarity to the anorectum, where we also found smooth muscle bundles and autonomic nerves outside the ventral wall, which we think work in functional coactivity to the longitudinal internal bundles (Aigner et al. 2004). Nevertheless, it seems to be sure that the function of the so-called pubovesical ligaments which receive a presumptive cholinergic innervation (Wilson et al. 1983) is not fixing the urethra to the pubic bone but maintaining its position relative to the bone during micturition (Gosling 1999). In contrast the contraction of the levator ani muscle and the external urethral sphincter leads to a narrowing of the preurethral space and to an ascending movement of the urethra as can be seen in dynamic MRI (Fielding et al. 1998; Sprenger et al. 2000).

Due to our results that in principle support the hammock hypothesis of DeLancey (DeLancey 1994), an operative "refixation" of the urethra and the bladder neck should result in an ascending dorsocranial traction (nerve-guiding plate), as well as a descending ventrocaudal traction (tendinous arch of the pelvic fascia). Though there are innovative ideas regarding the surgical reconstruction of the female urinary tract (Ulmsten 2001), most procedures are not performed according to the morphological needs, because they mostly consider only one part of the so-called fixation system.

3.2.4 Important Vessels, Nerves, and Lymphatics of the Anterior Compartment

- Inferior vesical artery
- Branches to the ureter
- Superior vesical artery
- Vesical lymph nodes
- Internal iliac lymph nodes
- Internal iliac artery
- Inferior hypogastric plexus
- Paravesical fat pad

(Veins have a corresponding course.)

3.3 Middle Compartment

3.3.1 Connective Tissue Structures

In macroscopic dissections of the adult female pelvis it is impossible to isolate ligaments fastening the cervix uteri or the vagina to the lateral pelvic wall and thus separating the middle compartment from the anterior or the posterior one laterally. In a refined macroscopic dissection performed with a binocular dissecting microscope it is possible—as well as in any other part of the pelvic subperitoneal tissue—to isolate connective tissue septa within the adipose tissue surrounding uterus and vagina (DeBlok 1982a, b). Our study of female fetal and adult pelvic sections reveals the true nature of the connective tissue structures surrounding uterus and vagina. The only connective tissue belonging to the middle compartment accompanies the vessels of uterus and vagina, thus running parallel to the lateral walls of these organs. In fetuses, the connective tissue is still loose, and without a differentiated structure, in the adult it mainly consists of adipose tissue with regular connective tissue septa (Fig. 12a–d) and it is continuous with the broad ligaments (see

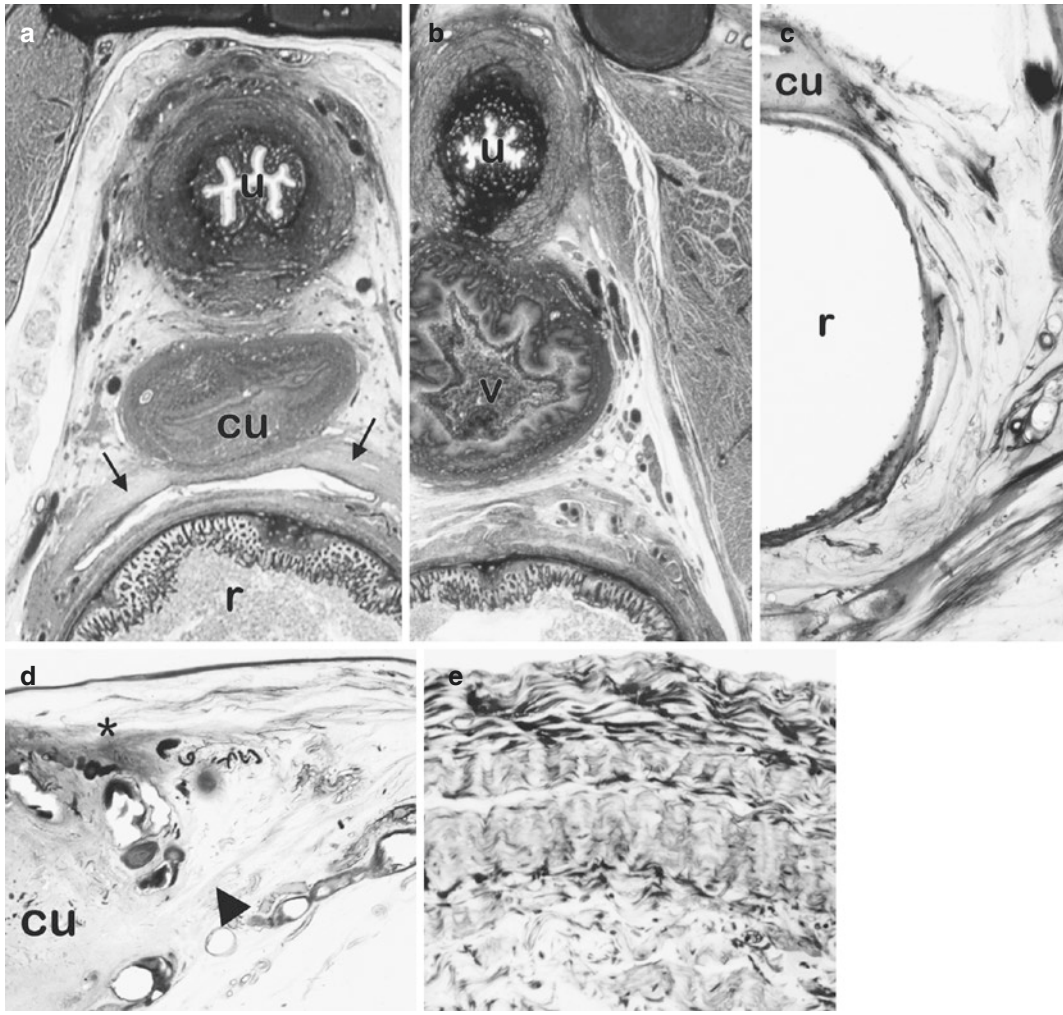

Fig. 12 Paracervical and paravaginal tissue. (**a**) Axial section (400 µm) of a 24-week-old female fetus at a level with the rectouterine pouch covered by dense connective tissue (*arrow*). ×8. (**b**) Axial section (400 µm) of the same fetus at a level with the vagina embedded in loose paravaginal tissue. Vagina and urethra are intimately connected. ×8. (**c**) Axial section (3 mm) of an adult female with the paracervical tissue. ×0.8. (**d**) Enlargement of an axial section (3 mm) of the same specimen with origin of the round ligament (*asterisk*) and the uterosacral ligament (*arrowhead*). ×3.5. (**e**) Enlargement of (**a**) with parallel oriented connective tissue fibers constituting the subperitoneal part of the uterosacral ligament. ×40. *u* urethra, *cu* cervix uteri, *r* rectum, *v* vagina

Table 1) laterally. The paracervical connective tissue abuts to the paravesical adipose tissue laterally and the paravaginal connective tissue abuts to the pelvic parietal fascia caudally (Fig. 12a, b). The broad ligaments themselves are part of the rectouterine and the vesicouterine folds (see Table 1) that tangentially cover the anterior and posterior uterine walls (Fritsch 1992). Apart from dense subperitoneal connective tissue that covers the rectouterine pouch (see Table 1) (Fig. 12e) and mainly consists of collagenous fibers, no supportive ligaments are found for the female fetal uterus. In the adult, this condensation of subperitoneal connective tissue has developed to the uterosacral ligaments (see Table 1). They are visible in the transparent sections as well as on MRI and form semicircular cords varying in thickness individually. They originate from the lateral margin of the cervix uteri and the vaginal vault and course dorsocranially where they are connected to

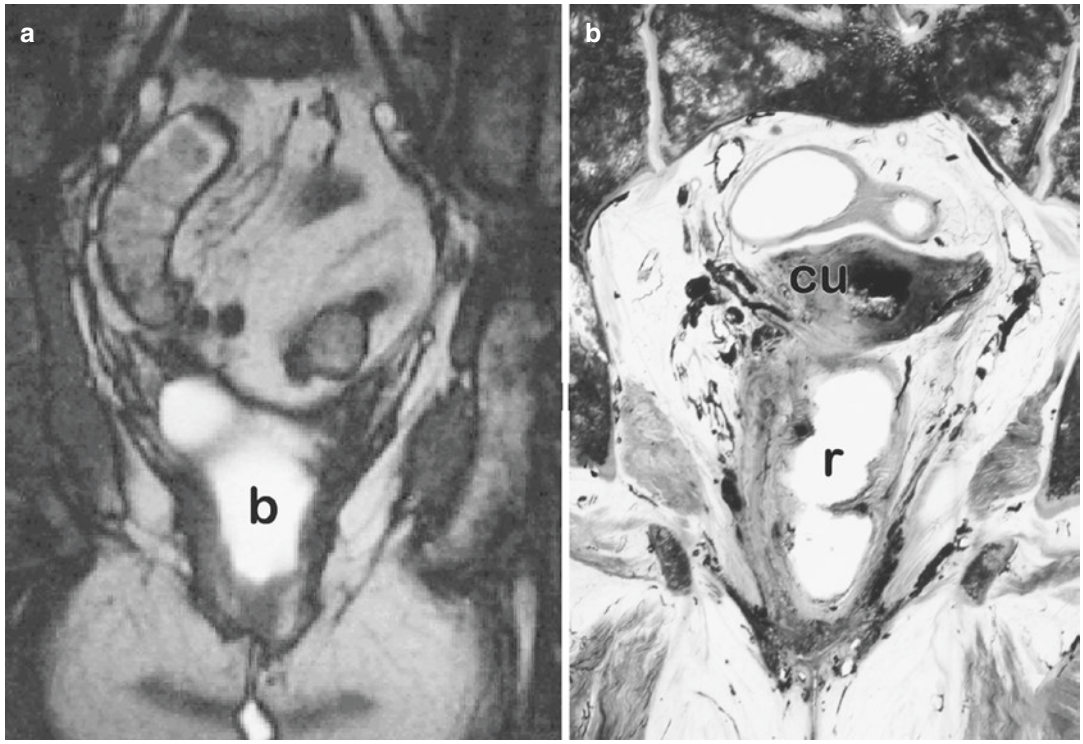

Fig. 13 Subperitoneal connective tissue and nerve vessel-guiding plate. (**a**) Coronal section (3 mm) of an adult female with pararectal and paracervical tissue. ×0.4. (**b**) Coronal MR image of an adult female with paravesical and paracervical tissue

the pelvic parietal fascia covering the sacrospinous ligaments and the sacrum. As they are part of the rectouterine ligaments they cover the perirectal tissue laterally. Our study undoubtedly confirmed the existence of the round ligaments as well as their course and their components. However, ligamentous structures constituting cardinal or transverse ligaments (see Table 1) (Kocks 1880; Mackenrodt 1895) that are to be supposed to fasten the cervix uteri and the vaginal vault with the lateral pelvic wall cannot be found in the adult pelvis. Our findings that have been taken from anatomic sections of elder specimens unrestrictedly correlate with the results of the MRI taken from young adult female pelves (Fig. 13).

Subperitoneally, the middle compartment and its organs abut the anterior compartment ventrally. This area is predominated by the dense connective tissue bridge intimately connecting the ventral vaginal wall with the dorsal urethral wall (Fig. 12b) (see also Sect. 3.2).

Dorsomedially, the middle compartment abuts the posterior compartment. The border between these compartments is demarcated by the rectovaginal fascia/septum (see also Sect. 3.1) that is composed of dense connective tissue, elastic fibers (Richardson 1993) and smooth muscle cells that belong to the longitudinal layer of the rectal wall.

The uterine tubes lie on each side of the uterus in the upper margin of the broad ligament (see Table 1; broad ligament). Each tube is attached on its inferior surface to a double fold of peritoneum called mesosalpinx (see Table 1). The lateral and superior part of the tube is the ampulla that opens into the funnel-shaped infundibulum with its fimbria at the abdominal orifice. The ovaries lie in the ovarian fossa, i.e., close to the lateral pelvic wall, and are suspended by a double fold of peritoneum, the mesovarium (see Table 1). The latter is attached to the broad ligament posteriorly. Behind the ovarian fossa are

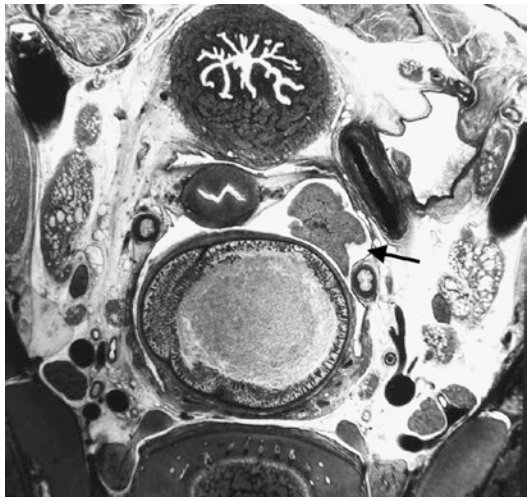

Fig. 14 Axial section (400 µm) of a 24-week-old female fetus at a level with the ovarian fossa (*arrow*). ×4

extraperitoneal structures, especially the ureter and the internal iliac vessels as well as the origin of the uterine artery (Fig. 14).

3.3.2 Muscles

The middle compartment does not have any specific striated muscles. The lateral vaginal wall comes in close contact to the puborectalis portion of the levator ani muscle. Both structures are always separated by the superior fascia of this muscle (Fig. 6b).

3.3.3 Reinterpreted Anatomy and Clinical Relevance

Though there are a lot of anatomical and clinical terms describing the tissue surrounding uterus and vagina, neither their definitions nor their origins are clear. The mesometrium (see Table 1) for example may be considered to be the largest part of the broad ligament extending from the pelvic floor to the uterine body enclosing the uterine artery or the connective tissue lying directly beneath the peritoneal covering of the uterus. As has been reemphasized by Höckel et al. (Höckel et al. 2005) the knowledge of the possible extent of local tumor spread is essential for the planning of surgery and radiotherapy, especially in the female pelvis. Like the posterior compartment with its mesorectum, the "mesometrium" (see Table 1) has been redefined and was identified to be the anatomical territory derived from common precursor tissues. Thus a new operation technique was proposed to operate carcinoma of the uterine cervix (stages IB–IIA). It is termed total mesometrial resection and is identified as the morphogenetic unit for the cervix and the proximal vagina including its neurovasculature.

Surgical techniques for the fixation of uterus and vagina are numerous. They all depend on the idea that there are sheath-like condensations within the pelvic cavity that are commonly called fascia. Moreover, these fasciae are thought to be responsible for acting as supportive structures to the uterus and vagina and thus they need to be reconstructed during operation. We think this point is one of the most critical to be discussed in this chapter.

Our reinterpreted anatomy of the connective tissue surrounding uterus and vagina is as follows:

- In accordance with former Anglo-American authors (Berglas and Rubin 1953; Koster 1933; Uhlenhuth and Nolley 1957) we do not find any visceral fascia covering uterus and vagina. Both organs are accompanied by adventitial connective tissue. The rectovaginal fascia/septum develops in situ (Ludwikowski et al. 2002) and is connected to the uterosacral ligaments, to the longitudinal muscular layer of the rectum, and to the perineum (see Sects. 3.1 and 4).
- As has been clearly summarized by Bastian and Lassau (Bastian and Lassau 1982) various ligaments are supposed to exist in the pelvis of the adult female. Our results show that—apart from the uterosacral and the round ligaments—no ligaments of the uterus can be found in conventional anatomical specimens, sections, or by MRI. We showed, however, that the paracervical and paravaginal region contains adipose tissue, numerous vessels, nerves, and connective tissue septa. All together these components may be confounded with a ligamentous structure, especially in the older female. The connective tissue septa have carefully been described by new morphological approaches (DeBlok 1982b; DeLancey 1996), but they have been over-interpreted as to their functional meaning.

There is no doubt that some of these connective tissue septa are connected to the fascia of the levator ani muscle and the contraction of this muscle is directly transferred to the septa and thus also to the vagina. But due to their morphological characteristics they are not supposed to act as supportive structures.

Our results are still in disagreement with the classical descriptions found in clinical and anatomical textbooks. We are aware of the fact that the variability of nomenclature is also misleading. But, nevertheless, the only fixation of the uterus is provided by the sacrouterine ligaments running in a dorsocranial direction. These ligaments are connected to the pelvic parietal fascia at a level with the sacrospinous ligaments, thus producing an upward traction for the whole uterovaginal complex.

There are various surgical procedures to reconstruct the so-called supportive ligaments in patients with genital prolapse. Due to our morphological data, it is useful to carry out a sacral fixation of the uterovaginal complex in terms of prolapse (Niemen and Heinonen 2001; Thakar and Stanton 2002), taking into account that the pudendal vessels and the pudendal nerve are not injured during operation (Occelli et al. 2001). New techniques include meshes that are suggested to support all female pelvic organs (Berrocal et al. 2004). The results of these techniques seem to open the field of female hernia surgery.

3.3.4 Important Vessels, Nerves, and Lymphatics of the Middle Compartment

- Uterine artery
- Inferior hypogastric plexus (veins have a corresponding course)

4 Perineal Body

4.1 Connective Tissue Structures and Muscles in the Female

The perineal body separates the urogenital and anal hiatus. It is situated between rectum and vagina, i.e., between the posterior and middle compartments. Within the region of the perineal body the skin is firmly attached to the underlying connective tissue. The perineal body consists of dense connective tissue. It does not possess its own musculature, but it serves muscles of the perineal region to originate or to attach (Fig. 15a). Whereas the external anal sphincter is attached to it dorsally (Fig. 15a), the muscles of the cavernous tissue are attached ventrally (Fig. 15b). A deep transverse perineal muscle that may be attached ventrally does not exist in the female (Oelrich 1983). As has already been pointed out above (see Sect. 3.1) the additional smooth rectal muscle bundles that are situated in the rectovaginal fascia/septum are integrated and attached to the connective tissue of the perineal body (Fig. 15c). As the region of the female's perineal body is of high clinical interest in terms of damage during childbirth and/or episiotomies (Woodmann and Graney 2002), again it is described according to the gynecologist's point of view, i.e., from outside (inferior) to the inside (superior): At a level below the orifice of the vagina the external anal sphincter is attached to the perineal body (Fig. 15a), whereas at a level with the orifice of the vagina and above the internal sphincter abuts the perineal body and thus indirectly the dorsal wall of the vagina (Fig. 15b). At these levels the external sphincter embraces the anal canal, the perineal body, and the dorsal wall of the vagina laterally.

The intralevatoric side of the perineal body is connected with connective tissue septa of the ischioanal fossa (DeBlok and DeJong 1980) that are also connected to the inferior fascia of the levator ani muscle (Janssen et al. 2001).

4.2 Reinterpreted Anatomy and Clinical Relevance

A detailed knowledge of the anatomy of the perineal body has become of interest since transperineal or even dynamic transperineal ultrasound (Beer-Gabel et al. 2002) has been carried out. With the help of these techniques, the infralevatoric viscera, the soft tissues, and the puborectalis can be viewed and defined.

For a long time there has been no doubt about the existence of the fibrous components of this

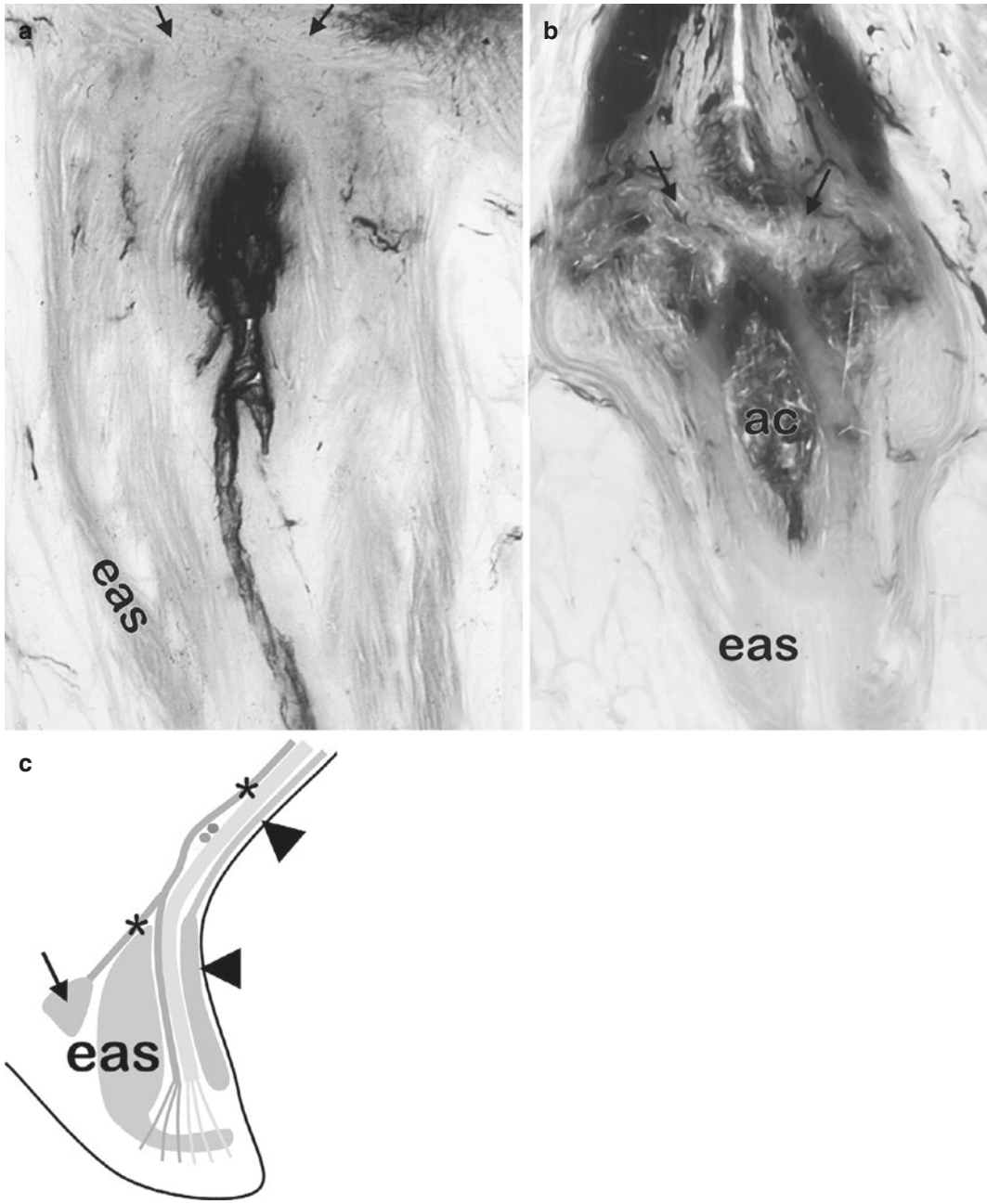

Fig. 15 Perineal body (*arrows*) and attached muscles. (**a**) Axial section (5 mm) of an adult female at a level with the anal cleft. ×2.2. (**b**) Axial section of the same specimen (**a**) at a level with the vaginal hiatus. ×1.2. (**c**) The sagittal plane pointing out the ventral anorectal wall (*arrowheads*) and the different muscle layers including the longitudinal muscle cells (*asterisks*). *eas*, external anal sphincter

region. However, defined in the actual *Terminologia Anatomica* (Federative Committee on Anatomical Terminology 1998), the perineal body should be a fibromuscular rather than a tendinous structure. We categorically disagree with this opinion. The perineal body itself is a fibrous structure, but it is intermingled with all originating and inserting muscles. It has to be considered as a tendinous center for all the muscles that do not have a bony origin or attachment. There is no

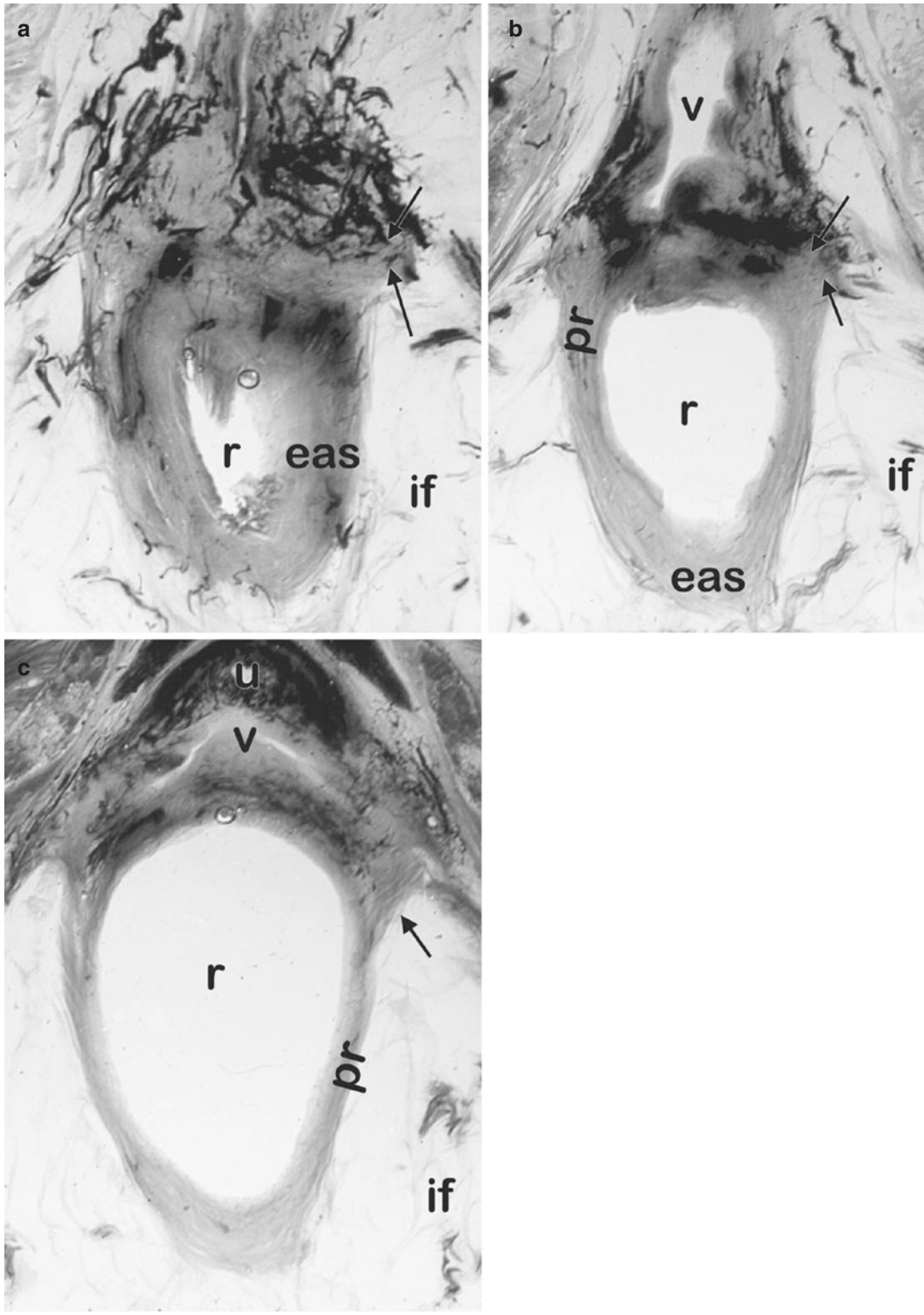

Fig. 16 Scar (*arrows*) of an old perineal rupture in axial sections (4 mm) of an adult female. (**a**) At a level with the perineum. ×0.8. (**b**) At a level with the fusion of external anal sphincter and puborectalis muscle. ×0. (**c**) At a level with the rectal ampulla. ×0.8. *r* rectum, *eas* external anal sphincter, *if* ischioanal fossa, *pr* puborectalis muscle, *v* vagina

doubt that it is an important region for absorbing part of the intrapelvic (intra-abdominal) pressure. A stretched or even destroyed perineal body may be the cause for urogenital or rectal prolapse (Zbar et al. 2003).

From a morphological as well as a functional point of view there is need for discussion as to how and whether a surgical approach through an intact perineal body should be performed.

The discussion of pelvic floor damage during vaginal delivery and/or after episiotomies has been kindled through the remarkable statistics of Sultan et al. (Sultan et al. 1993), who showed that episiotomies do not prevent tearing. We think that the indication for episiotomies should clearly be defined by an international committee and it should be restricted to special cases. Perineal damage may occur not only spontaneously but also iatrogenically through the execution of an episiotomy. It is not at all "old-fashioned" to protect the perineum during vaginal delivery by hands-on methods.

We recommend not carrying out median and lateral episiotomies and being careful with mediolateral ones: As can be seen from a pathological specimen in Fig. 16, a perineal tear and/or a lateral episiotomy has led to a scar of the perineal body and the external anal sphincter. The connective tissue septa of the ischioanal fossa are irregular (Fig. 16a). At the border between the infralevatoric and levatoric level, it becomes visible that the vaginal wall is slightly displaced, the puborectalis is rather thin, and the ischioanal fossa is not symmetric with the contralateral side (Fig. 16b), a diagnosis that still remains on supralevatoric levels (Fig. 16c). Refined and functional surgical treatment of perineal tears seems to be necessary to avoid such situations. As modern imaging techniques allow a fast and reliable examination, it is the gynecologists' task to improve the surgical treatment.

References

Aigner F, Zbar AP, Kovacs P, Ludwikowski B, Kreczy A, Fritsch H (2004) The rectogenital septum: morphology, function and clinical relevance. Dis Colon Rectum 47:131–140

Bastian D, Lassau JP (1982) The suspensory mechanism of the uterus. Surg Radiol Anat 4:147–160

Beer-Gabel M, Teshler M, Barzilai N, Lurie Y, Malnick S, Bass D, Zbar A (2002) Dynamic transperineal ultrasound in the diagnosis of pelvic floor disorders. Dis Colon Rectum 45:239–248

Beets-Tan RGH, Beets GL, Vliegen RFA, Kessels AGH, Van Boven H, De Bruine A, von Meyenfeldt MF, CGMI B, van Engelshoven JMA (2001) Accuracy of magnetic resonance imaging in prediction of tumour-free resection margin in rectal cancer surgery. Lancet 357:497–505

Berglas B, Rubin IC (1953) Histologic study of the pelvic connective tissue. Surg Gynecol Obstet 97:277–289

Berrocal J, Clave H, Cosson M, Dedodinance P, Garbin O, Jacquetin B, Rosenthal C, Salet-Lizee D, Villet R (2004) Conceptual advances in the surgical management of genital prolapse. J Gynecol Obstet Biol Reprod 33:577–587

Brown G, Radcliffe AG, Newcombe RG, Dallimore NS, Bourne MW, Williams GT (2003) Preoperative assessment of prognostic factors in rectal cancer using high resolution magnetic resonance imaging. Br J Surg 90:355–364

Cundiff GW, Weidner AC, Visco AG, Addison A, Bump RC (1998) An anatomic and functional assessment of the discrete defect rectocele repair. Am J Obstet Gynecol 179:1451–1457

DeBlok S (1982a) The connective tissue of the female fetal pelvic region. Acta Morphol Neerl Scand 20:65–92

DeBlok S (1982b) The connective tissue of the adult female pelvic region. Acta Morphol Neerl Scand 20:325–346

DeBlok S, DeJong E (1980) The fibrous tissue architecture of the female perineal region. Acta Morphol Neerl Scand 18:181–194

DeLancey JO (1994) Structural support of the urethra as it relates to stress urinary incontinence: the hammock hypothesis. Am J Obstet Gynecol 170:1713–1723

DeLancey JO (1996) Standing anatomy of the pelvic floor. J Pelvic Surg 2:260–263

Dorschner W, Stolzenburg JV, Neuhaus J (2001) Structure and function of the bladder neck. Adv Anat Embryol Cell Biol 159:III–XII. 1–109

Federative Committee on Anatomical Terminology (1998) Terminologia anatomica: international anatomical terminology. Georg Thieme Verlag, Stuttgart

Fielding JR, Griffiths DJ, Versi E, Mulkern RV, Lee ML, Jolesz FA (1998) MR imaging of pelvic floor continence mechanisms in the supine and sitting positions. Am J Roentgenol 171:1607–1610

Fritsch H (1990) Development of the rectal fascia. Anat Anz 170:273–280

Fritsch H (1992) The connective tissue sheath of uterus and vagina in the human female fetus. Ann Anat 174:261–266

Fritsch H (1994) Topography and subdivision of the pelvic connective tissue. Surg Radiol Anat 16:259–265

Fritsch H, Fröhlich B (1994) Development of the levator ani muscle in human fetuses. Early Hum Dev 37:15–25

Fritsch H, Kühnel W (1992) Development and distribution of adipose tissue in the pelvis. Early Hum Dev 28:79–88

Fritsch H, Kühnel W, Stelzner F (1996) Entwicklung und klinische Anatomie der Adventitia recti. Langenbecks Arch Chir 381:237–243

Fritsch H, Brenner E, Lienemann A, Ludwikowski B (2002) Anal sphincter complex. Dis Colon Rectum 45:188–194

Fritsch H, Lienemann A, Brenner E, Ludwikowski B (2004) Clinical anatomy of the pelvic floor. Adv Anat Embryol Cell Biol 175:1–64

Gasparri F, Brizzi E (1961) Significato anatomo-chirurgico delle formazioni connecttivali del piccolo bacino. Arch Ital Anat Embriol 66:151–169

Gosling J (1999) Gross anatomy of the lower urinary tract. In: Abrams P, Khoury S, Wein AJ (eds) Incontinence. Plymbridge, Plymouth, pp 21–56

Grabbe E, Lierse W, Winkler R (1982) Die Hüllfascien des Rektums. Fortsch Röntgenstr 136:653–659

Heald RJ (1995) Total mesorectal excision is optimal surgery for rectal cancer. Br J Surg 82:1297–1299

Höckel M, Horn L-C, Fritsch H (2005) Association between the mesenchymal compartment of uterovaginal organogenesis and local tumour spread in stage IB–IIB cervical carcinoma: a prospective study. Lancet Oncol 6:751–756

Janssen U, Lienemann A, Fritsch H (2001) Die Bedeutung des M. levator ani – Fossa ischioanalis-Glutaeus maximus (LFG) – Komplexes für den weiblichen Beckenboden. Ann Anat Suppl 183:11

Khubchandani IT, Sheets JA, Stasik JJ, Hakki AR (1983) Endorectal repair of rectocele. Dis Colon Rectum 26:792–796

Kocks J (1880) Normale und pathologische Lage und Gestalt des Uterus sowie deren Mechanik. Cohen, Bonn, pp 1–60

Koster H (1933) On the supports of the uterus. Am J Obstet Gynecol 25:67–74

Kux M, Fritsch H (2000) On the extraperitoneal origin of hernia. Hernia 4:259–263

Lierse W (1984) Becken. In: von Lanz T, Wachsmuth W (eds) Praktische Anatomie, Bd 2, Teil 8A. Springer, Berlin

Ludwikowski B, Oesch-Hayward I, Brenner E, Fritsch H (2001) The development of the external urethral sphincter in humans. BJU Int 87:565–568

Ludwikowski B, Oesch-Hayward I, Fritsch H (2002) Rectovaginal fascia: an important structure in pelvic visceral surgery? About its development, structure, and function. J Pediatr Surg 37:634–638

Mackenrodt A (1895) Ueber die Ursachen der normalen und pathologischen Lage des Uterus. Arch Gynaekol 48:393–421

Niemen K, Heinonen PK (2001) Sacrospinous ligament fixation for massive genital prolapse in women aged over 80 years. BJOG 108:817–821

Nobis A (1988) Untersuchungen zur feineren Struktur des retrorektalen Raumes beim Menschen. Inaugural Dissertation, Bonn

Occelli B, Narducci F, Hautefeuille J, Francke JP, Querleu D, Crepin G, Cosson M (2001) Anatomic study of arcus tendineus fasciae pelvis. Eur J Obstet Gynecol Reprod Biol 97:213–219

Oelrich TM (1983) The striated urogenital sphincter in the female. Anat Rec 205:223–232

Pernkopf E (1941) Topographische Anatomie des Menschen. Urban & Schwarzenberg, Berlin; Bd 2, Teil 1: Bd 2, Teil 2

Richardson AC (1993) The rectovaginal septum revisited: its relationship to rectocele and its importance in rectocele repair. Clin Obstet Ggynecol 36:976–983

Richter K (1998) Gynäkologische Chirurgie des Beckenbodens. In: Heinz F, Terruhn V (eds) Georg Thieme Verlag, Stuttgart

Richter K, Frick H (1985) Die Anatomie der Fascia pelvic visceralis aus didaktischer Sicht. Geburtsh Frauenheilk 45:282–287

Sprenger D, Lienemann A, Anthuber C, Reiser M (2000) Funktionelle MRT des Beckenbodens: normale anatomische und pathologische Befunde. Radiologe 40:458–464

Stelzner F (1989) Die Begründung, die Technik und die Ergebnisse der knappen transabdominalen Kontinenzresektion. Langenbecks Arch Chir 374:303–314

Stelzner F (1998) Chirurgie an vizeralen Abschlusssystemen. Georg Thieme, Stuttgart

Sultan AH, Kamm MA, Hudson CN, Thomas JM, Bartram CI (1993) Anal sphincter disruption during vaginal delivery. N Engl J Med 329:1905–1911

Thakar R, Stanton S (2002) Management of genital prolapse. BMJ 324:1258–1262

Tobin CE, Benjamin JA (1945) Anatomical and surgical study of Denonvilliers fascia. Surg Gynecol Obstet 80:373

Uhlenhuth E, Nolley GW (1957) Vaginal fascia, a myth? Obstet Gynecol 10:349–358

Ulmsten U (2001) The basic understanding and clinical results of tension-free vaginal tape for stress urinary incontinence. Urologe 40:269–273

Waldeyer W (1899) Das Becken. Cohen, Bonn

WEW R, Tucker WG (1986) Thickening of the pelvic fascia in carcinoma of the rectum. Dis Colon Rectum 29:117–119

Wilson PD, Dixon JS, ADG B, Gosling JA (1983) Posterior pubo-urethral ligaments in normal and genuine stress incontinent women. J Urol 130:802–805

Woodmann PJ, Graney DO (2002) Anatomy and physiology of the female perineal body with relevance to obstetrical injury and repair. Clin Anat 15:321–334

Zbar AP, Lienemann A, Fritsch H, Beer-Gabel M, Pescatori M (2003) Rectocele: pathogenesis and surgical management. Int J Color Dis 29:1–11

MR and CT Techniques

João Lopes Dias and Teresa Margarida Cunha

Contents

Abstract

Magnetic resonance imaging (MRI) and computed tomography (CT) are routinely used in female pelvis imaging. MRI is primarily useful for locoregional characterization of benign and malignant diseases. CT is less accurate in locoregional evaluation, but remains useful in the follow-up of treated gynecological malignancies, as well as in the setting of emergency and in the guidance of biopsies. Although transabdominal and transvaginal ultrasonography (US) is not under the scope of this chapter, it remains the first-line imaging method for most gynecological conditions.

1 Introduction

Magnetic resonance imaging (MRI) and computed tomography (CT) are routinely used in female pelvis imaging. MRI has a higher soft-tissue contrast and allows an accurate anatomic characterization of the pelvis as a whole, and a detailed depiction of the zonal anatomy. Thus, it is primarily useful for locoregional characterization of benign and malignant diseases. CT is less accurate in locoregional evaluation, but remains useful in the follow-up of treated gynecological malignancies, as well as in the setting of emergency (assessment of postsurgical complications and

J. Lopes Dias (✉)
Centro Hospitalar de Lisboa Central, Lisbon, Portugal

Hospital Lusíadas de Lisboa, Lisbon, Portugal

New Medical School, Lisbon, Portugal
e-mail: joaolopesdias85@gmail.com

T.M. Cunha
Instituto Português de Oncologia de Lisboa Francisco Gentil, Lisbon, Portugal
e-mail: tmargarida@gmail.com

Med Radiol Diagn Imaging (2017)
DOI 10.1007/174_2017_51, © Springer International Publishing AG
Published Online: 03 May 2017

pelvic infectious diseases) and in the guidance of biopsies. Although transabdominal and transvaginal ultrasonography (US) is not under the scope of this chapter, it remains the first-line imaging method for most gynecological conditions.

This chapter aims to focus on some important, hands-on topics regarding MRI and CT techniques, trying not to exhaustively develop issues with isolated historical interest.

2 Magnetic Resonance Imaging

2.1 Introduction

The introduction of modern phased-array coils with eight or more elements led to high signal-to-noise ratios (SNR) and consequently increased image quality. Additionally, pelvic examinations have become faster as turbo (TSE) and fast spin-echo (FSE) sequences have replaced conventional spin-echo (SE) sequences. Most MRI examinations are now performed at 1.5 and 3 Tesla (T) magnets. Despite significant improvement on SNR with higher field strength, 3 T magnets are more prone to magnetic susceptibility artifacts, which may be particularly prominent on diffusion-weighted imaging (DWI).

2.2 Patient Preparation and Positioning

Before performing an MR exam, the patient should be informed about its approximate duration as well as the necessity to use earplugs to protect against loud noises and to place a surface coil close to the skin. Moreover, all patients should be asked about contraindications and claustrophobia. Sedation may be required for those patients who would really benefit from the examination, but are unable to proceed due to claustrophobia. Any implanted device must be previously known and considered to be safe for the patient undergoing an MR procedure. Intrauterine devices (IUD) can be normally scanned, and usually appear as a hypointense linear structure within the endometrial cavity on both T2-weighted images (T2WI).

Finally, patients should also be informed about the utility of intravenous (IV) contrast and spasmolytic agent administration, as well as their side effects (see next sections).

Whenever a pregnant woman is undergoing an MR exam, issues about the fetus development are raised. As a general rule, the risk-benefit ratio should be evaluated for every patient. Fetal deleterious effects have not been documented on 1.5 T magnets. However, some experts still recommend avoiding the exam in the first trimester unless the potential benefits compensate the hypothetical risks. Since most of the studies were performed on 1.5 T scanners, far less is known about potential effects on 3 T (Masselli et al. 2013; Ray et al. 2016).

Some authors advocate that patients should void about 1 h before the examination to ensure that the bladder is only moderately filled. A full bladder may hamper T2WI and give rise to motion artifacts due to patient discomfort.

A 4-h fast helps to reduce bowel peristalsis and is recommended in some centers when intravenous contrast administration is required. The administration of a fast-acting laxative enema to clean the bowel may also improve image quality.

It is uncommon to perform bowel preparation with diluted barium sulfate or other solutions as it increases preparation and imaging time and does not seem to bring significant advantages.

Vaginal tampon should be avoided. Vaginal opacification with ultrasound gel makes the evaluation of vaginal walls easy and may be recommended when studying vagina tumors and deep endometriosis. Moreover, rectal and/or vaginal opacification with ultrasound gel may be useful in dynamic pelvic floor and deep endometriosis studies (Beddy et al. 2012; Sala et al. 2013; Bazot et al. 2016).

Female pelvis imaging is usually performed with patients in supine position with the arms placed by their side. The placement of a bolster

under the knees makes the examination more comfortable. Two important procedures are generally taken in order to decrease motion artifacts during abdominal and pelvic examinations: the use of a belt covering phased-array body coils, which restricts respiratory excursions, and the application of a spatial presaturation slab in a sagittal scout view, which is particularly useful in sequences without breathhold, because of its ability to reduce artifacts from the movement of the anterior abdominal wall (Sala et al. 2013; Forstner et al. 2016; Froehlich et al. 2009).

2.2.1 Spasmolytic Medication

The administration of antispasmodic agents such as scopolamine *N*-butyl bromide (Buscopan®) or glucagon is indicated to reduce artifacts from small bowel and bladder motion. It is particularly useful in the assessment of peritoneal implants on both morphological and functional sequences, especially on DWI. The administration of intravenous Buscopan® (20–40 mg) immediately before the examination is the most consensual option. Longer examinations may justify a second identical dose, because IV Buscopan® action only lasts about 15 min. Intramuscular (IM) administration (20 mg) has an increased length of action (approximately 30–60 min). This anticholinergic drug should not be administered in patients who have demonstrated prior hypersensitivity to scopolamine *N*-butyl bromide, as well as in those with myasthenia gravis, narrow-angle glaucoma, megacolon, tachycardia, prostatic enlargement with urinary retention, paralytic ileus, or mechanical stenosis in the gastrointestinal tract. Data regarding contraindications during pregnancy is scarce; therefore Buscopan® is not recommended. Common undesirable effects may be accommodation disorders, tachycardia, dizziness, or dry mouth. If accommodation changes occur, patients should be advised not to drive.

When Buscopan® is contraindicated, glucagon (1 mg) can be administrated intravenously (Beddy et al. 2012; Sala et al. 2013; Bazot et al. 2016). In a study of Froehlich et al., glucagon had more reliable onset of action and induced longer bowel paralysis when compared to scopolamine *N*-butyl bromide. Glucagon is contraindicated in patients with known hypersensitivity to the substance, as well as in those with known pheochromocytoma (due to the risk of stimulating catecholamine release). In patients with a known insulinoma, glucagon should be administered cautiously since its initial hyperglycemic effect may stimulate the release of insulin and cause subsequent hypoglycemia (Froehlich et al. 2009).

2.3 Coils, Scan Planes, and General Protocols

Female pelvic MRI is generally performed with a phased-array body coil with at least four elements. The introduction of modern coils improved SNR and allowed parallel imaging, thus reducing scan time on T1W and T2W conventional sequences. Intracavitary coils, either endovaginal or endorectal, have no current scientific support (Sala et al. 2013; Allen et al. 2014).

A general female pelvis protocol usually begins with a coronal localizer, which provides an anatomic overview of both lower abdomen and pelvis. It is helpful not only to guide pelvic sequences but also to exclude other conditions like hydronephrosis or renal malformations. Fast sequences like single-shot turbo or fast spin echo are generally used.

Specific protocols depend on the study target, but usually include an axial T1WI sequence and at least two T2WI sequences in different planes (Fig. 1). Dynamic contrast-enhanced magnetic resonance imaging (DCE-MRI) and DWI have become part of the standard imaging protocols for most of female pelvis MR examinations (Forstner et al. 2010, 2016; Allen et al. 2014; Sala et al. 2011).

Table 1 resumes a suitable general protocol for gynecological MRI. Specific parameters should always be adapted according to the magnet and coils available in each center.

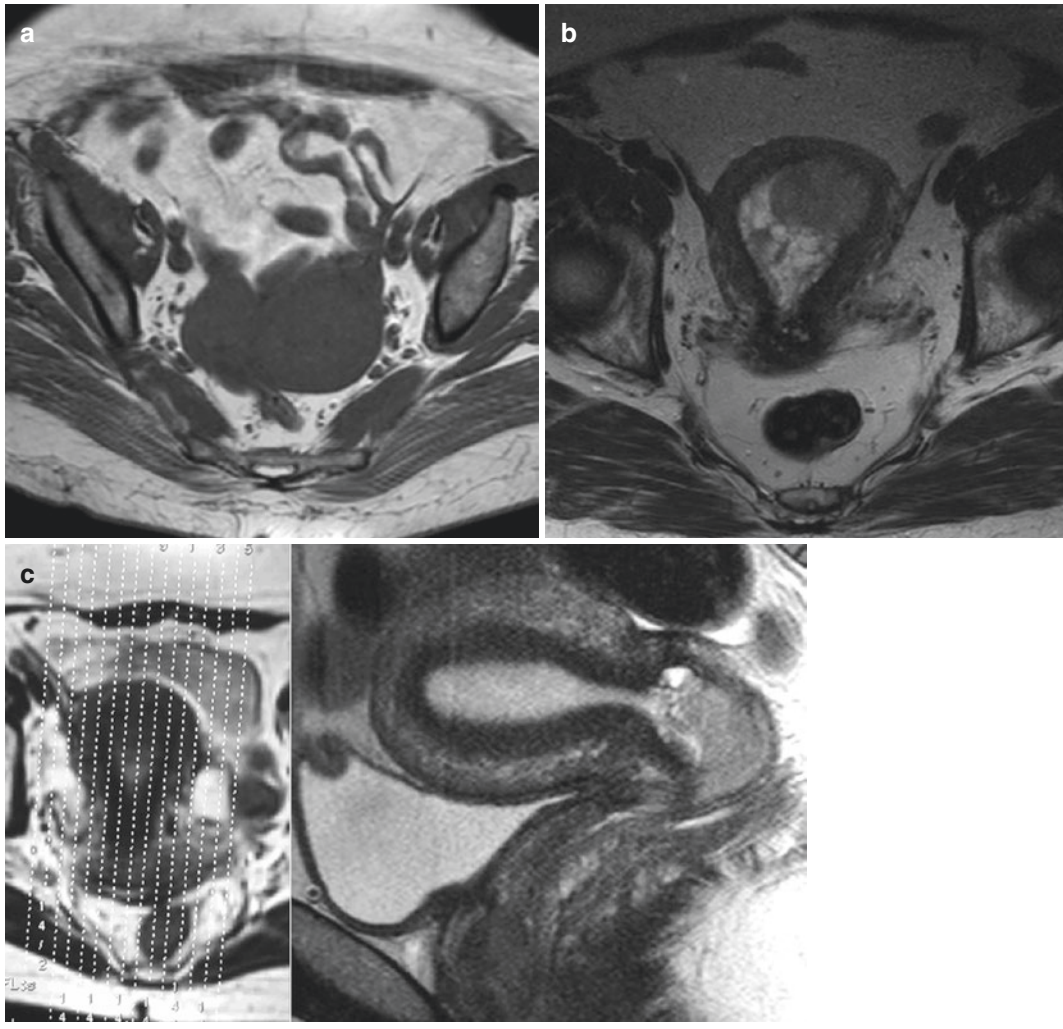

Fig. 1 Examples of different orientations on MRI in distinct patients. Axial T1W image of the pelvis (**a**). Axial T2W image through the pelvis showing the uterus with an endometrial carcinoma associated with a polyp (**b**). Oblique sagittal according to the uterine axis T2W image showing the normal uterine zonal anatomy and a cervical cancer (**c**). Oblique coronal according to the long axis of the uterus, parallel to the endometrial cavity (**d**). Axial oblique T2W image, perpendicular to the long axis of the cervix, for evaluation of parametrial invasion while staging a cervical cancer (**e**). Axial oblique TIW images after gadolinium with fat saturation, perpendicular to the long axis of the uterus, for local staging of an endometrial cancer (**f**)

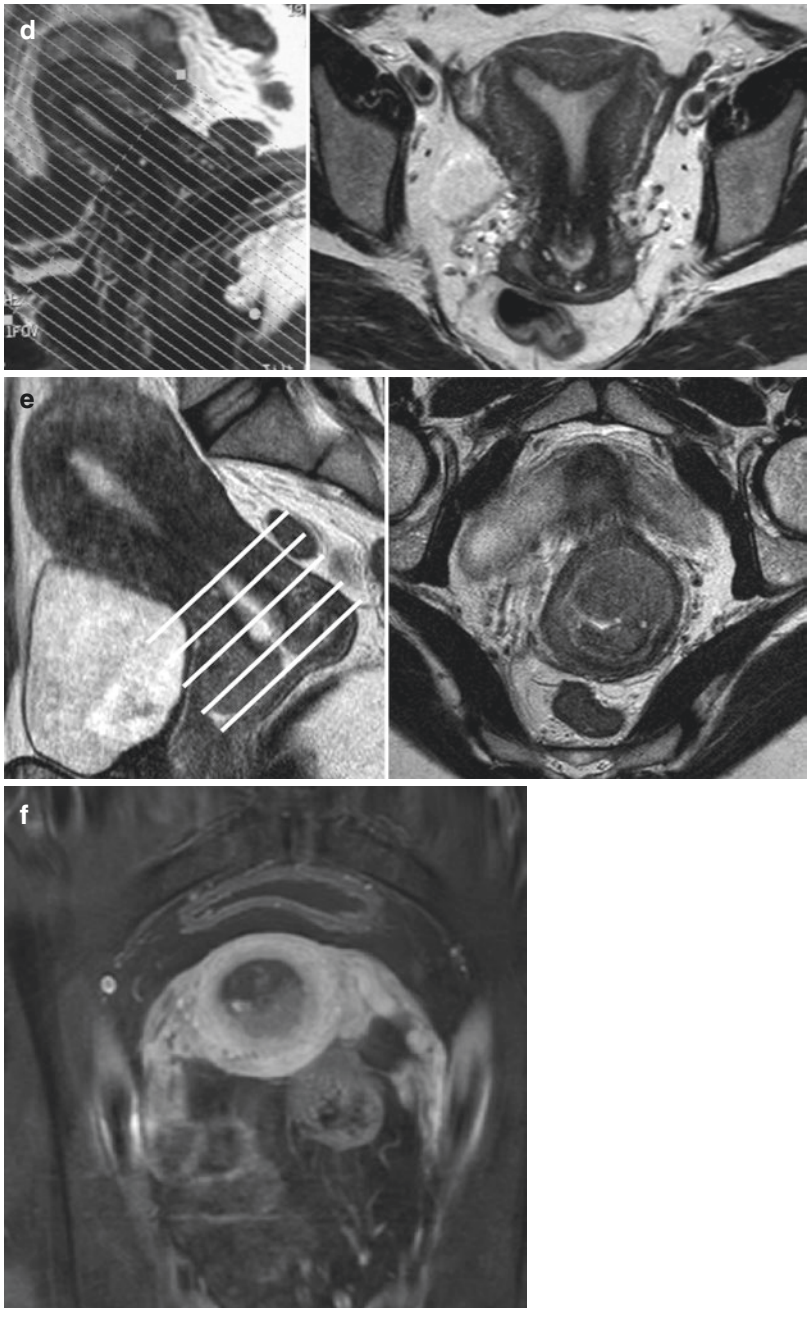

Fig. 1 (continued)

Table 1 Suitable general protocol for gynecological MRI at a 1.5 T magnet

• 4–6 h of fasting • Voiding and ingestion of two glasses of water 1 to 2 h before the exam • Avoid the use of vaginal tampon • Vaginal opacification with ultrasound gel – May be useful for vaginal tumors and deep endometriosis • Rectal and/or vaginal opacification with ultrasound gel – May be useful for dynamic pelvic floor studies and deep endometriosis • Administration of a fast-acting laxative enema to clean the bowel, one on the day before the exam and another during the morning of the exam (optional)
• Supine position • Pelvic phased-array coils with at least four elements • Belt covering phased-array body coils • Anterior and superior saturation band • Antispasmodic agents: – Buscopan 20/40 mg IM/IV – Glucagon 1 mg IV
• Matrix: 512 × 512 • Coronal localizer: single-shot turbo or fast spin-echo • Morphological sequences: axial T1WI and at least two different planes on T2WI (or single 3D T2WI with posterior multiplanar post processing) • DWI: field-of-view and thickness equal to T2WI (preferentially axial) – Pelvis (b values: 0, 600 and 1000 s/mm^2) – Abdomen (b values: 0, 500 and 1000 s/mm^2) – High b values may reach 1200–1400 s/mm^2 • DCE-MRI: 2D or 3D fat-suppressed T1W GRE sequence – Scan plane, region of interest, and acquisition timing depending on the specific target of the study – Gadolinium standard dose: 0.1 mmol Gd/kg body weigh

2.3.1 T1- and T2-Weighted Imaging

Typical SE T1WI is usually performed to assess spontaneous hyperintense content that may correspond to fat or blood. Axial fat-saturated T1WI in the same plane and with the same thickness should be performed for their distinction. Some centers perform T1W in- and opposed-phase images, which allow the detection of intravoxel lipid within masses (manifesting as a signal loss on the opposed-phase images). If a short scan time is needed, gradient-echo (GRE) sequences may be applied; however anatomic detail will be decreased. Fat saturation may also be achieved by the Dixon method, a chemical shift-based technique that acquires both in- and opposed-phase images simultaneously, thus allowing mathematical combinations into fat-only and water-only sequences. It results in a more uniform suppression of the fat signal, and allows the detection and quantification of microscopic lipid (Allen et al. 2014).

Multiplanar high-resolution nonfat-saturated T2W sequences are the most relevant for the majority of female pelvic diseases, because of their ability to depict uterine and ovarian zonal anatomy and to provide good contrast between normal and pathological tissues. TSE or FSE sequences are typically used. A single 3D T2W sequence with later multiplanar postprocessing can alternatively be performed. Single-shot TSE sequences during breath-hold (HASTE) may be useful in the coronal plane to exclude hydronephrosis or to assess renal malformations.

Fat-suppressed T2W sequences are not routinely used for female pelvic imaging. However, they may be helpful to identify intraperitoneal, extraperitoneal, and endoluminal fluid; enlarged lymph nodes; and bone changes (for example, in the setting of bone metastases or of edematous changes due to postradiotherapy insufficiency fractures). When compared to nonfat-suppressed T2WI, it also helps to assess for macroscopic lipid content (Allen et al. 2014).

2.3.2 Diffusion-Weighted Imaging

DWI is a functional MR technique that assesses the random movement or the Brownian motion of water molecules in different physical media. The diffusion properties of a biological tissue are related to the amount of interstitial free water and permeability, therefore reflecting tissue cellularity and presence of intact cellular membranes. In general, high-cellularity tumors show restricted diffusion when compared to normal tissue, because of their higher cellular density. Coagulative necrosis, highly viscous fluid, and

abscesses may behave similarly. DWI is performed using two or more *b* values (a measure of the gradient strength), including one or more low *b* values (0 or 50 s/mm^2) and a high *b* value (1000 s/mm^2 or higher). Apparent diffusion coefficients (ADC) are mathematical transformations of *b* value acquisitions that represent the slope of the line of the natural logarithm of signal intensity (*y*-axis) versus *b* values (*x*-axis). ADC maps are displayed parametrically as grayscale images. Suspicious areas with true water molecule movement restriction appear bright at high *b* values and dark on the ADC map. High *b* value sequences and the ADC map should always be interpreted together with morphological sequences to avoid potential pitfalls. In order to facilitate this evaluation, fusion images between T2WI and DWI may be generated. However, they can be altered by patient motion and bladder distention during the examination, which may change the relative position of pelvic organs.

Whole-body diffusion-weighted MRI protocols have been developed over the last years, mainly for cancer staging and follow-up. Short-time examinations are now possible on both 1.5- and 3-T magnets due to the evolution of echo-planar and parallel imaging, generation of high-performance gradients, and introduction of phased-array multichannel surface coils. Advantages include absence of ionizing radiation and no injection of isotopes or intravenous contrast media (Sala et al. 2013; Whittaker et al. 2009; Hameeduddin and Sahdev 2015; Qayyum 2009).

2.3.3 Dynamic Contrast Enhancement

Gadolinium-based contrast agents act by shortening T1 relaxation time, which is better seen on T1WI. Thus, dynamic contrast-enhanced MRI (DCE-MRI) is usually performed using a 2D or 3D fat-suppressed T1W GRE sequence. 3D sequences like volumetric interpolated breath-hold examination (VIBE) allow the acquisition of thinner slices. The injection should be preferentially performed using an MR-compatible automatic injector, but manual administration may also be performed. Serial image acquisitions are then performed every few seconds over a length of a few minutes. The protocol—including scan plane, region of interest, and acquisition time—will depend on the specific target of the study (see appropriate chapters). Qualitative, semi-quantitative, and quantitative analysis may be performed. The enhancement of a given structure may be directly and qualitatively accessed as an area of increased signal intensity (SI) on T1WI. Semiquantitative analysis implies recording the SI of a region of interest before and after contrast administration in order to get dynamic time-signal intensity (TSI) curves, which enable the extraction of some data like time to onset of enhancement, relative signal intensity, maximum postcontrast SI-to-precontrast SI ratio, rate of enhancement, and area under the curve (overall enhancement). Quantitative analysis—namely Ktrans (volume transfer constant between the plasma and the extracellular extravascular space)—remains under study and is not currently available in many centers (Beddy et al. 2012; Hameeduddin and Sahdev 2015; Bernardin et al. 2012).

Initial unenhanced imaging is helpful to detect hyperintense hemorrhagic or proteinaceous content, and also allows performing subtraction imaging, which requires cautious breath-holding instructions to guarantee similar registration between unenhanced and contrast-enhanced images. Regardless of those instructions, some artifacts may be found due to bladder filling during the examination.

2.4 Gadolinium-Based Contrast Media

A standard dose of 0.1 mmol/kg body weight of gadolinium is typically administered. For MR angiography, it may be increased to 0.2 mmol/kg body weight. The risk of nephrotoxicity is very low when gadolinium-based contrast media are used in approved doses (Beckett et al. 2015).

The risk of an acute reaction to a gadolinium-based contrast agent is low when compared to iodine-based contrast agents. However, similar cautions should be taken. Risk patients are those with a history of previous acute reaction to gadolinium-based contrast agent, asthma, and allergy requiring medical treatment. Unlike iodine-based contrast agents, the risk of reaction to gadolinium-based contrast agents is not related to osmolality (Beckett et al. 2015).

Nephrogenic systemic fibrosis (NSF) is recognized as a very late reaction to gadolinium-based contrast media since 2006. It usually starts with pain, pruritus, swelling, and erythema in the legs, and progresses to thickening of the skin and subcutaneous tissues, as well as to fibrosis of internal organs and respiratory muscles, which may lead to variable consequences ranging from contractures to cachexia and death. The severity of the disease implies the prompt recognition of high-risk patients, which are those with chronic kidney disease (CKD) 4 and 5 (GFR <30 mL/min), including patients on dialysis, and those with acute kidney insufficiency. Gadolinium-based contrast agents with higher risk of NSF are gadodiamide (DTPA-BMA), gadopentetate dimeglumine (DTPA), and gadoversetamide (DTPA-BMEA). These high-risk agents should never be given in higher doses than 0.1 mmol/kg and are contraindicated in patients with stage 4 and 5 CKDM, including those on dialysis, in patients with acute renal insufficiency, in pregnant women, and in neonates (Beckett et al. 2015; Thomsen et al. 2013, 2016; Mathur and Weinreb 2016).

Low-risk gadolinium contrast agents may be used in pregnancy when there is a strong need and no neonatal tests are necessary. Lactating women are frequently object of concern. If the above-mentioned high-risk agents are used, breastfeeding should be stopped for 24 h (Beckett et al. 2015; Thomsen et al. 2013, 2016; Mathur and Weinreb 2016).

3 CT Technique

3.1 Introduction

The advent of helical scanning movement and multislice data collection gave rise to a new era of fast and high-resolution acquisitions.

Modern CT scans show substantial improvement on volume coverage, scan speed, as well as a more efficient use of X-ray tubes. Helical CT scans allow near-isotropic acquisitions, thus enabling high-resolution multiplanar reconstructions (MPR) and volume rendering. Moreover, the detector size decreased and multiple arrays were incorporated inside. Therefore, several slices can be recorded simultaneously, shortening the exposure time; thus thinner slices can be obtained and partial volume artifacts can be decreased.

The high speed of current CT scanners allows a complete thoracic, abdominal, and pelvic examination in only one breath-hold. A CT pelvic acquisition is rarely performed alone. The scan is usually extended to the upper abdomen not only for staging and for the follow-up of malignant diseases but also when characterization of vascular, inflammatory, or infectious entities is needed.

By shortening the scan time, motion artifacts are also reduced and distinct phases of enhancement may be accurately obtained after intravenous contrast administration. Overall, multidetector CT (MDCT) scans yield high spatial, temporal, and contrast resolution, thus increasing diagnostic accuracy. MDCT has rapidly evolved from 4-detector row systems to 256-slice and 320-detector row CT systems. Currently, most centers use scanners with at least 8- to 16-detector rows. Submillimeter or millimeter volumetric acquisitions with subsequent reconstruction into 2–5 mm thick axial, sagittal, and coronal images is a suitable protocol for routine CT scans (Thomsen et al. 2016; Rydberg et al. 2000; Goldman 2007; Yitta et al. 2009) (Fig. 2). Table 2 resumes a suitable general protocol for gynecological CT scans.

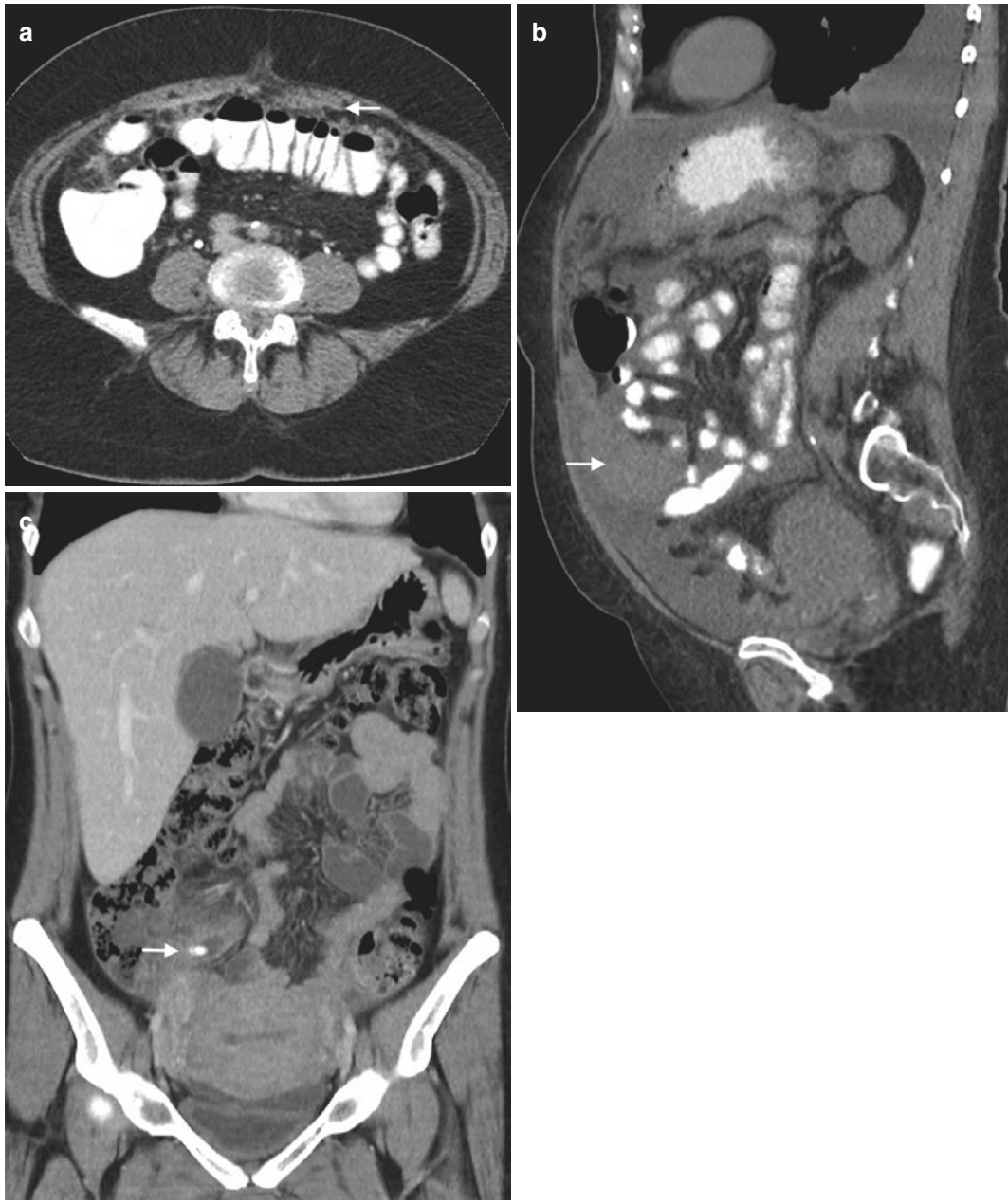

Fig. 2 Examples of different orientations on CT in three distinct patients. Axial image, after oral and intravenous contrast administration, depicting anterior peritoneal carcinomatosis (*arrow*) in a patient with endometrial carcinoma (**a**). Sagittal image, after oral contrast administration (intravenous contrast was contraindicated), showing ascites and huge solid peritoneal implants (*arrow*) in a patient with ovarian carcinoma (**b**). Coronal image, after intravenous contrast administration, identifying an acute appendicitis (*arrow*) in a young patient during early puerperium (**c**)

Table 2 Suitable general protocol for gynecological CT at a 64-detector scanner

• 4–6 h of fasting • Administration of a fast-acting laxative enema to clean the bowel, one on the day before the exam and another during the morning of the exam (optional) • Water or iodine-based oral contrast: 1000–1500 mL of contrast medium administered in separate doses 45 to 60 min prior to the examination • Water or iodine-based rectal contrast: catheter and enema bag; 200 mL to the rectosigmoid and 900–1200 mL to the entire colon
• Supine and "foot-first" positions • Range from diaphragm to pubic bone • Inspiration • Scout image: 120 kV, 10–50 mA • Final acquisition: (20 kV, 100–200 mAs) • Sub-mm or mm volumetric acquisitions with subsequent reconstruction into 2 to 5 mm thick axial, sagittal and coronal images • Correction of hip prosthesis artifacts if need: filtered back projection, adaptive filtering or iterative algorithms • Intravenous iodine-based contrast: 100–150 mL at 3–4 mL/s • Scan delay – 70–100 s (covering all range) – 3–5 min (if pelvic vein thrombosis is suspected) – 5–10 min (if bladder and ureteral opacification is needed)

3.2 Technical Disadvantages

Among the main disadvantages of CT, there are two with great relevance in daily practice: ionizing radiation exposure and metallic artifacts. Despite the kind of CT scan, radiation reduction and protection should always be considered. Both technicians and radiologists should be familiarized with some technical features including the tube current, X-ray beam collimation, and pitch, and cautiously select both the number and length of scan sequences. Dose quantification parameters like volume CT dose index (CTDIvol) and dose-length product (DLP) are usually displayed in current CT scans and should be routinely checked. Hip prosthesis causes substantial artifacts due to photon starvation and beam hardening, consequently hampering not only the joint and the surrounding muscles, but also pelvic organs. Methods may be used to reduce these artifacts: filtered back projection (FBP), which uses information from areas adjacent to regions affected by metal artifacts and replaces the metal-corrupted raw data by the interpolated values; adaptive filtering, which corrects the excessive noise produced by the photon starvation effect; or iterative algorithms, which use a combination of different metal artifact reduction algorithms and algebraic reconstruction techniques (Morsbach et al. 2013). Iterative reconstruction techniques also enable performing reduced-dose CT examinations (due to either tube current or tube potential lowering) without altering image quality (Padole et al. 2014).

3.3 Patient Preparation and Positioning

Before a CT scan, an inquiry about the patient medical history, routine medication, and potential contraindications is mandatory. Pregnancy is not a formal contraindication to CT; however, it should be avoided mainly during the first trimester. Patient preparation for CT scans is mainly related to contrast material administration (see next sections). Due to the need of intravenous contrast, patients are optimally asked to fast at least for 4 h. Administrating a fast-acting laxative enema to clean the bowel may also be recommended.

Patients are usually scanned in supine and "foot-first" positions, with their arms raised above their heads. Claustrophobic patients tolerate lying with the head outside the gantry better. Moreover, these positions allow for a face-to-face communication with the patient and facilitate the access to the patient whenever the examination has to be interrupted. "Foot-first" positioning also eases the connection of contrast medium tubes, which can be done immediately after inserting the venous access.

3.4 Oral and Rectal Contrast

Oral and rectal contrast media are frequently used in abdominal and pelvic CT imaging. Classically, it is given in cases of suspected bowel perforation or of anastomosis leakage. However, opacification

of the digestive tract is also helpful for distinguishing collapsed loops from lymph nodes, peritoneal implants, pelvic masses, and fluid collections.

Water as negative or positive iodinated solutions may be used for bowel opacification. In female pelvis imaging, positive contrast is particularly useful for staging and follow-up of ovarian and endometrial cancer. Iodinated solutions are preferable over barium suspensions due to its moderate effect on peristalsis and easier distribution along the digestive tract. Contrarily, barium suspensions are more prone to flocculate and may give rise to streak artifacts that hamper wall evaluation. Both types of contrast are usually safe, with only rare cases of mild diarrhea being reported. However, if bowel perforation is suspected, only iodinated solution should be administered due to the higher peritoneal toxicity of barium-based contrast media. As 1–2% of oral contrast is absorbed through the gut patients who had previous moderate to severe IV contrast allergy should be managed carefully.

Protocols for oral contrast vary according to the center. Typically, 1000–1500 mL of contrast medium is ingested in separate doses 45–60 min prior to the examination. Some authors advocate the administration of 20 mg metoclopramide at the beginning of the ingestion, in order to shorten patient preparation.

Rectal contrast is administered when the patient lies on the scanning table by using a catheter and an enema bag. 200 mL of contrast usually opacifies the rectum and the sigmoid colon adequately, whereas the entire colon may require 900–1200 mL of contrast. Sometimes, anal diseases like hemorrhoids and fissures hamper the introduction of the rectal tube due to pain. Special care should also be taken in patients with anal and lower third rectal carcinoma due to the risk of ulceration or perforation (Beckett et al. 2015).

3.5 Intravenous Iodine-Based Contrast Media

Intravenous iodine-based contrast media are usually given as a rapid bolus via an IV cannula, by using a pump injector. A suitable protocol for abdominal and pelvic CT scan is to administer 100–150 mL of 350 mg iodine contrast media at 3–4 mL/s. As the time to contrast material arrival and peak enhancement are affected by the choice of intravenous access sites, particularly when forearm or hand veins are used, lower flow rates are desirable (Bae 2010).

A suitable routine gynecological CT scan includes the upper abdomen and is acquired 70–100 s after contrast injection. Liver metastases from gynecological malignancies are typically hypovascular, so an arterial phase is usually unnecessary. Delayed images are recommended whenever pelvic vein thrombosis is suspected (3–5 min) or bladder and ureteral opacification is needed (5–10 min).

In order to reduce the risk of an acute reaction to iodine-based contrast media, some procedures should be taken according to the European Society of Urogenital Radiology (ESUR) guidelines: a nonionic contrast medium should be used; the patient should be kept in the Radiology Department for 30 min after the injection; and drugs and equipment for resuscitation have to be readily available. For patients at increased risk of reaction (history of previous moderate or severe acute reaction to an iodine-based contrast agent, asthma, and allergy requiring medical treatment), an alternative imaging tool not requiring an iodine-based contrast agent should be considered. The use of premedication for allergy prevention is widely accepted, despite its underlying limited clinical evidence. The ESUR guidelines recommend oral administration of prednisolone 30 mg (or methylprednisolone 32 mg), 12 and 2 h before contrast medium administration (Thomsen et al. 2016).

There is usually some concern regarding thyrotoxicosis, a potential very late reaction to iodine-based contrast media that usually occurs more than 1 week after injection. As a general rule, iodinated contrast media should not be given to patients with manifest hyperthyroidism. Patients at risk—those with untreated Graves' disease, or multinodular goiter and thyroid autonomy, especially if they are elderly and/or live in areas of dietary iodine deficiency—should be strictly monitored by endocrinologists after injection (Van der Molen et al. 2004).

Pregnancy and lactation are also usual sources of concern for both clinicians and radiologists.

Iodine-based contrast media may be given to pregnant patients in extraordinary conditions, but thyroid function should be checked in the neonate during the first week following the exam. When iodine-based agents are given to lactating mothers, breastfeeding may be continued normally (Thomsen et al. 2016).

In patients with renal impairment (eGFR less 45 mL/min/1.73 m^2 for intravenous administration), an alternative imaging method without iodine-based contrast media should be considered. However, if it is really needed, volume expansion should be done. According to the ESUR guidelines, intravenous normal saline, 1.0–1.5 mL/kg/h, for at least 6 h before and after contrast medium administration is recommended. An alternative suitable protocol is intravenous sodium bicarbonate (154 mEq/L in dextrose 5% water), 3 mL/kg/h for 1 h before contrast medium administration and 1 mL/kg/h for 6 h after contrast medium administration. Moreover, the lowest dose of a low or iso-osmolar contrast medium should be used (Thomsen et al. 2016).

Finally, some recommendations should be followed in patients taking metformin due to the risk of lactic acidosis after IV iodine-based contrast exposure when significant renal impairment is present. Patients with an eGFR between 30 and 44 mL/min/1.73 m^2 (CKD 3) should stop metformin 48 h before contrast medium injection and should only restart it 48 h after the examination if renal function has not deteriorated. In patients with eGFR less than 30 mL/min/1.73 m^2 (CKD 4 and 5), iodine-based contrast media should be avoided (Beckett et al. 2015; Thomsen et al. 2016).

References

Allen BC, Hosseinzadeh K, Qasem SA, Varner A, Leyendecker JR (2014) Practical approach to MRI of female pelvic masses. Am J Roentgenol 202(6):1366–1375. doi:10.2214/AJR.13.12023

Bae KT (2010) Intravenous contrast medium administration and scan timing at CT: considerations and approaches. Radiology 256(1):32–61. doi:10.1148/radiol.10090908

Bazot M, Bharwani N, Huchon C, Kinkel K, Cunha TM, Guerra A, Manganaro L, Buñesch L, Kido A, Togashi K, Thomassin-Naggara I, Rockall AG (2016) European Society of Urogenital Radiology (ESUR) guidelines: MR imaging of pelvic endometriosis. Eur Radiol. doi:10.1007/s00330-016-4673-z2016

Beckett KR, Moriarity AK, Langer JM (2015) Safe use of contrast media: what the radiologist needs to know. Radiographics 35(6):1738–1750. doi:10.1148/rg.2015150033

Beddy P, O'Neill AC, Yamamoto AK, Addley HC, Reinhold C, Sala E (2012) FIGO staging system for endometrial cancer: added benefits of MR imaging. Radiographics 32(1):241–254. doi:10.1148/rg.321115045

Bernardin L, Dilks P, Liyanage S, Miquel ME, Sahdev A, Rockall A (2012) Effectiveness of semi-quantitative multiphase dynamic contrast-enhanced MRI as a predictor of malignancy in complex adnexal masses: radiological and pathological correlation. Eur Radiol 22(4):880–890. doi:10.1007/s00330-011-2331-z

Forstner R, Sala E, Kinkel K, Spencer JA (2010) ESUR guidelines: ovarian cancer staging and follow-up. Eur Radiol 20(12):2773–2780. doi:10.1007/s00330-010-1886-4

Forstner R, Thomassin-Naggara I, Cunha TM, Kinkel K, Marselli G, Kubik-Huch R, Spencer JA, Rockall A (2016) ESUR recommendations for MR imaging of the sonographically indeterminate adnexal mass: an update. Eur Radiol. doi:10.1007/s00330-016-4600-3

Froehlich JM, Daenzer M, von Weymarn C, Erturk SM, Zollikofer CL, Patak MA (2009) Aperistaltic effect of hyoscine *N*-butylbromide versus glucagon on the small bowel assessed by magnetic resonance imaging. Eur Radiol 19:1387–1393. doi:10.1007/s00330-008-1293-2

Goldman LW (2007) Principles of CT and CT technology. J Nucl Med Technol 35(3):115–130. doi:10.2967/jnmt.107.042978

Hameeduddin A, Sahdev A (2015) Diffusion-weighted imaging and dynamic contrast-enhanced MRI in assessing response and recurrent disease in gynaecological malignancies. Cancer Imaging 15:3. doi:10.1186/s40644-015-0037-1

Masselli G, Derchi L, McHugo J, Rockall A, Vock P, Weston M, Spencer J (2013) Acute abdominal and pelvic pain in pregnancy: ESUR recommendations. Eur Radiol 23:3485–3500. doi:10.1007/s00330-013-2987-7

Mathur M, Weinreb JC (2016) Imaging patients with renal impairment. Abdom Radiol 41(6):1108–1121. doi:10.1007/s00261-016-0709-8

Morsbach F, Bickelhaupt S, Wanner GA, Krauss A, Schmidt B, Alkadhi H (2013) Reduction of metal artifacts from hip prostheses on CT images of the pelvis: value of iterative reconstructions. Radiology 268(1):237–244. doi:10.1148/radiol.13122089

Padole A, Khawaja R, Kalra M, Singh S (2014) CT radiation dose and iterative reconstruction techniques. Am J Roentgenol 204:W384–W392. doi:10.2214/AJR.14.13241

Qayyum A (2009) Diffusion-weighted imaging in the abdomen and pelvis: concepts and applications. Radiographics 29(6):1797–1810

Ray J, Vermeulen M, Bharatha A, Montanera W, Park A (2016) Association between MRI exposure during pregnancy and fetal and childhood outcomes. JAMA 316(9):952–961. doi:10.1001/jama.2016.12126

Rydberg J, Buckwalter KA, Caldemeyer KS et al (2000) Multisection CT: scanning techniques and clinical applications. Radiographics 20(6):1787–1806. doi:10.1148/radiographics.20.6.g00nv071787

Sala E, Rockall A, Kubik-Huch R (2011) Advances in magnetic resonance imaging of endometrial cancer. Eur Radiol 21(3):468–473. doi:10.1007/s00330-010-2010-5

Sala E, Rockall AG, Freeman SJ, Mitchell DG, Reinhold C (2013) The added role of MR imaging in treatment stratification of patients with gynecologic malignancies: what the radiologist needs to know. Radiology 266(3):717–740. doi:10.1148/radiol.12120315

Thomsen HS, Morcos SK, Almen T et al (2013) Nephrogenic systemic fibrosis and gadolinium-based contrast media: updated ESUR contrast medium safety committee guidelines. Eur Radiol 23(2):307–318. doi:10.1007/s00330-012-2597-9

Thomsen HS et al (2016) ESUR Guidelines on Contrast Media Version:9.0. http://www.esur.org/esur-guidelines/

Van der Molen AJ, Thomsen HS, Morcos SK (2004) Effect of iodinated contrast media on thyroid function in adults. Eur Radiol 14(5):902–907. doi:10.1007/s00330-004-2238-z

Whittaker CS, Coady A, Culver L, Rustin G, Padwick M, Padhani AR (2009) Diffusion-weighted MR imaging of female pelvic tumors: a pictorial review. Radiographics 29(3):759–774. doi:10.1148/rg.293085130discussion 774–8

Yitta S, Hecht EM, Slywotzky CM, Bennett GL (2009) Added value of multiplanar reformation in the multidetector CT evaluation of the female pelvis: a pictorial review. Radiographics 29:1987–2005. doi:10.1148/rg.297095710

Uterus: Normal Findings

Athina C. Tsili

Contents

1 Introduction

Radiologists should be familiar with the normal appearances of the uterus on CT and MRI when interpreting uterine pathologies. Although CT is not generally recommended as the first-line imaging modality for the assessment of uterine diseases, it is often used for the initial evaluation of patients referred to the emergency settings. Multidetector CT with multiplanar reformations allows improved visualization of the normal anatomy of the uterus. MRI is a superb modality for evaluation of the normal uterus. Uterine and cervical zonal anatomy is nicely displayed on T2WI. The zonal appearance of the uterine corpus changes significantly in response to a variety of physiological stimuli, including menstrual phase, age and hormonal effects. Functional imaging techniques including dynamic contrast-enhanced MRI and diffusion-weighted imaging enable the radiologist to move from morphological to functional assessment of the normal uterus.

2 Embryonic Development and Normal Anatomy of the Uterus

In females, the paramesonephric (Müllerian) ducts arise from the mesoderm, lateral to the mesonephric ducts in the seventh week. The

A.C. Tsili
Department of Clinical Radiology, Medical School, University of Ioannina, University Campus, 45110, Ioannina, Greece
e-mail: a_tsili@yahoo.gr; atsili@cc.uoi.gr

Med Radiol Diagn Imaging (2017)
DOI 10.1007/174_2017_43, © Springer International Publishing AG
Published Online: 09 April 2017

paramesonephric ducts grow caudally, coursing lateral to the urogenital ridges. In the eighth week, the paired paramesonephric ducts lie medial to the mesonephric ducts. The paramesonephric ducts fuse to form a confluence. This process is called Müllerian organogenesis and represents the initial stage in the development of the upper two-thirds of the vagina, the cervix, uterus and both fallopian tubes. The cranial end of the fused ducts gives rise to the future uterus. The caudal end of the fused ducts will form the upper two-thirds of the vagina. The lower third of the vagina is formed as the sinovaginal node (bulb) canalizes. The sinovaginal node inserts into the urogenital sinus at Müller's tubercle (Mann et al. 2012).

The uterus is a pear-shaped organ, approximately 8 cm long, 5 cm at its widest part and 2.5 cm or less at its thickest part (Fig. 1) (Mann et al. 2012; Basmajian 1971; Siddall and Rubens 2005). It is composed of three distinct anatomic regions, namely the fundus, the body and the cervix. The fundus and body form the upper two-thirds and the cervix the lower third. The fundus is the part that lies above the tubes and is covered by peritoneum. The lower uterine segment (isthmus) together with the internal os forms the junction between the uterine corpus and cervix (Mann et al. 2012).

The zonal anatomy of the uterus as classically described consists of: the endometrium composed of the mucosal stratum functionalis and the region of glandular interdigitation into the myometrium or stratum basale; the subendometrial region of densely packed smooth muscle bundles with an orientation primarily parallel to the endometrial stratum basale; the stratum vasculature, where the arcuate arteries are branching through the randomly oriented and loosely organized smooth muscle bundles of the myometrium proper; and the thin subserosal zone of dense fibrous tissue (Fig. 2) (Brown et al. 1991; Kaur et al. 1998). The

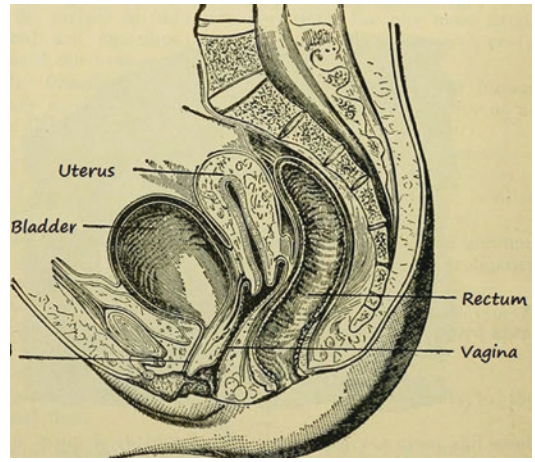

Fig. 1 Anatomic draft of the normal female pelvis in sagittal orientation

potential cavity of the uterine body is only a thin cleft. The anterior and posterior walls are applied to each other.

The uterus is thick-walled and muscular. The arrangement of muscle fibres in the human uterus has been extensively evaluated, and the uterine wall consists of two counter-rotating systems of spiral fibres. Fibres in the myometrium are divided into the internal layer (stratum subvasculature), which mostly run in a circular pattern, and the external layer (stratum supravasculature), which mostly run in a longitudinal pattern. There is also an intermediate layer (stratum vasculature) in which the fibres run in random directions (Fiocchi et al. 2012).

The cervical canal extends from the internal os to the external os of the uterus. It is spindle-shaped and 2–3 cm in length. The uterine cervix consists of the supravaginal cervical canal (endocervix) and the vaginal portion that projects into the vagina. The wall of the cervix is primarily made up of firm connective tissue. The muscular part accounts for less than 10% of the cervical wall and primarily consists of smooth muscle cells in circular arrangement. The cervical canal is coated with

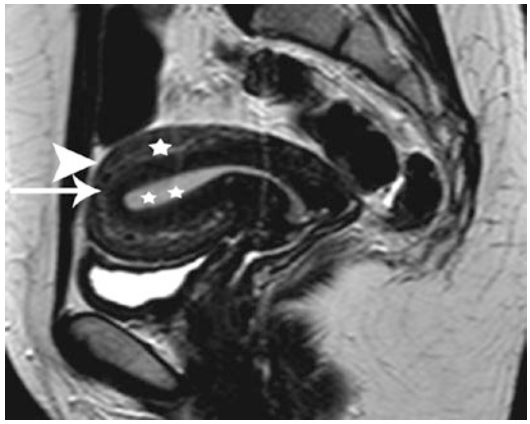

Fig. 2 Sagittal T2WI image of a healthy premenopausal woman shows normal uterine zonal anatomy: the endometrium (*asterisks*) appears hyperintense, the junctional zone (*long arrow*) shows low signal intensity, the outer myometrium (*asterisk*) demonstrates intermediate signal intensity and a subserosal zone of the myometrium is detected hypointense (*arrowhead*)

mucus-producing columnar epithelium and contains numerous gland-like units, the crypts. The squamocolumnar junction is the transition from the columnar epithelium of the endocervix to the non-keratinizing squamous epithelium of the ectocervix and is situated at the level of the external os of the uterus (Mann et al. 2012).

The uterine artery supplies the uterus and gives off superior and inferior branches to the cervix, fallopian tubes and upper vagina. It arises from the anterior branch of the internal iliac artery and crosses the ureter as it enters the bladder. The uterine artery gives branches that penetrate the outer myometrium, proceed to the middle third of the myometrium and divide to form the arcuate arteries. The arcuate arteries give off radial branches, which travel into the uterine lumen, called 'spiral' arteries as they pass the myometrial–endometrial junction. After entering the endometrium, the spiral arteries give off small branches, the basal arteries, which supply the basal layer and, unlike the spiral arteries, are not affected by hormonal stimuli. The arcuate arteries give off branches to the outer myometrium and a plexus of small, radically oriented arteries is formed immediately beneath the serosa (Fig. 3) (Kaur et al. 1998). The uterine veins drain into the internal iliac veins. Lymphatic drainage from the corpus is through the broad ligament into the paraaortic lymph nodes and from the cervix into the parametrial and iliac lymph nodes.

The broad ligament is formed by two layers of peritoneum, which drape over the uterus and extend laterally from the uterus to the pelvic sidewall. Its superior free edge is formed by the fallopian tube medially and the suspensory ligament of the ovary laterally. The lower margin of the broad ligament ends at the cardinal ligament. Between the two leaves of the broad ligament can be found loose extraperitoneal connective tissue, smooth muscle and fat known as the parametrium, which contains the fallopian tube, round ligament, ovarian ligament, uterine and ovarian blood vessels, nerves, lymphatic vessels, mesonephric remnants and a portion of the ureter (Foshager and Walsh 1994). The round ligament is a band of fibromuscular tissue that attaches to the anterolateral uterine fundus just below and anterior to the fallopian tube and ovarian ligament (Fig. 4). The cardinal ligament forms the base of the broad ligament and provides the major ligamentous support for the uterus and upper vagina. It extends laterally from the cervix and upper vagina to merge with a fascia overlying the obturator internus muscle (Fig. 4b). The uterine artery lies along its superior border. The uterosacral ligament lies posteriorly, extending from the lateral cervix and vagina at the level of the internal cervical os and forming a curved arc toward the anterior body of the sacrum at S2 or S3 level (Foshager and Walsh 1994).

Most of the uterus is covered by peritoneum. The peritoneum passes from the

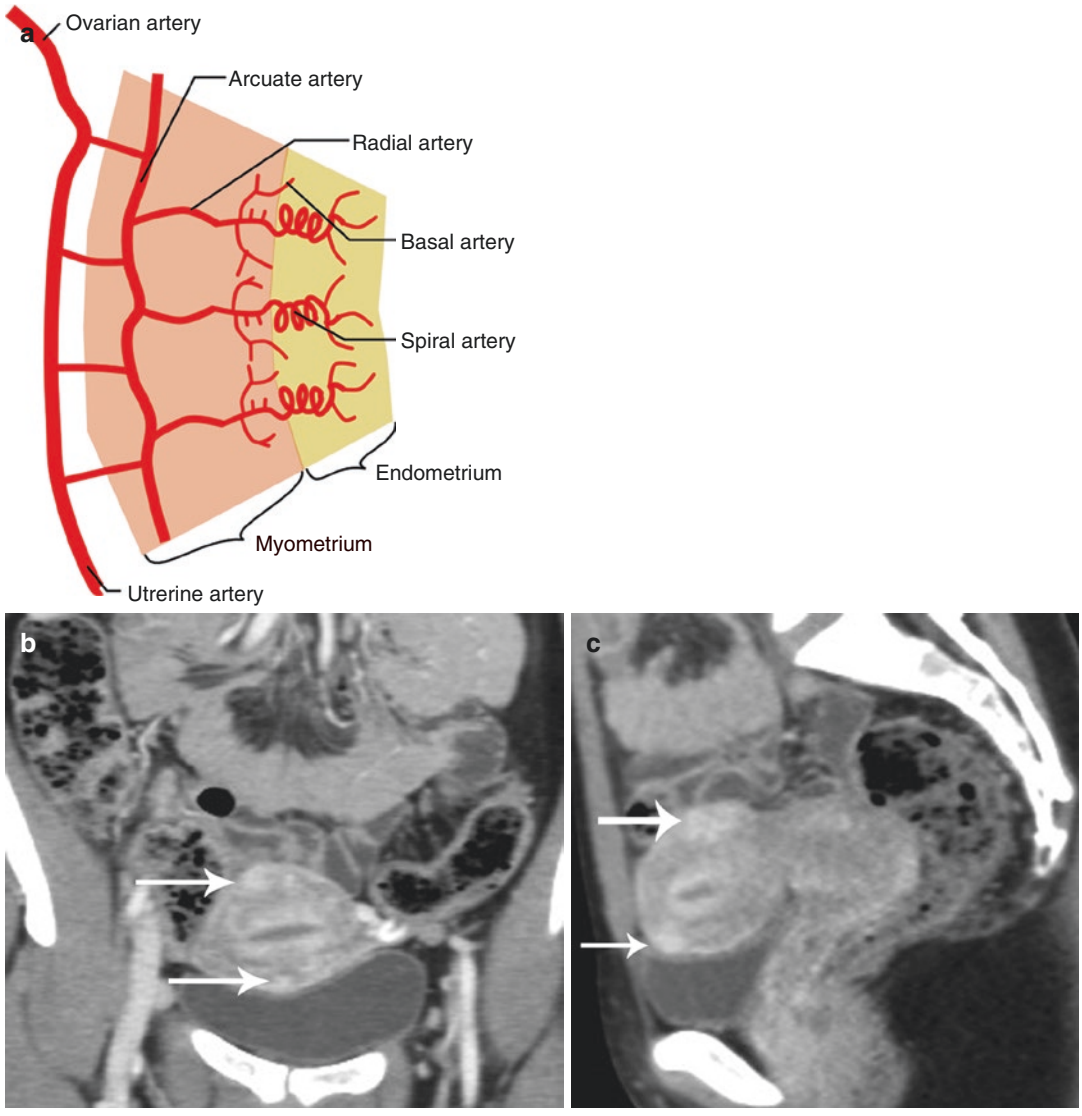

Fig. 3 (**a**) Arterial vasculature of the human uterus. CT examination (**b**) coronal and (**c**) sagittal multiplanar reformatted images (portal phase) depict uterine arcuate arteries (*long arrow*)

symphysis pubis on to the upper surface of the bladder and from the third piece of the sacrum to rectum. The homologue of the rectovesical pouch of peritoneum in the male is divided into an anterior and a posterior part by a transverse partition, formed by the uterus and the broad ligament. The anterior subdivision is the vesicouterine pouch and the posterior subdivision the rectouterine pouch (Douglas space) (Basmajian 1971).

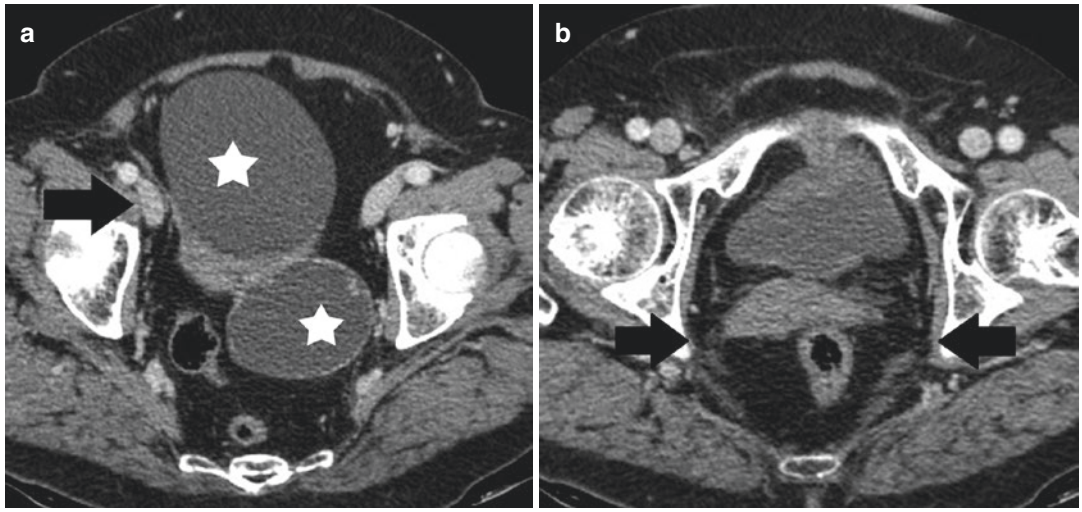

Fig. 4 Transverse contrast-enhanced CT images (portal phase) in a postmenopausal woman with bilateral serous ovarian cystadenomas (*asterisk*, **a**) depict normal right round ligament (*arrow*, **a**) and cardinal (*arrow*, **b**) ligaments

3 Uterine Corpus: Normal CT and MRI Findings

Although CT is generally not the primary imaging modality for the assessment of the uterus, it is often the initial diagnostic examination for evaluating nongynecologic pelvic diseases, especially in emergency settings. Therefore, radiologists should be familiar with normal uterine CT findings, to avoid misdiagnosis and/or unnecessary additional diagnostic tests (Yitta et al. 2011; Yitta et al. 2009; Kormano et al. 1981; Grossman et al. 2008; Lim et al. 2002). Multidetector CT (MDCT) with two-dimensional multiplanar reformatted (MPR) images has improved visualization of the normal anatomy of the female pelvis (Yitta et al. 2011; Yitta et al. 2009). Standard sagittal and coronal MPRs and when necessary additional oblique or curved planar MPRs are generated with no additional time or labor required on the part of the radiologist (Yitta et al. 2011; Yitta et al. 2009). Sagittal reconstructions are particularly recommended in cases of a retroverted and retroflexed uterus and in cases of a prominent or triangular endometrium (Fig. 5) (Yitta et al. 2011; Yitta et al. 2009; Kormano et al. 1981; Grossman et al. 2008; Lim et al. 2002).

At unenhanced images, the uterus exhibits relative uniform soft-tissue density, with a central slightly hypodense region, corresponding to endometrial canal (Fig. 6). With conventional CT, the uterine wall appears relatively featureless with lack of distinction between layers after intravenous contrast material administration. Multidetector CT with rapid scanning during different phases of contrast enhancement allows the detection of a uterine enhancement pattern, closely resembling that at dynamic gadolinium-enhanced MRI (Kaur et al. 1998; Yitta et al. 2011; Yitta et al. 2009; Yamashita et al. 1993).

However, few data regarding normal uterine and cervical contrast enhancement with MDCT exist in the literature (Kaur et al. 1998; Yitta et al. 2011; Yitta et al. 2009; Kormano et al. 1981). Three types of early enhancement of the uterine body have been described with single-section helical CT: type 1, subendometrial enhancement with or without associated subserosal enhancement, predominantly seen in premenopausal women; type 2, absence of early subendometrial enhancement with enhancement either progressing from the subserosa or diffuse from the outset, equally seen in both premenopausal and postmenopausal women and type 3, faint diffuse enhancement of the myometrium, predominantly seen in postmenopausal women (Fig. 7) (Kaur

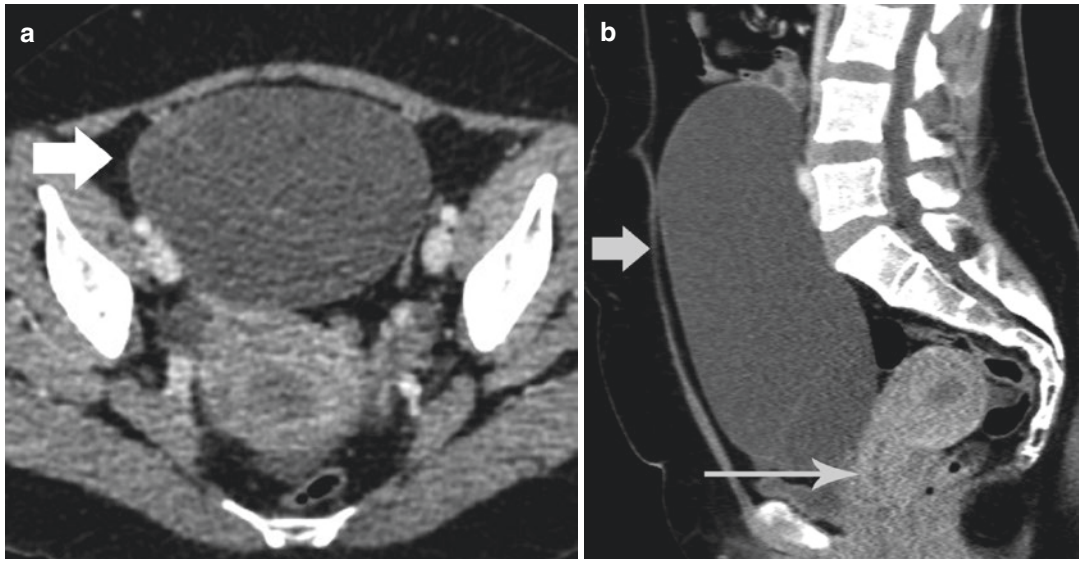

Fig. 5 (**a**) Transverse and (**b**) sagittal MPRs (portal phase) in a 35-year-old woman with ovarian mucinous cystadenoma (*arrow*) and retroverted and retroflexed uterus. Normal cervical enhancement is seen (*long arrow*)

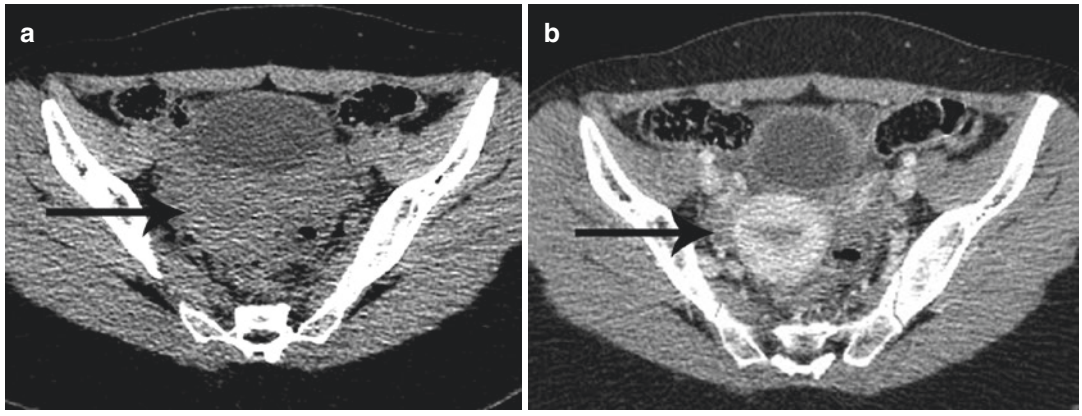

Fig. 6 Transverse unenhanced (**a**) and contrast-enhanced (**b**) CT images of normal uterus in a 23-year-old woman. The endometrium appears hypodense (*long arrow*)

et al. 1998; Yitta et al. 2009). Recently, another pattern has been described, including patchy, heterogeneous enhancement throughout the myometrium (Yitta et al. 2011). The visualization of these enhancement patterns is transient, depending on various factors, including age and menstrual status. On delayed imaging, diffuse uniform enhancement of the myometrium is seen. The lower uterine segment and cervix is often less enhancing compared to the myometrium on early phase and this may falsely simulate a mass (Fig. 7c).

On CT, the endometrium is defined as the central hypodense region. However, endometrial cavity often represents a source of confusion at CT (Yitta et al. 2009; Grossman et al. 2008; Lim et al. 2002). CT is considered relatively insensitive in detecting mild endometrial thickening, but better able to identify gross thickening (Grossman et al. 2008). Endometrial thickness may be exaggerated on standard axial and coronal images, especially in cases of uterine version, where the endometrium is imaged in an oblique plane. Sagittal MPRs are

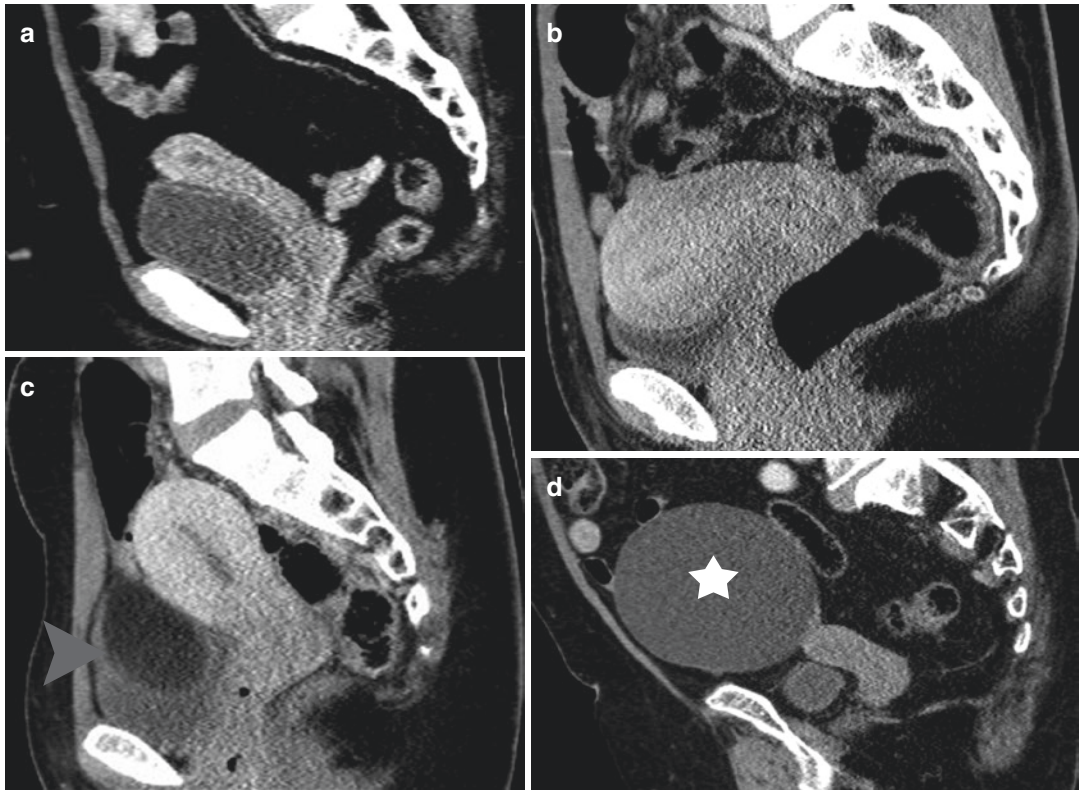

Fig. 7 Patterns of normal uterine enhancement on MDCT (sagittal MPRs, portal phase). Type 1, (**a**) thin and (**b**) thick subendometrial enhancement. (**c**) Type 2, diffuse myometrial enhancement. Normal hypodense cervix. Ovarian mature cystic teratoma (*arrowhead*). (**d**) Type 3, minimal diffuse myometrial enhancement. Ovarian serous cystadenoma (*asterisk*, same patient as in Fig. 4)

often helpful to confirm or exclude gross endometrial thickening in these cases. CT criteria for characterizing normal endometrial thickness are lacking (Yitta et al. 2009; Grossman et al. 2008; Lim et al. 2002). A maximum of 7.5 mm in mean short-axis thickness of normal endometrium in asymptomatic postmenopausal women has been reported, greater than that for US measurements, in which 5 mm is an accepted upper limit of normal (Lim et al. 2002).

The normal dimensions of the uterus during reproductive life vary depending on patient age and parity. Normal uterus in women of childbearing age measures approximately 8 cm in length, 4 cm height and 5 cm width, with multiparous uterus being larger than nulliparous uterus by approximately 1 cm in each dimension (Takeuchi et al. 2010). The uterus is typically pear-shaped, with uterine body approximately twice the size of the cervix. The normal position of the uterus may vary depending on the degree of distention of the urinary bladder. Uterine position is characterized in relation to the angle of the long axis of the uterine body to the long axis of the cervix (flexion) and the long axis of the uterus to the long axis of the vagina (version). The uterus is more often in an anteverted and anteflexed position (Takeuchi et al. 2010).

Uterine zonal anatomy on MRI is visualized on T2-weighted images (T2WI) consisting of a high signal intensity central zone, corresponding to endometrium, a subjacent low signal intensity junctional zone (JZ) of myometrium, a moderately intense zone of myometrium and a thin, hypointense subserosal zone of myometrium (Fig. 8) (Brown et al. 1991; Hricak et al. 1983; Togashi et al. 2001). The low signal intensity of the JZ is explained by its lower water content, decreased extracellular

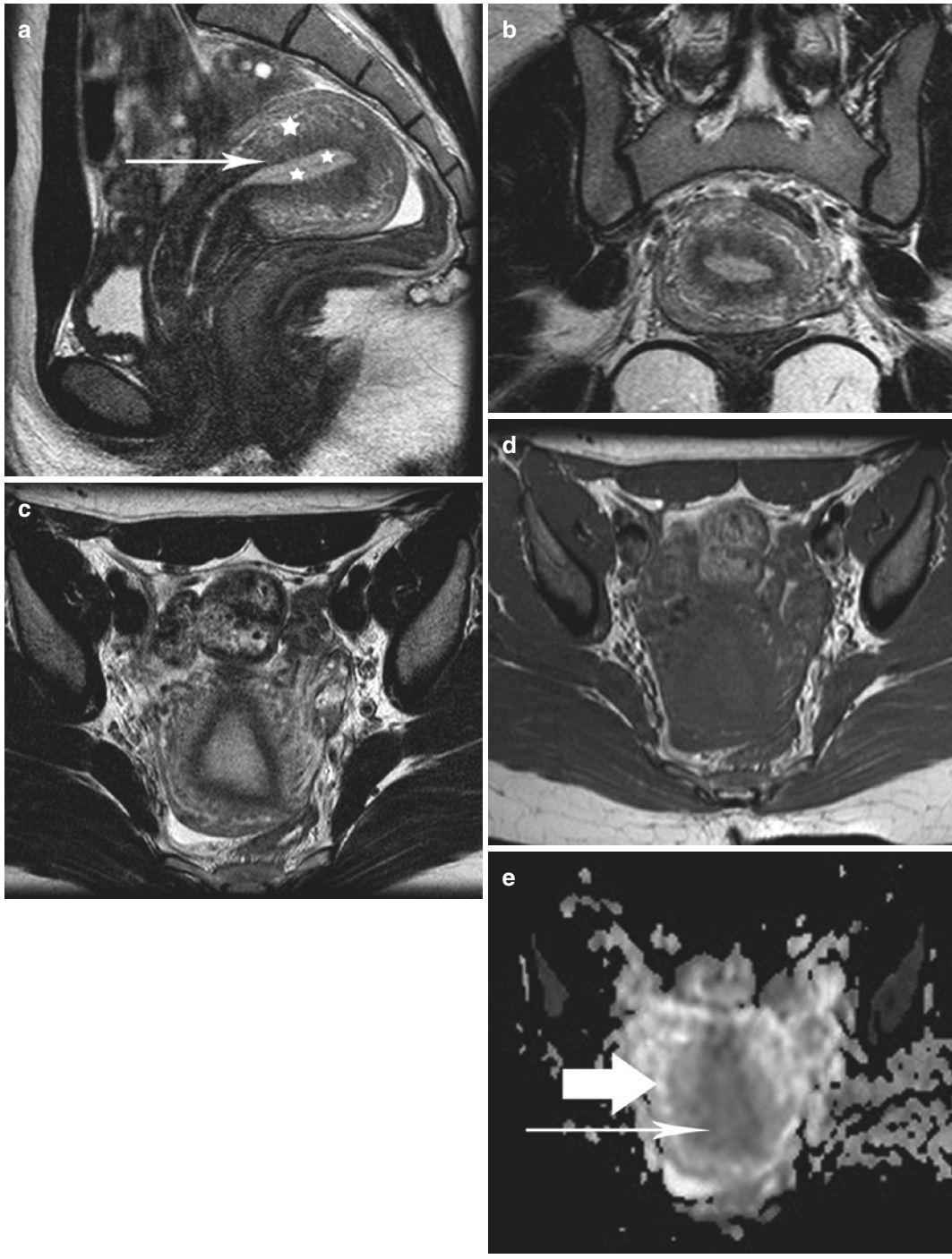

Fig. 8 MRI of a healthy 31-year-old woman with retroverted and retroflexed uterus during secretory phase. T2WI in (**a**) sagittal, (**b**) coronal and (**c**) transverse orientation. The endometrium is thick (*asterisks*), the myometrium appears hyperintense (*asterisk*) and the interface between outer myometrium and JZ is relatively indistinct (*arrowhead*). (**d**) Transverse T1WI shows relatively homogeneous uterine body with signal intensity similar to that of muscles. (**e**) Transverse apparent diffusion coefficient (ADC) map. The ADC of normal endometrium (*long arrow*) and myometrium (*arrow*) is 1.26×10^{-3} mm^2/s and 1.55×10^{-3} mm^2/s, respectively

matrix, tightly packed muscle cells and a threefold increase in nuclear area (Togashi et al. 2001; Hauth et al. 2007; Novellas et al. 2011; Brosens et al. 1995). The first studies in the 1980s proposed a maximum threshold of between 2 and 5 mm for the thickness of the normal JZ. Over the past two decades, this criterion has been gradually revised, resulting in an upper limit of normal of 5–8 mm for the thickness of the JZ. A width larger than 12 mm for JZ on MRI has been proposed as a criterion for the diagnosis of diffuse adenomyosis (Togashi et al. 2001; Hauth et al. 2007; Novellas et al. 2011; Brosens et al. 1995). Uterine body appears homogeneous and featureless on T1-weighted images (T1WI), isointense compared to skeletal muscles (Brown et al. 1991; Hricak et al. 1983; Togashi et al. 2001) (Fig. 8d).

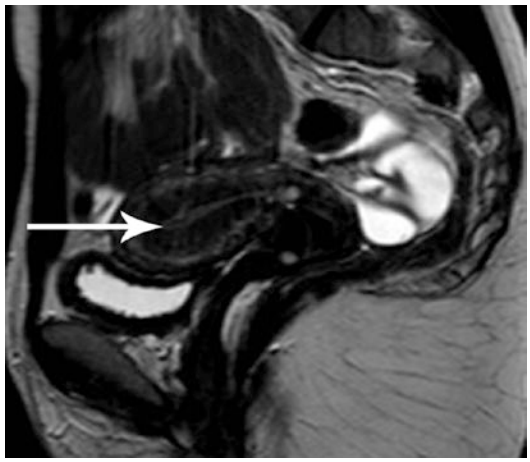

Fig. 9 MRI of a healthy 33-year-old woman during menstrual phase. T2WI in sagittal orientation. The endometrium appears thin. Within the cavity, the menstrual blood (*long arrow*) is detected as a stripe of low signal intensity

Uteri of women in the reproductive age, not taking exogenous hormones show variations in endometrial and myometrial width, and signal intensity throughout the menstrual cycle (Takeuchi et al. 2010; Togashi et al. 2001; Hauth et al. 2007; McCarthy et al. 1986; Demas et al. 1986; Haynor et al. 1986; Langer et al. 2012; He et al. 2016). The endometrium is thin just after menstruation. As the estrogen level increases during the proliferative (follicular) phase, the endometrium thickens. During ovulation, there are no obvious changes in the endometrium. During the secretory (luteal) phase, under the influence of both estrogen and progesterone, the endometrium reaches its maximum thickness, up to 7–14 mm. The myometrium shrinks on menstrual phase and has decreased signal intensity on T2WI (Fig. 9). Myometrial thickness gradually increases during the proliferative phase. The contrast between outer myometrium and JZ is more prominent in the proliferative phase (Fig. 10), and it becomes indistinct in the secretory and menstrual phases. Myometrial signal intensity

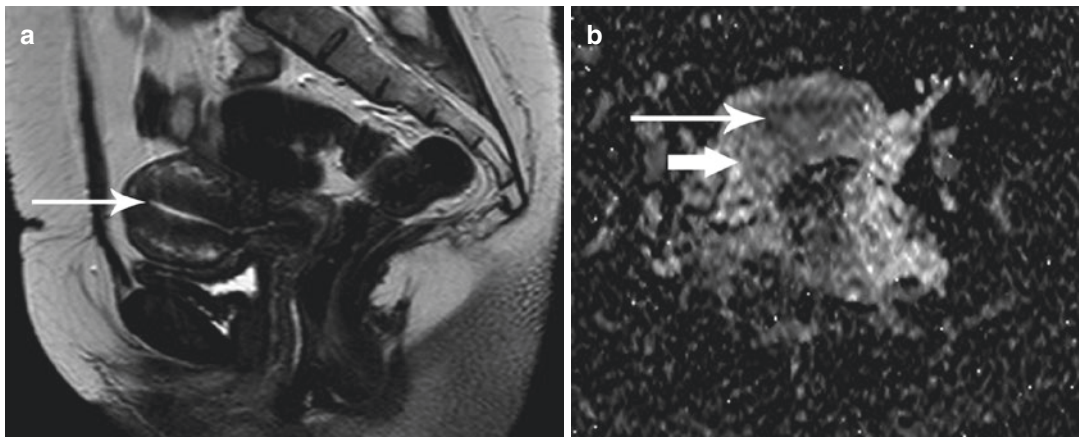

Fig. 10 MRI of a healthy 32-year-old woman during proliferative phase. (**a**) Sagittal T2WI image. The endometrium appears thin (*long arrow*) and the contrast between outer myometrium and JZ is evident. (**b**) Axial ADC map. The ADC of normal endometrium (*long arrow*) and myometrium (*arrow*) is 1.56×10^{-3} mm^2/s and 1.47×10^{-3} mm^2/s, respectively

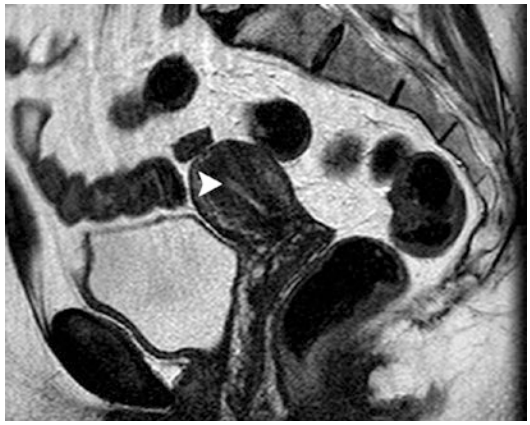

Fig. 11 T2WI in sagittal plane of a healthy 64-year-old woman depicts a small uterus, with a normal thin hyperintense endometrium (*arrowhead*)

increases and myometrial arcuate vessels are more clearly defined during the midsecretory phase (Fig. 8). The higher water content of the myometrium during this phase results in increased signal intensity (Takeuchi et al. 2010; Togashi et al. 2001; Hauth et al. 2007; McCarthy et al. 1986; Demas et al. 1986; Haynor et al. 1986; Langer et al. 2012; He et al. 2016).

Patient age has a significant effect on MRI features of female reproductive organs (Takeuchi et al. 2010; Hauth et al. 2007; Demas et al. 1986; Langer et al. 2012). In the premenarchal girl and in the postmenopausal woman, the uterine corpus is small and relatively featureless, with faint myometrial-endometrial interface on T2WI (Fig. 11) (Takeuchi et al. 2010; Demas et al. 1986; Langer et al. 2012).

Exogenous hormonal replacement affects the appearance of the uterus (Togashi et al. 2001; McCarthy et al. 1986; Demas et al. 1986). In premenopausal women using oral contraceptives, the JZ is significantly thinner than usual, the uterus has a thin endometrium and a bright myometrium, the latter due to edema. Women treated with GnRH analogue exhibit a uterus similar to that found in postmenopausal women. Although tamoxifen is antiestrogenic, it has paradoxical estrogenic effects in postmenopausal women, resulting in a heterogenous and thickened endometrium. These findings may mimic endometrial cancer, although they regress after withdrawal of the drug (Togashi et al. 2001; McCarthy et al. 1986; Demas et al. 1986).

The normal uterus presents two types of physiologic myometrial contractions: transient sustained contraction and uterine peristalsis (Togashi et al. 1993a, b, 2001; Masui et al. 2001). Transient myometrial contraction appears as sporadic focal bulging of myometrium, persisting for several minutes. It may be detected as a focal hypointense area on T2WI, simulating a leiomyoma or adenomyosis, although it may disappear on subsequent images (Fig. 12). Uterine peristalsis is caused by contractions of the inner myometrium, with retrograde direction (cervico-fundal) in mid-cycle and antegrade during menstruation. This movement is considered to play a major role in rapid sperm transport, discharge of menstrual blood and in maintenance of early pregnancies. Uterine peristalsis subsides during the secretory phase, most likely to facilitate implantation of the embryo. Fast MRI in a kinematic fashion depicts myometrial contraction, which appears as a series of changes in configuration, thickness and signal intensity of the myometrium and JZ (Togashi et al. 1993a, 2001; Masui et al. 2001).

Functional MRI by means of dynamic multiphase contrast-enhanced MRI (DCE-MRI) and diffusion-weighted MRI (DW-MRI) is now part of the standard imaging protocols for evaluation of the female pelvis. Both techniques enable the radiologist to move from morphological to functional assessment of diseases of the female pelvis (Sala et al. 2013; Punwani 2011).

Three types of uterine enhancement on DCE-MRI have been described: type 1, a thin early enhancing layer between the endometrium and myometrium (called subendometrial enhancement [SEE]), followed by enhancement of the entire myometrium, more often seen during the proliferative phase or in postmenopausal women; type 2, a thick layer corresponding to the JZ with marked initial enhancement, usually seen during the secretory phase and type 3, enhancement of the whole myometrium, more often detected in the menstrual phase (Kaur et al. 1998; Yamashita et al. 1993; Hricak and Kim 1993) (Fig. 13).

Perfusion-MRI although mainly used as a research tool confirmed the presence of different myometrial components, especially during reproductive age, where both microcirculation and

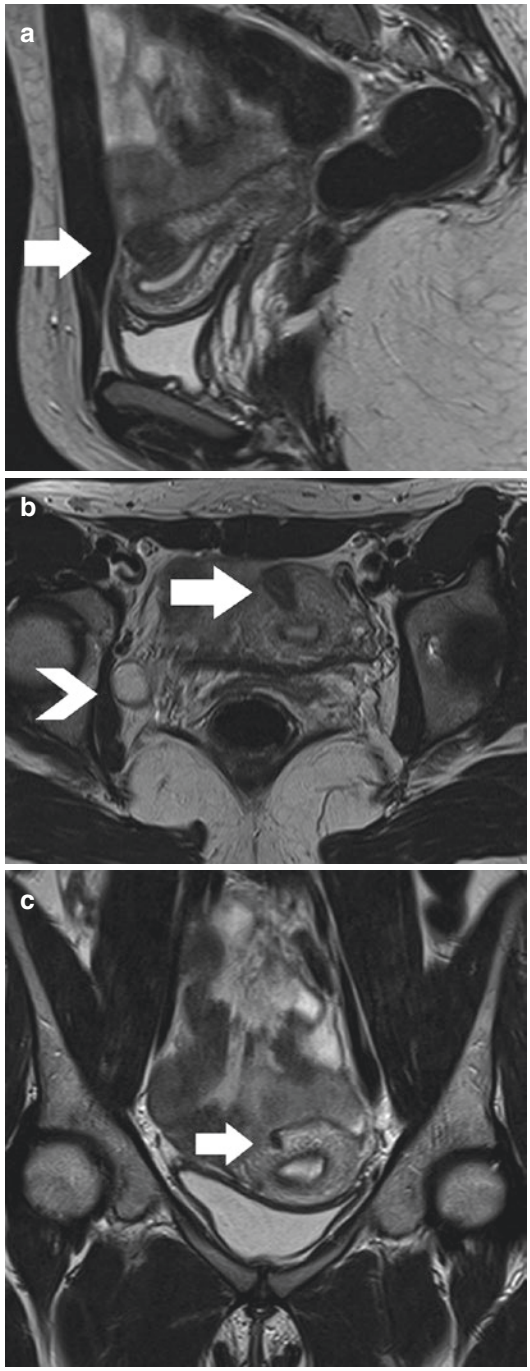

Fig. 12 Transient myometrial contraction. T2WI in (**a**) sagittal and (**b**) transverse orientation shows focal low signal intensity myometrial mass (*arrow*), mimicking leiomyoma. Small right ovarian follicle (*arrowhead*). (**c**) Subsequent coronal T2WI shows significant resolution of the findings (*arrow*) (Courtesy Dr. Cunha TM, Lisbon, Portugal)

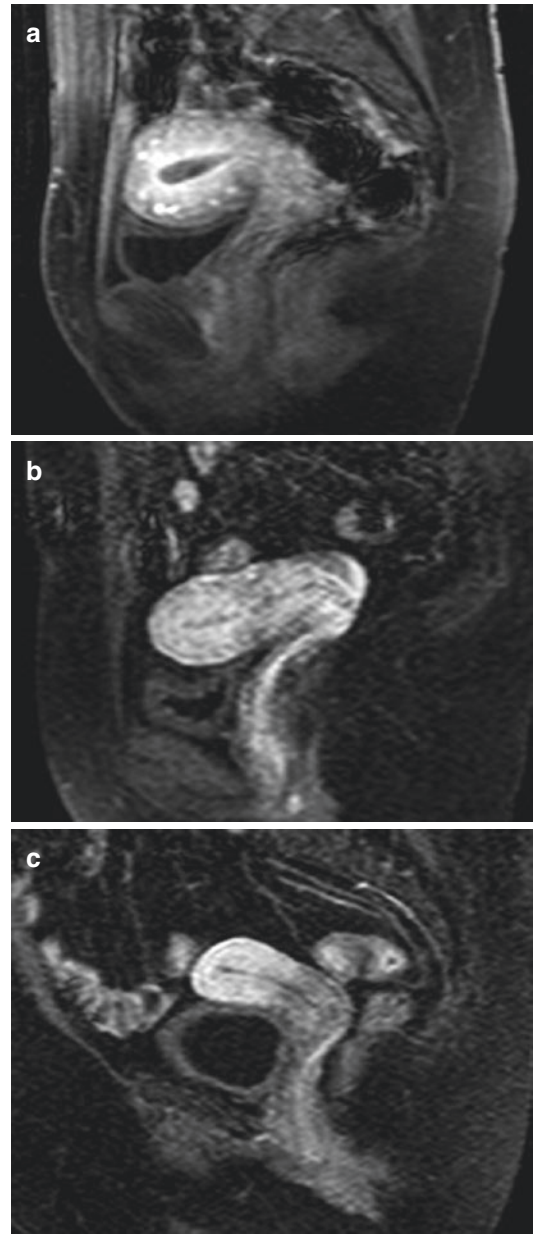

Fig. 13 Patterns of early uterine enhancement on DCE-MRI. (**a**) Type 1, thin enhancing layer between the endometrium and myometrium (subendometrial enhancement); (**b**) Type 2, thick enhancing layer corresponding to the JZ and (**c**) Type 3, enhancement of the whole myometrium

ultrastructural features such as the extracellular matrix differ between the inner and the outer myometrium. Specifically, DCE-MRI has shown higher tissue blood flow (F) and permeability-surface area product (PS), lower blood volume fraction (Vb) and interstitial volume (Ve), and longer lag time (Dt) in the inner myometrium, compared to the outer myometrium (Thomassin-Naggara et al. 2010). During the menstrual cycle no differences for all perfusion imaging parameters are seen in the outer myometrium. By contrast, the inner myometrium shows microvascular variations with higher F, higher Vb and shorter Dt during the proliferative phase compared with the secretory phase (Thomassin-Naggara et al. 2010).

Blood oxygenation level dependent (BOLD) MRI has shown significantly lower T2* values for the JZ compared to that of the outer myometrium and lower T2* values of both JZ and outer myometrium throughout the menstrual cycle, probably related to decreased blood perfusion and subsequently decreased pO2 (Kido et al. 2007).

Uterine zone, age and phase of the menstrual cycle in premenopausal women should be taken into consideration when interpreting the apparent diffusion coefficient (ADC) values of uterine structures (He et al. 2016; Fujimoto et al. 2013; Kido et al. 2010; Tsili et al. 2012; Kuang et al. 2012; Fornasa and Montemezzi 2012; He et al. 2015). Normal ADC is higher for outer myometrium, followed by endometrium and JZ (Fujimoto et al. 2013). A wide variation of ADC for the normal endometrium/myometrium during the different phases of the menstrual cycle has been found. The ADC of the normal endometrium is lower during the menstrual phase when compared with the proliferative and the secretory phases. The ADC is also lower during the proliferative phase when compared with the secretory phase (Figs. 8e and 10b) (Kido et al. 2010; Tsili et al. 2012; Kuang et al. 2012; Fornasa and Montemezzi 2012; He et al. 2015). On the contrary, the ADC of myometrium shows significant increase from menstrual phase to secretory phase (Figs. 8e and 10b) (Tsili et al. 2012; He et al. 2015). The ADC of normal JZ increases with age in premenopausal women (He et al. 2016). During menstrual cycle, ADC of JZ is lower in menstrual phase compared to the secretory phase (He et al. 2016). Histopathologic changes of the normal uterus in premenopausal women explain the variations of the ADC of the endometrium/myometrium during the menstrual cycle. Endometrial discharge consisting of blood and sloughing of stromal and epithelial cells coupled by the torn ends of veins, arteries and glands cause restricted diffusion by the endometrium during the menstrual phase. The presence of large uterine glands and more prominent arteries in stratum functionalis of the normal endometrium and increased interstitial fluid are the possible explanations for the higher ADC of the endometrium during the secretory phase when compared to the proliferative phase. The higher water content of the myometrium during secretory phase also possibly contributes to the higher ADC of the myometrium in this phase.

Diffusion tensor imaging (DTI) of the normal uterus in vivo using 3 T system reveals differences in fibre number, length and orientation (Fiocchi et al. 2012; He et al. 2016; Fujimoto et al. 2013). Anisotropy is found in most parts of the uterine body and two fibre directions have been described: circular and longitudinal, as in ex vivo studies (Fiocchi et al. 2012). Fractional anisotropy (FA) is highest for JZ, followed by outer myometrium and normal endometrium (He et al. 2016). During menstrual cycle, endometrial FA declines (He et al. 2016).

4 Uterine Cervix: Normal CT and MRI Findings

The cervix represents the lower third of the uterus, usually measuring 2–3 cm in length. On axial CT images, the exact boundary between the uterine body and the cervix may be difficult to detect. The oblique orientation of the cervix or the presence of fluid in the vaginal fornices may mimic a mass. Sagittal MPRs, with respect to the orientation of the cervix are helpful in delineating normal cervix, closely mimicking sagittal T2WI (Yitta et al. 2009). After intravenous contrast material administration, the cervix overall usually shows differential or delayed enhancement in comparison with the uterine body. This results in a hypodense appearance and may probably be related to the presence of greater amount of fibrous tissue in the cervix (Fig. 7c) (Yitta et al. 2011).

Dynamic enhancement patterns of the normal uterine cervix at MDCT closely resemble those at MRI (Kaur et al. 1998; Yitta et al. 2011; Yitta et al. 2009). These patterns are seen in women with a type 1 or type 2 uterine enhancement patterns, but not with a type 3. The cervical zonal enhancement of the cervix is typically characterized by early, intense central circumferential enhancement, corresponding to the richly glandular central mucosa, with secondary less intense enhancement of the surrounding inner fibromuscular stroma (Fig. 5b). The outer fibromuscular stroma enhances later, more intensely compared to the inner fibromuscular stroma, but less intensely compared to the central cervical mucosa. The combination of the three layers produces a target-like appearance of the normal cervix on axial images (Kaur et al. 1998; Yitta et al. 2011; Yitta et al. 2009).

Nabothian cysts are essentially benign retention cysts of the cervix, probably due to chronic inflammation. They are usually asymptomatic, more often detected incidentally. At MDCT, nabothian cysts are well-defined cystic structures, with a density similar to that of fluid, of variable size. Sagittal and coronal MPRs show them as well-defined, thin-walled cystic structures, separate from the endocervical canal (Yitta et al. 2011).

On MRI, the cervix and the uterine body can be differentiated, the lower uterine segment (isthmus) creating a gradual separation between the corpus uteri and the cervix (Brown et al. 1991). T2WI delineates the following four discrete zones of the endocervix: the high signal intensity central region of cervical mucus; the high signal intensity endocervix with its mucosal folds; the cervical stroma, which displays a predominantly low T2 signal and is in contiguity with the JZ of the uterus and an intermediate signal intensity outer zone, which is continuous with the outer myometrium (Fig. 14). Both the middle and outer zones correspond to the fibromuscular stroma of the cervix (Brown et al. 1991; Yitta et al. 2011; Togashi et al. 2001; Scoutt et al. 1993; deSouza et al. 1994). The percentage of nuclear area in the inner zone of the fibromuscular stroma is 2.5 times greater than in the outer zone, which may account for

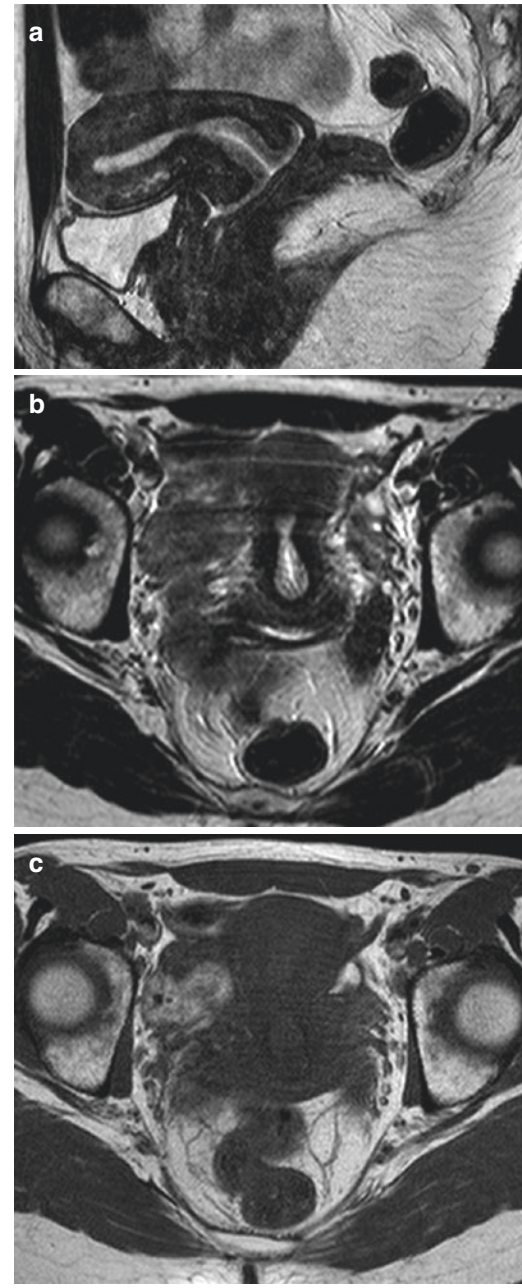

Fig. 14 T2WI in (**a**) sagittal and (**b**) transverse orientation in a healthy premenopausal woman shows normal zonal anatomy of the uterine cervix: mucus in the cervical canal as a stripe of very high signal intensity centrally, the mucosa of the endocervix with high signal intensity, the cervical stroma with predominantly low signal intensity and the outermost layer with intermediate signal intensity. (**c**) Transverse T1WI depicts normal cervix relatively homogeneous, with signal intensity similar to that of the uterine body

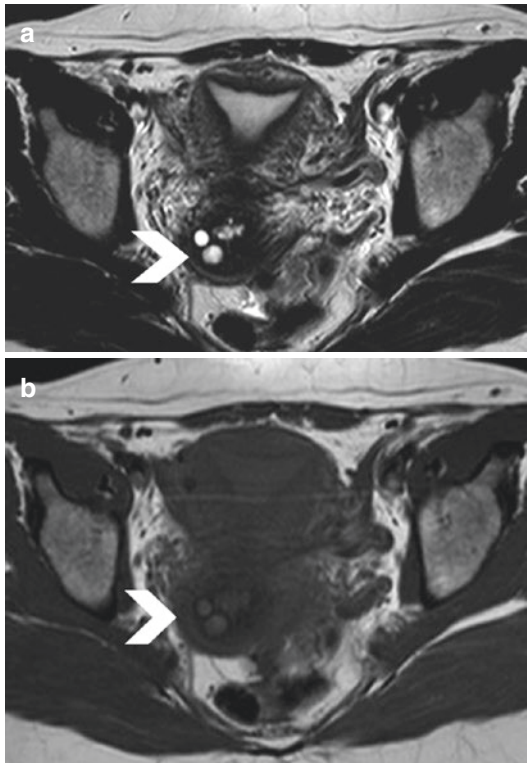

Fig. 15 Axial (**a**) T2WI and (**b**) T1WI showing Nabothian cysts (*arrowhead*)

the lower signal intensity of the inner zone (deSouza et al. 1994). Uterine cervix appears homogeneous, featureless of intermediate signal intensity on TIWI (Fig. 14c) (Brown et al. 1991). Nabothian cysts exhibit intermediate or slightly high T1 signal and prominently high T2 signal (Fig. 15).

The plicae palmatae is a normal endocervical fold, consisting of lateral parts of numerous smaller folds and a large elevation at the midline, which is thought to be a developmental remnant of the Müllerian ductal fusion. It is demonstrated as a longitudinal ridge of distinct low T2 signal at the midline of either anterior and/or posterior wall which protrudes into the cervical canal (Takahata et al. 2009). The prevalence of this finding is reported 44.5–53.2%, more often seen during the fourth decade. The incidence of plicae palmatae is significantly lower in postmenopausal women (Takahata et al. 2009) (Fig. 16).

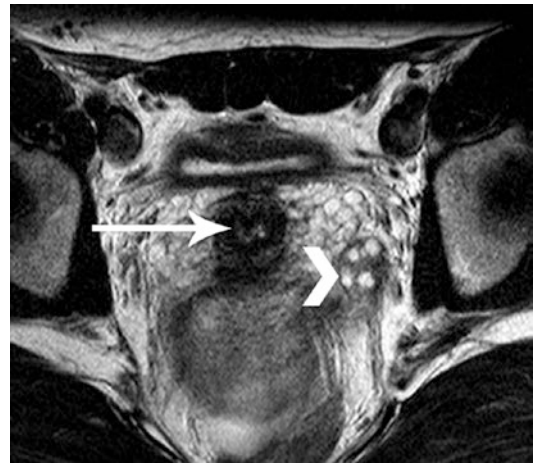

Fig. 16 Axial T2WI in a 24-year-old woman showing plicae palmatae (*long arrow*). Normal left ovary is also seen (*arrowhead*)

The cervix is relatively stable on MRI during the menstrual cycle, although some studies report an increase in thickness of cervical stroma late in the cycle (Fiocchi et al. 2012; Haynor et al. 1986). The configuration of the cervix changes from elongated, seen in the premenarchal and nulliparous female to a wide short cervix of the multiparous women (Brown et al. 1991).

References

Basmajian JV (1971) Grant's method of anatomy. The Williams & Wilkins Co, Baltimore

Brosens JJ, de Souza NM, Barker FG (1995) Uterine junctional zone: function and disease. Lancet 26:558–560

Brown HK, Stoll BS, Nicosia SV, Fiorica JV, Hambley PS, Clarke LP, Silbiger ML (1991) Uterine junctional zone: correlation between histologic findings and MR imaging. Radiology 179:409–413

Demas BE, Hricak H, Jaffe RB (1986) Uterine MR imaging: effects of hormonal stimulation. Radiology 159:123–126

Fiocchi F, Nocetti L, Siopis E, Currá S, Costi T, Ligabue G, Toricelli P (2012) In vivo 3 T MR diffusion tensor imaging for detection of the fibre architecture of the human uterus: a feasibility and quantitative study. Br J Radiol 85:e1009–e1017

Fornasa F, Montemezzi S (2012) Diffusion-weighted magnetic resonance imaging of the normal endometrium: temporal and spatial variations of the apparent diffusion coefficient. Acta Radiol 53:586–590

Foshager MC, Walsh JW (1994) CT anatomy of the female pelvis: a second look. Radiographics 14:51–64

Fujimoto K, Kido A, Okada T, Uchikoshi M, Togashi K (2013) Diffusion tensor imaging (DTI) of the normal human uterus in vivo at 3 tesla: comparison of DTI parameters in the different uterine layers. J Magn Reson Imaging 38:1494–1500

Grossman J, Ricci ZJ, Rozenblit A, Freeman K, Mazzariol F, Stein MW (2008) Efficacy of contrast-enhanced CT in assessing the endometrium. AJR 191:664–669

Hauth EAM, Jaeger HJ, Libera H, Lange S, Forsting M (2007) MR imaging of the uterus and cervix in healthy women: determination of normal values. Eur Radiol 17:734–742

Haynor DR, Mack LA, Soules MR, Shuman WP, Montana MA, Moss AA (1986) Changing appearance of the normal uterus during the menstrual cycle: MR studies. Radiology 161:459–462

He Y, Ding N, Li Y, Li Z, Xiang Y, Jin Z, Xue H (2015) 3-T diffusion tensor imaging (DTI) of normal uterus in young and middle-aged females during the menstrual cycle: evaluation of the cyclic changes of fractional anisotropy (FA) and apparent diffusion coefficient (ADC) values. Br J Radiol 88:20150043

He YL, Ding N, Li Y, Li Z, Xiang Y, Jin ZY, Xue HD (2016) Cyclic changes of the junctional zone on 3 T MRI images in young and middle-aged females during the menstrual cycle. Clin Radiol 71:341–348

Hricak H, Kim B (1993) Contrast-enhanced MR imaging of the female pelvis. J Magn Reson Imaging 3:297–306

Hricak H, Alpers C, Crooks LE, Sheldon PE (1983) Magnetic resonance of the female pelvis: initial experience. Airman 141:1119–1128

Kaur H, Loyer EM, Minami M, Charnsangavej C (1998) Patterns of uterine enhancement with helical CT. Eur J Radiol 28:250–255

Kido A, Koyama T, Kataoka M, Yamamoto A, Saga T, Turner R, Togashi K (2007) Physiological changes of the human uterine myometrium during menstrual cycle: preliminary evaluation using BOLD MR imaging. J Magn Reson Imaging 26:695–700

Kido A, Kataoka M, Koyama T, Yamamoto A, Saga T, Togashi K (2010) Changes in apparent diffusion coefficients in the normal uterus during different phases of the menstrual cycle. Br J Radiol 83:524–528

Kormano MJ, Goske MJ, Hamlin DJ (1981) Attenuation and contrast enhancement of gynecologic organs and tumors in CT. Eur J Radiol 1(4):307–311

Kuang F, Ren J, Huan Y, Chen Z, Zhong Q (2012) Apparent diffusion coefficients of normal uterus in premenopausal women with 3.0-T magnetic resonance imaging. J Comput Assist Tomogr 36:54–59

Langer JE, Oliver ER, Lev-Toaff AS, Coleman BG (2012) Imaging of the female pelvis through the life cycle. Radiographics 32:1575–1597

Lim PS, Nazarian LN, Wechsler RJ, Kurtz AB, Parker L (2002) The endometrium on routine contrastenhanced CT in asymptomatic postmenopausal women: avoiding errors in interpretation. Clin Imaging 26:325–329

Mann GS, Blair JC, Garden AS (2012) Imaging of gynecological disorders in infants and children. Springer-Verlag, Berlin Heidelberg

Masui T, Katayama M, Kobayashi S, Nakayama S, Nozaki A, Kabasawa H, Ito T, Sakahara H (2001) Changes in myometrial and junctional zone thickness and signal intensity: demonstration with kinematic T2-weighted MR imaging. Radiology 221:75–85

McCarthy S, Tauber C, Gore J (1986) Female pelvic anatomy: MR assessment of variations during the menstrual cycle and with use of oral contraceptives. Radiology 160:119–123

Novellas S, Chassang M, Delotte J, Toullalan O, Chevallier A, Bouaziz J, Chevallier P (2011) MRI characteristics of the uterine junctional zone: from normal to the diagnosis of adenomyosis. AJR Am J Roentgenol 196:1206–1213

Punwani S (2011) Diffusion weighted imaging of female pelvic cancers: concepts and clinical applications. Eur J Radiol 78:21–29

Sala E, Rockall AG, Freeman SJ, Mitchell DG, Reinhold C (2013) The added role of MR imaging in treatment stratification of patients with gynecologic malignancies: what the radiologist needs to know. Radiology 266:717–740

Scoutt LM, McCauley TR, Flynn SD, Luthringer DJ, McCarthy SM (1993) Zonal anatomy of the cervix: correlation of MR imaging and histologic examination of hysterectomy specimens. Radiology 186:159–162

Siddall KA, Rubens DJ (2005) Multidetector CT of the female pelvis. Radiol Clin N Am 43:1097–1118

deSouza NM, Hawley IC, Schwieso JE, Gilderdale DJ, Soutter WP (1994) The uterine cervix on in vitro and in vivo MR images: a study of zonal anatomy and vascularity using an enveloping cervical coil. Am J Roentgenol 163:607–612

Takahata A, Koyama T, Kido A, Kataoka M, Umeoka S, Nishizawa S, Nishimura T, Togashi K (2009) The frequency of the plicae palmatae in the uterine cervix on MR imaging. Abdom Imaging 34:277–279

Takeuchi M, Matsuzaki K, Nishitani H (2010) Manifestations of the female reproductive organs on MR images: changes induced by various physiologic states. Radiographics 30:1147

Thomassin-Naggara I, Balvay D, Cuenod CA, Daraï E, Marsault C, Bazot M (2010) Dynamic contrast-enhanced MR imaging to assess physiologic variations of myometrial perfusion. Eur Radiol 20:984–994

Togashi K, Kawakami S, Kimura I, Asato R, Okumura R, Fukuoka M, Mori T, Konishi J (1993a) Uterine contractions: possible diagnostic pitfall at MR imaging. J Magn Reson Imaging 3:889–893

Togashi K, Kawakami S, Kimura I, Asato R, Takakura K, Mori T, Konishi J (1993b) Sustained uterine contractions: a cause of hypointense myometrial bulging. Radiology 187:707–710

Togashi K, Nakai A, Sugimura K (2001) Anatomy and physiology of the female pelvis: MR imaging revisited. J Magn Reson Imaging 3:842–849

Tsili AC, Argyropoulou MI, Tzarouchi L, Dalkalitsis N, Koliopoulos G, Paraskevaidis E, Tsampoulas K (2012)

Apparent diffusion coefficient values of the normal uterus: interindividual variations during menstrual cycle. Eur J Radiol 81:1951–1956

Yamashita Y, Harada M, Sawada T, Takahashi M, Miyazaki H, Okamura H (1993) Normal uterus and FIGO stage I endometrial carcinoma: dynamic gadolinium-enhanced MR imaging. Radiology 186: 495–501

Yitta S, Hecht EM, Slywotzky CM, Bennett GL (2009) Added value of multiplanar reformation in the multidetector CT evaluation of the female pelvis: a pictorial review. Radiographics 29:1987–2005

Yitta S, Hecht EM, Mausner EV, Bennett GL (2011) Normal or abnormal? Demystifying uterine and cervical contrast enhancement at multidetector CT. Radiographics 31:647–666

Congenital Malformations of the Uterus

Justus Roos, Gligor Milosevic, Martin Heubner, and Rahel A. Kubik-Huch

Contents

Abstract

Congenital malformations of the uterus, also termed Müllerian duct anomalies (MDA), are an uncommon, but often treatable, cause of infertility. Estimates of its frequency vary widely owing to different patient populations, nonstandardized classification systems, and differences in diagnostic data acquisition. Because normal pregnancies can occur in women with MDA and the anomalies are mostly discovered in cases of patients presenting with infertility, the reported prevalence of MDA in the general population is probably underestimated.

1 Clinical Background

1.1 Epidemiology

Congenital malformations of the uterus, also termed Müllerian duct anomalies (MDA), are an uncommon, but often treatable, cause of infertility. Estimates of its frequency vary widely owing to different patient populations, nonstandardized classification systems, and differences in diagnostic data acquisition. Because normal pregnancies can occur in women with MDA and the anomalies are mostly discovered in cases of patients presenting with infertility, the reported prevalence of MDA in the general population is probably underestimated.

The overall published data suggest a prevalence range of uterovaginal anomalies of around

J. Roos, MD
Institute of Radiology, Luzerner Kantonsspital, CH-6000, Luzern, Switzerland

G. Milosevic, MD • R.A. Kubik-Huch, MD, MPH (✉)
Institute of Radiology, Kantonsspital Baden AG, CH-5404, Baden, Switzerland
e-mail: rahel.kubik@ksb.ch

M. Heubner, MD
Department of Gynaecology and Obstetrics, Kantonsspital Baden AG, CH-5404, Baden, Switzerland

Med Radiol Diagn Imaging (2017)
DOI 10.1007/174_2017_1, © Springer International Publishing AG
Published Online: 11 February 2017

1–10% (Acién 1997; Ashton et al. 1988; Homer et al. 2000; Raga et al. 1997; Saleem 2003; Simón et al. 1991; Troiano and McCarthy 2004; Chan et al. 2011a) in the general population among women with normal and abnormal fertility. Arcuate and septate uteri appear to be the most common malformations in an unselected population (Dreisler and Stampe 2014). While conceiving is a minor problem for the majority of women with MDA, the risk of pregnancy loss is truly associated with MDA. Its prevalence in women with repeated miscarriage is considered to be around 5–13% (Homer et al. 2000; Raga et al. 1997; Chan et al. 2011a; Clifford et al. 1994; Nahum 1998; Raziel et al. 1994) and up to 25% in women with combined infertility and recurrent miscarriage (Chan et al. 2011a). No racial predilection is noted in the literature.

1.2 Clinical Presentation

Mild forms of MDA, especially arcuate uteri, may never be diagnosed. Major forms of MDA may become clinically evident at different ages depending on their specific characteristics and associated disorders. The distribution among the different classes of MDA and their clinical presentations is summarized in Table 1. In the newborn/infant age, an initial presentation of a palpable abdominal or pelvic mass due to a uterine or/and vaginal obstruction causing intraluminal fluid retention is possible. In the adolescent age group, a delayed menarche or primary amenorrhea with or without fluid retention in the uterus (hematometra) and/or vagina (hematocolpos) may present as a painful intra-abdominal tumor in case of obstruction or complete obliteration. Some patients also have cyclical pain, usually due to retrograde menstruation through the fallopian tubes. The most common MDA often become significant for the first time in the childbearing age. Patients can present with various problems of infertility, repeated spontaneous abortions, premature delivery, fetal intrauterine growth retardation, and difficulties during delivery like breech presentation or transverse lie (Zlopasa et al. 2007).

By understanding the defective embryological development, one can understand the potential for the presence of associated congenital malformations of other organ systems. Most frequently, renal malformations like renal agenesis or ectopia can occur. Much less frequent are bony malformations – most of them occur in a complex of varying symptoms – like abnormal scapula, supernumerary or fused ribs, vertebral malsegmentation, fusion of the vertebral column (i.e., Klippel–Feil syndrome), and radiocarpal hypoplasia. The nonrandom association

Table 1 Distribution among the different classes of MDA and their clinical presentations

Müllerian duct anomalies (MDA)	Influence on reproductive/obstetric outcome			Other major associations
	Spontaneous abortion	Premature delivery	Fetal survival rate	
Class I: Dysplasia (4–10%)	No potential for reproduction			
Class II: Unicornuate uterus (5–20%)	50%[a] (41–62%)	15% (10–20%)	40% (38–57%)	Renal agenesis 67%
Class III: Uterus didelphys (5–11%)	45% (32–52%)	38% (20–45%)	55% (41–61%)	Longitudinal vaginal septum 75%
Class IV: Bicornuate uterus (10–39%)	30% (28–35%)	20% (14–23%)	60% (57–63%)	High cervical incompetence 38%
Class V: Septate uterus (34–55%)	65% (26–94%)	20% (9–33%)	30% (10–75%)	Vaginal septum 25%
Class VI: Arcuate uterus (7%)	Mostly compatible with normal-term gestation			
Class VII: DES-exposed uterus	Increased	Increased	Decreased	Cervical anomalies 44%

All percentage data are pooled from the current literature (Simón et al. 1991; Troiano and McCarthy 2004; Nahum 1998; Rennell 1979; Chan et al. 2011b); values in brackets represent percentage ranges

of MDA, renal agenesis/ectopia, and cervicothoracic somite dysplasia are subsumed under the so-called MURCS associations (Pittock et al. 2005). Although other malformations such as cardiac defects have been described, it remains unclear if some of the associated malformations are caused in the same development field or if early exposure to teratogenic agents was causative (Pittock et al. 2005). The literature does not show increased mortality for patients carrying an MDA compared to the general population, whereas the morbidity may be increased in some specific types of MDA causing obstructed Müllerian systems with the presence of hematosalpinx (retention of blood in the fallopian tubes), hematocolpos (retention of blood in the vagina), or retrograde menses causing the potential problem of endometriosis.

Once an MDA is suggested based on evidence from patient history and physical examination, the next diagnostic step includes an imaging workup, which often detects the underlying anomaly and guides further (surgical) interventions. Apart from the precise anatomic evaluation of the female genital tract, attention should be paid to associated malformations (e.g., of ureter or pelvic vessels), as this additional information might impact upon therapeutic measures, especially reconstructive or corrective surgery.

1.3 Embryology

The understanding of the embryogenesis of the urogenital female tract is of paramount importance to understand the pathogenesis of the different types of MDA. The female reproductive system develops from the two paired Müllerian ducts (synonym: paramesonephric ducts) that start off in the embryonal mesoderm lateral to each Wolffian duct (synonym: mesonephric duct). The paired Müllerian ducts develop in medial and caudal directions, and the cranial part remains nonfused and forms the fallopian tubes. The caudal part fuses to a single canal forming the uterus and the upper two thirds of the vagina. This is called lateral fusion. In a process called vertical fusion, the intervening midline septum of both ducts undergoes regression. The caudal part of the vagina arises from the sinovaginal bulb and fuses with the lower fused Müllerian ducts. The ovaries originate from the gonadal ridge, a completely different tissue than the mesoderm, forming both the urinary and genital systems. Hence, associated malformations of the kidney, but not of the ovaries, are frequently observed together with MDA. Pathogenesis of Müllerian duct anomalies can be basically classified into the presence of agenesis, hypoplasia, and defects in vertical and lateral fusion of the paired ducts.

In 1988, the American Society for Reproductive Medicine (ASRM; formerly known as American Fertility Society) (1988) presented a consensus in classification of uterovaginal anomalies and published a schematization system that is widely accepted among specialists. Other used classification systems are referenced (Buttram and Gibbons 1979; Rock and Schlaff 1985; Rock 2000). A more recent classification was proposed in 2013 by the European Society of Human Reproduction and Embryology (ESHRE) and the European Society for Gynaecological Endoscopy (ESGE) (Grimbizis et al. 2013), in an attempt to improve the characterization of anomalies which did not fit into any group of the older classifications. Its reliability in clinical practice and effect on reproductive outcome still warrant further scientific evaluation, as it has been reported to lead to possible overdiagnosis and unnecessary operative treatment of septate uteri in cases which would have been classified as normal or arcuate uteri according to the ASRM classification (Ludwin and Ludwin 2015).

Although most Müllerian duct anomalies occur sporadically, there is a known association with in utero exposure to teratogenic agents such as diethylstilbestrol (DES) or thalidomide (Kaufman et al. 2000). Currently there are no known specific patterns of inheritance.

1.4 Pathology

Whatever steps in embryogenesis are defective, different types of MDA can occur. The ASRM

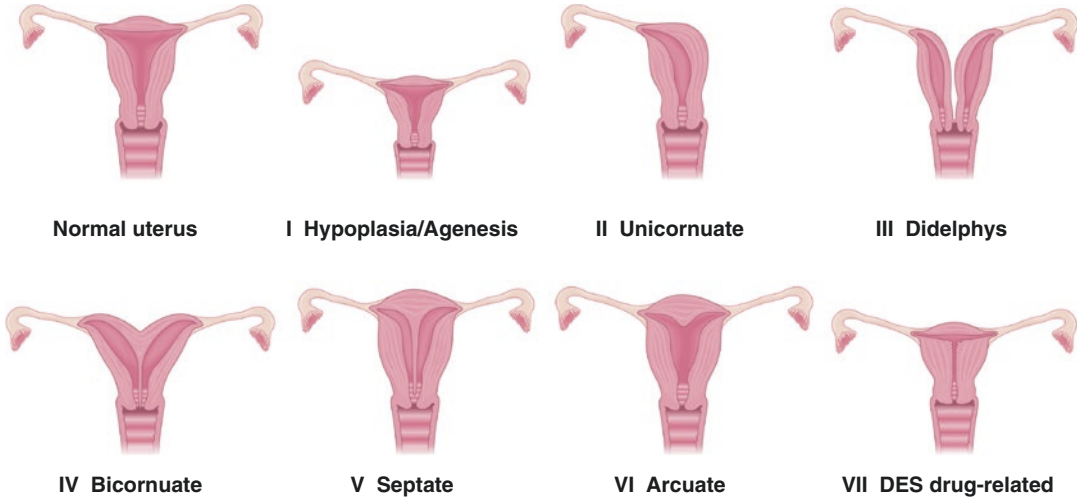

Fig. 1 Classification system of Müllerian duct anomalies (American Society for Reproductive Medicine) (1988)

introduced a classification system in 1988 (1988) that stratifies MDA into seven different classes of uterine anomalies (Fig. 1). It is based on a previous classification system introduced by Buttram et al. (Buttram and Gibbons 1979). Other classification systems followed and included broader collections of anomalies in order to avoid conflicting observations and oversimplicity (Rock 2000; Grimbizis et al. 2013). With all classification systems, one must emphasize that with the overlap of associated cervical and vaginal anomalies, the classifications describe primarily the uterine defects, whereas cervicovaginal defects as well as associated malformations must be added separately in the form of a subset. The distribution among the different classes of MDA and their clinical presentations is summarized in Table 1. The diagnosis of MDA is based upon the clinical presentation, physical examination, and subsequent imaging workup with different imaging methods available, of which magnetic resonance imaging (MRI) takes a leading role, especially in complex uterine malformation (Minto et al. 2001; Olpin and Heilbrun 2009). For the following descriptions of the specific pathologies, we use the ASRM classification system and provide definitions of the different types of MDA in the imaging section.

2 Imaging

2.1 Technique

Once an MDA is suggested based on evidence from patient history and physical examination, the next diagnostic step includes different imaging workups in order to detect and specify MDA and to guide further treatment options. Before ultrasound (US) and MRI were capable of visualizing MDA with a high accuracy, imaging of MDA was limited to hysterosalpingography (HSG) (Krysiewicz 1992), a fluoroscopic spot film technique in combination with endoluminal filling of the uterine cavity with radiopaque contrast agent. Since the diagnostic imaging properties of MDA include mainly the configuration of the endometrial cavity and the external uterine contour, HSG is able to depict only certain types of MDA, whereas it fails in other cases and stays nonspecific for precise diagnosis, the latter mainly due to the lack of the visualization of the outer uterine contour. Because of this drawback, HSG did not provide diagnoses with high degrees of confidence and US and MRI soon began to play a larger role in assessment and treatment of patients. As HSG provides, besides the morphological, also the functional information of tubal

patency, it may still be used in the primary imaging workup in case of infertility clarification. A newer technique using MR for the visualization of the tubal patency, the so-called 3D MR-HSG, avoids exposure of the ovaries to ionizing radiation and has been found to be a reliable imaging alternative to conventional HSG in a couple of smaller studies (Winter et al. 2010; Ma et al. 2012). Nevertheless, it is not widely used due to the better availability of saline contrast hysterosonography (see below).

Nowadays, the first imaging modality in the MDA assessment includes pelvic US (Byrne et al. 2000; Goldberg et al. 1997) – (1) transabdominal US (performed with a 2.5- to 5-Mhz probe) for evaluation of the entire abdomen, especially for associated renal malformations, and (2) transvaginal US (performed with a 5- to 8-Mhz endovaginal probe) for better delineation of the uterus, vagina, and ovaries. Hysterosonography, a technique consisting of transvaginal US with prior infusion of saline or ultrasound contrast agent into the endometrial canal, further increases the delineation of the endometrial cavity. It is performed only for selected indications, i.e., in patients with a history of infertility. US is highly accurate for the detection of MDA (Pellerito et al. 1992). Newer techniques, such as 3D US (Wu et al. 1997; Bermejo et al. 2010), even further improved the imaging diagnostics by giving better information about the external contour of the uterus and its volume.

Magnetic resonance imaging (MRI) is today considered standard in the evaluation of MDA and accepted as the leading imaging modality for further surgical planning (Behr et al. 2012; Steinkeler et al. 2009; Robbins et al. 2012). MRI provides high-resolution images of the entire uterine anatomy (internal and external contour), as well as of secondary findings like renal malformations. Among the three major imaging methods, MRI has the best accuracy in the evaluation of uterine anomalies and accuracies of up to 100% have been reported (Pellerito et al. 1992; Carrington et al. 1990).

According to the author's institution's imaging protocol (Siemens Magnetom Aera, 1.5-Tesla MR unit, Siemens Medical; Erlangen, Germany) for the assessment of congenital uterine anomalies, MRI of the uterus includes six basic native sequences without intravenous contrast using a bodyflex phased-array MR surface coil as shown in Table 2.

If possible, patients should be scheduled in the second half of the menstrual cycle, since the thickness of the endometrial stripe increases

Table 2 MR imaging protocol for assessment of MDA

Sequence	Region	Slice thickness (mm)	Slice spacing (%)	Matrix	TR (ms)	TE (ms)	Flip angle (°)	Field of view (mm)
TRUFISP coronal	Abdomen	6	20	256 × 256	3.45	1.73	70	400 × 400
TRUFISP fs axial	Abdomen	6	20	256 × 256	4.64	2.32	70	360 × 292
T2 TSE sagittal	Pelvis	4	30	384 × 384	4000	90	150	210 × 210
T2 TSE axial oblique	Pelvis	4	20	384 × 384	3500	100	150	210 × 210
T2 TSE coronal oblique	Pelvis	4	20	384 × 384	3500	100	150	210 × 210
T1 VIBE Dixon axial	Pelvis	2.5	20	320 × 320	7.2	2.39 4.77	12	240 × 240

Exemplary protocol from the authors' institution, performed on a 1.5 T MR-Unit (Siemens Medical, Germany)
TRUFISP "fast induction steady state potential" gradient sequence; *TSE* turbo spin echo; also known as *FSE* fast spin echo; *VIBE* Volumetric Interpolated Breath Hold Examination; *TR* repetition time; *TE* time to echo; *coronal oblique*, parallel to the long axis of the uterus; *axial oblique*, parallel to the short axis of the uterus

during the follicular and secretory phase and thus the normal zonal anatomy of the uterus can be better appreciated. No specific patient preparation is necessary. It may be debated if the application of a tampon by the patient or endovaginal administration of sterile gel prior to the examination might be helpful to delineate the vaginal lumen in selected cases. Intravenous injection of antiperistaltic agents like glucagon or scopolamine butylbromide (Buscopan®) can be performed to reduce artifacts caused by intestinal motion.

Native axial T1-weighted sequences are standard techniques for the assessment of the female pelvis. In this patient population with suspected MDA, they are mainly performed in order not to miss any associated pathologies, e.g., ovarian disease or peritoneal implants in endometriosis. In addition, the demonstration of hemorrhage within the endometrial cavity (hematometra) and/or vagina (hematocolpos) benefits from T1-weighted imaging. High-resolution T2-weighted images are most important for the assessment of the uterus. Sagittal sections are best suited to image the uterus and its zonal anatomy. Additional oblique sections parallel to the endometrial cavity results in a long-axis view, which is most helpful for imaging the fundal contour. An oblique sequence obtained perpendicular to the cervical canal results in a short-axis view and allows accurate assessment of the cervix, i.e., the diagnosis of duplication or septation. The protocol further includes fast sequences of the upper abdomen in axial and coronal orientation to diagnose or exclude renal pathology.

2.2 Classes of Müllerian Duct Anomalies (MDA)

The percentage distribution of the different MDA classes and their influence on reproductive and obstetric outcome, as well as their major associations, are summarized in Table 1.

2.2.1 Class I Anomalies: Dysgenesis

Definition: Dysgenesis (segmental agenesis and variable hypoplasia) of the Müllerian ducts (uterus and upper two thirds of the vagina) (Pittock et al. 2005; Strübbe et al. 1993) (Fig. 2). Mayer–Rokitansky–Küster syndrome is the most common form of Class I anomaly and includes agenesis of uterus and vagina.

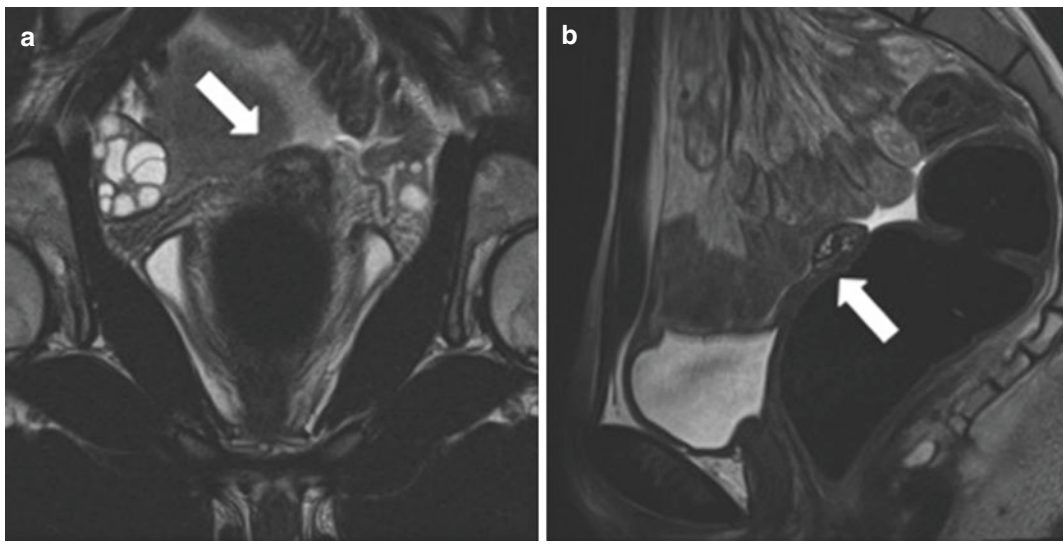

Fig. 2 (**a**–**d**) Two patients with primary amenorrhea. In both cases, MRI showed a small fibrous uterine remnant (*arrow*), consistent with Mayer–Rokitansky–Küster Syndrome

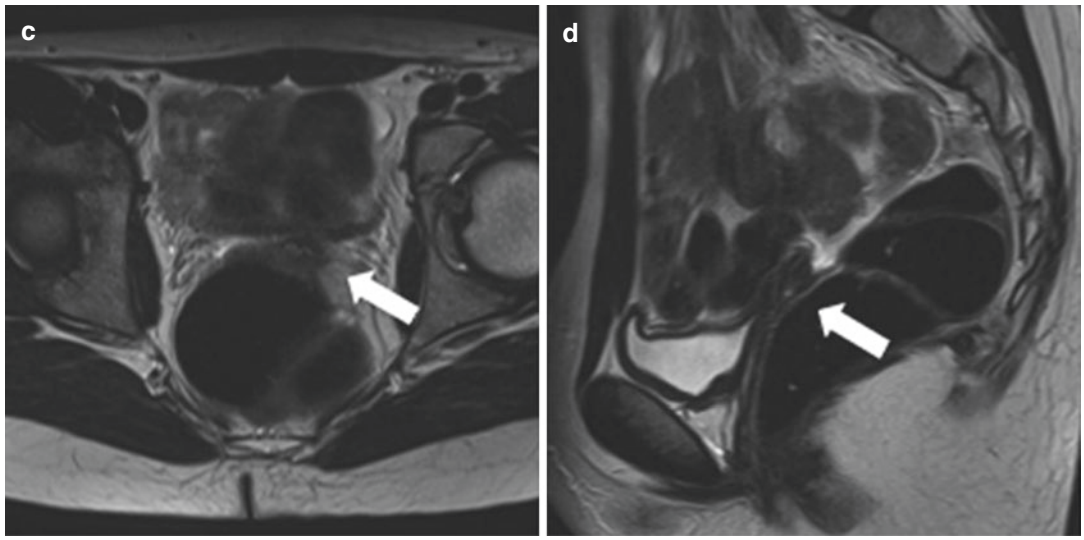

Fig. 2 (continued)

2.2.2 Class II Anomalies: Unicornuate Uterus

Definition: Unicornuate uterus is the result of partial or complete hypoplasia of one Müllerian duct (Brody et al. 1998) (Fig. 3).

Unicornuate uterus may be isolated (35%) or associated with a contralateral rudimentary horn. These rudimentary horns present with or without communication to the endometrial cavity and may or may not contain endometrium, the latter variant being also called no cavity rudimentary horn. In patients with cavity noncommunicating rudimentary horn, dysmenorrhea and hematometra may occur. Surgical resection to either relieve symptomatic pain or to reduce the risk of potential ectopic pregnancy is justified. As with every obstructed system, the risk of endometriosis is also increased with a noncommunicating rudimentary horn. Renal malformations are common with unicornuate uterus and occur mostly on the same side as the rudimentary horn is found.

2.2.3 Class III Anomalies: Uterus Didelphys

Definition: Uterus didelphys is the result of complete nonfusion of the Müllerian ducts forming a complete uterine duplication with no communication between each other (Carrington et al. 1990; Fedele et al. 1989; Fedele et al. 1988) (Fig. 4).

Uterus didelphys may be associated with a longitudinal (75%) or, more rarely, a transverse vaginal septum, the latter causing obstructive hematometrocolpos of one uterine horn. Renal agenesis might occur in these patients and are usually located on the same side as the septum. Endometriosis, as a result of retrograde menstruation, may also be an issue in these conditions. A nonobstructive uterus didelphys is usually asymptomatic.

2.2.4 Class IV Anomalies: Bicornuate Uterus

Definition: Bicornuate uterus is the result of incomplete fusion of the cranial parts of the Müllerian ducts (Pellerito et al. 1992; Toaff et al. 1984) (Fig. 5).

Two uterine cavities with normal zonal anatomy can be depicted. The leading imaging feature is a fundal cleft greater than 1 cm of the external uterine contour that helps to distinguish bicornuate uterus from septate uterus.

Bicornuate uterus occurs with wide variability. Extension of the intervening fundal cleft to the internal cervical os characterizes the complete bicornuate uterus with a single cervix (bicornuate,

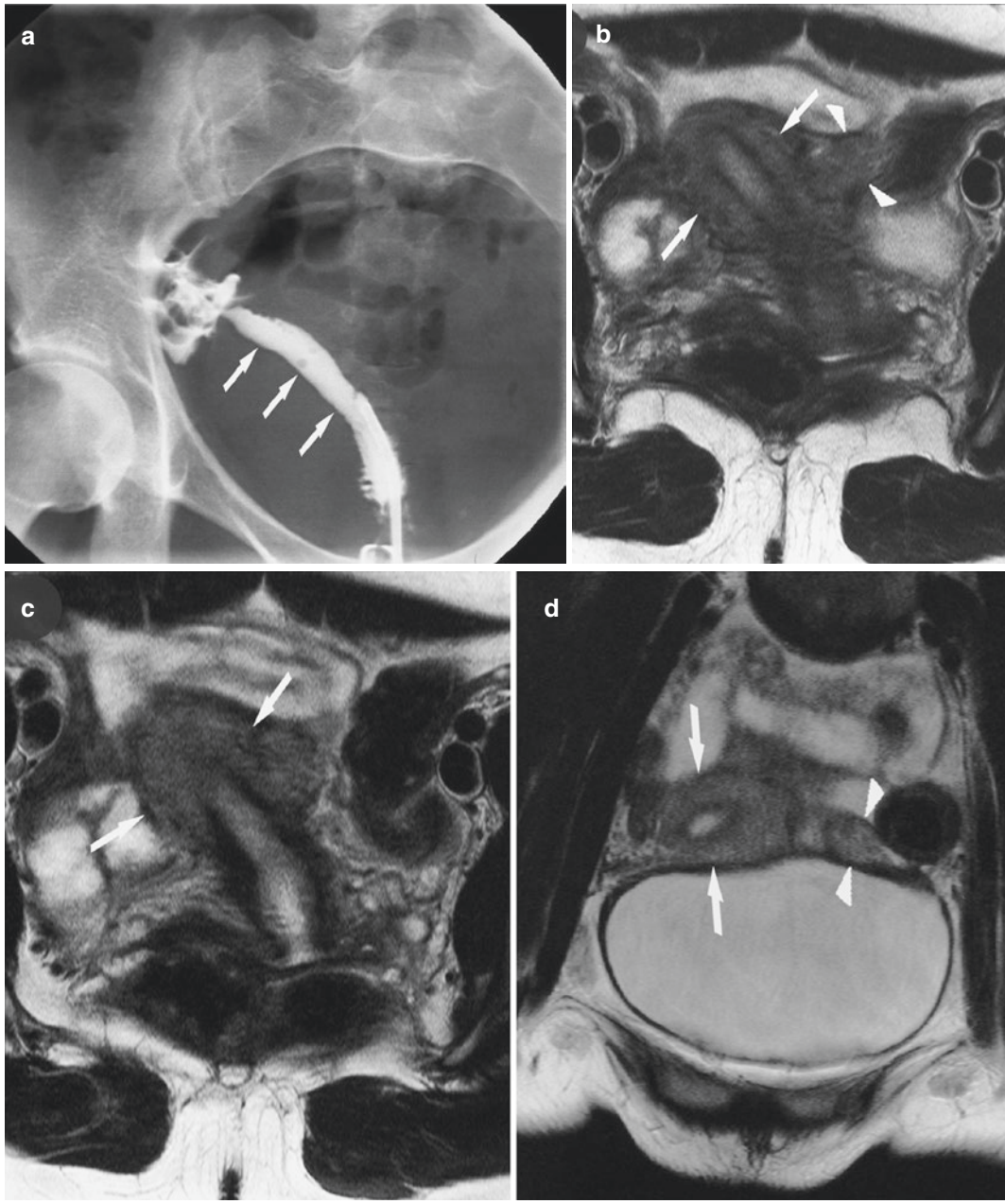

Fig. 3 (**a**–**d**) A 28-year-old female patient with infertility. HSG (**a**) shows a fusiform "banana-shaped" configuration of one small endometrial cavity (*arrows*) that is deviated to the right and drains into one fallopian tube. Note the absence of the normal triangular appearance of the fundal cavity. This configuration is highly suggestive of the presence of a unicornuate uterus. Iatrogenic filling defects in the uterine cavity by air bubbles. Oblique T2-weighted MR images (**b**, **c**) and coronal T2-weighted MR image (**d**) confirm the diagnosis of a unicornuate uterus with the presence of a small elongated uterus that shows normal zonal anatomy (*arrows*). A rudimentary horn with low signal intensity and no zonal anatomy – thus corresponding to a rudimentary horn with no endometrium – can be depicted on the right side (*arrowheads*). No surgical resection is needed in this case

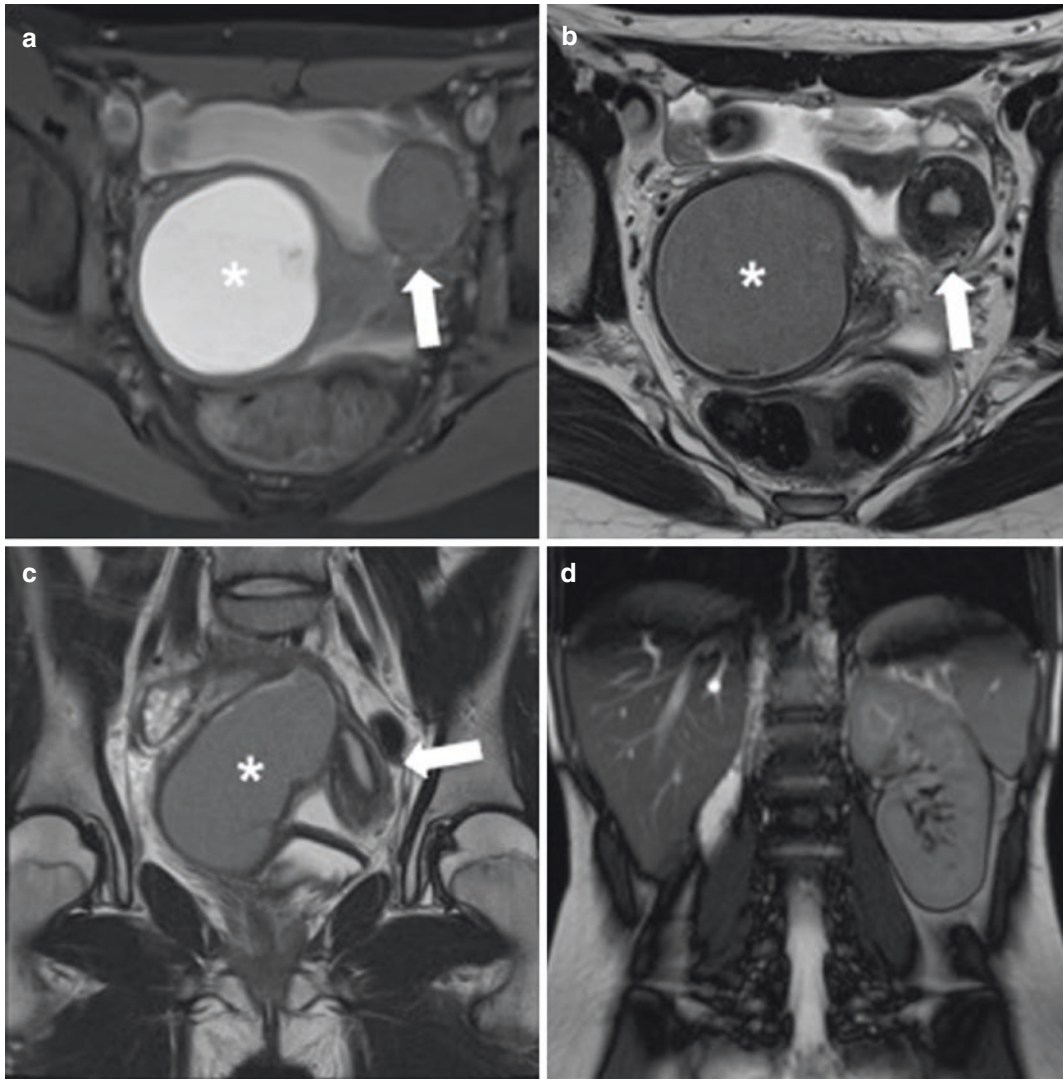

Fig. 4 (**a**, **b**) A 14-year-old female patient with abdominal pain. MRI shows uterine fusion anomaly with two separate cavities, the right one markedly dilated (asterisk) due to retention of blood caused by an obstructing septum ((**a**): axial T1-weighted image with fat suppression; (**b**, **c**): axial and coronal T2-weighted images); the left cavity shows a normal zonal anatomy (*arrow*). Coronal TRUFISP shows associated agenesis of the right kidney (**d**). Schematic drawing shows uterus didelphys with an obstructing septum on the right side (medical illustrator: W. Herzig) (**e**)

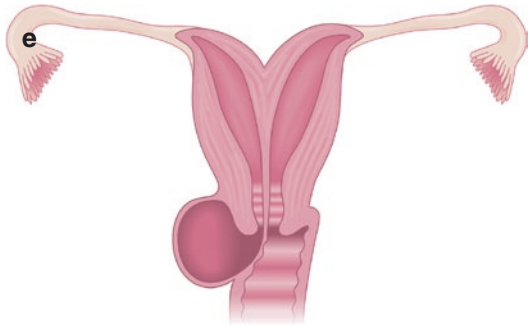

Fig. 4 (continued)

unicollis uterus), whereas variants of partial bicornuate uterus exist if the cleft is of variable length. Bicornuate uterus may be associated with a duplicated cervix (bicornuate bicollis uterus), as well as with a longitudinal vaginal septum that coexists in up to 25% of bicornuate uterus. Nevertheless, a degree of communication is always present between both uterine cavities. Still controversial is the need for surgical intervention, and it is probably only necessary in specific cases. A higher rate of cervical incompetence seems to be associated with bicornuate uterus.

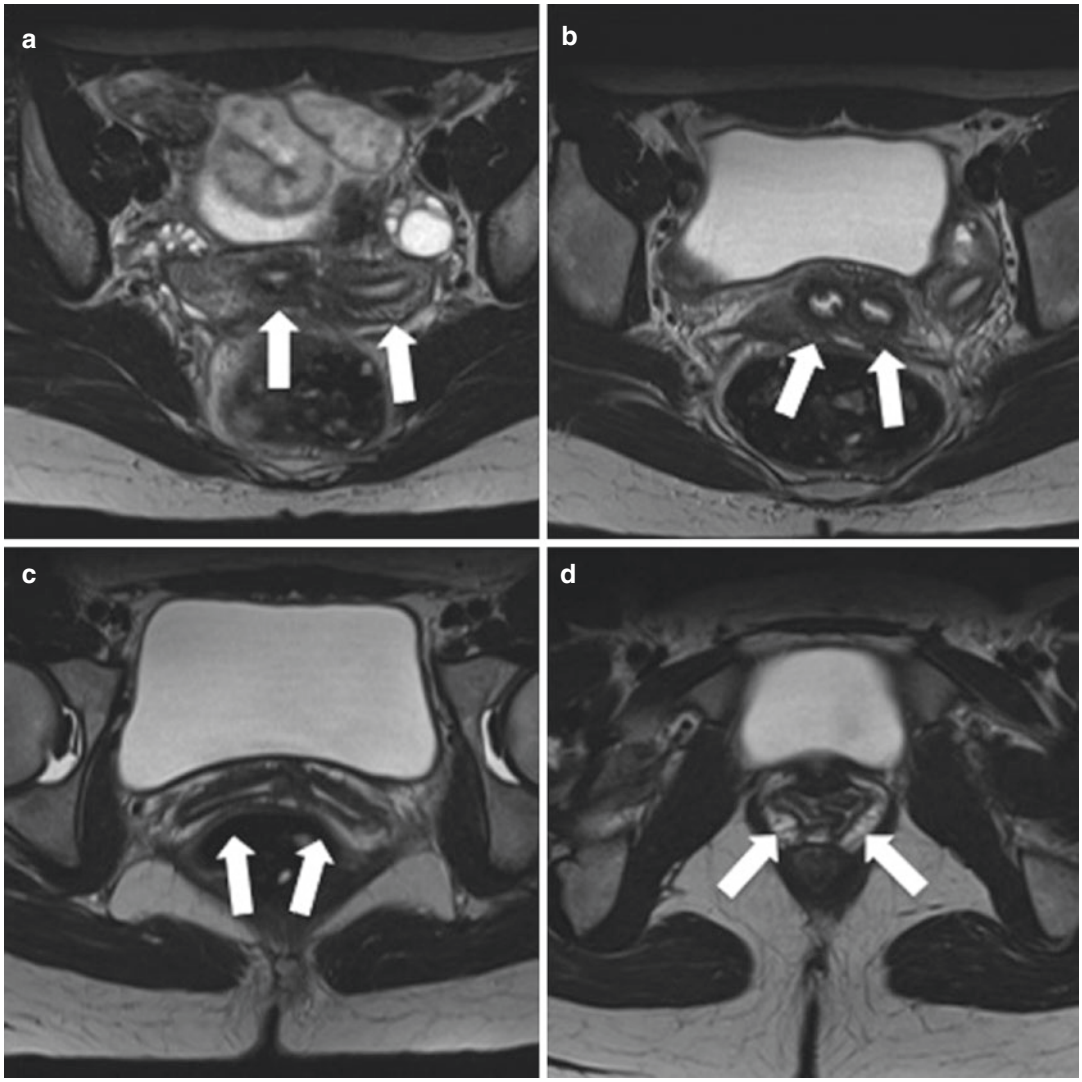

Fig. 5 (**a**–**d**) MRI in a 29-year-old female patient shows uterus didelphys with two separate uterine cavities, cervices, and upper part of the vagina (*arrows*) without an associated obstructing septum

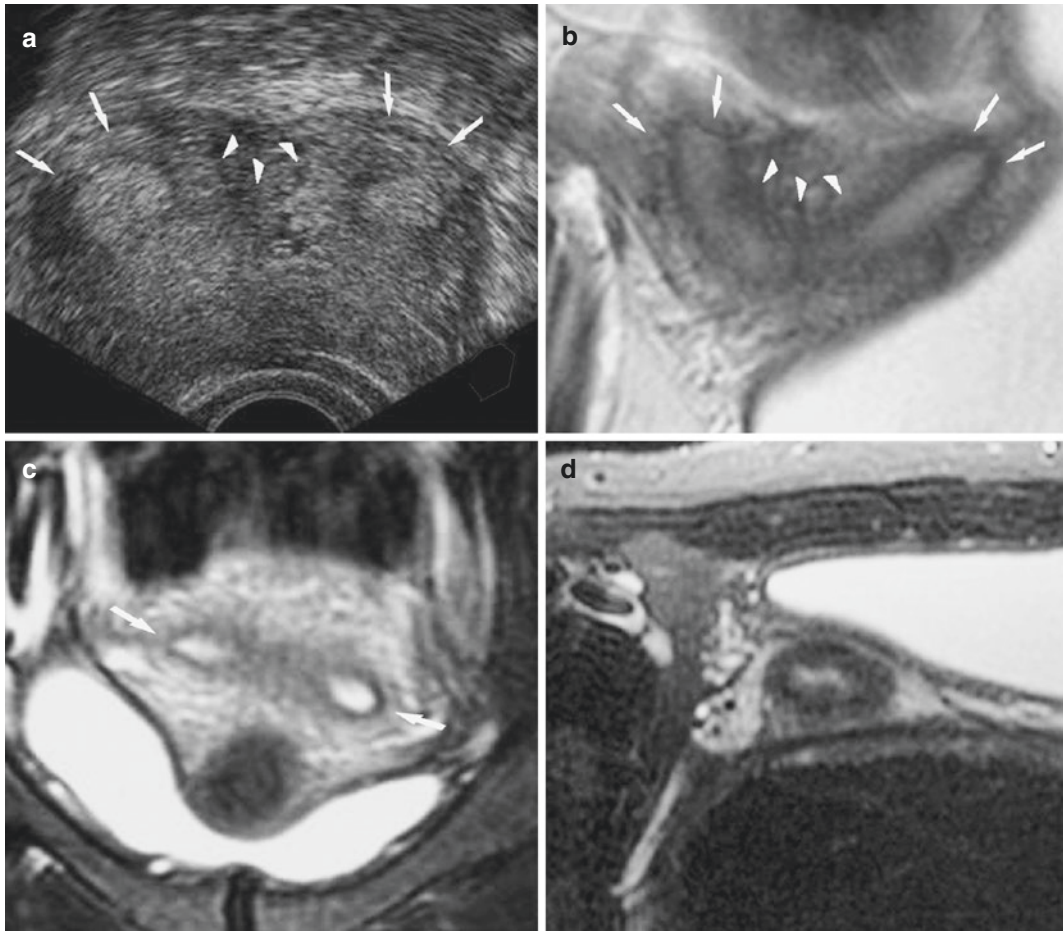

Fig. 6 (**a**–**d**) A 17-year-old female patient. Transvaginal US (**a**) depicts two endometrial cavities (*arrows*) in the coronal plane consisting of a hyperechogenic endometrial stripe and a hypoechogenic myometrial layer. An intervening external fundal cleft was visible during the examination by interactively turning the image plane (*arrowheads*). The highly suspected presence of a bicornuate uterus was confirmed by MR with a coronal T2-weighted image (**b**) showing two uterine cavities (*arrows*) separated by a deep external fundal cleft (*arrowheads*). In the same image plane, the separation of both cavities (*arrows*) are visible to the level of the internal cervical os (**c**) before they conjoin to one single cervix (**d**) as shown in a T2-weighted axial image (bicornuate, unicollis uterus)

2.2.5 Class V Anomalies: Septate Uterus

Definition: Septate uterus is the result of partial or complete nonregression of the midline uterovaginal septum (Pellerito et al. 1992; Carrington et al. 1990; Fedele and Bianchi 1995; Fedele et al. 1996; Reuter et al. 1989; Valle 1996) (Fig. 6). The main imaging feature is that the external contour of the uterine fundus may be either convex or mildly concave (<1 cm) and not with a cleft greater than 1 cm, the latter defining a bicornuate or didelphic uterus (Homer et al. 2000; Carrington et al. 1990) (Fig. 7).

Septate uterus is the most common Müllerian duct anomaly and is unfortunately associated with the poorest reproductive outcome. Because of different treatment options, septate uterus must be differentiated from bicornuate and didelphic uterus. A widely accepted definition therefore – empirically invented during laparoscopy procedures – states that a uterus is septate if the outer contour of the uterine fundus is only mildly concave in the presence of a septum. The cutoff of concavity is 1 cm; deeper concavity is associated with bicornuate uterus and uterus didelphys. In a complete septate uterus, the septum extends to the

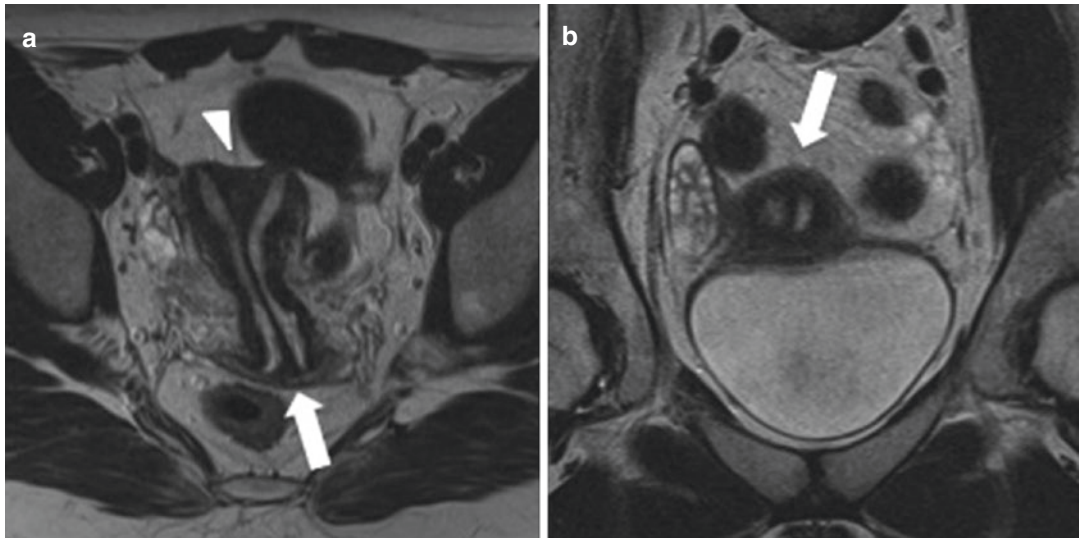

Fig. 7 (**a**, **b**). A 21-year-old female patient with infertility. (**a**) Coronal T2-weighted MR image demonstrates an uterine contour with mild external fundal cleft (*arrowhead*), as well as a hypointense thin septum dividing the endometrial cavity at the level of the uterine body and cervix (*arrows*). (**b**) Axial T2-weighted image shows the extension of the longitudinal septum to the external cervix os

external cervical os. In 25% of septate uteri, the septum extends even further into the upper part of the vagina.

Obstetric outcome seems not to be correlated with the length of the septum. The septum may be composed of muscle or fibrous tissue and is not a reliable means of distinguishing septate and bicornuate uteri. Resection of the septum by hysteroscopic metroplasty is indicated and may improve the reproductive outcome significantly.

2.2.6 Class VI Anomalies: Arcuate Uterus

Definition: Arcuate uterus is the result of a near complete regression of the uterovaginal septum forming a mild and broad, saddle-shaped indentation of the fundal endometrium (Buttram and Gibbons 1979) (Fig. 8).

Differentiation from bicornuate uterus is based on the complete fundal unification; however, a partial septate uterus with a broad-based muscular septum is difficult to distinguish from an arcuate uterus. There is much controversy as to whether an arcuate uterus should be considered a real anomaly or an anatomic variant. Reports finding a higher risk of second-term miscarriage mostly used suboptimal diagnostic tests like two-dimensional ultrasound or HSG, while studies relying upon more accurate methods could not reproduce these results (Chan et al. 2011a). Fact is that MRI may detect this abnormality, but typically, it is not clinically relevant because arcuate uterus has no proven significant negative effects on pregnancy outcome.

2.2.7 Class VII Anomalies

DES-exposed uterus. DES (synthetic estrogen, diethylstilbestrol, 1948–1971) may induce abnormal myometrial hypertrophy in the fetal uterus forming small T-shaped endometrial cavities (Rennell 1979), as well as increase the risk of developing a clear cell carcinoma of the vagina (Herbst et al. 1971; Hatch et al. 1998). The characteristic uterine abnormalities must be categorized in the group of complex uterine anomalies and may occur with or without the exposure of DES.

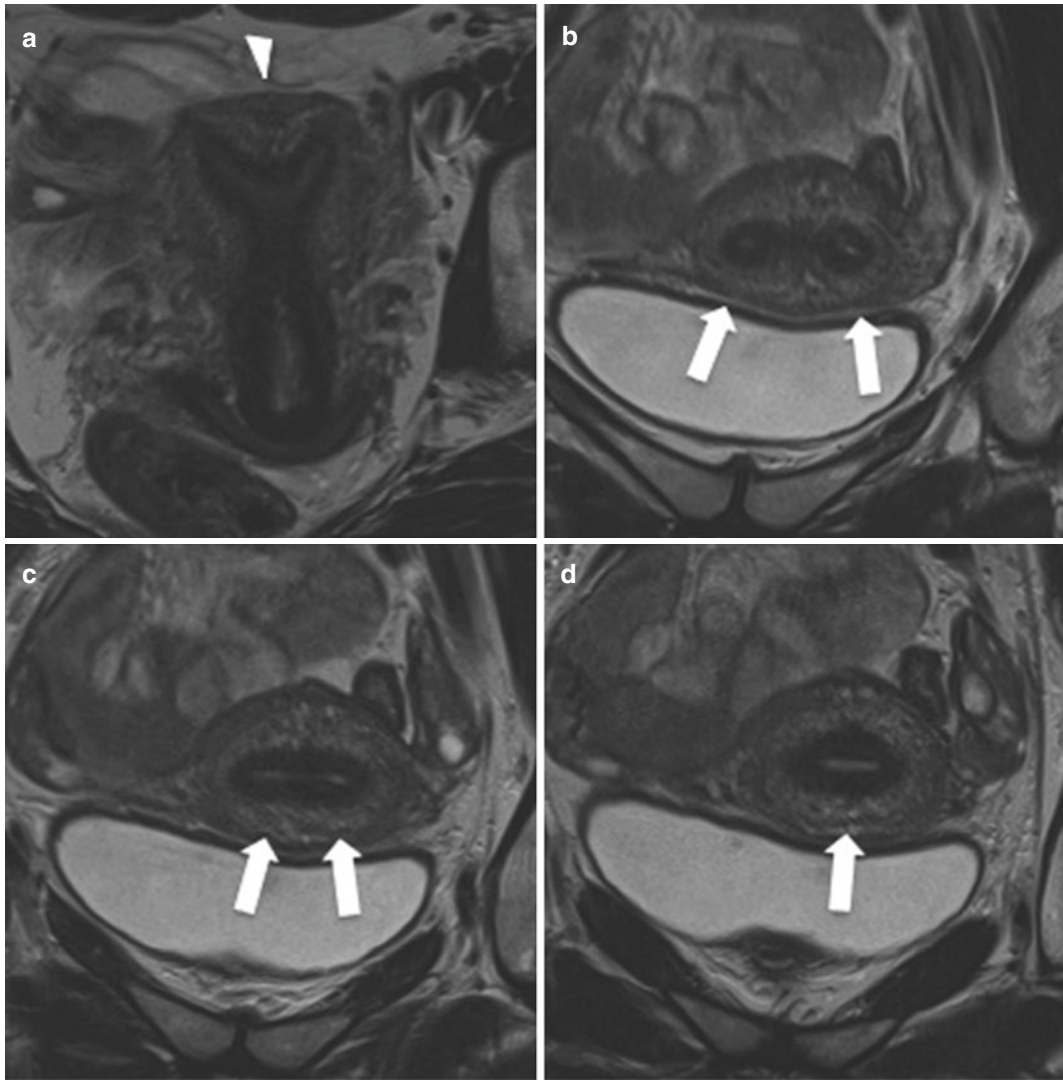

Fig. 8 (**a**–**d**) MRI in a 34-year-old patient demonstrates an arcuate uterus. T2-weighted long-axis view of the uterus (**a**) shows a normal external uterine contour *(arrowhead)* and broad-based indentation of the endometrium. Sequential T2-weighted short-axis images (**b**–**d**) at the level where the two "horns" of the uterine cavity merge show no discernible fibrous septum

References

Acién P (1997) Incidence of Müllerian defects in fertile and infertile women. Hum Reprod 12(7): 1372–1376

Ashton D, Amin HK, Richart RM, Neuwirth RS (1988) The incidence of asymptomatic uterine anomalies in women undergoing transcervical tubal sterilization. Obstet Gynecol 72(1):28–30

Behr SC, Courtier JL, Qayyum A (2012) Imaging of müllerian duct anomalies. Radiographics 32(6):E233–E250

Bermejo C, Martínez Ten P, Cantarero R et al (2010) Three-dimensional ultrasound in the diagnosis of Müllerian duct anomalies and concordance with magnetic resonance imaging. Ultrasound Obstet Gynecol 35(5):593–601

Brody JM, Koelliker SL, Frishman GN (1998) Unicornuate uterus: imaging appearance, associated anomalies, and clinical implications. AJR Am J Roentgenol 171(5):1341–1347

Buttram VC, Gibbons WE (1979) Müllerian anomalies: a proposed classification. (An analysis of 144 cases). Fertil Steril 32(1):40–46

Byrne J, Nussbaum-Blask A, Taylor WS et al (2000) Prevalence of Müllerian duct anomalies detected at ultrasound. Am J Med Genet 94(1):9–12

Carrington BM, Hricak H, Nuruddin RN, Secaf E, Laros RK, Hill EC (1990) Müllerian duct anomalies: MR imaging evaluation. Radiology 176(3):715–720

Chan YY, Jayaprakasan K, Zamora J, Thornton JG, Raine-Fenning N, Coomarasamy A (2011a) The prevalence of congenital uterine anomalies in unselected and high-risk populations: a systematic review. Hum Reprod Update 17(6):761–771

Chan YY, Jayaprakasan K, Tan A, Thornton JG, Coomarasamy A, Raine-Fenning NJ (2011b) Reproductive outcomes in women with congenital uterine anomalies: a systematic review. Ultrasound Obstet Gynecol 38(4):371–382

Clifford K, Rai R, Watson H, Regan L (1994) An informative protocol for the investigation of recurrent miscarriage: preliminary experience of 500 consecutive cases. Hum Reprod 9(7):1328–1332

Dreisler E, Stampe SS (2014) Müllerian duct anomalies diagnosed by saline contrast sonohysterography: prevalence in a general population. Fertil Steril 102(2):525–529

Fedele L, Bianchi S (1995) Hysteroscopic metroplasty for septate uterus. Obstet Gynecol Clin N Am 22(3):473–489

Fedele L, Ferrazzi E, Dorta M, Vercellini P, Candiani GB (1988) Ultrasonography in the differential diagnosis of "double" uteri. Fertil Steril 50(2):361–364

Fedele L, Dorta M, Brioschi D, Massari C, Candiani GB (1989) Magnetic resonance evaluation of double uteri. Obstet Gynecol 74(6):844–847

Fedele L, Bianchi S, Marchini M, Franchi D, Tozzi L, Dorta M (1996) Ultrastructural aspects of endometrium in infertile women with septate uterus. Fertil Steril 65(4):750–752

Goldberg JM, Falcone T, Attaran M (1997) Sonohysterographic evaluation of uterine abnormalities noted on hysterosalpingography. Hum Reprod 12(10):2151–2153

Grimbizis GF, Gordts S, Di Spiezio SA et al (2013) The ESHRE/ESGE consensus on the classification of female genital tract congenital anomalies. Hum Reprod 28(8):2032–2044

Hatch EE, Palmer JR, Titus-Ernstoff L et al (1998) Cancer risk in women exposed to diethylstilbestrol in utero. JAMA 280(7):630–634

Herbst AL, Ulfelder H, Poskanzer DC (1971) Adenocarcinoma of the vagina. Association of maternal stilbestrol therapy with tumor appearance in young women. N Engl J Med 284(15):878–881

Homer HA, Li TC, Cooke ID (2000) The septate uterus: a review of management and reproductive outcome. Fertil Steril 73(1):1–14

Kaufman RH, Adam E, Hatch EE et al (2000) Continued follow-up of pregnancy outcomes in diethylstilbestrol-exposed offspring. Obstet Gynecol 96(4):483–489

Krysiewicz S (1992) Infertility in women: diagnostic evaluation with hysterosalpingography and other imaging techniques. AJR Am J Roentgenol 159(2):253–261

Ludwin A, Ludwin I (2015) Comparison of the ESHRE-ESGE and ASRM classifications of Müllerian duct anomalies in everyday practice. Hum Reprod 30(3):569–580

Ma L, Wu G, Wang Y et al (2012) Fallopian tubal patency diagnosed by magnetic resonance hysterosalpingography. J Reprod Med 57(9–10):435–440

Minto CL, Hollings N, Hall-Craggs M, Creighton S (2001) Magnetic resonance imaging in the assessment of complex Müllerian anomalies. BJOG 108(8):791–797

Nahum GG (1998) Uterine anomalies. How common are they, and what is their distribution among subtypes? J Reprod Med 43(10):877–887

Olpin JD, Heilbrun M (2009) Imaging of Müllerian duct anomalies. Clin Obstet Gynecol 52(1):40–56

Pellerito JS, McCarthy SM, Doyle MB, Glickman MG, DeCherney AH (1992) Diagnosis of uterine anomalies: relative accuracy of MR imaging, endovaginal sonography, and hysterosalpingography. Radiology 183(3):795–800

Pittock ST, Babovic-Vuksanovic D, Lteif A (2005) Mayer-Rokitansky-Küster-Hauser anomaly and its associated malformations. Am J Med Genet A 135(3):314–316

Raga F, Bauset C, Remohi J, Bonilla-Musoles F, Simón C, Pellicer A (1997) Reproductive impact of congenital Müllerian anomalies. Hum Reprod 12(10):2277–2281

Raziel A, Arieli S, Bukovsky I, Caspi E, Golan A (1994) Investigation of the uterine cavity in recurrent aborters. Fertil Steril 62(5):1080–1082

Rennell CL (1979) T-shaped uterus in diethylstilbestrol (DES) exposure. AJR Am J Roentgenol 132(6):979–980

Reuter KL, Daly DC, Cohen SM (1989) Septate versus bicornuate uteri: errors in imaging diagnosis. Radiology 172(3):749–752

Robbins JB, Parry JP, Guite KM et al (2012) MRI of pregnancy-related issues: müllerian duct anomalies. AJR Am J Roentgenol 198(2):302–310

Rock JAAR (2000) Surgery to repair disorders of development. In: Nichols DHC-PD (ed) Gynecologic, obstetric and related surgery, 2nd edn. Mosby, St. Louis, pp 780–830

Rock JA, Schlaff WD (1985) The obstetric consequences of uterovaginal anomalies. Fertil Steril 43(5):681–692

Saleem SN (2003) MR imaging diagnosis of uterovaginal anomalies: current state of the art. Radiographics 23(5):e13

Simón C, Martinez L, Pardo F, Tortajada M, Pellicer A (1991) Müllerian defects in women with normal reproductive outcome. Fertil Steril 56(6):1192–1193

Steinkeler JA, Woodfield CA, Lazarus E, Hillstrom MM (2009) Female infertility: a systematic approach to radiologic imaging and diagnosis. Radiographics 29(5):1353–1370

Strübbe EH, Willemsen WN, Lemmens JA, Thijn CJ, Rolland R (1993) Mayer-Rokitansky-Küster-Hauser

syndrome: distinction between two forms based on excretory urographic, sonographic, and laparoscopic findings. AJR Am J Roentgenol 160(2):331–334

1988 The American Fertility Society classifications of adnexal adhesions, distal tubal occlusion, tubal occlusion secondary to tubal ligation, tubal pregnancies, müllerian anomalies and intrauterine adhesions. Fertil Steril 49(6):944–55.

Toaff ME, Lev-Toaff AS, Toaff R (1984) Communicating uteri: review and classification with introduction of two previously unreported types. Fertil Steril 41(5):661–679

Troiano RN, McCarthy SM (2004) Mullerian duct anomalies: imaging and clinical issues. Radiology 233(1):19–34

Valle RF (1996) Hysteroscopic treatment of partial and complete uterine septum. Int J Fertil Menopausal Stud 41(3):310–315

Winter L, Glücker T, Steimann S et al (2010) Feasibility of dynamic MR-hysterosalpingography for the diagnostic work-up of infertile women. Acta Radiol 51(6):693–701

Wu MH, Hsu CC, Huang KE (1997) Detection of congenital müllerian duct anomalies using three-dimensional ultrasound. J Clin Ultrasound 25(9):487–492

Zlopasa G, Skrablin S, Kalafatić D, Banović V, Lesin J (2007) Uterine anomalies and pregnancy outcome following resectoscope metroplasty. Int J Gynaecol Obstet 98(2):129–133

Benign Uterine Lesions

Thomas J. Kröncke

Contents

T.J. Kröncke
Klinik für Diagnostische und Interventionelle Radiologie und Neuroradiologie, Klinikum Augsburg, Stenglinstr. 2, 86152 Augsburg, Germany
e-mail: radiologie@klinikum-augsburg.de

1 Background

1.1 Uterine Leiomyomas

1.1.1 Epidemiology

Leiomyomas, or leiomyomas, are the most common benign tumors of the uterus. The incidence of leiomyomas is difficult to estimate and frequencies reported in the literature range between 25 and 50%. In autopsy studies, leiomyomas of the uterus have been found in up to 77% of women (ACOG 1994; Buttram and Reiter 1981; Cramer and Patel 1990). Only about one-third of affected women have leiomyomas that become clinically apparent before menopause. Leiomyomas may cause abnormal menstrual bleeding (menorrhagia with secondary anemia, dysmenorrhea, sensation of increased abdominal girth) or pelvic pressure due to their mass effect (urinary urgency, constipation, pelvic pain, dyspareunia). Finally, leiomyomas of the uterus are also implicated in female infertility and are the most common indication for hysterectomy in Western industrialized countries. In the USA, 430,000 hysterectomies were performed in 2010 most commonly for leiomyomas (40.7%) and endometriosis (17.7%) (Wright et al. 2013).

Leiomyomas are smooth muscle tumors of the uterus that are influenced by steroid hormones and develop in women of reproductive age. They do not occur before puberty and leiomyoma-related symptoms become less severe or resolve altogether with the onset of menopause as a result of decreasing levels of steroid hormones (estrogen,

Med Radiol Diagn Imaging (2017)
DOI 10.1007/174_2017_146, © Springer International Publishing AG
Published Online: 13 September 2017

progesterone) and cessation of the menstrual cycle. However, women on hormone replacement therapy may suffer from leiomyoma-related complaints even after the sixth decade of life (Reed et al. 2004). Hormonal stimulation during pregnancy can lead to considerable growth of leiomyomas and spontaneous infarction (Coronado et al. 2000; Hasan et al. 1991). Uterine leiomyomas are more common in black women compared with Caucasians or Asians. A black woman has a two to three times higher relative risk of developing leiomyomas than a white woman (Marshall et al. 1997). Reproductive factors also play a role. Leiomyomas are two times more common in nulliparous women as compared with women who have given birth and multiple pregnancies reduce the risk further (Parazzini et al. 1988; Samadi et al. 1996; Ross et al. 1986). Other factors associated with an increased risk (early menarche and late menopause, obesity, tamoxifen therapy) or reduced risk (smoking, low-meat diet) of leiomyoma development have been described (Flake et al. 2003; Faerstein et al. 2001; Stewart et al. 2017).

1.1.2 Pathogenesis

Uterine leiomyomas are monoclonal tumors arising from the myometrium. Genetic factors, steroid hormones, and growth factors play a role in the development and growth of uterine leiomyoma. Two mechanisms involved in the development of leiomyomas can be distinguished: the initial neoplastic transformation of normal myocytes and the further increase in size under the influence of hormones and growth factors (Flake et al. 2003; Schwartz 2001). While only little is known about the initial stimulus, it is undisputed that leiomyomas exhibit a variety of characteristic changes of the karyotype which give rise to a similar phenotype whose further growth occurs via clonal expansion (Townsend et al. 1970; Hashimoto et al. 1995). Recently, the discovery of stem cells and their paracrine interactions with more differentiated cell populations within leiomyoma has led to an increasing body of evidence supporting the hypothesis that uterine fibroids originate from stem cells in the myometrium (Mas et al. 2012; Ono et al. 2012). Estrogen and progesterone promote the development of leiomyomas whereas growth factors are assumed to act as mediators or effectors of these steroid hormones in leiomyomas (Flake et al. 2003; Friedman et al. 1990). Estrogens are assigned a central role both in the development of leiomyomas and with regard to local effects resulting from a so-called leiomyoma-related hyperestrogenic environment. Compared to normal myometrium, leiomyoma tissue is more sensitive to estradiol, has more estrogen receptors, and has an increased aromatase activity, which enhances the synthesis of estrogens within the leiomyomas (Lumsden et al. 1989; Sadan et al. 1987; Tamaya et al. 1985; Shozu et al. 2004). Finally, glandular hyperplasia of the endometrium has been demonstrated in the immediate vicinity of submucosal leiomyomas and is attributed to the effect of local hyperestrogenism (Buttram and Reiter 1981). Traditionally, estrogens were assumed to have the most important role in leiomyoma growth. Alternatively, it has been hypothesized that progesterones have a crucial role as it has been observed that the highest progesterone levels that occur during the secretory phase of the uterus coincide with the highest mitotic rate in leiomyomas (Kawaguchi et al. 1989; Rein et al. 1995).

1.1.3 Histopathology

Leiomyomas are benign tumors composed of uterine smooth muscle cells. They typically develop in the uterine corpus or fundus but may also originate in the cervix (<8%) or rarely in the supporting structures of the uterus such as the broad ligament. So-called parasitic leiomyomas are no longer contiguous with the uterus and develop an atypical blood supply (Lurie et al. 1991; Yeh et al. 1999). Two-thirds of affected women have multiple leiomyomas. The majority of leiomyomas are round lesions with a well-defined margin (Fig. 1). Growing leiomyomas displace the surrounding tissue, giving rise to a pseudocapsule of condensed myometrium, which allows surgical enucleation of the tumors. Macroscopically, the cut surface of leiomyomas has a whorl-like appearance. Histologically, leiomyomas are made up of intertwined smooth muscle cells arranged in fascicles forming whorl-like patterns (Fig. 2). These smooth muscle cells are embedded in a stroma of collagen fibers. Microscopically, the

uniform cells have cigar-shaped nuclei and an eosinophilic fibrillary cytoplasm. The majority of leiomyomas show higher cell density than the surrounding myometrium. Mitosis and atypia are not found in leiomyomas. Histologically, different subtypes are distinguished, of which cellular and myxoid leiomyoma as well as lipoleiomyoma can also be differentiated by magnetic resonance imaging. Rare manifestations are diffuse leiomyomatosis of the uterus and forms that extend beyond the uterus. The latter comprise benign metastatic leiomyomatosis, peritoneal disseminated leiomyomatosis, and intravenous leiomyomatosis (Ueda et al. 1999; Robboy et al. 2000; Suginami et al. 1990; Hayasaka et al. 2000). Diffuse leiomyomatosis (Fig. 3) is characterized by the presence of many small ill-defined leiomyomas that may be confluent. The tumors are found throughout the myometrium

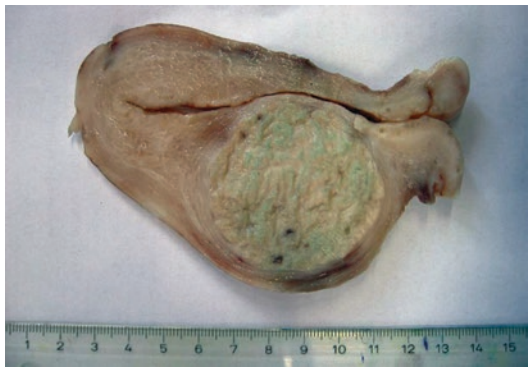

Fig. 1 Macroscopic pathology of leiomyoma. Macroscopic uterine specimen showing a single intramural leiomyoma in the wall of the uterine corpus abutting the endometrial cavity and deforming the outer contour of the uterus. A surrounding pseudocapsule of compressed myometrium can also be depicted

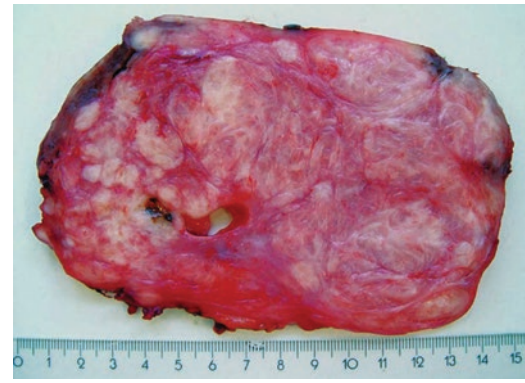

Fig. 3 Macroscopic pathology of diffuse leiomyomatosis of the uterus. Macroscopic uterine specimen showing multiple ill-defined leiomyomas throughout all uterine layers ranging from millimeters to several centimeters in size. The leiomyomas are partially confluent and have replaced almost the entire normal myometrium, a condition also known under the term of (diffuse) leiomyomatosis

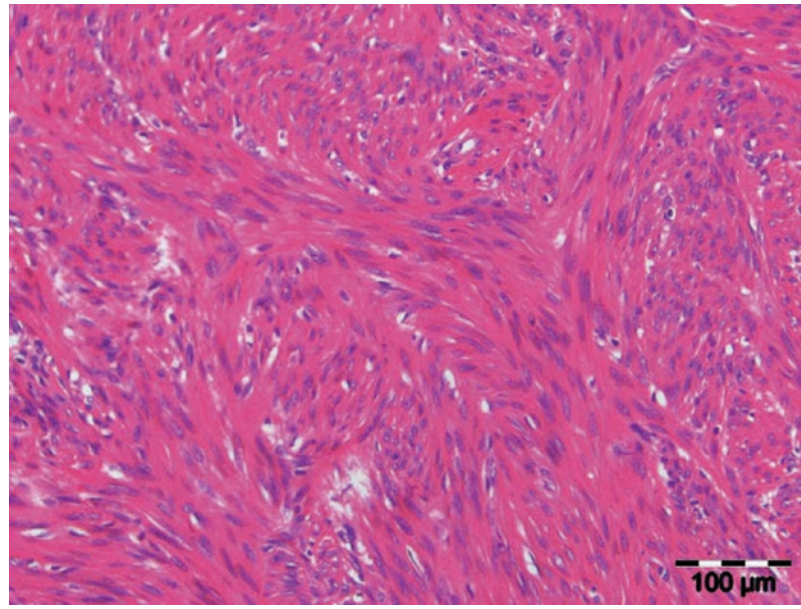

Fig. 2 Histopathology of uterine leiomyoma. H&E-stained section of a leiomyoma specimen showing monomorphic smooth muscle cells arranged in fascicles forming whorl-like patterns

and cause symmetrical enlargement of the uterus (Mulvany et al. 1995; Robles-Frias et al. 2001).

Another factor contributing to the very heterogeneous imaging appearance of uterine leiomyomas is the presence of degenerative changes. Leiomyomas undergo degeneration when the tumors outgrow their blood supply. Typical degenerative changes such as hyaline degeneration, which is present in over 60% of leiomyomas, as well as hemorrhagic (red), myxoid, and (rare) cystic degeneration (4%) can be differentiated by MRI (Zaloudek and Hendrickson 2002). Other typical changes are amorphous or plaque-like calcifications, which are present in 3–8% of leiomyomas (Casillas et al. 1990). Most of the leiomyoma subtypes that can be distinguished histologically or by imaging as well as the degenerative changes outlined above have no clinical relevance for therapeutic decision making. An exception is hemorrhagic infarction of a leiomyoma during pregnancy, which is identified by MRI in a straightforward manner (Hasan et al. 1991). Criteria that are being used for the differentiation of leiomyosarcoma from leiomyomas are an increased mitosis rate, the presence of cytologic atypia, as well as the presence of coagulation necrosis with or without intralesional hemorrhage (Bell et al. 1994; Jones and Norris 1995; Goto et al. 2002; Kawamura et al. 2002; Hanley et al. 2017). Hemorrhage and necrosis within leiomyomas only occur in the rare cases of spontaneous or pregnancy-related hemorrhagic infarction but are common early after interventional therapy by means of uterine artery embolization (UAE). Postinterventional hemorrhage and necrosis may in this setting affect large portions or the whole leiomyoma (Weichert et al. 2005).

1.1.4 Clinical Presentation

Leiomyomas of the uterus are rare below the age of 30. They usually become manifest during the fourth to six decade of life. Typical symptoms are excessive and/or prolonged menstrual bleeding (hypermenorrhea and menorrhagia). Bleeding between periods or irregular bleeding may be observed in patients with pedunculated submucosal leiomyomas but is not characteristic and therefore requires diagnostic evaluation of the endometrium (endometrial biopsy, dilatation, and curettage). Women with heavy periods frequently develop iron-deficiency anemia. Other frequently reported complaints are bulk symptoms manifesting as a premenstrual sensation of fullness (increased abdominal/pelvic girth), urinary urgency, and indigestion. Affected women usually complain of painful periods (dysmenorrhea), and less common is unspecific pain radiating into the flank or the back or pain during intercourse (dyspareunia). These symptoms alone are not characteristic of uterine leiomyomas and must be interpreted in conjunction with a patient's history and imaging findings.

The patient's symptoms vary with the location and size of the leiomyomas. For example, submucosal leiomyomas can cause severe menstrual bleeding even when they are very small. In women with this type of leiomyoma, abnormal menstrual bleeding has been attributed to ulceration and thinning of the endometrium over the leiomyoma due to compression, reduced uterine contractility, and congestion of endometrial veins. Intramural leiomyomas are associated with an especially high incidence of abnormal and painful menstrual bleeding. Although location has been suggested to influence symptoms objective evidence for this is limited and there is no consistent relationship between symptoms and size and location of leiomyoma (Hapangama and Bulmer 2016).

In patients presenting with dysmenorrhea as the leading clinical symptom, the examiner should always consider uterine adenomyosis and endometriosis in the differential diagnosis (Zacharia and O'Neill 2006). Subserosal leiomyomas can become very large without causing any symptoms. Compression of the intestine and urinary bladder with urinary frequency or urgency and abdominal bloating around periods are more commonly associated with subserosal leiomyomas. Moreover, there is some evidence suggesting that symptoms are not only due to merely mechanical local effects but that additional factors associated with specific biological activities of the leiomyomas also play a considerable role. Such functional factors influence the subendometrial vascular bed through dysregulation of growth and angiogenic factors and are primarily implicated to cause leiomyoma-related abnormal

menstrual bleeding (Stewart and Nowak 1996; deSouza and Williams 2002).

The impairment of quality of life caused by leiomyoma-related problems and the measurable loss of economic productivity due to absence from work are considerable.

In a national survey study conducted in the USA it was reported that women waited an average of 3.6 years before seeking treatment for leiomyomas and 28% of employed respondents reported missing work due to leiomyoma symptoms (Borah et al. 2013).

For the USA it has been estimated that at least 5 million workdays are lost per year due to leiomyomas and that the annual treatment cost amounts to US$ 3 billion (Greenberg and Kazamel 1995). The high incidence of leiomyomas and its socioeconomic implications as well as individual loss of quality of life are in sharp contrast to our still limited understanding of the pathogenesis of uterine leiomyomas and inadequate therapeutic options. A lack of research into the epidemiology, pathogenesis, and pathophysiology of leiomyomas of the uterus as well as their "benign nature" are the most important factors that have so far inhibited the search for alternative therapeutic options to replace the radical surgical approach of hysterectomy (Myers et al. 2002). Surgical removal of the uterus continues to be the most widely used therapeutic approach in patients with symptomatic leiomyomas. In Western industrialized countries, uterine leiomyomas are the most frequent indication for removal of the uterus, accounting for 175,000 hysterectomies per year in the USA alone (Wright et al. 2013). Women are increasingly asking for alternative nonsurgical, uterus-sparing therapies and research and scientific evaluation of alternative therapeutic options such as uterine artery embolization have markedly increased over the last two decades (Borah et al. 2013; ACOG 2001).

1.1.5 Therapy

1.1.5.1 Indications

Treatment of uterine leiomyomas is indicated when they cause symptoms (American College of Obstetricians and Gynecologists 2008) while a wait-and-see approach is in order in women without symptoms. Whether treatment is indicated or not does not depend on the size of the uterus or that of individual leiomyoma tumors since there is no evidence that marked enlargement of the uterus is associated with an increased surgical morbidity. Traditionally, rapid growth of a leiomyoma has been interpreted as a sign of malignancy (leiomyosarcoma) while the results of larger studies do not confirm this assumption (Leibsohn et al. 1990; Parker et al. 1994). A relative indication for treating asymptomatic leiomyomas exists in women who want to conceive and have a history of miscarriage and proven leiomyoma-related deformity of the uterine cavity. In these cases treatment may be indicated because the leiomyomas can interfere with placentation and pregnancy is associated with additional risks (Hasan et al. 1991; Phelan 1995; Pritts 2001; Rice et al. 1989). A systematic review, however, concluded that there is no conclusive evidence that intramural or subserosal leiomyomas adversely affect fecundity and good maternal and neonatal outcomes are expected in pregnancies with uterine leiomyomas (Klatsky et al. 2008).

1.1.5.2 Medical Therapy and Ablation

Medical therapy is usually symptomatic and aims to relieve leiomyoma-related abnormal menstrual bleeding (hypermenorrhea, menorrhagia), dysmenorrhea, and bulk symptoms. Oral contraceptives of different hormonal composition and nonsteroidal anti-inflammatory drugs with analgesic and antifibrinolytic effects are used although evidence for their long-term effectiveness in treating uterine leiomyomas is not available (Myers et al. 2002; Stewart 2001). Moreover, there is no data demonstrating a growth-reducing effect of oral contraceptives. These therapeutic options are used in the routine clinical setting to bridge the time until definitive therapy is performed. Treatment with GnRH analogues improves leiomyoma-related symptoms and leads to a transient reduction of leiomyoma size. Maximum size reduction is seen after about 3 months of treatment. Once GnRH analogues are discontinued, however, leiomyomas will again increase in size. This is why GnRH analogues

are given only to reduce leiomyoma size prior to surgery (Ylikorkala et al. 1995). GnRH administration is also beneficial to minimize blood loss in case of larger leiomyomas or for the transient treatment of anemia resulting from heavy menstrual bleeding. However, GnRH treatment causes softening of leiomyomas, which is a disadvantage for surgical enucleation. Progesterone receptor modulators (PRMs) have recently demonstrated effectiveness for intermittent treatment of symptomatic uterine leiomyomas (Donnez et al. 2012, 2014, 2015).

The severity of menstrual bleeding can be reduced by insertion of a *levonorgestrel-releasing intrauterine device* (IUD) (Mercorio et al. 2003; Wildemeersch and Schacht 2002). The effect of such IUDs is based on the local activity of continuously released progesterone, which effectively suppresses the endometrium. A recent systematic review concluded that levonorgestrel-releasing intrauterine systems could decrease uterine volume and endometrial thickness and reduce menstrual blood loss and increase blood hemoglobin, ferritin, and hematocrit levels significantly. However, no evidence for decreasing uterine leiomyoma volume was found (Jiang et al. 2014). It is known that an IUD for the treatment of hypermenorrhea has a higher failure rate in the presence of submucosal leiomyomas (Wildemeersch and Schacht 2002).

Endometrial ablation is a permanent and invasive therapeutic option which relieves excessive menstrual bleeding in 62–79% of cases (Soysal et al. 2001). Thermoablation of the endometrium is performed using a balloon or roller ball technique and a hysteroscopic access. The success of endometrial ablation in the presence of leiomyomas is small because not the entire endometrium is accessible in women with multiple leiomyomas because of enlargement and deformity of the uterine cavity.

1.1.5.3 Surgical Therapy

Hysterectomy is a definitive cure in patients with a symptomatic multileiomyoma uterus. Both abdominal and vaginal hysterectomy is associated with a low mortality and morbidity. However, given that uterine leiomyomas are benign lesions, the large number of hysterectomies performed worldwide to treat this condition appears to be disproportionate (Broder et al. 2000; Stewart et al. 2012). As an alternative to hysterectomy, uterus-sparing operative, ablative, and interventional radiological procedures are available, depending on location and size of leiomyomas present, the patient's age, desire to have children, and personal preferences.

Depending on their location, leiomyomas can be resected or enucleated using a hysteroscopic or laparoscopic access or open laparotomy. Hysteroscopic resection is suitable to remove submucosal leiomyomas. Hysteroscopic resection is generally considered unsuitable for submucosal leiomyomas larger than 5 cm in size, if more than three leiomyomas are present, or if the uterine cavity is very large (length of uterine probe >12 cm). Moreover, the size of the intramural component is a risk factor of the hysteroscopic resection because the risk of perforation increases when the residual myometrium is thin (Wamsteker et al. 1993). A laparoscopic access is used to remove visible subserosal and intramural leiomyomas in combination with reconstruction of the uterus. This approach is unsuitable in the presence of very large leiomyomas or a markedly enlarged uterus because these factors limit the use of the laparoscope and visibility. Using the laparoscopic approach, multiple leiomyomas can be enucleated in one session. Only visible leiomyomas can be removed while intramural tumors are not easily accessible to laparoscopic removal. Incision of the uterine cavity necessary for the removal of transmural leiomyomas is considered a disadvantage because it is associated with the risk of synechia. Adhesions are observed in 33–54% of patients following laparoscopic interventions (Hasson et al. 1992; Dubuisson et al. 1998; Malzoni et al. 2003). The risk of recurrence after laparoscopic leiomyoma removal is between 21 and 50% in women followed up for up to 5 years (Doridot et al. 2001; Radosa et al. 2014). (Mini-) Laparotomy is primarily used in patients with one or more large leiomyomas, which are

removed using an adjusted abdominal incision. The perioperative risks of laparotomy are comparable to those of hysterectomy while the rate of adhesions may be as high as 90% (Sawin et al. 2000; Tulandi et al. 1993). The reported recurrence rate after abdominal myomectomy is 10% within 5 years and up to 27% after 10 years. One-third of the patients with recurrent leiomyomas will ultimately undergo hysterectomy (Candiani et al. 1991; Fauconnier et al. 2000).

1.1.5.4 Uterine Artery Embolization (UAE)

Uterine artery embolization (UAE) is an established technique that has been used to stop life-threatening vaginal hemorrhage in women with malignancy, postpartum uterine atony, or traumatic injury since the mid-1970s (Margolies et al. 1972; Goldstein et al. 1975; Athanasoulis et al. 1976; Higgins et al. 1977; Brown et al. 1979). The first successful treatment of symptomatic leiomyomas of the uterus by UAE was reported by Ravina et al. in 1994 (Ravina et al. 1994).

Embolization of the uterine artery induces infarction of leiomyomas while uterine perfusion is maintained (Katsumori et al. 2001; McCluggage et al. 2000). Infarction leads to coagulation necrosis and subsequent complete hyalinization of the leiomyomas (Weichert et al. 2005; McCluggage et al. 2000; Colgan et al. 2003). Further transformations cause softening and shrinkage of the tumors. Follow-up for 3–24 months has shown that there is an average size reduction of the uterus of 23–60% while the dominant leiomyoma decreases by 42–78% on average. Progressive shrinkage of the leiomyomas has been documented for a period of 12 months (Kroncke et al. 2005; Brunereau et al. 2000; Hutchins et al. 1999; McLucas et al. 2001a; Prollius et al. 2004; Pron et al. 2003; Spies et al. 2001a; Walker and Pelage 2002). Several studies provide evidence for a relief of bleeding-related symptoms in 80–100% of patients and a regression of bulk symptoms in 60–100% of patients followed up for 3–60 months (Kroncke et al. 2005; Brunereau et al. 2000; Hutchins et al. 1999; McLucas et al. 2001a; Prollius et al. 2004; Pron et al. 2003; Spies et al. 2001a; Walker and Pelage 2002; Andersen et al. 2001; Katsumori et al. 2002). Studies comparing UAE with hysterectomy and myomectomy in the treatment of symptomatic uterine leiomyomas suggest that UAE has a similar success rate in terms of symptom relief and patient satisfaction while it has a lower complication rate and shorter recovery period as compared with the surgical procedures (Razavi et al. 2003; Broder et al. 2002; Spies et al. 2004a; Mara et al. 2005). These results are confirmed by two randomized studies (Pinto et al. 2003; Hehenkamp et al. 2005). Long-term results after UAE are limited but the available data suggests that permanent improvement of symptoms can be expected in two-thirds of women (Broder et al. 2002; Spies et al. 2005a; Scheurig-Muenkler et al. 2011). Complications during the intervention are extremely rare (Spies et al. 2002a; Kroncke et al. 2004). Following UAE, 5–10% of the patients report vaginal discharge with or without tissue passage and expulsion of infarcted leiomyomas may occur (Kroencke et al. 2003; Park et al. 2005; Berkowitz et al. 1999; Abbara et al. 1999). Leiomyoma expulsion occurs weeks to months after the intervention and may necessitate administration of antibiotics and pain medication if complicated by superinfection and in rare cases surgically assisted removal or hysteroscopic resection (Hutchins et al. 1999; McLucas et al. 2001a; Spies et al. 2001a). Transient amenorrhea persisting for up to three cycles is not unusual while permanent amenorrhea is rare and occurs more commonly in patients above 45 years old than in younger ones (Walker and Pelage 2002; Chrisman et al. 2000; Tropeano et al. 2004). UAE can be performed in patients with single or multiple leiomyomas but, based on current knowledge, patients who wish to preserve their fertility should be treated by UAE only if alternative, uterus-sparing therapeutic approaches have been attempted or are not an option. All uterus-sparing therapeutic approaches share the risk of newly occurring leiomyomas and may require repeat interventions or hysterectomy due to complications of surgical or interventional treatment.

1.1.5.5 Magnetic Resonance-Guided Focused Ultrasound

Magnetic resonance-guided focused ultrasound (MRgFUS) is an image-guided therapy whereby ultrasound energy is used to heat and destroy tissue. In a randomized placebo-controlled trial MRgFUS demonstrated efficacy in symptom and volume reduction and improvement in quality of life (Jacoby et al. 2016). MRgFUS requires proper patient selection since technical restrictions exist which subsequently limit its application. This includes leiomyoma characteristics (leiomyoma number, location, distance to the skin or to the sacral bone, signal intensity) and obstacles to the ultrasound beam among others. A high variability regarding eligibility for MRgFUS is reported (range: 14–74% of women with leiomyomas) (Pron 2015). In the largest trial using MRgFUS to treat symptomatic leiomyomas, symptom reduction and rate of re-intervention were correlated to the degree of ablation as measured by the non-perfused volume (Stewart et al. 2007). Reported complication rate in clinical cohort studies involving 1594 patients was 1.6% (Pron 2015). Long-term data on safety and efficacy and comparative evidence are still lacking.

2 Adenomyosis of the Uterus

2.1 Epidemiology

Adenomyosis (endometriosis genitalis interna) of the uterus affects premenopausal women and is predominantly seen in multiparous women and women over 30 years of age (Parazzini et al. 1997; Azziz 1989). Because its symptoms are unspecific, adenomyosis rarely comes to clinical attention, which is why the incidence of this uterine condition is underestimated (Azziz 1989). Until recently, the diagnosis was established almost exclusively after hysterectomy. Histologic examination of hysterectomy specimens demonstrates adenomyosis in 19–63% of cases (Azziz 1989). Adenomyosis often occurs in conjunction with leiomyomas and endometriosis (endometriosis genitalis externa et extragenitalis) (Zacharia and O'Neill 2006; Kunz et al. 2005).

2.2 Pathogenesis

Adenomyosis is a nonneoplastic condition which results from the dislocation of basal endometrial glands and stroma into the underlying myometrium (Ferenczy 1998). It has been shown that adenomyosis progresses with age, suggesting that there is continuous progression from superficial to deep myometrial involvement (Kunz et al. 2000). The dislocated endometrial glands in adenomyosis do not undergo cyclic changes, which has been attributed to the predominance of the zona basalis in these glands (Azziz 1989). The mechanism underlying the dislocation of basal endometrium is largely unknown. Estrogen-mediated and mechanical effects seem to play a role. Since adenomyosis is seen predominantly in parous women, a breakdown of the basal layer of the endometrium and myometrium due to postpartum endometritis has also been proposed as a possible cause (Siegler and Camilien 1994). Tissue injury and repair at large have been postulated as primary events in the disease process (Leyendecker et al. 2015).

2.3 Histopathology

Adenomyosis presents morphologically as focal areas or diffuse involvement of the uterus. Grossly, the cut surface is characterized by a whorled texture which results from the irregular trabeculations of the thickened myometrium (Fig. 4). Another common feature is cyst-like lesions. Hemorrhagic foci within the myometrium may be seen as well on gross inspection. The diagnosis is based on the histologic demonstration of dispersed endometrial glandular tissue in the myometrium and requires the presence of at least one glandular nest at a depth of more than 2.5 mm or one-half of a low-power field (X 100) within the myometrium measured from the endomyometrial junction (Zaloudek and Hendrickson 2002). The islets of glandular tissue are surrounded by hypertrophied myometrium (Fig. 5). Pathologically a superficial form of adenomyosis which only involves the inner myometrium can be differentiated from deep-infiltrating adenomyosis which

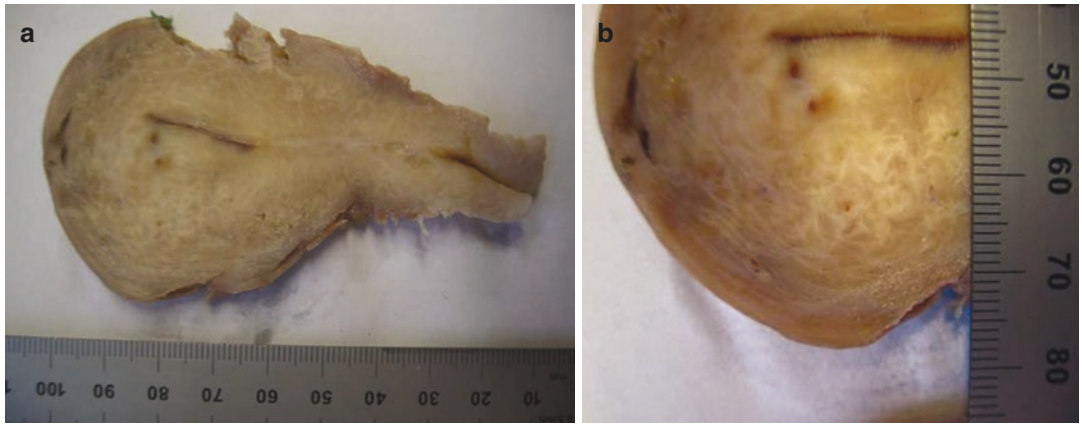

Fig. 4 Macroscopic pathology of adenomyosis of the uterus. (**a**) Macroscopic uterine specimen showing focal adenomyosis. A thickened anterior uterine wall with broadening of the myometrium as well as irregular myometrial trabeculations and multiple micro-cysts are visible. (**b**) Magnified area of the anterior uterine wall showing coarse trabeculation of the myometrium without a mass lesion and small brownish cysts corresponding to hemorrhagic foci of dislocated endometrial glands

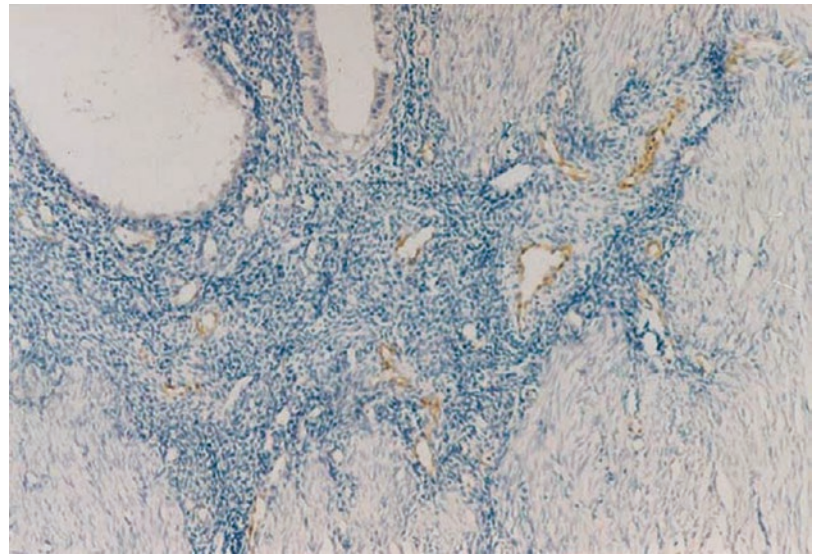

Fig. 5 Histopathology of adenomyosis of the uterus. Dislocated endometrial glands are surrounded by hypertrophied myometrium (reproduced with permission from Keckstein J, Ulrich U (2004) Gynäkologische Endokrinologie. Springer Verlag, Berlin Heidelberg New York, 2:11–18)

considerably enlarges the uterine wall due to smooth muscle hyperplasia adjacent to deep-infiltrating endometrial glands (Ferenczy 1998).

2.4 Clinical Presentation

The clinical presentation of adenomyosis is unspecific and includes symptoms such as dysmenorrhea, menorrhagia, and pelvic pain, which are also common in disorders like dysfunctional bleeding, leiomyoma, and endometriosis. The uterus is frequently enlarged in women with adenomyosis but not distorted in its shape like with uterine leiomyoma. Women with superficial or focal adenomyosis may be asymptomatic in contrast to women with extensive disease in whom the uterus usually is also markedly enlarged. The depth of involvement of the uterine wall correlates to some degree with clinical symptoms (Benson and Sneeden 1958; Bird et al. 1972; McCausland 1992). Dysmenorrhea has been

reported to be more frequent when involvement of the myometrium by adenomyosis exceeds 80% of the diameter of the uterine wall (Nishida 1991).

2.5 Therapy

Hysterectomy is still considered the definitive treatment in patients with symptomatic adenomyosis. However, less invasive therapeutic options should be considered initially taking into account the patient's age, symptom severity, and desire of future fertility as well as the presence of associated disorders such as leiomyomas and endometriosis. Symptom relief can be achieved with nonsteroidal anti-inflammatory drugs but suppression of the endometrium may be needed. A broad range of suppressive hormonal treatments are applied which induce regression of adenomyosis and improve symptoms (Pontis et al. 2016). Intrauterine devices (IUD) which release levonorgestrel have been shown to be effective in controlling menorrhagia caused by adenomyosis although symptoms return once the IUD is removed (Fedele et al. 1997). Endometrial ablation or resection denudes the endometrial layer of the uterus and is an option for women with predominantly abnormal uterine bleeding. Adenomyosis of the superficial type with less than 2 mm penetration responds better than deep-infiltrating adenomyosis to endometrial ablation (McCausland and McCausland 1996).

Uterus-conserving surgery is hampered by the lack of a clearly defined dissection plane but may be of value in the infertile patient (Ozaki et al. 1999). Laparoscopic resection of adenomyosis has been shown to reduce pain, menorrhagia, and dysmenorrhea in small case series with limited follow-up (Wood et al. 1994; Morita et al. 2004). Uterine artery embolization (UAE) has been reported to be successful in relieving menorrhagia and dysmenorrhea at short term. The long-term results are encouraging with improvement rates for dysmenorrhea and menorrhagia reported to be 70.4% and 68.8%, respectively, at 5-year follow-up. After 7 years of follow-up, in 82% of UAE-treated patients with symptomatic adenomyosis a hysterectomy could be avoided (Siskin et al. 2001; Kim et al. 2004; Pelage et al. 2005; Kitamura et al. 2006; Zhou et al. 2016; de Bruijn et al. 2017).

3 Imaging

3.1 Diagnostic Imaging for Uterine Leiomyomas and Adenomyosis: Overview

Uterine leiomyomas and adenomyosis cannot be reliably differentiated on the basis of clinical grounds because both conditions cause similar symptoms.

Leiomyomas of the uterus, once they have reached a certain size, can be palpated and differentiated from the uterine wall as solid tumors that tend to be mobile. Bimanual palpation is typically supplemented by *transvaginal ultrasound* (*TVUS*) or, in patients with a markedly enlarged uterus, transabdominal ultrasound. The ultrasound examination allows assessment of the uterus and especially TVUS provides additional information on the endometrium and ovaries. TVUS is the primary imaging modality in the diagnostic workup of women with uterine leiomyomas. Ultrasound (US) depicts leiomyomas as hypoechoic round lesions which are sharply demarcated from the remainder of the uterus (Fig. 6). Anechoic cystic portions and degenerative changes with a heterogeneous echo pattern within the lesions are quite common. US enables reliable assessment of the location of leiomyomas and their topographic relationship to surrounding

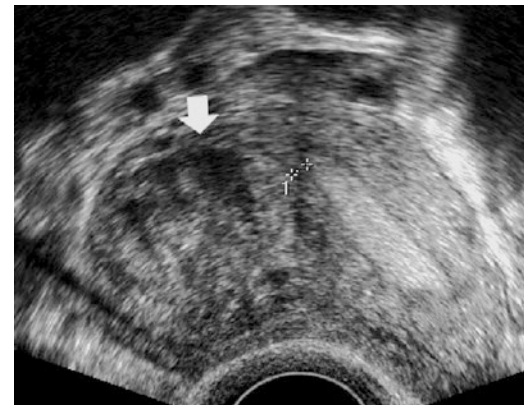

Fig. 6 Transvaginal ultrasound (TVUS) of uterine leiomyoma. TVUS demonstrates a well-defined subserosal leiomyoma (*arrow*) distorting the outer contour of the uterine wall. The leiomyoma shows a heterogeneous echotexture and is hypoechoic compared to the adjacent myometrium and endometrium. The endometrium is seen as a hyperechoic stripe

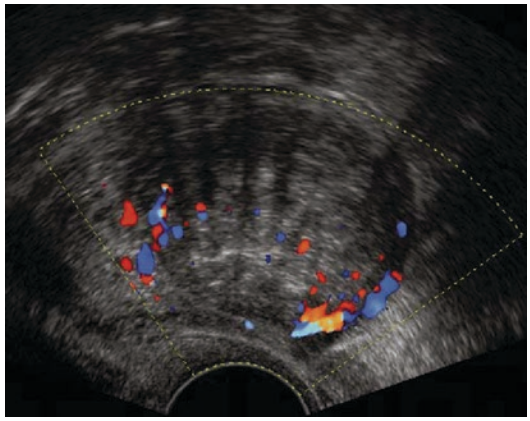

Fig. 7 Transvaginal ultrasound of leiomyoma. Transvaginal color-coded duplex ultrasound demonstrates the perifibroid plexus vessels surrounding the leiomyoma

structures, and in particular the uterine cavity, in most cases. Additional Doppler US will depict tumor vascularity and demonstrate typical features such as a central vessel or a marginal vascular network (Fig. 7). *Hysterosonography* with the instillation of fluid into the uterine cavity improves the diagnostic accuracy of TVUS in detecting submucosal leiomyomas, differentiating from endometrial polyps, and determining depth of myometrial (uterine wall) involvement (Dueholm et al. 2002a).

Endoscopic procedures such as *laparoscopy* or *hysteroscopy* have a role in patients with suspected leiomyomas and inconclusive US findings. Moreover, hysteroscopy is performed in conjunction with endometrial sampling in women with abnormal menstrual bleeding and for specific diagnostic purposes such as evaluation of the uterine cavity and tubes in infertile women with leiomyomas. In patients with known uterine leiomyomas, laparoscopy and hysteroscopy have their main role as therapeutic procedures for the uterus-sparing resection of known uterine leiomyomas.

Magnetic resonance imaging (*MRI*) is the most accurate diagnostic modality for assessing uterine leiomyomas (Dueholm et al. 2002b). MRI enables assessment of the uterus in multiplanar orientation and without interference from superimposed structures. MRI provides accurate information not only on the number and size of leiomyomas but also on their location within the uterus (cervix, corpus, fundus) and within the wall (submucosal, intramural, subserosal) as well as their relationship to neighboring structures such as the tubes and ovaries (Figs. 8 and 9).

The unique soft-tissue contrast afforded by MRI enables good delineation of the leiomyomas from adjacent myometrium, the junctional

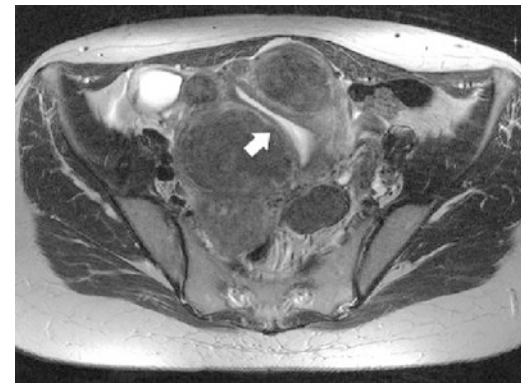

Fig. 8 MRI of leiomyoma—locations. Transaxial T2-weighted image depicts multiple, mainly subserosal uterine leiomyoma. There is mild distortion of the uterine cavity by a transmural (full thickness) leiomyoma (*arrow*)

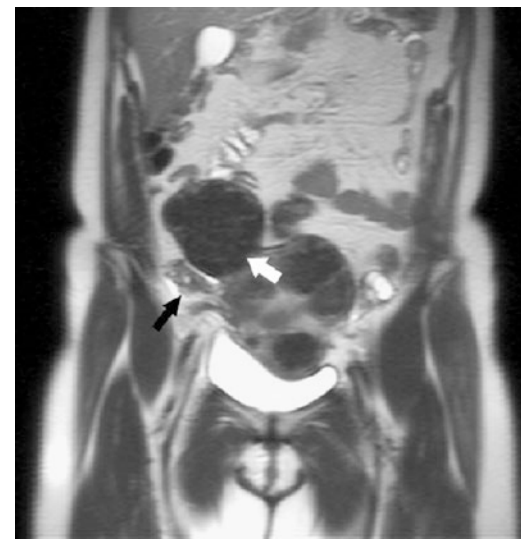

Fig. 9 MRI of leiomyoma—locations. T2-weighted coronal image of a polyfibroid uterus. A subserosal pedunculated uterine fibroid (*white arrow*) is easily identified by its low signal intensity and continuity with the right lateral aspect of the uterine fundus while sonographically the lesion could not be separated from the right ovary (*black arrow*) (reproduced with permission from reference 840, Kröncke TJ, Hamm B (2003) Role of magnetic resonance imaging (MRI) in establishing the indication for planning and following up uterine artery embolization (UAE) for treating symptomatic leiomyomas of the uterus [article in German]. Radiologe 43:624–633)

zone, which is important for the differential diagnosis, and the endometrium. It also enables evaluation of the internal make-up of leiomyomas including secondary degenerative changes. These features thus make MRI superior to all other imaging modalities in characterizing uterine leiomyomas. MRI is of use in patients with inconclusive US findings with regard to the differential diagnosis of a pelvic lesion or the origin of a lesion from the uterus or the ovary (Scoutt et al. 1994; Weinreb et al. 1990). MRI is increasingly being used to evaluate the feasibility of uterus-sparing surgical therapy or a radiologic intervention (Dudiak et al. 1988). To establish the indication for hysteroscopic or laparoscopic resection, it is necessary to know the number and size of leiomyomas as well as their precise position, in particular their relationship to the uterine cavity and their depth within the wall (Dueholm et al. 2002c; Hurst et al. 2005). In evaluating potential candidates for UAE, MRI provides information on the size of the individual leiomyomas, the presence of pedunculated or parasitic leiomyomas, the nature of degenerative changes, the degree of leiomyoma vascularization, and the vascular supply of the uterus.

Computed tomography (*CT*) with its poor soft-tissue contrast is of limited value in diagnosing benign changes of the uterus. CT does not allow adequate differentiation of the different uterine layers and hence fails to reliably assign uterine lesions to a specific layer. Intravenous contrast medium administration improves the differentiation of adjacent structures but does not improve the differential diagnosis (Fig. 10). On CT scans, uterine leiomyomas are isodense with muscle and can occasionally be identified by the presence of typical calcifications on unenhanced images. There are no specific CT criteria for the presence of adenomyosis.

Adenomyosis—when severe—causes enlargement of the uterus but differs from leiomyoma-related enlargement in that the uterus is soft on palpation. *TVUS* will depict areas of reduced echogenicity or a heterogeneous appearance in about 75% of patients with adenomyosis (Reinhold et al. 1995; Brosens et al. 1995; Fedele et al. 1992). Apart from asymmetric thickening of the myometrium in the presence of focal adenomyosis, other morphologic features that are indicative of adenomyosis are a poor definition of the endomyometrial junction, presence of myometrial cysts (<5 mm) in up to 50% of affected patients, as well as echogenic lines or spots within the myometrium (Fedele et al. 1992; Iribarne et al. 1994). Circumscribed lesions are absent in the majority of cases. Good diagnostic performance can be expected if diagnostic criteria as described above are combined and real-time examination is used. An increased vascularization demonstrated by *color duplex US* is indicative of adenomyosis (Hirai et al. 1995; Chiang et al. 1999). Transvaginal ultrasound has a reported sensitivity of 53–89% and a specificity ranging from 50 to 99% (Reinhold et al. 1995; Brosens et al. 1995; Fedele et al. 1992; Ascher et al. 1994). The wide variation is primarily attributable to the examiner dependence of US. The diagnostic accuracy is limited in the presence of leiomyomas (Bazot et al. 2001). Many of the features of adenomyosis seen on US are depicted more clearly on T2-weighted MR images, which clearly show changes in zonal anatomy based on the excellent

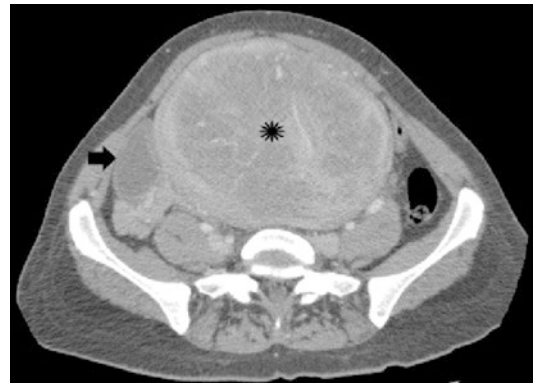

Fig. 10 CT of uterine leiomyoma. Contrast-enhanced CT of the pelvis in a 39-year-old women with a known uterine leiomyoma shows a large oval mass within the uterus with heterogeneous enhancement (*asterisk*) which displays the hypodense right ovary (*arrow*) and distends the abdomen

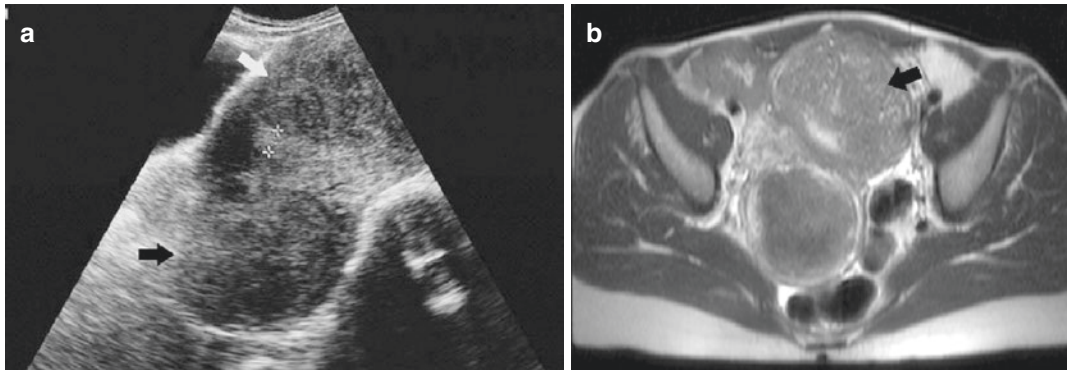

Fig. 11 Correlation of transvaginal ultrasound (TVUS) and magnetic resonance imaging (MRI) in a patient with leiomyoma and adenomyosis of the uterus. (**a**) TVUS of a 48-year-old woman with menorrhagia and dysmenorrhea. Two leiomyoma were reported to be present, one in a subserosal location (*black arrow*) of the posterior wall and a second intramurally in the anterior uterine wall (*white arrow*). However, a poor definition of the endomyometrial junction and asymmetric myometrial thickening of the anterior uterine wall rather than a clear mass lesion is seen. Calipers indicate measurement of endometrial thickness. (**b**) Corresponding T2-weighted transaxial image shows a subserosal leiomyoma of the posterior uterine wall and focal adenomyosis of the anterior uterine wall (*black arrow*) characterized by a broadening of the junctional zone and cyst-like inclusions in the myometrium corresponding to endometrial glands

soft-tissue contrast of this imaging modality (Fig. 11). Despite its sensitivity of 86–100% and specificity of 85–90.5% for the diagnosis of adenomyosis and its high diagnostic accuracy in establishing the differential diagnosis, MRI is rarely used in the routine clinical setting, for two reasons: adenomyosis is rarely suspected as the cause of hypermenorrhea or dysmenorrhea before surgery and reliable pretherapeutic demonstration of adenomyosis as the underlying cause in symptomatic women in the fourth or fifth decade of life was considered irrelevant for therapeutic decision making (hysterectomy) (Ascher et al. 1994; Reinhold et al. 1996; Togashi et al. 1989; Mark et al. 1987). MRI is thus not indicated and cost effective in the initial evaluation of patients with unspecific complaints suggestive of adenomyosis. However, MRI has its place as an adjunctive tool in patients with diffusely enlarged uteri of unknown cause, in the workup of infertile women, and for follow-up of patients receiving GnRH therapy for adenomyosis or prior to uterus-conserving surgical therapy and UAE (Ozaki et al. 1999; Kim et al. 2004; Kido et al. 2003a; Imaoka et al. 2002).

3.2 Magnetic Resonance Imaging

3.2.1 Magnetic Resonance Imaging: Technique

A short clinical history including menstrual status, previous pelvic surgery, clinical symptoms, time point within the menstrual cycle, and current hormonal therapy should be taken prior to an MR examination of the female pelvis. Due to the cyclic changes of the uterus, imaging is best performed in the second half of the menstrual cycle to take advantage of maximum signal differences between the uterine layers. The pelvis should be imaged on a high-field (1.5T) scanner using a pelvic or torso phased-array coil. Motion artifacts caused by bowel peristalsis can degrade image quality significantly and should be eliminated. Measures to reduce such artifacts include asking the patient to fast for 4–6 h prior to the examination and intramuscular injection of butylscopolamine in patients who have no contraindications. Patients should also be instructed to void prior to the examination. The standard protocol for pelvic MR imaging should include both T1- and T2-weighted sequences. Breath-hold T2-weighted sequences

acquired in the true axial, sagittal, and coronal planes (T2-HASTE, SSFSE) are sufficient to diagnose uterine leiomyomas and adenomyosis in the majority of cases (Ascher et al. 1999; Masui et al. 2001). However, the relationship of a uterine lesion to the uterine cavity may be difficult to recognize on breath-hold images alone. Additional high-resolution T2-weighted TSE sequences acquired in the axial and sagittal planes in conjunction with presaturation of the anterior abdominal wall are recommended in cases of inconclusive breath-hold images or a severely distorted uterine cavity (Yamashita et al. 1998). T1-weighted pulse sequences with and without fat saturation acquired in the axial plane provide information on fatty components and blood products within a lesion and accentuate areas of calcification otherwise not seen on T2-weighted imaging. Gadolinium-enhanced T1-weighted images can provide additional information on the vascularity of uterine leiomyomas, improve the visualization of the surrounding pseudocapsule, and may help to delineate the uterine origin of a subserosal leiomyoma but are not necessary to diagnose uterine leiomyomas and adenomyosis (Hricak et al. 1992). Diffusion-weighted magnetic resonance imaging (DW-MRI) and dynamic multiphase contrast-enhanced magnetic resonance imaging (DCE-MRI) are now part of the standard imaging protocols for evaluation of the female pelvis with the latter being rather used in research settings. DCE-MRI and DWI may be of added value in benign uterine conditions. Both functional imaging techniques can assist in distinguishing between various subtypes of benign leiomyomas and leiomyosarcomas. Leiomyomas show low signal intensity on T1W, T2W, and DW images (Tamai et al. 2008). Uterine sarcomas show high or low signal intensity on T2W images and high signal intensity (i.e., restricted diffusion) on DW images. It is known from contrast-enhanced imaging studies that leiomyosarcomas tend to show a much stronger and inhomogeneous enhancement pattern with areas of necrosis compared to leiomyomas. However, there is some overlap with degenerated and cellular leiomyomas (Lin et al. 2016). Additional MRA gradient-echo sequences are recommended in patients with leiomyomas and adenomyosis in whom uterine artery embolization is planned (Kroencke et al. 2006).

3.2.2 MR Appearance of Uterine Leiomyomas

Leiomyomas of the uterus present as well-defined round or oval low-signal-intensity masses on T2-weighted MR images. They are characterized by expansive growth but do not infiltrate surrounding structures and therefore distort the shape of the uterus in relation to their size and location. MRI performed in three orthogonal planes allows one first to accurately localize leiomyomas as submucosal, intramural, transmural (full thickness), subserosal, pedunculated, or (extrauterine) intraligamentous and second to assign them to the cervix (less than 8%), corpus uteri (anterior, posterior, lateral uterine wall), or fundus. Uterine leiomyomas can be single but usually are multiple and may reach considerable size. In a multileiomyoma uterus normal myometrium often represents only a minor portion of the uterine tissue (Fig. 12). Diffuse

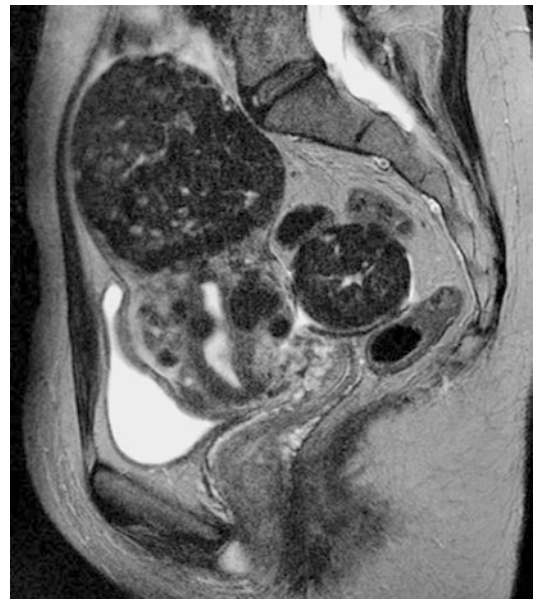

Fig. 12 Polyfibroid uterus—MRI appearance. T2-weighted sagittal image of a 44-year-old woman shows multiple uterine leiomyoma, the largest extending subserosal from the fundus of the uterus. All leiomyomas are well marginated and show typical hypointense signal intensity with some speckled hyperintense spots. A pedunculated subserosally leiomyoma is present in the posterior cul-de-sac

leiomyomatosis is a rare form where the myometrium is displaced by confluent leiomyomas (Kido et al. 2003b) (Fig. 13).

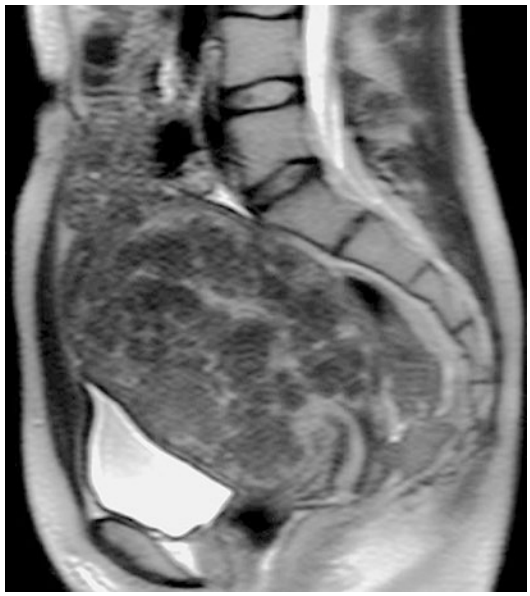

Fig. 13 MRI of diffuse leiomyomatosis of the uterus. T2-weighted sagittal image of a 41-year-old woman shows multiple uterine leiomyoma throughout the uterine layers ranging from millimeters to several centimeters in size. The leiomyomas are partially confluent and have replaced almost the entire normal myometrium (compare also with Fig. 3)

3.2.3 Locations, Growth Patterns, and Imaging Characteristics

The localization of leiomyomas by imaging is of clinical importance because symptoms are related to and treatment varies based on the position of a leiomyoma within the uterus. Recently, a detailed classification system has been devised and advocated by the International Federation of Gynecology and Obstetrics (FIGO) (Munro et al. 2011). Whether a submucosal leiomyoma can be resected depends on its size and ingrowth into the uterine wall (Wamsteker et al. 1993). A subserosal leiomyoma can be surgically treated by enucleation but opening and surgical reconstruction of the uterine cavity may be necessary if the leiomyoma grows transmurally (Stringer et al. 2001). Leiomyomas are characterized by expansive growth with displacement of neighboring tissue and therefore already have a mass effect when they are still small. Deformity of the uterine contour is primarily associated with submucosal and subserosal leiomyomas because they distend neighboring layers such as the endometrium and serosa (Fig. 14). In patients with a markedly enlarged uterus due to multiple leiomyomas, these tumors are often difficult to differentiate from extrauterine or ovarian lesions on ultrasound. The presence of a claw-like

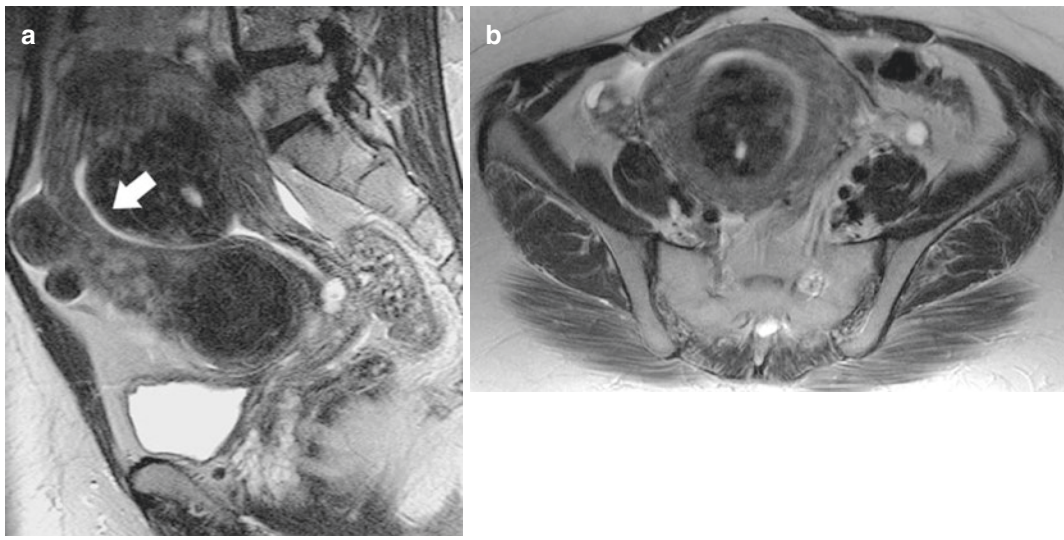

Fig. 14 Mass effect of uterine leiomyoma. (**a**) T2-weighted sagittal image shows a multifibroid uterus with a large submucosal leiomyoma that exerts mass effect on the underlying endometrium (*arrow*). (**b**) T2-weighted axial image at corresponding level

extension of myometrium surrounding the lesion and corkscrew-like flow voids at the interface between lesion and normal uterine tissue, which can be detected on T1-weighted images, and less commonly on T2-weighted images, indicate uterine leiomyomas with a high degree of certainty (Scoutt et al. 1994; Weinreb et al. 1990; Torashima et al. 1998; Kim et al. 2000). These flow voids represent the arteries arising from the uterine artery and feeding the large-caliber vascular plexus of a leiomyoma (Fig. 15). The MR imaging signs of uterine leiomyomas are summarized in Table 1.

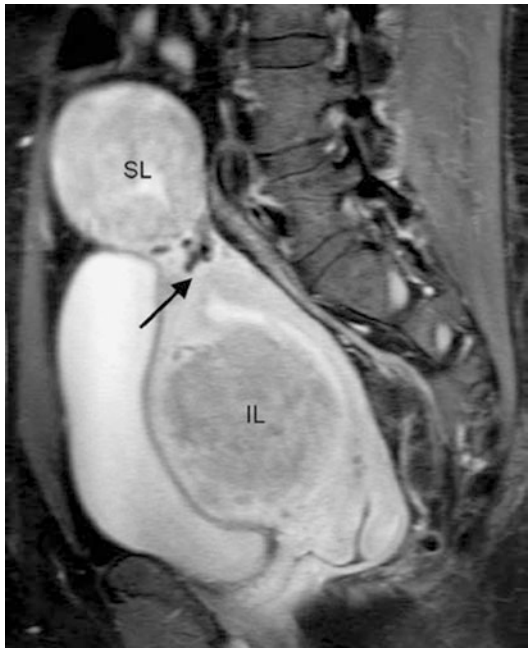

Fig. 15 Bridging vascular sign in a pedunculated leiomyoma. T1-weighted contrast-enhanced fat-suppressed sagittal image depicts a large pedunculated subserosal leiomyoma originating from the uterine fundus. Flow voids are seen within the vessel stalk (*arrow*). A second intramural leiomyoma in the anterior wall is seen displacing the endometrial stripe (reproduced with permission from reference 840, Kröncke TJ, Hamm B (2003) Role of magnetic resonance imaging (MRI) in establishing the indication for planning and following up uterine artery embolization (UAE) for treating symptomatic leiomyomas of the uterus [article in German]. Radiologe 43:624–633)

Table 1 MRI criteria for leiomyoma

Location	• Corpus, fundus, less often cervical or within uterine ligaments, subserosal, intramural, transmural, submucous, pedunculated, in statu nascendi
Morphology	• Spherical, sharply marginated, pseudocapsule may be present, mass effect even if small, deforming the uterine outline and/or cavity may be singular but often numerous
	• Size range from 0.5 to >20 cm
	• Claw-like extension of myometrium surrounding the lesion
Appearance on T1	• Isointense to the myometrium
	• Peripheral hypointense rim indicates calcification
	• Hyperintense areas related to hemorrhage
	• Peripheral high SI rim or homogenous high SI indicates hemorrhagic infarction
Appearance on T2	• Variable, in general hypointense mass relative to myometrium but different SI seen in individual leiomyomas
	• Homogenously high SI often seen in cellular leiomyomas
	• High SI rim represents dilated lymphatics in large leiomyoma
Appearance on Gd-enhanced T1	• Can appear hypo-, iso-, and hyperintense relative to myometrium hypervascularity often seen in cellular leiomyomas
	• Pseudocapsule more prominent
	• Absence of enhancement seen in partially or completely infarcted leiomyoma (bridging-vascular-sign)
Additional findings	• Flow voids in the periphery (best seen on T1-weighted images) indicate the perifibroid plexus vessels
	• A vessel stalk may be seen in pedunculated leiomyomas

3.2.4 Histologic Subtypes and Forms of Degeneration

Different histologic subtypes of leiomyomas exist, some of them showing characteristic features on MRI. Cellular leiomyomas, a subgroup of leiomyomas characterized by compact smooth muscle cells with little intervening collagen, exhibit a homogenously high signal intensity on T2-weighted images (Fig. 16). They are isointense to surrounding myometrium on T1-weighted images and tend to enhance fairly homogenously after gadolinium administration (Yamashita et al. 1993). Lipoleiomyoma is a rare type of leiomyoma which displays a signal intensity similar to subcutaneous fat on all pulse sequences due to the presence of various amounts of fat cells. Chemical shift imaging or spectral fat suppression may be useful to determine the fatty nature of these leiomyomas (Tsushima et al. 1997). While MRI can distinguish among the different subtypes in only 69% of all cases, the method is highly sensitive and specific in identifying simple leiomyomas without any major degenerative changes, leiomyomas having undergone hemorrhagic infarction, and leiomyomas with cystic degenerative changes (Schwartz et al. 1998). Degeneration of uterine leiomyomas is common and is attributed to an inadequate blood supply. It is a sudden event in case of hemorrhagic degeneration while degenerative changes may develop gradually when a tumor outgrows its blood supply.

The typical MRI appearance of a smoothly marginated tumor with a nearly homogeneous low signal intensity relative to surrounding myometrium on T2-weighted images and intermediate signal on T1-weighted images (Fig. 17) is attributable to hyalinization (Oguchi et al. 1995).

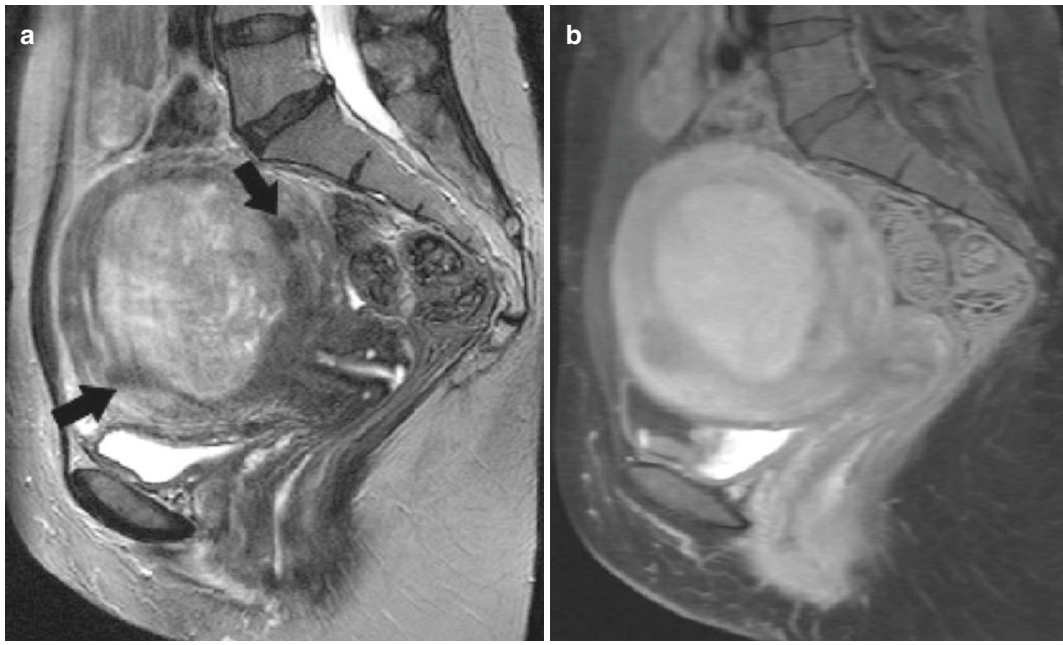

Fig. 16 MRI of cellular leiomyoma. (**a**) T2-weighted sagittal image of the uterus demonstrating a large intramural cellular leiomyoma with homogenous high signal intensity compared to surrounding myometrium. Two small intramural leiomyomas show the typical low-intensity signal (*arrows*). (**b**) T1-weighted contrast-enhanced fat-suppressed sagittal image showing marked enhancement of the intramural cellular leiomyoma which appears hyperintense compared to surrounding myometrium

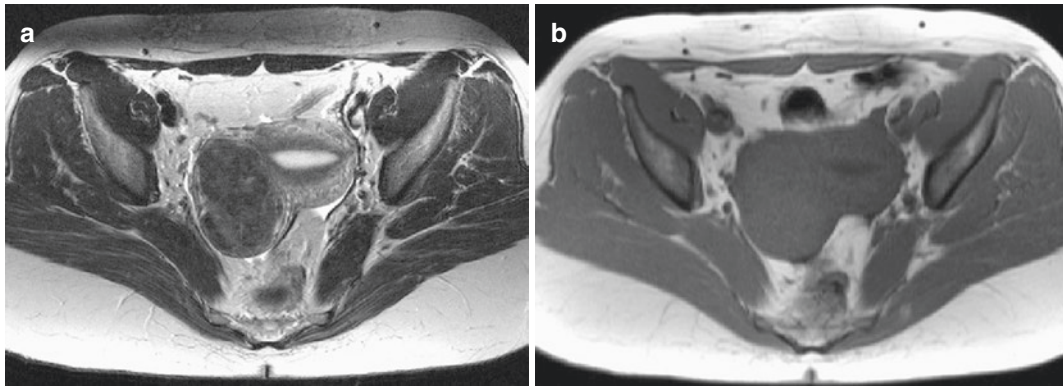

Fig. 17 Signal intensity characteristics of leiomyoma. (**a**) T2-weighted transaxial image of the uterus (secretory phase of menstrual cycle) showing a subserosal leiomyoma with typical low signal intensity compared to adjacent myometrium. Note the bright signal of the endometrium and intermediate signal intensity of the junctional zone. (**b**) Corresponding T1-weighted transaxial image of the uterus showing intermediate signal intensity of the leiomyoma which can hardly be differentiated from the adjacent myometrium

Hyaline degeneration is the predominant form of degeneration and is present in about 60% of all leiomyomas. It is characterized by the accumulation of high-protein eosinophilic substrate in the extracellular spaces between strands of muscle cells. Other types of degeneration that can be differentiated are cystic, myxoid, and hemorrhagic (red) degeneration. *Cystic degeneration* is characterized by the presence of clearly delineated cystic lesions with a signal intensity isointense to fluid on T1- and T2-weighted images. *Myxoid degeneration* is seen as intralesional areas of very high signal intensity on T2-weighted images. These portions are of intermediate to low signal on T1-weighted images and typically do not show enhancement after contrast medium administration (Fig. 18).

Histology demonstrates gelatinous portions containing hyaluronic mucopolysaccharides. *Haemorrhagic or red degeneration* is more common during pregnancy or in women on gestagen therapy. It is attributed to sudden infarction of leiomyoma tissue with secondary intralesional hemorrhage (Hasan et al. 1991). MRI shows a lesion with an increased internal signal and a low-signal-intensity margin on T2-weighted images while T1-weighted images depict a lesion with a heterogeneous high signal that varies with the amount of blood degradation products present and is often confined to the margin (Fig. 19) (Kawakami et al. 1994). Hemorrhagic leiomyomas typically show no enhancement after contrast medium administration. MRI confirms the diagnosis of acute hemorrhagic degeneration in conjunction with the clinical symptoms comprising acute pain, subfebrile temperature, and leukocytosis (Kawakami et al. 1994; Hamlin et al. 1985). Hydropic degeneration of a leiomyoma has been described as a rare form of degeneration and usually presents as a large and lobulated complex mass on US that displays heterogeneous mainly high T2 signal with strands of low

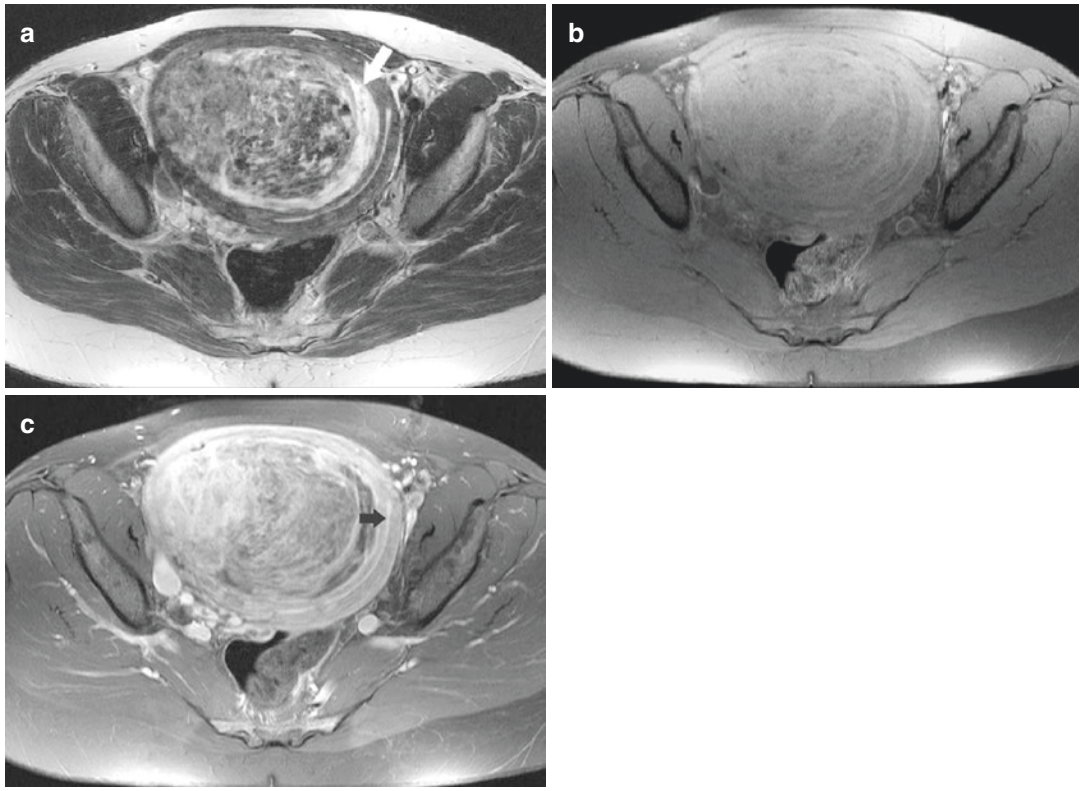

Fig. 18 MRI of myxoid leiomyoma. (**a**) T2-weighted transaxial image of the uterus showing also heterogeneous signal intensity of the leiomyoma and a C-shaped area at the left border of the leiomyoma (*arrow*) of high signal intensity corresponding to myxoid degeneration. Note that high-signal-intensity stripe of the endometrium is displaced laterally. (**b**) On the corresponding T1-weighted fat-suppressed transaxial image the whole leiomyoma has a heterogeneous intermediate signal intensity and the C-shaped area shows no low signal as expected if liquefaction had occurred. (**c**) Contrast-enhanced T1-weighted fat-suppressed transaxial image shows heterogeneous enhancement of the leiomyoma including septations of myxoid tissue, Note enhancement of endometrial stripe (*arrow*)

signal on MRI. A solid component as well as prominent intralesional blood vessels may be present. This appearance can be a diagnostic challenge since these imaging features overlap with malignant tumors. "Pseudo-Meigs' syndrome" has been associated with hydropic leiomyomas associated with ascites and elevated serum levels of CA-125 (Horta et al. 2015).

MRI is methodologically limited in that it does not reliably show intralesional *calcifications*, which are frequently identified on conventional radiographs or CT scans by their popcorn-like appearance (Schwartz et al. 1998). Occasionally, calcifications take the form of a peripheral rim after hemorrhagic infraction and can be identified on T1-weighted MR images (Fig. 20).

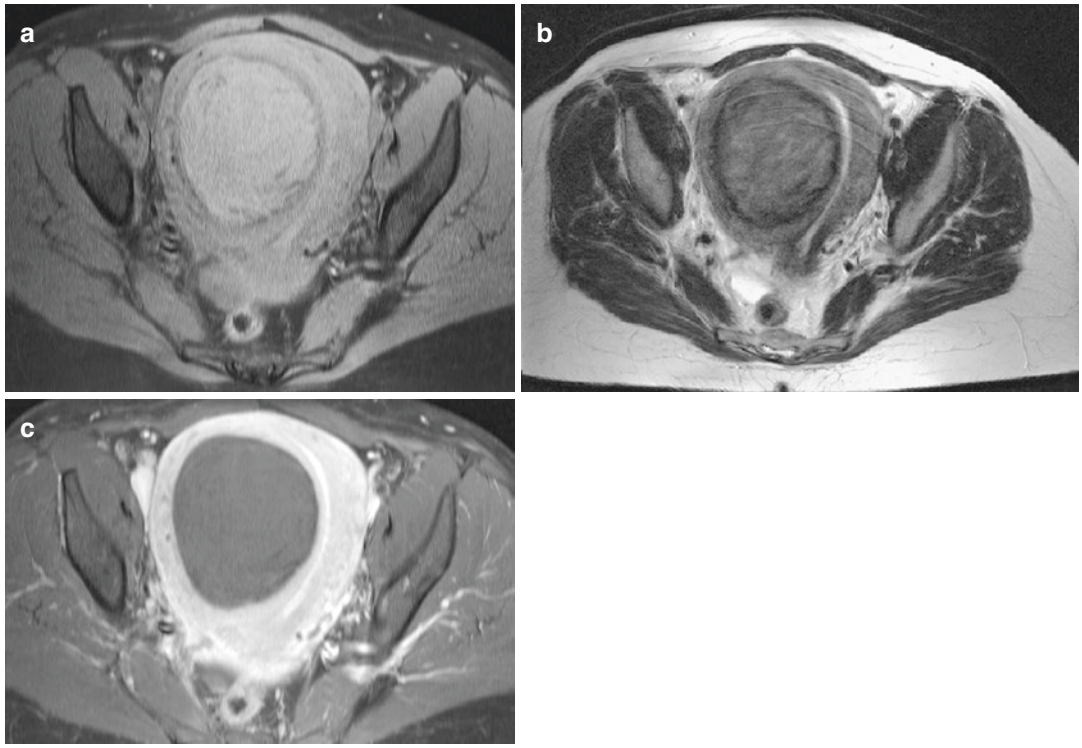

Fig. 19 MRI of spontaneously infarcted leiomyoma. (**a**) T1-weighted fat-suppressed transaxial image of a spontaneously infarcted submucosal leiomyoma. The central portion shows a slightly hyperintense signal intensity compared to the surrounding myometrium. (**b**) T2-weighted transaxial image of a spontaneous infarcted submucosal leiomyoma. The central portion shows a signal intensity isointense to the myometrium while a marked hypointense rim is seen which corresponds to blood degradation products (hemosiderin) after hemorrhagic infarction. (**c**) Contrast-enhanced T1-weighted fat-suppressed transaxial image confirms infarction of the leiomyoma while the surrounding myometrium is well perfused (reproduced with permission from reference 840, Kröncke TJ, Hamm B (2003) Role of magnetic resonance imaging (MRI) in establishing the indication for planning and following up uterine artery embolization (UAE) for treating symptomatic leiomyomas of the uterus [article in German]. Radiologe 43:624–633)

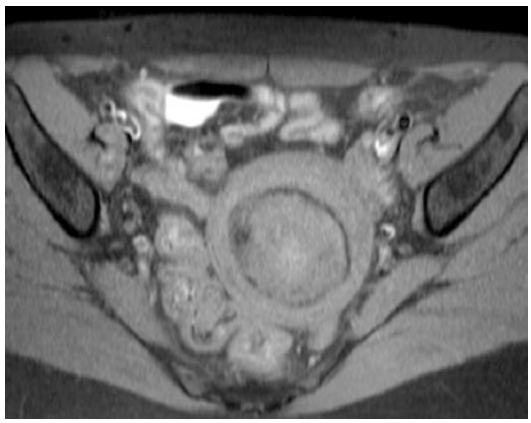

Fig. 20 MRI of rim calcification of a leiomyoma. T1-weighted fat-suppressed transaxial image showing a leiomyoma with a discontinuous, markedly hypointense rim corresponding to asymmetrical calcification

3.2.5 Differential Diagnosis

In evaluating lesions in close topographic relationship to the uterus, the examiner must consider *ovarian masses* in the differential diagnosis. If it is not possible to definitely assign the lesion to the uterus, an intraligamentous or ovarian leiomyoma may be present if the lesion shows homogeneous low signal intensity on T2-weighted images and an intermediate signal on T1-weighted images relative to the signal intensity of the myometrium of the uterus. However, an inhomogeneous intermediate or high signal relative to the myometrium may indicate both a leiomyoma with degenerative changes or an extrauterine benign or malignant tumor.

Myometrial contractions can mimic submucosal leiomyomas or focal adenomyosis (Togashi et al. 1993a). Uterine contractions involve the

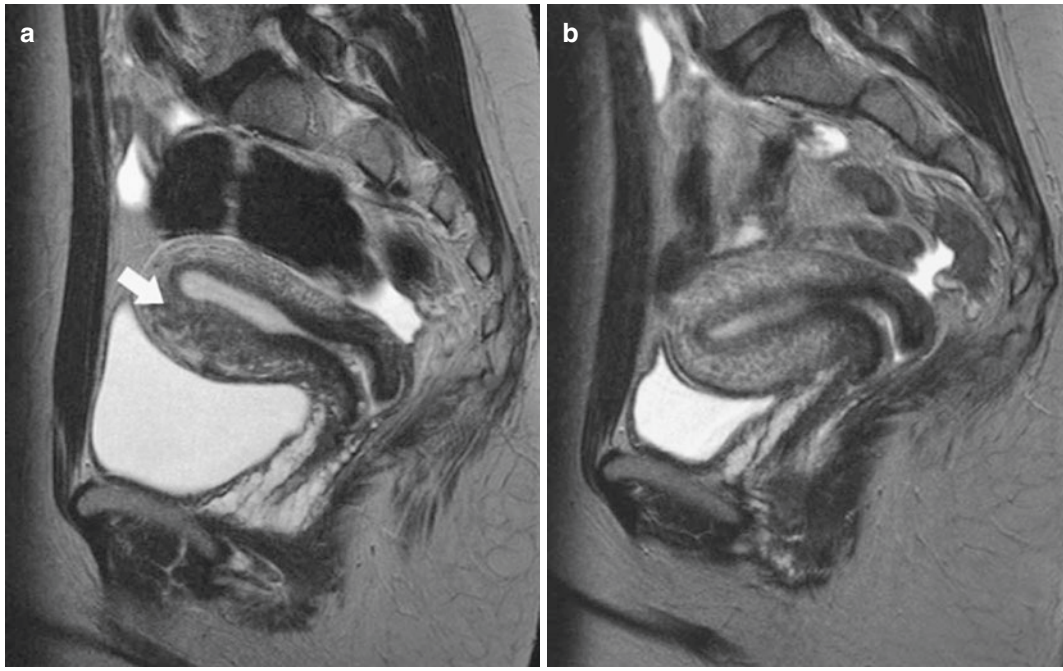

Fig. 21 Transient uterine contraction. (**a**) T2-weighted sagittal image of the uterus depicting a broadening of the inner myometrium of the anterior uterine wall with bulging into the uterine cavity (*arrow*). (**b**) T2-weighted sagittal image of the uterus obtained 5 min before (**a**) shows absence of any structural abnormality, a finding consistent with myometrial contraction

endo- and myometrium but spare the outer uterine contour (Fig. 21). They are characterized by band- or stick-like low-signal-intensity areas on T2-weighted images (Masui et al. 2003). These signal changes are transient and changing appearances can be noted on sequential images obtained with a delay of 30–45 min (Togashi et al. 1993a, b).

Endometrial polyps are seen most frequently in perimenopausal and postmenopausal women, and are usually asymptomatic but may cause uterine bleeding especially in postmenopausal women (DeWaay et al. 2002). In 20% of the cases polyps are multiple. They can be broad based or pedunculated and may occur in conjunction with endometrial hyperplasia. On T2-weighted images a central fibrous core or intratumoral cysts may be visible (Grasel et al. 2000). On T1-weighted images endometrial polyps show an intermediate signal while they exhibit a slightly hypointense or isointense signal intensity relative to the endometrium on T2-weighted images and present as localized endometrial thickening (Fig. 22). Small polyps enhance and become more conspicuous after gadolinium administration, especially on

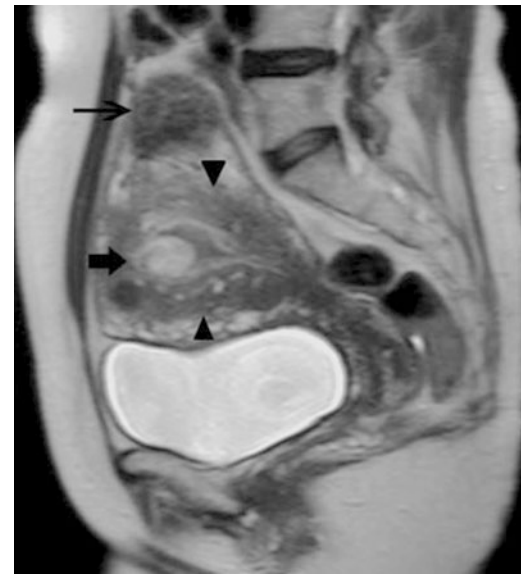

Fig. 22 Leiomyoma, diffuse adenomyosis and endometrial polyp on MRI. T2-weighted sagittal image of a patient depicts diffuse adenomyosis (*arrowheads*) with symmetrical broadening of the junctional zone. An endometrial polyp exhibiting similar high signal intensity as the endometrium can be clearly identified within the uterine cavity (*short arrow*). A fibroid is present in the fundus (*long arrow*)

early enhanced scans, while large polyps exhibit a heterogeneous enhancement pattern (Hricak et al. 1992; Grasel et al. 2000). Submucosal leiomyomas are best distinguished from endometrial polyps by their rather spherical shape, their obvious connection to the myometrium, and lower signal intensity on T2-weighted images.

Leiomyosarcoma (LMS) is a rare tumor that accounts for approximately 1% of all uterine malignancies and contributes to nearly 70% of all uterine sarcomas. The incidence of uterine LMS is 1.5–3 per 100.000 women (Brooks et al. 2004). Most occur in women over 40 years of age, with incidence increasing after age 50. They are predominantly observed in older women (sixth decade of life) as compared to women with leiomyoma (fourth decade of life) (Rammeh-Rommani et al. 2005). It is felt that leiomyosarcomas arise de novo and may be unrelated to benign leiomyomas (Levy et al. 2000). While rapid growth is not an indicator of malignancy in premenopausal women, it is always suspicious in postmenopausal women, although not specific (Parker et al. 1994; Okamoto et al. 2004). The imaging appearance does not enable reliable differentiation of leiomyosarcoma from benign leiomyoma (Parker et al. 1994; Schwartz et al. 1998; Janus et al. 1989; Takemori et al. 1992). Besides frank signs of invasiveness or metastatic disease, an irregular contour, nodular borders, inhomogeneous appearance with pockets of high signal intensity on T2, T2 "dark" area in a myometrial mass, hemorrhagic changes with high signal intensity on T1, as well as presence of central unenhanced areas have been demonstrated to be MR features indicative of a leiomyosarcoma rather than a leiomyoma (Goto et al. 2002; Schwartz et al. 1998; Sahdev et al. 2001; Pattani et al. 1995; Lakhman et al. 2017). Early enhancement on dynamic scans after administration of contrast medium together with serum determination of LDH and its isoenzyme was reported to be highly sensitive and specific in differentiating leiomyosarcoma from degenerated leiomyoma (Goto et al. 2002). The mean ADC value in leiomyosarcomas has been reported to be significantly lower than in degenerated leiomyomas (Li et al. 2016).

3.2.6 MR Appearance of Uterine Adenomyosis

Adenomyosis of the uterus is diagnosed on T2-weighted images where it is characterized by ill-defined low-signal-intensity areas representing diffuse or focal broadening of the junctional zone as a result of smooth muscle hyperplasia associated with heterotopic endometrial glands (Reinhold et al. 1996; Outwater et al. 1998). A junctional zone thickness of ≥12 mm (Fig. 23) is the threshold for which a high degree of accuracy in the diagnosis of adenomyosis has been reported (Reinhold et al. 1998; Kang et al. 1996). Adenomyosis can be excluded if the junctional zone thickness is 8 mm or less (Reinhold et al. 1996). Bright foci and cyst-like inclusions may be seen on T2-weighted images in up to 50% of patients and represent heterotopic endometrial glands, cystic dilatations, or hemorrhagic foci (Reinhold et al. 1996; Togashi et al. 1989). Corresponding high signal on T1-weighted images is less frequently observed but highly

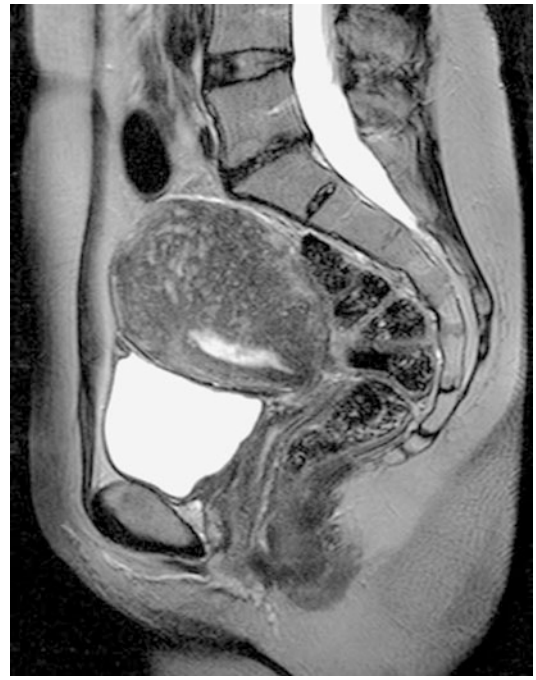

Fig. 23 Focal adenomyosis of the uterus. T2-weighted sagittal image of a patient with focal adenomyosis of the uterus. There is enlargement with only mild deformity of the uterus. The fundus and posterior uterine wall is thickened due to marked broadening of the junctional zone. Hyperintense foci are seen within the lesion (reproduced with permission from reference 840, Kröncke TJ, Hamm B (2003) Role of magnetic resonance imaging (MRI) in establishing the indication for planning and following up uterine artery embolization (UAE) for treating symptomatic leiomyomas of the uterus [article in German]. Radiologe 43:624–633)

suggestive of adenomyosis (Fig. 24). Additionally, striations of high signal intensity extending from the endometrium into the myometrium as a result of direct invasion of the myometrium may be seen and result in pseudo-widening of the endometrium (Reinhold et al. 1999). These high-signal-intensity changes associated with adenomyosis may fluctuate during the menstrual cycle. The MR imaging signs of adenomyosis are summarized in Table 2.

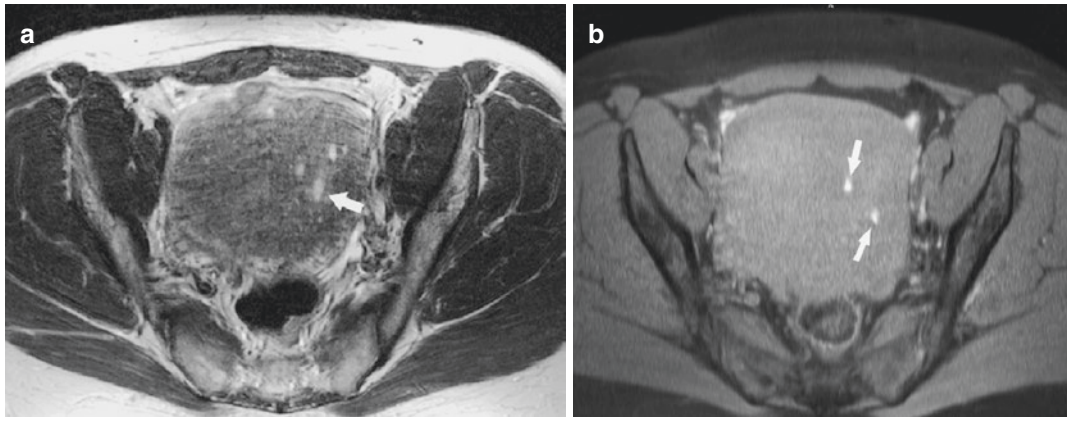

Fig. 24 MRI of diffuse adenomyosis of the uterus. (**a**) T2-weighted transaxial image of a patient with diffuse adenomyosis of the uterus. The uterine wall is thickened, there is poor definition of the endomyometrial junction, and the junctional zones blend with the myometrium. No focal mass is present. Cyst-like inclusions of hyperintense signal intensity are present (*arrow*). (**b**) Corresponding fat-suppressed T1-weighted transaxial image showing hyperintense spots within the myometrium indicating fresh blood related to the dislocated endometrial glands (*arrows*)

Table 2 MRI criteria for adenomyosis

Location	• Focal or diffuse widening of junctional zone (JZ) > 12 mm
	• More often found in the posterior uterine wall
	• Not seen in the cervix
	• Seldom seen as focal lesion without contact to JZ (adenomyoma)
Morphology	• Either diffusely involving the uterus or presenting as a lesion with ill-defined margins blending with the surrounding myometrium
	• Poor definition of endomyometrial junction
	• If focal, may be globular, elliptical but usually not round, spherical
	• Significant mass effect missing, even if large lesion present
	• Mild distortion of endometrium but marked enlargement of the uterus in diffuse adenomyosis
	• Adenomyoma may rarely present as round lesion located away from JZ
	• Lesion may include large cystic areas (cystic adenomyosis)
Appearance on T1	• Mostly isointense to the myometrium
	• May show hyperintense foci corresponding to small areas of hemorrhage
Appearance on T2	• Low SI uterine lesion with or without punctuate high SI foci scattered throughout the lesion or high SI linear striations extending from the edometrium that may lead to a pseudo-widening of the endometrium
	• High SI (micro) cysts may be seen (<5 mm)
	• Rarely large cystic spaces within a lesion (cystic adenomyosis)
Appearance on Gd-enhanced T1	• Can appear hypo-, iso-, and hyperintense relative to myometrium
	• Perfusion abnormalities may be seen on dynamic contrast-enhanced MRI
Additional findings	• No pseudocapsule
	• Adenomyosis frequently seen in combination with findings of endometriosis

3.2.7 Locations, Growth Patterns, and Imaging Characteristics

Uterine adenomyosis is found more often in the posterior than in the anterior wall of the uterus and the fundus (Byun et al. 1999). Adenomyosis does not involve the cervix uteri. A focal type can be differentiated from a diffuse type of thickening of the junctional zone. Diffuse adenomyosis (Fig. 25) may lead to a markedly enlarged uterus with a surprisingly small or disproportional mass effect on the uterine contour and cavity. Focal adenomyosis (Fig. 26) manifests as an oval or a round lesion which leads to thickening of the uterine wall but differs from leiomyoma in that there is only little distortion of the uterine cavity or serosal surface. The lesion shows poorly defined margins and blends with surrounding myometrium. It lacks the pseudocapsule that may be seen with uterine leiomyoma. Signal voids at the periphery of the lesion are rare in focal adenomyosis (Byun et al. 1999). Gadolinium-enhanced T1-weighted imaging does not increase the accuracy in diagnosing adenomyosis of the uterus although perfusion abnormalities may be seen (Hricak et al. 1992). Unusual growth patterns include adenomyoma of the uterus which represents a localized form that manifests as a myometrial or subserosal mass without a direct connection to the junctional zone (Gilks et al. 2000; Tamai et al. 2005). Another rare variant is cystic adenomyosis which is thought to result from extensive hemorrhage within adenomyotic implants, leading to a well-circumscribed cystic myometrial lesion which may show different stages of blood product degradation such as a low-intensity rim on T2-weighted images corresponding to hemosiderin and areas of high signal intensity on T1-weighted images representing fresh blood (Reinhold et al. 1999; Tamai et al. 2005; Troiano et al. 1998). Treatment of adenomyosis by GnRH agonists may also alter its appearance on MR imaging and a decrease in junctional zone thickness and a better lesion demarcation may be observed (Imaoka et al. 2002).

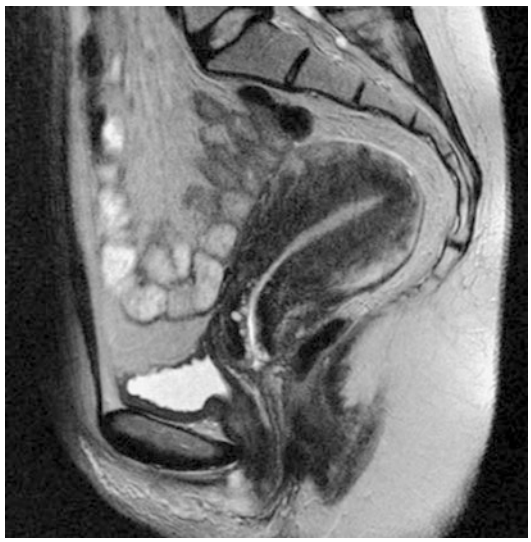

Fig. 25 MRI of diffuse adenomyosis of the uterus. T2-weighted sagittal image of the uterus. A broadened junctional zone (>12 mm) is seen with poor definition of the endomyometrial junction. The junctional zone blends with the myometrium

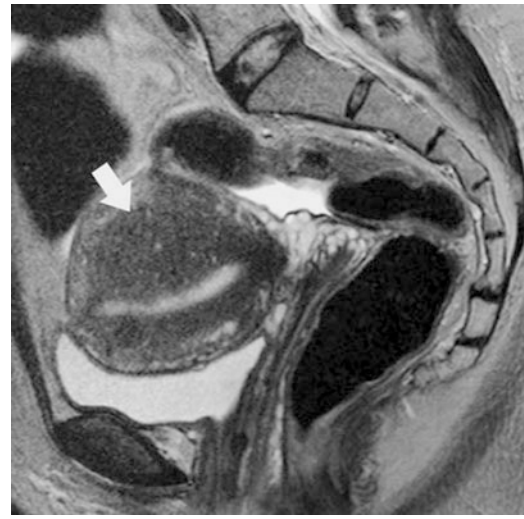

Fig. 26 MRI of focal adenomyosis of the uterus. T2-weighted sagittal image of the uterus. The posterior wall of the uterus is thickened and a focally broadened junctional zone with hyperintense foci appearing as a globular lesion is seen (*arrow*). The uterus is enlarged but no mass effect is seen

3.2.8 Differential Diagnosis

Leiomyomas of the uterus are part of the differential diagnosis for adenomyosis and differentiation is especially important since therapeutic options differ for both entities. Imaging features that favor adenomyosis are poorly defined lesion borders, minimal mass effect, an elliptical instead of a globular shape, and high-signal-intensity spots, cysts, and striations on T2-weighted imaging. Adenomyoma and cystic adenomyosis, however, may be indistinguishable from degenerated leiomyomas at MR imaging or may resemble an aggressive uterine neoplasm (Tamai et al. 2005; Connors et al. 2003). Myometrial contractions may also mimic focal adenomyosis but are transient phenomena.

Endometrial carcinoma can show some overlap with the imaging features associated with adenomyosis such as an irregular endomyometrial junction, high-signal-intensity linear striations on T2-weighted imaging, as well as pseudo-widening of the endometrium. Contrast-enhanced MR imaging has been reported to be useful in case of endometrial carcinoma invading adenomyosis (Utsunomiya et al. 2004). Endometrial stroma sarcoma (ESS) must also be considered when both endometrial and myometrial involvement of an apparently infiltrative lesion with cystic changes is detected (Koyama et al. 1999). A rare differential diagnosis is an adenocarcinoma arising in adenomyosis (Koshiyama et al. 2002; Kuwashima et al. 1994).

3.3 Computed Tomography

3.3.1 CT Technique

Given the availability and cost-effectiveness of ultrasound as a first-line imaging tool to diagnose benign uterine lesions and the proven benefits of MRI in delineating soft-tissue masses of the uterus, little room is left for the use of CT in this setting. With the advent of multislice spiral CT (MSCT) spatial resolution has improved considerably. Current scanner technology allows the acquisition of slices as thin as 0.5 mm. The generation of isotropic voxels allows multiplanar reformations in the desired plane of interest and can aid in determining the exact location of a presumed uterine lesion with respect to surrounding tissues. However, the improvement in spatial resolution is of little benefit for the diagnosis of benign uterine conditions.

3.3.2 CT Appearance of Uterine Leiomyoma and Adenomyosis

While there are no specific CT features of leiomyomas, their presence may be suggested by uterine enlargement, contour deformity, and depiction of calcifications. Calcification is the most specific sign of a leiomyoma and can be found in up to 10% of cases. Calcifications may be mottled, whorled, or streaked in appearance but can also present as a well-defined peripheral rim surrounding the leiomyoma (Casillas et al. 1990). Calcifications may be found only in one of multiple leiomyomas and may be only present in a part of a leiomyoma. On CT, leiomyomas usually exhibit a similar density as surrounding myometrium but may show low-density areas that represent degenerative cystic changes (Fig. 27). CT cannot reliably identify adenomyosis of the uterus. As with uterine leiomyomas, enlargement of the uterus may be present. In adenomyosis there is enlargement while a clear mass lesion or distortion of the uterine contour is absent.

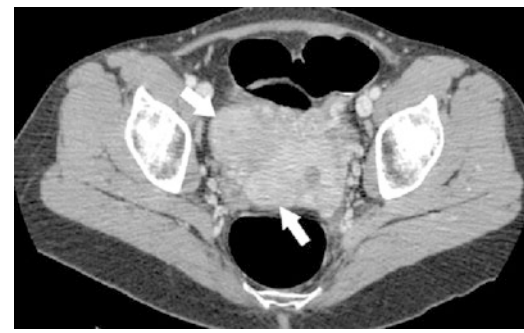

Fig. 27 CT of uterine leiomyomas of the uterus. Contrast-enhanced CT shows subserosal leiomyomas distorting the uterine contour (*arrows*). The fibroids show similar enhancement to adjacent myometrium

3.3.3 Atypical Appearances on CT and Differential Diagnosis

Leiomyomas may undergo spontaneous infarction, which presents clinically as an acute abdomen. Infarction may be related to rapid growth during pregnancy or may be due to acute torsion (Fig. 28) of a pedunculated subserosal leiomyoma (Roy et al. 2005). On unenhanced images small areas of high attenuation indicate hemorrhagic infarction, which is confirmed on contrast-enhanced images (Roy et al. 2005). Superinfection of leiomyomas may occur secondary to degeneration or hemorrhagic infarction if predisposing factors such as diabetes, adnexitis, or an ascending infection that can spread to leiomyomas with contact to the endometrial cavity are present. Pyomyoma develops slowly over days and weeks, particularly in patients after delivery or abortion (Karcaaltincaba and Sudakoff 2003). Specific findings are hypodense areas in combination with pockets of gas within the leiomyoma. If perforation into the peritoneal cavity occurs, discontinuity of the uterine wall,

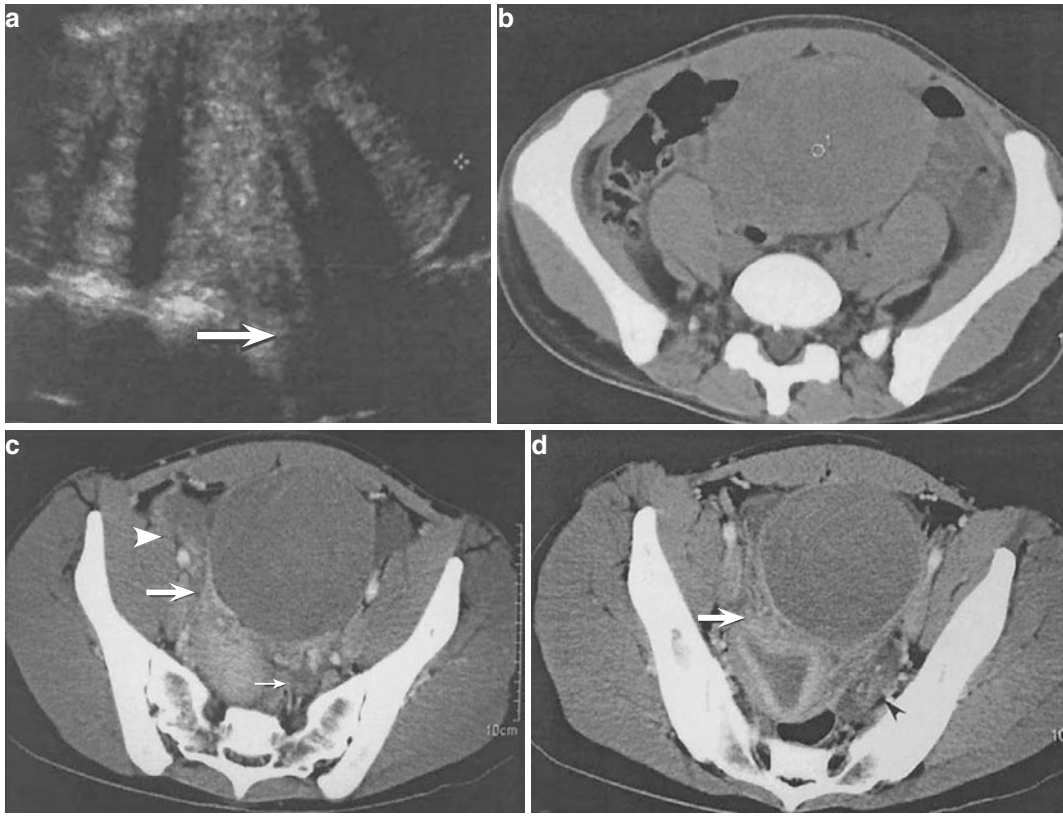

Fig. 28 Acute torsion of a uterine leiomyoma. A 30-year-old-woman with torsion of a pedunculated subserosal leiomyoma. (**a**) Suprapubic US examination in the sagittal plane shows a large (13 cm in diameter), echogenic, heterogeneous mass that compresses the bladder. The uterus is displaced posteriorly (*arrow*). Shadows inside the mass are due to acoustic reflections. (**b**) Unenhanced CT scan shows a large, slightly heterogeneous, abdominopelvic mass (mean value 45 HU). Some linear parts have a higher value of 55 HU. (**c**) Contrast-enhanced CT scan shows intense rim enhancement localized against uptake of contrast medium inside tortuous vessels between the upper anterior part of the corpus uteri and the mass (*large arrow*). There is no enhancement inside the mass. The left ovary is normal and far from the mass (*arrowhead*). Note fluid inside the cul-de-sac (*small arrow*). (**d**) Contrast-enhanced CT scan at a level inferior to that depicted in (**c**) shows thin rim enhancement that is more intense in contact with persistent uptake of contrast medium against the anterior part of the uterus (*arrow*). No enhancement inside the mass was recorded. The endometrial cavity is normally enlarged during the second part of the menstrual cycle. The right ovary is normal (*arrowhead*) (reproduced with permission from reference 928, Roy C, Bierry G, Ghali SE, Buy X, Rossini A (2005) Acute torsion of uterine leiomyoma: CT features. Abdom Imaging. 30:120–123)

intraperitoneal gas, and fluid are usually present, and peritoneal enhancement is seen with peritonitis (Karcaaltincaba and Sudakoff 2003).

The differential diagnosis of acute torsion of a pedunculated leiomyoma includes ovarian/adnexal torsion and uterine torsion (Ghossain et al. 1994; Jeong et al. 2003). The most valuable sign to diagnose acute adnexal torsion is thought to be thickening of the fallopian tube due to venous congestion and edema. Coronal and sagittal reformations from thin-section contrast-enhanced MSCT also aid in identifying the ovarian vascular pedicle and confirm the ovarian origin of a pelvic tumor (Lee et al. 2003). Uterine torsion has been reported to occur more often during pregnancy and is characterized by torsion along the corpus and cervix uteri. A whorled structure of the uterine cervix or a twisting upper vagina is seen on CT (Jeong et al. 2003).

4 UAE for the Treatment of Leiomyoma and Adenomyosis

4.1 Indications

UAE is an established treatment for symptomatic leiomyomas. The gynecologist and interventional radiologist should closely cooperate in establishing the indication for leiomyoma embolization and carefully weigh the indications and contraindications in light of the range of therapeutic options available for the individual patient. UAE must not be performed without careful preinterventional diagnostic workup of the patient's symptoms by the gynecologist. UAE is an alternative therapeutic option only in patients with symptomatic leiomyoma who would otherwise undergo surgery. The "ideal" candidate for UAE is a premenopausal woman with a symptomatic multileiomyoma uterus in whom surgery is indicated and who does not desire to preserve fertility and prefers a minimal invasive intervention. As a rule, both single and multiple leiomyomas can be treated by UAE. The number and location of the individual tumors (subserosal, intramural, transmural, submucosal) do not affect the approach, technique, or outcome of UAE. Nevertheless, one must always thoroughly evaluate the clinical symptoms, imaging findings, and patient's preferences on an individual basis to decide when UAE should be preferred to uterus-sparing surgical approaches or hysterectomy.

Embolization of subserosal pedunculated and intraligamentous leiomyomas is considered to be more risky because postprocedural necrosis of the tumors may cause peritoneal adhesions and decomposition of the leiomyomas into the free abdominal cavity. A number of studies, however, have not demonstrated a higher complication rate of UAE for subserosal pedunculated leiomyomas (Katsumori et al. 2005). From the interventional radiologist's perspective, there is no size limit above which it becomes technically impossible to perform UAE. Early reports on higher complication rates in leiomyomas >10 cm were not confirmed by later studies, which found good clinical results after embolization of large uterine leiomyomas (Prollius et al. 2004; Katsumori et al. 2003). However, the patient must be aware that a markedly enlarged uterus will persist after UAE despite shrinkage of the leiomyomas in case of a multileiomyoma uterus associated with pronounced enlargement before the intervention. UAE is not indicated in patients with contraindications to angiography (clotting disorder, renal insufficiency, manifest hyperthyroidism) and in women with pelvic or urogenital infections (adnexitis, endometritis, urinary tract infection), an adnexal tumor, status post-pelvic radiotherapy, and suspected malignant tumor. An unwillingness to undergo follow-up examinations is a relative contraindication because follow-up is absolutely necessary to evaluate the success of the intervention and to identify and treat possible complications. Since data on the effect of UAE on fertility and the course of pregnancy after UAE is still inadequate, the wish to conceive is considered a contraindication to UAE while a desire to have further children is a relative contraindication to embolization in those women in whom other therapeutic approaches (e.g., laparoscopic/abdominal leiomyoma resection) are an option (McLucas et al. 2001b; Ravina et al. 2000; Spies et al. 2005b; Kakarla

and Ash 2005; Price et al. 2005; Kim et al. 2005). In addition to the gynecologic examination, a recent Pap smear is required, and women with irregular periods (menorrhagia, metrorrhagia) should undergo endometrial sampling before UAE. UAE for adenomyosis occurring either alone or in conjunction with uterine leiomyomas is still under investigation (see also 2.5 Therapy, p. 10). Contrary to previous reports, UAE has been shown to be effective in the midterm for both scenarios (Siskin et al. 2001; Kim et al. 2004; Pelage et al. 2005; Kitamura et al. 2006; Goldberg 2005; McLucas et al. 2002; Jha et al. 2003).

4.2 Technique

UAE is performed under local anesthesia, which may be supplemented by sedation where required, using a transfemoral access and standard Seldinger technique. Prior to embolization, patients receive an intravenous line and a bladder catheter. A 4F or 5F catheter sheath is placed and the internal iliac artery is probed using end-hole catheters. An abdominal aortogram or selective angiographic series of the pelvic arteries is required only in those cases where the road map of the internal iliac artery in left or right anterior oblique projection does not provide adequate information on the origin of the uterine artery. When the uterine artery is strong and its origin takes a straight course, it can be catheterized with the diagnostic catheter. However, coaxial advanced microcatheters should be used deliberately to prevent vascular spasm, in particular when the uterine artery has a small caliber or its origin is at a right angle or twisted. The embolic agent is administered with the blood flow in a fractionated manner (free-flow embolization) once the catheter comes to lie in the horizontal segment of the uterine artery and the angiogram shows good contrast medium flow. Spasm sometimes results in complete cessation of flow and should then be addressed with intra-arterial administration of nitroglycerin or tolazoline. In case of strong spasm, the interventional radiologist should first proceed to embolize the contralateral uterine artery and then try again. Particulate agents are used for UAE in treating both symptomatic uterine leiomyomas and adenomyosis. Well-documented experience is available with polyvinyl alcohol (PVA), Gelfoam, and trisacryl gelatin-coated microspheres (TGM) (Kroncke et al. 2005; McLucas et al. 2001a; Katsumori et al. 2002; Siskin et al. 2001; Kim et al. 2004; Pelage et al. 2005; Hutchins and Worthington-Kirsch 2000; Pelage et al. 2000; Spies et al. 2004b; Spies et al. 2001b). Nonspherical particles measuring 350–750 μm and microspheres ranging in size from 500 to 900 μm are used. PVA particles are used to occlude the uterine artery and stop blood flow in this vessel while the aim of injecting trisacryl gelatin microspheres is to preserve sluggish antegrade flow while occluding the tumoral vascular plexus (Spies et al. 2001b; Pelage et al. 2001). The level of occlusion is documented by last image hold or a final selective series. Following embolization of the contralateral side, the ipsilateral uterine artery is catheterized by formation of a Waltman loop or by simply pulling down a curved catheter such as the Rösch inferior mesenteric catheter which acts like a hook and easily enters the internal iliac artery. When confronted with a difficult anatomic situation on the ipsilateral side, it may become necessary to puncture the other groin. A controversy exists regarding the necessity of obtaining a final aortogram at the time of the intervention to exclude relevant collateral flow to the uterus (e.g., ovarian artery). If MR angiography is performed, relevant blood supply to the uterus through the ovarian artery can be identified noninvasively already before embolization (Kroencke et al. 2006). The technical success rate is over 95% for primary bilateral embolization. Postprocedural management during the first 24(−48) h comprises adequate pain relief using intravenous opioid analgesics or placement of a peridural catheter and administration of nonsteroidal anti-inflammatory agents and antiemetic medication.

4.3 MR Imaging in the Setting of UAE and Uterus-Conserving Surgery

MR imaging prior to UAE or uterus-conserving surgery offers a comprehensive view of the pelvis without superimposed structures even in patients with a markedly enlarged polyleiomyoma uterus. It has been demonstrated that MRI affects patient treatment by reducing unnecessary surgery and identifying co-pathologies prior to UAE (Schwartz et al. 1994; Omary et al. 2002). MR imaging can aid in the preoperative planning for myomectomy by its ability to accurately determine the size and position of individual leiomyomas within the uterine wall and to differentiate conditions which may mimic leiomyoma both clinically and on ultrasound (Weinreb et al. 1990; Battista et al. 2016). Preoperative classification of leiomyomas is of clinical significance since a submucosal tumor with a minor intramural component may be treated by hysteroscopic resection whereas a laparoscopic or transabdominal approach may be required in intramural or subserosal leiomyomas (Dudiak et al. 1988). Knowing the position of a leiomyoma and the thickness of the surrounding myometrium helps one to minimize the risk of uterine perforation during hysteroscopic resection and inadvertent entry into the uterine cavity at myomectomy, which is associated with synechia and may require endometrial repair (Stringer et al. 2001). MR imaging is also useful in monitoring the effect of GnRH therapy on leiomyomas (Andreyko et al. 1988; Zawin et al. 1990).

Besides its high accuracy in the diagnosis of leiomyomas and additional pathologies of the adnexae prior to UAE, MR imaging enables identification of tumors in which embolization is associated with a higher risk such as subserosal pedunculated leiomyomas (Fig. 15) with a narrow stalk or those which will probably not respond to embolization due to their parasitic blood supply such as intraligamentous leiomyomas. However, the ability of MR imaging to predict a successful clinical outcome based on the location, size, and signal intensity of a leiomyoma is still under investigation (Burn et al. 1999; Jha et al. 2000; Spies et al. 2002b). Three-dimensional contrast-enhanced MR angiography can show the uterine arteries and collateral flow via enlarged ovarian arteries and may serve as a "road map" prior to embolization (Fig. 29).

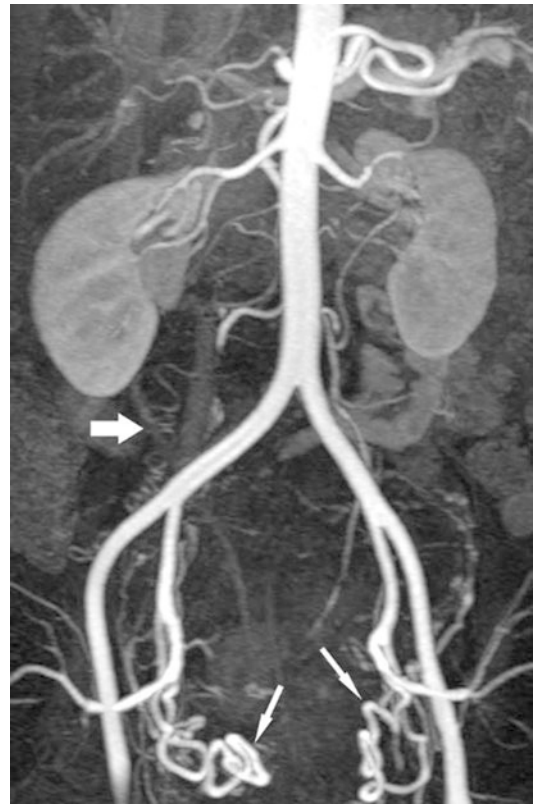

Fig. 29 UAE. Maximum intensity projection of a contrast-enhanced MR angiography depicts the uterine arteries (*long white arrows*) as well as an enlarged the right ovarian artery (*thick white arrow*)

Typical imaging features are observed after leiomyoma embolization (Fig. 30). The tumors show a homogeneous low signal intensity on T2-weighted images after UAE and high signal intensity on T1-weighted images due to hemorrhagic infarction (Fig. 31).

MR imaging also depicts morphologic changes such as sloughing of leiomyomas in contact with the uterine cavity (Fig. 32). The latter may be associated with vaginal discharge in patients having undergone UAE but do not require additional treatment in the majority of cases (Walker et al. 2004). MRI also identifies side effects and complications associated with UAE such as ongoing leiomyoma expulsion, endometritis, and uterine necrosis (Kitamura et al. 2005; Torigian et al. 2005). In case of

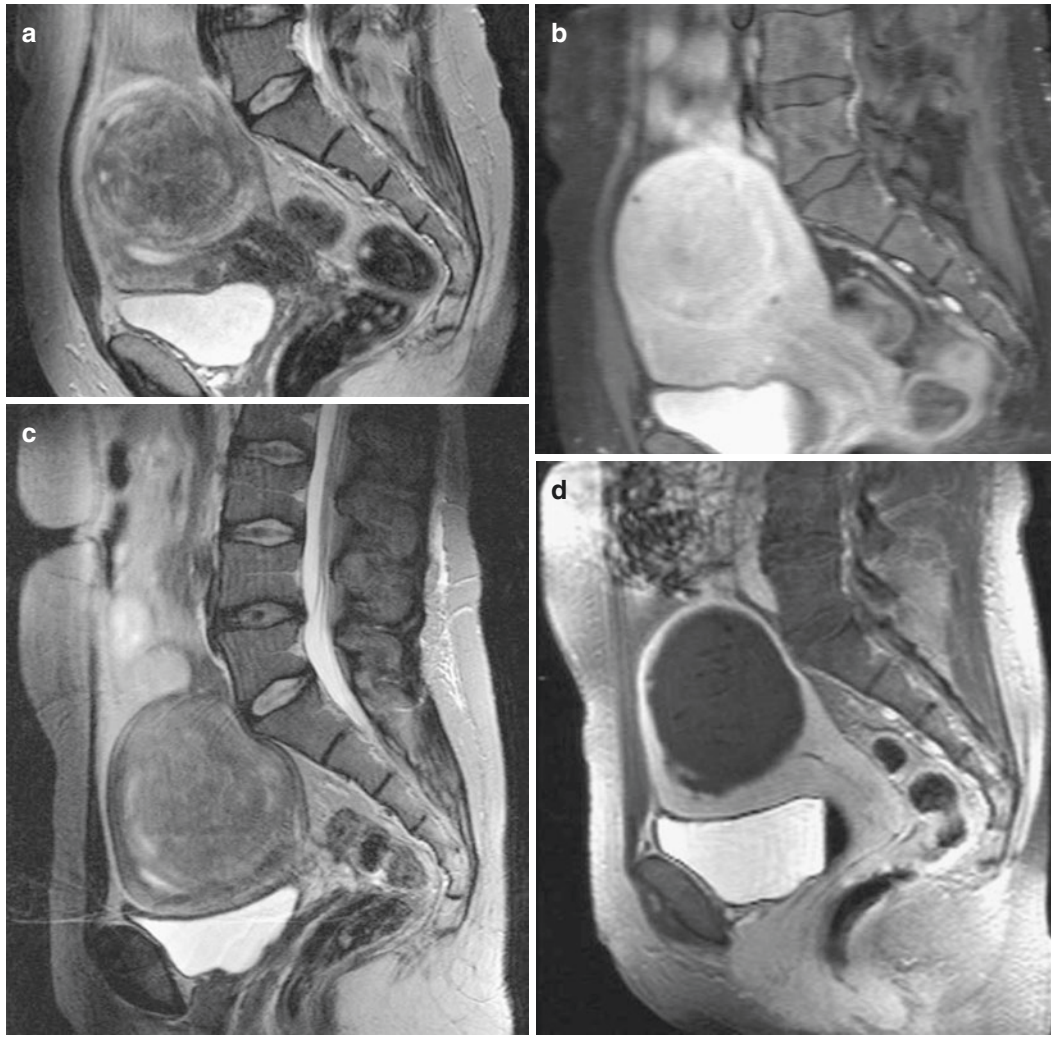

Fig. 30 MR imaging features of leiomyoma before and after UAE. (**a**) T2-weighted sagittal image prior to UAE depicts an intramural leiomyoma with iso- to hypointense signal intensity compared to the adjacent myometrium of the uterus. (**b**) Contrast-enhanced T1-weighted fat-suppressed sagittal image prior to UAE. Strong enhancement of the uterus and leiomyoma. (**c**) T2-weighted sagittal image 72 h after UAE. The leiomyoma shows an increased signal intensity due to edema. (**d**) Contrast-enhanced T1-weighted sagittal image obtained 72 h after UAE shows complete lack of enhancement of the leiomyoma consistent with infarction. The myometrium shows normal perfusion (reproduced with permission from reference 840, Kröncke TJ, Hamm B (2003) Role of magnetic resonance imaging (MRI) in establishing the indication for planning and following up uterine artery embolization (UAE) for treating symptomatic leiomyomas of the uterus [article in German]. Radiologe 43:624–633)

ongoing leiomyoma expulsion a dilated cervical os and leiomyoma tissue pointing towards the cervix may be observed (Fig. 33). Endometritis is seen in 0.5% of cases after UAE, is associated with leiomyoma expulsion, and usually responds well to antibiotics but may spread and result in septicemia if left untreated. At MR imaging tissue within the uterine cavity may be observed together with high-signal-intensity fluid on T2-weighted images indicating retained fluid. Punctuate foci of low signal intensity represent signal voids due to the presence of air on T1- and T2-weighted images. Contrast-enhanced MR images increase the conspicuity of intracavitary fluid collections and also depict hyperperfusion of inflamed adjacent endometrium

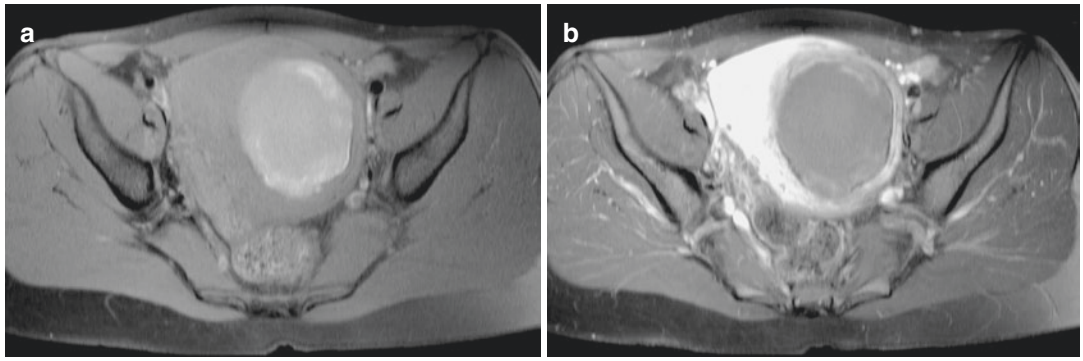

Fig. 31 MRI of hemorrhagic leiomyoma infarction: "bag-of-blood-sign." (**a**) Transaxial T1-weighted fat-suppressed image obtained 3 months after UAE. Peripherally accentuated hyperintense signal intensity of the leiomyoma indicating hemorrhagic transformation of the leiomyoma ("bag-of-blood-sign"). (**b**) Transaxial contrast-enhanced T1-weighted fat-suppressed image obtained 3 months after UAE. Lack of enhancement of the leiomyoma consistent with infarction (reproduced with permission from reference 840, Kröncke TJ, Hamm B (2003) Role of magnetic resonance imaging (MRI) in establishing the indication for planning and following up uterine artery embolization (UAE) for treating symptomatic leiomyomas of the uterus [article in German]. Radiologe 43:624–633)

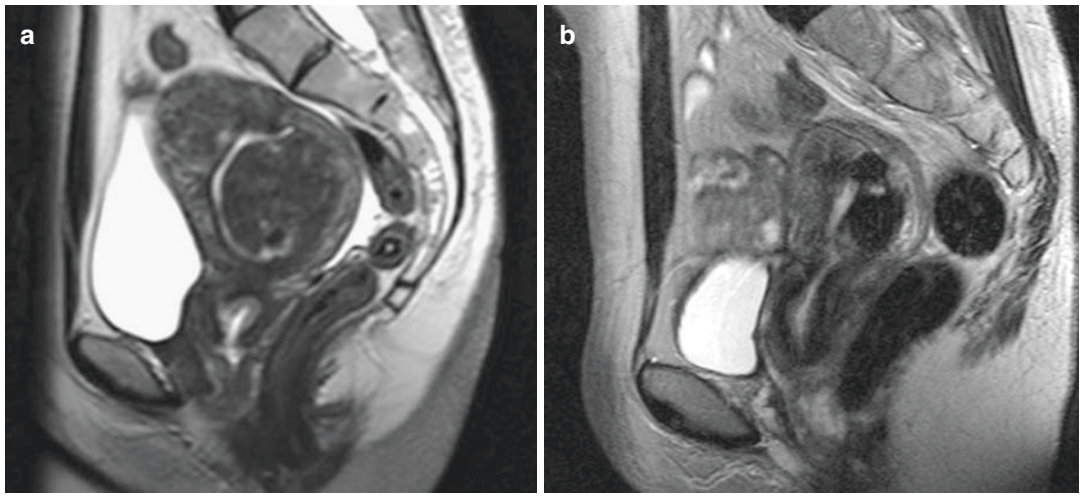

Fig. 32 Sloughing of uterine fibroids after UAE. (**a**) Sagittal T2-weighted prior to UAE shows an intramural leiomyoma in the fundus and a submucosal leiomyoma in the posterior uterine wall. (**b**) Sagittal T2-weighted 24 months after UAE. While the patient reported marked improvement of leiomyoma-associated menorrhagia as early as 3 months after UAE, a late follow-up MRI shows marked decrease in size of the leiomyoma due to ongoing fibroid sloughing

(Kitamura et al. 2005). Contrast-enhanced MRI is helpful in determining persistent perfusion of leiomyomas and adenomyosis after UAE. It has been demonstrated that persistent perfusion may lead to regrowth of leiomyoma tissue and recurrence of symptoms (Pelage et al. 2004). It is important to know that uterine or individual leiomyoma size reduction is not a good indicator of successful embolization since even a partially infarcted leiomyoma undergoes shrinkage while at the same time perfused areas may be present from which the tumor may regrow. The frequency of recurrence of symptoms in cases of persistent perfusion is largely unknown but it is generally accepted among interventional radiologists that persistent perfusion of leiomyoma tissue in the setting of recurrent symptoms indicates technical failure of UAE, which may be attributable to

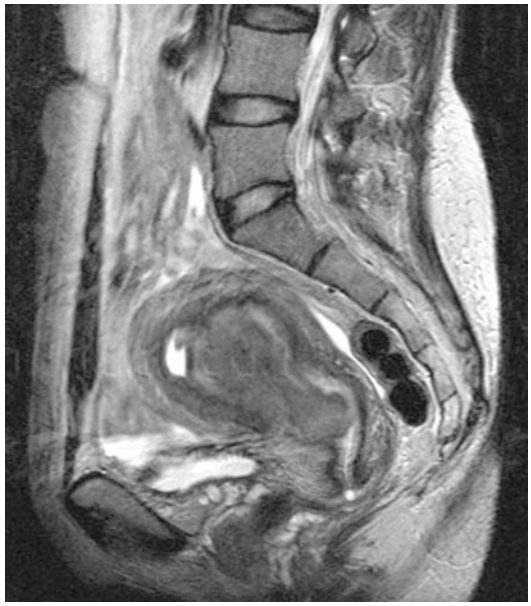

Fig. 33 MRI of ongoing leiomyoma expulsion. T2-weighted sagittal image of a patient 72 h after UAE. A submucosal fibroid shows the typical homogenous high signal intensity of edematous change after embolization. The leiomyoma is deformed, mainly within the uterine cavity, and points towards the cervix. This finding, together with clinical signs (crampy pain), is indicative of ongoing fibroid expulsion

underembolization (causes: vasospasm during UAE, inadequate choice of level of occlusion or of embolic agent) or collateral supply. Complete infarction of leiomyomas indicates technical success of UAE and is associated with long-term clinical success (Pelage et al. 2004; Kroencke et al. 2010).

Bibliography

Abbara S, Spies JB, Scialli AR, Jha RC, Lage JM, Nikolic B (1999) Transcervical expulsion of a fibroid as a result of uterine artery embolization for leiomyomata. J Vasc Interv Radiol 10(4):409–411

ACOG (1994) Uterine leiomyomata. ACOG technical bulletin Number 192—May 1994. Int J Gynaecol Obstet 46(1):73–82

ACOG (2001) ACOG practice bulletin. Surgical alternatives to hysterectomy in the management of leiomyomas. Number 16, May 2000 (replaces educational bulletin number 192, May 1994). Obstet Gynecol 73(3):285–293

American College of Obstetricians and Gynecologists (2008) ACOG practice bulletin. Alternatives to hysterectomy in the management of leiomyomas. Obstet Gynecol 112(2 Pt 1):387–400

Andersen PE, Lund N, Justesen P, Munk T, Elle B, Floridon C (2001) Uterine artery embolization of symptomatic uterine fibroids. Initial success and short-term results. Acta Radiol 42(2):234–238

Andreyko JL, Blumenfeld Z, Marshall LA, Monroe SE, Hricak H, Jaffe RB (1988) Use of an agonistic analog of gonadotropin-releasing hormone (nafarelin) to treat leiomyomas: assessment by magnetic resonance imaging. Am J Obstet Gynecol 158(4):903–910

Ascher SM, Arnold LL, Patt RH et al (1994) Adenomyosis: prospective comparison of MR imaging and transvaginal sonography. Radiology 190(3):803–806

Ascher SM, O'Malley J, Semelka RC, Patt RH, Rajan S, Thomasson D (1999) T2-weighted MRI of the uterus: fast spin echo vs. breath-hold fast spin echo. J Magn Reson Imaging 9(3):384–390

Athanasoulis CA, Waltman AC, Barnes AB, Herbst AL (1976) Angiographic control of pelvic bleeding from treated carcinoma of the cervix. Gynecol Oncol 4(2):144–150

Azziz R (1989) Adenomyosis: current perspectives. Obstet Gynecol Clin N Am 16(1):221–235

Battista C, Capriglione S, Guzzo F et al (2016) The challenge of preoperative identification of uterine myomas: is ultrasound trustworthy? A prospective cohort study. Arch Gynecol Obstet 293(6):1235–1241

Bazot M, Cortez A, Darai E et al (2001) Ultrasonography compared with magnetic resonance imaging for the diagnosis of adenomyosis: correlation with histopathology. Hum Reprod 16(11):2427–2433

Bell SW, Kempson RL, Hendrickson MR (1994) Problematic uterine smooth muscle neoplasms. A clinicopathologic study of 213 cases. Am J Surg Pathol 18(6):535–558

Benson RC, Sneeden VD (1958) Adenomyosis: a reappraisal of symptomatology. Am J Obstet Gynecol 76(5):1044–1057; discussion 1057-1061

Berkowitz RP, Hutchins FL Jr, Worthington-Kirsch RL (1999) Vaginal expulsion of submucosal fibroids after uterine artery embolization. A report of three cases. J Reprod Med 44(4):373–376

Bird CC, McElin TW, Manalo-Estrella P (1972) The elusive adenomyosis of the uterus—revisited. Am J Obstet Gynecol 112(5):583–593

Borah BJ, Nicholson WK, Bradley L, Stewart EA (2013) The impact of uterine leiomyomas: a national survey of affected women. Am J Obstet Gynecol 209(4):319 e311–319 e320

Broder MS, Kanouse DE, Mittman BS, Bernstein SJ (2000) The appropriateness of recommendations for hysterectomy. Obstet Gynecol 95(2):199–205

Broder MS, Goodwin S, Chen G et al (2002) Comparison of long-term outcomes of myomectomy and uterine artery embolization. Obstet Gynecol 100(5 Pt 1):864–868

Brooks SE, Zhan M, Cote T, Baquet CR (2004) Surveillance, epidemiology, and end results analysis

of 2677 cases of uterine sarcoma 1989-1999. Gynecol Oncol 93(1):204–208
Brosens JJ, de Souza NM, Barker FG, Paraschos T, Winston RM (1995) Endovaginal ultrasonography in the diagnosis of adenomyosis uteri: identifying the predictive characteristics. Br J Obstet Gynaecol 102(6):471–474
Brown BJ, Heaston DK, Poulson AM, Gabert HA, Mineau DE, Miller FJ Jr (1979) Uncontrollable postpartum bleeding: a new approach to hemostasis through angiographic arterial embolization. Obstet Gynecol 54(3):361–365
de Bruijn AM, Smink M, Hehenkamp WJK et al (2017) Uterine artery embolization for symptomatic adenomyosis: 7-year clinical follow-up using UFS-Qol questionnaire. Cardiovasc Intervent Radiol 40(9):1344–1350
Brunereau L, Herbreteau D, Gallas S et al (2000) Uterine artery embolization in the primary treatment of uterine leiomyomas: technical features and prospective follow-up with clinical and sonographic examinations in 58 patients. AJR Am J Roentgenol 175(5):1267–1272
Burn P, McCall J, Chinn R, Healy J (1999) Embolization of uterine fibroids. Br J Radiol 72(854):159–161
Buttram VC Jr, Reiter RC (1981) Uterine leiomyomata: etiology, symptomatology, and management. Fertil Steril 36(4):433–445
Byun JY, Kim SE, Choi BG, Ko GY, Jung SE, Choi KH (1999) Diffuse and focal adenomyosis: MR imaging findings. Radiographics 19 Spec No:S161–170
Candiani GB, Fedele L, Parazzini F, Villa L (1991) Risk of recurrence after myomectomy. Br J Obstet Gynaecol 98(4):385–389
Casillas J, Joseph RC, Guerra JJ Jr (1990) CT appearance of uterine leiomyomas. Radiographics 10(6):999–1007
Chiang CH, Chang MY, Hsu JJ et al (1999) Tumor vascular pattern and blood flow impedance in the differential diagnosis of leiomyoma and adenomyosis by color Doppler sonography. J Assist Reprod Genet 16(5):268–275
Chrisman HB, Saker MB, Ryu RK et al (2000) The impact of uterine fibroid embolization on resumption of menses and ovarian function. J Vasc Interv Radiol 11(6):699–703
Colgan TJ, Pron G, Mocarski EJ, Bennett JD, Asch MR, Common A (2003) Pathologic features of uteri and leiomyomas following uterine artery embolization for leiomyomas. Am J Surg Pathol 27(2):167–177
Connors AM, deSouza NM, McIndoe GA (2003) Adenomyoma mimicking an aggressive uterine neoplasm on MRI. Br J Radiol 76(901):66–68
Coronado GD, Marshall LM, Schwartz SM (2000) Complications in pregnancy, labor, and delivery with uterine leiomyomas: a population-based study. Obstet Gynecol 95(5):764–769
Cramer SF, Patel A (1990) The frequency of uterine leiomyomas. Am J Clin Pathol 94(4):435–438
DeWaay DJ, Syrop CH, Nygaard IE, Davis WA, Van Voorhis BJ (2002) Natural history of uterine polyps and leiomyomata. Obstet Gynecol 100(1):3–7
Donnez J, Tomaszewski J, Vazquez F et al (2012) Ulipristal acetate versus leuprolide acetate for uterine fibroids. N Engl J Med 366(5):421–432
Donnez J, Vazquez F, Tomaszewski J et al (2014) Long-term treatment of uterine fibroids with ulipristal acetate. Fertil Steril 101(6):1565–1573 e1561-1518
Donnez J, Hudecek R, Donnez O et al (2015) Efficacy and safety of repeated use of ulipristal acetate in uterine fibroids. Fertil Steril 103(2):519–527.e513
Doridot V, Dubuisson JB, Chapron C, Fauconnier A, Babaki-Fard K (2001) Recurrence of leiomyomata after laparoscopic myomectomy. J Am Assoc Gynecol Laparosc 8(4):495–500
Dubuisson JB, Fauconnier A, Chapron C, Kreiker G, Norgaard C (1998) Second look after laparoscopic myomectomy. Hum Reprod 13(8):2102–2106
Dudiak CM, Turner DA, Patel SK, Archie JT, Silver B, Norusis M (1988) Uterine leiomyomas in the infertile patient: preoperative localization with MR imaging versus US and hysterosalpingography. Radiology 167(3):627–630
Dueholm M, Lundorf E, Olesen F (2002a) Imaging techniques for evaluation of the uterine cavity and endometrium in premenopausal patients before minimally invasive surgery. Obstet Gynecol Surv 57(6):388–403
Dueholm M, Lundorf E, Hansen ES, Ledertoug S, Olesen F (2002b) Accuracy of magnetic resonance imaging and transvaginal ultrasonography in the diagnosis, mapping, and measurement of uterine myomas. Am J Obstet Gynecol 186(3):409–415
Dueholm M, Lundorf E, Sorensen JS, Ledertoug S, Olesen F, Laursen H (2002c) Reproducibility of evaluation of the uterus by transvaginal sonography, hysterosonographic examination, hysteroscopy and magnetic resonance imaging. Hum Reprod 17(1):195–200
Faerstein E, Szklo M, Rosenshein N (2001) Risk factors for uterine leiomyoma: a practice-based case-control study. I. African-American heritage, reproductive history, body size, and smoking. Am J Epidemiol 153(1):1–10
Fauconnier A, Chapron C, Babaki-Fard K, Dubuisson JB (2000) Recurrence of leiomyomata after myomectomy. Hum Reprod Update 6(6):595–602
Fedele L, Bianchi S, Dorta M, Arcaini L, Zanotti F, Carinelli S (1992) Transvaginal ultrasonography in the diagnosis of diffuse adenomyosis. Fertil Steril 58(1):94–97
Fedele L, Bianchi S, Raffaelli R, Portuese A, Dorta M (1997) Treatment of adenomyosis-associated menorrhagia with a levonorgestrel-releasing intrauterine device. Fertil Steril 68(3):426–429
Ferenczy A (1998) Pathophysiology of adenomyosis. Hum Reprod Update 4(4):312–322
Flake GP, Andersen J, Dixon D (2003) Etiology and pathogenesis of uterine leiomyomas: a review. Environ Health Perspect 111(8):1037–1054
Friedman AJ, Rein MS, Pandian MR, Barbieri RL (1990) Fasting serum growth hormone and insulin-like growth factor-I and -II concentrations in women with

leiomyomata uteri treated with leuprolide acetate or placebo. Fertil Steril 53(2):250–253
Ghossain MA, Buy JN, Bazot M et al (1994) CT in adnexal torsion with emphasis on tubal findings: correlation with US. J Comput Assist Tomogr 18(4):619–625
Gilks CB, Clement PB, Hart WR, Young RH (2000) Uterine adenomyomas excluding atypical polypoid adenomyomas and adenomyomas of endocervical type: a clinicopathologic study of 30 cases of an underemphasized lesion that may cause diagnostic problems with brief consideration of adenomyomas of other female genital tract sites. Int J Gynecol Pathol 19(3):195–205
Goldberg J (2005) Uterine artery embolization for adenomyosis: looking at the glass half full. Radiology 236(3):1111–1112; author reply 1112
Goldstein HM, Medellin H, Ben-Menachem Y, Wallace S (1975) Transcatheter arterial embolization in the management of bleeding in the cancer patient. Radiology 115(3):603–608
Goto A, Takeuchi S, Sugimura K, Maruo T (2002) Usefulness of Gd-DTPA contrast-enhanced dynamic MRI and serum determination of LDH and its isozymes in the differential diagnosis of leiomyosarcoma from degenerated leiomyoma of the uterus. Int J Gynecol Cancer 12(4):354–361
Grasel RP, Outwater EK, Siegelman ES, Capuzzi D, Parker L, Hussain SM (2000) Endometrial polyps: MR imaging features and distinction from endometrial carcinoma. Radiology 214(1):47–52
Greenberg MD, Kazamel TI (1995) Medical and socioeconomic impact of uterine fibroids. Obstet Gynecol Clin N Am 22(4):625–636
Hamlin DJ, Pettersson H, Fitzsimmons J, Morgan LS (1985) MR imaging of uterine leiomyomas and their complications. J Comput Assist Tomogr 9(5):902–907
Hanley KZ, Birdsong GG, Mosunjac MB (2017) Recent developments in surgical pathology of the uterine corpus. Arch Pathol Lab Med 141(4):528–541
Hapangama DK, Bulmer JN (2016) Pathophysiology of heavy menstrual bleeding. Womens Health (Lond) 12(1):3–13
Hasan F, Arumugam K, Sivanesaratnam V (1991) Uterine leiomyomata in pregnancy. Int J Gynaecol Obstet 34(1):45–48
Hashimoto K, Azuma C, Kamiura S et al (1995) Clonal determination of uterine leiomyomas by analyzing differential inactivation of the X-chromosome-linked phosphoglycerokinase gene. Gynecol Obstet Investig 40(3):204–208
Hasson HM, Rotman C, Rana N, Sistos F, Dmowski WP (1992) Laparoscopic myomectomy. Obstet Gynecol 80(5):884–888
Hayasaka K, Tanaka Y, Fujii M, Himi K, Negishi N (2000) Intravenous leiomyomatosis. J Comput Assist Tomogr 24(1):83–85
Hehenkamp WJ, Volkers NA, Donderwinkel PF et al (2005) Uterine artery embolization versus hysterectomy in the treatment of symptomatic uterine fibroids (EMMY trial): peri- and postprocedural results from a randomized controlled trial. Am J Obstet Gynecol 193(5):1618–1629
Higgins CB, Bookstein JJ, Davis GB, Galloway DC, Barr JW (1977) Therapeutic embolization for intractable chronic bleeding. Radiology 122(2):473–478
Hirai M, Shibata K, Sagai H, Sekiya S, Goldberg BB (1995) Transvaginal pulsed and color Doppler sonography for the evaluation of adenomyosis. J Ultrasound Med 14(7):529–532
Horta M, Cunha TM, Oliveira R, Magro P (2015) Hydropic leiomyoma of the uterus presenting as a giant abdominal mass. BMJ Case Rep. https://doi.org/10.1136/bcr-2015-211929
Hricak H, Finck S, Honda G, Goranson H (1992) MR imaging in the evaluation of benign uterine masses: value of gadopentetate dimeglumine-enhanced T1-weighted images. AJR Am J Roentgenol 158(5):1043–1050
Hurst BS, Matthews ML, Marshburn PB (2005) Laparoscopic myomectomy for symptomatic uterine myomas. Fertil Steril 83(1):1–23
Hutchins FL Jr, Worthington-Kirsch R (2000) Embolotherapy for myoma-induced menorrhagia. Obstet Gynecol Clin N Am 27(2):397–405
Hutchins FL Jr, Worthington-Kirsch R, Berkowitz RP (1999) Selective uterine artery embolization as primary treatment for symptomatic leiomyomata uteri. J Am Assoc Gynecol Laparosc 6(3):279–284
Imaoka I, Ascher SM, Sugimura K et al (2002) MR imaging of diffuse adenomyosis changes after GnRH analog therapy. J Magn Reson Imaging 15(3):285–290
Iribarne C, Plaza J, De la Fuente P, Garrido C, Garzon A, Olaizola JI (1994) Intramyometrial cystic adenomyosis. J Clin Ultrasound 22(5):348–350
Jacoby VL, Kohi MP, Poder L et al (2016) PROMISe trial: a pilot, randomized, placebo-controlled trial of magnetic resonance guided focused ultrasound for uterine fibroids. Fertil Steril 105(3):773–780
Janus C, White M, Dottino P, Brodman M, Goodman H (1989) Uterine leiomyosarcoma—magnetic resonance imaging. Gynecol Oncol 32(1):79–81
Jeong YY, Kang HK, Park JG, Choi HS (2003) CT features of uterine torsion. Eur Radiol 13(Suppl 4):L249–L250
Jha RC, Ascher SM, Imaoka I, Spies JB (2000) Symptomatic fibroleiomyomata: MR imaging of the uterus before and after uterine arterial embolization. Radiology 217(1):228–235
Jha RC, Takahama J, Imaoka I et al (2003) Adenomyosis: MRI of the uterus treated with uterine artery embolization. AJR Am J Roentgenol 181(3):851–856
Jiang W, Shen Q, Chen M et al (2014) Levonorgestrel-releasing intrauterine system use in premenopausal women with symptomatic uterine leiomyoma: a systematic review. Steroids 86:69–78
Jones MW, Norris HJ (1995) Clinicopathologic study of 28 uterine leiomyosarcomas with metastasis. Int J Gynecol Pathol 14(3):243–249
Kakarla A, Ash AK (2005) Pregnancy after embolisation of a fibroid: emergency caesarean myomectomy. J Obstet Gynaecol 25(3):300–301

Kang S, Turner DA, Foster GS, Rapoport MI, Spencer SA, Wang JZ (1996) Adenomyosis: specificity of 5 mm as the maximum normal uterine junctional zone thickness in MR images. AJR Am J Roentgenol 166(5):1145–1150

Karcaaltincaba M, Sudakoff GS (2003) CT of a ruptured pyomyoma. AJR Am J Roentgenol 181(5):1375–1377

Katsumori T, Nakajima K, Tokuhiro M (2001) Gadolinium-enhanced MR imaging in the evaluation of uterine fibroids treated with uterine artery embolization. AJR Am J Roentgenol 177(2):303–307

Katsumori T, Nakajima K, Mihara T, Tokuhiro M (2002) Uterine artery embolization using gelatin sponge particles alone for symptomatic uterine fibroids: midterm results. AJR Am J Roentgenol 178(1):135–139

Katsumori T, Nakajima K, Mihara T (2003) Is a large fibroid a high-risk factor for uterine artery embolization? AJR Am J Roentgenol 181(5):1309–1314

Katsumori T, Akazawa K, Mihara T (2005) Uterine artery embolization for pedunculated subserosal fibroids. AJR Am J Roentgenol 184(2):399–402

Kawaguchi K, Fujii S, Konishi I, Nanbu Y, Nonogaki H, Mori T (1989) Mitotic activity in uterine leiomyomas during the menstrual cycle. Am J Obstet Gynecol 160(3):637–641

Kawakami S, Togashi K, Konishi I et al (1994) Red degeneration of uterine leiomyoma: MR appearance. J Comput Assist Tomogr 18(6):925–928

Kawamura N, Ichimura T, Ito F et al (2002) Transcervical needle biopsy for the differential diagnosis between uterine sarcoma and leiomyoma. Cancer 94(6):1713–1720

Kido A, Togashi K, Koyama T, Yamaoka T, Fujiwara T, Fujii S (2003a) Diffusely enlarged uterus: evaluation with MR imaging. Radiographics 23(6):1423–1439

Kido A, Monma C, Togashi K et al (2003b) Uterine arterial embolization for the treatment of diffuse leiomyomatosis. J Vasc Interv Radiol 14(5):643–647

Kim JC, Kim SS, Park JY (2000) "Bridging vascular sign" in the MR diagnosis of exophytic uterine leiomyoma. J Comput Assist Tomogr 24(1):57–60

Kim MD, Won JW, Lee DY, Ahn CS (2004) Uterine artery embolization for adenomyosis without fibroids. Clin Radiol 59(6):520–526

Kim MD, Kim NK, Kim HJ, Lee MH (2005) Pregnancy following uterine artery embolization with polyvinyl alcohol particles for patients with uterine fibroid or adenomyosis. Cardiovasc Intervent Radiol 28(5):611–615

Kitamura Y, Ascher SM, Cooper C et al (2005) Imaging manifestations of complications associated with uterine artery embolization. Radiographics 25(Suppl 1):S119–S132

Kitamura Y, Allison SJ, Jha RC, Spies JB, Flick PA, Ascher SM (2006) MRI of adenomyosis: changes with uterine artery embolization. AJR Am J Roentgenol 186(3):855–864

Klatsky PC, Tran ND, Caughey AB, Fujimoto VY (2008) Fibroids and reproductive outcomes: a systematic literature review from conception to delivery. Am J Obstet Gynecol 198(4):357–366

Koshiyama M, Suzuki A, Ozawa M et al (2002) Adenocarcinomas arising from uterine adenomyosis: a report of four cases. Int J Gynecol Pathol 21(3):239–245

Koyama T, Togashi K, Konishi I et al (1999) MR imaging of endometrial stromal sarcoma: correlation with pathologic findings. AJR Am J Roentgenol 173(3):767–772

Kroencke TJ, Gauruder-Burmester A, Enzweiler CN, Taupitz M, Hamm B (2003) Disintegration and stepwise expulsion of a large uterine leiomyoma with restoration of the uterine architecture after successful uterine fibroid embolization: case report. Hum Reprod 18(4):863–865

Kroencke TJ, Scheurig C, Kluner C, Taupitz M, Schnorr J, Hamm B (2006) Contrast-enhanced magnetic resonance angiography to predict ovarian artery supply of uterine fibroids—initial experience. Radiology 241(1):181–189

Kroencke TJ, Scheurig C, Poellinger A, Gronewold M, Hamm B (2010) Uterine artery embolization for leiomyomas: percentage of infarction predicts clinical outcome. Radiology 255(3):834–841

Kroncke TJ, Gauruder-Burmester A, Gronewold M et al (2004) Technical success rate, peri-interventional complications and radiation exposure of the transarterial embolization for leiomyomas of the uterus. Rofo 176(4):580–589

Kroncke TJ, Gauruder-Burmester A, Scheurig C et al (2005) Transarterial embolization for uterine fibroids: clinical success rate and results of magnetic resonance imaging. Rofo 177(1):89–98

Kunz G, Beil D, Huppert P, Leyendecker G (2000) Structural abnormalities of the uterine wall in women with endometriosis and infertility visualized by vaginal sonography and magnetic resonance imaging. Hum Reprod 15(1):76–82

Kunz G, Beil D, Huppert P, Noe M, Kissler S, Leyendecker G (2005) Adenomyosis in endometriosis—prevalence and impact on fertility. Evidence from magnetic resonance imaging. Hum Reprod 20(8):2309–2316

Kuwashima Y, Uehara T, Kishi K et al (1994) Intramural adenocarcinoma of the uterus, arisen from adenomyosis uteri, showing unique histologic appearances. Report of two cases. Eur J Gynaecol Oncol 15(6):418–423

Lakhman Y, Veeraraghavan H, Chaim J et al (2017) Differentiation of uterine leiomyosarcoma from atypical leiomyoma: diagnostic accuracy of qualitative MR imaging features and feasibility of texture analysis. Eur Radiol 27(7):2903–2915

Lee JH, Jeong YK, Park JK, Hwang JC (2003) "Ovarian vascular pedicle" sign revealing organ of origin of a pelvic mass lesion on helical CT. AJR Am J Roentgenol 181(1):131–137

Leibsohn S, d'Ablaing G, Mishell DR Jr, Schlaerth JB (1990) Leiomyosarcoma in a series of hysterectomies performed for presumed uterine leiomyomas. Am J Obstet Gynecol 162(4):968–974. discussion 974–966

Levy B, Mukherjee T, Hirschhorn K (2000) Molecular cytogenetic analysis of uterine leiomyoma and leiomyosarcoma by comparative genomic hybridization. Cancer Genet Cytogenet 121(1):1–8

Leyendecker G, Bilgicyildirim A, Inacker M et al (2015) Adenomyosis and endometriosis. Re-visiting their association and further insights into the mechanisms of auto-traumatisation. An MRI study. Arch Gynecol Obstet 291(4):917–932

Li HM, Liu J, Qiang JW, Zhang H, Zhang GF, Ma F (2016) Diffusion-weighted imaging for differentiating uterine leiomyosarcoma from degenerated leiomyoma. J Comput Assist Tomogr 41(4):599–606

Lin G, Yang LY, Huang YT et al (2016) Comparison of the diagnostic accuracy of contrast-enhanced MRI and diffusion-weighted MRI in the differentiation between uterine leiomyosarcoma/smooth muscle tumor with uncertain malignant potential and benign leiomyoma. J Magn Reson Imaging 43(2):333–342

Lumsden MA, West CP, Hawkins RA, Bramley TA, Rumgay L, Baird DT (1989) The binding of steroids to myometrium and leiomyomata (fibroids) in women treated with the gonadotrophin-releasing hormone agonist Zoladex (ICI 118630). J Endocrinol 121(2):389–396

Lurie S, Gorbacz S, Caspi B, Borenstein R (1991) Parasitic leiomyoma: a case report. Clin Exp Obstet Gynecol 18(1):7–8

Malzoni M, Rotond M, Perone C et al (2003) Fertility after laparoscopic myomectomy of large uterine myomas: operative technique and preliminary results. Eur J Gynaecol Oncol 24(1):79–82

Mara M, Fucikova Z, Maskova J, Kuzel D, Haakova L (2005) Uterine fibroid embolization versus myomectomy in women wishing to preserve fertility: preliminary results of a randomized controlled trial. Eur J Obstet Gynecol Reprod Biol 126(2):226–233

Margolies MN, Ring EJ, Waltman AC, Kerr WS Jr, Baum S (1972) Arteriography in the management of hemorrhage from pelvic fractures. N Engl J Med 287(7):317–321

Mark AS, Hricak H, Heinrichs LW et al (1987) Adenomyosis and leiomyoma: differential diagnosis with MR imaging. Radiology 163(2):527–529

Marshall LM, Spiegelman D, Barbieri RL et al (1997) Variation in the incidence of uterine leiomyoma among premenopausal women by age and race. Obstet Gynecol 90(6):967–973

Mas A, Cervello I, Gil-Sanchis C et al (2012) Identification and characterization of the human leiomyoma side population as putative tumor-initiating cells. Fertil Steril 98(3):741–751. e746

Masui T, Katayama M, Kobayashi S, Sakahara H, Ito T, Nozaki A (2001) T2-weighted MRI of the female pelvis: comparison of breath-hold fast-recovery fast spin-echo and nonbreath-hold fast spin-echo sequences. J Magn Reson Imaging 13(6):930–937

Masui T, Katayama M, Kobayashi S, Shimizu S, Nozaki A, Sakahara H (2003) Pseudolesions related to uterine contraction: characterization with multiphase-multisection T2-weighted MR imaging. Radiology 227(2):345–352

McCausland AM (1992) Hysteroscopic myometrial biopsy: its use in diagnosing adenomyosis and its clinical application. Am J Obstet Gynecol 166(6 Pt 1):1619–1626; discussion 1626–1618

McCausland AM, McCausland VM (1996) Depth of endometrial penetration in adenomyosis helps determine outcome of rollerball ablation. Am J Obstet Gynecol 174(6):1786–1793; 1793–1784

McCluggage WG, Ellis PK, McClure N, Walker WJ, Jackson PA, Manek S (2000) Pathologic features of uterine leiomyomas following uterine artery embolization. Int J Gynecol Pathol 19(4):342–347

McLucas B, Adler L, Perrella R (2001a) Uterine fibroid embolization: nonsurgical treatment for symptomatic fibroids. J Am Coll Surg 192(1):95–105

McLucas B, Goodwin S, Adler L, Rappaport A, Reed R, Perrella R (2001b) Pregnancy following uterine fibroid embolization. Int J Gynaecol Obstet 74(1):1–7

McLucas B, Perrella R, Adler L (2002) Embolization for the treatment of adenomyosis. AJR Am J Roentgenol 178(4):1028–1029

Mercorio F, De Simone R, Di Spiezio Sardo A et al (2003) The effect of a levonorgestrel-releasing intrauterine device in the treatment of myoma-related menorrhagia. Contraception 67(4):277–280

Morita M, Asakawa Y, Nakakuma M, Kubo H (2004) Laparoscopic excision of myometrial adenomyomas in patients with adenomyosis uteri and main symptoms of severe dysmenorrhea and hypermenorrhea. J Am Assoc Gynecol Laparosc 11(1):86–89

Mulvany NJ, Ostor AG, Ross I (1995) Diffuse leiomyomatosis of the uterus. Histopathology 27(2):175–179

Munro MG, Critchley HO, Broder MS, Fraser IS, Disorders FWGM (2011) FIGO classification system (PALM-COEIN) for causes of abnormal uterine bleeding in nongravid women of reproductive age. Int J Gynaecol Obstet 113(1):3–13

Myers ER, Barber MD, Gustilo-Ashby T, Couchman G, Matchar DB, McCrory DC (2002) Management of uterine leiomyomata: what do we really know? Obstet Gynecol 100(1):8–17

Nishida M (1991) Relationship between the onset of dysmenorrhea and histologic findings in adenomyosis. Am J Obstet Gynecol 165(1):229–231

Oguchi O, Mori A, Kobayashi Y, Horiuchi A, Nikaido T, Fujii S (1995) Prediction of histopathologic features and proliferative activity of uterine leiomyoma by magnetic resonance imaging prior to GnRH analogue therapy: correlation between T2-weighted images and effect of GnRH analogue. J Obstet Gynaecol 21(2):107–117

Okamoto T, Koshiyama M, Yamamoto K (2004) Rapidly growing leiomyoma in a postmenopausal woman. J Obstet Gynaecol Res 30(4):316–318

Omary RA, Vasireddy S, Chrisman HB et al (2002) The effect of pelvic MR imaging on the diagnosis and

treatment of women with presumed symptomatic uterine fibroids. J Vasc Interv Radiol 13(11):1149–1153
Ono M, Qiang W, Serna VA et al (2012) Role of stem cells in human uterine leiomyoma growth. PLoS One 7(5):e36935
Outwater EK, Siegelman ES, Van Deerlin V (1998) Adenomyosis: current concepts and imaging considerations. AJR Am J Roentgenol 170(2):437–441
Ozaki T, Takahashi K, Okada M, Kurioka H, Miyazaki K (1999) Live birth after conservative surgery for severe adenomyosis following magnetic resonance imaging and gonadotropin-releasing hormone agonist therapy. Int J Fertil Womens Med 44(5):260–264
Parazzini F, La Vecchia C, Negri E, Cecchetti G, Fedele L (1988) Epidemiologic characteristics of women with uterine fibroids: a case-control study. Obstet Gynecol 72(6):853–857
Parazzini F, Vercellini P, Panazza S, Chatenoud L, Oldani S, Crosignani PG (1997) Risk factors for adenomyosis. Hum Reprod 12(6):1275–1279
Park HR, Kim MD, Kim NK et al (2005) Uterine restoration after repeated sloughing of fibroids or vaginal expulsion following uterine artery embolization. Eur Radiol 15(9):1850–1854
Parker WH, Fu YS, Berek JS (1994) Uterine sarcoma in patients operated on for presumed leiomyoma and rapidly growing leiomyoma. Obstet Gynecol 83(3):414–418
Pattani SJ, Kier R, Deal R, Luchansky E (1995) MRI of uterine leiomyosarcoma. Magn Reson Imaging 13(2):331–333
Pelage JP, Le Dref O, Soyer P et al (2000) Fibroid-related menorrhagia: treatment with superselective embolization of the uterine arteries and midterm follow-up. Radiology 215(2):428–431
Pelage JP, Beregi J, LeDref O, Nonent M, Robert YH, Rymer R (2001) Uterine artery embolization for fibroids using a different end-point for embolization: preliminary results using calibrated microspheres. Radiology 221(P):356
Pelage JP, Guaou NG, Jha RC, Ascher SM, Spies JB (2004) Uterine fibroid tumors: long-term MR imaging outcome after embolization. Radiology 230(3):803–809
Pelage JP, Jacob D, Fazel A et al (2005) Midterm results of uterine artery embolization for symptomatic adenomyosis: initial experience. Radiology 234(3):948–953
Phelan JP (1995) Myomas and pregnancy. Obstet Gynecol Clin N Am 22(4):801–805
Pinto I, Chimeno P, Romo A et al (2003) Uterine fibroids: uterine artery embolization versus abdominal hysterectomy for treatment—a prospective, randomized, and controlled clinical trial. Radiology 226(2):425–431
Pontis A, D'Alterio MN, Pirarba S, de Angelis C, Tinelli R, Angioni S (2016) Adenomyosis: a systematic review of medical treatment. Gynecol Endocrinol 32(9):696–700
Price N, Gillmer MD, Stock A, Hurley PA (2005) Pregnancy following uterine artery embolisation. J Obstet Gynaecol 25(1):28–31
Pritts EA (2001) Fibroids and infertility: a systematic review of the evidence. Obstet Gynecol Surv 56(8):483–491
Prollius A, de Vries C, Loggenberg E, du Plessis A, Nel M, Wessels PH (2004) Uterine artery embolisation for symptomatic fibroids: the effect of the large uterus on outcome. BJOG 111(3):239–242
Pron G (2015) Magnetic resonance-guided high-intensity focused ultrasound (MRgHIFU) treatment of symptomatic uterine fibroids: an evidence-based analysis. Ont Health Technol Assess Ser 15(4):1–86
Pron G, Bennett J, Common A, Wall J, Asch M, Sniderman K (2003) The Ontario Uterine Fibroid Embolization Trial. Part 2. Uterine fibroid reduction and symptom relief after uterine artery embolization for fibroids. Fertil Steril 79(1):120–127
Radosa MP, Owsianowski Z, Mothes A et al (2014) Long-term risk of fibroid recurrence after laparoscopic myomectomy. Eur J Obstet Gynecol Reprod Biol 180:35–39
Rammeh-Rommani S, Mokni M, Stita W et al (2005) Uterine smooth muscle tumors: retrospective epidemiological and pathological study of 2760 cases. J Gynecol Obstet Biol Reprod (Paris) 34(6):568–571
Ravina J, Merland J, Herbetreau D, Houdart E, Bouret J, Madelenat P (1994) Embolisation pré-opératoire des fibromes utérins. Presse Med 23(33):1540
Ravina JH, Vigneron NC, Aymard A, Le Dref O, Merland JJ (2000) Pregnancy after embolization of uterine myoma: report of 12 cases. Fertil Steril 73(6):1241–1243
Razavi MK, Hwang G, Jahed A, Modanloo S, Chen B (2003) Abdominal myomectomy versus uterine fibroid embolization in the treatment of symptomatic uterine leiomyomas. AJR Am J Roentgenol 180(6):1571–1575
Reed SD, Cushing-Haugen KL, Daling JR, Scholes D, Schwartz SM (2004) Postmenopausal estrogen and progestogen therapy and the risk of uterine leiomyomas. Menopause 11(2):214–222
Rein MS, Barbieri RL, Friedman AJ (1995) Progesterone: a critical role in the pathogenesis of uterine myomas. Am J Obstet Gynecol 172(1 Pt 1):14–18
Reinhold C, Atri M, Mehio A, Zakarian R, Aldis AE, Bret PM (1995) Diffuse uterine adenomyosis: morphologic criteria and diagnostic accuracy of endovaginal sonography. Radiology 197(3):609–614
Reinhold C, McCarthy S, Bret PM et al (1996) Diffuse adenomyosis: comparison of endovaginal US and MR imaging with histopathologic correlation. Radiology 199(1):151–158
Reinhold C, Tafazoli F, Wang L (1998) Imaging features of adenomyosis. Hum Reprod Update 4(4):337–349
Reinhold C, Tafazoli F, Mehio A, et al (1999) Uterine adenomyosis: endovaginal US and MR imaging features with histopathologic correlation. Radiographics 19 Spec No:S147–160
Rice JP, Kay HH, Mahony BS (1989) The clinical significance of uterine leiomyomas in pregnancy. Am J Obstet Gynecol 160(5 Pt 1):1212–1216

Robboy SJ, Bentley RC, Butnor K, Anderson MC (2000) Pathology and pathophysiology of uterine smooth-muscle tumors. Environ Health Perspect 108(Suppl 5):779–784

Robles-Frias A, Severin CE, Robles-Frias MJ, Garrido JL (2001) Diffuse uterine leiomyomatosis with ovarian and parametrial involvement. Obstet Gynecol 97(5 Pt 2):834–835

Ross RK, Pike MC, Vessey MP, Bull D, Yeates D, Casagrande JT (1986) Risk factors for uterine fibroids: reduced risk associated with oral contraceptives. Br Med J (Clin Res Ed) 293(6543):359–362

Roy C, Bierry G, Ghali SE, Buy X, Rossini A (2005) Acute torsion of uterine leiomyoma: CT features. Abdom Imaging 30(1):120–123

Sadan O, van Iddekinge B, van Gelderen CJ et al (1987) Oestrogen and progesterone receptor concentrations in leiomyoma and normal myometrium. Ann Clin Biochem 24(Pt 3):263–267

Sahdev A, Sohaib SA, Jacobs I, Shepherd JH, Oram DH, Reznek RH (2001) MR imaging of uterine sarcomas. AJR Am J Roentgenol 177(6):1307–1311

Samadi AR, Lee NC, Flanders WD, Boring JR 3rd, Parris EB (1996) Risk factors for self-reported uterine fibroids: a case-control study. Am J Public Health 86(6):858–862

Sawin SW, Pilevsky ND, Berlin JA, Barnhart KT (2000) Comparability of perioperative morbidity between abdominal myomectomy and hysterectomy for women with uterine leiomyomas. Am J Obstet Gynecol 183(6):1448–1455

Scheurig-Muenkler C, Lembcke A, Froeling V, Maurer M, Hamm B, Kroencke TJ (2011) Uterine artery embolization for symptomatic fibroids: long-term changes in disease-specific symptoms and quality of life. Hum Reprod 26(8):2036–2042

Schwartz SM (2001) Invited commentary: studying the epidemiology of uterine leiomyomata—past, present, and future. Am J Epidemiol 153(1):27–29. discussion 30

Schwartz LB, Panageas E, Lange R, Rizzo J, Comite F, McCarthy S (1994) Female pelvis: impact of MR imaging on treatment decisions and net cost analysis. Radiology 192(1):55–60

Schwartz LB, Zawin M, Carcangiu ML, Lange R, McCarthy S (1998) Does pelvic magnetic resonance imaging differentiate among the histologic subtypes of uterine leiomyomata? Fertil Steril 70(3):580–587

Scoutt LM, McCarthy SM, Lange R, Bourque A, Schwartz PE (1994) MR evaluation of clinically suspected adnexal masses. J Comput Assist Tomogr 18(4):609–618

Shozu M, Murakami K, Inoue M (2004) Aromatase and leiomyoma of the uterus. Semin Reprod Med 22(1):51–60

Siegler AM, Camilien L (1994) Adenomyosis. J Reprod Med 39(11):841–853

Siskin GP, Tublin ME, Stainken BF, Dowling K, Dolen EG (2001) Uterine artery embolization for the treatment of adenomyosis: clinical response and evaluation with MR imaging. AJR Am J Roentgenol 177(2):297–302

deSouza NM, Williams AD (2002) Uterine arterial embolization for leiomyomas: perfusion and volume changes at MR imaging and relation to clinical outcome. Radiology 222(2):367–374

Soysal ME, Soysal SK, Vicdan K (2001) Thermal balloon ablation in myoma-induced menorrhagia under local anesthesia. Gynecol Obstet Investig 51(2):128–133

Spies JB, Ascher SA, Roth AR, Kim J, Levy EB, Gomez-Jorge J (2001a) Uterine artery embolization for leiomyomata. Obstet Gynecol 98(1):29–34

Spies JB, Benenati JF, Worthington-Kirsch RL, Pelage JP (2001b) Initial experience with use of tris-acryl gelatin microspheres for uterine artery embolization for leiomyomata. J Vasc Interv Radiol 12(9):1059–1063

Spies JB, Spector A, Roth AR, Baker CM, Mauro L, Murphy-Skrynarz K (2002a) Complications after uterine artery embolization for leiomyomas. Obstet Gynecol 100(5 Pt 1):873–880

Spies JB, Roth AR, Jha RC et al (2002b) Leiomyomata treated with uterine artery embolization: factors associated with successful symptom and imaging outcome. Radiology 222(1):45–52

Spies JB, Cooper JM, Worthington-Kirsch R, Lipman JC, Mills BB, Bennetati JF (2004a) Outcome of uterine embolization and hysterectomy for leiomyomas: results of a multicenter study. Obstet Gynecol Surv 59(12):819–820

Spies JB, Allison S, Flick P et al (2004b) Polyvinyl alcohol particles and tris-acryl gelatin microspheres for uterine artery embolization for leiomyomas: results of a randomized comparative study. J Vasc Interv Radiol 15(8):793–800

Spies JB, Bruno J, Czeyda-Pommersheim F, Magee ST, Ascher SA, Jha RC (2005a) Long-term outcome of uterine artery embolization of leiomyomata. Obstet Gynecol 106(5):933–939

Spies JB, Patel AA, Epstein NB, White AM (2005b) Recent advances in uterine fibroid embolization. Curr Opin Obstet Gynecol 17(6):562–567

Stewart EA (2001) Uterine fibroids. Lancet 357(9252):293–298

Stewart EA, Nowak RA (1996) Leiomyoma-related bleeding: a classic hypothesis updated for the molecular era. Hum Reprod Update 2(4):295–306

Stewart EA, Gostout B, Rabinovici J, Kim HS, Regan L, Tempany CM (2007) Sustained relief of leiomyoma symptoms by using focused ultrasound surgery. Obstet Gynecol 110(2 Pt 1):279–287

Stewart EA, Shuster LT, Rocca WA (2012) Reassessing hysterectomy. Minn Med 95(3):36–39

Stewart EA, Cookson CL, Gandolfo RA, Schulze-Rath R (2017) Epidemiology of uterine fibroids: a systematic review. BJOG. https://doi.org/10.1111/1471-0528.14640

Stringer NH, Strassner HT, Lawson L et al (2001) Pregnancy outcomes after laparoscopic myomectomy with ultrasonic energy and laparoscopic suturing of the endometrial cavity. J Am Assoc Gynecol Laparosc 8(1):129–136

Suginami H, Kaura R, Ochi H, Matsuura S (1990) Intravenous leiomyomatosis with cardiac extension: successful surgical management and histopathologic study. Obstet Gynecol 76(3 Pt 2):527–529

Takemori M, Nishimura R, Sugimura K (1992) Magnetic resonance imaging of uterine leiomyosarcoma. Arch Gynecol Obstet 251(4):215–218

Tamai K, Togashi K, Ito T, Morisawa N, Fujiwara T, Koyama T (2005) MR imaging findings of adenomyosis: correlation with histopathologic features and diagnostic pitfalls. Radiographics 25(1):21–40

Tamai K, Koyama T, Saga T et al (2008) The utility of diffusion-weighted MR imaging for differentiating uterine sarcomas from benign leiomyomas. Eur Radiol 18(4):723–730

Tamaya T, Fujimoto J, Okada H (1985) Comparison of cellular levels of steroid receptors in uterine leiomyoma and myometrium. Acta Obstet Gynecol Scand 64(4):307–309

Togashi K, Ozasa H, Konishi I et al (1989) Enlarged uterus: differentiation between adenomyosis and leiomyoma with MR imaging. Radiology 171(2):531–534

Togashi K, Kawakami S, Kimura I et al (1993a) Uterine contractions: possible diagnostic pitfall at MR imaging. J Magn Reson Imaging 3(6):889–893

Togashi K, Kawakami S, Kimura I et al (1993b) Sustained uterine contractions: a cause of hypointense myometrial bulging. Radiology 187(3):707–710

Torashima M, Yamashita Y, Matsuno Y et al (1998) The value of detection of flow voids between the uterus and the leiomyoma with MRI. J Magn Reson Imaging 8(2):427–431

Torigian DA, Siegelman ES, Terhune KP, Butts SF, Blasco L, Shlansky-Goldberg RD (2005) MRI of uterine necrosis after uterine artery embolization for treatment of uterine leiomyomata. AJR Am J Roentgenol 184(2):555–559

Townsend DE, Sparkes RS, Baluda MC, McClelland G (1970) Unicellular histogenesis of uterine leiomyomas as determined by electrophoresis by glucose-6-phosphate dehydrogenase. Am J Obstet Gynecol 107(8):1168–1173

Troiano RN, Flynn SD, McCarthy S (1998) Cystic adenomyosis of the uterus: MRI. J Magn Reson Imaging 8(6):1198–1202

Tropeano G, Di Stasi C, Litwicka K, Romano D, Draisci G, Mancuso S (2004) Uterine artery embolization for fibroids does not have adverse effects on ovarian reserve in regularly cycling women younger than 40 years. Fertil Steril 81(4):1055–1061

Tsushima Y, Kita T, Yamamoto K (1997) Uterine lipoleiomyoma: MRI, CT and ultrasonographic findings. Br J Radiol 70(838):1068–1070

Tulandi T, Murray C, Guralnick M (1993) Adhesion formation and reproductive outcome after myomectomy and second-look laparoscopy. Obstet Gynecol 82(2):213–215

Ueda H, Togashi K, Konishi I et al (1999) Unusual appearances of uterine leiomyomas: MR imaging findings and their histopathologic backgrounds. Radiographics 19:131–145

Utsunomiya D, Notsute S, Hayashida Y et al (2004) Endometrial carcinoma in adenomyosis: assessment of myometrial invasion on T2-weighted spin-echo and gadolinium-enhanced T1-weighted images. AJR Am J Roentgenol 182(2):399–404

Walker WJ, Pelage JP (2002) Uterine artery embolisation for symptomatic fibroids: clinical results in 400 women with imaging follow up. BJOG 109(11):1262–1272

Walker WJ, Carpenter TT, Kent AS (2004) Persistent vaginal discharge after uterine artery embolization for fibroid tumors: cause of the condition, magnetic resonance imaging appearance, and surgical treatment. Am J Obstet Gynecol 190(5):1230–1233

Wamsteker K, Emanuel MH, de Kruif JH (1993) Transcervical hysteroscopic resection of submucous fibroids for abnormal uterine bleeding: results regarding the degree of intramural extension. Obstet Gynecol 82(5):736–740

Weichert W, Denkert C, Gauruder-Burmester A et al (2005) Uterine arterial embolization with tris-acryl gelatin microspheres: a histopathologic evaluation. Am J Surg Pathol 29(7):955–961

Weinreb JC, Barkoff ND, Megibow A, Demopoulos R (1990) The value of MR imaging in distinguishing leiomyomas from other solid pelvic masses when sonography is indeterminate. AJR Am J Roentgenol 154(2):295–299

Wildemeersch D, Schacht E (2002) The effect on menstrual blood loss in women with uterine fibroids of a novel "frameless" intrauterine levonorgestrel-releasing drug delivery system: a pilot study. Eur J Obstet Gynecol Reprod Biol 102(1):74–79

Wood C, Maher P, Hill D (1994) Biopsy diagnosis and conservative surgical treatment of adenomyosis. J Am Assoc Gynecol Laparosc 1(4 Pt 1):313–316

Wright JD, Herzog TJ, Tsui J et al (2013) Nationwide trends in the performance of inpatient hysterectomy in the United States. Obstet Gynecol 122(2 Pt 1):233–241

Yamashita Y, Torashima M, Takahashi M et al (1993) Hyperintense uterine leiomyoma at T2-weighted MR imaging: differentiation with dynamic enhanced MR imaging and clinical implications. Radiology 189(3):721–725

Yamashita Y, Tang Y, Abe Y, Mitsuzaki K, Takahashi M (1998) Comparison of ultrafast half-Fourier single-shot turbo spin-echo sequence with turbo spin-echo sequences for T2-weighted imaging of the female pelvis. J Magn Reson Imaging 8(6):1207–1212

Yeh HC, Kaplan M, Deligdisch L (1999) Parasitic and pedunculated leiomyomas: ultrasonographic features. J Ultrasound Med 18(11):789–794

Ylikorkala O, Tiitinen A, Hulkko S, Kivinen S, Nummi S (1995) Decrease in symptoms, blood loss and uterine size with nafarelin acetate before abdominal hysterectomy: a placebo-controlled, double-blind study. Hum Reprod 10(6):1470–1474

Zacharia TT, O'Neill MJ (2006) Prevalence and distribution of adnexal findings suggesting endometriosis

in patients with MR diagnosis of adenomyosis. Br J Radiol 79(940):303–307

Zaloudek C, Hendrickson MR (2002) Mesenchymal tumors of the uterus. In: Kurman RJ, Ellenson H, Lora R, Brigitte M (eds) Blaustein's pathology of the female genital tract. Springer, New York, p 567ff

Zawin M, McCarthy S, Scoutt LM, Comite F (1990) High-field MRI and US evaluation of the pelvis in women with leiomyomas. Magn Reson Imaging 8(4):371–376

Zhou J, He L, Liu P et al (2016) Outcomes in adenomyosis treated with uterine artery embolization are associated with lesion vascularity: a long-term follow-up study of 252 cases. PLoS One 11(11):e0165610

Cervical Cancer

Federico Collettini and Bernd Hamm

Contents

F. Collettini, M.D. (✉)
Klinik für Radiologie (Campus Virchow-Klinikum), Charité—Universitätsmedizin Berlin, Augustenburger Platz 1, Berlin 13353, Germany
e-mail: federico.colletini@charite.de

B. Hamm, M.D.
Institut für Radiologie (Campus Mitte), Klinik für Radiologie (Campus Virchow-Klinikum), Klinik und Hochschulambulanz für Radiologie (Campus Benjamin Franklin), Charité—Universitätsmedizin Berlin, Charitéplatz 1, Berlin 10117, Germany
e-mail: Bernd.Hamm@charite.de

1 Background

1.1 Epidemiology

Cervical cancer is the fourth most commonly diagnosed cancer among females worldwide, with an estimated 528,000 cases and 266,000 deaths in 2012 (http://globocan.iarc.fr/old/FactSheets/cancers/cervix-new.asp). In less developed countries the incidence of cervical cancer remains substantially higher than in industrialized countries and accounts for almost 12% of all female cancers. High-risk regions include Eastern Africa, Melanesia, and Southern and Middle Africa (http://globocan.iarc.fr/old/FactSheets/cancers/cervix-new.asp). In Europe, about 58,000 women are diagnosed with invasive cervical cancer per year and about 24,000 women die from the disease (Ferlay et al. 2013). In Germany, approximately 5000 new cases are diagnosed per year and approximately 1500 women die from cervical cancer every year (Ferlay et al. 2013). Historically, the mean age of onset used to be 52 years, but there is a tendency toward earlier onset. In fact, recent data show that on average each year approximately 52% of cervical cancer cases were diagnosed in females aged under 45, with a peak in the age-specific incidence rates in the 25–29 age group (Cancer Research UK 2016).

The overall incidence of invasive cervical cancer has dropped dramatically in the last 50 years. European age-standardized incidence rates peaked in 1985–1987, decreased by 50% to their

Med Radiol Diagn Imaging (2017)
DOI 10.1007/174_2017_54, © Springer International Publishing AG
Published Online: 12 July 2017

lowest point in 2004–2006, and have since remained stable. The largest decreases have been in females aged 50–64 and 65–79, with European age-standardized incidence rates decreasing by 62% and 64%, respectively, between 1985–1987 and 2011–2013. This decline is attributable to the availability of cytological screening, which has led to the identification and therapy of precursor lesions, thus preventing their progression to invasive cervical cancer (Gustafsson et al. 1997; Womack and Warren 1998; Plaxe and Saltzstein 1999). The overall mortality from cervical cancer has declined by over 50% since 1970 and the figures continue to decrease slightly. The annual mortality rate today is 2.4 per 100,000 women in the USA and ranges between 0.7 (Iceland) and 14.2 (Romania) in Europe. In addition, there has been a change in therapeutic strategies as it has been shown, for instance, that certain subgroups of patients benefit from the combination of surgery and radiochemotherapy. Novel and minimally invasive operative techniques primarily aim to improve the patient's postoperative quality of life. Despite these advances, there has been only slight change in the prognosis of invasive cervical cancer over the last decades. The average relative 5-year survival rate in the USA raised from 69% in 1975 to 70% in 2010 (Siegel et al. 2015).

1.2 Pathogenesis

The main cause of cervical cancer is infection of the cervical epithelium by one of the oncogenic human papilloma virus (HPV) types. The high-risk types of HPV are 16 and 18, which have been shown to have a high oncogenic potential (Castle et al. 2002; Lorincz et al. 2002; Walboomers et al. 1999; Yamada et al. 1997; Bosch et al. 1995; Munoz et al. 2002). HPV16/18 account for at least two-thirds of cervical carcinomas in all continents. The overall prevalence of cervical HPV infections is 5–20%, with a peak between 20 and 25 years of age. Spontaneous regression and clearance of HPV infection with complete eradication of the virus by cell-mediated immunity within 1–2 years of exposure are common (Walboomers et al. 1999). Persistence of the virus is only associated with the risk of epithelial changes of the cervical mucosa. Especially women with cofactors such as multiple sexual partners, poor genital hygiene, or immunosuppression as in women with AIDS are at risk of developing invasive cancer (Smith et al. 2002a, b). Cervical cancer of the squamous cell type develops in several stages from local epithelial proliferation, through definitive epithelial changes and dysplasia, to a truly precancerous lesion. The precancerous stages are referred to as cervical intraepithelial neoplasia (CIN) (Richart 1973) or squamous intraepithelial lesion (SIL) and first progress to carcinoma in situ before they become invasive cancers. About 3–5% of sexually mature women have CIN. The incidence of advanced precancerous conditions (CIN II, III) is about 100 times higher than the incidence of cervical cancer. CIN often resolves spontaneously but may also progress to carcinoma in situ—typically between 25 and 35 years of age—and finally to invasive cervical cancer at around age 40. Cervical cancer usually arises from the cervical transformation zone, a ring of mucosa at the junction between the squamous epithelium of the portio and the columnar epithelium of the cervical canal (Schiffman et al. 2007).

1.3 Screening

The ultimate goal of cervical screening tests is to decrease the incidence and the subsequent mortality from invasive cervical cancer through the identification of precursor lesions. In fact since the introduction of the conventional cytology test (commonly referred to as the Pap smear) in the mid-twentieth century cervical cancer incidence and mortality rates have declined significantly (Smith et al. 2015). For the period from 2002 to 2011, cervical cancer incidence rates decreased at an average annual rate of 1.2% per year in women younger than 50 years and by 1.5% per year in women aged 50 years and older (Smith et al. 2015). Following the indications of current guidelines, cervical screening should begin at age 21 years and should be discontinued after the age of 65 years in case of three consecutive negative cytology tests (Smith et al. 2015). While women of 21–29 years should receive cytology screening every 3 years, for women of 30–65 years, the preferred approach

is the combination of cytology and human papillomavirus (HPV) testing every 5 years (Smith et al. 2015). Thanks to these efforts, today over 80% of cervical carcinomas are detected at stage I when the tumor is still locally confined.

1.4 HPV Vaccination

Due to the etiologic role of HPV in the pathogenesis of cervical neoplasia, immunization against HPV infection offers a primary prevention strategy. In the past 10 years, most industrialized countries have introduced national HPV vaccination programs targeting adolescent girls (Kahn 2009). Ten years ago, in 2006, the first vaccine targeting HPV was approved by the US Food and Drug Administration. This quadrivalent vaccine using a late protein L1 construct to induce antibody-mediated immunity is active against HPV genotypes 6, 11, 16, and 18, which are responsible for approximately 66% of cervical cancers and 90% of genital warts. In 2009, a bivalent (HPV-16, -18) vaccine was approved, with similar efficacy profile against cervical cancers caused by these HPV genotypes. More recently, in 2014 a vaccine targeting nine HPV types was approved and demonstrated over 95% efficacy against the additional HPV genotypes in Phase III trials (Castle and Maza 2016). Current guidelines indorse routine HPV vaccination principally for females aged 11–12 years; all forms of HPV vaccine are currently recommended as a three-dose schedule across a 6-month period.

1.5 Clinical Presentation

Early forms of cervical cancer do not present any symptoms. Clinical symptoms occur fairly late, typically when the tumor has reached the stage of invasive ulcerating cancer. The symptoms include vaginal bleeding after intercourse, vaginal discharge, and dyspareunia. Diffuse pelvic and back pain radiating into the legs may indicate advanced cervical cancer with infiltration of adjacent structures. Large cervical cancers may cause pain or bleeding with urination or passage of stools. Tumor-induced disturbance of lymphatic drainage causes unilateral leg edema, peritoneal seeding, and increased body circumference. General symptoms of advanced cervical cancer are a decline of physical performance and weight loss. Late complications include respiratory disturbance and cough in patients with metastatic spread to the lungs.

1.6 Histopathology

Histologically, approximately 80% of all cervical cancers are of the keratinizing or nonkeratinizing squamous cell type. Adenocarcinoma is the second most common histologic type, accounting for about 15% of all cervical cancers (Vizcaino et al. 2000). Although infection with a carcinogenic HPV is a necessary cause of both squamous cell carcinoma and adenocarcinoma, the latter has been found to correlate with recurrent or chronic cervicitis and the intake of estrogen-containing drugs. Stage II and III adenocarcinomas have a slightly more unfavorable prognosis than squamous cell carcinoma (Davidson et al. 1989). A small proportion (about 3%) of adenocarcinomas is of the histologic subtype of highly differentiated mucinous adenocarcinoma. This so-called adenoma malignum has a very poor prognosis because of its early spread into the abdominal cavity and poorer response to chemotherapy or radiotherapy (Kaminski and Norris 1983; Fu et al. 1982). At the same time, its well-differentiated morphology may lead to misinterpretation of its malignancy. MRI depicts a solid tumor containing multiple cysts arising from the endocervical glands and invading the cervical stroma (Doi et al. 1997). This malignant tumor is difficult to differentiate from cystic cervical lesions, which have a similar appearance. The solid tumor portions provide the key to the diagnosis (Li et al. 1999). Adenoma malignum is often seen in patients with Peutz-Jeghers syndrome, which is characterized by pigmentation of the skin and mucous membranes, multiple hamartomas of the gastrointestinal tract, and ovarian tumors (Chen 1986). Among the rarer histologic types of cervical cancer is adenosquamous carcinoma with a proportion of 3% and a poorer prognosis than squamous cell carcinoma and adenocarcinoma (Sheridan et al. 1996). Other types of cervical tumors are

neuroendocrine tumors, small-cell tumors, and rhabdomyosarcoma. Small-cell cervical cancer has a poor prognosis due to early metastatic spread. Neuroendocrine tumors account for 0.3% of cervical cancers and show aggressive growth. Accompanying carcinoid syndrome is rare and the clinical symptoms do not differ from those of squamous cell carcinoma (Lea et al. 2002; Koch et al. 1999; Ueda and Yamasaki 1992; Sheridan et al. 1996).

1.7 Staging

The most widely used staging system for patients with cervical cancer is the Féderation Internationale de Gynécologie et d'Obstétrique (FIGO) classification, introduced before the advent of modern imaging modalities and hence based on solely clinical parameters including physical examination under anesthesia, colposcopy, endocervical curettage, hysteroscopy, cystoscopy, proctoscopy, intravenous urography, barium enema, and radiography of the lungs and skeleton (Pecorelli and Odicino 2003) (Table 1). Findings obtained with MRI, CT, ultrasound, and scintigraphy are not taken into consideration in determining the FIGO stage, which is regarded as a drawback of this staging system. In fact, while the vaginal extent of cervical cancer can be determined with a high degree of accuracy by means of rectovaginal examination and colposcopy, clinical examination has proved to be less accurate in evaluating tumor size (especially in primary endocervical tumors), parametrial and pelvic sidewall invasion, and metastatic spread including nodal status. The concordance between the clinical FIGO staging and surgical staging has been reported to be 85.4%, 77.4%, 35.3%, and 20.5% for stage IB, IB2, IIA, and IIB, respectively (Qin et al. 2009). In addition to the inaccuracies of clinical staging, the evaluation of nodal status, which is a crucial prognostic factor and a determinant in treatment planning, is not considered in the FIGO staging system (Lagasse et al. 1980; LaPolla et al. 1986). Despite these limitations, while the use of modern imaging modalities is expressly encouraged in a revised version of the FIGO staging system implemented in 2009, cross-sectional imaging techniques such as ultrasound, CT, and MRI remain excluded from the FIGO staging system due to their high cost and lack of availability in the underdeveloped regions of the world, where invasive cervical cancer is most prevalent (Pecorelli et al. 2009).

Table 1 FIGO staging of cervical cancer (Wiebe et al. 2012)

FIGO stage	Description
I	Cervical carcinoma strictly confined to the cervix
IA	Invasive cancer identified only microscopically. Invasion is limited to measured stromal invasion with a maximum depth of 5 mm and no wider than 7 mm
IA1	Stromal invasion no greater than 3 mm in depth and no wider than 7 mm
IA2	Stromal invasion greater than 3 mm but no greater than 5 mm in depth and no wider than 7 mm
IB	Invasion of stroma greater than 5 mm in depth or greater than 7 mm in diameter or clinically visible lesion confined to the cervix
IB1	Clinically visible lesion no greater than 4 cm in size
IB2	Clinically visible lesion greater than 4 cm in size
II	Carcinoma extending beyond the uterus but not involving the pelvic wall or lower third of vagina
IIA	Tumor involves the vagina but not its lower third. No obvious parametrial involvement
IIA1	Clinically visible lesion ≤4 cm
IIA2	Clinically visible lesion >4 cm
IIB	Obvious parametrial invasion but not onto the pelvic sidewall
III	Tumor involves the lower third of the vagina and/or extends to the pelvic sidewall and/or causes hydronephrosis/nonfunctioning kidney
IIIA	Tumor involves the lower third of the vagina but no extension onto pelvic sidewall
IIIB	Tumor extends to pelvic sidewall or causes hydronephrosis/nonfunctioning kidney.
IV	The carcinoma has extended beyond the true pelvis or has clinically involved (biopsy proven) the mucosa of the bladder and/or rectum
IVA	Spread to adjacent pelvic organs
IVB	Metastatic spread to distant organs

Important factors for staging according to the FIGO classification comprise tumor size, vaginal

or parametrial involvement, bladder/rectum extension, and distant metastases. In FIGO stage I, cervical carcinoma is confined to the cervix. Microscopically invasive cervical carcinoma with a maximal depth of stromal invasion <0.5 cm and maximal width <0.7 cm in horizontal diameter is defined as FIGO stage IA. Clinically visible lesions up to 4.0 cm and limited to the cervix or preclinical cancers greater than stage IA define FIGO stage IB1, while clinically visible lesions greater than 4.0 cm in size define stage IB2. FIGO stage II comprises cervical carcinoma invading beyond the uterus but not to pelvic wall or lower third of vagina. If there is no obvious parametrial involvement, the cancer is staged as FIGO IIA; parametrial invasion defines stage FIGO IIB. In FIGO stage III the tumor has invaded the lower third of vagina (IIIA) or has extended to the pelvic wall and/or has caused hydronephrosis or a nonfunctioning kidney (IIIB). All cases with hydronephrosis or nonfunctioning kidney are included in stage IIIB, unless they are known to be due to other causes. FIGO stage IVA is characterized by invasion of the bladder or rectum or by tumor extension beyond the true pelvis. The presence of distant metastases establishes stage IVB disease.

1.8 Growth Patterns

The vast majority of cervical carcinomas arise from the squamocolumnar junction and typically show exophytic growth in the outer cervix in younger women. With retraction of the transformation zone into the cervical canal in older women, endophytic growth patterns of cervical cancer become more common (Fig. 1).

Cervical cancer is characterized by continuous invasive growth with extension into the vagina, parametria, uterine corpus, bladder, rectum, and peritoneal cavity. In the same way, the tumor spreads to pelvic lymph nodes. Preferred sites of nodal metastases are the obturator fossa, the nodes along the external, internal, and common iliac vessels, the presacral lymph nodes, and the paraaortic nodes (Fig. 2). The risk of lymph node

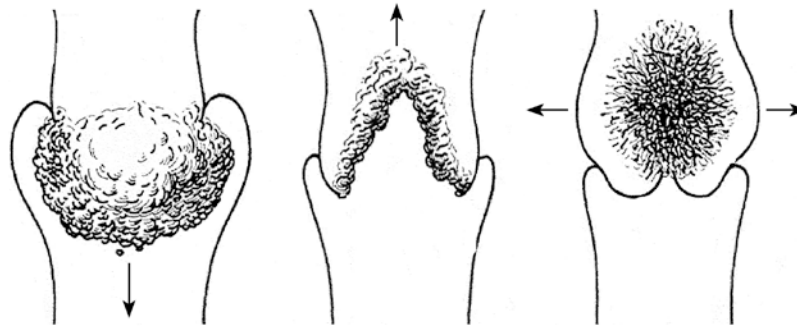

Fig. 1 Growth patterns of cervical cancer: exophytic, endophytic ulcerative, and endophytic expansion with barrel-shaped configuration of the cervix (from Schmidt-Matthiesen and Wallwiener 2005)

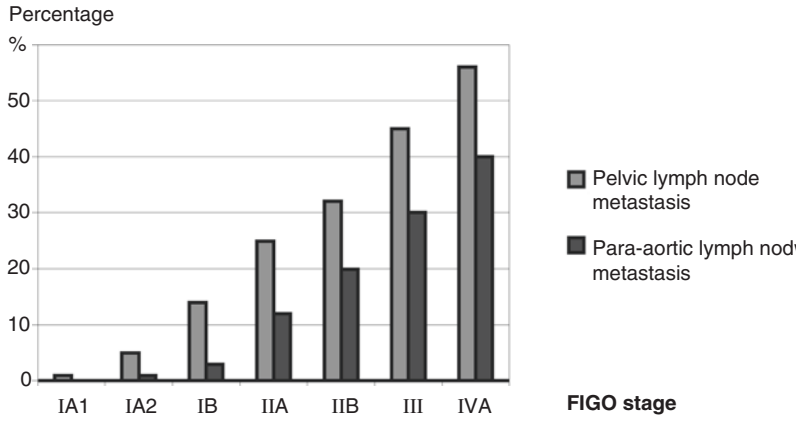

Fig. 2 Probability of lymph node metastasis by tumor stage

metastasis correlates with the stage of cervical cancer. In stage IA1 disease (microscopic infiltration of stroma) without vascular space involvement, the probability of pelvic lymph node metastasis is less than 1% (Metcalf et al. 2000) vs. 10–20% in stage IB disease. When there is cancer extension beyond the cervix with involvement of the upper vagina in stage IIA, the risk of pelvic or para-aortic nodal metastases increases to 25% and to over 30% when there is parametrial invasion (stage IIB). The risk is 45% in stage III tumors with involvement of the lower third of the vagina or extension to the pelvic wall and 55% in stage IVA with infiltration of the bladder or rectum. The probability of metastatic spread to para-aortic nodes becomes relevant for stage IIA and above, where it is 8–17%. Para-aortic nodal metastases are regarded as distant metastases and are rare when the pelvic nodes are negative.

Hematogenous dissemination is rare and is seen only in advanced cervical cancer. The 10-year risk of distant metastases varies with the stage and ranges from 3% for IB cervical cancer and 75% for stage IVA. Preferred sites of distant metastases are the para-aortic and supraclavicular lymph nodes, lungs, abdominal cavity, and skeleton (Fagundes et al. 1992).

The probability of tumor recurrence correlates with the disease stage and is 10–20% for stages IB and IIA with negative lymph nodes and 50–70% in advanced tumors of stages IIB–IVA and in patients with nodal metastases (Fig. 3) (Perez et al. 1995). The incidence of pelvic recurrence and metastatic spread is highest during the first 2 years after diagnosis and primary therapy (Friedlander and Grogan 2002). The true pelvis is the site of recurrent disease in 60–80% of cases (Fagundes et al. 1992; Stehman et al. 1991; Burghardt et al. 1992; Perez et al. 1986).

1.9 Treatment

Treatment of cervical cancer is individualized to the patient's disease stage. Although radiation therapy and surgery are equally effective in patients with early-stage disease, younger patients are usually treated surgically in order to preserve the ovaries and avoid radiation-induced complications of the lower genital tract. Chemoradiotherapy is the standard of care for patients with bulky (IB2, IIA2) or locally advanced (IIB–IVA) cervical cancer. Standard concurrent chemoradiation therapy includes external pelvic irradiation plus brachytherapy.

1.9.1 Treatment of Microinvasive Cervical Cancer

FIGO stage IA1 disease with no lymphovascular invasion has less than a 1% chance of lymphatic metastasis and may be managed conservatively with conization without lymphadenectomy to preserve fertility or with total hysterectomy when preservation of fertility is not desired or relevant. Patients with stage IA2 cervical cancer without lymphovascular invasion can be treated by extrafascial hysterectomy or by conization (to preserve fertility). In the presence of lymphovas-

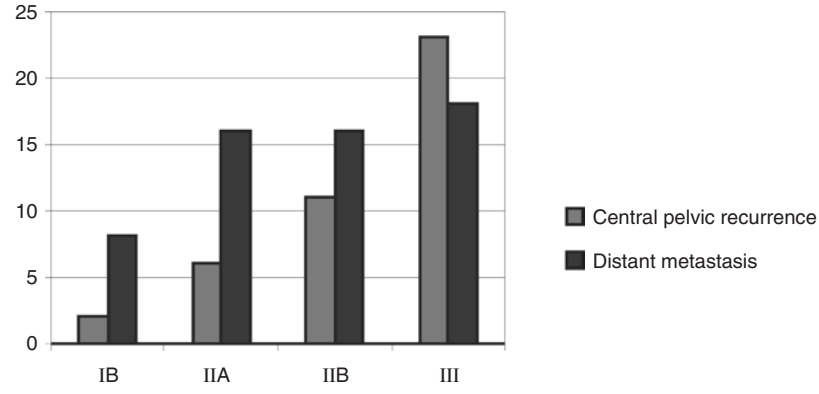

Fig. 3 Probability of central pelvic recurrence and distant metastasis by tumor stage

cular invasion, modified radical hysterectomy or radical trachelectomy with pelvic lymphadenectomy should be performed. Radical trachelectomy with laparoscopic lymphadenectomy procedure offers a fertility-sparing option for carefully selected patients with stage IA2 or stage IB1 lesions of 2 cm diameter or less situated at least 1 cm away from internal cervical os. Further criteria for patient eligibility for radical trachelectomy comprise among others the absence of capillary space involvement in intraoperative pathologic specimens and limited endocervical involvement at colposcopic examination (Dargent et al. 2000).

1.9.2 Treatment of Grossly Invasive Cervical Carcinoma (FIGO IB-IVA)

In patients with stage IB1 and IIA1 cervical carcinoma radical surgery and primary curative radiotherapy have proven to be equally effective. Generally, radical surgery is preferred in younger women because it has less deleterious consequences for the ovaries and vagina and less severe long-term effects on the urinary bladder and rectum as compared with radiotherapy. Radical hysterectomy according to Wertheim (Fig. 4a) and pelvic lymphadenectomy is considered the standard surgical approach to treat stage IB1 and IIA1 cervical cancer (Piver et al. 1974).

Lymph node dissection is performed in all cases of vascular space invasion regardless of depth of infiltration (Piver et al. 1974; Benedet and Anderson 1996; Committee on Practice B-G 2002). Surgical removal and examination of the so-called sentinel lymph node as part of surgical staging are under clinical evaluation. The results available so far suggest a high negative predictive value (Martinez-Palones et al. 2004; Marchiole et al. 2004). The sentinel lymph node is the regional lymph node that is assumed to be the first lymph node affected in case of metastatic spread.

Alternatively to surgery, primary or neoadjuvant radiochemotherapy is used to treat cervical carcinomas with a large volume, with infiltration of the vagina, or with parametrial involvement.

Following surgery, adjuvant radiochemotherapy is performed in patients with an increased risk of local pelvic recurrence. An increased risk of recurrence is assumed when there is a large tumor volume, a positive surgical margin, a very small safety margin, invasion of blood and lymphatic vessels, parametrial infiltration (Plaxe and Saltzstein 1999), or lymph node metastasis. A higher recurrence rate has also been identified for the histologic types of adenocarcinoma and clear cell carcinoma (Sedlis et al. 1999).

Advanced cervical carcinomas (FIGO stages III and IV) and bulky cervical cancers (FIGO IB2 and FIGO IIA2) are not amenable to primary

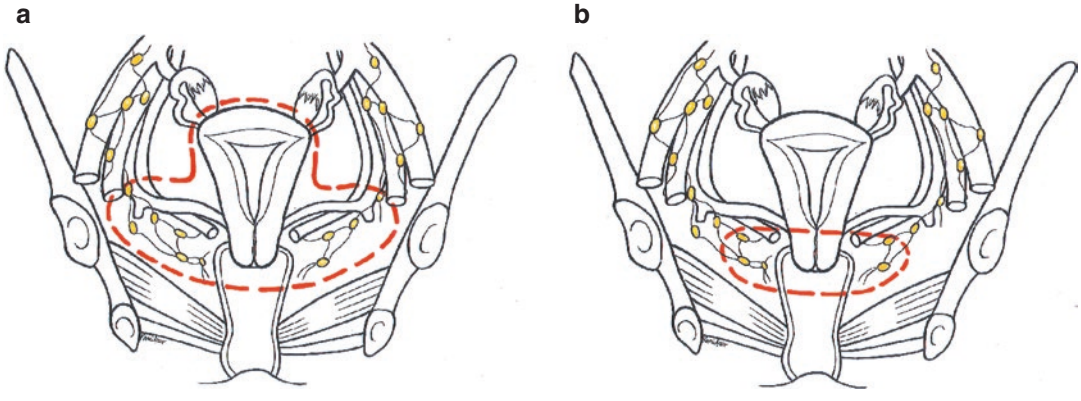

Fig. 4 Operative techniques. (**a**) Radical hysterectomy with removal of the uterus, vaginal cuff, parametria, and parailiac and para-aortic lymph nodes. Depending on the extent of parametrial removal, different types of hysterectomy are distinguished according to Piver. (**b**) Radical trachelectomy with removal of the uterine cervix, parametria, a vaginal cuff, and parailiac lymph nodes with subsequent uterovaginal anastomosis (from the lecture script of the Dept. of Gynecology and Obstetrics, Jena University Hospital, Germany)

curative surgery. For these tumor stages, primary definitive radiochemotherapy is the treatment of choice. Pretreatment surgical lymph node staging may be performed to exclude para-aortic lymph node metastases and may additionally serve to perform oophoropexy or to reduce the tumor bulk.

Radiotherapy consists of external beam irradiation of the uninvolved pelvic lymphatics and uninvolved parametrial tissue with a dose of up to 45 Gy in 180–200 cGy per fraction and image-guided brachytherapy. The dose delivered by external beam radiotherapy is adjusted to the local tumor extent and metastatic nodal involvement (boost). A larger field of external irradiation is chosen in patients with para-aortic lymph node metastases.

Alternatively, stage IVA cervical cancer with invasion of adjacent pelvic organs can be treated with primary pelvic exenteration. The most common therapies according to stage are summarized in Table 2.

Table 2 Therapy of cervical cancer

Stage	Standard treatment options
FIGO IA	Conization
	Total hysterectomy
	Modified radical hysterectomy with lymphadenectomy
	Radical trachelectomy (in patients wishing to preserve their fertility)
	Intracaviatry radiation therapy
FIGO IB, IIA	Radical hysterectomy and bilateral pelvic lymphadenectomy with or without pelvic radiation therapy plus chemotherapy
	Radiation therapy with concomitant chemotherapy
	Neoadjuvant chemotherapy
	Radiation therapy alone
	Intensity modulated radiation therapy (IMRT)
FIGO IIB, III, IVA	Radiation therapy with concomitant chemotherapy
	Interstitial brachytherapy
	Neoadjuvant chemotherapy
FIGO IVB	Palliative radiation therapy
	Palliative chemotherapy
Recurrent cervical cancer	Radiation therapy and chemotherapy
	Palliative chemotherapy
	Pelvic exenteration

1.9.3 Treatment of Recurrent Disease

Local tumor recurrence with infiltration of the bladder or rectum but without extension to the pelvic sidewall can be treated by potentially curative pelvic exenteration. With strict patient selection, the 5-year survival rate is 82% (Holtz and Dunton 2002). Various other surgical options are available for removal of recurrent tumor. In patients not having undergone radiotherapy or chemotherapy before, these therapeutic options are available for treating central pelvic recurrence. Repeat radiotherapy achieves successful local control with improvement of symptoms in cases of recurrent tumor outside the primary radiation field. Palliative chemotherapy is the final option available to all patients in whom curative surgery or radio(chemo)therapy is no longer possible.

1.9.4 Treatment of Cervical Cancer During Pregnancy

The diagnosis of cervical cancer in a pregnant woman presents a therapeutic dilemma. CIN lesions or microinvasive cancer (stage IA1) can be treated with conization and cerclage with continuation of the pregnancy. Following delivery, thorough repeat evaluation is performed. In patients with more advanced cervical cancer diagnosed in early pregnancy, hysterectomy with termination of the pregnancy is recommended. Patients in advanced pregnancy have the option of premature delivery by cesarean section with subsequent definitive cancer treatment. Continuation of pregnancy with delay of cancer treatment is advocated only after the patient has been fully informed of the potential risks and counseled about the options available and undergoes close follow-up for evaluation of further tumor development.

1.10 Prognosis

There is a strong correlation between the prognosis of patients with cervical cancer and stage of disease at diagnosis. Consistently, while the overall 5-year survival rate for patients with cervical cancer is 68%, survival rates vary markedly according to the different clinical stages. The 5-year survival rate is 93% for stage IA cervical carcinoma and 80% for stage IB tumors. In patients with more advanced

cervical cancer, 5-year survival is 58% for those with parametrial invasion (stage IIB), 16% for patients with infiltration of pelvic organs (IVA), and 15% when distant metastases (IVB) are present. Patients with negative lymph nodes have a 5-year survival rate of 90% as opposed to 60–20% for patients with lymph node metastases. Tumor extension to para-aortic lymph nodes reduces survival by half. For instance, the 5-year survival rate of stage IB decreases from 85% to 50–60% in patients with pelvic lymph node metastases and to only 25% in patients with para-aortic lymph nodes (Kosary 2007; Tewari et al. 2014).

The prognosis for patients with recurrent cervical carcinoma is reported to be less than 10% but there are subgroups of patients with markedly better prognosis. Five-year survival rates range from 30 to 70% in patients with curative pelvic exenteration for central tumor recurrence (Brenner 2002; Sant et al. 2001). Similar survival rates of 40–70% are reported for curative radiotherapy of recurrent cervical carcinoma in patients not having undergone primary radiation therapy. However, the prognosis strongly depends on the size of the recurrent tumor and its location. Recurrent tumor in the pelvic sidewall is associated with a disease-free 5-year survival rate of 20–50%, which is below that of central tumor recurrence (Hille et al. 2003).

2 Imaging

2.1 Indications

Currently, MRI is recommended for pretreatment assessment of local tumor extent in patients with histologically proven FIGO stage IB or greater (Balleyguier et al. 2011). It provides relevant information for deciding between primary operation and radiotherapy. It is the method of choice for local tumor staging: assessing the depth of infiltration, tumor volume, and involvement of adjacent structures. The clinical examination is inadequate to exclude parametrial invasion and infiltration of the urinary bladder and rectum while the extent of vaginal involvement can be determined more reliably by means of colposcopy. MRI is the most accurate imaging modality (90%) for distinguishing cancer confined to the cervix from cancer with parametrial infiltration (stage IB from IIB). A recent meta-analysis of the available literature on the diagnostic performance of clinical examination and MRI in detecting parametrial invasion and advanced-stage disease (FIGO stage ≥IIB) revealed a pooled sensitivity of 40% (95% CI 25–58) for the evaluation of parametrial invasion with clinical examination comparing with 84% (95% CI 76–90) with MRI and 53% (95% CI 41–66) for the evaluation of advanced disease with clinical examination as opposed to 79% (95% CI 64–89) with MRI (Thomeer et al. 2013). Conventional radiologic modalities such as cystoscopy, rectosigmoidoscopy, or double-contrast barium enema, as recommended in the FIGO classification, have been abandoned in most cases since MRI has become firmly established as the first-line modality for evaluating the local extent of cervical cancer. MR urography has also replaced conventional IV urography, which used to be the standard procedure in patients with advanced or recurrent cervical cancer and clinically suspected urinary obstruction. In this way, MRI evaluation of cervical cancer is even cost effective (Hricak et al. 1996). Cervical cancer of stages 0 (carcinoma in situ) and IA (microinvasive cervical cancer) cannot be assessed directly by MRI or CT. Nevertheless, in clinical practice, pelvic MRI could be performed for pretherapeutic evaluation of the pelvic organs and for radiologic lymph node staging at these early stages as well. Most patients already have a histologic diagnosis of cervical cancer at the time of the exam. This means that MRI is performed to evaluate the extent of the cervical carcinoma and not to detect it.

MRI is considered the best method for planning radiochemotherapy and for following up tumor response to therapy. Pelvic CT scanning is the established technique for planning radiotherapy in cervical cancer.

In the aftercare of patients, MRI can distinguish postoperative scar formation or postactinic changes from recurrent tumor after about 6 months, and guidelines also recommend pelvic MRI in patients with suspected recurrence of cervical cancer.

With its lower soft-tissue contrast, CT is widely less used for assessing the local extent of cervical cancer.

2.1.1 Role of CT and MRI

The most important advantages of multislice CT over MRI are the shorter examination time and the high spatial resolution. Reported staging accuracy for computed tomography ranges from 32 to 80% in literature. The major drawback of CT is the markedly poorer soft-tissue contrast compared with MRI and the resulting inadequate differentiation between tumor and normal cervical stroma or parametrial structures (Fig. 5). The sensitivity for parametrial invasion ranges from 17 to 100%, with an average of 64%. Specificity ranges from 50 to 100%, with an average of 81%. Hence, the diagnostic accuracy of CT is inadequate for the detection of small cervical cancers and early parametrial infiltration, having only a minor role in the local staging (Brenner et al. 1982; Villasanta et al. 1983; Tsili et al. 2013; Hricak et al. 2005). Unenhanced CT identifies tumors only indirectly as cervical enlargement, while tumors are depicted after contrast medium administration as contrast-enhancing lesions. Parametrial infiltration is detected indirectly by an irregular cervical demarcation or larger intraparametrial lesions. CT depicts rectal or bladder infiltration only indirectly as consumption of the fat lamella or in advanced tumor stages when there is wall thickening or a tumoral mass protruding into the lumen. In cases where pelvic CT is performed, combined oral and rectal contrast medium administration is recommended.

On the other hand, CT is the method of choice for excluding pulmonary metastases, which is the reason why guidelines in Germany recommend a chest CT scan for patients with FIGO stage III or IV (Schmidt-Matthiesen and Wallwiener 2005). CT of the chest is performed with IV contrast administration and including the supraclavicular lymph nodes. Finally, CT can be used as an alternative modality for lymph node staging and liver imaging and is indicated for evaluating the extent of osseous damage in patients with bone metastases.

With its excellent soft-tissue contrast on T2-weighted images, MRI is the imaging modality of choice for assessment of cervical cancer. This is ensured by multiplanar capabilities of imaging planes and imaging in two planes (Table 3) (Hricak et al. 1988; Kim and Han 1997), allowing optimal adjustment to pelvic

Table 3 Sensitivity and specificity of MRI in pretreatment staging of cervical cancer

FIGO stage	MRI accuracy (%)	CT accuracy (%)
IB (tumor localization)	91	
IIA (vaginal infiltration)	93	
IIB (parametrial infiltration)	94	70
IIIB (extension to pelvic sidewall)	75	
IVA (bladder infiltration)	99	
Average stage	83	63

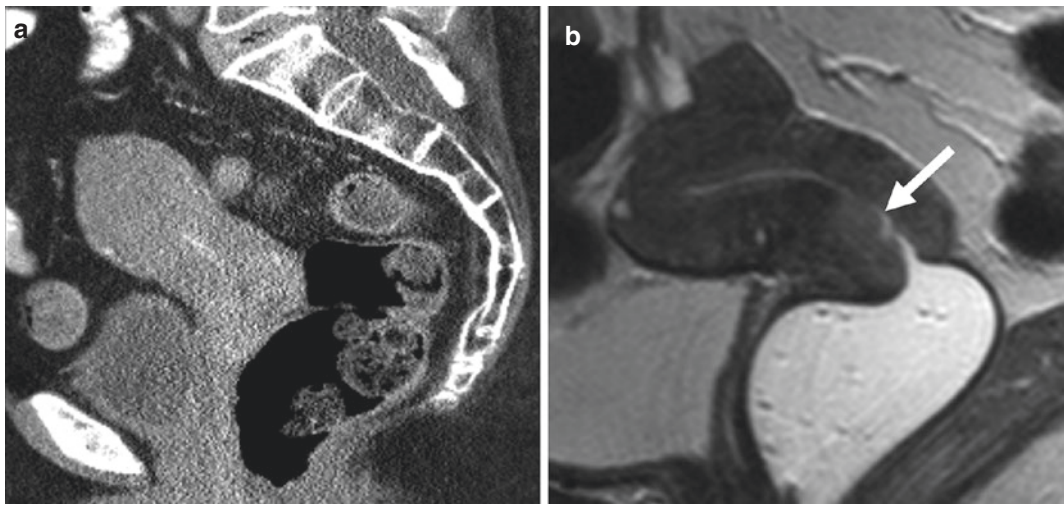

Fig. 5 Comparison of CT and MRI. (**a**) No cervical tumor can be delineated in the sagittal reconstruction of a CT scan. (**b**) Cervical carcinoma is shown in the ventral cervix (*arrow*) in T2-weighted (T2w) sagittal MRI

anatomy. MRI differentiates a tumorous lesion from surrounding tissue and permits precise determination of its size. T2-weighted images depict the organs of the true pelvis, and their zonal anatomy, which is the basis for identification of intra- and extracervical tumor extension. Furthermore, the calculated apparent diffusion coefficients of cervical cancer have shown to be lower than those of normal cervical stroma, providing increased contrast between the normal cervical stroma and cervical tumor (Hoogendam et al. 2010). In fact, the addition of diffusion-weighted imaging improves interobserver agreement, especially when T2-weighted images are equivocal (Chen et al. 2010). MRI is superior to clinical evaluation in assessing tumor size; its measurements are within 0.5 cm of the surgical size in 70–94% of cases (Hricak et al. 1988; Mitchell et al. 2006). For the assessment of small-volume disease, the use of an endovaginal coil has been reported to be more sensitive than an external-array coil (Downey et al. 2016). Studies in the literature report accuracy of 88–97% for MRI in the detection of parametrial invasion as compared to 72% for CT (Brodman et al. 1990; Sala et al. 2007; Scheidler and Heuck 2002). The superior depiction of the vaginal anatomy by MRI with differentiation of the mucosal and muscular layers of the wall results in earlier detection of vaginal involvement, with an accuracy of 90% as opposed to 77–82% for CT (Togashi et al. 1989). Infiltration of the bladder and rectum is demonstrated directly by MRI and identified with an accuracy of 96–100% (Preidler et al. 1996; Ebner et al. 1994). The overall staging accuracy of MRI ranges from 75 to 96% (Sala et al. 2007; Scheidler and Heuck 2002; Ascher et al. 2001).

With regard to lymph node staging, MRI and CT have similar sensitivities of only up to 70%, while specificity is high at approximately 95% (Hricak et al. 1988; Togashi et al. 1989; Boss et al. 2000). Both imaging modalities primarily rely on morphometric criteria for identifying metastatic nodes and therefore fail to detect micrometastases that do not affect lymph node size and shape. Preliminary studies evaluating the use of diffusion-weighted imaging for lymph node assessment have revealed that nodal metastases show significantly decreased apparent diffusion coefficients compared with benign lymph nodes, and abnormal nodes as small as 5 mm may be detected with diffusion imaging (Lin et al. 2008; Kim et al. 2008).

MRI is also a valuable imaging technique for excluding or demonstrating local tumor recurrence. In particular, MRI enables differentiation of postoperative or radiation-induced scars from recurrent tumor. Additional contrast-enhanced dynamic Tl-weighted studies are helpful to differentiate therapy-related changes from tumor tissue. In contrast, CT demonstrates most local recurrences only when they produce a mass effect or infiltrate adjacent structures or organs (Heron et al. 1988).

2.2 Imaging Technique

2.2.1 MRI

Streamlined technical guidelines for uterine cervical cancer staging and follow-up with MRI were recently issued by the female imaging subcommittee of the ESUR (European Society of Urogenital Radiology) and may serve as an excellent guide to achieve state of the art examinations (Balleyguier et al. 2011).

A brief gynecologic history should be obtained prior to the MRI examination. As the morphologic appearance of the uterus varies with the patient's hormonal status, information on the phase of the menstrual cycle or postmenopausal status as well as on hormone therapy should be gathered. Moreover, the history should comprise information on pregnancies and cesarean sections as well as on invasive diagnostic procedures such as cervical conization or curettage. In patients undergoing follow-up MRI, information on earlier pelvic surgery or radiochemotherapy is important. The radiologist needs these data to correctly interpret the morphologic MR appearance.

MRI is performed with the patient in the supine position. Fasting is not necessary prior to the examination.

Moderate bladder filling will straighten an anteflexed uterus. Too much bladder filling may lead to restlessness during the course of the examination and may even make it necessary to discontinue the examination.

For an optimal image quality, artifacts caused by intestinal peristalsis should be minimized, in general by administration of a spasmolytic agent at the beginning of the examination. The usual agent is butylscopolamine bromide (Buscopan) administered intravenously or intramuscularly at a dose of 40 mg. This spasmolytic agent has an elimination half-life of 2–3 h. The onset of spasmolytic activity is immediately after IV administration while it is delayed by a few minutes after IM administration. Alternatively, patients with contraindications to butylscopolamine bromide (hypersensitivity, glaucoma, driving immediately after the examination) are given an IV dose of 2 mg glucagon (GlucaGen). Technically, motion artifacts can be reduced by rapid image acquisition.

A high signal-to-noise ratio (SNR) and a high spatial resolution are important for optimal pelvic evaluation by MRI. For this reason, body phased-array surface coils are most frequently used. The resolution can also be improved with the use of a small field of view (FOV), for instance 20 × 20 cm, in combination with phase oversampling to prevent wrap-around artifacts (aliasing). With surface coils being highly susceptible to artifacts caused by respiratory motion of the abdominal wall, all sequences must be acquired with presaturation of the abdominal wall.

A valuable alternative to the phased-array surface coils, in case of small-volume cervical carcinomas, is the endovaginal MRI technique consisting of a ring-design endovaginal receiver coil of solenoid geometry inserted into the vagina and positioned around the cervix (deSouza et al. 2006).

The imaging area should comprise not only the pelvis but also the abdomen up to the renal hilum in order to include the para-aortic lymph nodes. This applies especially to patients with cervical cancer stage IIB and above.

The MRI examination begins with a localizer scan in transverse, sagittal, and coronal orientation, followed by T2-weighted imaging in two planes. T2-weighted sequences have the highest soft-tissue contrast and thus provide most of the information on the localization and extent of a cervical carcinoma. They are the basis of any pelvic MRI examination.

The first T2-weighted sequence should be acquired in the sagittal plane and cover the uterus and vagina to the pelvic floor. This sequence should be acquired with high resolution using thin slices and a small FOV, i.e., a 384 × 256 matrix size, a FOV of 240 mm, and a slice thickness of 4–5 mm.

The sagittal T2-weighted images may serve to plan the transverse angulated T2-weighted sequence. The transverse sequence should be angulated for alignment perpendicular to the axis of the cervical canal. As with the sagittal sequence, the imaging field in transverse orientation extends from the fundus uteri to the pelvic floor. Images should be acquired with a slice thickness of 4–5 mm, a 384 × 256 matrix, and a phase resolution of at least 75% (Table 4 and Fig. 11).

The cervix uteri is normally anteversed and forms an angle of about 90° with the axis of the vagina. The uterine corpus is flexed forward, resulting in an angle of 70°–100° relative to the cervix. The degree of anteflexion varies with bladder filling and is also affected by the size of the uterine corpus. From puberty onwards, the cervix-to-corpus ratio is 1:2, and the corpus becomes again smaller after menopause and descends into the true pelvis. The positions of the uterus are shown in Fig. 6.

Angulated image acquisition ensures optimal depiction of the cervix and parametria and their topographic relationships (Fig. 7). It is important that the angulation does not exceed 45° to avoid acquisition in coronal orientation with reversal of left and right.

In cases of vaginal involvement with the risk of parametrial infiltration through the paravaginal tissue from below, additional angulation perpendicular to the vagina is useful. For optimal evaluation of vaginal infiltration, the vagina may be distended with ultrasound gel. Involvement of the pelvic floor muscles in advanced tumors is evaluated on coronal T2-weighted images, which is especially suited for evaluation of the levator ani muscle. Information on muscle involvement is important for planning of the surgical procedure.

Table 4 Recommended MRI imaging protocol (adapted from Sala et al. 2013)

Parameter	Axial T1w	Axial T2w	Sagittal T2w	Axial oblique T2w	Axial upper abdomen T1w	Sagittal DW	Axial oblique DW
Sequence	FSE	FRFSE	FRFSE	FRFSE	SE	EPI	EPI
Echo time	Minimum full	85	85	85	Minimum full	Minimum	Minimum
Repetition time	470	4500	4500	4500	700	5000	5000
No. of sections	20	20	24	26	20	21	26
FOV (cm)	240	240	240	240	280	240	280
Section thickness (mm)	5	5	5	4	10	4.5	4.5
Matrix size	488 × 288	384 × 256	384 × 256	384 × 256	256 × 192	128 × 128	128 × 128
B value (s/mm^2)	–	–	–	–	–	500	800
Acquisition time	4:50	4:53	4:53	4:53	5:00	2:10	4:10

DW Diffusion weighted, EPI Echo planar imaging, SE spin echo, FSE fast SE, and FRFSE fast recovery FSE

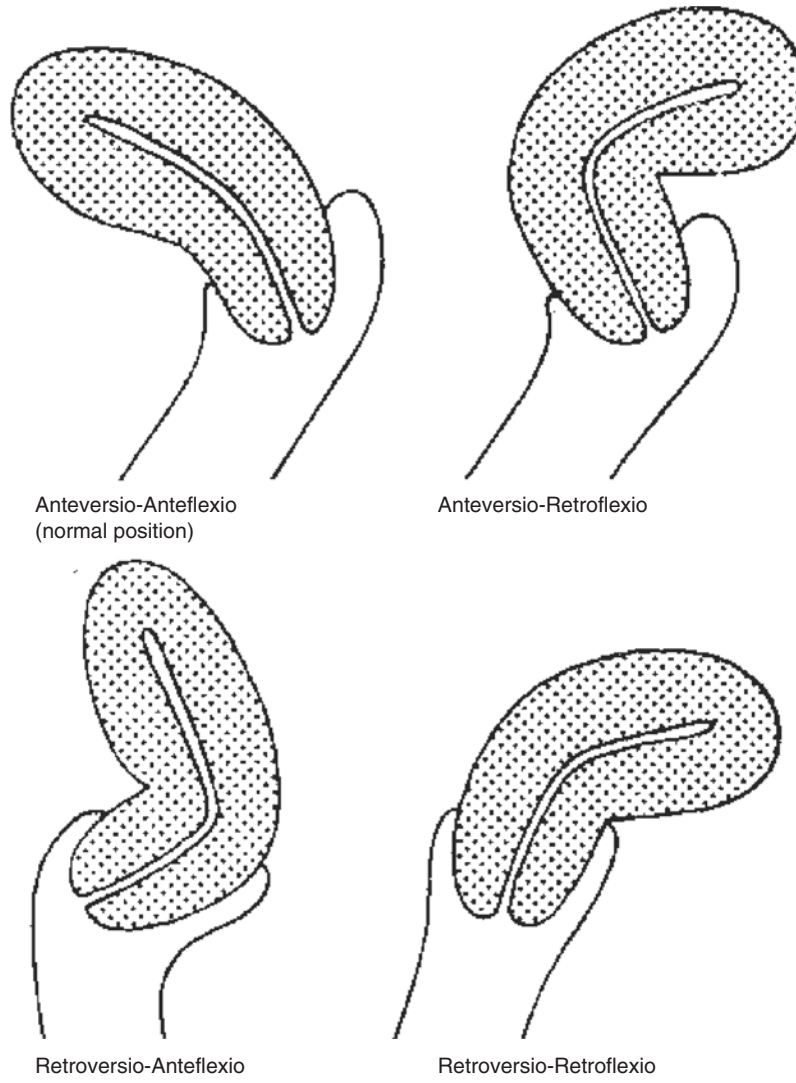

Fig. 6 Positions of the uterus. Version is the tilting of the uterus relative to the vagina and varies with bladder filling (typically 90°). Flexion refers to the position of the uterine corpus relative to the cervix (typically 70°–100°) (from Rohen 1999)

For evaluation of the pelvic sidewall and lymph node staging, an additional proton-density or a T1-weighted sequence in transverse orientation should be performed (see Fig. 10). The acquisition starts at the level of the aortic bifurcation and extends to below the pelvic floor. A slice thickness of 6 mm is used, with a 512 matrix and a phase resolution of at least 60%. Complete coverage of the inguinal lymph nodes should be attempted in patients with cervical cancers involving the lower third of the vagina (stage IIIA or higher), which are more likely to be associated with inguinal lymph node metastasis.

Although intravenous contrast medium administration is not routinely used for primary staging of cervical cancer, recent studies have shown that contrast-enhanced T1-weighted imaging may be superior to T2-weighted imaging in terms of cervical cancer tumor localization and tumor margin detection, especially for patients with small tumors (Akita et al. 2011) (Figs. 8 and 9).

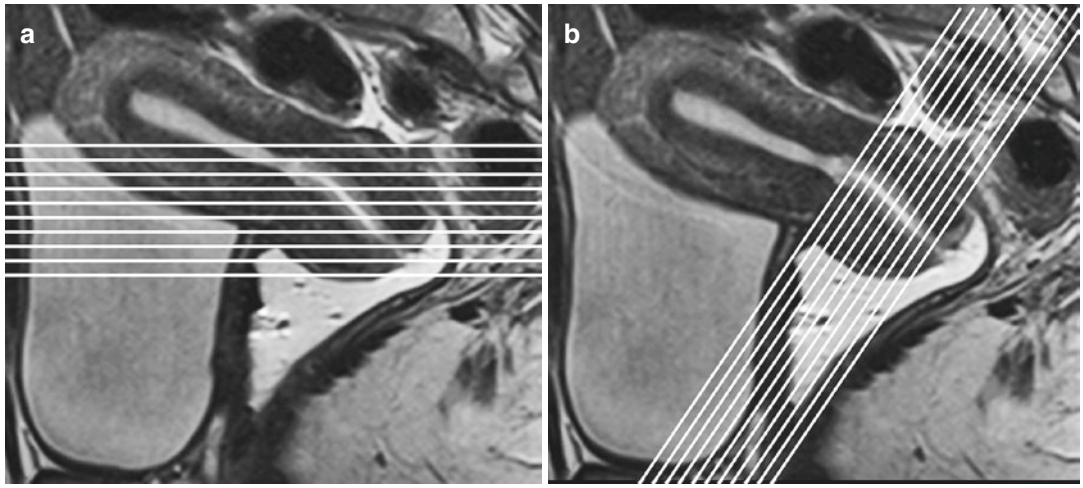

Fig. 7 Angulation. T2w TSE images in sagittal orientation of a normal cervix. The cervix is shown in strictly axial orientation (**a**) and in angulated axial orientation (**b**). With angulated image acquisition, a superior anatomic view is obtained of the structures that are crucial for staging (cancer, cervical stroma, parametria) and the cervix is depicted in more slices

Contrast-enhanced images can also improve the diagnostic accuracy of identifying tumorous infiltration of the urinary bladder or rectum. The extent of infiltration is visualized as a disruption of the muscular wall of these organs, which is of lower signal intensity on T1-weighted images. It has been shown that contrast-enhanced MRI can improve the differentiation of an edematous stromal reaction of the vesical or rectal wall (no enhancement) from tumorous infiltration (positive enhancement) (Hawighorst et al. 1997). Contrast-enhanced pelvic MRI is performed by acquiring T1-weighted sequences before and after contrast medium (CM) administration. The CM generally used is an unspecific gadolinium-based low-molecular agent administered at a dose of 0.5 mmol/kg body weight. The contrast-enhanced T1-weighted study can be planned by adopting the imaging area and orientation of the T2-weighted sequences.

CM administration is indicated to differentiate recurrent tumor from postoperative and postactinic changes at follow-up MRI (Fig. 10). A dynamic T1-weighted postcontrast study with repeated acquisitions enables temporally resolved quantification of CM enhancement.

Diffusion-weighted imaging (DWI) is a functional MR technique that helps characterization of biological tissues based on water proton mobility, providing valuable information on extracellular space tortuosity, tissue cellularity, and cellular membrane integrity (Bammer 2003; Liu et al. 2015). The architectural malformations associated with cancer result in shrinkage of the extracellular space, which in turn restricts the diffusion of water. The calculated diffusion of water in vivo is expressed as apparent diffusion coefficient (ADC). In the last decade DWI has gained great acceptance and has nowadays become part of the routine imaging protocol for gynecologic oncology imaging. Several studies have demonstrated the value of DWI in the detection, staging, and characterization of malignant tumors of the uterine cervix. DWI enables accurate discrimination of cervical cancer from benign cervical lesions and normal cervical tissue, which may be useful in patients with isointense tumors in T2-weighted images or in patients with small-

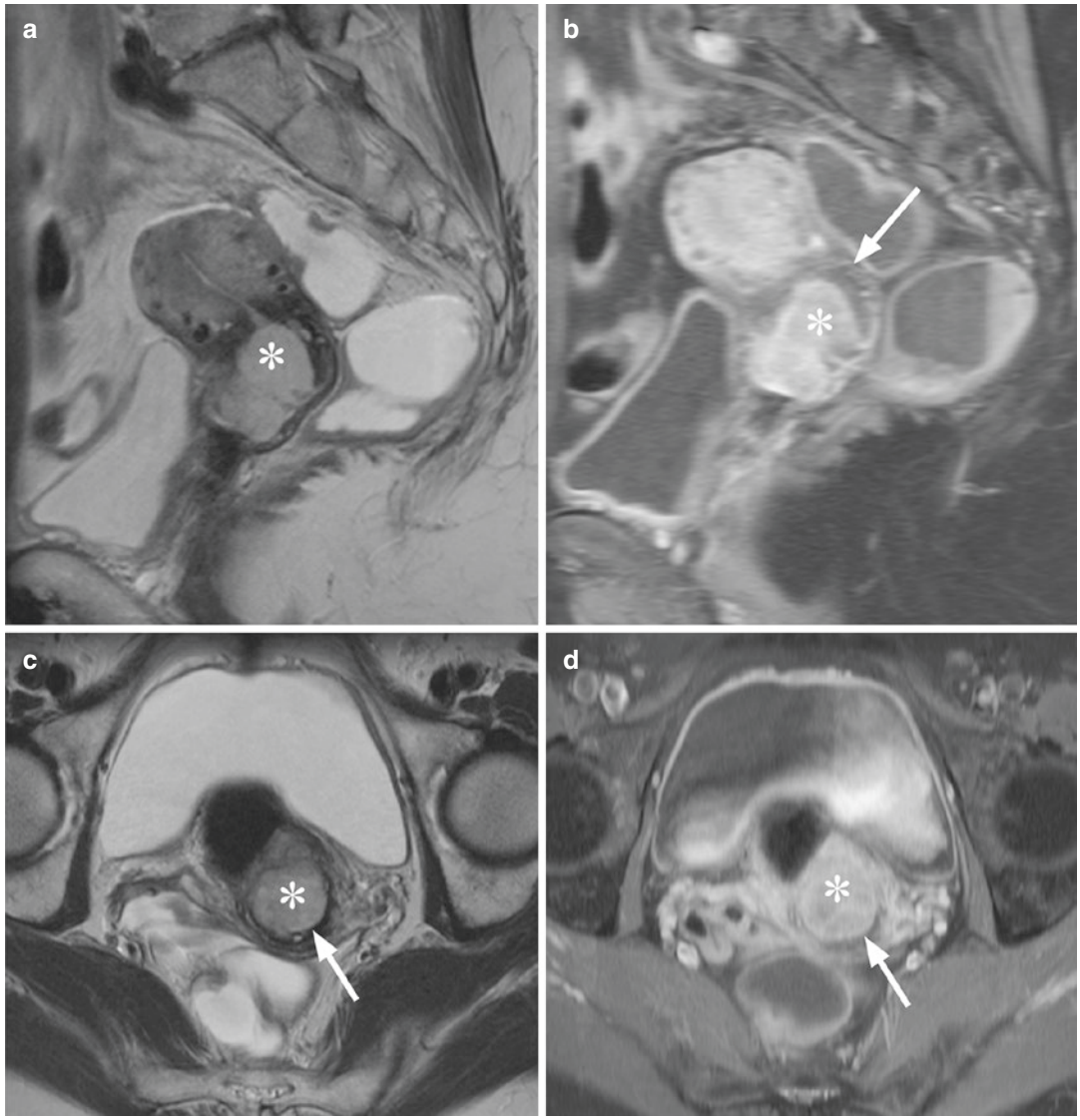

Fig. 8 Contrast enhancement of cervical cancer. (**a**, **b**) T2w turbo-spin echo (TSE image) in sagittal and transverse orientation. The cervical cancer (*asterisks*) is seen as a hyperintense mass in the surrounding low-signal-intensity cervical stroma (*arrow*). (**c**, **d**) T1w TSE images with fat saturation (FS) in sagittal and transverse orientation with fat saturation acquired 1 min after administration of Gadopentetate dimeglumine (Gd-DTPA). There is pronounced contrast medium enhancement of the hypervascularized cervical cancer with less enhancement of the hypointense normal cervical stroma (*arrows*)

volume cervical cancer. Recent studies have shown the potential ability of DWI to indicate the histologic type of cervical cancer as well as the grade of tumor differentiation (Liu et al. 2013, 2015; Thoeny et al. 2012).

Various other sequences are available to answer specific queries and provide specific information as required according to tumor stage. Cervical cancer extending beyond the cervix and recurrent tumors are associated with a significantly higher risk of metastatic spread to paraaortic lymph nodes. These lymph nodes are best evaluated with high-resolution respiratory-triggered T2-weighted sequences for imaging of the

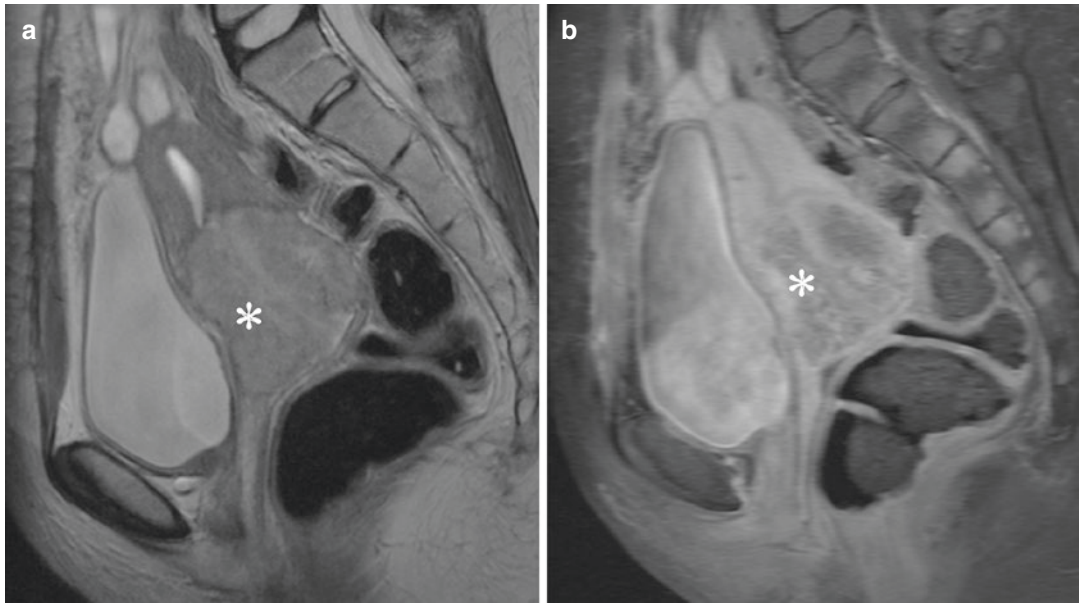

Fig. 9 Contrast enhancement of cervical cancer. (**a**) T2w TSE image in sagittal orientation. The cervical cancer (*asterisk*) is seen as a large mass of intermediate to high signal intensity that is delineated against a very thin margin of low-signal-intensity cervical stroma and against the more hypointense myometrium of the uterine corpus. There is barrel-shaped expansion of the cervix. (**b**) T1w TSE image with FS in sagittal orientation 1 min after Gd-DTPA administration. Enhancement of the hypointense and hypovascularized cervical cancer is inhomogeneous (*asterisk*) and tumor delineation is not improved by contrast medium administration

abdomen in transverse orientation from the renal hili to the aortic bifurcation (Fig. 11).

In patients with locally advanced or recurrent cervical cancer, it is often necessary to exclude ureteral obstruction, which can be done on transverse T2-weighted images that also serve to assess the para-aortic lymph nodes. In addition, coronal T2-weighted turbo-spin echo (TSE) sequences enable excellent evaluation for possible urinary retention and require little extra time to acquire. In addition, contrast-enhanced MR urography can be performed to exclude tumor-induced hydronephrosis.

Rectouterine or vesicouterine fistulas may develop as a complication of radiochemotherapy. A clinically suspected fistula is an indication for contrast-enhanced MRI using an unspecific gadolinium-based low-molecular contrast medium. Fat-saturated T1-weighted sequences in transverse and sagittal planes are acquired before and after CM administration. The postcontrast sequence is started 60 s after CM administration to image the venous phase. A fistula is typically a filiform structure of low-signal-intensity lumen showing contrast enhancement of the wall. In addition, T2-weighted inversion recovery sequences that null the signal of fat have a high accuracy in detecting fistulas.

A technical overview of the recommended MR protocol is given in Table 4.

2.2.2 Dynamic MRI

Dynamic contrast-enhanced MRI of the uterine cervix is performed to evaluate the course of contrast enhancement in a region of interest (ROI) placed in a suspicious area. First, an unenhanced sequence with an acquisition time of about 23 s is acquired, followed by the first postcontrast acquisition about 15–20 s after CM administration. Postcontrast acquisition for measurement of signal intensity in the ROI is repeated over a period of about 10 min. A dynamic MRI study is part of the routine protocol for differentiation of post-therapeutic changes from recurrent tumor but is rarely necessary in the pretreatment evaluation of patients with cervical cancer. Although vital tumor tissue typically shows earlier arterial enhancement than

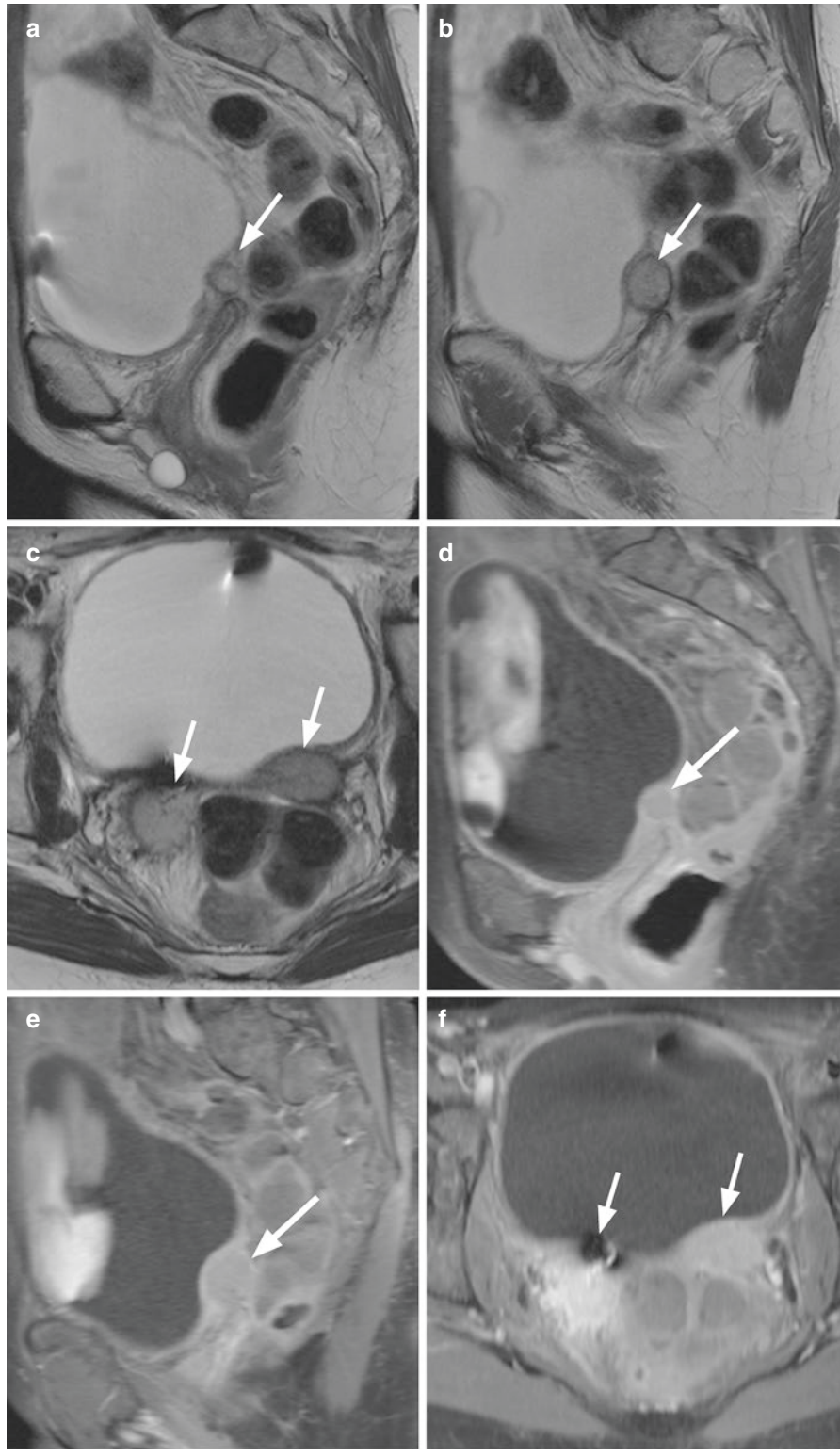

Fig. 10 Contrast enhancement of cervical cancer. (**a**–**c**) T2w TSE images in sagittal and transverse orientation. Local recurrence of cervical cancer (*arrows*) is seen as a tumor of intermediate signal intensity above the vaginal stump. (**d**–**f**) T1w TSE images with fat saturation in sagittal and transverse orientation 1 min after Gd-DTPA administration show local recurrence as an enhancing tumor (*arrows*). Accessory finding in (**a**): Bartholin cyst (*asterisk*)

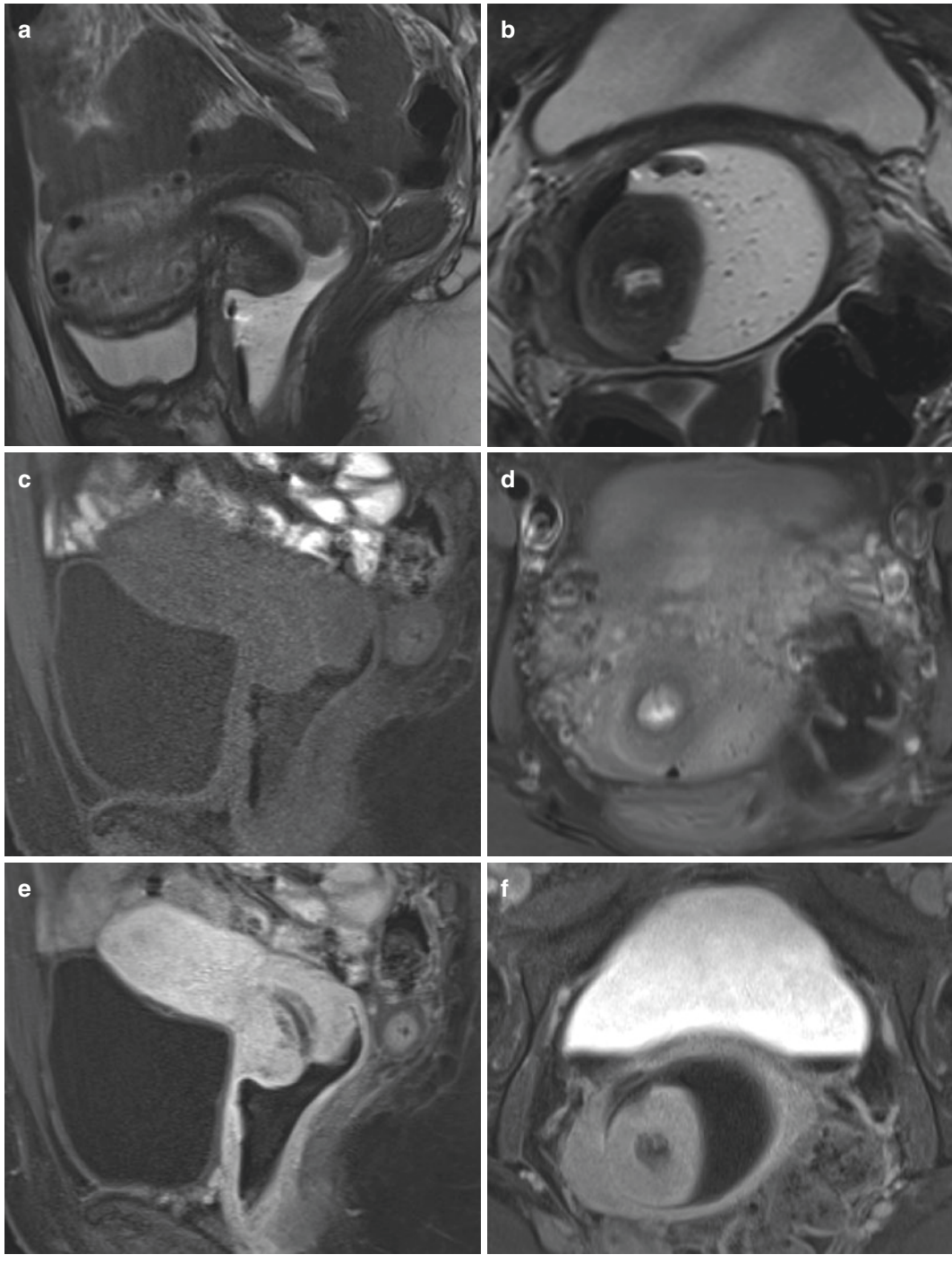

Fig. 11 Illustration of imaging protocol. (**a**, **b**) T2w TSE images in sagittal and transverse orientation. (**c**, **d**) T1w TSE images with fat saturation in sagittal and transverse orientation. (**e**, **f**) T1w TSE images with FS after contrast medium administration in sagittal and transverse orientation. (**g**, **h**) Axial DWI. (**i**) PD-TSE image for lymph node assessment in the true pelvis. (**j**) T2w TSE image with respiratory-gating (PACE) for lymph node assessment in the abdomen

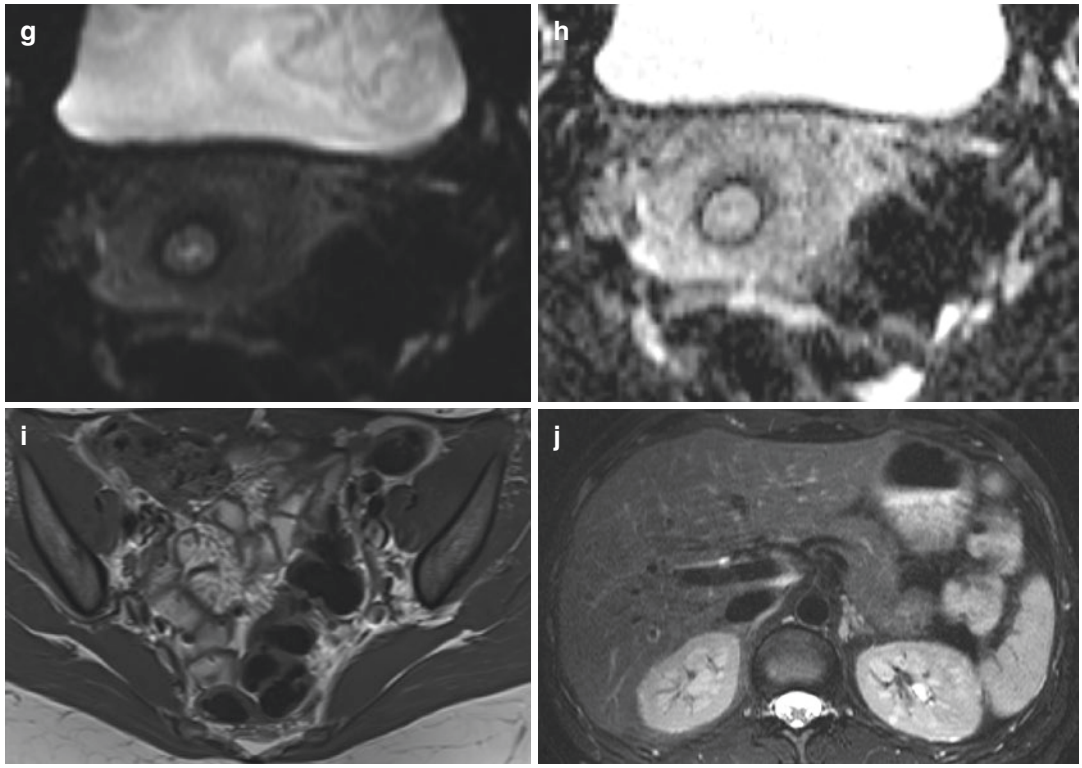

Fig. 11 (continued)

the surrounding cervical stroma (Hricak et al. 1991), no benefit was found for differentiation of the tumor or demonstration of parametrial infiltration in studies that evaluated color-coded dynamic MR images (Postema et al. 1998, 1999). However, the demonstration of necrosis and determination of tumor vascularization might help to estimate the radiosensitivity of a tumor prior to therapy. Moreover, a correlation was found between contrast medium time-intensity curves and angiogenic activity as an indicator of infiltration of the lymphatic system (Hawighorst et al. 1998). No correlation was found for other malignancy criteria such as infiltration depth and metastatic pelvic nodes.

2.2.3 Coil Technique

Morphologic MRI staging of cervical cancer implies high demands on SNR, signal homogeneity, and spatial resolution. Therefore, body phased-array surface coils are recommended because they increase the SNR in comparison to volume coils and can also increase the spatial resolution, or, alternatively, shorten the acquisition time. The surface coil is placed on the torso and must cover the entire imaging area. Although local coils such as endorectal or endovaginal coils have proven to be more accurate than external array for detecting small cervical cancers, they are rarely used as they distort anatomy, for instance, by compressing lipid lamellae (deSouza et al. 2006). Moreover, an additional examination with a body phased-array coil is required in most cases to evaluate the entire pelvis including the lymph nodes. Since body phased-array coils offer a high SNR, are easy to handle, and provide better patient comfort, local coils have not yet become widely accepted (Fig. 12).

2.2.4 Vaginal Opacification

Evaluation of vaginal involvement is not the most important goal of MRI staging, as the vagina can be adequately evaluated by clinical examination and colposcopy in most patients. On the other hand, imaging vaginal infiltration is important for

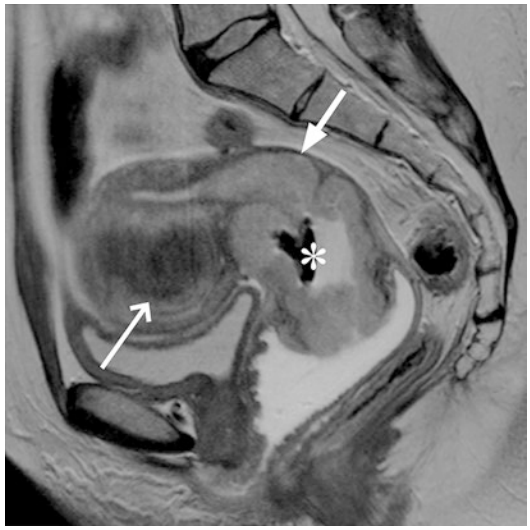

Fig. 12 Tumor growth and vaginal opacification. T2w TSE image in sagittal orientation. The high-signal-intensity cervical cancer has a central necrotic cavity (*asterisk*) with an air-fluid level. There is barrel-shaped expansion of the cervix and portio through the tumor. Tumor growth into the uterine cavity (*arrow*). Accessory finding: leiomyoma of the uterine corpus (*open arrow*). The vagina and fornix are distended by gel, which allows exclusion of vaginal infiltration

planning brachytherapy. The insertion of a vaginal tampon soaked with contrast medium has been abandoned because distention of the vagina is incomplete while anatomic relationships are distorted. However, intravaginal application of a contrast medium, e.g., ultrasound gel as a negative contrast medium (Fig. 13), was found to improve evaluation of vaginal involvement and is part of the routine protocol in many centers.

2.3 Staging

2.3.1 General MR Appearance

The basis of the radiologic evaluation of cervical cancer is T2-weighted MRI sequences (Shiraiwa et al. 1999), which provide high soft-tissue contrast for optimal differentiation of tumor from normal cervical stroma and adjacent organs. Cervical cancer is characterized by a higher signal intensity and is thus delineated against the cervical stroma, which has a lower signal intensity. Cervical cancer typically develops as a circumscribed focal lesion arising from the mucosal layer of the cervix. It may grow superficially in a circular pattern and increases in depth with invasion of the cervical stroma. Sagittal and transverse T2-weighted sequences serve to determine the localization and size of the tumor as well as the depth of cervical stroma infiltration. These sequences are also crucial for excluding extracervical extension and infiltration of the parametria, vagina, bladder, and rectum. The two critical issues—depth of infiltration and parametrial involvement—can be assessed most reliably on transverse images angulated perpendicular to the cervical axis.

Cervical cancer arises in the transitional zone that marks the junction of the squamous epithelium of the external cervix with the columnar epithelium of the cervical canal. This zone is usually located on the portio in younger women, which is where cervical cancer usually occurs with exophytic growths. In contrast, older women with retraction of the transformation zone into the cervical canal typically develop cervical cancer with an endocervical growth pattern (Fig. 13). This growth type usually gives rise to the typical barrel-shaped configuration of the cervix as the tumor increases in size or an endocervical ulcer develops when there is necrosis.

On T1-weighted MR images, cervical cancer is similar in signal intensity to the normal cervical stroma. Demarcation from the corpus uteri, vagina, and parametria is also difficult (Fig. 14). Only large cervical carcinomas can be identified based on their mass effect.

However, T1-weighted images can be useful in delineation of the tumor within the lateral parametria, which have a higher fat content than the medial parametria, resulting in improved contrast between high-signal-intense fat and low-signal-intense carcinoma. In the routine clinical setting, T1-weighted sequences are primarily used for lymph node staging and for unenhanced imaging in cases where contrast medium administration is planned.

Cervical carcinomas show early enhancement 15–30 s after contrast medium administration.

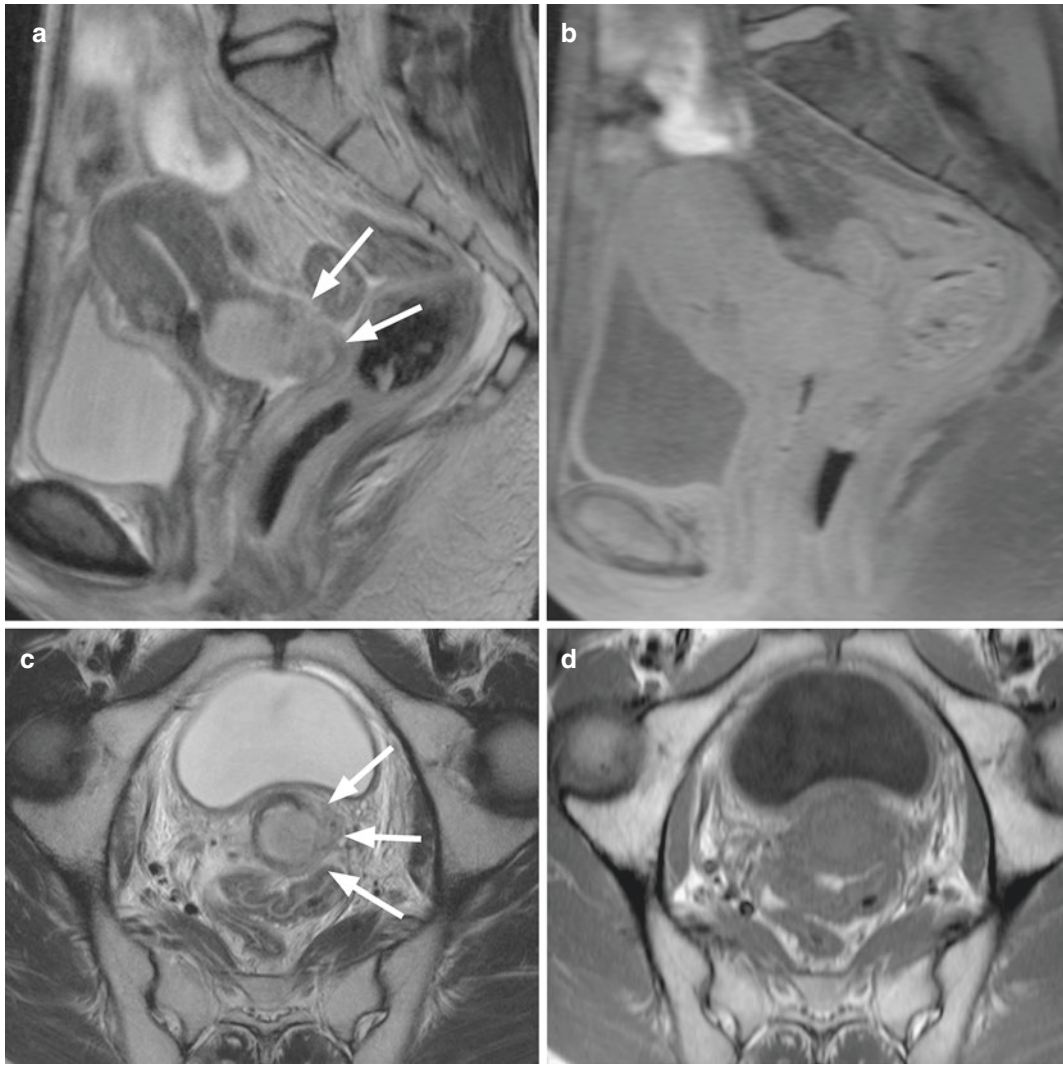

Fig. 13 Comparison of T2w and T1w imaging. (**a**, **b**) T2w TSE images in sagittal and transverse orientation showing stage IIB cancer of the posterior cervix. There is posterior (*sagittal*) and left lateral (*transverse*) disruption of the hypointense cervical stroma (*arrows*). (**c**, **d**) T1w TSE images with FS in identical sagittal and transverse orientation. The extent of the cervical cancer in the stroma cannot be assessed due to the lower soft-tissue contrast of T1w sequences

The increase in signal intensity can improve the contrast between the hypointense cervical stroma and the hyperintense tumor on T1-weighted images. Altogether, however, the signal intensity of cervical cancer is heterogeneous and varies with vascularization. In pretherapeutic staging where precise determination of the extent of the tumor in the cervix and its relationship to the corpus uteri, parametrial tissue, and vagina is important, most cervical carcinomas are seen more clearly on T2-weighted images than on contrast-enhanced T1-weighted images. This does not hold true for advanced cervical carcinomas with infiltration of the bladder or rectum or extension to the pelvic sidewall and for the exclusion of recurrent tumor by post-therapeutic MRI.

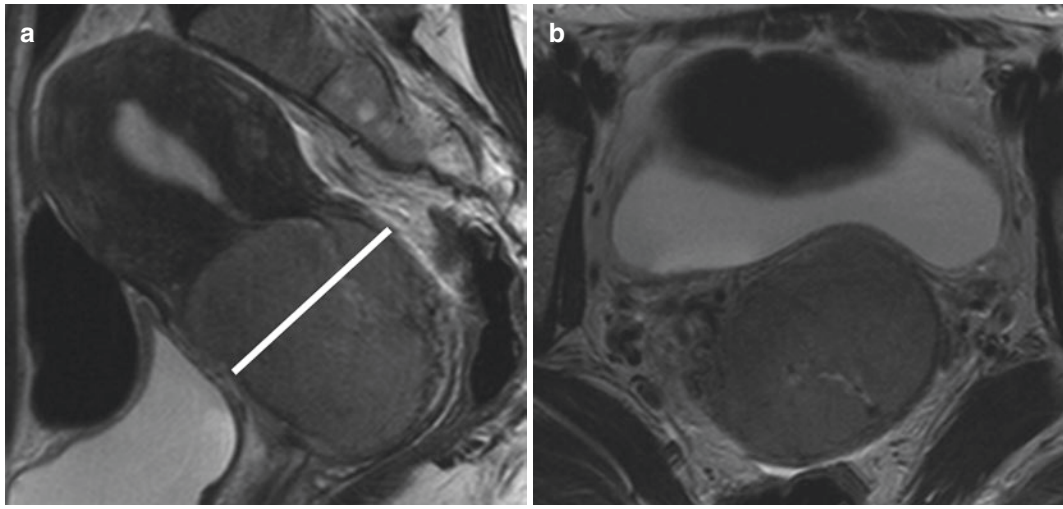

Fig. 14 Determination of tumor size. (**a**, **b**) T2w TSE images in sagittal and transverse orientation (*arrows*) with barrel-shaped expansion of the cervix. Maximum tumor diameter is determined according to the RECIST criteria of the WHO, in the example on the sagittal image (*line*)

2.3.2 Rare Histologic Types

Squamous cell carcinoma is by far the most common histologic type, accounting for about 90% of all cervical carcinomas. Descriptions in this chapter and in the literature on cervical cancer in general usually refer to this histologic type, unless explicitly stated otherwise. In this section, other histologic types of cervical cancer, especially adenocarcinoma, are briefly described with regard to their clinical status and imaging features (see also Sects. 1.5 and 2.6). In general, it is not possible to distinguish these less common histologic types from squamous cell carcinoma of the cervix based on their MR appearance.

With a proportion of 10–15% of all cervical cancers, adenocarcinoma is the most frequent of the rarer histologic types. The histologic distinction is important. Adenocarcinomas arise from the columnar epithelium and are associated with a higher risk of infiltration of the uterine corpus, lymphatic spread, and local recurrence compared with squamous cell carcinoma. Adenocarcinoma is more difficult to demonstrate histologically, which is why the diagnosis is often delayed until the tumor has reached an advanced stage. The clinical and radiologic evaluation of tumor extent also presents a challenge, as some adenocarcinomas are characterized by subepithelial growth and diffuse infiltration. Parametrial infiltration is not always associated with a macroscopic disruption of the cervical stroma. A focal lesion is not always apparent on MRI since small adenocarcinomas often grow diffusely and have a signal intensity similar to that of normal cervical tissue. The morphologic MR appearance varies with the histologic subtype. Mucinous adenocarcinoma is the most common subtype and may be endocervical or ectocervical in location. T2-weighted images show a tumor with an intermediate to slightly hyperintense signal intensity, depending on the mucin content. The margin is irregular and blurred. The second most common subtype is adenoma malignum, an extremely well-differentiated mucinous adenocarcinoma that is very difficult to confirm histopathologically. Adenoma malignum is composed of clusters of cystic lesions within an otherwise more or less solid tumor tissue of high signal intensity. The solid portions are key to the differentiation from dilated cervical glands and nabothian cysts. Other histologic subtypes are endometrioid, clear cell, and serous adenocarcinoma of the cervix,

which are histologically similar to carcinomas of the uterine corpus. They are of an intermediate to slightly high signal intensity on MRI and arise in the endocervix, from where they infiltrate the cervical stroma. In this type of tumor, it may be difficult to determine whether the origin is in the cervix or in the uterine corpus. In general, the part of the uterus from which the tumor arises shows deeper infiltration and more marked enlargement to the respective other part (cervix or corpus). The rare subtype of adenosquamous cervical carcinoma resembles squamous cell carcinoma with regard to its growth pattern and morphologic appearance on MR images.

Neuroendocrine cervical carcinoma is the second most frequent of the rare histologies. With its heterogeneous appearance and high signal intensity on T2-weighted images, neuroendocrine cervical carcinoma resembles squamous cell carcinoma at MRI (Lopes Dias et al. 2015).

2.3.3 Tumor Size

Cervical cancer is revealed by MRI when tumors are large enough to be macroscopically visible, which is the case when the tumor has a diameter of 1–2 cm or a volume of 2–4 cm (Cancer Research UK 2016) (FIGO stage IB). Tumor size is the most important prognostic factor besides lymphatic metastasis. T2-weighted MRI in at least two planes is the method of first choice for determining tumor size (Hawighorst et al. 1997), since cervical cancer is best distinguished from surrounding tissue in these sequences. While gynecologic examination tends to underestimate tumor size with reported accuracy rates as low as 60%, MR imaging is very accurate in evaluating tumor size with 93% of cases within 5 mm of the histologic size (Hricak et al. 1988; Mitchell et al. 2006; Shiraiwa et al. 1999; Lopes Dias et al. 2015; Nicolet et al. 2000; Okamoto et al. 2003; Sahdev et al. 2007). Exact assessment of tumor size is crucial not only in patients with early-stage cervical cancer scheduled for fertility-sparing surgery, but also for patients with stage IIA cervical cancer or less, since patients with tumors larger than 4 cm are considered nonsurgical candidates. Preliminary comparative studies have shown that tumor delineation and determination of size can be further enhanced by contrast medium administration. Preliminary comparative studies have shown that contrast-enhanced T1-weighted imaging may by superior to T2-weighted imaging in terms of cervical cancer localization and tumor margin detection, especially in patients with small tumors (Akita et al. 2011).

Tumor size is usually determined by measuring the longest diameter and its perpendicular. Two-dimensional measurement is based on the WHO guidelines for evaluating the response of solid tumors to chemotherapy or radiotherapy. Since a precise description of the spatial extent of a tumor is crucial prior to surgery, the tumor should also be measured in the third dimension. In patients where it is important to evaluate the response to radiochemotherapy, tumor size should be measured according to the revised RECIST[1] (response evaluation criteria in solid tumors) guideline which uses one-dimensional measurements (Eisenhauer et al. 2009) (Fig. 13). These guidelines have superseded the two-dimensional WHO measurement as the standard.

Techniques of tumor volumetry can additionally be applied. These techniques relied on formula such as height × width × length × $\pi/6$ to calculate approximate tumor volume or determined the volume by integration of the individual slice volumes (Fig. 12).

2.3.4 Local Staging

2.3.4.1 Stage IA

There is no role for MR imaging in patients with microinvasive cervical cancer (stage IA). Microinvasive cervical cancers do not alter the normal morphologic MR appearance of the cervix (Fig. 15). The normal endocervix is depicted on T2-weighted images with a hyperintense, continuous mucosal layer surrounded by hypointense cervical stroma, consisting of connective tissue and smooth muscle. Hence, imaging is optional in patients with tumors IB1 or lower. Colposcopy and conization are the

[1] RECIST is a set of rules defining the criteria for tumoral response, stability, or progression during treatment. The longest diameter of the non-nodal lesions is measured.

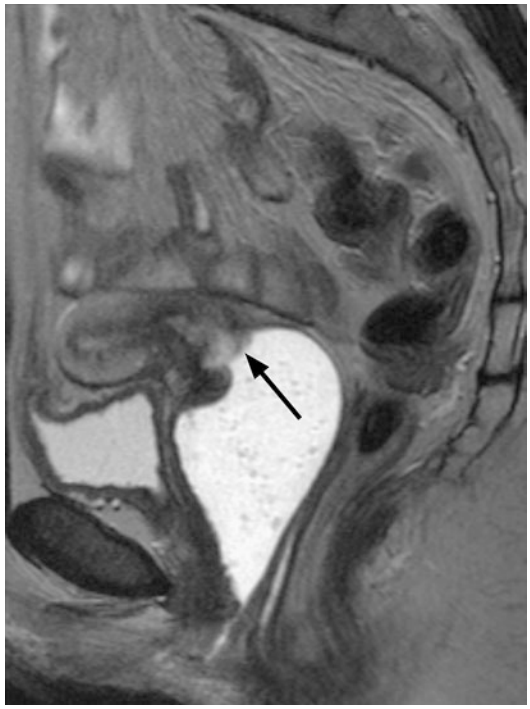

Fig. 15 Stage IB. T2w TSE image in sagittal orientation. High-signal-intensity cervical cancer (*arrow*) primarily involving the anterior cervix and the portio. Gel filling of the vagina

methods of choice for evaluating these early forms of cervical carcinoma. The conization defect is depicted on MR images as a circumscribed lesion of the external os, quite often associated with an adjacent seroma or clot. In the further course, shrinkage of the portio can sometimes be seen.

2.3.4.2 Stage IB

Stage IB cervical carcinoma has a depth of more than 5 mm and a diameter of more than 7 mm or is visible clinically. The tumor is still confined to the cervix but is characterized by invasive local growth. This is the earliest stage that can be demonstrated by MRI (Mitchell et al. 2006). The average MRI detection rate is 95%. Stage IB1 (diameter <4 cm) and stage IB2 (diameter >4 cm) are distinguished based on their size. Stage IB2 cervical cancer has a poorer prognosis and should be treated with concomitant chemotherapy and radiation therapy. Transverse and sagittal T2-weighted images depict cervical carcinoma as a high- or intermediate-intensity lesion within the low-signal-intensity oval cervical stroma (Figs. 11, 16, 17, 18, and 19). Cervical cancer at this stage is fairly smoothly marginated and completely surrounded by low-signal-intensity cervical stroma. Occasional exophytic bulging of a stage IB tumor into the vagina or the parametrium may be mistaken for infiltration.

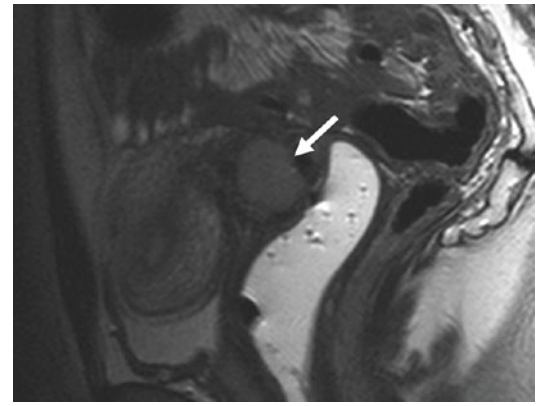

Fig. 16 Stage IB. T2w TSE image in sagittal orientation. High-signal-intensity cervical cancer (*arrow*) primarily involving the anterior cervix and the portio. Gel filling of the vagina

A large stage IB2 cervical carcinoma can obstruct the cervical canal and lead to hydrometra or hematometra. Hydro- or serometra is suggested by a fluid collection in the uterine cavity showing hyperintensity in T2-weighted and low-signal-intensity in T1-weighted images, whereas a hematometra is characterized by high signal intensity in T2- and T1-weighted images.

The rationale of using MR imaging at this stage of disease is to accurately assess tumor size, parametrial invasion, lower vaginal involvement, and lymph node metastases. Identification of this prognostic factors would preclude surgical treatment and is thus crucial for therapy planning (Freeman et al. 2013; Cheng et al. 2004; Kupets and Covens 2001).

2.3.4.3 Stage IIA

In stage IIA cervical cancer, infiltration involves up to two-thirds of the proximal vagina while sparing the lower third. On T2-weighted MR images, vaginal involvement is seen as a

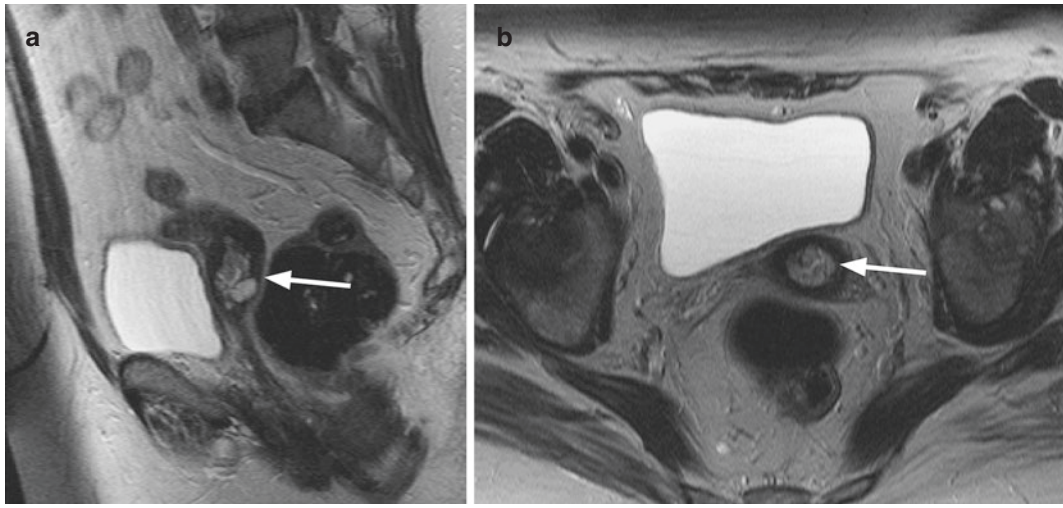

Fig. 17 Stage IB. (**a**, **b**) T2w TSE images in sagittal and transverse orientation. The cervical cancer is seen as a high-signal-intensity lesion within the cervix (*arrows*). The cancer is surrounded by low-signal-intensity cervical stroma on both sagittal and transverse images. Accessory finding: Nabothian cysts

hyperintense segmental disruption or lesion in the otherwise low-signal-intensity vaginal wall. Infiltration of the anterior and posterior fornix and of the wall is best seen in sagittal orientation (Figs. 20, 21, 22, and 23). The radiologist interpreting the images must be aware that a large exophytic cervical cancer may lead to widening of the fornix and thus mimic vaginal infiltration. In such cases, opacification and distention of the vagina can be helpful. Similarly to stage IB, stage IIA is further subdivided into IIA1 (if the tumor is 4 cm or smaller in diameter) and IIA2 (for tumors greater than 4 cm in diameter). Stage IIA is further defined by the absence of parametrial invasion. Parametrial infiltration can be reliably excluded if the tumor is surrounded by a low-signal-intensity rim on transverse angulated T2-weighted images.

2.3.4.4 Stage IIB

Stage IIB cervical cancer is characterized by parametrial infiltration but without extension to the pelvic sidewall. Parametrial infiltration has important implications for the therapeutic approach. While gross parametrial invasion can be usually detected by experienced clinicians, early invasion usually remains undetected. Reported accuracy of clinical staging for detection of parametrial and pelvic side wall invasion amounts to only 29–53% (Hricak et al. 1988; Zand et al. 2007). MRI is the only noninvasive modality that allows adequate evaluation of parametrial infiltration with a reported sensitivity of 69%, specificity of 93%, and negative predictive values of 100% for depicting parametrial invasion (Zand et al. 2007). Sagittal and transverse T2-weighted images angulated perpendicular to the cervical canal are most suitable to evaluate parametrial infiltration. It is indicated by a disruption of the low-signal-intensity cervical stroma and tumoral extension into the parametria. Visualization of an uninterrupted rim of cervical stromal rim thicker than 3 mm ("hypointense rim sign") reliably excludes parametrial infiltration with a specificity as high as 99% (Zand et al. 2007). The accuracy of MRI in the evaluation of parametrial invasion varies according to the tumor size, with 96% accuracy in small tumors and 70% in large tumors (Zand et al. 2007). Early microscopic parametrial infiltration must be suggested if high-signal-intensity tumor tissue shows irregular and unsharp margins and is disrupting the hypointense cervical stroma with no normal cervical stroma left that separates the tumor from the parametria. The most reliable MRI criterion of parametrial infiltration is the direct visualization

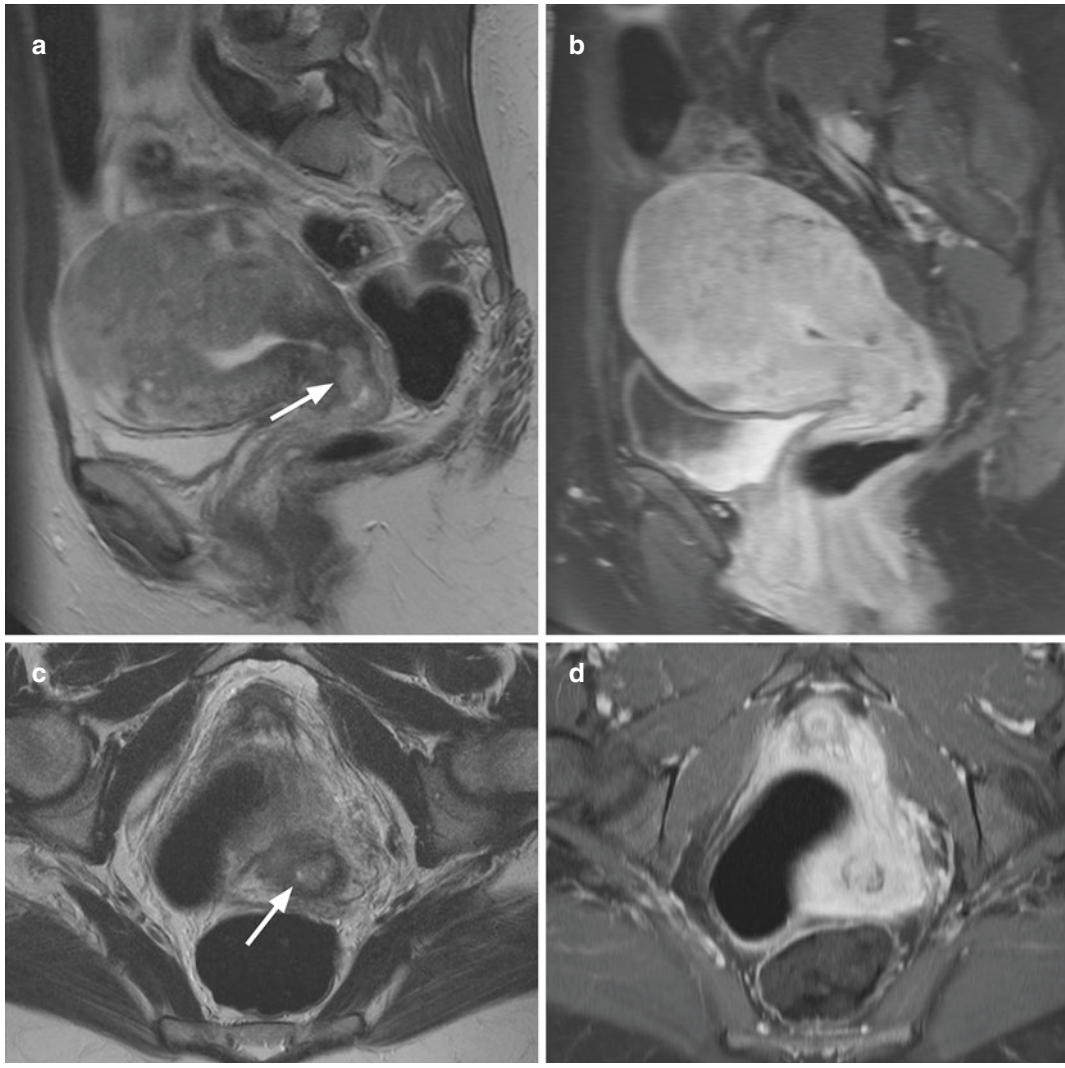

Fig. 18 Stage IB. (**a**, **b**) T2w TSE images in sagittal and transverse orientation. High-signal-intensity lesion of the cervix (*arrows*) with preservation of low-signal intensity stroma around the tumor. (**c**, **d**) T1w TSE images in sagittal and transverse orientation. No circumscribed cervical cancer is seen on the image obtained 1 min after Gd-DTPA administration. Accessory finding: uterine adenomyosis

of a tumor mass extending into the parametria (Figs. 24, 25, 26, and 27). Occasionally, the parametria may be invaded from below, through the paravaginal space. The anatomy of the true pelvis determines the further routes of spread of cervical cancer. Infiltration of the rectouterine or vesicouterine ligaments at their cervical attachments is seen on MR images as focal thickening. In rare cases, parametrial invasion can cause retraction with displacement of the cervix to the side of infiltration.

2.3.4.5 Stage IIIA

Stage IIIA tumor is established when there is involvement of the lower third of the vagina. As with stage IIA tumor, sagittal and oblique transverse T2-weighted sequences are most suitable to evaluate vaginal infiltration. Tumor infiltration is indicated by a hyperintense disruption and continuous or discontinuous thickening of the vaginal wall that extends to the lower third of the vagina. This stage is also associated with an increased risk of metastatic spread to the

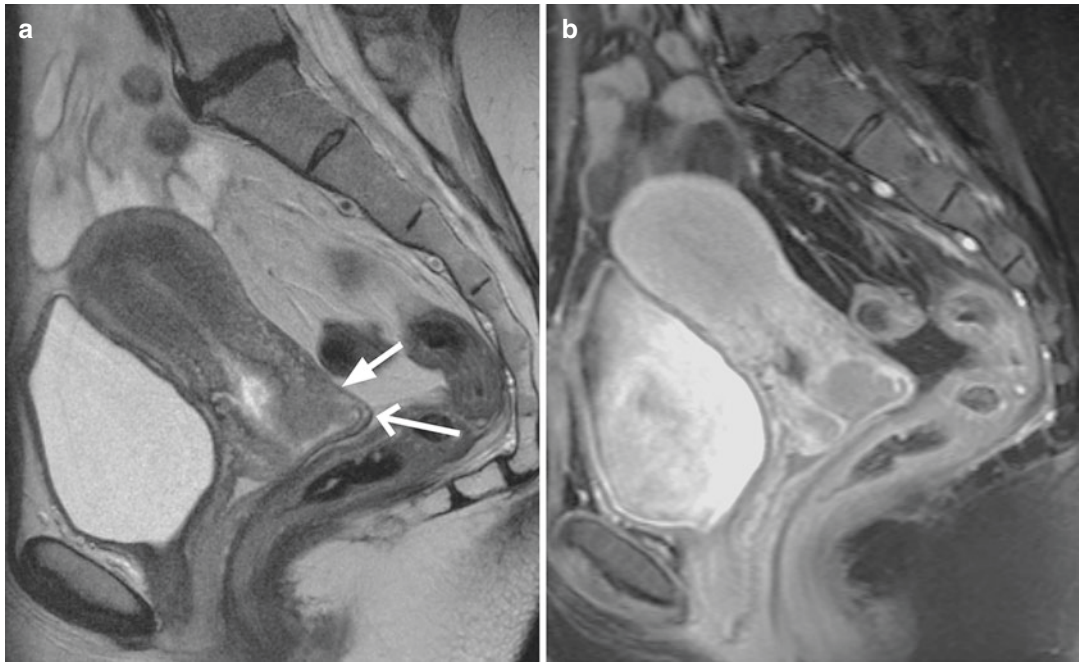

Fig. 19 Stage IB. (**a**) T2w TSE image in sagittal orientation. The cervical cancer (*arrow*) is depicted as a high-signal-intensity tumor that primarily involves the posterior cervix and is surrounded by low-signal-intensity cervical stroma. There is no infiltration of the posterior vaginal fornix (*open arrow*). (**b**) T1w TSE image with FS in sagittal orientation. Following administration of Gd-DTPA, a partially necrotic tumor is depicted

superficial inguinal lymph nodes, which must be taken into account in the diagnostic evaluation. The lower third of the vagina corresponds to the length of the urethra (from the pelvic floor to the level of the urinary bladder).

2.3.4.6 Stage IIIB

Cervical cancer with invasion of the pelvic sidewall corresponds to stage IIIB. Cervical cancer can reach the pelvic sidewall by continuous lateral growth through the parametrial tissue and the sacral bone and through posterior extension along the sacrouterine ligaments (Fig. 28). T2-weighted images depict tumor infiltration as hyperintense lesions in the intermediate signal intensity of the muscle, or low signal intensity of the cortical bone, or as thickening of the vascular wall. T1-weighted imaging allows evaluation of the extent of advanced parametrial infiltration and possible extension to the pelvic sidewall with good delineation of the hypointense tumor mass from the lateral parametrial tissue and the intermediate-signal-intensity muscle tissue. The tumor-related consumption of the lateral fat plane seen on T1-weighted images may already suggest extension to the pelvic sidewall from the surgical perspective even if direct infiltration of the sidewall is not yet apparent (Zand et al. 2007). Visualization of tumor within 3 mm from the obturator internus, levator ani, and piriform muscle or the iliac vessels is considered highly suggestive of stage IIIB disease (Freeman et al. 2013; Zand et al. 2007).

Ureteral infiltration and obstruction with hydronephrosis is also classified as stage IIIB disease (Fig. 29). The ureter courses over the psoas muscle from dorsolaterally before it descends into the pelvis. In the true pelvis, the ureter takes an anteromedial course from the pelvic sidewall in the inferior segment of the parametria toward the base of the bladder. At the level of the uterine isthmus, the ureter courses lateral to the uterine cervix at a distance of 1–2.5 cm and is over-crossed by the uterine artery anteriorly. The ureter is typically infiltrated when there is lateral tumor growth through the parametria. A thickening of the ure-

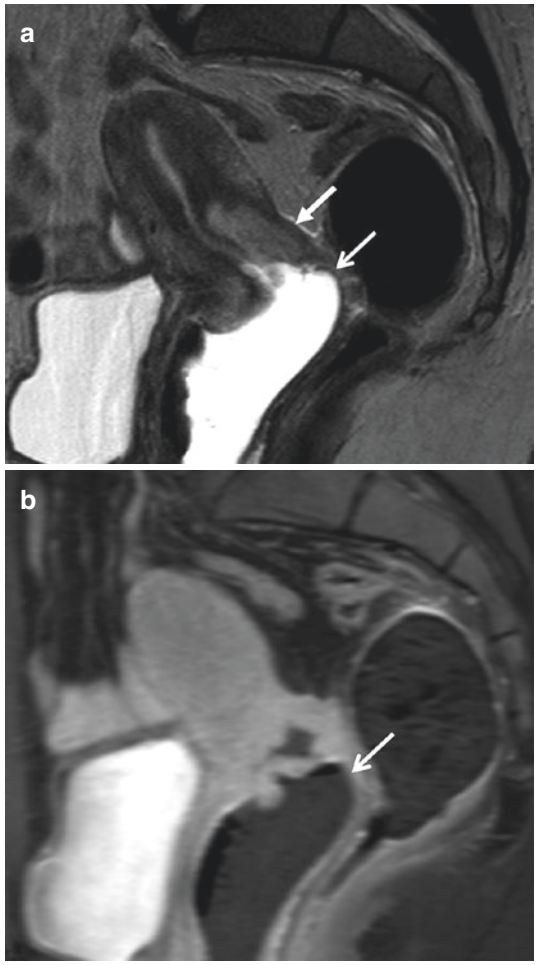

Fig. 20 Stage IB. (**a**) T2w TSE image in sagittal orientation. The cervical cancer (*arrow*) is depicted as a high-signal-intensity tumor that primarily involves the posterior cervix and is surrounded by low-signal-intensity cervical stroma. There is no infiltration of the posterior vaginal fornix (*open arrow*). (**b**) T1w TSE image with FS in sagittal orientation. Following administration of Gd-DTPA, a well vascularized cervical cancer is depicted

teral wall or hydronephrosis is seen. In patients with a tumor mass in the parametria, the kidneys and urinary tract should be included in the imaging volume in order to confirm or exclude ureteral obstruction and hydronephrosis.

2.3.4.7 Stage IVA

Stage IVA cervical cancer is characterized by infiltration of the mucosa of the rectum or urinary bladder. The FIGO classification is based on mucosal infiltration of these organs because the outer wall layers are not amenable to evaluation by endoscopy and biopsy. MRI, on the other hand, can identify infiltration of the outer muscular layer of the bladder and rectum. Tumor extension to the rectum is either through invasion of the sacrouterine ligament or through direct infiltration of the pouch of Douglas with subsequent extension of the tumor to the anterior rectal wall (Fig. 30). The peritoneal fold of the rectouterine space (pouch of Douglas) acts as a natural barrier that aggravates extension to the anterior rectal wall.

The urinary bladder is infiltrated through continuous anterior growth of the cervical tumor along the peritoneal fold between the cervix and the bladder, also referred to as the vesicouterine ligament (Figs. 31 and 32). Sagittal and transverse T2-weighted MR images depict infiltration as segmental disruption of the hypointense muscular layer of the wall of the bladder or rectum by hyperintense tumor. Contrast-enhanced Tl-weighted images often enable a more reliable identification of segmental disruption because of stronger enhancement of the tumor as compared with the muscular layer. Infiltration of the wall of the bladder and/or the rectum as well as contiguity of cervical cancer with either of these organs have important therapeutic implications. Bladder or rectal invasion can be depicted by means of MR imaging with a sensitivity and specificity of 71–100% and 89–91%, respectively (Rockall et al. 2006). For the exclusion of bladder and rectal invasion MR images achieve negative predictive values of 100%, making invasive endoscopic examinations obsolescent (Rockall et al. 2006).

Tumor infiltration of these hollow organs is quite often associated with the development of fistulas. A collection of air in the urinary bladder may indicate a vesicouterine fistula especially in patients under chemo- or radiotherapy (Figs. 46, 47, and 48). A fistula can be best demonstrated with fat-saturated, contrast-enhanced T1-weighted sequences, which will depict the fistula as an enhancing formation with a nonenhancing filiform lumen. Alternatively, a fistula can be demonstrated as a hyperintense filiform structure with a high sensitivity by using a T2-weighted inversion recovery sequence.

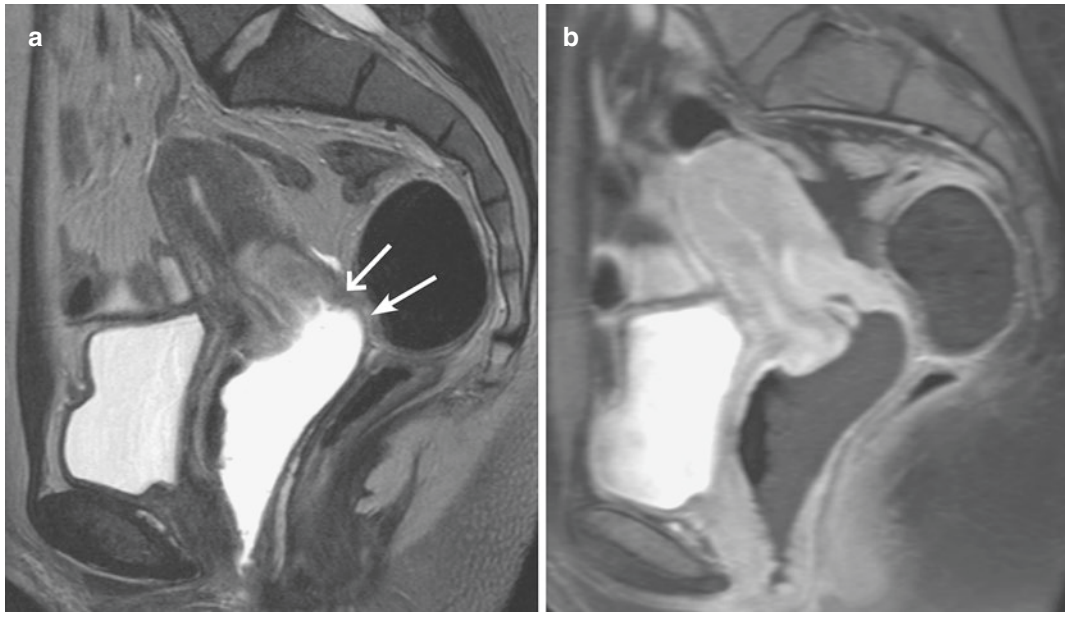

Fig. 21 Stage IIA. (**a**) T2w TSE image in sagittal orientation. High-signal-intensity cervical cancer with ulceration (*open arrow*) of its posterior portion and infiltration of the posterior vaginal fornix (*arrow*). (**b**) T1w TSE image in sagittal orientation. Following administration of Gd-DTPA, a low-signal intensity (hypovascularized) cervical cancer with ulceration and tumor infiltration of the posterior vaginal fornix is seen. Gel filling of the vagina

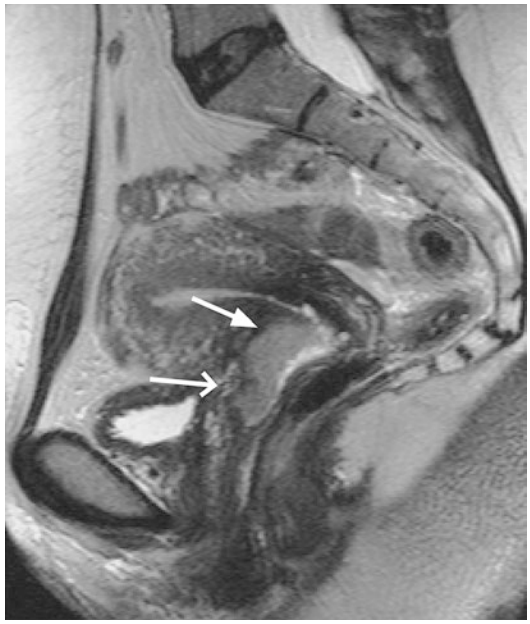

Fig. 22 Stage IIA. (**a**) T2w TSE image in sagittal orientation. Cervical cancer seen as a high-signal-intensity mass of the anterior cervix (*arrow*) with infiltration of the proximal vagina (*open arrow*)

2.3.4.8 Stage IVB

Stage IVB cervical cancer is characterized by hematogenous dissemination.

2.3.5 Lymph Node Staging

Following invasion of the dense network of lymphatic vessels in the parametria, cervical cancer can spread to the pelvic and para-aortic lymph nodes. The presence of lymph node metastases affects treatment planning and survival. Although several studies have shown that the presence of nodal metastases is among the most important prognostic factors in patients with cervical cancer, the nodal status is not taken into account by the FIGO classification. The earliest tumor stage associated with lymph node metastasis is IB (20%) and the risk increases with tumor size and stage (see Sects. 1.7 and 1.9). The risk of metastatic lymph nodes is increased in tumor recurrence and in patients with adenocarcinoma as compared with squamous cell carcinoma. Lymphatic spread usually first affects the primary

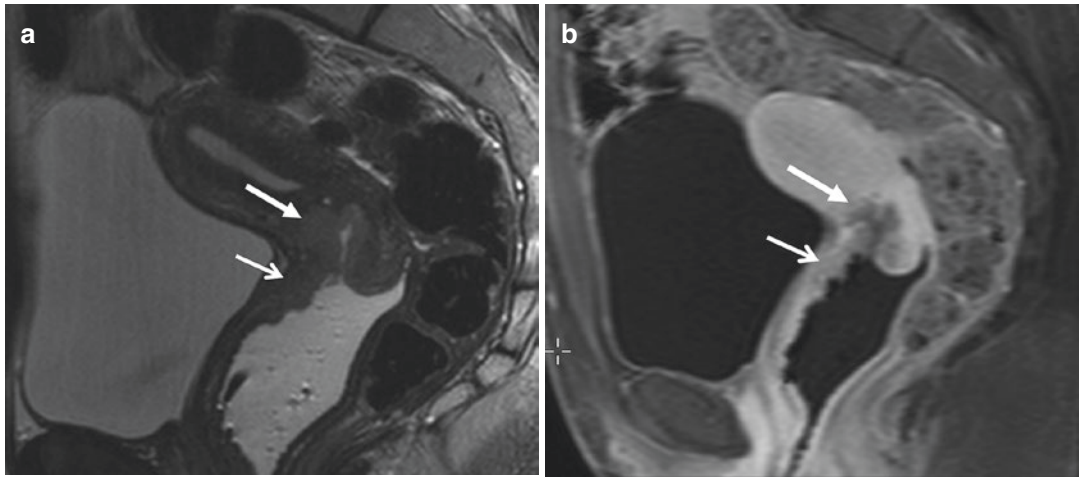

Fig. 23 Stage IIA. (**a**) T2w TSE image in sagittal orientation. Cervical cancer seen as a high-signal-intensity mass of the anterior proximal cervix (*arrow*) with infiltration of the upper two-thirds of the vagina (*open arrow*). (**b**) T1w TSE image with FS in sagittal orientation. Following administration of Gd-DTPA, a hypovascularized cervical cancer is depicted

lymph node stations in the parametrium, along the internal and external iliac arteries, from where the tumor spreads to the secondary, presacral lymph nodes along the common iliac artery and to the para-aortic lymph nodes (Figs. 33, 34, 35, and 36).

Finally, there may be spread to extra-abdominal lymph nodes. These are primarily the supraclavicular lymph nodes in the venous angle (Fig. 37), at the termination of the azygos and hemiazygos veins into the superior vena cava, besides the less commonly affected parabronchial and axillary lymph node stations. The morphologic changes caused by nodal metastases range from slight increases in size of isolated nodes to large lymph node conglomerates.

Surgical lymphadenectomy remains the gold standard in the diagnosis of nodal metastases. However, despite dramatic advantages in minimally invasive surgical techniques and technologies, surgical lymphadenectomy remains a potential source of severe complications. For this reason, in recent years, a great research effort has been directed at identifying imaging techniques able to reliably assess the nodal status in a noninvasive manner. Historically, radiologic evaluation of the lymph nodes is based on merely morphologic criteria including size and shape. A parametrial node is considered suspicious when its short axis is 5 mm or longer. A pelvic or para-aortic lymph node with a short axis longer than 10 mm and oval in shape or with an axis longer than 8 mm and round shape is interpreted as a potentially metastatic lymph node at MRI and CT (Scheidler et al. 1997; Kim et al. 1994). Other morphologic criteria are an irregular contour, inhomogeneous contrast enhancement and central necrosis. Intravascular contrast medium administration is especially useful to differentiate vascular structures and identify necrotic areas. While traditional size criteria display a specificity of almost 90% to exclude lymph node metastasis in early-stage cervical cancer patients, reported sensitivity rates are limited by the inability of merely morphological imaging techniques to detect lymphatic metastasis in normal-sized and -shaped nodes (Klerkx et al. 2010). Diffusion-weighted MR imaging (DWI), a sequence that provides functional information about the integrity of cell membranes and tissue consistency, has been proposed to improve the distinction between normal and metastatic lymph nodes by means of

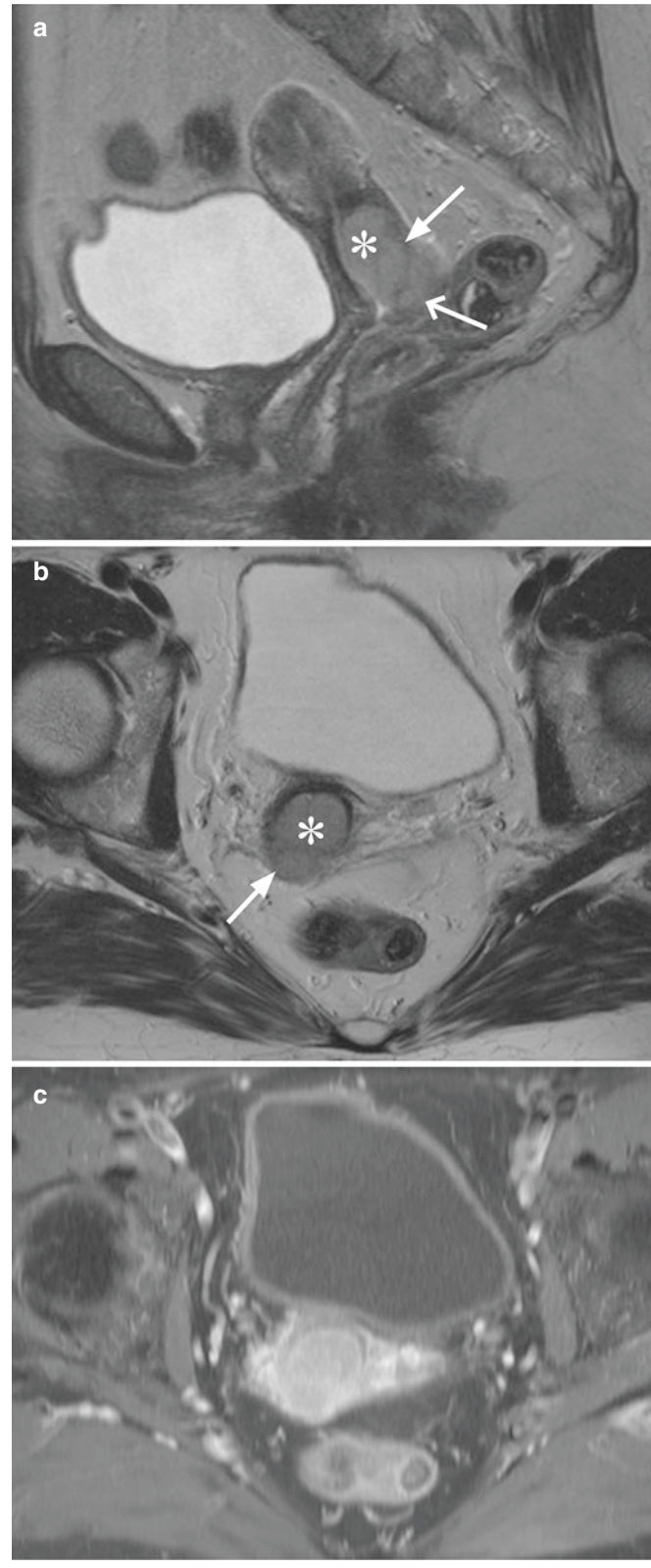

Fig. 24 Stage IIB. (**a**, **b**) T2w TSE images in sagittal and transverse orientation. Cervical cancer (*asterisks*) with infiltration of the posterior vagina (*open arrow*). Posterior disruption of the cervical stroma and a solid tumor extending in a posterior direction (*arrows*) are seen as signs of parametrium infiltration. (**c**) T1w TSE image with FS in transverse orientation 1 min after administration of Gd-DTPA showing a moderately hypervascularized cervical cancer with hypovascularized cervical stroma and hypervascularized lateral parametrial tissue

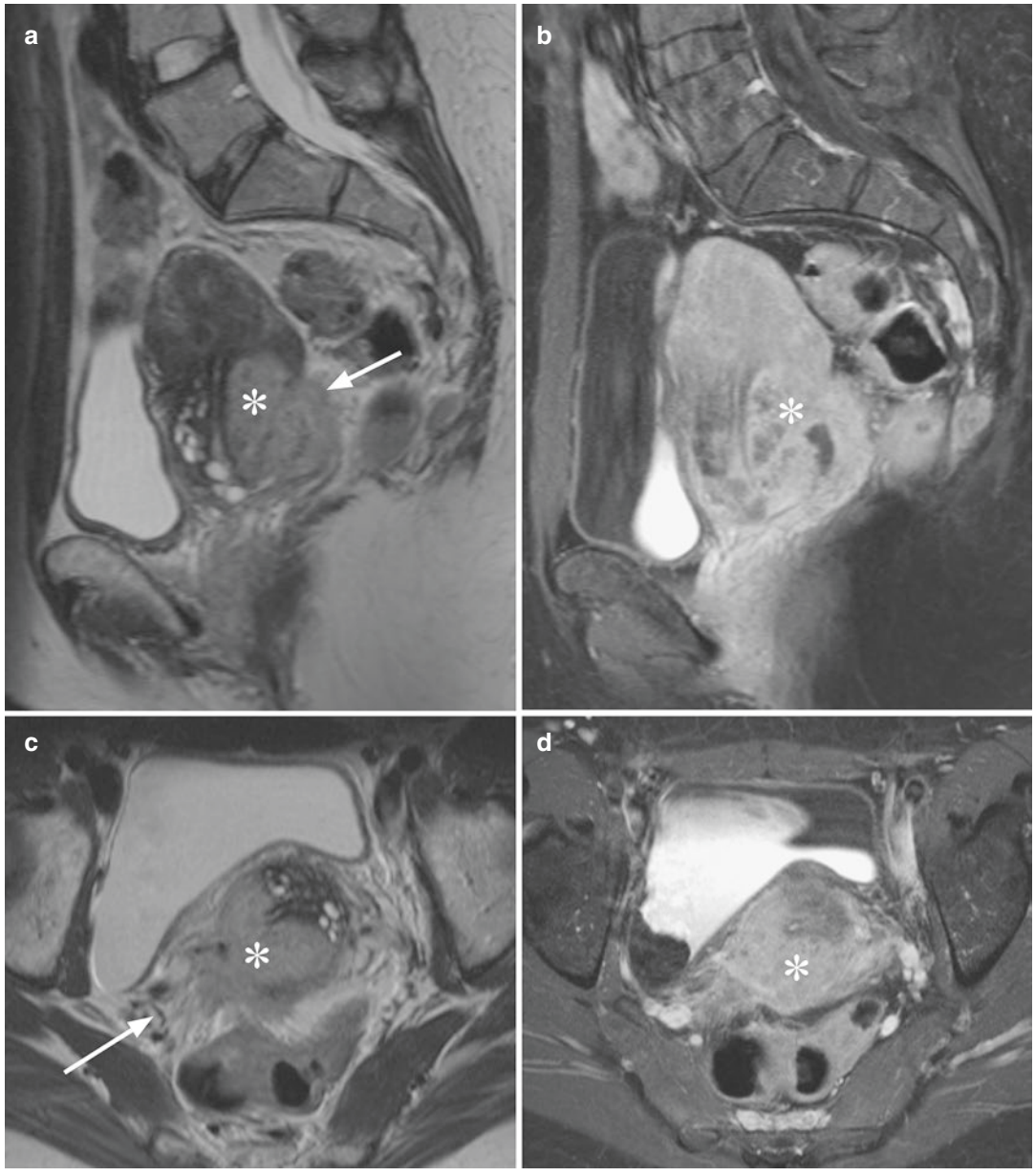

Fig. 25 Stage IIB. (**a**, **b**) T2w TSE images in sagittal and transverse orientation. Cervical cancer (*asteriks*) with infiltration of the posterior vaginal fornix. Clearly seen are parametrium tumor extensions (*arrows*) in a posterior direction and to the right without infiltration of the pelvic sidewall or of the rectum. (**c**, **d**) T1w TSE images in sagittal and transverse orientation 1 min after administration of Gd-DTPA. Heterogeneous hypervascularized cervical cancer (*asterisks*) with hypovascularized, necrotic portions. Accessory finding: cervical cysts

differences in signal intensity quantified as the apparent diffusion coefficient (ADC). In recent years, numerous studies have demonstrated that DWI is able to distinguish metastatic from benign lymph nodes in cervical cancer patients. Chen et al. (2011) reported that DWI with ADC measurements could differentiate metastatic from hyperplastic nodes with a sensitivity of 83.3%, specificity of 74.7%, and accuracy of 78.4%. By using the minimum ADC ($\leq 0.881 \times 10^{-3}$ mm^2/s)

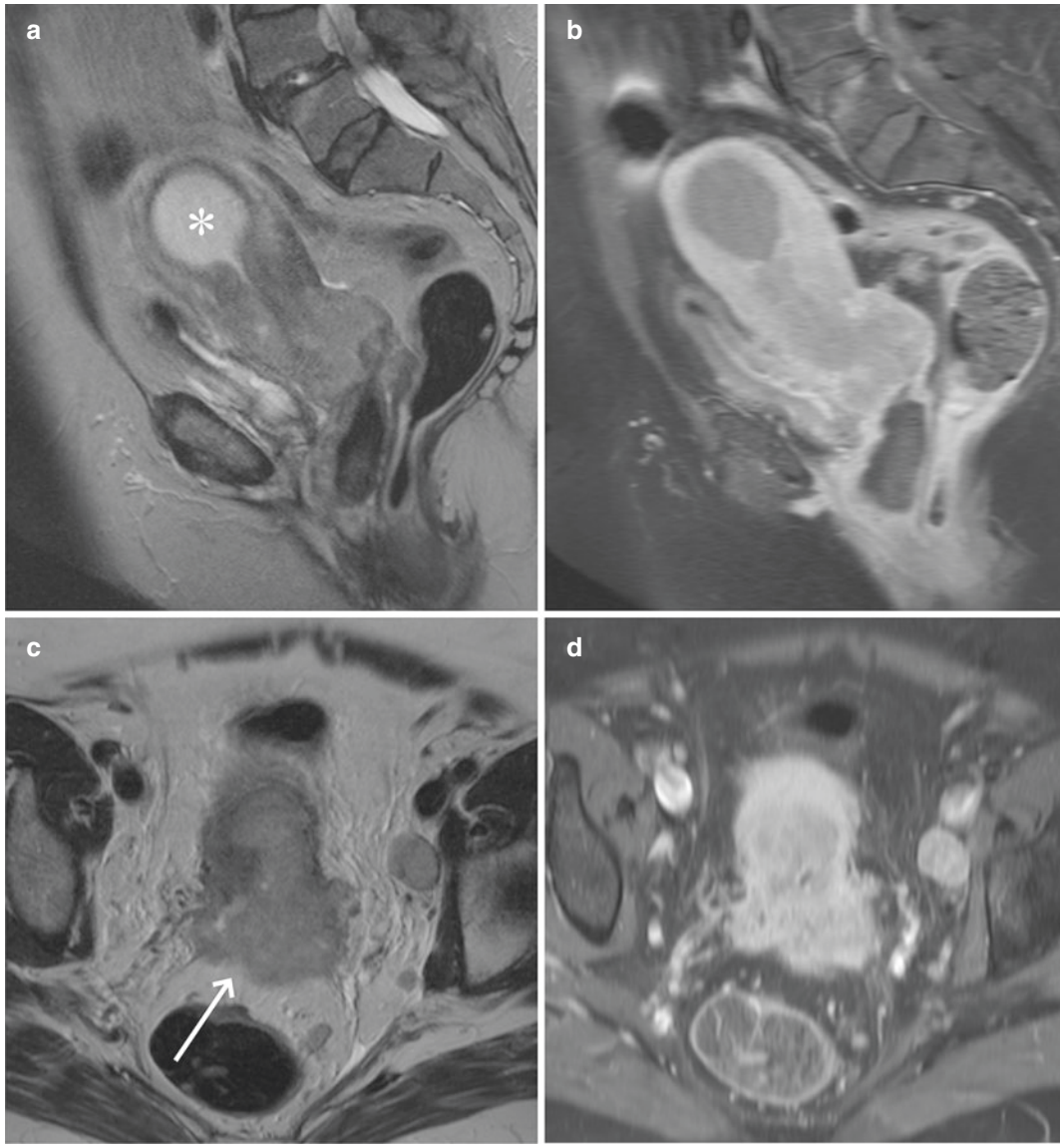

Fig. 26 Stage IIB. (**a**, **b**) T2w TSE images in sagittal and transverse orientation. Cervical cancer with infiltration of the uterine corpus and hematometra (*asterisk*) due to tumorous stenosis of the cervical canal. Large solid tumor portions extend into the parametria posteriorly (*open arrow*) but do not infiltrate the rectum. Also seen are nodal metastases of the internal obturator group, along the internal iliac artery, and of pararectal nodes on the left. (**c**, **d**) T1w TSE images in sagittal and transverse orientation 1 min after administration of Gd-DTPA

as a cutoff, Liu et al. reported a sensitivity and specificity for differentiating metastatic from nonmetastatic nodes of 95.7% and 96.5%, respectively (Liu et al. 2011). In a recent meta-analysis, Shen et al. reported pooled estimates of 0.86 (95% CI, 0.84–0.89) for sensitivity and 0.84 (95% CI, 0.83–0.86) for specificity, suggesting that DWI could be beneficial in the assessment of pelvic nodal metastases in patients with cervical cancer (Shen et al. 2015).

Another modality, whole-body FDG-PET (5-fluor-odesoxyglucosis-positron emission tomography), can be used as a supplementary test for lymph node staging in follow-up (Reinhardt

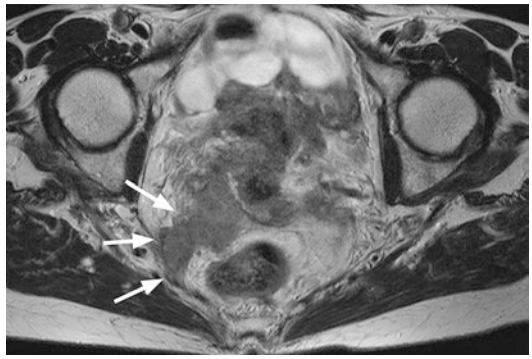

Fig. 27 Stage IIIB. T2w TSE image in transversal orientation. Cervical cancer with right lateral parametrial infiltration and infiltration of the right pelvic wall (*arrows*)

et al. 2001) but has similar limitations to established imaging modalities, which include identification of micrometastases and differentiation of tumor from inflammatory changes. FDG PET provides no morphologic information and has to be combined with CT or MRI, possibly using the technique of image fusion (Lemke et al. 2004; Kim et al. 2009). Integrated PET and computed tomography (PET/CT) scanners are nowadays widely used in clinical practice. Kitajima et al. compared DWI and FDG-PET/CT in evaluation of nodal metastases from cervical and endometrial cancer and reported lower sensitivity (38.9% vs. 83.3%) but a higher specificity (96.3% vs.

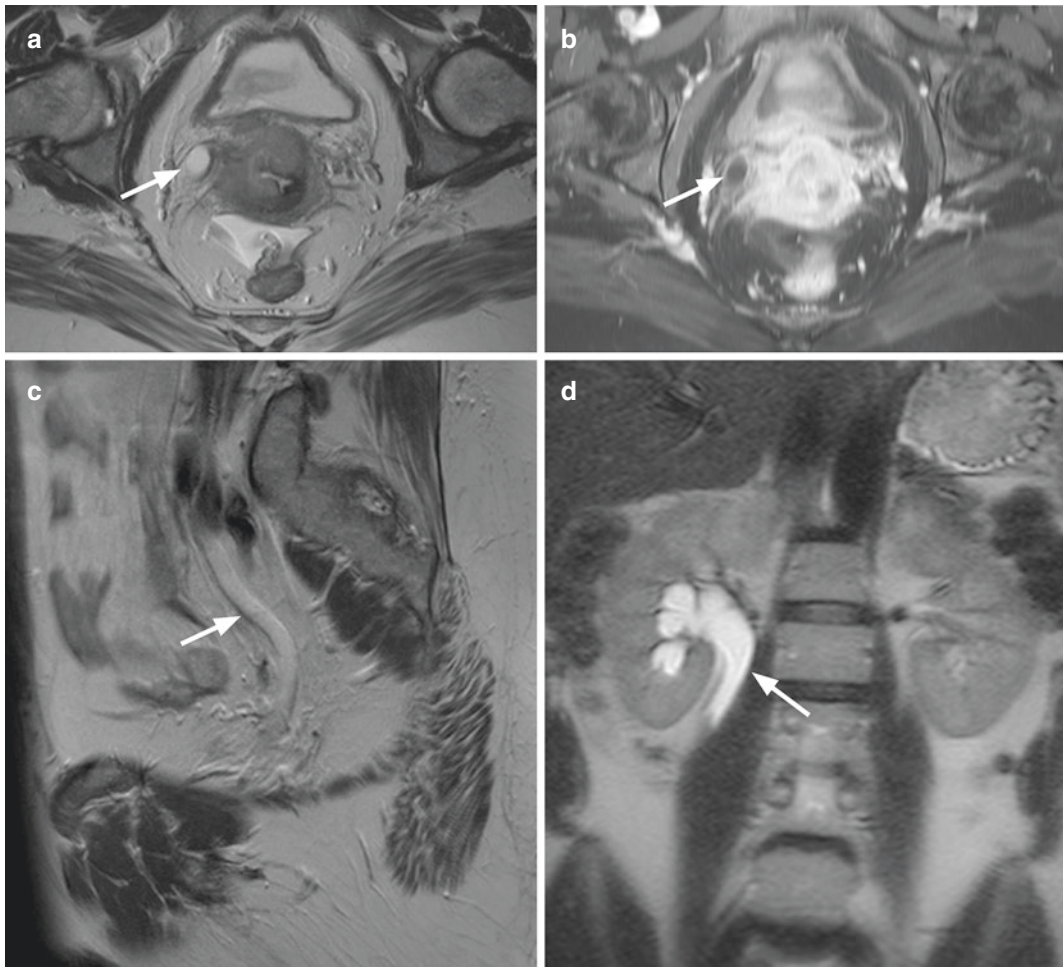

Fig. 28 Stage IIIB. (**a**, **b**) T2w TSE images in sagittal and transverse orientation. (**c**) HASTE TSE image in coronal orientation. (**d**) T1w TSE image in transverse orientation 1 min after administration of Gd-DTPA. Cervical cancer with right lateral parametrial infiltration and infiltration of the right ureter, which is distended as a consequence (*arrows*)

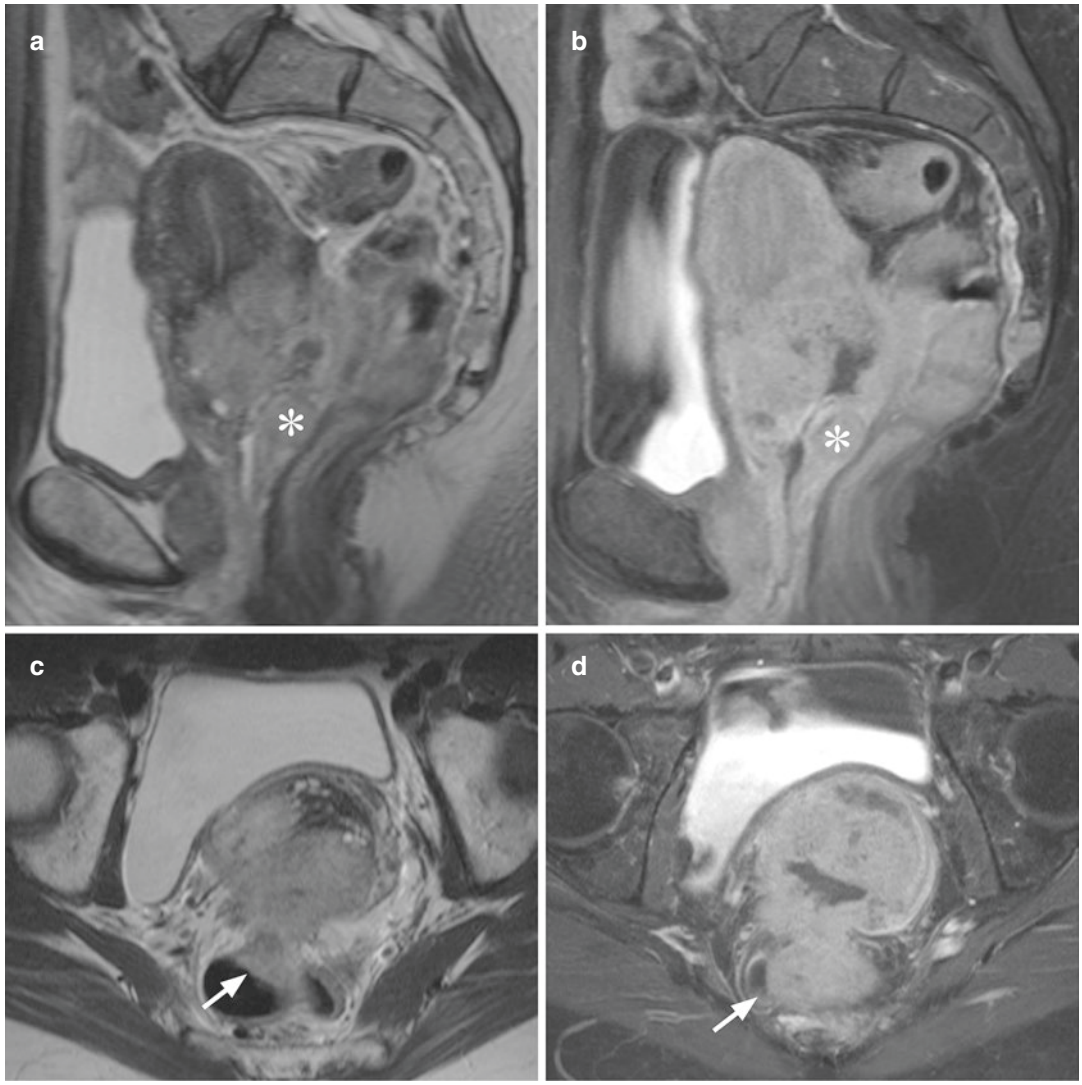

Fig. 29 Stage IVA. (**a**, **b**) T2w TSE images in sagittal and transverse orientation. (**c**, **d**) Tlw TSE images in sagittal and transverse orientation 1 min after administration of Gd-DTPA. Cervical cancer with infiltration of the posterior parametria. Rectal infiltration (*arrows*) is seen as hyperintense tumor extension disrupting the anterior rectal wall, which is of low signal intensity before and of intermediate signal intensity after CM administration. Tumor is also seen in the posterior vaginal wall (*asterisks*)

51.2%) for FDG-PET/CT compared to DWI (Kitajima et al. 2012).

2.3.6 Distant Metastases

Distant metastases are characteristic of stage IVB cervical cancer. In the FIGO classification, metastases of the para-aortic lymph nodes count as distant metastases. Hematogenous dissemination occurs late in cervical cancer or typically in patients with local tumor recurrence. Organ metastases most commonly affect the lungs and are less frequent in the liver, peritoneum, and skeleton. Systemic staging for the exclusion of distant metastases is indicated in stage III and IV cervical cancer. In Germany, an additional helical CT scan of the chest, abdomen, and pelvis including the supraclavicular region, with oral opacification and IV bolus administration of contrast

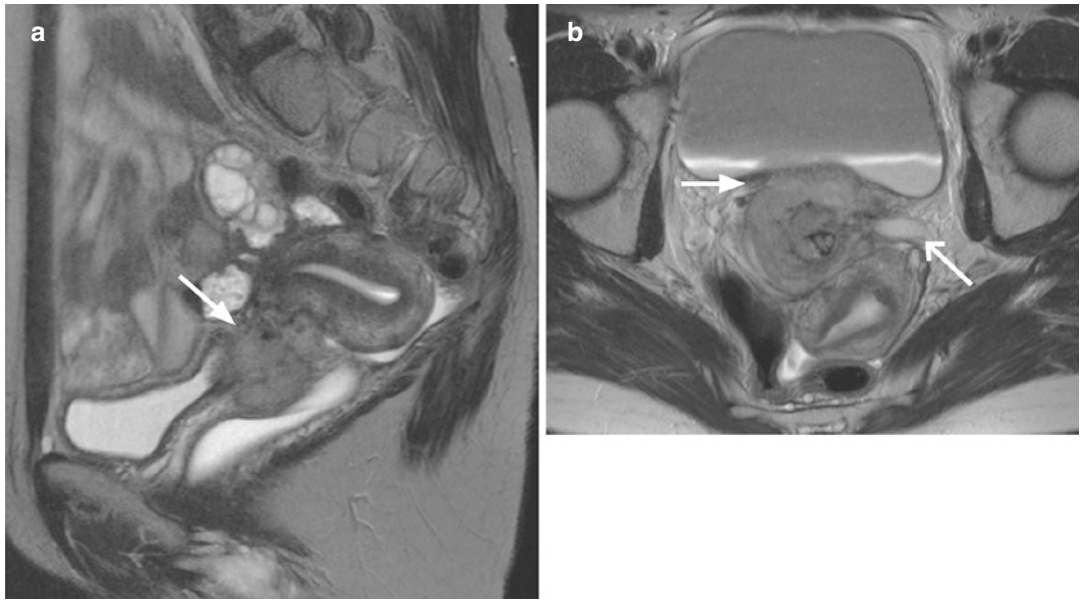

Fig. 30 Stage IVA. (**a**, **b**) T2w TSE images in sagittal and transverse orientation showing cervical cancer with infiltration of the urinary bladder. Disruption of the hypointense bladder wall and intravesical tumor growth are seen (*arrows*). In addition, there is infiltration of the left lateral parametria and the left ureter, which is distended as a consequence (*open arrow*)

medium, is recommended (Schmidt-Matthiesen and Wallwiener 2005).

Autopsy studies found pulmonary metastases in about 35% of patients with recurrent cervical cancer. The probability of lung metastases is similar for squamous cell carcinoma and adenocarcinoma of the cervix. Solitary or multiple nodular pulmonary metastases may occur and are comparable to pulmonary metastases from other primaries in that clinical symptoms occur late. Chest CT is recommended as the first-line modality for exclusion of pulmonary metastases. Alternatively, routine chest radiography performed before therapy for assessment of the cardiopulmonary status can likewise be used to exclude pulmonary metastases but is less sensitive than CT. Pulmonary metastases are associated with mediastinal or hilar lymphadenopathy in 30% of cases and with pleural metastases in about 27% (autopsy studies). A slightly higher risk of pleural metastases has been reported for cervical adenocarcinoma. Rare findings are pericardial metastases, bronchial spread with endobronchial obstruction (5%), and pulmonary lymphangiosis carcinomatosa (3%) (Choi et al. 2000).

Liver metastases occur in about 30% of patients with recurrent cervical carcinoma (Drescher et al. 1989) (Fig. 37). They are identified by ultrasound as multiple focal lesions of low echogenicity and as focal lesions with heterogeneous contrast medium uptake on CT and MRI. MRI has the highest sensitivity in detecting liver metastases, especially when performed with administration of a liver-specific contrast medium (Hamm et al. 1997). Metastases in the peritoneum (Fig. 38), major omentum, or mesentery were identified at autopsy studies in 5–27% of cases (Nicolet et al. 2000; Sahdev et al. 2007). Clinical symptoms occur late and comprise abdominal pain and an increase in abdominal circumference. Metastases in these locations are sensitively identified by MRI and CT (Outwater et al. 1996; Low et al. 1997). MRI is performed with contrast-enhanced fat-saturated T1-weighted sequences, optionally supplemented by oral opacification. Characteristic signs of peritoneal metastases are a wavy contour of the liver resulting from impressions by the focal lesions, nodular peritoneal masses, and irregular peritoneal thickening. Ascites is unspecific but may indicate peritoneal metastases (Badib et al. 1968).

Recurrent cervical cancer is associated with bone metastases (Fig. 38) in 15–29% of patients at autopsy (Badib et al. 1968). Typical locations are the bony pelvis as well as the lumbar and other vertebral bodies. Bone metastases in the ribs and extremities are less common. Skeletal metastases typically have an osteolytic character and originate from locally advanced or recurrent tumor in the pelvic sidewall or arise through retrograde tumor spread in patients with para-aortic lymph node metastasis.

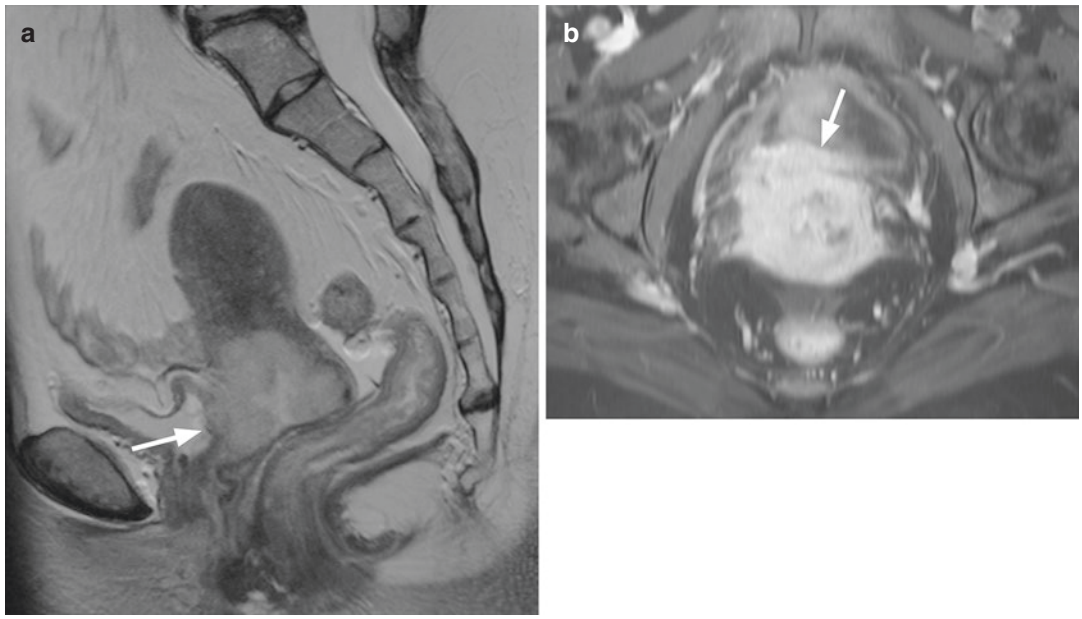

Fig. 31 Stage IVA. (**a**) T2w TSE image in sagittal orientation. Cervical cancer with infiltration of the vesicouterine ligament and of the low-signal-intensity posterior bladder wall (*arrow*). Tlw TSE image with FS transverse orientation 1 min after administration of Gd-DTPA. (**b**) After CM administration, a hypervascularized tumor (transverse image) is seen in the posterior bladder wall (*arrow*) (from Nicolas et al. 2005)

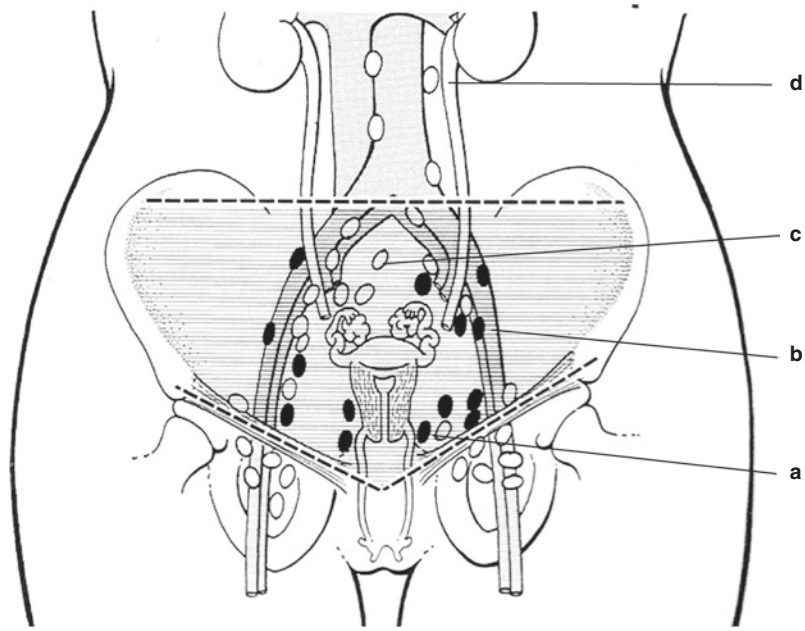

Fig. 32 Lymph node staging. Stages of metastatic spread to the lymph nodes in cervical cancer. (**a**) Parametrial nodes. (**b**) Nodes along the external and common iliac arteries. (**c**) Presacral nodes. (**d**) Para-aortic nodes (regarded as distant metastases) (from Wittekind et al. 2005)

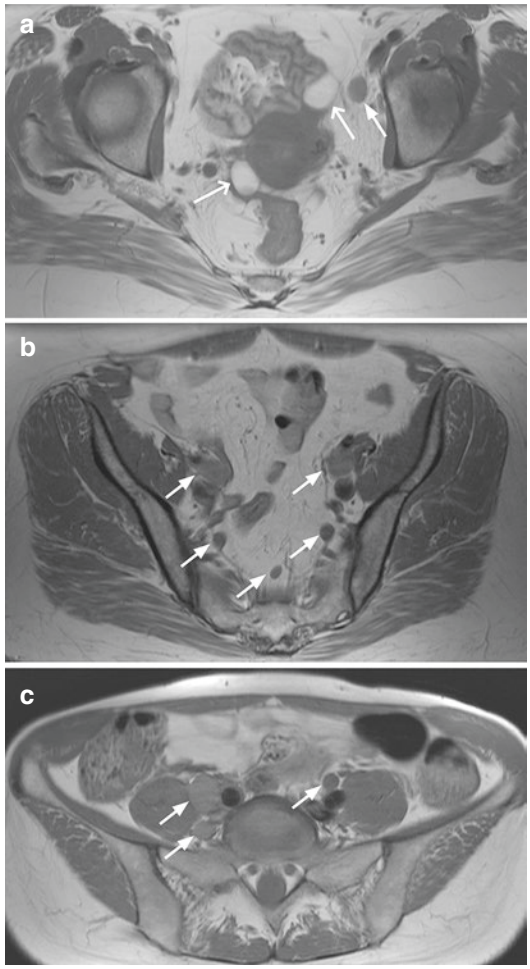

Fig. 33 Lymph node staging in different patients. (**a**–**c**) PD-TSE images in transverse orientation. (**a**) Suspicious lymph node of round configuration measuring 1 cm in diameter of the external iliac artery group on the left (*arrow*) in a patient with cervical cancer with bilateral parametrial infiltration and ureteral distention (*open arrows*). (**b**) Suspicious round and enlarged lymph nodes along the external iliac artery on both sides and an increase in the number of presacral lymph nodes with round configuration (*arrows*). (**c**) Suspicious round and enlarged lymph nodes of the common iliac artery group on both sides (*arrows*). The presence of pelvic lymph node metastases is not taken into account in the FIGO staging system

Hematogenous dissemination to the skeleton occurs late. MRI with unenhanced and contrast-enhanced fat-saturated T1-weighted sequences depicts bone metastases as hyperintense lesions in the low-intensity bone marrow with high sensitivity. CT primarily shows the extent of osseous destruction.

About 15% of patients with recurrent cervical cancer develop adrenal metastases (Badib et al. 1968). Splenic, pancreatic, gastrointestinal, and renal metastases are very rare.

2.4 Specific Diagnostic Queries

2.4.1 Preoperative Imaging

Pretherapeutic local tumor staging is crucial to determine resectability and to select the most suitable operative procedure (simple hysterectomy, radical hysterectomy, trachelectomy, extent of lymphadenectomy), which is primarily based on tumor size, lymph node status, and parametrial involvement. The surgical procedure chosen based on the MRI findings is often specified further by surgical lymph node staging. If no primary surgery and no surgical lymph node staging are performed, the MRI findings serve to determine the target volume to be irradiated. MRI after adjuvant therapy serves to reconsider the indication for surgery. In patients with local recurrence, the MRI findings have an important role in deciding to reoperate and the surgical technique. Contraindications to curative exenteration are intraperitoneal implantation, nonresectable nodes, extensive involvement of the pelvic sidewall and liver or lung metastases.

Furthermore, MRI plays a crucial role in establishing the indication for radical trachelectomy. Only patients in whom MRI demonstrates a tumor-free internal os of the cervical canal at the isthmus uteri are candidates for trachelectomy (Peppercorn et al. 1999). Therefore it is additionally important to estimate the distance of the tumor from the uterine isthmus and from the vaginal vault. Trachelectomy is not performed if there is infiltration of the isthmus or of the myometrium of the uterine corpus. The isthmus is identified by its small diameter and the entrance of the uterine vessels.

2.4.2 Imaging Before Radiotherapy

In patients scheduled for primary radiotherapy without surgical staging, the pretreatment radiologic evaluation together with the clinical findings gains in importance. Although exter-

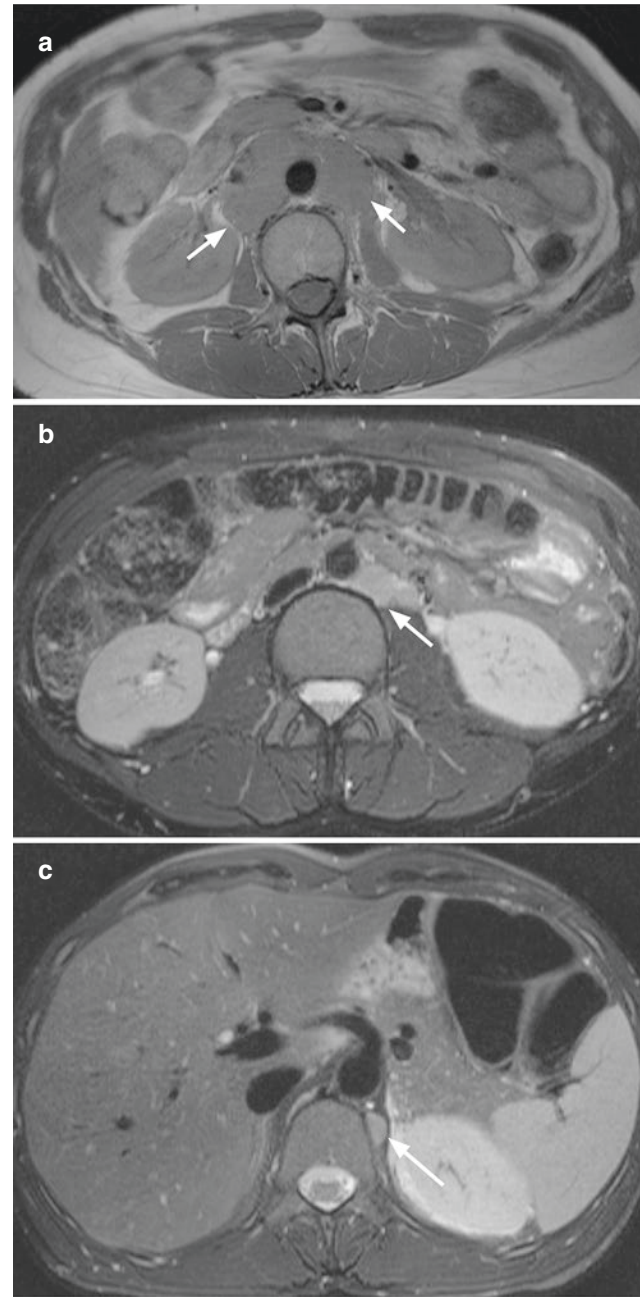

Fig. 34 Lymph node staging in different patients. (**a**) PD-TSE images in transverse orientation shows para-aortic and interaortocaval lymph node metastases (*arrows*). (**b**, **c**) T1w TSE images (PACE) in transverse orientation. Suspicious round and enlarged para-aortic and retrocrural lymph nodes (*arrows*). Para-aortic lymph node metastases are regarded as distant metastases, the patient thus has FIGO stage IVB

nal beam radiotherapy is still usually planned by means of a CT scan, MRI has an increasing role in treatment planning and controlling radiation (Figs. 39 and 40). The superior accuracy of T2-weighted images in the delineation of the primary tumor and the adjacent soft-tissue invasion make MR imaging more and more appreciated. The CT scan performed to plan radiotherapy serves to determine the physical parameters of irradiation such as number and direction of the radiation fields, collimation, and dose distribution. The use of 3D-based individual planning of radiation fields has almost completely replaced the four-field box technique (Fig. 39).

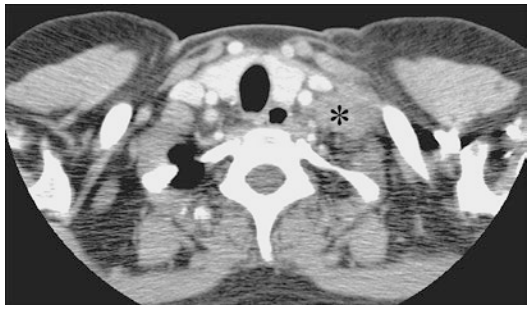

Fig. 35 Lymph node staging. Contrast-enhanced CT image. Supraclavicular lymph node metastasis on the left (*asterisk*). FIGO stage IVB

Dose-volume histograms serve to determine the respective dose corresponding to a specific organ volume such as the bladder or rectum, which are especially at risk. In planning the target volume to be irradiated (PTV, physical target volume), the primary tumor volume (GTV, gross tumor volume), the area of potential tumor extent (CTV, clinical target volume), and a safety margin that takes into account patient and organ motion are defined. The CTV comprises the uterus, at least the proximal third of the vagina, the parametrial tissue up to the pelvic wall, and the pelvic lymphatic drainage system, which is irradiated with a dose high enough to eliminate both micrometastases and manifest metastases. The only proven indication for para-aortic irradiation is metastatic para-aortic nodes. To spare the intestine, planning and irradiation are usually performed with the patient positioned prone on a belly board.

Modern radiation therapy for patients with cervical cancer is generally delivered with a combination of external beam radiation therapy (EBRT) and brachytherapy (BT), the latest being essential especially when therapy is administered with curative intent.

The advent of three-dimensional treatment planning of BT, allowing precise dose delivery to the target volume while limiting the dose to organs at risk, represents one of the most significant advancements in the treatment of cervical cancer. The introduction of computer tomography-based 3D treatment planning enables the delineation the organs at risk as volumetric structures rather than arbitrary reference points, resulting in better estimation of maximum doses to the surrounding organs at risk as well as in improved local tumor control (Harkenrider et al. 2015). MR imaging is becoming increasingly used for image-based brachytherapy as it allows accurate demonstration of tumor size, location, and extension thanks to its superior soft-tissue resolution. In studies comparing MRI with CT-based treatment planning, MRI has shown to enable better tumor delineation and greater dose escalation (Harkenrider et al. 2015).

2.5 Follow-Up

2.5.1 Findings After Surgery

Scar tissue being older than 6 months has low signal intensity similar to that of muscle on T1- and T2-weighted MR images. Fresh scars are of a higher signal intensity on T2-weighted images due to inflammation and neovascularization in the first months after surgery. Signal intensity decreases with fibrosis. This is why MRI should be performed not earlier than 6 months after the end of therapy and even then the signal intensities of recurrent tumor and scar tissue may still overlap on T2-weighted images. In these situations, a dynamic contrast-enhanced study could be necessary and help to better distinguish recurrent tumor on the basis of its earlier and more pronounced CM enhancement.

After radical hysterectomy, the uterus and the vaginal vault are absent (Brown et al. 1992). The vaginal stump is depicted with a smooth end and as a symmetrical, elongated, or rectangular structure that is sharply demarcated from the surrounding fatty tissue between the bladder and the rectum (Fig. 41). Cranial to the stump, the resection cavity is filled by the urinary bladder and bowel. Images in sagittal orientation are most suitable to evaluate the vaginal wall (Brown et al. 1992). On T2-weighted images, the vagina is characterized by a high-signal-intensity inner mucosal layer and a smooth outer muscular layer of low signal intensity. Surgical clips are depicted

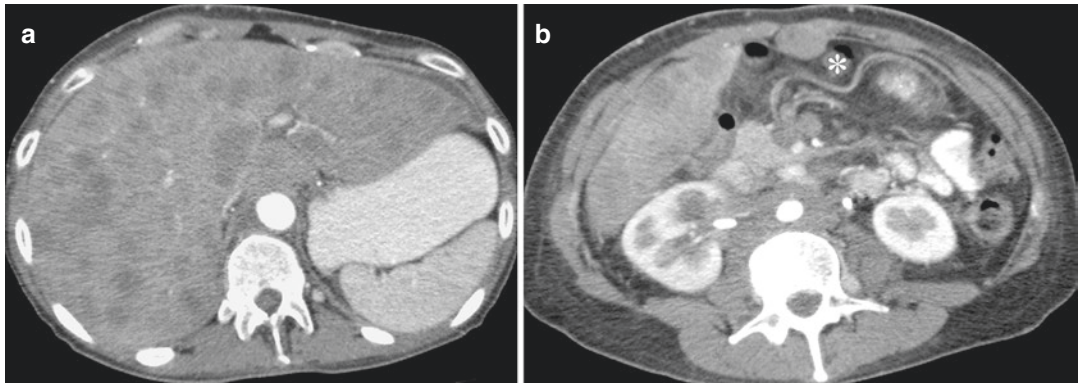

Fig. 36 Distant metastases. (**a**, **b**) Contrast-enhanced CT images. Numerous hypovascularized metastases are seen in the liver. In addition, metastatic spread to the peritoneum (*asterisk*) and extensive para-aortic lymph node metastases. FIGO stage IVB

on MRI images as small signal voids at the vaginal stump. Some patients develop fibrotic scar tissue at the roof of the vaginal stump. It is characterized by an intermediate to low signal intensity on T2-weighted and T1-weighted images and may be difficult to differentiate from recurrence if it is of nodular configuration.

The peri- and postoperative complications include the development of vesicovaginal fistulas, which typically occur on the basis of necrosis roughly 1–2 weeks after the surgery. If they do not close spontaneously, they are operated on at 8 weeks or later in patients undergoing adjuvant radiotherapy. Injury to the urinary bladder occurs in 3–5% of patients undergoing radical hysterectomy and ureteral damage in 2%. Ureteral damage is usually treated by primary surgical repair. Ureterovaginal fistulas typically develop in the second postoperative week and have an incidence of about 1%. They spontaneously close after placement of a double-J catheter. Lymph edema of the legs has an incidence of 3% after surgery and of 5–15% after adjuvant radiotherapy. Clinically, approximately 15% of patients develop acute bladder voiding difficulties after radical hysterectomy with lymph node dissection, due to mechanical factors as well as damage to bladder innervation. The incidence increases with the radicalness of the operation.

In radical trachelectomy, MRI depicts the end-to-end anastomosis and the development of a posterior neofornix (Fig. 42). The latter may develop in the process of healing and must be carefully distinguished from a recurrent tumor. The few recurrences of cervical cancer observed after trachelectomy seem to occur at the site of anastomosis (Sahdev et al. 2005). Occasionally, stenosis has been observed after trachelectomy. Moreover, mobilization of the parametrial and paravaginal tissue can lead to diffuse thickening of the vaginal wall, which may mimic recurrent invasive tumor at MRI. Most of these postoperative changes recede spontaneously. In some patients, asymptomatic widening of the parametrial venous plexus has been observed. In patients becoming pregnant after trachelectomy, a cerclage is placed to keep the cervix closed.

Following lymph node dissection, metal clips are often seen at the pelvic wall as focal artifacts of low signal intensity at MRI or as metal-dense structures at CT. Lymphoceles most frequently develop after lymphadenectomy. They are usually small, cause no symptoms, and recede without therapy. If a lymphocele becomes symptomatic or infection is suspected due to contrast enhancement of the wall, therapy may be required in the form of repeat operation, puncture, drainage, or sclerotherapy.

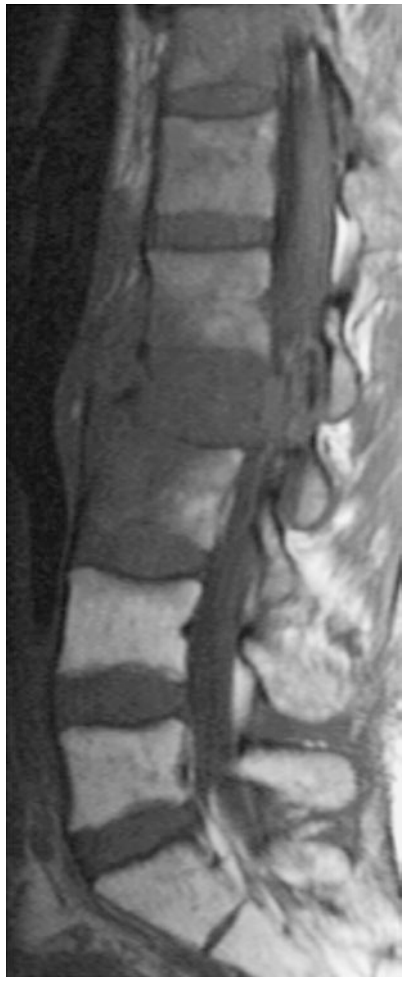

Fig. 37 Distant metastases. T1w TSE image in sagittal orientation. Para-aortic lymph node metastases with vertebral infiltration of L1–L3. Consecutive total collapse of vertebral body of L2. FIGO stage IVB

Pelvic exenteration is the curative method of choice in patients with central pelvic tumor recurrence and comprises colpectomy and hysterectomy with removal of the bladder (anterior exenteration) or of the bladder and rectosigmoid (complete exenteration). In addition, the intervention may be performed as supralevator exenteration with partial resection of the levator plate or as translevator exenteration with vulvectomy and radical resection of the levator muscle, urogenital diaphragm, and vulvoperineal soft tissue. The patient's quality of life is improved by subsequent reconstruction of the pelvic organs with deep rectal anastomosis, creation of a urinary pouch, and possibly creation of a neovagina. The intervention-related mortality is about 5%.

2.5.2 Findings After Chemotherapy

The main criterion for a response to chemotherapy is a reduction of tumor size. For follow-up of tumor size under chemotherapy, the largest transverse diameter of the lesion is measured according to the RECIST criteria (Eisenhauer et al. 2009). A size reduction of at least 30% is defined as partial response to therapy. Tumor progression is assumed when there is an increase in size of at least 20%. MRI is the method of choice for evaluating the response to chemotherapy in patients with cervical cancer. However, in patients on chemotherapy, both vital tumor tissue and inflammatory reactive areas are present, which are of high signal intensity on T2-weighted images and show early contrast enhancement on T1-weighted images. This is why reliable evaluation of tumor tissue on the basis of signal intensity at T2-weighted imaging and contrast enhancement at T1-weighted imaging is not always possible at this stage. Therefore, the most important criterion for a response to therapy at this stage is the size reduction of the tumor. The concomitant reaction of the surrounding tissue and fibrosis impairs not only the radiologic diagnosis but also later surgical treatment. In recent years, diffusion-weighted imaging (DWI) has been investigated as an alternative imaging modality for following up tumor response to chemotherapy. The idea behind the use of DWI to monitor tumor response relies on the fact that as the tumor shrinks with treatment, water mobility increases. Thus, the apparent diffusion coefficient (ADC) may increase and may serve as an early indicator of tumor response. Preliminary studies using DWI-MRI as an early biomarker to assess tumor response to neoadjuvant chemotherapy have been promising, raising the need for future large-scale prospective studies (Fu et al. 2012).

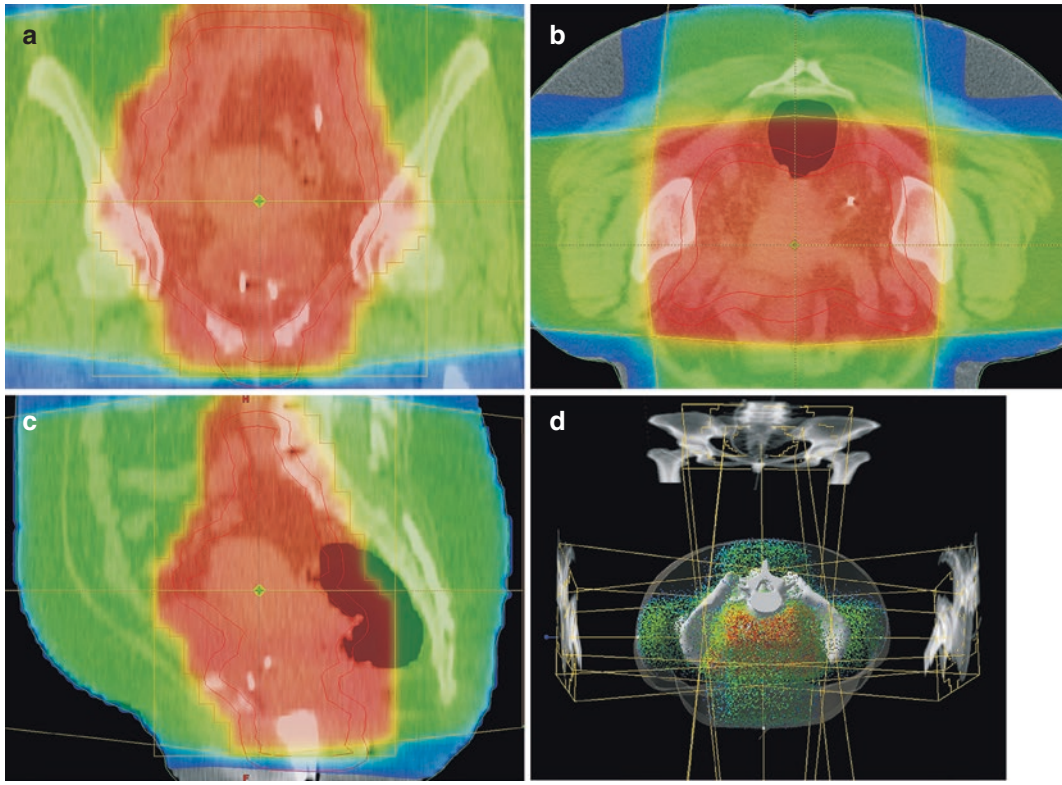

Fig. 38 Planning CT scan prior to radiotherapy. (**a**–**c**) Planning of irradiation therapy with determination of the target volume using the transverse planes of the CT scan and transfer to the sagittal and coronal planes. (**d**) Dose target volume and arrangement of fields using a four-field technique. The target volume comprises the vagina, uterus, and locoregional lymphatic drainage system including a safety margin. Irradiation in the prone position to spare the small intestine (Courtesy of Dr. L. Moser, Berlin)

2.5.3 Findings After Radiotherapy

MRI is the first-line radiologic modality for follow-up after radiation therapy. It may be performed 6 and 12 months after completion of irradiation and whenever tumor recurrence is suggested by the clinical or gynecologic findings. During and shortly after radiotherapy, the entire irradiated field shows a reactive signal increase on T2-weighted images and more pronounced contrast enhancement on T1-weighted images. This is why differentiation of tumor tissue from reactively inflamed tissue is impaired during and shortly after irradiation. Hence, MRI during or within the first 6 months after radiotherapy is indicated in exceptional cases for the

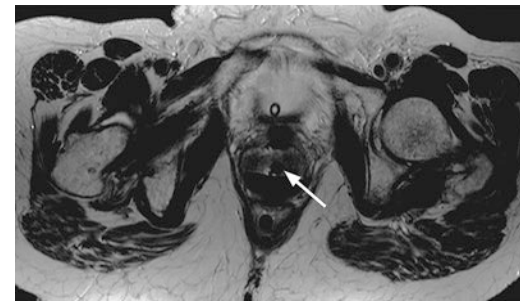

Fig. 39 MR imaging during intracavitary brachytherapy. Axial T2w image during intracavitary brachytherapy facilitates treatment planning and is useful in controlling the relationships between tumor and applicator (*arrow*). Measuring probes are placed in the rectum (courtesy of Prof. Dr. S. Marnitz, Köln)

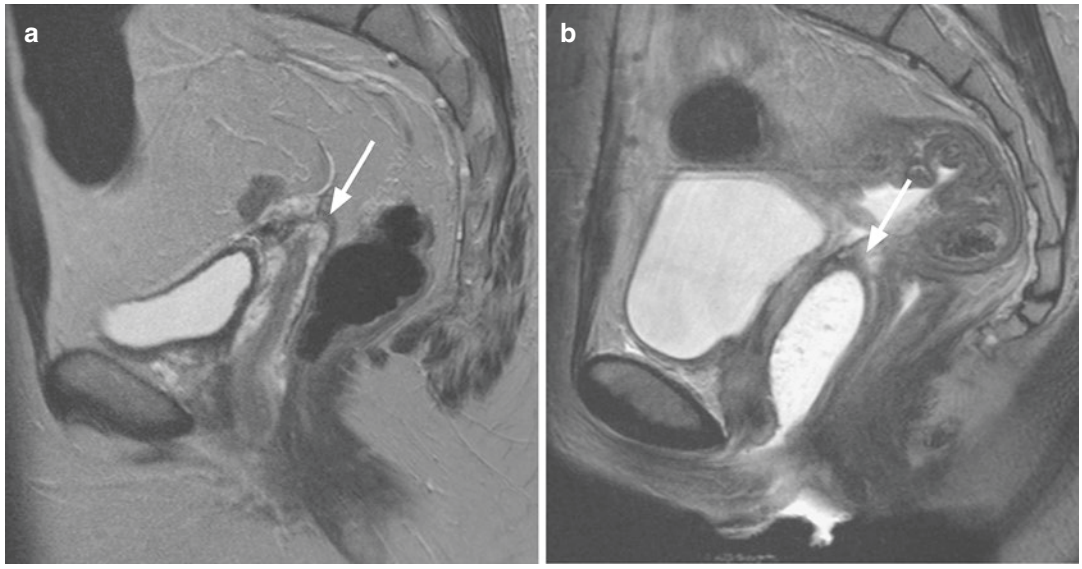

Fig. 40 Status after hysterectomy. (**a**, **b**) T2w TSE images of different patients in sagittal orientation. Normal appearance of the vaginal stump (*arrows*) after hysterectomy without (**a**) and with (**b**) filling of the vagina. Patient is catheterized

evaluation of tumor shrinkage or assessment of a fistula.

Effective radiation therapy leads to a significant reduction or complete disappearance of the tumor and a decrease in signal intensity on T2-weighted images (Figs. 43 and 44). A reliable sign of complete tumor remission is the return of the normal anatomy of the cervix and proximal vagina, which is suggested by the depiction of a homogeneous stroma of low signal intensity with a smooth mucosal layer often accompanied by shrinkage of the cervix. Recurrent tumor is typically seen as a high-signal-intensity mass corresponding to the original tumor on T2-weighted images.

The signal changes seen at MRI correlate with the overall radiation dose applied. Radiation-induced edema persists in the myometrium of the uterine corpus for up to 6 months after irradiation. After completion of radiation, there is a decrease in signal intensity on T2-weighted images, the endometrium becomes narrower, and the zonal anatomy of the myometrium is eliminated. In postmenopausal women, the uterus returns to its former MRI appearance without zonal anatomy after resolution of radiation-induced edema. The vagina also has an increased signal intensity on T2-weighted

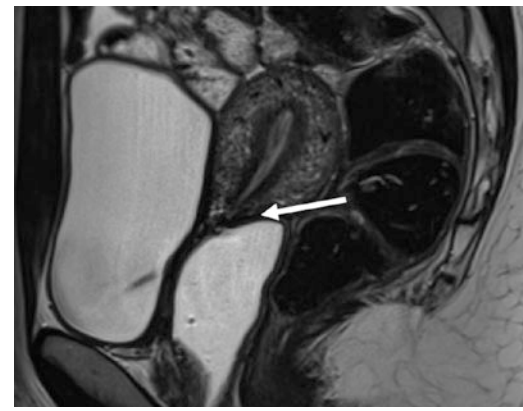

Fig. 41 Status after trachelectomy. A T2w TSE image in sagittal orientation. Markedly shortened uterine cervix after radical trachelectomy with fertility-sparing uterovaginal reanastomosis (*arrow*). Gel filling of the vagina

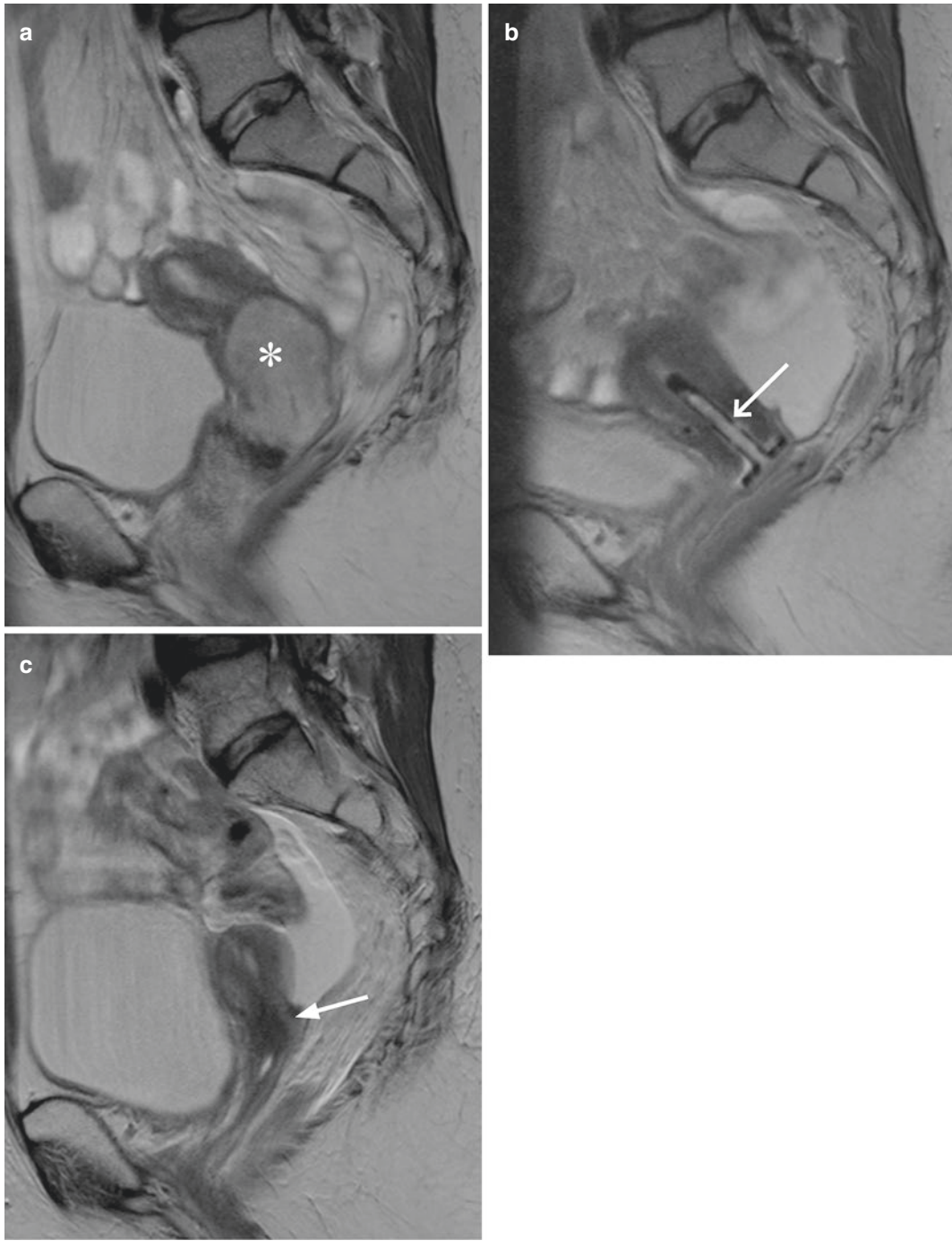

Fig. 42 Monitoring of radiotherapy, (**a**–**c**) T2w TSE images in sagittal orientation, (**a**) cervical cancer (*asterisk)* with infiltration of the vagina and parametria. (**b**) Tumorous mass of the cervix has disappeared 2 months after radiotherapy. Endocervical sheath in place (*arrow*). (**c**) Normal appearance of the cervix and atrophy of the uterus 12 months after completion of irradiation (*arrow*). Small amounts of free fluid

images due to edematous and inflammatory changes in the acute and subacute phase after irradiation. About 6 months after the end of radiation therapy, there is a fibrosis-related signal reduction on T2-weighted images. Shrinkage of the cervix and vagina may occasionally lead to an effective stenosis (radiogenic fibrosis) with subsequent development of hydrometra or hematometra. This condition is associated with symmetric enlargement of the uterus with a central fluid collection, which is of high signal intensity on T2-weighted images and also on T1-weighted images if the protein or blood content is high.

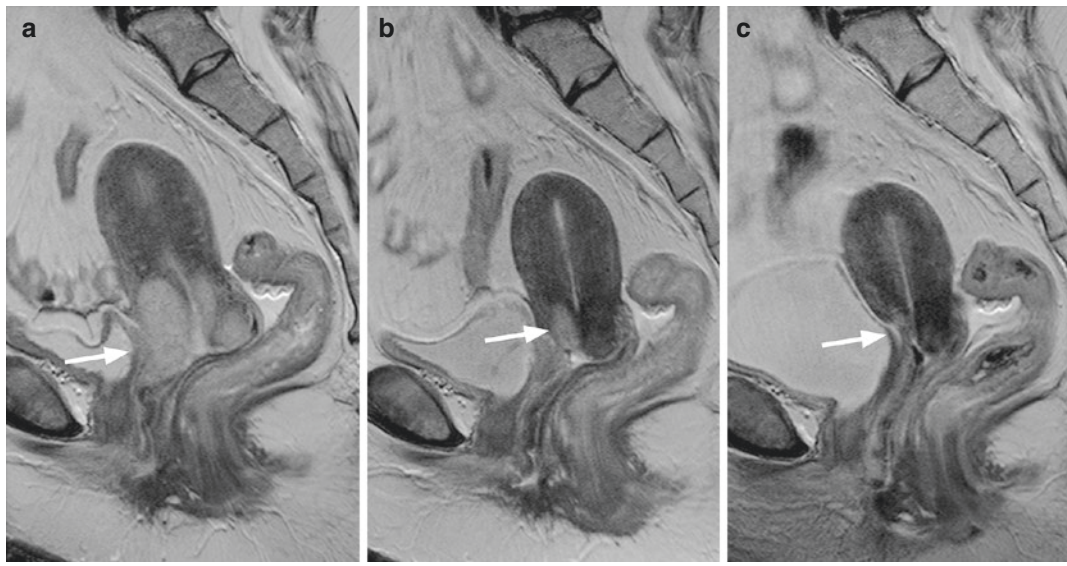

Fig. 43 Monitoring of radiotherapy. (**a**–**c**) T2w TSE images in sagittal orientation. (**a**) Cervical cancer (*arrow*) with infiltration of the urinary bladder. (**b**) Size reduction of the tumor (*arrow*) during radiotherapy. (**c**) No circumscribed tumor of the cervix is depicted 3 months after completion of irradiation (*arrow*)

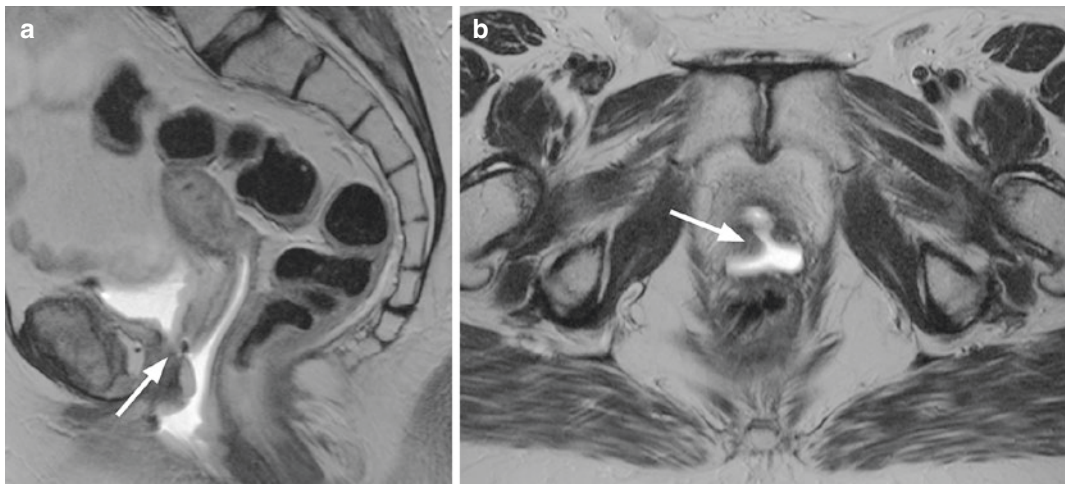

Fig. 44 Fistula after radiochemotherapy. (**a**, **b**) T2w TSE images in sagittal and transverse orientation. Following radiochemotherapy of advanced cervical cancer, a fistula depicted as a high-signal-intensity fluid-filled connection is seen between the vagina and urinary bladder (*arrows*). There is urine in the vagina

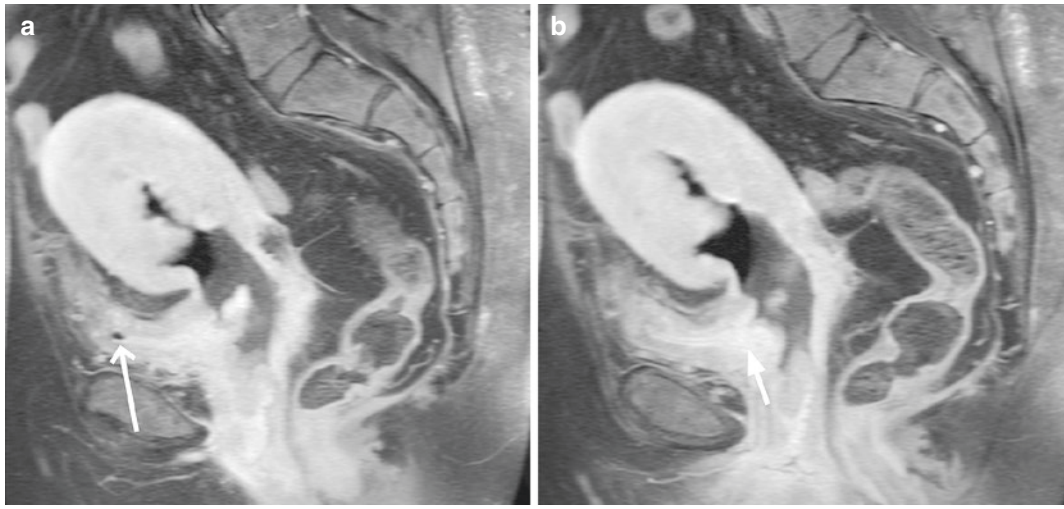

Fig. 45 Fistula after radiochemotherapy. (**a**, **b**) T2w TSE images in sagittal and transverse orientation. Following radiochemotherapy of advanced cervical cancer, a fistula depicted as a high-signal-intensity fluid-filled connection is seen between the vagina and urinary bladder (*arrow*). There is air in the bladder (*open arrow*)

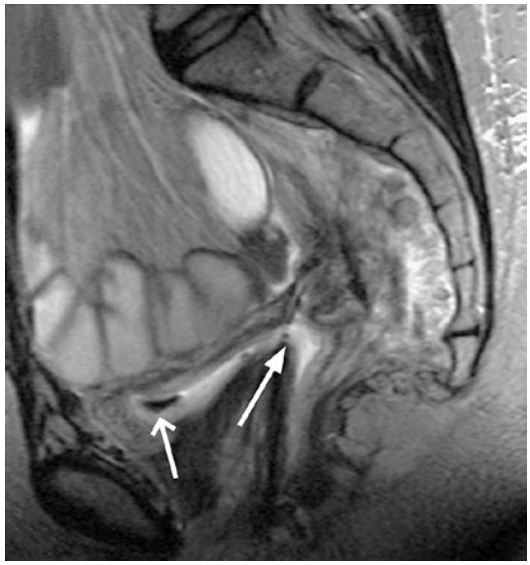

Fig. 46 Fistula after hysterectomy. A T2w TSE image in sagittal orientation. Following hysterectomy for cervical cancer, a fistula depicted as a high-signal-intensity fluid-filled connection is seen between the vagina and urinary bladder (*arrow*). There is air in the bladder (*open arrow*)

A complication after irradiation is the development of fistulas due to therapy-induced regression of invasive cervical cancer (Figs. 45, 46, and 47). Contrast-enhanced T1-weighted images identify a fistula as abnormal enhancement surrounding the low-signal-intensity fistular canal. A fistula from the uterus or vagina to the bladder is suggested when there is air in the bladder (Kim and Han 1997).

Postactinic radiogenic colitis is characterized by concentric edematous thickening of the intestinal wall with preservation of the layered structure and may be associated with additional edematous thickening and infiltration of the perirectal fat. Radiation-induced stricture of the ureter or insufficiency fracture of the sacral bone has become rare. The bone marrow of the pelvic bone in the irradiated field is regularly replaced with fat marrow, which is depicted on T1-weighted images with a high signal intensity.

In recent years, several authors have investigated the potentials of functional MRI including diffusion- and perfusion-weighted imaging in evaluating the therapeutic response and predicting the clinical outcome after radiation therapy alone or in combination with chemotherapy. DCE-MRI, that involves intravenous application of low-molecular-weight paramagnetic intravascular contrast agents, enables the noninvasive assessment of tumor perfusion and oxygenation, major factors in response of tumor cells

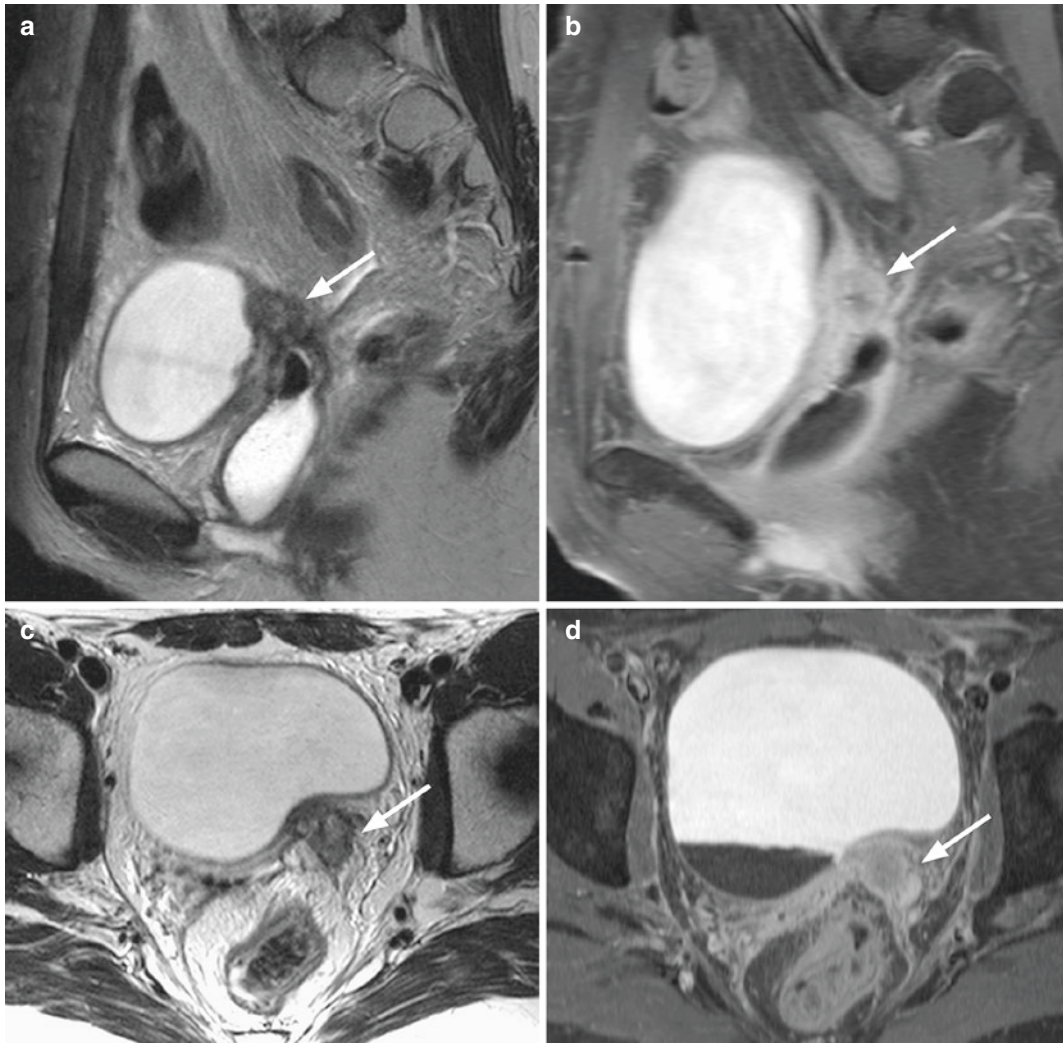

Fig. 47 Recurrent cervical cancer after hysterectomy. (**a**, **b**) T2w TSE images in sagittal and transverse orientation. (**c**, **d**) T1w TSE images in sagittal and transverse orientation 1 min after administration of Gd-DTPA. MRI after hysterectomy depicts a nodular lesion at the roof of the vagina with enhancement on the postcontrast images (*arrows*). Note the unusually low signal intensity of the lesion (*like a scar*); however, tumor recurrence is indicated by the strong contrast enhancement. Gel filling of the vagina

to radiation. Numerous studies published in the last years have demonstrated that pretreatment DCE parameters of high relative signal intensity or peak enhancement are associated with better response to treatment (Zahra et al. 2009; Mayr et al. 1996, 2010). Similarly, other groups were able to demonstrate that mid-treatment ADC may be a useful surrogate biomarker of treatment response (Harry et al. 2008) and even patient's survival (Somoye et al. 2012).

2.5.4 Recurrent Cervical Cancer

Cervical cancer tends to recur within 2 years after the initial diagnosis. Recurrence is defined as the demonstration of renewed local tumor growth, development of nodal metastases, or hematogenous distant metastases after a tumor-free interval of at least 6 months. About 30% of patients with invasive cervical carcinoma die because of recurrent disease. Some guidelines recommend follow-up examinations at 3-month

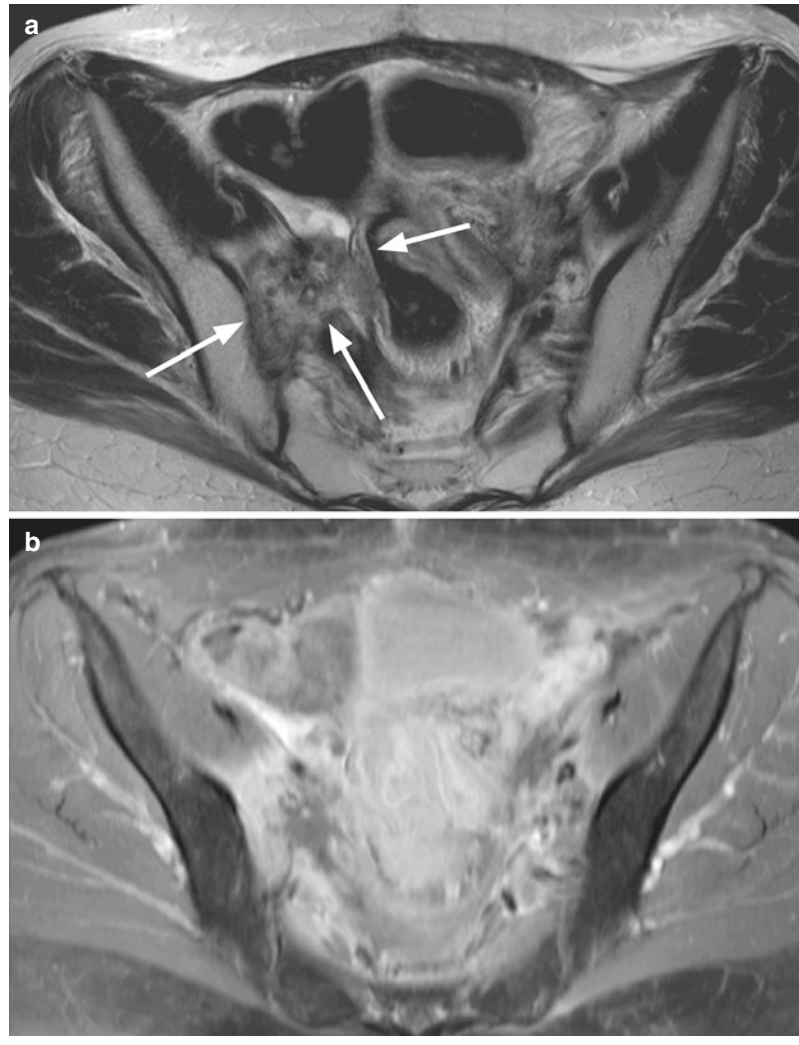

Fig. 48 Recurrent tumor of the pelvic sidewall after hysterectomy. (**a**) T2w TSE image in transverse orientation. At the right pelvic sidewall, a solid, heterogeneous mass (*arrows*) is depicted that infiltrates the pelvic wall and extends to the iliac bone. Tumor adhesion to the sigmoid colon. (**b**) T1w TSE image with FS transverse orientation 1 min after administration of Gd-DTPA. MRI depicts an enhancement on the postcontrast image and central necrosis

intervals during the first 3 years, every 6 months during the next 2 years, and once a year thereafter. A survival advantage from inclusion in structured follow-up has not been demonstrated. The routine follow-up tests are merely clinical and comprise history taking, physical, and vaginal examination, which may be supplemented by colposcopy and cytology, and a transvaginal ultrasound examination. More extensive tests are performed in patients with clinically suspected locoregional tumor recurrence. Recurrence is suggested by the findings of the gynecologic follow-up examination or if the patient reports difficulties passing urine or stools or other suspicious symptoms. Recurrent tumor of the pelvic

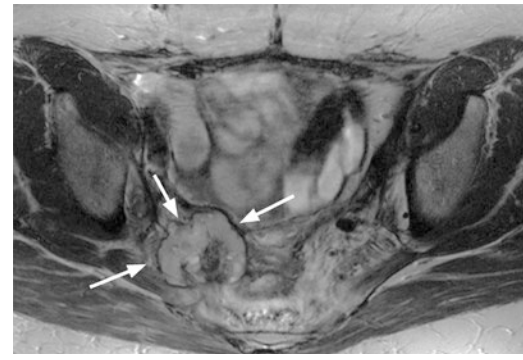

Fig. 49 Recurrent tumor of the pelvic sidewall after hysterectomy. T2w TSE image in sagittal orientation. A solid, heterogeneous mass with irregular margins (*arrows*) and infiltration of muscle is seen anterior to the sciatic foramen

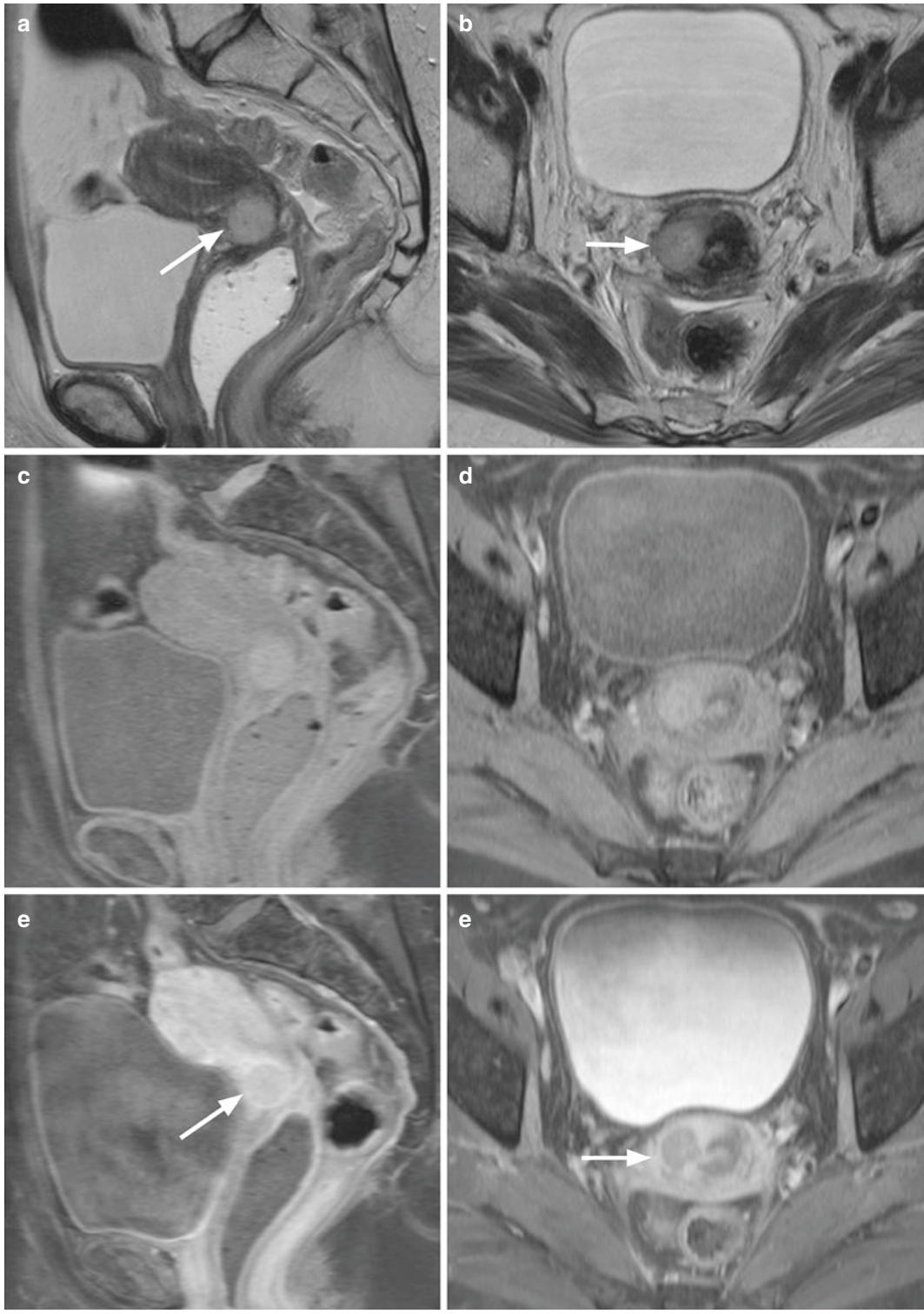

Fig. 50 Recurrent cervical cancer after radiochemotherapy. (**a**, **b**) T2w TSE images in sagittal and transverse orientation. Recurrent cervical cancer 6 months after primary radiochemotherapy. The high-signal-intensity mass (*arrows*) is located eccentrically on the right side of the cervix. Gel filling of the vagina. (**c**, **d**) T1w TSE images with FS in sagittal and transverse orientation showing recurrent cervical cancer with slightly higher signal intensity. (**e**, **f**) T1w TSE images with FS in sagittal and transverse orientation 1 min after administration of Gd-DTPA. MRI depicts a moderate enhancement on the postcontrast image (*arrows*)

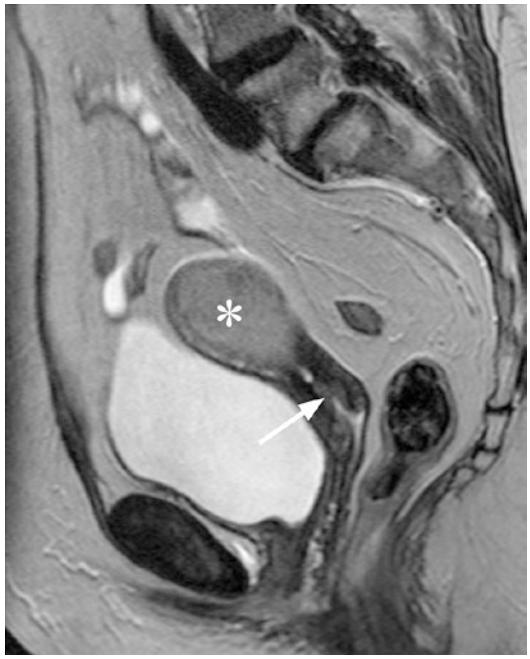

Fig. 51 Other tumors of the cervix. T2w TSE image in sagittal orientation. Cervical manifestation (*asterisk*) of endometrial cancer (*arrow*)

sidewall may manifest with pain due to nerve infiltration or leg edema due to obliteration of the lymphatics.

CT, MRI, and PET-CT are recognized techniques for the detection of recurrent cervical cancer. MRI is particularly accurate in detecting suspected local recurrence and for evaluation following radiation therapy. When the clinical symptoms suggest the presence of distant metastases either CT or PET-CT are preferable to MRI. For the assessment of lymph node metastases, PET-CT has a greater sensitivity and specificity than either MRI or CT.

Usually follow-up MRI is not indicated during the first 6 months after completion of primary therapy due to its limitations in differentiating recurrent tumor from acute peri- or postoperative changes (Hricak et al. 1993). As with primary staging, follow-up MRI should be performed by using sagittal and transverse T2-weighted sequences as well as a respiratory-gated T1-weighted abdominal PACE sequence and a T1-weighted pelvic sequence for lymph node staging. In contrast to pretreatment MRI, the follow-up examination should always comprise a contrast-enhanced T1-weighted sequence. These are always performed in combination with an unenhanced T1-weighted examination in identical orientations. Ideally, the contrast-enhanced images should allow differentiation of recurrent tumor, which shows early and pronounced enhancement, from scar tissue. If there is extension to the pelvic floor, this basic protocol can be supplemented by T2-weighted sequences in coronal orientation. If hydronephrosis is suspected, an additional coronal T2-weighted sequence or contrast-enhanced MR urography is indicated. Besides the standard anatomical sequences, the use of diffusion-weighted imaging (DWI) is becoming more and more common in both European and American centers. In a recently published study the addition of DWI to T2-weighted sequences considerably improved the accuracy of MRI (92.1% vs. 80%) in the detection of cervical cancer recurrence (Lucas et al. 2015).

Recurrent cervical cancer has a variable appearance at MRI. The tumor may have a nodular appearance with a blurred contour and extension into surrounding tissue, which may lead to fixation of bowel loops. The irregular contour is due to tumor extension and desmoplastic reactions. Alternatively, a recurrent tumor may show diffuse growth. In this case, the absence of a circumscribed mass makes the tumor especially difficult to distinguish from a postoperative scar. By clinical examination, both scar and recurrent tumor may appear indurated. Recurrent cancer can be differentiated from scar tissue and muscle by its higher signal intensity on T2-weighted images as well as earlier and more pronounced enhancement on dynamic contrast-enhanced T1-weighted images. Regressive tumor portions may be identified by lack of enhancement. In contrast, scar tissue resembles muscle, with a low signal intensity on T1- and T2-weighted images. Moreover, scars show only little and late enhancement if MRI is performed not earlier than 6 months after the end of therapy.

Despite the short examination time and absence of artifacts caused by bowel motion, CT has little use in differentiating post-therapeutic changes and recurrent tumor in the true pelvis.

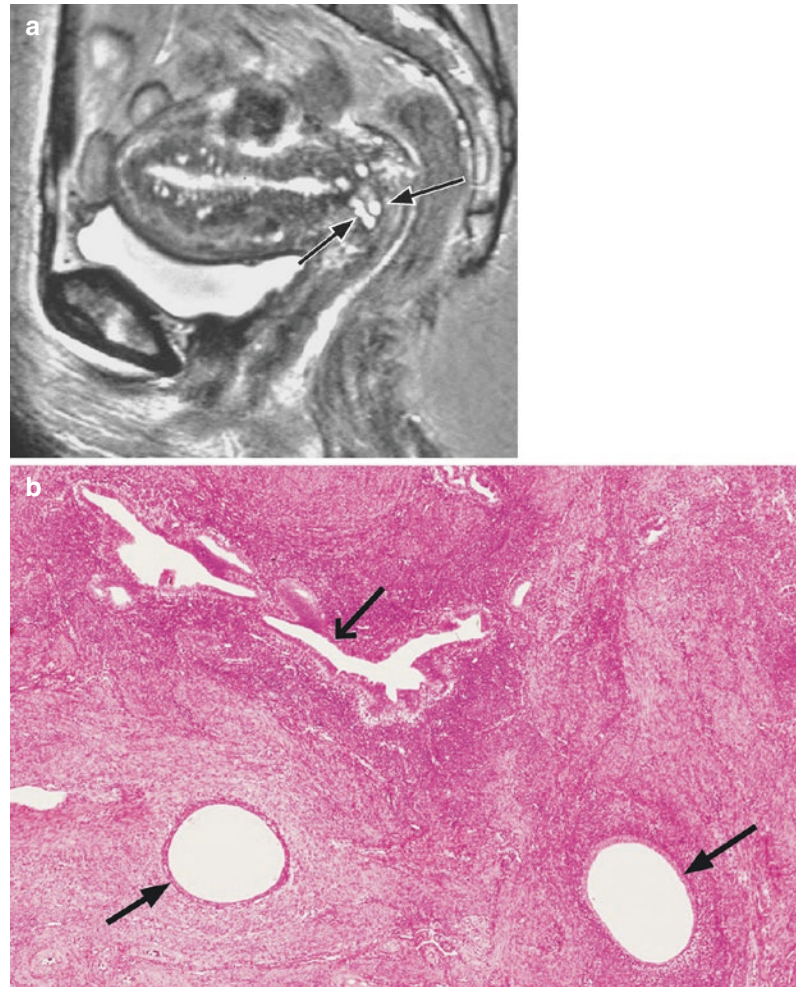

Fig. 52 Nabothian cysts. (**a**) T2w TSE image in sagittal orientation. Cystic lesions in the cervical stroma (*arrows*). (**b**) H&E-stained specimen of the cervix with intrastromal cystic lesions (*arrows*). Also seen are cervical glands (*open arrow*)

However, CT of the chest, abdomen, and pelvis after oral opacification and IV contrast medium administration can be used in the follow-up of cervical cancer to exclude distant metastases and postoperative complications.

Recurrent tumor after surgery is most frequently seen in the operative bed, primarily the vaginal stump, and at the resection margins, in particular the pelvic sidewalls. After radical hysterectomy, most tumors show supravaginal recurrence (20%) at the roof of the vaginal stump and in the rectovaginal space, typically between the bladder and the rectum. An occasional patient may develop fibrotic scar tissue at the roof of the vaginal stump, which is characterized by moderate to low signal intensity on T2-weighted and T1-weighted images. When recurrent tumor is identified, its relationship to the vaginal stump should be described and infiltration of the urinary bladder and rectum should be excluded (Figs. 10 and 48).

Posterior tumor growth leads to infiltration of the presacral space and sacral bone or of the perirectal space and rectum. Recurrent cervical cancer is associated with rectal infiltration in about 17% of cases. The most common site is the rectosigmoid junction. Laterally, recurrent tumor may extend to the pelvic sidewall. If the recurrent local tumor grows anteriorly along the peritoneal fold, there will be infiltration of the urinary bladder. Advanced recurrent cervical cancer may involve the remaining colon or the small intestine, is typically associated with adhesion of bowel loops, and may cause intestinal obstruction.

The second most common site of recurrence is the pelvic sidewall, which is the preferred site of nodal metastasis (Figs. 49 and 50). An important issue is their topographic relationship to the bony pelvis and the iliac vessels because of its implications for the surgical technique. Regarding the iliac vessels, infra- and peri-iliac metastases should be distinguished; regarding the bones, a distinction should be made between ischiopubic, acetabular, iliosacral, and sacrococcygeal metastases. Further progression may lead to destruction of the bony pelvis.

Pelvic tumor recurrence typically leads to external ureteral obstruction through encasement of the ureters and their orifices, which manifests as hydronephrosis. Follow-up MRI enables evaluation of both the etiology and the site of the obstruction.

Local recurrence after primary radiochemotherapy is characterized by the development of a new tumor in the cervix or infiltration of the vagina (Fig. 51). Alternatively, there may be recurrence in the parametria with lateral extension at the level of the cervix and vagina (Choi et al. 2000). A large recurrent tumor with a mass effect within the cervix may obstruct the internal os with development of hydrometra or pyometra. Alternatively, the cervix can be obstructed by radiation-induced stenoses. This is depicted by CT and MRI as a symmetrically enlarged uterine corpus containing nonenhancing fluid.

Patients with central pelvic tumor recurrence are operated on with curative intention if possible. Curative pelvic exenteration is more difficult when the pelvic wall is infiltrated. Hence, recurrent tumor of the pelvic wall is typically treated by radiochemotherapy, which can be performed with a curative dose in patients not having undergone irradiation before. Local control of recurrence in the pelvic wall is poorer and has a more unfavorable prognosis than central pelvic recurrence. Specific surgical procedures and possibly reduced radiotherapy are available for patients having been irradiated before. These aggressive measures are, however, associated with considerable side effects. Lymph node metastasis is typically treated by radiotherapy and hematogenous distant metastasis by chemotherapy.

2.6 Role of Other Diagnostic Modalities

2.6.1 Ultrasound

While ultrasonography has a role in endometrial cancer, it is of little use in detection and staging of cervical cancer. Ultrasonography does not allow reliable demonstration of parametrial infiltration. Direct imaging of cervical cancer in controlling tumor response to radiochemotherapy by 3D ultrasound is under evaluation. The sonographic evaluation of the pelvic and para-aortic lymph nodes is limited due to their location at the pelvic wall or retroperitoneally and due to overlying bowel gas (Mamsen et al. 1995). Transabdominal or transrectal ultrasound is routinely used in pretherapeutic staging, typically to exclude liver metastases and at follow-up, above all to exclude ureteral obstruction (Innocenti et al. 1992; Magee et al. 1991). Ultrasonography is limited by its dependence on the examiner and the equipment used and lacks adequate documentation and reproducibility of the findings.

2.6.2 PET/CT

In recent years, 18F-fluorodeoxyglucose (FDG) positron emission tomography—computed tomography (PET/CT) has gained acceptance in the initial evaluation of disease extent of patients with locally advanced cervical cancer, especially in the assessment of lymph node status and distant metastasis. Furthermore, FDG-PET/CT has been used for image-guided radiation therapy and for the detection of distal, extrapelvic recurrent tumor after therapy (Balleyguier et al. 2011; Herrera and Prior 2013).

2.7 Other Malignant Tumors of the Cervix

2.7.1 Metastasis

Most metastases to the cervix are from endometrial cancer (Fig. 52) (or by tumor infiltration per continuitatem), less commonly from other primary tumors of the ovaries, breast, or stomach. On imaging, it is virtually impossible to differentiate a metastasis from a primary carcinoma.

2.7.2 Malignant Melanoma

Between 1 and 3% of malignant melanomas in women occur in the genital tract, where they typically arise in the vaginal mucosa and infiltrate the uterine cervix. Primary cervical melanoma is rare. Melanomas of the female genital tract are characterized by high signal intensity on T1-weighted images and low signal on T2-weighted images. The degree of signal shortening on T1-weighted images varies with the melanin content. The signal is further altered by intralesional hemorrhage, which is quite common (Moon et al. 1993; Miyagi et al. 1997; Kristiansen et al. 1992).

2.7.3 Lymphoma

Malignant lymphoma of the cervix is typically due to secondary infiltration by advanced lymphoma from other sites. Primary manifestations in the uterus account for only 2% of all primary extranodal malignant lymphomas and typically affect the cervix. Cervical lymphoma is of low signal intensity on T1-weighted images and of high signal intensity on T2-weighted images and thus resembles cervical squamous cell carcinoma. In most cases, lymphoma can be distinguished from cervical carcinomas by its typically large size and the absence of infiltration of surrounding structures. Another distinctive feature is the avid and diffuse contrast enhancement of primary cervical lymphomas (Dang et al. 1991; Kim et al. 1997).

2.8 Benign Lesions of the Cervix

2.8.1 Nabothian Cyst

Nabothian cysts are retention cysts of the cervical glands that develop secondary to chronic cervicitis and are often discovered incidentally. Cervicitis is associated with epithelial proliferation and may lead to localized overgrowth and obstruction of glands. Nabothian cysts usually measure only a few millimeters but may grow in size to over 4 cm and then produce a mass effect. They have an intermediate to higher signal intensity on T1-weighted images that reflects the protein content of the cyst content. On T2-weighted images, they have high signal intensity and are depicted as round to oval lesions with smooth margins. Their differentiation from the rare adenoma malignum (well-differentiated cervical adenocarcinoma with cystic portions) may be difficult by MRI. The depiction of solid portions surrounding or separating the cysts suggests malignancy (Li et al. 1999).

2.8.2 Leiomyoma

Fewer than 10% of leiomyomas of the uterus affect the cervix. The typical clinical symptoms of cervical leiomyoma are infertility and complications during pregnancy. The lesions are characterized on T2-weighted images by low signal intensity, smooth contour, and a roundish shape (see Sect. 2.7.2).

2.8.3 Polyps

Cervical polyps are the most common benign lesions of the cervix. They typically occur in perimenopausal women and often cause bleeding between periods. They are usually pedicled and range in size from a few millimeters to 3 cm. Their pathogenesis is mutifactorial and includes metaplastic processes and inflammatory changes of the cervical glands. Cervical polyps are diagnosed by hysteroscopy. Imaging modalities typically depict them as masses of the endocervix.

2.8.4 Rare Benign Tumors

The rare benign tumors of the cervix comprise capillary or cavernous hemangioma, lymphangioma, papillary adenofibroma, adenomyoma, fibroadenoma, and mesonephric papilloma.

2.8.5 Cervicitis

Cervicitis is caused by the same pathogens as vaginitis. These include *Trichomonas vaginalis, Candida albicans,* and Herpes simplex virus. They invade the epithelium of the portio and cause inflammation of the ectocervix. In contrast, bacteria such as *Neisseria gonorrhoeae* and *Chlamydia trachomatis* affect the cervical glands and cause mucopurulent endocervicitis. Bacterial infection may manifest with vaginal discharge or dull pelvic pain. Occasionally, retention cysts may develop in the cervix and can be demonstrated by MRI but may be difficult to differenti-

ate from glandular hyperplasia or adenoma malignum based on their MRI appearance alone when clinical symptoms are absent (Mikami et al. 1999).

2.8.6 Endometriosis

Cervical endometriosis is rare and, when present, typically affects the portio or the endocervical canal. The solid tissue portions of an endometriosis lesion are of low signal intensity on T1-weighted and T2-weighted images and exhibit pronounced contrast enhancement. The lesions usually contain blood that often gives rise to the development of cystic portions with high signal intensity on T1-weighted images. Alternatively, endometriosis of the uterine corpus may protrude into the cervical canal as a polypoid mass that is covered by endometrial mucosa as the lesion arises from the junctional zone of the myometrium.

2.8.7 Ectopic Cervical Pregnancy

The number of cervical pregnancies is increasing as more women have abortions. Its rate is one per 1000–24,000 pregnancies. MRI depicts a cervical pregnancy as a cervical mass of heterogeneous signal intensity with a low-signal-intensity margin that may not surround the lesion on all sides (Werber et al. 1983). It is usually an exclusion diagnosis.

References

Akita A, Shinmoto H, Hayashi S, Akita H, Fujii T, Mikami S, Tanimoto A, Kuribayashi S (2011) Comparison of T2-weighted and contrast-enhanced T1-weighted MR imaging at 1.5 T for assessing the local extent of cervical carcinoma. Eur Radiol 21(9):1850–1857

Ascher SM, Takahama J, Jha RC (2001) Staging of gynecologic malignancies. Top Magn Reson Imaging 12(2):105–129

Badib AO, Kurohara SS, Webster JH, Pickren JW (1968) Metastasis to organs in carcinoma of the uterine cervix. Influence of treatment on incidence and distribution. Cancer 21:434–439

Balleyguier C, Sala E, Da Cunha T, Bergman A, Brkljacic B, Danza F, Forstner R, Hamm B, Kubik-Huch R, Lopez C, Manfredi R, McHugo J, Oleaga L, Togashi K, Kinkel K (2011) Staging of uterine cervical cancer with MRI: guidelines of the European Society of Urogenital Radiology. Eur Radiol 21(5):1102–1110

Bammer R (2003) Basic principles of diffusion-weighted imaging. Eur J Radiol 45(3):169–184

Benedet JL, Anderson GH (1996) Stage IA carcinoma of the cervix revisited. Obstet Gynecol 87:1052–1059

Bosch FX, Manos MM, Munoz N, Sherman M, Jansen AM, Peto J, Schiffman MH, Moreno V, Kurman R, Shah KV (1995) Prevalence of human papillomavirus in cervical cancer: a worldwide perspective. International biological study on cervical cancer (IBSCC) Study Group. J Natl Cancer Inst 87:796–802

Boss EA, Barentsz JO, Massuger LF, Boonstra H (2000) The role of MR imaging in invasive cervical carcinoma. Eur Radiol 10:256–270

Brenner H (2002) Long-term survival rates of cancer patients achieved by the end of the 20th century: a period analysis. Lancet 360:1131–1135

Brenner DE, Whitley NO, Prempree T, Villasanta U (1982) An evaluation of the computed tomographic scanner for the staging of carcinoma of the cervix. Cancer 50:2323–2232

Brodman M, Friedman F Jr, Dottino P, Janus C, Plaxe S, Cohen C (1990) A comparative study of computerized tomography, magnetic resonance imaging, and clinical staging for the detection of early cervix cancer. Gynecol Oncol 36:409–412

Brown JJ, Gutierrez ED, Lee JK (1992) MR appearance of the normal and abnormal vagina after hysterectomy. AJR Am J Roentgenol 158:95–99

Burghardt E, Baltzer J, Tulusan AH, Haas J (1992) Results of surgical treatment of 1028 cervical cancers studied with volumetry. Cancer 70:648–655

Cancer Research UK (2016) Cervical cancer incidence by age. Cancer Research UK, London

Castle PE, Maza M (2016) Prophylactic HPV vaccination: past, present, and future. Epidemiol Infect 144(3):449–468

Castle PE, Wacholder S, Lorincz AT, Scott DR, Sherman ME, Glass AG, Rush BB, Schussler JE, Schiffman M (2002) A prospective study of high-grade cervical neoplasia risk among human papillomavirus-infected women. J Natl Cancer Inst 94:1406–1414

Chen KT (1986) Female genital tract tumors in Peutz-Jeghers syndrome. Hum Pathol 17:858–861

Chen YB, Liao J, Xie R, Chen GL, Chen G (2011) Discrimination of metastatic from hyperplastic pelvic lymph nodes in patients with cervical cancer by diffusion-weighted magnetic resonance imaging. Abdom Imaging 36:102–109

Chen J, Zhang Y, Liang B, Yang Z (2010) The utility of diffusion-weighted MR imaging in cervical cancer. Eur J Radiol 74(3):e101–e106

Cheng X, Cai S, Li Z, Tang M, Xue M, Zang R (2004) The prognosis of women with stage IB1-IIB node-positive cervical carcinoma after radical surgery. World J Surg Oncol 2:47

Choi JI, Kim SH, Seong CK, Sim JS, Lee HJ, Do KH (2000) Recurrent uterine cervical carcinoma: spectrum of imaging findings. Korean J Radiol 1:198–207

Committee on Practice B-G (2002) ACOG practice bulletin. Diagnosis and treatment of cervical carcinomas, number 35, May 2002. Obstet Gynecol 99:855–867

Dang HT, Terk MR, Colletti PM, Schlaerth JB, Curtin JP (1991) Primary lymphoma of the cervix: MRI findings with gadolinium. Magn Reson Imaging 9:941–944

Dargent D, Martin X, Sacchetoni A, Mathevet P (2000) Laparoscopic vaginal radical trachelectomy: a treatment to preserve the fertility of cervical carcinoma patients. Cancer 88(8):1877–1882

Davidson SE, Symonds RP, Lamont D, Watson ER (1989) Does adenocarcinoma of uterine cervix have a worse prognosis than squamous carcinoma when treated by radiotherapy? Gynecol Oncol 33:23–26

deSouza NM, Dina R, McIndoe GA, Soutter WP (2006) Cervical cancer: value of an endovaginal coil magnetic resonance imaging technique in detecting small volume disease and assessing parametrial extension. Gynecol Oncol 102(1):80–85

Doi T, Yamashita Y, Yasunaga T, Fujiyoshi K, Tsunawaki A, Takahashi M, Katabuchi H, Tanaka N, Okamura H (1997) Adenoma malignum: MR imaging and pathologic study. Radiology 204:39–42

Downey K, Attygalle AD, Morgan VA, Giles SL, MacDonald A, Davis M, Ind TE, Shepherd JH, deSouza NM (2016) Comparison of optimised endovaginal vs external array coil T2-weighted and diffusion-weighted imaging techniques for detecting suspected early stage (IA/IB1) uterine cervical cancer. Eur Radiol 26(4):941–950

Drescher CW, Hopkins MP, Roberts JA (1989) Comparison of the pattern of metastatic spread of squamous cell cancer and adenocarcinoma of the uterine cervix. Gynecol Oncol 33:340–343

Ebner F, Tamussino K, Kressel HY (1994) Magnetic resonance imaging in cervical carcinoma: diagnosis, staging, and follow-up. Magn Reson Q 10:22–42

Eisenhauer EA, Therasse P, Bogaerts J, Schwartz LH, Sargent D, Ford R, Dancey J, Arbuck S, Gwyther S, Mooney M, Rubinstein L, Shankar L, Dodd L, Kaplan R, Lacombe D, Verweij J (2009) New response evaluation criteria in solid tumours: revised RECIST guideline (version 1.1). Eur J Cancer 5(2):228–247

Fagundes H, Perez CA, Grigsby PW, Lockett MA (1992) Distant metastases after irradiation alone in carcinoma of the uterine cervix. Int J Radiat Oncol Biol Phys 24:197–204

Ferlay J, Steliarova-Foucher E, Lortet-Tieulent J, Rosso S, Coebergh JW, Comber H, Forman D, Bray F (2013) Cancer incidence and mortality patterns in Europe: estimates for 40 countries in 2012. Eur J Cancer 49(6):1374–1403

Freeman SJ, Aly AM, Kataoka MY, Addley HC, Reinhold C, Sala E (2013) The revised FIGO staging system for uterine malignancies: implications for MR imaging. Radiographics 32(6):1805–1827

Friedlander M, Grogan M (2002) Guidelines for the treatment of recurrent and metastatic cervical cancer. Oncologist 7:342–347

Fu C, Bian D, Liu F, Feng X, Du W, Wang X (2012) The value of diffusion-weighted magnetic resonance imaging in assessing the response of locally advanced cervical cancer to neoadjuvant chemotherapy. Int J Gynecol Cancer 22(6):1037–1043

Fu YS, Reagan JW, Fu AS, Janiga KE (1982) Adenocarcinoma and mixed carcinoma of the uterine cervix. II. Prognostic value of nuclear DNA analysis. Cancer 49:2571–2577

Gustafsson L, Ponten J, Bergstrom R, Adami HO (1997) International incidence rates of invasive cervical cancer before cytological screening. Int J Cancer 71:159–165

Hamm B, Mahfouz AE, Taupitz M, Mitchell DG, Nelson R, Halpern E, Speidel A, Wolf KJ, Saini S (1997) Liver metastases: improved detection with dynamic gadolinium-enhanced MR imaging? Radiology 202:677–682

Hamm B et al (1999) MRT von Abdomen und Becken. Thieme, Berlin

Harkenrider MM, Alite F, Silva SR, Small W Jr (2015) Image-based brachytherapy for the treatment of cervical cancer. Int J Radiat Oncol Biol Phys 92(4):921–934

Harry VN, Semple SI, Gilbert FJ, Parkin DE (2008) Diffusion-weighted magnetic resonance imaging in the early detection of response to chemoradiation in cervical cancer. Gynecol Oncol 111(2):213–220

Hawighorst H, Knapstein PG, Knopp MV, Weikel W, Schaeffer U, Zuna I, Schonberg SO, Essig M, Hoffmann U, Brix G, van Kaick G (1998) Angiogenesis of cervix carcinoma. Contrast-enhanced dynamic MRI, histologic quantification of capillary density and lymphatic system infiltration. Radiologe 38:50–57

Hawighorst H, Knapstein PG, Weikel W, Knopp MV, Schaeffer U, Essig M, Brix G, Zuna I, Schonberg S, van Kaick G (1997) Invasive cervix carcinoma (pT2b-pT4a). Value of conventional and pharmacokinetic magnetic resonance tomography (MRI) in comparison with extensive cross sections and histopathologic findings. Radiologe 37:130–138

Heron CW, Husband JE, Williams MP, Dobbs HJ, Cosgrove DO (1988) The value of CT in the diagnosis of recurrent carcinoma of the cervix. Clin Radiol 39:496–450

Herrera FG, Prior JO (2013) The role of PET/CT in cervical cancer. Front Oncol 3:34

Hille A, Weiss E, Hess CF (2003) Therapeutic outcome and prognostic factors in the radiotherapy of recurrences of cervical carcinoma following surgery. Strahlenther Onkol 179:742–747

Holtz DO, Dunton C (2002) Traditional management of invasive cervical cancer. Obstet Gynecol Clin N Am 29:645–657

Hoogendam JP, Klerkx WM, de Kort GA, Bipat S, Zweemer RP, Sie-Go DM, Verheijen RH, Mali WP, Veldhuis WB (2010) The influence of the b-value combination on apparent diffusion coefficient based differentiation between malignant and benign tissue in cervical cancer. J Magn Reson Imaging 32(2):376–382

Hricak H, Gatsonis C, Chi DS, Amendola MA, Brandt K, Schwartz LH, Koelliker S, Siegelman ES, Brown JJ, RB MG, Iyer R, Vitellas KM, Snyder B, Long HJ, Fiorica JV, Mitchell DG, American College of

Radiology Imaging Network 6651; Gynecologic Oncology Group 183 (2005) Role of imaging in pretreatment evaluation of early invasive cervical cancer: results of the intergroup study American College of Radiology Imaging Network 6651-Gynecologic Oncology Group 183. J Clin Oncol 23:9329–9337

Hricak H, Hamm B, Semelka RC, Cann CE, Nauert T, Secaf E, Stern JL, Wolf KJ (1991) Carcinoma of the uterus: use of gadopentetate dimeglumine in MR imaging. Radiology 181:95–106

Hricak H, Lacey CG, Sandles LG, Chang YC, Winkler ML, Stern JL (1988) Invasive cervical carcinoma: comparison of MR imaging and surgical findings. Radiology 166:62363

Hricak H, Powell CB, Yu KK, Washington E, Subak LL, Stern JL, Cisternas MG, Arenson RL (1996) Invasive cervical carcinoma: role of MR imaging in pretreatment work-up-cost minimization and diagnostic efficacy analysis. Radiology 198:403–409

Hricak H, Swift PS, Campos Z, Quivey JM, Gildengorin V, Goranson H (1993) Irradiation of the cervix uteri: value of unenhanced and contrast-enhanced MR imaging. Radiology 189:381–388

Innocenti P, Pulli F, Savino L, Nicolucci A, Pandimiglio A, Menchi I, Massi G (1992) Staging of cervical cancer: reliability of transrectal US. Radiology 185:201–205

Kahn JA (2009) HPV vaccination for the prevention of cervical intraepithelial neoplasia. N Engl J Med 361(3):271–278

Kaminski PF, Norris HJ (1983) Minimal deviation carcinoma (adenoma malignum) of the cervix. Int J Gynecol Pathol 2:141–152

Kasales CJ, Langer JE, Arger PH (1995) Pelvic pathology after hysterectomy. A pictorial essay. Clin Imaging 19:210–217

Kim SK, Choi HJ, Park SY, Lee HY, Seo SS, Yoo CW (2009) Additional value of MR/PET fusion compared with PET/CT in the detection of lymph node metastases in cervical cancer patients. Eur J Cancer 45(12):2103–2109

Kim SH, Han MC (1997) Invasion of the urinary bladder by uterine cervical carcinoma: evaluation with MR imaging. AJR Am J Roentgenol 168:393–397

Kim SH, Kim SC, Choi BI, Han MC (1994) Uterine cervical carcinoma: evaluation of pelvic lymph node metastasis with MR imaging. Radiology 190:807–811

Kim JK, Kim KA, Park BW, Kim N, Cho KS (2008) Feasibility of diffusion-weighted imaging in the differentiation of metastatic from nonmetastatic lymph nodes: early experience. J Magn Reson Imaging 28(3):714–719

Kim YS, Koh BH, Cho OK, Rhim HC (1997) MR imaging of primary uterine lymphoma. Abdom Imaging 22:441–444

Kitajima K, Yamasaki E, Kaji Y, Murakami K, Sugimura K (2012) Comparison of DWI and PET/CT in evaluation of lymph node metastasis in uterine cancer. World J Radiol 4(5):207–214

Klerkx WM, Bax L, Veldhuis WB, Heintz AP, Mali WP, Peeters PH, Moons KG (2010) Detection of lymph node metastases by gadolinium-enhanced magnetic resonance imaging: systematic review and meta-analysis. J Natl Cancer Inst 102(4):244–253

Koch CA, Azumi N, Furlong MA, Jha RC, Kehoe TE, Trowbridge CH, O'Dorisio TM, Chrousos GP, Clement SC (1999) Carcinoid syndrome caused by an atypical carcinoid of the uterine cervix. J Clin Endocrinol Metab 84:4209–4213

Kosary CL (2007) Cancer of the uterine cervix. In: Ries LAG, Young JL, Keel GE, Eisner MP, Lin YD, Horner M-J (eds) SEER Survival Monograph: Cancer Survival Among Adults: U.S. SEER Program, 1988-2001, Patient and Tumor Characteristics. National Cancer Institute, SEER Program, NIH Pub. No. 07-6,215, Bethesda, MD

Kristiansen SB, Anderson R, Cohen DM (1992) Primary malignant melanoma of the cervix and review of the literature. Gynecol Oncol 47:398–403

Kupets R, Covens A (2001) Is the International Federation of Gynecology and Obstetrics staging system for cervical carcinoma able to predict survival in patients with cervical carcinoma?: an assessment of clinimetric properties. Cancer 92(4):796–804

Lagasse LD, Creasman WT, Shingleton HM, Ford JH, Blessing JA (1980) Results and complications of operative staging in cervical cancer: experience of the Gynecologic Oncology Group. Gynecol Oncol 9:90–98

LaPolla JP, Schlaerth JB, Gaddis O, Morrow CP (1986) The influence of surgical staging on the evaluation and treatment of patients with cervical carcinoma. Gynecol Oncol 24:194–206

Lea JS, Sheets EE, Wenham RM, Duska LR, Coleman RL, Miller DS, Schorge JO (2002) Stage IIB-IVB cervical adenocarcinoma: prognostic factors and survival. Gynecol Oncol 84:115–119

Lemke AJ, Niehues SM, Amthauer H, Rohlfing T, Hosten N, Felix R (2004) Clinical use of digital retrospective image fusion of CT, MRI, FDG-PET and SPECT – fields of indications and results. Rofo 176:1811–1818

Li H, Sugimura K, Okizuka H, Yoshida M, Maruyama R, Takahashi K, Miyazaki K (1999) Markedly high signal intensity lesions in the uterine cervix on T2-weighted imaging: differentiation between mucin-producing carcinomas and nabothian cysts. Radiat Med 17:137–143

Lin G, Ho KC, Wang JJ, Ng KK, Wai YY, Chen YT, Chang CJ, Ng SH, Lai CH, Yen TC (2008) Detection of lymph node metastasis in cervical and uterine cancers by diffusion-weighted magnetic resonance imaging at 3T. J Magn Reson Imaging 28(1):128–135

Liu Y, Liu H, Bai X, Ye Z, Sun H, Bai R, Wang D (2011) Differentiation of metastatic from non-metastatic lymph nodes in patients with uterine cervical cancer using diffusion-weighted imaging. Gynecol Oncol 122:19–24

Liu Y, Ye Z, Sun H, Bai R (2013) Grading of uterine cervical cancer by using the ADC difference value and its correlation with microvascular density and vascular endothelial growth factor. Eur Radiol 23(3): 757–765

Liu Y, Ye Z, Sun H, Bai R (2015) Clinical application of diffusion-weighted magnetic resonance imaging in uterine cervical cancer. Int J Gynecol Cancer 25(6):1073–1078

Lopes Dias J, Cunha TM, Gomes FV, Callé C, Félix A (2015) Neuroendocrine tumours of the female genital tract: a case-based imaging review with pathological correlation. Insights Imaging 6:43–52

Lorincz AT, Castle PE, Sherman ME, Scott DR, Glass AG, Wacholder S, Rush BB, Gravitt PE, Schussler JE, Schiffman M (2002) Viral load of human papillomavirus and risk of CIN3 or cervical cancer. Lancet 360:228–229

Low RN, Barone RM, Lacey C, Sigeti JS, Alzate GD, Sebre-chts CP (1997) Peritoneal tumor: MR imaging with dilute oral barium and intravenous gadolinium-containing contrast agents compared with unenhanced MR imaging and CT. Radiology 204:513–520

Lucas R, Lopes Dias J, Cunha TM (2015) Added value of diffusion-weighted MRI in detection of cervical cancer recurrence: comparison with morphologic and dynamic contrast-enhanced MRI sequences. Diagn Interv Radiol 21(5):368–375

Magee BJ, Logue JP, Swindell R, McHugh D (1991) Tumour size as a prognostic factor in carcinoma of the cervix: assessment by transrectal ultrasound. Br J Radiol 64:812–815

Mamsen A, Ledertoug S, Horlyck A, Knudsen HJ, Rasmussen KL, Nyland MH, Jakobsen A (1995) The possible role of ultrasound in early cervical cancer. Gynecol Oncol 56:187–190

Marchiole P, Buenerd A, Scoazec JY, Dargent D, Mathevet P (2004) Sentinel lymph node biopsy is not accurate in predicting lymph node status for patients with cervical carcinoma. Cancer 100:2154–2159

Martinez-Palones JM, Gil-Moreno A, Perez-Benavente MA, Roca I, Xercavins J (2004) Intraoperative sentinel node identification in early stage cervical cancer using a combination of radiolabeled albumin injection and isosulfan blue dye injection. Gynecol Oncol 92:845–850

Mayr NA, Wang JZ, Zhang D, Grecula JC, Lo SS, Jaroura D (2010) Longitudinal changes in tumor perfusion pattern during the radiation therapy course and its clinical impact in cervical cancer. Int J Radiat Oncol Biol Phys 77(2):502–508

Mayr NA, Yuh WT, Magnotta VA, Ehrhardt JC, Wheeler JA, Sorosky JI (1996) Tumor perfusion studies using fast magnetic resonance imaging technique in advanced cervical cancer: a new noninvasive predictive assay. Int J Radiat Oncol Biol Phys 36(3): 623–633

Metcalf KS, Johnson N, Calvert S, Peel KR (2000) Site specific lymph node metastasis in carcinoma of the cervix: is there a sentinel node? Int J Gynecol Cancer 10:411–416

Mikami Y, Hata S, Fujiwara K, Imajo Y, Kohno I, Manabe T (1999) Florid endocervical glandular hyperplasia with intestinal and pyloric gland metaplasia: worrisome benign mimic of "adenoma malignum". Gynecol Oncol 74:504–511

Mitchell DG, Snyder B, Coakley F, Reinhold C, Thomas G, Amendola M, Schwartz LH, Woodward P, Pannu H, Hricak H (2006) Early invasive cervical cancer: tumor delineation by magnetic resonance imaging, computed tomography, and clinical examination, verified by pathologic results, in the ACRIN 6651/GOG 183 Intergroup Study. J Clin Oncol 24(36):5687–5694

Miyagi Y, Yamada S, Yamamoto J, Kawanishi K, Yoshinouchi M, Kodama J, Kamimura S, Takamoto N, Kudo T, Tagu-chi K (1997) Malignant melanoma of the uterine cervix: a case report. J Obstet Gynaecol Res 23:511–519

Moon WK, Kim SH, Han MC (1993) MR findings of malignant melanoma of the vagina. Clin Radiol 48:326–328

Munoz N, Franceschi S, Bosetti C, Moreno V, Herrero R, Smith JS, Shah KV, Meijer CJ, Bosch FX (2002) Role of parity and human papillomavirus in cervical cancer: the IARC multicentric case-control study. Lancet 359:1093–1101

Nicolas CG et al (2005) Radiologic-pathologic correlations. Springer, Berlin

Nicolet V, Carignan L, Bourdon F, Prosmanne O (2000) MR imaging of cervical carcinoma: a practical staging approach. Radiographics 20(6):1539–1549

Okamoto Y, Tanaka YO, Nishida M, Tsunoda H, Yoshikawa H, Itai Y (2003) MR imaging of the uterine cervix: imaging-pathologic correlation. Radiographics 23(2):425–445

Outwater EK, Siegelman ES, Wilson KM, Mitchell DG (1996) Benign and malignant gynecologic disease: clinical importance of fluid and peritoneal enhancement in the pelvis at MR imaging. Radiology 200:483–488

Pecorelli S, Odicino F (2003) Cervical cancer staging. Cancer J 9(5):390–394

Pecorelli S, Zigliani L, Odicino F (2009) Revised FIGO staging for carcinoma of the cervix. Int J Gynaecol Obstet 105(2):107–108

Peppercorn PD, Jeyarajah AR, Woolas R, Shepherd JH, Oram DH, Jacobs IJ, Armstrong P, Lowe D, Reznek RH (1999) Role of MR imaging in the selection of patients with early cervical carcinoma for fertility-preserving surgery: initial experience. Radiology 212:395–399

Perez CA, Camel HM, Kuske RR, Kao MS, Galakatos A, Hederman MA, Powers WE (1986) Radiation therapy alone in the treatment of carcinoma of the uterine cervix: a 20-year experience. Gynecol Oncol 23: 127–140

Perez CA, Grigsby PW, Camel HM, Galakatos AE, Mutch D, Lockett MA (1995) Irradiation alone or combined with surgery in stage IB, IIA, and IIB carcinoma of uterine cervix: update of a nonrandomized comparison. Int J Radiat Oncol Biol Phys 31:703–716

Piver MS, Rutledge F, Smith JP (1974) Five classes of extended hysterectomy for women with cervical cancer. Obstet Gynecol 44:265–272

Plaxe SC, Saltzstein SL (1999) Estimation of the duration of the preclinical phase of cervical adenocarcinoma

suggests that there is ample opportunity for screening. Gynecol Oncol 75:55–56

Postema S, Pattynama PM, Broker S, van der Geest RJ, van Rijswijk CS, Baptist Trimbos J (1998) Fast dynamic contrast-enhanced colour-coded MRI in uterine cervix carcinoma: useful for tumour staging? Clin Radiol 53:729–734

Postema S, Pattynama PM, van Rijswijk CS (1999) Trimbos JB (1999) Cervical carcinoma: can dynamic contrast-enhanced MR imaging help predict tumor aggressiveness? Radiology 210:217–220

Preidler KW, Tamussino K, Szolar DM, Ranner G, Ebner F (1996) Staging of cervical carcinomas. Comparison of body-coil magnetic resonance imaging and endorectal surface coil magnetic resonance imaging with histopathologic correlation. Investig Radiol 31:458–462

Qin Y, Peng Z, Lou J, Liu H, Deng F, Zheng Y (2009) Discrepancies between clinical staging and pathological findings of operable cervical carcinoma with stage IB-IIB: a retrospective analysis of 818 patients. Aust N Z J Obstet Gynaecol 49(5):542–544

Reinhardt MJ, Ehritt-Braun C, Vogelgesang D, Ihling C, Hogerle S, Mix M, Moser E, Krause TM (2001) Metastatic lymph nodes in patients with cervical cancer: detection with MR imaging and FDG PET. Radiology 218:776–782

Richart RM (1973) Cervical intraepithelial neoplasia. Pathol Annu 8:301–328

Rockall AG, Ghosh S, Alexander-Sefre F, Babar S, Younis MT, Naz S, Jacobs IJ, Reznek RH (2006) Can MRI rule out bladder and rectal invasion in cervical cancer to help select patients for limited EUA? Gynecol Oncol 01(2):244–249

Rohen JW (1999) Topographische Anatomie. Schattauer, Stuttgart

Sahdev A, Jones J, Shepherd JH, Reznek RH (2005) MR imaging appearances of the female pelvis after trachelectomy. Radiographics 25:41–52

Sahdev A, Sohaib SA, Wenaden AE, Shepherd JH, Reznek RH (2007) The performance of magnetic resonance imaging in early cervical carcinoma: a long-term experience. Int J Gynecol Cancer 17(3):629–636

Sala E, Rockall AG, Freeman SJ, Mitchell DG, Reinhold C (2013) The added role of MR imaging in treatment stratification of patients with gynecologic malignancies: what the radiologist needs to know. Radiology 266(3):717–740

Sala E, Wakely S, Senior E, Lomas D (2007) MRI of malignant neoplasms of the uterine corpus and cervix. AJR Am J Roentgenol 188(6):1577–1587

Sant M, Capocaccia R, Coleman MP, Berrino F, Gatta G, Micheli A, Verdecchia A, Faivre J, Hakulinen T, Coebergh JW, Martinez-Garcia C, Forman D, Zappone A (2001) Cancer survival increases in Europe, but international differences remain wide. Eur J Cancer 37:1659–1667

Scheidler J, Heuck AF (2002) Imaging of cancer of the cervix. Radiol Clin N Am 40(3):577–590

Scheidler J, Hricak H, Yu KK, Subak L, Segal MR (1997) Radiological evaluation of lymph node metastases in patients with cervical cancer. A meta-analysis. JAMA 278:1096–1101

Schiffman M, Castle PE, Jeronimo J, Rodriguez AC, Wacholder S (2007) Human papillomavirus and cervical cancer. Lancet 370(9590):890–907

Schmidt-Matthiesen H, Wallwiener D (2005) Gynäkologie und Geburtshilfe. Schattauer, Stuttgart

Sedlis A, Bundy BN, Rotman MZ, Lentz SS, Muderspach LI, Zaino RJ (1999) A randomized trial of pelvic radiation therapy versus no further therapy in selected patients with stage IB carcinoma of the cervix after radical hysterectomy and pelvic lymphadenectomy: a Gynecologic Oncology Group Study. Gynecol Oncol 73:177–183

Shen G, Zhou H, Jia Z, Deng H (2015) Diagnostic performance of diffusion-weighted MRI for detection of pelvic metastatic lymph nodes in patients with cervical cancer: a systematic review and meta-analysis. Br J Radiol 88:20150063

Sheridan E, Lorigan PC, Goepel J, Radstone DJ, Coleman RE (1996) Small cell carcinoma of the cervix. Clin Oncol (R Coll Radiol) 8:102–105

Shiraiwa M, Joja I, Asakawa T, Okuno K, Shibutani O, Akamatsu N, Kudo T, Hiraki Y (1999) Cervical carcinoma: efficacy of thin-section oblique axial T2-weighted images for evaluating parametrial invasion. Abdom Imaging 24:514–551

Siegel RL, Miller KD, Jemal A (2015) Cancer statistics, 2015. CA Cancer J Clin 65(1):5–29

Smith JS, Herrero R, Bosetti C, Munoz N, Bosch FX, Eluf-Neto J, Castellsague X, Meijer CJ, Van den Brule AJ, Franceschi S, Ashley R (2002a) Herpes simplex virus-2 as a human papillomavirus cofactor in the etiology of invasive cervical cancer. J Natl Cancer Inst 94:1604–1613

Smith RA, Manassaram-Baptiste D, Brooks D, Doroshenk M, Fedewa S, Saslow D, Brawley OW, Wender R (2015) Cancer screening in the United States, 2015: a review of current American cancer society guidelines and current issues in cancer screening. CA Cancer J Clin 65(1):30–54

Smith JS, Munoz N, Herrero R, Eluf-Neto J, Ngelangel C, Franceschi S, Bosch FX, Walboomers JM, Peeling RW (2002b) Evidence for Chlamydia trachomatis as a human papillomavirus cofactor in the etiology of invasive cervical cancer in Brazil and the Philippines. J Infect Dis 185:324–331

Somoye G, Harry V, Semple S, Plataniotis G, Scott N, Gilbert FJ (2012) Early diffusion weighted magnetic resonance imaging can predict survival in women with locally advanced cancer of the cervix treated with combined chemo-radiation. Eur Radiol 22(11):2319–2327

Stehman FB, Bundy BN, DiSaia PJ, Keys HM, Larson JE, Fowler WC (1991) Carcinoma of the cervix treated with radiation therapy. I. A multi-variate analysis of prognostic variables in the Gynecologic Oncology Group. Cancer 67:2776–2785

Tewari KS, Sill MW, Long HJ 3rd, Penson RT, Huang H, Ramondetta LM, Landrum LM, Oaknin A, Reid TJ, Leitao MM, Michael HE, Monk BJ (2014) Improved survival with bevacizumab in advanced cervical cancer. N Engl J Med 370(8):734–743

Thoeny HC, Forstner R, De Keyzer F (2012) Genitourinary applications of diffusion-weighted MR imaging in the pelvis. Radiology 263(2):326–342

Thomeer MG, Gerestein C, Spronk S, van Doorn HC, van der Ham E, Hunink MG (2013) Clinical examination versus magnetic resonance imaging in the pretreatment staging of cervical carcinoma: systematic review and meta-analysis. Eur Radiol 23(7):2005–2018

Togashi K, Nishimura K, Sagoh T, Minami S, Noma S, Fujisawa I, Nakano Y, Konishi J, Ozasa H, Konishi I et al (1989) Carcinoma of the cervix: staging with MR imaging. Radiology 171:245–251

Tsili AC, Tsangou V, Koliopoulos G, Stefos T, Argyropoulou MI (2013) Early-stage cervical carcinoma: the role of multidetector CT in correlation with histopathological findings. J Obstet Gynaecol 33:882–887

Ueda G, Yamasaki M (1992) Neuroendocrine carcinoma of the uterus. Curr Top Pathol 85:309–335

Villasanta U, Whitley NO, Haney PJ, Brenner D (1983) Computed tomography in invasive carcinoma of the cervix: an appraisal. Obstet Gynecol 62:218–224

Vizcaino AP, Moreno V, Bosch FX, Munoz N, Barros-Dios XM, Borras J, Parkin DM (2000) International trends in incidence of cervical cancer: II. Squamous-cell carcinoma. Int J Cancer 86:429–435

Walboomers JM, Jacobs MV, Manos MM, Bosch FX, Kummer JA, Shah KV, Snijders PJ, Peto J, Meijer CJ, Munoz N (1999) Human papillomavirus is a necessary cause of invasive cervical cancer worldwide. J Pathol 189:12–19

Werber J, Prasadarao PR, Harris VJ (1983) Cervical pregnancy diagnosed by ultrasound. Radiology 149:279–280

Wiebe E, Denny L, Thomas G (2012) Cancer of the cervix uteri. Int J Gynaecol Obstet 119(Suppl 2):S100

Wittekind C, Klimpfinger M, Sobin LH (2005) TNM-Atlas. Springer, Berlin

Womack C, Warren AY (1998) The cervical screening muddle. Lancet 351:1129

Yamada T, Manos MM, Peto J, Greer CE, Munoz N, Bosch FX, Wheeler CM (1997) Human papillomavirus type 16 sequence variation in cervical cancers: a worldwide perspective. J Virol 71:2463–2472

Zahra MA, Tan LT, Priest AN, Graves MJ, Arends M, Crawford RA (2009) Semiquantitative and quantitative dynamic contrast-enhanced magnetic resonance imaging measurements predict radiation response in cervix cancer. Int J Radiat Oncol Biol Phys 74(3):766–773

Zand KR, Reinhold C, Abe H, Maheshwari S, Mohamed A, Upegui D (2007) Magnetic resonance imaging of the cervix. Cancer Imaging 7:69–76

Endometrial Cancer

Mariana Horta and Teresa Margarida Cunha

Contents

Abstract

Endometrial cancer is the most common gynecological malignancy in well-developed countries. Biologically and clinicopathologically, endometrial carcinomas are divided into two types: type 1 or estrogen-dependent carcinomas and type 2 or estrogen-independent carcinomas. Type 1 cancers correspond mainly to endometrioid carcinomas and account for approximately 90 % of endometrial cancers, whereas type 2 cancers correspond to the majority of the other histopathological subtypes.

The vast majority of endometrial cancers present as abnormal vaginal bleedings in postmenopausal women. Therefore, 75 % of cancers are diagnosed at an early stage, which makes the overall prognosis favorable.

The first diagnostic step to evaluate women with an abnormal vaginal bleeding is the measurement of the endometrial thickness with transvaginal ultrasound. If endometrial thickening or heterogeneity is confirmed, a biopsy should be performed to establish a definite histopathological diagnosis.

Magnetic resonance imaging is not considered in the International Federation of Gynaecology and Obstetrics staging system. Nonetheless it plays a relevant role in the preoperative staging of

The original version of this chapter was revised: The affiliation details of the authors were corrected. The erratum to this chapter is available at DOI: 10.1007/174_2017_91.

M. Horta (✉)
Serviço de Radiologia, Instituto Português de Oncologia de Lisboa Francisco Gentil, Rua Prof. Lima Basto, 1099-023 Lisboa, Portugal
e-mail: mariana.sf.horta@gmail.com

T.M. Cunha, M.D.
Serviço de Radiologia, Instituto Português de Oncologia de Lisboa Francisco Gentil, Rua Prof. Lima Basto, 1099-023 Lisboa, Portugal
e-mail: tmargarida@gmail.com

Med Radiol Diagn Imaging (2016)
DOI 10.1007/174_2016_84, © Springer International Publishing Switzerland
Published Online: 17 December 2016

endometrial carcinoma, helping to define the best therapeutic management. Moreover, it is important in the diagnosis of treatment complications, in the surveillance of therapy response, and in the assessment of recurrent disease.

1 Endometrial Cancer: Background

1.1 Epidemiology

Endometrial cancer is the fifth most common malignancy in females worldwide, after breast, colorectal, cervical, and lung cancers, accounting for 4.8 % of all cancers in women (Ferlay et al. 2013).

In contrast to cervical cancer, endometrioid cancer peak incidence rates occur in well-developed countries (Europe and North America), where it is the most common gynecological malignancy (Ferlay et al. 2013). This is probably due to lifestyle factors, in particular obesity, which has been linked to about 50 % endometrial cancers in these countries (Epstein and Blomqvist 2014; Calle and Kaaks 2004). The increase in life expectancy is also responsible for its rising (Koh et al. 2014).

Endometrial cancer is more likely to occur in postmenopausal women in their sixth and seventh decades, with cases only rarely reported under the age of 35 in the United Kingdom (Patel et al. 2010; Cancer Incidence Statistics 2015).

Despite its relatively high prevalence, approximately 82 % of endometrial cancers are diagnosed at an early stage, which makes its overall prognosis favorable (Cancer Incidence Statistics 2015). Its worldwide mortality rate is low and it has been estimated at 2.2 % (Ferlay et al. 2013).

1.2 Pathology and Risk Factors

The World Health Organization (WHO) classification of uterine corpus tumors was revised in 2014 (Kurman et al. 2014). Endometrial carcinomas (also known as adenocarcinoma of the endometrium) are classified under the "Epithelial Tumours and Precursors" group and clinicopathologically divided into the following types: endometrioid carcinoma; mucinous carcinoma; serous endometrial intraepithelial carcinoma; serous carcinoma; clear-cell carcinoma; neuroendocrine tumors; mixed cell adenocarcinoma; undifferentiated carcinoma; and dedifferentiated carcinoma (Table 1) (Kurman et al. 2014).

Table 1 World Health Organization classification of epithelial tumors and precursors of the uterine corpus

Precursors
Hyperplasia without atypia
Atypical hyperplasia/endometrioid intraepithelial neoplasia
Endometrial cancer
Endometrioid carcinoma
Squamous differentiation
Villoglandular
Secretory
Mucinous carcinoma
Serous endometrial intraepithelial carcinoma
Serous carcinoma
Clear-cell carcinoma
Neuroendocrine tumors
Low-grade neuroendocrine tumor (carcinoid tumor)
High-grade neuroendocrine carcinoma (small cell neuroendocrine carcinoma; large cell neuroendocrine carcinoma)
Mixed cell adenocarcinoma
Undifferentiated carcinoma
Dedifferentiated carcinoma

Adapted from Kurman et al. (2014)

Although carcinosarcoma belongs to the "Mixed Epithelial and Mesenchymal Tumours" group of the uterine corpus, it should be staged as an endometrial carcinoma (Kurman et al. 2014).

Biologically and clinicopathologically, endometrial carcinomas are divided into two types: type 1 or estrogen-dependent carcinomas and type 2 or estrogen-independent carcinomas (Table 2).

Type 1 correspond mainly to endometrioid carcinomas and accounts for approximately 90 % of endometrial cancers, whereas type 2 cancers correspond to the majority of the other histopathological subtypes (Epstein and Blomqvist 2014).

Type 1 endometrial cancers are associated with prolonged unopposed estrogen exposure, therefore with the following risk factors: estrogen replacement therapy; tamoxifen therapy for breast cancer; polycystic ovarian syndrome; estrogen producing ovarian tumors; obesity (conversion of androgen to estrone in adipose tissue); diabetes; early menarche and late menopause and

Table 2 Types of endometrial cancer

Type 1 endometrial cancer
Endometrioid carcinoma (90 %)
Mucinous carcinoma (rarely)
Commonly associated with endometrial hyperplasia
Estrogen-dependent carcinomas
Risk factors:
Estrogen replacement therapy
Tamoxifen therapy for breast cancer
Polycystic ovarian syndrome
Estrogen producing ovarian tumors
Obesity (conversion of androgen to estrone in adipose tissue)
Diabetes
Early menarche and late menopause
Nulliparity
Usually diagnosed at an early stage
Good prognosis
Type 2 endometrial cancer
Other histological types, namely, serous carcinoma and clear-cell carcinoma
Generally develops in a polyp or in an atrophic endometrium (serous carcinoma)
May present with distant disease even without myometrial invasion (serous carcinoma and clear-cell carcinoma)
Usually diagnosed at a high stage
Aggressive clinical behavior
Poor prognosis

nulliparity (Shapiro et al. 1985; Fisher et al. 1994; Renehan et al. 2008; Soliman et al. 2006; McPherson et al. 1996).

Endometrioid cancers are endometrial glandular neoplasms that can be preceded or associated with endometrial hyperplasia (Kurman et al. 2014; Colombo et al. 2013). They are subdivided into three grades of differentiation (well to poorly differentiated) according to the amount of solid components (Colombo et al. 2013; Tirumani et al. 2013). Low-grade tumors are usually diagnosed at an early stage and generally have a good outcome, whereas high-grade endometrioid cancers are associated with a poor prognosis (Tirumani et al. 2013).

Endometrioid cancers are characteristically associated with PTEN, K-RAS, and CTNNB gene mutations (Tirumani et al. 2013).

Mucinous carcinomas are a rare form of type 1 endometrial cancer, where more than 50 % of glandular cells mucin can be found. They are in the majority of times well differentiated and associated with good prognosis (Kurman et al. 2014; Jalloul et al. 2012).

Type 2 tumors are constituted by the other histological types, namely, serous carcinoma and clear-cell carcinoma (Tirumani et al. 2013; Jalloul et al. 2012). They have a more aggressive clinical behavior, a poorer prognosis, and are usually diagnosed at higher stage (Tirumani et al. 2013; Jalloul et al. 2012).

Genetics changes such as p53 and p16 inactivation genes and gene overexpression of HER-2/neu are frequently present in these types of carcinomas (Tirumani et al. 2013; Hecht and Mutter 2006).

Although classically considered estrogen-independent cancers, Setiawan and her colleagues found an overlap between risk factors of type 1 and type 2 endometrial cancers (Setiawan et al. 2013). Parity, oral contraceptives use, age at menarche, diabetes and smoking were associated with both type 2 (mainly serosal and mixed carcinomas) and type 1 cancers (Setiawan et al. 2013). The risk factors of type 2 endometrial cancer and high-grade endometrioid tumors were similar, whereas body mass index was more associated with type 1 cancer (Setiawan et al. 2013).

Serous carcinomas make up the majority of type 2 endometrial cancers. They are characterized by the presence of complex papillary architecture associated with remarkable nuclear pleomorphism (Kurman et al. 2014). They are not associated with endometrial hyperplasia, but may be preceded by serous endometrial intraepithelial carcinoma, a noninvasive form of carcinoma confined to the epithelium that generally develops in a polyp or in an atrophic endometrium (Kurman et al. 2014).

Clear-cell carcinoma is a rare form of type 2 cancer that resembles its ovarian counterpart (Kurman et al. 2014).

Undifferentiated and dedifferentiated carcinomas of the endometrium are also rare types. The former is characterized by the presence of cells with no differentiation, whereas the latter is composed partially by undifferentiated type carcinoma and by International Federation of Gynaecology Obstetrics (FIGO) grade 1 or 2 endometrioid carcinoma (Kurman et al. 2014).

Mixed carcinomas are made of two or more types of endometrial carcinomas, with at least one being a type 2 carcinoma (Kurman et al. 2014).

Neuroendocrine tumors of the endometrium are extremely rare tumors.

Although they present different pathological and epidemiological features, in the latest WHO classification they have been grouped under endometrial carcinomas (Kurman et al. 2014).

Endometrial neuroendocrine tumors may be of low grade (carcinoid tumors) or of high grade (small cell neuroendocrine carcinomas and large cell neuroendocrine tumors).

The majority of cases reported in the literature are of small cell neuroendocrine carcinomas, which present as their lung counterpart (Lopes Dias et al. 2015).

They tend to be aggressive tumors with a poor prognosis. Women are generally in the postmenopausal age and tend to present with vaginal bleeding, but sometimes due to their aggressiveness, metastatic pain can be present (Lopes Dias et al. 2015; Eichhorn and Young 2001).

Carcinosarcomas are an admixture of carcinomatous and mesenchymal sarcomatous components (Kurman et al. 2014). Carcinomatous elements are generally high-grade endometrioid, serous, clear-cell, or undifferentiated carcinomas. Carcinosarcomas are classified under the "Mixed epithelial and mesenchymal" group (Kurman et al. 2014). However, due to their carcinomatous component and to the fact that their risk factors present symptoms and behavior similar to those of high-grade endometrial carcinomas, they are staged as such.

The radiological and pathological appearances of these tumors tend to differ from the other histopathological endometrial cancer subtypes, as they tend to present as large hemorrhagic and necrotic masses that distend the endometrial cavity, compressing and frequently invading the myometrium and the cervical stroma. Their prognosis is poor since they tend to present lymphatic and sometimes hematogenous spread at the time of diagnosis. Recurrence is also frequent.

The majority of endometrial cancers are sporadic. Nonetheless, about 5 % of endometrial cancers are caused by genetic mutations (e.g., Lynch syndrome, Cowden syndrome). These cancers tend to occur 10–20 years before the sporadic type (Koh et al. 2014; Resnick et al. 2009).

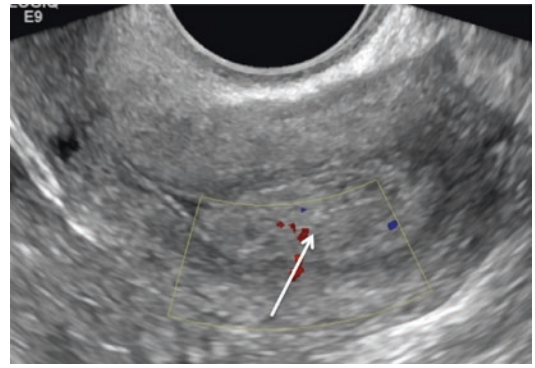

Fig. 1 Serous endometrial carcinoma in a 59-year-old woman presenting with vaginal bleeding. Transvaginal ultrasonography detected thickening of the endometrium (*arrow*), which was posteriorly submitted to biopsy that diagnosed a serous endometrial carcinoma

1.3 Symptoms and Diagnosis

About 90 % of patients with endometrial carcinoma present with abnormal vaginal bleeding (Koh et al. 2014; Colombo et al. 2013). Therefore, endometrial carcinoma is often diagnosed at an early and treatable stage, at which the prognosis is good.

Some women also seek care owing to pelvic pain or pressure (usually patients with advanced stage disease). Moreover, patients may present with atypical glandular cells on cervical cytology, which requires further evaluation for premalignant or malignant diseases of the endocervix and of the endometrium.

The first diagnostic step to evaluate women with pre- and postmenopausal abnormal vaginal bleeding should be the measurement of endometrial thickness with transvaginal ultrasound (TVUS) (Fig. 1) (Bennet et al. 2011). Transabdominal ultrasound may also be used as an adjunct modality, particularly in large leiomyomatous uterus or when women cannot tolerate TVUS (Bennet et al. 2011).

In postmenopausal women with vaginal bleeding an upper threshold of 5 mm or of 4 mm for normal endometrial thickness should be considered (Bennet et al. 2011; Gull et al. 2003; Karlsson et al. 1995; Smith-Bindman et al. 1998). In this age group, an endometrial thickness measurement

≤5 mm is associated with the absence of endometrial cancer (Gupta et al. 2002). This cut-off value should also be used in women under hormone replacement therapy and under tamoxifen (Bennet et al. 2011).

In symptomatic patients in premenopausal age, an upper threshold of normal endometrial thickness is more difficult to establish due to its variations during the menstrual cycle. In this group of women, the assessment of the endometrium should be performed during the early first half of the menstrual cycle (Bennet et al. 2011). In these women, an endometrial thickness >16 mm has shown to have a sensitivity of 67 % and a specificity of 75 % for detecting endometrial abnormalities (Bennet et al. 2011; Hulka et al. 1994). A heterogeneous endometrium or an area of focal thickness should be also further investigated (Bennet et al. 2011; Goldstein et al. 2001).

If the endometrium is thickened or heterogeneous, a sample of the endometrium must be undertaken to establish a definite histopathological diagnosis. In these cases a hysteroscopy with biopsy or resection should be performed.

Before treatment, the initial evaluation should include a medical history, a physical and gynecological examination, a complete blood count, and a chest radiograph (Koh et al. 2014).

If the age of the onset of the disease is <50 years and if there is history of familiar colorectal or endometrial cancer, screening for genetic mutations should be performed (Koh et al. 2014).

Women with Lynch syndrome, without endometrial cancer, should be screened annually with an endometrial biopsy (Koh et al. 2014; Järvinen et al. 2009; Meyer et al. 2009). Prophylactic hysterectomy with bilateral salpingoophorectomy may be considered in these patients (Koh et al. 2014; Schmeler et al. 2006).

2 Endometrial Cancer Staging

Endometrial carcinoma is staged with the International Federation of Gynaecology Obstetrics (FIGO) system, which was last revised in 2009 (Table 3) (Creasman 2009; Pecorelli 2009). This classification defines that endometrial carcinoma is staged on the basis of surgicopathological findings.

Table 3 Endometrial Cancer Staging: FIGO[a] 2009

Stage I—The tumor is confined to the uterine corpus
IA—Absence or invasion of <50 % of the myometrium
IB—Invasion of ≥50 % of the myometrium
Stage II—The tumor invades the cervical stroma, but not beyond the uterus
Stage III—There is local or regional involvement
IIIA—The tumor invades the serosa and/or the adnexa
IIIB—Presence of vaginal and/or parametrial involvement
IIIC—Presence of pelvic or para-aortic lymphadenopathies
III_{C1}—Presence of pelvic lymphadenopathies
III_{C2}—Presence of para-aortic lymphadenopathies, with or without pelvic lymphadenopathies
Stage IV—The tumor invades the bladder mucosa and/or the intestinal mucosa, and/or there are distant metastases
IVA—The tumor invades the bladder mucosa and/or the intestinal mucosa
IVB—Presence of distant metastases, including abdominal metastases and/or inguinal lymphadenopathies.

Adapted from Pecorelli (2009)
[a]*FIGO* International Federation of Gynaecology and Obstetrics

The complete surgical staging procedure implies hysterectomy with bilateral salpingoophorectomy, assessment of the abdominal cavity with biopsies of suspicious peritoneal lesions, cytology of peritoneal washings, and pelvic and retroperitoneal lymphadenectomy (Koh et al. 2014). In patients with serous carcinoma, clear-cell carcinoma, and carcinosarcoma, the surgical staging procedure should be the same as for ovarian cancer (Koh et al. 2014).

The FIGO 2009 staging classification is as follows (Table 3) (Pecorelli 2009):

In stage I, the tumor is confined to the uterus. This stage is subdivided in two substages: stage IA (the tumor invades <50 % of the myometrium) and stage IB (the tumor invades ≥50 % of the myometrium).

In stage II, the tumor invades the cervical stroma, but not beyond the uterus.

Stage III is subdivided into three substages. In stage IIIA, the tumor invades the serosa or/and the adnexa (direct extension or metastasis). In stage IIIB, there is involvement of the parametria and/or the vagina (direct extension or metastasis). In stage IIIC, there is lymph node involvement (III_{C1} if there are positive pelvic lymph nodes and III_{C2} if there are positive para-aortic lymph nodes).

Stage IV is also subdivided into two substages. The tumor is in stage IVA if there is mucosal invasion of the bladder or/and the bowel and it is in stage IVB if there are distant metastasis including abdominal metastasis and/or the presence of positive inguinal lymph nodes.

MR imaging is not considered in the FIGO staging of endometrial carcinoma, but due to its high contrast resolution and reproducibility, it has an important role in the preoperative staging of the disease. Thus, it is crucial for tailoring the surgical approach to these patients.

There is still no consensus on whether complete surgical staging with primary pelvic and para-aortic lymphadenopathy should be performed at stage I, namely, in patients with low recurrence risk (Bonatti et al. 2015; Todo et al. 2010; May et al. 2010). However, it is known that the tumor histological type and grade, the presence of myometrial invasion ≥50 %, and the presence of lymphovascular space invasion correlate with the presence of lymph node metastasis and with overall survival (Rechichi et al. 2010; Sala et al. 2013; Boronow 1990; Larson et al. 1996). From these features, only the histological type and grade can be assessed preoperatively without imaging. Nonetheless, discrepancies of up to 15 % between the pre- and postoperative tumoral histopathological results have been described (Sala et al. 2013; Frei et al. 2000).

MR can accurately determine the depth of myometrial invasion. Therefore, in conjunction with the histopathological grade it may be used to select the patients that might be candidates for pelvic and para-aortic lymphadenectomy, precluding surgery in low-risk patients, thus avoiding the morbidities associated with this procedure. Presence of lymph node metastases has been reported in more than 30 % of the cases of endometrial cancer with ≥50 % of myometrial invasion and in only 5 % of cases when the tumor invades <50 % of the myometrium (Larson et al. 1996; Gallego et al. 2014).

Lymphovascular invasion is generally assessed postoperatively. It is related not only to the likelihood of lymph node involvement, but with tumor relapse and poor survival (Sala et al. 2013; Fujii et al. 2015; Briët et al. 2005). Not many studies have addressed the role of MR in diagnosing lymphovascular space involvement. However, a study by Nougaret et al. showed that whole tumor volume and ADC could be useful in its prediction (Nougaret et al. 2015).

Cervical stromal invasion is also associated with lymph node metastasis and poor survival. MR can accurately diagnose cervical stromal invasion and parametrial invasion. This is particularly important so surgeons can avoid cutting through the tumor and thus perform an extensive resection (Sala et al. 2013).

Moreover, MR is helpful is diagnosing advanced disease involving the adnexa and the peritoneum, which generally are contraindications to laparoscopic and robotic surgery (Sala et al. 2013; Venkat et al. 2012; Amant et al. 2007). Other extra-uterine coexistent pathologies can also be diagnosed that may help determining the surgical approach.

Therefore, MR is useful not only in planning surgical treatment but also in selecting more advanced and difficult surgical cases that should be guided to specialized oncologic centers.

MR is also useful in determining the origin (cervical or endometrial) of a biopsy proven adenocarcinoma (Fig. 2). Vargas and colleagues showed that by assessing the epicenter of the tumor, the endometrial versus the cervical origin of an adenocarcinoma could be determined with an accuracy of 85–88 % (Vargas et al. 2011). Furthermore, endometrial thickening, expansion of the endometrial cavity by a mass, and the presence of a tumor invading the myometrium may aid the discrimination between these two types of tumors (Haider et al. 2006). This distinction is particularly important, because early stage cervical adenocarcinomas are

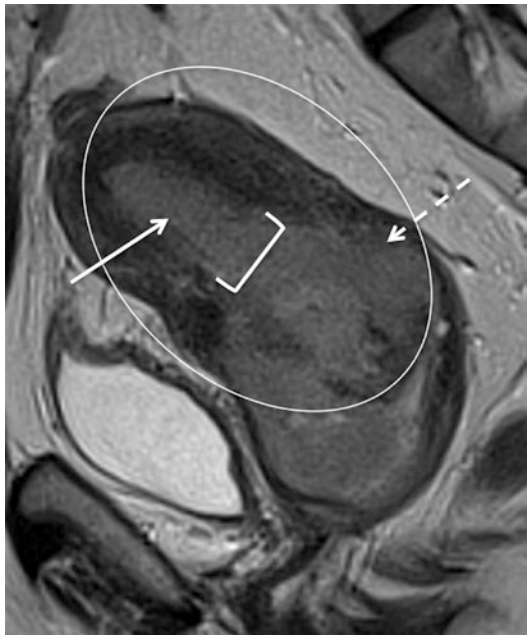

Fig. 2 Endometrial carcinoma that invades the cervical stroma in a 53-year-old woman. Sagittal T2-weighted image. Distinction between endometrial and cervical origin of an adenocarcinoma may be challenging. Radiologists should look for the epicenter of the tumor (>50 %) (*circle*), and other signs that may help defining endometrial origin, such as endometrial thickness (*arrow*), expansion of the uterine cavity by a mass (*squared brackets*), and invasion of the myometrium (*dashed arrow*)

Table 4 MR protocol scheme for endometrial cancer staging

MRI protocol for endometrial cancer staging
Abdomen
T2 FSE axial (6 mm/1 mm)—from the diaphragm to the iliac crests
Axial DWI and the respective ADC maps (6 mm)
Pelvis
T1 FSE axial (5 mm/0.5 mm)
T2 FSE axial (5 mm/0.5 mm); T2 FSE sagittal (4 mm/0.4 mm); T2 FSE axial oblique of the uterine corpus (perpendicular to the uterine cavity; 4 mm/0.4 mm)
Dynamic contrast-enhanced study in the axial oblique plane of the uterine corpus: 3D T1, FS pre- and postcontrast administration, five acquisition phases (until 150 s; 2 mm)
Axial DWI and the respective ADC maps (5 mm/0.5 mm)
Protocol variants
If there is suspicion of cervix invasion:
T2 FSE axial oblique of the uterine cervix (perpendicular to the cervical canal; 4 mm/0.4 mm)
Dynamic contrast-enhanced study in the sagittal plane: 3D T1, FS pre- and postcontrast administration, five acquisition phases (until 150 s; 2 mm)
Axial oblique plane of the uterine cervix postcontrast injection 3D T1, FS in late phase (4 min; 2 mm)

treated with surgery, advanced stage cervical adenocarcinomas are treated with chemotherapy and radiotherapy and endometrial carcinomas are treated primarily with surgery.

Although fertility-sparing progesterone therapy is not the standard of care for endometrial cancers, it might be considered according to patients request in treatment of low-grade endometrial cancers that do not invade the myometrium. In these cases, MR is essential in defining which patients are candidates to this approach.

2.1 MR Protocol for Staging Endometrial Carcinoma

In our institution the MR protocol for staging endometrial carcinoma is as follows (Table 4):

Patients are advised to fast 4–6 h before the procedure. A fast acting laxative enema to clean the bowel is administered the day before the exam and during the morning of the exam. Patients are encouraged to void before the examination since a full bladder degrades the quality of T2-weighted images.

In order to reduce bowel peristalsis and hence improve image quality, 1 mg of glucagon intravenous is administered before the exam. Alternatively, 20 mg or 40 mg of hyoscine butylbromide intramuscular/intravenous can be administered.

Patients are advised to avoid the use of vaginal tampon.

MR imaging can either be performed in a 1.5 T or a 3 T MR machine. 3 T MR has been not shown to offer significant benefit over 1.5 T MR in the evaluation of endometrial cancer, since 3 T MR is more prone to susceptibility and chemical-shift artifacts that impair the image quality (Wakefield et al. 2013; Haldorsen and Salvesen 2012; Hori et al. 2013).

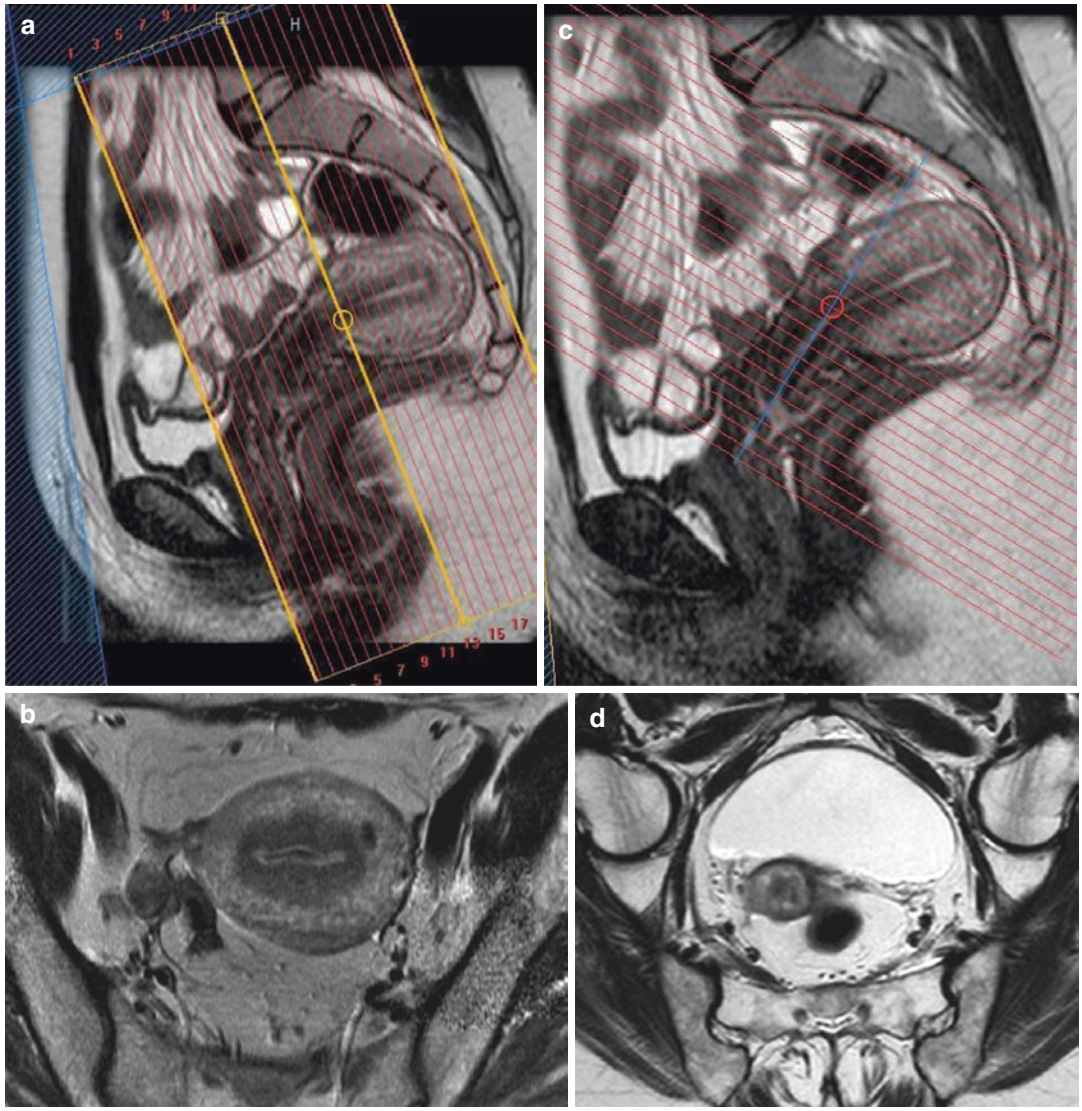

Fig. 3 (**a**, **b**) Axial oblique plane of the uterine corpus (perpendicular to the uterine cavity); (**c**, **d**) axial oblique plane of the uterine cervix (perpendicular to the cervical canal)

A pelvic phase array is used along with anterior and superior saturation bands.

The patient should be placed in a supine position for the whole exam. However, prone position may be used in uncooperative patients.

Axial imaging of the abdomen (from diaphragm to iliac crests) should be performed for the evaluation of advanced disease, with fast recovery, fast spin-echo T2-weighted images (6 mm/1 mm, breath-hold). Abdominal axial diffusion-weighted images (DWI) (6 mm, *b-values*—0, 500, 1000 s/mm^2) and the respective ADC maps should also be obtained.

Evaluation of the pelvis should be performed with axial fast spin-echo T1-weighted images (5 mm/0.5 mm), axial fast spin-echo T2-weighted images (5 mm/0.5 mm), and sagittal fast spin-echo T2-weighted images (4 mm/0.4 mm).

Fast spin-echo T2-weighted axial oblique images (perpendicular to the uterine cavity, 4 mm/0.4 mm) are helpful in assessing myometrial invasion (Fig. 3).

The dynamic contrast-enhanced MR images are obtained after the injection of 0.1 mmol/kg of gadolinium at a rate of 2 mL/s. In our institution, images are acquired using a 3D-recalled echo fat-suppressed T1-weighted sequence, pre- and post-contrast injection during five acquisition phases in the axial-oblique plane (perpendicular to the uterine cavity), until 150 s (2 mm). The dynamic study tends to be avoided in patients with renal impairment.

DWI study (*b-values*—0, 600, 1000 s/mm^2, 5 mm/0.5 mm) and the respective ADC maps are performed in the axial plane.

If there is suspicion of cervix invasion, axial oblique of the cervix fast spin-echo T2-weighted images (perpendicular to the cervical canal, 4 mm/0.4 mm) are obtained to evaluate parametrial invasion (Fig. 3). In these cases, the dynamic study should be performed in the sagittal plane using a 3D-reccaled echo fat-suppressed T1-weighted sequence, pre- and postcontrast injection during five acquisition phases until 150 s (2 mm). Furthermore, axial oblique of the cervix (perpendicular to cervical canal) postcontrast injection 3D-reccaled echo fat-suppressed T1-weighted images are obtained in a late phase (4 min, 2 mm), to better assess cervical stromal invasion (Fig. 3).

2.2 MR Findings According to the Stage of Endometrial Carcinoma

On conventional imaging, the normal uterus anatomy is better depicted on T2-weighted images. The endometrium tends to be hyperintense, the junctional zone is hypointense and the outer myometrium shows intermediate intensity (Fig. 4).

Endometrial cancer is isointense to the endometrium on T1-weighted images and it most frequently shows heterogeneous moderate to high-signal intensity on T2-weighted images. However, it can also show low-signal intensity on T2-weighted images (Fig. 5).

On DCE-MR, in the arterial phase (≈30 s) endometrial tumors enhance earlier than does the normal endometrium, as this is the most adequate sequence to depict small endometrial tumors confined to the endometrium. At the equilibrium phase (≈120–180 s), tumors tend to be hypointense relative to the myometrium. However, they can remain isointense and a minority can even be hyperintense (Figs. 5 and 6).

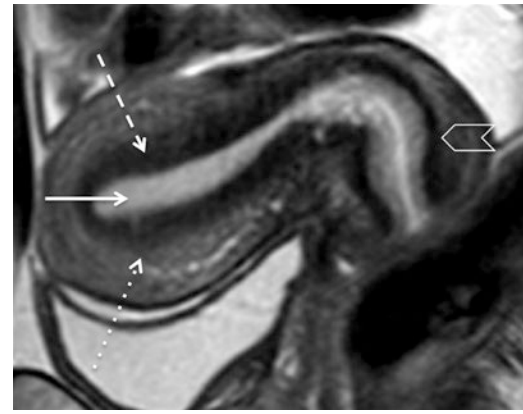

Fig. 4 Normal uterine T2-weighted anatomy. Sagittal T2-weighted image. Hyperintense endometrium (*arrow*); hypointense junctional zone (*dashed arrow*); outer myometrium showing intermediate intensity (*dotted line*); hypointense cervical stroma (*arrowhead*)

On DWI-MR the tumors usually show restricted diffusion (hyperintensity on high b-value sequences and hypointensity on the respective ADC map) (Fig. 6). ADC values have shown to be significantly lower in endometrial carcinoma than in normal endometrium and benign conditions such as endometrial polyps and submucosal leiomyomas (Fujii et al. 2008; Tamai et al. 2007; Takeuchi et al. 2009; Rechichi et al. 2011) (Fig. 7).Therefore, this functional sequence can be helpful in diagnosing an endometrial tumor when biopsy cannot be easily performed (i.e., in the case of cervical stenosis) or when the histopathological diagnosis is not conclusive. Cross-reference with conventional sequences is, however, mandatory to avoid pitfalls, since restricted diffusion may be present also in retained secretions in the endometrial cavity.

Several studies have shown that there is no relation between the tumor grade, aggressiveness, and ADC values (Rechichi et al. 2011;

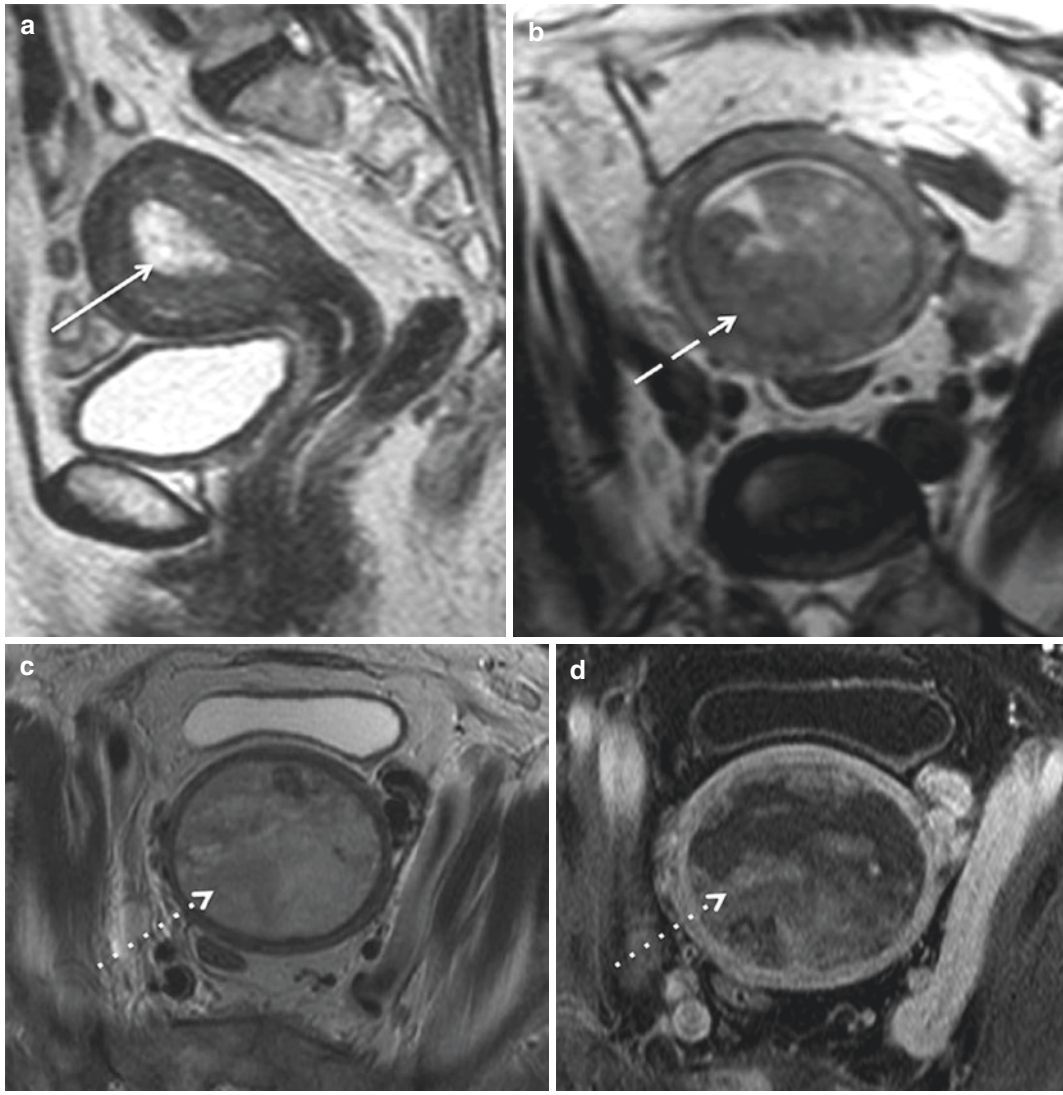

Fig. 5 MR features of endometrial cancer. (**a**) endometrioid cancer showing heterogeneous high-signal intensity on sagittal T2-weighted image (*arrow*); (**b**) endometrioid cancer showing hyposignal intensity on axial oblique T2-weighted image, a less common appearance (*dashed arrow*); (**c**, **d**) endometrioid cancer distending the uterine cavity and compressing the myometrium showing a remarkable heterogeneous high-signal intensity on axial oblique T2 weighted image (*dotted arrows*) and mixed hypointensity and isointensity relative to outer myometrium after administration of gadolinium in the equilibrium phase (*dotted arrows*)

Bharwani et al. 2011). However, in one study higher grade tumors were associated with lower ADC values but there was a considerable overlap in estimation of histological grade based on ADC values (Tamai et al. 2007). Moreover, high ADC values may be found in high-grade tumors with a large necrotic component (Sala et al. 2010).

2.2.1 Stage I Disease

Stage I endometrial carcinomas account for approximately 74 % of endometrial cancers (Cancer Incidence Statistics 2015). The most important role of the radiologist, when facing a stage I endometrial cancer is to determine the extent of myometrial invasion, since stage I disease is subdivided into stage IA disease, if the

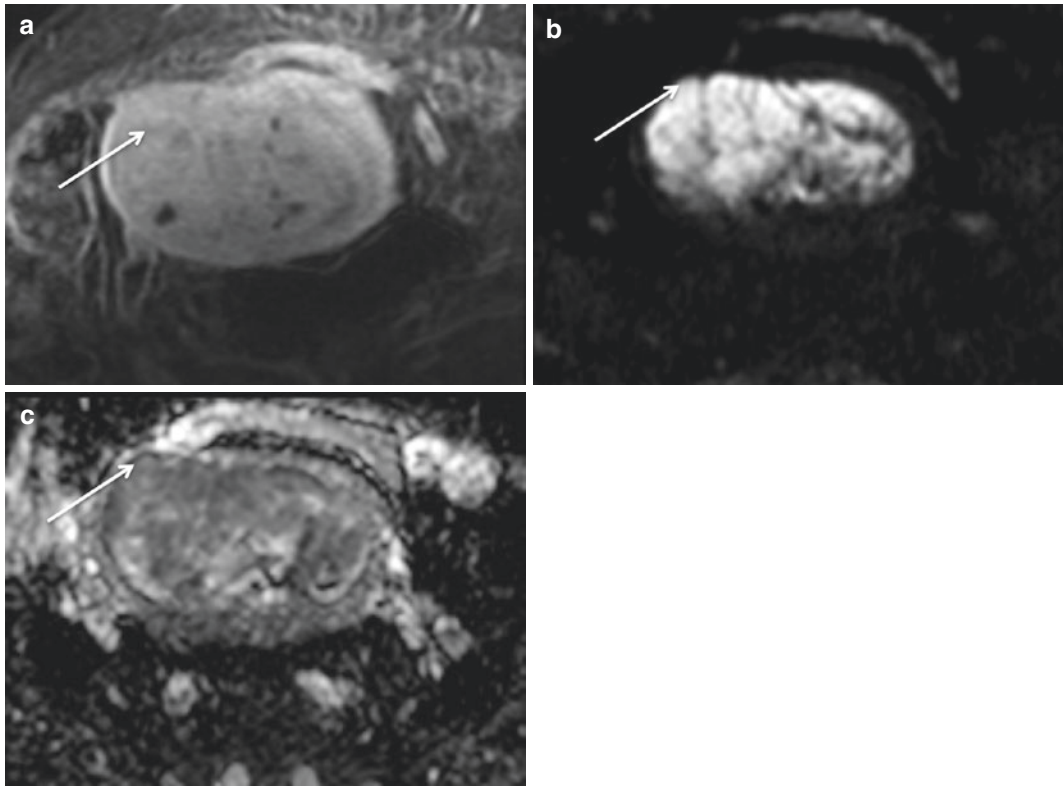

Fig. 6 (**a**) Endometrioid carcinoma in a 79-year-old woman, isointense to the myometrium after administration of gadolinium in the equilibrium phase, making it difficult to access the depth of myometrial invasion (*arrow*); (**b**, **c**) diffusion-weighted image ($b = 1000$ mm/s^2) and the respective ADC map show typical tumoral restricted diffusion, enabling the radiologist to diagnose invasion of ≥50 % the myometrium (stage IB) (*arrow*)

tumor only invades <50 % of the myometrium, and stage IB disease, if the tumor invades ≥50 % of the myometrium (Figs. 8 and 9) (Pecorelli 2009). If the patient is considering fertility-sparing treatment, it is also important to clearly define if the tumor is confined to the endometrium or if it invades the superficial myometrium, which precludes this approach (Fig. 10) (Jafari Shobeiri et al. 2013; Kesterson and Fanning 2012).

T2-weighted images are useful in determining myometrial invasion. A focal or diffuse thickening of the endometrium with a clearly visualized intact junctional zone is a sign that the tumor is confined to the endometrium (Fig. 8). Breaching and irregularity of the hypointense signal of the junctional zone implies superficial myometrial invasion (Manfredi et al. 2005).

The depth of myometrial invasion should be based on the thickness of remaining myometrium where the tumor is at its deepest point into the myometrium (Haldorsen and Salvesen 2012; Koyama et al. 2007).

However, there are situations where the evaluation of myometrial invasion by T2-weighted images may be difficult or even impossible, such as the presence of: a tumor in the cornua (Fig. 11); a fibromatous uterus (Fig. 11); a less conspicuous junctional zone in postmenopausal women (Fig. 12); a thinned myometrium in postmenopausal women (Fig. 13); an adenomyotic uterus (Fig. 14); a polypoid uterus; a congenital abnormality (Fig. 15); and the presence of poor tumor signal difference/isointensity between the tumor and the myometrium (Figs. 6 and 16) (Kinkel 2006; Scoutt et al. 1995; Yamashita et al. 1993a; Saez et al. 2000; Fanning et al. 1990). In these cases, DCE-MR and DWI-MR play an important role, when combined with T2-weighted images.

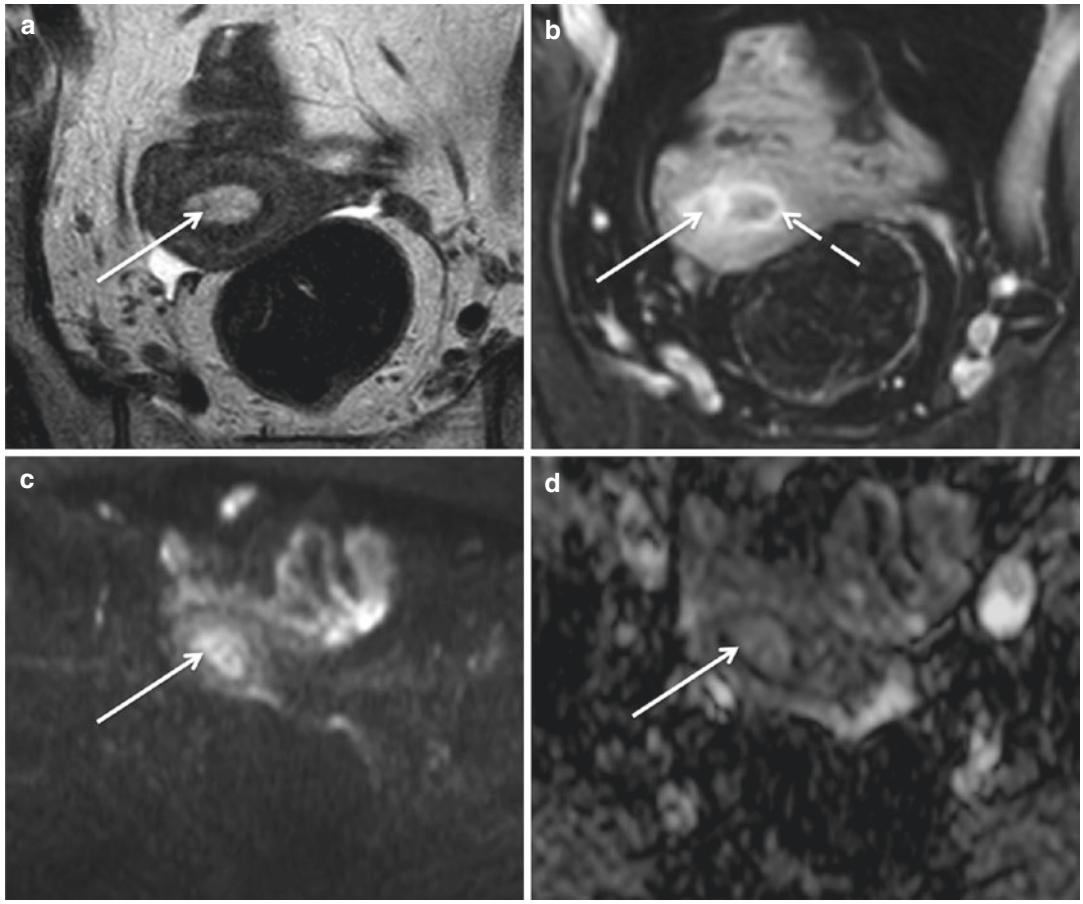

Fig. 7 Benign polyp in a 60-year-old woman. (**a**) Axial oblique T2-weighted image shows a heterogeneous hyperintense filling of the endometrial cavity; (**b**) axial oblique 3D fat-suppressed T1-weighted sequence after the administration of gadolinium in the arterial phase (30 s) shows lesional heterogeneous enhancement (*arrow*). Note the avid enhancement of the junctional zone in this phase when compared to the outer myometrium (*dashed arrow*). Both T2 and DCE-MR characteristics of this benign polyp mimic those of endometrial carcinoma; (**c**) axial diffusion-weighted image (b = 1000 s/mm^2) shows high-signal intensity of the tumor; (**d**) the apparent diffusion coefficient map also shows high-signal intensity. In contrast to what would be expected in an endometrial carcinoma, this benign polyp does not show restricted diffusion

On DCE-MR imaging, in the arterial phase (≈ 30 s), the junctional zone typically enhances avidly when compared to the endometrial tumor (Manfredi et al. 2005). Disruption of this subendometrial enhancement usually indicates myometrial invasion (Fujii et al. 2015; Manfredi et al. 2005; Nakao et al. 2006; Yamashita et al. 1993b; Kaneda et al. 2011; Frei and Kinker 2001). This is particularly important when the patient is being considered for fertility-sparing treatment since the FIGO 2009 division of stage I disease is only based on the presence of invasion of the inner or outer portions of the myometrium (Fig. 10) (Jafari Shobeiri et al. 2013; Kesterson and Fanning 2012).

On the other hand, it is in the equilibrium phase (≈120 s) that is better diagnosed deep myometrial invasion. In this phase there is more pronounced contrast-to-noise ratio between the outer myometrium, which is markedly hyperintense, and the endometrial tumor, which is usually hypointense (Figs. 9, 13 and 15) (Manfredi et al. 2005). Attention must be paid to the presence of peritumoral inflammatory enhancement, which

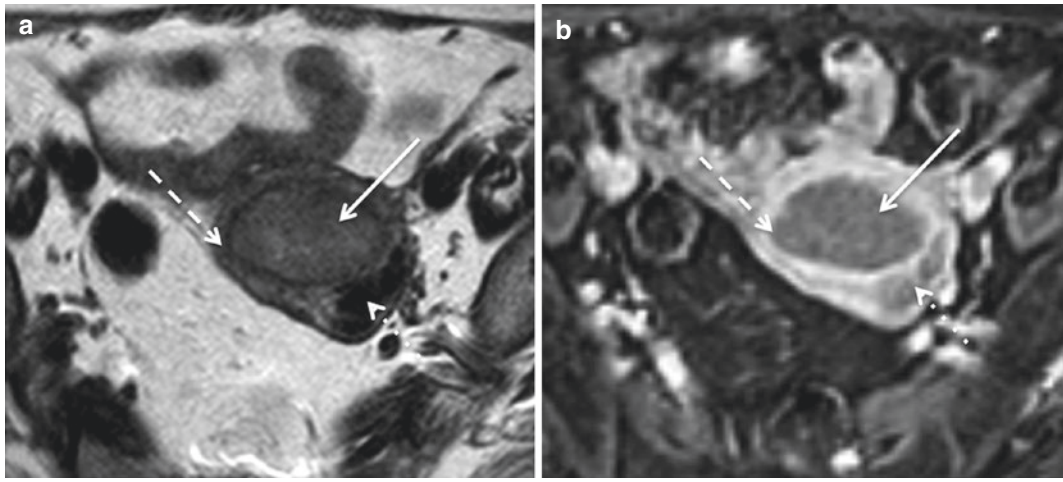

Fig. 8 Stage IA endometrioid carcinoma. (**a**) Axial oblique T2-weighted image; (**b**) axial oblique 3D fat-suppressed T1-weighted sequence after the administration of gadolinium in the arterial phase (30 s). There is preservation of the regular hypointense signal on T2-weighted image and of the regular enhancement of the junctional zone after administration of gadolinium in the arterial phase (*dashed arrow*), thus the tumor is confined to the endometrial cavity (*arrow*). Note the intramural leiomyoma in the posterior corpus (*dotted arrow*)

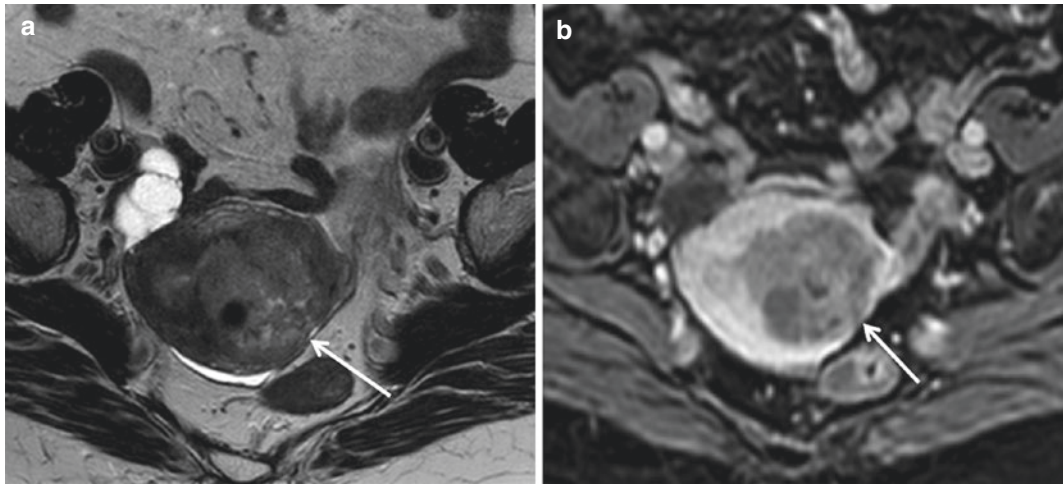

Fig. 9 Stage IB endometrioid carcinoma in an 85-year-old woman. (**a**) Axial oblique T2-weighted image; (**b**) axial oblique 3D fat-suppressed T1-weighted sequence after the administration of gadolinium in the equilibrium phase (120 s). There is extension of the tumor to the outer portion of the left posterior myometrium (*arrow*), which is clearly depicted after the administration of gadolinium in the equilibrium phase, where there is more pronounced contrast-to-noise ratio between the hypointense tumor and the hyperintense outer myometrium

can exaggerate the appearance of myometrial invasion (Sala et al. 2013).

DWI-MR has shown to be very useful in assessing myometrial invasion, especially in patients who cannot receive intravenous contrast, in patients with isointense or hyperintense tumors relative to the myometrium following contrast administration, and in patients with adenomyosis (Figs. 16, 14 and 16) (Takeuchi et al. 2009; Sala et al. 2010).

Moreover, DWI-MR is very accurate in assessing myometrial invasion.

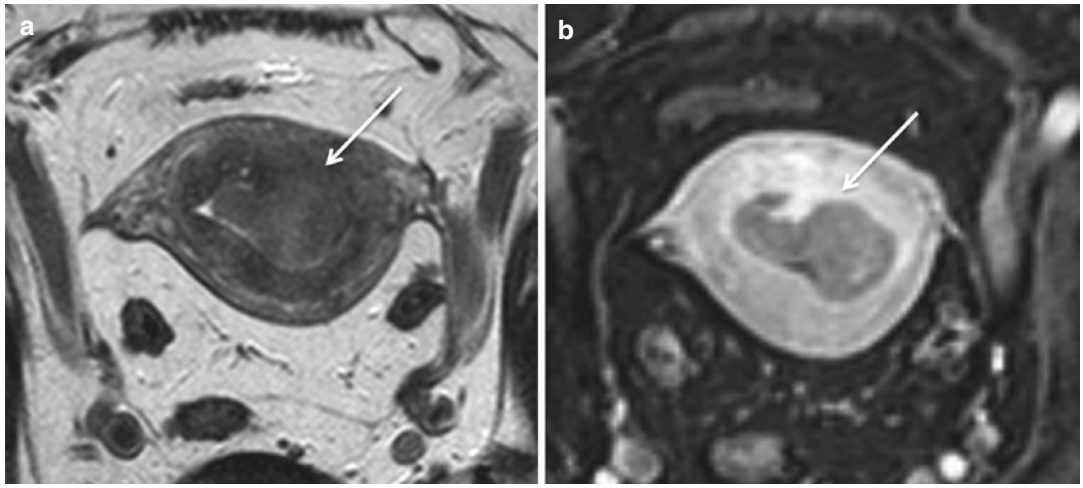

Fig. 10 Endometrioid carcinoma in a woman considering fertility-sparing therapy. (**a**) Axial oblique T2-weighted image; (**b**) axial oblique 3D fat-suppressed T1-weighted sequence after the administration of gadolinium in the arterial phase (30 s). Axial oblique T2-weighted image is inconclusive regarding myometrial invasion, whereas DCE-MR in the arterial phase clearly shows that there is no disruption of the junctional zone enhancement and therefore the tumor does not invade the myometrium

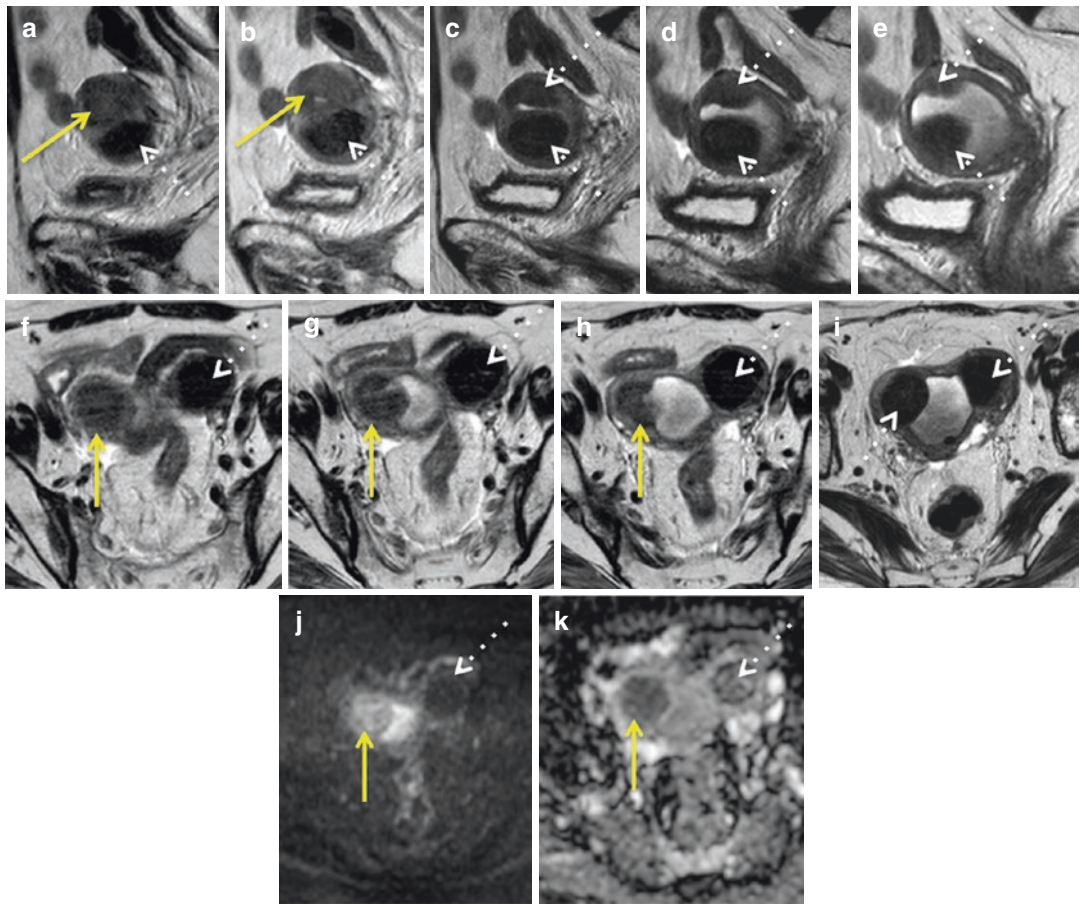

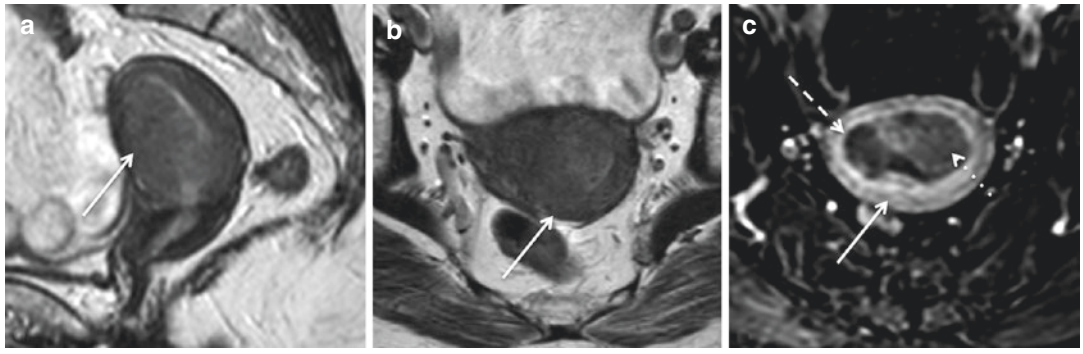

Fig. 12 Stage IA mucinous carcinoma of the endometrium in a 72-year-old woman with a thinned junctional zone. (**a**) Sagittal T2-weighted image; (**b**) axial oblique T2-weighted image; (**c**) axial oblique 3D fat-suppressed T1-weighted sequence after the administration of gadolinium in the arterial phase (30 s). The junctional zone of this postmenopausal woman cannot be identified in T2-weighted images, making it difficult to assess the depth of tumoral myometrial invasion. The use of T2-weighted images alone might suggest that the tumor invades the outer portion of the myometrium (*arrow*). However contrast-enhanced image in the arterial phase clearly shows an enhancing regular junctional zone (*dashed arrow*) and the tumor confined to the endometrial cavity (*dotted arrow*)

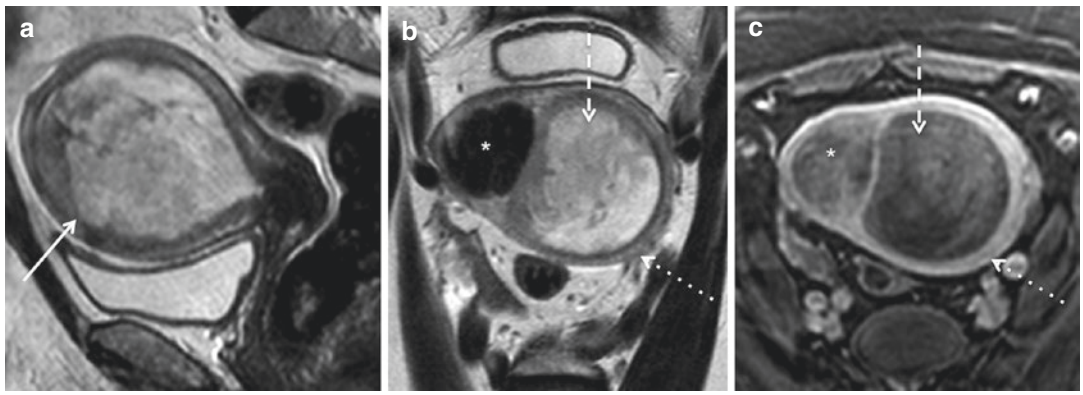

Fig. 13 Stage IA endometrioid carcinoma in a 72-year-old woman with myometrial thinning secondary to stretching due to a large tumor. (**a**) Sagittal T2-weighted image; (**b**) axial T2-weighted image; (**c**) axial oblique 3D fat-suppressed T1-weighted sequence after the administration of gadolinium in the equilibrium phase (120 s). Distortion at the base of this polypoid tumor is difficult to distinguish from outer myometrial tumoral invasion on T2 weighted images (*arrow*). Contrast-enhanced image in the equilibrium phase clearly shows a hypointense tumor (*dashed arrow*) that does not invade the outer hyperintense myometrium (*dotted arrow*). Note the T2 hypointense intramural leiomyoma (*asterisk*)

Fig. 11 Endometrial adenocarcinoma in a 71-year-old patient, previously submitted to radiation therapy due to cervical cancer. (**a**–**e**) Sagittal T2-weighted images fail to clearly show a small isointense tumor in the right uterine cornua (*yellow arrow*), due to the coexistence of submucosal leiomyomas (*dotted arrow*); (**f–i**) axial oblique T2-weighted images better depict this isointense lesion and clearly differentiate it from the hypointense leiomyomas; (**j**) axial diffusion-weighted image (b = 1000 s/mm^2) shows high-signal intensity of the tumor; (**k**) the apparent diffusion coefficient map shows hyposignal intensity, therefore tumoral restricted diffusion. In contrast, the leiomyoma present in the left cornua, does not show restricted diffusion

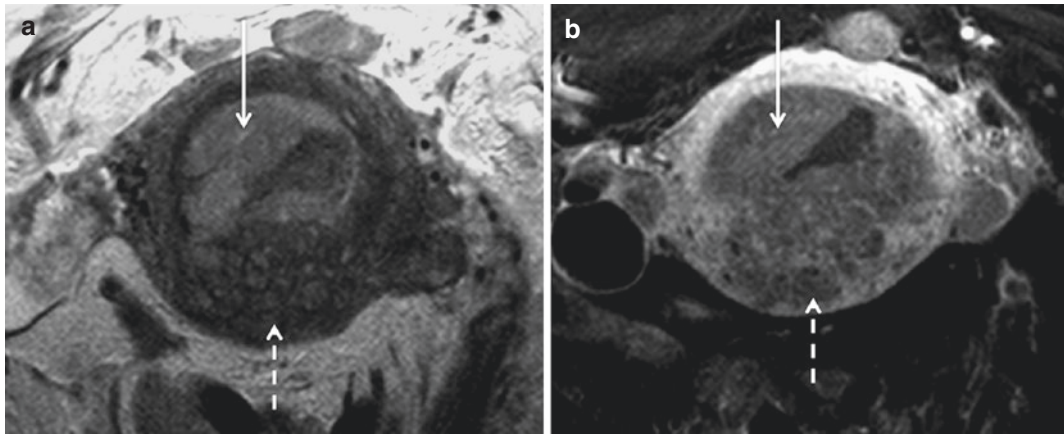

Fig. 14 Endometrioid carcinoma in a 71-year-old woman with an adenomyotic uterus. (**a**) Axial oblique T2-weighted image. (**b**) Axial oblique 3D fat-suppressed T1-weighted sequence after the administration of gadolinium in the equilibrium phase (120 s). The presence of posterior adenomyosis (*dashed arrow*) impedes the assessment of tumoral (*arrow*) myometrial invasion on both T2-weighted image and contrast-enhanced image. Diffusion-weighted images could be useful in this case

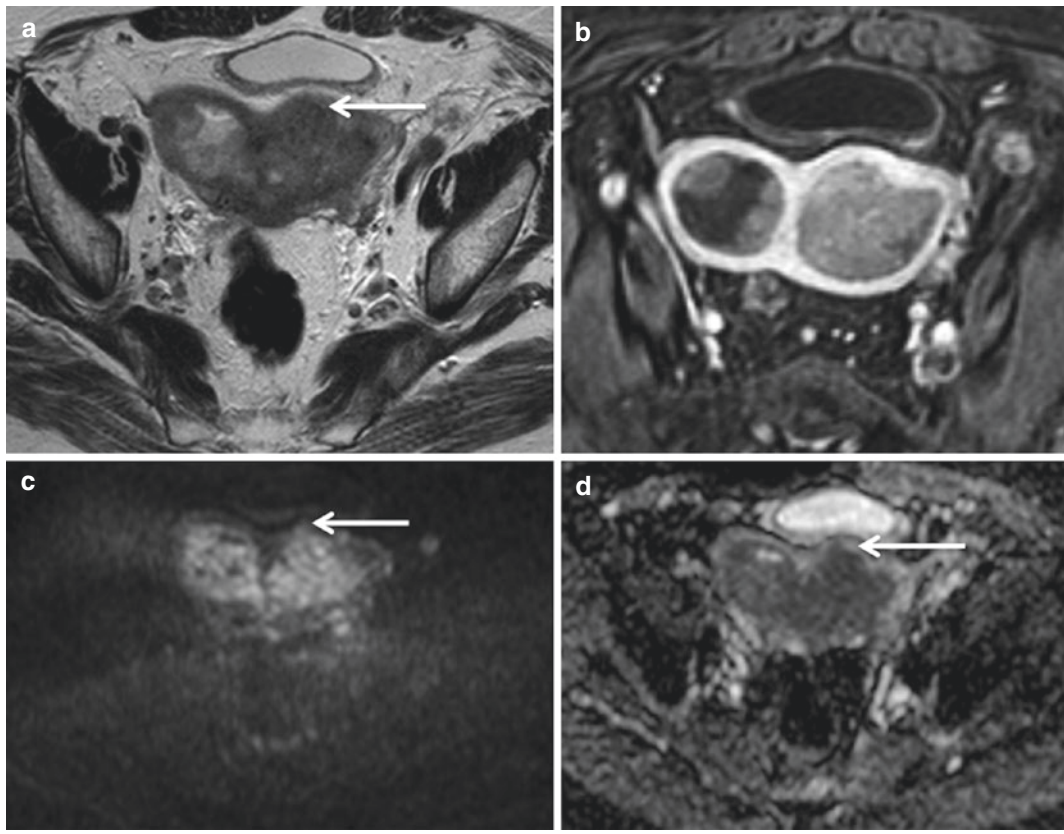

Fig. 15 Stage IB endometrioid carcinoma in a 76-year-old woman with a bicornuate bicollis uterus. (**a**) Axial T2-weighted image; (**b**) axial oblique 3D fat-suppressed T1-weighted sequence after the administration of gadolinium in the equilibrium phase (120 s); (**c**) axial diffusion-weighted image (b = 1000 s/mm^2). (**d**) ADC map. In this bicornuate bicollis uterus, the tumoral invasion of the anterior outer myometrium is difficult to depict on both T2-weighted image and after administration of contrast. Diffusion-weighted image and the respective ADC map clearly identify a focal area of restricted diffusion in the anterior outer myometrium, staging the tumor as IB

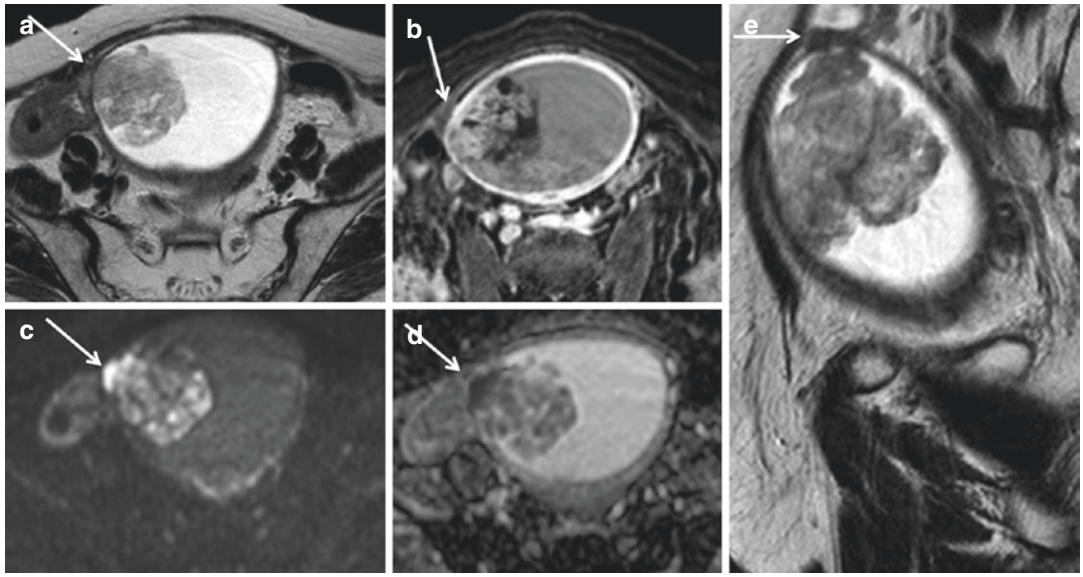

Fig. 16 Stage IB polypoid endometrioid carcinoma that distends the uterine cavity and causes myometrial thinning in a 68 year-old woman. (**a**) Axial T2-weighted image; (**b**) axial oblique 3D fat-suppressed T1-weighted sequence after the administration of gadolinium in the equilibrium phase (120 s); (**c**) axial diffusion-weighted image (b = 1000 s/mm^2); (**d**) ADC map; (**e**) sagittal T2-weighted image. The endometrial tumor is heterogeneous and shows both areas of hypointense and hyperintense signal relatively to the outer myometrium after administration of gadolinium in the equilibrium phase. This makes it difficult to assess myometrial invasion. Outer tumoral myometrial invasion in this thinned myometrium is better depicted in the diffusion-weighted image and in the respective ADC map (*arrows*)

Recent studies have shown that DWI-MR is significantly superior in the assessment of myometrial invasion when compared to DCE-MR (Bonatti et al. 2015; Rechichi et al. 2010; Takeuchi et al. 2009; Beddy et al. 2012).

A prospective study conducted by Rechichi et al. has concluded that DWI-MR is highly accurate in assessing the depth of myometrial invasion and perhaps it could replace DCE-MR as a complement to T2-weighted images in the preoperative evaluation of endometrial carcinoma (Rechichi et al. 2010). These findings were also supported by the study of Bonatti et al. that also stated that T2-weighted images and DWI could replace the combination of T2-weighted images and contrast-enhanced T1-weighted images in the preoperative staging of endometrial carcinoma (Bonatti et al. 2015).

Takeuchi and coworkers also reported an accuracy of 94 % for DWI and of 88 % for DCE-MR in the assessment of myometrial invasion (Takeuchi et al. 2009).

ADC maps have also shown to provide accurate measurement of the depth of myometrial invasion (Gallego et al. 2014).

Nonetheless, a recent meta-analysis assessing only nine studies showed that although DWI-MR has a slightly higher specificity in the diagnosis of myometrial invasion, DCE-MR and DWI-MR do not differ significantly in sensitivity and specificity in presurgical diagnosis of myometrial invasion (Andreano et al. 2014).

2.2.2 Stage II Disease

Stage II disease is characterized by cervical stromal invasion (Pecorelli 2009).

In the majority of cases, T2-weighted images are helpful in diagnosing cervical stromal invasion by depicting a heterogeneous hyperintense tumor disrupting the hypointense cervical stroma (Manfredi et al. 2005).

Axial oblique plane of the cervix (perpendicular to the cervical canal) postcontrast injection 3D-reccaled echo fat-suppressed T1-weighted images in a late phase (≈80–240 s) are also very useful in assessing cervical stromal invasion, as they show the disruption of cervical enhancement by the tumor (Fig. 17) (Tirumani et al. 2013; Haldorsen and Salvesen

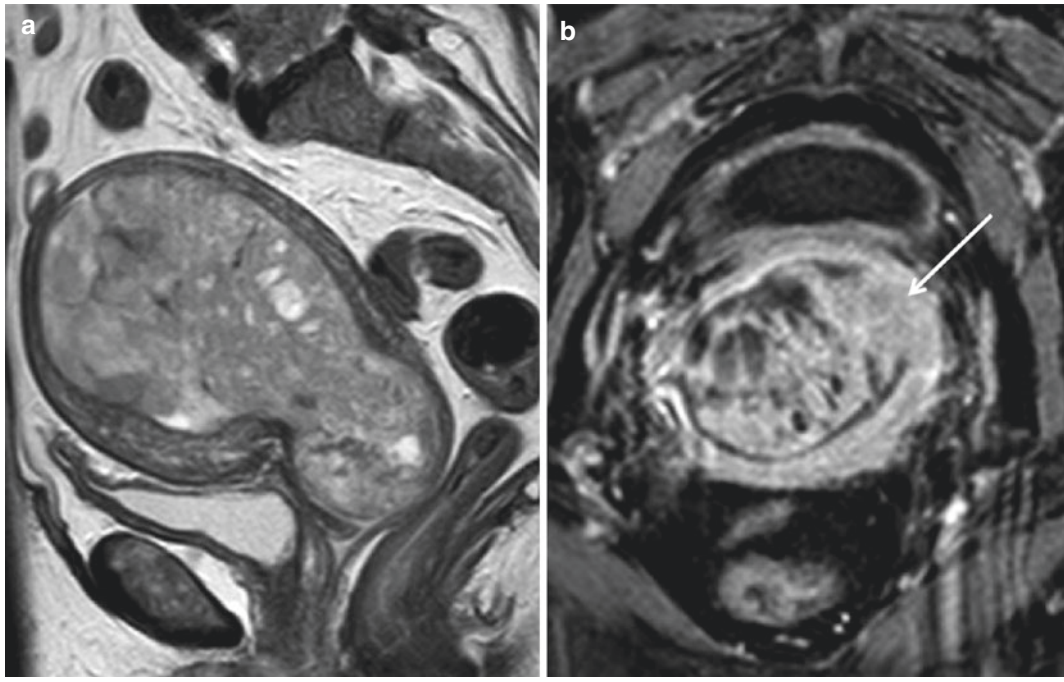

Fig. 17 Stage II endometrioid carcinoma in an 83-year-old woman (**a**) sagittal T2-weighted image; (**b**) axial oblique plane of the cervix (perpendicular to the cervical canal) postcontrast injection 3D-reccaled echo fat-suppressed T1-weighted images in a late phase (4 min). Sagittal T2-weighted image shows a voluminous endometrial tumor that prolapses in the cervical canal. The axial oblique plane of the cervix is very useful in detecting stromal invasion, especially after the administration of gadolinium in a late phase (4 min) (*arrow*)

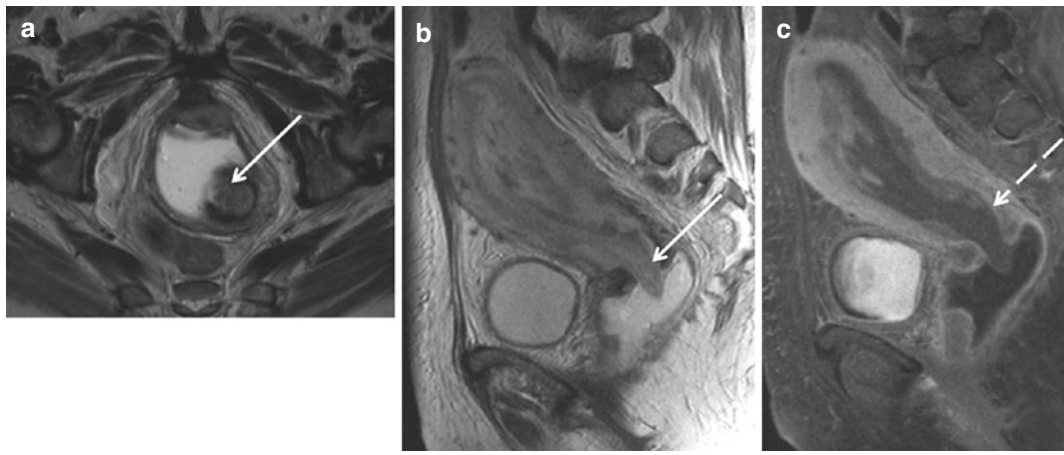

Fig. 18 Endometrial cancer prolapsed into the endocervical canal (**a**) Axial oblique plane of the cervix (perpendicular to the cervical canal) T2-weighted image: (**b**) sagittal T2-weighted image; (**c**) sagittal postcontrast injection 3D-reccaled echo fat-suppressed T1-weighted images in the equilibrium phase (120 s). Both axial oblique and sagittal T2-weighted images raise the suspicion of cervical invasion. However, there is normal enhancement of the cervical epithelium without any disruption, which excludes stage II disease

2012; Seki et al. 2000). Normal enhancement of the cervical epithelium is present in tumors that project into the endocervical canal but do not invade the cervical stroma (Fig. 18) (Tirumani et al. 2013; Haldorsen and Salvesen 2012).

2.2.3 Stage III Disease

Stage III disease is defined by local or regional spread of the tumor and it is subdivided into three substages (Pecorelli 2009).

In stage IIIA endometrial cancer, the tumor invades the serosa or/and the adnexa (Figs. 19 and 20).

Disruption of the serosal hypointense signal on T2-weighted images or loss of the enhancing myometrial outer margin on DCE-MR indicates serosal invasion (Fig. 19) (Tirumani et al. 2013; Manfredi et al. 2005).

The invasion of the ovaries may be due to direct extension via transmyometrial invasion or due to metastasis. Nodular foci in the adnexa are particularly frequent in type II endometrial cancer and in high-grade endometrioid carcinoma (Tirumani et al. 2013). DWI-MR is very useful in depicting these cases as well as pelvic peritoneal disease (Fig. 20) (Tirumani et al. 2013; Sala et al. 2010; Shen et al. 2008).

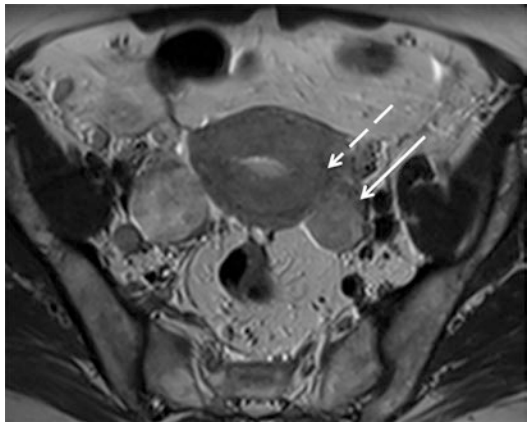

Fig. 19 Stage IIIA endometrioid carcinoma. (**a**) Axial oblique T2-weighted image shows disruption of the T2 hypointense serosal signal (*dashed arrow*) and tumoral invasion of the left ovary (*arrow*)

In stage IIIB disease, there is tumoral involvement of the parametria and/or the vagina by direct extension or by skip metastasis (Figs. 21, 22 and 23) (Pecorelli 2009). Images of the axial oblique plane of the cervix (perpendicular to the cervical canal) are very helpful in detecting parametrial invasion (Fig. 21). Detection of parametrial invasion is particularly important so surgeons can avoid perform a simple hysterectomy and thus perform a more extensive resection (Sala et al. 2013).

In stage IIIC endometrial cancer there is lymph node involvement (III_{C1} if there are positive pelvic lymph nodes and III_{C2} if there are positive paraaortic lymph nodes) (Fig. 24) (Pecorelli 2009).

MR sensitivity for detecting tumoral lymph node involvement is mostly low (Haldorsen and Salvesen 2012). The assessment of lymphadenopathies on MR imaging is still based on morphologic criteria (shortest axis diameter >10 mm) (Haldorsen and Salvesen 2012; Manfredi et al. 2004). DWI-MR helps detect lymph nodes, but there is a significant overlap with the ADC values of benign and malignant nodes (Nougaret et al. 2013; Nakai et al. 2008; Roy et al. 2010).

2.2.4 Stage IV Disease

Stage IV endometrial cancers are subdivided in two substages: stage IVA if there is invasion of

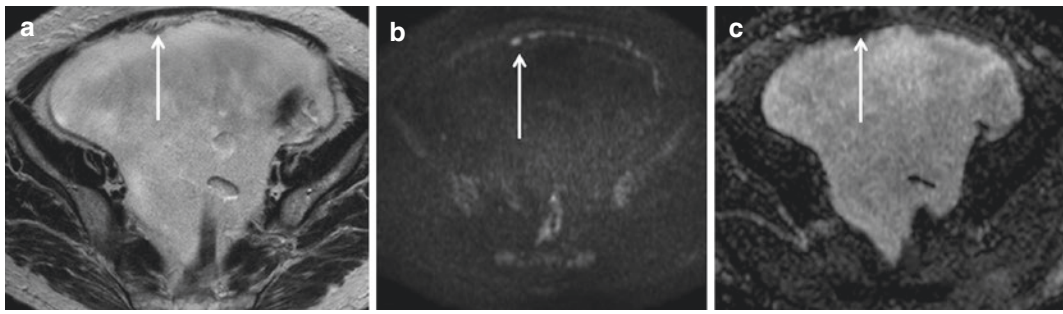

Fig. 20 Stage IIIA endometrioid carcinoma with subtle peritoneal nodules (**a**) axial T2-weighted image; (**b**) axial diffusion-weighted image (b = 1000 s/mm^2); (**c**) ADC map. Subtle peritoneal implants can be better depicted with diffusion-weighted images (*arrow*)

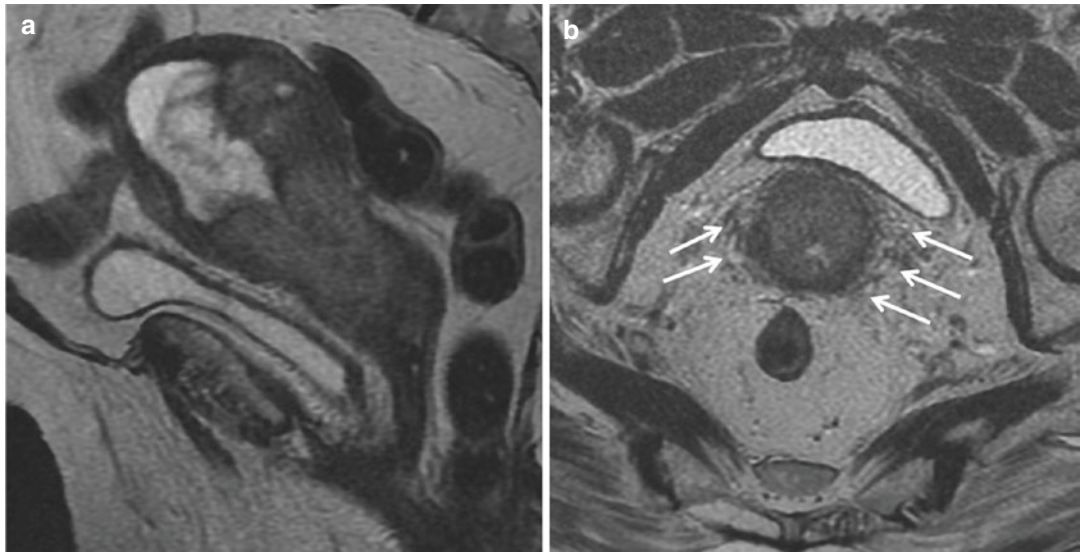

Fig. 21 Stage IIIB endometrioid carcinoma (**a**) sagittal T2-weighted image; (**b**) axial oblique plane of the cervix (perpendicular to the cervical canal) T2-weighted image**.** Parametrial invasion can be better depicted in the axial oblique plane of the cervix, where disruption of the hypointense stromal signal can be seen as well as tumor extending to both parametria (*arrows*)

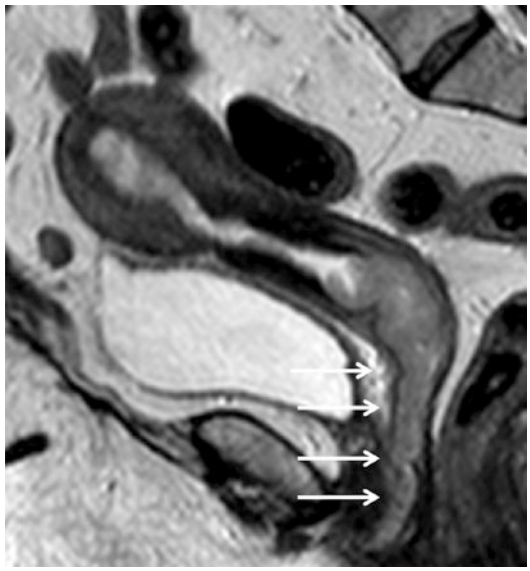

Fig. 22 Stage IIIB endometrioid carcinoma. (**a**) Sagittal T2-weighted image shows disruption of the T2 hypointense vaginal signal with invasion of the inferior third of the vagina (*arrows*)

the bladder or/and the bowel (Figs. 25 and 26); stage IVB if there are distant metastasis including abdominal metastasis and/or the presence of positive inguinal lymph nodes or/and para-aortic nodes above the renal hila (Fig. 27) (Pecorelli 2009).

For an endometrial tumor to be considered as stage IVA, a lesion transgressing the hypointense T2-signal of the muscularis propria of the bladder and/or of the bowel must be clearly seen, as well as disrupting the hyperintense signal of the mucosa (Figs. 25 and 26) (Tirumani et al. 2013). Moreover, tumoral enhancement within the lumen should also be present (Figs. 25 and 26). This is particularly important in the differential diagnosis of bladder bullous edema (a sign of tumoral involvement of the bladder serosa and muscular layer, but not of the mucosa), since it is not considered stage IVA disease (Sala et al. 2013).

Although rare at presentation, distant hematogenous disease most commonly affects the liver, lungs, and bone (Fig. 27) (Numazaki et al. 2009).

In type 2 endometrial cancer, and in high-grade endometrioid endometrial cancer, stage IVB disease may present as in ovarian cancers with peritoneal carcinomatosis (Tirumani et al. 2013; Sala et al. 2013).

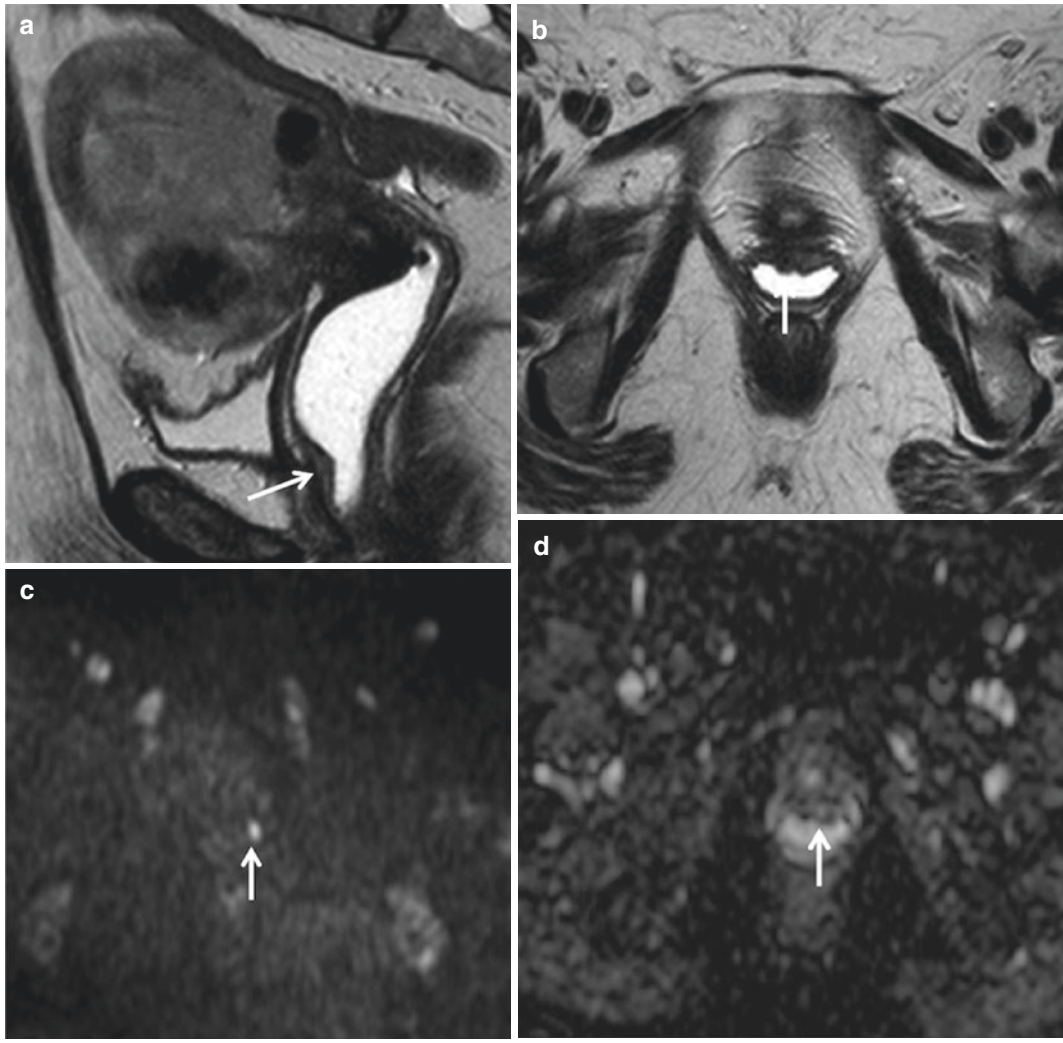

Fig. 23 Stage IIIB endometrioid carcinoma in a 62-year-old woman with skip vaginal metastasis. (**a**) Sagittal T2-weighted image; (**b**) axial T2-weighted image; (**c**) axial diffusion-weighted image (b = 1000 s/mm^2); (**d**) ADC map. In the anterior lower third of the vagina a small lesion showing restricted diffusion can be seen (*arrow*). It was diagnosed as a vaginal metastasis

3 Recent Advances in Functional MR Imaging in Assessing Endometrial Carcinoma

In perfusion MR, repeated acquisitions of sequential images during the passage of gadolinium through the tumor are performed. Tumoral signal intensity versus time graphs and quantitative perfusion maps may be obtained, making it possible to evaluate microvascularity parameters (Haldorsen and Salvesen 2012). The value of perfusion MR in assessing endometrial cancer is not yet established and validation studies are necessary to study its potential benefit.

Haldorsen et al. suggested that DCE-MRI may offer new information about the histological subtype and clinical course of endometrial carcinoma (Haldorsen et al. 2013). On the other hand, other studies regarding DCE-perfusion MR and tumor grading have shown contradictory results (Haldorsen et al. 2013; Ippolito et al. 2014a, b).

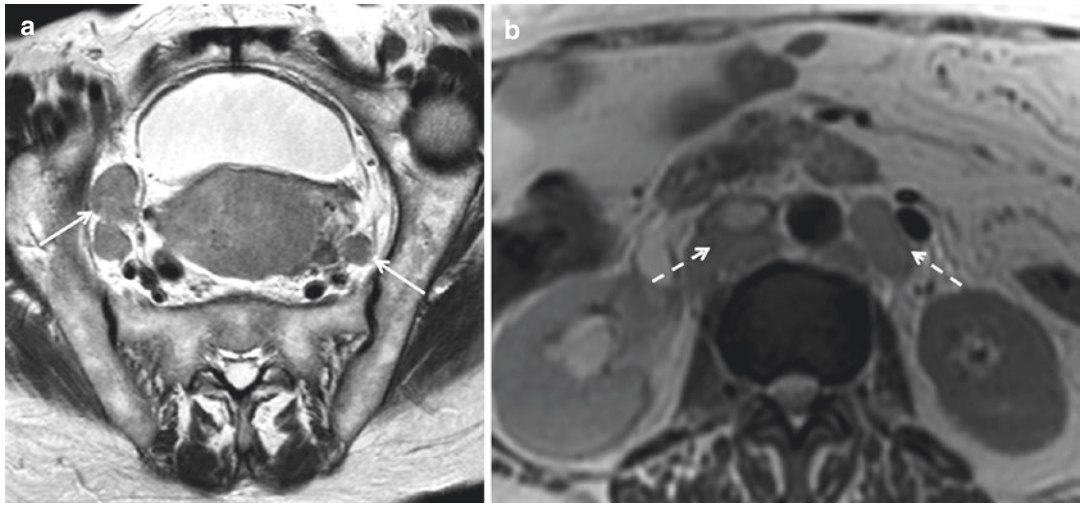

Fig. 24 Stage IIIC endometrial cancer (**a**) axial T2-weighted image shows pelvic lymphadenopathies (*arrows*) (stage III_{C1} disease); (**b**) axial T2-weighted image shows para-aortic lymphadenopathies (*dashed arrows*) (Stage III_{C2} disease)

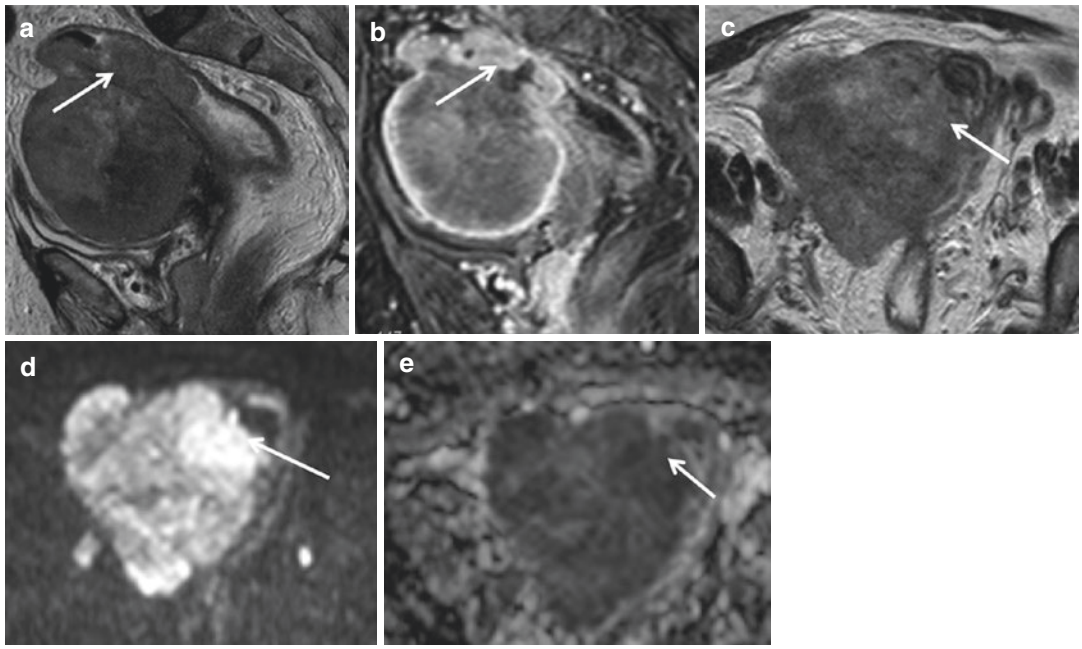

Fig. 25 Stage IVA endometrioid carcinoma that invades the sigmoid colon in a 75-year-old woman. (**a**) Sagittal T2-weighted image; (**b**) sagittal 3D fat-suppressed T1-weighted sequence after the administration of gadolinium in the equilibrium phase (120–180 s); (**c**) axial T2-weighted image; (**d**) axial diffusion-weighted image (b = 1000 s/mm^2); (**e**) ADC map. T2-weighted images show disruption of the hypointense signal of the sigmoid colon wall and mucosal invasion. There is tumoral enhancement within the lumen. The tumor shows also marked restricted diffusion, which can also be seen in the sigmoid lumen

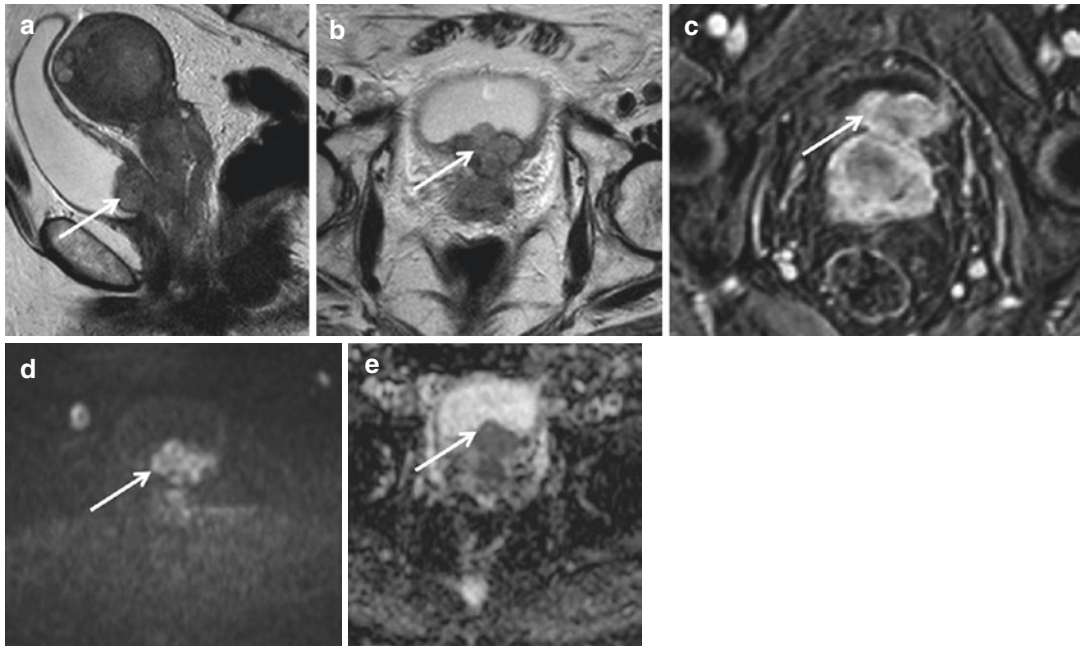

Fig. 26 Stage IVA endometrioid carcinoma that invades the bladder in a 76-year-old woman. (**a**) Sagittal T2-weighted image; (**b**) axial T2-weighted image; (**c**) axial oblique 3D fat-suppressed T1-weighted sequence after the administration of gadolinium in the equilibrium phase (120 s); (**d**) axial diffusion-weighted image (b = 1000 s/mm^2); (**e**) ADC map. T2-weighted images show disruption of the hypointense signal of the bladder wall and mucosal invasion. There is tumoral enhancement within the lumen. The tumor shows also marked restricted diffusion, which can also be seen in the bladder lumen

4 Therapeutic Approaches

4.1 Surgery

All medical operable patients with endometrial cancer should be considered for surgery (Koh et al. 2014).

The standard surgical approach of endometrial cancer consists of total hysterectomy with bilateral salpingo-oophorectomy, assessment of the abdominal cavity with biopsies of suspicious peritoneal lesions, cytology of peritoneal washing, and at least excision of enlarged lymph nodes (Koh et al. 2014).

Although, systematic pelvic and para-aortic lymphadenopathy is considered part of FIGO surgico-pathological staging, there is still no consensus if it should be performed in cases of treatment of stage I endometrial cancer (Koh et al. 2014; Colombo et al. 2013; Soliman et al. 2010).

A randomized study has shown that in patients where systematic lymphadenectomy was performed, a higher rate of postoperative complications was detected with no improvement of disease-free and overall survival rates (Benedetti Panici et al. 2008). The ASTEC surgical trial also concluded that pelvic lymphadenectomy in patients with early disease did not improve overall or recurrence-free survival (ASTEC study group et al. 2009). These two studies had important limitations and caution must be taken to avoid overinterpretation.

On the other hand, a large retrospective study, the SEPAL study, showed survival benefits in patients with intermediate (FIGO IA and IB, grade 3 endometrioid carcinoma; FIGO IB, grade 1 and 2 endometrioid carcinoma with lymphovascular space invasion; FIGO IC and II endometrioid carcinoma; any type of type 2 endometrial cancer) and high risk (FIGO III and IV endometrioid carcinoma) endometrial carcinoma when

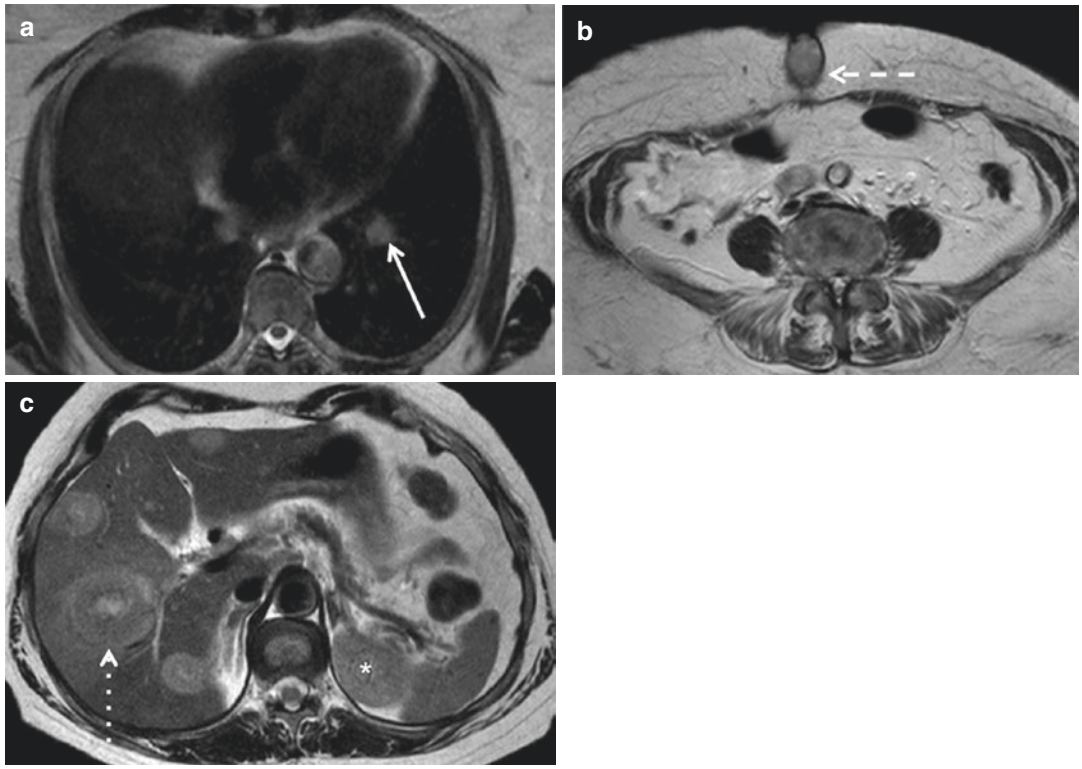

Fig. 27 Stage IVB disease (**a**) axial T2-weighted image showing a pulmonary metastasis *(arrow)*; (**b**) axial T2-weighted image showing an umbilical metastasis (Sister Mary Joseph node) (*dashed arrow*); (**c**) axial T2-weighted image showing hepatic metastasis (*dotted arrows*) and a left adrenal metastasis (*asterisk*)

submitted to combined pelvic and para-aortic lymphadenectomy (Todo et al. 2010).

Women with stage II should be considered for radical hysterectomy with bilateral salpingo-oophorectomy and pelvic and para-aortic lymphadenectomy (Colombo et al. 2013).

In patients with a good performance status with advanced stage disease (FIGO stage III and IV), maximum debulking surgery of resettable tumors should be performed. Anterior and posterior pelvic exenteration can be considered for stage IVA disease as well as palliative surgery in patients with metastatic disease (Colombo et al. 2013).

Women with serous, clear-cell carcinomas and carcinosarcomas should be submitted to the same surgical-pathological staging of ovarian cancer (Koh et al. 2014). Serous and clear-cell carcinomas can occur in atrophic endometrium and may present with distant disease even without myometrial invasion; therefore, omentectomy, diaphragmatic cytology or biopsy, and random peritoneal biopsies should be performed (Koh et al. 2014; Colombo et al. 2013). Pelvic and para-aortic lymphadenectomy is mandatory (Colombo et al. 2013).

4.2 Adjuvant Treatment

Radiation therapy is usually used in the adjuvant setting, in the form of external beam radiation therapy (EBRT) and vaginal brachytherapy (VBT).

The purpose of adjuvant radiation therapy is to eliminate microscopic disease in the lymph nodes and in the central pelvic region, including the vaginal cuff; thus reducing the risk of recurrence.

According to the 2014 guidelines of the American Society for Radiation Oncology (ASTRO), patients with endometrioid carcinoma

that do not require adjuvant radiotherapy (RT) are women with no residual disease in the hysterectomy specimen and patients with grade 1 or 2 endometrial cancer with no myometrial invasion or with <50 % of myometrial invasion, especially when no high risk features are present (Klopp et al. 2014). Patients with grade 3 endometrioid carcinoma without myometrial invasion and patients with grade 1 or 2 cancer with <50 % of myometrial invasion and higher risk factors, such as being age >60 years and/or lymphovascular space invasion, can be adequately treated with or without VBT (Klopp et al. 2014).

These guidelines also identify the patients with endometrioid cancer for whom vaginal cuff brachytherapy is as effective as pelvic radiation therapy and consequently should be preferred. These patients are women with grade 1 or 2 cancers with ≥50 % of myometrial invasion and women with grade 3 tumors with <50 % of myometrial invasion (Klopp et al. 2014).

In order to decrease pelvic recurrence, the following women with early phase endometrial cancer should receive adjuvant EBRT: patients with stage I, grade 3 cancer with ≥50 % of myometrial invasion or patients with cervical stromal invasion; patients with stage I, grade 1 or 2 cancer, with ≥50 % of myometrial invasion and other risk factors such as being of age >60 years and/or lymphovascular space invasion (Klopp et al. 2014).

If there is a negative prognostic factor, pelvic RT and/or chemotherapy should be performed for stage I and stage II disease (Colombo et al. 2013).

In patients with stage III and IVA disease, external EBRT and adjuvant chemotherapy are justifiable options. These patients can be considered for concurrent chemoradiation followed by adjuvant chemotherapy (Klopp et al. 2014).

If metastatic disease is present, chemotherapy-radiotherapy can be performed for palliative treatment (Colombo et al. 2013).

Patients with serous carcinomas, clear-cell carcinomas, and carcinosarcomas should be considered for platinum-based adjuvant chemotherapy with or without radiation therapy (Koh et al. 2014).

4.3 Fertility-Sparing Treatment

Fertility-sparing treatment with progestin hormonal therapy may be considered for women who express the desire to preserve fertility and have atypical endometrial hyperplasia or grade 1 endometrioid carcinoma without myometrial involvement in MR (Jafari Shobeiri et al. 2013; Kesterson and Fanning 2012; Colombo et al. 2016). However, this is not the standard of care and the decision to proceed with conservative management is associated with several hazards. Risks include an inadequately staged and treated advanced endometrial cancer; the presence of a synchronous or meta-synchronous cancer; the presence of an inherited genetic predisposition; and the absence of standard medical management and surveillance (Kesterson and Fanning 2012).

5 Follow-Up and Recurrent Endometrial Carcinoma

The majority of recurrences will occur within the first 3 years (80 %) (Tirumani et al. 2013). However, only 15 % of patients will develop recurrent disease (Sala et al. 2013; Magrina et al. 2011).

The recommended follow-up is a clinical and gynecological exam at 3–4 months intervals during the first 2 years and then every 6 months until 5 years (Colombo et al. 2013).

During follow-up, radiological exams should only be performed if clinically indicated (Colombo et al. 2013).

Most of endometrial cancer recurrences occur in the lymph nodes (46 %) and in the vaginal vault (42 %) (Sohaib et al. 2007). The peritoneum and lungs are also reported sites of recurrence, although less frequent (Sohaib et al. 2007).

MR imaging is very useful in diagnosing vaginal vault recurrences, which characteristically display the same signal characteristics as of those of the primary tumor (Tirumani et al. 2013). They tend to appear as a mass disrupting the low signal intensity of the vaginal vault (Sala et al. 2013). MR in these cases plays a role in defining surgical resectability of pelvic recurrences.

PET-CT has shown high sensitivity (93 %), specificity (93 %), and accuracy (93 %) in detecting recurrent disease (Kitajima et al. 2008). However, more prospective larger studies must determine its role for routine screening (Salani et al. 2011).

5.1 Treatment of Recurrence

Treatment of recurrence varies according to the site, to previous treatments, and to the initial stage of the disease.

Vaginal recurrence is the most common and the standard of treatment is EBRT plus VBP (Colombo et al. 2013).

Central pelvic recurrence is usually treated with surgery and radiation therapy, whereas regional pelvic recurrence is treated with radiation therapy plus chemotherapy if possible (Colombo et al. 2013).

Recurrent serous and clear-cell carcinomas should be treated with the same chemotherapeutic regimens of ovarian cancer (Colombo et al. 2013).

6 Prognosis

As stated previously, endometrial carcinoma generally has a good outcome. Prognostic factors include histological subtype; histological grade; tumor stage; depth of invasion; and lymphovascular space invasion (Colombo et al. 2013).

Reported 5-year survival rates for stage IA and IB are of 88 % and of 75 %, respectively. The prognosis of the different types of stage III substages differs significantly from one another, with estimated 5-year survival rates of 58 % for stage III_{C1} and of 47 % for stage III_{C2}. Stage IV disease 5-year survival is estimated at 15–17 % (American Cancer Society 2016).

The presence of lymph node metastasis, namely para-aortic, has shown to have a strong effect on prognosis (Todo et al. 2010). Tumor grade, lymphovascular space involvement, and the depth of myometrial invasion have been reported as high risk factors for the tumoral involvement of lymph nodes (Patel et al. 2010).

Invasion of the outer half of the myometrium is also strongly associated with a diminished 5-year survival rate (Patel et al. 2010; Amant et al. 2005). Furthermore, it was demonstrated that patients with lymphovascular space involvement had an overall 5-year survival rate of 64 %, and on the other hand women without lymphovascular space involvement had an overall 5-year survival rate of 88 % (Colombo et al. 2013).

Conclusion

Magnetic resonance imaging is not considered in the International Federation of Gynaecology and Obstetrics staging system. However, it plays a relevant role in the preoperative staging of endometrial carcinomas, helping to define the best therapeutic approaches. Moreover, it is important in the diagnosis of treatment complications, in the surveillance of therapy response, and in the assessment of recurrent disease.

Functional MR techniques and specific MR sequence planes play an important role in preventing errors in endometrial cancer staging.

To help prevent diagnostic errors and in order to guide appropriate therapeutic management, radiologists should be aware of common magnetic resonance imaging endometrial appearances for all stages and the frequent mistakes in the assessment of endometrial cancer.

References

Amant F, Moerman P, Neven P, Timmerman D, Van Limbergen E, Vergote I (2005) Endometrial cancer. Lancet 366(9484):491–505

Amant F, Moerman P, Neven P, Timmerman D, Van Limbergen E, Vergote I (2007) Treatment modalities in endometrial cancer. Curr Opin Oncol 19(5):479–485

American Cancer Society (2016) http://www.cancer.org/cancer/endometrialcancer/detailedguide/endometrial-uterine-cancer-survival-rates. Accessed 25 May 2016

Andreano A, Rechichi G, Rebora P, Sironi S, Valsecchi MG, Galimberti S (2014) MR diffusion imaging for preoperative staging of myometrial invasion in patients with endometrial cancer: a systematic review and

meta-analysis. Eur Radiol 24(6):1327–1338. doi:10.1007/s00330-014-3139-4

ASTEC Study Group, Kitchener H, Swart AM, Qian Q, Amos C, Parmar MK (2009) Efficacy of systematic pelvic lymphadenectomy in endometrial cancer (MRC ASTEC trial): a randomised study. Lancet 373(9658):125–136. doi:10.1016/S0140-6736(08)61766-3

Beddy P, Moyle P, Kataoka M, Yamamoto AK, Joubert I, Lomas D et al (2012) Evaluation of depth of myometrial invasion and overall staging in endometrial cancer: comparison of diffusion-weighted and dynamic contrast-enhanced MR imaging. Radiology 262(2): 530–537. doi:10.1148/radiol.11110984

Benedetti Panici P, Basile S, Maneschi F, Alberto Lissoni A, Signorelli M, Scambia G et al (2008) Systematic pelvic lymphadenectomy vs no lymphadenectomy in early-stage endometrial carcinoma: randomized clinical trial. J Natl Cancer Inst 100(23):1707–1716. doi:10.1093/jnci/djn397

Bennet GL, Andreotti RF, Lee SI, Dejesus Allison SO, Brown DL, Dubinsky T et al (2011 Jul) ACR Appropriateness Criteria® on Abnormal Vaginal Bleeding. J Am Coll Radiol 8(7):460–468. doi:10.1016/j.jacr.2011.03.011

Bharwani N, Miquel ME, Sahdev A, Narayanan P, Malietzis G, Reznek RH et al (2011) Diffusion-weighted imaging in the assessment of tumour grade in endometrial cancer. Br J Radiol 84(1007):997–1004. doi:10.1259/bjr/14980811

Bonatti M, Stuefer J, Oberhofer N, Negri G, Tagliaferri T, Schifferle G et al (2015) MRI for local staging of endometrial carcinoma: is endovenous contrast medium administration still needed? Eur J Radiol 84(2):208–214. doi:10.1016/j.ejrad.2014.11.010

Boronow RC (1990) Advances in diagnosis, staging, and management of cervical and endometrial cancer Stages I and II. Cancer 65(3 Suppl):648–659

Briët JM, Hollema H, Reesink N, Aalders JG, Mourits MJE, Hoor ten KA et al (2005) Lymphvascular space involvement: an independent prognostic factor in endometrial cancer. Gynecol Oncol 96(3):799–804

Calle EE, Kaaks R (2004) Overweight, obesity and cancer: epidemiological evidence and proposed mechanisms. Nat Rev Cancer 4(8):579–591

Cancer Incidence Statistics (2015) http://www.cancerresearchuk.org/health-professional/cancer-statistics/statistics-by-cancer-type/uterine-cancer. Accessed on 22 May 2015

Colombo N, Preti E, Landoni F, Carinelli S, Colombo A, Marini C et al (2013) Endometrial cancer: ESMO Clinical Practice Guidelines for diagnosis, treatment and follow-up. Ann Oncol 24(Suppl 6):vi33–vi38. doi:10.1093/annonc/mdt353

Colombo N, Creutzberg C, Amant F, Bosse T, González-Martín A, Ledermann J et al (2016) ESMO-ESGO-ESTRO consensus conference on endometrial cancer: diagnosis, treatment and follow-up. Int J Gynecol Cancer 26(1):2–30. doi:10.1097/IGC.0000000000000609

Creasman W (2009) Revised FIGO staging for carcinoma of the endometrium. Int J Gynaecol Obstet 105(2):109. doi:10.1016/j.ijgo.2009.02.010

Eichhorn JH, Young RH (2001) Neuroendocrine tumors of the genital tract. Am J Clin Pathol 115(Suppl):S94–112

Epstein E, Blomqvist L (2014) Imaging in endometrial cancer. Best Pract Res Clin Obstet Gynaecol 28(5):721–739. doi:10.1016/j.bpobgyn.2014.04.007

Fanning J, Tsukada Y, Piver MS (1990) Intraoperative frozen section diagnosis of depth of myometrial invasion inendometrial adenocarcinoma. Gynecol Oncol 37(1):47–50

Ferlay J, Soerjomataram I, Ervik M, Dikshit R, Eser S, Mathers C, Rebelo M et al (2013) Cancer Incidence and Mortality Worldwide: IARC CancerBase No. 11 [Internet]. Lyon: International Agency for Research on Cancer. Available from: http://globocan.iarc.fr. Accessed 23 May 2015

Fisher B, Costantino JP, Redmond CK, Fisher ER, Wickerham DL, Cronin WM (1994) Endometrial cancer in tamoxifen-treated breast cancer patients: findings from the National Surgical Adjuvant Breast and Bowel Project (NSABP) B-14. J Natl Cancer Inst 86(7):527–537

Frei KA, Kinker K (2001) Staging endometrial cancer: role of magnetic resonance imaging. J Magn Reson Imaging 13(6):850–855

Frei KA, Kinkel K, Bonél HM, Lu Y, Zaloudek C, Hricak H (2000) Prediction of deep myometrial invasion in patients with endometrial cancer: clinical utility of contrast-enhanced MR imaging–a meta-analysis and bayesian analysis. Radiology 216(2):444–449

Fujii S, Matsusue E, Kigawa J, Sato S, Kanasaki Y, Nakanishi J et al (2008) Diagnostic accuracy of the apparent diffusion coefficient in differentiating benign from malignant uterine endometrial cavity lesions: initial results. Eur Radiol 18(2):384–389

Fujii S, Kido A, Baba T, Fujimoto K, Daido S, Matsumura N (2015) Subendometrial enhancement and peritumoral enhancement for assessing endometrial cancer on dynamic contrast enhanced MR imaging. Eur J Radiol 84(4):581–589. doi:10.1016/j.ejrad.2015.01.004

Gallego JC, Porta A, Pardo MC, Fernández C (2014) Evaluation of myometrial invasion in endometrial cancer: comparison of diffusion-weighted magnetic resonance and intraoperative frozen sections. Abdom Imaging 39(5):1021–1026. doi:10.1007/s00261-014-0134-9

Goldstein RB, Bree RL, Benson CB, Benacerraf BR, Carlos R et al (2001) Evaluation of the woman with postmenopausal bleeding: society of radiologists in ultrasound-sponsored consensus conference statement. J Ultrasound Med 20(10):1025–1036

Gull B, Karlsson B, Milsom I, Granber S (2003) Can ultrasound replace dilation and curettage? A longitudinal evaluation of postmenopausal bleeding and transvaginal sonographic measurement of the endometrium as predictors of endometrial cancer. Am J Obstet Gynecol 188(2):401–408

Gupta JK, Chien PF, Voit D, Clark TJ, Khan KS (2002) Ultrasonographic endometrial thickness for diagnosing endometrial pathology in women with postmenopausal bleeding: a meta-analysis. Acta Obstet Gynecol Scand 81(9):799–816

Haider MA, Patlas M, Jhaveri K, Chapman W, Fyles A, Rosen B (2006) Adenocarcinoma involving the uterine cervix: magnetic resonance imaging findings in tumours of endometrial, compared with cervical, origin. Can Assoc Radiol J 57(1):43–48

Haldorsen IS, Salvesen HB (2012) Staging of endometrial carcinomas with MRI using traditional and novel MRI techniques. Clin Radiol 67(1):2–12. doi:10.1016/j.crad.2011.02.018

Haldorsen IS, Grüner R, Husby JA, Magnussen IJ, Werner HMJ, Salvesen ØO et al (2013) Dynamic contrast-enhanced MRI in endometrial carcinoma identifies patients at increased risk of recurrence. Eur Radiol 23(10):2916–2925. doi:10.1007/s00330-013-2901-3

Hecht JL, Mutter GL (2006) Molecular and pathologic aspects of endometrial carcinogenesis. J Clin Oncol 24(29):4783–4791

Hori M, Kim T, Onishi H, Imaoka I, Kagawa Y, Murakami T et al (2013) Endometrial cancer: preoperative staging using three-dimensional T2-weighted turbo spin-echo and diffusion-weighted MR imaging at 3.0 T: a prospective comparative study. Eur Radiol 23(8):2296–2305. doi:10.1007/s00330-013-2815-0

Hulka CA, Hall DA, McCarthy K, Simeone JF (1994) Endometrial polyps, hyperplasia, and carcinoma in postmenopausal women: differentiation with endovaginal sonography. Radiology 191(3):755–758

Ippolito D, Minutolo O, Cadonici A, Talei Franzesi C, Bonaffini P, Perego P et al (2014a) Endometrial cancer: diagnostic value of quantitative measurements of microvascular changes with DCE-MR imaging. MAGMA 27(6):531–538. doi:10.1007/s10334-014-0435-6

Ippolito D, Cadonici A, Bonaffini PA, Minutolo O, Casiraghi A, Perego P et al (2014b) Semiquantitative perfusion combined with diffusion-weighted MR imaging in pre-operative evaluation of endometrial carcinoma: Results in a group of 57 patients. Magn Reson Imaging 32(5):464–472. doi:10.1016/j.mri.2014.01.009

Jafari Shobeiri M, Mostafa Gharabaghi P, Esmaeili H, Ouladsahebmadarek E, Mehrzad-Sadagiani M (2013) Fertility sparing treatment in young patients with early endometrial adenocarcinoma: case series. Pak J Med Sci 29(2):651–655

Jalloul RJ, Elshaikh MA, Ali-Fehmi R, Haley MM, Yoon J, Mahan M et al (2012) Mucinous adenocarcinoma of the endometrium. Int J Gynecol Cancer 22(5):812–818. doi:10.1097/IGC.0b013e31824a

Järvinen HJ, Renkonen-Sinisalo L, Aktán-Collán K, Peltomäki P, Aaltonen LA, Mecklin J-P (2009) Ten years after mutation testing for Lynch syndrome: cancer incidence and outcome in mutation-positive and mutation-negative family members. J Clin Oncol 27(28):4793–4797. doi:10.1200/JCO.2009.23.7784

Kaneda S, Fujii S, Fukunaga T, Kakite S, Kaminou T, Kigawa J et al (2011) Myometrial invasion by endometrial carcinoma: evaluation with 3.0 T MR imaging. Abdom Imaging 36(5):612–618. doi:10.1007/s00261-011-9719-8

Karlsson B, Granberg S, Wikland M, Ylostalo P, Torvid K, Marsal K et al (1995) Transvaginal ultrasonography of the endometrium in women withpostmenopausal bleeding—a Nordic multicenter study. Am J Obstet Gynecol 172(5):1488–1494

Kesterson JP, Fanning J (2012) Fertility-sparing treatment of endometrial cancer: options, outcomes and pitfalls. J Gynecol Oncol 23(2):120–124. doi:10.3802/jgo.2012.23.2.120

Kinkel K (2006) Pitfalls in staging uterine neoplasm with imaging: a review. Abdom Imaging 31(2):164–173

Kitajima K, Murakami K, Yamasaki E, Domeki Y, Kaji Y, Morita S et al (2008) Performance of integrated FDG-PET/contrast-enhanced CT in the diagnosis of recurrent uterine cancer: comparison with PET and enhanced CT. Eur J Nucl Med Mol Imaging 36(3):362–372. doi:10.1007/s00259-008-0956-1

Klopp A, Smith BD, Alektiar K, Cabrera A, Damato AL, Erikson B et al (2014) The role of postoperative radiation therapy for endometrial cancer: Executive Summary of an American Society for Radiation Oncology evidence-based guideline. Pract Radiat Oncol 4(3):137–144. doi:10.1016/j.prro.2014.01.003

Koh WJ, Greer BE, Abu-Rustum NR, Apte SM, Campos SM, Chan J et al (2014) Uterine Neoplasms, version 1.2014. J Natl Compr Canc Netw 12(2):248–280

Koyama T, Tamai K, Togashi K (2007) Staging of carcinoma of the uterine cervix and endometrium. Eur Radiol 17(8):2009–2019

Kurman RJ, Carcangiu ML, Herrington CS, Young RH (2014) Tumours of the Uterine Corpus. In: WHO classification of tumours of female reproductive organs, vol 6, 4th edn. International Agency for Research on Cancer, Lyon, pp. 121–155

Larson DM, Connor GP, Broste SK, Krawisz BR, Johnson KK (1996) Prognostic significance of gross myometrial invasion with endometrial cancer. Obstet Gynecol 88(3):394–398

Lopes Dias J, Cunha TM, Gomes FV, Callé C, Félix A (2015) Neuroendocrine tumours of the female genital tract: a case-based imaging review with pathological correlation. Insights Imaging 6(1):43–52. doi:10.1007/s13244-014-0378-5

Magrina JF, Zanagnolo V, Giles D, Noble BN, Kho RM, Magtibay PM (2011) Robotic surgery for endometrial cancer: comparison of perioperative outcomes and recurrence with laparoscopy, vaginal/laparoscopy and laparotomy. Eur J Gynaecol Oncol 32(5):476–480

Manfredi R, Mirk P, Maresca G, Margariti PA, Testa A, Zannoni GF et al (2004) Local-regional staging of endometrial carcinoma: role of MR imaging in surgical planning. Radiology 231(2):372–378

Manfredi R, Gui B, Maresca G, Fanfani F, Bonomo L (2005) Endometrial cancer: magnetic resonance imaging. Abdom Imaging 30(5):626–636

May K, Bryant A, Dickinson HO, Kehoe S, Morrison J (2010) Lymphadenectomy for the management of endometrial cancer. Cochrane Database Syst Rev 20(1):CD007585. doi:10.1002/14651858.CD007585.pub2

McPherson CP, Sellers TA, Potter JD, Bostick RM, Folsom AR (1996) Reproductive factors and risk of endometrial cancer. The Iowa Women's Health Study. Am J Epidemiol 143(12):1195–1202

Meyer LA, Broaddus RR, Lu KH (2009) Endometrial cancer and Lynch syndrome: clinical and pathologic considerations. Cancer Control 16(1):14–22

Nakai G, Matsuki M, Inada Y, Tatsugami F, Tanikake M, Narabayashi I et al (2008) Detection and evaluation of pelvic lymph nodes in patients with gynecologic malignancies using body diffusion-weighted magnetic resonance imaging. J Comput Assist Tomogr 32(5):764–768. doi:10.1097/RCT.0b013e318153fd43

Nakao Y, Yokoyama M, Hara K, Koyamatsu Y, Yasunaga M, Araki Y et al (2006) MR imaging in endometrial carcinoma as a diagnostic tool for the absence of myometrial invasion. Gynecol Oncol 102(2):343–347

Nougaret S, Tirumani SH, Addley H, Pandey H, Sala E, Reinhold C (2013) Pearls and pitfalls in MRI of gynecologic malignancy with diffusion-weighted technique. AJR Am J Roentgenol 200(2):261–276. doi:10.2214/AJR.12.9713

Nougaret S, Reinhold C, Alsharif SS, Addley H, Arceneau J, Molinari N et al (2015) Endometrial cancer: combined MR volumetry and diffusion-weighted imaging for assessment of myometrial and lymphovascular invasion and tumor grade. Radiology 276(3):797–808. doi:10.1148/radiol.15141212

Numazaki R, Miyagi E, Konnai K, Ikeda M, Yamamoto A, Onose R et al (2009) Analysis of stage IVB endometrial carcinoma patients with distant metastasis: a review of prognoses in 55 patients. Int J Clin Oncol 14(4):344–350. doi:10.1007/s10147-009-0878-3

Patel S, Liyanage SH, Sahdev A, Rockall AG, Reznek RH (2010) Imaging of endometrial and cervical cancer. Insights Imaging 1(5–6):309–328

Pecorelli S (2009) Revised FIGO staging for carcinoma of the vulva, cervix, and endometrium. Int J Gynaecol Obstet 105(2):103–104

Rechichi G, Galimberti S, Signorelli M, Perego P, Valsecchi MG, Sironi S (2010) Myometrial invasion in endometrial cancer: diagnostic performance of diffusion-weighted MR imaging at 1.5-T. Eur Radiol 20(3):754–762. doi:10.1007/s00330-009-1597-x

Rechichi G, Galimberti S, Signorelli M, Franzesi CT, Perego P, Valsecchi MG et al (2011) Endometrial cancer: correlation of apparent diffusion coefficient with tumor grade, depth of myometrial invasion, and presence of lymph node metastases. AJR Am J Roentgenol 197(1):256–262. doi:10.2214/AJR.10.5584

Renehan AG, Tyson M, Egger M, Heller RF, Zwahlen M (2008) Body-mass index and incidence of cancer: a systematic review and meta-analysis of prospective observational studies. Lancet 371(9612):569–578. doi:10.1016/S0140-6736(08)60269-X

Resnick KE, Hampel H, Fishel R, Cohn DE (2009) Current and emerging trends in Lynch syndrome identification in women with endometrial cancer. Gynecol Oncol 114(1):128–134. doi:10.1016/j.ygyno.2009.03.003 Epub 2009 Apr 17

Roy C, Bierry G, Matau A, Bazille G, Pasquali R (2010) Value of diffusion-weighted imaging to detect small malignant pelvic lymph nodes at 3 T. Eur Radiol 20(8):1803–1811. doi:10.1007/s00330-010-1736-4

Saez F, Urresola A, Larena JA, Martín JI, Pijuán JI, Schneider J et al (2000) Endometrial carcinoma: assessment of myometrial invasion with plain and gadolinium-enhanced MR imaging. J Magn Reson Imaging 12(3):460–466

Sala E, Rockall A, Rangarajan D, Kubik-Huch RA (2010) The role of dynamic contrast-enhanced and diffusion weighted magnetic resonance imaging in the female pelvis. Eur J Radiol 76(3):367–385. doi:10.1016/j.ejrad.2010.01.026

Sala E, Rockall AG, Freeman SJ, Mitchell DG, Reinhold C (2013) The added role of MR imaging in treatment stratification of patients with gynecologic malignancies: what the radiologist needs to know. Radiology 266(3):717–740. doi:10.1148/radiol.12120315

Salani R, Backes FJ, Fung MF, Holschneider CH, Parker LP, Bristow RE et al (2011 Jun) Posttreatment surveillance and diagnosis of recurrence in women with gynecologic malignancies: society of Gynecologic Oncologists recommendations. Am J Obstet Gynecol 204(6):466–478. doi:10.1016/j.ajog.2011.03.008

Schmeler KM, Lynch HT, Chen LM, Munsell MF, Soliman PT, Clark MB et al (2006) Prophylactic surgery to reduce the risk of gynecologic cancers in the lynch syndrome. N Engl J Med 354(3):261–269

Scoutt LM, McCarthy SM, Flynn SD, Lange RC, Long F, Smith RC et al (1995) Clinical stage I endometrial carcinoma: pitfalls in preoperative assessment with MR imaging Work in progress. Radiology 194(2):567–572

Seki H, Takano T, Sakai K (2000) Value of dynamic MR imaging in assessing endometrial carcinoma involvement of the cervix. AJR Am J Roentgenol 175(1):171–176

Setiawan VW, Yang HP, Pike MC, McCann SE, Yu H, Xiang Y-B et al (2013) Type I and II endometrial cancers: have they different risk factors? J Clin Oncol 31(20):2607–2618. doi:10.1200/JCO.2012.48.2596

Shapiro S, Kelly JP, Rosenberg L, Kaufman DW, Helmrich SP, Rosenshein NB et al (1985) Risk of localized and widespread endometrial cancer in relation to recent and discontinued use of conjugated estrogens. N Engl J Med 313(16):969–972

Shen S-H, Chiou Y-Y, Wang J-H, Yen M-S, Lee R-C, Lai C-R et al (2008) Diffusion-weighted single-shot echo-planar imaging with parallel technique in assessment

of endometrial cancer. Am J Roentgenol 190(2):481–488. doi:10.2214/AJR.07.2155

Smith-Bindman R, Kerlikowske K, Feldstein VA, Subak L, Scheidler J, Segal M et al (1998) Endovaginal ultrasound to exclude endometrial cancer and other endometrial abnormalities. JAMA 280(17):1510–1517

Sohaib SA, Houghton SL, Meroni R, Rockall AG, Blake P, Reznek RH (2007) Recurrent endometrial cancer: patterns of recurrent disease and assessment of prognosis. Clin Radiol 62(1):28–34

Soliman PT, Wu D, Tortolero-Luna G, Schmeler KM, Slomovitz BM, Bray MS et al (2006) Association between adiponectin, insulin resistance, and endometrial cancer. Cancer 106(11):2376–2381

Soliman PT, Frumovitz M, Spannuth W, Greer MJ, Sharma S, Schmeler KM et al (2010 Nov) Lymphadenectomy during endometrial cancer staging: Practice patterns among gynecologic oncologists. Gynecol Oncol 119(2):291–294. doi:10.1016/j.ygyno.2010.07.011

Takeuchi M, Matsuzaki K, Nishitani H (2009) Diffusion-weighted magnetic resonance imaging of endometrial cancer: differentiation from benign endometrial lesions and preoperative assessment of myometrial invasion. Acta Radiol 50(8):947–953. doi:10.1080/02841850903099981

Tamai K, Koyama T, Saga T, Umeoka S, Mikami Y, Fujii S et al (2007) Diffusion-weighted MR imaging of uterine endometrial cancer. J Magn Reson Imaging 26(3):682–687

Tirumani SH, Shanbhogue AK, Prasad SR (2013) Current concepts in the diagnosis and management of endometrial and cervical carcinomas. Radiol Clin North Am 51(6):1087–1110. doi:10.1016/j.rcl.2013.07.003

Todo Y, Kato H, Kaneuchi M, Watari H, Takeda M, Sakuragi N (2010) Survival effect of para-aortic lymphadenectomy in endometrial cancer (SEPAL study): a retrospective cohort analysis. Lancet 375(9721):1165–1172. doi:10.1016/S0140-6736(09)62002-X

Vargas HA, Akin O, Zheng J, Moskowitz C, Soslow R, Abu-Rustum N et al (2011) The value of MR imaging when the site of uterine cancer origin is uncertain. Radiology 258(3):785–792. doi:10.1148/radiol.10101147

Venkat P, Chen LM, Young-Lin N, Kiet TK, Young G, Amatori D et al (2012) An economic analysis of robotic versus laparoscopic surgery for endometrial cancer: costs, charges and reimbursements to hospitals and professionals. Gynecol Oncol 125(1):237–240. doi:10.1016/j.ygyno.2011.11.036

Wakefield JC, Downey K, Kyriazi S, deSouza NM (2013) New MR techniques in gynecologic cancer. AJR Am J Roentgenol 200(2):249–260. doi:10.2214/AJR.12.8932

Yamashita Y, Mizutani H, Torashima M, Takahashi M, Miyazaki K, Okamura H et al (1993a) Assessment of myometrial invasion by endometrial carcinoma: transvaginal sonography vs contrast-enhanced MR imaging. AJR Am J Roentgenol 161(3):595–599

Yamashita Y, Harada M, Sawada T, Takahashi M, Miyazaki K, Okamura H (1993b) Normal uterus and FIGO stage I endometrial carcinoma: dynamic gadolinium-enhanced MR imaging. Radiology 186(2):495–501

Uterine Sarcomas

Rita Lucas and Teresa Margarida Cunha

Contents

1 Epidemiology

The term sarcoma comes from a Greek word meaning "fleshy growth".

Gynaecological sarcomas are uncommon tumours with aggressive behaviour that account for approximately 1% of all female genital tract malignancies and 3–7% of uterine cancers (D'Angelo and Prat 2010; Major et al. 1993). Although rare, the most frequent of all gynaecological sarcomas is leiomyosarcoma.

The great majority of sarcomas arise in the uterus and are classified according to the histologic tissue from which they are derived, either smooth muscle or endometrial stroma. Although uncommon, the histopathological diversity of gynaecological sarcomas have contributed to many inaccuracies and lack of consensus in nomenclature in the past.

Sarcomas can also develop at other sites in the female genital tract with different features, for example, ovarian fibrosarcoma, vulvovaginal leiomyosarcoma or rhabdomyosarcoma; however these tumours are extremely rare and are outside the scope of this chapter.

2 Pathology

The current World Health Organization (WHO) classification of tumours of the female reproductive organs (Kurman et al. 2014), recently revised and published in 2014, classifies mesenchymal

R. Lucas (✉)
Hospital dos Lusíadas de Lisboa, Lisbon, Portugal
e-mail: ritalucas1@gmail.com

T.M. Cunha
Instituto Português de Oncologia de Lisboa Francisco Gentil, Lisbon, Portugal
e-mail: tmargarida@gmail.com

Med Radiol Diagn Imaging (2016)
DOI 10.1007/174_2016_90, © Springer International Publishing Switzerland
Published Online: 07 December 2016

tumours of the uterine corpus into smooth muscle origin, endometrial stromal origin, mixed epithelial-mesenchymal origin and miscellaneous tumours.

In comparison with the previous WHO 2003 classification, the new classification reintroduces high-grade endometrial stromal sarcoma as a separate entity, supported by emerging recent molecular and morphological data, and replaces the designation "undifferentiated endometrial sarcoma" by undifferentiated uterine sarcoma to reflect the fact that an endometrial origin is not certain (McCluggage et al. 2014).

Uterine sarcomas more frequently exhibit early peritoneal and haematogenous spread with distant metastases, instead of starting to spread locally in the pelvis and to lymph nodes as carcinomas do (Seddon and Davda 2011).

2.1 Smooth Muscle Tumours

Smooth muscle tumours are composed of cells showing smooth muscle differentiation arising within the myometrium that can be either benign or malignant. Because they arise in the stroma, the classic histological criteria for invasion are not so easy to define as in epithelial tumours.

This designation comprises:

- Classic benign leiomyoma (i.e., the most frequent uterine tumour)
- Smooth muscle tumour of uncertain malignant potential (STUMP), also called atypical smooth muscle neoplasm, a lesion not fulfilling entirely the criteria for a leiomyoma or leiomyosarcoma
- Leiomyosarcoma, a malignant tumour that occasionally shows epithelioid or myxoid features

Leiomyosarcomas and leiomyomas are independent entities with differing cytogenetic abnormalities that can however coexist (McCluggage et al. 2014; Bodner et al. 2003). Classical teaching books state that malignant transformation should be suspected in rapid growth of a leiomyoma in a menopausal woman; however the most recent evidence supports that uterine sarcomas do not generally arise from pre-existing leiomyomas, with only very rare exceptions (about 0.2% of cases). By consensus from genetic studies, the current concept is that most sarcomas arise independently (Hodge and Morton 2007; McCluggage 2002a). Furthermore, rapid growth can also occur in premenopausal women in leiomyoma.

2.2 Endometrial Stromal Tumours

Endometrial stromal neoplasms are a subset of uterine mesenchymal neoplasms that account for less than 10% of all uterine sarcomas (Chan et al. 2008). These rare uterine neoplasms mimic proliferative endometrium; however, they have myometrial and/or vascular invasion (Kurman et al. 2014).

Recent molecular genetics and immunohistochemistry advances have improved the understanding of these lesions and helped to redefine the WHO classification into more meaningful categories with distinct prognosis (Kurman et al. 2014; Ali and Rouzbahman 2015; Conklin and Longacre 2014; Xue and Cheung 2011), namely

- Low-grade endometrial stromal sarcoma
- High-grade endometrial stromal sarcoma
- Undifferentiated uterine sarcoma

In tumours in which a focal smooth muscle differentiation coexists, the neoplasm is considered an endometrial stromal sarcoma if the smooth muscle component involves <30% of the total lesion volume. Tumours composed of a larger smooth muscle component are designated as "mixed endometrial stromal and smooth muscle neoplasms" or *stromomyomas*. However, there is still few data regarding these lesions (Kurman et al. 2014).

2.3 Mixed Epithelial and Mesenchymal Tumours

This category includes adenosarcoma, a rare tumour that accounts for 5–9% of uterine sarcomas. In this lesion the epithelial component

is benign or atypical, and the stromal component is low-grade malignant (Tse et al. 2011). It is a difficult diagnosis to make requiring an experienced gynaecological pathologist (Blom and Guerrieri 1999).

Even though adenosarcomas typically have a low malignant potential, there is however a subgroup defined as having sarcomatous overgrowth, with pure sarcoma occupying at least 25% of the tumour (McCluggage et al. 2014).

Carcinosarcoma, previously called malignant Müllerian tumour, has recently been reclassified as a dedifferentiated or metaplastic form of endometrial carcinoma (type II cancer). In addition, the epidemiology, risk factors, and clinical behaviour associated with carcinosarcoma suggest a closer relationship to endometrial carcinoma than to other sarcomas (McCluggage 2002a, b).

2.4 Miscellaneous Mesenchymal Tumours

This group includes rhabdomyosarcoma, which is a notably rare tumour that shows skeletal muscle differentiation, occurring both in the vagina and uterine corpus and cervix, typically arising in children and adolescents.

For this chapter only, malignant uterine sarcomas with mesenchymal and mixed epithelial-mesenchymal origin will be considered as summarized in Table 1.

Table 1 Malignant uterine sarcomas

Mesenchymal origin	Mixed epithelial and mesenchymal origin
Smooth muscle origin	Adenosarcoma
Leiomyosarcoma	
Endometrial stroma and related origin	
Low-grade endometrial stromal sarcoma	
High-grade endometrial stromal sarcoma	
Undifferentiated uterine sarcoma	

3 Clinical Background

The clinical presentation of uterine sarcomas is non-specific, with a peak incidence between 50 and 65 years of age. Of note, low-grade endometrial stromal sarcomas occur mainly in premenopausal women (D'Angelo and Prat 2010; Conklin and Longacre 2014).

Frequently there is history of a rapidly growing uterine mass, abnormal vaginal bleeding and pelvic or abdominal pain.

Less frequently, leiomyosarcoma can present hemoperitoneum (due to tumour rupture), or symptoms resulting from extrauterine extension or metastases (D'Angelo and Prat 2010).

The diagnosis of uterine sarcomas is frequently unexpected, discovered incidentally on histopathology analysis following hysterectomy, often for benign diseases. Of those patients undergoing hysterectomy for a preoperative diagnosis of leiomyoma, 0.5% is subsequently diagnosed with leiomyosarcoma (Wu et al. 2011).

African-american women have an approximately twofold higher incidence of leiomyosarcomas (but not other types of uterine sarcoma) than caucasian women (Sherman and Devesa 2003).

Occasional cases are associated with long-term tamoxifen therapy, polycystic ovarian disease, prolonged estrogenic stimulation or pelvic irradiation. There are also some associated hereditary conditions such as *hereditary leiomyomatosis/renal cell carcinoma syndrome* and survivors of childhood retinoblastoma (Toro et al. 2003; Yu et al. 2009).

Obesity, diabetes and younger age at menarche have been associated with increased risk of endometrial stromal sarcomas, although the molecular mechanisms involved are yet to be elucidated (Felix et al. 2013).

Compared with the more common endometrial carcinomas (epithelial neoplasms), uterine sarcomas behave aggressively and are associated with a poorer prognosis.

4 Staging

Staging is surgical, including total hysterectomy with bilateral salpingo-oophorectomy, and remains the most powerful prognostic factor for

Table 2 2009 FIGO staging systems for uterine sarcomas

Uterine leiomyosarcoma and endometrial stromal sarcoma	
Stage I	Tumour limited to uterus
IA	≤5 cm
IB	>5 cm
Stage II	Tumour extends beyond the uterus, within the pelvis
IIA	Adnexal involvement
IIB	Involvement of other pelvic tissues
Stage III	Tumour invades abdominal tissues (not just protruding into the abdomen)
IIIA	One site
IIIB	More than one site
IIIC	Metastasis to pelvic and/or para-aortic lymph nodes
Stage IV	
IVA	Tumour invades bladder and/or rectum
IVB	Distant metastasis
Uterine adenosarcoma	
Stage I	Tumour limited to uterus
IA	Tumour limited to endometrium/endocervix with no myometrial invasion
IB	Less than or equal to half myometrial invasion
IC	More than half myometrial invasion
Stage II	Tumour extends beyond the uterus, within the pelvis
IIA	Adnexal involvement
IIB	Involvement of other pelvic tissues
Stage III	Tumour invades abdominal tissues (not just protruding into the abdomen)
IIIA	One site
IIIB	More than one site
IIIC	Metastasis to pelvic and/or para-aortic lymph nodes
Stage IV	
IVA	Tumour invades bladder and/or rectum
IVB	Distant metastasis

uterine sarcomas. However in pretreatment evaluation, staging largely depends on imaging as the clinical evaluation is very limited.

Due to their different biologic behaviour, in 2009 FIGO introduced two new dedicated staging systems, specifically designed for uterine sarcomas, in which the morphological tumour subtype determines which staging system is used: one staging system for leiomyosarcoma and endometrial stromal sarcoma and a different system for adenosarcoma (Prat 2009a, b) (Table 2).

Adenosarcoma tends to arise at the endometrial or cervical surface, progressively invading the myometrium or cervical stroma in a similar way to endometrial carcinomas. The staging system is comparable to endometrial carcinomas, whereas leiomyosarcoma and endometrial stromal sarcoma that usually arise within the myometrium and have a different tumoural progression are staged in a different fashion.

5 Imaging

Imaging plays an important role in the evaluation of disease extent and treatment decision, even though the diagnosis relies on the histological examination. Endometrial sampling may yield the correct diagnosis but not in all patients: cases that arise within the endometrium may be indistinguishable from endometrial carcinoma, whereas those that arise from the myometrium may be indistinguishable from degenerating leiomyomas (Sala et al. 2013).

Table 3 Key points in the evaluation of sarcomatous uterine lesions

Tumour limits/interface	Early-stage uterine leiomyosarcomas can be well-circumscribed, while more advanced lesions typically have an irregular contour. On the other hand, endometrial stromal sarcomas may exhibit a diffusely infiltrative pattern of myometrial invasion
Depth of myometrial invasion	Important in the substaging of stage I adenosarcomas: Stage IA tumours are limited to the endometrium, stage IB invades less than or half of myometrium thickness and stage IC equates to more than one half myometrial invasion. It is also considered a risk factor for recurrence Since most other uterine sarcomas are predominantly myometrial-based lesions, myometrial invasion is not considered in the staging of these neoplasms
Cervical involvement	It has an adverse influence on prognosis, for example, in the case of a leiomyosarcomas
Adnexal involvement	Adnexal involvement affects the tumour stage (FIGO stage IIA) and may occur as result of direct extension or metastatic spread of tumour
Lymph nodes	Pelvic or para-aortic lymph node involvement upstages uterine sarcomas to stage IIIC
Involvement of pelvic tissues	Other sites of pelvic tumour involvement should be documented since this equates to FIGO stage IIB
Involvement of omentum and other abdominal tissues	The number of affected locations in peritoneal tissue is important as FIGO stage IIIA equates to one site of abdominal involvement and IIIB to more than one site

Pre-surgical subtyping of uterine sarcomas is very important for therapeutic management. Even though the imaging findings of uterine sarcomas have a considerable overlap, there are however some specific features that can narrow the differential diagnosis list.

Ultrasound is usually the first-line study to evaluate women for potential uterine pathology as it is a readily available, non-invasive and relatively inexpensive technique. It gives an initial evaluation of the size and location of the lesion and may identify features suggestive of aggressiveness; however, the accuracy is very low.

Computed tomography (CT) is mainly used for staging in the assessment of extra-pelvic disease, distant metastases and follow-up.

The primary modality for imaging uterine sarcomas is magnetic resonance imaging (MRI) due to the improved ability of this technique to delineate local disease.

When evaluating a possible sarcomatous uterine lesion with MRI, there are some specific key points that are important to evaluate as described in Table 3 (McCluggage et al. 2014).

5.1 Leiomyosarcoma

Leiomyosarcomas are rare typically large lesions (>10 cm) presenting as solitary masses with areas of haemorrhage and necrosis that may bulge into and distort the uterine cavity, but the epicentre is in the myometrium (Kurman et al. 2014).

Pelvic ultrasound is commonly the first-line study to evaluate women for potential uterine pathology. Some findings such as heterogeneous echo texture, central necrosis and colour Doppler findings of irregular vessel distribution might suggest the diagnosis of leiomyosarcoma; however sonographic evaluation is highly unspecific and hard to differentiate from leiomyomas (the most common myometrial tumour) (Amant et al. 2009).

Leiomyosarcomas commonly cause massive uterine enlargement, demonstrating heterogeneous low to intermediate signal intensity and scattered hyperintense foci on T1-weighted images (WI), whereas on T2-WI they are irregular and ill-defined lesions with intermediate to high signal intensity with cystic areas denoting necrosis (present in >50% of cases) (Santos and Cunha 2015). Detection of scattered foci of haemorrhages or necrosis may suggest the diagnosis; however signal intensity alone is not a reliable indicator of malignancy (Amant et al. 2009) (Fig. 1).

As stated before, leiomyosarcomas and leiomyomas are independent entities with differing cytogenetic abnormalities that can however coexist (Bodner et al. 2003; Hodge and Morton 2007;

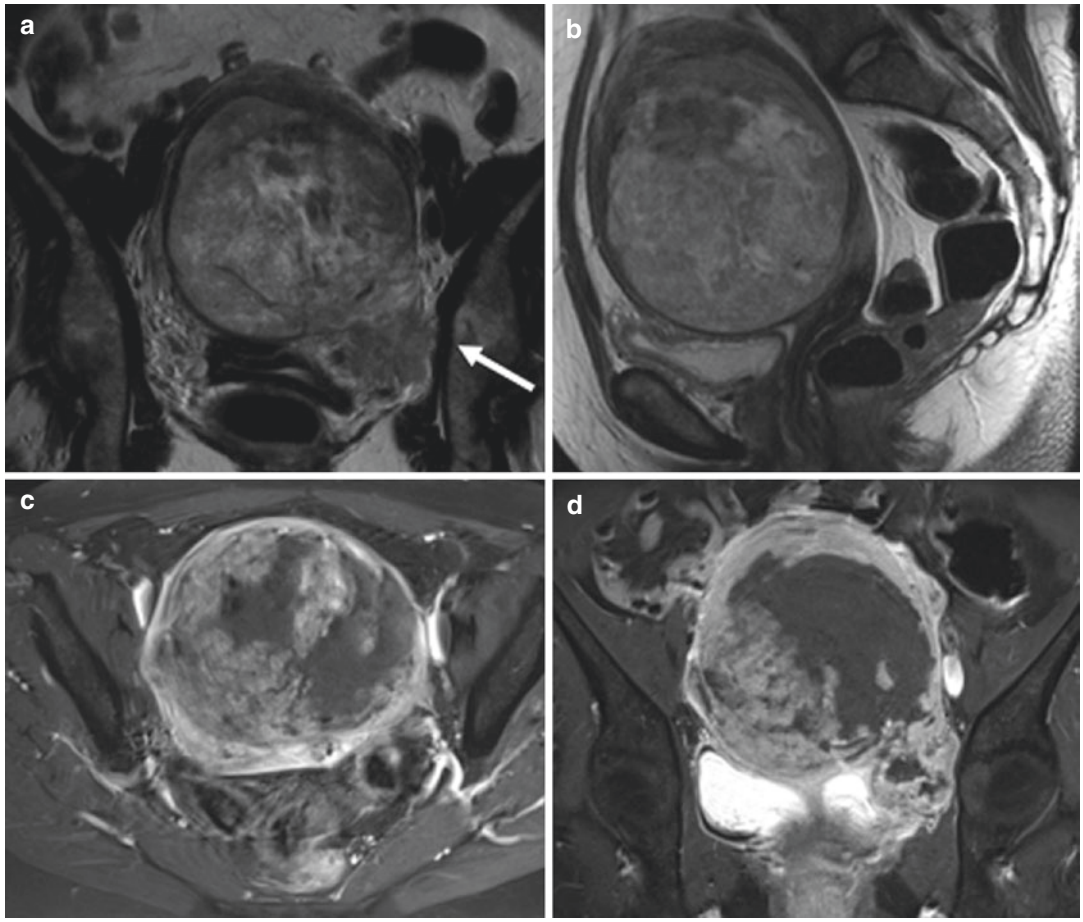

Fig. 1 Leiomyosarcoma in a 56-year-old woman. Coronal (**a**) and sagittal (**b**) T2-WI show marked uterine enlargement due to a heterogeneous myometrial tumour that invades the pelvic wall on the left (*arrow*), with intense enhancement in solid areas showed here in axial (**c**) and coronal (**d**) gadolinium-enhanced T1-WI with fat suppression and extensive areas of tumoural necrosis

McCluggage 2002a). Benign leiomyomas develop primarily in women of reproductive age and typically stabilize or diminish in size following menopause. In contrast, increasing age is a significant risk factor for uterine sarcomas, and new or a rapidly growing uterine mass warrants further evaluation in menopausal women.

There is however a considerable overlap in the MR appearance, signal intensity and enhancement characteristics of leiomyosarcoma and leiomyomas with atypical imaging features (Schwartz et al. 1998; Cornfield et al. 2010). As so the diagnosis of uterine sarcomas can be incidental in histopathology analysis following hysterectomy (Sagae et al. 2004). It should also be highlighted that with the development of laparoscopic surgery, morcellation of presumed leiomyomas has resulted in suboptimal treatment in patients with previously undiagnosed uterine sarcomas and reinforcing the need of better preoperative tumour characterization (Sutton 2013).

It has been suggested that an irregular contour, high signal on T2-WI and hyperintense areas on T1-WI could favour leiomyosarcoma against leiomyoma, but the specificity of this finding has not been established (Cornfield et al. 2010; Murase et al. 1999; Tanaka et al. 2004). The absence of calcifications is also a consistent finding in leiomyosarcomas (Schwartz et al. 1998).

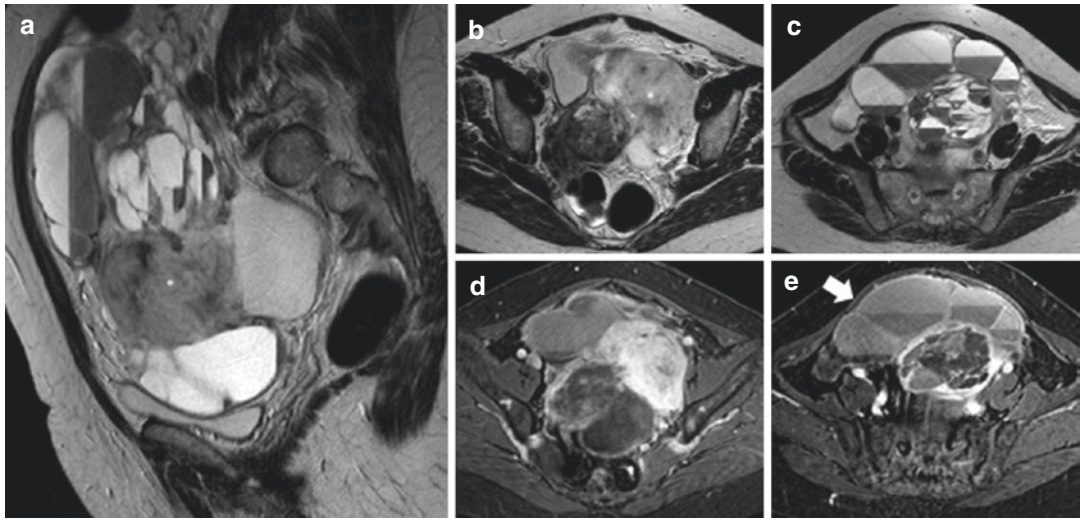

Fig. 2 Myxoid leiomyosarcoma in a 60-year-old, appearing to grow from a solid anterior myometrial nodule (*asterisk* on sagittal – **a** and axial T2-WI – **b**) and communicating with an exuberant multiloculated cystic component, with multiple fluid levels (**c**). On axial T1-WI with fat saturation and contrast administration (**d** and **e**), some levels have high signal (*arrow*) related to haemorrhagic content

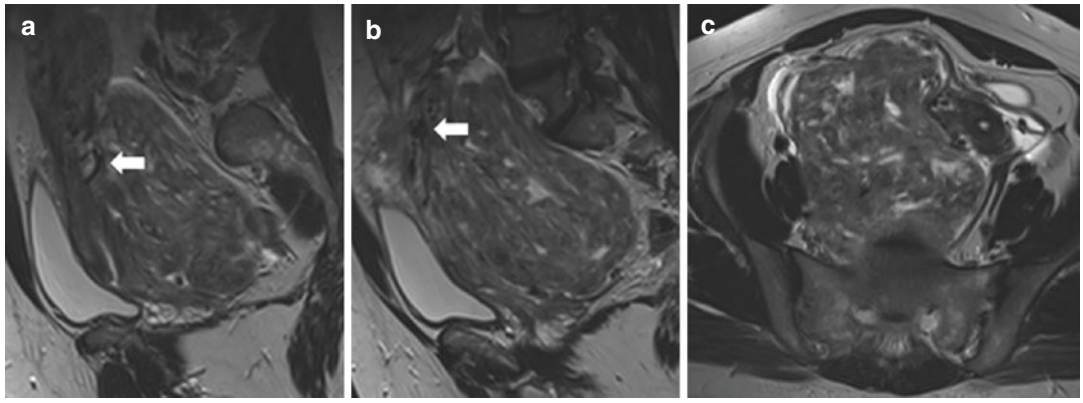

Fig. 3 Epithelioid leiomyosarcoma in a 43-year-old woman. This subserosal tumour arises from the right posterior uterine wall. On sagittal T2-WI (**a** and **b**) the flow voids of the connecting vessels are easily seen (*arrows*). On axial T2-WI (**c**) this lesion is seen on the right of the uterine cervix. The endometrial cavity is indistinct

The myxoid and epithelioid variants can have a more diverse appearance, and the establishment of the diagnosis is particularly difficult in these cases (Figs. 2 and 3).

Leiomyosarcomas demonstrate early haematogenous spread to the lungs and liver (Sala et al. 2013). Involvement of pelvic lymph nodes is uncommon and usually associated with advanced intra-abdominal disease and decreased survival (Leitao et al. 2003; Kapp et al. 2008) (Fig. 4).

The major advantage of diffusion-weighted imaging (DWI) sequences is the delineation of malignant lesions DWI seems to be a potentially useful tool in soft tissue characterization of large uterine lesions: the high nuclear-to-cytoplasm ratio in tumour cells limits intracellular motion of water molecules in uterine sarcomas and these lesions are depicted as hyperintense lesions on DWI and low signal on the corresponding apparent diffusion coefficient (ADC) maps.

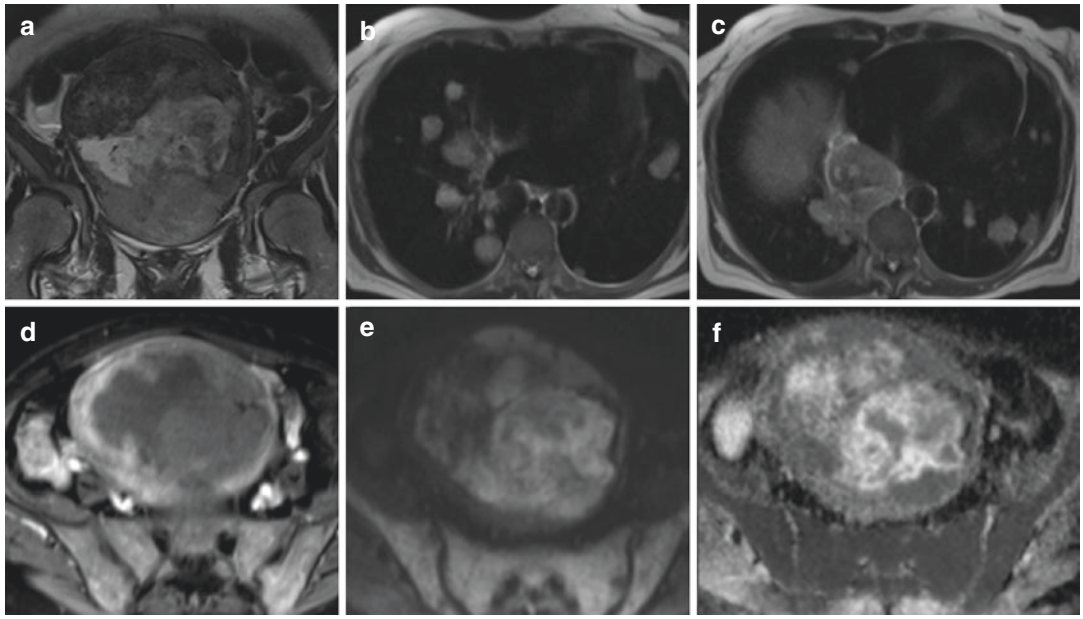

Fig. 4 Leiomyosarcoma in a 55-year-old woman. Coronal T2-WI of the pelvis (**a**) shows marked uterine enlargement due to a heterogeneous myometrial tumour with areas of high signal. Axial T2-WI, at the level of the pulmonary bases (**b** and **c**), reveals pulmonary metastases and posterior mediastinum enlarged lymph nodes (**c**). In axial gadolinium-enhanced T1-WI with fat suppression (**d**), the tumour demonstrates early intense peripheral enhancement with irregular central zones of low signal intensity denoting extensive necrosis. Endometrial cavity is difficult to depict. DWI-MR (**e**) and ADC map (**f**) show restricted diffusion in the solid areas of the lesion

Leiomyosarcomas display restriction in DWI studies.

DWI proved to reduce misdiagnoses of uterine sarcoma as benign leiomyoma with high accuracy (Thomassin-Naggara et al. 2013). DWI combined with T2-WI is even better than DWI alone in the differentiation of uterine sarcomas from benign leiomyomas (Namimoto et al. 2009). It is however important to recall, as a potential pitfall, that non-malignant lesions with high cellular density, such as high celular leiomyomas, may have restricted diffusion.

Positron emission tomography (PET) combined with CT adds metabolic information to morphologic data; However the main role of PET-CT is confined to post-therapy surveillance in order to detect distant metastasis or local recurrence, it appears to exist a significant variability in fluorodeoxyglucose (FDG) mean standard uptake values (SUVs) between benign and malignant neoplasms (Tirumani et al. 2013; Kao et al. 2011).

5.2 Endometrial Stromal Sarcomas

The ultrasonographic evaluation of these lesions is highly unspecific. They appear as heterogeneous hypoechoic endometrial masses with irregular endometrial-myometrial interface, sometimes with fingerlike invasive myometrial projections and low-resistance intralesional arteries on Doppler (Amant et al. 2009; Gandolfo et al. 2000).

T2-WI are the most helpful MR sequences in detecting the endometrial nature of the tumours and its relationships with surrounding myometrium (Gandolfo et al. 2000).

Another feature that may suggest endometrial stromal sarcoma, observed in about one third of the cases, is the continuous extension of the lesion into adjacent structures most commonly the ovary, but also the fallopian tubes, the surrounding ligaments and vessels (Koyama et al. 1999). Digitiform tumour extension is best delineated on DWI (Tamai et al. 2008), differing from

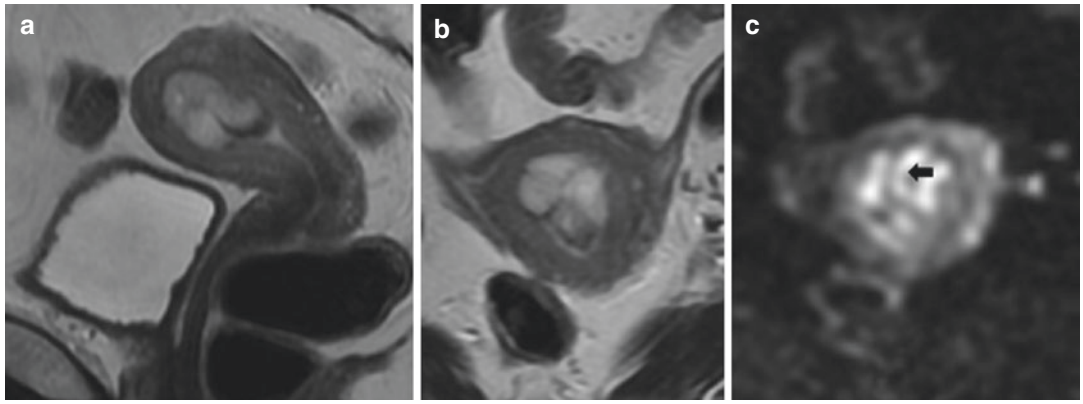

Fig. 5 Low-grade endometrial stromal sarcoma in a 62-year-old woman with postmenopausal bleeding. Sagittal (**a**) and axial (**b**) T2-WI of the pelvis demonstrate a high signal endometrial polypoid lesion, with ill-defined endometrial/myometrial border and without evidence of a well-defined myometrial mass. DWI-MRI (**c**) allowed better identification of the lesion and revealed bands of low signal intensity (*arrow*) representing preserved bundles of the myometrium. Histopathology revealed internal myometrial invasion

intravenous leiomyomatosis due to tumoural high signal (Riopel et al. 2005).

Lymph node metastases occur in up to 30% of patients, and besides pelvic chain, spread to paraaortic nodes has also been reported (Fekete and Vellios 1984).

5.2.1 Low-Grade Endometrial Stromal Sarcoma

These tumours occur in a younger age group compared to high-grade lesions, usually involve the endometrium forming a polyp of homogeneous high signal intensity on T2-WI, which may be infarcted or haemorrhagic (Fig. 5).

There is myometrial invasion and an infiltrative growth pattern that may form deceptively well-demarcated nodules in the myometrium or may cause myometrial diffuse thickening without evidence of a well-defined tumour (Tamai et al. 2008). In some cases this diffuse thickening can be been misinterpreted as adenomyosis and, if more localized, can present as a myometrial mass mimicking a degenerated cystic leiomyoma, however without the typical well-defined border. In the presence of a large myometrial lesion, it is extremely important to evaluate the adjacent endometrial thickness, endometrial-myometrial border and lesion margin (Koyama et al. 1999).

On MRI, these lesions have heterogeneous signal intensity on both T1- and T2-WI (Gandolfo et al. 2000; Koyama et al. 1999), and the most important imaging feature is the presence of bands of low signal intensity on T2-WI invading the myometrium, representing preserved muscular bundles.

Tumour enhancement is commonly heterogeneous and iso- or hyperintense when compared with normal myometrium (in contrast to endometrial carcinoma, which enhances less than normal myometrium) (Sala et al. 2013). Sometimes signal voids can be observed reflecting the hypervascular nature of these tumours (Koyama et al. 1999).

Although low-grade endometrial stromal sarcomas have an indolent clinical course there is a significant tendency for recurrence (Fig. 6).

5.2.2 High-Grade Endometrial Stromal Sarcoma

Recently a subset of endometrial stromal sarcomas has been discovered with a unique gene rearrangement, distinct morphologic features and an intermediate prognosis between low-grade and undifferentiated stromal sarcomas, supporting the need to consider these tumours a separated category (Lee et al. 2012).

On MRI, the T2-WI hypointense preserved bundles of myometrial fibres are much thinner, scattered and harder to depict compared to low-grade lesions, due to a more aggressive growth (Koyama et al. 1999) (Fig. 7).

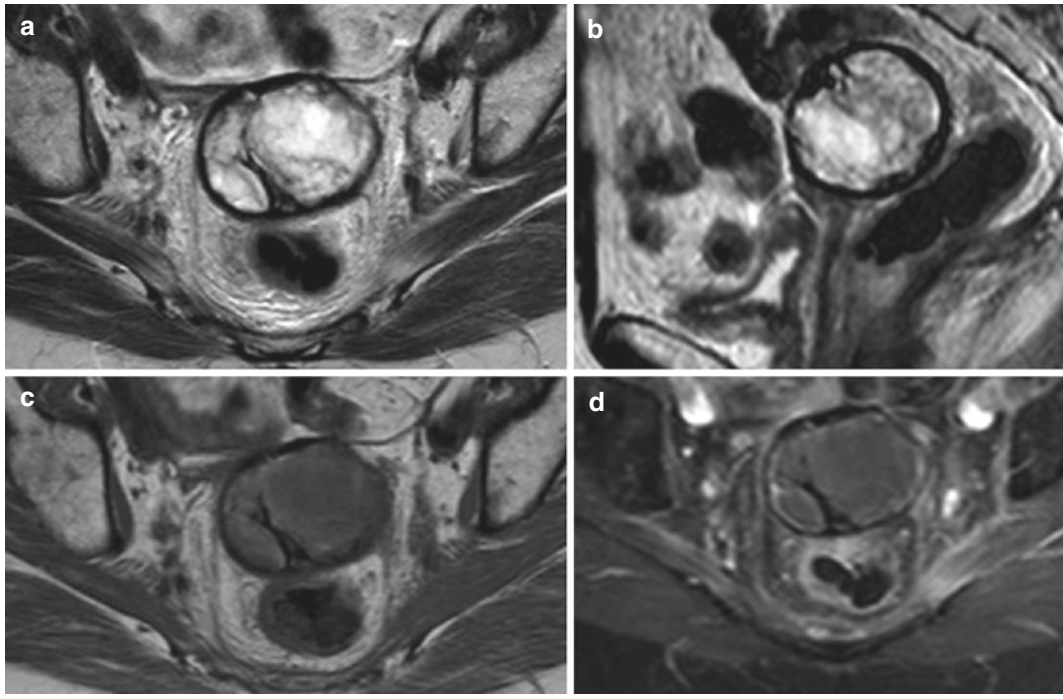

Fig. 6 Low-grade endometrial stromal sarcoma recurrence in a 70-year-old woman 2 years after surgery. Axial (**a**) and sagittal (**b**) T2-WI images demonstrate a large heterogeneous cystic and solid mass in the vaginal cuff. On axial T1-WI (**c**) the lesion in hypointense, with faint enhancement after contrast on T1-WI fat supressed acquisition (**d**).

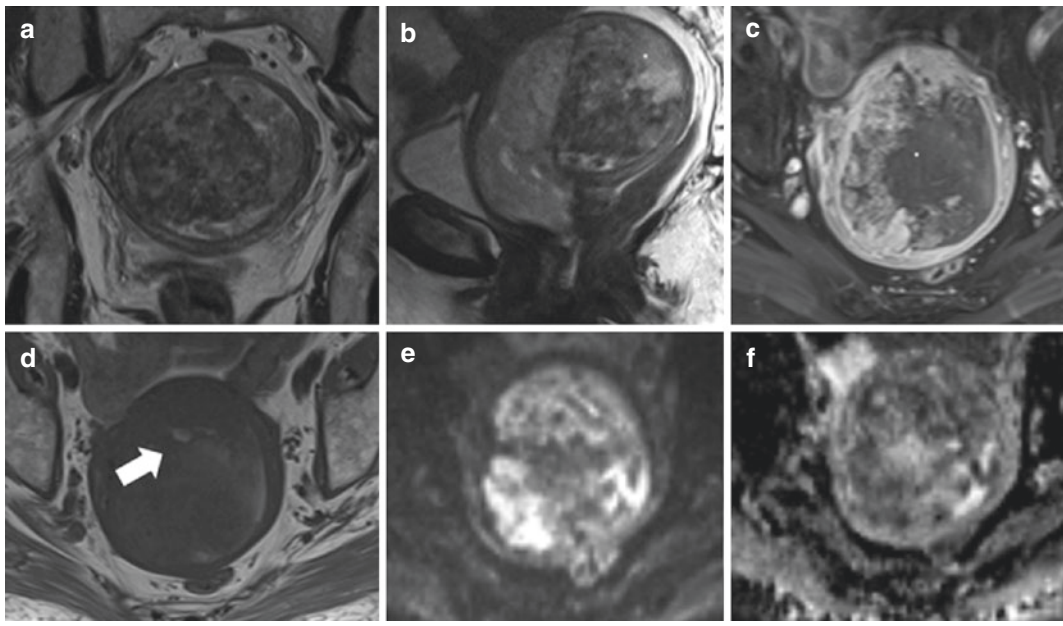

Fig. 7 High-grade endometrial stromal sarcoma in a 75-year-old woman. Coronal (**a**) and sagittal T2-WI (**b**) revealed a heterogeneous mass with necrotic areas (*asterisk*) extending to the cervix, with heterogeneous enhancement after gadolinium administration (**c**), high-signal foci on T1-WI (**d**) (*arrow*) denoting haemorrhage, and marked restriction on DWI (**e**) and ADC map (**f**). The gross examination of the specimen revealed a heterogeneous endometrial mass invading the myometrium and reaching the cervix denoting aggressive growth

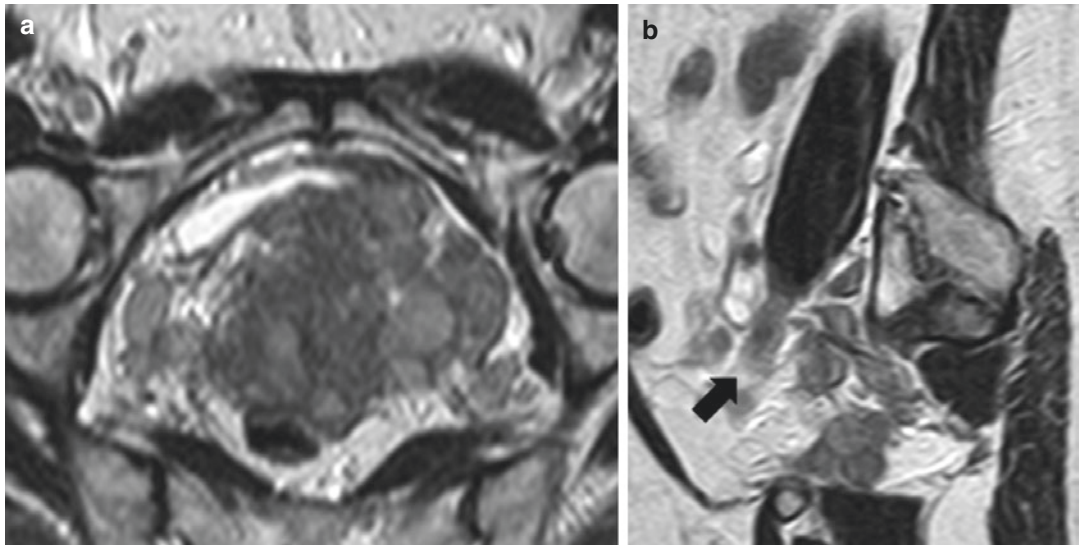

Fig. 8 High-grade endometrial stromal sarcoma in a 64-year-old woman. Axial (**a**) and sagittal (**b**) T2-WI show a heterogeneous multinodular tumour with extensive myometrial invasion and high-signal tumoural extension along pelvic vessels (*black arrow*)

The tumoural extension to adjacent organs, supporting structures and vascular elements is also characteristic (Fig. 8).

5.2.3 Undifferentiated Uterine Sarcoma

This is a tumour arising in the endometrium or the myometrium, lacking any resemblance to proliferative-phase endometrial stroma.

There are few studies describing the characteristic appearance of undifferentiated uterine sarcoma, suggesting that they appear similarly to high-grade endometrial stromal sarcomas and as so presenting as polypoid masses that frequently fill the endometrial cavity, with irregular margins, multiple marginal tumour nodules, extensive areas of haemorrhage, necrosis and myometrial invasion (Tirumani et al. 2013) (Fig. 9).

These tumours are typically characterized by a haphazard arrangement of variably sized blood vessels, as so manifesting as enhancing masses that can have marked vascular and lymphatic invasion (Amant et al. 2009; Santos and Cunha 2015) (Fig. 10).

Also metastatic extrauterine disease is more frequent than in the previously described types of endometrial stromal sarcoma (Tanner et al. 2012).

5.3 Adenosarcoma

The majority of adenosarcomas are present in the endometrium, but they may also arise from the myometrium, cervix or extrauterine Müllerian tissues (Huang et al. 2014).

Sonographic features of adenosarcoma may include expansion of endometrial cavity associated with a thickened heterogeneous and cystic complex mass. These features can mimic gestational trophoblastic disease (Santos and Cunha 2015; Chourmouzi et al. 2003).

These neoplasms present as polypoid solid, well-circumscribed multiseptated cystic mass with heterogeneous solid components. They usually arise from the fundus, sometimes protrude through the cervical os, and typically cause marked enlargement of the uterus with a thin myometrium (Amant et al. 2009; Santos and Cunha 2015; Chourmouzi et al. 2003) (Fig. 11). On MR the cysts have hight signal on T2-WI, representing glandular epithelial components or necrosis, solid component shows T2-WI hypointensity, resulting in a latticework appearance due to the intervening septa that enhance after contrast (Chourmouzi et al. 2003; Szklaruk et al. 2003) (Fig. 12).

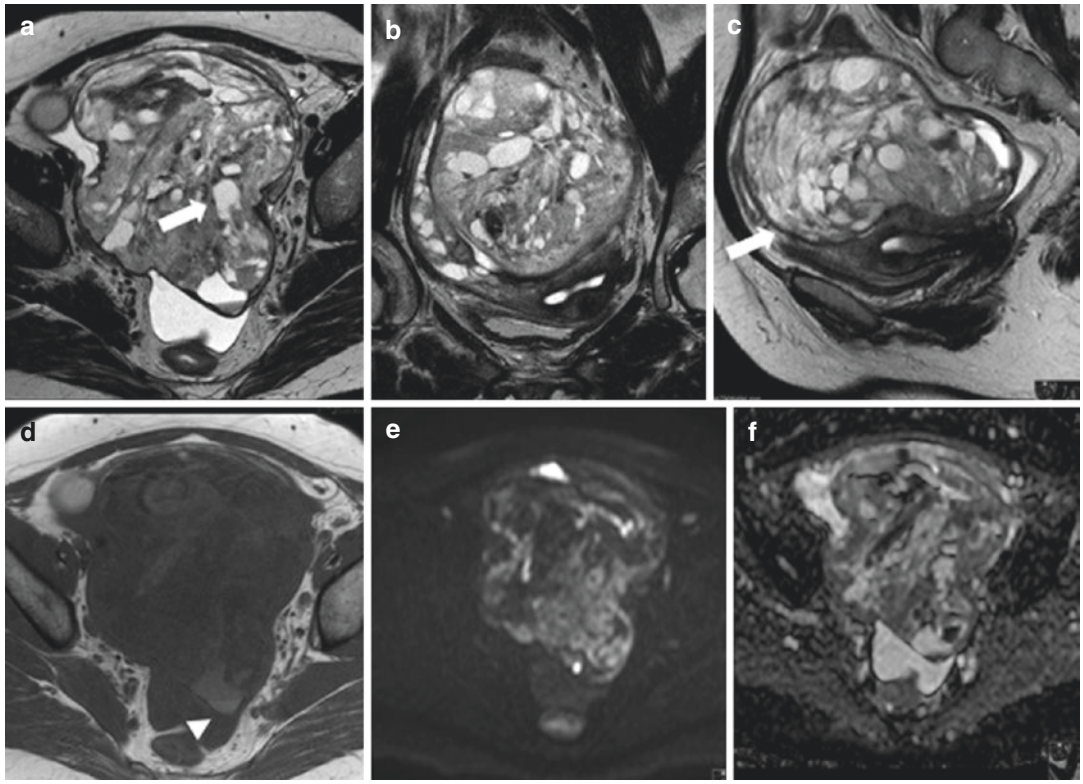

Fig. 9 Undifferentiated uterine sarcoma in a 56-year-old woman. Axial (**a**), coronal (**b**) and sagittal (**c**) T2-WI show marked uterine enlargement due to a large subserosal heterogeneous tumour, with lobulated contours, showing extensive cystic and necrotic areas (*arrows*). On T1-weighted image (**d**) haemorrhage can be appreciated (*arrow-head*). The tumour shows marked restriction on DWI (**e**) and on the ADC map (**f**)

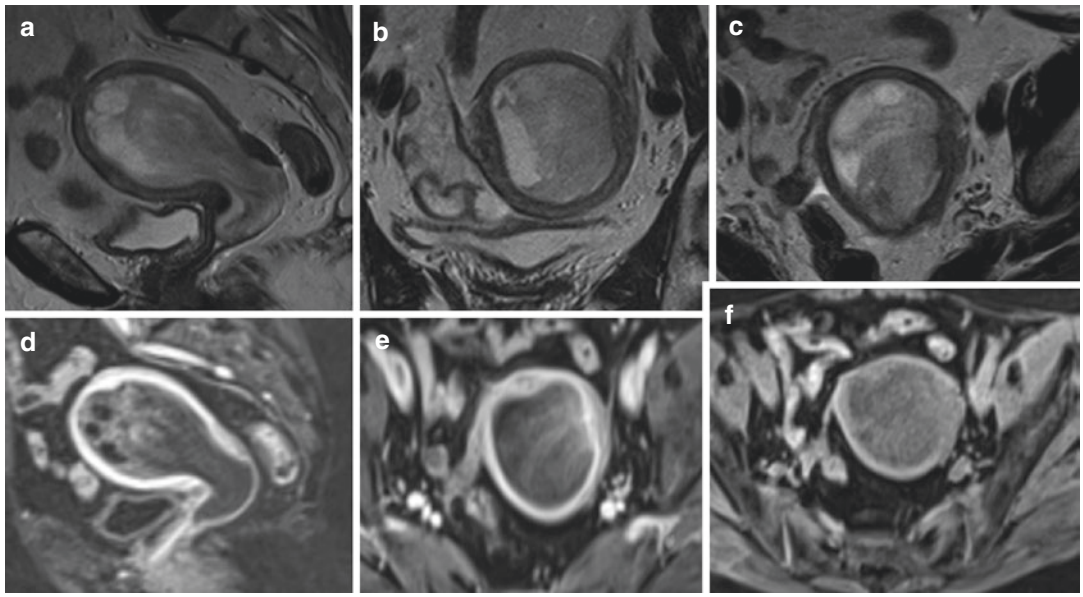

Fig. 10 Undifferentiated uterine sarcoma in a 72-year-old woman. Sagittal (**a**), coronal (**b**) and axial and (**c**) T2-WI show a polypoid mass with heterogeneous high signal intensity within the endometrial cavity, protruding through the cervical os into the vagina. On T1-WI FS after gadolinium administration, in the same three planes (**d**–**f**) the lesion enhances heterogeneously compared to the peripheral myometrium

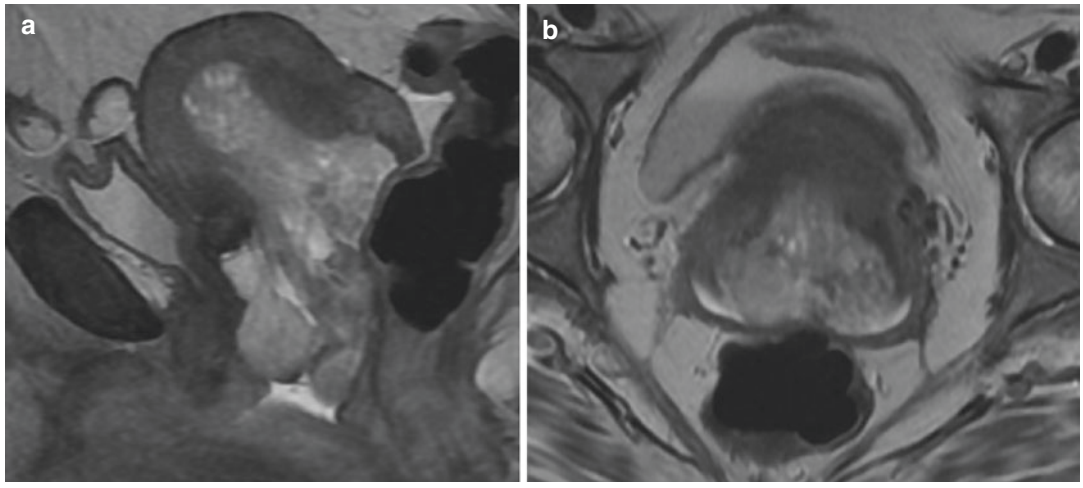

Fig. 11 Adenosarcoma in a 48-year-old woman presenting with pelvic mass and vaginal discharge. Sagittal (**a**) and axial (**b**) T2-WI demonstrate a large, heterogeneous, high-signal intensity mass centred in the endometrial cavity, protruding trough the cervical canal and prolapsing

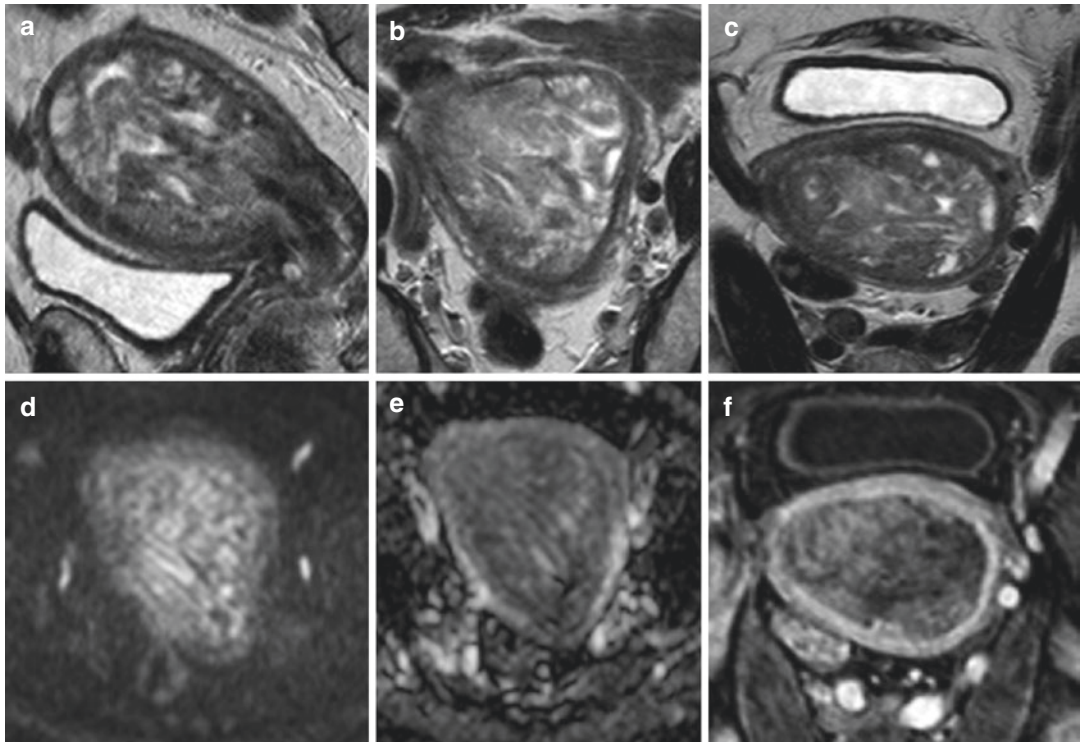

Fig. 12 Adenosarcoma in a 77-year-old woman presenting with post-menopausal bleeding. Sagittal (**a**), axial (**b**) and axial of the uterine body (**c**) T2-WI of the pelvis demonstrate a huge endometrial mass with cystic spaces and heterogeneous solid components. The uterine contour is preserved. Axial DWI-MR (**d**) reveals high signal intensity and low signal on the ADC map (**e**). T1-WI fat suppressed after administration of contrast (**f**) shows early enhancement of the septa and solid areas. No myometrial invasion was present on pathology

The cases of adenosarcoma with sarcomatous overgrowth are described in the literature as large pelvic masses with heterogeneous signal intensity, cystic areas and transperitoneal extension with contiguous intravascular growth (Kim et al. 2011).

6 Prognosis and Treatment

Overall 5-year survival for uterine sarcomas ranges between around 18–55%, considerably lower than for endometrial carcinomas (Koivisto-Korander et al. 2008). Prognostic factors include age, clinical stage, tumour size, tumour circumscription, mitotic index and lymphovascular invasion (D'Angelo and Prat 2010; Abeler et al. 2009).

Leiomyosarcomas and undifferentiated uterine sarcomas are highly aggressive neoplasms with a marked propensity for extrauterine spread and systemic metastasis; and nodal metastasis is not so common (McCluggage et al. 2014; Kapp et al. 2008).

In undifferentiated uterine sarcomas, a significant proportion of patients (>60%) has advanced-stage disease at the time of diagnosis, with extrauterine spread of tumour to the upper abdomen, pelvic lymph nodes or even more distant sites such as the lungs (Leath et al. 2007).

On the other hand, low-grade endometrial stromal sarcomas have an indolent clinical course with good long-term survival, despite the tendency for late recurrence. Stage is the most important prognostic factor, with FIGO stage I and II tumours having an excellent 5-year survival rate.

Adenosarcomas are mixed tumours of low malignant potential containing a benign epithelial and a malignant stromal component, usually of low grade. They usually have a favourable prognosis with a 5-year survival rate above 80% unless associated with sarcomatous overgrowth or deep myometrial invasion (McCluggage et al. 2014; Abeler et al. 2009).

The current standard of care for uterine sarcomas remains surgery: total abdominal hysterectomy with bilateral salpingo-oophorectomy. In younger patients preservation of the ovaries can be considered in early-stage disease.

For patients with evidence of extrauterine disease, surgical staging and cytoreduction are performed only if intra-abdominal metastases are resectable and there is no extra-abdominal disease. If patients are not surgical candidates, medical treatment should be offered. Whether systematic lymphadenectomy is needed is still controversial (Prat and Mbatani 2015).

Adjuvant chemotheraphy is decided in a case-to-case base and not consensually indicated. Radiotherapy is also not routinely performed as it does not appear to provide a benefit in survival, but it may reduce local recurrence in high-risk women (Seddon and Davda 2011).

Recurrence can be treated either by surgical resection or by systemic chemotherapy, with hormonotherapy in particular cases, when hormonal receptors are present (Amant et al. 2009).

References

Abeler VM, Royne O, Thoresen S et al (2009) Uterine sarcomas in Norway. A histopathological and prognostic survey of a total population from 1970 to 2000 including 419 patients. Histopathology 54:355–364

Ali RH, Rouzbahman M (2015) Endometrial stromal tumours revisited: an update based on the 2014 WHO classification. J Clin Pathol 68(5):325–332

Amant F, Coosemans A, Debiec-Rychter M, Timmerman D, Vergote I (2009) Clinical management of uterine sarcomas. Lancet Oncol 10:1188–1198

Blom R, Guerrieri C (1999) Adenosarcoma of the uterus: a clinicopathologic, DNA flow cytometric, p53 and mdm-2 analysis of 11 cases. Int J Gynecol Cancer 9(1):37–43

Bodner K, Bodner-Adler B, Kimberger O et al (2003) Estrogen and progesterone receptor expression in patients with uterine leiomyosarcoma and correlation with different clinicopathological parameters. Anticancer Res 23:729

Chan JK, Kawar NM, Shin JY et al (2008) Endometrial stromal sarcoma: a population-based analysis. Br J Cancer 99(8):1210–1215

Chourmouzi D, Boulogianni G, Zarampoukas T, Drevelengas A (2003) Sonography and MRI of tamoxifen-associated Mullerian adenosarcoma of the uterus. AJR Am J Roentgenol 181:1673–1675

Conklin CM, Longacre TA (2014) Endometrial stromal tumours: the new WHO classification. Adv Anat Pathol 21(6):383–393

Cornfield D, Israel G, Martel M et al (2010) MRI appearance of mesenchymal tumors of the uterus. Eur J Radiol 74:241–249

D'Angelo E, Prat J (2010) Uterine sarcomas: a review. Gynecol Oncol 116:131–139

Fekete PS, Vellios F (1984) The clinical and histologic spectrum of endometrial stromal neoplasms: a report of 41 cases. Int J Gynecol Pathol 3:198–212

Felix AS, Cook LS, Gaudet MM et al (2013) The etiology of uterine sarcomas: a pooled analysis of the epidemiology of endometrial cancer consortium. Br J Cancer 108:727–734

Gandolfo N, Gandolfo NG, Serafini G, Martinoli C (2000) Endometrial stromal sarcoma of the uterus: MR and US findings. Eur Radiol 10:776–779

Hodge JC, Morton CC (2007) Genetic heterogeneity among uterine leiomyomata: insights into malignant progression. Hum Mol Genet 16(1):R7

Huang PS, Chang WC, Huang SC (2014) Müllerian adenosarcoma: a review of cases and literature. Eur J Gynaecol Oncol 35(6):617–620

Kao YH, Saad U, Tan AE, Magsombol BM, Padhy AK (2011) Fluorine-18-fluorodeoxyglucose PET/CT for the evaluation of suspected recurrent uterine leiomyosarcomas. Acta Radiol 52:463–466

Kapp DS, Shin JY, Chan JK (2008) Prognostic factors and survival in 1396 patients with uterine leiomyosarcomas: emphasis on impact of lymphadenectomy and oophorectomy. Cancer 112:820–830

Kim SA, Jung JS, Ju SJ, Kim YT, Kim KR (2011) Mullerian adenosarcoma with sarcomatous overgrowth in the pelvic cavity extending into the inferior vena cava and the right atrium. Pathol Int 61:445–448

Koivisto-Korander R, Butzow R, Koivisto AM, Leminen A (2008) Clinical outcome and prognostic factors in 100 cases of uterine sarcoma: experience in Helsinki University Central Hospital 1990–2001. Gynecol Oncol 111:74–81

Koyama T, Togashi K, Konishi I et al (1999) MR imaging of endometrial stromal sarcoma: correlation with pathologic findings. AJR Am J Roentgenol 173:767–772

Kurman RJ, Carcangiu ML, Herrington S, Young RH (eds) (2014) WHO classification of tumours of the female reproductive organs, 4 edn. IARC, Lyon

Leath CA III, Huh WK, Hyde J Jr et al (2007) A multiinstitutional review of outcomes of endometrial stromal sarcoma. Gynecol Oncol 105:630–634

Lee C-H, Mariño-Enriquez A, Ou W et al (2012) The clinicopathologic features of YWHAE-FAM22 endometrial stromal sarcomas: a histologically high-grade and clinically aggressive tumor. Am J Surg Pathol 36:641–653

Leitao MM, Sonoda Y, Brennan MF, Barakat RR, Chi DS (2003) Incidence of lymph node and ovarian metastases in leiomyosarcoma of the uterus. Gynecol Oncol 91(1):209–212

Major FJ, Blessing JA, Silverberg SG et al (1993) Prognostic factors in early stage uterine sarcoma. A Gynecologic Oncology Group study. Cancer 71(Suppl 4):1702–1709

McCluggage WG (2002a) Malignant biphasic uterine tumours: carcinosarcomas or metaplastic carcinomas? J Clin Pathol 55:321–325

McCluggage WG (2002b) Uterine carcinosarcomas (malignant mixed Mullerian tumors) are metaplastic carcinomas. Int J Gynecol Cancer 12:687–690

McCluggage WG, Fisher C, Hirschowitz L; On behalf of the Working Group for Cancer Services of The Royal College of Pathologists (2014) Standards and datasets for reporting cancers. Dataset for histological reporting of uterine sarcomas. London: The Royal College of Pathologists

Murase E, Siegelman ES, Outwater EK, Perez-Jaffe LA, Tureck RW (1999) Uterine leiomyomas: histopathologic features, MR imaging findings, differential diagnosis, and treatment. Radiographics 19(5):1179–1197

Namimoto T, Yamashita Y, Awai K et al (2009) Combined use of T2-weighted and diffusion-weighted 3-T MR imaging for differentiating uterine sarcomas from benign leiomyomas. Eur Radiol 19:2756–2764

Prat J (2009a) Corrigendum to 'FIGO staging for uterine sarcomas' [Int J Gynaecol Obstet 2009; 104:179]. Int J Gynaecol Obstet 106:277

Prat J (2009b) FIGO staging for uterine sarcomas. Int J Gynaecol Obstet 104:177–178

Prat J, Mbatani N (2015) Uterine sarcomas. Int J Gynaecol Obstet 131(Suppl 2):S105–S110

Riopel J, Plante M, Renaud M-C et al (2005) Lymph node metastases in low-grade endometrial stromal sarcoma. Gynecol Oncol 96:402–406

Sagae S, Yamashita K, Ishioka S et al (2004) Preoperative diagnosis and treatment results in 106 patients with uterine sarcoma in Hokkaido, Japan. Oncology 67(1):33–39

Sala E, Rockall AG, Freeman SJ, Mitchell DG, Reinhold C (2013) The added role of MR imaging in treatment stratification of patients with gynecologic malignancies: what the radiologist needs to know. Radiology 266:717–740

Santos P, Cunha TM (2015) Uterine sarcomas: clinical presentation and MRI features. Diagn Interv Radiol 21(1):4–9

Schwartz LB, Zawin M, Carcangui MA, Lange R, McCarthy S (1998) Does pelvic magnetic resonance imaging differentiate among the histologic subtypes of uterine leiomyomata? Fertil Steril 70:580–587

Seddon BM, Davda R (2011) Uterine sarcomas – recent progress and future challenges. Eur J Radiol 78(1): 30–40

Sherman ME, Devesa SS (2003) Analysis of racial differences in incidence, survival, and mortality for malignant tumors of the uterine corpus. Cancer 98:176–186

Sutton G (2013) Uterine sarcomas 2013. Gynecol Oncol 130(1):3–5

Szklaruk J, Tamm EP, Choi H, Varavithya V (2003) MR imaging of common and uncommon large pelvic masses. Radiographics 23:403–424

Tamai K, Koyama T, Saga T et al (2008) The utility of diffusion-weighted MR imaging for differentiating uterine sarcomas from benign leiomyomas. Eur Radiol 18:723–730

Tanaka YO, Nishida M, Tsunoda H, Okamoto Y, Yoshikawa H (2004) Smooth muscle tumors of uncertain malignant potential and leiomyosarcomas of the uterus: MR findings. J Magn Reson Imaging 20: 998–1007

Tanner EJ, Garg K, Leitao MM Jr, Soslow RA, Hensley ML (2012) High grade undifferentiated uterine sarcoma: surgery, treatment, and survival outcomes. Gynecol Oncol 127(1):27–31

Thomassin-Naggara I, Dechoux S, Bonneau C et al (2013) How to differentiate benign from malignant myometrial tumours using MR imaging. Eur Radiol 23:2306–2314

Tirumani SH, Ojili V, Shanbhogue AK, Fasih N, Ryan JG, Reinhold C (2013) Current concepts in the imaging of uterine sarcoma. Abdom Imaging 38(2):397–411

Toro JR, Nickerson ML, Wei MH et al (2003) Mutations in the fumarate hydratase gene cause hereditary leiomyomatosis and renal cell cancer in families in North America. Am J Hum Genet 73:95–106

Tse KY, Crawford R, Ngan HY (2011) Staging of uterine sarcomas. Best Pract Res Clin Obstet Gynaecol 25(6):733–749

Wu TI, Yen TC, Lai CH (2011) Clinical presentation and diagnosis of uterine sarcoma, including imaging. Best Pract Res Clin Obstet Gynaecol 25:681–689

Xue WC, Cheung AN (2011) Endometrial stromal sarcoma of uterus. Best Pract Res Clin Obstet Gynaecol 25(6):719–732

Yu CL, Tucker MA, Abramson DH et al (2009) Cause-specific mortality in long-term survivors of retinoblastoma. J Natl Cancer Inst 101:581–591

Ovaries and Fallopian Tubes: Normal Findings and Anomalies

Rosemarie Forstner

Contents

Abstract

Identification of the normal ovaries is one of the cornerstones of assessing pelvic masses by imaging. Due to its excellent soft tissue contrast MRI allows visualization of the ovaries in typical and atypical position. Using anatomical landmarks, particularly the ovarian vascular pedicles and attaching ligaments even in CT both pre and postmenopausal ovaries can usually be identified. Folliclular derivates, including follicular and corpus luteum cysts are the most common incidental finding. Size criteria have recently been published that guide management of ovarian cysts.

This chapter covers the normal ovaries and fallopian tubes and their vascular and ligamentous attachments. Although malformations are much rarer than uterine anomalies, their knowledge is pivotal in the work-up of infertility and variations may also be a source of misinterpretations. This is also true for ovaries that had undergone ovarian transposition before pelvic radiotherapy.

1 Ovaries and Fallopian Tubes: Normal Findings

1.1 Anatomical Relationships

The female adnexal structures are located in the lesser pelvis and include the fallopian tubes, the ovaries, and ligamentous attachments. The fallopian

R. Forstner
Salzburger Landeskliniken, Paracelsus Medical University, Müllner Hauptstr. 48, Salzburg 5020, Austria
e-mail: R.Forstner@salk.at

Med Radiol Diagn Imaging (2017)
DOI 10.1007/174_2017_15, © Springer International Publishing AG
Published Online: 21 February 2017

tubes are 8–12 cm long paired tubular structures at the superior aspect of the broad ligament (Ghattamaneni et al. 2009). They connect the uterus to the ovaries and are divided into four anatomical segments: intramural portion, isthmus, ampulla, and infundibulum with the abdominal ostium. The latter is trumpet shaped, opens at the ovarian end into the peritoneal cavity, and is composed of irregular fingerlike extensions, the fimbriae, which overhang the ovary (Stevens 1992). The infundibulum narrows gradually from about 15 mm to about 4 mm in diameter and merges medially with the serpiginous ampullary portion of the tube, which comprises more than half of the length of the fallopian tube. Due to its circumferential muscular thickening, the isthmus presents the narrowest part of the fallopian tube. Within the uterus, the 1–2 cm long intramural segment joins the uterotubal junction. At its extrauterine course, the fallopian tubes are attached to the upper edge of the broad ligament via its mesentery (Ghattamaneni et al. 2009).

The ovaries are typically located in the ovarian fossa close to the lateral pelvic sidewalls (Fig. 1). In most women, the ovaries can be identified laterally and superiorly of the uterine cornua near the bifurcation of the common iliac artery between internal and external iliac arteries (Outwater et al. 1996). Alternatively, the "ovarian axis" defined by sections parallel to the uterine long axis allows visualization of the ovaries and their relationship to the uterus (Fig. 1) (Spencer et al. 2010). Occasionally, the ovaries may be found at atypical sites, e.g., adjacent to the uterine corpus, superior (Fig. 2) and posterior to the uterine fundus, or in the posterior cul-de sac. Due to its anchoring to the posterior border of the broad ligament, the ovary is typically located in the posterior pelvic compartment and above the uterine fundus, but not in the anterior cul-de-sac

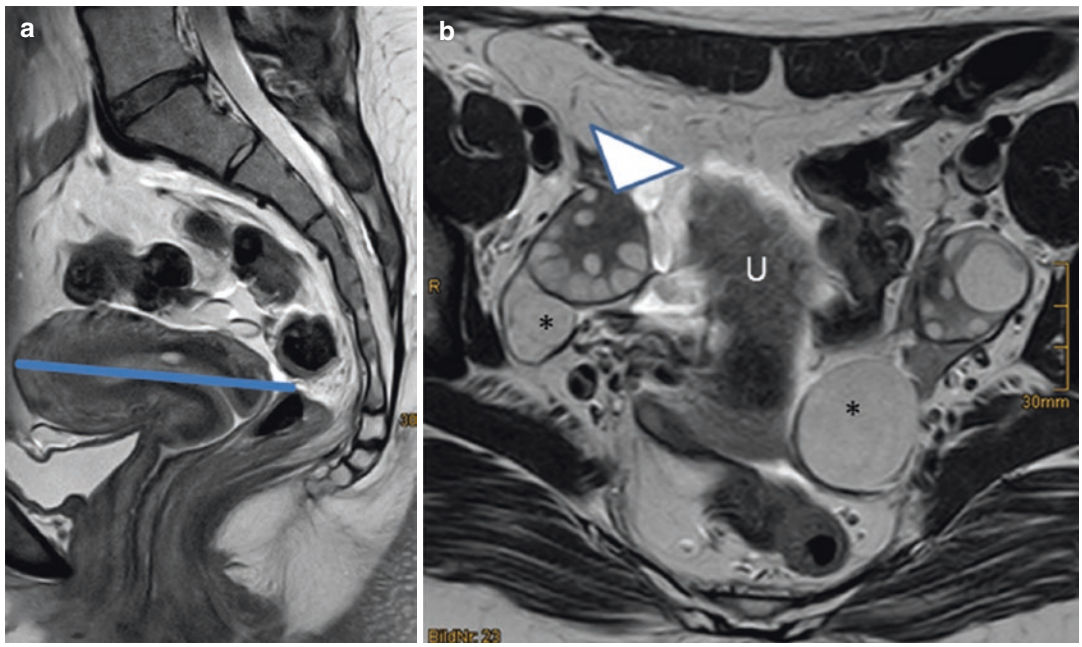

Fig. 1 Uterine axis and ovarian fossa. Sagittal T2WI demonstrates the ovarian axis parallel to the long axis of the uterus (**a**). In this plane (**b**), the ovaries are visualized adjacent to the uterus (*U*) in the ovarian fossa, which is a shallow peritoneal groove between external and internal iliac vessels. The ovaries can be easily identified on T2WI due to small cystic structures, the follicles. These are located peripherally to the ovarian stroma that displays intermediate SI on T2WI (*arrowhead*). Adjacent to the ovaries paraovarian cysts (*) are demonstrated

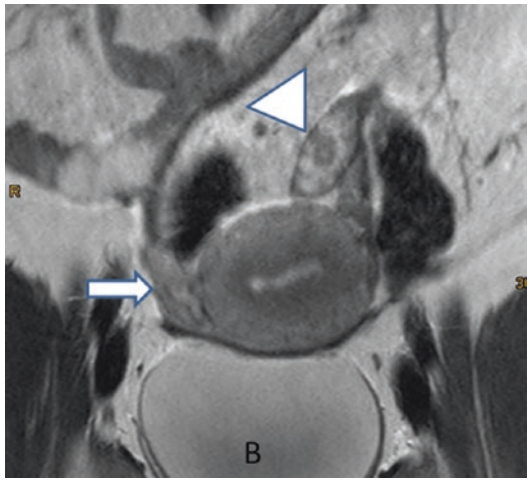

Fig. 2 Ovarian location in a woman of childbearing age. Coronal T2WI shows the left ovary in high position (*arrowhead*), whereas the right ovary (*arrow*) is normally located adjacent and lateral to the uterus. *B* bladder

(Saksouk and Johnson 2004). When the uterus, however, is retroverted one or both ovaries may be found anterior or posterior to the uterus. Furthermore, pregnancy, diseases associated with uterine enlargement such as fibroids, or pelvic masses can displace the ovaries outside the lesser pelvis (Saksouk and Johnson 2004).

1.2 Normal Ovaries in the Reproductive Age

Adult ovaries measure approximately 3–5 cm in length, 1.5–3 cm in width, and 0.5–1.5 cm in thickness. Their appearance and size, however, varies considerably, depending on age, hormonal status, menstrual cycle, and the contents of follicular derivates (Clement 2002). Normal ovarian volume in reproductive age ranges from 4 to 16 cm^3 (Langer et al. 2012). In a larger series, mean ovarian volumes obtained by sonography were highest in the age group younger than 30 years with 6.6 cm^3 (Pavlik et al. 2000). Increased ovarian volumes are also noted in pregnancy (Cohen et al. 1990). The ovaries are of ovoid, almond shape with a smooth surface in early reproductive age, that becomes more irregular afterwards. The ovary is encapsulated by a thin fibrous layer, the tunica albuginea. Within the capsule lies the ovarian stroma, which consists of fibroblasts, smooth muscle cells, arteries, veins, lymphatics, nerves, and follicles. Histologically, the ovaries contain three ill-defined zones: the outer cortex, the highly vascular inner medulla, and the hilum (Clement 2002). The cortex is predominantly composed of follicles, corpora lutea, fibroblasts, and smooth muscle cells.

In childbearing age during each menstrual cycle, a number of follicles are stimulated to begin to mature, but usually only a single follicle completes the process. At midcycle, the preovulatory dominant follicle can be identified as a thin-walled cyst attaining a size of approximately 15–25 mm (Outwater and Mitchell 1996). After formation of the corpus luteum the wall may involute and become irregular. Corpus lutea may be cystic or involuted and noncystic (Outwater et al. 1996). Furthermore, abundant vascularization may give rise to hemorrhage (Fig. 3) (Clement 2002).

The normal fallopian tube contains a small amount of intraluminal fluid that is dispersed within multiple infoldings of the fallopian tube mucosa (Outwater et al. 1996). These infoldings usually prevent visualization of the normal tubes as fluid-filled structures by MRI or CT. Furthermore, due to its small caliber they are difficult to differentiate from adjacent ligaments and vessels on cross-sectional imaging, unless outlined with ascites, where the normal fallopian tubes appear as thin serpentine structures adjacent to the uterus, often extending either anteriorly or posteriorly in the cul-de sac (Rezvani and Shaabab 2011). In tubal ligation, clips allow identification of the fallopian tube (Fig. 4).

Imaging findings

Ovaries can be identified in CT and MRI due to their juxtauterine position. The landmarks of the ovaries are the follicles which are best appreciated on T2W MRI (Outwater and Mitchell 1996) (Figs. 1 and 5). In CT, positive bowel contrast

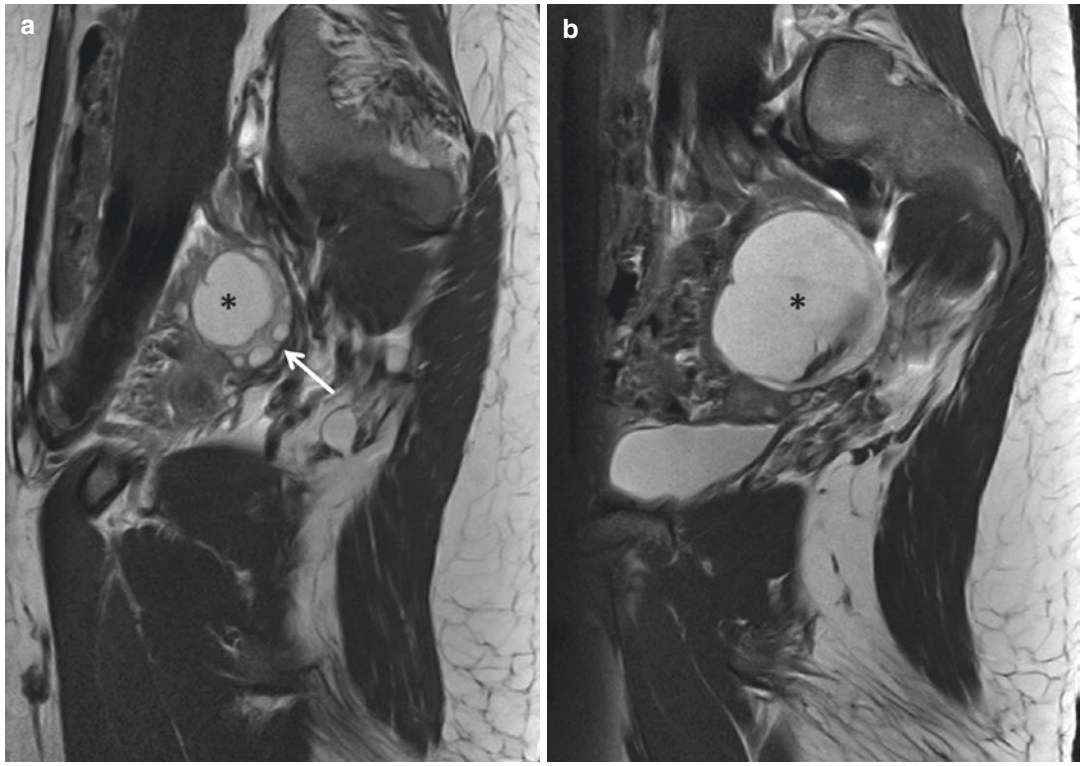

Fig. 3 Hemorrhagic cyst in a 24-year-old femaleT2 WI (**a**, **b**) obtained within interval of 1 week. The ovary demonstrates multiple small follicles (*arrow*) and a mature follicle (*) in (**a**). The follow-up (**b**) shows its enlargement in size and low SI at the bottom presenting hemorrhage

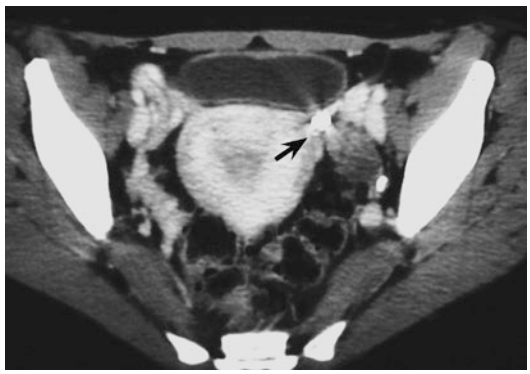

Fig. 4 Tubal ligation. The left fallopian tube is located at the superior margin of the broad ligament and can be identified by the clip in CT (*arrow*). Dilated tortuous vascular structures along the parametria and the right pelvic sidewall present pelvic varices

opacification facilitates visualization of normal ovaries (Fig. 6). They present as ovoid soft tissue structures with cystic areas which represent normal follicles. Presence of a dominant follicle ranging more than 1 cm in size assists in ovarian identification. Another physiologic finding, the corpus luteum can be distinguished from follicles by its thickened wall (Fig. 6). It may also be identified by high attenuation values or a fluid-fluid level in CT (Outwater and Mitchell 1996).

In MRI in the majority of premenopausal women (95%), ovaries can be identified by the presence of follicles within the ovary (Outwater et al. 1996). The ovaries are of low to intermediate SI on T1 (Fig. 5). In premenopausal women, most ovaries (70%) display a zonal differentiation with a higher signal intensity of the medulla compared to the low-signal-intensity cortex on T2WI (Fig. 1) (Outwater and Mitchell 1996). As the ovarian stroma remains of relatively low signal intensity, follicular structures can be well discriminated on T2WI. Follicles are of very high signal intensity with a discrete thin-walled low-signal-intensity rim and are predominantly located in the cortex and range between 0.2 and 4.7 cm in size

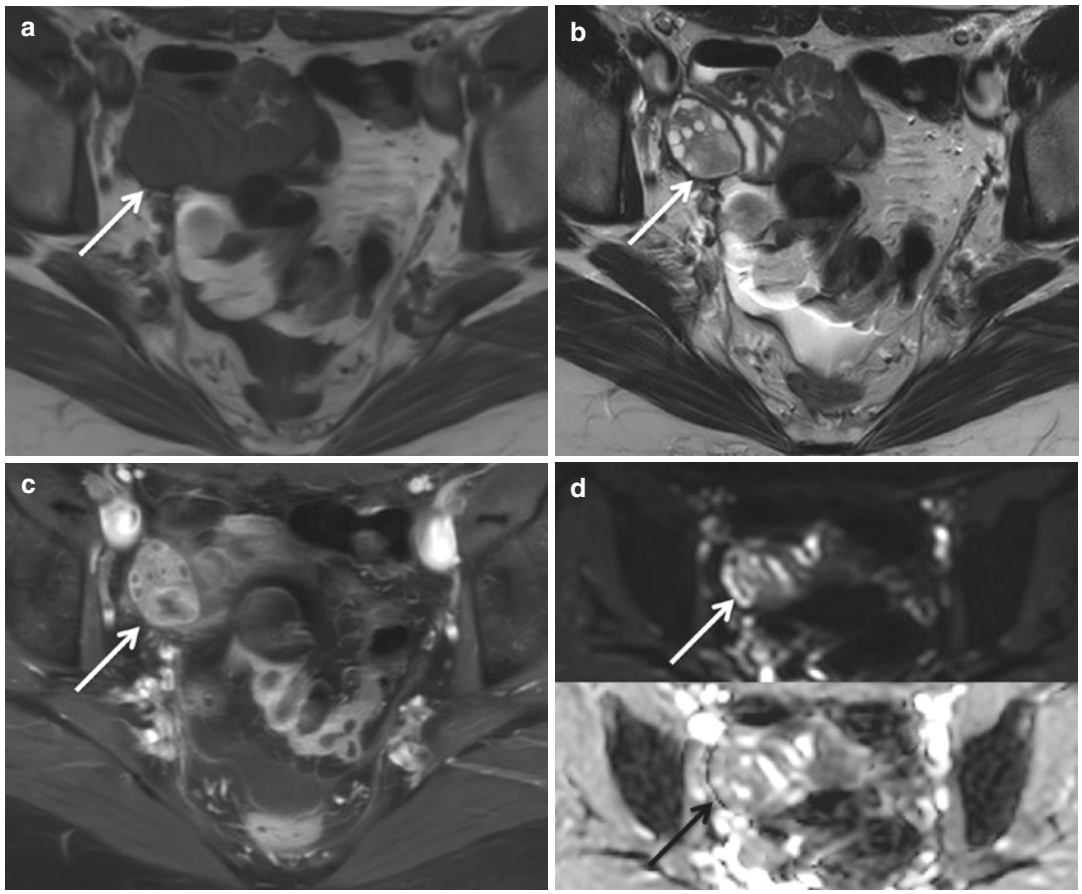

Fig. 5 Normal right ovary in a premenopausal woman. Transaxial T1WI (**a**), T2WI (**b**), Gd T1FS (**c**), and DWI (b = 800 s/mm^2 and ADC) (**d**). The right ovary contains multiple small follicles which show intermediate signal on T1WI (**a**) and very bright signal on the T2WI (**b**). At its posterior aspect a corpus luteum (*arrow*) is seen with intermediate SI on T1WI (**a**) and low SI on T2WI (**b**) corresponding with hemorrhage. It displays an irregular enhancing wall (**c**) and areas of restricted diffusion (**d**). Physiologic free fluid is seen in the cul-de sac

(Outwater and Mitchell 1996). In fertile age, a unilocular cystic lesion up to 3 cm in either ovary or other smaller cysts is a normal finding and presents follicular elements. According to recent management recommendations for US and CT, in a premenopausal woman a unilocular thin-walled cyst with watery contents up to 3 cm is a normal finding and such cysts ranging from 3 to 5 cm in size should be mentioned in the report, but do not require further follow-up (Levine et al. 2010; Spencer and Gore 2011). Alternatively a 6-month follow-up for simple cysts >3 cm and ≤5 cm may be considered (Kim et al. 2016).

Following intravenous contrast application, corpus luteum demonstrates avid enhancement and a thicker enhancing wall than follicles (Figs. 5 and 6). Corpus luteum may contain blood with bright signal on T1 and T2 as a sign of subacute hemorrhage (Outwater and Mitchell 1996). Resolution is expected in a follow-up after two to three menstrual cycles and thus enables the differentiation from an endometrioma. Imaging features on DWI depend on the menstrual cycle. On DWI, normal ovaries display high SI throughout the cycle, that is most prominent in the luteal phase. However, no significant cyclic change of ADC values has been reported (Morisawa et al. 2012).

In premenopausal age, physiological ^{18}FDG PET uptake is noted in the ovaries, particularly in the corpus luteum (Well et al. 2007). Thus, caution is warranted due to overlap of SUV in

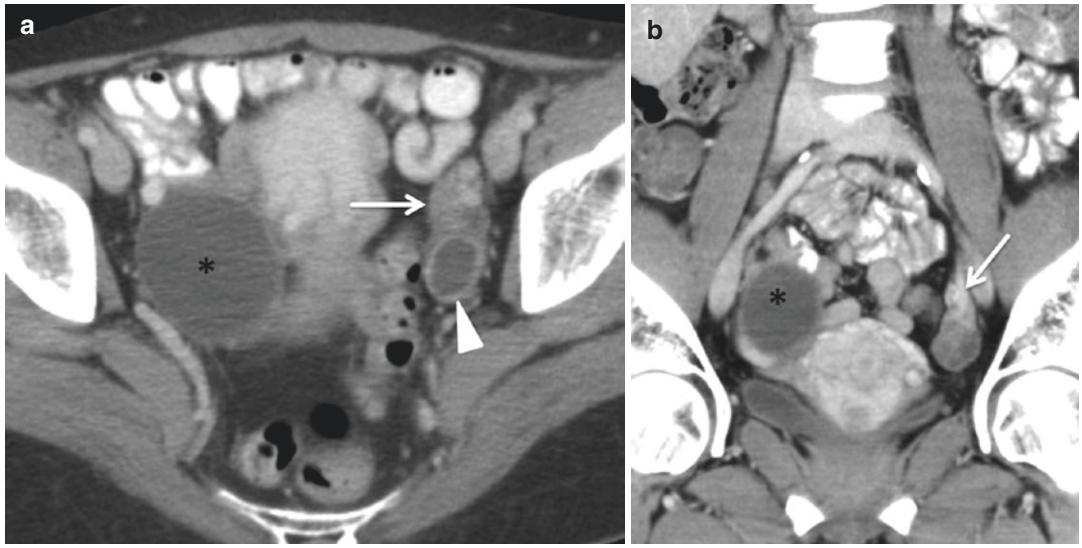

Fig. 6 Functional ovarian cyst on CT. The ovaries contain small cystic elements, the follicles. The corpus luteum (*arrowhead*) can be differentiated by its mural enhancement. Ovarian vessels are entering the left ovary via the suspensory ovarian ligament (*arrow*). The thin-walled cyst (*) of 6 cm in size presents a functional cyst or a cystadenoma. Regression within a 3-month follow-up proofs the diagnosis of a functional cyst

functional and malignant ovarian lesions in this age group (Lerman et al. 2004). Timing of PET/CTs within a week before or shortly after the menses, when corpus luteum typically is not present will reduce the risk of misinterpretations (Lerman et al. 2004).

1.3 Normal Peri- and Postmenopausal Ovaries

After menopause, which is associated with an average age of 51 years in normal women, the ovaries typically shrink to a size of half of the reproductive age (Welt 2016). Ovarian volumes range from 1.6 to 4.6 cm^3 with a reported mean ovarian volume of 2.6 cm^3 in early menopause (Langer et al. 2012; Pavlik et al. 2000).

Most ovaries display a shrunken gyriform shape; some may also have a smooth contour. The ovarian stroma increases variably in volume, and unresolved corpora lutea may be found (Clement 2002). Follicles may persist for several years after cessation of menses. They may account for sporadic ovulation and follicle cyst formation. Follicular activity is typically not found after 4–5 years after menopause (Outwater and Mitchell 1996). Mild hyperplasia of the medullary and cortical stroma is commonly found in postmenopausal women. The clinical findings are secondary to excess androgen production of the stroma, and these findings can be associated with diabetes, obesity, and hypertension (Cohen et al. 1990). Other factors that may increase the ovarian size in postmenopausal women include multiparity or hormonal replacement therapy (Clement 2002). Ovaries may also display stromal atrophy and become extremely fibrotic (Clement 2002). Multiple small (1–3 mm) cysts, probably presenting secondary follicles as well as surface epithelium inclusion cysts, are a common finding in postmenopausal ovaries (Welt 2016). With increasing age, ovarian vessels within the stroma may calcify or become hyalinous (Clement 2002).

Imaging findings

In CT, postmenopausal ovaries are more difficult to identify than premenopausal ovaries, and are best differentiated from bowel loops if bowel opacification was performed (Fig. 7) (Lee et al. 2003). Tracking down the ovarian ovarian vessels along the psoas muscle usually allows identification even of small ovaries (Lee et al. 2003). Postmenopausal ovaries appear in

CT as triangular or bandlike soft tissue structures that show low or moderate contrast enhancement (Figs. 7 and 8). Punctate dystrophic calcifications or identification of small cysts, typically presenting inclusion cysts, or follicles at early menopause aids in the detection of the ovaries.

In MRI, postmenopausal ovaries can be visualized as oval structures most commonly of uniformly intermediate to low signal intensity on T1 and T2WI (Fig. 8) (Outwater and Mitchell 1996). They can be identified in most postmenopausal women despite their small size and nonspecific characteristics by their location in relationship to the uterus and ovarian vessels. Due to the superior soft tissue contrast, small ovarian cysts are more commonly identified in MRI than in CT in postmenopausal women (Fig. 8). As these present common findings, ovarian cysts of ≤1 cm in size are now considered as normal finding and do not require a follow-up (Levine et al. 2010). Neither diffusion restriction is found in MRI nor FDG/PET uptake in postmenopausal ovaries (Lerman et al. 2004).

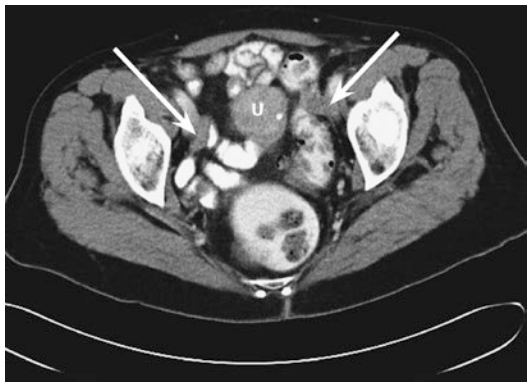

Fig. 7 Postmenopausal ovaries in CT. The ovaries (*arrows*) appear as bandlike soft tissue structures and are located between the iliac vessels and the bowel loops. Without bowel opacification, identification of normal postmenopausal ovaries is usually not possible. Uterus (*U*) with a calcified fibroid of the fundus

1.4 Pelvic Fluid

Small amounts of pelvic fluid are best identified in the cul-de-sac or with increasing volume as tiny fluid pockets outlining bowel loops throughout the pelvis (Welt 2016; Lee et al. 2003). Pelvic free fluid is a common finding throughout the menstrual cycle and peaks in the secretory phase (Davis and Gosink 1986). Although some fluid may be related to ovarian cyst rupture, it seems that most of the fluid is not related to cyst rupture. Pelvic free fluid is a common sequelae after pelvic

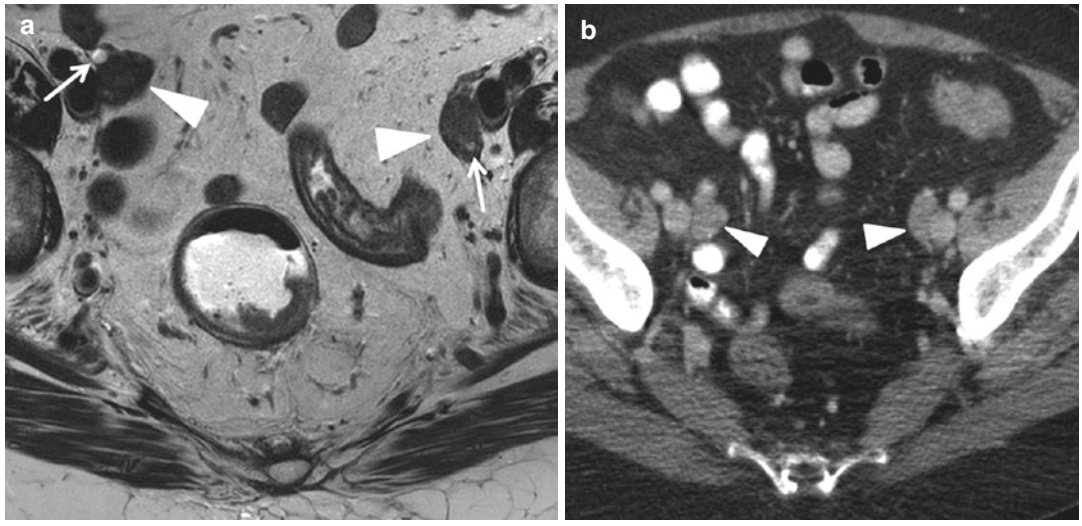

Fig. 8 Normal postmenopausal ovaries in MRI and in CT in a 74-year-old female. Transaxial T2 WI (**a**) and corresponding CT (**b**) show normal small ovaries (*arrowheads*) that are located adjacent to the external iliac vessels and display tiny calcifications. Small cystic structures (*arrows*) are seen on MRI, likely presenting inclusion cysts are a normal finding (**a**)

radiotherapy (Addley et al. 2010). In postmenopausal age, presence of pelvic free fluid is uncommon and further assessment is warranted. In premenopausal age, only larger amounts of pelvic fluid should alert to scrutinize the peritoneum for signs of peritoneal spread (Diop et al. 2014). Normal peritoneum does not enhance after the application of iv contrast media and shows no restricted diffusion on DWI. Diffuse enhancement, however, is not specific and is found in benign, mostly inflammatory and in malignant diseases (Diop et al. 2014).

1.5 Ovarian Attachments and Vascular Supply

The broad ligament is formed by two layers of peritoneum which drape over the uterus and extend laterally to the pelvic sidewalls (Foshager and Walsh 1994). Its caudal margin is defined by the cardinal ligament. The superior free margin is formed by the fallopian tube medially and the suspensory ligament of the ovary laterally. Between these peritoneal folds lies the parametrium which contains the fallopian tube, round ligament, ovarian ligament, uterine and ovarian blood vessels, nerves, lymphatics, mesonephric remnants, and the parts of the ureter (Foshager and Walsh 1994).

Each ovary is suspended in the peritoneal cavity by three supporting structures: the mesovarium which anchors the ovary to the posterior aspect of the broad ligament; the ovarian ligament which attaches the ovary to the uterine cornu; and the suspensory ligament or infundibulopelvic which anchors the ovary to the pelvic sidewall (Clement 2002).

The ovarian ligament and the suspensory ligament are not tight supporting structures but more comparable to a mesentery (Saksouk and Johnson 2004). The ovarian blood vessels and lymphatics course within the peritoneal folds of the mesovarium and enter and exit the ovary through the ovarian hilum. Anastomosing branches of the ovarian and uterine vessels in close relationship with lymphatics are located within the mesovarium (Clement 2002).

The suspensory ligament of the ovary is located at the superior lateral aspect of the broad ligament (Clement 2002). It extends from the ovary anterolaterally over the external and common iliac vessels and blends with connective tissue over the psoas muscle (Foshager and Walsh 1994). Ovarian blood vessels and lymphatics traverse the suspensory ligament to reach the ovarian hilum along the mesovarium.

The ovarian ligament is a rounded fibromuscular band extending from the ovary to the uterine cornu (Clement 2002). Its position varies with that of the ovary. It is located immediately posterior and inferior to the fallopian tube and round ligament (Foshager and Walsh 1994). The ovarian branches of the uterine artery pass through the ovarian ligament and anastomose with branches of ovarian artery in the mesovarium.

The ovarian artery originates from the lumbar aorta near the renal hilum. It is accompanied along its retroperitoneal course by the ovarian vein and the ureter on the anterior surface of the psoas muscle. It then crosses the ureter and common iliac vessels near the pelvic brim to enter the suspensory ligament of the ovary. The ovarian artery courses inferiorly and medially between the two layers of the broad ligament near the mesovarian border (Saksouk and Johnson 2004). It forms multiple branches that enter the ovarian hilum via the mesovarium. It has a tortuous course that is most evident near the ovary.

The ovarian vein is typically single, but may also be multiple and accompanies the ovarian artery. The venous drainage is into the left renal vein, and into the inferior vena cava on the right side. At the pelvic level, they can be identified at the medial aspect of the external iliac vessels. The ovarian lymphatics ascend with the ovarian vessels along the psoas muscle and drain almost exclusively into the para-aortal lymph nodes at the level of the lower pole of the kidneys. In some patients, accessory channels pass the broad ligament and drain into the internal and common iliac and interaortic lymph nodes, or course along the round ligament to the external iliac and inguinal lymph nodes (Clement 2002). In the fallopian tube, additional lymphatic channels to presacral nodes, and occasionally from the ampulla, to gluteal nodes may exist (Clement 2002).

Identifying the ligaments on imaging

The broad ligament and the mesovarium are usually not discernable by cross-sectional imaging unless they are surrounded by large amounts of ascites. Their position, however, can be identified by the structures they contain (Foshager and Walsh 1994). In ascites, the ovaries can be seen suspended from the posterior surface of the broad ligament (Fig. 9) (Saksouk and Johnson 2004). The ovarian ligament may occasionally be visualized as a short and narrow soft tissue band extending between the uterus and the ovary.

In the retroperitoneum, at the level of the inferior renal pole, the ovarian artery and vein can be identified along the psoas muscle medial to the ureter (Fig. 10) (Karaosmanoglu et al. 2009). The ovarian artery is located medial to the vein and due to its smaller size is less constantly conspicuous on CT or MRI. They cross obliquely anterior the ureter at the middle to the lower lumbar region and are then located laterally to the ureter in the lower abdomen and pelvis (Figs. 10 and 11).

Tracking these vessels continuously downwards from the retroperitoneum to the pelvis leads to the suspensory ovarian ligament (Fig. 6) (Lee et al. 2003). The latter is an excellent landmark for localizing the ovary. It is a short and narrow fan-shaped soft tissue band that widens as it approaches the ovary. Sometimes it can also be identified as a linear band that is thicker than the ovarian vein. Due to its vascular landmarks, it is more commonly identifiable than the other ovarian ligaments (Saksouk and Johnson 2004). This ovarian vascular pedicle sign serves also as a useful imaging sign to differentiate between pelvic masses of ovarian from those of uterine origin.

2 Developmental Anomalies

Developmental anomalies of the ovaries are very rare. Although ovaries have a different developmental origin from uterus and fallopian tubes, ovarian anomalies are significantly more often associated with congenital uterine anomalies (22%), particularly with unicornuate uterus (Dabirash et al. 1994). Uterus and fallopian tubes develop from the paramesonephric ducts. Defects of the paramesonephric tubes result not only in abnormalities of the uterus but also of the fallopian tubes, kidneys, and ureters.

In utero the primordial ovaries are located on the medial surface of the urogenital ridge on each side of the lower thoracic and upper lumbar spine, inside the Wolffian body. The ovaries descend during the 3rd month of fetal life with the ovaries located at the level of the iliac crest by the 3rd month of life. They take their place in the ovarian fossa at the end of the first year of life (Stevens 1992). Ovarian migration is guided by

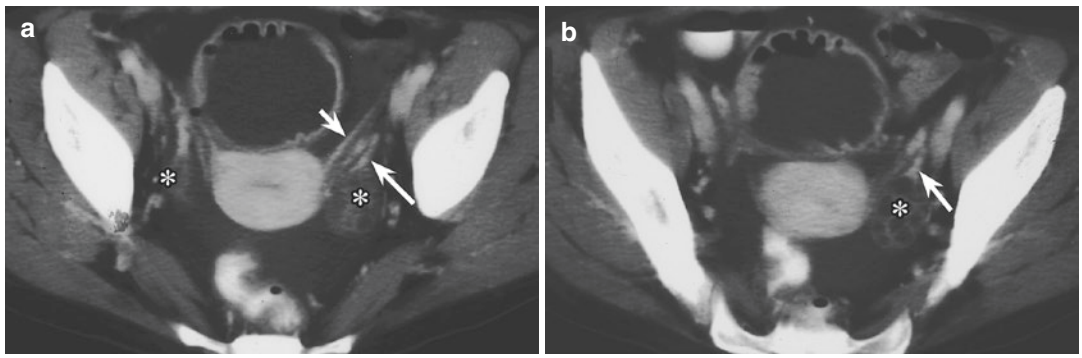

Fig. 9 Broad ligament and ovary in CT. In a patient with free fluid, the ovaries (*) can be visualized posterolaterally of the broad ligament. The left round ligament (*small arrow*) is visualized at the anterior aspect of the broad ligament and courses anterolaterally towards the internal inguinal canal (**a**). At the lateral free margin of the broad ligament, the suspensory ligament attaches to the anterior margin of the left ovary. It transmits the ovarian artery and vein (*long arrow*) and is contiguous to the mesovarium (**a**, **b**)

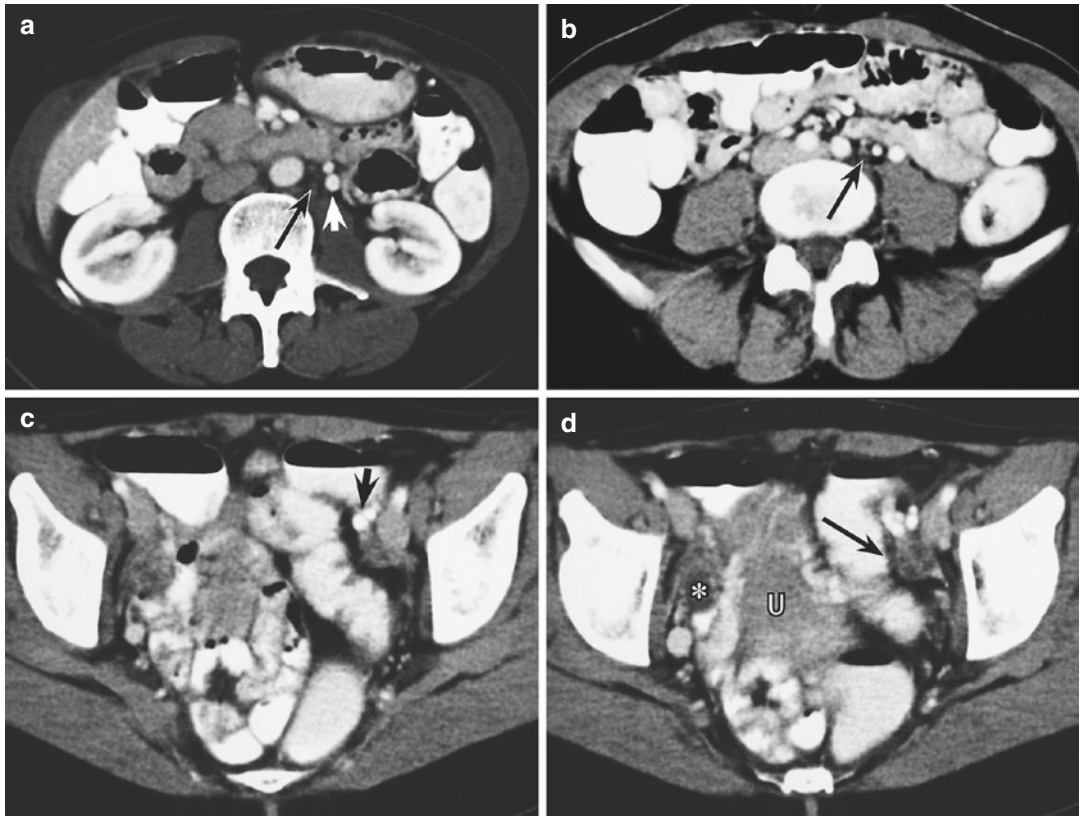

Fig. 10 Ovarian vessels in the retroperitoneum and suspensory ligament "ovarian vascular pedicle." CT scans at level below the renal hilum (**a**) aortic bifurcation (**b**), upper pelvis (**c**), and mid pelvis (**d**). Ovarian artery and vein (*arrow*) course along the psoas muscle parallel to the ureter (*long arrow*) (**a**). At the lower lumbar region, they cross obliquely (*arrow*) and are visualized lateral to the ureter (*long arrow*). The ovarian vessels (*arrow*) are continuous with the suspensory ligament, which is identified near the external iliac vessels (**c**). It demonstrates a wedging as it approaches the ovary. The latter can be identified by multiple small cystic follicles (**d**). Follicle cyst in the right ovary (*). *U* uterus

the gubernaculum which connects the lower pole of the gonad and attaches to the uterus, forming the ovarian and round ligaments of the uterus (Trinidad et al. 2004).

2.1 Congenital Abnormalities

In phenotypic females, absence of both ovaries is usually associated with abnormal karyotypes and a syndrome of gonadal dysgenesis. These patients may have underdeveloped gonads, or uni- or bilateral streak gonads (Fig. 12), which carry a risk of malignancy (Clement 2002). Congenital unilateral agenesis of an ovary in a normal female is extremely rare and usually asymptomatic. It presents more likely the result of torsion with atrophy, particularly in the prenatal period. It may be accompanied by ipsilateral renal or ureteric agenesis and/or malformation of the ipsilateral fallopian tube (Dueck et al. 2001).

Accessory or supernumerary ovaries are extremely rare, and may also be associated with other congenital genitourinary abnormalities. An accessory ovary contains ovarian tissue and is usually located in vicinity of a normal ovary (Clement 2002). Supernumerary ovaries are not attached to the ovary, but may be found at various sites within and outside

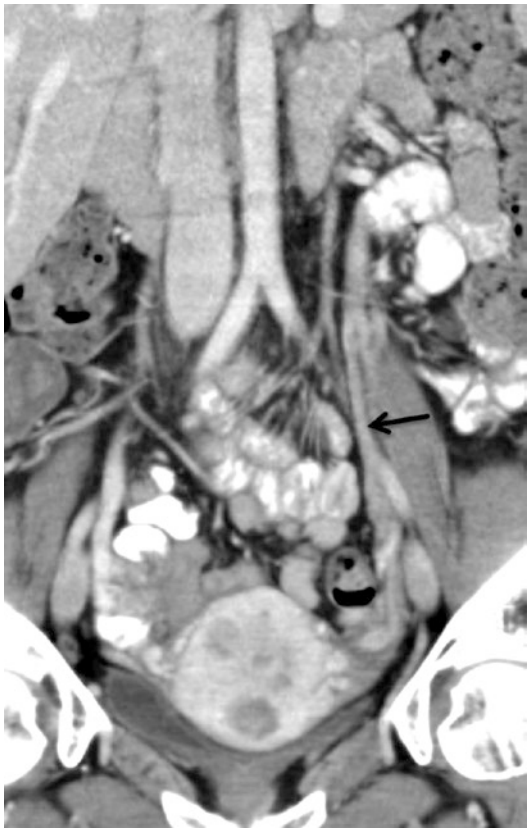

Fig. 11 Ovarian veins. Coronal CT demonstrates the ovarian veins. The left ovarian vein (*arrow*) can be tracked from the left ovary to the retroperitoneum

the pelvis. In most cases, they are smaller than 1 cm in size (Hahn-Pedersen and Larsen 1984). The ectopic ovarian tissue possesses the functional as well as the pathological potential of normal ovaries and may give rise to primary carcinoma of the peritoneum (Seidman et al. 2002).

Adrenal cortical rests may be observed within the wall of the fallopian tubes and broad ligament.

Congenital abnormalities of the fallopian tubes are also extremely rare. As in the ovaries, they result more likely from torsion or an inflammatory process. Isolated congenital abnormalities include aplasia, duplication, accessory ostia, and congenital diverticula of the fallopian tubes (Rezvani and Shaabab 2011). Tubes may also be partially atretic or hypoplastic and these may be associated with uterine abnormalities such as rudimentary uterine horn or bicornuate uterus. Offspring of women exposed to diethylstilbestrol may suffer from infertility due to tubal anomalies including short sacculated or dilated fallopian tubes (Nunley et al. 1984).

2.2 Ovarian Maldescent

Ovarian maldescent has an incidence of 0.2–0.5% (Allen et al. 2012). It may be uni- or bilateral and is more common in Müllerian malformations (17%), with the highest association with didelphis and uni- or bicornuate uterus, and hypoplastic uterus (Allen et al. 2012). In ovarian maldescent, ovaries may be found in an ectopic position along its migration pathway from the lumbar region to the ovarian fossa. Rarely, ovaries may descend too far down until the inguinal canal (Ghattamaneni et al. 2009).

A common location of ovarian maldescent above the pelvic brim is the paracolic gutters (Fig. 13). After pregnancy, the ovaries may be hindered to return to their original position due to adhesions. Furthermore, an ectopic ovarian position may be associated with adhesions, inflammation, and surgery, or result from abnormal ovarian mobility due to elongation of the broad ligaments (Spencer et al. 2010).

Imaging findings

Identification of the upper pole of the ovary at or above the level of the iliac bifurcation defines ovarian malposition (Allen et al. 2012). In women of childbearing age, ovaries in atypical positions can be identified in the majority of patients due to the typical morphology of follicles. MRI is the preferred examination technique to diagnose maldescended or ectopic ovaries due to their excellent visualization on the T2WI (Fig. 13). An ovary not visualized in the ovarian fossa should be sought in other locations in proximity to the uterus and above the pelvic brim, rarely may it be located near the inguinal canal.

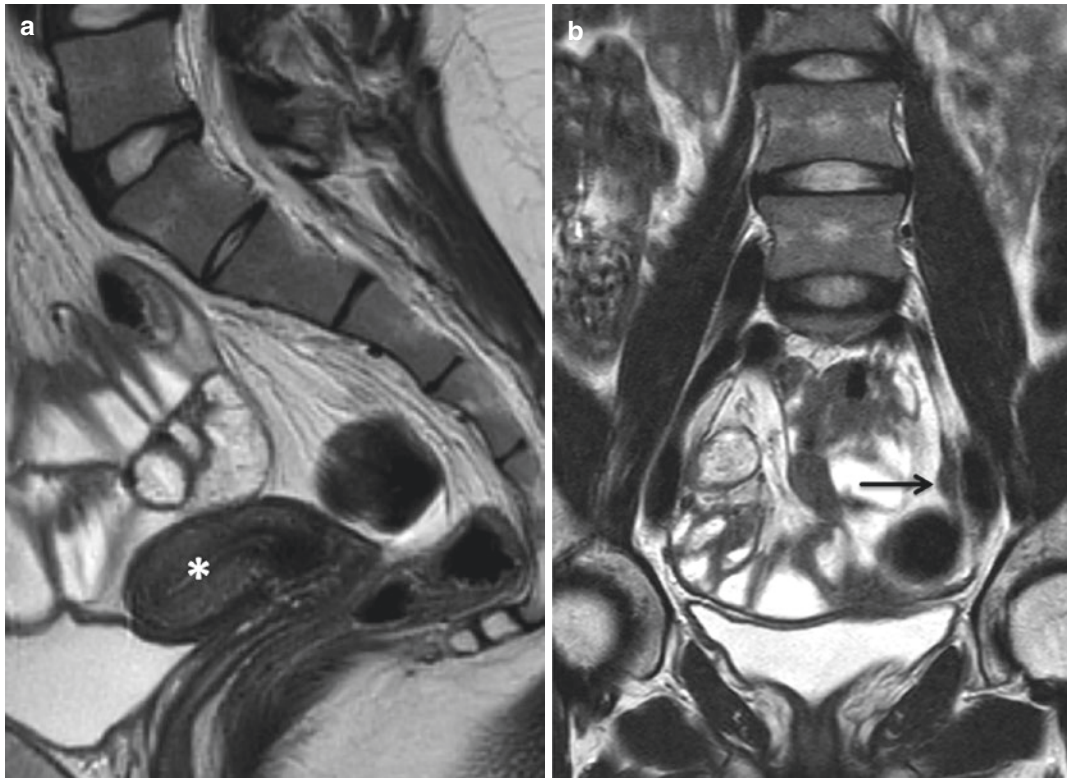

Fig. 12 Streak gonads. In a 23-year-old female, uterine hypoplasia (*) is demonstrated on the sagittal T2WI (**a**). Normal ovaries are not identified. A bandlike soft tissue structure (*arrow*) adjacent to the external iliac vessel presents a left streak gonad (**b**)

Differential diagnosis Differential diagnosis of a unilateral missing ovary includes ectopic ovary and atrophy resulting from adnexal torsion. Mullerian duct anomalies support congenital etiology and warrant search along the psoas muscle outside the pelvis.

3 Ovarian Transposition

Surgical transposition of the ovaries is accomplished before therapeutic irradiation of the pelvis in women to preserve ovarian function. Ovaries, supportive ligaments, and their vascular supply are surgically mobilized outside the pelvis, most commonly laterally to the paracolic gutters anterior of the psoas muscles (Wo and Viswanathan 2009).

Other sites of transposition are the lower paracolic gutters close to the iliac fossa. Lateral transposition is performed in patients with cervical cancer, vaginal cancer, pelvic sarcoma, and Hodgkin disease. Medial transposition refers to attachment of the ovaries to the surface of the uterus (Kier and Chambers 1989; Bashist and Freidman 1989). Surgical clips are typically affixed to each ovary to mark its location.

Imaging findings

Transposed ovaries can be identified by their characteristic morphologic feature of follicles that undergo follicular maturation. Metallic clips help to identify the ovaries on CT (Fig. 14) (Bashist and Freidman 1989). Furthermore, following the ovarian vessels downwards from the mid-lumbar region aids in identifying the ovaries (Lee et al. 2003).

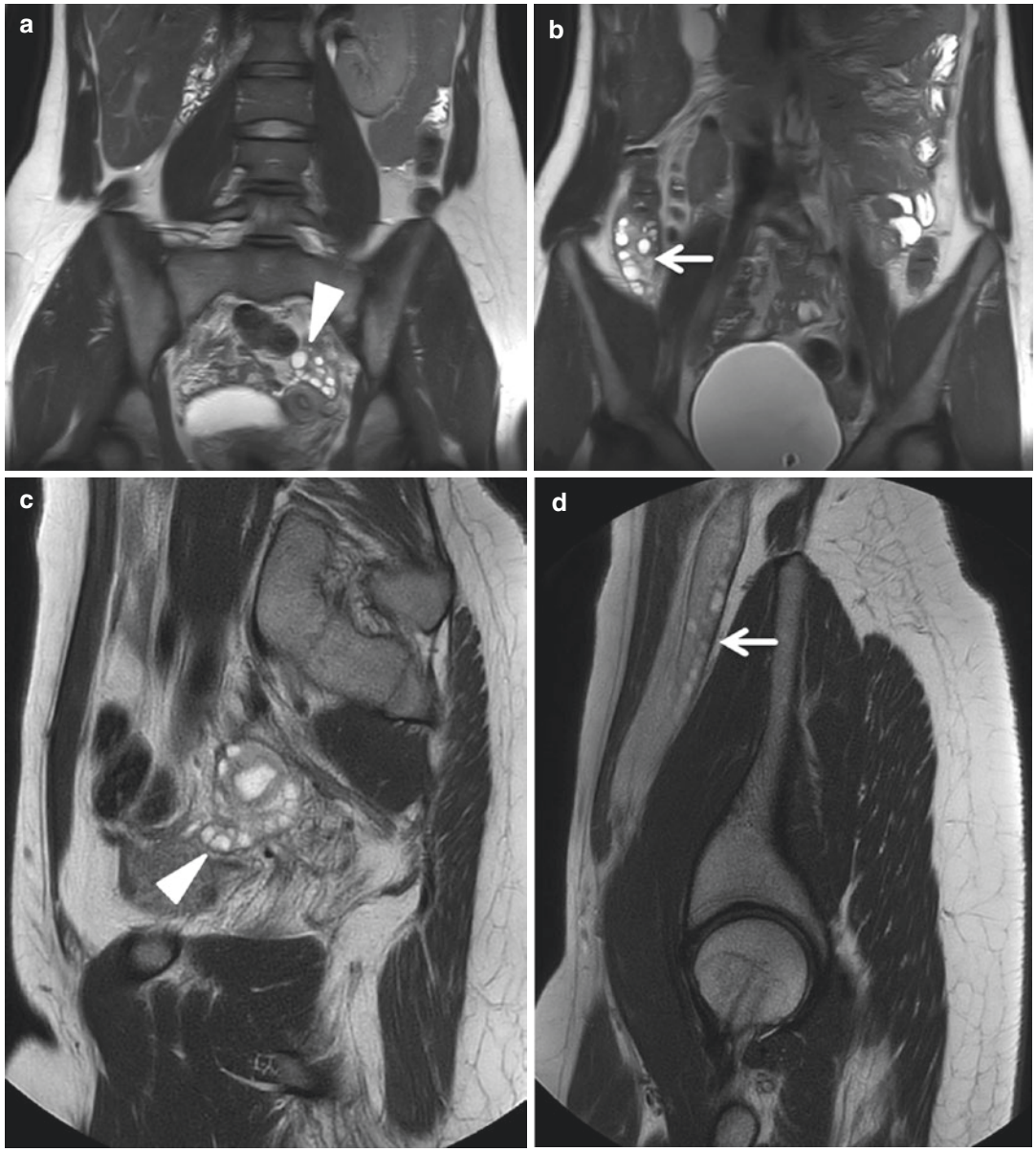

Fig. 13 Ovarian maldescent associated with uterine malformation. Coronal (**a**, **b**) and sagittal (**c**, **d**) T2WI. The left ovary is in normal position adjacent to the unicornuate uterus (*arrowhead*) (**a**, **c**). The left ovary is in atypical high position anterior to the psoas muscle (**d**). It contains multiple peripheral follicles (**b**) and displays an atypical elongated shape (*arrow*) (**d**)

Ovarian vessels in lateral transposition deviate laterally near the iliac fossa instead of coursing inferiorly (Saksouk and Johnson 2004). Transposed ovaries should not be misdiagnosed as peritoneal implants. Medical history and metallic surgical clip markings in CT will facilitate differentiation, as well as meticulous analysis of ovarian morphology including ovarian follicles on T2WI (Sella et al. 2005). Identification of featureless and small atrophic ovaries is feasible due to the surgical clips in CT, but it may be difficult in MRI.

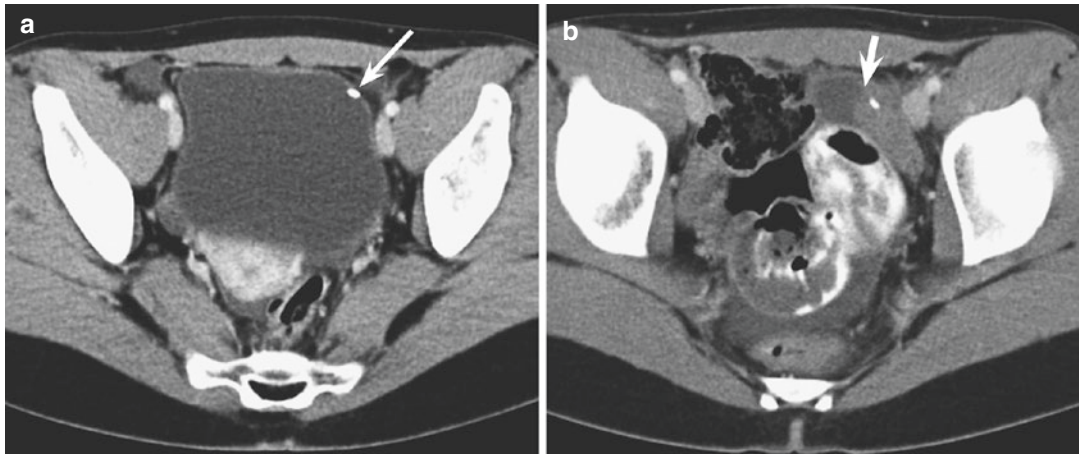

Fig. 14 Surgical transposition. Transaxial CT after transposition of the ovary (**a**) and after radiation therapy (**b**). During endoscopical transposition, the left ovary was marked by a clip (*arrow*). In the follow-up, the cystic and solid lesion presents the normal transposed ovary which undergoes cyclic changes. Without the clip (*arrow*), it may easily be misdiagnosed as a tumor. Ascites is a sequelae of radiation

Differential diagnosis Familiarity with history of ovarian transposition is crucial to establish the correct diagnosis. The differential diagnosis includes mucocele of appendix, peritoneal implants, colonic masses, lymphoceles, and lymph node metastases.

References

Addley HC, Vargas HA, Moyle PL, Crawford R, Sala E (2010) Pelvic imaging following chemotherapy and radiation therapy for gynecologic malignancies. Radiographics 3:1843–1856

Allen JW, Cardall S, Kittijarukhajorn M, Siege CL (2012) Incidence of ovarian maldescent in women with müllerian duct anomalies: evaluation by MRI. AJR Am J Roentgenol 198:W381–W385

Bashist B, Freidman WN, Killackey MA (1989) Surgical transposition of the ovary: radiological appearance. Radiology 173:857–860

Clement PB (2002) Anatomy and histology of the ovary. In: Kurman RJ (ed) Blaustein's pathology of the female genital tract. Springer, New York, pp 649–674

Cohen HL, Tice HM, Mandel FS (1990) Ovarian volumes measured by US: bigger than we think. Radiology 177:189–192

Dabirash H, Mohammad K, Moghadami-Tabrizi N (1994) Ovarian malposition in women with uterine anomalies. Obstet Gynecol 83:293–294

Davis JA, Gosink BB (1986) Fluid in the female pelvis: cyclic patterns. J Ultrasound Med 5:75

Diop AD, Fontarensky M, Montoriol PF, Da Ines D (2014) CT imaging of peritoneal carcinomatosis and its mimics. Diagn Interv Imaging 95:861–872

Dueck A, Poenaru D, Jamieson MA (2001) Unilateral ovarian agenesis and fallopian tube maldescent. Pediatr Surg Int 17:228–229

Foshager MC, Walsh JW (1994) CT anatomy of the female pelvis: a second look. Radiographics 14:51–66

Ghattamaneni S, Bhuskute NM, Weston MJ, Spencer JA (2009) Discriminitive MRI features of fallopian tube masses. Clin Radiol 64:815–831

Hahn-Pedersen J, Larsen PM (1984) Supernumary ovaries. Acta Obstet Gynecol Scand 63:365–366

Karaosmanoglu D, Karcaaltincaba M, Karcaaltincaba D, Akata D, Ozmen M (2009) MDCT of the ovarian vein. Normal anatomy and pathology. AJR Am J Roentgenol 192:295–299

Kier R, Chambers SK (1989) Surgical transposition of the ovaries: imaging findings in14 patients. AJR 153:1003–1006

Kim DC, Bennett GL, Somberg M, Campbell N et al (2016) A multidisciplinary approach to improving appropriate follow-up imaging of ovarian cysts. A quality improvement initiative. J Am Coll Radiol 13:535–541

Langer JE, Oliver ER, Lev-Toaff AS, Coleman BG (2012) Imaging of the female pelvis through the life cycle. Radiographics 32:1575–1597

Lee JH, Jeong YK, Park JK et al (2003) Ovarian vascular pedicle sign revealing organ origin of mass lesion on helical CT. AJR 181:131–137

Lerman H, Metser U, Grisaru D et al (2004) Normal and abnormal 18F-DG endometrial and ovarian uptake in pre-and postmenopausal patients: assessment by PET/CT. J Nucl Med 45:266–271

Levine D, Brown DL, Andreotti RF et al (2010) Management of asymptomatic ovarian and other adnexal cysts imaged at US: Society of Radiologists in Ultrasound consensus conference statement. Radiology 256:943–954

Morisawa N, Kido A, Koyama T, Okada T, Kataoka M et al (2012) Changes in the normal ovary during menstrual cycle in reproductive age on the diffusion-weighted image. J Comput Assist Tomogr 36:319–322

Nunley WC, Pope TL, Bateman BG (1984) Upper reproductive tract radiographic findings in DES-exposed female offspring. AJR 142:337–339

Outwater EK, Mitchell DG (1996) Normal ovaries and functional cysts: MR appearance. Radiology 198:397–402

Outwater EK, Talerman A, Dunton C (1996) Normal adnexa uteri specimens: anatomic basis of MR imaging features. Radiology 201:751–755

Pavlik EJ, DePriest PD, Gallion HH, Ueland FR, Reedy MB, Kryscio RJ, van Nagell JR Jr (2000) Ovarian volume related to age. Gynecol Oncol 77:410–412

Rezvani M, Shaabab AM (2011) Fallopian tube disease in the nonpregnant patient. Radiographics 31: 527–548

Saksouk FA, Johnson SC (2004) Recognition of the ovaries and ovarian origin of pelvic masses with CT. Radiographics 24:133–146

Seidman JD, Russell P, Kurman RJ (2002) Surface epithelial tumors of the ovary. In: Kurman RJ (ed) Blaustein's pathology of the female genital tract. Springer, New York, pp 791–904

Sella T, Mironov S, Hricak H (2005) Imaging of transposed ovaries in patients with cervical carcinoma. AJR Am J Roentgenol 184:1602–1610

Spencer JA, Gore RM (2011) The adnexal incidentaloma: a practical approach to management. Cancer Imaging 11:48–51

Spencer JA, Forstner R, Cunha TM, Kinkel K, on behalf of the ESUR Female Imaging Sub-Committee (2010) ESUR guidelines for MR imaging of the sonographically indeterminate adnexal mass: an algorithmic approach. Eur Radiol 20:25–35

Stevens SK (1992) The adnexa. In: Higgins CB, Hricak H, Helms CA (eds) MRI of the body. Raven Press, New York, pp 865–889

Trinidad C, Tardaguila F, Fernandez GC (2004) Ovarian maldescent. Eur Radiol 14:805–808

Well D, Yang H, Houseni M, Iruvuri S, Alzeair S et al (2007) Age-related changes in the pelvic reproductive end organs. Semin Nucl Med 37:137–184

Welt CK (2016) Ovarian development and failure (menopause) in normal women. Barbeiri RL, Crowley WF (Section eds), Martin KA (Dep ed). www.uptodate.com

Wo JY, Viswanathan AN (2009) Impact of radiotherapy on fertility, pregnancy, and neonatal outcomes in female cancer patients. Int J Radiat Oncol Biol Phys 73:1304–1312

Adnexal Masses: Benign Ovarian Lesions and Characterization

Benign Ovarian Masses

Alexander Schlattau, Teresa Margarida Cunha, and Rosemarie Forstner

Contents

Abstract

Incidental adnexal masses are commonly identified in radiologists' daily practice. Most of them are benign ovarian lesions of no concern. However, sometimes defining the origin of a pelvic mass may be challenging, especially on ultrasound alone. Moreover, ultrasound not always allows the distinction between a benign and a malignant adnexal tumor.

Most of sonographically indeterminate adnexal masses turn out to be common benign entities that can be readily diagnosed by magnetic resonance imaging. The clinical impact of predicting the likelihood of malignancy is crucial for proper patient management.

The first part of this chapter will cover the technical magnetic resonance imaging aspects of ovarian lesions characterization as well as the imaging features that allow the radiologist to correctly define the anatomic origin of a pelvic mass. Next, the authors will go through different benign ovarian entities and through the different histologic types of benign ovarian tumors. Finally the functional ovarian tumors and the ovarian tumors in children, adolescents, young females, and pregnant women will be covered.

1 Introduction

Preoperative imaging plays a pivotal role in triaging management of patients with suspected adnexal masses (Forstner et al. 2016; Kaijser et al. 2014). It also aids in planning the adequate surgical

A. Schlattau, M.D. (✉) • R. Forstner
Salzburger Landeskliniken, Paracelsus Medical University,
Müllner Hauptstr. 48, Salzburg 5020, Austria
e-mail: A.Schlattau@salk.at; R.Forstner@salk.at

T.M. Cunha, M.D.
Serviço de Radiologia, Instituto Português de Oncologia de Lisboa Francisco Gentil,
Rua Prof. Lima Basto, 1099-023 Lisboa, Portugal
e-mail: tmargarida@gmail.com

Med Radiol Diagn Imaging (2017)
DOI 10.1007/174_2017_65, © Springer International Publishing AG
Published Online: 02 June 2017

approach. In this context, in benign ovarian lesions laparoscopy has been widely replacing open surgery. Although a definite histopathologic diagnosis is often not possible, imaging reliably assists in predicting the likelihood of malignancy which is crucial for proper patient management (Jung et al. 2002). In the assessment of adnexal masses the following parameters should be addressed by imaging: (a) defining the exact origin of the mass, (b) if the lesion is ovarian to define if it is a physiologic or neoplastic finding, and (c) when surgery is warranted for a neoplastic lesion, defining the risk of malignancy and providing a differential diagnosis (Sala and Atri 2003).

2 Technical Recommendations for Ovarian Lesion Characterization

MRI of the female pelvis is best performed after at least 4 h of fasting and with prior injection of peristaltic inhibitors to minimize artifacts due to bowel movement. The patient lies on her back in a supine position with a pelvic, torso, or cardiac coil attached around her pelvis or abdomen. Ovarian mass characterization requires anatomical coverage of the entire ovarian mass and the uterus to be able to confirm the ovarian versus uterine origin of the mass. High-resolution fast spin echo T2-weighted images are mandatory to confirm the anatomical origin and clearly identify the ovarian nature of the mass. A basic protocol includes a T2W sagittal sequence of the pelvis and pair of T1W and T2W sequences covering the adnexal mass in the same orthogonal (axial or coronal or oblique) plane with identical slice thickness (Forstner et al. 2016). Further tissue characterization takes into account signal intensity at T1- and T1FS-weighted sequences, and after intravenous injection of gadolinium.

Turbo spin echo (TSE) sequences are the sequences of choice due to their excellent spatial image resolution. Imaging parameters include a field of view of 200–300 mm with a matrix of 512 × 256, slice thickness between 3 and 5 mm. T2-weighted fast spin echo (FSE) sequences use a TR/TE around 4000/90 ms, whereas the TR for T1-weighted sequences is around 500 ms with a minimum TE. Due to time restrictions, faster T2-weighted sequences such as ultrafast half-Fourier single-shot turbo spin echo sequences (HASTE, 3 s per slice) or a 3D T2 WI sequences may be used. Because of its limited image resolution, the HASTE sequence can be used when the high-resolution TSE imaging is suboptimal or to provide additional imaging planes as a complement to high-resolution TSE.

DWI should be performed with a *b* value of 800–1000 s/mm^2. Diffusion restriction is found in solid aspects of both benign and malignant adnexal masses as well as in fatty and hemorrhagic masses, e.g., in endometriomas. In one study the diagnostic confidence was increased about 15% using DW additional to conventional images (Thomassin-Naggara et al. 2011). When the solid component of an indeterminate adnexal mass is of low signal intensity on T2W images and the entire mass is of low signal on DWI obtained with a *b* value of 800–1000 s/mm^2 there is a very high likelihood of benignity (Thomassin-Naggara et al. 2009). DWI is thus diagnostic in the majority of common predominantly solid benign adnexal masses such as ovarian fibroma or cystadenofibroma and for the majority of pedunculated uterine leiomyomas (Forstner et al. 2016). Moreover, a T2W solid mass with low DWI signal is highly likely to be benign irrespective of its pattern or profile of contrast enhancement. For ovarian lesion characterization, intravenous contrast injection has been shown to be useful because of its ability to identify solid intracystic portions such as papillary projections, necrosis within a solid mass,

Fig. 1 A 39-year-old woman presenting with a right adnexal mass and a sonographic diagnosis of atypical endometriosis. MRI is performed for additional lesion characterization. Axial oblique T2 (**a**) and T1-weighted images (**b**), sagittal T2-weighted images (**c**), contrast-enhanced T1-weighted images with fat saturation (FS) (**d**), gross specimen photography (**e**). A multilocular cystic mass of the right ovary (**a**) with a heterogeneous content in the most anterior loculation (*arrow*). The corresponding T1-weighted image (**b**) shows no evidence of hemorrhage excluding the diagnosis of endometrioma. Sagittal T2-weighted image through the heterogeneous part of the cyst shows a hypointense solid portion (*arrow*) with converging thin septa of the cyst, possibly suggesting normal ovarian parenchyma (**c**). Only minimal contrast enhancement the solid aspects and the walls of the cyst (*arrowheads*) is demonstrated in (**d**). Gross specimen photography (**e**) of the right ovary shows a multilocular cyst with tiny papillary projections within the wall of the posterior loculation (*arrowheads*) and a white fibrous portion. Histology diagnosed a serous cystadenofibroma of the ovary

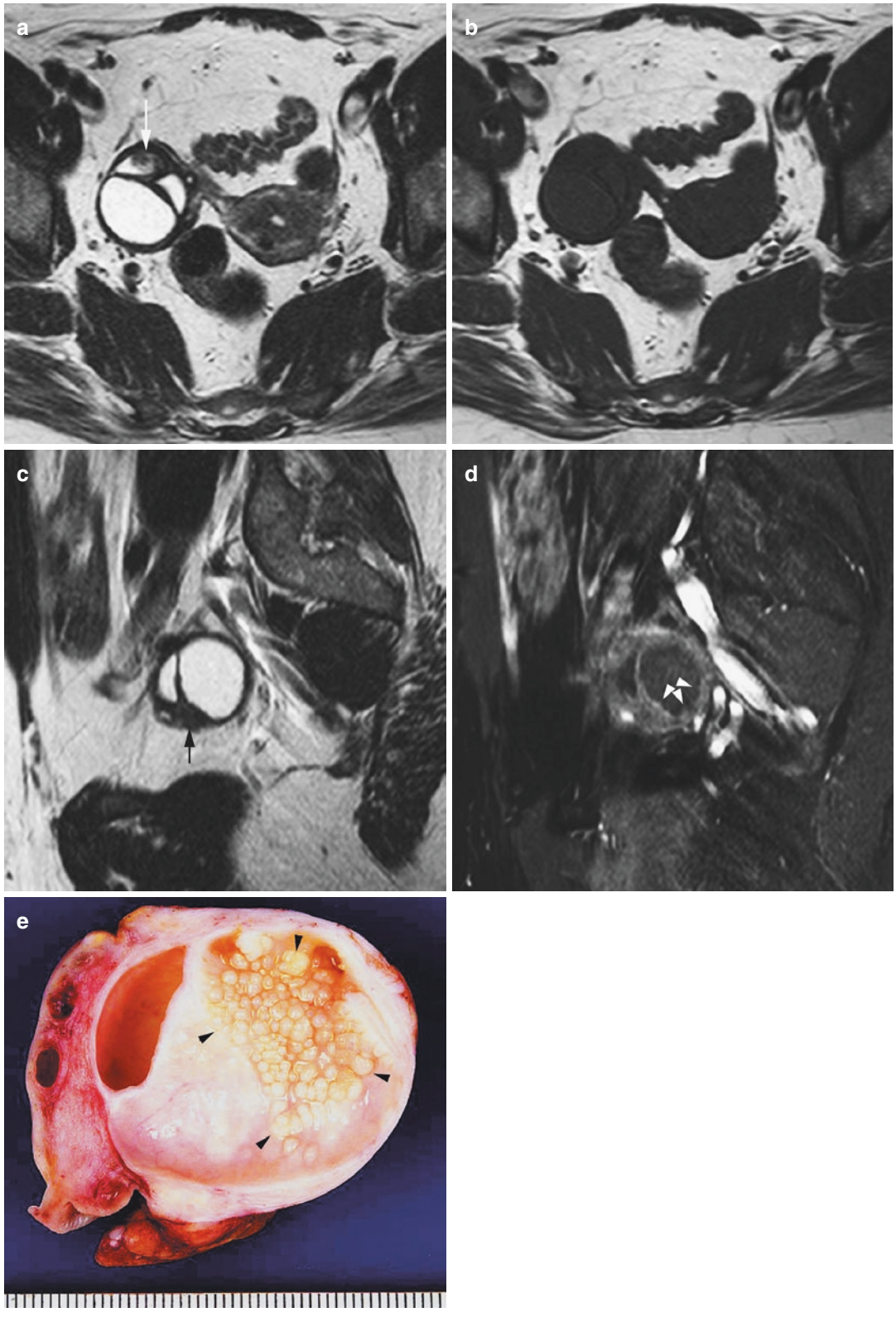
a
b
c
d
e

Table 1 Signal intensity of benign ovarian masses on MRI of the pelvis according to sequences and histological lesion type

Signal intensity					
Ovarian neoplasm	T2	T1	FS T1	Gd T1[a]	DWI[a] ($b > 800$ s/mm^2)
Serous cystadenoma	High	Low	Low	TIC 1	Low
Mucinous cystadenoma	High	Intermediate	Intermediate	TIC 1	Low
Mature cystic teratoma	Intermediate	High	Low	Rokitansky nodule may display TIC 3	Bright
Endometrioma	High	High	High	TIC 1 or 2	Bright
Fibroma	Low-intermediate	Intermediate	Intermediate	TIC 1, rarely TIC 2	Low, some areas bright

TIC time intensity curve
[a]Wall or septations, or solid areas in fibroma

septation, or wall thickening (Fig. 1) (Hricak et al. 2000). Recent data support that dynamic contrast enhancement is the best technique to differentiate between benign and malignant features in ovarian masses. It is based on the comparison of the time intensity curve (TIC) of the solid component in an adnexal mass with the time intensity curve of the external myometrium which is the internal reference. Thus, a DCE MR sequence should be acquired in a plane that involves the solid component of the adnexal mass (i.e., solid papillary projections, thickened irregular septa, or solid portion) and the myometrium (Forstner et al. 2016; Thomassin-Naggara et al. 2009, 2011). For details see also Chap. 66.

Dynamic contrast-enhanced imaging with acquisition of time intensity curves has been recommended by the latest ESUR guidelines on how to characterize sonographically indeterminate masses (Forstner et al. 2016). Table 1 demonstrates differences in signal intensity according to the histological type of the most frequent ovarian benign masses. Details on how to characterize adnexal masses with MRI are covered more in detail in Chap. 66.

Because of its inferior soft tissue contrast compared to MRI, CT is not the imaging modality of choice for characterization of sonographically indeterminate adnexal lesions. Indications for CT include contraindications for MRI, assessment of acute pelvic pain, of complications of pelvic inflammatory disease, and staging of ovarian cancer. Due to its wide clinical use, however, many adnexal lesions are incidentally detected by CT examinations. Published management recommendations of these incidentalomas assist in triaging these common findings (Spencer and Gore 2011; Patel et al. 2013). In CT the use of bowel opacification is generally recommended for assessment of adnexal lesions. It assists in the differentiation of fluid-filled bowel and cystic adnexal lesions and improves the identification of peritoneal seeding. Furthermore, especially in thin patients and in postmenopausal age, detection of normal ovaries is often only possible with bowel opacification. For this purpose, 1000 ml of diluted contrast media or alternatively water is administered 1 h prior to the CT study. Rectal opacification is also helpful in assessing involvement of the rectum or sigmoid colon. Intravenous contrast opacification is pivotal for assessing adnexal lesions. It allows better characterization of the internal architecture and the differentiation of pelvic vascular structures, including depiction of the ovarian vascular pedicle. In most cases, a venous phase enables best depiction of the internal architecture, as solid enhancing components and papillary projections may be missed in an early phase. If a mature teratoma is suspected sonographically, a study without i.v. contrast media may be sufficient.

3 Defining the Origin of a Pelvic Mass: Adnexal Versus Extra-adnexal Versus Extraperitoneal

Defining the origin is the first diagnostic step in assessing a suspected adnexal mass. Depending on the site of origin the differential diagnoses and

treatment options often differ completely. Size, architecture, and location may appear similar in adnexal, extra-adnexal peritoneal masses, and even extraperitoneal lesions. However, special features determining the anatomical relationship of the mass and the surrounding pelvic anatomical structures can assist in their differentiation (Saksouk and Johnson 2004). These parameters include visualization of ovarian structures, the type of contour deformity at the interface between the ovary and the pelvic mass, and the displacement pattern of the vessels, ureters, and other pelvic organs.

Identifying a mass separate from the ipsilateral ovary indicates its nonovarian origin (Fig. 2). However, especially in large pelvic lesions, the ovary may often be obscured or totally invaded by the mass (Levine et al. 1997). Especially in smaller lesions when the ovary is not completely obscured, identifying ovarian follicles indicates its ovarian origin (Fig. 3). Furthermore, for this purpose analyzing specific signs, such as the beak sign, and the embedded organ sign can aid in better defining its relationship with the ovary. When a mass deforms the edge of the ovary into a beak shape it is likely that it arises from the ovary (Fig. 3). In contrast, dull edges at the interface with the adjacent ovary suggest that the tumor compresses the ovary but does not arise from it (Saksouk and Johnson 2004).

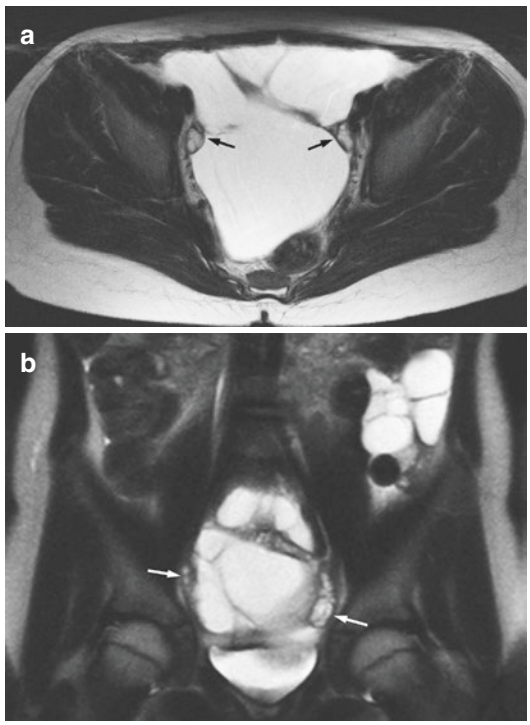

Fig. 2 Nonovarian cystic tumor. Transaxial (**a**) and coronal T2-weighted images (**b**) in a 14-year-old girl in whom sonography, to rule out an abscess after appendectomy, found a multicystic ovarian lesion. A large bilateral multiseptate lesion extending above the umbilical level is demonstrated in both planes. Identification of normal ovaries (*arrows*) allows exclusion of an ovarian origin of the lesion. Histopathology of the surgical specimen diagnosed a chyloma

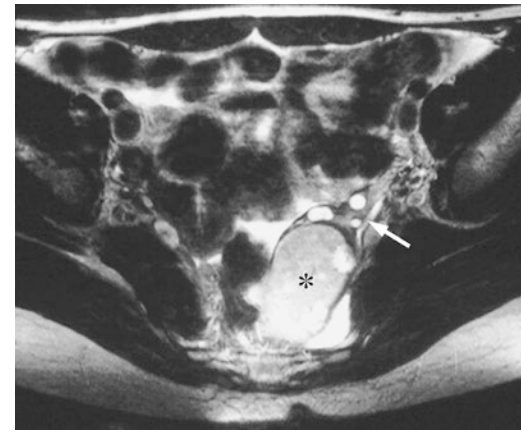

Fig. 3 Beak sign. Transaxial T2-weighted images show a mass in the left cul-de-sac (*asterisk*). Its ovarian origin can be clearly identified due to multiple follicles (*arrow*). The interface to the ovarian tissue is characterized by a sharp angulation, which is typical for the beak sign. A small amount of free fluid in the cul-de-sac as seen in this patient is a physiological finding in premenopausal age and peaks in the secretory phase

Large ovarian masses typically displace the ureter posteriorly or posterolaterally. The same displacement pattern can also be caused by other intraperitoneal lesions, such as the bladder, and masses arising from the uterus or bowel (Foshager et al. 1996). The iliac vessels are typically displaced laterally by an adnexal lesion. In contrast, medial displacement of the iliac vessels is typical for extraovarian masses, originating from the pelvic wall or in lymphadenopathy (Fig. 4). The origin of a mass may be further elucidated by tracking the vascular pedicle or the ovarian suspensory ligament (Saksouk and Johnson 2004). The presence of ovarian vessels leading to or emerging from an adnexal mass was identified in

92% of ovarian lesions in CT (Lee et al. 2003). Defining the ovarian vascular pedicle allows also the differentiation from lesions mimicking ovarian tumors, such as subserosal uterine leiomyoma. Furthermore, in the majority of leiomyomas, a vascular bridging sign at the interface between uterus and leiomyoma or the claw sign can be observed, which is not the case in ovarian lesions (Fig. 5) (Kim et al. 2000; Forstner et al. 2016).

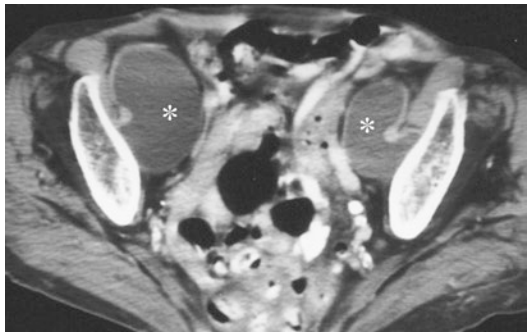

Fig. 4 Medial displacement of the iliac vessels. Transaxial CT in a patient with sonographically suspected bilateral ovarian cancer. Bilateral cystic lesions (*asterisks*) with mural thickening are simulating ovarian lesions. The displacement pattern of the iliac vessels, however, is typical for an origin from the pelvic sidewalls. The lesions are due to bilateral iliopectinea bursitis in a patient with rheumatoid arthritis

Because of their close anatomic relationship, masses arising from the fallopian tubes cannot be distinguished from ovarian lesions by identifying the ovarian vessels or the ovarian suspensory ligament. Incomplete septa emerging from the wall of a cystic adnexal mass indicate the fallopian origin of the mass (Ghattamaneni et al. 2009) (Fig. 6).

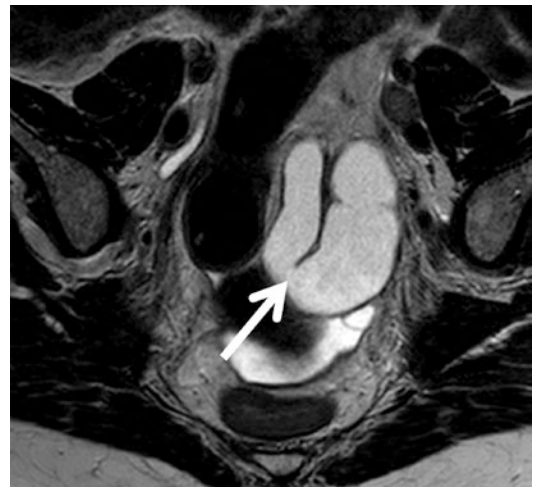

Fig. 6 Incomplete septations. Coronal oblique T2-weighted image of a left adnexal mass. Incomplete interdigitating septa (*arrow*) are typical findings of a hydrosalpinx

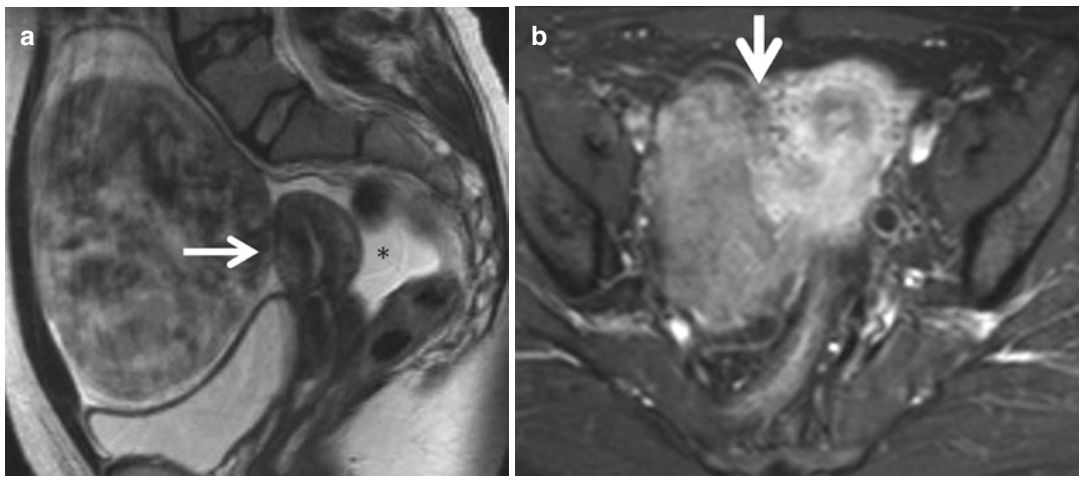

Fig. 5 Ovarian versus extraovarian mass. Sagittal T2-weighted image and axial Gd-enhanced fat-suppressed T1 image demonstrate solid lesions adjacent to the uterus in two women of reproductive age. In ovarian fibroma (**a**), the uterus can be separated from the ovarian mass (*arrow*). Ascites is found in the cul-de-sac and surrounding the ovarian fibroma (**a**). A subserosal uterine leiomyoma (**b**) can be differentiated from an ovarian mass by the demonstration of multiple bridging vessels. These (*arrow*) are found at the interface between the lesion and the myometrium

4 Benign Adnexal Lesions

4.1 Non-neoplastic Lesions of the Ovaries and Adnexa

4.1.1 Physiological Ovarian Cysts: Follicular and Corpus Luteum Cysts

The ovaries change their appearance periodically during their ovarian cycle. The ovarian cycle consists of development of the ovarian follicle, rupture, discharge of the ovum, formation, and regression of corpus luteum. Ovaries may contain follicles of various stages of development, corpus luteum cysts, and surface inclusion cysts.

Physiological ovarian cysts constitute the vast majority of cystic adnexal lesions. In the reproductive age ovarian cysts are defined as ovarian cysts if they are larger than 3 cm in size, whereas smaller lesions present follicles (Levine et al. 2010). Cysts may be classified as functional, which means they are associated with hormone production, or nonfunctional. In nonpregnant patients, corpus luteum cysts derive from failure of regression or hemorrhage into the corpus luteum.

Functional cysts are asymptomatic in the majority of cases. Progesterone production may persist in corpus luteum cysts, resulting in delayed menstruation or bleeding anomalies. Large physiologic cysts may cause abdominal pressure or low back pain. Acute abdomen is caused by complications such as rupture, hemorrhage, or torsion.

With an estimated prevalence of 18% ovarian cysts are a common finding in the reproductive age. Less commonly small cystic lesions may be also found in the postmenopausal age. In a series of 74 normal ovaries, the average size of the largest cyst was 1 cm (range, 0.2–4.7 cm) (Outwater and Mitchell 1996). Functional cysts usually do not exceed 5 cm in size, but may occasionally grow as large as 8–10 cm (Fig. 7). In most cases, they are self-limiting and will regress spontaneously. In contrast to follicular cysts, corpus luteum cysts often require a period of up to 3 months to regress.

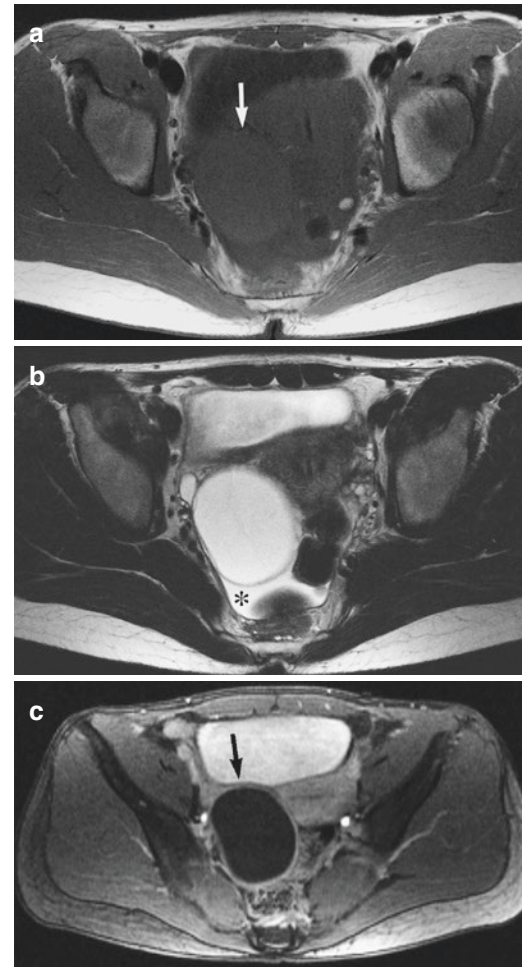

Fig. 7 Functional cyst in a 29-year-old woman. Transaxial T1 (**a**), T2-weighted (**b**), and contrast-enhanced T1-weighted images with FS (**c**). An 8-cm cystic ovarian lesion (*arrow*) displays intermediate signal intensity on T1-weighted image similar to the myometrium (**a**) and very high SI on T2-weighted image (**b**). It has a thin wall well demonstrated on T2-weighted image (**b**) and after contrast administration (**c**). A functional cyst, most likely a corpus luteum cyst, could not be differentiated from an ovarian cystadenoma. The sonographic follow-up showed a considerable decrease in size within 3 months. Small amount of physiologic fluid is seen in the cul-de-sac

4.1.1.1 Imaging Findings in Physiological Ovarian Cysts

Transvaginal sonography is the gold standard for the diagnosis of ovarian cysts. According to recent management guidelines simple ovarian cysts of less than 5 cm in size do not require

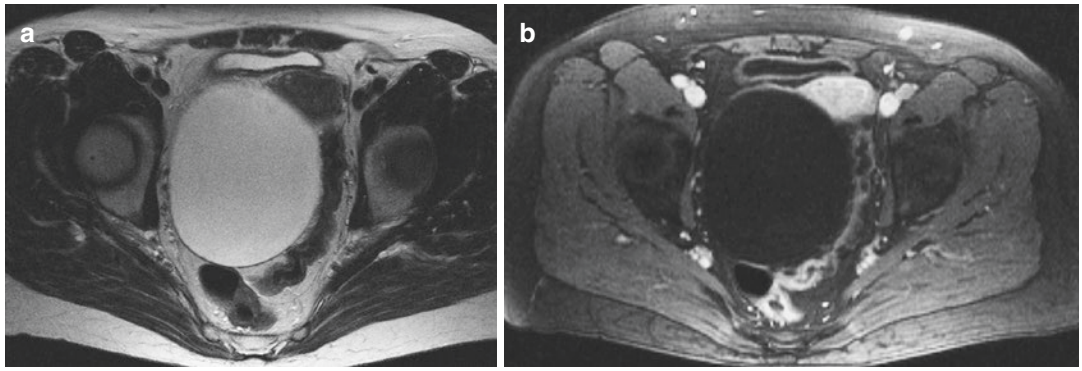

Fig. 8 Large cystic adnexal lesion in a 55-year-old woman. Transaxial T2-weighted image (**a**) and T1-weighted image with Gd and fat saturation (**b**) show a unilocular right adnexal cyst. It displaces the uterus and the adjacent sigmoid colon. There are no signs of malignancy. Due to postmenopausal age and the increase in size, surgery was performed. The histopathological diagnosis was serous cystadenoma

further assessment in an asymptomatic woman of reproductive age (Spencer and Gore 2011; Levine et al. 2010). Findings include anechoic thin-walled cysts for simple follicular cysts and a fishnet-like heterogeneous hypoechoic content for hemorrhagic follicular or luteal cysts also described with a fine trabecular jelly-like content (Levine et al. 2010). Most of these cysts will disappear or decrease in size at short-term follow-up. In a follow-up 65% of the cysts persisting after menstruation had resolved within 3 months, independently of the use of oral contraceptives (Christensen et al. 2002).

Simple ovarian cysts are a common incidental finding on CT and MRI. They are unilocular and display an imperceptible or thin (<3 mm) wall. On CT they appear as round or oval water-density lesions (<20 HU). Most cysts display intermediate to low signal intensity (SI) on T1-weighted images, and very high signal intensity on T2-weighted images, due to the presence of watery fluid. The thin wall is best depicted on T2-weighted images as hypointense and on contrast-enhanced images as hyperintense to ovarian stroma (Outwater and Mitchell 1996). Corpus luteum cysts demonstrate thicker walls with distinct enhancement due to their thick luteinized cell lining. Layering by debris and internal fibrin clots in corpus luteum cysts can be differentiated from papillary projections in epithelial tumors by their lack of enhancement.

4.1.1.2 Differential Diagnosis

Unilocular cystadenomas may mimic simple ovarian cysts (Fig. 8). Regression in a follow-up over two to three cycles confirms the diagnosis of a physiological cyst.

Both corpus luteum cysts and endometrioma may show intracystic hemorrhage. However, endometrioma tend to be bilateral, are often multiple, and typically demonstrate prominent T2 shortening ("shading") and the T2 dark spot sign presenting mural clot (Corwin et al. 2014).

4.1.2 Paraovarian Cysts

Paraovarian cysts (paratubal) cysts arising from Wolffian duct remnants in the mesovarium (Moyle et al. 2010) are common incidentalomas. Although encountered throughout life, they are most commonly found in middle-aged women. Surgical data suggest that they account for 10–20% of adnexal masses (Kier 1992). They are round or ovoid, unilocular thin-walled cysts ranging between 1 and 12 cm in size (Kim et al. 1997). Complications do not differ from those of other ovarian cysts. Secondary transformation with foci of benign and malignant papillary neoplasms is extremely rare (Honoré and O'Hara 1980).

4.1.2.1 Imaging Findings

Paraovarian cysts tend to be large thin-walled unilocular cysts, located typically within the broad ligament (Fig. 9). Rarely they may contain

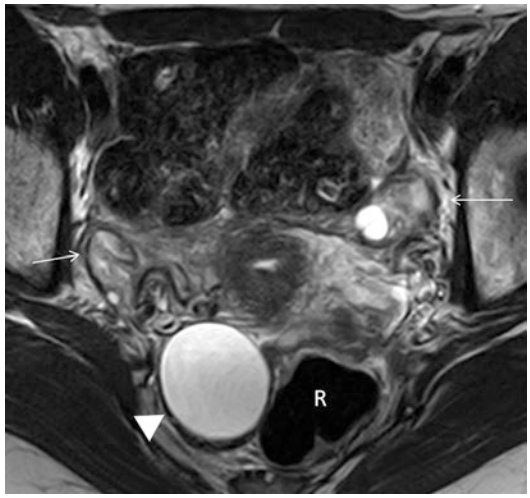

Fig. 9 Paraovarian cyst in a 53-year-old female. Transaxial T2WI demonstrates a 5 cm cyst (*arrowhead*) that is clearly separated from the postmenopausal right ovary (*arrow*). A 1 cm cyst with a thin septum is seen on the left ovary (*arrow*). Rectum (*R*)

internal septations. On CT and MRI, they display typical criteria of ovarian cysts, but are found separate from the ipsilateral ovary (Moyle et al. 2010).

4.1.2.2 Differential Diagnosis

A paraovarian cyst can only be distinguished from an ovarian cyst if it is clearly separated from the ovary. While paraovarian cysts are usually larger cysts, cysts of Morgagni, which arise from the fimbriated end of the tube, usually do not exceed 1 cm in diameter. The differential diagnosis of paraovarian cysts includes ovarian cystadenoma, an eccentric ovarian cyst, retroperitoneal cysts, and lymphoceles. The latter can be differentiated based on the clinical history and the pattern of vascular displacement. Hydrosalpinx may have a similar location within the broad ligament; however, it displays a tubular form and interdigitating septa (Moyle et al. 2010). In contrast to paraovarian cysts, the shape of peritoneal inclusion is defined by the surrounding structures.

4.1.3 Peritoneal Inclusion Cysts

Peritoneal inclusion cysts (pseudocysts or multilocular inclusion cysts) are accumulations of fluid produced by the ovaries that become entrapped by peritoneal adhesions. These lesions are of variable size and are typically encountered in premenopausal women with previous surgeries, endometriosis, or pelvic inflammatory disease (PID) (Moyle et al. 2010). Pseudocysts have an irregular shape because the outer surface is not a true wall but defined by surrounding structures. They may become clinically apparent due to mass effect, chronic pelvic pain, or present without symptoms (Kim et al. 1997).

4.1.3.1 Imaging Findings

Peritoneal inclusion cysts tend to take the shape of the space they are occupying. The ovary is entrapped and lies typically inside the cyst or within the cyst wall and may be mistaken as a solid nodule (Fig. 10). The internal architecture of peritoneal inclusion cysts depends on its contents. In most cases, they contain simple fluid with low SI on T1-weighted images and very high SI on T2-weighted images, and low density on CT. Hemorrhage and layering of hemosiderin can lead to high SI on T1 and low SI on T2 W, and higher densities on CT. In one study internal septa were found in 11/15 cases of peritoneal inclusion cysts (Kim et al. 1997).

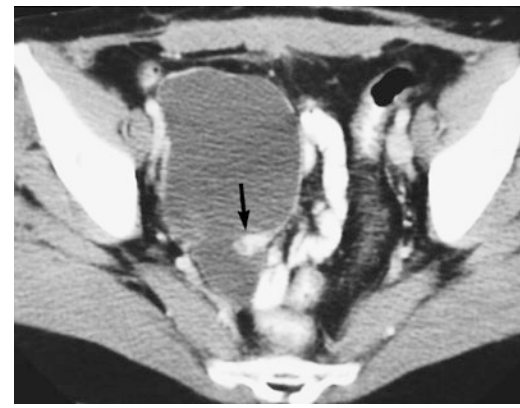

Fig. 10 Peritoneal inclusion cyst on CT. A cystic lesion of the right adnexa was found on sonography in a 33-year-old woman with a history of several previous pelvic surgeries. CT demonstrates a cystic lesion with thin enhancing walls and a solid ovoid structure (*arrow*) at its posterior wall. Surgery revealed a peritoneal inclusion cyst. The solid structure was the normal ovary

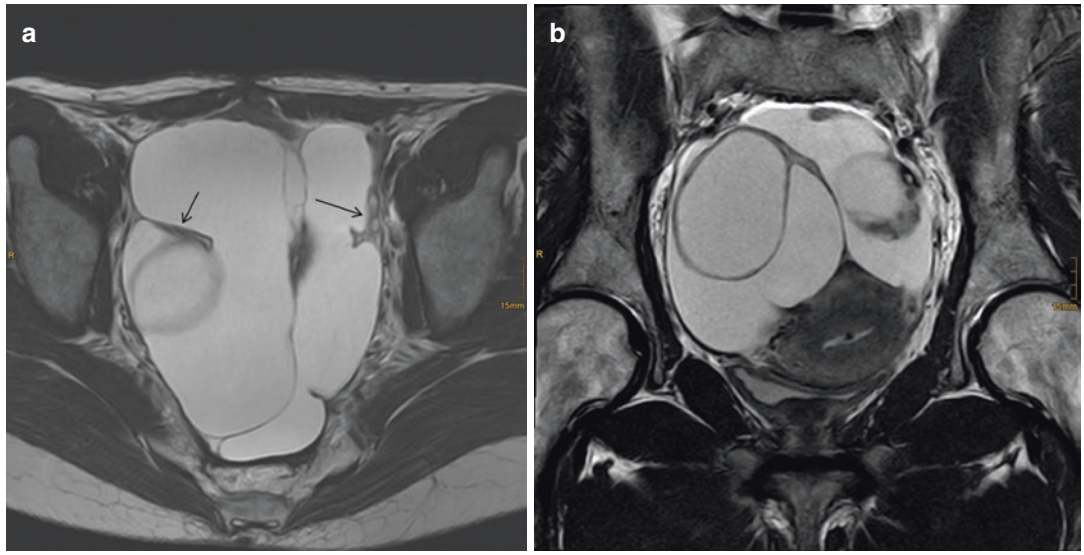

Fig. 11 Peritoneal pseudocyst on MRI. Transaxial (**a**) and coronal T2WI (**b**) show a multiseptate cystic bilateral mass. Imaging features typical of this entity include the ovary (*arrows*) displayed at the wall or within a septum, thin septas, and the contour following the predefined anatomical space

4.1.3.2 Differential Diagnosis

Particularly in CT differentiation of a pseudocyst from cystadenomas or ovarian cancer may be difficult due to internal septations and the murally located ovary mimicking a solid component within a cystic mass. Conforming to the peritoneal cavity and encasement rather than displacement of adjacent organs as well as a history of previous surgeries, PID, or Crohn's disease are key elements for the correct diagnosis (Fig. 11).

4.1.4 Theca Lutein Cysts

Theca lutein cysts are ovarian cysts that are lined by luteinized theca cells. They develop in patients with high levels of serum human chorionic gonadotropin and are associated with multiple gestations, trophoblastic disease, and pregnancies complicated by hydrops fetalis, or in patients with ovarian hyperstimulation syndrome (Fig. 12).

4.1.4.1 Imaging Findings

Theca lutein cysts are typically large, bilateral multiseptate ovarian cysts composed of simple fluid. They may cause gross enlargement of the ovaries to 10–20 cm in diameter. T2-weighted images or contrast-enhanced MRI or CT will typically display no evidence of mural thickening (Fig. 13).

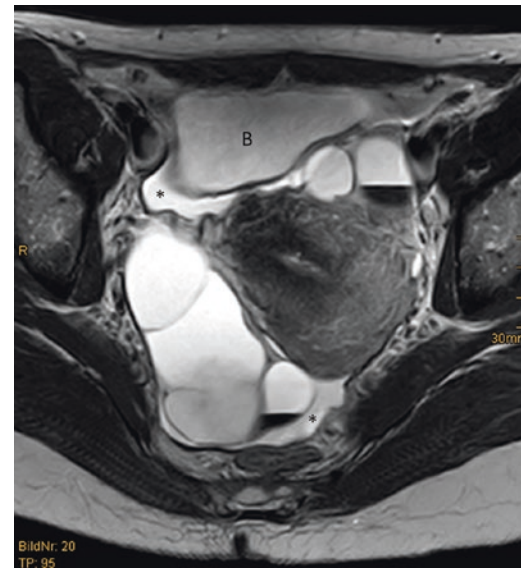

Fig. 12 Ovarian hyperstimulation syndrome in a 45-year-old female treated with tamoxifen. Bilateral enlarged ovaries with multiple thin-walled cysts are found. Some of these show hemorrhagic foci. Bladder (*B*). Ascites (*asterisk*)

4.1.4.2 Differential Diagnosis

Theca lutein cysts may resemble bilateral cystadenomas, but the clinical background is different.

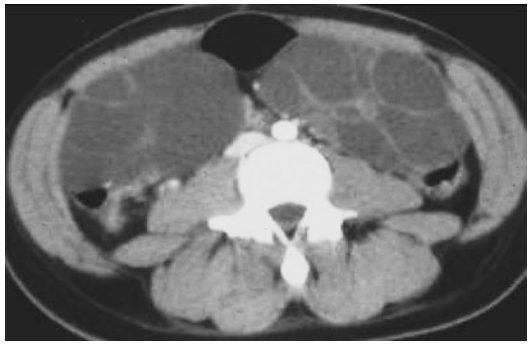

Fig. 13 Bilateral theca lutein cysts CT at the umbilical level in a 27-year-old patient with a hydatidiform mole. Bilaterally enlarged ovaries are demonstrated displaying numerous thin-walled cysts of water-like density. No enhancing solid structures or papillary projections could be identified. Theca lutein cysts are found in up to 20% of patients with a hydatidiform mole

4.1.5 Polycystic Ovary Syndrome

Polycystic ovary syndrome (PCOS) is a complex endocrinologic disorder characterized by inappropriate gonadotropin secretion that results in chronic anovulation. It affects 5–10% of women of reproductive age and is found in 50% of women with infertility problems (Lakhani et al. 2002).

Although most notable in Stein-Leventhal syndrome, which comprises the classical findings of amenorrhea, hirsutism, obesity, and sclerotic ovaries, a wide range of clinical presentations exist. Only one-quarter to one-half of the patients present the classical signs. Another feature is metabolic disorders including increased risk of diabetes, cardiovascular disease, and endometrial hyperplasia or endometrial cancer (Lee and Rausch 2012). The morphologic hallmark is mild enlargement of both ovaries, which contain numerous multiple small follicles surrounding the increased central ovarian stroma.

4.1.5.1 Imaging Findings

As there is an overlap of normal and polycystic ovaries in imaging, the diagnosis of polycystic ovary syndrome is based on hormonal changes as well as clinical and imaging findings (Johnstone et al. 2010).

The imaging modality of choice to assess PCOS is transvaginal US. The Rotterdam consensus defined a threshold of at least 12 or more follicles, measuring between 2 and 9 mm (FNPO), and/or an ovarian volume >10 cm^3 (Franks 2006). Newer data suggest follicle counting by 3D techniques and increasing the number of follicles (Lujan et al. 2013). MRI is usually not warranted to diagnose PCOS (Lee and Rausch 2012). In this setting the role of MRI is as an adjunct to US to exclude a virilizing ovarian tumor and to assess the adrenal glands.

The MRI findings in PCOS include bilateral moderately enlarged (up to 5 cm) spherical ovaries with an abnormally high number of follicles measuring less than 10 mm in size (Fig. 14). At least 12 follicles are found in a peripheral distribution (Fig. 9.24) in each ovary. Rarely, a normal contralateral ovary may be identified. The ovaries are surrounded by a thickened sclerotic capsule and typically display abundant low signal central stroma on T1- and T2-weighted images (Fig. 14).

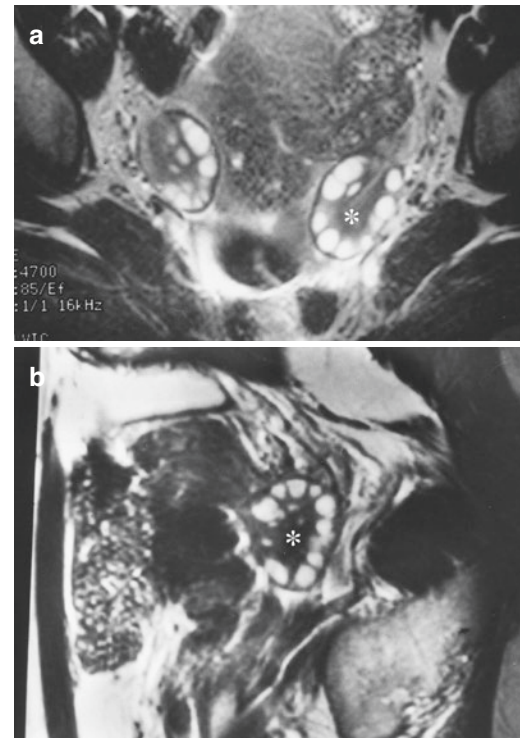

Fig. 14 Polycystic ovaries in MRI. Transaxial T2-weighted image (**a**) and parasagittal T2 WI (**b**) in a patient with Stein-Leventhal syndrome. Bilateral spherical ovaries are demonstrated showing numerous small follicles of uniform size. The latter are located in the periphery of the ovary much like a "string of pearls" surrounding the ovarian stroma (*asterisk*), which typically is of very low signal intensity on T2-weighted images in PCO

4.1.5.2 Differential Diagnosis

Multiple follicles in different stages of development including complex cysts constitute a common finding in adolescents, and present a normal finding in mid- to late puberty (Laufer 2017). Using the threshold of 12 follicles an overlap to PCOS exists also in normal young females (Duijkers and Klipping 2010). Multifollicular ovaries may also be found in hyperprolactinemia, hypothalamic anovulation, and weight-related amenorrhea. They may be differentiated from PCO by fewer cysts, the different size of follicles, lack of stromal hypertrophy, and the distribution of the often larger follicles throughout the ovary (Clement 2002). In contrast to PCO, the ovaries resume normal appearance after treatment.

4.2 Benign Neoplastic Lesions of the Ovaries

Benign ovarian neoplasm accounts for 57% of epithelial ovarian tumors and for 80% of all ovarian tumors (Seidman et al. 2002). Although there is large spectrum of benign ovarian neoplasm, the vast majority are encompassed by only a few different histologic types. It is a matter of debate whether cystadenomas or teratomas are most frequent. In a large series cystic teratomas accounted for the majority of benign tumors (58%) followed by serous cystadenomas (25%) and mucinous cystadenomas (12%), benign stromal tumors (fibromas/thecomas) (4%), and Brenner tumors (1%) (Koonings et al. 1989). In epithelial tumors a continuum between various subtypes of benign cystadenomas, borderline, and malignant epithelial tumors is found (Lengyel 2010).

4.2.1 Cystadenoma

Cystadenomas account for 37–50% of benign ovarian tumors in the reproductive age. Their frequency tends to increase with age, and after menopause, cystadenomas account for up to 80% of benign ovarian tumors (Jung et al. 2002). Cystadenomas are thin-walled unilocular or multilocular cystic lesions filled with serous, mucinous, and sometimes hemorrhagic contents. Small papillary projections within the cyst walls may be rarely found in serous cystadenomas (Hassen et al. 2011). Serous and mucinous cystadenomas differ in pathology, prognosis, and disease course. Serous cystadenomas are more common than mucinous cystadenomas, with a prevalence of 11.2% vs. 7.4% in the IOTA series analyzing more than 3000 patients with adnexal masses (Timmerman et al. 2016). Both types of cystadenomas have been recognized as precursors of ovarian cancer and may slowly transform to borderline tumors and invasive ovarian cancer (Lengyel 2010).

Serous cystadenomas account for up to 40% of all benign ovarian neoplasms. They show a peak incidence in the fourth and fifth decades and are in up to 20% bilateral. Mucinous cystadenomas account for 20–25% of all benign ovarian neoplasms, and are bilateral in only 5% of cases (Hochberg and Hoffman 2017). Both are cystic lesions filled with water-like or higher proteinaceous contents. Small coarse calcifications in mural location or within the cyst were found in >30% of mucinous cystadenomas, whereas tiny psammoma bodies in serous cystadenomas are a rare finding in CT (Okada et al. 2005). Mucinous cystadenomas tend to be larger at presentation and are typically multilocular with different contents of the loculi (Fig. 15) (Jung et al. 2002). These loculi are small and multiple and separated by thin septations. Rupture of a mucinous cystadenoma can result in pseudomyxoma peritonei.

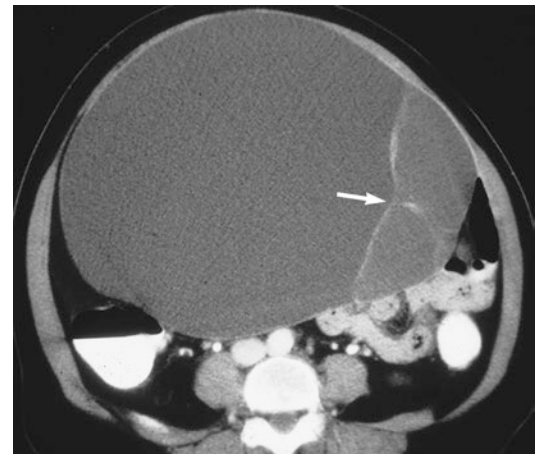

Fig. 15 Mucinous cystadenoma on CT. At the level of L5, a cystic ovarian lesion extending to the upper abdomen and measuring 25 cm in diameter is demonstrated. It bulges the abdominal wall and displaces bowel loops posteriorly. It displays multiple thin septations (*arrow*). Loculi in the left periphery display attenuation values which are higher than water. The large lesion size and different densities of the loculi are findings suggesting the diagnosis of a mucinous cystadenoma

4.2.1.1 Imaging Findings

Although an overlap exists, imaging features aid in the differentiation of serous from mucinous cystadenomas (Jung et al. 2002). In general, serous cystadenomas follow the pattern of a simple cyst and mucinous cystadenomas those of a multilocular lesion. For details see Chap. 66. Cystadenomas are well-circumscribed cystic tumors with enhancing thin walls and—if present—internal septations on CT and MRI (Fig. 15). The wall and septa are regular and thin (<3 mm) (Fig. 16). Papillary projections may be found in cystadenomas, but these tend to be small and a size of less than 3–5 mm indicates benignity (Timmerman et al. 2016) (Figs. 17 and 18).

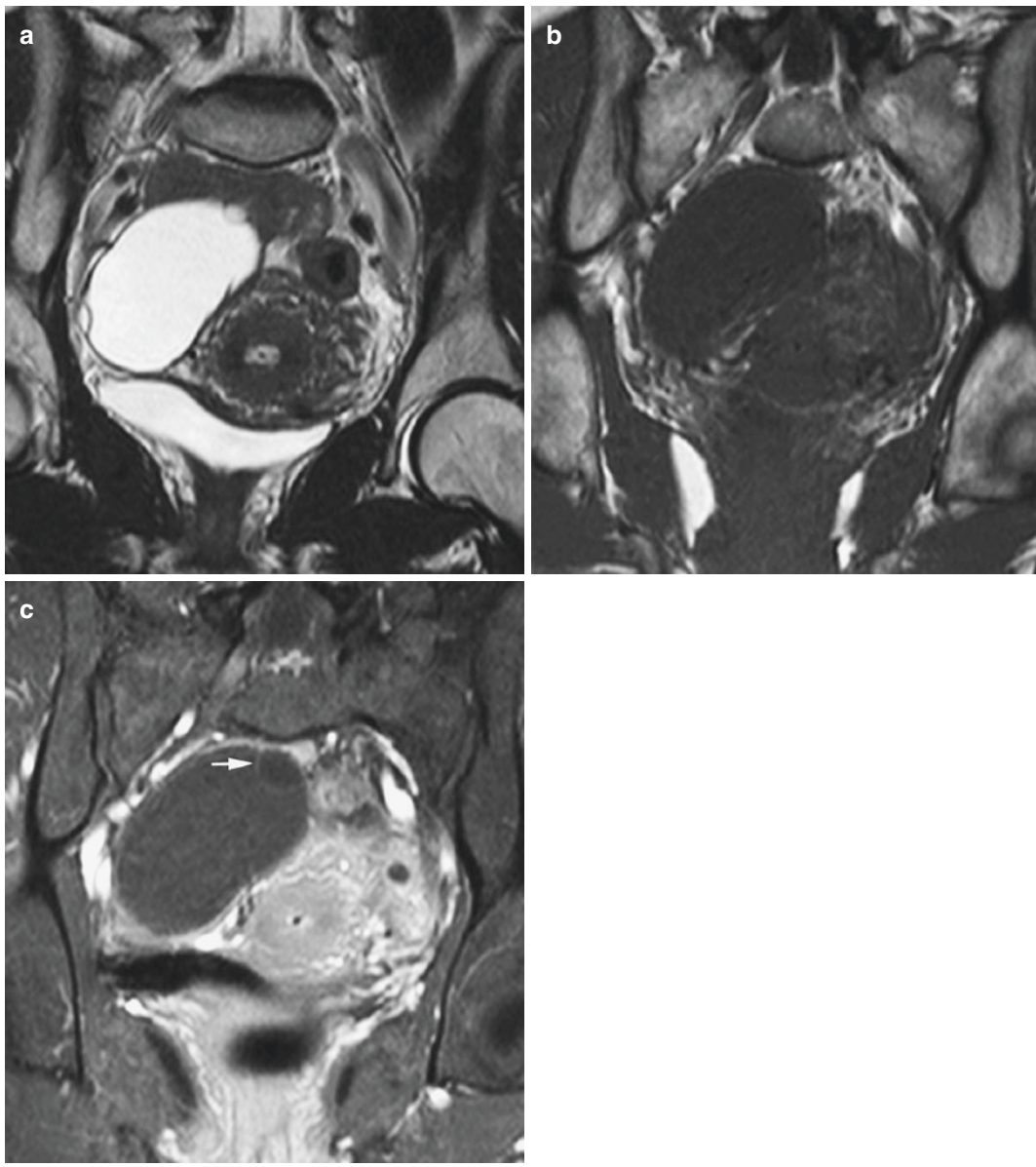

Fig. 16 Mucinous cystadenoma. In a 48-year-old woman with a cystic mass in sonography, complementary MRI with coronal T2-weighted image (**a**), coronal T1-weighted image (**b**), and fat-suppressed contrast-enhanced T1-weighted image (**c**) are demonstrated. Coronal T2-weighted MR image of the pelvis shows a hyperintense multilocular cystic mass with thin septation (**a**) in the right adnexal region. T1-weighted image confirms the purely cystic content of the cyst (**b**). The septations are thin and demonstrate contrast enhancement (**c**). Pathology after laparoscopic removal of the ovary showed benign mucinous cystadenoma of the ovary

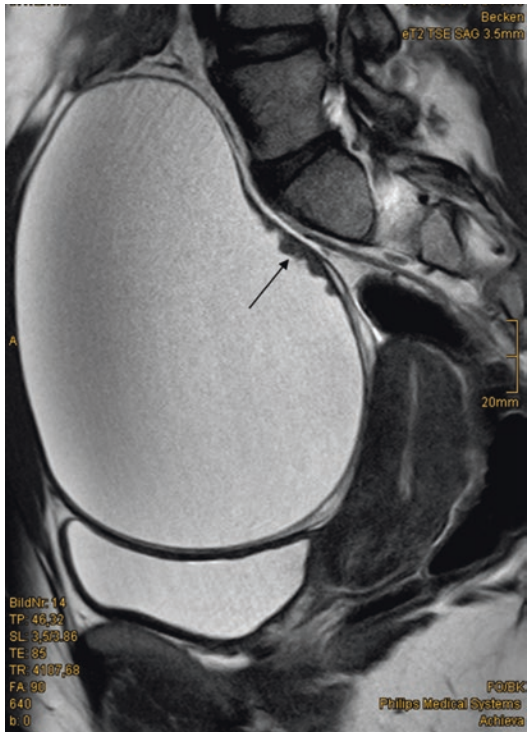

Fig. 17 Papillary projections in a mucinous cystadenoma. MRI was performed complementary to sonography in a persistent ovarian cyst. Sagittal T2WI displays a large unilocular cyst that shows small irregular mural thickening of the posterior wall presenting papillary projections (*arrow*)

The cystic loculi of serous cystadenomas display signal of simple fluid. In contrast, mucinous cystadenomas have often various signal intensities depending on the contents within the different loculi, which vary from watery to proteinaceous to hemorrhagic. They display SI intensity higher than water on T2 and lower SI on T2-weighted images relative to serous fluid. When hemorrhage is present, blood products may be identified on MRI. Rarely, mucinous cystadenomas can manifest as a simple cyst.

Mucinous cystadenomas tend to be large at diagnosis with a mean size of 10 cm, but may be as large as 30 cm (Jung et al. 2002).

4.2.1.2 Differential Diagnosis

Serous and mucinous cystadenomas may display similar imaging findings on CT and MRI. If papillary projections are found in cystadenomas, they tend to be fewer and smaller than in borderline tumors and display a type 1 time intensity curve. The presence of a mural nodule is highly indicative of a borderline or invasive malignancy (Fig. 18). Endometriomas may resemble mucinous cystadenomas, especially when these are complicated by hemorrhage. Low SI shading on the T2-weighted images is

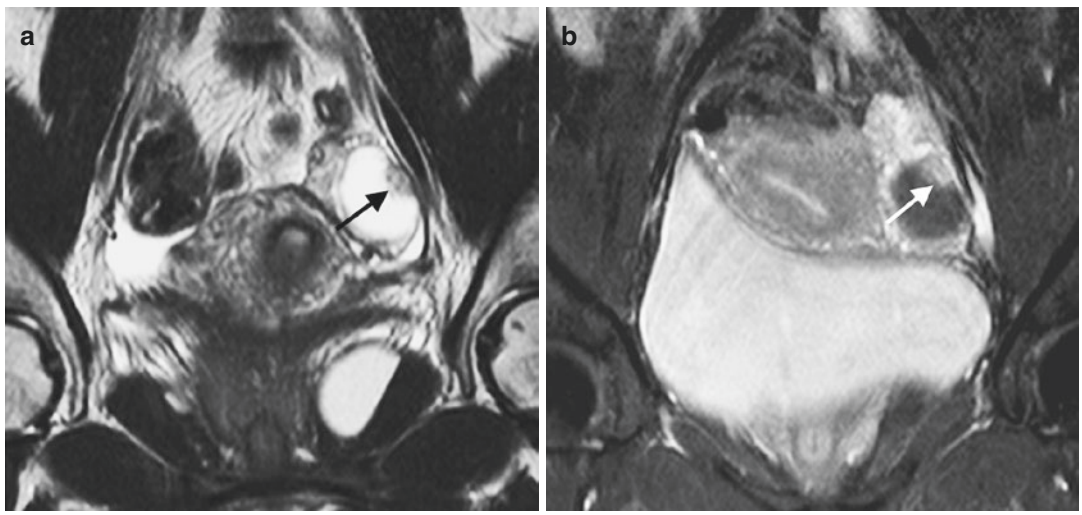

Fig. 18 Vegetation within a cyst. Coronal T2-weighted image (**a**) and fat-saturated contrast-enhanced T1-weighted image (**b**). In a 3.5 cm ovarian cyst, a mural nodule of 10 mm with intermediate signal intensity on T2-weighted image (**a**) and contrast enhancement (**b**) is demonstrated. This finding should warrant the suspicion of malignancy, especially a borderline tumor as in this patient. Papillary projections in cystadenomas tend to be smaller

not exclusive of endometriomas. Homogenous shading is the most prevalent pattern in endometriomas but focal/multifocal shading within a complex mass may also be found in endometroid carcinomas (Dias et al. 2015). Furthermore, the walls in endometriomas tend to be thicker and irregular and endometrioma usually are smaller than 10 cm. In CT the differentiation of cystadenomas from endometriomas is not possible. Hydrosalpinx can also display as a multiloculated uni- or bilateral adnexal lesion. In contrast to cystadenomas, the loculi communicate and incomplete septa are found (Ghattamaneni et al. 2009).

4.2.2 Cystadenofibroma

Cystadenofibromas account for 1.7% of ovarian tumors. They are benign cystic tumors composed of epithelial and various amounts of solid stromal elements. They can also be purely cystic with small foci of stroma detected microscopically. The margin tends to be well defined and smooth. Endocrine activity is not found (Jung et al. 2006).

4.2.2.1 Imaging Features

Cystadenofibroma present as uni- or bilateral ovarian predominantly cystic tumors. Solid stromal tissue displaying very low SI on T2WI is the key feature suggesting cystadenofibroma. This may be encountered in a diffuse or partially thickened cyst wall or in a multicystic or solid element within the lesion (Fig. 19). The reference most suitable for low SI in a benign lesion is the skeletal pelvic muscle (Forstner et al. 2016). On MRI small papillary projections may be displayed (Fig. 1). On CT coarse calcifications suggest benignity. Variable amounts of fibrous stroma in ovarian cystadenofibromas result in imaging features that vary from purely cystic to a complex cystic tumor with one or more solid components. In one series of 32 ovarian cystadenofibromas, 50% displayed as multiloculated masses identical to cystadenomas. The other half was complex cystic tumors with one or more solid components and smooth thickened septa of very low SI. This feature has been described as black sponge sign (Cho et al. 2004).

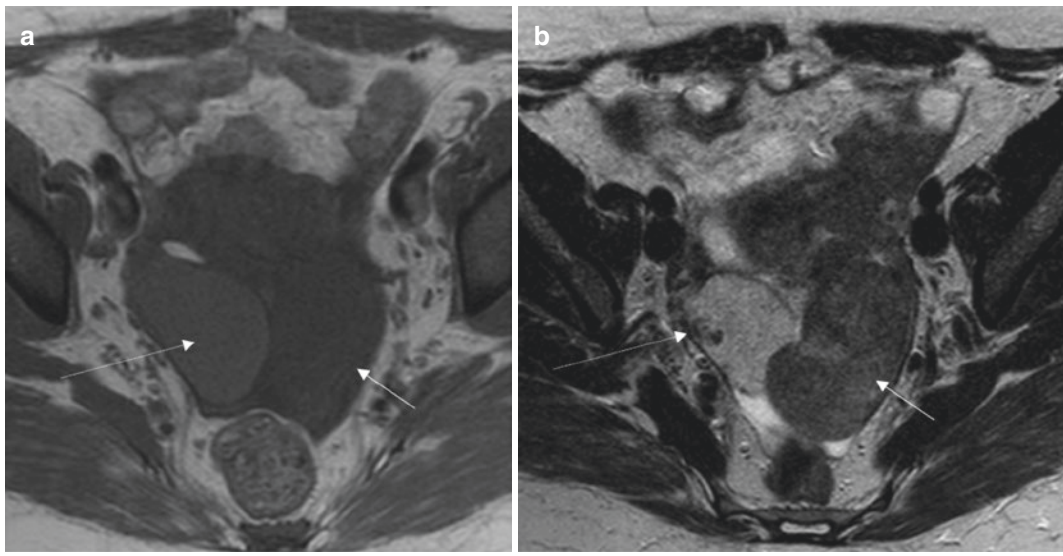

Fig. 19 A 45-year-old patient with a right cystadenofibroma and a left fibroma. (**a**) Axial T1-weighted image; (**b**) axial T2-weighted image; (**c**) fat-saturated axial gadolinium-enhanced T1-weighted image; (**d**) axial oblique T2-weighted image. T2-weighted images show a solid hypointense lesion in the left ovary that shows moderate contrast enhancement and therefore is compatible with a fibroma (*arrows*). In the right ovary there is a cystic lesion with small areas of low signal intensity on T2-weighted images that revealed to be a cystadenofibroma (*dashed arrows*)

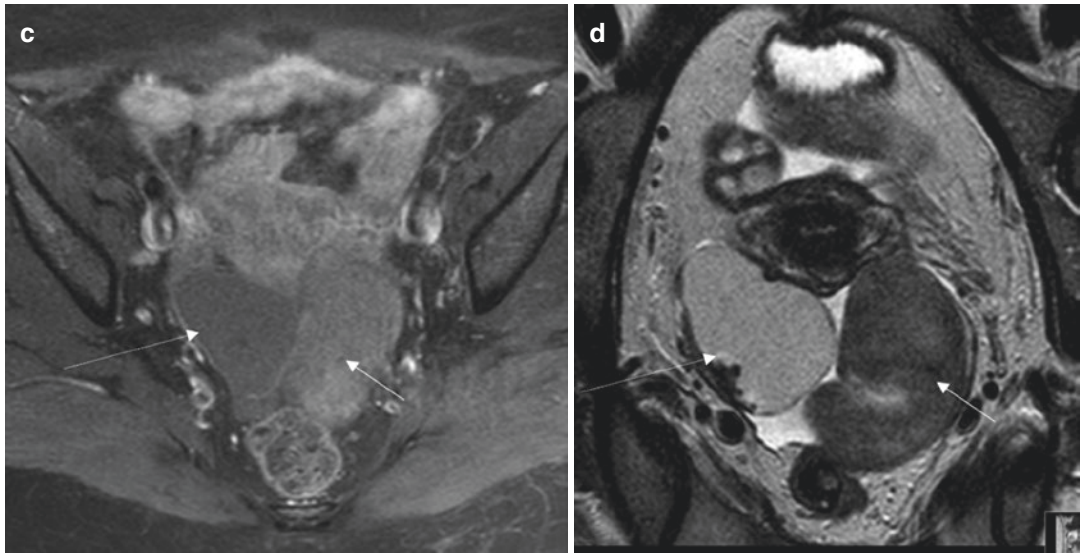

Fig. 19 (continued)

4.2.3 Mature Teratoma

Mature teratomas are the most common ovarian neoplasm in women under 45 years of age, and account for up to 70% of tumors in females less than 19 years of age (Koonings et al. 1989). In a large series it constitutes 10.6% of adnexal masses (Timmerman et al. 2016). Ovarian teratomas derive from germ cells and are classified into three main categories, among which the mature cystic teratomas account for 99%. Less common types of mature teratomas are the monodermal teratomas, which include struma ovarii and carcinoid tumors. Monodermal teratomas are not cystic but contain primarily solid structures. Mature cystic teratomas typically contain lipid material consisting of sebaceous fluid within the cyst cavity or adipose tissue within the cyst wall or the dermoid plug.

4.2.3.1 Mature Cystic Teratoma

Mature cystic teratomas or dermoid cysts are composed of mature tissue from at least two of the three germ cell layers: ectoderm, mesoderm, and endoderm. They are typically unilateral lesions, with only 10–15% of mature cystic teratomas found in both ovaries (Kurman et al. 2011). In the vast majority (88%), mature teratomas are unilocular cystic lesions filled with sebaceous material. A protuberance, the Rokitansky nodule, or dermoid plug projects into the cavity and is the hallmark of mature teratomas. It contains a variety of tissues, often including fat and calcifications, which represent teeth or abortive bone. Fat is detected in over 90%, teeth in 31%, and calcifications in the wall in 56% (Buy et al. 1989).

A minority of mature cystic teratomas will demonstrate no fat or only small foci of fat within the wall or the Rokitansky nodule (Yamashita et al. 1994). Yamashita et al. reported that 15% of mature teratomas did not show fat within the cystic cavity. Approximately half of these cases displayed small amounts of fat within the wall of the teratoma or the dermoid plug. In 8% of benign teratomas, no fat could be detected (Yamashita et al. 1994).

Mature teratomas are usually asymptomatic and tend to grow slowly. This is why watchful waiting is warranted in older females presenting with lesions smaller than 5 cm in size (Caspi et al. 1997). Complications encountered are malignant degeneration and rupture, and in up to 16% torsion (Rha et al. 2004). Malignant degeneration is extremely

rare and associated with large size (>10 cm) and postmenopausal age. Rupture of a mature teratoma can cause acute abdomen due to granulomatous peritonitis caused by leakage of the fatty contents (Rha et al. 2004). Rarely, giant teratomas are found occupying the pelvis and abdomen. Recently ovarian teratoma-associated anti-NDMDAR encephalitis has been described. It is a potentially fatal disease in young women who clinically present with encephalitis caused by an underlying mostly with mature teratoma (Acien et al. 2014).

Imaging Findings

Sonographic assessment of mature cystic teratomas may be limited by its variety of appearance. At CT and MRI, however, the diagnosis of fat within a cystic mass is pathognomonic for a mature cystic teratoma (Figs. 20 and 21). The fatty elements display characteristic low CT attenuation (−20 to −120 HU). Another typical feature on CT is the presence of calcifications within the cyst wall or the dermoid plug (Fig. 20).

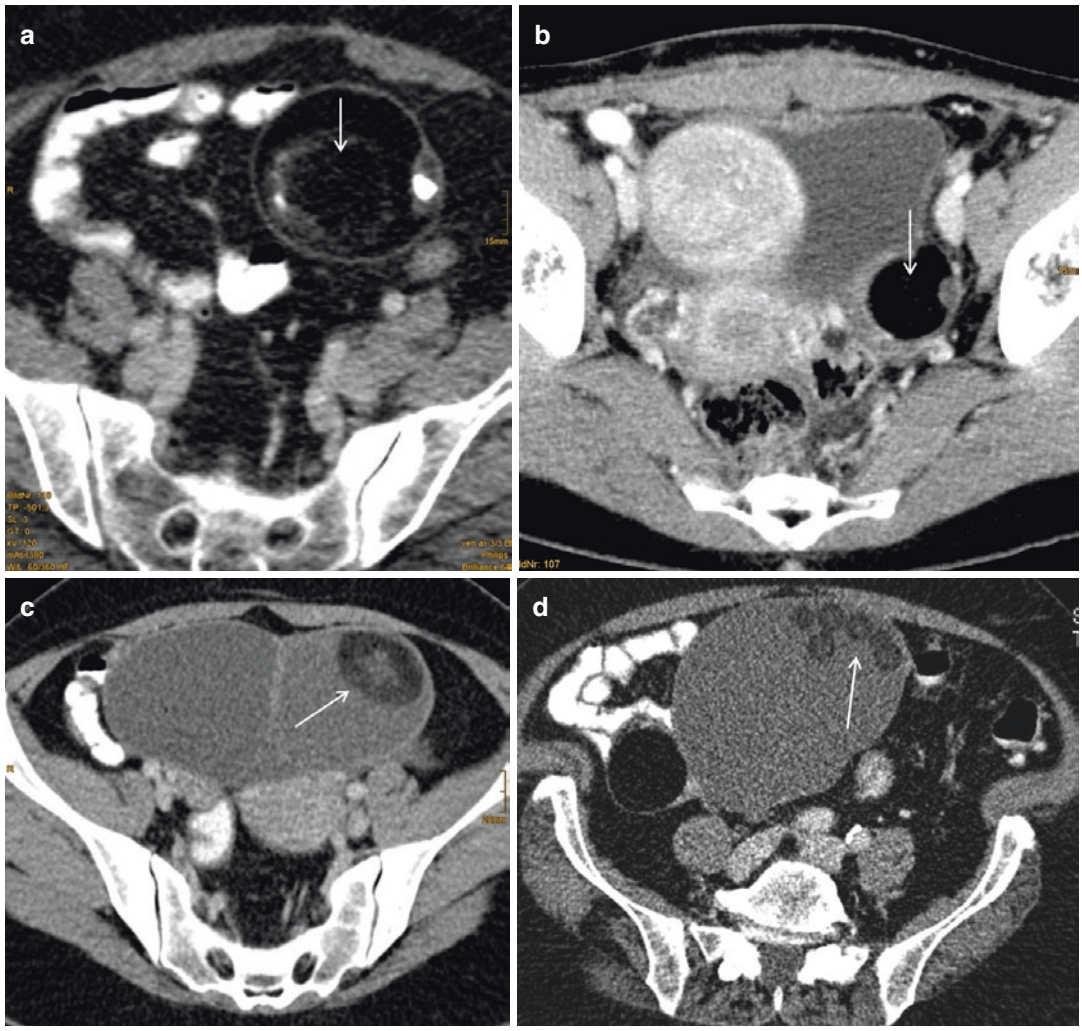

Fig. 20 A spectrum of CT findings in mature cystic teratomas in four different patients (**a**–**d**) is displayed. The *arrow* indicates fat as pathognomonic finding in this tumor type

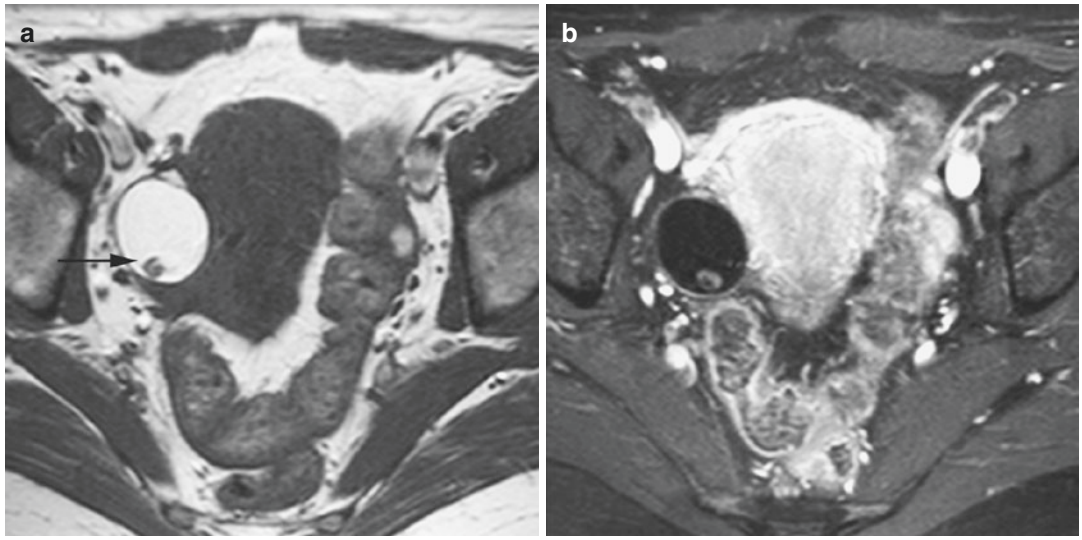

Fig. 21 Typical findings of a mature cystic teratoma on MRI. A 44-year-old woman complaining about irregular menstrual cycle and a suspicious adnexal mass at transvaginal ultrasound. Axial T1-weighted image (**a**) and contrast-enhanced T1-weighted image with fat suppression (**b**) at the acetabular level. The cystic structure of the right ovary demonstrates hyperintense content with a round nodule in the lower part of the cyst (*arrow*) (**a**). The hypointense content after fat suppression (**b**) confirms the fatty nature of the cyst. At pathology, the round nodule corresponded to a hair ball within a mature cystic teratoma

MRI findings include a round or oval, sharply delineated lesion with high SI on T1-weighted images, and loss of signal on the fat-saturated T1-weighted images, or signal loss in the out of phase chemical shift sequence. This fatty content may display a broad spectrum of appearance, including a fat-filled cavity, foci of fat within the lesion or its wall, and a fat-fluid interface often representing a floating mass of hair.

On T2-weighted images, the signal may be variable, but it tends to be similar to subcutaneous fat. Furthermore, chemical shift artifacts in the frequency-encoding direction can be observed, which confirms the presence of fat and differentiates it from hemorrhage. Calcification in the wall of or in the dermoid plug will often be missed on MRI due to the low SI on T1- and T2-weighted images. Caution is warranted in DWI because it may be misleading due to restricted diffusion (Forstner et al. 2016).

Differential Diagnosis

Although hemorrhagic lesions including endometrioma, hemorrhagic cysts, and neoplasm may appear similar on the T1-weighted images and T2-weighted images, fat-suppressed or chemical shift images are most reliable for the differentiation of fat from hemorrhage.

When no or only small amounts of fat are present (8%), teratomas are not distinguishable from benign cystic ovarian tumors or ovarian cancer (Fig. 22) (Rha et al. 2004).

Capsule penetration typically arising from the dermoid plug is a sign for malignant transformation of a mature teratoma (Rha et al. 2004). The rare liposarcoma or immature teratoma may contain fat and thus may be indiscernible from a teratoma. Immature teratomas, however, are extremely rare and occur in the first two decades of life. They may occur in association with an ipsilateral teratoma in 26% and a contralateral teratoma in 10%. However, at the time of presentation they are usually very

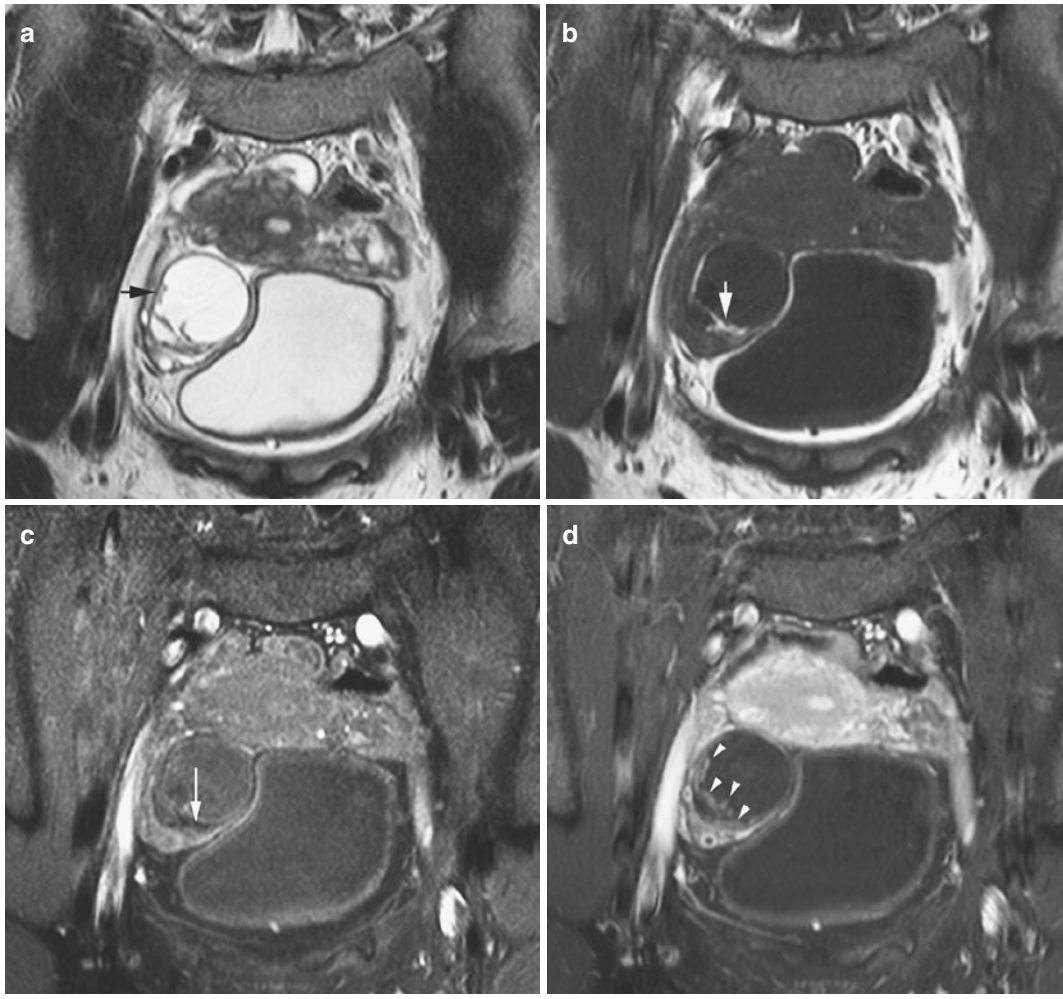

Fig. 22 Mature cystic teratoma with little fat. MRI was performed for further characterization of a sonographically suspicious cystic and solid mass in a 31-year-old woman. Coronal T2-weighted image (**a**), T1-weighted image (**b**), T1-weighted image with fat suppression (**c**), contrast-enhanced T1-weighted image with fat suppression (**d**). A multilocular mass with irregular wall thickening (*arrow*) (**a**) arising from the right adnexa is demonstrated. Coronal native T1-weighted image (**b**) confirms the cystic nature of the mass. A linear hyperintense portion is located at the lower part of the cyst (*white arrow*). The corresponding coronal fat-suppressed T1-weighted image (**c**) shows vanishing of the hyperintense linear part confirming the presence of a small amount of fat in the linear hypointense lower portion of the cyst (*white arrow*). The contrast-enhanced fat-suppressed T1-weighted image (**c**) shows enhancement of an irregular wall and septa (*arrowheads*) corresponding to the Rokitansky nodule of a mature cystic teratoma with little fat. Contrast enhancement of the mural protrusion of a mature cystic teratoma can be mistaken for ovarian cancer

large, are predominantly solid or cystic and solid, and contain only few foci of fat (Heifetz et al. 1998).

4.2.3.2 Monodermal Teratoma

Monodermal teratomas are composed mainly of one tissue type. They include struma ovarii, ovarian carcinoid tumors, and tumors with neural differentiation.

Struma ovarii is the most common type and accounts for 3% of all mature teratomas (Matsuki M 2000). It consists predominantly or solely of mature thyroid tissue. A mixed morphology with acini filled with thyroid colloid, hemorrhage, fibrosis, and necrosis is found. Rarely struma ovarii may produce thyrotoxicosis.

Carcinoid tumors are frequently associated with a mature cystic teratoma or a mucinous ovarian tumor. Unlike most cystic teratomas, they are predominantly found in postmenopausal women. The course is usually benign; there is a small subset of carcinoid tumors and of struma ovarii that are malignant. Carcinoid syndrome is uncommon.

Imaging Findings

On CT and MRI, a struma ovarii displays as a heterogeneous complex mass (Fig. 23). They present as cystic lesions or with a multilocular appearance with loculi displaying high signal intensity on T1 and T2, some with low signal intensity on T1- and T2-weighted images on MR. Fat is not seen in struma ovarii. Carcinoid tumors are solid tumors indistinguishable from solid ovarian malignancies.

4.2.4 Benign Sex Cord-Stromal Tumors

Sex cord-stromal tumors include neoplasms that are composed of granulosa cells, theca cells, and their luteinized derivates, including Sertoli cells,

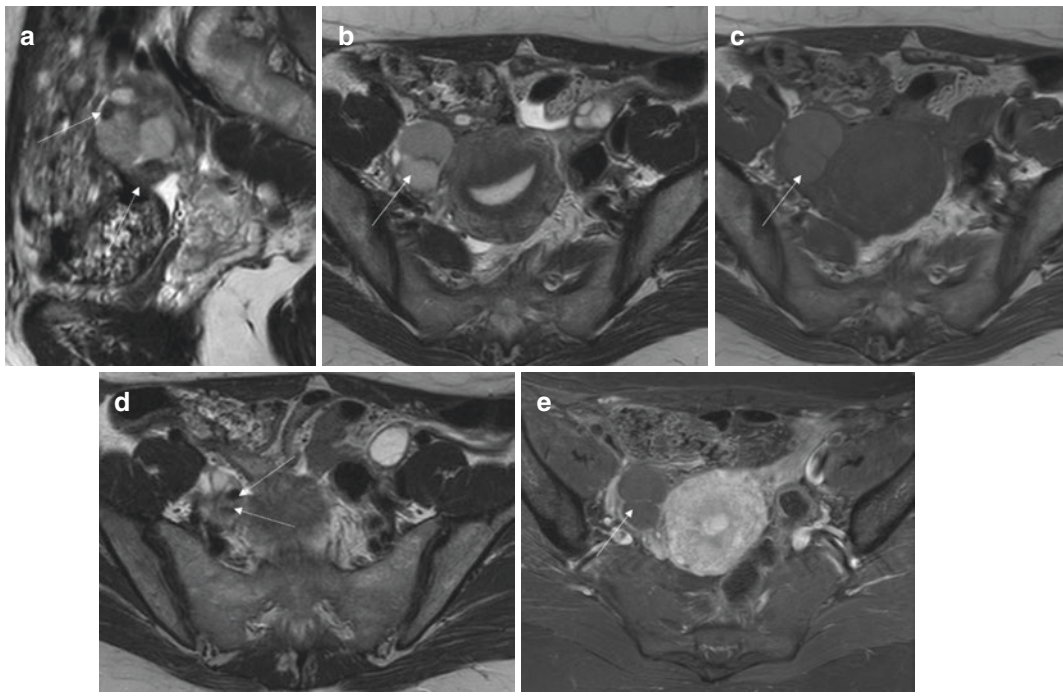

Fig. 23 Struma ovarii in a 49-year-old patient. (**a**) Sagittal T2-weighted image; (**b**) axial T2-weighted image; (**c**) axial T1-weighted image; (**d**) axial T2-weighted image; (**e**) axial fat-suppressed gadolinium-enhanced T1-weighted image. T1- and T2-weighted images show a multiloculated cystic mass in the right ovary, with locules of variable signal intensity. There are locules showing high signal both on T1- and T2-weighted images and low signal fat-suppressed gadolinium-enhanced T1-weighted images that are consistent with fat (*arrows*). Note the typical locules with low T2-weighted signal due to the presence of colloid content (*dashed arrows*)

Leydig cells, and fibroblasts of gonadal stromal origin (Young and Scully 2002). They present rare tumors that differ from epithelial neoplasm due to their hormonal activity (Horta and Cunha 2015). Sex cord-stromal tumors have recently been classified as pure stromal tumors, pure sex cord tumors, and mixed sex cord-stromal tumors (Kurman et al. 2014).

Among the pure stromal tumors fibroma and thecoma account for the vast majority of benign sex cord-stromal tumors.

4.2.4.1 Fibroma and Thecoma

Fibromas and thecomas are solid ovarian tumors accounting for 3–4% of all ovarian tumors and 10% of solid adnexal masses. They are typically unilateral (90%) and occur in peri- and postmenopausal age women. Histologically they present the majority of sex cord-stromal tumors.

Fibromas are composed mostly of fibroblasts and spindle cells and abundant collagen contents. Fibromas are not hormonally active. The triad of an ovarian fibroma, ascites, and pleural effusion constitutes the benign Meigs syndrome, which can be associated with elevated CA-125 levels (Timmerman et al. 1995). In basal cell nevus syndrome, numerous basal cell carcinomas are associated with abnormalities of bones, eyes, brain, and tumors, including ovarian bilateral fibromas.

Thecomas are composed of thecal cells with abundant and varying amounts of fibrosis and may rarely contain dense amorphous calcifications. Unlike fibromas, 60% of thecomas have estrogenic activity and may present with uterine bleeding. Furthermore, in more than 20%, endometrial carcinomas occur concomitantly (Outwater et al. 1997).

Imaging Findings

Small fibromas and thecomas are solid tumors with imaging features similar to nondegenerative uterine leiomyomas on CT and MRI (Figs. 24 and 25). They display intermediate to low SI on T1-weighted images and typically very low SI or low SI with intermediate SI on the T2-weighted images on MRI (Fig. 25). Large lesions may have an inhomogeneous architecture with areas of high signal intensity within the solid low signal intensity lesion, representing edema or cystic degeneration (Chung et al. 2015). They had in 40% atypical features with mixed solid/cystic and predominantly cystic morphology and displayed high SI on T1 and T2WI in almost half of the cases. Small amounts of ascites were a common finding (Chung et al. 2015). Another feature is dense amorphous calcifications, which are

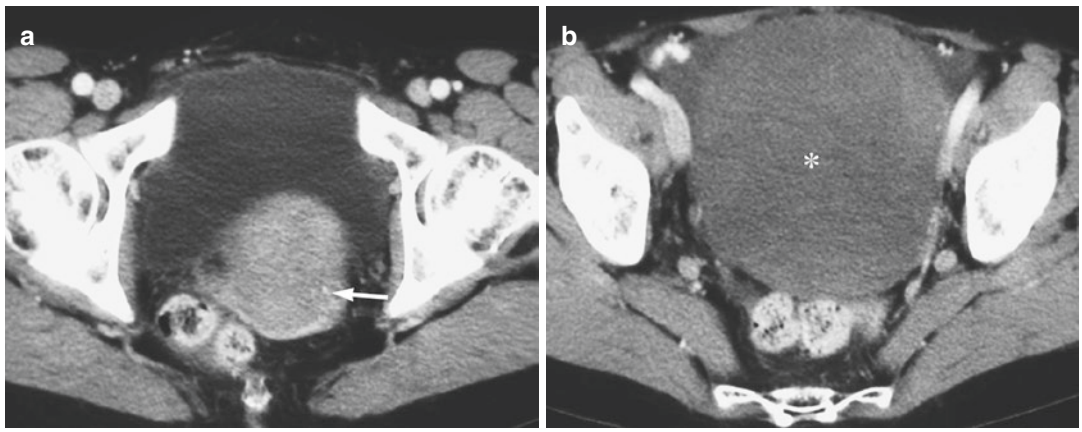

Fig. 24 Ovarian fibroma on CT. Transaxial pelvic CT at the uterine level (**a**) and above (**b**) in a 55-year-old woman with abdominal fullness. A large lesion (*asterisk*) is found in the mid pelvis above the level of the uterus and bladder (**b**). It is well demarcated and displays a slightly inhomogeneous solid structure. Contrast enhancement is distinctly less than that of the myometrium (*arrow*). No calcifications were found throughout the lesion. Minimal ascites was seen. Histopathology revealed a 9 cm fibroma of the left ovary

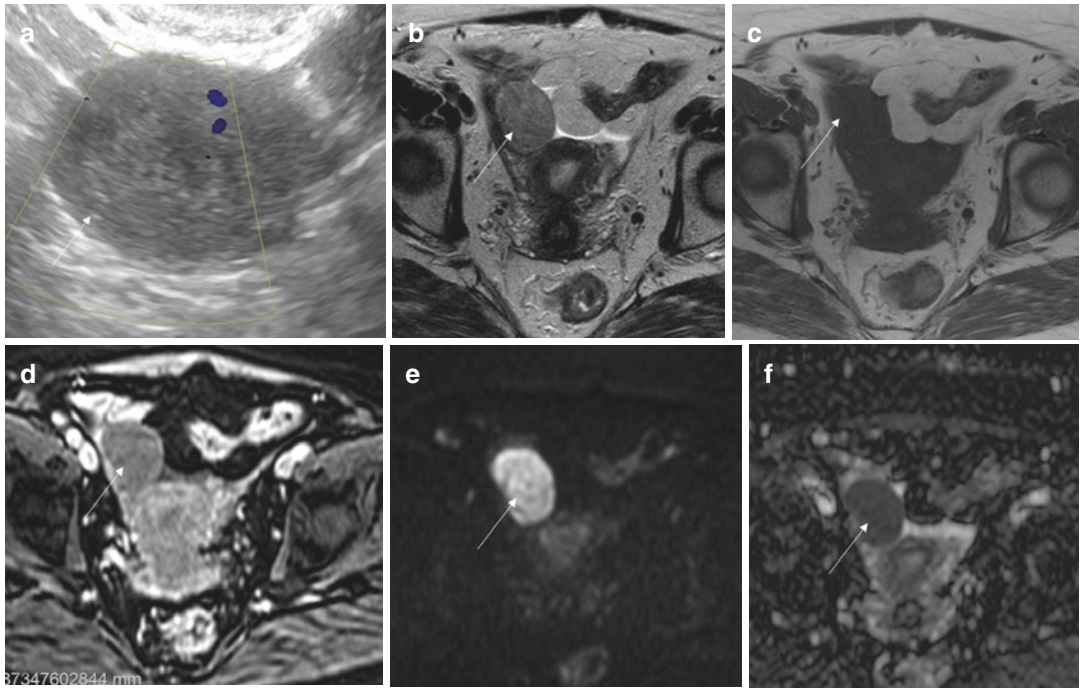

Fig. 25 A 67-year-old patient with a right ovarian thecoma. (**a**) Transvaginal ultrasound image; (**b**) axial T2-weighted image; (**c**) axial T1-weighted image; (**d**) fat-saturated axial gadolinium-enhanced T1-weighted image; (**e**) axial diffusion-weighted image (b = 1000 s/mm^2); (**f**) axial ADC map. Ultrasound image shows a right homogeneous vascularized solid mass. T2-weighted image shows a solid intermediate signal lesion. The lesion displays low signal intensity on T1-weighted image, only moderate contrast uptake, and restricted diffusion (*arrows*)

easily detected on CT. Fibromas and thecomas tend to show mild or delayed contrast enhancement and typically a type 1 time intensity pattern. They may also display a type 2 time intensity curve. Rarely cellular fibromas may be found, which tend to be well vascularized and have a low malignant potential (Horta and Cunha 2015) (Fig. 26). Low SI on the high b value in DWI allows the exclusion of malignancy in solid adnexal masses (Thomassin-Naggara et al. 2009). Ascites may be present and even large amounts are no sign of malignancy.

4.2.4.2 Sclerosing Stromal Tumor

Sclerosing stromal tumor of the ovary is a rare subtype of sex cord-stromal tumors. It is a benign tumor affecting most commonly young girls and women younger than 30 years of age, which is much earlier in other stromal tumor types (Matsubayashi et al. 1999; Palmeiro et al. 2016). Macroscopically, these tumors display peripheral edematous ovarian cortical stroma surrounding nodular highly vascular cellular components (Matsubayashi et al. 1999; Palmeiro et al. 2016). Some of these tumors may have an estrogenic effect and rarely androgenic effects, which cause prolonged menstrual irregularities or pelvic pain. Ascites may be rarely found.

Imaging Findings

Sclerosing stromal tumors of the ovary tend to be unilateral well-encapsulated multiloculated cystic or heterogeneous ovarian lesions with a characteristic centripetal contrast enhancement pattern (Fig. 27). On T1- and T2-weighted images, a thin low-intensity rim representing a capsule is seen. On T2-weighted images, in the periphery an irregular low-signal-intensity rim is found adjacent to a very bright more central portion, which has a nodular appearance. On dynamic imaging, the arterial phase shows minimal contrast uptake, whereas in the venous

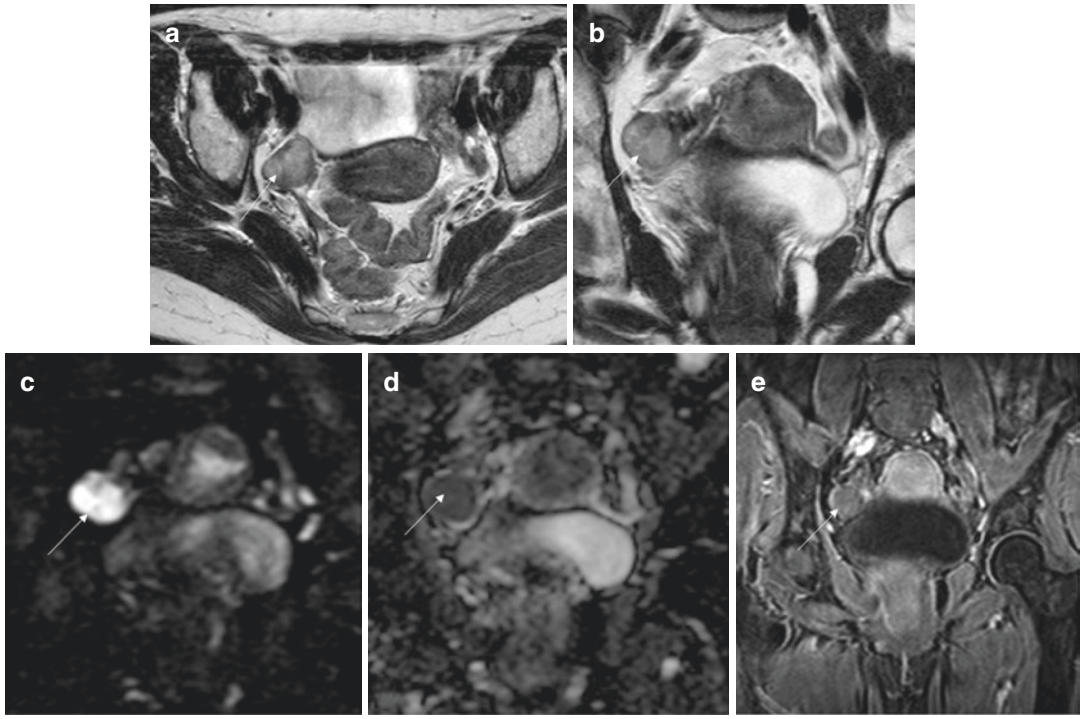

Fig. 26 Cellular fibroma of the right ovary in a 60-year-old patient. (**a**) Axial T2-weighted image; (**b**) axial oblique T2-weighted image; (**c**) axial oblique diffusion-weighted image (b = 1000 s/mm^2); (**d**) axial oblique ADC map; (**e**) fat-saturated axial oblique gadolinium-enhanced T1-weighted image. On T2-weighted images the intermediate signal intensity of the cellular fibromas is shown (**a**) and (**b**)

phase high contrast uptake and a pseudolobular pattern are seen. Slow centripetal progression on delayed images has been described as a typical imaging feature (Matsubayashi et al. 1999).

4.2.5 Brenner Tumors

Brenner tumors are rare ovarian tumors that occur at a mean age of 50 years. Brenner tumors constitute 1–3% of ovarian tumors. They are mostly benign, with less than 2% demonstrating borderline or malignant transformation. They are typically small, solid, unilateral ovarian tumors, with 60% of these tumors found fewer than 2 cm in size. Extensive calcification may be found. The vast majority is discovered incidentally in pathologic specimen of the adnexa. Brenner tumors rarely produce estrogen, and then they may be associated with endometrial thickening (Moon et al. 2000). If cystic components are found in Brenner tumors, they may be associated with cystadenomas (Seidman et al. 2002). Up to 20% of Brenner tumors are associated with mucinous cystadenomas or other epithelial neoplasm (Fig. 28).

4.2.5.1 Imaging Findings

The typical finding of Brenner tumors is a small solid tumor that displays very low SI on the T2-weighted images (Moon et al. 2000). Dense amorphous calcifications in a small solid ovarian tumor are a typical CT finding. In one series of eight Brenner tumors, the mean size was 11.5 cm, and tumors displayed a mixed solid and cystic appearance in half of the cases, which mimicked ovarian cancer (Moon et al. 2000). The combination of a multiseptate ovarian tumor with a solid part displaying extensive calcifications on CT or very low SI on MRI may suggest the diagnosis of a collision tumor of Brenner tumor and a cystic ovarian neoplasm, e.g., cystadenoma (Fig. 28).

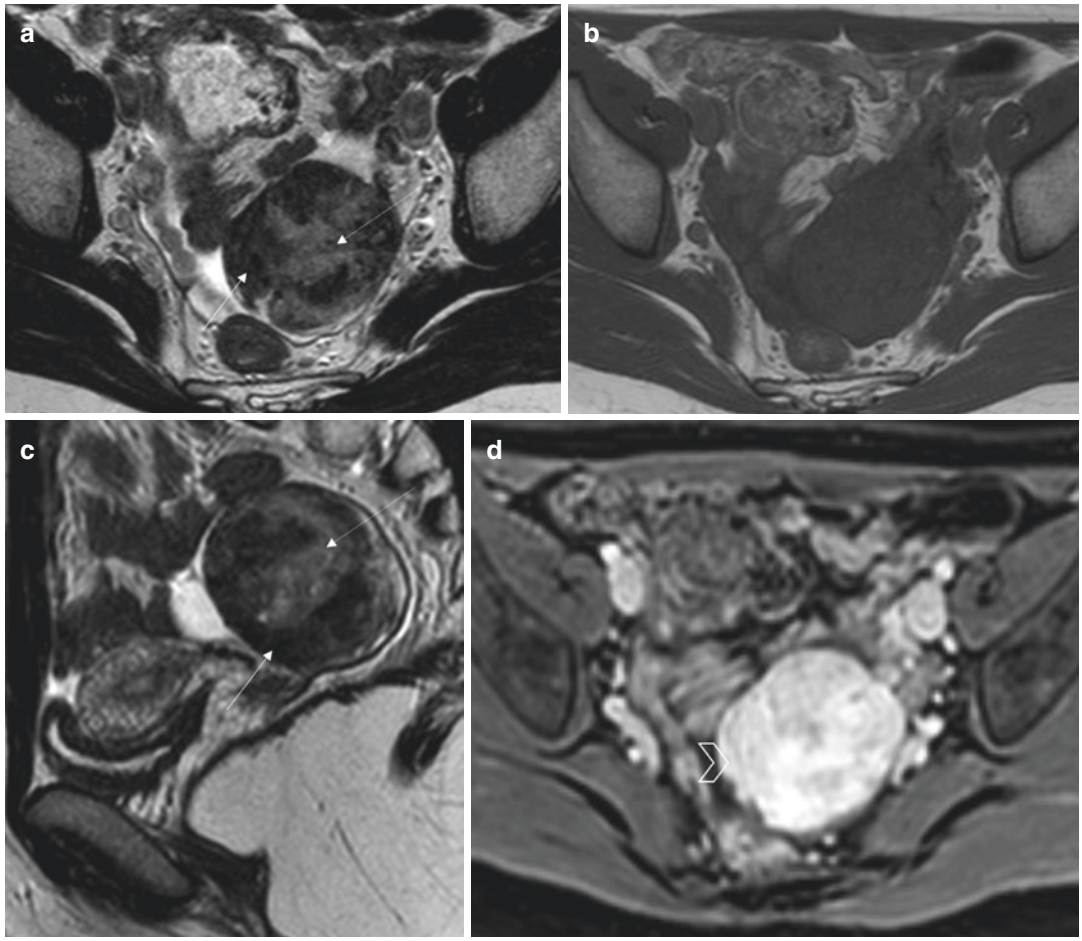

Fig. 27 Sclerosing stromal tumor of the left ovary in an 18-year-old patient. (**a**) Axial T2-weighted image; (**b**) axial T1-weighted image; (**c**) sagittal T2-weighted image; (**d**) axial fat-suppressed gadolinium-enhanced T1-weighted image. T2-weighted images show a left ovarian mass with a pseudolobular spoke-wheel pattern that is characterized by outer hypointense solid component (*arrows*) and a central intermediate signal intensity area (*dashed arrows*). The outer solid component shows avid enhancement after gadolinium administration (*arrowhead*)

4.2.5.2 Differential Diagnosis

The solid morphology and the very low SI on the T2WI of fibromas and thecomas are fairly characteristic. Pedunculated uterine leiomyomas and leiomyomas of the broad ligaments can display similar imaging characteristics. Subserosal pedunculated leiomyomas can be discriminated by the bridging vascular sign. Unilateral or bilateral ovarian leiomyomas are extremely rare and cannot be reliably differentiated by imaging. High-contrast media uptake in such a lesion might suggest ovarian leiomyoma (Yoshitake et al. 2005). Fibromas with large central necrotic area mimic malignant ovarian masses, especially Krukenberg tumors. DWI and most importantly DCE will allow the differentiation in the majority of cases (see Chap. 66). Dense amorphous calcifications in CT support also the diagnosis of

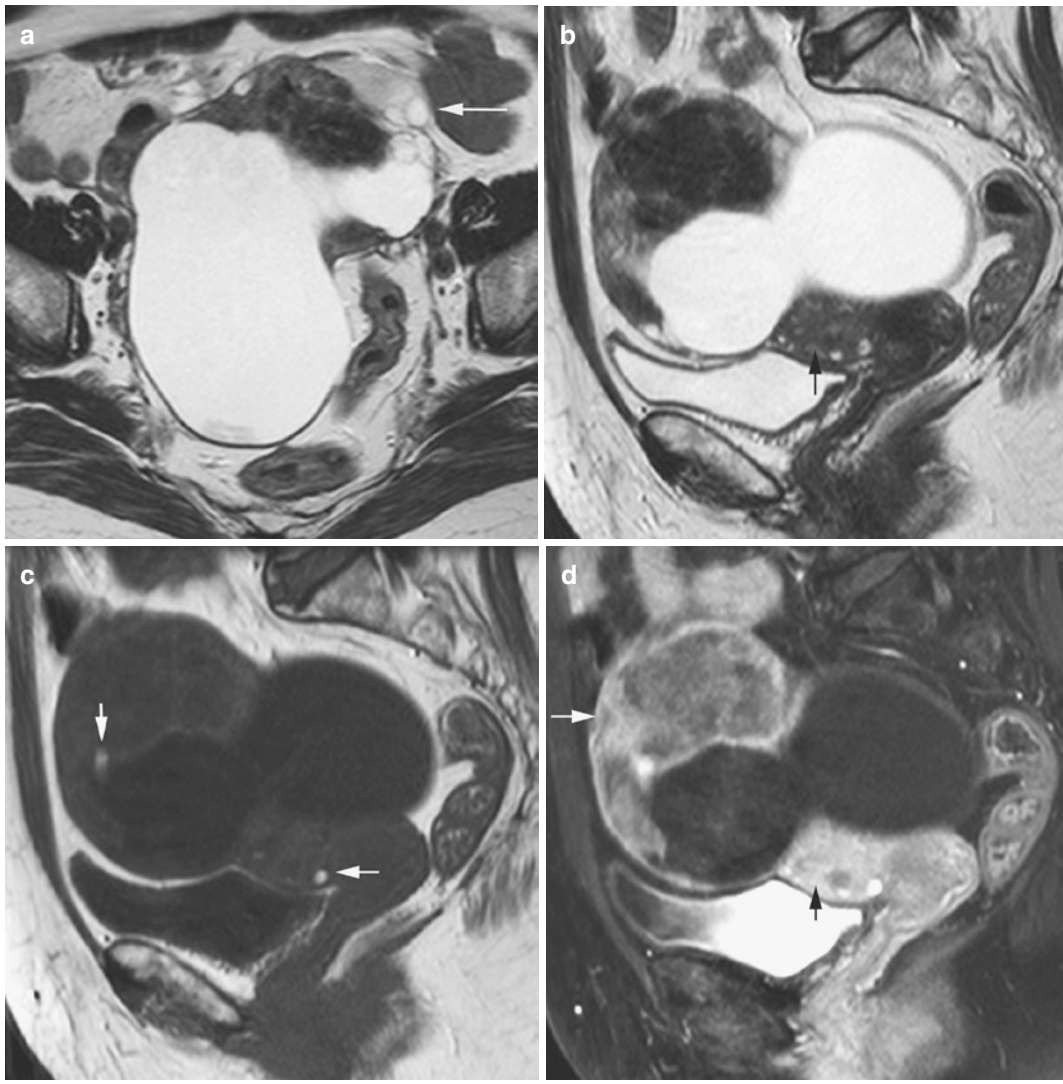

Fig. 28 Large Brenner tumor with mucinous portion. A 75-year-old woman presenting with a large suspicious pelvic mass at ultrasound and moderate increase in CA-125 level. Axial T2-weighted image (**a**), sagittal T2-weighted image (**b**), sagittal T1-weighted image (**c**), sagittal T1-weighted image with fat suppressed. (**d**). A cystic mass with a solid hypointense anterior portion is demonstrated (**a**). Ovarian parenchyma with two follicles is seen at the left anterior side (*arrow*). The small uterus (*arrow*) is identified below the left ovarian mass (**b**). The interface between the cystic and solid portion of the mass is regular. Sagittal T1-weighted image (**c**) shows absent blood within the cyst except for two blood vessels seen within the solid portion of the mass and the anterior myometrium (*arrows*). At the same level as (**b**) and (**c**) contrast-enhanced T1-weighted image with fat suppression (**d**) shows heterogeneous decreased contrast enhancement of the solid portion of the cyst (*white arrow*) compared to the strongly enhancing myometrium (*black arrow*). Histology after hysterectomy and bilateral oophorectomy diagnosed a benign Brenner tumor of the left ovary with an associated benign mucinous portion

stromal tumors. Small calcified solid tumors favor the diagnosis of Brenner tumors. Unlike in benign stromal tumors, calcifications in ovarian cancer tend to be small punctuating foci, the so-called psammoma bodies.

Sclerosing stromal cell tumors have a pathognomonic centripetal contrast media uptake. Morphologically, they may resemble Krukenberg tumors, but young age is characteristic of this entity.

5 Functioning Ovarian Tumors

Clinical and imaging findings may lead to the diagnosis of a functioning ovarian tumor.

The imaging findings comprise an ovarian mass, but also indirect findings as abnormalities of the uterus with uterine enlargement, a thickened endometrium in pre- and postmenopausal women, abnormal bleeding, features of virilization, or endocrinologic symptoms (Tanaka et al. 2004).

Sex cord-stromal tumors account for the majority of functioning ovarian tumors. These benign masses as well as neoplasms of low malignant potential account for the majority of estrogen-producing tumors. Granulosa cell tumors and thecomas are the most common estrogen-producing tumors (Fig. 29). Some mucinous cystadenomas and rarely ovarian cancer and metastases may also produce estrogens (Young and Scully 2002). In the majority of women of reproductive age, virilization is associated with the benign polycystic ovaries syndrome (PCOS). Virilizing ovarian tumors are rare and present mostly solid ovarian tumors (Fig. 30). Sertoli-Leydig cell tumors are typically found in young women and account for two-thirds of these tumors causing hirsutism or virilization. In middle-aged women, steroid cell tumors can cause virilization and/or Cushing's syndrome. Furthermore, rarely granulosa cell tumors, Brenner tumors, and thecomas may also have virilizing effects.

Thyroid hormones are typically produced in struma ovarii in subclinical levels. Hyperthyreosis seems to be present in only 25%, and thyrotoxicosis occurs in only 5% of patients with struma ovarii (Young and Scully 2002). Primary carcinoids of the ovary are rarely associated with carcinoid syndrome. Metastatic carcinoids involving the ovary, however, are associated with carcinoid syndrome in 50% of cases. Benign and malignant mucinous ovarian tumors may produce gastrin within the cyst wall and present clinically with Zollinger-Ellison syndrome (Garcia-Villanueva et al. 1990).

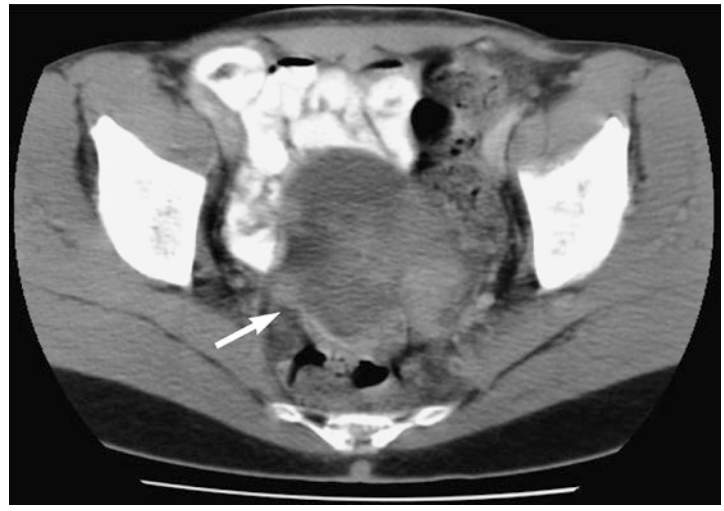

Fig. 29 Granulosa cell tumor. A 52-year-old female with a history of hysterectomy and unilateral oophorectomy for granulosa cell tumors several years before. A solid and cystic pelvic tumor with irregular margins displacing bowel loops is seen at the acetabular level. From imaging, it cannot be differentiated from an ovarian cancer

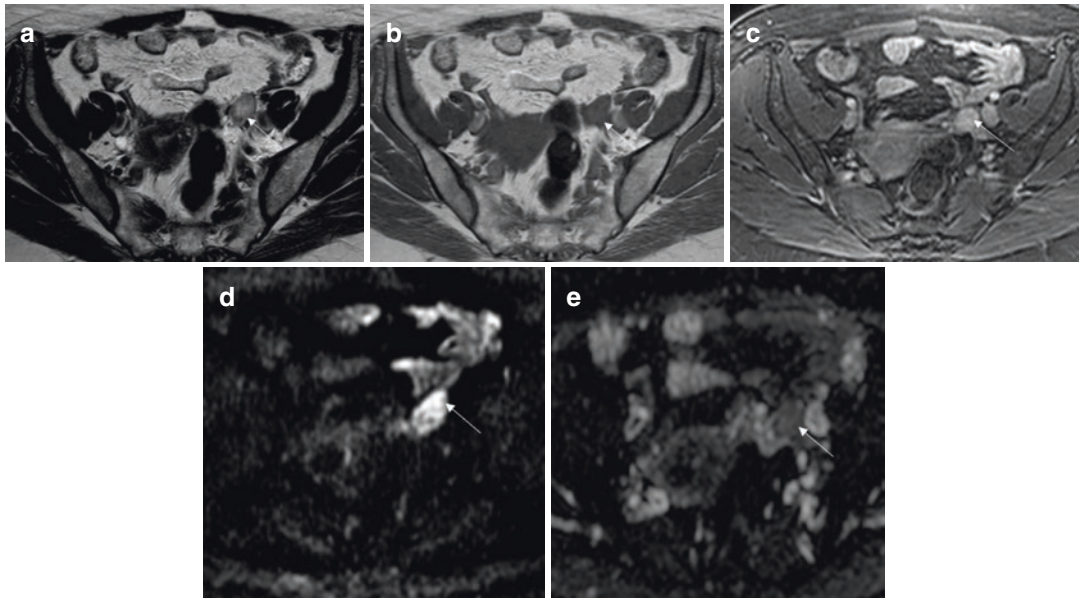

Fig. 30 A 63-year-old patient with a left steroid cell tumor (former stromal luteoma) presenting with hirsutism. (**a**) Axial T2-weighted image; (**b**) axial T1-weighted image fat; (**c**) saturated axial gadolinium-enhanced T1-weighted image; (**d**) axial diffusion-weighted image (b = 1000 s/mm^2); (**e**) axial ADC map. Images show a small solid tumor that on T2-weighted images is hyperintense to the ovarian stroma. There is enhancement of the lesion as well as restricted diffusion (*arrows*)

6 Ovarian Tumors in Children, Adolescents, and Young Women

The majority of ovarian masses in children older than 9 years and young women are benign and include follicular cysts and mature cystic teratomas, with fewer than 5% of ovarian malignancies occurring in this age group. However, lesions with complex architecture should be carefully assessed, as 35% of all malignant ovarian neoplasms occur during childhood and adolescence. This is especially true for children younger than 9 years, where approximately 80% of ovarian neoplasms are malignant (Norris and Jensen 1972). A solid ovarian mass in childhood should also be considered malignant until proven otherwise by histology (Laufer 2017). Differential diagnosis includes dysgerminoma, neuroblastoma rhabdomyosarcoma, lymphoma, and nongenital tumors in the pelvis. Some ovarian neoplasms occurring in this age group excrete protein tumor markers, which may aid in diagnosis and follow-up. They include alpha-fetoprotein, which is produced by endodermal sinus tumors, mixed germ cell tumors, and immature teratomas, lactate dehydrogenase, which is secreted by dysgerminomas, and human chorionic gonadotropin, which is elevated in pregnancy and pregnancy-related tumors and in embryonal ovarian carcinomas (Laufer 2017). Torsion is a special problem in children and young adults presenting with an ovarian mass. Ovarian masses associated with torsion present benign cystic lesions (Fig. 31) with a size greater than 5 cm seem to be under a high risk for torsion (Cass et al. 2001). In children also normal ovaries may undergo torsion. Acute pelvic pain is the mainstay in the differential diagnosis of a torsed ovary; however, imaging findings may sometimes be subacute and misleading and simulate a malignant ovarian tumor.

Ovarian cysts are uncommon before puberty. Most of these are physiologic follicular cysts that will resolve spontaneously. Some ovarian cysts may be hormonally active and result in precocious pseudopuberty, e.g., in McCune-Albright syndrome (Frisch et al. 1992). Ovarian cysts are

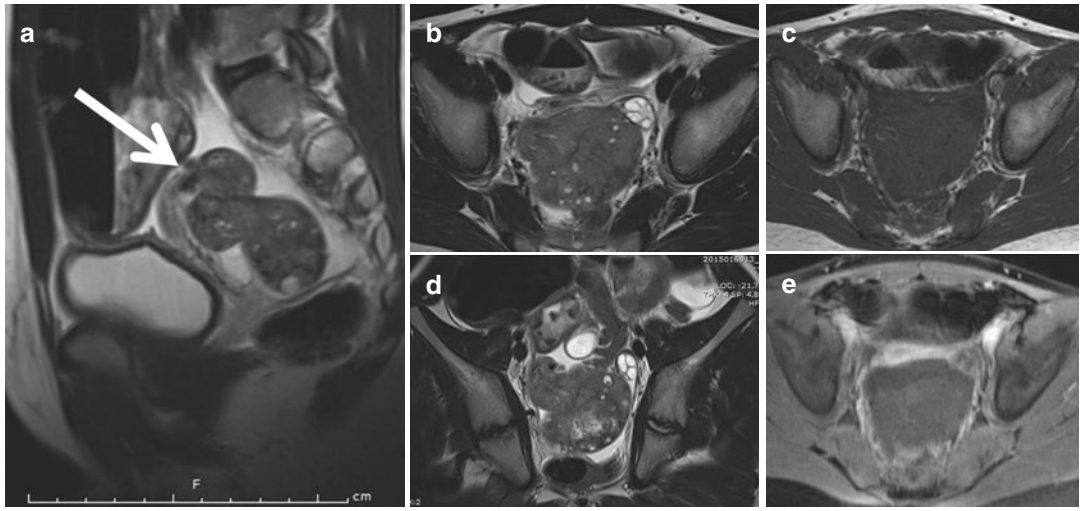

Fig. 31 Right ovarian torsion in a 10-year-old girl. Sagittal T2-weighted image (**a**), axial T2-weighted image (**b**), coronal T2-weighted image (**c**), axial T1-weighted image (**d**), axial T1-weighted image with FS (**e**). Common findings are somewhat nonspecific and include an adnexal mass that may be in the midline, rotated toward the contralateral side of the pelvis; deviation of the uterus to the side of the affected ovary (**e**); and ascites. An enlarged right ovary with peripheral cysts (up to 1 cm in diameter) and no evidence of blood flow is seen. A small amount of pelvic free fluid is also noted. A beaked protrusion at the periphery of the affected ovary, a finding consistent with engorged blood vessels (*arrow*) (**a**) and absence of enhancement (**e**) can be observed. At surgery, the ovary was hemorrhagic and necrotic, appearing with a 360° twist of the pedicle. At pathologic analysis, a congested hemorrhagic ovary with no normal ovarian tissue was identified

extremely common between puberty and 18 years of age. Most of these cysts are functional ovarian cysts and may attain a size of up to 8–10 cm. In this age group, paraovarian or mesothelial cysts, hydrosalpinx, and obstructive genital lesions may also simulate cystic ovarian lesions. Germ cell tumors account for half to two-thirds of the tumors in girls up to 18 years; they present 70% of ovarian tumors in the age between 10 and 30 years (van Winter et al. 1994). The vast majority is unilateral and present benign teratomas. Only 3% of ovarian germ cell tumors are malignant. Dysgerminomas account for approximately 50% of the malignant germ cell tumors in adolescents and young adults and are followed by endodermal sinus tumors (20%) and immature teratomas (19%) (van Winter et al. 1994). As in many ovarian malignancies, rapid growth is a typical finding; however, bilateral manifestation is more common in dysgerminomas than in other malignant germ cell tumors. Juvenile granulosa cell tumors are stromal cell tumors of low malignant potential, which occur before the age of 30. Rarely, they develop before puberty and may become clinically apparent as precocious puberty. Immature teratomas are commonly associated with a mature teratoma; they comprise 1% of all teratomas and occur most commonly in the first two decades of life. Tumor markers are usually negative.

7 Adnexal Masses in Pregnancy

Adnexal masses have been reported to occur in 1–2% of pregnancies (Chiang and Levine 2004). Most of these masses are found incidentally, present functional cysts and will disappear during the first 16 weeks of pregnancy (Hermans et al. 2003). The incidence of ovarian cancer associated with a persistent adnexal mass varies from 3% to 5.9%. In a retrospective analysis of 60 adnexal masses during pregnancy, 50% included mature cystic teratomas, 20% cystadenomas, 13% functional ovarian cysts, and 13% malignant tumors. Among the latter, six

out of eight were tumors of low malignant potential, and all malignant lesions were FIGO stage IA tumors (Sherard et al. 2003). The management of an adnexal mass during pregnancy depends on the size, sonomorphologic criteria, and gestational age. MRI offers incremental benefit in diagnosing exophytic leiomyomas, atypical mature cystic teratomas, and in assessing distant spread in frankly malignant adnexal masses (Telischak et al. 2008). Well-vascularized adnexal masses that are pregnancy related include decidualized endometriomas and pregnancy luteomas. These may mimic malignancy, but clinical background combined with US and MRI may suggest the correct diagnosis and warrant a follow-up (Telischak et al. 2008; Tannus et al. 2009). Pain or an acute abdomen should alert to complications due to hemorrhage, rupture, and torsion of the adnexal mass or nongynecological pelvic conditions.

References

Acien P, Acien N, Ruiz-Macia E, Martin-Estefania C (2014) Ovarian teratoma-associated anti-NDMDAR encephalitis: a systematic review of reported cases. Orphanet J Rare Dis 9:157. doi:10.1186/s13023-014-0157-x

Buy JN, Ghossain MA, Moss AA et al (1989) Cystic teratoma of the ovary: CT detection. Radiology 171:697–670. doi:10.1148/radiology.171.3.2717741.

Caspi B, Appelman Z, Rabinerson D et al (1997) The growth pattern of ovarian dermoid cysts: a prospective study in premenopausal and postmenopausal women. Fertil Steril 68:501–505

Cass DL, Hawkins E, Brandt ML et al (2001) Surgery for ovarian masses in infants, children, and adolescents: 102 consecutive patients treated in a 15-year period. J Pediatr Surg 36:693–699. doi:10.1053/jpsu.2001.22939

Chiang G, Levine D (2004) Imaging of adnexal masses in pregnancy. J Ultrasound Med 23:805–819

Christensen JT, Boldsen JL, Westergaard JG (2002) Functional ovarian cysts in premenopausal and gynecologically healthy women. Contraception 66:153–157

Cho SM, Byun JY, Rha SE et al (2004) CT and MRI findings of cystadenofibromas of the ovary. Eur Radiol 14:798–804. doi:10.1007/s00330-003-2060-z

Chung BM, Park SB, Lee JB, Park HJ, Kim YS, Oh YJ (2015) Magnetic resonance imaging features of ovarian fibroma, fibrothecoma, and thecoma. Abdom Imaging 40:1263–1272. doi:10.1007/s00261-014-0257-z

Clement PB (2002) Non-neoplastic lesions of the ovary. In: Kurman RJ (ed) Blaustein's pathology of the female genital tract. Springer Verlag, New York, pp 675–728

Corwin MT, Gerscovich EO, Lamba R, Wilson M, McGahan JP (2014) Differentiation of ovarian endometriomas from hemorrhagic cysts at MR imaging: utility of the T2 dark spot sign. Radiology 271:126–132. doi:10.1148/radiol.13131394

Dias JL, Veloso Gomes F, Lucas R, Cunha TM (2015) The shading sign: is it exclusive of endometriomas? Abdom Imaging 40:2566–2572. doi:10.1007/s00261-015-0465-1

Duijkers IJ, Klipping C (2010) Polycystic ovaries, as defined by the 2003 Rotterdam consensus criteria, are found to be very common in young healthy women. Gynecol Endocrinol 26:152–160. doi:10.1080/09513590903247824

Forstner R, Thomassin-Naggara I, Cunha TM et al (2016) ESUR recommendations for MR imaging of the sonographically indeterminate adnexal mass: an update. Eur Radiol Oct 21 [Epub ahead of print] Erratum in: Eur Radiol. 2016 Dec 5. doi:10.1007/s00330-016-4600-3

Foshager MC, Hood LL, Walsh JW (1996) Masses simulating gynaecologic diseases at CT and MRI. RadioGraphics 16:1085–1099. doi:10.1148/radiographics.16.5.8888392

Franks S (2006) Controversy in clinical endocrinology: diagnosis of polycystic ovarian syndrome: in defense of the Rotterdam criteria. J Clin Endocrinol Metab 91:786–789. doi:10.1210/jc.2005-2501

Frisch LS, Copeland KC, Boepple PA (1992) Recurrent ovarian cysts in childhood: diagnosis of McCune-Albright syndrome by bone scan. Pediatrics 90: 102–104

Garcia-Villanueva M, Badia Figuerola N, Ruiz del Arbol L, Hernandez Ortiz MJ (1990) Zollinger Ellison syndrome due to a borderline mucinous cystadenoma of the ovary. Obstet Gynecol 75:549–552

Ghattamaneni S, Bhuskute N, Weston MJ, Spencer JA (2009) Discriminative MR imaging features of Fallopian tube masses. Clin Radiol 64:815–831. doi:10.1016/j.crad.2009.03.007

Hassen K, Ghossain MA, Rousset P et al (2011) Characterization of papillary projections in benign versus borderline and malignant ovarian masses on conventional and color Doppler ultrasound. AJR Am J Roentgenol 196:1444–1449. doi:10.2214/AJR.10.5014

Hermans RH, Fisher DC, van der Putte HW et al (2003) Adnexal masses in pregnancy. Onkologie 26:167–172. doi:69838

Heifetz SA, Cushing B, Giller R et al (1998) Immature teratomas in children: pathologic considerations: a report from the combined Pediatric Oncology Group/Children's Cancer Group. Am J Surg Pathol 22:1115–1124

Hochberg L, Hoffman MS (2017) Differential diagnosis of adnexal mass. www uptodate 2017

Honoré LH, O'Hara KE (1980) Serous papillary neoplasms arising in paramesonephric paraovarian cysts: a report of 8 cases. Acta Obstet Gynecol Scand 59:525–528

Horta M, Cunha TM (2015) Sex cord-stromal tumors of the ovary: a comprehensive review and update for radiologists. Diagn Interv Radiol 21:277–286. doi:10.5152/dir.2015.34414

Hricak H, Chen M, Coakley FV et al (2000) Complex adnexal masses: detection and characterization with MRI—multivariate analysis. Radiology 214:39–46. doi:10.1148/radiology.214.1.r00ja3939

Johnstone EB, Rosen MP, Neri R et al (2010) The polycystic ovary post-Rotterdam: a common, age-dependent finding in ovulatory women without metabolic significance. J Clin Endocrinol Metab 95:4965–4972. doi:10.1210/jc.2010-0202

Jung SE, Lee JM, Rha SE, Byun JY, Jung JI, Hahn ST (2002) CT and MRI of ovarian tumors with emphasis on the differential diagnosis. RadioGraphics 22:1305–1325. doi:10.1148/rg.226025033

Jung DC, Kim SH, Kim SH (2006) MR imaging findings of ovarian cystadenofibroma and cystadenocarcinofibroma: clues for the differential diagnosis. Korean J Radiol 7:199–204. doi:10.3348/kjr.2006.7.3.199

Kaijser J, Vandecaveye V, Deroose CM et al (2014) Imaging techniques for the pre-surgical diagnosis of adnexal tumours. Best Pract Res Clin Obstet Gynaecol 28:683–695. doi:10.1016/j.bpobgyn.2014.03.013

Kier R (1992) Nonovarian gynaecologic cysts: MR imaging findings. AJR Am J Roentgenol 158:1265–1269. doi:10.2214/ajr.158.6.1590120

Kim JS, Lee HJ, Woo SK, Lee TS (1997) Peritoneal inclusion cysts and their relationship to the ovaries: evaluation with sonography. Radiology 204:481–484. doi:10.1148/radiology.204.2.9240539

Kim JC, Kim SS, Park JY (2000) Bridging vascular sign in the MR diagnosis of exophytic uterine leiomyoma. J Comput Assist Tomogr 24:57–60

Koonings PP, Campbell K, Mishell DR Jr, Grimes DA (1989) Relative frequency of primary ovarian neoplasm: a 10-year review. Obstet Gynecol 74:921–926

Kurman RJ, Ellenson LH, Ronnett B (2011) Blaustein's pathology of the female genital tract, 6th edn. Springer, New York

Kurman RJ, Carcangiu ML, Herrington CS, Young RH (2014) Classification of tumors of the ovary. In: WHO classification of tumours, vol. 6, 4th edn. IARC, Lyon, pp 44–56

Lakhani K, Seifalian AM, Atiomo WU, Hardiman P (2002) Polycystic ovaries. Br J Radiol 75:9–16. doi:10.1259/bjr.75.889.750009

Laufer MR (2017) Ovarian cysts and neoplasm in infants, children, and adolescents. www.uptodate.com

Lee JH, Jeong YK, Park JK, Hwang JC (2003) "Ovarian vascular pedicle" sign revealing organ of origin of a pelvic mass lesion on helical CT. AJR Am J Roentgenol 181:131–137

Lee TT, Rausch ME (2012) Polycystic ovarian syndrome: role of imaging in diagnosis. RadioGraphics 32:1643–1657

Lengyel E (2010) Ovarian cancer development and metastasis. Am J Pathol 177:1053–1064. doi:10.2353/ajpath.2010.100105

Levine CD, Patel UJ, Ghanekar D, Wachsberg RH, Simmons MZ, Stein M (1997) Benign extraovarian mimics of ovarian cancer: distinction with imaging studies. Clin Imaging 21:350–358

Levine D, Brown DL, Andreotti RF et al (2010) Management of asymptomatic ovarian and other adnexal cysts imaged at US: society of radiologists in ultrasound consensus conference statement. Radiology 256:943–954. doi:10.1148/radiol.10100213

Lujan ME, Jarrett BY, Brooks ED et al (2013) Updated ultrasound criteria for polycystic ovary syndrome: reliable thresholds for elevated follicle population and ovarian volume. Hum Reprod 28:1361–1368. doi:10.1093/humrep/det062

Matsubayashi R, Matsuo Y, Doi J, Kudo S, Matsuguchi K, Sugimori H (1999) Sclerosing stromal tumor of the ovary: radiologic findings. Eur Radiol 9:1335–1338. doi:10.1007/s003300050844

Matsuki M, Kaji Y, Matsuo M, Kobashi Y (2000) Struma ovarii: MRI findings. Br J Radiol 73:87–90. doi:10.1259/bjr.73.865.10721328

Moon WJ, Koh BH, Kim SK et al (2000) Brenner tumor of the ovary: CT and MR findings. J Comput Assist Tomogr 24:72–76

Moyle PL, Kataoka MY, Nakai A, Takahata A, Reinhold C, Sala E (2010) Nonovarian cystic lesions of the pelvis. RadioGraphics 30:921–938. doi:10.1148/rg.304095706

Norris HJ, Jensen RD (1972) Relative frequency of ovarian neoplasm in children and adolescents. Cancer 30:713–719

Okada S, Ohaki Y, Inoue K et al (2005) Calcifications in mucinous and serous cystic ovarian tumors. J Nippon Med Sch 72:29–33

Outwater EK, Mitchell DG (1996) Normal ovaries and functional cysts: MR appearance. Radiology 198:397–402. doi:10.1148/radiology.198.2.8596839

Palmeiro MM, Cunha TM, Loureiro AL, Esteves G (2016) A rare benign ovarian tumour. BMJ Case Rep (2016) Mar 1;2016. pii: bcr2015214101. doi: 10.1136/bcr-2015-214101

Patel MD, Ascher SM, Paspulati RM et al (2013) Managing incidental findings on abdominal and pelvic CT and MRI, part 1: white paper of the ACR Incidental Findings Committee II on adnexal findings. J Am Coll Radiol 10:675–681. doi:10.1016/j.jacr.2013.05.023

Rha SE, Byun JY, Jung SE et al (2004) Atypical CT and MRI manifestations of mature ovarian cystic teratomas. AJR Am J Roentgenol 183:743–750. doi:10.2214/ajr.183.3.1830743

Sala EJ, Atri M (2003) MRI of benign adnexal disease. Top Magn Reson Imaging 14:305–327

Saksouk FA, Johnson SC (2004) Recognition of the ovarian origin of pelvic masses with CT. RadioGraphics 24(Suppl 1):S133–S146. doi:10.1148/rg.24si045507

Seidman JD, Russell P, Kurman RJ (2002) Surface epithelial tumors of the ovary. In: Kurman RJ (ed) Blaustein's pathology of the female genital tract. Springer Verlag, New York, pp 791–904

Sherard GB 3rd, Hodson CA, Williams HJ, Semer DA, Hadi HA, Tait DL (2003) Adnexal masses and pregnancy: a 12-year experience. Am J Obstet Gynecol 189:358–362. discussion 362–363

Spencer JA, Gore RM (2011) The adnexal incidentaloma: a practical approach to management. Cancer Imaging 11:48–51. doi:10.1102/1470-7330.2011.0008

Tanaka YO, Tsunoda H, Kitagawa Y, Ueno T, Yoshikawa H, Saida Y (2004) Functioning ovarian tumors: direct and indirect findings at MR imaging. RadioGraphics 24(Suppl 1):S147–S166. doi:10.1148/rg.24si045501

Tannus JF, Hertzberg BS, Haystead CM, Paulson EK (2009) Unilateral luteoma of pregnancy mimicking a malignant ovarian mass on magnetic resonance and ultrasound. J Magn Reson Imaging 29:713–717. doi:10.1002/jmri.21530

Telischak NA, Yeh BM, Joe BN, Westphalen AC, Poder L, Coakley FV (2008) MRI of adnexal masses in pregnancy. AJR Am J Roentgenol 191:364–370. doi:10.2214/AJR.07.3509

Timmerman D, Moerman P, Vergote I (1995) Meigs syndrome with elevated CA-125 levels: two case reports and review of the literature. Gynecol Oncol 59:405–408. doi:10.1006/gyno.1995.9952

Timmerman D, Van Calster B, Testa A et al (2016) Predicting the risk of malignancy in adnexal masses based on the Simple Rules from the International Ovarian Tumor Analysis group. Am J Obstet Gynecol 214:424–437. doi:10.1016/j.ajog.2016.01.007

Thomassin-Naggara I, Daraï E, Cuenod CA et al (2009) Contribution of diffusion-weighted MR imaging for predicting benignity of complex adnexal masses. Eur Radiol 19:1544–1552. doi:10.1007/s00330-009-1299-4

Thomassin-Naggara I, Toussaint I, Perrot N et al (2011) Characterization of complex adnexal masses: value of adding perfusion- and diffusion-weighted MR imaging to conventional MR imaging. Radiology 258:793–803. doi:10.1148/radiol.10100751

van Winter JT, Simmons PS, Podratz KC (1994) Surgically treated adnexal masses in infancy, childhood, and adolescence. Am J Obstet Gynecol 170:1780–1786. discussion 1786–1789

Young RH, Scully RE (2002) Sex cord stromal, steroid cell, and other ovarian tumors. In: Kurman RJ (ed) Blaustein's pathology of the female genital tract. Springer Verlag, New York, pp 903–966

Yamashita Y, Hatanaka Y, Torashima M, Takahashi M, Miyazaki K, Okamura H (1994) Mature cystic teratomas of the ovary without fat in the cystic cavity: MR features in 12 cases. AJR Am J Roentgenol 163:613–616. doi:10.2214/ajr.163.3.8079854

Yoshitake T, Asayama Y, Yoshimitsu K et al (2005) Bilateral ovarian leiomyomas: CT and MRI features. Abdom Imaging 30:117–119. doi:10.1007/s00261-004-0202-7

Adnexal Masses: Characterization of Benign Adnexal Masses

I. Thomassin-Naggara, B. Fedida, and E. Kermarrec

Contents

I. Thomassin-Naggara (✉)
Sorbonne Universités, UPMC Univ Paris 06, IUC, 75005 Paris, France

INSERM, UMR970, Equipe 2, Imagerie de l'angiogenèse, 75005 Paris, France

Department of Radiology, AP-HP, Hôpital Tenon, 4 rue de la Chine, 75020 Paris, France

Service de Radiologie, Hôpital Tenon, 4 rue de la Chine, 75020 Paris, France
e-mail: isabelle.thomassin@aphp.fr

B. Fedida
Sorbonne Universités, UPMC Univ Paris 06, IUC, 75005 Paris, France

Department of Radiology, AP-HP, Hôpital Tenon, 4 rue de la Chine, 75020 Paris, France

E. Kermarrec
Department of Radiology, AP-HP, Hôpital Tenon, 4 rue de la Chine, 75020 Paris, France

Abstract

Pelvic MR imaging is the best second-line technique to characterize indeterminate or complex adnexal masses detected at transvaginal ultrasonography. The aim of this text is to explain the added value of MR and CT in the diagnostic management of a slightly symptomatic indeterminate or complex adnexal mass. The objectives of this chapter are to describe the place of MR imaging and CT imaging and to learn how to combine features from morphologic and functional sequences to accurately diagnose an adnexal mass.

The analysis is divided into two steps: The first step is to estimate the risk of malignancy based on the ADNEX MR Scoring system or EURAD score and the second step is to suggest an histopathological hypothesis combining EURAD score with the age of the patient and the morphology of the tumor.

1 Introduction

Pelvic MR imaging is the best second-line technique to characterize indeterminate or complex adnexal masses detected at transvaginal ultrasonography.

In clinical routine, there are two very different circumstances for detecting these masses at ultrasonography. The first situation is the context of acute or subacute pelvic pain and the second one is incidental finding of an adnexal mass during

Med Radiol Diagn Imaging (2017)
DOI 10.1007/174_2017_66, © Springer International Publishing AG
Published Online: 26 April 2017

the assessment of a nonspecific symptom such as bleeding, chronic pelvic pain, or infertility.

In this chapter, we are not going to develop the first clinical situation which will be covered in the "Acute and chronic pelvic pain disorders" chapter about pelvic inflammatory disease and adnexal torsion. The aim of this text is to explain the added value of MR and CT in the diagnostic management of a slightly symptomatic indeterminate or complex adnexal mass.

The objectives of this chapter are to describe the place of MR imaging and CT imaging and to learn how to combine features from morphologic and functional sequences to accurately diagnose an adnexal mass.

2 Part 1: MR Imaging in Diagnostic Pathway

2.1 Context

Most of the medical imaging publications recommend MR imaging to characterize complex adnexal masses without any consensus on the definition of the word "complex". Despite a high level of evidence on the performance of MR imaging in this issue, many clinicians perform laparoscopy just based on ultrasonographic features. However, recent data on the impact of ovarian surgery on fertility are modifying the practices and render MR imaging useful especially to obtain criteria to avoid unnecessary surgery in patients with benign lesions (Buys et al. 2005). Another significant impact of MRI is the possibility to plan the surgical procedure time and then to improve the organization of our overloaded theater schedule. The surgeon needs to correctly plan the surgery and also to inform the patient of the possibility and the risks to discover unexpected lesions during the surgery. That's why we perform more and more MR imaging in this indication.

2.2 Which Lesions Should Be Assessed with MR Imaging?

MR imaging is a second-line technique after ultrasonography which is the first imaging technique to assess pelvis abnormalities. More than 70% of adnexal masses are accurately identified using transvaginal ultrasonography with color Doppler. According to the literature, even using accurate ultrasonographic models, 20–25% of adnexal masses remain indeterminate after ultrasonography and need further examination (Kinkel et al. 2005).

To approach the definition of a complex adnexal mass, pattern recognition analysis or simple rules, which are currently the most reliable model published until now, can be used (Brun et al. 2014).

2.2.1 Indications According to Ultrasonographic Patterns

The main ultrasonographic patterns are divided into the following six categories:

US pattern 1: Simple cyst (i.e., unilocular anechoic cyst without solid component)

US pattern 2: Nonsimple cyst (i.e., unilocular echoic cyst without solid component)

These two first US patterns are included in the first categories of International Ovarian Tumor Analysis group classification named "Unilocular cyst" (Buys et al. 2005). This group includes the tubal benign abnormalities like hydrosalpinx, hematosalpinx, and the different echoic signal like "ground glass," "hemorrhagic content," and "mixed content."

US pattern 3: Bi- or multilocular cyst (i.e., bi- or multilocular cyst without solid component)

US pattern 4: Cyst with papillary projections

US pattern 5: Mixed heterogeneous mass

IOTA classification groups these two last patterns in the groups "unilocular solid" or "multilocular solid". In these two categories, there is a cystic and a solid component in the described lesion.

US pattern 6: Enlarged ovaries (including purely solid mass than means more than 80% of solid component in the lesion)

These last three patterns require an ultrasonographic characterization of their solid component looking for acoustic shadowing, irregularity of the margins, and feature of the Doppler flow. These elements are usually inadequate to accurately predict the risk of malignancy.

Therefore, MR imaging can be performed in the cases with US pattern 4, 5, or 6 to suggest a histopathological diagnosis. In pattern 3, MR

imaging allows to exclude a solid component and to characterize the different cystic components and it also helps to approach a histological diagnosis.

On the contrary, in categories 1 and 2, MR imaging has a very low added value except if the lesion is very large. Indeed, if an echoic cyst is larger than 7 cm or an anechoic cyst is larger than 10 cm, MRI is better to exclude a small solid component distant from the endovaginal probe that could be missed. MRI is also efficient to evaluate any associated findings such as deep pelvic endometriosis associated with endometrioma.

2.2.2 Indications According to Simple Rules

The simple rules described by IOTA group consist in dividing ten sonographic features in two groups: benign features (B features) and malignant features (M features) (Table 1).

When at least one B feature is found and no M feature, the lesion is considered as benign whereas when at least one M feature is found and no B feature, the lesion is considered as malignant. When both B and M features are found, the lesion is considered as indeterminate as well as when none B or M features is found. Applying these rules, in the group of indeterminate lesion, the risk of malignancy is 40% and MR imaging is warranted (Timmerman et al. 2010).

Recently, Timmerman et al. reviewed the level of risk according to the simple rules' categories publishing a model of prediction of malignancy on a population of 4848 patients with a prevalence of malignancy of 34.3% (1665/4848) (Timmerman et al. 2010). This new publication suggests that the lesions categorized with an "intermediate risk" (i.e., risk of 8.3%) may also be referred for MR imaging to obtain additional findings to predict benignity (Table 2).

Table 1 Simples rules (Timmerman et al. 2010)

Benign features	Malignant features
B1 Unilocular cyst	M1 Irregular solid tumor
B2 Solid components present but <7 mm	M2 Ascites
B3 Acoustic shadows	M3 At least four papillary structures
B4 Smooth multilocular tumor with largest diameter <100 mm	M4 Irregular multilocular solid tumor with largest diameter > or equal to 100 mm
B5 No blood flow	M5 Very strong color Doppler

2.3 Why MR Imaging Is Useful to Characterize Adnexal Masses?

Adnexal masses usually have multiple cystic and solid components. If the cyst is anechoic, ultrasonography is accurate to diagnose simple fluid (water-like appearance). If the mass is echoic, the presence of positive Doppler Flow allows identifying solid components. But the presence of solid component does not correspond to malignancy whereas the absence of positive Doppler Flow does not help to distinguish hypovascular solid components from nonsimple fluid lesions. The motion of the echos and the presence of a fluid level are in keeping with a nonsimple cyst. However in this type of mass, a solid tissue can be difficult to exclude.

Using pelvic MR imaging, the absence of contrast enhancement in an adnexal mass allows to exclude the presence of solid tissue if the spatial resolution is thin enough (< or =3 mm). Moreover,

Table 2 Risk of malignancy of US lesions according the simples rules (Timmerman et al. 2010)

	Simple rules descriptors	PPV of malignancy
Very low risk	No M feature ··· + ··· >2B features	**0.6%** (1/175)
Low risk	No M feature ··· + ··· 2B features No M feature ··· + ··· B1 feature	**1.3%** (20/1560)
Intermediate risk	No M feature ··· + ··· 1B feature (except B1)	**8.3%** (60/722)
Elevated risk	No features Equal number of M and B features More B than M features present	**41.1%** (451/1096)
Very high risk	More M than B features present	**87.5%** (1133/1295)

$p<0.05$

the combination of T2W, T1W, DW, and T1W after intravenous injection of chelates of gadolinium allows recognizing most cystic components seen in adnexal masses. The addition of DW and DCE MR imaging is reliable to characterize solid components distinguishing between benign, borderline, and invasive malignant tissue. By definition, a solid tissue enhances after gadolinium injection. However, any internal enhancement does not correspond to solid tissue. A solid tissue includes solid papillary projection, irregular septa, mural nodule, and purely solid mass (Thomassin-Naggara et al. 2013). Smooth septa whatever the thickness is considered as solid component but not solid tissue.

Thus, MR imaging analysis is performed in two steps: the first step evaluates the risk of malignancy and the second step addresses the histopathological type of ovarian or tubal tumors.

3 Part 2: MR Protocol and Keys for Analysis

3.1 Step 1: Prediction of the Risk of Malignancy

When a pelvis mass is discovered, the first step is to determine its origin. Thus, normal ipsilateral ovarian parenchyma needs to be identified either as a crescent at the periphery of the mass or in a different site distant from the pelvic mass (suggestive of an extra-ovarian origin). If no ovarian parenchyma is visible, we should look for the ovarian pedicles to find the location of ovarian fossae and verify if the ovarian pedicle is adjacent to the mass. That's why the MR protocol should include an anatomical lombo-pelvic sequence with slices from the mid-kidneys to the pubal symphysis which is best performed with a T2W sequence. Moreover, a sagittal T2W sequence is recommended to evaluate the mass and its relationship with the uterus. At the end, when a tubal origin is suspected, coronal views in T2WI are useful to confirm this hypothesis.

The absence of solid tissue is a main feature to suggest a low risk of malignancy (<5%) (Thomassin-Naggara et al. 2013). By definition, a solid tissue enhances after gadolinium injection but any internal enhancement does not always correspond to solid tissue. Indeed, smooth septa are not considered as solid tissue. This feature is included in the expression "solid component" but not considered as solid tissue. Thus, a solid component groups unenhanced elements, such as clots and debris, and enhanced tissue including smooth septa and solid tissue. Solid tissue corresponds to irregular septa, solid papillary projection (>3 mm), mural nodule, and purely solid mass.

In our experience, unilocular cyst with solid tissue with a simple fluid content, or endometriotic contents or fatty contents have a very low risk of malignancy (<2%). A unilocular cyst with another type of fluid content has also a low risk of malignancy (<5%).

A bi- or a multilocular cyst without solid tissue again has a low risk of malignancy (<5%).

When a solid tissue is detected, the analysis of T2W signal, DW signal, and DCE MR signal within the solid tissue is useful. A solid tissue in low T2W signal and low DW signal has a very low risk of malignancy (<2%) (Thomassin-Naggara et al. 2013). If a solid tissue displays either an intermediate T2W signal or a high signal on DW sequence, time intensity curves comparing solid tissue to adjacent external myometrium are useful (Thomassin-Naggara et al. 2013). If the solid tissue enhances according to a type 1 time intensity curve, the PPV of malignancy is <5%. If the solid tissue enhances according to a type 3 time intensity curve, the PPV of malignancy is higher than 95%. If the solid tissue enhances according to a type 2 time intensity (Thomassin-Naggara et al. 2013). In our experience, less than 15% of the lesions remain indeterminate. Thus, an MR classification has been developed named ADNEX MR Score which is under European validation (EURAD study) (Table 3).

3.2 Step 2: Prediction of the Histopathological Diagnosis

If the first step is feasible by any junior radiologist or a general radiologist, this second step

Table 3 ADNEX MR score or EURAD score (Thomassin-Naggara et al. 2013)

		PPV of malignancy
Score 1	No adnexal mass	0%
Score 2	Unilocular simple cyst or tube Endometriotic lesion, no internal Gd+ Fatty lesion, no solid tissue No wall enhancement Solid tissue in low T2W and low DW signal	<2%
Score 3	Unilocular nonsimple cyst (excl. fatty and endometriotic) Multilocular cyst, no solid tissue Solid tissue with TIC type 1	<5%
Score 4	Solid tissue with TIC type 2	5–95%
Score 5	Solid tissue with TIC type 3 Peritoneal implants	>95%

A lesion with a solid tissue corresponds to MR categories 4, 5, and 6

requires deeper knowledge of functional and organic ovarian lesions. The analysis is based on the clinical history and the different MR parameters useful to analyze cystic and solid components characteristics, the shape, the wall, and the size of the lesion. Sometimes, the differentiation between functional and organic cysts is difficult and ultrasonographic follow-up helps to the make the differential diagnosis.

As for ultrasonography, we differentiate the following six categories of MR features:

MR pattern 1: Simple cyst

Simple cyst corresponds to a unilocular cyst lesion without internal enhancement with a fluid content that presents a low T1W signal, a high T2W signal, a low DW signal and a high ADC (Fig. 1). Nonspecific cyst, serous cystadenoma, follicular cyst, pseudo peritoneal cyst, and hydrosalpinx are usually classified in this pattern (Table 4).

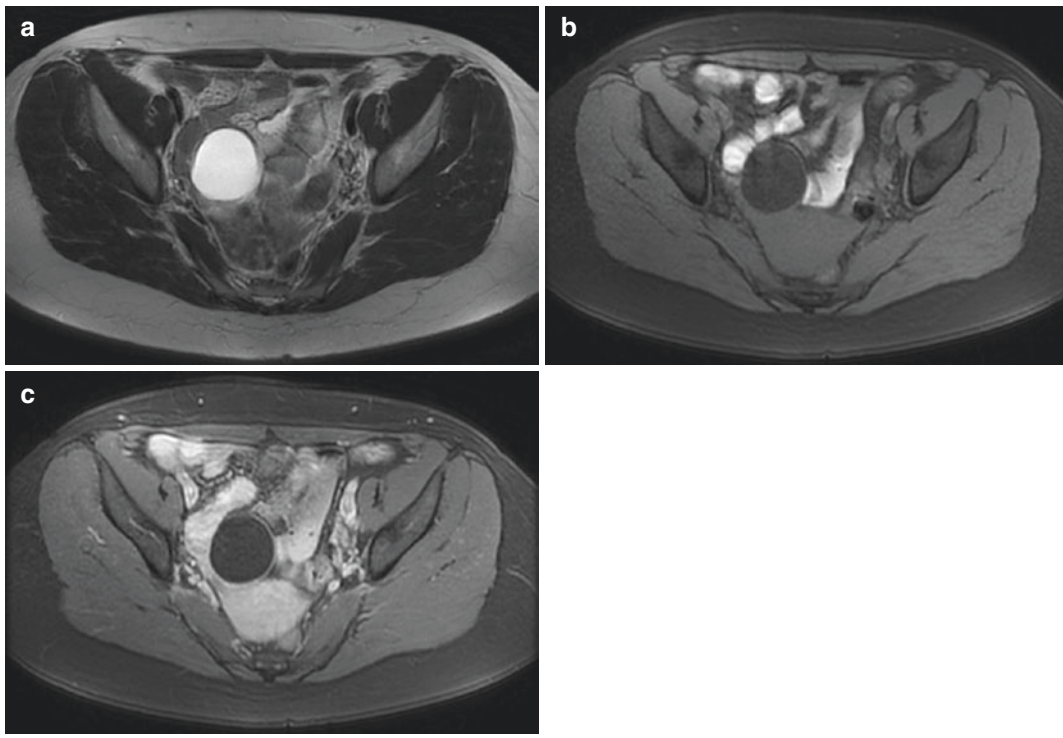

Fig. 1 MR pattern 1: Serous benign cystadenoma (**a**: Axial T2W sequence, **b**: Axial T1W sequence, **c**: Axial T1W sequence after gadolinium injection). Step 1: Unilocular cyst without internal enhancement with a fluid content in high T2W and low T1W signal corresponding to EURAD score 2. Step 2: There is no specific feature that helps to distinguish a functional cyst from an organic cyst

Table 4 Adnexal masses without solid tissue

Diagnostic hypothesis	Clinical history	Fluid	Shape	Wall	Specific sign
Pattern 1 = simple cyst					
Follicular cyst	Premenopausal woman	High T2	Oval	Fine Gd+	Spontaneous disappearance
Unspecified cyst	Menopausal	High T2	Oval	Gd−	–
Serous cystadenoma	40–50 year old	High T2	Oval	Gd+	Calcospherites
Hydrosalpinx	Any age	High T2	Tubular (CoroT2W)	Gd+	Partial septa
Pseudoperitoneal cyst	After surgery or pelvic inflammatory disease	High T2	Pelvic shape	Gd−	Deformable at palpation
Pattern 2 = nonsimple cyst					
Luteal cyst	Premenopausal	Variable T1W signal	Round	Thick Gd+/DW+	Spontaneous disappearance
Endometrioma	Premenopausal	Low T2W signal T1W>fat	Round	Gd−	Clots
Dermoid cyst	<45 year old	HypoT1 FS	Round		
Hématosalpinx	Premenopausal	Variable T1W signal	Tubular	Gd+ Franges+	
Tubo ovarian abscess	Premenopausal	High T1W and DW signal with low ADC value	Round + tubular	Thick Gd+	Fatty infiltration
Pattern 3 = multilocular lesion					
Mucinous benign cystadenoma	30–50 year old	Loculi with different signal intensity	Oval	Gd+	None
Struma ovarii	40–50 year old	Presence of colloid	Oval	Gd+	None
Adult granulosa	55 year old	Hemorrhagic loculi	Oval	Gd+	Endometrial thickening adenomyosis
Sertoli Leydig	20–30 year old	Hemorrhagic loculi	Oval	Gd+	Hyperandrogenic syndrome
Yolk sac	20 year old αFP > 1000	Hemorrhagic loculi			

MR pattern 2: Nonsimple cyst

Nonsimple cyst corresponds to a unilocular cyst that has no internal enhancement with a fluid content that presents an intermediate or high T1W signal, a variable T2W signal, DW signal, and ADC maps. The analysis is based on the signal of the cystic content before and after fat suppression, the presence or the absence of wall enhancement, and the signal on the DW sequence (Table 4).

MR pattern 3: Multilocular cyst

In a multilocular cyst, there are smooth septa that enhance after gadolinium injection. Smooth septa are not considered as solid tissue. On T2W sequence, a luteal cyst with fibrinous component may look like a multilocular cyst. The difference between septa and fibrinous components is the presence of septal enhancement.

Septal enhancement is a key feature that helps to distinguish septa from fibrinous components that do not enhance after contrast media injection. In that case, the cyst can be considered as unilocular indicating the luteal cyst. A lesion classified in this pattern "3" does not include any solid tissue.

MR imaging is useful in this group either in large lesion size or to characterize the cystic component owing to the combination of the different MR sequences to suggest a histopathological subtype. The different cystic fluid types found in ovarian tumors are:

- Mucin (moderate high T1W signal, intermediate T2W signal, high DW signal, high ADC value)
- Colloid (very low T2W signal, moderate high T1W signal)
- Blood (high T1W signal with and without fat suppression, intermediate T2W signal)
- Pus (moderate high T2W signal, intermediate T2W signal, high DW signal, low ADC value)
- Fat (high T1W signal that decreases after fat suppression) (Fig. 2)

MR pattern 4: Cyst with papillary projections

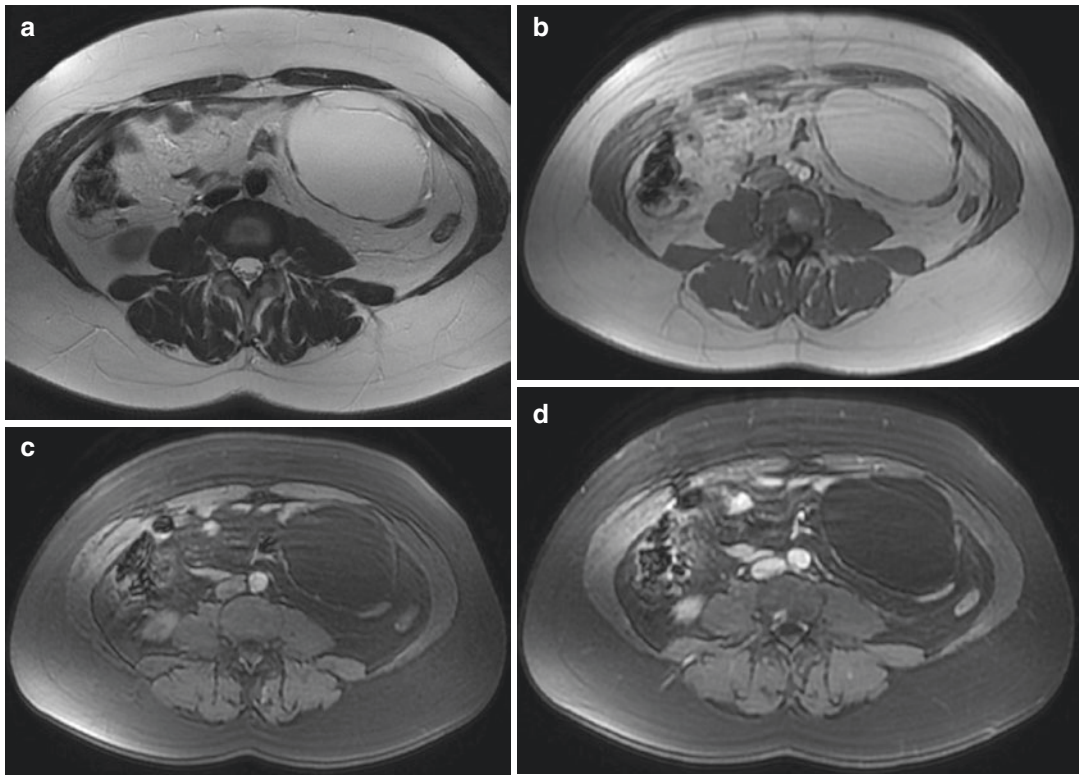

Fig. 2 MR pattern 3: Mature cystic teratoma (**a**: Axial T2W sequence, **b**: Axial T1W sequence, **c**: Axial T1W sequence with fat suppression, **d**: Axial T1W sequence with fat suppression after gadolinium injection). Step 1: Multilocular cyst without solid tissue with a fluid content in high T2W, high T1W signal, and low T1 after fat corresponding to EURAD score 2. Step 2: The presence of fatty content and the absence of colloid suggests a teratoma. The absence of protuberance in this case strongly suggests a mature cystic teratoma

A papillary projection corresponds to solid tissue and centrally enhances after gadolinium injection (Fig. 3). This feature is important to distinguish a solid papillary projection from a small loculus before performing any time intensity curve (cause of false positive). Moreover, in tubal distension pseudopapillary projections with the same size, regularly located on the cystic wall, indicate the cogwell sign (Ghattamaneni et al. 2009). A tubular shape in another plan may help to diagnose hydrosalpinx. Final differential diagnosis is a clot that does not enhance after gadolinium injection.

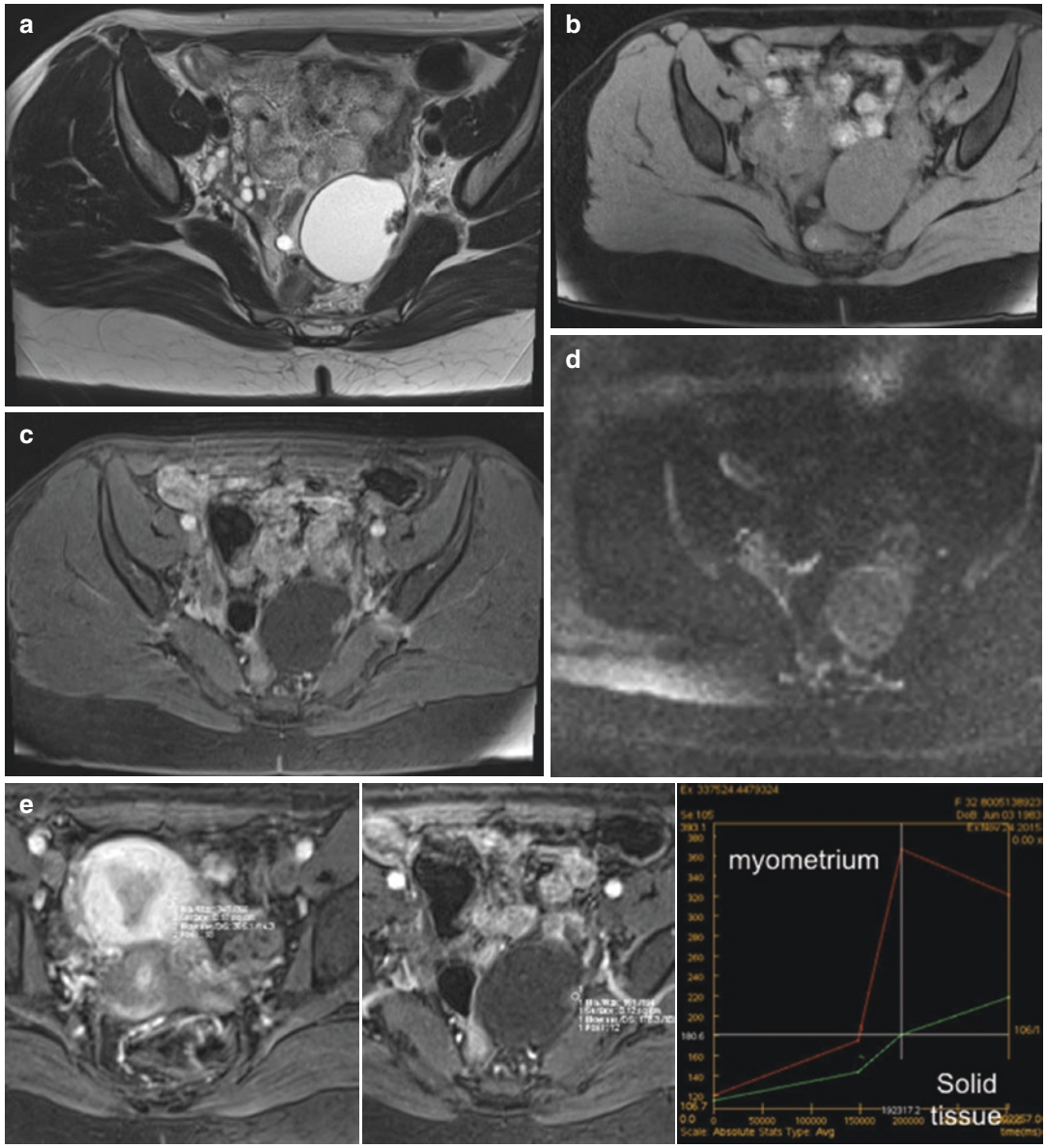

Fig. 3 MR pattern 4: Serous benign cystadenoma (**a**: Axial T2W sequence, **b**: Axial T1W sequence, **c**: Axial T1W sequence with fat suppression after gadolinium injection, **d**: Axial DWI sequence, **e**: Axial DCE MR sequence). Step 1: Unilocular cyst with solid tissue that corresponds to solid papillary projection that displays a high T2W signal, low DW signal, and enhances according a TIC type 1 corresponding to EURAD score 3 (probably benign). Step 2: Unilocular cyst with papillary projection higher than 1 mm suggests a serous cystadenoma. Benign characteristics suggest a benign serous cystadenoma

The presence of solid papillary projections is pathognomonic of the presence of epithelial tumors but is not synonymous of a borderline or benign lesion. There are two main types of solid papillary projections:

– Larger than 1 mm in size found in serous cystadenomas which displays in benign lesion a low T2W and low DW signal and a type 1 time intensity curve (TIC) and displays in borderline cystadenomas an intermediate T2W signal, a high DW signal and a type 2 TIC (Fig. 4).
– Smaller than 1 mm found in borderline mucinous cystadenomas. No papillary projection is

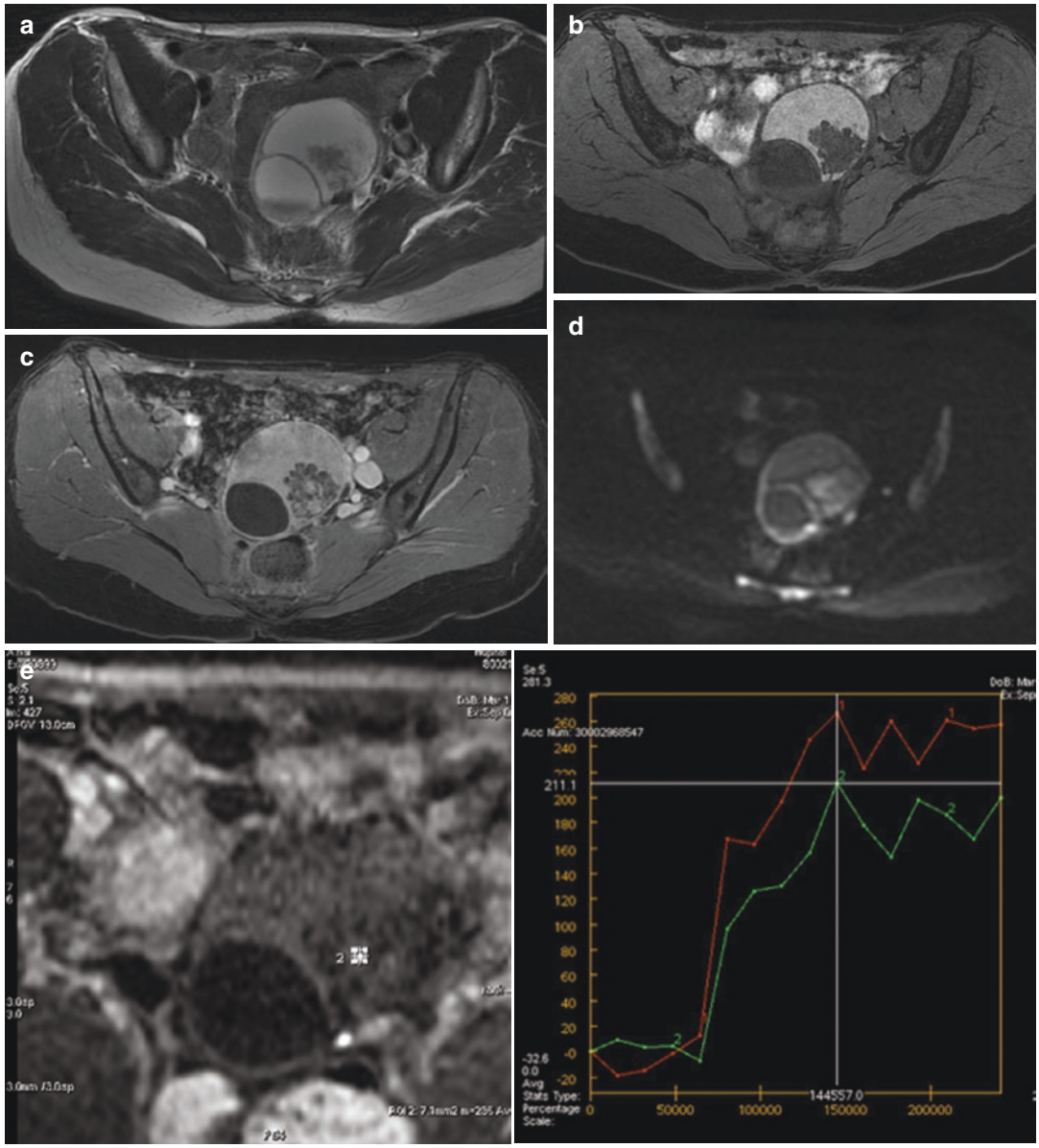

Fig. 4 MR pattern 4: Borderline serous cystadenoma (**a**: Axial T2W sequence, **b**: Axial T1W sequence, **c**: Axial T1W sequence with fat suppression after gadolinium injection, **d**: Axial DWI sequence, **e**: Axial DCE MR sequence). Step 1: Unilocular cyst with solid tissue that corresponds to grouped solid papillary projections that display a high T2W signal, high DW signal, and enhances according a TIC type 2 corresponding to EURAD score 4 (indeterminate). Step 2: Unilocular cyst with papillary projection higher than 1 mm suggests a serous cystadenoma. Suspicious characteristics suggest a borderline serous cystadenoma

found in benign mucinous cystadenoma that displays only smooth septa.

In this pattern, only unilocular or multilocular cyst with solid papillary projections and no other type of solid tissue is present (see below in pattern 5).

When solid papillary projections are grouped, the distinction with a mural nodule can be difficult. This is important to distinguish a borderline cystadenoma (with solid papillary projections) from invasive malignant cystadenocarcinoma (mural nodule) when this tissue displays an intermediate T2W signal, a high DW signal, and a type 2 TIC. A mural nodule (or "solid portion") corresponds to a pathological thickening of the wall due to malignant proliferation and thus an obtuse angle with the wall is seen. In contrast, a group of papillary projections has an acute angle with the wall.

MR Pattern 5: Mixed mass

This pattern corresponds to a large variety of tumors that includes both cystic and solid components (Fig. 5). The analysis of gadolinium enhancement helps identify tumors that truly display a solid portion (echoic cystic portion at ultrasonography may look like solid tissue). The differential diagnoses are enlisted in detail in Table 5 and this category comprises the largest number of diagnoses. MR imaging is also useful to determine the origin of the tumor and may help to recognize a non-ovarian mass.

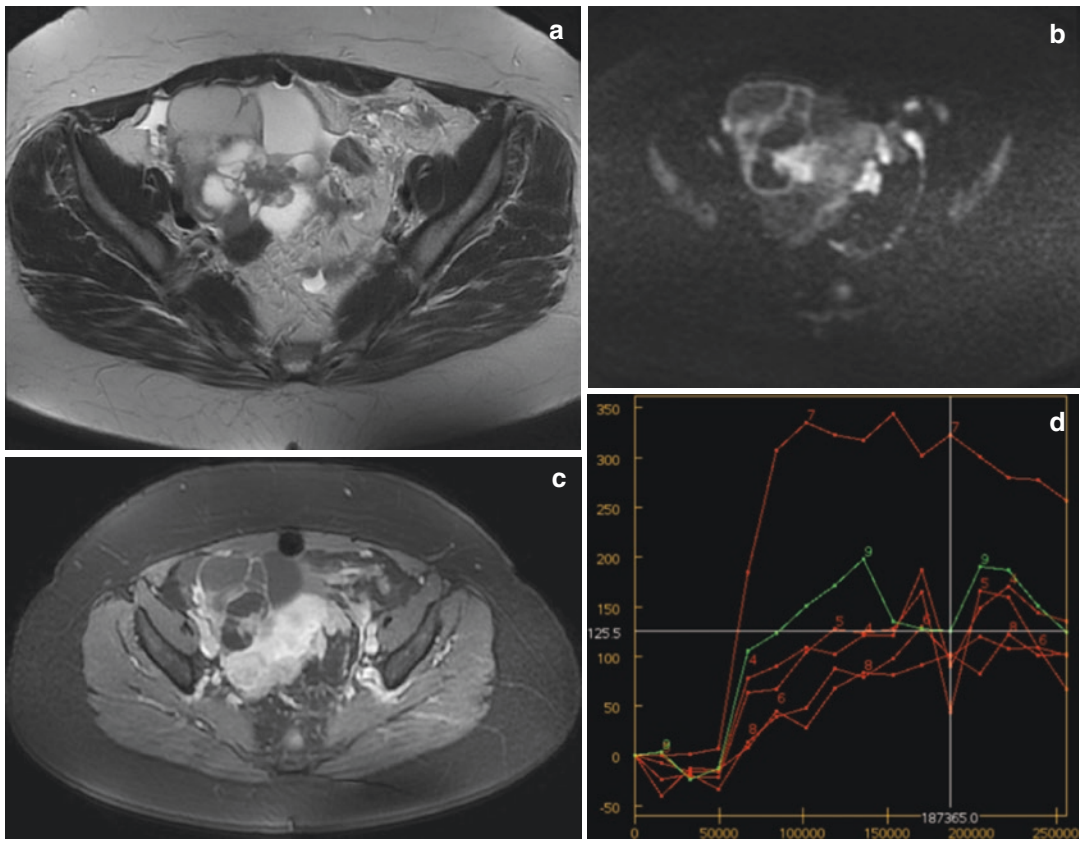

Fig. 5 5 MR pattern 5: Invasive cystadenocarcinoma (**a**: Axial T2W sequence, **b**: Axial DW sequence, **c**: Axial T1W sequence with fat suppression after gadolinium injection, **d**: Axial DCE MR sequence). Step 1: Mixed mass with solid tissue that corresponds to mural nodule that displays intermediate T2W signal, high DW signal, and enhances according a TIC type 2 corresponding to EURAD score 4. Step 2: The morphology, the age of the patient (65-year-old woman), and the suspicious findings suggest an invasive cystadenocarcinoma

MR Pattern 6: Purely solid mass

The initial finding is an enlarged ovary due to an ovarian edema that induces an intermediate T2W signal, a high DW signal, and a variable enhancement. Follicles are located in the periphery of the ovary. The different causes of ovarian edema are detailed in Table 5.

When there is a solid mass, the first question to answer is the origin of the lesion. The most common ovarian solid tumor is fibrothecoma, with the differential diagnosis of uterine leiomyoma which is the most frequent parauterine mass. The other diagnosis are neurogenic tumors such as schwannoma (main feature: anterior displace-

Table 5 Adnexal masses with solid tissue

Diagnosis	Clinical history	Fluid	Solid	Specific sign
Pattern 4 = cyst with papillary projections				
Benign serous cystadenoma	40–50 YO	Simple	Low T2 and DW signal/type 1 TIC	
Borderline serous cystadenoma	40–50 YO	Simple	Intermediate T2W signal/type 2 TIC	
Borderline mucinous cystadenoma	30–50 YO	Loculi of different SI	Low T2W signal/High DW signal	Large
Pattern 5 = mixed mass				
Cystadenofibroma	40–50 YO	Loculi of different SI	Low T2 and DW signal/type 1 or 2 TIC	
Ovarian and tubal cystadenocarcinoma	Ménopausal CA125 +++	Variable according pathological subtype	Intermediate T2W signal/type 3 TIC	Peritoneal implants
Mature cystic teratoma	<45 YO	Fat	Variable	None
Metastasis	Premenopausal	Multilocular		Intestinal primary tumor (colon)
Tubo ovarian abscess	Premenopausal	High DW signal with low ADC values	Intermediate T2W signal/thick wall with vascularization	Fatty infiltration
Pattern 6 = purely solid mass				
Fibrothecoma	50 YO	NA	Low T2 and DW signal type 1 TIC	Cellular subtype intermediate T2W signal
Brenner	40–80 YO	NA	Low T2 and DW signal type 1 or 2 TIC	Calcosphérites
Sclerosing stromal tumor	30 YO		Low T2 and DW signal type 2 TIC without wash out	
Granulosa cell tumor (young)	30 YO E2 et inhibin	NA	T2W intermediate signal—High DW signal type 2 or 3 TIC	Hemorrhagic center
Sertoli-Leydig	<30 YO	NA	Similar to granulosa cell tumor	Androgenic
Mature solid teratoma	<45 YO	NA	Intermediate T2W signal	High T1 signal fatty spots
Dysgerminoma	20–30 YO		Intermediate T2 signal—high DW signal, type 2 TIC	
Ovarian and tubal cystadenocarcinoma	>50 YO		Intermediate T2 signal—high DW signal—type 3 TIC	Peritoneal implants
Metastasis	Premenopausal	NA	Intermediate T2 signal—high DW signal—type 3 TIC	Breast or stomach cancer

ment of posterior peritoneum), GIST tumor (main feature: intense homogeneous enhancement with cystic changes in the center part of the lesion), and pelvic lymph nodes (main feature: perivascular).

When the lesion is originating from the ovary, MR criteria are accurate to differentiate benign from malignant tumors but less reliable for tissue characterization (Fig. 6). In this pattern, clinical history, biological markers, and CT scan are useful (Table 5). CT scan may help to detect calcifications which are suggestive of ovarian leiomyoma if they are coarse or suggestive of Brenner tumor if they are amorphous and central.

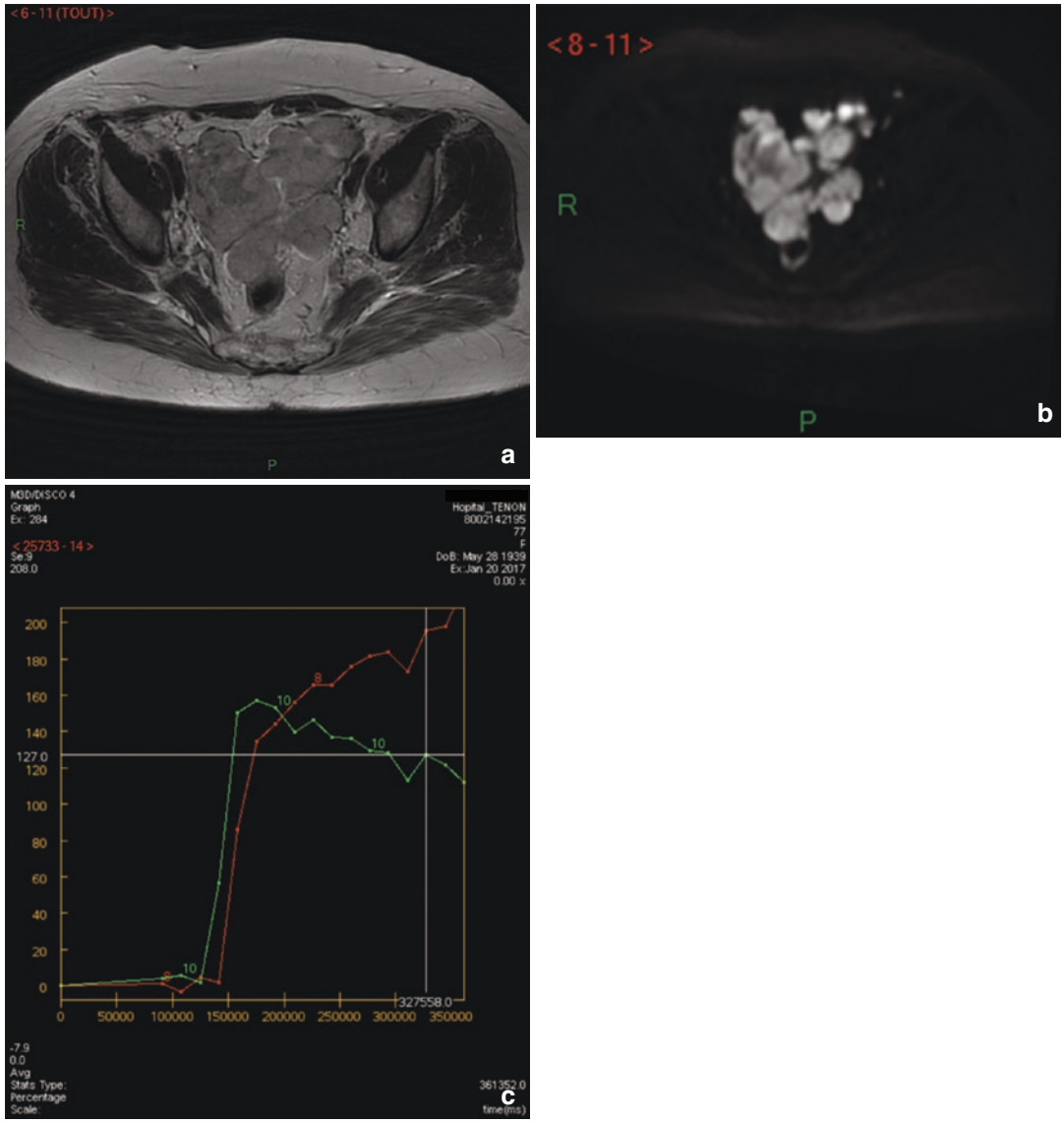

Fig. 6 MR pattern 6: Lymphoma (**a**: Axial T2W sequence, **b**: Axial DWI sequence, **c**: Axial DCE MR sequence). Step 1: Bilateral purely solid masses that display an intermediate T2W signal, high DW signal, and enhance according a TIC type 3 corresponding to EURAD score 5 (probably malignant). Step 2: The morphology and the score suggest invasive malignancy. The bilaterality and the age of the patient (45-year-old woman) suggest either hematological disorder or ovarian metastasis

Conclusion

If ultrasonography remains the first-line investigation, pelvic MR imaging allows to optimize complex or indeterminate adnexal masses characterization (Fig. 6). In a two step analysis, pelvic MR imaging allows to provide a risk of malignancy to the clinician independently of the reader experience by using a MRI score and may also suggest a histopathological diagnosis if the reader has a higher expertise. As six patterns are defined at ultrasonography, the same six patterns may be defined at MR imaging. However, MR imaging will sometimes correctly reclassify some lesions misdiagnosed at ultrasonography, as echoic structures do not always correspond to solid tissue.

References

Brun JL, Fritel X, Aubard Y et al (2014) Management of presumed benign ovarian tumors: updated French guidelines. Eur J Obstet Gynecol Reprod Biol 183:52–58

Buys SS, Partridge E, Greene MH et al (2005) Ovarian cancer screening in the Prostate, Lung, Colorectal and Ovarian (PLCO) cancer screening trial: findings from the initial screen of a randomized trial. Am J Obstet Gynecol 193(5):1630–1639

Ghattamaneni S, Bhuskute NM, Weston MJ, Spencer JA (2009) Discriminative MRI features of fallopian tube masses. Clin Radiol 64:815–831

Kinkel K, Lu Y, Mehdizade A et al (2005) Indeterminate ovarian mass at US: incremental value of second imaging test for characterization—meta-analysis and Bayesian analysis. Radiology 236(1):85–94

Thomassin-Naggara I, Aubert E, Rockall A et al (2013) Adnexal masses: development and preliminary validation of an MR imaging scoring system. Radiology 267(2):432–443

Timmerman D, Ameye L, Fischerova D et al (2010) Simple ultrasound rules to distinguish between benign and malignant adnexal masses before surgery: prospective validation by IOTA group. BMJ 341:c6839

CT and MRI in Ovarian Carcinoma

Rosemarie Forstner

Contents

Abstract

Primary ovarian cancer is categorized as surface epithelial cancer, germ cell tumors, and sex cord stromal tumors. Epithelial ovarian cancer is now understood as a spectrum of different cancer entities that vary considerably on a clinicopathological and molecular level. Disseminated peritoneal spread and ascites is typical of the most common cancer type, high grade serous ovarian cancer. Other cancer subtypes may show distinct features in imaging. CT and MRI are usually complementary techniques to ultrasonography to further assess indeterminate or frankly malignant ovarian lesions. In the latter CT is the imaging modality of choice for triaging patients with ovarian cancer. MRI is emerging as a new technique to assess peritoneal spread and is superior to CT in lesion characterization. This chapter will make familiar with recent concepts in ovarian cancer. Typical imaging findings and differential diagnostic aspects of various types of ovarian malignancies as well as the update of the FIGO staging classification and respectability criteria will be covered.

Abbreviations

ADC	Apparent diffusion coefficient
BT	Borderline tumor
CT	Computed tomography
DCE	Dynamic contrast enhanced

The original version of this chapter was revised. The erratum to this chapter is available online at DOI 10.1007/174_2018_189.

R. Forstner (✉)
Salzburger Landeskliniken, Paracelsus Medical University, Müllner Hauptstr. 48, Salzburg, 5020, Austria
e-mail: R.Forstner@salk.at

Med Radiol Diagn Imaging (2017)
DOI 10.1007/174_2017_17, © Springer International Publishing AG
Published Online: 17 March 2017

DWI	Diffusion-weighted imaging
IV	Intravenous
MRI	Magnetic resonance imaging
SI	Signal intensity

1 Introduction

The vast majority of ovarian carcinomas are epithelial in origin, accounting for more than 90% of the estimated 22,280 new cases of ovarian cancer diagnosed in 2016 in the United States (Cancer Fact and Figures 2016). Most fallopian tube carcinomas and peritoneal carcinomas are now considered a clinical entity with high-grade serous ovarian cancer. While early-stage cancer is often curable, advanced-stage ovarian cancer is one of the most lethal cancers in women, with a 5-year survival of approximately 28% when a patient is diagnosed with tumor spread outside the pelvis (Clarke-Pearson 2009). Nowadays ovarian cancer is understood as a spectrum of different cancer entities that vary considerably on a clinicopathological and molecular level. Genomic profiling may open new approaches of personalized medicine in treatment of ovarian cancer (Jayson et al. 2014).

2 Epidemiology and Risk Factors

In developed countries, ovarian cancer accounts for only 3% of cancer in females, but ranks fifth in cancer mortality, and is the leading cause of death among the gynecological cancers (Cancer Fact and Figures 2016). It is estimated that one woman in 75 will develop ovarian cancer, and one woman in 100 will die of the disease. Ovarian cancer is often clinically silent and about 75% of women present with advanced stages.

The incidence rate of ovarian cancer is higher in White women than in Black or Asian women and differs across the world (Cancer Fact and Figures 2016). The strongest patient-related risk factors for ovarian cancer are family history and increasing age. The vast majority of epithelial ovarian carcinomas are diagnosed in the postmenopausal period, with more than half of the cases diagnosed in the UK are females aged 65 years or older (Ovarian Cancer Statistics).

In patients with genetic predisposition, ovarian cancers occur approximately 10 years earlier (Jayson et al. 2014). In females younger than 20 years of age, germ cell tumors account for more than two-thirds of malignant ovarian tumors. Prolonged times of uninterrupted ovulations seem to play a role in the development of ovarian cancer. Infertility, nulliparity, late menopause, early menarche, polycystic ovary syndrome, endometriosis, and cigarette smoking harbor an increased risk of ovarian cancer (Carlson 2016).

2.1 Familial or Hereditary Ovarian Cancers

Genetic, reproductive, and environmental factors have been identified to play a role in the development of ovarian cancer. Approximately 5–15% of ovarian cancers are considered hereditary cancers. Families with three or more first-degree relatives with ovarian and/or ovarian and breast cancer carry a substantially (16–60%) increased risk for developing ovarian cancer (Pennington and Wsisher 2012).

Hereditary breast-ovarian cancer syndrome (HBOC) accounts for the vast majority (85–90%) of all hereditary ovarian cancers (Jayson et al. 2014; Ozols et al. 2001). In hereditary nonpolyposis colorectal cancer (HNPCC) syndrome, the Lynch syndrome, patients present with colon, endometrial, breast, ovarian, and other cancers (Pennington and Wsisher 2012). Their estimated ovarian cancer risk is 8–10% (Pennington and Wsisher 2012). BRCA mutation carriers have a substantially higher lifetime risk of 10–40% to develop ovarian cancer. It is higher in BRCA1 (35–60%) than in BRCA2 (12–25%) mutation carriers (Pennington and Wsisher 2012). Hereditary ovarian cancer has been attributed mainly to mutations in BRCA1 and BRCA2 genes, but numerous new high-risk genes including PTEN, TP53, CDH1, and STK11 and other germ line mutations have been identified with advances in genomic testing (Runnebaum and Arnold 2013). BRCA mutations are associated mostly with high-grade serous cancers that present

at an advanced stage at an average age of 48 years, which is younger than in non-hereditary ovarian cancer. Identification of these gene mutations, which are related to 10–13% of high-grade serous ovarian cancers, is important, as these patients have a better prognosis, and new therapeutic options can be offered (Jayson et al. 2014; Neto and Cunha 2015).

3 Screening for Ovarian Cancer

Successful screening for ovarian cancer, by definition, is able to decrease mortality and morbidity from the disease (Ozols et al. 2001). Large randomized trials have assessed transvaginal sonography and serum CA-125, or both, or included complex algorithms as screening tests for ovarian cancer (Clarke-Pearson 2009; Jayson et al. 2014; Buys et al. 2011; Moyer 2012). Due to lack of evidence that screening improves survival, screening for ovarian cancer is currently not recommended in the general population (Clarke-Pearson 2009; Jayson et al. 2014; Moyer 2012). This is based upon the fact that prevalence of ovarian cancer is very low and the issue of false-positive screening tests (Moyer 2012). In the randomized controlled PLCO (prostate, lung, colorectal, ovarian) cancer screening trial, no difference was found in stage at diagnosis and the ovarian cancer death rate, but approximately 10% of participants had a false-positive result. False-positive findings during screening may even lead to adverse effects with an increased morbidity due to unnecessary surgeries. The PLCO trial reported a ratio of surgeries to cancer of approximately 20:1 and considerable complication rates after surgery (Buys et al. 2011).

However, women at an increased personal risk, with relatives with BRCA1 and BRCA2 gene mutations, with Lynch syndrome or a strong familiar risk for ovarian cancer should be referred to formal genetic counseling, and multigene testing may be offered (Clarke-Pearson 2009; Moyer 2012; NCCN 2016). Because of their markedly increased lifetime risk of ovarian cancer, the National Comprehensive Cancer Network recommends screening with semiannual transvaginal US and CA-125 testing for women with *BRCA1* or *BRCA2* gene mutations beginning at age 30–35 years (NCCN 2016). Prophylactic salpingo-oophorectomy should also be considered to reduce the cancer risk in these women. It may be delayed until childbearing is completed, or at the ages of 35–40 years (Clarke-Pearson 2009).

4 Tumorigenesis of Ovarian Cancer

On the basis of distinct histological features, primary ovarian malignancies can be separated into three major entities: epithelial carcinomas, germ cell, and sex-cord stromal malignancies (Lengyel 2010). Rare malignancies include sarcomas and lymphomas. 5–15% of ovarian malignancies account for metastases. Primary tumors with a propensity to metastasize to the ovaries include colorectal, gastric, breast, and endometrial cancer. Epithelial ovarian cancer constitutes the vast majority (85–95%) of all ovarian malignancies (Koonings et al. 1989). A dualistic model of carcinogenesis of epithelial ovarian cancer that differentiates between cancer types I and II has been introduced (Kurman and Shih 2011). These two major cancer types not only develop along different pathways but differ considerably in terms of tumor biology, aggressiveness, precursors, and prognosis (Kurman and Shih 2011;). Cancer types I include low-grade serous cancers, endometrioid cancer, and clear cell, transitional, and mucinous cancers (Kurman and Shih 2011). They are characterized by specific gene mutations including KRAS, BRAF, ERBB2, etc. They exhibit a slow growth, mutate stepwisely from precursor lesions, and are less aggressive in their clinical course. In contrast, type II cancers are composed of high-grade serous cancers. They are clinically aggressive and usually present in an advanced stage. Often TP53 mutations and high cellular proliferations are found, and genetically, these tumors are typically instable (Kurman and Shih 2011). It is now accepted that the origin of high-grade serous, primary peritoneal cancer and most fallopian tube cancers is not the ovaries but that these tumors derive from the fallopian tube (STIC theory) (Lengyel 2010; Kurman and Shih 2011).

5 Tumor Markers

CA-125, a glycoprotein antigen, is currently the most widely used tumor marker for ovarian cancer. However, elevation of CA-125 of more than 35 U/ml is not specific for epithelial ovarian cancer but can be observed as well in other malignant epithelial cancers, including pancreatic, lung, breast, and colon cancer, and in non-Hodgkin's lymphoma (Bairey et al. 2003). Furthermore, the list of benign conditions associated with an elevated CA-125 level is long and includes cirrhosis, peritonitis, pancreatitis, endometriosis, uterine fibroids, pregnancy, benign ovarian cysts, pelvic inflammatory disease, and even ascites. The level of CA-125 is associated with the menstrual cycle, and more than 90% of false-positive findings are encountered in premenopausal women (Togashi 2003). This is why in premenopausal women, CA-125 is not useful as a single test, but its value is based upon the rise in serial measurements. In postmenopausal women, CA-125 is a better discriminator between benign and malignant diseases. More than 80% of women with advanced epithelial ovarian cancer present with CA-125 elevations. Of note, for early-stage disease, the sensitivity is only 25% (Togashi 2003). CA-125 is pivotal in the follow-up of patients with ovarian cancer to monitor efficacy of treatment and tumor recurrence (Chen and Berek 2016). Multiple novel tumor markers using monoclonal antibodies are now tested in ovarian cancer. Currently they are used in combination with CA-125 in tumor marker panels but are still under investigation (Chen and Berek 2016).

Serum alpha-fetoprotein (AFP) and human chorionic gonadotropin (HCG) have been helpful in recognizing preoperatively the presence of an endodermal sinus tumor, embryonal carcinoma, choriocarcinoma, or a mixed germ cell tumor. Serum lactate dehydrogenase (LDH) may be elevated in dysgerminomas, and anti-Mullerian hormone and inhibin have been used in the work-up of granulosa cell tumors in postmenopausal age (Anthuber et al. 2014).

6 Clinical Presentation

Ovarian cancer has been called a "silent killer" as it is in the majority of cases diagnosed only at an advanced stage. In early stage symptoms are usually nonspecific or may mimic gastrointestinal or urinary symptoms (Carlson 2016; Chen and Berek 2016). Abdominal bloating or abdominal swelling may indicate ascites. Vaginal discharge and vaginal bleeding are rare symptoms and have been associated with tubal origin of the cancer (Chen and Berek 2016). Rarely, hormonal effects causing abnormal uterine bleeding, virilization, or paraneoplastic effects may be seen and may also precede the diagnosis. Paraneoplastic syndromes include neurologic disorders, e.g., limbic encephalitis or subacute cerebellar degeneration, and collagen vascular diseases, e.g., dermatomyositis and polymyositis, hypercalcemia, or Cushing's syndrome (Lorraine et al. 2010).

7 Imaging of Ovarian Cancer

7.1 Imaging Findings in Ovarian Cancer

7.1.1 Imaging Characteristics of Malignant Ovarian Tumors

Imaging features used for prediction of malignancy include lesion size larger than 4 cm, thickness of wall or septa exceeding more than 3 mm, papillary projections, necrosis, partially cystic and solid architecture, a lobulated solid mass, presence of tumor vessels, and patterns and dynamics of contrast enhancement (Table 1) (Fig. 1) (Hricak et al. 2000; Tsili et al.

Table 1 Imaging findings suggesting malignancy in an adnexal mass

Primary findings[a]
Lesion size >4 cm
Wall/septal thickness >3 mm
Papillary projections
Lobulated mass
Necrosis
Solid and cystic architecture
Type 3 time-intensity curve
Ancillary findings
Lymph node enlargement
Peritoneal lesions
Ascites

[a]Not specific as single factors

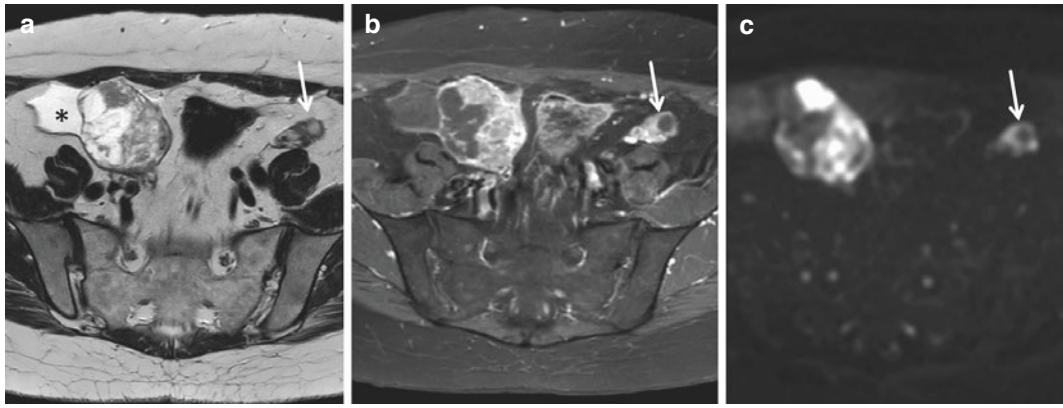

Fig. 1 Imaging characteristics of bilateral ovarian cancer. Transaxial T2WI (a) demontrates a right cystic and solid adnexal mass. Intermediate SI on T2WI (**a**), avid contrast enhancement (**b**), and high SI on DWI using b 1000 mm^2 (**c**) of the solid elements support the findings of malignancy. Ascites is seen adjacent to the right mass (*). Note similar architecture and SI characteristics of the normal-sized left ovary (*arrow*). At surgery bilateral high-grade serous ovarian cancer was found

2008; Buy et al. 1991; Sohaib et al. 2003; Stevens et al. 1991; Komatsu et al. 1996; Jung et al. 2002). None of these imaging criteria, however, were found specific enough as a single factor to reliably diagnose ovarian cancer. The likelihood of malignancy increases with solid nonfibrous elements, thickness of septa, and presence of necrosis (Hricak et al. 2000; Khasper et al. 2012). Ancillary findings such as the presence of lymphadenopathy, peritoneal lesions, and ascites improve the diagnostic confidence to diagnose ovarian cancer. The combination of tumor size and architecture with ancillary signs improves prediction of malignancy and yields an accuracy of 89–95% (Hricak et al. 2000; Tsili et al. 2008; Buy et al. 1991; Sohaib et al. 2003; Stevens et al. 1991; Komatsu et al. 1996; Jung et al. 2002).

Solid nonfatty nonfibrous tissue with or without necrosis has been reported as a valuable predictor of malignancy (Jung et al. 2002). Thus T2 WI signal intensity of solid aspects in adnexal masses may be used to predict malignancy. Masses that are as low or lower than skeletal muscle typically present benign entities, whereas lesions displaying a T2 intermediate SI or higher SI than skeletal muscle comprise a heterogenous group and include benign, borderline, and malignant lesions (Khasper et al. 2012). Thick walls and septations are less reliably signs of malignancy, as they may also occur in abscesses, endometriomas, and benign neoplasms such as cystadenofibromas and mucinous cystadenomas (Jung et al. 2002; Khasper et al. 2012).

Papillary projections present folds of the proliferating neoplastic epithelium growing over a stromal core. Identification of papillary projections is important because they are typical for an epithelial neoplasm. They are most often associated with epithelial cancers of low malignant potential (Fig. 2) and may also be found in 38% of invasive carcinomas. In the latter, the gross appearance is usually dominated by a solid component (Buy et al. 1991; Jung et al. 2002). Small papillary projections ranging in the size of less than 3 mm with low-contrast enhancement are a feature of mucinous cystadenomas (Kaijser et al. 2014).

Psammoma bodies, which are tiny calcifications, are found in CT in approximately 10% of serous epithelial ovarian cancers (Fig. 3). Calcifications may also occur in benign teratomas and in benign ovarian stromal tumors, e.g., Brenner tumors or thecomas. These tumors are typically solid and tend to show extensive coarse calcifications.

In CT and MRI, assessment of contrast enhancement is a cornerstone of tumor characterization. It improves assessment of papillary projections and necrosis and visualizes patterns of vascularization (Hricak et al. 2000; Buy et al. 1991; Thomassin-Naggara et al. 2008b, 2012, 2013; Bernardin et al. 2012; Dilks et al. 2010)

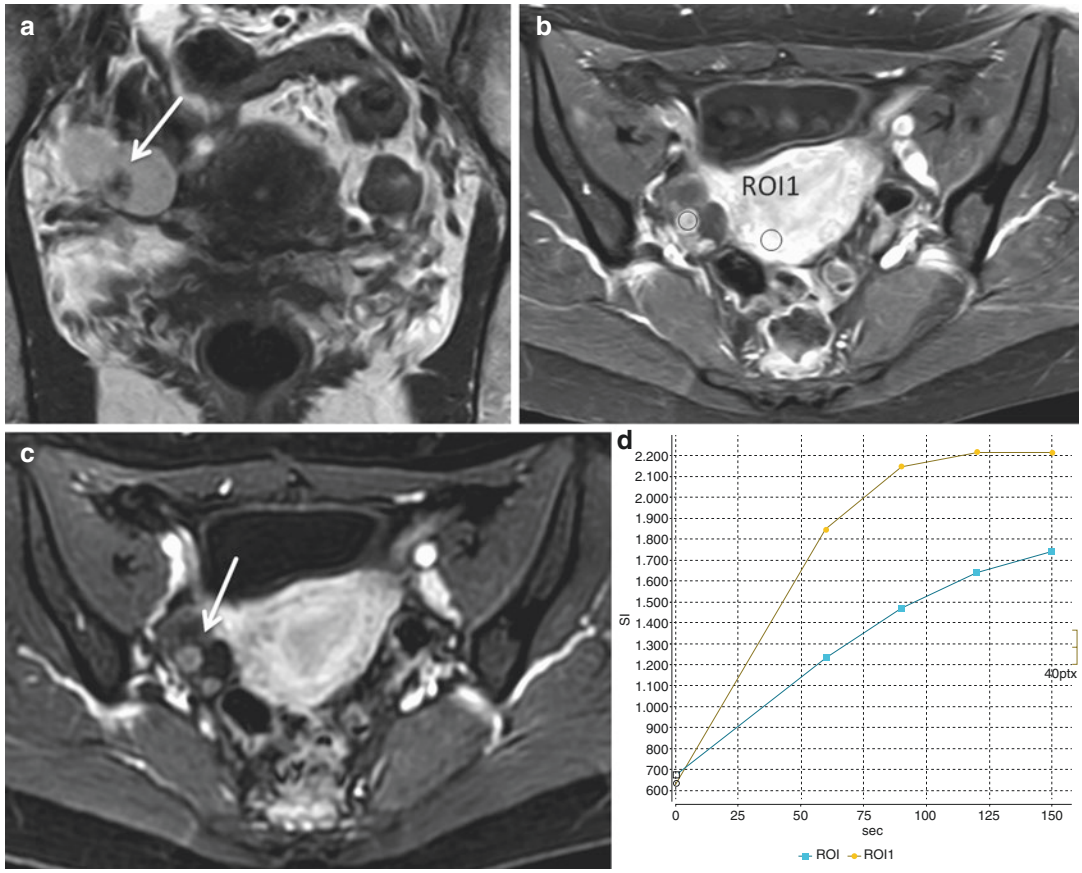

Fig. 2 Serous borderline cancer of the right ovary. Coronal T2WI (**a**) displays a thin septation and a low SI mural papillary projection (*arrow*). Transaxial FSGd T1 demonstrates two papillary projections (**b**, **c**) (*arrow*). The larger nodule displays a type 2 contrast enhancement curve (**b**, **d**), which is commonly found in borderline tumors

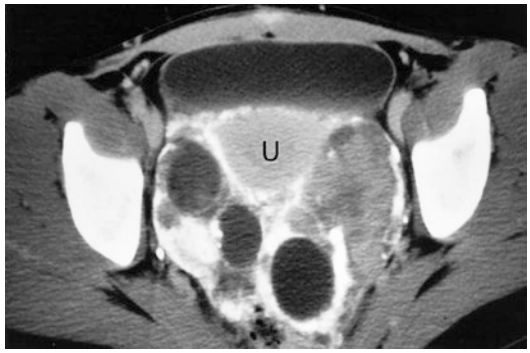

Fig. 3 Calcifications in ovarian cancer. Multiple plaque-like calcifications are demonstrated within a mixed solid and cystic bilateral ovarian tumor. They also cloak the peritoneal surface of the uterus (*U*). These small calcifications present psammoma bodies and are found in low-grade serous ovarian adenocarcinomas in CT. *B* bladder

(Figs. 1 and 2). DWI alone is limited due to overlap in benign and malignant adnexal lesions, and evidence is lacking supporting ADC quantification for reliable prediction of malignancy (Forstner et al. 2016a). DWI is most beneficial in adnexal mass characterization by excluding malignancy if a solid adnexal mass displays low SI using a high b value (Forstner et al. 2016a; Thomassin-Naggara et al. 2009). DCE using semiquantitative multiphase-dynamic contrast-enhanced MRI has become an important imaging tool for risk assessment in adnexal masses (Thomassin-Naggara et al. 2008b, 2012, 2013). Time-intensity curves are acquired of the solid areas within the adnexal lesion and the myometrium during multiphase-dynamic

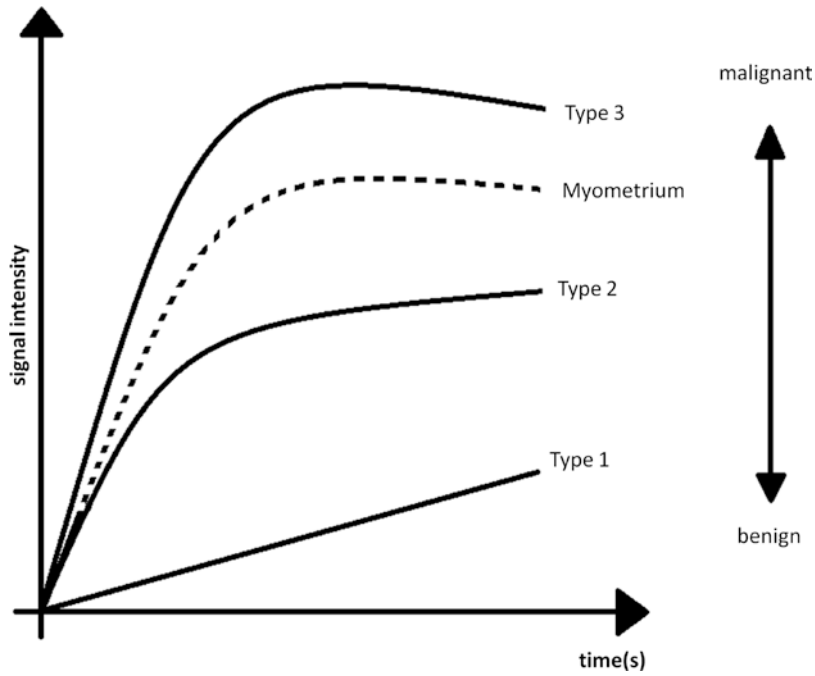

Fig. 4 Time-intensity curves. Time-intensity curves are acquired from the solid aspect of the ovarian mass and from the outer myometrium. Types 1, 2, and 3 curves assist in prediction of malignancy

Table 2 MR Adnex score

Score	Characteristics	Imaging findings
1	No mass	No adnexal lesion
2	Benign	Cysts, endometrioma, dermoid, cystadenoma, solid and low on T2WI and low on DWI (b 1000s/mm$^{2)}$
3	Probably benign	Cystic, no solid tissues; type 1 curve[a]
4	Indeterminate	Type 2 curve[a]
5	Probably malignant	Peritoneal implants Type 3 curve[a]

MR Adnex score (Adapted from Thomassin-Naggara et al. 2013)
[a]Assessed from solid tissue within the ovarian mass

contrast-enhanced series. Using the myometrial enhancement as reference, three types of enhancement curves can be identified which correlate with benign, borderline, and malignant tumors (Fig. 4) (Tsili et al. 2008; Thomassin-Naggara et al. 2008a). Type 1 time-intensity curves are characterized by a gradual uptake of contrast. It was more frequently encountered in benign than borderline lesion and never in malignant lesions. Type 2 time-intensity curves describing an early uptake of gadolinium – but less than myometrium – followed by a plateau were typical of borderline lesions (Fig. 2). Type 3 time-intensity curves describing an avid and early contrast uptake, followed by a washout, are typical of malignant tumors (Thomassin-Naggara et al. 2012, 2013). This technique is also pivotal in the MRI Adnex score system, a standardized MR imaging and reporting system for complex adnexal masses (Thomassin-Naggara et al. 2013). The MRI Adnex score assigns masses into five categories from score 1 correlating of no mass to score 5 that describes a probably malignant mass (Table 2). A feasibility study demonstrated excellent reproducibility and interobserver agreement for various levels of expertise (Thomassin-Naggara et al. 2013).

PET/CT is limited in prediction of malignancy of adnexal masses by false-positive findings, particularly in premenopausal ovaries due to physiologic uptake of the corpus luteum. It is more reliable in postmenopausal age, but false positives

in benign teratomas may occur at any age group. Currently, there is no evidence of an advantage of PET/CT over MRI for characterization of complex adnexal masses (Lee and Catalano 2015; Iver and Lee 2010).

7.1.2 Peritoneal Carcinomatosis

Peritoneal carcinomatosis is the typical pathway of tumor dissemination in advanced ovarian cancer (Fig. 5). It is determined by the complex anatomy of the peritoneal cavity and follows the clockwise pattern of the peritoneal fluid circulation along the paracolic gutters toward the diaphragm and downward (Lengyel 2010; Patel et al. 2011). Although all peritoneal parietal and visceral surfaces may be involved, common sites of peritoneal implants in ovarian cancer include greater omentum, paracolic gutters, the pouch of Douglas, surfaces of the liver and diaphragm, and bowel surface. Less frequent sites of dissemination are the mesentery, splenic surface, along the porta hepatis, lesser sac, and the gastrosplenic ligament (Forstner et al. 2010; Nougaret et al. 2012). Peritoneal metastases are characterized by a broad spectrum of imaging findings. They may display as nodular soft tissue lesions or as more subtle findings including linear or plaquelike thickening of the parietal or visceral peritoneum (Fig. 6). Implants from serous tumors may display tiny calcifications only. Besides nodular lesions, thickening of the root of the mesentery with a stellate radiating pattern or ill-defined nodular lesions have been described in metastases of the mesentery (Fig. 7) (Nougaret et al. 2012). The majority of peritoneal lesions show moderate enhancement after IV contrast medium.

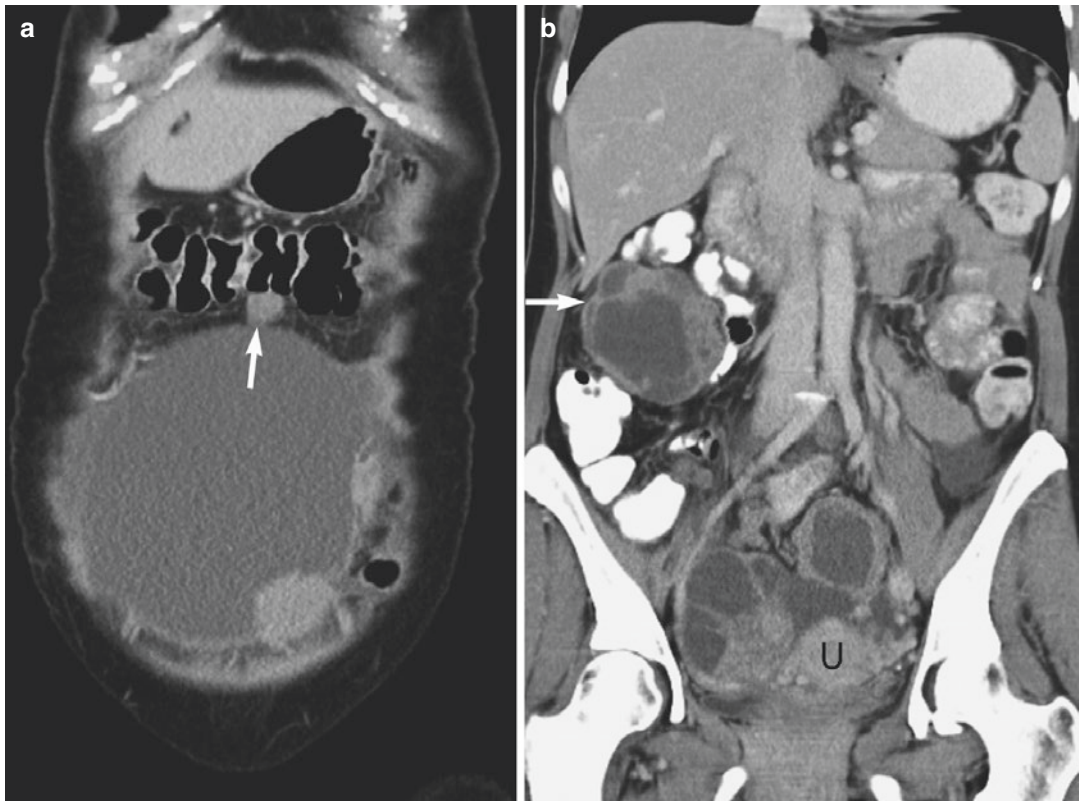

Fig. 5 Peritoneal implants. Findings in FIGO stage IIIC ovarian cancer are shown in an anterior (**a**) and posterior (**b**) coronal CT plane. Ascites, mild peritoneal thickening, and multiple solid peritoneal implants along the anterior abdominal wall and in the transverse mesocolon (*arrow*) are demonstrated in (**a**). A large implant in the right paracolic gutter (*arrow*) resembles the morphology of the thick-walled cystic and solid adnexal tumors, which present bilateral ovarian cancer (**b**). *U* uterus

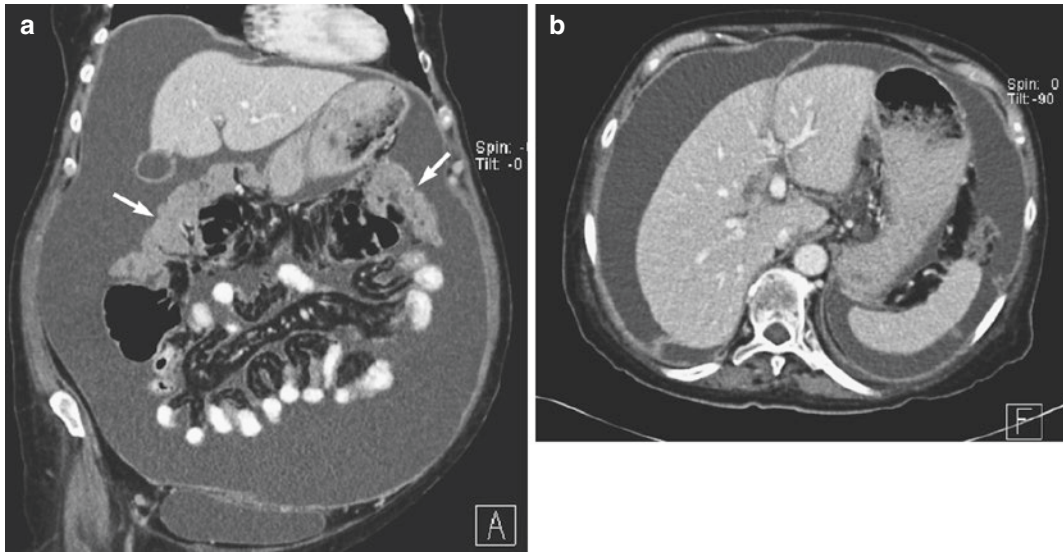

Fig. 6 Peritoneal implants. Coronal (**a**) and transaxial CT of the upper abdomen (**b**). Linear thickening of the parietal peritoneum is seen throughout the abdomen and pelvis in a patient with large amounts of ascites (**a**). The diffuse linear thickening of the diaphragm is better appreciated on the transaxial plane (**b**). Other findings include bilateral focal diaphragmatic implants and broad band-like tumors (*arrows*) adjacent to the transverse colon presenting omental cake

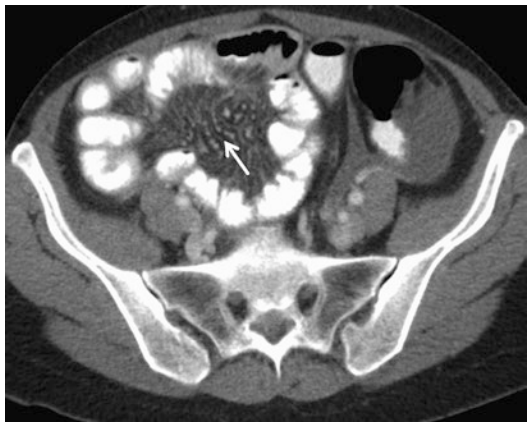

Fig. 7 Diffuse mesenterial involvement in high-grade serous cancer. Ill-defined mesenterial linear and nodular lesions (*arrow*) are seen in the root of the mesentery

Rarely, mixed solid and cystic or purely cystic lesions are found. The latter may mimic loculated ascites; however linear enhancement or tiny mural nodules may indicate the tumorous deposits. In MRI delayed enhancement at 3–10 min after gadolinium has been described to improve the detection of peritoneal metastases (Low et al. 2005). The omentum accounts for the most common site of peritoneal metastases, with the inframesocolic omentum more often involved than the supramesocolic omentum (Fig. 8). They are typically located between the abdominal wall and bowel loops. If they coalesce they are termed omental cake. Netlike omental involvement is more difficult to evaluate. In liver surface implants, peritoneal deposits of the liver capsule should be differentiated from invasive implants, as the latter usually are not resectable (Akin et al. 2008). Bowel surface or mesenterial implants can cause tethering of bowel loops and may lead to obstruction. However, this is more likely to occur in recurrent ovarian cancer (Low et al. 2003). Depiction of peritoneal implants depends on their size and on the presence of ascites. In CT the problem of diagnosing small peritoneal implants is expressed by the sensitivity of only 25–50% for lesion size of less than 1 cm in size (Coakley et al. 2002). The performance of CT, however, improved to a sensitivity of 85–93% and a specificity of 91–96% for peritoneal disease larger than 1 cm in size (Coakley et al. 2002). Although CT has been established as primary imaging modality to assess peritoneal malignant disease, MRI has the potential to become the new standard of the reference (Rockall 2014). It seems superior to CT

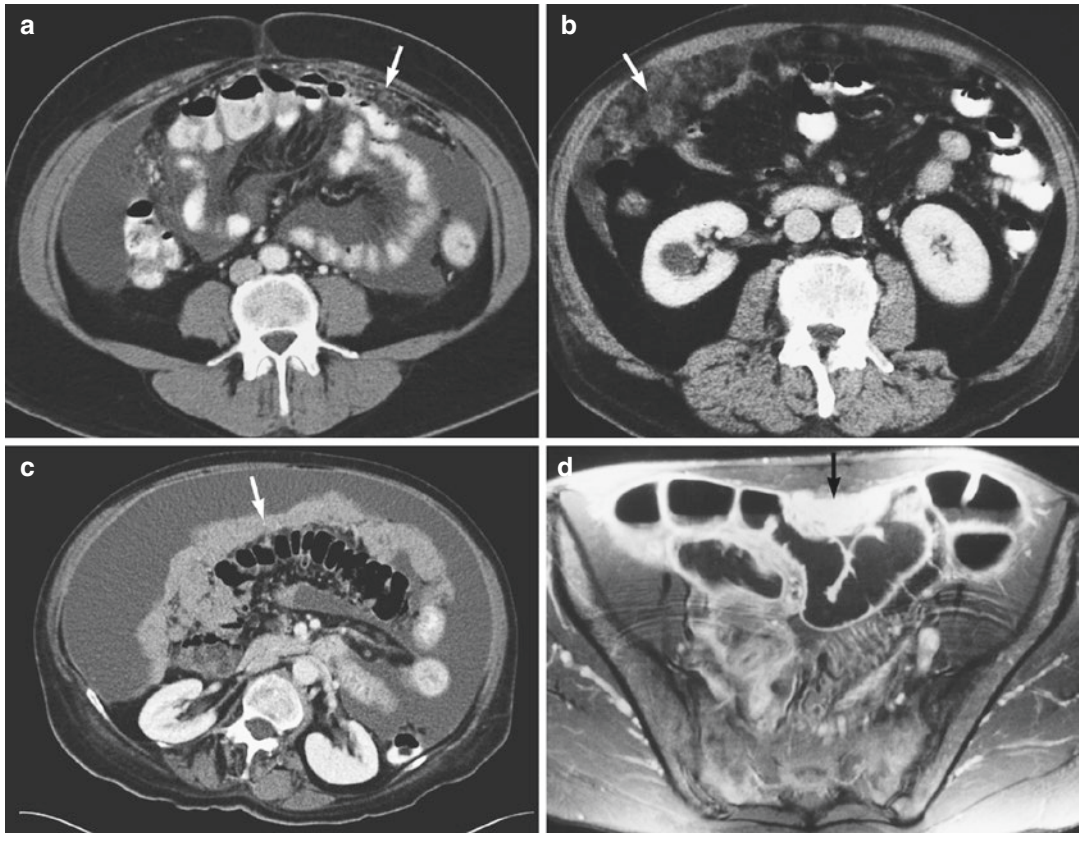

Fig. 8 Omental implants. Transaxial CT (**a**–**c**) and transaxial fat-saturated T1-weighted image (**d**) in four different patients. Omental implants (*arrows*) may display a broad spectrum of findings ranging from a netlike pattern (**a**) to cotton-like (**b**) and nodular lesions (**d**)

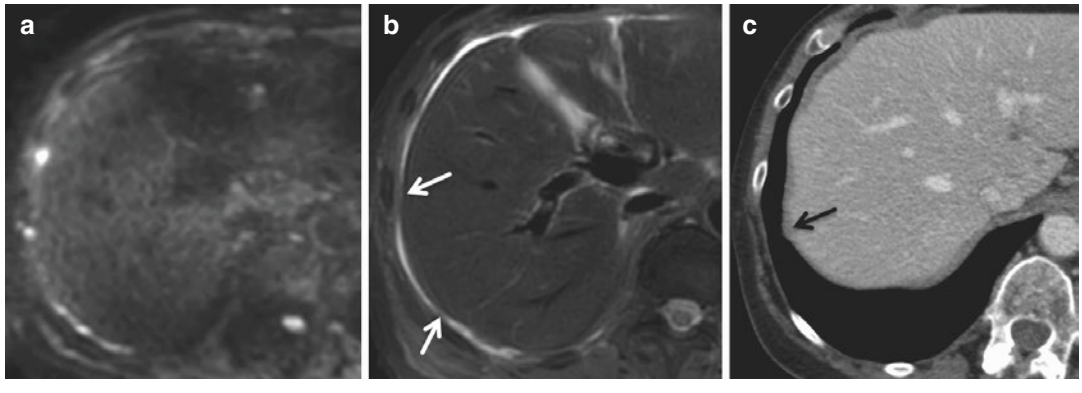

Fig. 9 Superiority of MRI (**a**, **b**) over CT (**c**) in visualization of small liver surface and diaphragmatic implants (*arrows*). The small deposits are best depicted on DWI (b = 800 mm^2) (**a**)

in detecting peritoneal implants (Fig. 9), particularly in the absence of ascites (Low et al. 1999, 2015). Diffusion-weighted MR imaging enables direct visualization of implants at sites that are otherwise difficult to assess throughout the peritoneal cavity and is superior in pelvic imaging to CT (Rockall 2014). In a prospective comparative study with surgery as standard of reference, whole-body MRI using DWI was superior to CT and to PET/CT in assessing bowel serosal and mesenteric disease (Michielsen et al. 2014). Another comparative study found no significant differences between CT, MRI, and PET/CT in assessing ovarian cancer. In this study PET/CT was best for assessment of supradiaphragmatic metastases (Schmidt et al. 2015). It seems that currently the role of PET/CT for staging primary ovarian cancer staging is limited (Rockall 2014). Most studies report slightly improved lesion conspicuity of PET/CT (sens. of 77–100%) over CT alone (sens. of 60–97%) (Pfanneberg et al. 2013). In one study combined PET/CT achieved a sensitivity of 88% compared to 84% for CT and 63% for PET alone in patients undergoing hyperthermic intraperitoneal chemotherapy (Pfanneberg et al. 2013). In PET/CT false negatives may occur due to small tumor size (5–10 mm) and FDG-negative tumors (Patel et al. 2011). False positives may occur in nonmalignant and inflammatory peritoneal diseases (Michielsen et al. 2014; Pfanneberg et al. 2013).

7.1.3 Ascites

Small amounts of pelvic fluid in the cul-de-sac present a physiological finding and may be found throughout the cycle in the reproductive age. Ascites is defined as fluid outside the pouch of Douglas according to the International Ovarian Tumor Analysis (IOTA) group (Timmerman et al. 2000). In ovarian cancer, pelvic ascites may be a finding of stage I disease. Large amounts of ascites in a patient with ovarian cancer usually indicate stage III disease. In ovarian cancer the presence of ascites alone had a PPV of 72–80% for peritoneal metastases (Coakley et al. 2002).

The absence of ascites may not exclude a malignant disease, as 50% of borderline tumors and 83% of early-stage ovarian cancers are not associated with ascites (Ozols et al. 2001). Peritoneal carcinomatosis is characterized by various amounts of ascites and diffuse or focal peritoneal thickening. Benign forms of ascites displaying the same pattern, such as postoperative inflammatory changes, bacterial peritonitis including tuberculosis, or chronic hemodialysis, often cannot be differentiated from peritoneal carcinomatosis (Diop et al. 2014; Levy et al. 2009).

7.2 Pathways of Spread in Ovarian Cancer

Knowledge of the pathways of tumor spread is pivotal for the interpretations of findings in CT and MRI, and they are the basis for staging of ovarian cancer. Ovarian cancer spreads primarily by direct extension to neighboring organs, by exfoliating cells into the peritoneal cavity that can implant on parietal and visceral peritoneum throughout the peritoneal cavity. It also disseminates by lymphatic pathways and less commonly metastasizes hematogenously. Locoregional spread of ovarian cancer occurs by continuous growth along the surfaces of the pelvic organs and pelvic sidewalls. Peritoneal spread and implantation outside the pelvis is caused by tumor cells that are able to slough off the ovary and enter the peritoneal circulation. Peritoneal implants are also disseminated throughout the lymphatic vessels of the peritoneum.

Tumor spread along the lymphatic pathways is found along three routes. The main pathway of lymphatic spread is along the broad ligament and parametria to the pelvic sidewall lymph nodes (external iliac and obturator chains) and along the ovarian vessels to the upper common iliac and para-aortic lymph nodes between the renal hilum and aortic bifurcation. Drainage to external and inguinal nodes via the round ligaments accounts for the rarest route of lymphatic tumor spread. In advanced ovarian cancer, the presence of nodal spread is reported in 40–60% (Ozols et al. 2001; Bachmann et al. 2016). In a series of 130 patients mostly with serous ovarian cancer, the rate of nodal metastases was 75%. In almost half of the cases, both metastases

to the pelvis and para-aortic lymph node were seen, whereas 13.5% was reported for pelvic resp for para-aortic lymph node metastases only (Bachmann et al. 2016).

Hematogenous spread occurs later in the course of the disease. Distant metastases are most commonly found in the liver, lung, pleura, and kidneys. At the time of the initial presentation, parenchymal liver metastases are extremely rare, and patients are more likely to present with liver surface metastases (Akin et al. 2008).

7.3 Staging of Ovarian Cancer

Staging of ovarian cancer is determined by the extent and location of disease found at surgical staging. The latter is considered the gold standard for staging and aims for obtaining the histopathological diagnosis and a complete cytoreductive surgery. It includes a total abdominal hysterectomy, bilateral salpingo-oophorectomy, infracolic omentectomy, and lymphadenectomy (Jayson et al. 2014; Ozols et al. 2001). Furthermore, peritoneal cytology and multiple peritoneal biopsies are obtained throughout the pelvis and upper abdomen. In an attempt for optimal debulking, agressive surgery techniques including multidisciplinary surgery teams may be needed (Jayson et al. 2014). Laparoscopic staging procedures for ovarian cancer have also been introduced. In clinical practice, understaging of ovarian cancer remains a common problem (20–40%). This may occur when the initial surgery had been performed under the presumption of a benign tumor, due to laparoscopy technique, and lack of oncologic specialist expertise (Ozols et al. 2001).

Ovarian cancer is staged using the TNM or the FIGO (International Federation of Gynecology and Obstetrics) classification. According to the 2014 revised FIGO classification, not only the tumor stage but also the histological subtypes and grade should be documented. Most important change is the fusion of epithelial ovarian, fallopian, and primary peritoneal cancers. The revised staging classification is also used in germ cell and sex-cord stromal malignancies (Kandukuri and Rao 2015).

7.3.1 Staging by CT and MRI

Surgical staging can be preceded by preoperative imaging. According to the ACR appropriateness criteria, radiographic studies such as contrast enema and urography have been replaced by CT and other cross-sectional imaging for staging ovarian cancer (Mitchell et al. 2013). Preoperative assessment by imaging has a major impact on treatment stratification, as the extent and anatomic location of peritoneal implants are major determinators for treatment decision (Forstner et al. 2010; Nougaret et al. 2012; Sala et al. 2013; Javadi et al. 2016).

Accurate mapping of the disease contributes to optimized surgery planning (Sala et al. 2013). This may also alert to need of multidisciplinary surgery teamwork. In case of extensive cancer load on CT or MRI, patients may also be triaged to undergo a neoadjuvant radiochemotherapy prior to surgery (Forstner et al. 2010; Sala et al. 2013).

Imaging Findings According to Tumor Stages

The FIGO classification system of ovarian cancer is summarized in Table 3.

Imaging findings in CT and MRI have also been adapted to the FIGO classification system (Forstner et al. 2010, 2016b; Nougaret et al. 2012; Javadi et al. 2016).

In *stage I*, tumor is confined to one ovary or the fallopian tube (stage IA) (Fig. 2) or both ovaries or the fallopian tubes (stage IB). The capsule of the tumor is intact, and there is no evidence of spread of the tumor outside of the ovary. In stage IC disease, tumor is detected on the ovarian or fallopian tube surface or capsule rupture has occurred. Malignant pelvic ascites may also be present (Fig. 1).

Stage II is characterized by local tumor extension into the pelvic soft tissues and to pelvic organs below the pelvic brim. In stage IIA, either direct tumor extension or implants on the uterus, ovaries, or fallopian tubes can be identified. Findings suggesting this stage include distortion or irregularity between the interface of the tumor and the myometrium. Stage IIB is characterized by involvement of pelvic tissues, such as the

Table 3 FIGO classification of ovarian cancer

FIGO Stage	Subcategory and Findings	
I	A	Tumor one ovary or fallopian tube
	B	Both ovaries fallopian tubes
	C	One or both ovaries or fallopian tubes plus C1: Surgical spill C2: Capsule ruptured or tumor on surface C3: M alignant cells in ascites or peritoneal washings
II	A	Extension/implants on uterus and/or ovaries and/or fallopian tubes
	B	Extension to other pelvic intraperi toneal tissues
III	A	A1 Positive retroperitoneal LN only
		A2 Microscopic extrapelvic peritoneal spread +/-LN
	B	Peritoneal implants outside pelvis up to 2cm +/-LN
	C	Peritoneal implants out side pelvis >2cm +/-LN
IV	A	Pleural effusion with positive cytology
	B	Parenchymal metastasis, metastasis to extraperitoneal organs, inguinal LN and LN outside abdominal cavity

Table modified from Kandukuri and Rao (2015) and Forstner et al. (2016b)
Changes in respect to the previous version are highlighted
LN lymph nodes

bladder, rectum, and pelvic peritoneum. Invasion of the sigmoid colon or rectum is diagnosed when loss of tissue plane between the solid components of the tumor, encasement, or localized wall thickening is noted (Fig. 10). A distance of less than 3 mm between the lesion and the pelvic sidewall or displacement or encasement of iliac vessels is suggestive of pelvic sidewall invasion (Fig. 11).

Stage III consists of extrapelvic peritoneal implants and/or retroperitoneal lymphadenopathy. Retroperitoneal lymph node metastases as the only disease outside the pelvis are found in less than 10%, but they demonstrate favorable prognosis than lymph node metastases in stages IIIB or IIIC (Kandukuri and Rao 2015). In imaging the diagnosis of lymphadenopathy is based on the short-axis diameter of lymph nodes of ≥1 cm. Peritoneal implants outside the pelvis, omental or mesenteric implants, and hepatic or splenic surface metastases are other findings defining stage III ovarian cancer. Stages IIIA2–IIIC differ in the size of abdominal peritoneal lesions. In stage IIIA2, tumor is grossly limited to the pelvis; however, large amounts of ascites are a sign of upper abdominal peritoneal tumor spread. In stage IIIB, lesion size is 2 cm or less and in stage IIIC it exceeds 2 cm (Fig. 12). Ascites is a common finding in stage III disease. In delayed contrast-enhanced MR imaging, ascites may enhance and thus obscure peritoneal implants.

Stage IV ovarian cancer is characterized by distant metastases that include pleura, parenchymal organs outside the pelvis, and extraabdominal lymph nodes. Malignant pleural effusion presents stage IVA1 and is characterized by pleural metastases proven either by positive cytology or biopsy. Typical imaging findings include pleural effusion associated with pleural nodularity and focal pleural thickening. Quantification of pleural effusion as small, moderate, or large has shown to be related with

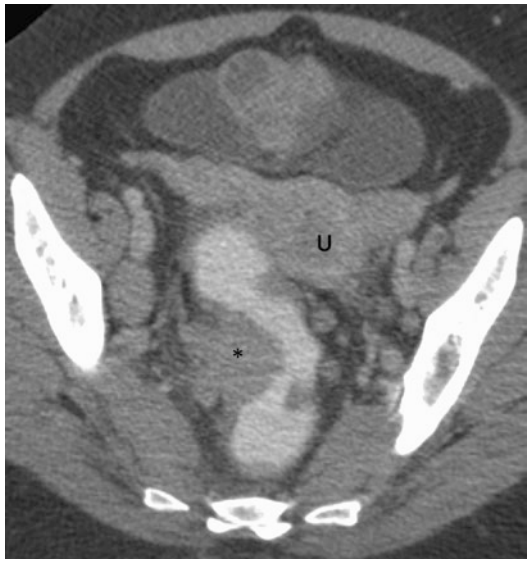

Fig. 10 Sigmoid colon wall invasion in CT. A peritoneal implant (*) shows a broad contact and impression of the colon wall. The ovarian cancer is located in the midline and compresses the bladder. Multiple pelvic lymph node metastases are seen, the largest in the right obturator region. *U* uterus

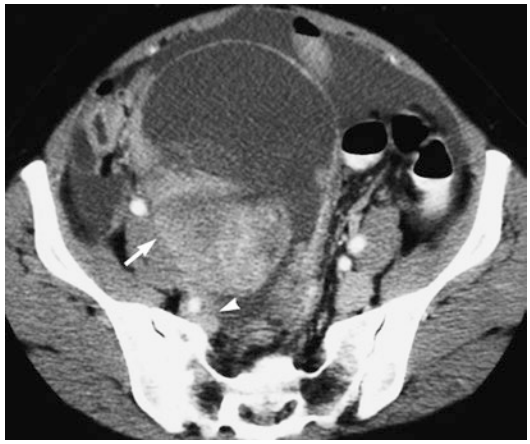

Fig. 11 Pelvic sidewall invasion. Transaxial CT at the level of the iliac bifurcation. A mixed solid and cystic adnexal tumor, which was nondifferentiated ovarian cancer at histopathology, is located in the pelvis. The left pelvic sidewall, including iliac vessels and psoas muscle, is clearly separated by fat. The right pelvic sidewall (*arrow*) is in direct contact with the solid tumor component. Furthermore, external and internal iliac arteries are displaced; the latter is encased by tumor (*arrowhead*)

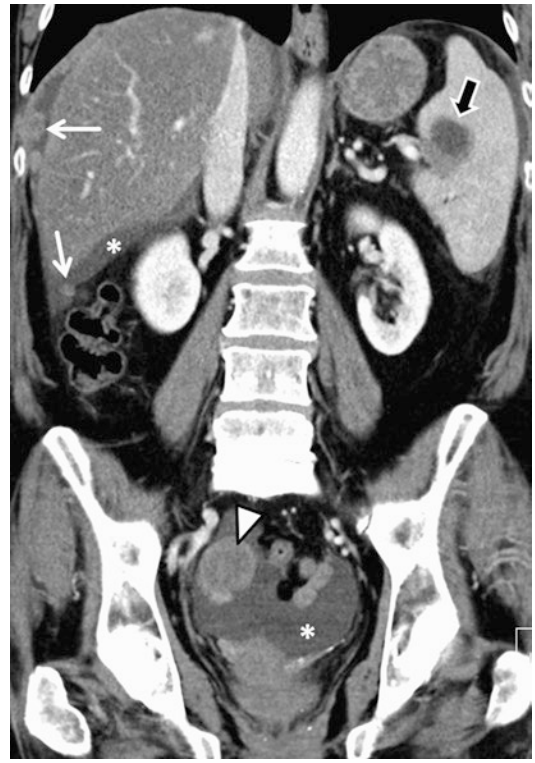

Fig. 12 Stage IIIC ovarian cancer. Peritoneal nodular implants are shown at the diaphragm and in the Morison's pouch (*arrows*). A surface metastases invading the spleen larger than 3 cm is also demonstrated (*arrow*). Ascites (*) is found in the pelvis and upper abdomen. Ovarian cancer (*arrowhead*)

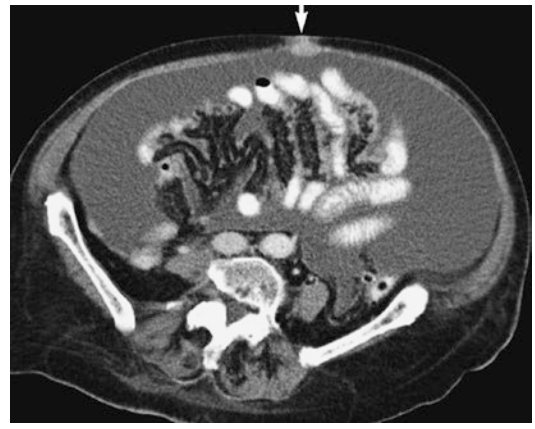

Fig. 13 Ovarian cancer stage IVB. Large amounts of ascites indicate peritoneal metastases. Umbilical metastasis (*arrow*) is a finding typical of stage IVB ovarian cancer

survival (Mironov et al. 2011). Lung or liver parenchymal metastases are also typical manifestations in stage IVB disease. It is particularly important to differentiate liver parenchymal metastases from liver surface metastases, which display smooth margins and an elliptic or biconvex shape. Umbilical metastasis (Fig. 13), the Sister Mary Joseph node, is now classified as stage IVB disease. It usually ranges from 1 to 1.5 cm in size but can attain a size of up to 10 cm. Cardiophrenic lymph node metastases are a typical findings in stage IV disease. They occur in approximately 30% of advanced ovarian cancer and are typically located in the anterior prepericardiac region, more commonly on the right than on the left side (Kim et al. 2016). A recent study reported a PPV of 86% for histologically proven cardiophrenic lymph nodes when a short-axis diameter of >7 mm was used in CT (Kim et al. 2016). Inguinal lymph node metastases are also classified as distant metastases (IVB).

Value of Imaging

CT and MRI perform similarly in staging of ovarian cancer, with reported accuracies of 70%–90%, sensitivities of 63–69%, and specificities of 100% (Mitchell et al. 2013; Forstner et al. 2010, 2016b; Nougaret et al. 2012; Sala et al. 2013; Javadi et al. 2016). The decision to use CT or MRI is based on many factors, including cost, availability, contraindications, radiologist expertise, and clinician's preference. Thus currently, CT is the primary imaging modality for staging ovarian cancer because of better availability and shorter examination times (Mitchell et al. 2013; Forstner et al. 2010). MRI is emerging as a potent alternative technique for staging ovarian cancer when standard MR sequences are combined with DWI (Forstner et al. 2010; Rockall 2014). This technique is recommended for staging of suspected ovarian cancer in pregnancy or in contraindications of IV contrast media (Forstner et al. 2010). In the latter PET/CT serves as an alternative modality to provide the relevant information for treatment decision. Similar to CT it is limited in small-volume peritoneal disease, but PET/CT seems most beneficial in advanced disease to assess metastases outside the peritoneal cavity (Forstner et al. 2010; Javadi et al. 2016). Detection of lymph node metastases is a major limitation of imaging. Based on a threshold of 1 cm in diameter, the sensitivity for lymph node metastases is only 50%, and the specificity is 95% for CT and MRI. PET/CT performs superiorly but is also limited by lymph node metastases in the size of less than 1 cm (Pfanneberg et al. 2013; Javadi et al. 2016).

7.3.2 Prediction of Resectability

Multidisciplinary consensus conferences (MDC) are the platform to define individualized optimal treatment regimen. If a patient with ovarian cancer will benefit from upfront surgery or rather from a neoadjuvant approach has to be decided on patient-related factors, e.g., the medical condition, surgical risks, and institutional preferences (Rockall 2014; Sala et al. 2013; Forstner et al. 2016b). The major limitation in the preoperative assessment of resectability is that no general accepted models exist and the impaired reproducibility due to different clinical practice (Forstner et al. 2016b). Imaging, mostly by CT, plays a pivotal role in patient triage by visualization of the size, site, and distribution of metastatic disease (Sala et al. 2013). Various CT criteria assessing different sites throughout the abdomen and CT scores without and with the incorporation of CA-125 or other clinical criteria have been proposed to predict preoperatively the success of optimal resectability (Suidan et al. 2014; Borley et al. 2015; Bristow et al. 2000; Quayyum et al. 2005). According to the ESUR guidelines for staging ovarian cancer, large disease (>2 cm) in the upper abdomen around the liver and spleen (Fig. 14), mesenteric deposits, and lymph node metastases above the renal hilum are sites likely to be nonoptimally resectable (Forstner et al. 2010). However, it has to be emphasized that resectability criteria may differ from center to center and predictive parameters have to be specified and agreed on in MDC (Forstner et al. 2010). CT and MRI performed similarly in detecting inoperable tumor and prediction of suboptimal debulking in ovarian cancer, with reported sensitivity of 76%, specificity of 99%, PPV of 99%, and NPV of 96% (Quayyum et al. 2005).

Conversely, Low et al. reported the superiority of MRI over CT to predict optimal cytoreduction (Low et al. 2015). A prospective multicenter trial identified three clinical and six CT criteria correlating with suboptimal debulking (Suidan et al. 2014). Another study reported lung metastases of >7 mm in size, pleural effusion, deposits of >10 mm in size on large- and small-bowel mesentery, and infrarenal para-aortic lymph node metastases to be associated with low debulking status (Borley et al. 2015). Despite advanced surgery techniques in both studies, bowel involvement is a major limitation for optimal cytoreduction. Thus, careful analysis of CT signs of bowel and mesenteric involvement, e.g., of bowel wall thickening and adhesions and mesenterial tethering, is warranted (Nougaret et al. 2012).

7.4 Tumor Types

Ovarian neoplasms are categorized as surface epithelial cell tumors, germ cell tumors, and sex-cord stromal tumors. The vast majority comprise epithelial cancers, whereas malignant germ cell and malignant stromal neoplasms are responsible for 7% each.

In epithelial tumors benign, malignant, and borderline tumors are differentiated according to their histological features. Malignant tumors of the ovary and borderline tumors account for 21% and 4–15% of primary ovarian tumors, respectively (Lengyel 2010; Koonings et al. 1989). In epithelial cancer distinct subtypes can be identified that not only differ in histopathology and genetic profiles but also in their imaging findings and clinical course. This is also reflected in the new WHO classification of ovarian, fallopian tube, and primary peritoneal cancer (Kurman et al. 2014). Clinicopathological and radiological characteristics of the major ovarian cancer subtypes are summarized in Table 4 (Forstner et al. 2016b; Höhn et al. 2014; Lalwani et al. 2011).

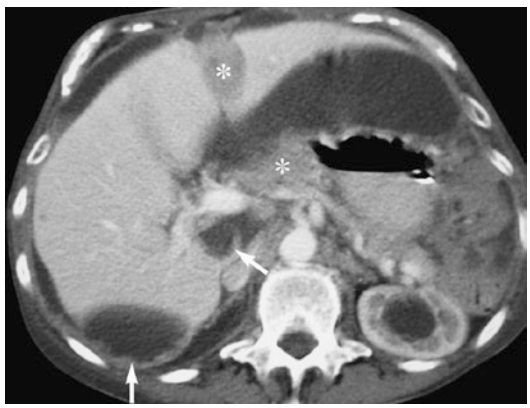

Fig. 14 Nonoptimally resectable ovarian cancer. Multiple peritoneal implants (*arrows*) are demonstrated on the liver surface and lesser sac. The latter is distended due to ascites. The implants located in the interlobar fissure (*) and lesser sac (*) are considered nonoptimally resectable

7.4.1 Epithelial Ovarian Cancer

High-Grade Serous Ovarian Cancer

High-grade serous epithelial cancer accounts for the majority (70–80%) of epithelial ovarian cancers. Two-thirds of these tumors involve both ovaries (Clarke-Pearson 2009; Ozols et al. 2001). Macroscopically, it displays typically as multilocular cystic tumors with intracystic papillary projections. These excrescences fill the cyst cavity, or they may contain serous, hemorrhagic, or turbid fluid (Fig. 1) (Lalwani et al. 2011). Some of these tumors may also present as solid masses with irregular contours. The typical imaging feature is advanced peritoneal disease with large amounts of ascites and often bilateral adnexal masses (Fig. 15) (Forstner et al. 2016b; Höhn et al. 2014; Tanaka et al. 2016). In up to 12%, the ovaries may be small and display predominantly surface involvement, a finding that previously defined primary carcinoma of the peritoneum but is now recognized as a variant of high-grade serous cancer (Kurman and Shih 2011). Almost all cancers related to BRACA1 and BRACA2 mutations fall into this tumor category (Jayson et al. 2014).

Low-Grade Serous Ovarian Cancer

This subtype accounts for approximately 5% of ovarian cancers. It seems to develop in a stepwise fashion from cystadenomas and serous borderline tumors. In imaging cystic and septate lesions or cystic lesions with papillary mural nodules

Table 4 Clinicopathological and radiological characteristics of ovarian cancer subtypes

	HG serous	LG serous	Mucinous	Endometrioid	Clear cell
Percentage	70–80%	5%	3%	10–20%	5–10%
Gene mutations	TP53, BRCA1/2	BRAF; KRAS3CA	KRAS	PTEN;CTNNB1, ARIDIA;PPP2RIA	KRAS, PTEN, PIK3CA, ZNF217; ARIDIA
Precursor	STIC	Serous cystadenoma BT	Mucinous cystadenoma; BT	Endometriosis	Endometriosis, clear cell adenofibroma
Tumor morphology	Cystic and solid; solid, irregular contour	Solid and cystic, psammoma bodies; serous BT	Large, cystic or solid; smooth contour	Smooth contour, endometrioma, solid and cystic	Large thick wall, uni- or multilocular, mural nodules; enhancing in endomtriosis
Disssemination	Diffuse abdominal	Nodules, abdomen	Ovary	Pelvis	Pelvis
Laterality[a]	Bilateral	Uni- and bilateral	Unilateral	Unilateral	Unilateral
Prognosis	Poor	Intermediate	Good	Good	Intermediate

Adapted from Forstner et al. (2016b), Höhn et al. (2014), Lalwani et al. (2011), and Tanaka et al. (2016)
STIC serous tubal intraepithelial cancer, *HG* high grade, *LG* low grade, *BT* borderline tumor
[a]Predominant pattern

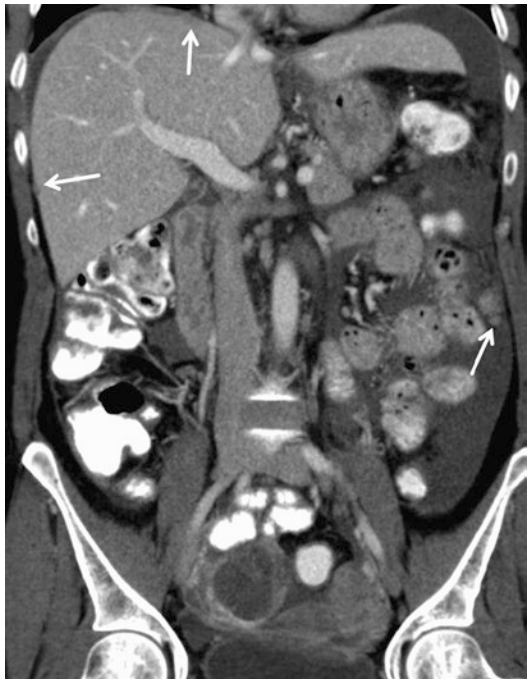

Fig. 15 Typical high-grade serous cancer in CT. Bilateral adnexal tumors and large amounts of ascites and peritoneal deposits in the abdomen (*arrows*) as sign of peritoneal spread outside the pelvis at time of diagnosis

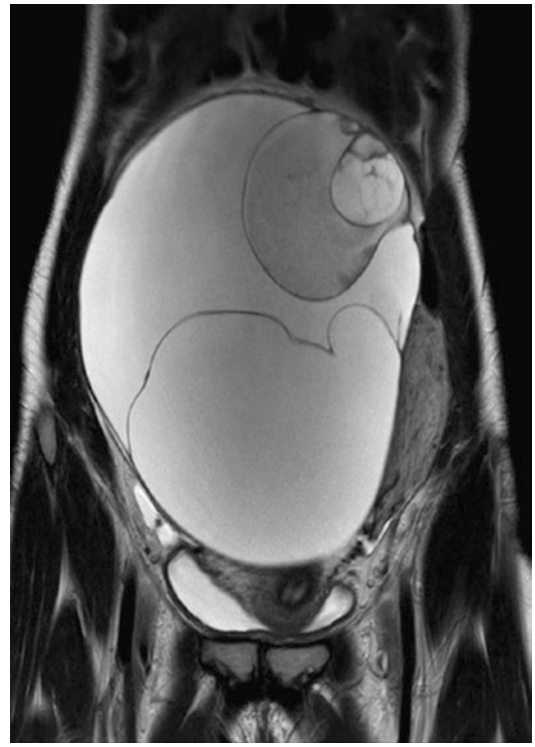

Fig. 16 Stage IA mucinous ovarian cancer arising within a BL mucinous tumor. A large multiloculated ovarian mass with loculi of different SI is shown on the T2WI indicating a mucinous lesion. At its superior aspect, areas of invasive cancers were found at surgery

may be found uni- or bilaterally. Both borderline tumors and low-grade serous cancers may coexist at diagnosis. Psammoma bodies within the tumor or implants, presenting tiny calcifications, are detected in 30% at histology but only in 12% of cases in CT (Ozols et al. 2001; Jung et al. 2002). Dissemination occurs later in the course of the disease, and nodular implants are identified throughout the abdomen (Höhn et al. 2014).

Mucinous Epithelial Ovarian Cancer

Mucinous cancers comprise approximately 3–5% of ovarian carcinomas. They tend to be large at diagnosis and contain loculi with hemorrhagic or proteinaceous content similar to their precursors mucinous borderline tumors. They present smooth contours and multiloculated cystic architecture with solid areas and intracystic nodules (Fig. 16). Rarely, the tumor may be predominantly solid. They are mostly unilateral and detected in early stages. Bilateral involvement is only found in 5–10% (Seidman et al. 2002). Pseudomyxoma peritonei with cystic peritoneal implants may be associated with mucinous ovarian cancers but seems more likely to result from spread by mucinous primaries of the GI tract.

Endometrioid Ovarian Carcinomas

Endometrioid carcinomas represent 10–20% of all ovarian carcinomas. They occur with synchronous endometrial carcinomas or endometrial hyperplasia in up to 33% of cases (Seidman et al. 2002). Endometrioid carcinoma may also arise from endometriosis (Tanaka et al. 2010). Bilateral ovarian involvement is encountered in 30–50% of cases. Macroscopically, these tumors are solid and cystic; the cysts may contain mucinous or greenish fluid. Rarely, solid tumors with extensive hemorrhage or necrosis may be found (Seidman et al. 2002). Another feature is cancer developing within an endometrioma (Lalwani et al. 2011; Tanaka et al. 2010).

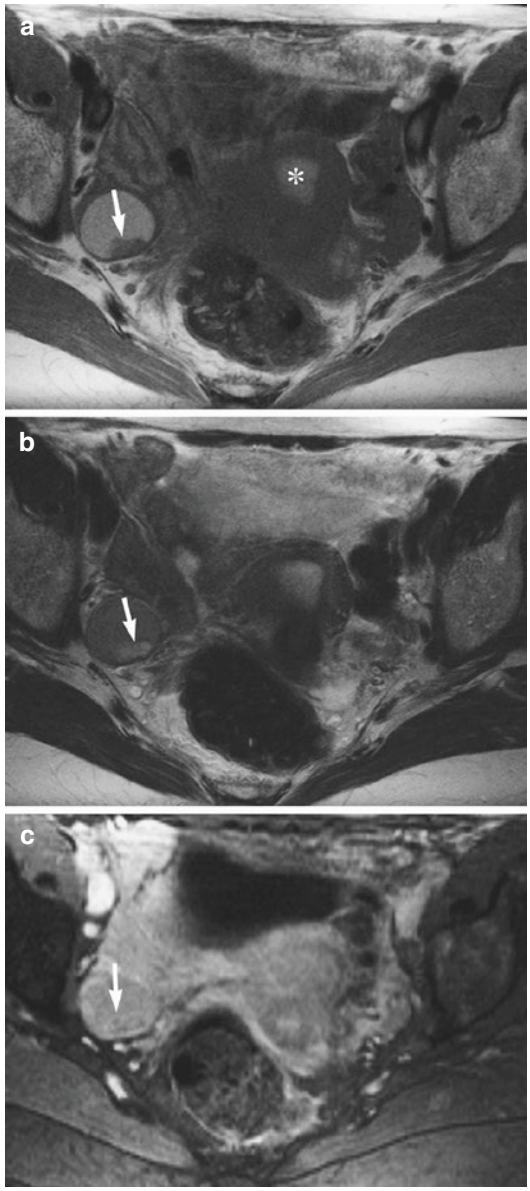

Fig. 17 Clear cell carcinoma arising in an endometrioma. Transaxial T1-weighted image (**a**), T2-weighted image (**b**), and contrast-enhanced fat-saturated (FS) T1-weighted image (**c**). A typical endometrioma of the right ovary is demonstrated in a and b, showing high signal intensity (SI) on T1- weighted image and shading with low SI on the T2-weighted image. Within the posterior wall of the endometrioma, a band-like mural lesion (*arrow*) with low SI on T1-weighted image (**a**) and high SI on T2-weighted image (**b**) is seen. Due to contrast enhancement, it is obscured in **c**. Contrast enhancement is not found in a clot in endometrioma, but is indicative of a tumor within the endometrial cyst. Hematometra (*)

Clear Cell Carcinomas

Clear cell carcinomas present approximately 5–10% of all ovarian cancers. The relationship with endometriosis is strongest among the ovarian cancers. The tumor may arise within an endometrioma (Fig. 17), or endometriotic implants may be found in relationship to the tumor or elsewhere in the pelvis (Lalwani et al. 2011). Hypercalcemia as a paraneoplastic syndrome and thromboembolic complications are more common than in other ovarian cancers (Lorraine et al. 2010). Typical imaging feature is a large thick-walled cyst with one or multiple nodules protruding into the mass (Tanaka et al. 2010).

Imaging Findings of Epithelial Ovarian Cancers

On CT and MRI, epithelial ovarian cancers present as complex cystic or multiloculated ovarian lesions. Although differentiation between the subtypes is not reliably possible by imaging, there might be some differential diagnostic clues. Disseminated peritoneal disease is typical of high-grade serous cancers. A large well-delineated multilocular mass is suggestive of mucinous cancer. Psammoma bodies, which can only be detected on CT, may be seen in low-grade serous ovarian cancers. Endometriosis is a precursor of endometrioid, and especially of clear cell cancer. The latter appears most commonly as a large unilocular cyst with one or more solid mural nodules (Tanaka et al. 2016). In endometrioid ovarian cancer, endometrial thickening or endometrial cancer may coexist. Details of histological, imaging, and clinical characteristics of the major ovarian cancer subtypes are enlisted in Table 4.

Differential Diagnosis

Benign serous and mucinous cystadenomas are usually entirely cystic and display thin walls and septa. Small papillary projections may also be present in cystadenomas. Metastases, particularly from primary cancer of the appendix or the gastrointestinal tract, can display similar imaging characteristics as ovarian cancer. Calcifications may also be present in metastases of mucinous adenocarcinoma of the colon

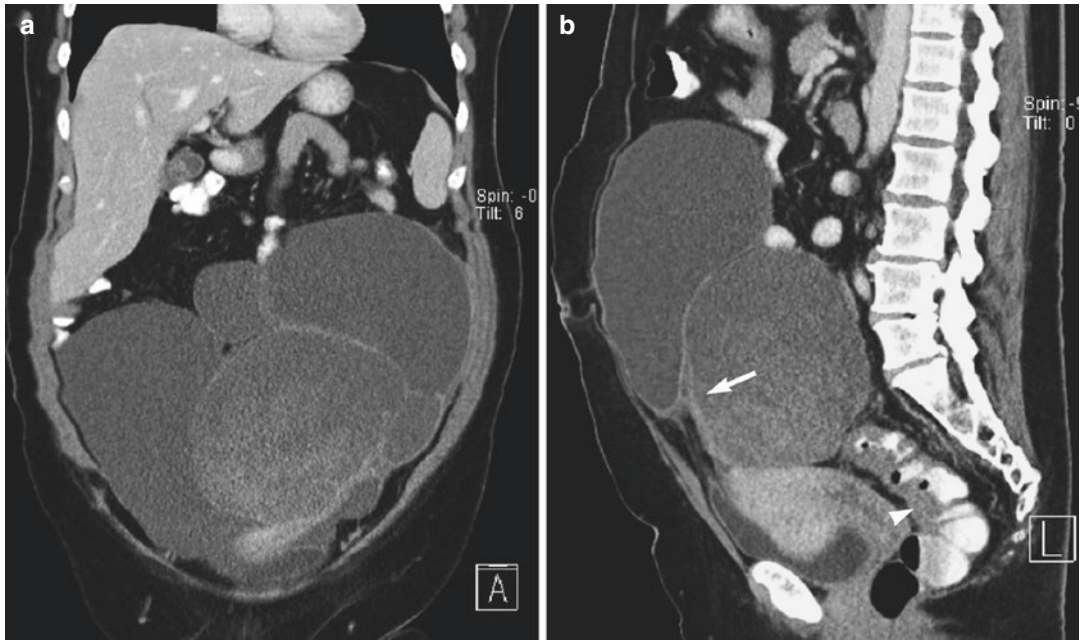

Fig. 18 Endometrioma mimicking ovarian cancer in CT. Coronal (**a**) and sagittal CT (**b**). In a 47-year-old woman with elevated tumor markers, a multicystic mass with a diameter of 25 cm occupies the pelvis and midabdomen. Focal mural and septal thickening (*arrow*) and high density within some cysts are demonstrated. There was no evidence of lymph node enlargement or ascites. At surgery, extensive endometriosis of the ovaries and peritoneum was found. Furthermore, mural wall thickening of the rectum and sigmoid colon by endometriosis (*arrowhead*) and thickening of the uterine corpus due to endometriosis were detected (**b**)

and papillary thyroid cancer (Kawamoto et al. 1999). Malignant ovarian germ cell and stromal tumors may display imaging characteristics similar as ovarian cancer. Age and hormonal effects may help in the differential diagnosis. Other differential diagnoses include benign cystic and/or solid tumors, e.g., cystadenofibroma and rarely dermoids without fat. In the majority of cases, tubo-ovarian abscesses can be distinguished from ovarian cancer based upon imaging and clinical findings. Endometriomas can be differentiated by MRI by typical findings such as shading, thick capsules, and lack of enhancing solid components. However, in CT, endometriomas may be a diagnostic problem and mimic ovarian cancer (Fig. 18). Enhancement of a mural nodule within an endometrioma is highly suggestive of malignant transformation.

Borderline Tumors

Borderline tumors account for up to 15% of all ovarian malignancies (Alvarez and Vazquez-Vicente 2015). They are distinct from invasive ovarian cancer in terms of younger age at presentation, better prognosis, and fertility-preserving treatment options. Histologic and cytogenetic features include atypical epithelial proliferations, multilayering of the epithelium, increased mitotic activity, nuclear atypia, and mostly KRAS and BRAF gene mutations but the absence of stromal invasion (Lalwani et al. 2010). Borderline tumors most commonly affect women in reproductive age. Most of these present with early-stage (70–80%) disease and are associated with an excellent prognosis. A 7-year follow-up of survival of stage I diseases was 99% and for stage II and III disease 92% (Ozols et al. 2001; Leake et al. 1992). In the presence of invasive elements, recurrence rates approach 45% and progression to invasive cancers may be found (Lalwani et al. 2010).

Borderline tumors may be large, with diameters ranging from 7 to 20 cm. Bilaterality is more common in serous tumor BT (25–50%) compared to the mucinous subtypes (5–10%) (Alvarez and Vazquez-Vicente 2015). Mucinous BT tends to be larger and may be associated with pseudomyxoma peritonei (Bent et al. 2009).

Imaging Findings

Borderline tumors tend to be large unilateral or bilateral ovarian tumors that cannot reliably be distinguished from invasive ovarian cancers in CT or MRI (Fig. 19). Imaging findings suggesting borderline tumors include a multicystic mass with papillary projections ranging from 10 to 15 mm in size protruding into the cyst wall (Jung et al. 2002). Rarely, BT may present as a purely cystic or solid lesion (Fig. 20), and psammoma bodies may be present (Bent et al. 2009). In a series of 60 borderline tumors, 6 were purely cystic and 29 mainly cystic with papillary projections and nodules; out of these one-third displayed vegetations of less than 1 cm in size; 14 were mixed cystic and solid and 10 mainly solid or solid (Zhao et al. 2014a). ADC values of the papillary projections tend to be higher than in invasive cancers. Using a threshold value of 1.039×10^3, Zao et al. attained sensitivity of 97% and specificity of 92.2% in

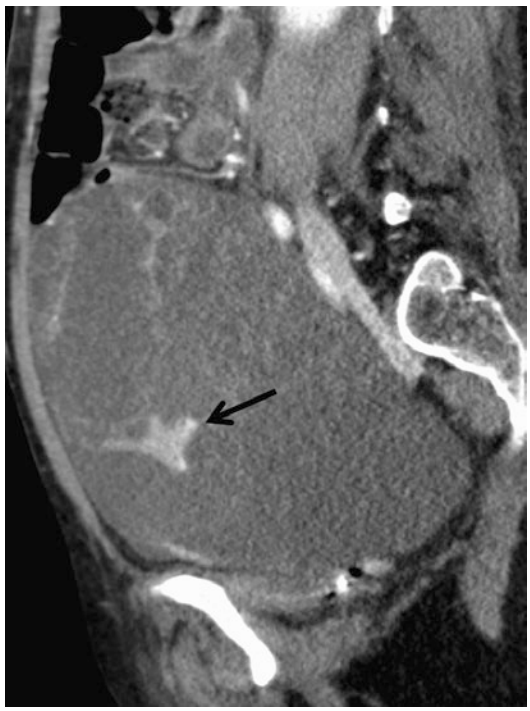

Fig. 19 Serous borderline tumor in CT. A large thin-walled cystic pelvic lesion is shown demonstrating slightly irregular enhancing septa at the cephalad aspect and a central irregular thickened septum with tiny calcifications (*arrow*)

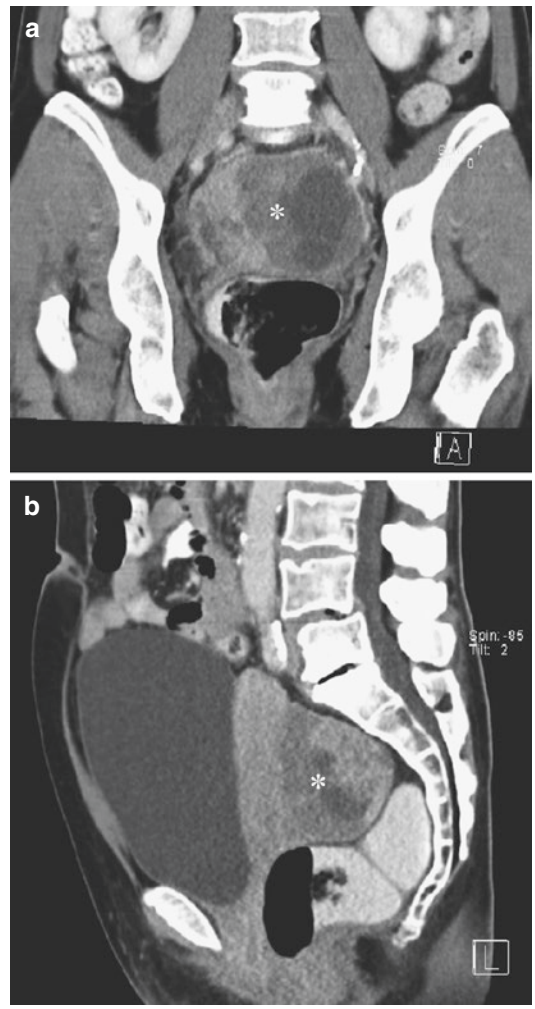

Fig. 20 Stage I borderline tumor. Coronal (**a**) and parasagittal (**b**) CT. A 7 cm predominantly solid tumor (*) with cystic areas is located in the cul-de-sac. The sagittal plane shows broad-based contact to the uterus (**b**). No evidence of ascites was found in the pelvis or abdomen. At surgery, a grayish tumor deriving from the left ovary was found. Histopathology revealed the rare endometrioid subtype of ovarian tumor of low malignant potential, which was classified as FIGO stage IA

their differentiation from invasive cancers. In DCE delayed enhancement and MRI type 2 time-intensity curves may be seen in BT (Fig. 2) (Thomassin-Naggara et al. 2013).

Differential Diagnosis

Borderline tumors are indistinguishable from invasive cancers due to overlap in imaging findings such as irregular thickened walls, enhancing vegetations, and solid components. Low ADC values of solid aspects in DWI favor cancer (Zhao et al. 2014a). Peritoneal implants or lymph node involvement is not a useful criterion for differentiation as these may be also found in approximately 30% of serous BT (Leake et al. 1992). Hemorrhagic and mucinous contents may be seen both in mucinous BT and mucinous cystadenomas. Features favoring BT are honeycomb appearance, thick septa (5 mm), and papillary projections of >5 mm (Zhao et al. 2014b).

Recurrent Ovarian Cancer

Although the initial response to treatment is good, persistence or recurrence of ovarian cancer remains a major problem. This is reflected by the overall likelihood of relapse for all stages of ovarian cancer of 62% and of up to 85% for women presenting with advanced ovarian cancer (Birrer 2016).

Survival correlates with the disease-free interval before tumor recurrence and the residual disease following primary cytorective surgery (Jayson et al. 2014; Ozols et al. 2001; Birrer 2016). Pelvic relapse develops after an average of 1.8 years and hematogenous metastases (liver, spleen, pleura, lungs, and brain) after an average of 2.5 years (Burghardt 1993). The pelvis, particularly the vaginal vault and the cul-de-sac, is the most common site of tumor recurrence, and it is followed by abdominal peritoneal implants. Typical abdominal locations include the surface of the diaphragm and liver, paracolic gutters, the large- and small-bowel surface, and mesentery (Kwek and Iyer 2006). Lymph node metastases are typically located in the para-aortic region and found in 18–33% (Burghardt 1993). Small- and large-bowel obstruction is a common complication in patients with recurrent ovarian cancer and remains the leading cause of mortality (Birrer 2016).

Unlike in primary ovarian cancer, recurrent ovarian cancer is not strongly associated with ascites. In one study, ascites was only found in 38% of patients with relapse of ovarian cancer, and in the vast majority, the amount of fluid detected was small (Forstner et al. 1995). Furthermore, small amounts of ascites were also demonstrated in patients without evidence of tumor recurrence. Large amounts of ascites are more likely to occur in platinum-resistant disease (Birrer 2016). Serum tumor markers (CA-125) are the cornerstone in the surveillance of patients with ovarian cancer. A rising CA-125 level in a patient in a clinically complete remission is highly predictive of recurrence. However, this may precede the median time to physical or radiographic evidence of recurrent disease by 4–6 months (Birrer 2016).

Imaging Findings

Recurrent ovarian cancer most frequently presents as solid or as mixed solid and cystic lesions located within the pelvis (Fig. 21). Entirely cystic lesions are rarely found (Forstner et al. 1995). In CT, recurrent disease usually displays moderate contrast enhancement. In MRI, the imaging findings depend on the morphology of the lesions. Usually smaller lesions display low to intermediate SI on T1-weighted images and intermediate to high SI on T2-weighted images. Contrast-enhanced images and DWI improve the detection of peritoneal surface lesions. Diffuse or focal peritoneal thickening presents peritoneal carcinomatosis. The pattern of peritoneal involvement is similar to primary ovarian cancer, with diffuse thin lining of the peritoneal surfaces to plaquelike lesions or nodules emerging from the peritoneal surfaces. Diffuse ascites is usually a sign of diffuse peritoneal recurrent disease. Omental caking is encountered only in patients treated with primary chemotherapy. Small-bowel obstruction is a typical complication as ovarian cancer advances and occurs in 5–42% (Low et al. 2003). Signs of malignant bowel obstruction include bowel dilatation, an obstructing mass, focal mural thickening, and peritoneal carcinomatosis (Low et al. 2003). A pseudo-small-bowel obstruction pattern can mimic small-bowel obstruction. It is typically

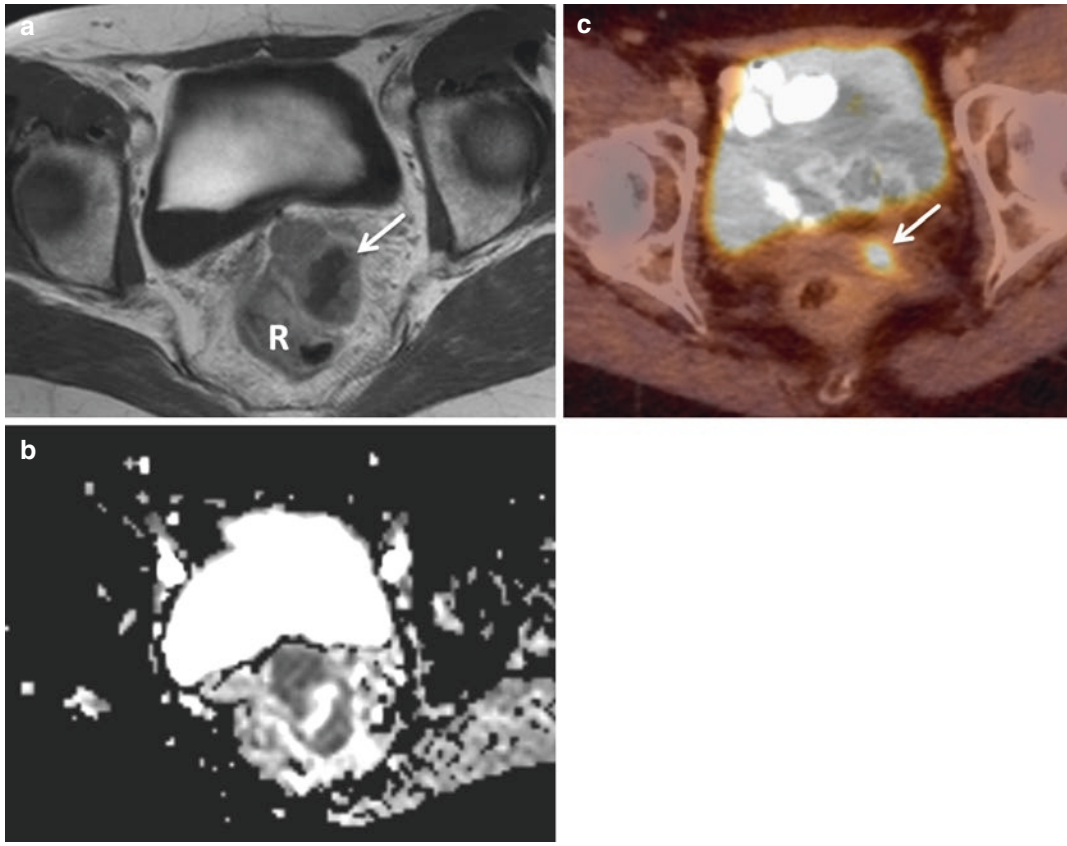

Fig. 21 Central pelvic recurrence (*arrow*) with rectal (R) invasion is demonstrated on Gd T1WI (**a**) and confirmed by its restricted diffusion on the ADC map (**b**). The PET/CT follow-up (**c**) after 6 months of chemotherapy demonstrates reduction in size but still vital residual cancer

encountered late in the course of the disease and is caused by tumor infiltration of the myenteric plexus of the small bowel (Ozols et al. 2001). Resection of recurrent disease, which is usually performed in pelvic recurrence, is only considered successful when complete resection without residual tumor is possible. Preoperatively, it is crucial to assess pelvic sidewall invasion rather than tumor size (Sala et al. 2013).

Differential Diagnosis

Postoperative hematomas, adhesions between bowel loops, or localized trapped fluid may mimic recurrent disease. Benign forms of diffuse peritoneal thickening such as a result of postoperative inflammatory complications or bacterial peritonitis cannot be differentiated from peritoneal relapse. Furthermore, chemical peritonitis following intraperitoneal chemotherapy also results in diffuse peritoneal thickening (Low et al. 2015).

Value of Imaging

Although large randomized trials showed no survival benefit of routine postoperative follow-up with CA-125, this tumor marker plays a pivotal role in monitoring patients with ovarian cancer in clinical practice (Birrer 2016; Spencer and Perren 2010). Imaging in conjunction with CA-125 is used to assess disease progression and response to therapy. Baseline CT examinations after surgery or before chemotherapy have been advocated to allow an objective follow-up (Sala et al. 2013). However, in many institutions imaging is only performed when tumor markers persist or increase or when the patients present with clinical symptoms. Demonstration of recurrence is pivotal in

patient triage for appropriate surgery or radiation therapy in selected cases (Kyriazi et al. 2010). Usually only patients with limited recurrent pelvic disease may be considered as candidates for cytoreductive surgery. Furthermore, patients can be selected who will benefit from a relieving colostomy (Birrer 2016). CT has been widely used for the assessment of recurrent ovarian cancer. MRI assists in predicting tumor resectability, particularly in the pelvis (Forstner et al. 2010). PET/CT is particularly useful in assessing persistent ovarian cancer and serves as a complementary imaging technique when tumor markers are rising and CT or MRI findings are inconclusive or negative (Mitchell et al. 2013; Iver and Lee 2010). It is superior to the other imaging techniques in assessing small implants, in differentiation metastases from scar tissues (Fig. 21). Although PET/MRI shows promising results and seems superior to PET/CT in advanced gynecological tumors, its value has still to be assessed (Queiroz et al. 2015).

7.4.2 Nonepithelial Ovarian Malignancies

Malignant Germ Cell Tumors

Malignant germ cell tumors are much less common than epithelial ovarian neoplasms. Although germ cell ovarian malignancies account for only 2–3% of all ovarian malignancies, their clinical importance is based upon their potential for cure and the typical age distribution (Ozols et al. 2001). In women younger than 20 years of age, they account for approximately two-thirds of all ovarian malignancies. They are often very large solid tumors with rapid and predominantly unilateral growth. The most frequent sites of dissemination are the peritoneum and retroperitoneal lymph nodes. Compared with epithelial tumors, they have a greater tendency for hematogenous metastases, and liver and lung involvement can be observed at diagnosis. Ascites is only found in approximately 20% of cases (Ozols et al. 2001). Histologically they mostly occur in pure forms.

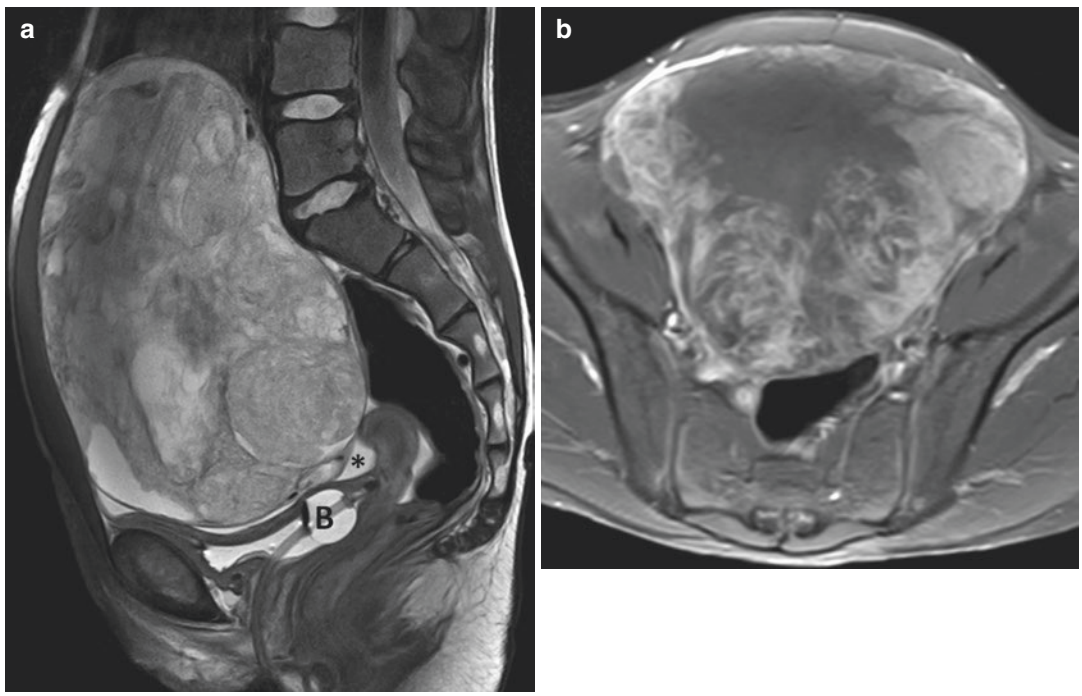

Fig. 22 Endodermal sinus tumor in a 14-year-old girl. Sag T2WI (**a**) and transaxial Gd T1FS (**b**). A large unilateral ovarian mass extends to the upper abdomen. It is well delineated but displays a very inhomogeneous architecture with areas of necrosis, hemorrhage, and solid well-vascularized elements. AFP levels were markedly elevated. *B* bladder. Ascites (*)

In mixed malignant germ tumors, the most malignant type defines the prognosis. Serum levels of HCG and AFP may assist in the diagnosis and in the follow-up of some germ cell tumors.

Malignant germ cell tumors comprise, in order of decreasing frequency, dysgerminomas, immature teratomas, endodermal sinus tumors, and embryonal and nongestational choriocarcinomas. The latter three are extremely rare. In these patients, tumor markers may be helpful for assessing response and tumor recurrence. Endodermal sinus tumors secrete AFP (Fig. 22). Embryonal carcinomas can secrete both AFP and HCG, whereas pure choriocarcinomas secrete only HCG (Ozols et al. 2001).

Dysgerminomas

Dysgerminomas present the most common type of malignant germ cell tumors and have been considered the female counterpart of seminoma of the testis. Seventy-five percent occur in early reproductive age, 10% in prepubertal girls, and 15–20% are diagnosed during pregnancy or postpartally (Hricak et al. 2004). In contrast to the other germ cell tumors, dysgerminomas may also occur bilaterally.

A minority (5%) of dysgerminomas arise in gonadal dysgenesis and may coexist with gonadoblastomas. Disorders of sexual differentiation, e.g., Turner syndrome and Swyer syndrome, harbor a considerably increased risk of dysgerminomas arising in streak gonads during adulthood (Tayfur et al. 2007). The vast majority of patients with dysgerminomas are diagnosed with early-stage disease, and fertility saving is an option in stage IA disease.

Imaging Findings

Dysgerminoma presents as a multilobulated, well-delineated solid lesion. In CT, speckled calcifications may be observed. Furthermore, they may contain low attenuation areas representing necrosis or hemorrhage. Contrast-enhanced CT may also demonstrate strongly enhancing fibrovascular septa. In MRI, the tumor displays low signal intensity on T1-weighted images and intermediate signal with low SI septa and high signal intensity areas of necrosis on T2-weighted images and restricted DWI (Fig. 23) As in CT, the intralesional septa may display strong enhancement (Tanaka et al. 1994).

Differential Diagnosis

Differential diagnosis includes solid ovarian tumors in younger age, e.g., granulosa cell tumors, yolk sac tumors, Sertoli cell tumor, and immature teratomas. The extremely rare ovarian lymphoma typically involves both ovaries. In MRI, uterine fibroma and fibrothecoma may display a similar appearance on T2-weighted images; however, contrast enhancement of uterine leiomyomas resembles that of myometrium, and fibrothecoma displays a type 1 time-intensity curve on DCE MRI (Forstner et al. 2016a). In CT, differentiation of subserosal uterine fibroids or ovarian fibromas from solid dysgerminomas is usually not feasible.

Immature Teratomas

Immature teratomas or malignant teratomas are the second most common germ cell malignancies. The typical age group is similar to dermoid cysts young age between 10 and 20 years. However, in contrast to benign teratomas, they are extremely rare, with less than 1% consisting of immature teratomas. They are typically large at the time of diagnosis and present as solid or predominantly solid tumors with cystic elements and areas of fat and calcifications. Immature teratomas are associated with dermoid cysts, more commonly in the ipsilateral (26%) than in the contralateral ovary (Young and Scully 2002a; Heifetz et al. 1998). They contain embryonic tissues and can also occur in combination with other germ cell tumors (mixed germ cell tumors). Yolk sac tumors within immature teratomas give rise to alpha-fetoprotein elevation and are an important prognostic factor (Heifetz et al. 1998). Immature teratomas may also rarely produce steroids and cause pseudoprecosity in prepubertal girls (Young and Scully 2002a; Heifetz et al. 1998).

Imaging Findings

Immature teratomas typically occur in young females and display mostly as heterogenous, predominantly solid lesions or as mixed solid and cystic lesions with scattered or coarse calcifications or hemorrhage (Heifetz et al.

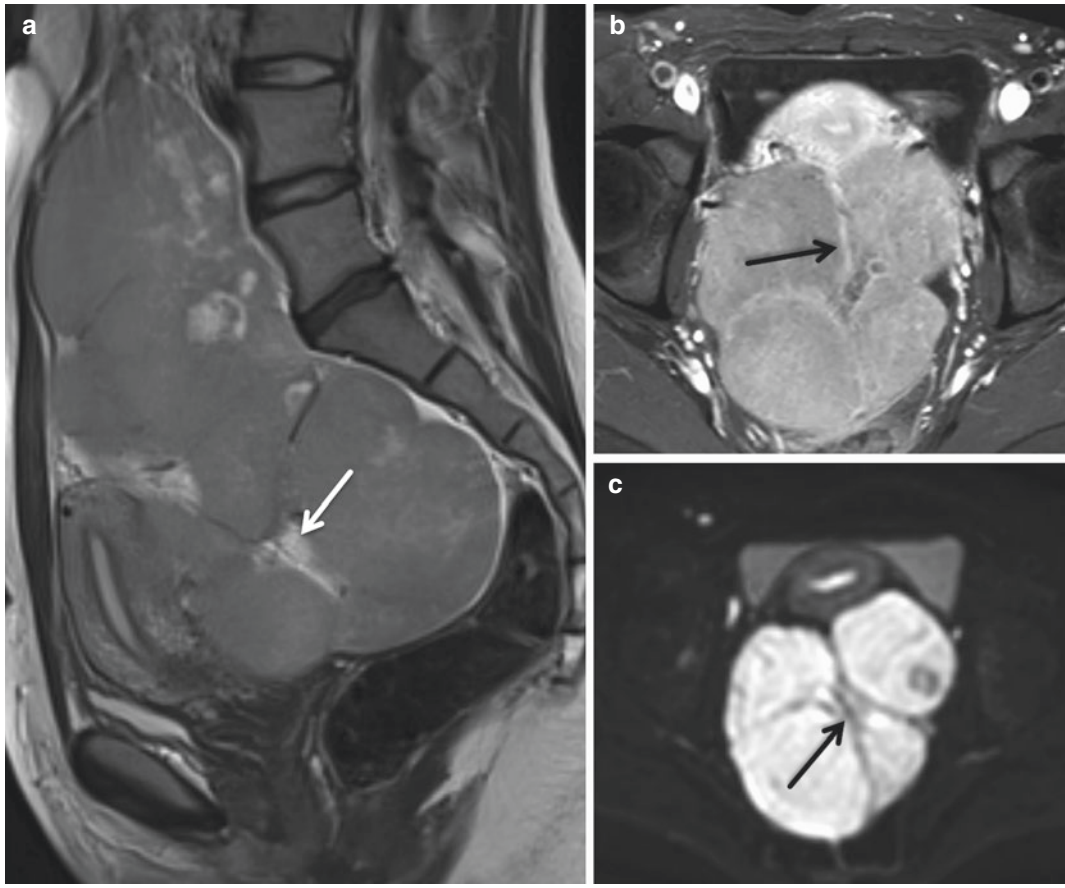

Fig. 23 Dysgerminoma of the right ovary in a 32-year-old female. A large, well-delineated multinodular solid lesion is located cranially and anterior of the uterus (**a**). It displays predominantly intermediate SI on the T2-weighted image (**a**) and moderate contrast enhancement (**b**), but clearly restricted diffusion (b = 1,000 mm^2) on DWI (**c**). Multiple septa (*arrows*) can be identified

1998; Bazot et al. 1999; Yamaoka et al. 2003). In CT, punctate foci of fat and calcifications are diagnostic clues for the presence of an immature teratoma (Bazot et al. 1999). In case of cystic lesions, they are typically filled with serous fluid and may rarely contain fatty sebaceous material (Diop et al. 2014). In MRI, small foci of fat with high SI on T1 (Fig. 24) and signal loss on the fat saturation sequence are typically found (Yamaoka et al. 2003). Malignant type of enhancement of the solid aspects may be seen. Capsular penetration is found in almost 50% of cases and is a pathognomonical feature of malignancy (Comerci et al. 1994).

Malignant Transformation in Benign Teratoma

Malignant transformation of benign teratomas is rare and reported in 0.17% of dermoid cysts (Comerci et al. 1994). It is associated with advanced age (mean 59 years) and a large (>6 cm) unilateral benign teratoma. In the vast majority, squamous cell cancer (up to 85%), or rarely carcinoid tumors, and adeno- or chorionic cancer arise from the cyst wall or from ectodermal elements of benign teratomas (Choudhary et al. 2009).

Imaging Findings

Fat within an ovarian mass is diagnostic of a teratoma. Signs indicative of malignancy include a

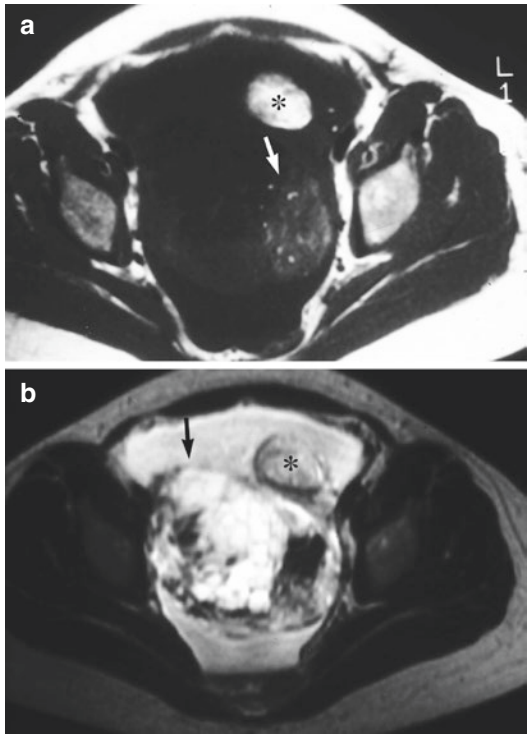

Fig. 24 Mature and immature teratoma in a 20-year-old female. T1- weighted image (**a**) and T2-weighted image with FS (**b**) at the acetabular level. Ascites surrounds bilateral ovarian lesions. The left tumor (*) represents a benign dermoid with predominantly fatty tissue. Posteriorly an inhomogeneous mixed solid and cystic lesion (*arrow*) with small hemorrhagic loculi is seen, which is better identified on the T2-weighted image (**b**). The tiny spots of high SI on T1-weighted image represent areas of fat (*arrow*) in (**a**). Courtesy of TM Cunha, Lisbon

solid well-vascularized large mural nodule, often arising from the Rokitansky protuberance, breach of the capsule, or extracapsular growth and metastases (Fig. 25) (Choudhary et al. 2009; Kido et al. 1999). Elevation of tumor markers CEA and CA-125 in an older female with a large fat-/sebaceum-containing mass is diagnostic of malignant degeneration of a dermoid cyst (Dos Santos et al. 2007).

Differential Diagnosis

Immature teratomas are usually large at presentation and occur in young females. In contrast to the majority of benign cystic teratomas, malignant teratomas tend to be predominantly solid with small foci of fat and scattered calcifications. Elevation of alpha-1-fetoprotein assists in establishing the diagnosis and is found in 33–65% of immature teratomas (Yamaoka et al. 2003). Mature and immature teratomas coexist in approximately 20% of cases. If no fat is identified, an immature teratoma cannot be differentiated from a monodermal benign teratoma, e.g., of struma ovarii, from malignant germ cell tumors, or from ovarian cancer (Dujardin et al. 2014). Pitfalls include struma ovarii, where nodules may show avid contrast enhancement similar to malignant degeneration (Forstner et al. 2016a). However, only capsular breach proves the malignant transformation (Choudhary et al. 2009).

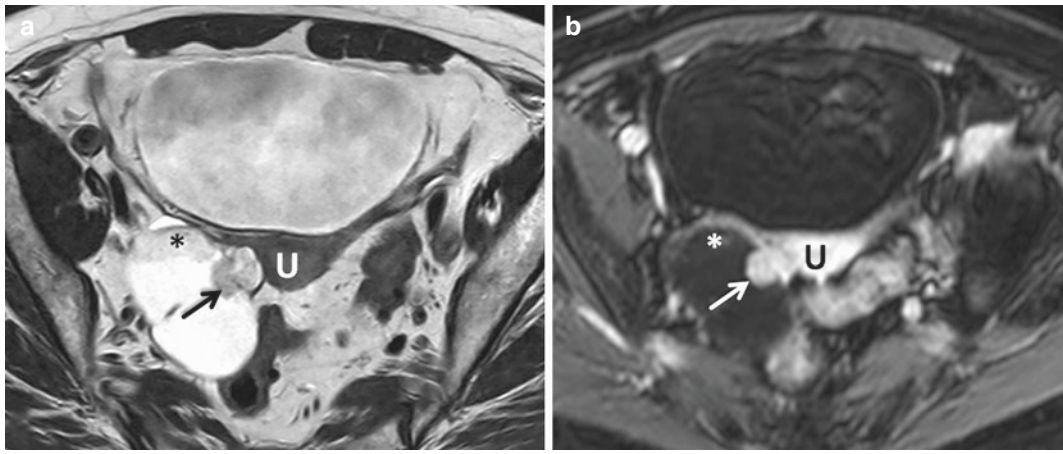

Fig. 25 Malignant transformation. In a 64-year-old female, a mural nodule breaching the capsule of a benign teratoma is seen on the T2WI (*arrow*) (**a**). FS GdT1 WI (**b**) shows the intensely enhancing nodule (*arrow*) with extracapsular growth. Fat (*) within the teratoma. *U* uterus

Sex-Cord Stromal Tumors

Sex-cord stromal tumors derive from coelomic epithelium or mesenchymal cells of the embryonic gonads (Young and Scully 2002a). Eight percent of all ovarian neoplasms account for this tumor type, with granulosa cell tumors, fibromas, thecomas, and Sertoli-Leydig cell tumors comprising the majority of these tumors. The 2014 revised WHO classification comprises pure stromal tumors, pure sex-cord tumors, and mixed sex-cord stromal tumors (Horta and Cunha 2015). Granulosa cell tumors are considered as low-grade malignant tumors. Sertoli-Leydig cell and steroid tumors may be malignant depending on the degree of differentiation (Young and Scully 2002a). Sex-cord stromal tumors affect all age groups but are commonly encountered in peri- and postmenopausal women (Tanaka et al. 2004). Their clinical and differential diagnostic importance is based upon their hormone activity. Granulosa cell tumors may typically produce estrogens, but a minority may be hyperandrogenic. Sertoli-Leydig cell tumors and steroid cell tumors are androgen-producing tumors. The majority of sex-cord stromal tumors are confined to the ovary at the time of diagnosis (Outwater et al. 1998).

Granulosa Cell Tumors

Granulosa cell tumors are classified as neoplasm of a low malignant potential. The juvenile and the adult subtype differ in several important aspects. Adult granulosa cell tumors account for 1–2% of all ovarian tumors and for 95% of all granulosa cell tumors (Young and Scully 2002a). FOXL2 gene mutation is seen in the vast majority and is diagnostic of the adult tumor type (Kottarathil et al. 2013). Granulosa cell tumors are the most common ovarian tumors presenting with hyperestrogenism. The rare juvenile granulosa cell tumors are hormonally active in 80% and occur typically before the age of 30 years. The majority is found in prepubertal girls who present with the signs of precocious pseudopuberty with development of breasts and pubic and axillary hair. An association with Ollier's disease (enchondromatosis) and Maffucci's syndrome (enchondromatosis and hemangiomatosis) has been reported in some cases (Young and Scully 2002a).

Adult granulosa cell tumors occur after the age of 30 years and have their peak incidence in the perimenopausal age (median 51 years) (Young and Scully 2002a; Kottarathil et al. 2013). Estrogen expression may become clinically manifest as abnormal uterine bleeding and endometrial hyperplasia. Endometrial cancer is associated with these tumors in 3–22% of cases (Outwater et al. 1998). Peutz-Jeghers syndrome and Potter's syndrome are also linked with granulosa cell tumors (Pennington and Wsisher 2012). Both types of granulosa cell tumors are typical unilateral ovarian tumors that vary considerably in size and show an average diameter of approximately 12 cm (Young and Scully 2002a). Unlike epithelial ovarian cancer, they are diagnosed in stage I in 71% of patients and in late stages (III and IV) in 19% (Kottarathil et al. 2013). Recurrence rates reach 25%, and recurrence tends to occur late at 4–5 years but may be seen even many years after the initial therapy (Young and Scully 2002a; Kottarathil et al. 2013). Relapse is typically confined to the pelvis and abdomen. However, distant metastases to the bone, supraclavicular lymph nodes, liver, and lungs have been reported (Kottarathil et al. 2013).

Imaging Findings

Granulosa cell tumors present typically unilateral, well-delineated often large masses. Irrespective of their distinct clinical features, both the juvenile and adult tumor type can display a broad spectrum of imaging features from entirely cystic to completely solid ovarian lesions (Fig. 26) (Jung et al. 2002).

Granulosa cell tumors may display homogenous contrast enhancement and intermediate to high SI on T2-weighted images. They may also manifest as a solid and cystic neoplasm, and cysts may contain hemorrhagic fluid. Papillary projections are not found and calcifications are rare (Horta and Cunha 2015). The adult type of granulosa cell tumors manifests mostly as a predominantly spongelike cystic multilocular tumor with blood clots and solid tissue (Kim 2002). In hormone-active tumors, the endometrial cavity may be widened due to hyperplasia or endometrial cancer (Kottarathil et al. 2013; Kim 2002).

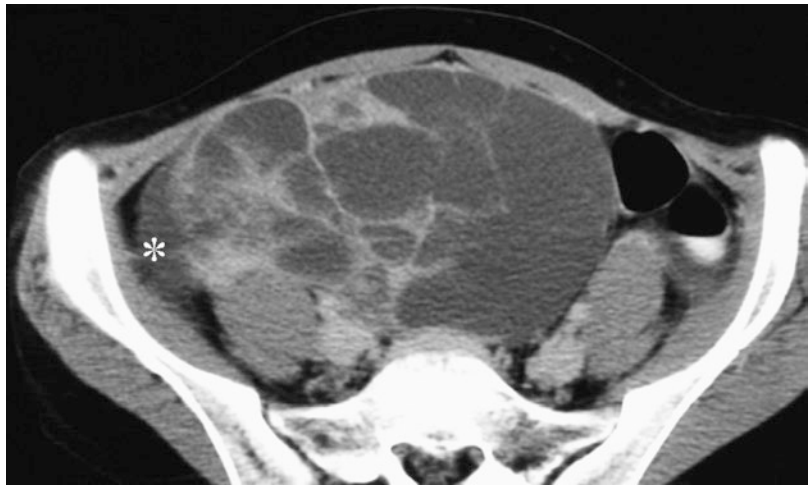

Fig. 26 Juvenile type of granulosa cell tumor. CT in a 17-year-old girl who presented with primary amenorrhea. A large, well-defined cystic ovarian tumor with multiple irregular septations and solid areas is demonstrated in the midpelvis. Small amount of ascites (*) without evidence of peritoneal seeding at surgery

Lymphatic spread is typically not found and peritoneal spread is rare (Kottarathil et al. 2013).

Sertoli-Leydig Cell Tumor

Sertoli-Leydig cell tumors account for less than 0.5% of ovarian tumors. The majority (75%) of Sertoli-Leydig cell tumors occur in women younger than 30 years (Tanaka et al. 2004). Less than 10% are found in women over 50 years of age (Young and Scully 2002a). Although virilization caused by androgen production is the most striking clinical feature, it occurs in only one-third of patients (Young and Scully 2002a). Other symptoms include menstrual irregularities or abnormal bleeding. Approximately 50% of women with Sertoli-Leydig tumors have no endocrine effects. Most Sertoli-Leydig cell tumors are unilateral and the majority is diagnosed as stage I disease. They vary in size between 5 and 15 cm (average, 13.5 cm). Some of these tumors may be very small and difficult to detect by imaging, although they produce hormonal effects (Outwater et al. 1998).

Depending upon the degree of differentiation, 1–59% of Sertoli-Leydig cell tumors were malignant in one series (Young and Scully 2002a). In contrast to granulosa cell tumors, Sertoli-Leydig cell tumors tend to relapse typically within the first year after surgery.

Imaging Findings

Sertoli-Leydig cell tumors vary broadly in gross appearance. They tend to be unilateral (98%) solid, sometimes lobulated masses. They may also appear as predominantly solid masses often with peripheral cysts or as a cystic lesion with polypoid mural structures (Fig. 27) (Tanaka et al. 2004). Cysts may display a slightly high signal intensity on T1-weighted images. The solid components display intermediate to high SI on T2-weighted images and avid contrast enhancement in MRI and CT (Jung et al. 2002). Rarely, these tumors may also manifest similar to Krukenberg tumors as a cystic lesion with well-vascularized solid aspects (Tanaka et al. 2004). Less differentiated types of Sertoli-Leydig cell tumors tend to display an inhomogeneous architecture with areas of necrosis and hemorrhage.

Ovarian Lymphoma

Ovarian involvement by lymphoma presents almost always a manifestation of systemic disease, mostly of B-cell lymphoma. Primary lymphoma of the ovary without lymph node or bone marrow involvement is extremely rare. It constitutes 5% of extranodal lymphomas, but the ovaries are leading among the gynecologic organ manifestations (Lagoo and Robboy 2006). Ovarian lymphoma tends to occur in

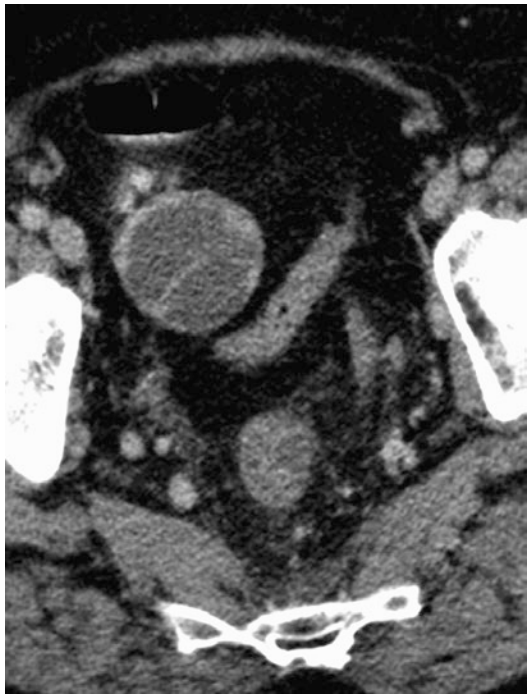

Fig. 27 Malignant Sertoli-Leydig cell tumor without hormonal activity. CT shows a well-delineated cystic lesion of the right ovary that was incidentally detected at a gynecological exam in a 64-year-old female

premenopausal women and appears most frequently as diffuse large B-cell non-Hodgkin lymphoma followed by Burkitt lymphoma (Onyiuke et al. 2013; Kosari et al. 2005). Follicular lymphoma and small lymphocytic lymphoma are encountered in more advanced ages (Onyiuke et al. 2013). Clinically, lymphoma may become apparent as a pelvic mass or with pelvic or abdominal pain.

Imaging Findings

Lymphomas appear as unilateral or more commonly as bilateral solid, homogenous ovarian masses without ascites (Ferrozzi et al. 2000). They also may demonstrate areas of cystic degeneration and hemorrhage. Margins are smooth and ovarian follicles may be preserved. In CT, lymphoma appears as well-defined solid nodular hypovascular masses. In MRI, they display intermediate signal on T1 and low to intermediate SI on T2-weighted images (Fig. 28) and distinct restricted DWI. Similar to CT, mild contrast enhancement is noted.

Differential Diagnosis

Thecomas are also hypovascular uni- or bilateral solid tumors that can be differentiated from lymphomas due to their low SI on T2WI. Their DWI SI may be variable, but if DWI restriction is

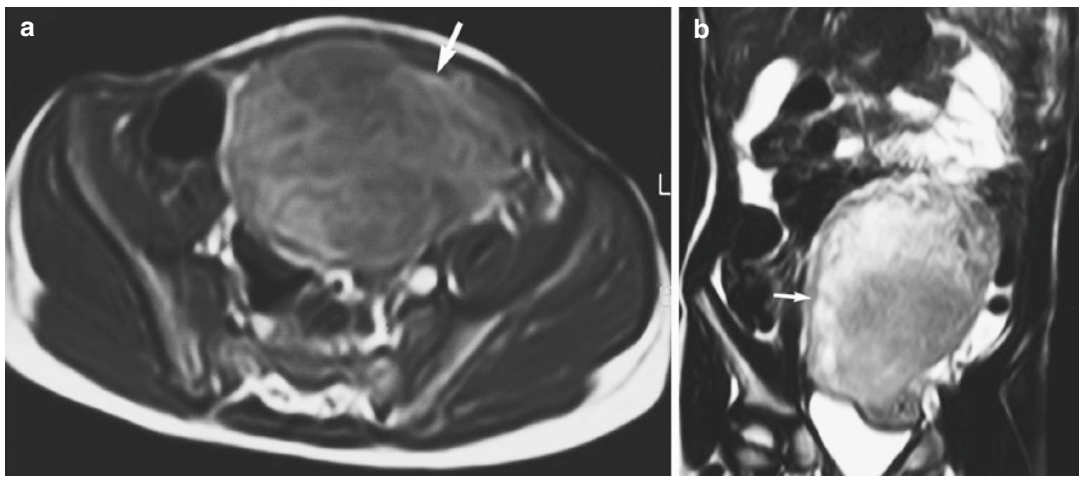

Fig. 28 Ovarian lymphoma in a child. Contrast-enhanced T1-weighted image in the midpelvis (**a**) and coronal T2-weighted image (**b**). Non-Hodgkin lymphoma only confined to the left ovary presents as a large solid mass (*arrow*) with moderate contrast enhancement (**a**) and inhomogeneous low to intermediate SI on T2-weighted image (**b**)

present in thecomas, it is much less than in lymphomas. Other malignant predominantly solid ovarian tumors, including ovarian cancer, metastases, and granulosa cell tumors, may resemble ovarian lymphoma, but these are more common than lymphomas. Bilaterally, high to intermediate SI on T2-weighted image and ascites favor the diagnosis of ovarian cancer. Metastases may also present as a lobulated unilateral or bilateral solid ovarian mass. They usually display strong contrast enhancement and central necrosis or cysts. History of cancer of the breast or the GI tract is pivotal for the differential diagnosis. Granulosa cell tumors tend to be unilateral and may cause estrogenic effects. Clinical history, presence of multiple lymph nodes, and splenomegaly support the diagnosis of secondary ovarian involvement in lymphoma.

7.4.3 Ovarian Metastases

5–15% of malignant ovarian tumors constitute metastases to the ovaries. The GI tract (39%), breast (28%), and endometrium (20%) are the most common primary sites (De Waal et al. 2009; Lee et al. 2009; Brown et al. 2001; Young and Scully 2002b). Rare cancer sources include pancreatic and gallbladder cancer, melanoma, and lymphoma (Young and Scully 2002b). Ovarian metastases seem more common in premenopausal women because of higher vascularity of the ovaries in this age, and they may be associated with hormonal activity (Young and Scully 2002b). Although metastases may occur unilaterally (especially in endometrial cancer), bilateral involvement is a typical feature and found in 70–80% of ovarian metastases (Togashi 2003). Approximately 50% of ovarian metastases are Krukenberg tumors from stomach or colorectal cancers. Compared to other histologies, Krukenberg tumors have a fourfold risk to metastasize to the ovaries. In a multicenter study assessing 86 patients with primary ovarian and 24 patients with secondary cancers, only multilocularity favored the diagnosis of a primary ovarian cancer (Brown et al. 2001). Despite their large size, ovarian metastases are often asymptomatic. Out of 147 patients with predominantly gastrointestinal tract cancers, 36% of metastases were detected synchronously (Li et al. 2012). In general, ovarian metastases are associated with a dismal prognosis. Colon cancer metastases have a significant better survival than stomach or breast cancer, where the majority of patients will die within the first year after detection (Li et al. 2012). Predisposing factors for metastases from breast cancer include premenopausal age, lobular carcinoma, and advanced stage. They typically develop 2–5 years after cancer diagnosis and are often also associated with peritoneal carcinomatosis (Bigorie et al. 2010).

Imaging Findings

Ovarian metastases may present as solid ovarian tumors with necrosis, as solid and cystic and rarely as multiseptate cystic masses (Koonings et al. 1989; Ha et al. 1995). Krukenberg tumors typically are bilateral oval or kidney-shaped tumors, which tend to preserve the contour of the ovary and have a nodular surface (Fig. 29). They are solid or predominantly solid with central necrosis or cysts and may attain a large size. On MRI, they display medium signal intensity on T1-weighted images and an inhomogeneous low to intermediate SI on T2-weighted images and DWI restriction (Ha et al. 1995; Kim et al. 1996). In CT and contrast-enhanced MRI, they tend to show strong enhancement of solid components or septations. Follicles may be preserved and displaced to the periphery. A transversing vessel may be present (Fig. 29). Ascites is commonly found and may be a sign of peritoneal seeding. Metastatic cancers different from Krukenberg tumors may have a variable appearance resembling other malignant ovarian lesions with cystic and mixed cystic and solid patterns (Brown et al. 2001; Young and Scully 2002b; Kim et al. 1996; Megibow et al. 1985). Colon cancer metastases commonly present as unilateral or bilateral, multiloculated, predominantly cystic tumors (Fig. 30) (Choi et al. 2006). Due to the high rate of synchronous ovarian metastases, careful assessment of the GI tract is warranted (Li et al. 2012). Further, in malignancy elsewhere, metastases to the ovaries should be suspected if the pattern of spread is atypical for ovarian cancer. In particular, the presence of pulmonary and hepatic metastases

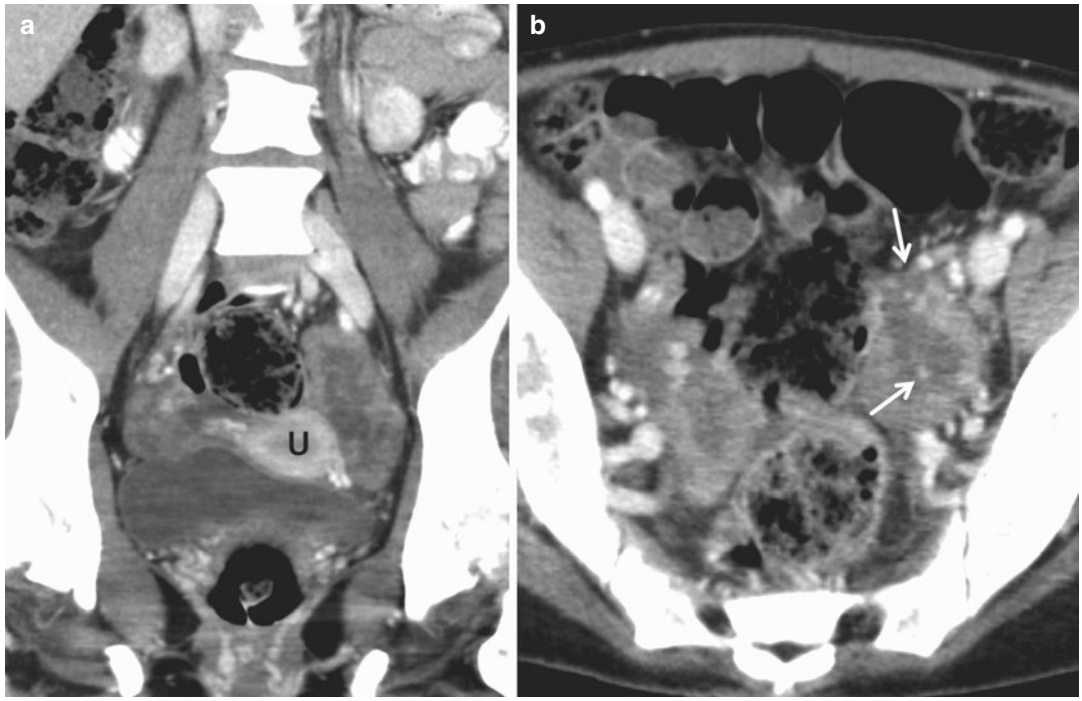

Fig. 29 Typical bilateral Krukenberg tumors in a patient with history of gastric cancer. Coronal (**a**) and transaxial (**b**) CT show bilateral ovarian tumors with central necrosis. On the left ovary, a transversing vessel can be identified in b (*arrows*). *U* uterus

in the absence of extensive peritoneal spread is unusual for ovarian cancer and favors another primary neoplasm (Young and Scully 2002b).

Differential Diagnosis

Confident distinction between primary and metastatic ovarian cancers is not feasible due to overlapping imaging findings. Bilateral, well-delineated, purely solid or predominantly solid tumors with necrosis strongly favor the diagnosis of Krukenberg tumors (Alcazar et al. 2003). Multinodularity at the ovarian surface is also a feature suggesting ovarian metastases, but this may also be seen in dysgerminomas and lymphomas (Horta and Cunha 2015; Li et al. 2012). Contrast uptake aids in the differentiation of solid ovarian metastases from stromal tumors. Stromal tumors typically display a mild and delayed contrast uptake resp type 1 time-intensity curves. If such a solid lesion shows low signal on a high b value DWI, the presence of metastases can be excluded (Thomassin-Naggara et al. 2009). If metastases are cystic and hemorrhagic, they may resemble endometriomas, which also occur in younger women. However, enhancing nodules and distinct contrast enhancement is not found in endometriomas. Abscesses usually present with different clinical features than the clinically silent metastases. Similar to sex-cord stromal tumors, ovarian metastases can produce estrogens or androgens. The clinical background is usually different, and history of a primary cancer prone to spread to the ovaries allows the correct diagnosis. Coexistence of a type II endometrial cancer or premenopausal age favor the presence of metastases to the ovaries rather than an independent ovarian cancer (Holschneider et al. 2005).

7.5 Fallopian Tube Cancer

Fallopian tube cancer has been thought to be extremely rare accounting for only 0.3–1.1% of all gynecologic cancers (Chen and Berek 2016).

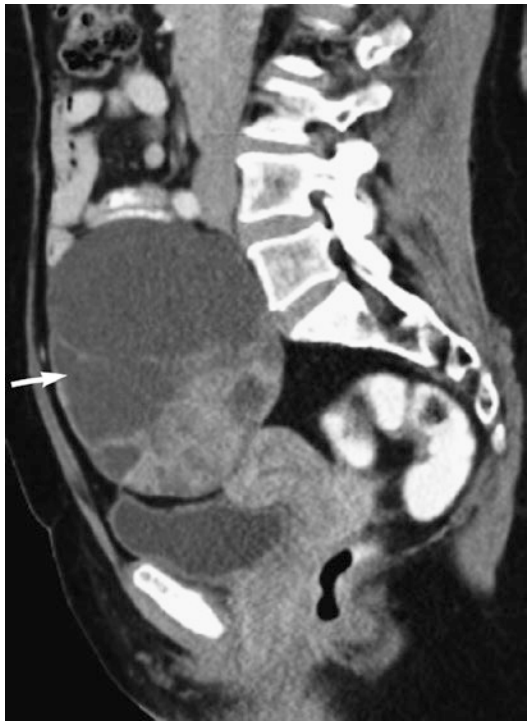

Fig. 30 Metastases from colon cancer. Sagittal CT shows a well-delineated mixed cystic and solid ovarian mass (*arrow*), which abuts the uterus fundus and elevates small-bowel loops. No ascites was found in the pelvis or abdomen. In this patient with stage T4 colon cancer, differentiation of metastasis from ovarian cancer is not possible by imaging

However, the tubal origin has been proven for most high serous ovarian cancers as well as for most of the hereditary ovarian cancers. Based on these new insights, the FIGO 2014 staging classification has unified ovarian, fallopian tube, and peritoneal cancer in its staging classification.

7.5.1 Imaging Findings

A unilateral adnexal complex cystic or solid mass associated with hydrosalpinx is the most common finding (Kawakami et al. 1993; Gomes et al. 2015). CT and MRI demonstrate complex solid and cystic enhancing masses similar to ovarian cancer. A cystic tubular structure with interdigitating septa adjacent to the mass represents the dilated tube. Signal intensity on T1 and T2 higher than serous fluid suggests hematosalpinx. Occasionally, focal nodularity within a hydrosalpinx may be found in fallopian cancer. Common associated findings are distension of the uterine cavity and ascites (Gomes et al. 2015). Peritoneal metastases are similar to those in ovarian cancer. Lymph node metastases may be found more often than in ovarian cancer (Gomes et al. 2015).

Differential Diagnosis

A solid mass arising within the dilated fallopian tube or a sausage-like adnexal mass has been described as a feature characterizing fallopian tubal cancer (Gomes et al. 2015). Especially with T2-weighted images, identification of the cystic components of the distended tube may be possible. Metastases to the fallopian tubes, which result most commonly from direct extension of gynecologic cancers, cannot be reliably differentiated from primary fallopian tube cancers. Rarely, leiomyomas of the fallopian tube may be encountered, which resemble ovarian stromal tumors or fibroids of the broad ligament.

References

Akin O, Sala E, Chaya S et al (2008) Perihepatic metastases from ovarian cancer: sensitivity and specificity of CT for the detection of metastases with and those without liver parenchymal invasion. Radiology 248:511–517

Alcazar JL, Galan MJ, Ceamanos C et al (2003) Transvaginal gray scale and color Doppler sonography in primary ovarian cancer and metastatic tumors to the ovary. J Ultrasound Med 22:243–247

Alvarez RM, Vazquez-Vicente D (2015) Fertility sparing treatment in borderline ovarian tumors. Ecancermedicalscience 9:507. doi:10.3332/ecancer.2015.507

Anthuber C, Engel J, Mayr D, Petrides P (2014) Keimstrangstromatumoren. www.journalonko.de 6:418–420

Bachmann C, Bachmann R, Kraemer B, Brucker SY et al (2016) Prevalence and distribution pattern of nodal metastases in advanced ovarian cancer. Mol Clin Oncol 5:483–487

Bairey O, Blickstein D, Stark P et al (2003) Serum CA 125 as a prognostic factor in non-Hodgkin's lymphoma. Leuk Lymphoma 44:1733–1738

Bazot M, Cortez A, Sananes S, Boudghene F et al (1999) Imaging of dermoid cysts with foci of immature tissue. J Comput Assist Tomogr 23:703–706

Bent CL, Sahdev A, Rockall A, Singh N, Sohaib A, Reznek RH (2009) MRI appearance of borderline ovarian tumors. Clin Radiol 64:430–438

Bernardin L, Dilks P, Liyanage S, Miquel ME, Sahdev A, Rockall A (2012) Effectiveness of semi-quantitative multiphase dynamic contrast-enhanced MRI as a predictor of malignancy in complex adnexal masses: radiological and pathological correlation. Eur Radiol 22:880–890

Bigorie V, Morice P, Pierre D, Antoine M et al (2010) Ovarian metastases from breast cancer: report of 29 cases. Cancer 116:799–804

Birrer MJ (2016) Medical treatment for relapsed ovarian fallopian tubal, or peritoneal cancer: platinum-resistant disease.www.uptodate.com

Borley J, Wilhelm-Benartzi C, Williamson R, Bharwani N et al (2015) Radiological predictors of cytoreductive outcomes in patients with advanced ovarian cancer. BJOG 122:843–849

Bristow RE, Duska LR, Lambrou NC et al (2000) A model for predicting surgical outcome in patients with advanced ovarian carcinoma using computed tomography. Cancer 89:1532–1540

Brown DL, Zou KH, Tempany CM et al (2001) Primary versus secondary ovarian malignancy: imaging findings of adnexal masses in the radiology diagnostic oncology group study. Radiology 219:213–218

Burghardt E (1993) Epithelial ovarian cancer. Recurrence. In: Burghardt E (ed) Surgical gynecological oncology. Thieme, Stuttgart, p 494

Buy JN, Ghossain MA, Sciot C et al (1991) Epithelial tumors of the ovary: CT findings and correlation with US. Radiology 178:811–818

Buys SS, Partrige EP, Black A, Johnson CC et al (2011) Effect of screening on ovarian cancer mortality. JAMA 305:2295–2303

Cancer Fact and Figures (2016) www.cancer.org/acs/groups/content/@research/documents/document/acspc-047079.pdf

Carlson KJ (2016) Ovarian cancer screening. www uptodate 2016

Chen C, Berek JS (2016) Epithelial cancer of the ovary, fallopian tube, and peritoneum. Clinical features and diagnosis. www.UpToDate.com

Choi HJ, Lee JH, Kang S et al (2006) Contrast-enhanced CT for differentiation of ovarian metastasis from gastrointestinal tract cancer: stomach cancer versus colon cancer. AJR Am J Roentgenol 187:741–745

Choudhary S, Fasih N, McInnes M, Marginean C (2009) Imaging of ovarian teratomas: appearances and complications. J Med Imaging Radiat Oncol 53:480–488

Clarke-Pearson DL (2009) Screening for ovarian cancer. N Engl J Med 361:170–177

Coakley FV, Choi PH, Gougoutas CA et al (2002) Peritoneal metastases: detection with spiral CT in patients with ovarian cancer. Radiology 223:495–499

Comerci JT, Jr Licciardi F, Bergh PA et al (1994) Mature cystic teratoma. A clinicopathological evaluation of 517 cases and review of the literature. Obstet Gynecol 84:22–28

De Waal YR, Thomas CM, Oei AL, Sweep FC, Massuger LF (2009) Secondary ovarian malignancies: frequency, origin, and characteristics. Int J Gynecol Cancer 19:1160–1165

Dilks P, Narayan P, Reznek R, Sahdev A, Rockall A (2010) Can quantitative dynamic contrast-enhanced MRI independently characterize an ovarian mass. Eur Radiol 20:2176–2183

Diop AD, Fontarensky M, Montoriol PF, Da Ines D (2014) CT imaging of peritoneal carcinomatosis and its mimics. Diagn Interv Imaging 95:861–872

Dos Santos L, Mok E, Iasonos A et al (2007) Squamous cell carcinoma arising in mature cystic teratoma of the ovary: a case series and review of the literature. Gynecol Oncol 105:321–324

Dujardin MI, Sekhri P, Turnbull LW (2014) Struma ovarii: role of imaging? Insights Imaging 5:41–51

Ferrozzi F, Tognini G, Bova D et al (2000) Non-Hodgkin lymphomas of the ovaries: MR findings. J Comput Assist Tomogr 24:416–420

Forstner R, Hricak H, Azizi L et al (1995) Ovarian cancer recurrence: value of MR imaging. Radiology 196:715–720

Forstner R, Sala E, Kinkel K, Spencer JA (2010) ESUR guidelines: ovarian cancer staging and follow-up. Eur Radiol 20:2773–2780

Forstner R, Thomassin-Naggara I, Cunha TM, Kinkel K, Masselli G, Kubik-Huch R, Spencer JA, Rockall A (2016a) ESUR recommendations for MR imaging of the sonographically indeterminate adnexal mass: an update. Eur Radiol [Epub ahead of print] PMID: 27921156

Forstner R, Meissnitzer M, Cunha TM (2016b) Update on imaging of ovarian cancer. Curr Radiol Rep 4:31

Genetic/Familial High-Risk Assessment: Breast and Ovarian, Version 1.2016 multigene testing National Comprehensive Cancer Network (NCCN). NCCN Clinical practice guidelines in oncology. http://www.nccn.org/professionals/physician_gls/f_guidelines.asp. Accessed on 27 Feb 2016

Gomes FV, Dias JL, Lucas R, Cunha TM (2015) Primary fallopian tube carcinoma: review of MR imaging findings. Insights Imaging 6:431–439

Ha HK, Baek SY, Kim SH et al (1995) Krukenberg's tumors of the ovary: MR imaging features. AJR Am J Roentgenol 164:1435–1439

Heifetz SA, Cushing B, Giller R et al (1998) Immature teratomas in children: pathologic considerations. Am J Surg Pathol 22:1115–1124

Höhn AK, Einenekel J, Wittekind C, Horn LC (2014) Neue FIGO-Klassifikation des Ovarial-Tuben und primären Peritonealkarzinoms. Pathologe 35:322–326

Holschneider C, Hoang Y, Tieu K, Karlan B, Cass I (2005) Coexisting ovarian malignancy in young women with endometrial cancer. Obstet Gynecol 106:693–699

Horta M, Cunha TM (2015) Sex cord-stromal tumors of the ovary: a comprehensive review and update for radiologists. DIR 21:277–286

Hricak H, Chen M, Coakley FV et al (2000) Complex adnexal masses: detection and characterization with MRI: multivariate analysis. Radiology 214:39–46

Hricak H, Reinhold C, Ascher SM (2004) Ovarian dysgerminomas. In: Hricak H, Reinhold C, Ascher SM (eds) Gynecology top 100 diagnoses. WB Saunders Company, Amirsys/Salt Lake City, pp 98–100

Iver VR, Lee SI (2010) MRI, CT and PET/CT for ovarian cancer detection and adnexal characterization. AJR 194:311–321

Javadi S, Ghaneshan DM, Quayyum A, Iyer RB, Bhosale P (2016) Ovarian cancer, the revised FIGO staging system, and the role of Imaging. AJR 206:1351–1360

Jayson GC, Kohn EC, Kitchener HC, Ledermann JA (2014) Ovarian cancer. Lancet 384:1376–1388

Jung SE, Lee JM, Rha SE et al (2002) CT and MR imaging of ovarian tumors with emphasis on differential diagnosis. Radiographics 22:1305–1325

Kaijser J, Vandecaveye V, Deroose CM et al (2014) Imaging techniques for the pre-surgical diagnosis of adnexal tumours. Best Pract Res Clin Obstet Gynaecol 28:683–695

Kandukuri SR, Rao J (2015) FIGO 2013 staging system for ovarian cancer: what is new in comparison to the 1988 staging system. Curr Opin Obstet Gynecol 27:48–52

Kawakami S, Togashi K, Kimura I et al (1993) Primary malignant tumor of the fallopian tube: appearance at CT and MR imaging. Radiology 186:503–508

Kawamoto S, Urban BA, Fishman EK (1999) CT of epithelial ovarian tumors. Radiographics 19:S85–S102

Khasper A, Addley HC, Abourokbah N, Nougaret S et al (2012) T2-hypointense adnexal lesions: an imaging algorithm. Radiographics 32:1047–1061

Kido A, Togashi K, Konishi I et al (1999) Dermoid cysts of the ovary with malignant transformation: MR appearance. AJR 172:445–449

Kim SH (2002) Granulosa cell tumor of the ovary: common findings and unusual appearances on CT and MR. J Comput Assist Tomogr 26:756–761

Kim SH, Kim WH, Park KL et al (1996) CT and MR findings of Krukenberg tumors: comparison with primary ovarian tumors. J Comput Assist Tomogr 20: 393–398

Kim TH, Lim MC, Kim SI, Seo SS et al (2016) Preoperative prediction of cardiophrenic lymph node metastasis in advanced ovarian cancer using CT. Ann Surg Oncol 23:1302–1308

Komatsu KI, Konishi I, Mandai M et al (1996) Adnexal masses: transvaginal US and gadolinium-enhanced MR imaging assessment of intratumoral structure. Radiology 198:109–115

Koonings PP, Campbell K, Mishell DR, Grimes DA (1989) Relative frequency of primary ovarian neoplasm: a 10-year review. Obstet Gynecol 74:921–926

Kosari F, Daneshbod Y, Parwaresch R, Krams M, Wacker HH (2005) Lymphomas of the female genital tract: a study of 186 cases and review of the literature. Am J Surg Pathol 29:1512–1520

Kottarathil VD, Anthony MA, Nair IR, Pvithran K (2013) Recent advances in granulosa cell tumory ovary: a review. Indian J Surg Oncol 4:37–47

Kurman R, Shih LM (2011) Molecular pathogenesis and extraovarian origin of epithelial ovarian cancer. Shifting the paradigm. Hum Pathol 42:918–931

Kurman RJ, Carcangiu ML, Herrington CS et al (2014) WHO classification of tumours of temale reproductive organs. In: WHO classification of tumours, 4th edn. WHO Press, Lyon

Kwek JW, Iyer RB (2006) Recurrent ovarian cancer: spectrum of imaging findings. Am J Roentgenol AJR 187:99–104

Kyriazi S, Kaye SB, deSouza NM (2010) Imaging ovarian cancer and peritoneal metastases – current and emerging techniques. Nat Rev Clin Oncol 7:381–393

Lagoo AS, Robboy SJ (2006) Lymphoma of the female genital tract: current status. Int J Gynecol Pathol 25:1–21

Lalwani N, Shanbhogue AKP, Vikram R, Nagar A, Jagirdar J, Prasad S (2010) Current update on Borderline ovarian neoplasm. AJR 194:330–336

Lalwani N, Prassad SR, Vikram R, Shanboghue AK et al (2011) Histologic, molecular, and cytogenetic features of ovarian cancers: implication for diagnosis and treatment. Radiographics 31:625–646

Leake JF, Currie JL, Rosenshein NB (1992) Long-term follow-up of serous ovarian tumors of low malignant potential. Gynecol Oncol 47:150–158

Lee SI, Catalano OA, Dehdashti F (2015) Evaluation of gynecologic cancer with MR imaging. ^{18}F-FDG PET/CT, and PET/MR imaging. J Nucl Med 56:436–443

Lee SJ, Bae JH, Lee AW, Tong SY, Park YG, Park JS (2009) Clinical characteristics of metastatic tumors to the ovaries. J Korean Med Sci 24:114–119

Lengyel E (2010) Ovarian cancer development and metastasis. Am J Pathol 177:1053–1064

Levy AD, Shaw JC, Sobin LH (2009) Secondary tumors and tumorlike lesions of the peritoneal cavity: imaging features with pathologic correlation. Radiographics 29:347–373

Li W, Wang H, Wang J et al (2012) Ovarian metastases resection from extragenital primary sites: outcome and prognostic factor analysis of 147 patients. BMC Cancer 12:278–286

Lorraine C, Pelosof LC, Gerber DE (2010) Paraneoplastic syndromes: an approach to diagnosis and treatment. Mayo Clin Proc 85:838–854

Low RN, Saleh F, Song SYT et al (1999) Treated ovarian cancer: comparison of MR imaging with serum CA-125 level and physical examination: a longitudinal study. Radiology 211:519–528

Low RN, Chen SC, Barone R et al (2003) Distinguishing benign from malignant bowel obstruction in patients with malignancy: findings at MRI. Radiology 228:157–165

Low RN, Duggan B, Barone RM et al (2005) Treated ovarian cancer: MR imaging, laparotomy reassessment, and serum CA-125 values compared with clinical outcome at 1 year. Radiology 235:918–926

Low RN, Barone RM, Lucero J (2015) comparison of MRI and CT for predicting the peritoneal cancer index (PCI) preoperatively in patients being considered for cytoreductive surgical procedures. Ann Surg Oncol 22:1708–1715

Megibow AJ, Hulnik DH, Bosniak MA et al (1985) Ovarian metastases: computed tomographic appearances. Radiology 156:161–164

Michielsen K, Vergote I, de Beeck O et al (2014) Whole–body MRI with diffusion-weighted sequence for staging of patients with suspected ovarian cancer: a clinical feasibility study in comparison to CT and FDG-PET/CT. Eur Radiol 24:889–901

Mironov O, Ishill NM, Mironov S, Vargas HA et al (2011) Pleural effusion detected at CT prior to primary cytoreduction for stage III or IV ovarian carcinoma: effect on survival. Radiology 258:776–784

Mitchell DG, Javitt MC, Glanc P et al (2013) ACR appropriateness criteria staging and follow-up of ovarian cancer. J Am Coll Radiol 10:822–827

Moyer VA (2012) Screening for ovarian cancer. US preventive service task force reaffirmation recommendation statement. Ann Intern Med 157:900–904

Neto N, Cunha TM (2015) Do hereditary syndrome-related gynecologic cancers have any specific features. Insights Imaging 6:545–552

Nougaret S, Addley HC, Colombo PE, Fujii S, Al Sharif SS, Tirumani SH, Jardon K, Sala E, Reinhold C (2012) Ovarian carcinomatosis: how the radiologist can help plan the surgical approach. Radiographics 32:1775–1800

Onyiuke I, Kirby AB, McCarthy S (2013) Primary gynecologic lymphoma: imaging findings. AJR 201:W648–W655

Outwater EK, Wagner BJ, Mannion C et al (1998) Sex cord stromal and steroid cell tumors of the ovary. Radiographics 18:1523–1546

Ovarian Cancer Statistics. www.cancerresearch uk.org

Ozols RF, Schwartz PE, Eifel PJ (2001) Ovarian cancer, fallopian tube carcinoma, and peritoneal carcinoma. In: De Vita Jr VT, Hellman S, Rosenberg SA (eds) Cancer: principles and practice of oncology, 6th edn. Lippincott Williams & Wilkins, Philadelphia, pp 1597–1632

Patel CM, Sahdev A, Reznek RH (2011) CT, MRI and PET imaging in peritoneal malignancy. Cancer Imaging 11:123–139

Pennington KP, Wsisher EM (2012) Hereditary ovarian cancer: beyond usual aspects. Gynecol Oncol 124: 347–353

Pfanneberg C, Schwenzer NF, Bruecher BL (2013) State of the Art Bildgebung bei Peritonealkarzinose. Fortschr Röntgenstr 184:205–213

Quayyum A, Coakley FV, Westphalen AC et al (2005) Role of CT and MRI in predicting optimal cytoreduction of newly diagnosed primary epithelial ovarian cancer. Gynecol Oncol 96:301–306

Queiroz MA, Kubik-Huch R, Hauser N, Freiwald-Chilla B et al (2015) PET/MRI and PET/CT in advanced gynecological tumors: initial experience and comparison. Eur Radiol 25:2222–2230

Rockall A (2014) Diffusion weighted MRI in ovarian cancer. Curr Opin Oncol 26:529–535

Runnebaum IB, Arnold N (2013) Genetik des Ovarialkarzinoms. Gynäkologe 46:553–559

Sala E, Rockall AG, Freeman SJ et al (2013) The added role of MR imaging in treatment stratification of patients with gynecologic malignancies: what the radiologists needs to know. Radiology 266:717–740

Schmidt S, Meuli RA, Achtari C, Prior JO (2015) Peritoneal carcinomatosis in primary ovarian cancer staging: comparison between MDCT, MRI and 18F-FDGPET/CT. Clin Nucl Med 40:371–377

Seidman JD, Russell P, Kurman RJ (2002) Surface epithelial tumors of the ovary. In: Kurman RJ (ed) Blaustein's pathology of the female genital tract. Springer, Berlin/Heidelberg/New York, pp 791–904

Sohaib SAA, Sahdev A, Trappen V et al (2003) Characterization of adnexal lesions on MRI. AJR Am J Roentgenol 180:1297–1304

Spencer JA, Perren TJ (2010) Recent EORTC and MRCUK studies: implications for imaging ovarian cancer. Cancer Imaging 10:135–136

Stevens SK, Hricak H, Stern JL (1991) Ovarian lesions: detection and characterization with gadolinium-enhanced MRI at 1.5 T. Radiology 181:481–488

Suidan RS, Ramirez PT, Sarasohn DM, Teitcher JB et al (2014) A multicenter prospective trial evaluating the ability of preoperative computed tomography scan and serum CA-125 to predict suboptimal cytoreduction at primary debulking surgery for advanced ovarian, fallopian tube, and peritoneal cancer. Gynecol Oncol 34:455–461

Tanaka YU, Kurosaki Y, Nishida M et al (1994) Ovarian dysgerminoma: MR and CT appearance. J Comput Assist Tomogr 18:443–448

Tanaka YO, Tsunoda H, Kitagawa Y et al (2004) Functioning ovarian tumors: direct and indirect findings at MRI. Radiographics 24:S147–S166

Tanaka YO, Okada S, Yagi T, Satoh T, Oki A, Tsunoda H, Yoshikawa H (2010) MRI of endometriotic cysts in association with ovarian carcinoma. AJR 194:355–361

Tanaka Y, Okada S, Satoh T, Matsumoto K, Oki A et al (2016) Differentiation of epithelial ovarian cancer subtypes by use of imaging and clinical data: a detailed analysis. Cancer Imaging 16:3

Tayfur M, Kocabas A, Kaygisiz A, Tiryaki S, Polat M, Cefle K (2007) Dysgerminoma arising in Swyer syndrome. Internet J Pathology 7:2

Thomassin-Naggara I, Daraï E, Cuenod CA et al (2008a) Dynamic contrast-enhanced magnetic resonance imaging: a useful tool for characterizing ovarian epithelial tumours. J Magn Reson Imaging 28:111–1120

Thomassin-Naggara I, Bazot M, Daraï E et al (2008b) Epithelial ovarian tumours: value of dynamic contrast-enhanced MR imaging and correlation with tumour angiogenesis. Radiology 248:148–159

Thomassin-Naggara I, Daraï E, Cuenod CA, Fournier L, Toussaint C, Bazot M (2009) Contribution of diffusion-weighted MR imaging for predicting benignity of complex adnexal masses. Eur Radiol 19:1544–1552

Thomassin-Naggara I, Balvay D, Aubert E et al (2012) Quantitative dynamic contrast-enhanced MR imaging analysis of complex adnexal masses: a preliminary study. Eur Radiol 22:738–745

Thomassin-Naggara I, Aubert E, Rockall A et al (2013) Adnexal masses: development and preliminary validation of an MR imaging scoring system. Radiology 267: 432–443

Timmerman D, Valentin L, Bourne TH, Collins WP, Verrelst H (2000) Terms, definitions and measurements to describe the sonographic features of adnexal tumors: a consensus opinion from the International Ovarian Tumor Analysis (IOTA) group. Ultrasound Obstet Gynecol 16:500–505

Togashi K (2003) Ovarian cancer: the role of US, CT and MRI. Eur Radiol 13(Suppl 4):L87–L104

Tsili AC, Tsampoulas C, Argyropoulou M et al (2008) Comparative evaluation of multidetector CT and MR imaging in the differentiation of adnexal masses. Eur Radiol 18:1049–1057

Yamaoka T, Togashi K, Koyama T et al (2003) Immature teratoma of the ovary: correlation of MR imaging and pathologic findings. Eur Radiol 13:313–319

Young RH, Scully RE (2002a) Sex-cord-stromal, steroid cell, and other ovarian tumors. In: Kurman RJ (ed) Blaustein's pathology of the female genital tract, 5th edn. Springer, Berlin\Heidelberg\New York, pp 905–965

Young RH, Scully RE (2002b) Metastatic tumors of the ovary. In: Kurmann RJ (ed) Blausteins's pathology of the female genital tract, 5th edn. Springer, Berlin\Heidelberg\New York, pp 1063–1101

Zhao SH, Quiang JW, Zhang GF, Ma FH, Cai SQ, LiHM WL (2014a) Diffusion-weighted MR imaging for differentiating borderline from malignant epithelial tumours of the ovary: pathological correlation. Eur Radiol 24:2292–2299

Zhao SH, Quiang JW, Zhang GF, Wang SJ, Qiu HJ, Wang L (2014b) MRI in differentiating ovarian borderline from benign mucinous cystadenoma: pathologic correlation. J Magn Reson Imaging 39:162–166

Endometriosis

Vera Schreiter and Karen Kinkel

Contents

V. Schreiter, MD, PD (✉)
Department of Radiology, Charité – Universitätsmedizin Berlin,
Augustenburger Platz 1, 13353 Berlin, Germany
e-mail: vera.schreiter@charite.de

K. Kinkel, MD, PD
Institut de Radiologie, Clinique des Grangettes,
ch. des Grangettes 7, 1224 Chêne-Bougeries, Geneva, Switzerland
e-mail: karen.kinkel@grangettes.ch

Abstract

While endometriosis is a benign disease of the female pelvis, it can be a very aggressive, invasive condition. The diagnosis is often delayed and difficult, and laparoscopy remains the gold standard. Among noninvasive diagnostic options, ultrasound has a role in diagnosing local manifestations of endometriosis, while magnetic resonance imaging (MRI) is gaining popularity. Patient preparation and selection of an adequate imaging protocol will help to fully exploit the diagnostic potential of MRI mapping of endometriotic lesion localization. The interpretation of MR images should use a checklist to search for lesions based on the most common locations of endometriosis and typical changes in MRI signal intensity.

1 Introduction

With an estimated prevalence of 10–15%, endometriosis is the third most common benign disease in women of premenopausal age after adenomyosis and fibroids of the uterus (Houston 1984). Endometriosis affects young women, peaking at age 28 (Bloski and Pierson 2008). Premenarchal onset and occurrence in men have been reported (Oliker and Harris 1971; Pinkert et al. 1979; Schrodt et al. 1980). Most women present with abdominal and pelvic pain, dysmenorrhea, dyschezia or other bowel-related symptoms, dysuria

Med Radiol Diagn Imaging (2017)
DOI 10.1007/174_2017_26, © Springer International Publishing AG
Published Online: 21 February 2017

or back pain, and fertility-related problems (Bloski and Pierson 2008). Many of these symptoms are attributable to the aggressive infiltrative nature of endometriosis. Endometrial tissue can occur anywhere in the body. Completely asymptomatic forms of endometriosis also exist (Balasch et al. 1996; Fedele et al. 2004).

The etiology of endometriosis has not been fully elucidated. Six different theories about the underlying mechanism exist, which are in part complementary and in part additive. Currently, the tissue injury and repair (TIAR) theory is considered the most plausible and most widely accepted explanation. This theory was proposed by Leyendecker and assumes that underlying microinjury and repair of the fundocornual raphe lead to enhanced hyper- and dysperistalsis with retrograde expulsion of basal endometrial tissue through the fallopian tubes into the abdominal cavity (Leyendecker et al. 2009). Leyendecker's explanation is a sensible supplement to the older transplantation theory of J. A. Sampson, known as retrograde menstruation (1927). The metaplasia theory proposed by R. Meyer (1919) assumes that endometrial tissue outside the uterus is composed of dedifferentiated celomic cells, which have undergone transformation under various influences and thus lead to extrauterine endometrial implants (Matsuura et al. 1999). Generally, there appears to be a strong association with estrogen (Da Costa e Silva Rde et al. 1992). This phenomenon plays a role in the aromatase theory, which assumes an increased formation of estrogen from C19 androgens, and in personalized treatment approaches (Zeitoun and Bulun 1999). The invasiveness and multifocal ectopic occurrence of the condition are explained by the cellular and molecular biological concepts with disturbed tissue integrity. Explanations for the lack of intrinsic defense mechanisms of the body against the invasive growth of endometriosis are proposed by immunological concepts involving cytokines, growth factors, and various hormones (Khorram et al. 1993; Halme et al. 1988; Vinatier et al. 1996).

The diagnosis of endometriosis is difficult and takes on average 6 years or even longer (Hadfield et al. 1996). Laparoscopy, combining visual inspection with the option of obtaining tissue for histology, remains the gold standard for the diagnosis of endometriosis (Dunselman et al. 2014). Besides the initial diagnosis comprising a gynecologic history and pelvic examination, laboratory testing (CA 125), and an ultrasound examination, magnetic resonance imaging (MRI) is gaining an increasing role, especially for preoperative mapping in women with extensive involvement and for diagnosis of recurrent endometriosis.

2 Imaging Techniques and Findings

2.1 Sonography

Vaginal ultrasound is the first-line diagnostic imaging modality in women with endometriosis; however, because of its limited range, it should be supplemented by additional examinations such as transrectal and/or transabdominal ultrasound and MRI, as well as endoscopic examinations including rectosigmoidoscopy and cystoscopy.

Vaginal ultrasound allows identification of ovarian manifestations of endometriosis as well as involvement of directly adjacent organs such as the urinary bladder and intestine and also provides information for differentiation of endometriosis from adenomyosis of the uterus (Lazzeri et al. 2014). Ovarian manifestations of endometriosis are known as endometriomas, chocolate cysts, or endometriotic cysts. They are categorized as benign cystic and cyst-like ovarian lesions and must be differentiated from other ovarian cystic lesions: functional ovarian cysts (follicular and corpus luteum cysts), surface epithelial inclusion cysts, ovarian dermoid cysts, ovarian cyst mimics (paraovarian cyst, paratubal cyst), cyst-like lesions (hydrosalpinx, tubo-ovarian abscess, lymphocele), benign epithelial ovarian tumors (serous cystadenomas, cystadenofibromas, mucinous cystadenomas), borderline tumors, and carcinoma of the ovary (Fleischer et al. 1978; Atri et al. 1994; Ekici et al. 1996). Sonographically, ovarian endometriotic cysts are hypoechoic cysts with low-level internal echoes and no demonstration of intralesional flow signals by color Doppler ultrasound (Patel et al. 1999). There is no hyperechoic solid node on the wall. In up to 30% of cases, small hyperechoic foci consistent with cell debris, cholesterol deposits, or small hemorrhages are seen within the lesion (Savelli 2009). Such hyperechoic internal foci must be differentiated from

wall-related hyperechoic structures with maximum diagnostic confidence to rule out a possible malignant component (ovarian cancer). This may necessitate an additional MRI examination since even additional functional assessment by color Doppler imaging often provides no reliable diagnosis either (Wu et al. 2004). With its high soft tissue contrast, MRI appears to be a valuable noninvasive diagnostic imaging modality for further evaluation of extragenital endometriotic lesions and second-line evaluation of some genital lesions: MRI primarily offers advantages in the characterization of nongenital endometric lesions, which often have a noncystic appearance (Bazot et al. 2004a).

Supplementary abdominal ultrasound should focus on the morphologic evaluation of both kidneys for ruling out possible secondary urinary stasis, evaluation of the filled bladder to rule out bladder endometriosis (supplemented by cystoscopy as needed), and on ruling out endometriosis of the appendix (Carmignani et al. 2010; Vercellini et al. 1996; Halis et al. 2010). When rectovaginal endometriosis is suspected, diagnostic workup should be supplemented by MRI and transrectal ultrasound and, possibly, followed by rectosigmoidoscopy (Halis et al. 2010; Fedele et al. 1998).

2.2 MRI

Based on current knowledge, MRI has the following indications: second-line imaging modality for pelvic endometriosis following ultrasound examination, patients with clinical symptoms and negative and/or indeterminate sonographic findings (Guerriero et al. 2015, 2016), and as a staging investigation prior to surgery in patients with multifocal deep infiltrating endometriosis (Medeiros et al. 2015).

Despite qualitative differences in terms of spatial resolution (Hottat et al. 2009; Rousset et al. 2014; Manganaro et al. 2012) and fat suppression (Manganaro et al. 2012; Cornfeld and Weinreb 2008), both 1.5 T and 3.0 T MRI appear to be suitable for examining women with endometriosis. The use of a pelvic phased-array coil is recommended because of the higher signal-to-noise ratio (McCauley et al. 1992; Kier et al. 1993). Patients should be examined supine; claustrophobic patients may be examined in prone position. Good bowel preparation is essential when looking for deep endometriotic nodules. Peristalsis should be eliminated to a maximum by administration of antiperistaltic medication (e.g., 1 mg glucagon (GlucaGen ®, Novo Nordisk ®; Bagsværd, Denmark) or 20 mg butylscopolamine (Buscopan ®, Boehringer Ingelheim GmbH; Ingelheim, Germany)) (Manganaro et al. 2014). Additional fasting for 3–6 h before the MRI examination is recommended (Manganaro et al. 2012; Saba et al. 2012; Abrao et al. 2007; Bazot et al. 2009; Fiaschetti et al. 2012; Bazot et al. 2004b; Chamie et al. 2011a). Expert consensus about the best time of the menstrual cycle to perform MRI does not exist according to the new ESUR guidelines (Bazot et al. 2016).

Further measures to be taken before the MRI examination depend on the clinical symptoms and suspected sites of endometriosis. For example, if bladder endometriosis is suspected, the patient should have a moderately filled urinary bladder, which can be accomplished, for example, by having the patient drink 1.5 l of water 45 min before the examination (Grasso et al. 2010; Takeuchi et al. 2005). Filling the rectum with ultrasound gel or water can potentially improve detection of endometrial lesions in the pouch of Douglas and the rectosigmoid junction (Fiaschetti et al. 2012; Takeuchi et al. 2005; Faccioli et al. 2010; Kikuchi et al. 2014) but is not mandatory. This should be done after prior bowel rinsing which is strongly recommended by several authors including the new ESUR guidelines (Chamie et al. 2011a; Bazot et al. 2016; Takeuchi et al. 2005; Yoon et al. 2010) and may possibly be supported by dietary measures starting up to 3 days before the MRI examination (Faccioli et al. 2010).

Vaginal filling with ultrasound gel is another optional measure and can potentially improve detection of endometriotic implants in the posterior vaginal fornix (Fiaschetti et al. 2012; Kikuchi et al. 2014).

The following MRI protocol is recommended for endometriosis mapping:

A T2-weighted (T2w) sequence is the sequence of choice for the detection of pelvic endometriosis, especially of the deep infiltrating type. At least two 2D T2w sequences – fast spin echo (FSE) and turbo spin echo (TSE) – in sagittal and axial planes (Hottat et al. 2009; Manganaro et al. 2012; Saba et al. 2012; Fiaschetti et al. 2012; Bazot

et al. 2004b; Di Paola et al. 2015; Roy et al. 2009; Del Frate et al. 2006; Chassang et al. 2010; Bazot et al. 2013; Kruger et al. 2013; Scardapane et al. 2014) should be acquired. An additional oblique axial T2w can be used to check for uterosacral and parametrial implants (Bazot et al. 2011a; Bazot et al. 2012). The protocol can be optionally supplemented by a 3D T2w sequence, which has high potential for detection of deep endometriotic lesions (Manganaro et al. 2012; Bazot et al. 2013).

T1-weighted (T1w) spin echo (SE) sequences in axial and sagittal planes with and without fat suppression (FS) are the sequences of choice/gold standard for the detection of ovarian endometriotic cysts, comparatively rated with T2w sequences for definitive diagnosis (Togashi et al. 1991). FS with a Dixon sequence enables simultaneous acquisition of four different T1w contrasts and stronger fat suppression, which is advantageous primarily when imaging is performed at 3 tesla (Cornfeld and Weinreb 2008; Cornfeld et al. 2008). Preliminary results suggest that T1w sequences with FS have advantages in the detection of peritoneal endometriosis (Ha et al. 1994; Tanaka et al. 1996).

Deep infiltrating endometriosis continues to be a challenge for morphologic imaging, which is why there is a long controversy about which additional pulse sequences are most beneficial. Currently available data suggest that contrast-enhanced T1w sequences, diffusion-weighted imaging (DWI), and susceptibility-weighted sequences do not improve detection of deep infiltrating endometriosis (Busard et al. 2010; Bazot et al. 2011b). Single-shot fast spin echo (SSFSE) or half-Fourier acquisition single-shot turbo spin echo (HASTE) imaging can be used to evaluate uterine function by assessing uterine peristalsis and possible adhesions to other organs (Hodler et al. 2014).

The radiologist interpreting the MRI dataset should use a checklist of all potential localizations of endometriosis for structured interpretation of images. These are:

1. Ovaries
2. Vesicouterine pouch and urinary bladder
3. The vaginal wall and in particular the posterior fornix of the upper vaginal wall
4. The uterine ligaments including the uterosacral ligaments and the round ligaments, the lateral and anterior pelvic wall, the parametrium, and the peritoneum
5. Bowel, specifically the anterior rectum and the sigmoid, the cecum, the ileum, and the appendix
6. Rare localizations, special types, and associated complications

3 MR Imaging Findings

3.1 Endometriosis of the Ovaries: Endometriotic Cysts or Endometriomas

Endometrial cysts or endometriomas in this location are hyperintense or isointense to subcutaneous fat on plain T1w images without a decrease in signal on T1w with FS; hyperintense foci on T1w images with FS indicate hemorrhagic deposits; the T2 appearance is characterized by a shading effect (Togashi et al. 1991) (Figs. 1 and 2). The wall appears thickened, and bilateral or multifocal lesions are common. It is important to identify any changes suspicious for malignancy

Fig. 1 (**a**–**d**) A 49-year-old woman with chronic left pelvic pain and an office ultrasound suspicious for bilateral ovarian cancer. (**a**) Oblique view of the right ovary at color Doppler transvaginal ultrasound demonstrates a heterogeneous right ovarian mass with small hyperechoic foci in the wall of the cyst (*arrowhead*). The intra- or extracystic location of peripheral color Doppler flow (*arrow*) is difficult to diagnose. Pelvic MRI is performed to exclude ovarian cancer. (**b**) Axial T2-weighted FSE image of the pelvis shows two right-sided ovarian cysts of intermediate signal intensity and one left-sided ovarian cyst with shading of signal intensity (*arrow*). (**c**) Axial T1-weighted image shows bilateral T1 hyperintense content of all three cysts and a speculated nodule between the two ovaries (*arrow*) with one hypointense line extending from the nodule toward the anterior rectum. (**d**) Axial T1-weighted fat-suppressed T1-weighted image at the same level as **c** confirms the hemorrhagic nature of all ovarian cysts and the interovarian peritoneal implant, suggesting endometriosis. At surgery, bilateral endometriomas were attached to each other (kissing ovaries) and associated with severe adhesions toward the rectosigmoid. Pathology confirmed bilateral endometriomas without malignancy

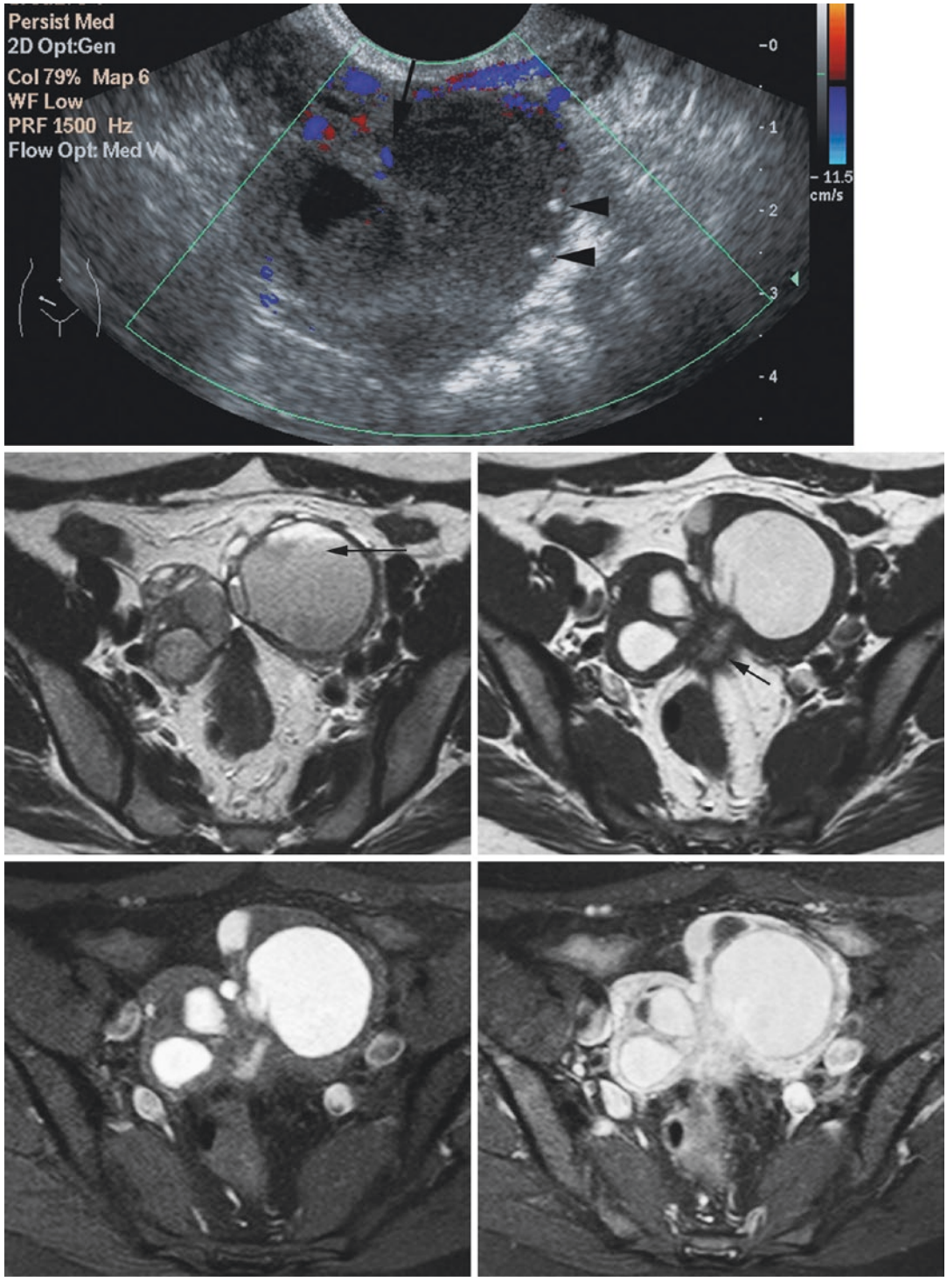
Persist Med
2D Opt:Gen
Col 79% Map 6
WF Low
PRF 1500 Hz
Flow Opt: Med V
-0
-1
-2
-3
-4
11.5
cm/s

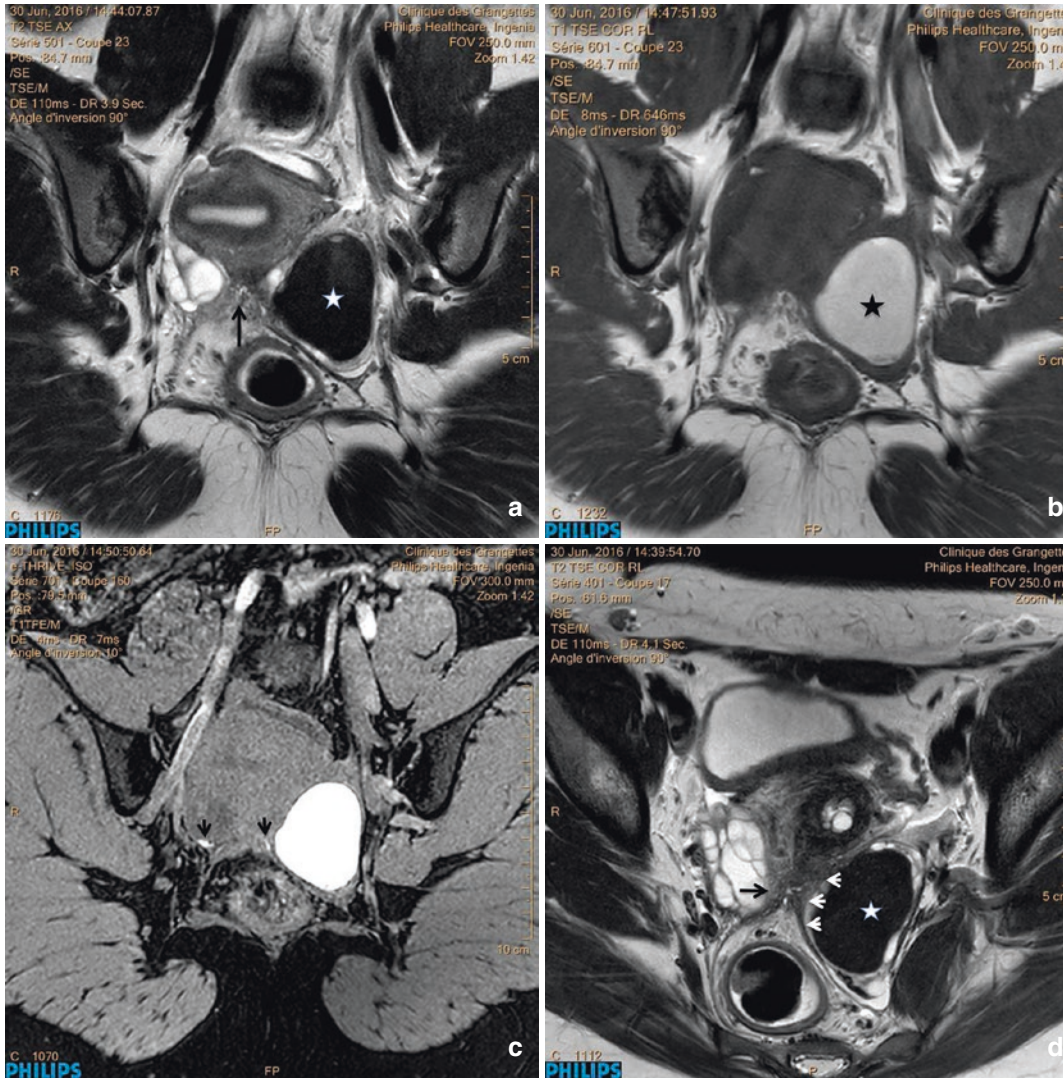

Fig. 2 (**a**–**d**) A 27-year-old woman undergoes MRI of the pelvis for characterization of a complex left ovarian mass with elevated serum CA 125 level. (**a**) Coronal T2-weighted image shows a hypointense mass in the left ovary (*white star*) and additional tissue between both ovaries and below the uterine isthmus (*black arrow*). (**b**) Coronal T1-weighted image at the same shows a hyperintense content of the left ovarian mass (*black star*) that remains hyperintense in the fat-suppressed T1-weighted image in (c). (**c**) In addition to the hemorrhagic cyst of the left ovary, the hyperintense spots (*black arrows*) within the fibrous structure below the uterus and at the periphery of the left ovary suggest peritoneal implants of endometriosis and possible deep endometriosis of the retrocervical region. (**d**) Axial T2-weighted image through the cervix shows the typical T2 hypointense shading of the left endometrioma (*white star*) and abnormal thickening of the right uterosacral ligament (*black arrow*). The left uterosacral ligament (*white arrows*) is displaced medially toward the right uterosacral ligament with a fibrous structure at the level of the torus uterinus. Subsequent surgery and pathology confirmed a left endometrioma and endometriosis of the torus uterinus and right uterosacral ligament

such as solid nodules of intermediate T2 signal intensity within the cyst, peritoneal metastases, or thickened intracystic septa (> 3 mm). If contrast-enhanced T1w images have been obtained, suspicious changes may be suggested by contrast enhancement within the cyst (Wu et al. 2004). According to the new ESUR guidelines for complex adnexal masses, contrast enhancement is mandatory (Bazot et al. 2016; Forstner et al. 2016).

3.2 Endometriosis of the Vesicouterine Pouch and the Urinary Bladder

As described above, it is helpful to prepare the patient to ensure moderate urinary bladder filling for optimal detectability of endometriotic tissue in the bladder wall. Manifestations appear as nodules of low T1 and T2 signal intensity and are most often located in the bladder wall at the level of the vesicouterine pouch forming an obtuse angle with the bladder. Hemorrhage within a nodule has high T1 signal intensity (Bazot et al. 2004b) (Fig. 3). In the event of bladder endometriosis, the distance to the ureterovesical junction and potential hydronephrosis can be assessed with both T2-weighted sequences and URO-MRI sequences.

3.3 Endometriosis of the Vaginal Wall and in Particular the Posterior Fornix of the Upper Vaginal Wall

Endometriosis of the vagina predominantly involves the upper posterior third of the vaginal wall. The extent of disease and locations in the posterior vaginal pouch profit from contrast filling of the vagina with sonographic gel (Dessole

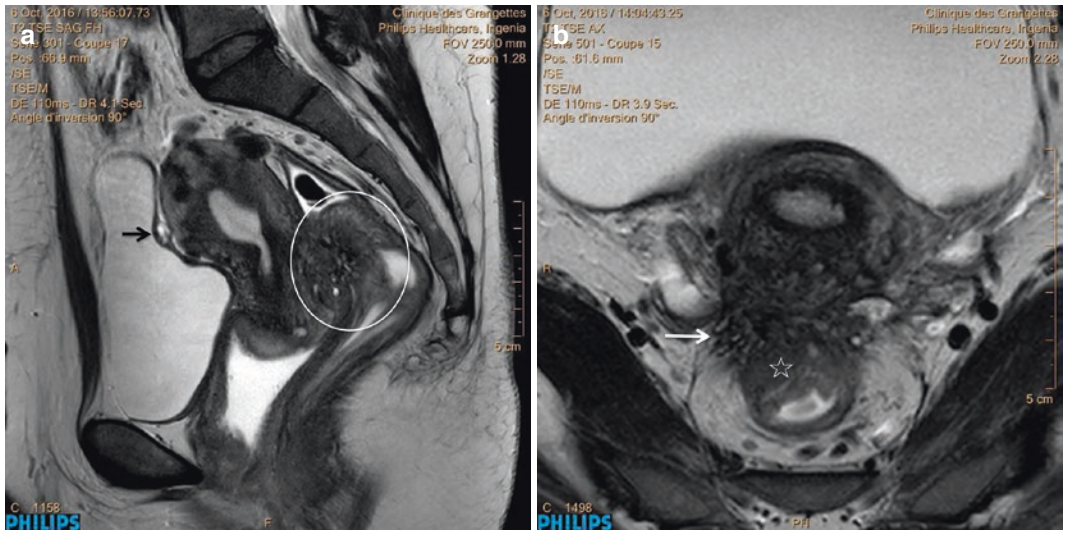

Fig. 3 (**a**–**e**) A 36-year-old woman with a painful retrocervical nodule and a history of surgery for endometriosis 1 year ago. (**a**) Sagittal T2-weighted image demonstrates a retrocervical mass extending into the rectosigmoid and the posterior vaginal fornix (*white ellipse*). The posterior bladder wall has a hyperintense nodule (*black arrow*). (**b**) Axial T2-weighted image through the center of the retrocervical nodule shows extension into the initial portion of the right uterosacral ligament (*white arrow*) and the anterior rectal wall (*white star*). (**c**) Coronal T2-weighted image through the rectal wall demonstrates an extension of the rectal nodule into the pararectal fat (*white arrows*). (**d**) Sagittal T1-weighted fat-suppressed image after intravenous injection of paramagnetic contrast confirms vascularity of the vaginal and rectal extension of the retrocervical nodule (*black star*) and shows small subserosal leiomyomas (*white arrows*). (**e**) Axial T1-weighted fat-suppressed image through the nodule of the bladder wall demonstrates a hemorrhagic portion (*white arrow*). Surgery and pathology confirms bladder, vaginal, retrocervical, and rectosigmoid deep endometriosis

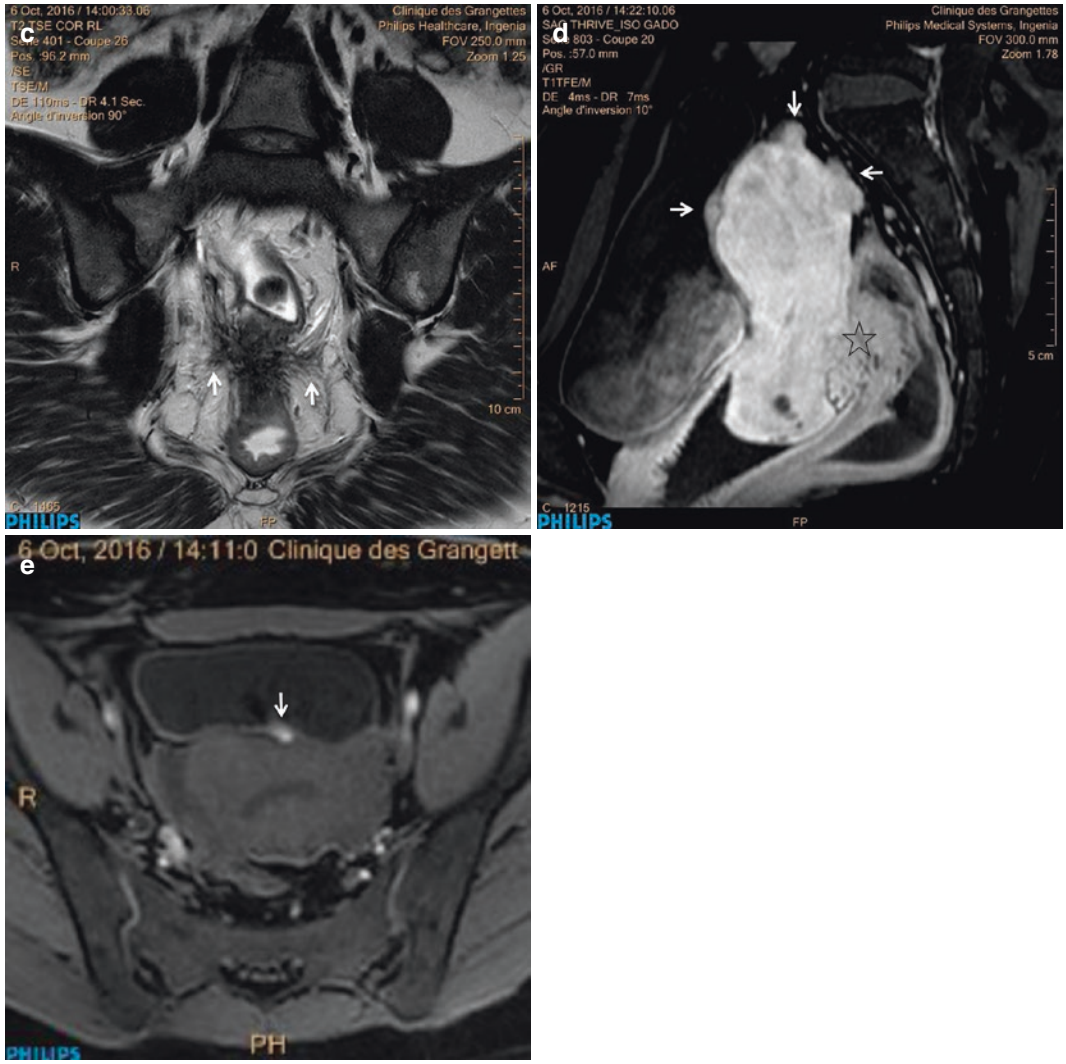

Fig. 3 (continued)

et al. 2003). Vaginal endometriosis is hypointense on T2w images and isointense on T1w images (Bazot et al. 2009), and the lesions may contain hyperintense spots in both sequences. Endometriosis of the posterior vagina is often associated with a thickened posterior cervical wall (Bazot and Darai 2005). Most vaginal lesions are associated with an obliteration of the pouch of Douglas extending in the upper retrocervical region, the lower or anterior rectosigmoid, or both (Figs. 3 and 4).

Endometriotic tissue in the rectovaginal septum can be associated with endometriotic lesions of the vagina, the rectosigmoid or uterosacral ligaments most notably in association with deep infiltrating endometriosis (Bazot and Darai 2005).

In up to 61% of cases, endometriotic lesions of the rectouterine pouch have high-signal-intensity areas on T1w images, which correspond to cystic hemorrhagic components in pathologic correlation (Bazot et al. 2004b; Kinkel et al.

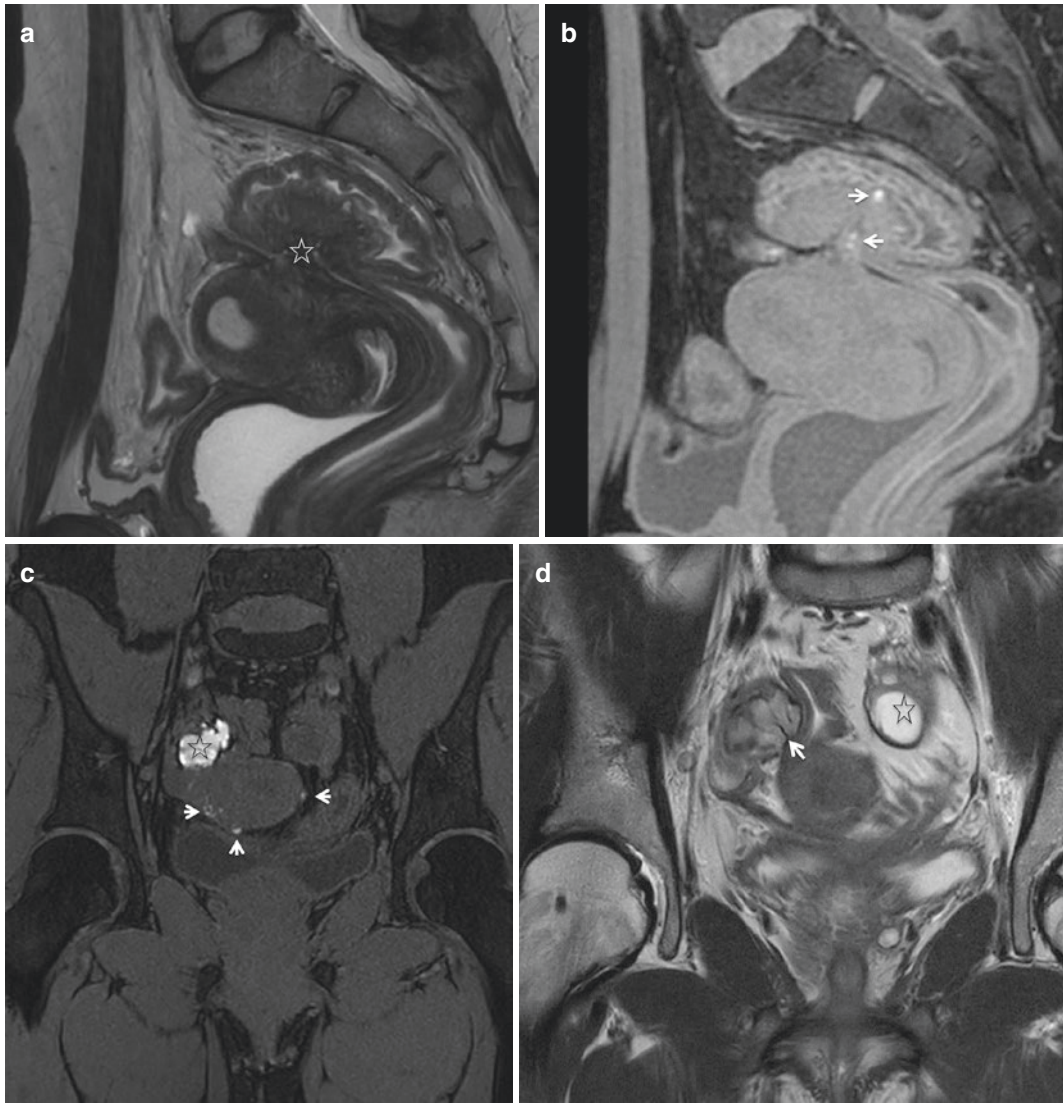

Fig. 4 (**a**–**d**) A 30-year-old woman with persistent dysmenorrhea 3 years after laparoscopic removal of a left endometrioma. (**a**) Sagittal T2-weighted image shows additional tissue at the posterior wall of the uterus (*white star*) extending into the inferior wall of the sigmoid. (**b**) Sagittal T1-weighted image (same level as **a**) indicates a small hemorrhagic portion (*white arrows*) in the submucosal of the abnormal bowel wall and within the adhesion between the sigmoid and the retroisthmic part of the uterus. (**c**) Coronal T1-weighted fat-suppressed image through the midportion of the uterus demonstrates a tubular hemorrhagic right adnexal structure compatible with hematosalpinx (*white arrow*). Other hyperintense spots in contact with the uterus suggest peritoneal implants. (**d**) The T2-weighted image at the same level as **c** shows multiple incomplete septa (*white arrow*) and confirms the tubular origin of the hemorrhagic right mass. A normal follicule can be seen in the left ovary (*black star*). Laparoscopic resection of the thickened sigmoid wall and the right tube confirmed deep endometriosis of the sigmoid and endometriosis of the right tube

1999). However, the absence of T1 hyperintense areas does not exclude the diagnosis.

3.4 Endometriosis of the Uterine Ligaments Including the Uterosacral Ligaments and the Round Ligaments, the Lateral and Anterior Pelvic Wall, and the Parametrium and the Peritoneum

Endometriotic infiltration of the uterine ligaments such as the uterosacral ligament or the round ligament is seen as unilateral or bilateral nodular lesions (regular or with stellate margins) and/or fibrotic thickening of the affected ligaments (Bazot et al. 2004b; Novellas et al. 2010) (Figs. 4, 5, 6, and 7). Endometriotic lesions of the upper posterior cervix are seen as band-like structures of low T2 and T1 signal intensity extending laterally to one or both uterosacral ligaments (Bazot et al. 2004b) (Figs. 5, 6, and 7). Nodular thickening with regular or stellate margins at the initial uterine portion of the uterosacral ligament is easier to identify on T2-weighted images obtained in an oblique orientation perpendicular to the long axis of the cervical channel (Bazot and Darai 2005; Kinkel et al. 2006).

Parametrial and pelvic wall endometriosis (with muscle infiltration) is characterized by low T2 signal intensity, and the lesions may contain hyperintense spots (Bazot et al. 2012). Pelvic wall endometriosis may affect the pelvic muscles such as the piriformis, coccygeus, or obturator muscles leading to extension of the endometriosis to the sciatic or pudendal nerve.

3.5 Endometriosis of the Bowel, Specifically the Anterior Rectum and the Sigmoid, the Cecum, the Ileum, and the Appendix

Deep infiltrating endometriotic lesions are defined by their morphologic appearance and signal intensity and may be found anywhere in the body. Most endometriotic lesions of the bowel are of a deep infiltrating nature and detected by abnormal wall thickening (Figs. 4 and 6). They are isointense to muscle on T2w and T1w images (Busard et al. 2012). Hyperintense foci on T1w images (+/− FS) correspond to hemorrhagic spots (Chamie et al. 2011b). Cavities have high

Fig. 5 (**a**–**e**) A 40-year-old woman with unexplained dysmenorrhea, perimenstrual hematuria, and infertility. (**a**) Sagittal T2-weighted image shows bladder wall thickening (*white star*), small cystic spaces within the myometrium, and nabothian cysts within the cervical stroma. (**b**) Coronal oblique T2-weighted image confirms a cystic and solid mass of the bladder wall (*black arrow*) typical of bladder endometriosis. (**c**) Axial oblique T2-weighted image through the upper portion of the bladder mass (*white star*) shows an irregular contour of the anterior uterus with a fibrous nodule (*white arrow*) in the pouch between the bladder and the uterus as well as cystic spaces in the myometrium suggesting adenomyosis. The enlarged right uterosacral ligament (*black arrow*) and anterior rectal wall close to the posterior uterus (*white circle*) suggest deep endometriosis of the rectum and the right uterosacral ligament. (**d**) Contrast-enhanced T1-weighted sagittal image of the mid-pelvis shows the abnormally thickened bladder wall (*white star*) and a small retrocervical nodule (*black arrow*). There are indistinct margins between the anterior sigmoid and the posterior myometrium (*white arrow*). (**e**) The axial fat-suppressed T1-weighted image through the cervix shows hemorrhagic spots (*white arrows*) within the right uterosacral ligament, the torus uterinus, and the bladder wall. Surgery performed partial cystectomy and ablation of the right uterosacral ligament. Associated bowel endometriosis and adenomyosis were treated medically

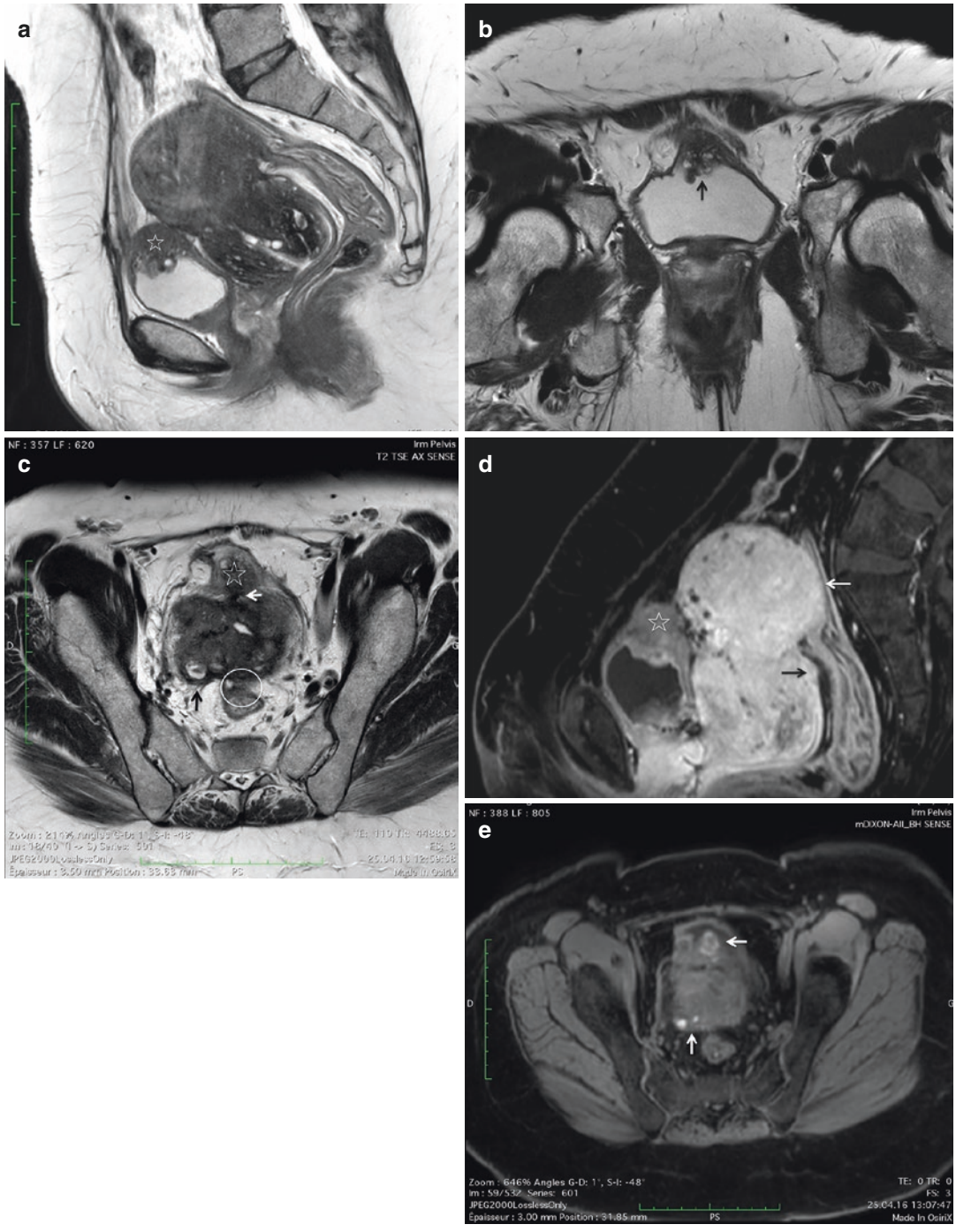
a
b
c
NF : 357 LF : 620
Irm Pelvis
T2 TSE AX SENSE
d
e
NF : 388 LF : 805
Irm Pelvis
mDIXON-All_BH SENSE
Zoom : 646% Angles G-D: 1°, S-I: -48°
im : 59/532 Series: 601
JPEG2000LosslessOnly
Épaisseur : 3.00 mm Position : 31.85 mm
PS
TE: 0 TR: 0
FS: 3
25.04.16 13:07:47
Made In OsiriX

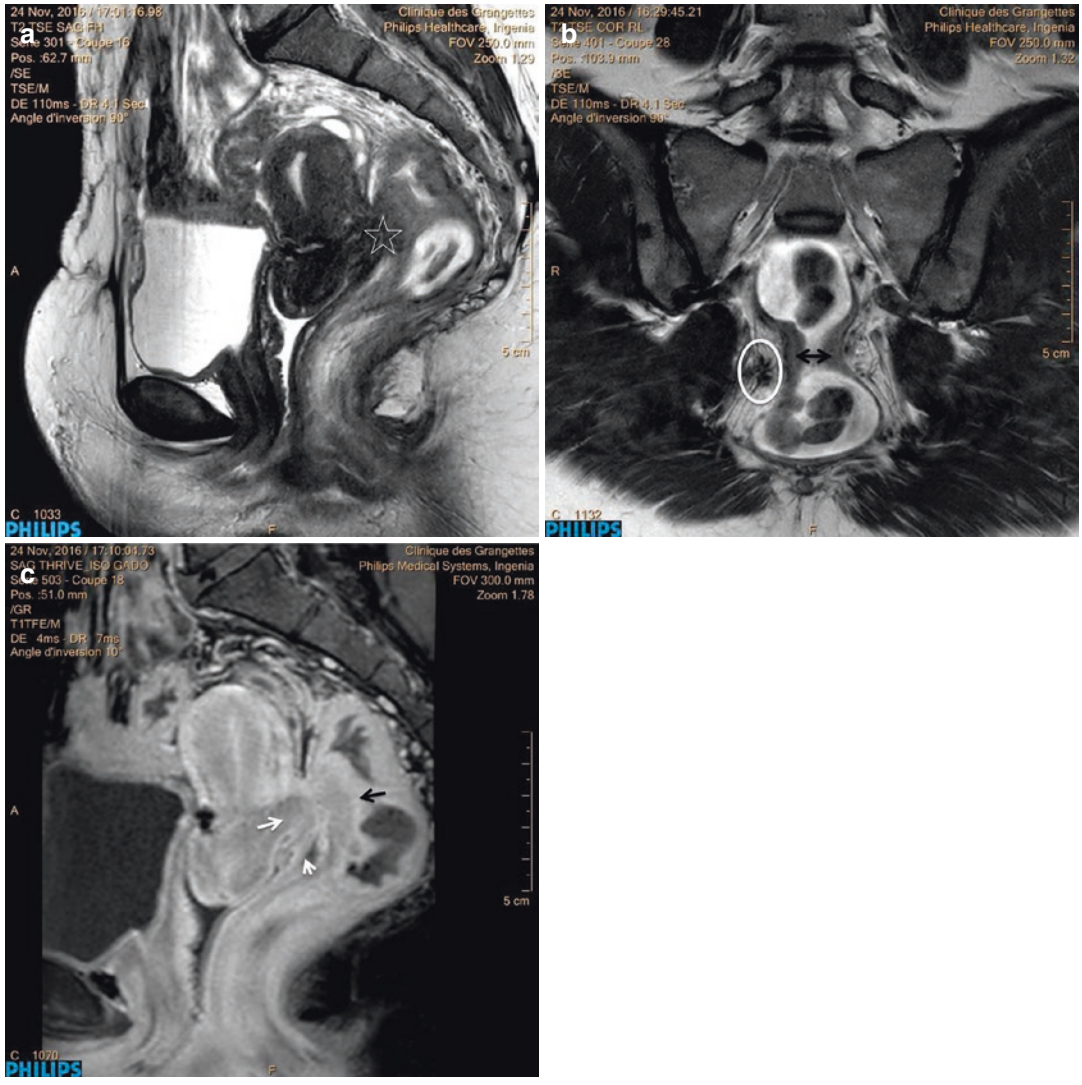

Fig. 6 (**a**–**c**) A 40-year-old woman with a palpable nodule in the Douglas pouch and three unsuccessful in vitro fertilization after a cesarean section 10 years ago. (**a**) Sagittal T2-weighted image with gel filling of the vagina confirms a heterogeneous mass between the uterus and the rectum extending to the posterior vaginal fornix (*white star*). (**b**) Coronal T2-weighted image through the rectum shows localized wall thickening (*black arrow*) and a spiculated nodule in the right pararectal fat (*white ellipse*) corresponding to a thickened portion of the mid right uterosacral ligament. (**c**) Sagittal contrast-enhanced T1-weighted fat-suppressed image depicts all the solid portions of the deep endometriotic nodule: the rectosigmoid junction (*black arrow*), the torus uterinus (*long white arrow*), and the posterior vaginal cuff (*short white arrow*) confirmed by subsequent surgery and pathology

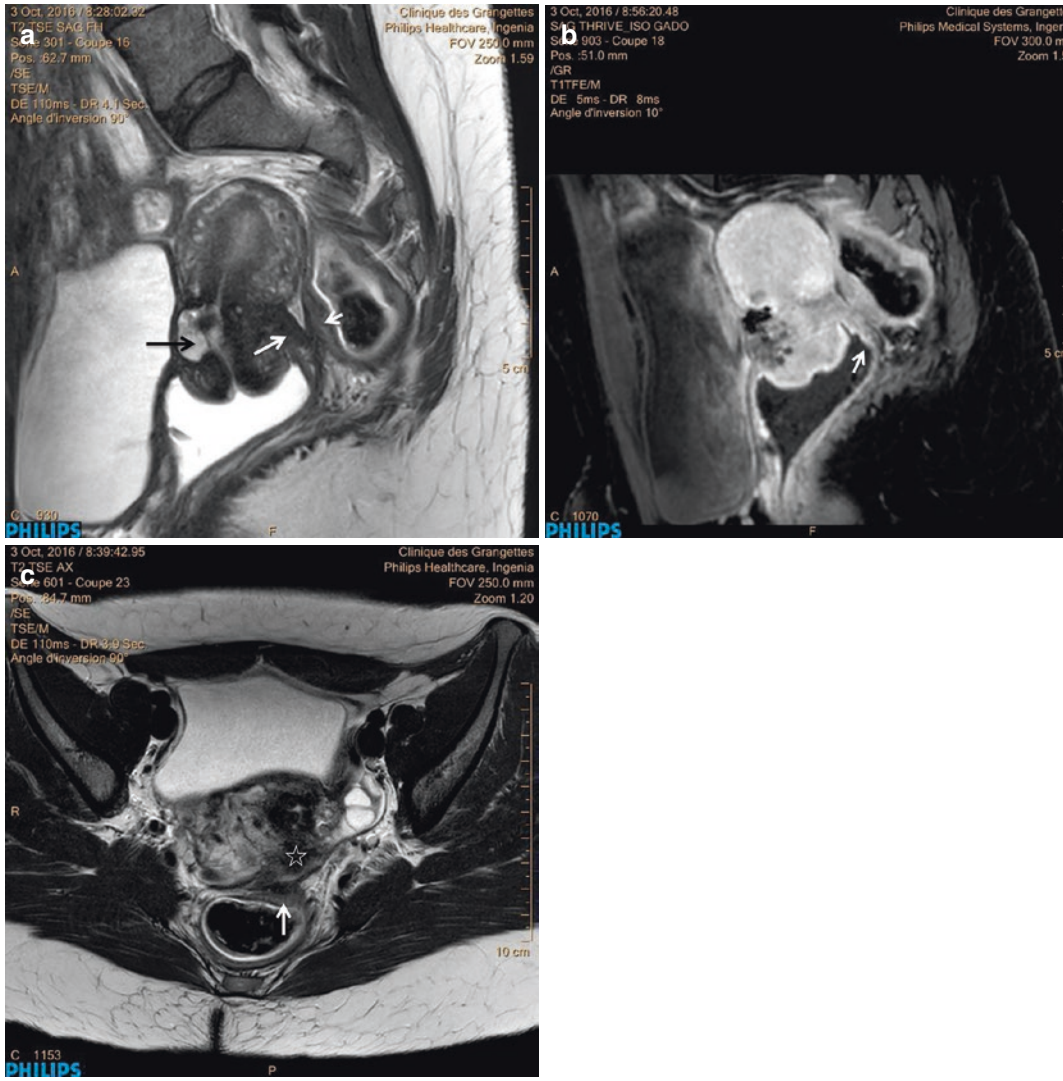

Fig. 7 (**a**–**c**) A 36-year-old woman with painful defecation during menstruation and a sonographic suspicion of retrocervical endometriosis. (**a**) Sagittal T2-weighted image with gel filling of the vagina shows a "butterfly"-shaped mass behind the cervix with the posterior wing in the anterior rectosigmoid junction (*short white arrow*) and the anterior wing at the torus uterinus and the posterior vaginal cuff (*long white arrow*). Ectasia of the cesarean scar (*black arrow*) displays T2 hyperintensity due to colonization by normal endometrium. (**b**) Sagittal T1-weighted fat-suppressed image at the same level confirms the extension of deep endometriosis into the upper posterior vagina (*white arrow*). The hypointense portion of the cesarean section is due to artifacts. (**c**) Axial T2-weighted image through the cervix shows the larger part of the hypointense mass behind the cervix at the torus uterinus (*white star*) and the second smaller portion in the anterior rectal wall (*white arrow*). Extensive surgery with transvaginal and laparoscopic approach allowed complete resection of all portions of deep endometriosis, confirmed by pathology

T2 signal intensity (Del Frate et al. 2006). The low-signal-intensity border of the intestinal wall on T2w images and surrounding fatty layers are obliterated. Extension into the surrounding fat can affect the intermediate portion of uterosacral ligaments (Fig. 5). Diagnosis of depth of wall infiltration is a difficult task but crucial for surgical decision-making (superficial shaving versus bowel resection). The lesion usually starts at the peritoneal portion of the wall before growing more deeply into the muscular and submucosal portion of the bowel wall. Extension into the mucosa is a rare finding. Other important findings include number of location (one or multiple), size of the lesion (length, thickness, transversal diameter), circumference involved, and the distance of the lowest portion of the lesions to the anal verge.

3.6 Endometriosis in Rare Localizations, Special Types, and Associated Complications

Rare sites of endometriosis include the parietal wall, cecum, appendix, small intestine, diaphragm, perineum, perigastric tissue, and surrounding nerves (sciatic or pudendal nerve) (Novellas et al. 2010; Alizadeh Otaghvar et al. 2014; Idetsu et al. 2007; Ceccaroni et al. 2013; Decker et al. 2004; Vercellini et al. 2003).

A special but common type is deep infiltrating endometriosis, which is particularly challenging for imaging. Deep implants can occur in all locations. Their morphologic MRI appearance has been described in the previous section. Adhesions, or bands of fibrous tissue, are the most common complications of endometriosis and can occur between all genital structures, causing destruction of the normal anatomy (Liakakos et al. 2001; Woodward et al. 2001). Adhesions can be associated with endometriosis and are difficult to identify by imaging; often they are only seen when they are surrounded by fluid. Therefore, it is important to pay attention to secondary imaging signs of adhesions, which include anterior rectal triangular attraction, angulation of bowel loops, abrupt changes in intestinal caliber (possibly with concomitant nodules), obliterated or distorted genital anatomy due to strictures causing traction such as elevation of the posterior vaginal fornix, posterior displacement of the uterus or the ovaries, loculated fluid collections, and hydrosalpinx (Woodward et al. 2001). Spiculated low-signal intensity strands converging toward deep peritoneal lesions of endometriosis are also suggestive of adhesions (McCauley et al. 1992; Togashi 2002).

References

Abrao MS, Goncalves MO, Dias JA Jr, Podgaec S, Chamie LP, Blasbalg R (2007) Comparison between clinical examination, transvaginal sonography and magnetic resonance imaging for the diagnosis of deep endometriosis. Hum Reprod 22:3092–3097

Alizadeh Otaghvar H, Hosseini M, Shabestanipour G, Tizmaghz A, Sedehi Esfahani G (2014) Cecal endometriosis presenting as acute appendicitis. Case Rep Surg 2014:519631

Atri M, Nazarnia S, Bret PM, Aldis AE, Kintzen G, Reinhold C (1994) Endovaginal sonographic appearance of benign ovarian masses. Radiographics 14:747–760

Balasch J, Creus M, Fábregues F, Carmona F, Ordi J, Martinez-Román S, Vanrell JA (1996) Visible and non-visible endometriosis at laparoscopy in fertile and infertile women and in patients with chronic pelvic pain: a prospective study. Hum Reprod 11:387–391

Bazot M, Darai E (2005) Sonography and MR imaging for assessment of deep pelvic endometriosis. J Minim Invasive Gynecol 12:178–185

Bazot M, Thomassin I, Hourani R, Cortez A, Darai E (2004a) Diagnostic accuracy of transvaginalsonography for deep pelvic endometriosis. Ultrasound Obstet Gynecol 24:180–185

Bazot M, Darai E, Hourani R, Thomassin I, Cortez A, Uzan S, Buy JN (2004b) Deep pelvic endometriosis: MR imaging for diagnosis and prediction of extension of disease. Radiology 232:379–389

Bazot M, Lafont C, Rouzier R, Roseau G, Thomassin-Naggara I, Darai E (2009) Diagnostic accuracy of physical examination, transvaginal sonography, rectal endoscopic sonography, and magnetic resonance imaging to diagnose deep infiltrating endometriosis. Fertil Steril 92:1825–1833

Bazot M, Gasner A, Ballester M, Darai E (2011a) Value of thin-section oblique axial T2-weighted magnetic resonance images to assess uterosacral ligament endometriosis. Hum Reprod 26:346–353

Bazot M, Gasner A, Lafont C, Ballester M, Darai E (2011b) Deep pelvic endometriosis: limited additional diagnostic value of postcontrast in comparison with conventional MR images. Eur J Radiol 80:331–339

Bazot M, Jarboui L, Ballester M, Touboul C, Thomassin-Naggara I, Darai E (2012) The value of MRI in assessing parametrial involvement in endometriosis. Hum Reprod 27:2352–2358

Bazot M, Stivalet A, Darai E, Coudray C, Thomassin-Naggara I, Poncelet E (2013) Comparison of 3D and 2D FSE T2-weighted MRI in the diagnosis of deep pelvic endometriosis: preliminary results. Clin Radiol 68:47–54

Bazot M, Bharwani N, Huchon C, Kinkel K, Cunha TM, Guerra A, Manganaro L, Buñesch L, Kido A, Togashi K, Thomassin-Naggara I, Rockall AG (2016) European society of urogenital radiology (ESUR) guidelines: MR imaging of pelvic endometriosis. Eur Radiol [Epub ahead of print]

Bloski T, Pierson R (2008) Endometriosis and chronic pelvic pain: unraveling the mystery behind this complex condition. Nurs Womens Health 12:382–395

Busard MP, Mijatovic V, van Kuijk C, Pieters-van den Bos IC, Hompes PGA, van Waesberghe JH (2010) Magnetic resonance imaging in the evaluation of (deep infiltrating) endometriosis: the value of diffusion-weighted imaging. J Magn Reson Imaging 31:1117–1123

Busard MP, van der Houwen LE, Bleeker MC, van den Bos IC P, Cuesta MA, van Kuijk C, Mijatovic V, Hompes PG, van Waesberghe JH (2012) Deep infiltrating endometriosis of the bowel: MR imaging as a method to predict muscular invasion. Abdom Imaging 37:549–557

Carmignani L, Vercellini P, Spinelli M, Fontana E, Frontino G, Fedele L (2010) Pelvic endometriosis and hydroureteronephrosis. Fertil Steril 93:1741–1744

Ceccaroni M, Roviglione G, Giampaolino P, Clarizia R, Bruni F, Ruffo G, Patrelli TS, De Placido G, Minelli L (2013) Laparoscopic surgical treatment of diaphragmatic endometriosis: a 7-year single-institution retrospective review. Surg Endosc 27:625–632

Chamie LP, Pereira RM, Zanatta A, Serafini PC (2011a) Transvaginal US after bowel preparation for deeply infiltrating endometriosis: protocol, imaging appearances, and laparoscopic correlation. Radiographics 30:1235–1249

Chamie LP, Blasbalg R, Pereira RM, Warmbrand G, Serafini PC (2011b) Findings of pelvic endometriosis at transvaginal us, MR imaging, and laparoscopy. Radiographics 31:E77–100

Chassang M, Novellas S, Bloch-Marcotte C, Delotte J, Toullalan O, Bongain A, Chevallier P (2010) Utility of vaginal and rectal contrast medium in MRI for the detection of deep pelvic endometriosis. Eur Radiol 20:1003–1010

Cornfeld D, Weinreb J (2008) Simple changes to 1.5-T MRI abdomen and pelvis protocols to optimize results at 3 T. AJR Am J Roentgenol 190:W140–W150

Cornfeld DM, Israel G, McCarthy SM, Weinreb JC (2008) Pelvic imaging using a T1 W fat-suppressed three-dimensional dual echo Dixon technique at 3 T. J Magn Reson Imaging 28:121–127

Da Costa e Silva Rde C, Moura KK, Ribeiro Júnior CL, Guillo LA (1992) Estrogen signaling in the proliferative endometrium: implications in endometriosis. Rev Assoc Med Bras 62:72–77

Decker D, König J, Wardelmann E, Richter O, Popat S, Wolff M, Hirner A, Ulrich U (2004) Terminal ileitis with sealed perforation – a rare complication of intestinal endometriosis: case report and short review of the literature. Arch Gynecol Obstet 269:294–298

Del Frate C, Girometti R, Pittino M, Del Frate G, Bazzocchi M, Zuiani C (2006) Deep retroperitoneal pelvic endometriosis: MR imaging appearance with laparoscopic correlation. Radiographics 26:1705–1718

Dessole S, Farina M, Rubattu G, Cosmi E, Ambrosini G, Nardelli GB (2003) Sonovaginography is a new technique for assessing rectovaginal endometriosis. Fertil Steril 79:1023–1027

Di Paola V, Manfredi R, Castelli F, Negrelli R, Mehrabi S, Pozzi Mucelli R (2015) Detection and localization of deep endometriosis by means of MRI and correlation with the ENZIAN score. Eur J Radiol 84:568–574

Dunselman GA, Vermeulen N, Becker C, Calhaz-Jorge C, D'Hooghe T, De Bie B, Heikinheimo O, Horne AW, Kiesel L, Nap A, Prentice A, Saridogan E, Soriano D, Nelen W (2014) ESHRE guideline: management of women with endometriosis. Hum Reprod 29:400–412

Ekici E, Soysal M, Kara S, Dogan M, Gokmen O (1996) The efficiency of ultrasonography in the diagnosis of dermoid cysts. Zentralbl Gynakol 118:136–141

Faccioli N, Foti G, Manfredi R, Mainardi P, Spoto E, Ruffo G, Minelli L, Mucelli RP (2010) Evaluation of colonic involvement in endometriosis: double-contrast barium enema vs. magnetic resonance imaging. Abdom Imaging 35:414–421

Fedele L, Bianchi S, Portuese A, Borruto F, Dorta M (1998) Transrectal ultrasonography in the assessment of rectovaginal endometriosis. Obstet Gynecol 91:444–448

Fedele L, Bianchi S, Zanconato G, Raffaelli R, Berlanda N (2004) Is rectovaginal endometriosis a progressive disease? Am J Obstet Gynecol 191:1539–1542

Fiaschetti V, Crusco S, Meschini A, Cama V, Di Vito L, Marziali M, Piccione E, Calabria F, Simonetti G (2012) Deeply infiltrating endometriosis: evaluation of retro-cervical space on MRI after vaginal opacification. Eur J Radiol 81:3638–3645

Fleischer AC, James AE, Millis JB, Julian C (1978) Differential diagnosis of pelvic masses by gray scale sonography. Am J Roentgenol 131:469–476

Forstner R, Thomassin-Naggara I, Cunha TM, Kinkel K, Masselli G, Kubik-Huch R, Spencer JA, Rockall A (2016) ESUR recommendations for MR imaging of the sonographically indeterminate adnexal mass: an update. Eur Radiol [Epub ahead of print]

Grasso RF, Di Giacomo V, Sedati P, Sizzi O, Florio G, Faiella E, Rossetti A, Del Vescovo R, Zobel BB (2010) Diagnosis of deep infiltrating endometriosis: accuracy of magnetic resonance imaging and transvaginal 3D ultrasonography. Abdom Imaging 35:716–725

Guerriero S, Ajossa S, Orozco R, Perniciano M, Jurado M, Melis GB, Alcazar JL (2015) Accuracy of transvaginal ultrasound for diagnosis of deep endometriosis in the recto-sigmoid: a meta-analysis. Ultrasound Obstet Gynecol 46:534–545

Guerriero S, Ajossa S, Minguez JA, Jurado M, Mais V, Melis GB, Alcazar JL (2016) Accuracy of transvaginal ultrasound for diagnosis of deep endometriosis regarding locations other than recto-sigmoid: systematic review and meta-analysis. Ultrasound Obstet Gynecol 47:281–289

Ha HK, Lim YT, Kim HS, Suh TS, Song HH, Kim SJ (1994) Diagnosis of pelvic endometriosis: fat-suppressed T1-weighted vs conventional MR images. AJR Am J Roentgenol 163:127–131

Hadfield R, Mardon H, Barlow DH, Kennedy S (1996) Delay in the diagnosis of endometriosis: a survey of women from the USA and the UK. Hum Reprod 11:878–880

Halis G, Mechsner S, Ebert AD (2010) The diagnosis and treatment of deep infiltrating endometriosis. Dtsch Arztebl Int 107:446–455

Halme J, White C, Kauma S, Estes J, Haskill S (1988) Peritoneal macrophages from patients with endometriosis release growth factor activity in vitro. J Clin Endocrinol Metab 66:1044–1049

Hodler J, Kubik-Huch RA, Schulthess GKV, Zollikhover CL (2014) Diseases of the abdomen and pelvis 2014–2017: diagnostic imaging and interventional techniques: 46th International Diagnostic Course in Davos (IDKD), Davos, 30 Mar – 4 Apr 2014

Hottat N, Larrousse C, Anaf V, Noël JC, Matos C, Absil J, Metens T (2009) Endometriosis: contribution of 3.0-T pelvic MR imaging in preoperative assessment – initial results. Radiology 253:126–134

Houston DE (1984) Evidence for the risk of pelvic endometriosis by age, race and socioeconomic status. Epidemiol Rev 6:167–191

Idetsu A, Ojima H, Saito K, Yamauchi H, Yamaki E, Hosouchi Y, Kuwano H (2007) Laparoscopic appendectomy for appendiceal endometriosis presenting as acute appendicitis: report of a case. Surg Today 37:510–513

Khorram O, Taylor RN, Ryan IP, Schall TJ, Landers DV (1993) Peritoneal fluid concentrations of the cytokine RANTES correlate with the severity of endometriosis. Am J Obstet Gynecol 169:1545–1549

Kier R, Wain S, Troiano R (1993) Fast spin-echo MR images of the pelvis obtained with a phased-array coil: value in localizing and staging prostatic carcinoma. AJR Am J Roentgenol 161:601–606

Kikuchi I, Kuwatsuru R, Yamazaki K, Kumakiri J, Aoki Y, Takeda S (2014) Evaluation of the usefulness of the MRI jelly method for diagnosing complete cul-de-sac obliteration. Biomed Res Int 2014:437962

Kinkel K, Chapron C, Balleyguier C, Fritel X, Dubuisson JB, Moreau JF (1999) Magnetic resonance imaging characteristics of deep endometriosis. Hum Reprod 14:1080–1086

Kinkel K, Frei KA, Balleyguier C, Chapron C (2006) Diagnosis of endometriosis with imaging: a review. Eur Radiol 16:285–298

Kruger K, Behrendt K, Niedobitek-Kreuter G, Koltermann K, Ebert AD (2013) Location-dependent value of pelvic MRI in the preoperative diagnosis of endometriosis. Eur J Obstet Gynecol Reprod Biol 169:93–98

Lazzeri L, Di Giovanni A, Exacoustos C, Tosti C, Pinzauti S, Malzoni M, Petraglia F, Zupi E (2014) Preoperative and postoperative clinical and transvaginal ultrasound findings of adenomyosis in patients with deep infiltrating endometriosis. Reprod Sci 21:1027–1033

Leyendecker G, Wildt L, Mall G (2009) The pathophysiology of endometriosis and adenomyosis: tissue injury and repair. Arch Gynecol Obstet 280:529–538

Liakakos T, Thomakos N, Fine PM, Dervenis C, Young RL (2001) Peritoneal adhesions: etiology, pathophysiology, and clinical significance. Dig Surg 18:260–273

Manganaro L, Fierro F, Tomei A, Irimia D, Lodise P, Sergi ME, Vinci V, Sollazzo P, Porpora MG, Delfini R, Vittori G, Marini M (2012) Feasibility of 3.0 T pelvic MR imaging in the evaluation of endometriosis. Eur J Radiol 81:1381–1387

Manganaro L, Porpora MG, Vinci V, Bernardo S, Lodise P, Sollazzo P, Sergi ME, Saldari M, Pace G, Vittori G, Catalano C, Pantano P (2014) Diffusion tensor imaging and tractography to evaluate sacral nerve root abnormalities in endometriosis-related pain: a pilot study. Eur Radiol 24:95–101

Matsuura K, Ohtake H, Katabuchi H, Okamura H (1999) Coelomic metaplasia theory of endometriosis: evidence from in vivo studies and an in vitro experimental model. Gynecol Obstet Investig 47:18–22

McCauley TR, McCarthy S, Lange R (1992) Pelvic phased array coil: image quality assessment for spin-echo MR imaging. Magn Reson Imaging 10:513–522

Medeiros LR, Rosa MI, Silva BR, Reis ME, Simon CS, Dondossola ER, da Cunha Filho JS (2015) Accuracy of magnetic resonance in deeply infiltrating endometriosis: a systematic review and meta-analysis. Arch Gynecol Obstet 291:611–621

Meyer R (1919) Über den stand der Frage der Adenomyositis und Adenomyome im Allgemeinen und insbesondere über Adenomyositis seroepithelialis und Adenomyometritis sarcomatosa. Zentralbl Gynakol 36:745–750

Novellas S, Chassang M, Bouaziz J, Delotte J, Toullalan O, Chevallier EP (2010) Anterior pelvic endometriosis: MRI features. Abdom Imaging 35:742–749

Oliker AJ, Harris AE (1971) Endometriosis of the bladder in a male patient. J Urol 106:858–859

Patel MD, Feldstein VA, Chen DC, Lipson SD, Filly RA (1999) Endometriomas: diagnostic performance of US. Radiology 210:739–745

Pinkert TC, Catlow CE, Straus R (1979) Endometriosis of the urinary bladder in a man with prostatic carcinoma. Cancer 43:1562–1567

Rousset P, Peyron N, Charlot M, Chateau F, Golfier F, Raudrant D, Cotte E, Isaac S, Réty F, Valette PJ (2014)

Bowel endometriosis: preoperative diagnostic accuracy of 3.0-T MR enterography-initial results. Radiology 273:117–124

Roy C, Balzan C, Thoma V, Sauer B, Wattiez A, Leroy J (2009) Efficiency of MR imaging to orientate surgical treatment of posterior deep pelvic endometriosis. Abdom Imaging 34:251–259

Saba L, Guerriero S, Sulcis R, Pilloni M, Ajossa S, Melis G, Mallarini G (2012) MRI and "tenderness guided" transvaginal ultrasonography in the diagnosis of rectosigmoid endometriosis. J Magn Reson Imaging 35:352–360

Sampson JA (1927) Peritoneal endometriosis due to the menstrual dissemination of endometrial tissue into the peritoneal cavity. Am J Obstet Gynecol 14:422–469

Savelli L (2009) Transvaginalsonography for the assessment of ovarian and pelvic endometriosis: how deep is our understanding? Ultrasound Obstet Gynecol 33:497–501

Scardapane A, Lorusso F, Scioscia M, Ferrante A, Stabile Ianora AA, Angelelli G (2014) Standard high-resolution pelvic MRI vs. low-resolution pelvic MRI in the evaluation of deep infiltrating endometriosis. Eur Radiol 24:2590–2596

Schrodt GR, Alcorn MO, Ibanez J (1980) Endometriosis of the male urinary system: a case report. J Urol 124:722–723

Takeuchi H, Kuwatsuru R, Kitade M, Sakurai A, Kikuchi I, Shimanuki H, Kinoshita K (2005) A novel technique using magnetic resonance imaging jelly for evaluation of rectovaginal endometriosis. Fertil Steril 83:442–447

Tanaka YO, Itai Y, Anno I, Matsumoto K, Ebihara R, Nishida M (1996) MR staging of pelvic endometriosis: role of fat-suppression T1-weighted images. Radiat Med 14:111–116

Togashi K (2002) MR imaging in obstetrics and gynecology. Nippon Igaku Hoshasen Gakkai Zasshi 62:7–16

Togashi K, Nishimura K, Kimura I, Tdsuda Y, Yamashita K, Shibata T, Nakano Y, Konishi J, Konishi I, Mori T (1991) Endometrial cysts: diagnosis with MR imaging. Radiology 180:73–78

Vercellini P, Meschia M, De Giorgi O, Panazza S, Cortesi I, Crosignani PG (1996) Bladder detrusor endometriosis: clinical and pathogenetic implications. J Urol 155:84–86

Vercellini P, Chapron C, Fedele L, Frontino G, Zaina B, Crosignani PG (2003) Evidence for asymmetric distribution of sciatic nerve endometriosis. Obstet Gynecol 102:383–387

Vinatier D, Dufour P, Oosterlynck D (1996) Immunological aspects of endometriosis. Hum Reprod Update 2:371–384

Woodward PJ, Sohaey R, Mezzetti TP Jr (2001) Endometriosis: radiologic-pathologic correlation. Radiographics 21:193–216

Wu TT, Coakley FV, Qayyum A, Yeh BM, Joe BN, Chen LM (2004) Magnetic resonance imaging of ovarian cancer arising in endometriomas. J Comput Assist Tomogr 28:836–838

Yoon JH, Choi D, Jang KT, Kim CK, Kim H, Lee SJ, Chun HK, Lee WY, Yun SH (2010) Deep rectosigmoid endometriosis: "mushroom cap" sign on T2-weighted MR imaging. Abdom Imaging 35:726–731

Zeitoun KM, Bulun SE (1999) Aromatase: a key molecule in the pathophysiology of endometriosis and a therapeutic target. Fertil Steril 72:961–969

Vagina and Vulva

Athina C. Tsili

Contents

A.C. Tsili
Department of Clinical Radiology, Medical School, University of Ioannina, University Campus, Ioannina 45110, Greece
e-mail: a_tsili@yahoo.gr; atsili@cc.uoi.gr

1 Introduction

Normal vaginal and vulvar anatomy and pathology can often be missed at CT and MRI performed either for gynecologic diseases or for other reasons. Radiologists should be familiar with the normal anatomy of the vagina and vulva to detect and interpret pathologic findings. MRI represents an important diagnostic tool for the assessment of vaginal and vulvar diseases due to its multiplanar ability and superb contrast resolution. It is an essential adjunct to sonography in the evaluation of complex Müllerian duct anomalies prior to consideration for surgery. MRI is also useful in staging both vaginal and vulval malignancies.

2 Embryonic Development and Normal Anatomy

The paramesonephric ducts (Müllerian ducts) represent the precursors of the uterus, fallopian tubes, cervix, and upper vagina. The upper two-thirds of the vagina are formed by

Med Radiol Diagn Imaging (2017)
DOI 10.1007/174_2017_44, © Springer International Publishing AG
Published Online: 09 April 2017

the caudal end of the fused Müllerian ducts. Lateral fusion of the paramesonephric ducts occurs between the seventh and ninth weeks of gestation, when the lower segments of the paramesonephric ducts fuse. At this stage, a midline septum is present in the uterus, which usually regresses at about 20 weeks, although it may persist. Vertical fusion occurs in the eighth week, when the lower most fused paramesonephric ducts fuse with the ascending endoderm of the sinovaginal bulb. The lower third of the vagina is formed as the sinovaginal node (bulb) canalizes. The sinovaginal node inserts into the urogenital sinus at Müller's tubercle. The hymen, a membrane separating the vagina from the urogenital sinus develops and is normally perforated by birth (Mann et al. 2012).

The external genitalia begin to display sexual differentiation during the tenth week, with complete differentiation occurring around the 12th week (Mann et al. 2012). The unfused parts of the genital swellings give rise to the labia majora, the folds fuse anteriorly to form the mons pubis and anterior labial commissure, and posteriorly the posterior labial commissure. The urethral folds fuse posteriorly to form the frenulum of the labia minora. The unfused urethral folds give rise to the labia minora. The unfused genital swellings enable the urogenital sinus to open into the anterior urethral part of the vagina and the vaginal vestibule. The genital tubercle becomes the clitoris by the 14th week (Mann et al. 2012).

The vagina is a 7–9-cm-long fibromuscular tube, extending from the vulvar vestibule to the uterus. It is attached to the levator ani at the level of the urogenital diaphragm, and is in close proximity to the urethra and neck-trigone area of the urinary bladder anteriorly, and to the anal canal and lower rectum posteriorly (Fig. 1) (Basmajian 1971; Siegelman et al. 1997; Walker et al. 2011; Hricak et al. 1988; Chang 2002; Griffin et al. 2010; Gardner et al. 2015). The vagina is anatomically divided into thirds, important for classifying tumor location

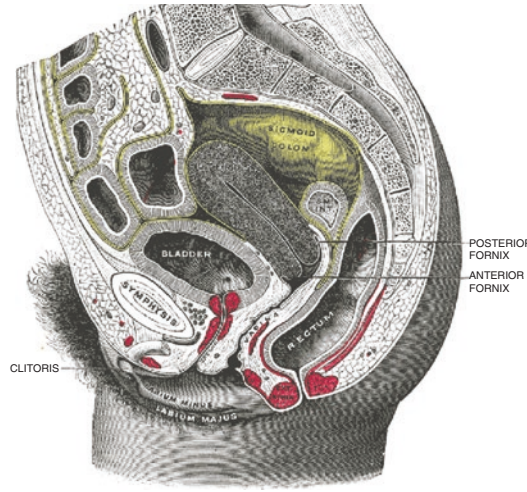

Fig. 1 Anatomic draft of the normal female pelvis in sagittal orientation

and lymphatic drainage (Griffin et al. 2010; Gardner et al. 2015). The lower third is defined below the level of the bladder base, with the urethra anteriorly. The middle third corresponds to the level of the bladder base, and the upper third is at the level of the vaginal fornices (Fig. 2). The posterior vaginal wall is longer and ends in the posterior fornix, and the shorter anterior wall ends in the anterior fornix (Fig. 3). The vagina is lined with estrogen-sensitive stratified squamous epithelium. This epithelium lines a tunica propria, which has numerous transverse folds (rugae). Outside the tunica propria there is a thin muscular coat of longitudinal fibers and some interlacing circular ones and a thick fibro-areolar adventitious coat (Mann et al. 2012).

The vagina is supplied by a network of vessels formed by an anastomosis between the vaginal and uterine branches of the internal iliac artery. The middle rectal artery and internal pudendal artery provide additional blood supply to the mid and lower third of the vagina, respectively. Venous drainage is via the uterine and vaginal venous plexuses into the internal iliac veins. Posteriorly, this plexus forms the rectovaginal septum. Lymphatic drainage of the upper two-thirds of the vagina is into the internal and

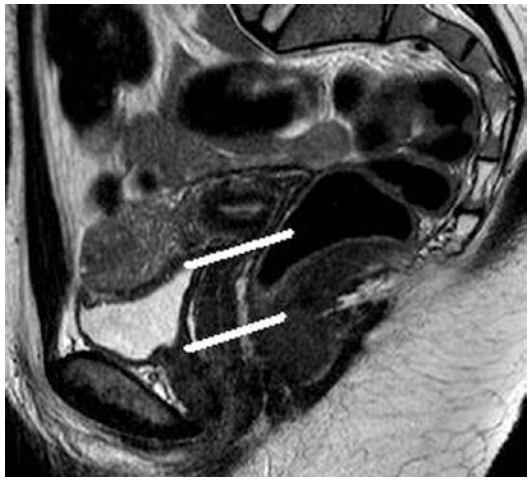

Fig. 2 Normal anatomy of the vagina in a premenopausal woman. Sagittal T2WI shows the three anatomic divisions of the vagina

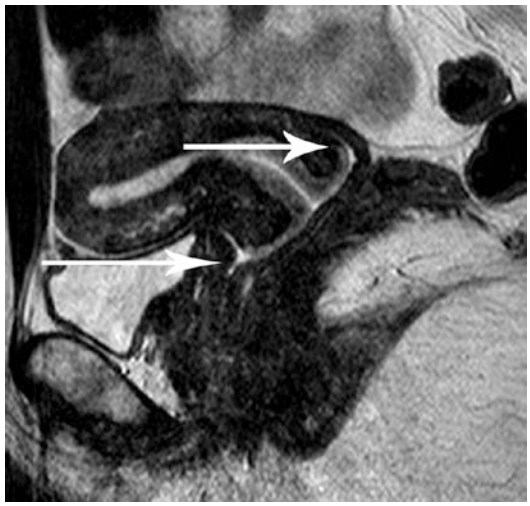

Fig. 3 Sagittal T2WI in a premenopausal woman delineates anterior and posterior vaginal fornices (*long arrow*)

external iliac lymph nodes. The lower third drains into the superficial inguinal nodes (Griffin et al. 2010).

The vulva is comprised of the mons pubis, the labia majora and minora, the clitoris, the vestibular bulb, the Bartholin glands, and the vestibule of the vagina. The mons pubis is composed of adipose tissue overlying the symphysis pubis and separating inferiorly into the

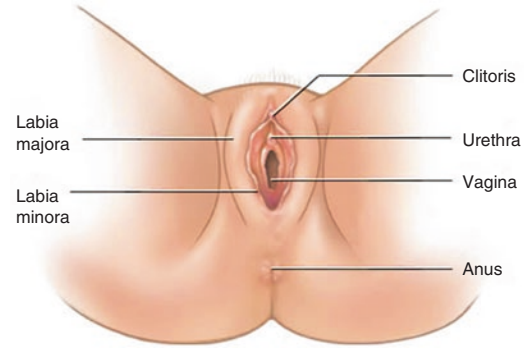

Fig. 4 The female external genitalia (vulva)

labia majora. The labia minora, the two thin skin folds lying between the labia majora, fuse at the level of the glans of the clitoris. The area between the labia minora is the vestibule of the vulva, containing the vaginal introitus and external urethral meatus. The Bartholin glands located posterolateral to the vaginal introitus secrete lubricant via ducts into the vestibule (Fig. 4) (Griffin et al. 2010; Hosseinzadeh et al. 2012; Lee et al. 2011). The vulva is supplied by branches of the external and internal pudendal arteries, with lymphatic drainage into the medial group of superficial inguinal nodes. Subsequent lymphatic flow is to the deep inguinal nodes, and then to the caudal external iliac nodes (Griffin et al. 2010; Lee et al. 2011).

3 Imaging Appearance of the Normal Vagina and Vulva

3.1 CT Appearance

CT is not considered the modality of choice for the evaluation of vaginal and vulvar diseases, due to its poor tissue characterization and the use of ionizing radiation. Based on the American College of Radiology Appropriateness Criteria, CT may be used to assess the local extent of vaginal cancer and to evaluate for nodal and distant metastases, although the sensitivity of the

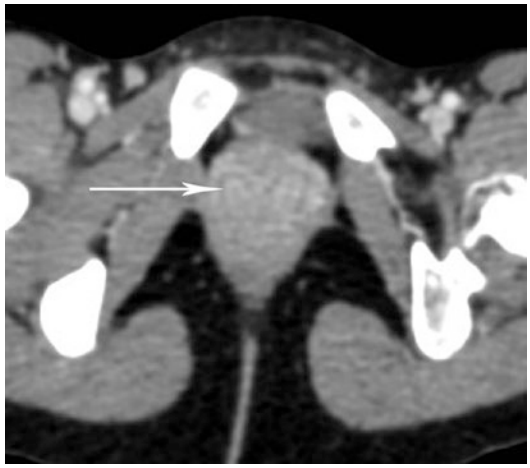

Fig. 5 Transverse MPR (portal phase) in a young woman depicts normally enhancing vaginal mucosa (*long arrow*)

technique is modest compared to MRI (American College of Radiology 2013). However, CT is often the initial diagnostic examination in the emergency settings in patients presenting with abdominal pain and nonspecific clinical symptoms. In these cases, knowledge of the normal CT appearance of the vagina and vulva is useful to avoid misdiagnosis (Walker et al. 2011; Yitta et al. 2009). Multidetector CT with two-dimensional multiplanar reformatted (MPR) images has improved visualization of the normal anatomy and pathology of the female pelvis (Yitta et al. 2009). If vaginal pathology is suspected, a vaginal tampon or vaginal gel may be inserted to better define the vagina.

The normal vagina demonstrates intense central enhancement, which corresponds to the vaginal mucosa, and a poorly enhancing peripheral vaginal wall, in women of childbearing age (Fig. 5). In postmenopausal women, the vaginal mucosa has similar CT density to that of the vaginal wall and adjacent pelvic structures (Walker et al. 2011; Yitta et al. 2009). Vaginal pathology may be difficult to assess on CT due its similar density with the surrounding soft-tissue structures (Walker et al. 2011).

The vulva appears as a triangular soft-tissue structure within the perineum, bounded by the symphysis pubis anteriorly, the anal sphincter posteriorly, and the ischial tuberosities laterally (Griffin et al. 2010).

3.2 MRI Protocol

Conventional MRI sequences obtained with a phased-array pelvic coil are usually diagnostic for the evaluation of the normal vaginal and vulvar anatomy and diseases (Walker et al. 2011; Griffin et al. 2010; Gardner et al. 2015; López et al. 2005). The use of a dry tampon or vaginal gel, although not included in routine practice provides better distension and visualization of the vagina, especially recommended in the assessment of vaginal malignancies (Gardner et al. 2015). The endoanal endoluminal coil can also be used to provide high-resolution images of the rectum, anal canal, rectovaginal septum, and vagina, although the small field of view represents a limitation (Griffin et al. 2010). Axial T1-weighted (T1WI) and T2-weighted images (T2WI) and sagittal T2WI are included in the standard MRI protocol. High-resolution axial T2WI with thin slices and small field of view is useful in imaging vaginal and vulvar pathology and especially tumors. Coronal T2WI is used for the assessment of congenital anomalies, with a large field of view to include the kidneys. Fat-suppressed axial T1WI improves detection of hemorrhagic or proteinaceous lesions and distinguish them from fat. T2WI with fat suppression is useful for the assessment of vaginal fistulas (Walker et al. 2011; Griffin et al. 2010; Gardner et al. 2015; López et al. 2005). Three-dimensional dynamic contrast-enhanced (DCE) images after intravenous administration of gadolinium are recommended in a sagittal orientation in cases of vaginal malignancies (Gardner et al. 2015). The role of diffusion-weighted imaging is currently unknown, but may be promising.

3.3 MRI Appearance

At MRI, the vagina has uniform T1 signal, resembling that of skeletal muscles (Fig. 6a). The vaginal wall anatomy is best depicted on T2WI, similar to the zonal anatomy of the uterus. The mucosa along with any intraluminal secretions appears as a thin layer of bright T2 signal. Surrounding the vaginal mucosa is a submucosal layer of collagen and elastic fibers and a muscularis consisting of

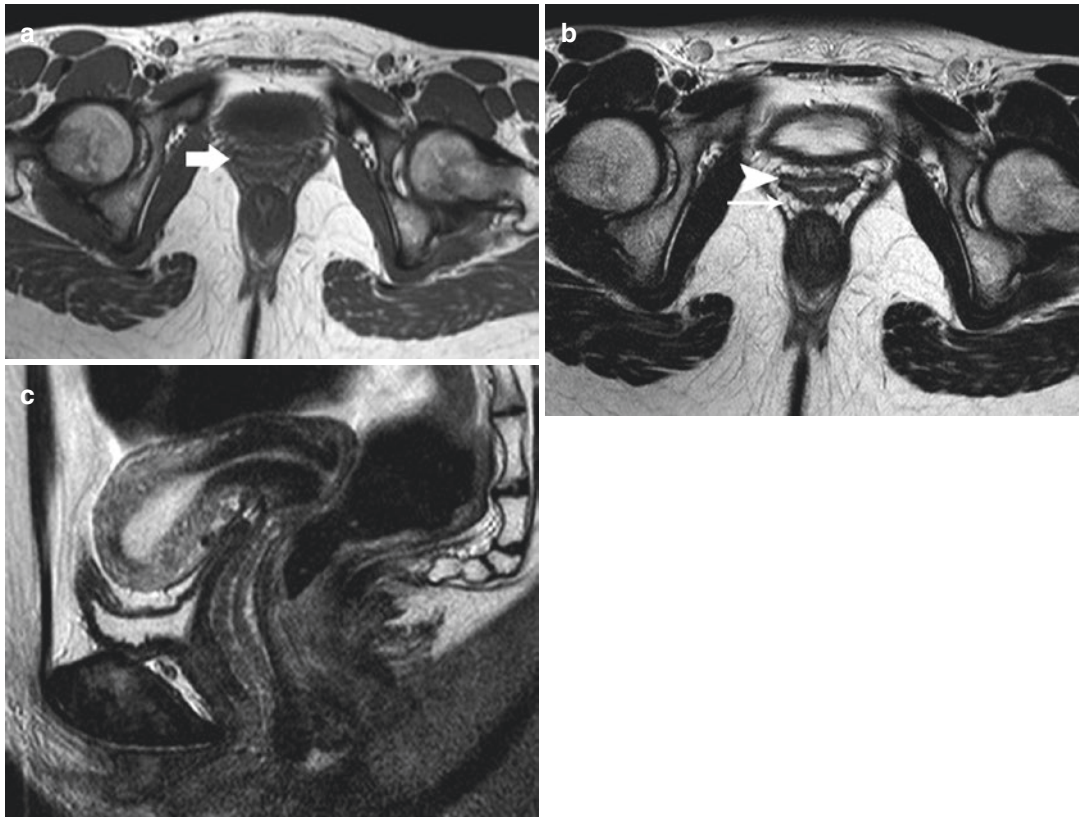

Fig. 6 Normal vaginal anatomy at MRI in a 25-year-old woman. (**a**) Axial T1WI depicts normal vagina mainly isointense to the surrounding muscles. Note that the middle layer of the vagina has low signal intensity (*arrow*). T2WI in (**b**) transverse and (**c**) sagittal orientation depicting the zonal anatomy of the vagina. The fibromuscular wall is of low signal intensity (*arrowhead*), surrounding a thin hyperintense layer, which corresponds to the vaginal mucosa and intraluminal mucus. External to the fibromuscular wall is a hyperintense layer containing a prominent venous plexus (*arrow*).

inner longitudinal and outer circular smooth muscle, exhibiting a low T2 signal. The outer connective tissue layer of the vaginal wall contains a prominent plexus of veins as well as the vaginal arteries and nerves. This layer appears hyperintense on T2WI, due to slow venous blood flow (Fig. 6b, c) (Siegelman et al. 1997; Walker et al. 2011; Griffin et al. 2010; Gardner et al. 2015; López et al. 2005; Taylor et al. 2007). Following intravenous administration of gadolinium, the vaginal mucosa enhances (Fig. 7). With the use of vaginal gel, the hyperintense mucosal layer is obscured by the hyperintense gel and only two layers are seen, the hypointense muscularis and the hyperintense adventitia (Gardner et al. 2015).

The MRI appearance of the normal vagina changes with patient age and phase of the men-

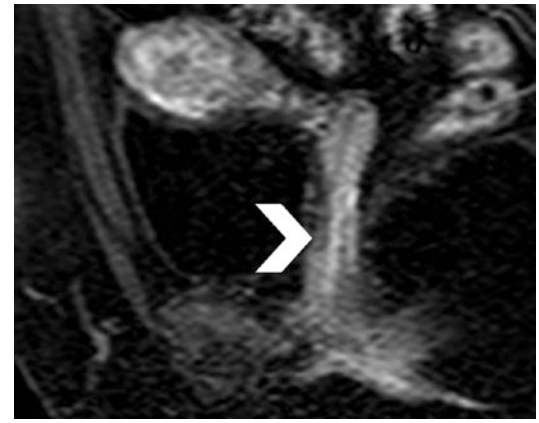

Fig. 7 Dynamic contrast-enhanced subtracted MR image (early phase) in sagittal orientation in a premenopausal woman shows normal enhancement of the vaginal mucosa (*arrowhead*)

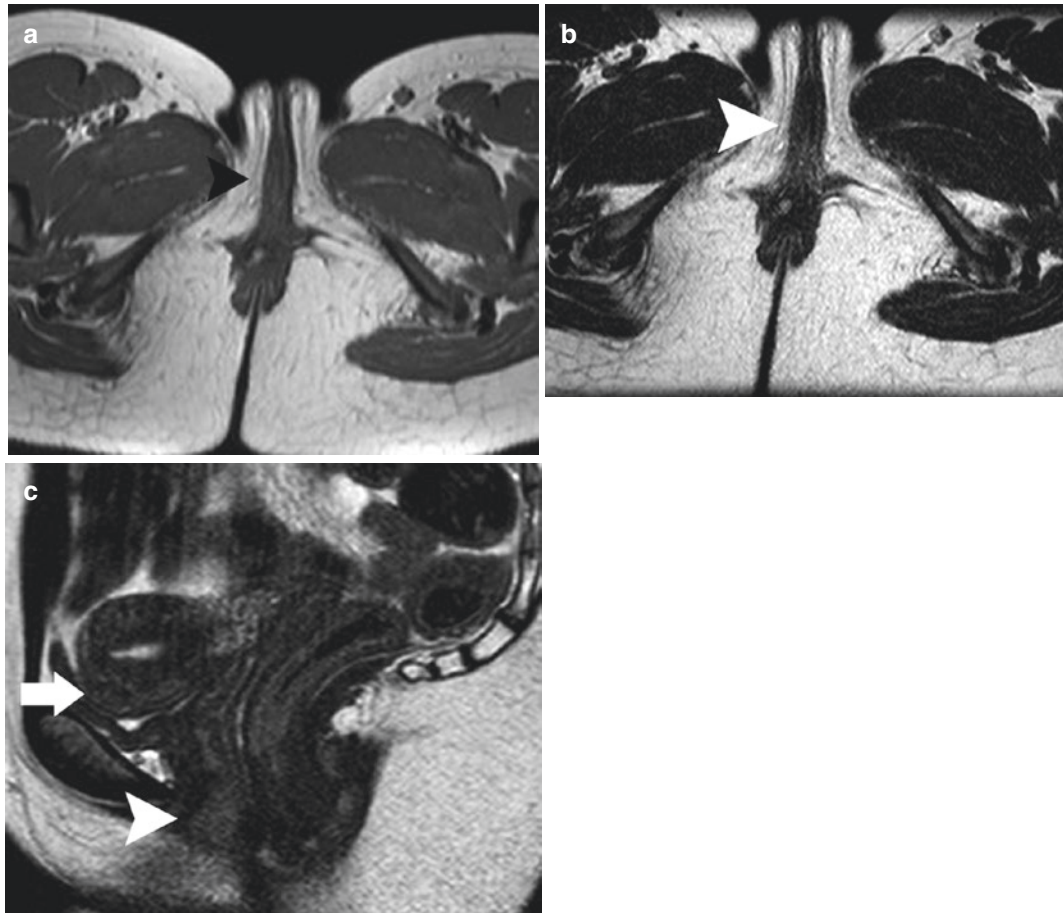

Fig. 8 (**a**) Axial T1WI shows normal vulva (*arrowhead*) with intermediate signal intensity, similar to that of muscles. T2WI in (**b**) axial and (**c**) sagittal orientation depicts vulva (*arrowhead*) with intermediate signal intensity, similar to that of normal myometrium (*arrow*)

strual cycle (Siegelman et al. 1997; Walker et al. 2011; Griffin et al. 2010; López et al. 2005; Taylor et al. 2007). Vaginal mucosa is relatively thin before menarche and after menopause. The vaginal wall and central mucus have the highest T2 signal and maximal thickness during the midsecretory phase of the menstrual cycle. Maximal T2 contrast between the vaginal wall and the surrounding pelvic fat is seen during the early proliferative or late secretory phase. In postmenopausal women who are undergoing hormone replacement therapy, the MRI appearance of the vagina is similar to that in premenopausal females (Walker et al. 2011).

At MRI, the vulva shows low to intermediate T1 signal and slightly high T2 signal (Fig. 8) (Griffin et al. 2010).

4 Congenital Anomalies of the Vagina and Vulva

Congenital anomalies of the vagina are associated with other Müllerian duct anomalies (MDAs) which result from non-development or fusion defects of the Müllerian ducts. The true incidence and prevalence of MDAs are difficult to assess. The close embryologic proximity of the Müllerian and Wolffian systems explains the association of MDAs with renal anomalies, the latter reported in 30–80% of cases. MRI is currently the modality of choice for the evaluation of patients with ambiguous genitalia and suspected MDAs, helping to demonstrate the presence or absence of the vagina, uterus, and ovaries, therefore, obviating unnecessary diagnostic laparoscopy.

In cases of congenital vaginal anomalies, MRI provides information about the location, thickness, and type of congenital obstruction, all of which are important factors in surgical planning (Walker et al. 2011; Griffin et al. 2010; López et al. 2005; Junqueira et al. 2009; Troiano and McCarthy 2004).

4.1 Imperforate Hymen

Imperforate hymen is the commonest congenital anomaly of the female genital tract. It is usually detected after menarche, when the patient presents with cyclic abdominal pain and primary amenorrhea. Imaging is rarely indicated, since the diagnosis is made at clinical examination (Walker et al. 2011).

4.2 Congenital Vaginal Septa

Congenital vaginal septa, both longitudinal and transverse may occur either in isolation or with other MDAs. These septa appear as thin, hypointense structures on MRI, best detected on T2WI (Walker et al. 2011; Griffin et al. 2010; López et al. 2005).

Longitudinal vaginal septa arise either as a failure of lateral fusion of the Müllerian ducts or due to incomplete resorption of the vaginal septum. They are present in 75% of cases of uterine didelphys. A transverse vaginal septum may also be seen, usually in the upper third of the vagina. Longitudinal vaginal septa may go unrecognized, both clinically and radiologically, if no obstruction is present. When obstruction is present, the septum is best delineated on T2WI, which helps differentiate the hypointense septum from the hyperintense intracavitary secretions and blood (Fig. 9) (Walker et al. 2011; Griffin et al. 2010).

A transverse vaginal septum may present in an adolescent girl with primary amenorrhoea, abdominal pain, and an abdominal mass if the septum is complete, or later in life with dyspareunia and dysmenorrhoea, if the septum is incomplete. It is not associated with other urological congenital anomalies or MDAs (López et al. 2005). It may occur at any level within the vagina, although it is more often seen at the junction of the upper and middle thirds, or at the junction of the embryologic sinovaginal plate and the fused Müllerian ducts. MRI is the modality of choice for the identification of transverse vaginal septum, providing useful information for

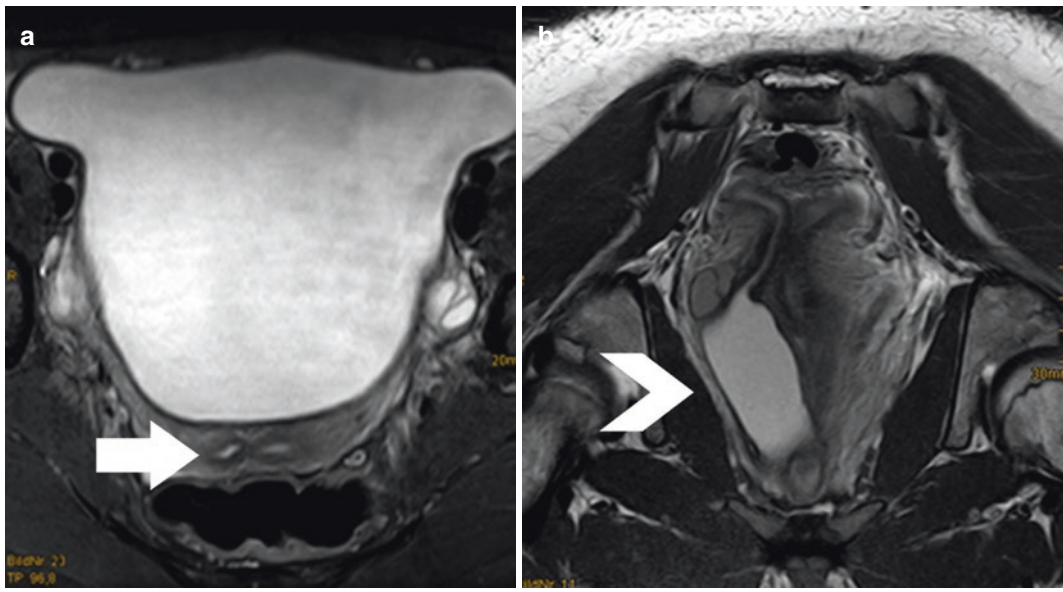

Fig. 9 Longitudinal vaginal septum in the context of a uterus bicornuate and bicollis, with right vagina obstructed. (**a**) Axial fat-suppressed T2WI depicts double vagina (*arrow*) (**b**) Coronal T2WI shows obstructed right vagina (*arrowhead*) (Courtesy Dr. Forstner R, Salzburg, Austria)

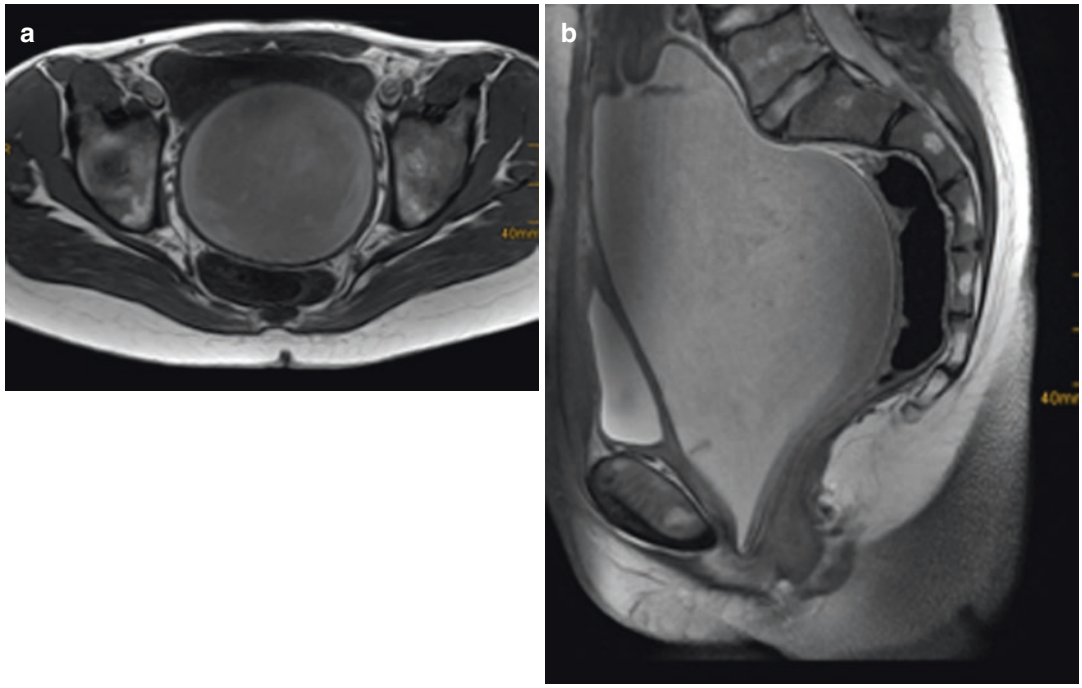

Fig. 10 Vaginal atresia in a 16-year-old female caused by a transverse vaginal septum. T1WI in (**a**) transverse and (**b**) sagittal orientation shows a massively dilated vagina containing blood products (Courtesy Dr. Forstner R, Salzburg, Austria)

surgical planning (Fig. 10). The detection of the cervix at MRI is important in these patients, for differentiating between a high transverse septum and congenital absence of the cervix. The surgical procedure of choice for the latter condition is hysterectomy, instead of reconstructive surgery (Walker et al. 2011; López et al. 2005).

4.3 Vaginal Agenesis

Vaginal agenesis, both complete and partial is rare and may be isolated or associated with other MDAs. The commonest cause is Mayer–Rokitansky–Kuster–Hauser (MRKH) syndrome, presenting with two types. Type 1 is an isolated abnormality, with normal ovaries, fallopian tubes, and external genitalia. Type 2 is associated with urinary tract abnormalities in 40% of cases. Although the diagnosis of vaginal agenesis is primarily made at clinical examination, imaging is often performed, especially in patients who present with a palpable abdominal mass (Walker et al. 2011; Griffin et al. 2010; López et al. 2005).

5 Benign Conditions of the Vagina and Vulva

5.1 Vaginal Cysts

Vaginal cysts are often seen as incidental findings at imaging evaluation. MRI helps in assessing the anatomic location of these cysts and in differentiating them from other regional cystic structures, including periurethral cysts (skene gland cysts), cervical (nabothian) cysts, and urethral diverticula (Walker et al. 2011; Griffin et al. 2010; Hahn et al. 2004; Chaudhari et al. 2010). Vaginal cysts are typically detected as well-delineated lesions, isointense relative to fluid at MRI, with low T1 signal and very high T2 signal. In the presence of proteinaceous, mucinous, or hemorrhagic contents, intermediate to high T1 signal may be seen. Neither the cyst nor its wall normally enhances. Infection should be suggested if there is thickening of the cyst wall or wall enhancement (Fig. 11) (Walker et al. 2011; Griffin et al. 2010; Hahn et al. 2004; Chaudhari et al. 2010).

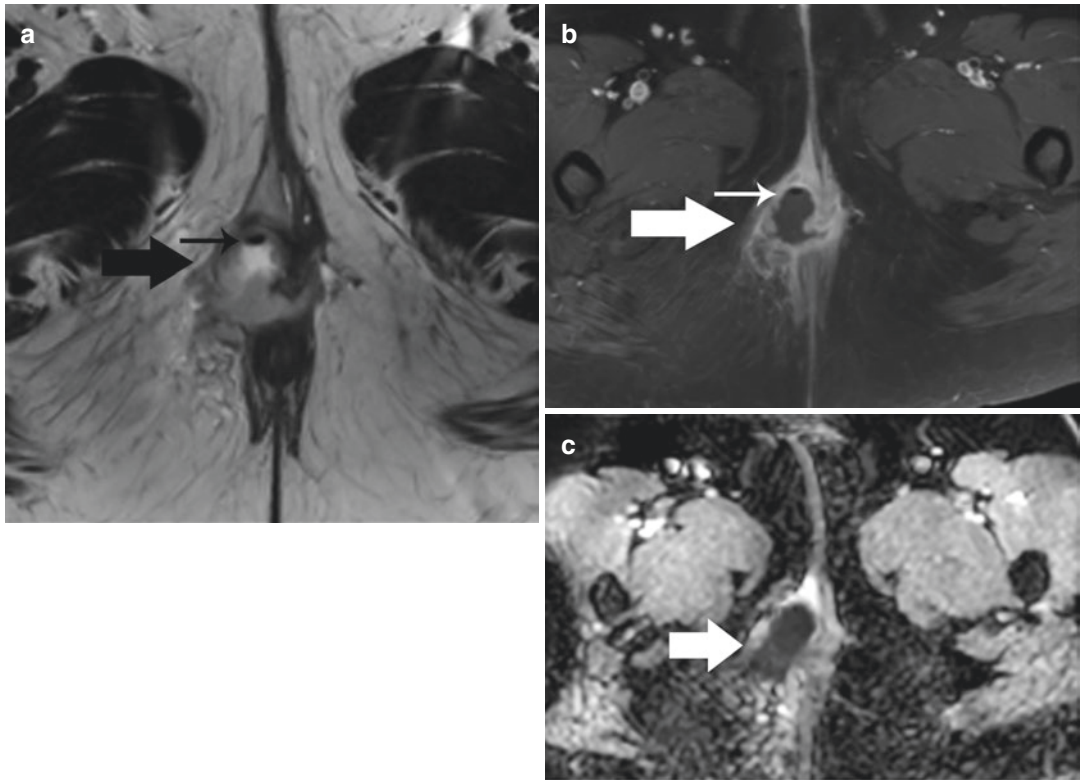

Fig. 11 Bartholinitis complicated by abscess in a 31-year-old woman presenting with a painful vulvar mass. Axial (**a**) T2WI, (**b**) fat-saturated T1WI after gadolinium administration, and (**c**) ADC map demonstrate a thick-walled cystic mass within the distal right posterolateral vaginal wall (*arrow*). The lesion is hyperintense on T2WI, with high signal intensity in the surrounding tissues due to edema and irregular rim enhancement. The presence of a small amount of air (*arrowhead*) within the mass and significantly restricted diffusion suggests abscess formation (Courtesy Dr. Forstner R, Salzburg, Austria)

5.1.1 Gardner Duct Cyst (Mesonephric Cyst)

Gartner duct cysts are embryologic secretory retention cysts that arise from incomplete regression of the mesonephric ducts. These cysts typically occur in the anterolateral wall of the upper third of the vagina, above the level of the most inferior aspect of the pubic symphysis. They are detected in 1–2% of female pelvic MRIs. They are usually small, less than 2 cm in diameter and asymptomatic. Occasionally, Gartner duct cysts are seen in association with other Wolffian abnormalities, such as unilateral renal agenesis, renal hypoplasia, and ectopic ureteral insertion. On imaging, differential diagnosis from urethral diverticula is usually not difficult, because diverticula form around the urethra, and Gartner duct cysts are located posteriorly in the vagina (Siegelman et al. 1997; Walker et al. 2011; Griffin et al. 2010; López et al. 2005; Hahn et al. 2004; Chaudhari et al. 2010).

5.1.2 Bartholin Gland Cyst

Bartholin glands are small, mucin-secreting glands that derive from the urogenital sinus and are located at the posterolateral vaginal introitus, medial to the labia minora. Bartholin gland cyst formation results from blockage of the drainage duct by a stone or a stenosis related to prior infection or trauma. It represents the commonest vulval cyst predominantly seen in women of reproductive age. These cysts are usually small, 1–4 cm in diameter and asymptomatic, but may require drainage in cases of superimposed infection or abscess formation (Fig. 11). Their typical location in the posterolateral inferior third of the vagina, medial to the labia minora and at or below the level of the pubic symphysis, helps to differentiate

them from Gartner duct cysts (Walker et al. 2011; Griffin et al. 2010; López et al. 2005; Hahn et al. 2004; Chaudhari et al. 2010).

5.2 Inflammatory Conditions of the Vagina and Vulva

5.2.1 Vaginal Infections

Infections of the vagina are common, caused by number of pathogens (viral, bacterial, fungal). It is a clinical diagnosis and imaging is rarely needed. On MRI, thickening of the vaginal wall may be seen, associated with increased T2 signal of the vaginal mucosa or of the entire wall, as well as enhancement after gadolinium administration.

5.2.1.1 Vulvar Infections

The vulva is vulnerable to community-acquired infections. Predisposing risk factors include obesity and diabetes mellitus. An increase in community-acquired methicillin-resistant *Staphylococcus aureus* colonization of the perineum and lower genital tract has been reported, representing the cause of infection in healthy, non-immunocompromised women, which leads to abscess formation and tissue necrosis. Vulvar edema in pregnancy may also be complicated with secondary infections such as cellulitis, abscess, and necrotizing fasciitis or Fournier gangrene. CT represents the modality of choice for the diagnosis, estimation of the extent of the disease, and guidance of the surgical approach in complicated vulvar infections. CT findings in Fournier gangrene include soft-tissue thickening, inflammation, abscess formation, and subcutaneous emphysema. Subcutaneous gas may diffuse along fascial planes, extending from the perineum to the inguinal regions, thighs, body wall, and retroperitoneum (Hosseinzadeh et al. 2012).

5.2.1.2 Vulvar Thrombophlebitis

Vulvar or labial thrombophlebitis is a rare condition, seen in preexisting varicose veins, either during pregnancy or the postpartum period. MRI and Doppler US are both reliable in helping establish the diagnosis, although MRI provides a larger field of view for assessing the extent of the thrombosis. At MRI, acute occlusive venous clots result in hyperintense T1 and T2 lesions within an expanded vessel. Perivascular inflammation is a useful ancillary finding in acute venous thrombosis (Hosseinzadeh et al. 2012).

5.3 Vulvar Trauma

Genital traumatic injuries may be related to sexual abuse and iatrogenic obstetric conditions. Nonobstetric accidental genital trauma is more often the result of straddle injuries (accounting for 70% of cases), but may also be due to non-straddle blunt and penetrating trauma (Hosseinzadeh et al. 2012; Ssi-Yan-Kai et al. 2015). The labia are the most frequent site of injury, but extension to the perineum may be seen in 20% of patients. CT is useful in detecting a heterogenous, mainly hyperdense mass, representing hematoma, and assessing for active extravasation with the use of intravenous contrast material (Hosseinzadeh et al. 2012; Ssi-Yan-Kai et al. 2015).

5.4 Vaginal Fistula

Vaginal fistulas can form between the vagina and neighboring organs, namely the urinary bladder, ureter, urethra, or bowel. The two commonest vaginal fistulas are vesicovaginal and rectovaginal. Most cases are related to complications of hysterectomy. Other causes include congenital anomalies, birth trauma, malignancies, pelvic irradiation, inflammatory bowel disease, diverticular disease, or genitourinary instrumentation. MRI has great potential for both the detection and characterization of fistulas in and around the vagina, with a reported accuracy of 91%. Fistulous tracts are usually detected hyperintense on T2WI and fat-suppressed T2WI or as an air-filled tract of low signal intensity. Wall enhancement and loss of intervening fat planes may be seen on fat-suppressed delayed contrast-enhanced T1WI. Sagittal orientation is recommended for the detection of vesicovaginal fistulas (Fig. 12). Both CT and MRI may provide additional information regarding extralu-

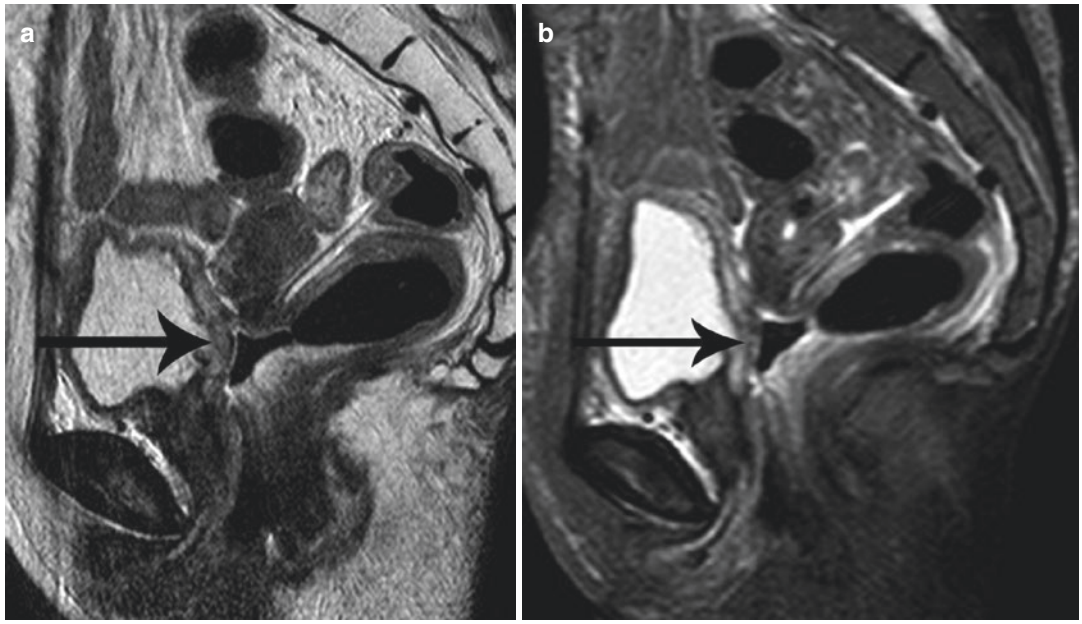

Fig. 12 Sagittal (**a**) T2WI and (**b**) dynamic contrast-enhanced subtracted MR image (early phase) depict an air-filled rectovaginal fistula (*long arrow*) in a 60-year-old woman with a history of prior hysterectomy and radiation therapy for cervical carcinoma. Radiation also induced fatty bone marrow replacement

minal disease and possible complications (e.g., abscesses) (Siegelman et al. 1997; Griffin et al. 2010; Gardner et al. 2015).

5.5 Post-Radiation Changes

In the first 6 months following pelvic irradiation, the vaginal wall may appear hyperintense on MRI, due to mucosal and intramuscular edema. These acute changes are usually transient and reversible. Mild chronic post-radiation changes may include mucosal atrophy, narrowing and foreshortening of the canal, and vaginal stenosis. Vaginal wall may have low signal intensity in this stage. In cases of severe radiation injury, vaginal necrosis and fistulation may occur (Fig. 12) (Siegelman et al. 1997; Griffin et al. 2010).

In the context of malignancy, differentiation between post-radiation fibrosis and tumor recurrence may be made on T2WI in most cases, 12–18 months after treatment, since fibrosis appears hypointense compared to tumor, which is hyperintense. Before this period, fibrosis may show high T2 signal due to inflammation and edema related to acute radiation changes and therefore, differentiation from recurrent malignancy is difficult (Siegelman et al. 1997; Griffin et al. 2010). In these cases, DCE-MRI is particularly helpful. Fibrosis usually does not show early and strong enhancement, while malignancy enhances early and avidly (Siegelman et al. 1997).

5.6 Benign Tumors

A variety of benign tumors may arise in the vagina, including leiomyoma, cavernous hemangioma, fibroepithelial polyp, and rhabdomyoma. Most solid vaginal masses are readily diagnosed at clinical examination and are easily excised to establish a histologic diagnosis. However, MRI may provide the best differentiation between normal vagina and vaginal masses, proved helpful in tumors that are not assessed at clinical examination (Walker et al. 2011; Griffin et al. 2010).

Vaginal leiomyomas are rare and may derive from the smooth muscle of the vagina, local arterial musculature, or smooth muscle of the

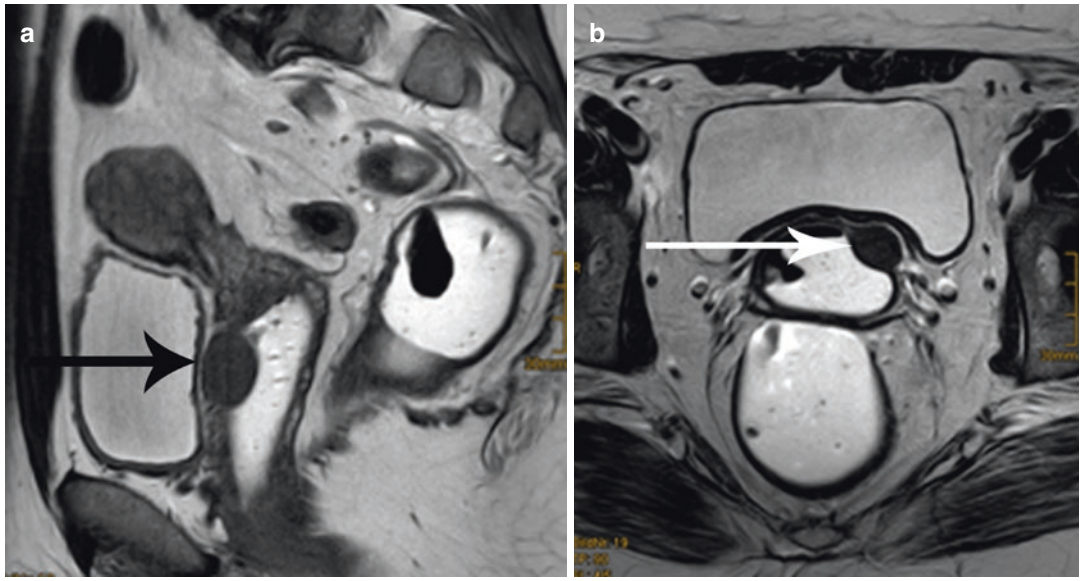

Fig. 13 Leiomyoma of the anterior vaginal wall. T2WI in (**a**) sagittal and transverse (**b**) orientation (vagina with gel) demonstrates a well-circumscribed vaginal mass (*long arrow*) of decreased signal intensity (Courtesy Dr. Forstner R, Salzburg, Austria)

bladder or urethra. The commonest location for vaginal leiomyomas is the anterior vaginal wall. Imaging findings resemble those of uterine leiomyomas. Typical leiomyomas appear homogeneous of low T1 and T2 signal (Fig. 13). They may undergo degeneration, with hyaline degeneration demonstrating low T2 signal, myxoid and cystic degeneration showing high T2 signal, and hemorrhagic degeneration demonstrating high signal on both T1WI and T2WI (Walker et al. 2011; Griffin et al. 2010). MRI is particularly useful for distinguishing a vaginal leiomyoma from an "aborting" uterine leiomyoma or other atypical vaginal mass (Walker et al. 2011).

6 Malignant Neoplasms of the Vagina and Vulva

6.1 Vaginal Malignancies

6.1.1 Primary Vaginal Carcinoma

Primary vaginal carcinoma is rare, accounting for only 2–3% of gynecological malignancies and less than 20% of vaginal neoplasms. It is defined as arising only from the vagina, with no involvement of the external os superiorly or the vulva inferiorly, the importance of this definition correlating with the different approaches in the treatment of cervical and vulval carcinoma.

Squamous cell carcinoma (SCC) accounts for approximately 90% of vaginal malignancies. It is more common in postmenopausal females (median age at presentation, 60 years) and frequently involves the proximal third of the vagina and the posterior wall. Clinically, most women present with painless vaginal bleeding, or less often with abnormal vaginal discharge, urinary tract symptoms, pelvic pain, or a feeling of a mass in the vagina. SCC of the vagina tends to spread early by direct invasion of the bladder and urethra anteriorly and the rectum posteriorly. Approximately, one-third of patients have pelvic or inguinal lymph node metastases at diagnosis.

The precursor for vaginal carcinoma, vaginal intraepithelial neoplasia, and invasive vaginal cancer is strongly associated with human papillomavirus (HPV) infection. Both have similar risk factors as those for cervical carcinoma, including tobacco use, younger age at coitarche, HPV, and multiple sexual partners. Increased incidence of vaginal carcinoma is observed in women with a

Table 1 TNM and FIGO staging for vaginal cancer

TNM	FIGO	Definition
Tx		Primary tumor cannot be assessed
T0		No evidence of primary tumor
Tis		Carcinoma in situ (preinvasive)
T1	I	Tumor confined to vagina
T2	II	Tumor invades paravaginal tissues but does not extend to pelvic wall
T3	III	Tumor extends to pelvic wall
T4	IVA	Tumor invades mucosa of the bladder or rectum or shows direct extension beyond the true pelvis; bullous edema is not sufficient to allow classification as T4
M1	IVB	Distant metastases

previous diagnosis of cervical cancer or cervical intraepithelial neoplasia (Walker et al. 2011; Griffin et al. 2010; Gardner et al. 2015; López et al. 2005; Chang et al. 1988; Parikh et al. 2008).

Staging of the disease is primarily based on clinical examination by the International Federation of Gynecology and Obstetrics (FIGO) system (Table 1) (FIGO Committee on Gynecologic Oncology 2009). Pelvic examination continues to be the primary modality for the evaluation of the extent of the disease, although it has limitations, such as the inability to detect metastatic lymphadenopathy and the difficulty to assess local tumor infiltration. Therefore, FIGO encourages the use of cross-sectional imaging, including CT and MRI (FIGO Committee on Gynecologic Oncology 2009). Although CT is recommended for staging, MRI may provide superior evaluation of tumor volume and local extension, both for initial staging and follow-up, to allow for better treatment planning (Walker et al. 2011; Gardner et al. 2015; López et al. 2005; Parikh et al. 2008). Furthermore, MRI may be valuable in depicting pelvic anatomy for surgical and radiation therapy planning.

Primary vaginal carcinoma has a 5-year survival rate of about 80% for stage I or II disease, falling to 20% for stage III or IV disease. Because vaginal carcinoma is rare, treatment planning remains less well defined, often individualized and extrapolated from institutional experience and outcomes in cervical cancer. There is an increasing trend towards organ preservation and treatment strategies based on combined external beam radiation and brachytherapy, often with concurrent chemotherapy, with surgery being reserved for patients with in situ or very early stage disease (American College of Radiology 2013).

6.1.1.1 MRI Findings

Vaginal carcinoma is best detected on T2WI, as a mass of intermediate to high signal intensity that can be seen as separate from the hypointense vaginal wall. Some neoplasms may contain hyperintense foci, probably representing tumoral necrosis; this finding should raise the possibility of a poorly differentiated component, including adenosquamous carcinoma, mucinous adenocarcinoma, or metastases. The tumor appears isointense on T1WI, and its presence could be suggested in lesions large enough to alter the vaginal contour (Walker et al. 2011; Gardner et al. 2015; Taylor et al. 2007).

Stage I tumors are limited to the vaginal mucosa and appear as a mass expanding and filling the vagina, but with preservation of the low T2 signal of the vaginal wall. In stage II, tumor extension into the paravaginal tissues is well appreciated on MRI by loss of the low T2 signal of the vaginal wall and the presence of abnormal low T1 signal in the paravaginal fat, best detected on axial plane. In stage III, tumor extends laterally to the pelvic sidewall, which is best seen on axial and coronal orientations. On MRI, pelvic sidewall invasion is defined as tumor spread within 3 mm of the internal obturator, levator ani or piriformis muscles, and/or iliac vessels. Increased T2 signal related to edema or direct invasion of the tumor into the musculature may be seen. Tethering of the musculature is also occasionally detected. In stage II and III tumors, coronal T2WI should be performed to evaluate also for possible hydronephrosis. In stage IVA, disease has directly spread beyond the true pelvis and/or invaded the rectum or urinary bladder. Loss of the intervening fat planes and of the normal hypointense T2 signal of the bladder or rectal wall, sometimes associated with contour abnormality such as irregularity and nodularity along the wall are findings suggestive of invasion (Fig. 14). Abnormal enhancement of the bladder or rectal wall and/or direct extension of neoplasm

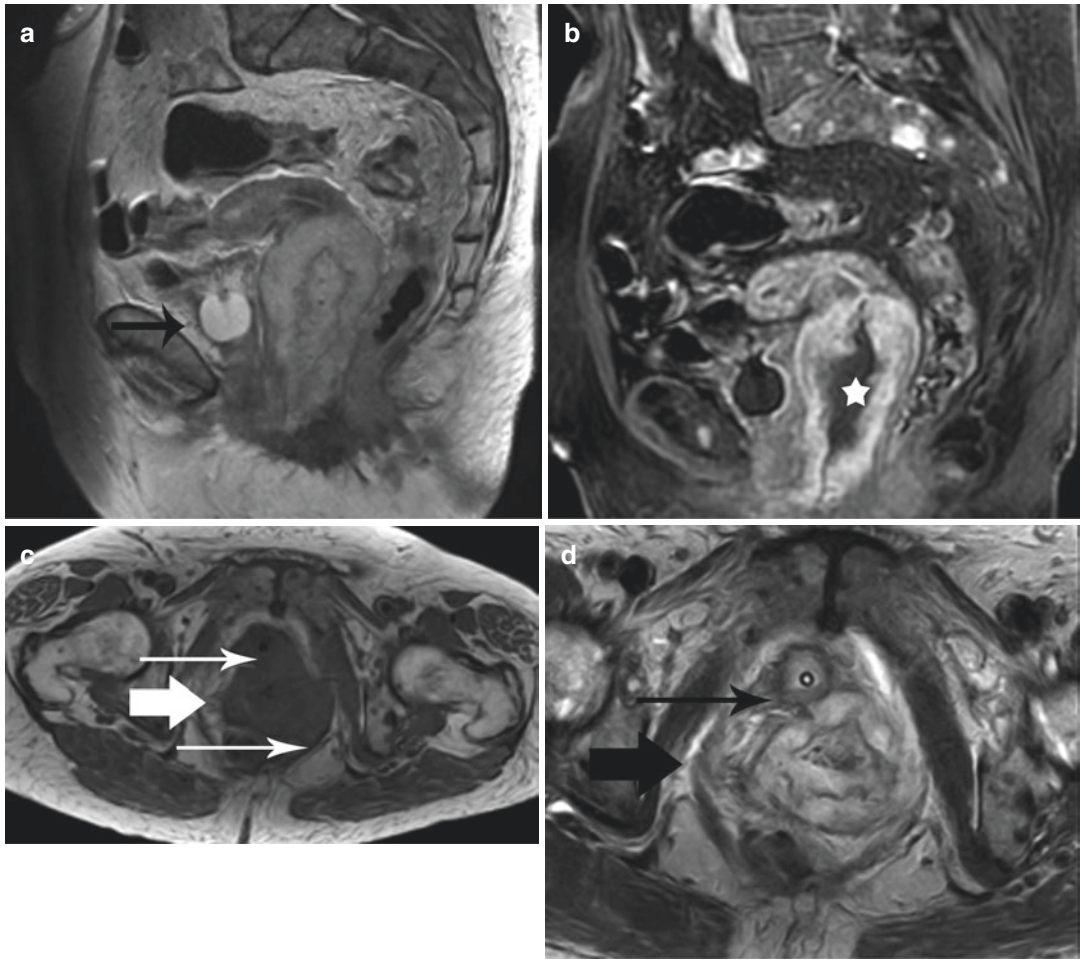

Fig. 14 FIGO stage IVA squamous cell carcinoma of the vagina. (**a**) T2WI and (**b**) post-gadolinium fat-saturated T1WI in sagittal orientation show a large, heterogenous mass replacing the vagina. The tumor appears mainly hyperintense on T2WI, strongly and inhomogeneously enhancing after gadolinium administration. Non-enhancing parts of the mass (*asterisk*) corresponded to areas of necrosis on pathology. Loss of the intervening fat planes between the neoplasm and the urethra/rectum suggests invasion. Foley catheter (*arrow*). (**c**) T1WI and (**d**) T2WI in transverse orientation depict vaginal carcinoma (*arrow*) invading the urinary bladder and the left puborectalis muscle (*long arrows*) (Courtesy Dr. Forstner R, Salzburg, Austria)

into the bladder or rectum are other signs suggestive of infiltration. Multiple planes are often necessary to verify the presence or absence of neighboring organ invasion. The overall accuracy of MRI in diagnosing bladder and rectal invasion is high, ranging from 96 to 99%. However, MRI may overstage bladder involvement as it is difficult to differentiate peritumoral edema (bullous edema) and inflammation from tumor infiltration; in these cases correlation with cystoscopy is necessary. In stage IVB, disease spreads beyond the pelvis and may involve the peritoneum and small or large bowel loops. The most common sites of distant metastases are the lung, liver, and bones (Walker et al. 2011; Gardner et al. 2015; López et al. 2005; Parikh et al. 2008).

MRI findings of staging primary vaginal carcinoma are presented in Table 2.

6.1.1.2 Lymph Node Drainage

Lymph node drainage is important as vaginal carcinoma commonly appears with metastatic lymphadenopathy, even in early stages, with reported rates 6–14% for stage I and 26–32% for stage II disease. The upper third of the vagina drains into the external iliac and para-

Table 2 MRI staging of vaginal cancer

Stage	MRI findings
I	Tumor confined within the vagina, with preservation of the low T2 signal of the vaginal wall
II	Disruption of the low T2 signal of the vaginal wall, abnormal low T1 signal in the paravaginal fat
III	Tumor spread within 3 mm of the internal obturator, levator ani, or piriformis muscles and/or iliac vessels. Increased T2 signal of the musculature and/or direct invasion of the tumor
IV	Tumor spreads beyond the true pelvis and/or invades the bladder or rectum
IVA	Loss of the intervening fat planes, loss of the normal hypointense T2 signal of the bladder or rectal wall, contour abnormality, abnormal enhancement of the bladder or rectal wall, or direct extension of neoplasm into the bladder or rectum
IVB	Distant metastases (lung, liver, bones)

aortic chain, the middle third into the common and internal iliac chains, and the lower third into the superficial inguinal, femoral, and perirectal nodal chains. However, these patterns of lymphatic drainage are highly variable and unreliable (Gardner et al. 2015). Both CT and MRI may be used for the evaluation of metastatic lymphadenopathy.

6.1.1.3 Recurrence and Complications

Local recurrences in vaginal cancer are the most common, usually seen within the first few years after initial diagnosis, almost 80% by 2 years and 90% by 5 years. The stage of the disease has been proved to be the main predictive variable for recurrence, reported to occur at 24% of cases for stage I disease, up to 73–83% of cases for stage IV disease. Tumors of the upper third of the vagina tend to recur locally, whereas those of the lower third are more often associated with pelvic sidewall invasion or even distant recurrence. In patients with recurrence, 5-year survival rate is poor, approximating 12% (Gardner et al. 2015; Parikh et al. 2008). MRI is useful in staging patients with vaginal carcinoma recurrence, with an overall accuracy of 82–95% (Gardner et al. 2015).

Common posttreatment complications in patients with vaginal carcinoma include radiation-induced bladder, rectal, and vaginal toxicity. Complications usually occur within the first 5 years of treatment, but may be seen up to 20 years later. FIGO stage, tumor size, and total radiation dose predict higher likelihood of complications. On imaging, post-radiation complications are common, reported in up to 30% of patients, with rectovaginal and vesicovaginal fistulas seen in 21%. Cystitis, proctitis, bowel stricture and perforation, pelvic bone osteonecrosis, and stress fractures may also occur. Various imaging modalities can be used to assess complications, including MRI (Gardner et al. 2015; Parikh et al. 2008).

6.1.2 Non-squamous Cell Carcinomas of the Vagina

Non-squamous cell carcinomas account for 15% of all primary vaginal carcinomas. These tumors usually are diagnosed at early stage, in younger age, and have better prognosis. However, they are more likely to recur than SCCs, often within 1–7 years after the diagnosis of primary tumor (Parikh et al. 2008; Tsuda et al. 1999).

6.1.2.1 Adenocarcinoma

Adenocarcinomas account for 9% of primary vaginal malignancies. The mean age at diagnosis is 19 years; two-thirds of those women have a history of exposure to diethylstilbestrol in utero, dating from the 1950–1970s, when diethylstilbestrol was given to mothers at risk for miscarriage. Primary vaginal adenocarcinoma mainly involves the upper third and the anterior wall of the vagina. On MRI, it appears either as a bulky lobulated vaginal mass, hyperintense on T2WI or as diffuse circumferential thickening of the vaginal wall (Parikh et al. 2008; Tsuda et al. 1999).

6.1.2.2 Melanoma

Primary vaginal malignant melanoma accounts for less than 3% of all vaginal malignancies. Only less than 0.5–2% of all melanomas in women affect the vagina, the vulva representing the commonest site. It often manifests in postmenopausal women, with a predilection for the lower vaginal third and the anterior and lateral

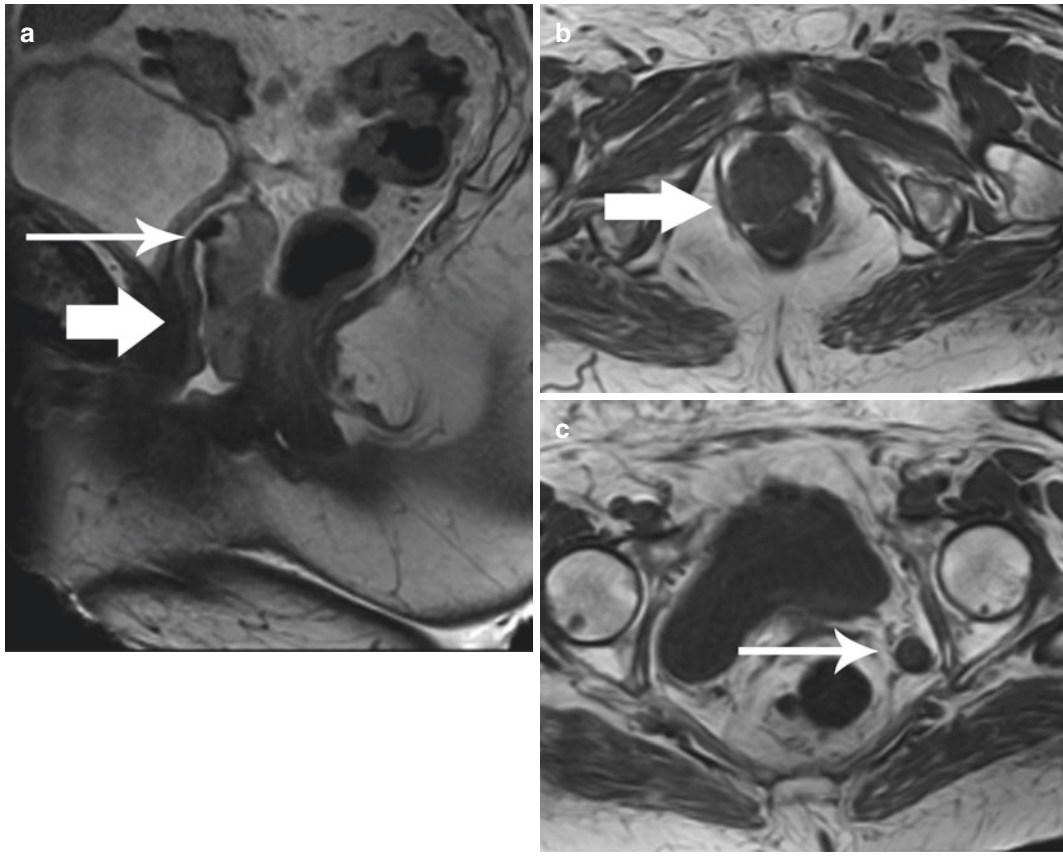

Fig. 15 FIGO stage II vaginal melanoma. (**a**) Sagittal T2WI depicts heterogeneous vaginal tumor (*arrow*), mainly hyperintense. Area of necrosis is detected within the mass with very high signal intensity and a small amount of air (*long arrow*). Axial T1WI shows vaginal neoplasm extending into the paravaginal tissues (**b**, *arrow*). An enlarged left internal iliac node (**c**, *long arrow*) is also seen (Courtesy Dr. Forstner R, Salzburg, Austria)

walls. MRI features are variable. These tumors may present with typical high T1 signal and low T2 signal, due to the paramagnetic effects of melanin and methemoglobin from intratumoral necrosis or hemorrhage. Amelanotic melanomas may appear with low T1 signal and intermediate to high T2 signal (Fig. 15). Melanomas are much more easily detected on fat-suppressed T1WI with brighter signal, as the dynamic range becomes narrower, allowing detection of subtle differences (López et al. 2005; Parikh et al. 2008; Tsuda et al. 1999; Moon et al. 1993).

6.1.2.3 Sarcomas

Sarcomas account for less than 3% of primary vaginal malignancies. Primary vaginal leiomyosarcoma represents the commonest vaginal soft-tissue sarcoma in adults. The average age is 50 years and may occur after radiation therapy to the genital tract. This tumor is thought to originate from the rectovaginal septum, mainly involving the upper vagina. Early hematogenous spread and local recurrence frequently occurs. MRI usually shows a bulky cystic-solid mass arising from the vagina, with areas of high T2 signal corresponding to cystic necrosis and pockets of high T1 signal corresponding to acute hemorrhage, strongly and heterogeneously enhancing (Fig. 16) (Griffin et al. 2010; Parikh et al. 2008).

6.1.2.4 Lymphoma

Primary lymphoma of the vagina is rare, representing approximately 1% of primary extranodal lymphomas. Secondary lymphoma is more

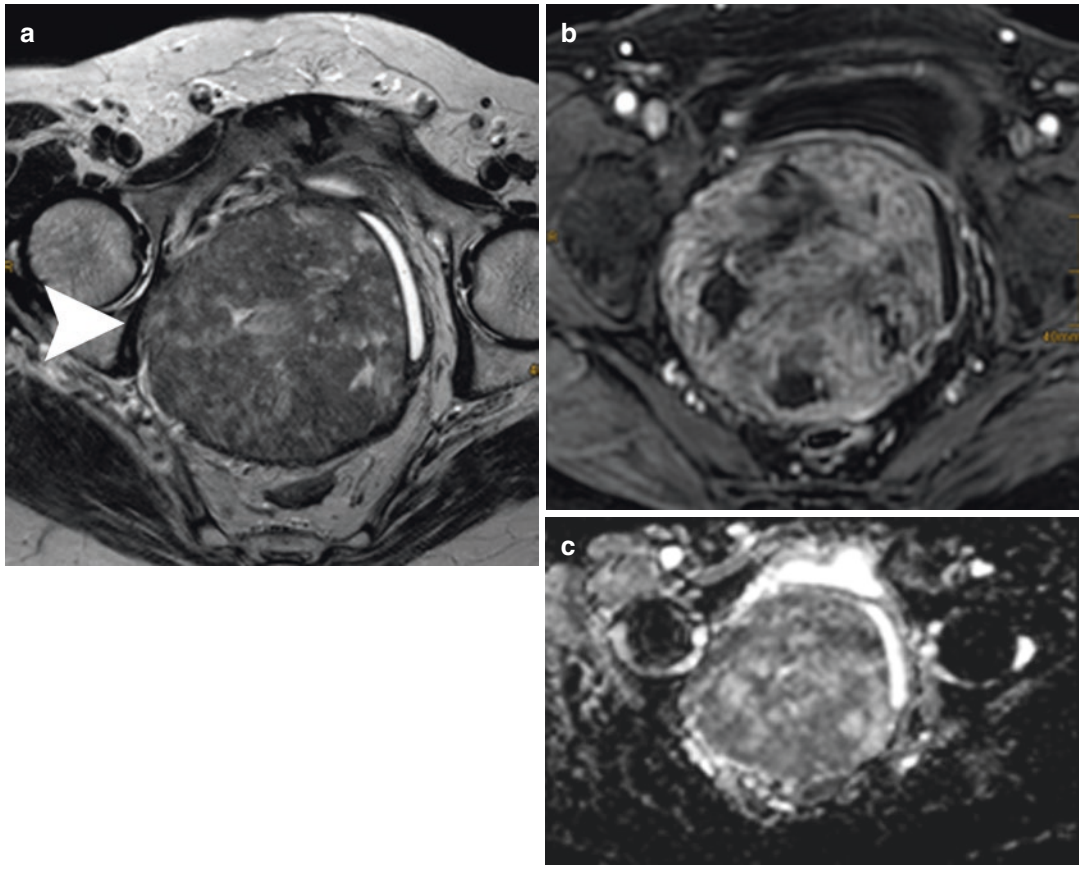

Fig. 16 FIGO stage III vaginal leiomyosarcoma. Axial (**a**) T2WI, (**b**) post-gadolinium fat-suppressed T1WI, and (**c**) ADC map demonstrate a large, heterogeneous vaginal mass, with strong, inhomogeneous contrast enhancement, and restricted diffusion. The neoplasm is in direct contact with the right internal obturator muscle (*arrowhead*), a finding suggestive of pelvic sidewall invasion (Courtesy Dr. Forstner R, Salzburg, Austria)

common. Both are usually B-cell, non-Hodgkin's lymphomas. The mean age at presentation is 50 years. The tumor is infiltrative or mass-like of homogeneous low T1 signal and intermediate-to-high T2 signal. Homogeneous enhancement is seen after intravenous contrast medium administration. An intact mucosa is considered characteristic for the diagnosis of lymphoma (Griffin et al. 2010; McNicholas et al. 1994).

6.1.3 Secondary Vaginal Malignancies

Secondary malignancies of the vagina are far more common than primary tumors and account for more than 80% of all vaginal neoplasms. The majority of vaginal metastases occur through direct contiguous spread from malignancies of adjacent tumors, e.g., primary cervical (Fig. 17), endometrial, vulval, rectal, or bladder carcinoma. Distant vaginal metastases may occur through lymphatic or hematogenous spread. The most common malignancies to metastasize to the vagina are ovarian, cervical, endometrial (Fig. 18), and rectal cancer. Very rarely, extragenital cancers including adenocarcinoma of the colon (Fig. 19), breast, pancreas, and small bowel may metastasize to the vagina. The vagina can also be the site for local recurrence, e.g., from endometrial and cervical carcinoma. The majority (80%) of vaginal metastases occur within the first three years after the diagnosis of primary malignancy, and 67% occur after surgical removal of the primary lesion. Disseminated metastatic disease is often present in patients

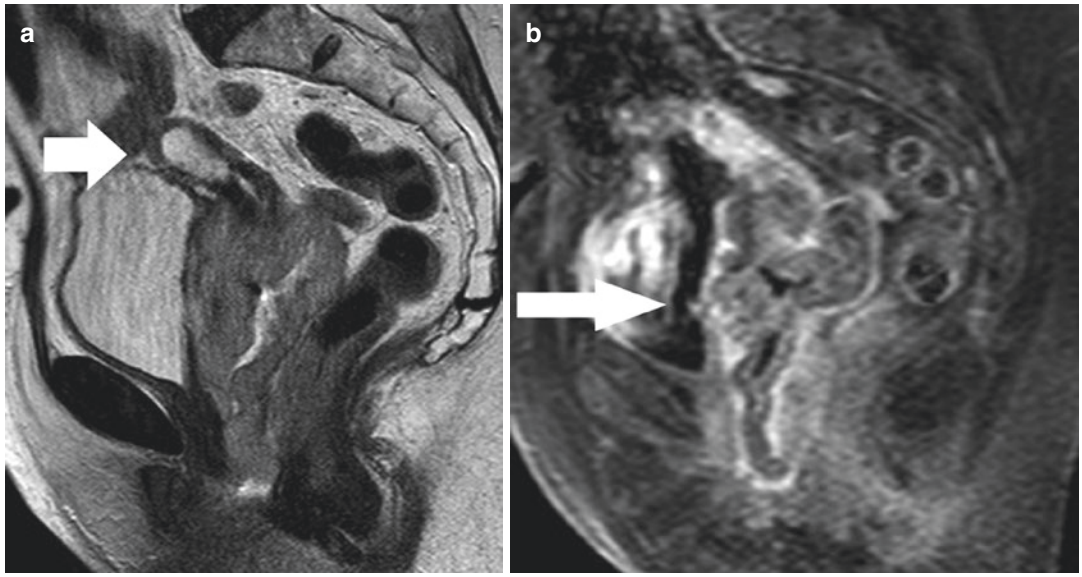

Fig. 17 FIGO stage IVA cervical carcinoma in 50-year-old woman. Sagittal (**a**) T2WI and (**b**) dynamic contrast-enhanced subtracted MR image (early phase) show a bulky heterogeneous mass that arises from the cervix and extends to the lower third of the vagina. The tumor appears with T2 signal mainly similar to that of normal myometrium, enhancing inhomogeneously, less than myometrium after gadolinium administration, with areas of necrosis and a small amount of air. The mass invades the posterior wall of the urinary bladder (*long arrow*). Obstruction of the endocervical canal by the neoplasm causes distention of the endometrial cavity (*arrow*)

with vaginal metastases and therefore the prognosis is extremely poor.

Seventy-five percent of squamous vaginal metastases arise from the cervix and 14% from the vulva. Of the vaginal metastases that are adenocarcinomas, 92.5% of lesions in the upper third and anterior wall arise from the upper genital tract, while 90% of lesions in the lower third and posterior wall arise from the gastrointestinal tract. The overall accuracy of MRI in assessing vaginal metastases has been reported as 92%. The MRI features of vaginal metastases mimic the MRI features of the primary tumor, usually detected with low to intermediate T1 signal and intermediate to high T2 signal (Walker et al. 2011; Griffin et al. 2010; Parikh et al. 2008).

6.2 Vulvar Malignancies

6.2.1 Vulvar Carcinoma

Vulval carcinoma is rare, accounting for 4% of all gynecologic malignancies. The disease has a bimodal distribution, with approximately 66% of cases seen over the age of 70 years and fewer than 20% occurring in women younger than 50 years (Griffin et al. 2010; Hosseinzadeh et al. 2012; Lee et al. 2011; Ssi-Yan-Kai et al. 2015; Sohaib et al. 2002). Human papilloma virus-positive tumors occur in younger age, may be multifocal, and show an association with vulvar intraepithelial neoplasia. Patients may present with a palpable mass, bleeding due to ulceration, pruritus, pain, and discharge.

Vulval cancer involves the labia in two-thirds of cases. The clitoris and Bartholin glands are less commonly involved. It is locally infiltrative and may extend to the urethra, anorectum, and vagina, and rarely to the bladder. It typically spreads to the ipsilateral superficial inguinofemoral lymph nodes, followed by the deep inguinofemoral lymph nodes, before pelvic lymph nodes. Rarely, it extends beyond the pelvis (Griffin et al. 2010; Hosseinzadeh et al. 2012; Lee et al. 2011; Ssi-Yan-Kai et al. 2015; Sohaib et al. 2002).

More than 85% are squamous cell carcinomas; other primary histologic types include adenocarcinoma, sarcoma, Bartholin gland cancer, basal cell cancer, and extramammary Paget disease. The most important prognostic

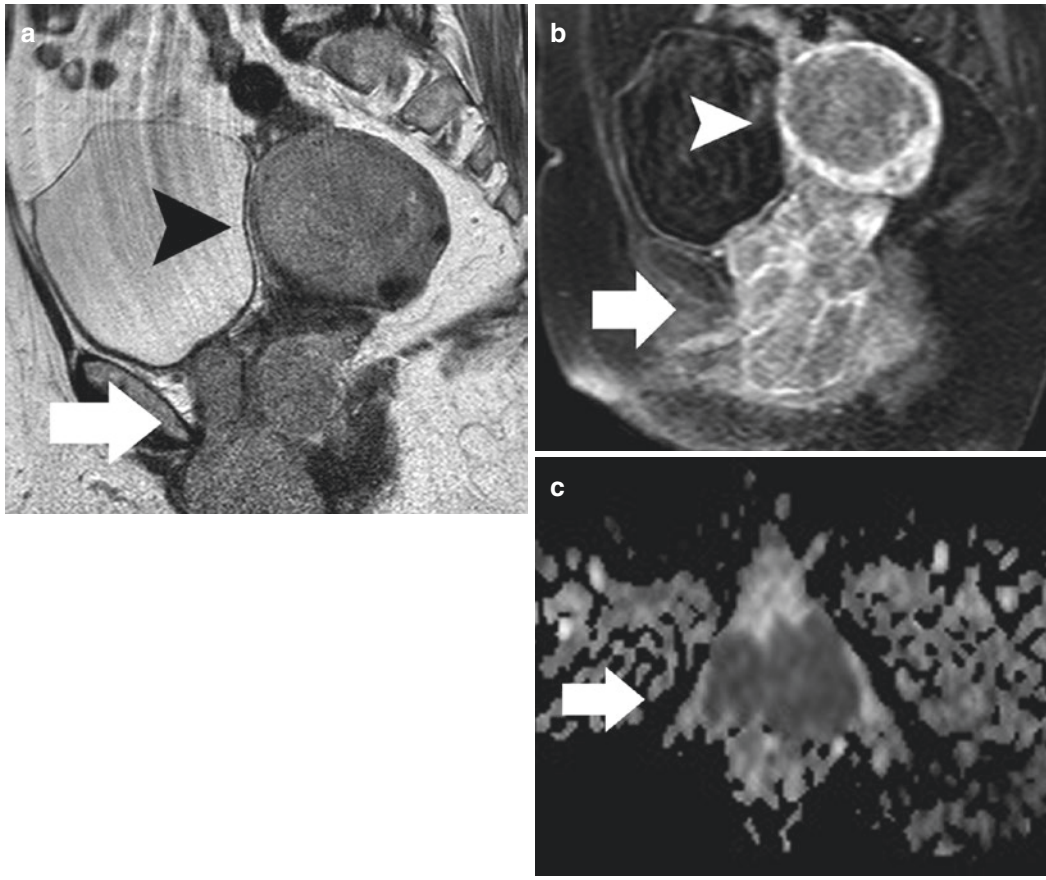

Fig. 18 Vaginal metastases from endometrial carcinoma (skip lesions) in an 80-year-old woman. Sagittal (**a**) T2WI and (**b**) dynamic contrast-enhanced subtracted MR image (early phase) demonstrate large heterogeneous masses replacing the uterus (*arrowhead*) and the vagina (*arrow*). The neoplasms have similar imaging findings, detected mainly with intermediate T2 signal and heterogeneous contrast enhancement. (**c**) Transverse ADC map at the level of vaginal mass shows tumor with low signal intensity (*arrow*), due to restricted diffusion

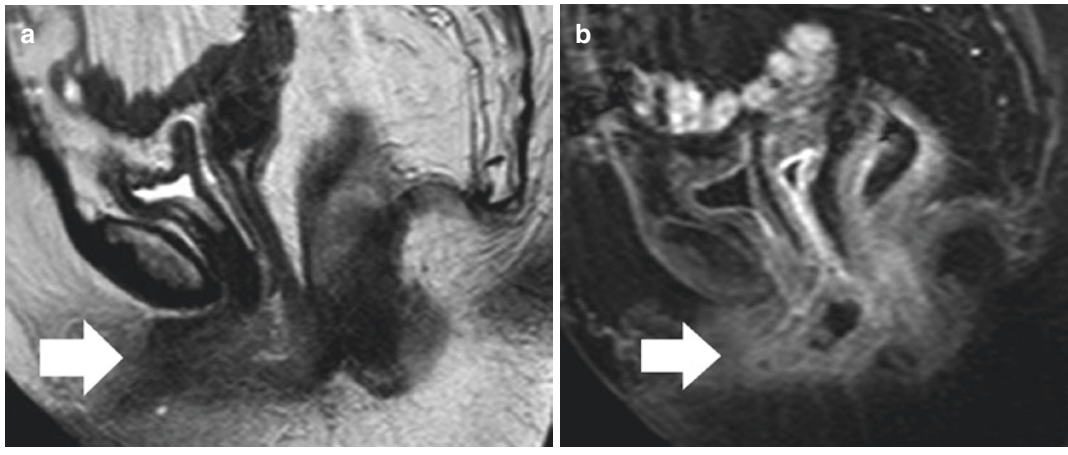

Fig. 19 Vaginal metastasis from colon adenocarcinoma in 82-year-old woman. Sagittal T2WI (**a**) and (**b**) fat-suppressed TIW1 after gadolinium administration depict heterogeneous vaginal mass (*arrow*), inhomogeneously enhancing. (**c**) Axial fat-saturated TIW1 after gadolinium administration shows left inguinal metastatic lymphadenopathy (*arrowhead*)

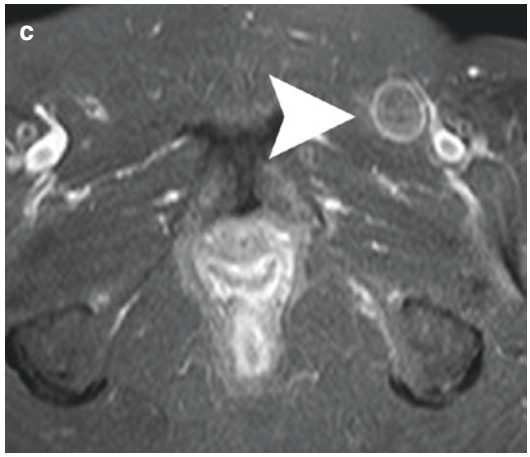

Fig. 19 (continued)

Table 3 FIGO staging for vulvar cancer

FIGO	Definition
IA	Tumor confined to vulva or perineum, ≤2 cm in size with stromal invasion ≤1 mm, negative nodes
IB	Tumor confined to vulva or perineum, >2 cm in size or with stromal invasion >1 mm, negative nodes
II	Tumor of any size with adjacent spread (1/3 lower urethra, 1/3 lower vagina, anus), negative nodes
IIIA	Tumor of any size with positive inguinofemoral lymph nodes (1) 1 lymph node metastasis greater than or equal to 5 mm (2) 1–2 lymph node metastasis(es) of less than 5 mm
IIIB	(1) 2 or more lymph node metastases greater than or equal to 5 mm (2) 3 or more lymph node metastases less than 5 mm
IIIC	Positive node(s) with extracapsular spread
IVA	(1) Tumor invades other regional structures (2/3 upper urethra, 2/3 upper vagina), bladder mucosa, rectal mucosa, or fixed to pelvic bone (2) Fixed or ulcerated inguinofemoral lymph nodes
IVB	Any distant metastasis including pelvic lymph nodes

factors determining survival include tumoral size, depth of invasion, and presence of lymph node metastases. The FIGO staging classification (Tan et al. 2012) is presented in Table 3. Patients with negative groin nodes have a 90% survival, compared to 50% survival with positive nodes. Recurrences are usually seen within 2 years after initial treatment, mostly in the vulva (57%), groin (22%), pelvis (4%), or distant sites (23%) (Griffin et al. 2010; Hosseinzadeh et al. 2012; Lee et al. 2011; Ssi-Yan-Kai et al. 2015; Sohaib et al. 2002).

MRI is the modality of choice to allow proper tumoral delineation, evaluation of the local extent of vulvar cancer, and its relationship to adjacent structures, to aid in surgical planning and to reduce surgical morbidity (Griffin et al. 2010; Hosseinzadeh et al. 2012; Lee et al. 2011; Ssi-Yan-Kai et al. 2015; Sohaib et al. 2002). The tumor appears as a solid mass with nonspecific low T1 signal, intermediate-to-high T2 signal, and variable contrast enhancement (Figs. 20 and 21). The reported sensitivity and specificity of MRI in detecting metastatic lymphadenopathy in patients with vulvar carcinoma is reported 52–86% and 82–85%, respectively (Lee et al. 2011). Location, size, shape, and internal architecture on CT or MRI should be assessed to diagnose lymph node involvement. Size criteria show suboptimal accuracy; almost 60% of metastatic lymph nodes are smaller than 5 mm in diameter. Loss of the fatty hilum and a more round rather than elongated shape are features suggestive of tumor involvement. A decrease in central enhancement, indicating necrosis, and T2 signal heterogeneity on MRI are features suspicious for metastatic infiltration (Lee et al. 2011).

6.2.2 Melanoma

Melanoma is the second most common vulval malignancy, accounting for 5% of malignant vulval neoplasms. MRI features are similar to those described for vaginal melanoma (Griffin et al. 2010; Hosseinzadeh et al. 2012; Ssi-Yan-Kai et al. 2015).

6.2.3 Lymphoma

Primary or secondary non-Hodgkin lymphoma (NHL) of the female genital tract is rare, more often seen as a manifestation of systemic disease. Rarely, NHL may arise primarily in gynecologic organs, with the vulva being the least commonly affected organ. Primary NHL of the vulva is aggressive, mostly occurring in the elderly. The final diagnosis is made through percutaneous core or

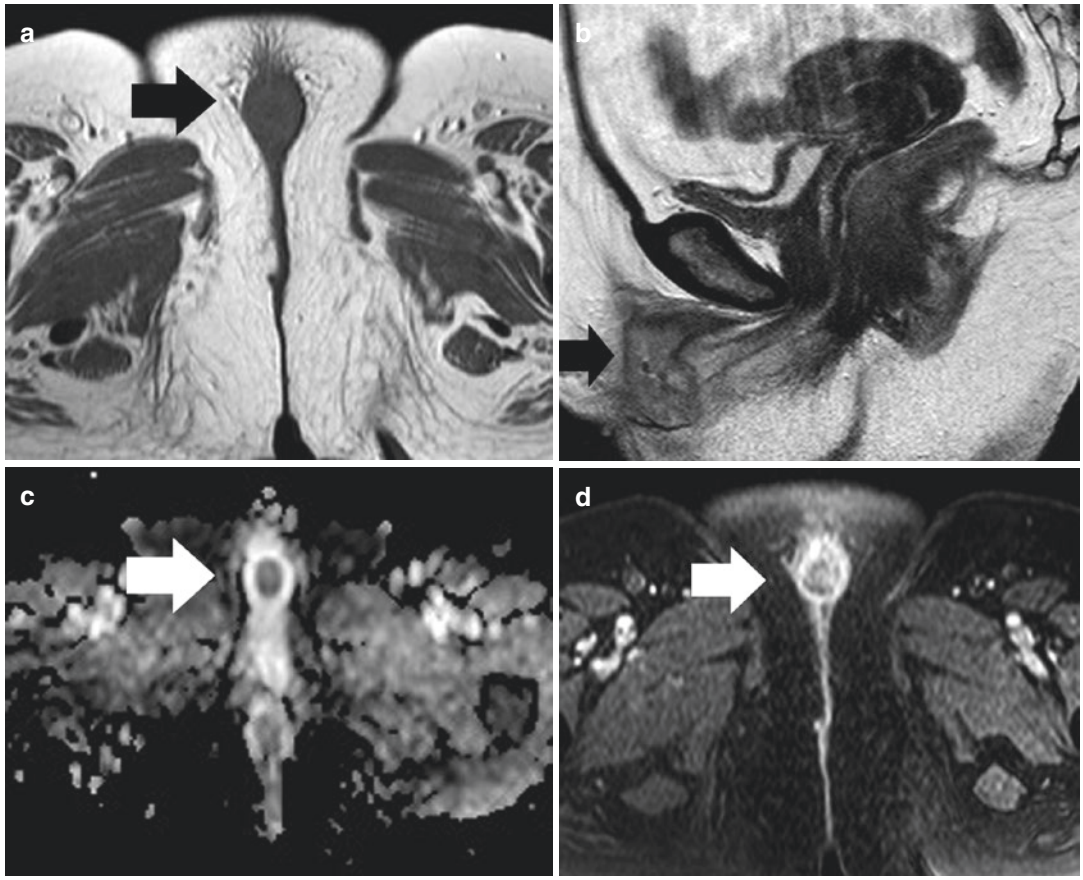

Fig. 20 (**a**) Axial T1WI, (**b**) sagittal T2WI, transverse (**c**) ADC map, and (**d**) subtracted DCE image show vulvar carcinoma in a 76-year-old woman. The tumor (*arrow*) appears isointense compared to surrounding muscles on T1WI, heterogeneous, mainly hyperintense on T2WI, with restricted diffusion and heterogeneous contrast enhancement. Areas of necrosis within the mass have very high signal intensity on T2WI and reduced enhancement. A small amount of air is seen within the tumor

excisional tissue biopsy. Lymphoma is detected as a homogeneous solid vulvar mass, centrally located and strongly enhancing (Hosseinzadeh et al. 2012).

6.2.4 Aggressive Angiomyxoma of the Vulva

Aggressive angiomyxoma is a rare tumor that affects the pelvis and perineum, usually seen in premenopausal women. It appears as a large, solid infiltrative mass that tends to displace rather than invade adjacent structures. It does not metastasize and is treated by wide local excision. There is a tendency for local recurrence if incompletely excised. Imaging is important to determine extent and, thus, the optimal surgical approach. High T2 signal is detected, probably reflecting the myxomatous stroma and high water content (Fig. 22). Swirled or layered tissue within the tumor produces a distinctive appearance, with slightly lower signal intensity than the remainder of the tumor on T2WI and enhancement after gadolinium administration (Griffin et al. 2010).

7 Vaginal Cuff Disease

The vaginal cuff represents the apex of the vagina, where the apposed upper walls are sutured together at hysterectomy. In cases where surgical history is unclear regarding total versus partial hysterectomy, imaging is important to define whether a cervical remnant is present. The vaginal cuff represents a common site of recurrent gynecologic malignancy

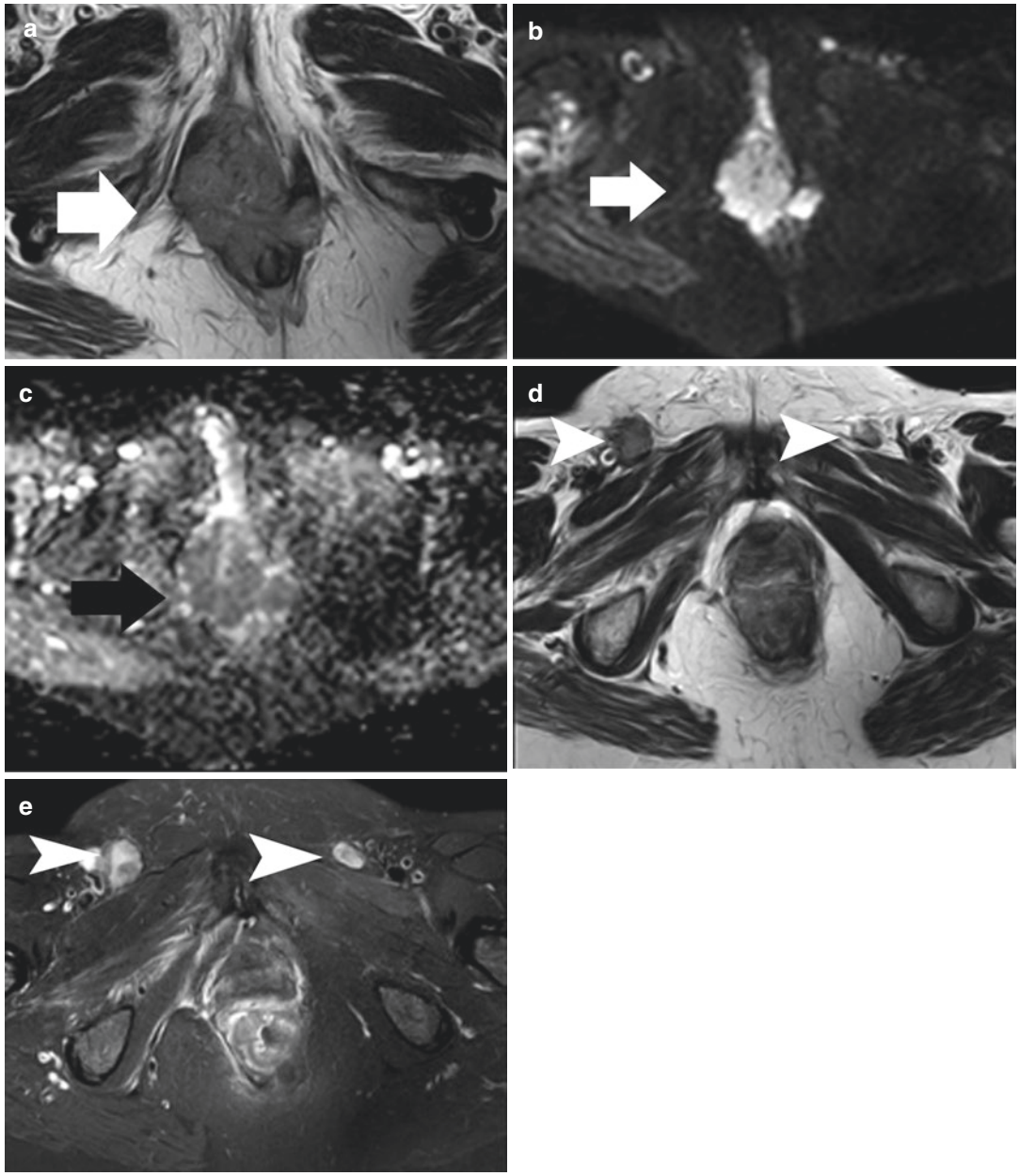

Fig. 21 Locally advanced vulvar carcinoma with bilateral inguinofemoral lymph node metastases. (**a**) Axial T2WI depicts large, heterogeneous vulvar carcinoma (*arrow*) invading the surrounding organs. The tumor (*arrow*) causes restricted diffusion and is detected hyperintense and hypointense on axial (**b**) DWI and (**c**) ADC map, respectively. (**d**) T2WI and (**e**) post-contrast T1WI with fat saturation show enlarged superficial inguinofemoral nodes (*arrowhead*), heterogeneously enhancing (Courtesy Dr. Forstner R, Salzburg, Austria)

after hysterectomy. Recurrence is usually seen in women with a history of cervical carcinoma, but also with endometrial carcinoma and, rarely, with ovarian carcinoma. Sometimes, on imaging the vaginal cuff appears bulky and/or asymmetric and differentiation of a prominent cuff or cervical remnant from tumor recurrence can be difficult. The vaginal cuff and cervical remnant are well assessed at MRI, which is generally superior to CT (Walker et al. 2011; Brown et al. 1992).

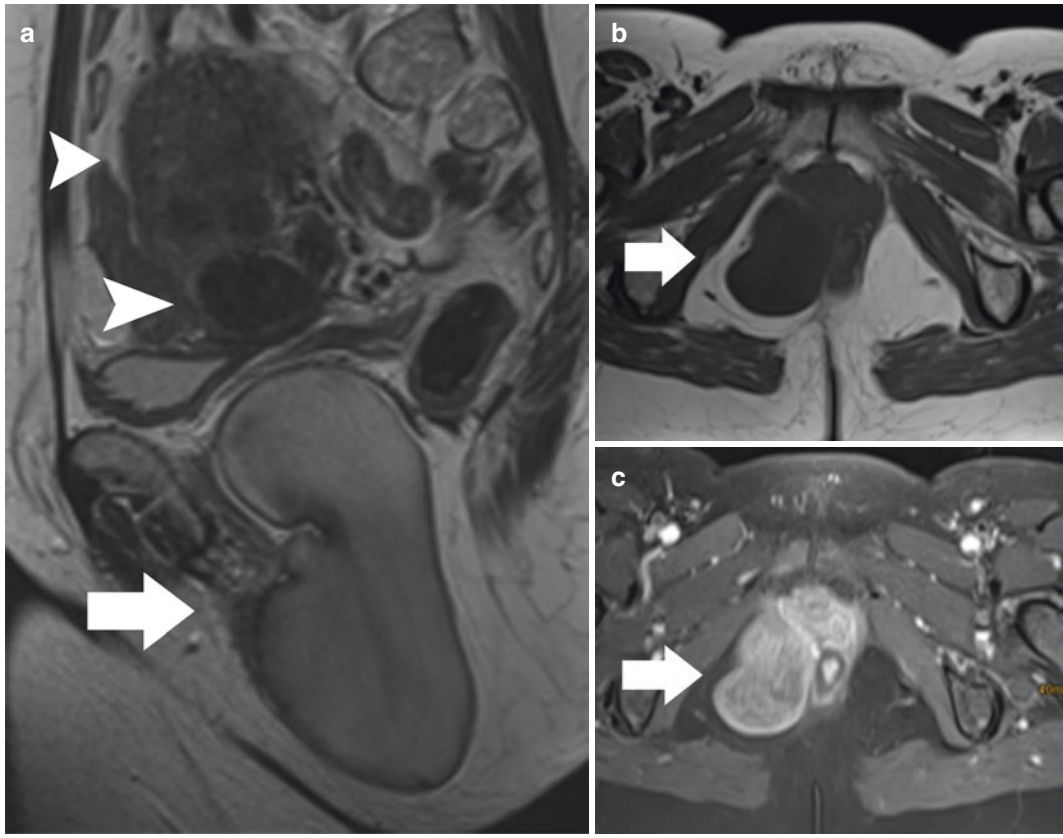

Fig. 22 Aggressive angiomyxoma of the vulva. (**a**) Sagittal T2WI depicts large heterogeneous, sharply defined perineal mass, mainly hyperintense (*arrow*). Uterus leiomyomas (*arrowheads*) are also seen as hypointense lesions. Axial (**b**) T1WI and (**c**) fat-saturated contrast-enhanced T1WI. The tumor (*arrow*) appears of intermediate T1 signal and enhances strongly after gadolinium administration. The characteristic swirled internal architecture of the neoplasm is seen on both T2WI and post-contrast T1WI (Courtesy Dr. Forstner R, Salzburg, Austria)

7.1 MRI Findings

The vaginal cuff may be linear and smooth or partially obscured by surgical clip artifacts. It may also have a nodular appearance, with a signal intensity similar to that of muscle that closely mimics a vaginal mass on TIWI. Differentiation is possible on T2WI, where the vagina has a normal appearance, and the hypointense layer of the vaginal smooth muscle can be distinguished from the bright outer layer of the connective tissue (Fig. 23). In cases of recurrence, the tumor is relatively hyperintense on T2WI, obliterating the hypointense vaginal muscularis (Fig. 24) (Walker et al. 2011; Brown et al. 1992).

8 Foreign Bodies

Knowledge of the imaging characteristics of vaginal foreign bodies aids in assessing the vagina and in avoiding a misdiagnosis of pelvic disease (Fig. 25). Patients often inadvertently leave tampons in place during imaging examinations. Vaginal pessary devices have been used for over 100 years for the treatment of uterine, vaginal, urinary bladder, and rectal prolapse as well as urinary incontinence. They are simple mechanical devices of variable size and shape, which can be left in place for long periods, even years (Walker et al. 2011; Hunter and Taljanovic 2005).

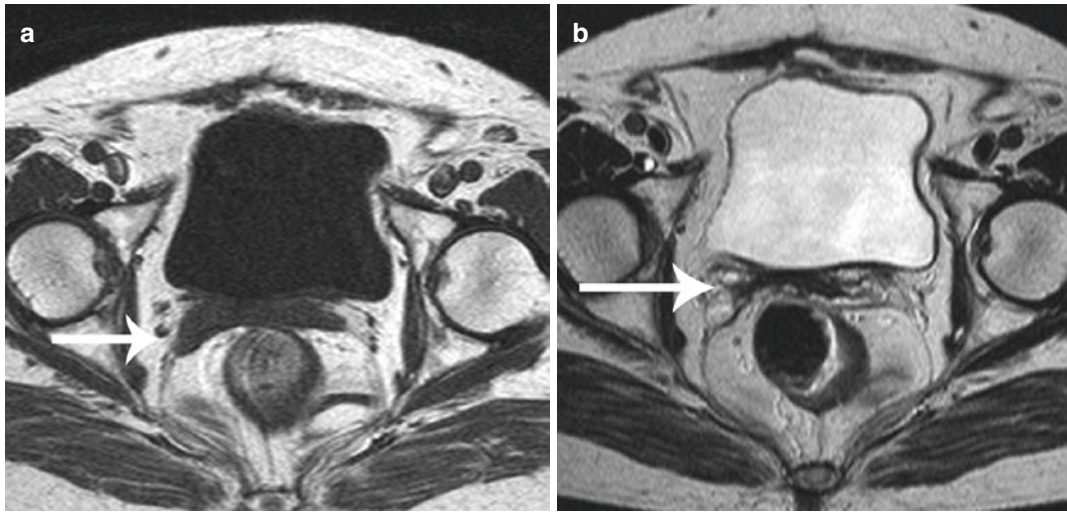

Fig. 23 Normal appearance of the vaginal cuff (*long arrow*) in a 74-year-old woman after total hysterectomy for endometrial carcinoma. (**a**) T1WI and (**b**) T2WI in axial orientation depict muscularis of vaginal cuff with low T2 signal, surrounded by bright connective tissue layer of vaginal wall

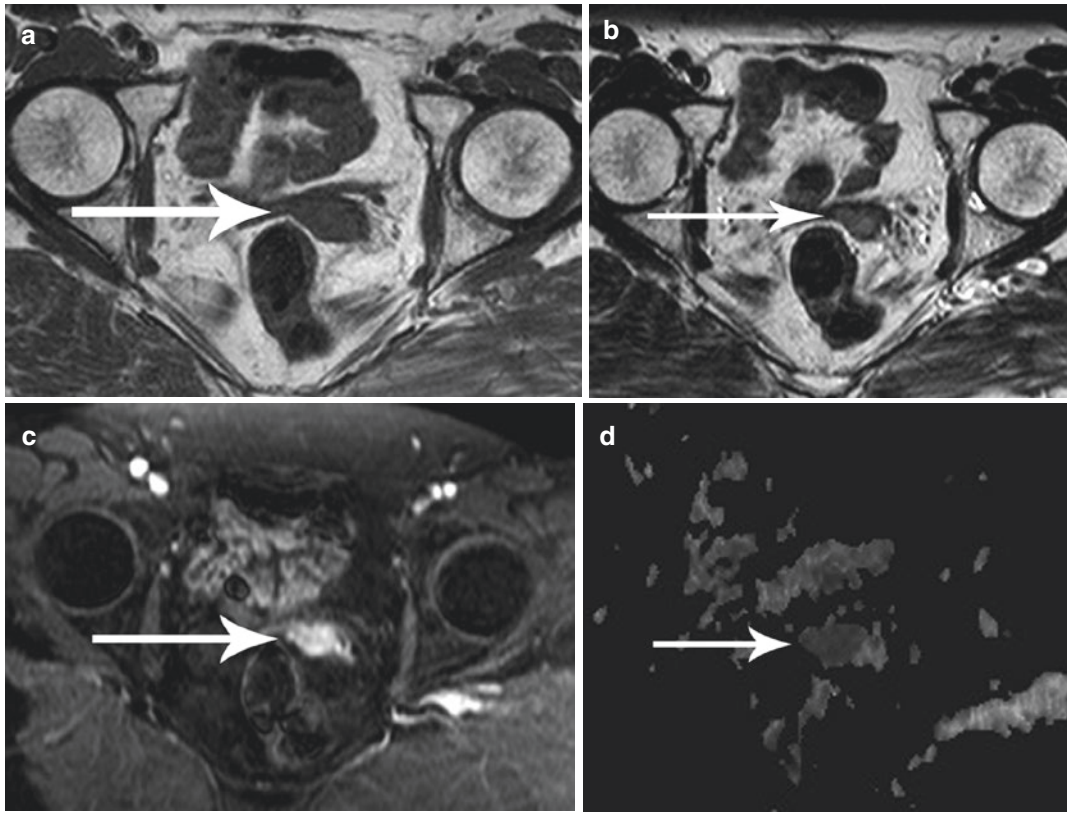

Fig. 24 Axial (**a**) T1WI, (**b**) T2WI, (**c**) dynamic contrast-enhanced subtracted MR image (early phase), and (**d**) ADC map depict cervical carcinoma recurrence at the vaginal cuff. The tumor (*long arrow*) is detected with intermediate and slightly high signal intensity on T1WI and T2WI, respectively, enhancing strongly on early imaging and causing restricted diffusion

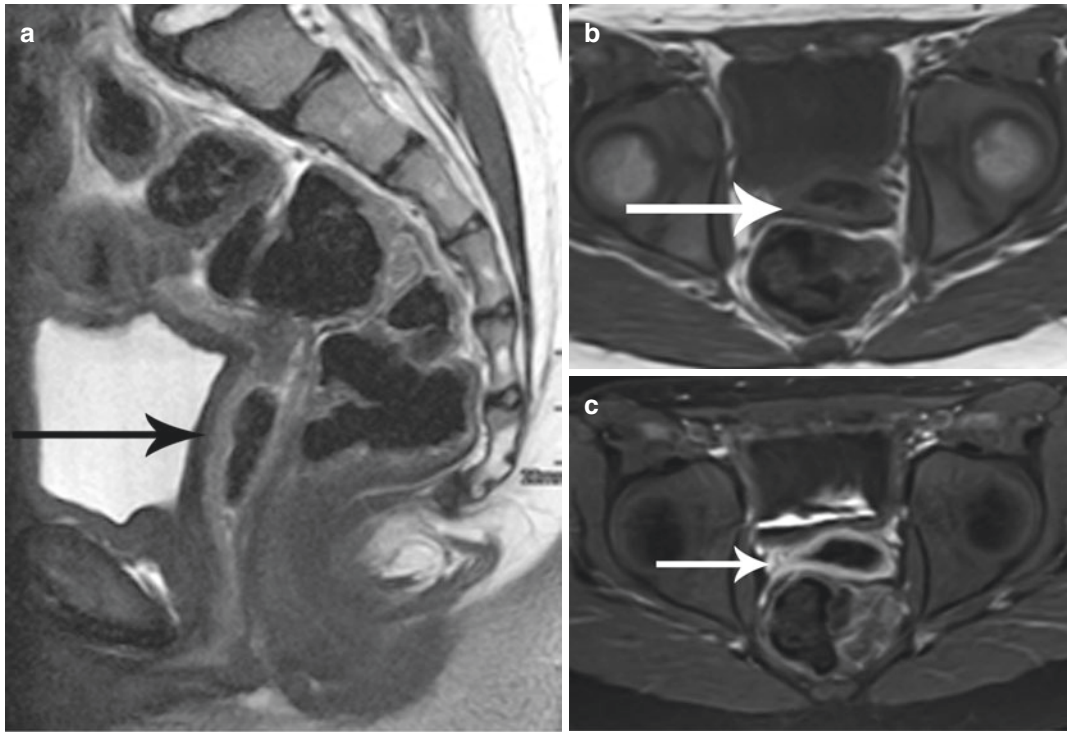

Fig. 25 Eight-year-old female presenting with vaginal bleeding, without signs of precocious puberty. (**a**) Sagittal T1WI and axial (**b**) unenhanced and (**c**) contrast-enhanced T1WI with fat saturation depict intravaginal lesion (*long arrow*) with very low signal intensity on all sequences, proved to correspond to foreign body (Courtesy Dr. Forstner R, Salzburg, Austria)

References

American College of Radiology (2013) ACR Appropriateness Criteria. Available at: https://acsearch.acr.org/docs/3082701/Narrative

Basmajian JV (1971) Grant's method of anatomy. The Williams & Wilkins Co, Baltimore

Brown JJ, Gutierrez ED, Lee JK (1992) MR appearance of the normal and abnormal vagina after hysterectomy. Am J Roentgenol 158:95–99

Chang SD (2002) Imaging of the vagina. Radiol Clin N Am 40:637–658

Chang YCF, Hricak H, Thumher S, Lacey CG (1988) Vagina: evaluation with MR imaging. Part II. Neoplasms. Radiology 169:175–179

Chaudhari VV, Patel MK, Douek M, Raman SS (2010) MR imaging and US of female urethral and periurethral disease. Radiographics 30:1857–1874

FIGO Committee on Gynecologic Oncology (2009) Current FIGO staging for cancer of the vagina, fallopian tube, ovary, and gestational trophoblastic neoplasia. Int J Gynaecol Obstet 105:3–4

Gardner CS, Sunil J, Klopp AH, Devine CE, Sagebiel T, Viswanathan C, Bhosale PR (2015) Pri0MRI in diagnosis, staging and treatment. Br J Radiol 88(1052):20150033

Griffin N, Grant LA, Sala E (2010) Congenital and acquired conditions of the vulva and vagina on magnetic resonance imaging: a pictorial review. Semin Ultrasound CT MR 31:347–362

Hahn WY, Israel GM, Lee VS (2004) MRI of female urethral and periurethral disorders. Am J Roentgenol 182:677–682

Hosseinzadeh K, Heller MT, Houshmand G (2012) Imaging of the female perineum in adults. Radiographics 32:E129–E168

Hricak H, Chang YCF, Thurnher S (1988) Vagina: evaluation with MR imaging. Part I. Normal anatomy and congenital anomalies. Radiology 69:169–174

Hunter TB, Taljanovic MS (2005) Medical devices of the abdomen and pelvis. Radiographics 25:503–523

Junqueira BL, Allen LM, Spitzer RF, Lucco KL, Babyn PS, Doria AS (2009) Müllerian duct anomalies and mimics in children and adolescents: correlative intraoperative assessment with clinical imaging. Radiographics 29:1085–1103

Lee SI, Oliva E, Hahn PF, Russell AH (2011) Malignant tumors of the female pelvic floor: imaging features that determine therapy: pictorial review. AJR 196:S15–S23

López C, Balogun M, Ganesan R, Olliff JF (2005) MRI of vaginal conditions. Clin Radiol 60:648–662

Mann GS, Blair JC, Garden AS (2012) Imaging of gynecological disorders in infants and children. Springer-Verlag, Berlin Heidelberg

McNicholas MM, Fennelly JJ, MacErlaine DP (1994) Imaging of primary vaginal lymphoma. Clin Radiol 49:130–132

Moon WK, Kim SH, Han MC (1993) MR findings of malignant melanoma of the vagina. Clin Radiol 48:326–328

Parikh JH, Barton DPJ, Ind TEJ, Sohaib SA (2008) MR imaging features of vaginal malignancies. Radiographics 28:49–63

Siegelman ES, Outwater EK, Banner MP, Ramchandani P, Anderson TL, Schnall MD (1997) High-resolution MR imaging of the vagina. Radiographics 17:1183–1203

Sohaib SA, Richards PS, Ind T, Jeyarajah AR, Shepherd JH, Jacobs IJ, Reznek RH (2002) MR imaging of carcinoma of the vulva. AJR 178:373–377

Ssi-Yan-Kai G, Thubert T, Rivain AL, Prevot S, Deffieux X, De Laveaucoupet J (2015) Female perineal diseases: spectrum of imaging findings. Abdom Imaging 40:2690–2709

Tan J, Chetty N, Kondalsamy-Chennakesavan S, Crandon A, Garrett A, Land R, Nascimento M, Nicklin J, Perrin L, Obermair A (2012) Validation of the FIGO 2009 staging system for carcinoma of the vulva. Int J Gynecol Cancer 22:498–502

Taylor MB, Dugar N, Davidson SE, Carrington BM (2007) Magnetic resonance imaging of primary vaginal carcinoma. Clin Radiol 62:549–555

Troiano RN, McCarthy SM (2004) Mullerian duct anomalies: imaging and clinical issues. Radiology 233:19–34

Tsuda K, Murakami T, Kurachi H, Narumi Y, Kim T, Takahashi S, Tomoda K, Ohi H, Murata Y, Nakamura H (1999) MR imaging of non-squamous vaginal tumors. Eur Radiol 9:1214–1218

Walker DK, Salibian RA, Salibian AD, Belen KM, Palmer SL (2011) Overlooked diseases of the vagina: a directed anatomic-pathologic approach for imaging assessment. Radiographics 31:1583–1598

Yitta S, Hecht EM, Slywotzky CM, Bennett GL (2009) Added value of multiplanar reformation in the multidetector CT evaluation of the female pelvis: a pictorial review. Radiographics 29:1987–2005

Imaging of Lymph Nodes

Sebastiano Barbieri, Kirsi H. Härmä,
and Harriet C. Thoeny

Contents

Abstract

This chapter provides an overview of lymph node imaging in the female pelvis. We start by outlining the importance and implications of detecting metastatic lymph nodes in gynecological cancer patients. Thereafter, indications are given about the use of different magnetic resonance imaging (MRI) sequences (e.g., T2-weighted and diffusion-weighted MRI), as well as computed tomography (CT), in the context of metastatic lymph node detection. Further, we discuss the potential advantages and disadvantages of intravenous unspecific and tissue-specific contrast agents. The chapter concludes with a description of common imaging findings in benign and malignant lymph nodes, together with corresponding MRI and CT examples.

1 Background

The most common gynecological malignancies are endometrial cancer and uterine sarcomas (estimated number of new cases in Europe in 2012: 98,900 women; mortality: 23,700 women), ovarian cancer (incidence: 65,500 women; mortality: 42,700 women), and uterine cervical cancer (incidence: 58,300 women; mortality: 24,400 women) (Ferlay et al. 2013). According to the guidelines published by the

S. Barbieri • K.H. Härmä • H.C. Thoeny (✉)
Department of Diagnostic, Interventional and Pediatric Radiology, Inselspital, University of Bern, Bern, Switzerland
e-mail: sebastiano.barbieri@insel.ch; kirsihannele.haermae@insel.ch; harriet.thoeny@insel.ch

Med Radiol Diagn Imaging (2017)
DOI 10.1007/174_2017_64, © Springer International Publishing AG
Published Online: 03 June 2017

International Federation of Gynecology and Obstetrics (FIGO) cancer of the corpus uteri is up-staged because of metastases to pelvic and/or para-aortic lymph nodes; similarly, ovarian cancer is up-staged because of positive retroperitoneal lymph nodes (Stage III) and further up-staged if cardiophrenic lymph nodes are considered or proven to be metastatic (Stage IVB) (Berek et al. 2015).

In ovarian cancer, lymph node enlargement above the renal hilum suggests that neo-adjuvant chemotherapy (NACT) might be preferable to primary debulking surgery (PDS) aiming at optimal cytoreduction (Qayyum et al. 2005; Vergote et al. 2010). Cardiophrenic lymph nodes larger than 5 mm are also of interest: upon review of computed tomography (CT) scans of 78 ovarian carcinoma patients, they have been found to be a significant adverse prognostic factor for both progression-free survival and overall survival and to be associated with peritoneal metastases. Thus, the involvement of paracardiac lymph nodes should be regarded as suspicious for stage IV ovarian cancer (Holloway et al. 1997). These results are supported by a more recent retrospective study on 31 patients which suggests that a cut-off value of 7 mm on the short axis can be used to detect metastatic cardiophrenic lymph nodes in advanced ovarian cancer patients with 83% specificity and 63% sensitivity (Raban et al. 2015).

In another study, a significant number of patients (20 out of 30) with advanced epithelial ovarian cancer (EOC) showed supradiaphragmatic lymph node metastases in pretreatment PET-CT findings, suggesting that the route of EOC cells from the peritoneal cavity to the lymphatic system permeates the diaphragm mainly to cardiophrenic lymph nodes and continues to parasternal lymph nodes (Hynninen et al. 2012). The lack of histopathological correlation is a substantial limitation of many studies on cardiophrenic lymph node involvement in EOC patients, due to the fact that it requires additional thoracic surgery and is generally not part of clinical routine. In a recent study, suspicious cardiophrenic lymph nodes with a short axis greater than 10 mm on preoperative CT were removed in case of optimal intra-abdominal debulking; 90% of patients (27 out of 30) had histologically confirmed metastases (Prader et al. 2016).

In the future, further knowledge about the involvement of small cardiophrenic lymph nodes, together with growing experience and technical advances in transdiaphragmatic cardiophrenic lymph node resection, could have an impact on whether NACT or PDS is chosen to treat advanced ovarian cancer patients.

Lymph node involvement has considerable implications on patients' treatment management and prognosis. Metastatic lymph nodes have been found to correlate with histological tumor grade and depth of myometrial invasion (Boronow et al. 1984) and to be associated with both progression-free survival and overall survival (Polterauer et al. 2012). Further, pelvic radiotherapy might be unnecessary for endometrial cancer patients with negative lymph nodes after extended pelvic lymph node dissection (Bottke et al. 2007). Recently, risk-scoring systems have been published to predict lymph node involvement and distant metastases in endometrial carcinoma; a cut-off on the corresponding risk score was found to be associated with an acceptable lymphadenectomy rate (Tuomi et al. 2015). Further, lymphatic dissemination and high-risk tumor features as per the risk-scoring systems were found to be predictors of survival independently of tumor stage (Tuomi et al. 2017).

Metastatic pelvic lymph nodes are recognized as an important prognostic factor in uterine cervical cancer as well (Piver and Chung 1975). In a retrospective study on 127 locally advanced cervical cancer patients, the status of lower pelvic lymph nodes was able to predict the pathologically assessed status of upper pelvic lymph nodes and of the parametrium (Ferrandina et al. 2007). In another study on 70 consecutive patients, lymph node metastases were significantly associated with a higher likelihood of uterine body involvement and of higher FIGO

stage. Moreover, the average tumor volume was determined to be larger in node-positive patients (69 cm^3) than in node-negative patients (49 cm^3) (Narayan et al. 2003).

2 Indications and Value of Imaging Techniques

There are no specific indications for the imaging of pelvic lymph nodes by magnetic resonance imaging (MRI) or CT. Lymph node evaluation is always done in conjunction with imaging performed for tumor staging and evaluation of general metastatic spread.

Traditionally, the standard technique used to differentiate normal from metastatic lymph nodes consists in applying a threshold to the short axis diameter of the node: lymph nodes with a short axis of 10 mm or more are considered metastatic. Nonetheless, this method does not allow discriminating between enlarged inflammatory lymph nodes and metastatic ones; further, the employed threshold value is a matter of debate: 10 mm guarantee a relatively high specificity (90% or more), but are also associated with low sensitivity; increasing this threshold value, e.g., to 12 mm, increases sensitivity but decreases specificity (Jager et al. 1996; Yang et al. 2000).

In recent years, diffusion-weighted magnetic resonance imaging (DW-MRI) has emerged as a promising additional technique for detecting metastatic lymph nodes. Due to the impeded diffusivity within metastatic tissue, positive lymph nodes appear as noncontinuous, hyperintense, ovoid or round structures on high *b*-value images (*b* in the 800–1000 s/mm^2 range) and as hypointense structures on corresponding apparent diffusion coefficient maps (ADC). Several studies on cervical and uterine cancer patients have reported significant differences in ADC values between malignant and benign lymph nodes (Kim et al. 2008; Lin et al. 2008; Koplay et al. 2014). In one study the combined analysis of ADC values and nodal size increased sensitivity to 83%, compared with 25% using morphological MRI alone; at the same time specificities remained high at 99% and 98%, respectively (Lin et al. 2008). The smallest metastatic lymph node detected by combined diffusion-weighted and morphological MRI was 5 mm in short axis diameter. A recent meta-analysis of studies on cervical cancer patients indicates that, using DW-MRI, metastatic lymph nodes might be detected with a pooled sensitivity of 86% (95% confidence interval, CI: 84–89%) and a pooled specificity of 84% (CI: 83–89%) (Shen et al. 2015). Nevertheless, there is a considerable overlap between ADC values measured in positive and negative lymph nodes. Another study, possibly due to the relatively small patient sample, did not determine a significantly lower ADC in metastatic lymph nodes (Nakai et al. 2008). It is worth mentioning that also the authors of the latter study conclude that DW-MRI improved detection of lymph nodes compared with morphological MRI alone. While several threshold values on ADC have been proposed for the detection of metastatic lymph nodes (e.g., ADC value below 0.10×10^{-3} mm^2/s in (Lin et al. 2008)), the measured ADC values might depend on the hardware characteristics and field strength of the employed MR scanner which should therefore be carefully calibrated at each center (Donati et al. 2014). It should also be noted that ADC measurements might be underestimated due to the presence of fatty hila, overestimated because of necrosis, or generally affected by partial volume artifacts since lymph nodes are small relative to image resolution. Finally, to detect metastatic lymph nodes, we advise to always correlate DW-MRI with T2-weighted MRI (Thoeny et al. 2014).

Another interesting development is represented by hybrid imaging techniques such as positron emission tomography (PET)-CT and PET-MRI. A meta-analysis of cervical cancer studies indicates that the pooled sensitivity of PET or PET-CT for detecting nodal metastases is 54% (CI: 46–61%), significantly higher than morphological MRI (38%, CI: 32–43%), but similar to CT alone (52%, CI: 42–62%). On the contrary, the pooled specificity of PET or PET-CT is 97% (CI: 96–98%), significantly

higher than CT alone (92%, CI: 90–94%), but similar to morphological MRI (97%, CI: 97–98%) (Choi et al. 2010). A study comparing the evaluation of nodal metastases in uterine cancer patients by PET-CT and DW-MRI suggests that DW-MRI showed higher sensitivity but lower specificity than PET-CT; however, neither technique was sufficiently accurate to replace surgical lymphadenectomy (Kitajima et al. 2012). Similarly, a recent meta-analysis on the use of DW-MRI, PET or PET-CT, and CT for detecting lymph node metastases in patients with cervical cancer concludes that DW-MRI and PET or PET-CT are significantly better than CT; PET or PET-CT was associated with the highest specificity and DW-MRI with the highest sensitivity (Liu et al. 2017).

Concerning PET-MRI, sensitivity and specificity values above 90% have been reported by studies analyzing the nodal stage of cervical cancer patients; despite the high potential of this technique, further studies are needed before PET-MRI is established and integrated into clinical routine (Grueneisen et al. 2015; Kim et al. 2009).

Finally, we are not aware of any studies that analyze the role of dynamic contrast-enhanced magnetic resonance imaging (DCE-MRI) for detecting metastatic lymph nodes in gynecological cancer patients. However, there is some evidence indicating that DCE-MRI is useful to detect nodal involvement in patients with breast (Bahri et al. 2008; Loiselle et al. 2011), head and neck (Wendl et al. 2012; Yan et al. 2016), and prostate cancer (Lista et al. 2014). It is possible that similar results apply to corpus uteri and ovarian cancer patients as well; further studies are needed to address this knowledge gap.

3 Technique

There is currently no consensus regarding the type of patient preparation before a pelvic MRI exam (Balleyguier et al. 2011). To limit bowel motion artifacts 6 h of fasting before MRI (Engin 2006; Liu et al. 2009) or the intramuscular or intravenous injection of an antiperistaltic agent (Johnson et al. 2007) have been suggested. Antiperistaltic agents such as 1 mg glucagon (Glucagen®; Novo Nordisk, Bagsværd, Denmark) or 20 mg butyl-scopolamine (Buscopan®; Boehringer Ingelheim GmbH, Ingelheim, Germany) seem to be most effective but are contraindicated in case of, e.g., diabetes or pheochromocytoma (Van Hoe et al. 1999). The urinary bladder should be moderately distended to avoid distortion of pelvic anatomy (Bourgioti et al. 2016).

3.1 MRI

Lymph node assessment is included in the staging protocol of gynecological cancers (Balleyguier et al. 2011; Kinkel et al. 2009; Forstner et al. 2010). In cervical and endometrial cancer, the pelvis and retroperitoneum up to the level of the renal hilum should be covered. In vulvar and vaginal cancer, the inguinal lymph nodes have to be carefully assessed; in ovarian cancer, the pelvis, abdomen, and distal thorax should be analyzed for lymph node metastases.

Lymph nodes can be assessed on axial T2-weighted images. Additional three-dimensional T1- and T2-weighted sequences with an isotropic voxel size of approximately 1 mm^3 might be helpful to correctly evaluate lymph nodes which appear round in the axial plane but elongated or oval in additional planes. Further, 3D reconstructions might allow correct localization of nodes in relation to adjacent vessels and therefore improve guidance to suspicious nodes for the surgeon (Thoeny et al. 2014).

DW-MRI should be acquired with fat saturation to avoid that fatty hila around lymph nodes (generally considered to be a reliable criterion for benignity) lead to misleadingly low ADC measurements (Herneth et al. 2010). There is no

consensus regarding the optimal set of *b*-values to be acquired for diffusion-weighted imaging; commonly used values range between 500 and 1000 s/mm^2 (in addition to a $b = 0$ s/mm^2 scan) (Koplay et al. 2014; Thoeny et al. 2014, 2012; McVeigh et al. 2008). The reader should keep in mind that the computed ADC maps depend on the acquired b-values as well as on the hardware characteristics and field strength of the employed magnetic resonance scanner (Donati et al. 2014; Koc et al. 2012).

3.1.1 Intravenous Unspecific Contrast Agents

There are no indications regarding the use of extracellular gadolinium-based contrast agents for lymph node imaging. On T1-weighted imaging, unspecific contrast agents might improve the differentiation of lymph nodes from vessels and facilitate the detection of necrotic lymph node regions.

The optimal time-point at which contrast-enhanced images are acquired likely depends on the pathology at hand (Kinkel et al. 2009); however, imaging should be performed within 10 min of contrast medium injection to avoid diffusion into ascites (Forstner et al. 2010). 3D gradient echo MRI sequences might be preferable to standard 2D enhanced sequences as they allow the acquisition of relatively thin slices (e.g., 1 mm) with sufficient spatial resolution.

If the patient is pregnant or presents impaired renal function, the use of gadolinium-based contrast agents needs to be carefully assessed (Thomsen et al. 2013) and might be substituted by thin-slice T2-weighted imaging and axial DW-MRI with fat saturation (Forstner et al. 2010).

3.1.2 Intravenous Tissue-Specific Contrast Agents

Tissue-specific contrast agents that accumulate in healthy lymph node tissue could represent a valid additional tool for detecting metastatic lymph nodes. These contrast agents (e.g., ferumoxtran-10; previously marketed as Sinerem® in Europe and as Combidex® in the United States) are based on ultrasmall superparamagnetic iron oxide particles (USPIO) with a diameter of approximately 20 nm. They are administered intravenously 24–36 h prior to imaging. Due to macrophage uptake, they cause healthy lymph nodes to appear hypointense on T2*-weighted MRI, whereas metastatic lymph nodes remain unchanged. Early studies suggest that ferumoxtran-10-based contrast agents improve the sensitivity of metastatic lymph node detection in endometrial and cervical cancer patients (Rockall et al. 2005) and considerably decrease the time needed by the radiologist to interpret the images (Thoeny et al. 2009). However, there are currently no USPIO-based contrast agents approved for differentiating metastatic from nonmetastatic lymph nodes on the market.

3.2 CT

As lymph node assessment is an integral part of staging, the range of lymph nodes to be assessed is defined by the staging protocols of the different cancer types. CT imaging of gynecological cancer is usually performed with intravenous contrast medium; therefore, no special technique is necessary to assess lymph nodes. Multiplanar reconstructions facilitate the depiction of lymph nodes and their differentiation from bowel loops.

4 Imaging Findings in Benign and Malignant Lymph Nodes: MRI/CT

On morphological images signs of nodal involvement include: a short axis diameter greater than 10 mm, visible necrosis (hyperintense foci on STIR or T2-weighted MRI), signal intensity similar to the primary tumor, and an irregular

nodal contour or tumor extending beyond the nodal capsule (Yang et al. 2000; Brown et al. 2003; Sala et al. 2010). However, these morphological features are rarely seen on CT or MRI. The contrast resolution of CT is too low to differentiate between normal and metastatic lymph node tissue. MRI generally has a higher soft tissue contrast resolution; however, the T1 and T2 relaxation times, as well as the proton densities, in lymphatic tissue and tumors are similar (Dooms et al. 1985).

To detect malignant lymph nodes, hyperintense noncontinuous round or oval structures on DW-MRI acquired with a high *b*-value (800–1000 s/mm^2) should be noted and correlated with morphological 3D images. Structures corresponding to lymph nodes warrant further assessment.

If a lymph node is associated with a hypointense structure on the respective ADC map and/or on T2-weighted MRI, it is suspicious for malignancy. T1-weighted MRI should be employed to exclude that the low ADC is due to a fatty hilum. A short axis diameter greater than 10 mm, round shape, irregular or ill-defined border, and low signal intensity compared with muscle or groin lymph nodes on T2-weighted images are additional indicators of malignancy. On the contrary, eccentric fat and symmetric pelvic localization including similar shape and size on axial reconstructed images support benignancy (Thoeny et al. 2014).

Figure 1 shows an example of a negative external iliac lymph node in a bilateral ovarian adenocarcinoma patient: despite appearing as a hyperintense structure on high *b*-value DW-MRI it presents an elongated and regular contour as well as a normal size on T1-weighted MRI. Figure 2 highlights a metastatic external iliac lymph node in a patient with high grade uterine leiomyosarcoma. The positive lymph node can be clearly identified as a round and enlarged structure which is hyperintense on high *b*-value DW-MRI and hypointense on the respective ADC map and on T2-weighted MRI. After 4 weeks of percutaneous radiotherapy the lymph node showed no clear response in size but ADC values increased from 0.8 to 1.6 × 10^{-3} mm^2/s, corresponding to a favorable therapy response. Figure 3 illustrates an example of a cardiophrenic lymph node in a stage IIIC ovarian cancer patient which was suspicious for malignancy due to its hyperintense appearance on high *b*-value DW-MRI; however, its small size (short axis diameter less than 5 mm) on contrast-enhanced CT did not indicate malignancy (histopathological correlation is unavailable as this lymph node was not resected).

Efforts are underway to establish criteria that allow detecting pathologic cardiophrenic lymph

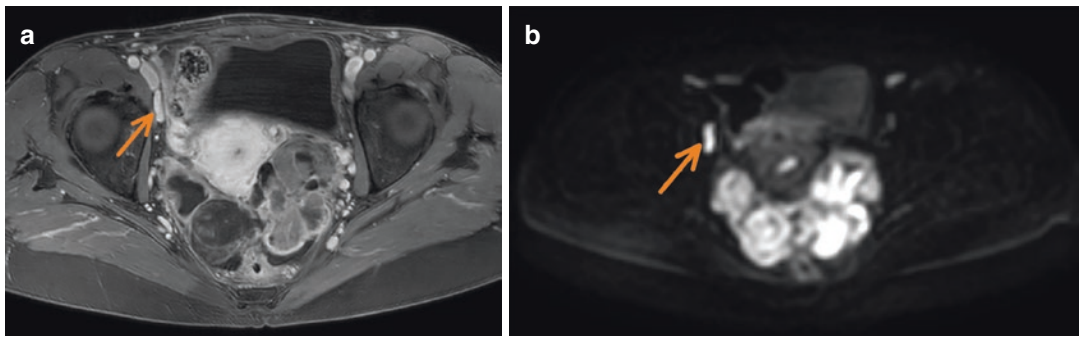

Fig. 1 A 53-year-old woman with bilateral ovarian adenocarcinoma with 16 histopathologic proven tumor-free pelvic lymph nodes. The *arrow* points to a negative external iliac lymph node with regular contour and normal size on axial T1-weighted Dixon water sequence (**a**) and on diffusion-weighted MRI with body background suppression (b = 1000 s/mm^2) (**b**)

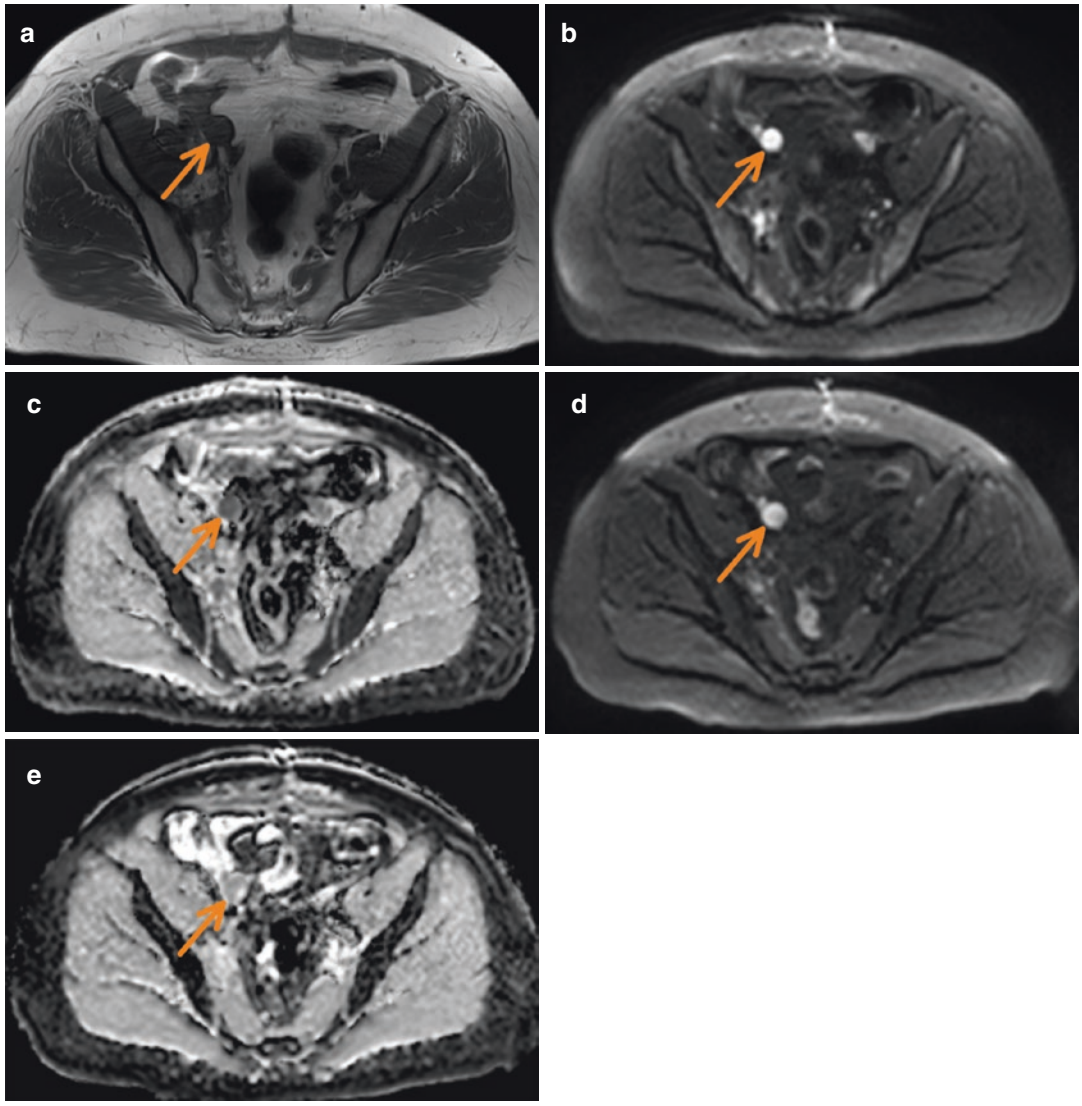

Fig. 2 A metastatic external iliac lymph node of a 65-year-old woman with high grade uterine leiomyosarcoma on axial T2-weighted (**a**), diffusion-weighted (b = 800 s/mm^2) MRI (**b**), and on the apparent diffusion coefficient map (**c**). After 4 weeks of percutaneous radiotherapy the lymph node showed no clear response in size but increase of ADC values from 0.8 to 1.6 × 10^{-3} mm^2/s diffusion-weighted MRI, (**d**), and corresponding ADC map, (**e**) corresponding to a favorable therapy response

nodes on CT. A recent study on 31 patients with advanced ovarian cancer suggests that a cut-off value of 7 mm on the short axis results in 63% sensitivity and 83% specificity. Figure 4 shows an example of enlarged, metastatic, cardiophrenic lymph nodes in a 61-year-old woman diagnosed with FIGO IIIC high grade serous ovarian carcinoma 10 years ago. CT was performed recently due to upper right abdominal pain. Besides enlarged cardiophrenic lymph nodes, metastatic diaphragmatic, perihepatic, and pleural lesions were detected. Ovarian

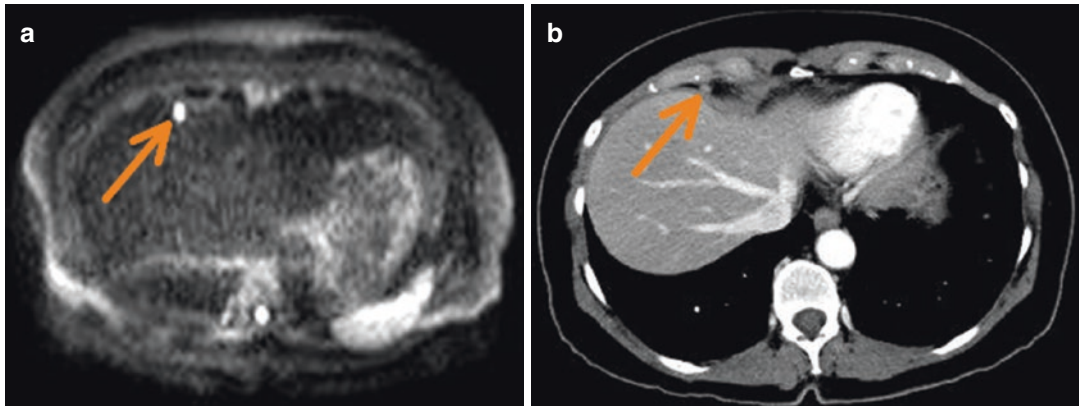

Fig. 3 A 71-year-old woman with newly diagnosed FIGO stage IIIC ovarian cancer with a suspected malignant cardiophrenic lymph node on axial diffusion-weighted MRI with body background suppression (DWIBS, b = 800 s/mm^2), without histopathological correlation (**a**). The same lymph node did not fulfill the size criteria (5 mm cut-off value) for malignancy on contrast-enhanced CT (**b**)

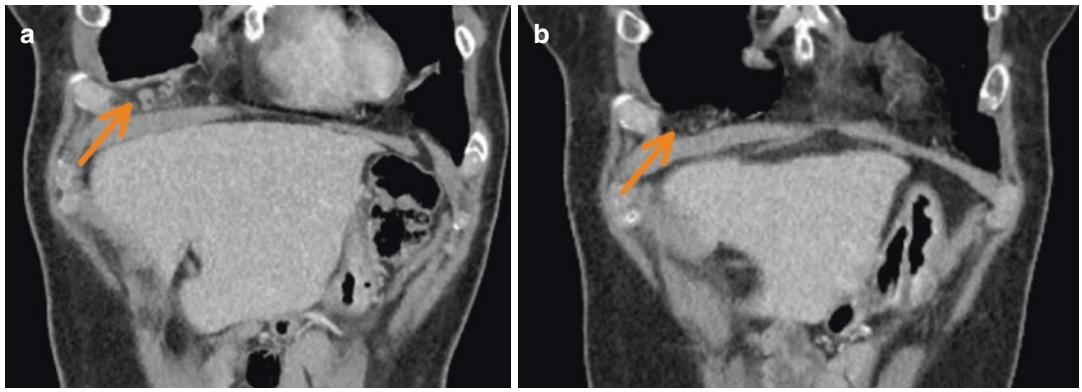

Fig. 4 A 61-year-old woman, initially with FIGO IIIC high grade serous ovarian carcinoma. Late recurrence after 10 years was established on CT performed due to upper right abdominal pain. Enlarged, metastatic, cardiophrenic lymph nodes were detected on CT (**a**). After six chemotherapy cycles the size of cardiophrenic lymph nodes decreased, indicating good therapy response (**b**)

carcinoma was proven in pleural fluid following histopathological analysis. A considerable decrease in the cardiophrenic lymph nodes' size was observed after six chemotherapy cycles, indicating good response to therapy.

References

Bahri S, Chen JH, HJ Y, Kuzucan A, Nalcioglu O, MY S (2008) Can dynamic contrast-enhanced MRI (DCE-MRI) predict tumor recurrence and lymph node status in patients with breast cancer? Ann Oncol 19(4):822–824. doi:10.1093/annonc/mdn043

Balleyguier C, Sala E, Da Cunha T, Bergman A, Brkljacic B, Danza F, Forstner R, Hamm B, Kubik-Huch R, Lopez C, Manfredi R, McHugo J, Oleaga L, Togashi K, Kinkel K (2011) Staging of uterine cervical cancer with MRI: guidelines of the European Society of Urogenital Radiology. Eur Radiol 21(5):1102–1110. doi:10.1007/s00330-010-1998-x

Berek JS, Crum C, Friedlander M (2015) Cancer of the ovary, fallopian tube, and peritoneum. Int J Gynaecol Obstet 131(Suppl 2):S111–S122. doi:10.1016/j.ijgo.2015.06.007

Boronow RC, Morrow CP, Creasman WT, Disaia PJ, Silverberg SG, Miller A, Blessing JA (1984) Surgical staging in endometrial cancer: clinical-pathologic findings of a prospective study. Obstet Gynecol 63(6):825–832

Bottke D, Wiegel T, Kreienberg R, Kurzeder C, Sauer G (2007) Stage IB endometrial cancer. Does

lymphadenectomy replace adjuvant radiotherapy? Strahlenther Onkol 183(11):600–604. doi:10.1007/s00066-007-1801-3

Bourgioti C, Chatoupis K, Moulopoulos LA (2016) Current imaging strategies for the evaluation of uterine cervical cancer. World J Radiol 8(4):342–354. doi:10.4329/wjr.v8.i4.342

Brown G, Richards CJ, Bourne MW, Newcombe RG, Radcliffe AG, Dallimore NS, Williams GT (2003) Morphologic predictors of lymph node status in rectal cancer with use of high-spatial-resolution MR imaging with histopathologic comparison. Radiology 227(2):371–377. doi:10.1148/radiol.2272011747

Choi HJ, Ju W, Myung SK, Kim Y (2010) Diagnostic performance of computer tomography, magnetic resonance imaging, and positron emission tomography or positron emission tomography/computer tomography for detection of metastatic lymph nodes in patients with cervical cancer: meta-analysis. Cancer Sci 101(6):1471–1479. doi:10.1111/j.1349-7006.2010.01532.x

Donati OF, Chong D, Nanz D, Boss A, Froehlich JM, Andres E, Seifert B, Thoeny HC (2014) Diffusion-weighted MR imaging of upper abdominal organs: field strength and intervendor variability of apparent diffusion coefficients. Radiology 270(2):454–463. doi:10.1148/radiol.13130819

Dooms GC, Hricak H, Moseley ME, Bottles K, Fisher M, Higgins CB (1985) Characterization of lymphadenopathy by magnetic resonance relaxation times: preliminary results. Radiology 155(3):691–697. doi:10.1148/radiology.155.3.4001371

Engin G (2006) Cervical cancer: MR imaging findings before, during, and after radiation therapy. Eur Radiol 16(2):313–324. doi:10.1007/s00330-005-2804-z

Ferlay J, Steliarova-Foucher E, Lortet-Tieulent J, Rosso S, Coebergh JW, Comber H, Forman D, Bray F (2013) Cancer incidence and mortality patterns in Europe: estimates for 40 countries in 2012. Eur J Cancer 49(6):1374–1403. doi:10.1016/j.ejca.2012.12.027

Ferrandina G, Distefano M, Ludovisi M, Morganti A, Smaniotto D, D'Agostino G, Fanfani F, Scambia G (2007) Lymph node involvement in locally advanced cervical cancer patients administered preoperative chemoradiation versus chemotherapy. Ann Surg Oncol 14(3):1129–1135. doi:10.1245/s10434-006-9252-0

Forstner R, Sala E, Kinkel K, Spencer JA, European Society of Urogenital R (2010) ESUR guidelines: ovarian cancer staging and follow-up. Eur Radiol 20(12):2773–2780. doi:10.1007/s00330-010-1886-4

Grueneisen J, Schaarschmidt BM, Heubner M, Aktas B, Kinner S, Forsting M, Lauenstein T, Ruhlmann V, Umutlu L (2015) Integrated PET/MRI for whole-body staging of patients with primary cervical cancer: preliminary results. Eur J Nucl Med Mol Imaging 42(12):1814–1824. doi:10.1007/s00259-015-3131-5

Herneth AM, Mayerhoefer M, Schernthaner R, Ba-Ssalamah A, Czerny C, Fruehwald-Pallamar J (2010) Diffusion weighted imaging: lymph nodes. Eur J Radiol 76(3):398–406. doi:10.1016/j.ejrad.2010.08.016

Holloway BJ, Gore ME, A'Hern RP, Parsons C (1997) The significance of paracardiac lymph node enlargement in ovarian cancer. Clin Radiol 52(9):692–697

Hynninen J, Auranen A, Carpén O, Dean K, Seppänen M, Kemppainen J, Lavonius M, Lisinen I, Virtanen J, Grénman S (2012) FDG PET/CT in staging of advanced epithelial ovarian cancer: frequency of supradiaphragmatic lymph node metastasis challenges the traditional pattern of disease spread. Gynecol Oncol 126(1):64–68

Jager GJ, Barentsz JO, Oosterhof GO, Witjes JA, Ruijs SJ (1996) Pelvic adenopathy in prostatic and urinary bladder carcinoma: MR imaging with a three-dimensional TI-weighted magnetization-prepared-rapid gradient-echo sequence. AJR Am J Roentgenol 167(6):1503–1507. doi:10.2214/ajr.167.6.8956585

Johnson W, Taylor MB, Carrington BM, Bonington SC, Swindell R (2007) The value of hyoscine butylbromide in pelvic MRI. Clin Radiol 62(11):1087–1093. doi:10.1016/j.crad.2007.05.007

Kim JK, Kim KA, Park BW, Kim N, Cho KS (2008) Feasibility of diffusion-weighted imaging in the differentiation of metastatic from nonmetastatic lymph nodes: early experience. J Magn Reson Imaging 28(3):714–719. doi:10.1002/jmri.21480

Kim SK, Choi HJ, Park SY, Lee HY, Seo SS, Yoo CW, Jung DC, Kang S, Cho KS (2009) Additional value of MR/PET fusion compared with PET/CT in the detection of lymph node metastases in cervical cancer patients. Eur J Cancer 45(12):2103–2109. doi:10.1016/j.ejca.2009.04.006

Kinkel K, Forstner R, Danza FM, Oleaga L, Cunha TM, Bergman A, Barentsz JO, Balleyguier C, Brkljacic B, Spencer JA, European Society of Urogenital I (2009) Staging of endometrial cancer with MRI: guidelines of the European Society of Urogenital Imaging. Eur Radiol 19(7):1565–1574. doi:10.1007/s00330-009-1309-6

Kitajima K, Yamasaki E, Kaji Y, Murakami K, Sugimura K (2012) Comparison of DWI and PET/CT in evaluation of lymph node metastasis in uterine cancer. World J Radiol 4(5):207–214. doi:10.4329/wjr.v4.i5.207

Koc Z, Erbay G, Ulusan S, Seydaoglu G, Aka-Bolat F (2012) Optimization of b value in diffusion-weighted MRI for characterization of benign and malignant gynecological lesions. J Magn Reson Imaging 35(3):650–659. doi:10.1002/jmri.22871

Koplay M, Dogan NU, Erdogan H, Sivri M, Erol C, Nayman A, Karabagli P, Paksoy Y, Celik C (2014) Diagnostic efficacy of diffusion-weighted MRI for preoperative assessment of myometrial and cervical invasion and pelvic lymph node metastasis in endometrial carcinoma. J Med Imaging Radiat Oncol 58(5):538–546 . doi:10.1111/1754-9485.12209quiz 648

Lin G, Ho KC, Wang JJ, Ng KK, Wai YY, Chen YT, Chang CJ, Ng SH, Lai CH, Yen TC (2008) Detection of lymph node metastasis in cervical and uterine cancers by diffusion-weighted magnetic resonance imaging at 3T. J Magn Reson Imaging 28(1):128–135. doi:10.1002/jmri.21412

Lista F, Gimbernat H, Caceres F, Rodriguez-Barbero JM, Castillo E, Angulo JC (2014) Multiparametric magnetic resonance imaging for the assessment of extracapsular invasion and other staging parameters in patients with prostate cancer candidates for radical prostatectomy. Actas Urol Esp 38(5):290–297. doi:10.1016/j.acuro.2013.11.003

Liu Y, Bai R, Sun H, Liu H, Zhao X, Li Y (2009) Diffusion-weighted imaging in predicting and monitoring the response of uterine cervical cancer to combined chemoradiation. Clin Radiol 64(11):1067–1074. doi:10.1016/j.crad.2009.07.010

Liu B, Gao S, Li S (2017) A comprehensive comparison of CT, MRI, positron emission tomography or positron emission tomography/CT, and diffusion weighted imaging-MRI for detecting the lymph nodes metastases in patients with cervical cancer: a meta-analysis based on 67 studies. Gynecol Obstet Invest. doi:10.1159/000456006

Loiselle CR, Eby PR, Peacock S, Kim JN, Lehman CD (2011) Dynamic contrast-enhanced magnetic resonance imaging and invasive breast cancer: primary lesion kinetics correlated with axillary lymph node extracapsular extension. J Magn Reson Imaging 33(1):96–101. doi:10.1002/jmri.22389

McVeigh PZ, Syed AM, Milosevic M, Fyles A, Haider MA (2008) Diffusion-weighted MRI in cervical cancer. Eur Radiol 18(5):1058–1064. doi:10.1007/s00330-007-0843-3

Nakai G, Matsuki M, Inada Y, Tatsugami F, Tanikake M, Narabayashi I, Yamada T (2008) Detection and evaluation of pelvic lymph nodes in patients with gynecologic malignancies using body diffusion-weighted magnetic resonance imaging. J Comput Assist Tomogr 32(5):764–768. doi:10.1097/RCT.0b013e318153fd43

Narayan K, McKenzie AF, Hicks RJ, Fisher R, Bernshaw D, Bau S (2003) Relation between FIGO stage, primary tumor volume, and presence of lymph node metastases in cervical cancer patients referred for radiotherapy. Int J Gynecol Cancer 13(5):657–663

Piver MS, Chung WS (1975) Prognostic significance of cervical lesion size and pelvic node metastases in cervical carcinoma. Obstet Gynecol 46(5):507–510

Polterauer S, Khalil S, Zivanovic O, Abu-Rustum NR, Hofstetter G, Concin N, Grimm C, Reinthaller A, Barakat RR, Leitao MM Jr (2012) Prognostic value of lymph node ratio and clinicopathologic parameters in patients diagnosed with stage IIIC endometrial cancer. Obstet Gynecol 119(6):1210–1218. doi:10.1097/AOG.0b013e318255060c

Prader S, Harter P, Grimm C, Traut A, Waltering K-U, Alesina PF, Heikaus S, Ataseven B, Heitz F, Schneider S, du Bois A (2016) Surgical management of cardiophrenic lymph nodes in patients with advanced ovarian cancer. Gynecol Oncolo 141(2):271–275

Qayyum A, Coakley FV, Westphalen AC, Hricak H, Okuno WT, Powell B (2005) Role of CT and MR imaging in predicting optimal cytoreduction of newly diagnosed primary epithelial ovarian cancer. Gynecol Oncol 96(2):301–306. doi:10.1016/j.ygyno.2004.06.054

Raban O, Peled Y, Krissi H, Goldberg N, Aviram A, Sabah G, Levavi H, Eitan R (2015) The significance of paracardiac lymph-node enlargement in patients with newly diagnosed stage IIIC ovarian cancer. Gynecol Oncol 138(2):259–262. doi:10.1016/j.ygyno.2015.05.007

Rockall AG, Sohaib SA, Harisinghani MG, Babar SA, Singh N, Jeyarajah AR, Oram DH, Jacobs IJ, Shepherd JH, Reznek RH (2005) Diagnostic performance of nanoparticle-enhanced magnetic resonance imaging in the diagnosis of lymph node metastases in patients with endometrial and cervical cancer. J Clin Oncol 23(12):2813–2821. doi:10.1200/JCO.2005.07.166

Sala E, Rockall A, Rangarajan D, Kubik-Huch RA (2010) The role of dynamic contrast-enhanced and diffusion weighted magnetic resonance imaging in the female pelvis. Eur J Radiol 76(3):367–385. doi:10.1016/j.ejrad.2010.01.026

Shen G, Zhou H, Jia Z, Deng H (2015) Diagnostic performance of diffusion-weighted MRI for detection of pelvic metastatic lymph nodes in patients with cervical cancer: a systematic review and meta-analysis. Br J Radiol 88(1052):20150063. doi:10.1259/bjr.20150063

Thoeny HC, Triantafyllou M, Birkhaeuser FD, Froehlich JM, Tshering DW, Binser T, Fleischmann A, Vermathen P, Studer UE (2009) Combined ultrasmall superparamagnetic particles of iron oxide-enhanced and diffusion-weighted magnetic resonance imaging reliably detect pelvic lymph node metastases in normal-sized nodes of bladder and prostate cancer patients. Eur Urol 55(4):761–769. doi:10.1016/j.eururo.2008.12.034

Thoeny HC, Forstner R, De Keyzer F (2012) Genitourinary applications of diffusion-weighted MR imaging in the pelvis. Radiology 263(2):326–342. doi:10.1148/radiol.12110446

Thoeny HC, Froehlich JM, Triantafyllou M, Huesler J, Bains LJ, Vermathen P, Fleischmann A, Studer UE (2014) Metastases in normal-sized pelvic lymph nodes: detection with diffusion-weighted MR imaging. Radiology 273(1):125–135. doi:10.1148/radiol.14132921

Thomsen HS, Morcos SK, Almen T, Bellin MF, Bertolotto M, Bongartz G, Clement O, Leander P, Heinz-Peer G, Reimer P, Stacul F, van der Molen A, Webb JA, Committee ECMS (2013) Nephrogenic systemic fibrosis and gadolinium-based contrast media: updated ESUR Contrast Medium Safety Committee guidelines. Eur Radiol 23(2):307–318. doi:10.1007/s00330-012-2597-9

Tuomi T, Pasanen A, Luomaranta A, Leminen A, Bützow R, Loukovaara M (2015) Risk-stratification of endometrial carcinomas revisited: a combined preoperative and intraoperative scoring system for a reliable prediction of an advanced disease. Gynecol Oncol 137(1):23–27

Tuomi T, Pasanen A, Leminen A, Bützow R, Loukovaara M (2017) Prediction of lymphatic dissemination in endometrioid endometrial cancer: comparison of three risk-stratification models in a single-institution cohort. Gynecol Oncol 144(3):510–514

Van Hoe L, Vanbeckevoort D, Oyen R, Itzlinger U, Vergote I (1999) Cervical carcinoma: optimized local staging with intravaginal contrast-enhanced MR imaging—preliminary results. Radiology 213(2):608–611. doi:10.1148/radiology.213.2.r99oc23608

Vergote I, Trope CG, Amant F, Kristensen GB, Ehlen T, Johnson N, Verheijen RH, van der Burg ME, Lacave AJ, Panici PB, Kenter GG, Casado A, Mendiola C, Coens C, Verleye L, Stuart GC, Pecorelli S, Reed NS, European Organization for R, Treatment of Cancer-Gynaecological Cancer G, Group NCT (2010) Neoadjuvant chemotherapy or primary surgery in stage IIIC or IV ovarian cancer. N Engl J Med 363(10):943–953. doi:10.1056/NEJMoa0908806

Wendl CM, Muller S, Meier J, Fellner C, Eiglsperger J, Gosau M, Prantl L, Stroszczynski C, Jung EM (2012) High resolution contrast-enhanced ultrasound and 3-tesla dynamic contrast-enhanced magnetic resonance imaging for the preoperative characterization of cervical lymph nodes: first results. Clin Hemorheol Microcirc 52(2-4):153–166. doi:10.3233/CH-2012-1593

Yan S, Wang Z, Li L, Guo Y, Ji X, Ni H, Shen W, Xia S (2016) Characterization of cervical lymph nodes using DCE-MRI: differentiation between metastases from SCC of head and neck and benign lymph nodes. Clin Hemorheol Microcirc 64(2):213–222. doi:10.3233/CH-162065

Yang WT, Lam WW, MY Y, Cheung TH, Metreweli C (2000) Comparison of dynamic helical CT and dynamic MR imaging in the evaluation of pelvic lymph nodes in cervical carcinoma. AJR Am J Roentgenol 175(3):759–766. doi:10.2214/ajr.175.3.1750759

Acute and Chronic Pelvic Pain Disorders

Amy Davis and Andrea Rockall

Contents

A. Davis (✉)
Department of Radiology, Epsom and St Helier University Hospitals NHS Trust, London, UK
e-mail: adavis@doctors.org.uk

A. Rockall
Department of Radiology, The Royal Marsden Hospital, NHS Foundation Trust, London, UK
e-mail: A.rockall@imperial.ac.uk

Abstract

This chapter will cover common gynecological and non-gynecological causes of acute and chronic pelvic pain, with particular focus on the differential diagnosis and imaging characteristics. The relative frequency of each diagnosis by MRI or CT is listed in Table 1. Gynecologic disorders highly associated with chronic pelvic pain such as endometriosis, uterine leiomyomas, and adenomyosis are discussed in previous chapters in this book.

1 Introduction

One of the most challenging problems in clinical practice is identifying the cause of pelvic pain. From a practical point of view, it is useful to classify pelvic pain as acute or chronic because these presentations differ in their differential diagnoses and therefore require different imaging strategies for their evaluation. Pelvic pain that has been present for 6 months or longer is defined as chronic pelvic pain.

The differential diagnosis of lower abdominal and pelvic pain encompasses gynecological, pregnancy-related, gastrointestinal, urological, neurological, and abdominal wall causes. Furthermore, psychological factors have been attributed to play an important role in women, especially those suffering from chronic pelvic pain.

The single most important laboratory test in assessing pelvic pain in a woman of reproductive

Med Radiol Diagn Imaging (2017)
DOI 10.1007/174_2017_103, © Springer International Publishing AG
Published Online: 13 July 2017

Table 1 Relative frequency of imaging by CT or MRI for pelvic pain in clinical routine

Gynecological pathologies	Frequency	Non-gynecological pathologies	Frequency
PID	+	Pelvic congestion syndrome	+
Tubo-ovarian abscess	++	Appendicitis	+++
Hydropyosalpinx	++	Diverticulitis	+++
Ovarian torsion	+	Epiploic appendagitis	+
Ovarian vein thrombosis	+	Crohn's disease	++
Endometriosis	++	Rectus sheath hematoma	+
Uterine leiomyomas	++		
Adenomyosis	++		

+, Low frequency; ++, medium frequency; +++, high frequency

age is a pregnancy test, in order to exclude a diagnosis of ectopic pregnancy. The most frequent gynecological emergencies occur in the premenopausal age group and include ectopic pregnancy, corpus luteum cyst rupture, and pelvic infection. Appendicitis accounts for most non-gynecological emergencies.

Sonography is the initial imaging modality of choice in gynecologic disorders causing pelvic pain. However in the emergency setting, with uncertainty related to the underlying cause of acute severe lower abdominal pain, CT of the abdomen and pelvis is often the first imaging performed allowing assessment of the gastrointestinal tract and urologic system. MRI is usually reserved for problem-solving, although it may be used when transvaginal ultrasound is not feasible.

This chapter will review some of the more common diagnoses of acute and chronic pelvic pain that are not covered elsewhere in this book (Table 1). Gynecologic disorders highly associated with chronic pelvic pain such as endometriosis, uterine leiomyomas, and adenomyosis are discussed in different chapters.

2 Gynecological Causes of Pelvic Pain

2.1 Ovarian Cysts: Acute Cyst Events

A follicular cyst may develop when an ovarian follicle enlarges physiologically during the menstrual cycle but does not rupture for ovulation. These functional simple cysts have no complex features on US, typically range from 3 to 6 cm, and usually resorb within a few menstrual cycles. In the case of a follicle that ovulates, a corpus luteum forms with wall thickening, increased wall vascularity and blood often accumulates in the central cavity. In some cases, these physiological cysts (follicular and corpus luteal) may undergo significant hemorrhage and/or there may be cyst rupture. These events may be sufficiently symptomatic to lead to an emergency presentation. Rupture of non-physiological cysts, including endometriotic cyst or mature cystic teratoma, also typically presents with acute pain.

2.1.1 Imaging Findings

A hemorrhagic ovarian cyst is usually readily diagnosed on US (Roche et al. 2012). Rupture of an ovarian cyst is also usually confidently diagnosed on US and there is no need for additional imaging on CT or MRI. However, in the acute presentation, CT may be the initial investigation due to diagnostic uncertainty. Ovarian cyst hemorrhage on CT may be seen as mixed attenuation material within an ovarian cyst due to the presence of blood (Fig. 1). The differentiation between blood and enhancing soft tissue may not be possible if there is no pre-contrast CT available. MRI is occasionally used in problem-solving. In the case of cyst rupture, there is free fluid in the pelvis; there may be no evidence of the ovarian cyst in cases where the cyst collapses following

rupture. If the cyst rupture was related to a hemorrhagic corpus luteum, there may be a visible disrupted corpus luteum in one ovary and the free fluid may be of higher attenuation than simple fluid, due to the presence of blood. Delayed post-contrast CT may demonstrate pooling of iodinated contrast in the pelvis. On MRI, free fluid in the pelvis may contain signs of visible hemoperitoneum (Fig. 2).

In the case of ruptured mature cystic teratoma, the presence of free globules of fat may be seen in the peritoneum and there are signs of inflammation. The original teratoma is typically seen in the adnexa (Fig. 3).

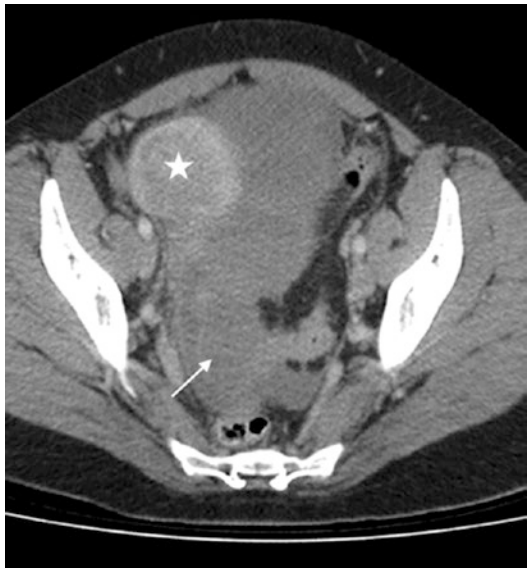

Fig. 1 CT of ruptured endometriotic cyst (*arrow*) showing mixed attenuation pelvic fluid consistent with blood. Uterus (*star*) is displaced to the right by the large complex left adnexal cyst

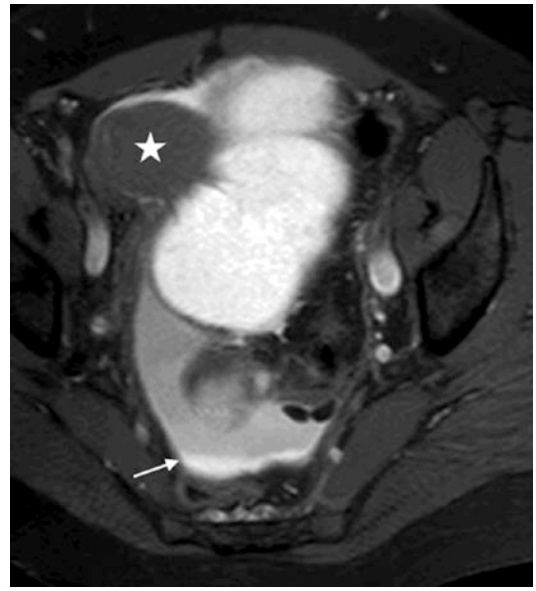

Fig. 2 Axial fat-saturated T1 MRI in the same patient as Fig. 1 shows a ruptured endometriotic cyst and layering of blood in the pelvis (*arrow*). Uterus (*star*) lies to the right of the large blood-filled cyst

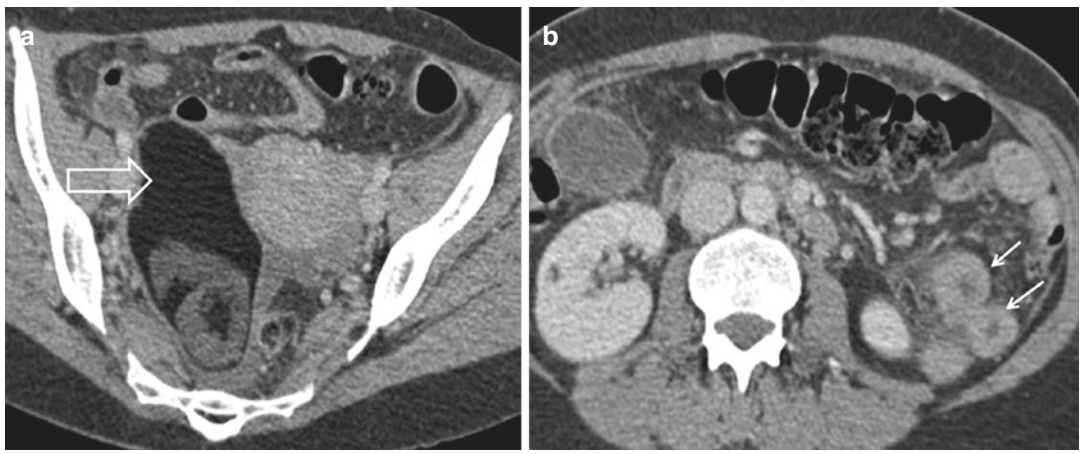

Fig. 3 CT of a patient presented with left upper quadrant pain. Image A shows the ruptured teratoma (*open arrow*); image B shows thickened bowel loops (*filled arrow*) secondary to chemical peritonitis. Stranding is seen in the adjacent fat and there is thickening of the left paracolic peritoneum. Courtesy of Prof. Evis Sala, New York

2.1.2 Differential Diagnosis

Ectopic pregnancy is the most critical differential diagnosis and exclusion of this diagnosis is essential. The differential diagnosis of the underlying cyst type can include physiological, endometriotic, benign cystic teratoma or neoplastic ovarian cyst. The finding of free fluid or blood in the pelvic cavity with no visible cyst or a collapsing cyst and an appropriate history is highly reassuring for physiological cyst rupture. Other causes of acute pelvic pain and free fluid include inflammatory processes such as pelvic inflammatory disease, appendicitis, or diverticulitis.

2.1.3 Value of Imaging

Imaging is used to confirm the findings of free pelvic fluid, identify the underlying cyst type if a cyst remains visible, and rule out alternative causes of the acute severe pelvic pain.

2.2 Pelvic Inflammatory

Pelvic inflammatory disease (PID) refers to an ascending infection of the upper genital tract in women who are typically of reproductive age. Infection can involve the uterus, fallopian tubes, and ovaries. Per definition, PID should be distinguished from pelvic infections caused by medical procedures, pregnancy, and other primary abdominal processes. PID usually results from sexually transmitted ascending infections typically by *Neisseria gonorrhoeae* or *Chlamydia trachomatis,* although 30–40% of cases are polymicrobial. Actinomycosis and tuberculosis account for rare causes of PID and may cause tubo-ovarian abscesses (Kim et al. 2004). Actinomycosis should be considered if there is a history of intrauterine contraceptive device (IUCD) and has also been reported following in vitro fertilization, as well as in those with no history of instrumentation (Atay et al. 2005). If PID is untreated or incompletely treated, there is a sixfold risk of ectopic pregnancy. Twenty percent of patients may complain of pelvic pain, and infertility is seen in 25–60% of women with more than one episode of PID (Ghiatas 2004). Occasionally patients with PID may develop Fritz-Hugh–Curtis syndrome due to peritonitis of the right upper quadrant surfaces and of the right lobe of the liver caused by bacterial spread along the paracolic gutters (Sam et al. 2002).

2.2.1 Imaging Findings

Imaging findings in early PID are typically subtle and their interpretation is based on the clinical findings. Findings on CT and MRI may include mild pelvic edema that results in thickening of the uterosacral ligaments and haziness and stranding of the pelvic fat, reactive lymphadenopathy, and free fluid (Revzin et al. 2016). Contrast enhancement and thickening of the fallopian tubes may be signs of salpingitis. Enlarged and abnormally enhancing ovaries may demonstrate a polycystic appearance and inflammatory changes (Fig. 4). Peri-ovarian stranding and enhancement of the adjacent peritoneum are common associated findings. In cases of endometritis, abnormal endometrial enhancement is seen as well as fluid in the endocervical canal which has similar imaging characteristics to that in the pouch of Douglas (Fig. 4). The uterine cervix may be enlarged with an abnormally enhancing endocervical canal if there is associated cervicitis. The uterine changes are better assessed on MRI than on CT (Sam et al. 2002).

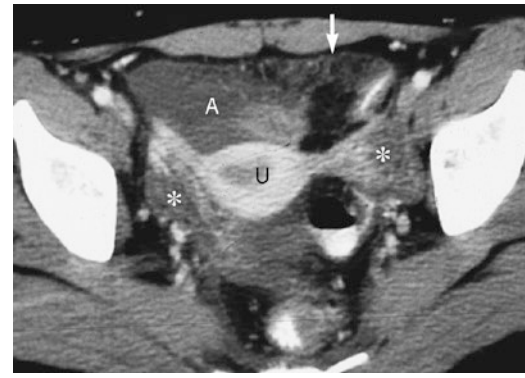

Fig. 4 CT findings in a 29-year-old woman with PID caused by *Chlamydia trachomatis* infection. Haziness and weblike fatty infiltration of pelvic fat (*arrow*), free fluid (*A*), marked swelling of the left ovary, and mild dilatation of the uterine cavity (*U*) are demonstrated. The ovaries (*asterisk*) are difficult to discriminate from ascites due to their polycystic appearance in oophoritis

2.3 Hydropyosalpinx

Salpingitis is the most important cause for obliteration of the fimbriated end of the tube, which leads to hydrosalpinx. Other etiologies include fallopian tube tumors, endometriosis, and adhesions from prior surgery. Serous fluid, blood, or pus may accumulate and cause distension of the fallopian tube.

2.3.1 Imaging Findings

Dilated fallopian tubes appear as fluid-filled tubular structures arising from the uterine fundus and separate from the ipsilateral ovary. The typical finding is a tortuous, cystic tubular structure with interdigitating incomplete mural septa (Fig. 5). These septa are thin and display low signal intensity on T2WI. Distinct septal enhancement on contrast-enhanced T1WI or CT may support the diagnosis of pyosalpinx (Tukeva et al. 1999). The nature of fluid within a dilated salpinx is best evaluated on MRI. The signal intensity varies in accordance with the contents, which ranges from water-like simple fluid to proteinaceous or hemorrhagic fluid. Multiplanar imaging and opacification of bowel loops with contrast allows identification of the tubal origin and differentiation from dilated bowel loops.

2.3.2 Differential Diagnosis

Tubal diameters can reach up to 10 cm and therefore hydrosalpinx may mimic multiloculated ovarian tumors, especially cystadenomas. Identification of the ovary separate from the lesion using multiplanar imaging helps to differentiate. Any enhancing component within a dilated tube, apart from fine incomplete smooth septations, should suggest the possibility of fallopian tube carcinoma or ectopic pregnancy (Kawakami et al. 1993). Pyosalpinx and hematosalpinx may be differentiated from hydrosalpinx by the signal intensity of the fluid content: a hydrosalpinx contains simple fluid (high on T2, low on T1, with no restricted diffusion, similar to CSF or urine) whereas a pyosalpinx contains pus (typically intermediate on T2, hyperintense on T1 and T1FS, with restricted diffusion); a hematosalpinx contains blood (typically hypointense on T2, hyperintense on T1 and T1FS with restricted diffusion).

2.4 Tubo-ovarian Abscess

In the majority of cases, tubo-ovarian abscess (TOA) results from PID. Other etiologies include complications of surgery or intra-abdominal

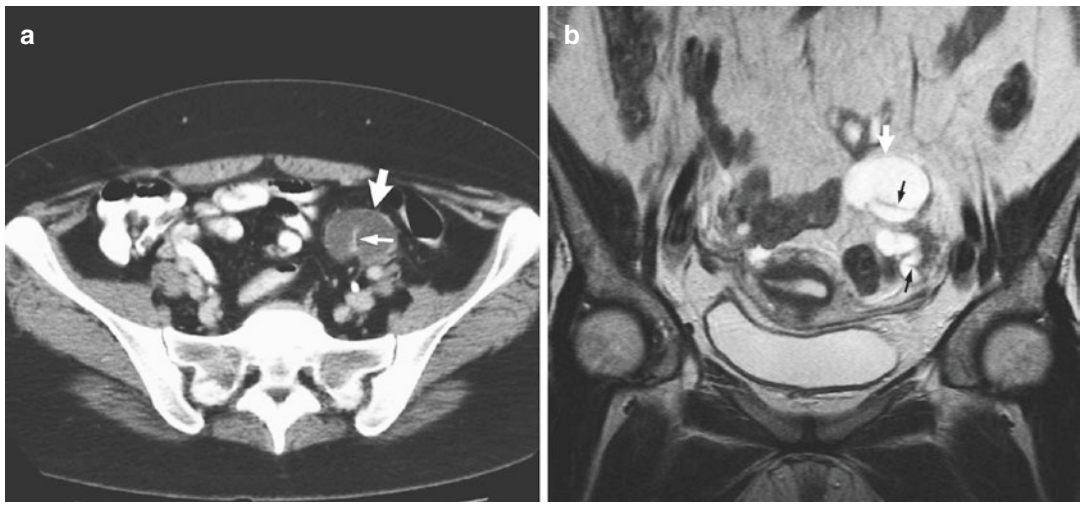

Fig. 5 Hydrosalpinx on CT and MRI. Transaxial CT (**a**) and coronal T2WI (**b**). A multiseptate lesion (*arrows*) in the left adnexal region is demonstrated on CT (**a**) and MRI (**b**): Its tubular nature with widening at the cephalad end is demonstrated on MRI (**b**). The thin incomplete, interdigitating septa (*small arrows*) are a typical finding of a dilated fallopian tube on CT and MRI

inflammatory bowel diseases, such as appendicitis, diverticulitis, or Crohn's disease. In most cases, TOA is caused by a polymicrobial infection with a high prevalence of anaerobes. Intrauterine contraceptive device (IUCD) users, especially in the first few months after insertion, also have a greater risk of PID. Pelvic actinomycosis is considered to be highly associated with the use of IUCD (Kim et al. 2004).

TOA most commonly occurs in women of reproductive age. Tubo-ovarian abscesses in postmenopausal women are rare, but can be seen in women with diabetes or previous radiation therapy. In postmenopausal women presenting with TOAs, a concomitant pelvic malignancy should be excluded as there is a significant association with malignancy (Protopapas et al. 2004).

The pathway of the inflammatory disease includes direct extension along the fallopian tubes. A hematogenous or lymphatic spread is found in the rare cases of tuberculous involvement of the genital tract (Kim et al. 2004).

2.4.1 Imaging Findings

On CT and MRI, tubo-ovarian abscesses are thick-walled, multilocular complex heterogeneous fluid-containing adnexal masses that can be unilateral or bilateral (Fig. 6). They may contain irregular inner contours, internal septa, gas, fluid, or a fluid-debris level (Sam et al. 2002). Necrosis or loculated fluid areas may resemble serous fluid, but can also be proteinaceous or hemorrhagic with T1 shortening. Tubo-ovarian abscesses most commonly display a heterogeneously intermediate or hyperintense signal on T2WI (Ghiatas 2004). They are surrounded by thick, markedly enhancing outer borders (Fig. 7). Due to dense pelvic adhesions or fibrosis, mesh-like strands in the pelvic fat planes are almost always seen; these demonstrate enhancement on CT or contrast-enhanced T1WI, and display a low signal on T2WI. The uterus and omentum usually become adherent. The abscess may enlarge and fill the pouch of Douglas or leak and produce metastatic abscesses and cause local peritonitis.

Involvement of adjacent structures includes thickened bowel loops with or without dilatation. Peritoneal enhancement, especially in the inferior pelvis, and small amounts of ascites are signs of associated peritonitis. Obstruction of the ureters may also be seen. Internal gas locules are the most specific radiologic sign of an abscess but are unusual in tubo-ovarian abscesses (Bennett et al. 2002). In the case of actinomycosis, there may be complex cystic

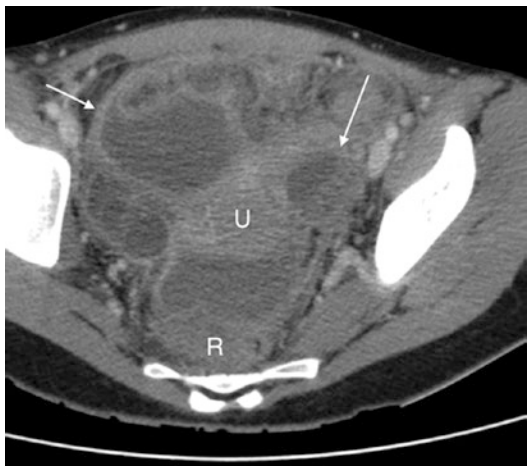

Fig. 6 Bilateral tubo-ovarian abscesses (*arrows*) are shown as thick-walled tubular, cystic adnexal masses. The rectum (*R*) and uterus (*U*) are also shown

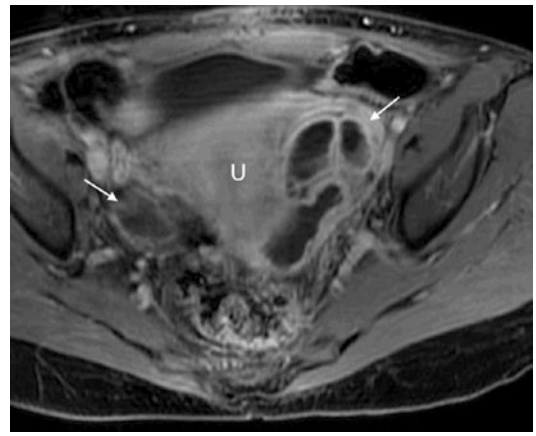

Fig. 7 Bilateral tubo-ovarian abscess on contrast-enhanced fat saturation T1WI. Bilateral adnexal cysts with thick walls and septations with avid enhancement (*arrows*). The uterus is shown for reference (*U*)

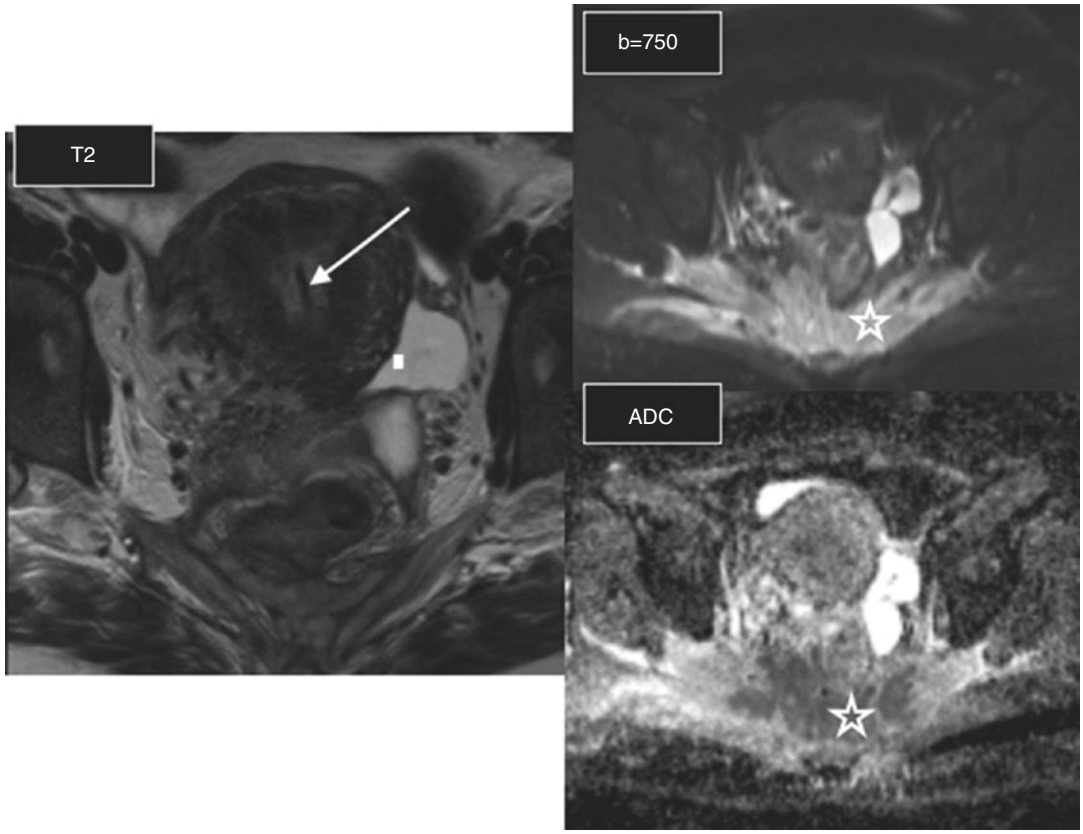

Fig. 8 MRI images in a patient with actinomycosis. An IUCD (*arrow*) can be seen in the uterine cavity on the axial T2WI. The diffusion-weighted image and ADC map shows thickening and fibrosis in the presacral space that demonstrates restricted diffusion (star). There is a complex lesion

solid ovarian masses and retroperitoneal thickening which may have the appearance of retroperitoneal fibrosis and a tendency for the inflammatory tissue to invade across tissue planes (Fig. 8) (Ha et al. 1993; Akhan et al. 2008). Appearances may mimic disseminated ovarian cancer with peritoneal deposits (Hildyard et al. 2013). However, presacral thickening is a typical finding and this should raise suspicion of actinomycosis (Hildyard et al. 2013).

2.4.2 Differential Diagnosis

Endometriomas may sometimes display similar imaging characteristics to TOA, with a thick rim; however, the clinical background is different. Ovarian cancer as well as ovarian metastases often present also as multiseptate ovarian masses (Willmott et al. 2012). In ovarian cancer, brightly enhancing solid tissue (irregular septae, papillary formations, or mural nodules) is typically found and signs of inflammation of the pelvic fat are absent. Furthermore, ovarian cancer is not frequently associated with tubal dilatation. However, in postmenopausal women with TOA, malignancy is a significant concern (Protopapas et al. 2004). If tubo-ovarian abscesses involve adjacent pelvic organs, the site of origin often cannot be reliably defined. Tuberculous peritonitis involving the adnexa mimics peritoneal carcinomatosis with nodularities along tubo-ovarian surfaces, and large amounts of ascites (Kim et al. 2004) (Fig. 9).

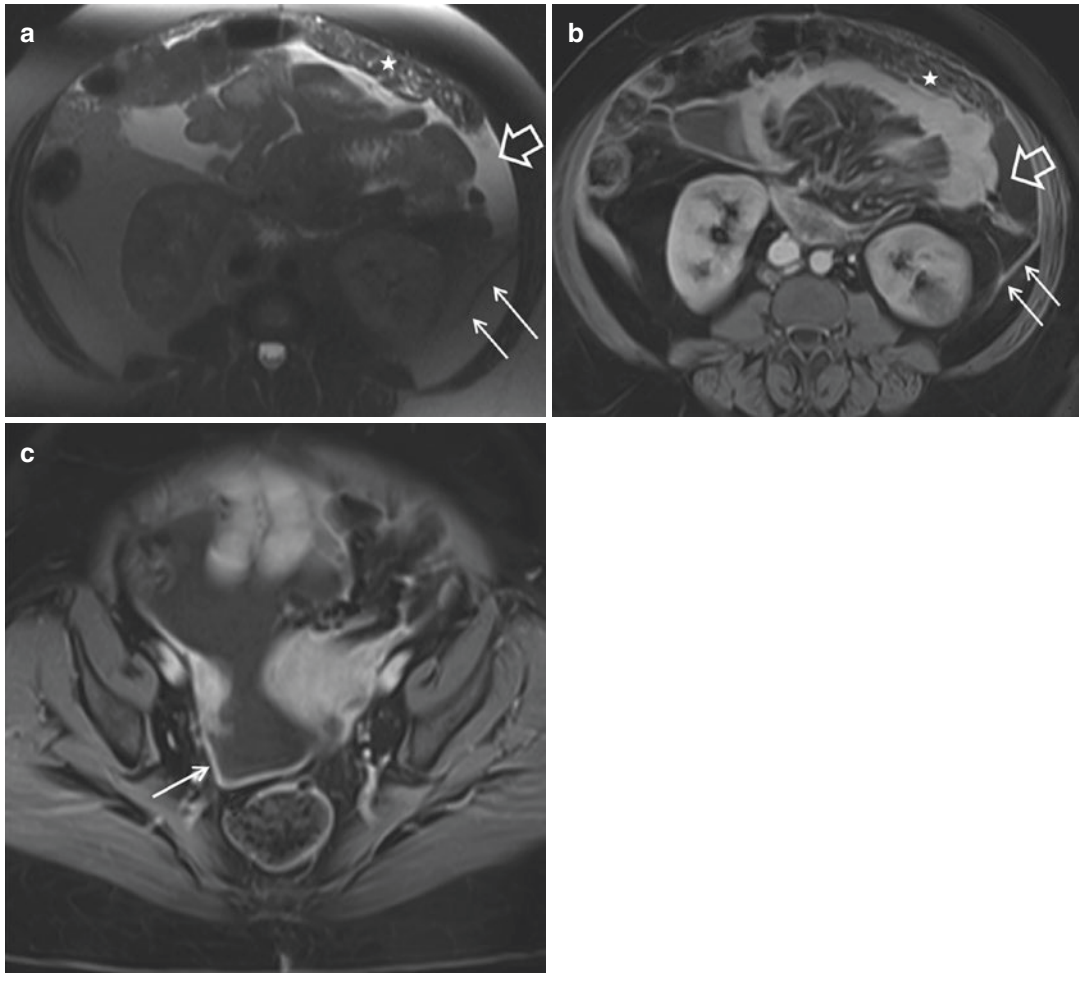

Fig. 9 MRI of peritoneal tuberculosis. Axial T2WI (**a**) demonstrates ascites (*open arrows*), omental thickening (*star*), and smooth thickening of the peritoneal reflections in the left flank (*filled arrows*). Axial T1 fat-saturated post-contrast MRI (**b**, **c**) confirm that the smooth peritoneal thickening in the mid-abdomen (**b**) and pelvis (**b**) enhances (*solid arrows*). There is no ovarian mass. There is also enhancement of the thickened omentum (*star*) and prominent mesenteric vessel enhancement—in keeping with an inflammatory process. The patient also had pleural effusions. A biopsy confirmed tuberculosis

2.4.3 Value of Imaging

The diagnosis of PID is based on clinical examination and laboratory studies, including assessment of vaginal secretions, and sonographic findings. In cases of nonspecific findings or suspected complications of PID, especially tubo-ovarian abscess or peritonitis, CT or MRI may serve as adjunct imaging modalities. CT is commonly used to assess complications of PID, especially when a tubo-ovarian abscess or peritonitis is suspected. Furthermore, it assists in defining the origin of the tubo-ovarian abscess and can differentiate it from inflammatory bowel disease. CT is also especially useful as a guide for surgery or a CT-guided drainage as well as identifying complications such as involvement of other organs (Fig. 10). MRI and CT are both useful in differentiating between an adnexal tumor and an abscess. The imaging findings, however, can only be interpreted in context with the clinical

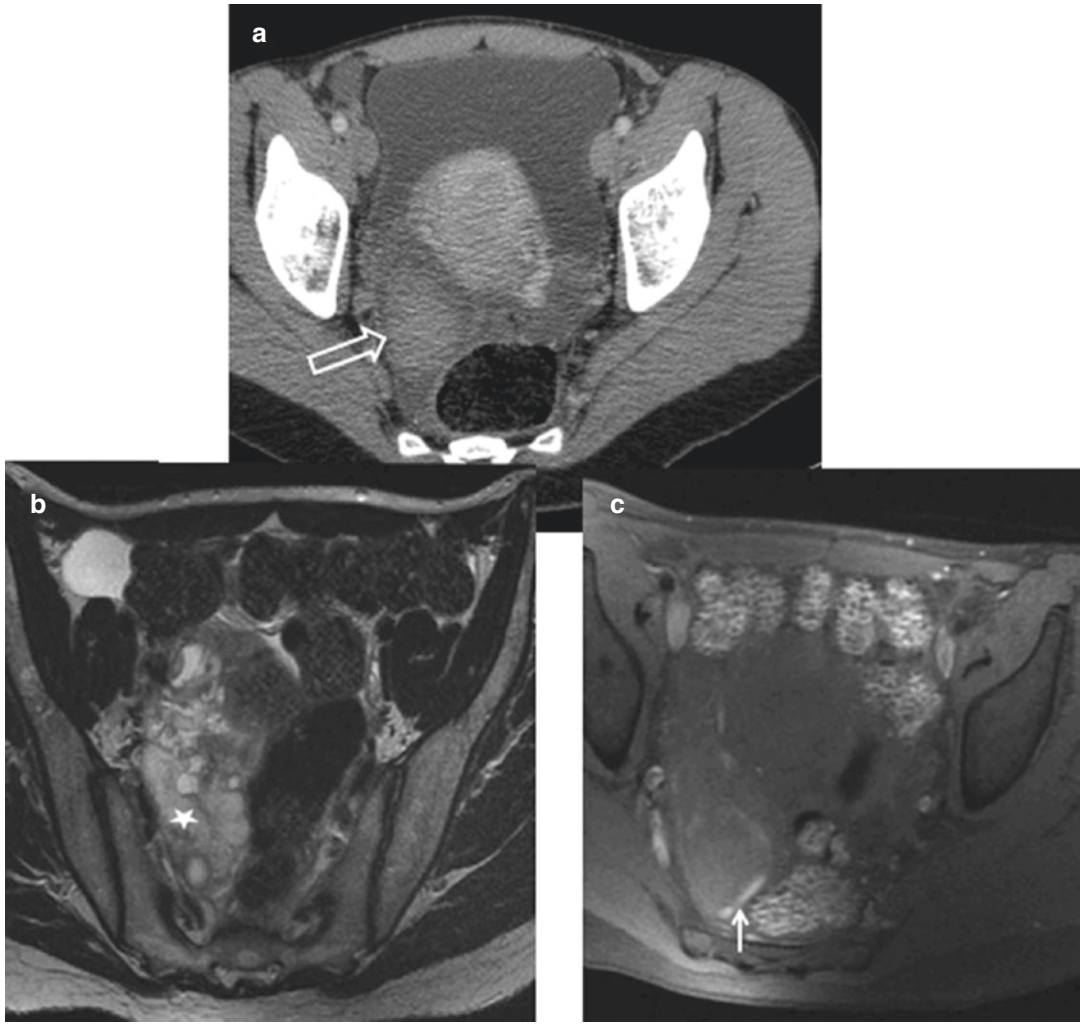

Fig. 10 Coronal (**a**) and sagittal (**b**) T2 weighted. MRI images show a bilateral tubo-ovarian abscess (TOA—*long arrows* on image **a**) with a fistulous communication (*long arrow* on image **b**) with the sigmoid colon (S). Cervix (C)

background. MRI is more useful than CT in differentiating a hydrosalpinx from a cystic ovarian tumor (Forstner et al. 2017).

2.5 Ovarian Torsion

Ovarian torsion is most commonly associated with tubal torsion. The age groups which tend to be affected are children, young women in their first three decades, and postmenopausal women. Presentation is usually with acute severe pelvic or lower abdominal pain and vomiting; the patient may have clinical signs of acute surgical abdomen.

Ovarian torsion is caused by partial or complete rotation of the ovarian vascular pedicle. While venous flow is initially compromised, causing swelling and edema, arterial flow is usually maintained until late in the course, a phenomenon that is attributed to the dual blood supply of the ovary (Lee et al. 1998).

Finally, hemorrhagic infarction leads to irreversible loss of the ovary. Predisposing factors for ovarian torsion include an underlying unilateral ovarian tumor (50–60%), most likely teratomas and cystic ovarian tumors including para-tubal cysts. Lesions larger than 6 cm have a greater risk for torsion (Sherard et al. 2003). However, torsion may also be encountered in normal-sized ovaries, particularly in children (Graif and Itzchak 1988). Furthermore, hypermobile adnexa or elongated fallopian tubes and increased abdominal pressure have been reported to be responsible for ovarian torsion. Women in their first three decades have the highest incidence of ovarian torsion, which is related to the higher frequency of physiological cysts and benign cystic tumors, infertility therapy and pregnancy. Approximately 20% of torsions occur during pregnancy, typically during the first and second trimesters. In postmenopausal women, torsion typically affects a benign adnexal tumor, most commonly serous cystadenomas, whereas malignant tumors tend not to undergo torsion (Koonings and Grimes 1989).

Benign massive edema of the ovary is a rare disorder found in the second and third decades of life and may be a variant of ovarian torsion. It results from partial or intermittent torsion and is characterized by an excessively enlarged edematous ovary (Machairiotis et al. 2016). There may be an acute or progressive clinical presentation with pain. Approximately 43% of cases are found to have signs of torsion at surgery (Praveen et al. 2013). The right ovary is more likely to twist than the left, suggesting that the sigmoid colon may help to prevent torsion.

2.5.1 Imaging Findings

The imaging findings depend on the degree and duration of torsion. Thickening of the fallopian tube with hemorrhage is suggestive of torsion, especially when associated with an enlarged ovary or an adnexal cystic mass; torsed adnexal masses are often located midline, cranial to the uterine fundus and there is often uterine deviation (Moribata et al. 2015). A twisted edematous pedicle can be seen connecting the lesion to the uterus with mixed signal intensity on all sequences on MRI (Haque et al. 2000). Sometimes when tracking down the ovarian vascular pedicle, a coiled vascular pedicle may produce the whirlpool sign (Fig. 11) (Lee et al. 1993). In a recent study using multivariate analysis, the whirlpool sign and a thickened fallopian tube (>10 mm) were associated with torsion, with substantial interreader agreement (Beranger-Gibert et al. 2016). In prepubertal and pubertal girls where torsion of a normal ovary occurs in 50%, a unilateral solid mass with peripheral small cysts is indicative of a torsed ovary (Fig. 12). In cases of hemorrhagic infarction, the enlarged ovary may show low signal intensity on T2WI due to interstitial hemorrhage, without wall enhancement of the displaced follicles (Haque et al. 2000). The presence of hemorrhage has been found to be associated with nonviable ovary in 70% of cases and viable ovary in 27% of cases (Beranger-Gibert et al. 2016).

The most common appearance in adults is of a mass with areas of hyperintensity on T1WI due to hemorrhage and hyperintensity on T2WI due to ovarian edema (Kimura et al. 1994). Smooth wall thickening of the twisted adnexal cystic mass and a thin hyperintense rim at the periphery of the lesion on T1WI are further signs of ovarian torsion.

A tubular or comma-like structure partially covering the ovary represents the fallopian tube and may also display hemorrhagic contents. CT studies have reported a diameter of the fallopian tube of 2–4 cm (Ghossain et al. 1994).

Contrast enhancement on CT and MRI depends on the degree of viability (Kimura et al. 1994). MR findings in hemorrhagic infarction include lack of enhancement, engorged vessels surrounding the lesion, and signal intensity of hematoma (Rha et al. 2002).

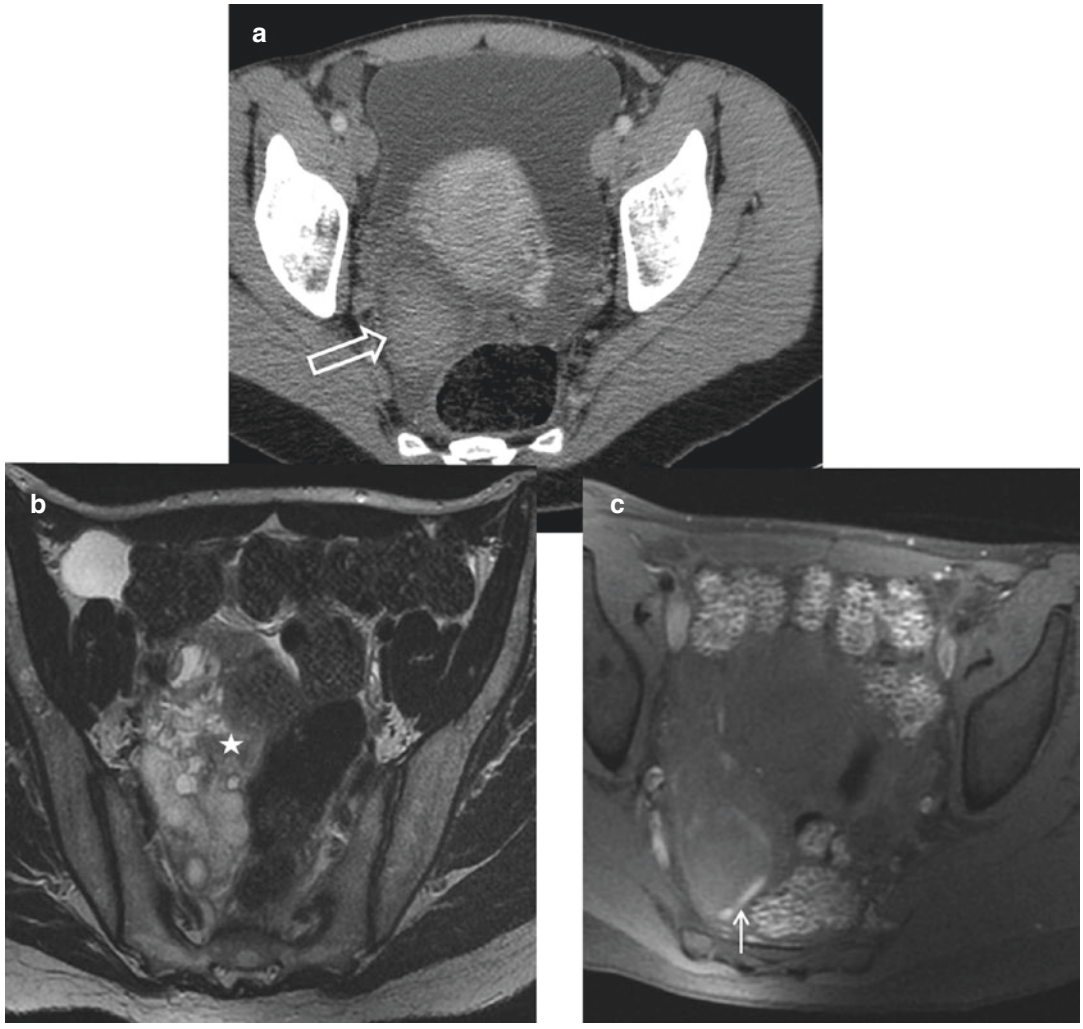

Fig. 11 CT and MRI images of a right ovarian torsion. The CT (**a**) shows a hyperdense right adnexal lesion (*open arrow*) in a lady presenting with acute abdominal pain. A transvaginal ultrasound could not be tolerated. On T2-weighted MRI (**b**) there is a whirlpool sign (*long arrow*) anterior to the enlarged edematous right ovary which is intermediate signal intensity on T2WI (*star*). Follicles are seen at the periphery of the ovary. The T1 fat saturation MRI (**c**) demonstrates blood at the periphery of the torsed ovary (*short arrow*)

Nonspecific findings include deviation of the uterus to the twisted side, ascites, and obliteration of the pelvic fat.

2.5.2 Differential Diagnosis

Clinically, ruptured ovarian cysts may resemble ovarian torsion. However, in the case of ruptured ovarian cyst, the ovary is usually normal in size and free fluid or blood may be seen in the pelvis; there is neither edema of an adnexal mass nor engorged adnexal vessels or dilatation of the fallopian tube. Tubo-ovarian abscess and hydrosalpinx may resemble advanced adnexal torsion. Lack of enhancement supports the diagnosis of ovarian torsion. In children, sonography usually allows the diagnosis of appendicitis as a cause of acute pelvic pain. In the case of a suspected abscess or an ovarian mass, MRI may

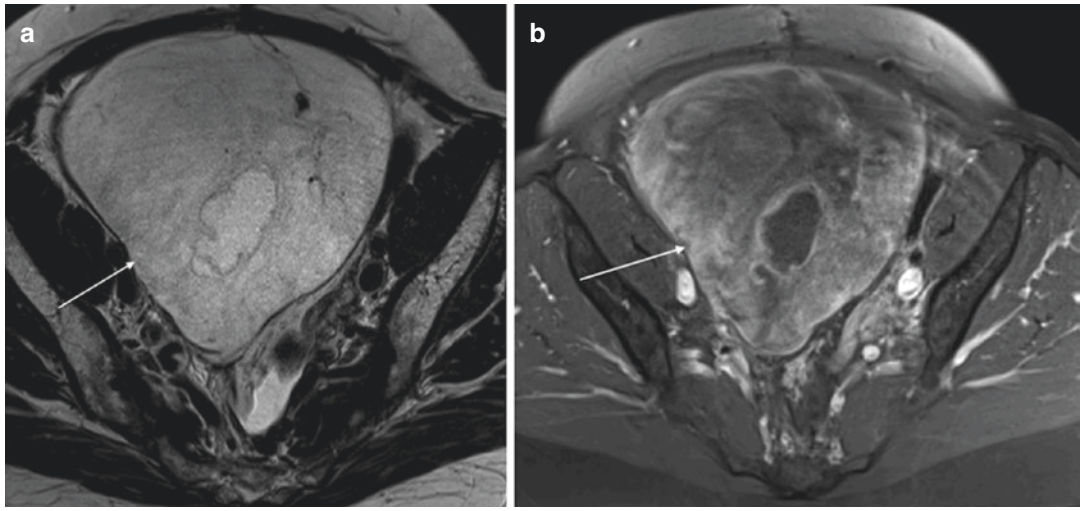

Fig. 12 Massive ovarian edema caused by infiltration from a mucinous colorectal tumor. The large pelvic mass (*arrow*) is of high signal intensity on axial T2wi (**a**) and demonstrates peripheral and heterogeneous contrast enhancement on dynamic contrast-enhanced T1 fat-saturated image (**b**)

assist in further assessment of the adnexa. Rarely, a calcified mass may result from chronic infarction which cannot reliably be differentiated from a calcified ovarian tumor (Currarino and Rutledge 1989). Malignant massive ovarian edema may be seen when there is metastatic infiltration of the lymphatics of the ovary (Krasevic et al. 2004; Bazot et al. 2003) (Fig. 12).

2.5.3 Diagnostic Value

Early diagnosis and treatment is crucial to prevent irreversible ovarian damage and prevent infectious complications. Most patients with suspected torsion clinically and on sonography will undergo immediate surgical untwisting. However, in patients that present with severe acute pain of uncertain diagnosis, CT may be the first line investigation and the signs of ovarian torsion may be difficult to appreciate. MRI and CT are often used in clinically atypical cases, especially in chronic torsion. In early torsion, the imaging signs may be indicative but not specific of ovarian torsion. MRI and CT are particularly useful in detecting twisted lesions displaced outside the pelvis, where sonography may be limited. In pregnancy and in children, MRI is the modality of choice to further assess suspected ovarian torsion.

2.6 Ectopic Pregnancy

Ectopic pregnancy describes implantation and growth of the fertilized ovum at any site other than the endometrial cavity. The fallopian tube accounts for the vast majority of all ectopic gestations (95%), with 75% found in the ampulla and the remainder occurring in the fimbrial and isthmic portions with roughly equal distribution (Bouyer et al. 2002). Rarely, ectopic pregnancy may occur within the ovary (3.2%), or within the peritoneal cavity (1.3%). Ectopic cervical pregnancy is more commonly found in pregnancies achieved through in vitro fertilization technologies (Ushakov et al. 1997). The major cause of ectopic pregnancy is disruption of normal tubal patency due to infection, surgery, müllerian anomalies, or tumors. The rise of ectopic pregnancies in the last decade is

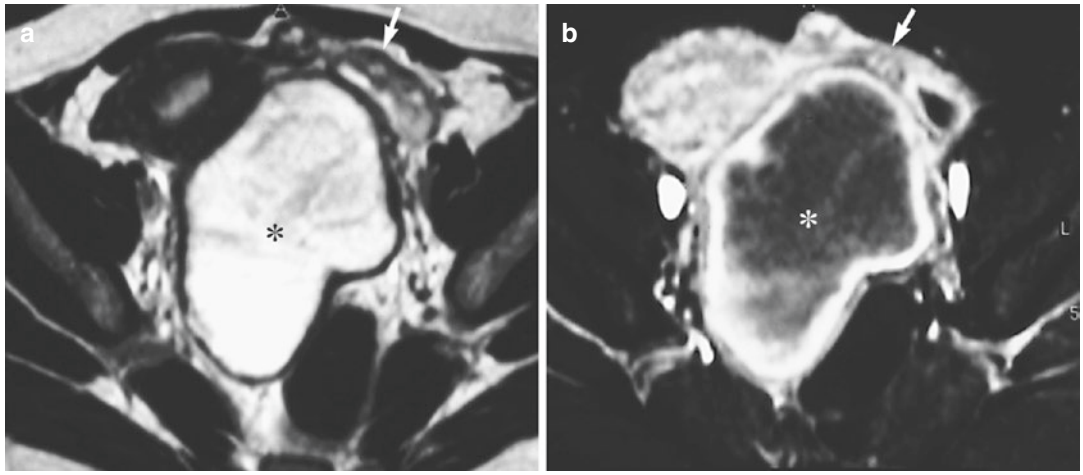

Fig. 13 Hematosalpinx in ectopic tubal pregnancy. Transaxial T2WI (**a**) and contrast-enhanced T1WI with fat saturation (FS) (**b**). In a 27-year-old woman with a positive pregnancy test, a cystic adnexal mass (*asterisk*) displaces the uterus. There is widening of the endometrial cavity. The adnexal lesion is separated from the adjacent left ovary (*arrow*) and displays inhomogeneous signal intensity with areas of high and low SI on T2WI (**a**) indicative of hemorrhage. The cystic content of the fallopian tube and distinct homogenous tubal wall enhancement is demonstrated following contrast media administration (**b**). Courtesy of Dr. Teresa Margarida Cunha, Lisbon

associated with the increased incidence of pelvic inflammatory disease. A history of PID with chronic salpingitis is found in 35–50% of patients with ectopic pregnancy.

2.6.1 Imaging Findings

On MRI, tubal wall enhancement and fresh tubal hematoma are highly specific for ectopic tubal pregnancy (Kataoka et al. 1999) (Fig. 13). The gestational sac is a cystic, centrally fluid-filled structure that is surrounded by a thick-walled peripheral rim. The latter displays inhomogeneous signal intensity on T2WI and medium signal intensity on T1WI, which may contain small areas of high signal intensity suggestive of blood (Nishino et al. 2002). When such a gestational sac-like structure is found separate from the uterus without tubal structures, this finding is equivocal due to the differential diagnostic problems of cystic ovarian masses (Kataoka et al. 1999). Identification of the uterine junctional zone between the gestational sac surrounded by myometrium and the uterine cavity is highly suggestive of a rare type of ectopic pregnancy, interstitial pregnancy (Filhastre et al. 2005). In suspected ectopic pregnancy, the combination of an adnexal mass and acute intraperitoneal hemorrhage is suggestive of tubal rupture.

2.6.2 Differential Diagnosis

In women of reproductive age presenting with elevated human chorionic gonadotropin levels, demonstration of a gestational sac-like structure is highly suggestive of ectopic pregnancy. However, ovarian cancer may rarely be detected during early pregnancy and be misdiagnosed as ectopic pregnancy (Riley et al. 1996). Based on the MRI findings alone, ectopic pregnancy may be misdiagnosed as an ovarian mass, e.g., ovarian cancer or endometriosis. Interstitial ectopic pregnancy may resemble cystic adenomyomas or necrotic leiomyomas (Filhastre et al. 2005).

2.6.3 Value of Imaging

The diagnosis of ectopic pregnancy is usually established by the combination of the clinical history, β-HCG levels, and transvaginal sonography. The role of MRI has not been defined. It may, however, provide additional information in the case of equivocal ultrasound,

especially to better determine the exact site of origin of the ectopic pregnancy (Filhastre et al. 2005).

3 Nongynecological Causes of Pelvic Pain

3.1 Pelvic Congestion Syndrome

Pelvic congestion syndrome or pelvic venous incompetence (PVI) is a common cause of chronic non-cyclical pelvic pain that affects most often multiparous women of reproductive age. The symptoms of chronic dull pelvic pain, pressure, and heaviness have been attributed to dilated, tortuous, and congested veins that are produced by retrograde flow through incompetent valves in ovarian veins, although the causal relationship between PVI and chronic pelvic pain is not established (Champaneria et al. 2016). Patients with pelvic congestion syndrome may also suffer from dyspareunia (71%), dysmenorrhea (66%), and postcoital ache (65%) (Kuligowska et al. 2005). The prevalence of pelvic congestion syndrome is closely related to the frequency of ovarian varices, which occur in 10% of the general population of women. Within this group of patients, up to 60% may develop pelvic congestion syndrome (Lopez 2015). The pathogenesis of pelvic congestion syndrome is most likely multifactorial and influenced by hormonal effects, multiparity, and previous surgery. Pelvic congestion syndrome may also result from obstructing anatomic anomalies such as a retro-aortic left renal vein or right common iliac vein compression (Kuligowska et al. 2005). It may be associated with asymptomatic hematuria in the nutcracker phenomenon, which is caused by left ovarian vein congestion secondary to compression of the left renal vein by the superior mesenteric artery (Umeoka et al. 2004). Dilated veins include veins in the broad ligaments, ovarian plexus, and pelvic sidewalls. Varices within the para-vaginal plexus, vulva, or the lower extremities may also be found (Umeoka et al. 2004). Polycystic changes in ovaries are associated in approximately 40% of cases (Park et al. 2004).

3.1.1 Imaging Findings

The typical imaging findings are dilated and tortuous vascular structures engorging the uterus and ovaries, which may extend to the pelvic sidewalls or communicate with para-vaginal veins. Ultrasound and MR imaging are noninvasive methods used to diagnose pelvic varices. The diagnosis of pelvic varicosities may also be made on CT by the demonstration of at least four ipsilateral dilated para-uterine veins of varying caliber, with a width of at least one vein larger than 4 mm or a diameter of the ovarian vein of more than 8 mm (Fig. 14) (Rozenblit et al. 2001). On T1-weighted MR images, pelvic varices display low signal intensity because of flow-void artifacts. On T2WI, the signal intensity depends on the velocity of blood flow. Contrast-enhanced magnetic resonance venogram (MRV) displays enhancing veins with maximal opacification in a venous phase. On gradient echo MR images, the varices typically display high signal intensity. MRV has been shown to have high sensitivity for pelvic venous congestion when using phlebography as a reference standard (Asciutto et al. 2008).

3.1.2 Differential Diagnosis

Incompetent and dilated ovarian veins are frequently seen on CT in asymptomatic parous women (Fig. 15) (Rozenblit et al. 2001). Congenital or acquired vascular malformations of the uterus or parametria present also as vascular lesions. Contrast-enhanced CT or MRI may aid in the differentiation by the early enhancement of arteriovenous malformations in contrast to a more delayed enhancement in varicosities (Gulati et al. 2000). Adnexal masses with torsion or rare uterine tumors, especially choriocarcinomas, may also be surrounded by thick, tortuous, well-enhanced vessels. The clinical background and imaging findings of an adnexal or uterine mass aid in the differential diagnosis.

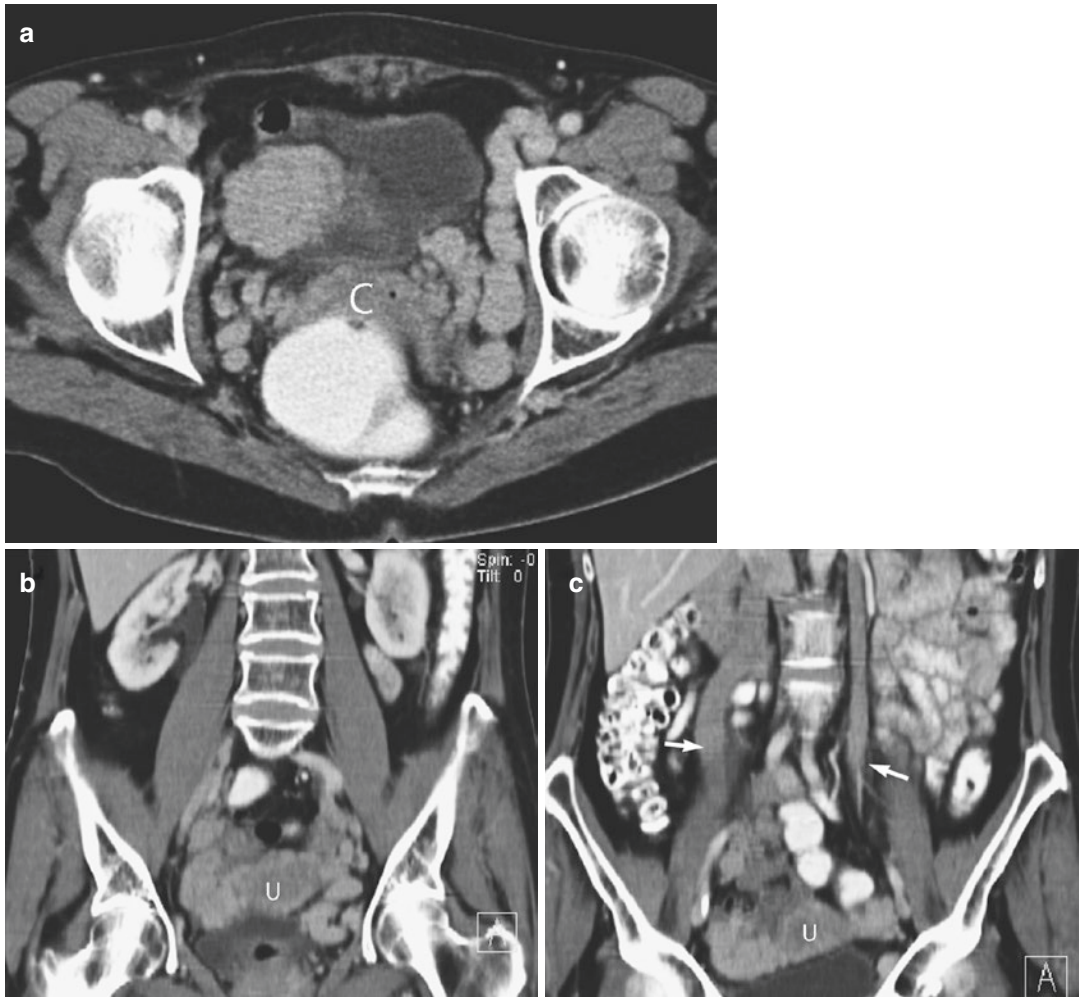

Fig. 14 Pelvic congestion syndrome. Transaxial CT at the level of the cervix uteri (**a**) and coronal scans in the pelvis and retroperitoneum (**b**, **c**). Multiple dilated tortuous pelvic vascular structures are demonstrated within the parametria and pelvic sidewalls (**a**). The coronal images demonstrate engulfment of the uterus (U) by these vascular structures (**b**, **c**). Dilatation of both ovarian veins (*arrows*), which display a diameter of more than 8 mm, is shown in (**c**). *U* uterine corpus, *C* cervix

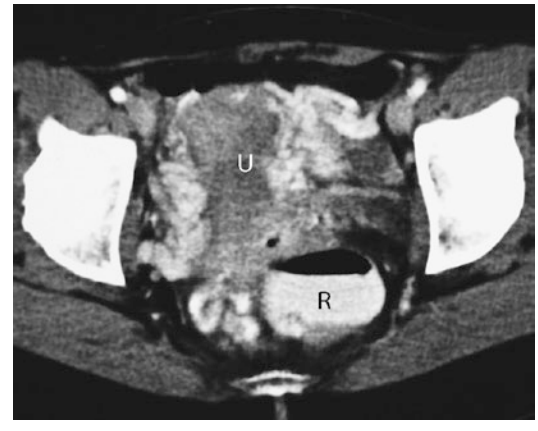

Fig. 15 Pelvic varices in an asymptomatic woman. CT shows numerous dilated para-uterine veins of varying diameter in an asymptomatic 37-year-old multiparous woman. *U* uterus, *R* rectum

3.1.3 Value of Imaging

The diagnosis of ovarian and pelvic varices is established by sonography. CT or MRI are used to confirm the diagnosis and to guide therapy (Arnoldussen 2015). However, these cross-sectional imaging techniques, which are not performed in an upright position, may underestimate the venous pathology.

Several treatment options for pelvic congestion syndrome, including laparoscopic transperitoneal ligation of ovarian veins, are currently under investigation. Percutaneous coil embolization of the gonadal vein seems to be a safe technique that relieves pelvic pain in many patients with pelvic congestion syndrome (Mathias et al. 1996).

3.2 Ovarian Vein Thrombosis

Ovarian vein thrombosis typically presents as a complication in the postpartum period, encountered most frequently after caesarean section, but may also be seen following gynecologic or pelvic surgery (Rottenstreich 2016; Assal et al. 2017). It is caused by venous stasis and hypercoagulability. The incidence of puerperal ovarian vein thrombosis (POVT) is approximately 1 in 2000 deliveries (Witlin et al. 1996). Other conditions such as infection, recent surgery, malignancy, and Crohn's disease increase the risk for ovarian vein thrombosis (Dunnihoo et al. 1991). Although a rare entity, ovarian vein thrombosis presents a differential diagnostic problem because of the nonspecific clinical symptoms, including fever, and the potential of fatal complications due to uterine necrosis or septic emboli (Savader et al. 1988). As the majority (80–90%) of ovarian vein thrombosis occurs in the right ovarian vein, right-sided pain is a typical clinical presentation.

3.2.1 Imaging Findings

Ovarian vein thrombosis is usually well depicted as a dilated tubular structure extending from the adnexa to the para-aortal region near the renal hilum. Contrast-enhanced CT allows direct visualization of the low attenuating central thrombus surrounded by vascular contrast enhancement

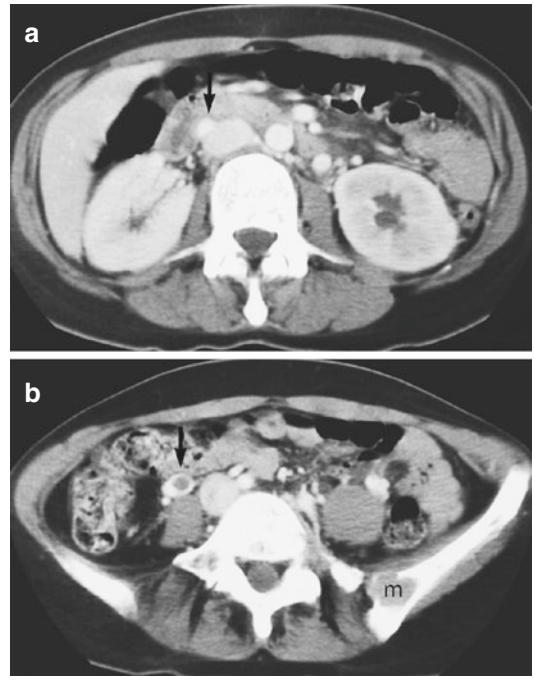

Fig. 16 Ovarian vein thrombosis. CT scans below the level of the renal hilum (**a**) and lower lumbar region (**b**). In a patient with metastatic breast cancer with bone involvement (*m*), a nonoccluding thrombus (*arrow*) is identified in a dilated right ovarian vein (**b**). The renal vein (*arrowhead*) is patent (**a**)

(Fig. 16) (Quane et al. 1998). On MRI, the thrombus may display high SI on T1 and T2WI. Transaxial gradient-echo images or contrast-enhanced T1WI images aid in differentiation of flow artifacts from thrombosis. Imaging in the coronal plane demonstrates the full extent of ovarian vein involvement.

3.2.2 Differential Diagnosis

The differential diagnosis includes other causes of right-sided pelvic pain such as appendicitis, adnexal torsion, pelvic abscess, pyelonephritis, and endometritis (Kubik-Huch et al. 1999).

3.2.3 Value of Imaging

Color Doppler ultrasound is the primary imaging modality in patients with suspected ovarian vein thrombosis. Especially in the postpartum period, its performance is often limited due to uterine enlargement, postoperative changes, or obesity. This is why CT or MRI are commonly performed to rule out ovarian vein thrombosis.

3.3 Appendicitis

Appendicitis affects all age groups, peaking in the early 20s and then gradually declining with increasing age. Appendicitis is 1.4 times more frequent in men compared to women. The most common causes of appendicitis are obstruction of the lumen by fecalith, lymphoid follicle hyperplasia, foreign bodies, and tumors. Variations in the appendiceal location make the clinical assessment of appendicitis difficult. The position of the appendix is retroperitoneal in about 30% of cases. In the remaining 70% of intraperitoneal appendices, the location can vary from retro-cecal to retro-ileal, deep pelvic, and rarely right upper quadrant location. Suspected appendicitis is the commonest cause of emergency abdominal surgery; however, clinical diagnosis can be difficult and approximately 20% of appendicectomy cases are false-positive diagnoses (Paulson et al. 2003). In women of reproductive age, the error rate can be as high as 40%, because acute gynecological processes can mimic the clinical findings of acute appendicitis (Andersson et al. 1992).

Perforation and abscess formation can complicate appendicitis in 38–55%, with the highest rates occurring in children and in elderly patients.

3.3.1 Imaging Findings

On CT the normal appendix appears as a tubular structure with a diameter of less than 6 mm that often contains air or contrast media. CT findings of acute appendicitis include enlargement of the appendix (>6 mm in outer diameter), enhancement of the thickened appendiceal wall, and fat stranding of the peri-appendiceal region (Fig. 17) (Rao et al. 1997). Signs indicative of perforation include extra-luminal air, extra-luminal appendicolith, a defect in the enhancing appendiceal wall, and an abscess or phlegmon (Horrow et al. 2003). A phlegmon is characterized by diffuse inflammation of the peri-appendiceal fat with no or small, ill-defined fluid collections. An abscess is a well-delineated fluid collection with rim enhancement (Horrow et al. 2003). Focal thickening of the cecum can be seen secondary to the inflammatory process and has been described as the arrowhead sign (Rao et al. 1997). The appearance on MR is similar to that described on CT, including thickening of the appendiceal wall, a dilated fluid-filled lumen, and increased intensity of peri-appendiceal tissue on T2-weighted imaging or contrast-enhanced images (Fig. 18) (Nitta et al. 2005). Extra-intestinal fluid-filled hyperintense lesions with walls that are hypointense on T2-weighted images and thick on the contrast-enhanced images are indicative of abscesses. The presence of air on MRI or CT allows the definitive diagnosis of an abscess (Oto et al. 2005).

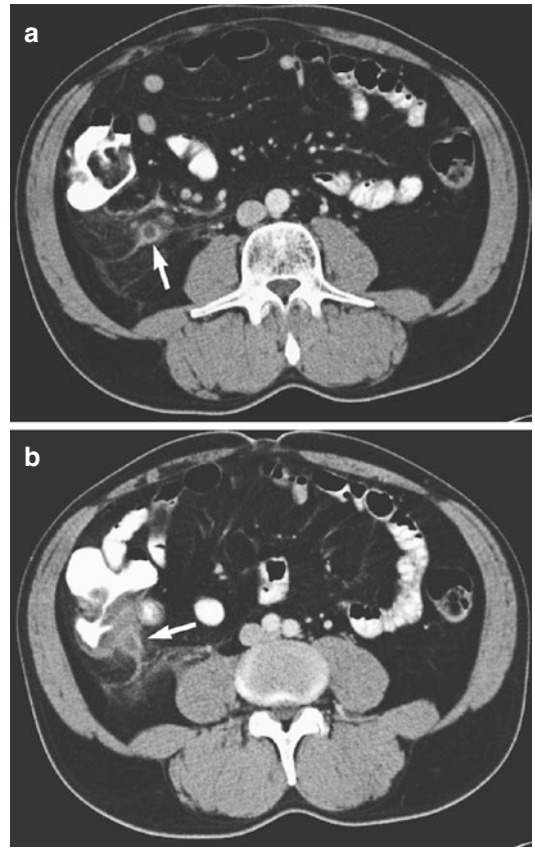

Fig. 17 CT findings in acute appendicitis. Axial Ct through the right lower quadrant (**a**, **b**). The tubular enhancing structure with a diameter of 9 mm is the dilated appendix (*arrow*). It is surrounded by marked fat stranding of the peri-cecal fat and adjacent facial thickening. At the base of the appendix (*arrow*), thickening of the cecum can be seen, which presents the arrowhead sign (**b**). A small fluid collection is seen along the surface of the psoas muscle (**b**)

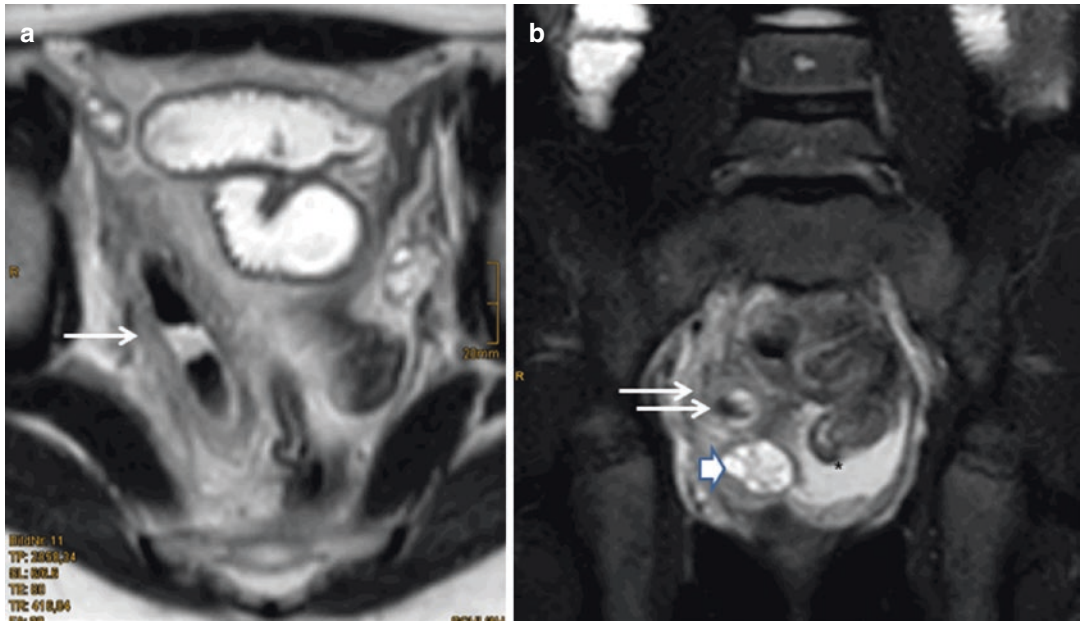

Fig. 18 10-year-old girl with advanced appendicitis. The appendix is fluid filled and enlarged with a diameter of 12 mm (*arrow*). Extensive adjacent inflammation is seen. There is also diffuse pelvic peritonitis and small amounts of ascites (*asterisk*). At surgery perforated appendicitis was found. Right ovary (*arrowhead*). Courtesy of Dr. Rosemarie Forstner

3.3.2 Value of Imaging

Ultrasound is the primary diagnostic imaging modality for suspected acute appendicitis; however, this is often non-diagnostic due to limitations in identifying the normal appendix, and variations in appendiceal location (Paulson et al. 2003). CT is highly sensitive and specific in the diagnosis of appendicitis (rates of 90–95% and 95–100%, respectively) is often performed when ultrasound is non-diagnostic. Due to its lack of ionizing radiation, MR is an alternative, highly useful imaging tool in the assessment of acute appendicitis (sensitivity and specificity rates of 96%) and is particularly useful as a first line investigation in pregnant women (sensitivity and specificity of 94% and 97%, respectively) and children (sensitivity and specificity of 96%) (Petkovska et al. 2016).

3.4 Diverticulitis

Colonic diverticulosis is a very common condition in Western society, affecting 5–10% of the population over 45 years, and 80% over 85 years of age (Ferzoco et al. 1998).

Diverticula are small sacculations of mucosa and submucosa through the muscularis of the colonic wall. They develop at the point where the nerve and blood vessel penetrate the muscularis between the teniae coli and mesentery (Horton et al. 2000). The most common location for diverticula is the sigmoid colon. Acute diverticulitis occurs when the neck of a diverticulum is occluded by food particles, stool, or inflammation, resulting in microperforation of the diverticulum with surrounding mild pericolic inflammation. This can lead to a localized abscess or, if adjacent organs are involved, a fistula. The inflammation is usually contained by peri-colonic fat and mesentery and without this free perforation and peritonitis can occur. The commonest clinical symptom is left-lower-quadrant pain and tenderness, which is often present for several days before admission. Low-grade fever and mild leukocytosis are common but their absence does not exclude diverticulitis.

Right-sided diverticulitis occurs in only 1.5% of patients in Western countries but is more common in Asian populations and tends to affect younger patients (Kang et al. 2004). Diverticulitis of small intestine or transverse colon is rare (Pereira et al. 2004).

3.4.1 Imaging Findings

On CT, diverticulae appear as small, air-filled outpouchings of the colonic wall. On MRI air-filled diverticulae are hypointense against the high-signal-intensity peri-colonic fat. The most common imaging finding in diverticulitis is paracolic fat stranding, which is characteristically more severe than the focal colonic wall thickening (Fig. 19). The key to distinguishing diverticulitis from other inflammatory conditions affecting the colon is the presence of diverticulae in the involved segment (Pereira et al. 2004). Contrast-enhanced CT or fat-suppressed T1-weighted contrast-enhanced images provide the best assessment of thickening of the colonic wall and the peri-colonic fat stranding. Other common imaging findings include thickening of the lateral conal fascia and a small volume of ascites in the cul-de-sac. Accumulation of fluid in the root of the sigmoid mesentery is known as the comma sign.

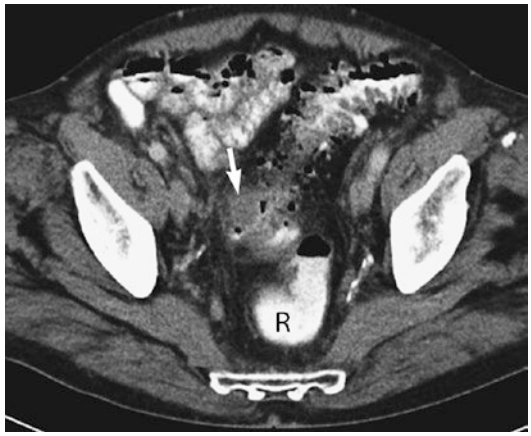

Fig. 19 Sigmoid diverticulitis. Multiple air containing diverticula are found along the sigmoid colon. In this patient with acute pelvic pain, focal wall thickening, stenosis, and paracolic fat stranding (*arrow*) are signs of acute diverticulitis involving the distal sigmoid colon. *R* rectum

Complications of diverticulitis include diverticular phlegmon and abscess, colo-vesical fistula, and perforation. Phlegmon is a heterogeneous inflammatory mass found adjacent to the diverticulitis (Onur et al. 2017). An abscess occurs in up to 30% of cases and on CT appears as a hypodense fluid collection with a contrast-enhancing rim and surrounding inflammatory changes. It may contain air or air–fluid levels (Horton et al. 2000). A colo-vesical fistula is suspected when air is seen in the bladder and there is thickening of the bladder wall adjacent to a diseased segment of bowel (Labs et al. 1988). Focal contained perforations can complicate diverticulitis; these appear as small extra-luminal deposits of air or extravasation of oral contrast material. Pneumoperitoneum is a rare finding in patients with diverticulitis (Horton et al. 2000).

3.4.2 Differential Diagnosis

The most important differential diagnosis is colon carcinoma. The presence of pericolic lymph nodes suggests the diagnosis of colon cancer rather than diverticulitis (Chintapalli et al. 1999). A long segment on involved colon (>10 cm), engorgement of adjacent sigmoid mesenteric vasculature, and the presence of fluid in the root of the sigmoid mesentery favor the diagnosis of diverticulitis (Horton et al. 2000; Cobben et al. 2003). It is not always possible to distinguish diverticulitis from colon cancer and the two entities can coexist in 3–18% of patients (Cobben et al. 2003). The presence of pelvic abscess may raise the possibility of PID in the differential diagnosis, although the extent of inflammatory change in the bowel is usually diagnostic.

3.4.3 Value of Imaging

The role of imaging in diverticulitis is to exclude complications and predict the necessity for emergent surgery. If an abscess is detected CT-guided percutaneous drainage may be performed. MR imaging can be useful in the diagnosis of right-sided diverticulitis in young or pregnant patients with suspected appendicitis.

3.5 Epiploic Appendagitis

Epiploic appendages are pedunculated fat-filled structures protruding from the external surface of the colon into the peritoneal cavity. They vary considerably in size, shape, and contour, but they are usually 1–2 cm thick and 0.5–5 cm long and they are larger on the left side of the colon. They are presumed to serve a protective cushion during peristalsis. Epiploic appendages have limited blood supply and are highly mobile which makes them prone to torsion, ischemia, and hemorrhagic infarction. When this happens it is known as epiploic appendagitis, hemorrhagic epiploitis, or epiploic appendicitis. It is a rare, benign, and self-limiting pathology. It occurs most commonly in the second to fifth decades of life, with a similar incidence among men and women (Almeida et al. 2009). The most common presentation is with sudden onset of abdominal pain without leukocytosis and fever (Rao and Novelline 1999).

3.5.1 Imaging Findings

Normal epiploic appendages are not usually seen on CT or MR unless there is a sufficient amount of surrounding intraperitoneal fluid, either ascites or hemoperitoneum (Fig. 20). Imaging findings of epiploic appendagitis include an oval-shaped fingerlike paracolic mass with fat attenuation and peri appendiceal fat stranding (Pereira et al. 2005). On CT, the density tends to be higher than uninvolved fat. A well-circumscribed hyperattenuating rim surrounding the mass representing the inflamed visceral peritoneal lining is a characteristic finding (Fig. 21). Adjacent colonic wall thickening and compression may also be seen (Rao and Novelline 1999). Sometimes a high attenuation central dot representing thrombosed central vessels or central areas of hemorrhage can be seen (Pereira et al. 2005). Rarely, dystrophic calcification from a previously infarcted appendage may be evident (Pickhardt and Bhalla 2005). On MRI, the inflamed epiploic appendage is slightly less hyperintense than the adjacent peritoneal fat and shows marked signal loss on fat suppression sequences. The inflammatory rim is hypointense on T1-weighted images and hyperintense on T2-weighted images. The central draining vein is hypointense on both T1- and T2-weighted images (Almeida et al. 2009).

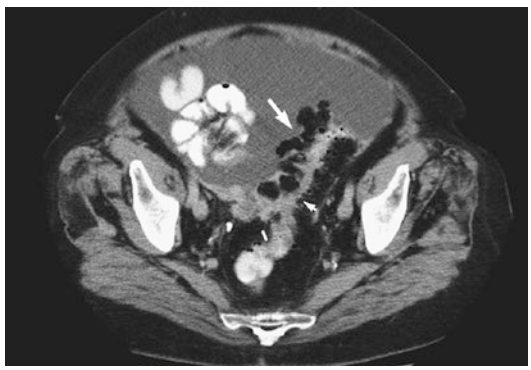

Fig. 20 Normal epiploic appendices on CT. Epiploic appendices of the sigmoid colon present pedunculated fat structures, which protrude from the sigmoid surface into the peritoneal cavity (*arrow*). They are easily visualized because of ascites in this woman with peritoneal carcinomatosis. Small sigmoid diverticula which present air-containing mural outpouchings into the peri-sigmoid fat tissue are also demonstrated (*arrowhead*)

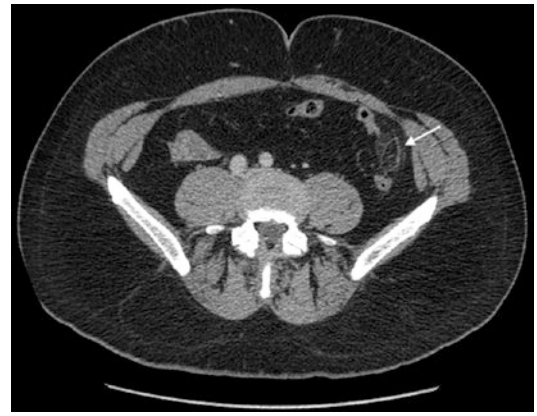

Fig. 21 Epiploic appendagitis. Axial CT shows soft-tissue infiltration (*arrow*) with adjacent reticular fatty infiltration in the left iliac fossa. The well-circumscribed hyper-attenuating rim is more consistent with epiploic appendagitis than omental infarction

3.5.2 Differential Diagnosis

Segmental omental infarction, which is often localized on the right side of the omentum, has a similar appearance to epiploic appendagitis. Imaging findings range from subtle focal hazy soft-tissue infiltration of the omentum to a

tumor-like inflammatory processes that may or may not lie immediately adjacent to the colon (Pereira et al. 2005; Pickhardt and Bhalla 2005). As features may also overlap with those of epiploic appendagitis, the term "focal fat infarction" has been suggested by some authors for both entities (Pereira et al. 2005).

3.5.3 Value of Imaging

Epiploic appendagitis and omental infarction are causes of acute pelvic pain that are often misdiagnosed clinically as acute appendicitis or diverticulitis. Imaging allows a definite diagnosis in most cases and patients can be managed conservatively.

3.6 Crohn's Disease

Crohn's disease is a chronic granulomatous inflammatory intestinal disease with a mean age of presentation in the third and fourth decades. It can affect any part of the gastrointestinal tract from the mouth to the anus, often involving multiple discontinuous sites. The small intestine is involved in 80% of cases, most commonly at the terminal ileum. The colon is affected either with or without involvement of the small intestine (Furukawa et al. 2004). Leading clinical manifestations are prolonged diarrhea with abdominal pain, weight loss, and fever. There is transmural inflammation of the bowel which may lead to adherent bowel loops inflammatory masses, fistulae, sinus tracts obstruction, and perforation. Perianal disease such as anal fissures, fistulas, and abscesses occur in 22% of patients with Crohn's disease, and are often the first clinical manifestation (Williams et al. 1981).

3.6.1 Imaging Findings

Bowel wall thickening, usually ranging from 1 to 2 cm, is the most consistent feature of Crohn's disease on CT and MR (Rollandi et al. 1999). Mural stratification (target appearance) is often seen in active lesions, particularly after contrast administration. The intensity of bowel wall enhancement correlates with the degree of inflammation (Gore et al. 1996). Luminal narrowing, pre-stenotic dilatation, fibro-fatty proliferation of the mesentery, and mesenteric lymph nodes ranging from 3 to 8 mm in size are further common findings (Fig. 22). On CT, fibro-fatty proliferation has a slightly increased attenuation. On MRI, the signal intensity is decreased compared with normal fat separating the bowel loops. Phlegmon and abscesses can occur in the small bowel mesentery, abdominal wall, or psoas muscle or perianally. They are well demonstrated on CT and fat-saturated T1W MR imaging (Furukawa et al. 2004). Fistulas and sinus tracts can also be identified on MR; however, the reported sensitivity (50–75%) is less than for conventional enteroclysis (Gourtsoyiannis et al. 2002).

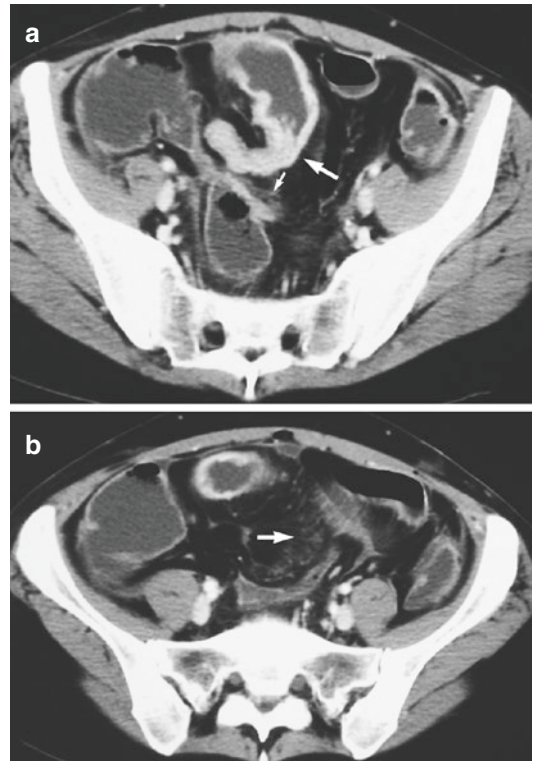

Fig. 22 Crohn's disease in CT. Small bowel loops with dilatation and stenoses are demonstrated in two pelvic CT scans (**a**, **b**). A loop of ileum shows transmural wall thickening and intense contrast enhancement (*arrow*) (**a**). Adjacent mesenteric hypervascularity represents the comb sign (*long arrow*) and is another sign of inflammatory activity (**b**). Heterogeneity of surrounding fat with increased attenuation presents fibrofatty proliferation (*arrowhead*) (**b**)

3.6.2 Differential Diagnosis

Ulcerative colitis is a mucosal disease that primarily affects the rectum. It is typically left-sided or diffuse, and only rarely involves the right colon exclusively (Philpotts et al. 1994). The mean wall thickness in Crohn's disease is usually greater than in ulcerative colitis (Fishman et al. 1987). The halo sign, a low-attenuation ring in the bowel wall caused by deposition of submucosal fat, is seen more commonly in ulcerative colitis than in Crohn's disease. Proliferation of mesenteric fat is almost exclusively seen in Crohn's disease, whereas proliferation of perirectal fat is nonspecific and can result from Crohn's disease, ulcerative colitis, pseudomembranous colitis, or radiation colitis (Philpotts et al. 1994). Abscesses are almost exclusively found in Crohn's disease and not in ulcerative colitis (Gore et al. 1996).

3.6.3 Value of Imaging

Cross-sectional imaging is able to demonstrate transmural extent, skip lesions beyond severe luminal stenoses, and intraperitoneal extraintestinal complications. MRI is preferred because of its lack of ionizing radiation and high diagnostic accuracy (sensitivity and specificity of up to 84% and 100%, respectively) (Laghi et al. 2003). MRI is also better at detecting complications such as fistulae that can be missed on CT. However, CT and MR imaging are both inferior compared to enteroclysis in the depiction of early disease manifestations (Furukawa et al. 2004).

3.7 Rectus Sheath Hematoma

Rectus sheath hematoma is an uncommon and often misdiagnosed condition resulting from either rupture of the epigastric vessels or the rectus muscle itself. The hematoma may be caused by coagulation disorders, trauma, or anticoagulation therapy (Fishman et al. 1987). Clinically, most patients present with acute abdominal pain, a peri- or infraumbilical mass, and anemic syndrome. Some patients also have a history of severe coughing episodes due to bronchial infection.

3.7.1 Imaging Findings

The shape of rectus sheath hematomas depends on the relationship to the arcuate line, which is 3.5–5 cm below the umbilical level (Fukuda et al. 1996). Above this level, they usually appear as spindle-shaped due to encasement by firm aponeurotic sheaths (Fig. 23). Below the arcuate line, hematomas tend to appear spherical and may communicate with extraperitoneal pelvic and perivascular pelvic spaces (Fukuda et al. 1996). On CT, hematomas present as homogeneous hyperdense lesions with thin circumferential halos of low density. Clot resorption leads to diminution of density and fluid–fluid levels because a hematocrit effect may be found within hematomas (Berna et al. 1996; Wolverson et al. 1983). Additional findings of rectus sheath hematoma include increased density of the adjacent subcutaneous fat and enlargement of the anterolateral muscles (Fukuda et al. 1996). On MRI, rectus sheath hematomas demonstrate heterogeneous signal intensities with areas of high signal intensity on T1-weighted and T2-weighted images. Fluid–fluid levels and a concentric ring sign can also be noted (Blum et al. 1995).

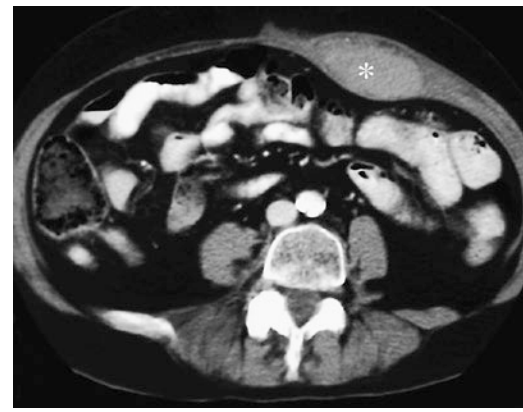

Fig. 23 Rectus sheath hematoma on CT. A spindle-shaped lesion is seen in the left rectus muscle (*arrow*). It shows homogenous high density and is surrounded at its anterior periphery by a minimal hypodense rim. Only minimal thickening of the adjacent lateral abdominal muscles can be noted

3.7.2 Differential Diagnosis

The acute clinical onset in a patient under anticoagulation supports the diagnosis of a rectus sheath hematoma. MR imaging may be useful in differentiation of chronic rectus sheath hematomas from anterior abdominal wall masses such as lipoma, hemangioma, neurofibroma, desmoid tumor, soft-tissue sarcoma, lymphoma, or metastatic lesions. Although bleeding into neoplasm may occur, hyperintense regions are rarely observed in tumors (Fukuda et al. 1996).

3.7.3 Value of Imaging

In the presence of a clinically suspected rectus sheath hematoma or equivocal findings in sonography, CT should be performed. CT usually allows the correct diagnosis and obviates unnecessary surgical interventions (Berna et al. 1996).

References

Akhan SE, Dogan Y, Akhan S, Iyibozkurt AC, Topuz S, Yalcin O (2008) Pelvic actinomycosis mimicking ovarian malignancy: three cases. Eur J Gynaecol Oncol 29(3):294–297

Almeida AT, Melao L, Viamonte B, Cunha R, Pereira JM (2009) Epiploic appendagitis: an entity frequently unknown to clinicians—diagnostic imaging, pitfalls, and look-alikes. AJR Am J Roentgenol 193(5):1243–1251

Andersson RE, Hugander A, Thulin AJ (1992) Diagnostic accuracy and perforation rate in appendicitis: association with age and sex of the patient and with appendicectomy rate. Eur J Surg 158(1):37–41

Arnoldussen CW (2015). Diagnostic imaging of pelvic congestive syndrome. In: de Wolf MA (ed), Phlebology. pp 67–72

Asciutto G, Mumme A, Marpe B, Koster O, Asciutto KC, Geier B (2008) MR venography in the detection of pelvic venous congestion. Eur J Vasc Endovasc Surg 36(4):491–496

Assal A, Kaner JD, Danda N, Cohen HW, Billett HH (2017) Risk factors and prognosis of ovarian vein thrombosis. Blood Coagul Fibrinolysis. DOI: 10.1097/MBC.0000000000000623

Atay Y, Altintas A, Tuncer I, Cennet A (2005) Ovarian actinomycosis mimicking malignancy. Eur J Gynaecol Oncol 26(6):663–664

Bazot M, Detchev R, Cortez A, Uzan S, Darai E (2003) Massive ovarian edema revealing gastric carcinoma: a case report. Gynecol Oncol 91(3):648–650

Bennett GL, Slywotzky CM, Giovanniello G (2002) Gynecologic causes of acute pelvic pain: spectrum of CT findings. Radiographics 22(4):785–801

Beranger-Gibert S, Sakly H, Ballester M, Rockall A, Bornes M, Bazot M et al (2016) Diagnostic value of MR imaging in the diagnosis of adnexal torsion. Radiology 279(2):461–470

Berna JD, Garcia-Medina V, Guirao J, Garcia-Medina J (1996) Rectus sheath hematoma: diagnostic classification by CT. Abdom Imaging 21(1):62–64

Blum A, Bui P, Boccaccini H, Bresler L, Claudon M, Boissel P et al (1995) Imaging of severe forms of hematoma in the rectus abdominis under anticoagulants. J Radiol 76(5):267–273

Bouyer J, Coste J, Fernandez H, Pouly JL, Job-Spira N (2002) Sites of ectopic pregnancy: a 10 year population-based study of 1800 cases. Hum Reprod (Oxford, England) 17(12):3224–3230

Champaneria R, Shah L, Moss J, Gupta JK, Birch J, Middleton LJ et al (2016) The relationship between pelvic vein incompetence and chronic pelvic pain in women: systematic reviews of diagnosis and treatment effectiveness. Health Technol Assess (Winchester, England) 20(5):1–108

Chintapalli KN, Chopra S, Ghiatas AA, Esola CC, Fields SF, Dodd GD 3rd (1999) Diverticulitis versus colon cancer: differentiation with helical CT findings. Radiology 210(2):429–435

Cobben LP, Groot I, Blickman JG, Puylaert JB (2003) Right colonic diverticulitis: MR appearance. Abdom Imaging 28(6):794–798

Currarino G, Rutledge JC (1989) Ovarian torsion and amputation resulting in partially calcified, pedunculated cystic mass. Pediatr Radiol 19(6–7):395–399

Dunnihoo DR, Gallaspy JW, Wise RB, Otterson WN (1991) Postpartum ovarian vein thrombophlebitis: a review. Obstet Gynecol Surv 46(7):415–427

Ferzoco LB, Raptopoulos V, Silen W (1998) Acute diverticulitis. N Engl J Med 338(21):1521–1526

Filhastre M, Dechaud H, Lesnik A, Taourel P (2005) Interstitial pregnancy: role of MRI. Eur Radiol 15(1):93–95

Fishman EK, Wolf EJ, Jones B, Bayless TM, Siegelman SS (1987) CT evaluation of Crohn's disease: effect on patient management. AJR Am J Roentgenol 148(3):537–540

Forstner R, Thomassin-Naggara I, Cunha TM, Kinkel K, Masselli G, Kubik-Huch R et al (2017) ESUR recommendations for MR imaging of the sonographically indeterminate adnexal mass: an update. Eur Radiol 27(6):2248–2257

Fukuda T, Sakamoto I, Kohzaki S, Uetani M, Mori M, Fujimoto T et al (1996) Spontaneous rectus sheath hematomas: clinical and radiological features. Abdom Imaging 21(1):58–61

Furukawa A, Saotome T, Yamasaki M, Maeda K, Nitta N, Takahashi M et al (2004) Cross-sectional imaging in Crohn disease. Radiographics 24(3):689–702

Ghiatas AA (2004) The spectrum of pelvic inflammatory disease. Eur Radiol 14(Suppl 3):E184–E192

Ghossain MA, Buy JN, Bazot M, Haddad S, Guinet C, Malbec L et al (1994) CT in adnexal torsion with

emphasis on tubal findings: correlation with US. J Comput Assist Tomogr 18(4):619–625
Gore RM, Balthazar EJ, Ghahremani GG, Miller FH (1996) CT features of ulcerative colitis and Crohn's disease. AJR Am J Roentgenol 167(1):3–15
Gourtsoyiannis N, Papanikolaou N, Grammatikakis J, Prassopoulos P (2002) MR enteroclysis: technical considerations and clinical applications. Eur Radiol 12(11):2651–2658
Graif M, Itzchak Y (1988) Sonographic evaluation of ovarian torsion in childhood and adolescence. AJR Am J Roentgenol 150(3):647–649
Gulati MS, Paul SB, Batra A, Sarma D, Dadhwal V, Nath J (2000) Uterine arteriovenous malformations: the role of intravenous 'dual-phase' CT angiography. Clin Imaging 24(1):10–14
Ha HK, Lee HJ, Kim H, Ro HJ, Park YH, Cha SJ et al (1993) Abdominal actinomycosis: CT findings in 10 patients. AJR Am J Roentgenol 161(4):791–794
Haque TL, Togashi K, Kobayashi H, Fujii S, Konishi J (2000) Adnexal torsion: MR imaging findings of viable ovary. Eur Radiol 10(12):1954–1957
Hildyard CA, Gallacher NJ, Macklin PS (2013) Abdominopelvic actinomycosis mimicking disseminated peritoneal carcinomatosis. BMJ Case Rep 2013 DOI: 10.1136/bcr-2013-201128
Horrow MM, White DS, Horrow JC (2003) Differentiation of perforated from nonperforated appendicitis at CT. Radiology 227(1):46–51
Horton KM, Corl FM, Fishman EK (2000) CT evaluation of the colon: inflammatory disease. Radiographics 20(2):399–418
Kang JY, Melville D, Maxwell JD (2004) Epidemiology and management of diverticular disease of the colon. Drugs Aging 21(4):211–228
Kataoka ML, Togashi K, Kobayashi H, Inoue T, Fujii S, Konishi J (1999) Evaluation of ectopic pregnancy by magnetic resonance imaging. Hum Reprod (Oxford, England) 14(10):2644–2650
Kawakami S, Togashi K, Kimura I, Nakano Y, Koshiyama M, Takakura K et al (1993) Primary malignant tumor of the fallopian tube: appearance at CT and MR imaging. Radiology 186(2):503–508
Kim SH, Kim SH, Yang DM, Kim KA (2004) Unusual causes of tubo-ovarian abscess: CT and MR imaging findings. Radiographics 24(6):1575–1589
Kimura I, Togashi K, Kawakami S, Takakura K, Mori T, Konishi J (1994) Ovarian torsion: CT and MR imaging appearances. Radiology 190(2):337–341
Koonings PP, Grimes DA (1989) Adnexal torsion in postmenopausal women. Obstet Gynecol 73(1):11–12
Krasevic M, Haller H, Rupcic S, Behrem S (2004) Massive edema of the ovary: a report of two cases due to lymphatic permeation by metastatic carcinoma from the uterine cervix. Gynecol Oncol 93(2):564–567
Kubik-Huch RA, Hebisch G, Huch R, Hilfiker P, Debatin JF, Krestin GP (1999) Role of duplex color Doppler ultrasound, computed tomography, and MR angiography in the diagnosis of septic puerperal ovarian vein thrombosis. Abdom Imaging 24(1):85–91
Kuligowska E, Deeds L 3rd, Lu K 3rd (2005) Pelvic pain: overlooked and underdiagnosed gynecologic conditions. Radiographics 25(1):3–20
Labs JD, Sarr MG, Fishman EK, Siegelman SS, Cameron JL (1988) Complications of acute diverticulitis of the colon: improved early diagnosis with computerized tomography. Am J Surg 155(2):331–336
Laghi A, Borrelli O, Paolantonio P, Dito L, Buena de Mesquita M, Falconieri P et al (2003) Contrast enhanced magnetic resonance imaging of the terminal ileum in children with Crohn's disease. Gut 52(3):393–397
Lee AR, Kim KH, Lee BH, Chin SY (1993) Massive edema of the ovary: imaging findings. AJR Am J Roentgenol 161(2):343–344
Lee EJ, Kwon HC, Joo HJ, Suh JH, Fleischer AC (1998) Diagnosis of ovarian torsion with color Doppler sonography: depiction of twisted vascular pedicle. J Ultrasound Med 17(2):83–89
Lopez AJ (2015) Female pelvic vein embolization: indications, techniques, and outcomes. Cardivasc Intervent Radiol 38(4):806–820
Machairiotis N, Stylianaki A, Kouroutou P, Sarli P, Alexiou NK, Efthymiou E et al (2016) Massive ovarian oedema: a misleading clinical entity. Diagn Pathol 11:18
Mathias SD, Kuppermann M, Liberman RF, Lipschutz RC, Steege JF (1996) Chronic pelvic pain: prevalence, health-related quality of life, and economic correlates. Obstet Gynecol 87(3):321–327
Moribata Y, Kido A, Yamaoka T, Mikami Y, Himoto Y, Kataoka M et al (2015) MR imaging findings of ovarian torsion correlate with pathological hemorrhagic infarction. J Obstet Gynaecol Res 41(9):1433–1439
Nishino M, Hayakawa K, Kawamata K, Iwasaku K, Takasu K (2002) MRI of early unruptured ectopic pregnancy: detection of gestational sac. J Comput Assist Tomogr 26(1):134–137
Nitta N, Takahashi M, Furukawa A, Murata K, Mori M, Fukushima M (2005) MR imaging of the normal appendix and acute appendicitis. J Magn Reson Imaging 21(2):156–165
Onur MR, Akpinar E, Karaosmanoglu AD, Isayev C, Karcaaltincaba M (2017) Diverticulitis: a comprehensive review with usual and unusual complications. Insights Imaging 8(1):19–27
Oto A, Ernst RD, Shah R, Koroglu M, Chaljub G, Gei AF et al (2005) Right-lower-quadrant pain and suspected appendicitis in pregnant women: evaluation with MR imaging—initial experience. Radiology 234(2):445–451
Park SJ, Lim JW, Ko YT, Lee DH, Yoon Y, Oh JH et al (2004) Diagnosis of pelvic congestion syndrome using transabdominal and transvaginal sonography. AJR Am J Roentgenol 182(3):683–688
Paulson EK, Kalady MF, Pappas TN (2003) Clinical practice. Suspected appendicitis. N Engl J Med 348(3):236–242
Pereira JM, Sirlin CB, Pinto PS, Jeffrey RB, Stella DL, Casola G (2004) Disproportionate fat stranding: a helpful CT sign in patients with acute abdominal pain. Radiographics 24(3):703–715

Pereira JM, Sirlin CB, Pinto PS, Casola G (2005) CT and MR imaging of extrahepatic fatty masses of the abdomen and pelvis: techniques, diagnosis, differential diagnosis, and pitfalls. Radiographics 25(1):69–85

Petkovska I, Duke E, Martin DR, Irani Z, Geffre CP, Cragun JM et al (2016) MRI of ovarian torsion: correlation of imaging features with the presence of perifollicular hemorrhage and ovarian viability. Eur J Radiol 85(11):2064–2071

Philpotts LE, Heiken JP, Westcott MA, Gore RM (1994) Colitis: use of CT findings in differential diagnosis. Radiology 190(2):445–449

Pickhardt PJ, Bhalla S (2005) Unusual nonneoplastic peritoneal and subperitoneal conditions: CT findings. Radiographics 25(3):719–730

Praveen R, Pallavi V, Rajashekar K, Usha A, Umadevi K, Bafna U (2013) A clinical update on massive ovarian oedema—a pseudotumour? Ecancermedicalscience 7:318

Protopapas AG, Diakomanolis ES, Milingos SD, Rodolakis AJ, Markaki SN, Vlachos GD et al (2004) Tubo-ovarian abscesses in postmenopausal women: gynecological malignancy until proven otherwise? Eur J Obstet Gynecol Reprod Biol 114(2):203–209

Quane LK, Kidney DD, Cohen AJ (1998) Unusual causes of ovarian vein thrombosis as revealed by CT and sonography. AJR Am J Roentgenol 171(2):487–490

Rao PM, Novelline RA (1999) Case 6: primary epiploic appendagitis. Radiology 210(1):145–148

Rao PM, Rhea JT, Novelline RA (1997) Sensitivity and specificity of the individual CT signs of appendicitis: experience with 200 helical appendiceal CT examinations. J Comput Assist Tomogr 21(5):686–692

Revzin MV, Mathur M, Dave HB, Macer ML, Spektor M (2016) Pelvic inflammatory disease: multimodality imaging approach with clinical-pathologic correlation. Radiographics 36(5):1579–1596

Rha SE, Byun JY, Jung SE, Jung JI, Choi BG, Kim BS et al (2002) CT and MR imaging features of adnexal torsion. Radiographics 22(2):283–294

Riley GM, Babcook C, Jain K (1996) Ruptured malignant ovarian tumor mimicking ruptured ectopic pregnancy. J Ultrasound Med 15(12):871–873

Roche O, Chavan N, Aquilina J, Rockall A (2012) Radiological appearances of gynaecological emergencies. Insights Imaging 3(3):265–275

Rollandi GA, Curone PF, Biscaldi E, Nardi F, Bonifacino E, Conzi R et al (1999) Spiral CT of the abdomen after distention of small bowel loops with transparent enema in patients with Crohn's disease. Abdom Imaging 24(6):544–549

Rottenstreich A (2016) Pregnancy and non-pregnancy related ovarian vein thrombosis: clinical course and outcome. Thromb Res 146:84–88

Rozenblit AM, Ricci ZJ, Tuvia J, Amis ES Jr (2001) Incompetent and dilated ovarian veins: a common CT finding in asymptomatic parous women. AJR Am J Roentgenol 176(1):119–122

Sam JW, Jacobs JE, Birnbaum BA (2002) Spectrum of CT findings in acute pyogenic pelvic inflammatory disease. Radiographics 22(6):1327–1334

Savader SJ, Otero RR, Savader BL (1988) Puerperal ovarian vein thrombosis: evaluation with CT, US, and MR imaging. Radiology 167(3):637–639

Sherard GB 3rd, Hodson CA, Williams HJ, Semer DA, Hadi HA, Tait DL (2003) Adnexal masses and pregnancy: a 12-year experience. Am J Obstet Gynecol 189(2):358–362; discussion 62–3

Tukeva TA, Aronen HJ, Karjalainen PT, Molander P, Paavonen T, Paavonen J (1999) MR imaging in pelvic inflammatory disease: comparison with laparoscopy and US. Radiology 210(1):209–216

Umeoka S, Koyama T, Togashi K, Kobayashi H, Akuta K (2004) Vascular dilatation in the pelvis: identification with CT and MR imaging. Radiographics 24(1):193–208

Ushakov FB, Elchalal U, Aceman PJ, Schenker JG (1997) Cervical pregnancy: past and future. Obstet Gynecol Surv 52(1):45–59

Williams DR, Coller JA, Corman ML, Nugent FW, Veidenheimer MC (1981) Anal complications in Crohn's disease. Dis Colon Rectum 24(1):22–24

Willmott F, Allouni KA, Rockall A (2012) Radiological manifestations of metastasis to the ovary. J Clin Pathol 65(7):585–590

Witlin AG, Mercer BM, Sibai BM (1996) Septic pelvic thrombophlebitis or refractory postpartum fever of undetermined etiology. J Matern Fetal Med 5(6):355–358

Wolverson MK, Crepps LF, Sundaram M, Heiberg E, Vas WG, Shields JB (1983) Hyperdensity of recent hemorrhage at body computed tomography: incidence and morphologic variation. Radiology 148(3):779–784

MRI of the Pelvic Floor

Rosemarie Forstner and Andreas Lienemann

Contents

R. Forstner (✉)
Universitätsinsitut für Radiologie Landeskliniken Salzburg, Paracelsus Medical University, Müllner Hauptstr., 48, Salzburg, Austria
e-mail: R.Forstner@salk.at

A. Lienemann
Radiologie Mühleninsel, Mühlenstrasse 4, Landshut 84028, Germany
e-mail: lienemann@muehleninsel.de

Abstract

Pelvic floor dysfunction comprises disorders related to pelvic floor descent and pelvic organ prolapse, urinary and fecal incontinence, defecation disorders, or pelvic pain. Although it may also occur in young age, typically postmenopausal women suffer from pelvic floor dysfunction that may significantly impair the quality of life. Its etiology is multifactorial, but female gender, increasing age and childbirths have been recognized as leading risk factors. MRI has emerged as an imaging technique to provide comprehensive information and has become an important diagnostic tool for treatment planning and for tailoring the surgical approach in pelvic floor pathologies.

This chapter reviews MRI for evaluation of the pelvic floor. The first part focuses on details of the examination technique, and provides information to assess qualitatively and quantitatively the pelvic floor. In the second part typical imaging findings associated with pathologies within the three anatomical compartments of the pelvic floor are covered. Finally, strengths and limitations of MRI of the pelvic floor will be discussed.

Med Radiol Diagn Imaging (2017)
DOI 10.1007/174_2017_53, © Springer International Publishing AG
Published Online: 19 April 2017

Abbreviations

MRI	Magnetic resonance imaging
PCL	Pubococcygeal line
POP	Pelvic organ prolapse
US	Ultrasonography
WI	Weighted images

1 Introduction

Pelvic floor dysfunction has become a major health care issue with the increasing ageing population. It is an umbrella term for different clinical disorders related to pelvic floor descent and pelvic organ prolapse, urinary and fecal incontinence, defecation disorders, or pelvic pain (Pannu et al. 2015). Pelvic floor dysfunction affects 30–50% of women, with approximately 10–20% of these becoming symptomatic and requiring surgery (Jundt et al. 2015). POP recurrence rates after surgery are high with a range between 30 and 70% (Tijdink et al. 2011). Although it may occur in young age, typically postmenopausal women suffer from pelvic floor dysfunction that may significantly impair the quality of life (Rogers and Fashokun 2016). Its etiology is multifactorial and associated with degradation of collagen, hormonal effects, obesity, multiparity, vaginal delivery, previous surgeries, constipation, muscle denervation, and menopause. But female gender, increasing age, and childbirths have been recognized as leading risk factors (Rogers and Fashokun 2016). Demographic developments in industrialized countries let expect the substantially increased need of imaging in patients with pelvic floor symptoms (Woodfield et al. 2010).

Among the imaging modalities MRI has emerged as an imaging technique to provide comprehensive information and has become an important diagnostic tool for treatment planning and for tailoring the surgical approach in pelvic floor pathologies (Pannu et al. 2015; El Sayed et al. 2016).

2 Imaging Techniques

Imaging modalities to assess the pelvic floor comprise conventional fluoroscopic techniques, ultrasonography, and MRI. Fluoroscopic X-ray techniques include cystourethrography, defecography or evacuation or voiding proctography, and colpocystoproctography. The latter requires opacification of multiple organs such as rectum, vagina, and small bowel and instillation of contrast media into the bladder via a urinary bladder catheter (Kim 2011). This widely available technique is performed in physiological sitting position, but is limited with respect of radiation exposure and inability to directly visualize the pelvic floor (Flusberg et al. 2011).

Various approaches including transabdominal, transvaginal, endoanal, transperineal, and translabial sonography have been used to assess urinary or fecal incontinence. Well-known advantages of this technique are short duration of exam, wide availability, and real-time imaging capabilities (Pannu et al. 2015). These, however, are outweighed by the small field of view, and its high operator dependence. Although its routine use is still limited, 3D and 4D US are emerging techniques to diagnose POP and are able to demonstrate pelvic musculature and fascias and otherwise difficult-to-assess mesh slings or implants (Dietz 2010). When performed by experts, good to excellent interobserver agreement can be achieved even in multicompartment ultrasound of the pelvic floor (Lone et al. 2016).

MRI has become the imaging method of choice to assess complex pelvic floor disorders, as it provides a comprehensive approach by combining static and dynamic MRI sequences (Maglinte et al. 2011). This technique has synonymously also been reported as dynamic MR, cine MR, MR defecography, MR proctography, or functional MR of the pelvic floor (Pannu et al. 2015; El Sayed et al. 2016). It was first introduced in 1991 by Yang et al. and Kruyt et al. They described movement of the bladder, vagina, and rectum in relation to the

pubococcygeal and symphysiosacral reference line in asymptomatic subjects and in patients. In 1993 Goodrich et al. recommended MRI for the pre- and postoperative evaluation of patients after pelvic floor surgery (Goodrich et al. 1993). Several consecutive publications showed at least equal results or its superiority compared to conventional colpocystoproctography and defecography (Gufler et al. 2004; Kelvin et al. 2000; Bump et al. 1996; Lienemann et al. 1996, 1997). Unfortunately for many years this technique showed inherent limitations in respect of standardization resulting in numerous variants of imaging techniques and protocols (El Sayed et al. 2016). A joint initiative of the ESUR and ESGAR pelvic floor working groups has overcome this problem and recommendations for the imaging technique and for reporting of pelvic floor disorders with MRI have been published in 2016 (El Sayed et al. 2016).

3 MRI Technique of the Pelvic Floor

3.1 Indications

Pelvic floor dysfunction may manifest with symptoms related specifically to affected structures, e.g., with urinary symptoms (stress and urge incontinence, or obstructed voiding), with defecatory symptoms (constipation, fecal incontinence, difficult or incomplete defecation), as pelvic pain or as adverse effects on sexual function (Rogers and Fashokun 2016). Among these bowel symptoms, those typically arising from the posterior pelvic compartment are leading indications for MRI (El Sayed et al. 2016). A specialist survey enlisted in order of decreasing frequency rectal outlet obstruction, rectocele, recurrent pelvic organ prolapse, enterocele, and dyssynergetic pelvic floor syndrome as clinical symptoms best suited to be assessed by MRI (El Sayed et al. 2016). In the postoperative setting MRI may assist to elucidate postoperative complications and the causes of failed POP repair by visualization of meshes, of relapsed POP, and of the integrity and movement of the pelvic floor muscles (Pannu et al. 2015; Alt et al. 2014).

3.2 Patient Preparation

An overextended bladder may impair the diagnosis of pelvic floor dysfunction. This is why according to the recent recommendations the bladder should be emptied 2 h before the exam, which will result in a midfull bladder during the exam (El Sayed et al. 2016). Cleansing of the rectum prior to the exam is helpful, but joint recommendations do not exist. Devices, e.g., pessar rings or intravaginal diaphragms, have to be removed before the exam.

3.3 Patient Instruction

Explaining the patient how to perform the required exercises is pivotal for a successful MRI study. Thus, optimally dedicated training for how to correctly perform the dynamic phases including straining, squeezing, and evacuation should precede the MR exam (El Sayed et al. 2016). As collaboration is pivotal, the patient has to be able to understand and follow the commands during the examination. Emptying of the rectum during the examination is required to assess the complex relationships in pelvic organ prolapse (Flusberg et al. 2011). This is why evacuation should be prolonged until complete defecation has been documented. Incomplete rectal evacuation results in a significantly lower sensitivity for the detection of pelvic floor defects by MRI compared to colpocystoproctography (Vanbeckevoort et al. 1999). If the patient is either too embarrassed to defecate inside the magnet or is unable to empty the rectum at all while lying supine, a triphasic approach may be performed with an additional post-toilet phase after the patient has evacuated in the bathroom (Kelvin et al. 2000).

3.4 Patient Positioning

In open-configuration MRI systems patients can be examined sitting on an MRI-compatible seat (Pannu et al. 2015; Lienemann et al. 1996). A physiological position for defecation cannot be achieved in close configuration systems where only horizontal positioning of the patient is feasible. In this case supine position is preferred to prone position, as it is more stable and convenient for the patient (Delemarre et al. 1994). Positioning with feed first will reduce claustrophobia. Furthermore, slight bending of the knees by a pillow underneath the knees and abduction of the hips will facilitate the process of defecation (Pannu et al. 2015; Bitti et al. 2014). Diapers and waterproof pads placed beneath the patient reliably prevent soiling of the table and help to improve the compliance (El Sayed et al. 2016; Lienemann et al. 1997; Healy et al. 1997a).

3.5 Organ Opacification

On T2-weighted imaging fluid-filled structures like the bladder or small bowel loops exhibit high signal intensity. But other organs like the vagina, rectum, or anal canal show an intermediate to low signal intensity. To improve their visualization and their differentiation from adjacent tissues during the dynamic phases vaginal and rectal opacification by ultrasound gel is performed (Lienemann et al. 1997; Sprenger et al. 2000). Some authors also advocated the placement of thin catheters to outline the urethra and to fill the bladder with 60 mL of saline solution and contrast media (Kelvin et al. 2000; Hodroff et al. 2002). But it is important to be aware that the catheter might impede the movement of the urethra and a rectocele or enterocele may be masked by a full bladder or a cystocele blocking the genital hiatus.

Emptying the bladder 2 h before the MRI will result in a midfull bladder. Lack of rectal contrast may result in a suboptimal study (Pannu et al. 2015). This is why rectum opacification is performed to improve visualization of the anorectal junction and to diagnose rectoceles. Instillation of 120–250 cm^3 of ultrasound gel improves also assessment of intususceptions and of rectal evacuation. A larger amount of gel is likely to facilitate the defecation (Lienemann et al. 1997). In the ESUR/ESGAR recommendations no agreement on opacification of the vagina was obtained (El Sayed et al. 2016). But opacification with 20 cm^3 of ultrasound gel allows visualization of the entire vagina and especially of the posterior fornix and its posterior vaginal wall (Lienemann et al. 1997). In addition, during Valsalva maneuver the gel in the vagina is emptied passively and thus the movement of the organ itself is not impeded (Hodroff et al. 2002).

3.6 Sequence Protocols

Technical prerequisites include mid- to high-field MR systems, surface array coils, and upright or supine position of the patient (Pannu et al. 2015; El Sayed et al. 2016; Fielding et al. 1998; Fielding 2003; Lienemann 1998). Pivotal in MR imaging of pelvic floor disorders is the acquisition of both static and dynamic imaging techniques. Static images provide multiplanar high spatial resolution of the pelvic floor anatomy, particularly the muscles and ligamentous structures (El Sayed et al. 2016; Lienemann et al. 1997; Delemarre et al. 1994). Integrity of the anal sphincter complex, position and morphology of the pelvic organs, and perivaginal space can also be assessed (Pannu et al. 2015; Fielding 2003). Furthermore, incidental findings (e.g., Bartholini, Gartner or ovarian cysts, or uterine leiomyomas) may be seen (Lienemann 1998).

Dynamic MRIs are performed at rest, squeezing, under maximal stress of the pelvic floor, and during defecation and displayed in cine mode (Fig. 1). Thus pelvic floor mobility, integrity of the pelvic floor or pelvic floor weakness, and organ prolapses are best visualized (El Sayed et al. 2016).

T2W imaging of the pelvic is performed at rest in three planes. This is followed by a dynamic acquisition in midsagittal plane at rest during squeezing, maximum straining, and evacuation of the rectal gel. Technical details of the MRI

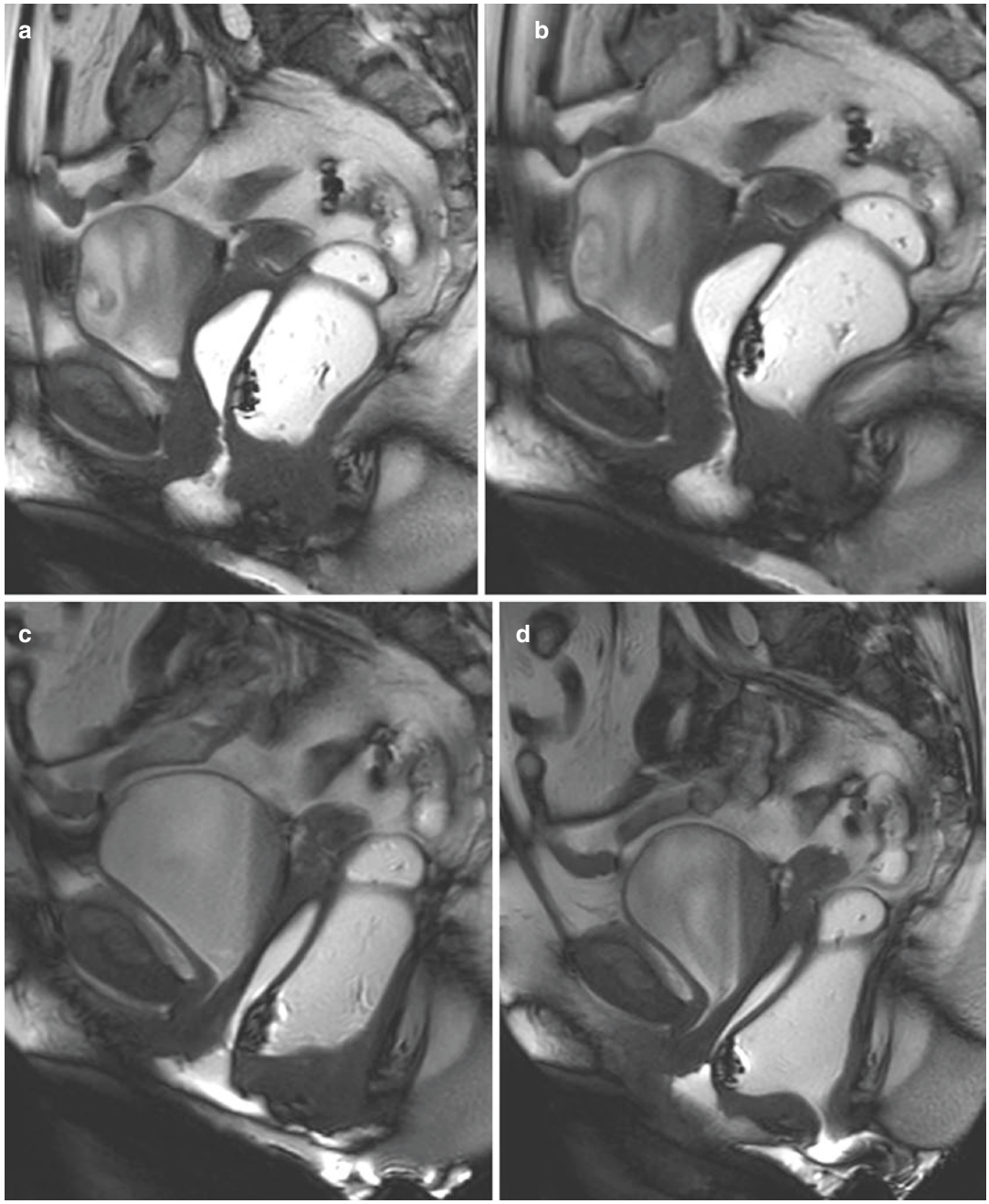

Fig. 1 Maneuvers of the dynamic series at rest (**a**), squeeze (**b**), straining (**c**), and defecation (**d**)

protocol as suggested by the ESUR/ESGAR recommendations are summarized in Table 1.

For the dynamic studies the midsagittal plane through the pelvis is the preferred slice orientation. It provides an excellent overview of all relevant organs within the different compartments of the pelvis and of the bony frame (Lienemann 1998) (Figs. 2, 3, and 4). This view is similar to conventional cystography or evacuation proctography. Owing to the complexity of the pelvic

Table 1 Recommended MR imaging protocol by ESUR/ESGAR

Plane		Sequence	Technique	TE(ms)	TR (ms)	mm	FOV (mm)	Matrix	Plane/angulation	Numbers of slices
Static MRI sequences 2D MRI										
	Sag.	T2WI	Turbo/fast spin echo	77–132	500–4210	4	200–300	256–448	Midsagittal	23
	Trans.	T2WI	Turbo/fast spin echo	88–132	500–7265	4	200–300	256–512	Perpendicular to urethra	25
	Cor.	T2WI	Turbo/fast spin echo	80–132	500–7265	4	200–260	256–512	Parallel to urethra	26
Dynamic MRI sequences										
Squeezing										
	Sag.	T2WI	GE[a]	1.27–1.88	3.3–397.4	8	250–310	126–280	Midsagittal	1 or 3
Straining										
	Sag.	T2WI	GE[a]	1.27–1.88	3.3–397.4	8	250–310	126–280	Midsagittal	1 or 3
Optional	Trans.	T2WI	GE[a]	1.6–80	5,0–1,200	5 or 6	250–310	126–280	Perpendicular to the urethra	5
Optional	Cor.	T2WI	GE[a]	1.6	5	5 or 6	300	256	Parallel to the urethra	5
MR-Defecography										
	Sag.	T2WI	GE[a]	1.27–1.88	3.3–397.4	8	250–310	168–280	Midsagittal	1 or 3
Optional	Cor.	T2WI	GE[a]	1.27–1.6	5–397	4 or 8	257–350	154–256	Parallel to anorectum	5

With permission from El Sayed et al. (2016)
[a]GE, ultrafast GE and balanced GE

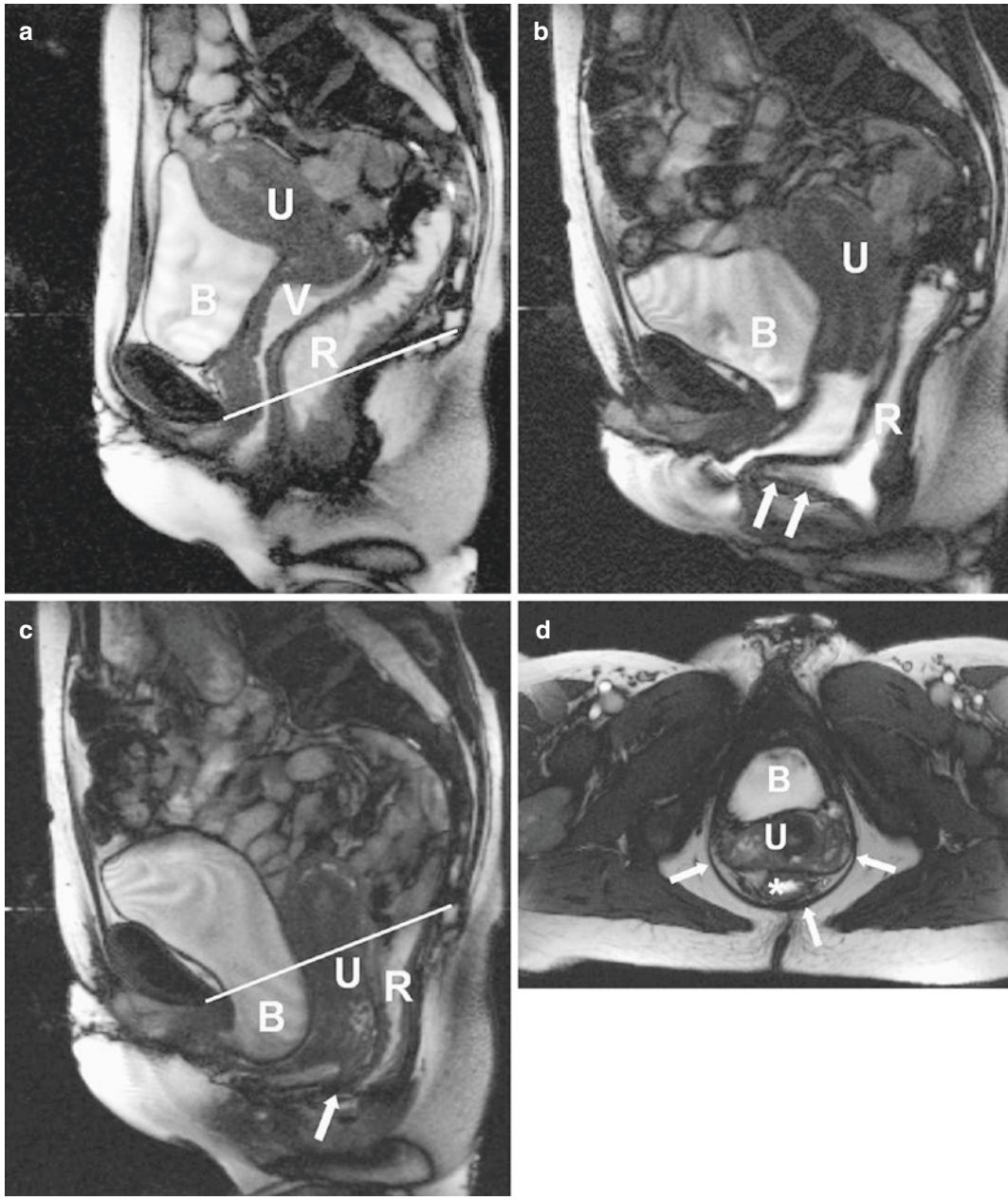

Fig. 2 Combined organ descent in a 40-year-old primiparous woman with stool outlet obstruction. T2-weighted functional MR images of the pelvis (**a–c** midsagittal; **d** transversal) obtained with the patient at rest (**a**) and during straining (**b–d**). (**a**) Normal position of the bladder (*B*), vagina (*V*), and uterus (*U*) above the pubococcygeal reference line (*white line*). The rectum (*R*) shows no anterior bulging. Vagina and rectum are filled with sonography gel. (**b**) During the first period of straining the anterior rectal wall is protruding in an anterior direction forming a deep rectocele (*arrows*). The bladder (*B*) and the uterus (*U*) descend only slightly. (**c**) After repeated straining and defecation now the rectum (*R*) and the rectocele (*arrow*) are emptied. Therefore, given more space to slide into the genital hiatus, a large cystocele (*B*) and a descensus of the uterus (*U*) far below the PC line occur causing a compression of the rectal lumen. Note the relaxed levator ani muscle with a nearly vertical orientation. (**d**) In the axial plane (level of the pubic symphysis) a ballooning of the levator ani muscle (*arrows*) resulting from muscular weakness can be seen. The descending bladder (*B*), lower parts of the uterus (*U*), and the rectum (*asterisk*) are located between the two sides of the puborectal muscle

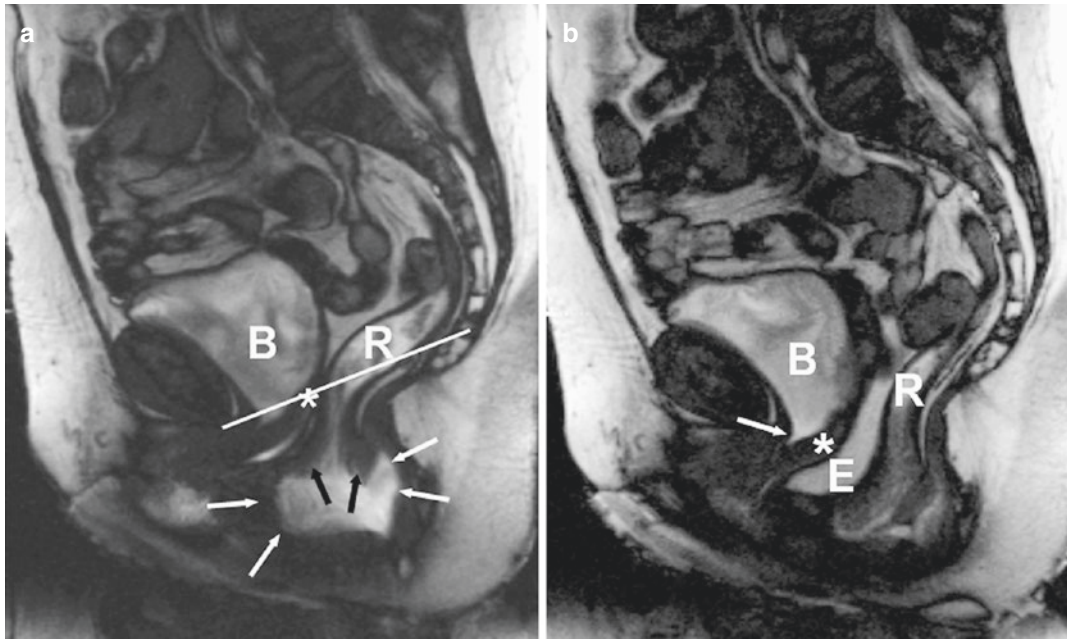

Fig. 3 Multiparous 71-year-old woman with defecation disorder. Midsagittal T2-weighted MR images of the pelvis obtained with the patient straining repeatedly. (**a**) During the first straining episode the well-gel-filled rectum (*R*) shows an extensive bulging of the rectal wall in the anterior-perineal as well as in the posterior direction (*white arrows*). This anterior and posterior rectocele stabilizes the position of both the bladder (*B*) and the vaginal vault (*asterisk*), which stay at the level of the PC line. Additionally, a thickening of the rectal mucosa (*black arrows*) is depicted marking a beginning intussusception. (**b**) After incomplete emptying of the rectocele and rectum (*R*) a large enterocele (*E*) has developed with mesenterial fatty tissue sliding down into the rectovaginal space. The sonography gel in the vagina has been evacuated passively. These findings are accompanied by a small cystocele with funneling of the urethra (*arrow*) and a vaginal vault descent (*asterisk*)

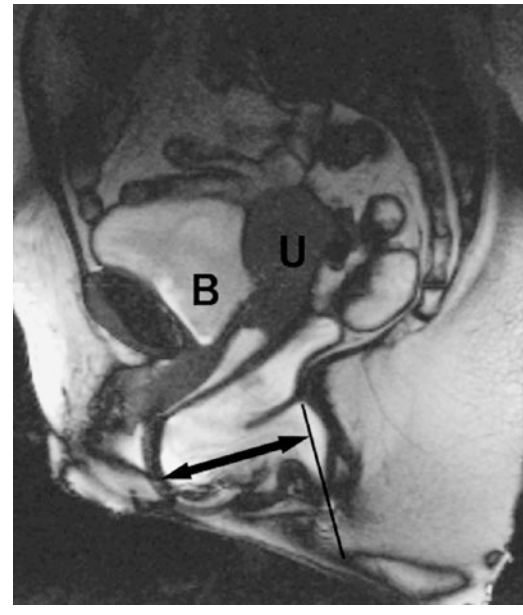

Fig. 4 A 69-year-old female with a partial prolapse of the posterior vaginal wall during clinical examination. Midsagittal T2-weighted MR images obtained with the patient straining. A huge bulging of the anterior rectal wall in an anterior direction occurs. The depth of the rectocele can be measured as the distance between the tip of the rectocele (*double arrow*) and a parallel line along the anal canal (*black line*). The bladder (*B*) and the uterus (*U*) descend only slightly

floor at least two additional slice orientations perpendicular to each other allow better depiction of pelvic floor abnormalities (Lienemann 1998). The ESUR guidelines advise angulated transaxial and coronal planes as optional (El Sayed et al. 2016) (Table 1).

4 MR Image Analysis

Image analysis should include the following aspects: bony pelvis, muscles and ligaments of the pelvic floor, and presence and degree of movement of organs and reference structures during evacuation. Static images provide detection and classification of structural abnormalities and dynamics are assessed to detect qualitatively and quantitatively assess the three compartments of the pelvic floor (El Sayed et al. 2016).

Measurements assist in quantifying the extent of pelvic floor organ prolapse and of pelvic floor relaxation. These MRI findings are optimally reported in a structured MRI report (El Sayed et al. 2016). Depending on the referring sites speciality-focused MRI reports may render more specific information according to urologic, urogynecologic, and proctologic focus (El Sayed et al. 2016; Macura et al. 2006).

4.1 Bony Pelvis

The bony pelvis and its inserting muscolofascial diaphragm, the pelvic floor are exposed to changing forces, which serve as inferior closure of the abdominal cavity and provides bladder and bowel control (Bitti et al. 2014). The pelvic bones as a surrounding frame protect and support the soft tissues and pelvic viscera (Retzky et al. 1996). A perpendicular relationship of the abdominal and pelvic cavity in a properly orientated bony pelvis, which directs the pressure towards the pubic symphysis and away from the pelvic floor, has been proposed (Retzky et al. 1996).

In MR pelvimetry a wider transverse inlet and a shorter obstetrical conjugate were associated with pelvic floor disorders (Handa et al. 2003). Incidental findings include Tarlov cysts, occult stress fractures of the sacral bone, or coccygodynia. In the latter, bone edema as well as a surrounding small rim of fluid can be seen (Maigne et al. 2012). Configuration and mobility of the coccygeal bone may vary. Bo et al. found a ventrocranial movement of 8.1 mm during contraction and a caudodorsal movement of 3.7 mm during straining, but there were no statistical difference between continent and incontinent women (Bo et al. 2001).

4.2 Pelvic Floor Muscles and Ligaments

The pelvic floor is composed of three layers: the endopelvic fascia which is too thin to be directly depicted on MRI, the pelvic floor muscles, and the perineal membrane which can be visualized at imaging as the perineal body, a connective soft-tissue condensation at the insertion of the perineal muscles, and external sphincter (Bitti et al. 2014).

The muscular pelvic floor including the components of the levator ani muscles does not represent a simple linear plate or hammock which is interconnected between the bony structures, but a complex 3D structure (Hjartardottir et al. 1997). Postprocessing with volume rendering techniques which are still a field of ongoing research assists in understanding the complexity of its anatomy and function (Bitti et al. 2014). Linear measurements on 2D MR images can vary considerably. In their study Hoyte et al. measured the anterior-posterior dimension of the levator hiatus using slightly rotated images (Hoyte and Ratiu 2001). Calculated and measured values differed and showed up to 15% variation. This may be explained as most cuts on MR images are not completely perpendicular to the muscle, and therefore oblique measurements will overestimate the muscular thickness (Bo et al. 2001). Positioning of the patient within the MR scanner may also impact on the measurements. It is highly recommended to position the patient on the coronal localizer with both acetabular bones at the same level. Tilting of the pelvis in the vertical axis during straining should also be avoided to prevent asymmetries (Bump et al. 1996). Interobserver accuracy has to be considered, especially in thin structures of only a few millimeters in size (Carr et al. 1996). In

the literature a variety of parameters concerning pelvic floor muscles have been analysed: width of the levator hiatus on axial on coronal and sagittal images, thickness of the iliococcygeal portion of the levator ani muscle on coronal and axial images, range of movement of the levator ani muscle on coronal images, urogenital hiatus on axial, as well as surface of the levator ani muscle assessed on coronal images (Woodfield et al. 2010; Hoyte and Ratiu 2001; Fielding 2002; Goh et al. 2000; Lienemann et al. 2000a; Pannu et al. 2000; Goodrich et al. 1993b; Hjartardottir et al. 1997b; Singh et al. 2002; Healy et al. 1997b). In addition, several different angles have been proposed: the levator-plate, levator-vaginal, and iliococcygeal angle (Goodrich et al. 1993; Hodroff et al. 2002; Goh et al. 2000; Healy et al. 1997b). The levator plate angle (LPA) is the angle between the posterior part of the levator ani muscle (iliococcygeal portion) as seen on the midsagittal image and the pubococcygeal reference line (PC line). In a similar way, the levator-vaginal angle is calculated by measuring the angle between the posterior portion of the levator ani plate and a line drawn through the horizontal axis of the upper third of the vagina (Singh et al. 2002). Another parameter to assess the orientation and slope of the iliococcygeal muscle is the angle between this muscle and the transverse plane of the pelvis on coronal images (Singh et al. 2002). However, measuring angles is challenging and limited by inter- and even intraobserver variability because of the often not completely even, but slightly curved, shape of the anatomical structures, e.g., the levator plate or the vaginal wall.

The shape of the various parts of the levator ani muscle reveals important additional information. Muscle defects with or without hernias are best seen on coronal images. A vertical orientation of the anococcygeal ligament on midsagittal images and a ballooning of the puborectal portion on axial images is indicative of pelvic floor weakness (Fig. 2c, d) (Bitti et al. 2014; Hoyte and Ratiu 2001). Normally the course of the anococcygeal ligament roughly parallels the PCL line at rest and during straining (Bitti et al. 2014).

Asymmetry or even complete loss of the right puborectal portion of the levator ani is a frequent finding in parous women after episiotomy. Intramuscular hematomas due to excessive straining or a thickened coccygeal portion in patients with levator ani syndrome or extensive scars due to previous surgery are other common findings.

Support to the pelvic floor is provided not only by the muscles, but also by ligaments and connective tissues (Bitti et al. 2014). Tears within these ligaments have been reported to be the cause of rectoceles or uterine/vaginal descent (Bitti et al. 2014; Bazot et al. 2011; El Sayed et al. 2008).

On MRI the rectovaginal septum, anococcygeal ligament, and sacrouterine ligaments can be clearly visualized. The first two structures are best seen on midsagittal images, whereas the sacrouterine ligaments can be delineated on coronal images or with oblique angulation (Bazot et al. 2011). The rectovaginal septum is seen between the posterior wall of the vagina and the anterior wall of the rectum, which are both of intermediate to low signal intensity. Separation of these two structures by a small rim of high signal intensity on T2-weighted images may just indicate a deep pouch of Douglas.

The connective tissues consist of fascias comprising the arcus tendinous levator ani and fascia pelvis (Bitti et al. 2014). It also wraps around the bladder, vagina, and uterus and suspends these organs to the pelvis (Bitti et al. 2014). The fascia itself is too thin to be visualized on imaging; however indirect signs of fascial defects have been described in MRI. Central to the understanding of fascial tears is the concept of the three levels of fascial support of the vagina: Level I consists of the posterior fornix and cervix, level II of the middle third of the vagina, and level III of the lower third of the vagina (Bitti et al. 2014; Huddleston et al. 1995). Imaging features of endofascial defects differ depending on the level involved. In *level I* defects due to loss of support of the vaginal apex by the uterosacral ligaments the upper vagina may appear flat or curved on a transaxial plane. This is typically found in multiparous women and usually caused by detachment from the ischial spine (Bitti et al. 2014). On MR imaging this facial defect is characterized by the chevron sign, a bilateral distortion of the upper vagina (Bitti et al. 2014).

In *level II* endofascial defects the normal H shape of the vagina is lost and due to loss of fascial suspension the bladder is displaced posteriorly and gives rise to the saddle bag sign (Bitti et al. 2014; Macura et al. 2006) (Fig. 5). Besides

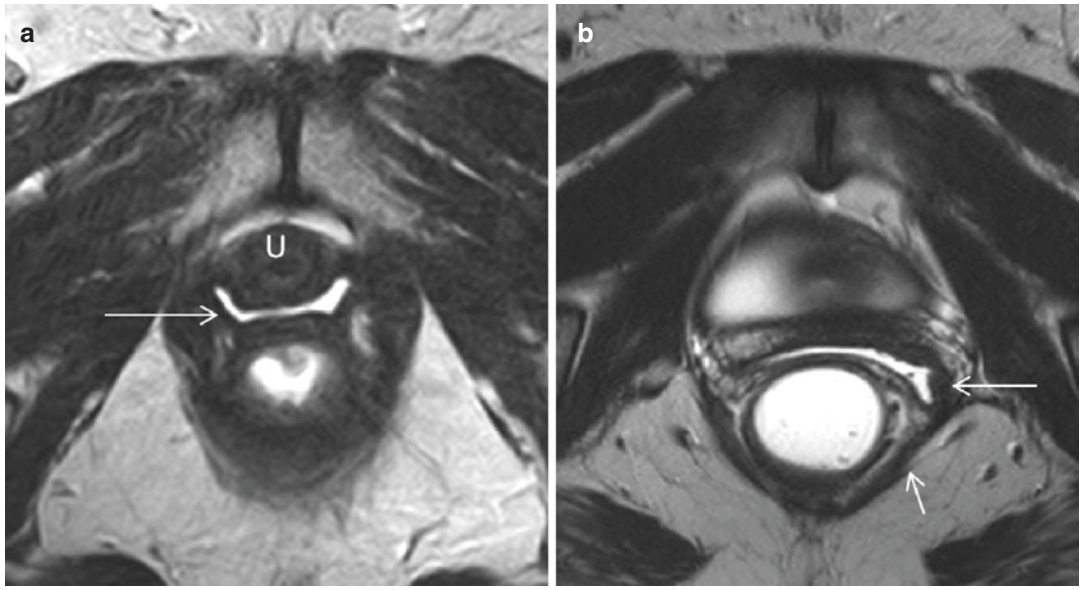

Fig. 5 Level II fascial defect. The normal H shape (*arrow*) of the vagina is seen in **a**. In contrast, in **b** displacement of the vagina and the saddle bag sign (*arrow*) is found. This finding supports the finding of level II fascial defects. Other findings: thinning and widening of the levator ani muscle (*short arrow*) in **b**

these lateral (paravaginal) defects central fascial defects at this level are postulated to predispose for enteroceles (Bitti et al. 2014).

Level III is defined by the lower vagina, perineal membrane, and urethral suspension ligaments. Disruption or complete absence of urethral suspension ligaments can lead to enlargement of the Retzius space between pubic bone and urethra, the drooping moustache sign (El Sayed et al. 2008).

4.3 Assessment of Pelvic Organ Mobility: Reference Lines

To evaluate the range of movement of the organs of the pelvic floor many reference lines have been published. On general consensus, the ideal reference line system should accomplish the following criteria: (1) mark the level of the levator ani muscle as the main supporting structure of the entire pelvic floor; (2) be independent of tilting of the pelvis by using two or more well-defined bony landmarks; (3) describe the range of organ movement in at least two different imaging planes; and (4) provide the possibility to compare findings on MR images with the results of the clinical examination and clinical classification systems. To date no single reference line or grading system meets all the above-mentioned criteria.

The most commonly used reference line is the pubococcygeal line (PC line) (Pannu et al. 2015; El Sayed et al. 2016; Yang et al. 1991b) (Figs. 2, 3, 4, and 6). This line is obtained on a midsagittal plane and connects the inferior aspect of the pubic symphysis to the last mobile coccygeal joint (Bertschinger et al. 2002). It is recommended by the ESUR as reference as it shows the lowest inter- and intraobserver variability (El Sayed et al. 2016). Three different variants of the PC line have been published in the literature. All PC lines are drawn on midsagittal images and start at the lower margin of the symphysis pubis. Apart from the above-described last coccygeal joint alternative second bony landmarks are either the first sacrococcygeal joint, or the point of insertion of the coccygeal portion of the levator ani (Vanbeckevoort et al. 1999; Healy et al. 1997a; Hjartardottir et al. 1997; Singh et al. 2001; Gufler et al. 1999).

The PCL serves as base for grading of POP. After defining the PCL the distance from each reference point within the three compartments is assessed perpendicularly to the PCL at

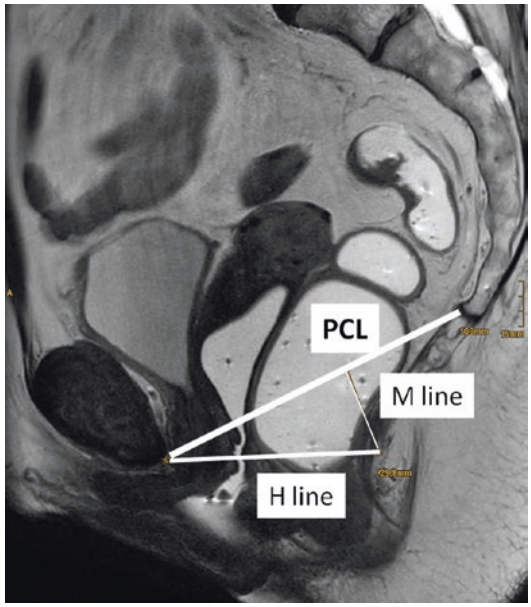

Fig. 6 H and M Lines to assess pelvic floor muscle insufficiency. *PCL* pubococcygeal line

rest and at maximum strain (El Sayed et al. 2016). Not only grading alone but also reporting the range of movement of the organs at rest and during straining are advised, as it provides more valuable information than grading alone (El Sayed et al. 2016).

The hiatus/muscle/organ (HMO) classification system is widely used to assess pelvic floor relaxation, which often coexists with POP but presents a different pathologic entity (Comiter et al. 1999). The reference lines in the HMO system are the H and M line (Fig. 6). The H line presents the length of the urogenital hiatus. It measures the distance between inferior symphysis pubis and puborectalis insertion. The M line is the perpendicular distance between the levator muscle plate and the PCL. Based on these reference lines pelvic relaxation is present in a symptomatic patient when the distance of the H line is >5 cm and the M line is >2 cm. A commonly used grading system is enlisted in Table 2 (El Sayed et al. 2016).

Numerous other reference lines of the pelvic floor have been published. The symphysiosacral line is obtained on midsagittal images between

Table 2 MR grading of pelvic floor descent

Grade	Length of M-Line (cm)
0 (normal)	<2
1 (mild)	2–4
2 (moderate)	4–6
3 (large)	>6

the superior border of the pubic bone and the distal sacral bone; the midpubic line extends through the longitudinal axis of the pubic bone (Lienemann 1998; Singh et al. 2002; Delemarre et al. 1994b). It represents approximately the level of the vaginal introitus and correlates with the clinical reference systems used in the quantification staging system of pelvic organ prolapsed (qPOP), where the hymen serves as a clinical reference (El Sayed et al. 2016; Bump et al. 1996; Singh et al. 2002).

4.4 Definition of Pathological Findings and Grading

Presence and extent of pelvic organ prolapse are analyzed in the cine mode display in the midsagittal plane by using points of reference for rest and during defecation. Optional display in a second plane allows detection of atypical rectoceles or enteroceles and facilitates the diagnosis of muscular defects (Lienemann 1998). Although the pelvic floor structures interact in a complex mode, abnormal descent and associated findings should be analyzed separately for each compartment. It is crucial to understand that complete emptying of the rectum maximizes detection of enteroceles and pelvic organ prolapse (Kelvin et al. 2000; Lienemann et al. 2000b).

Within the anterior compartment the bladder base or the most caudal part (mostly the dorsal wall) of the bladder is used as a landmark. In the middle compartment the anterior cervical lip or posterior fornix or after hysteroscopy the vaginal vault and in the posterior compartment the anorectal junction are used as references. Grading is then performed by measuring the perpendicular

distance of these structures in relationship to the reference PC line (El Sayed et al. 2016; Kelvin et al. 2000) (Table 3).

By definition an organ descent is diagnosed if one or all of these reference structures descend below the PL line. Therefore a cystocele or a uterine descent is diagnosed if these structures descend below the PC line. The grading is based upon the largest perpendicular distance to the PCL measured in cm and taken during maximum straining. (Pannu et al. 2015; Woodfield et al. 2010; Yang et al. 1991; vKruyt et al. 1991; Lienemann et al. 2000a). Grading systems unfortunately only poorly correlate with the clinical findings and symptoms (Pannu et al. 2015; Pizzoferrato et al. 2014). The recommended and most frequently used MRI grading system is enlisted in Table 3 (El Sayed et al. 2016; Kelvin et al. 2000).

Defects in the cul-de-sac include peritoneoceles, enteroceles, and sigmoideoceles (Fig. 7). Clinically these are difficult to assess as a posterior bulge may present one of the latter above or the rectum. The normal depth of the rectouterine pouch is about 5 cm (Kuhn and Hollyock 1982). A peritoneocele is defined as herniation of peritoneum through the rectovaginal septum and its extension beyond the upper third of the vagina (El Sayed et al. 2016; Kim 2011). In dynamic MRI a descent or widening of the pouch of Douglas below the PC line is considered to be pathological (El Sayed et al. 2016; Sprenger et al. 2000; Lienemann et al. 2000a, b). Small bowel loops and the sigmoid colon sliding down during straining constitute the diagnosis of an enterocele and sigmoidocele.

A rectocele presents mostly an anterior protrusion of the rectal wall. It is defined by the width of its outbulging beyond the expected anterior contour of the rectum (El Sayed et al. 2016). If its depth exceeds 2 cm the rectocele is considered pathological (El Sayed et al. 2016). Alternatively the distance from the anterior rectal wall to a reference line extending upwards from the anal canal has been used (Reiner et al. 2011). Of note, a considerable overlap between findings in normal volunteers and patients has been reported (Shorvon et al. 1989).

Table 3 MR grading of organ prolapse (cystoceles, uterine prolapse, enteroceles); modified from El Sayed et al. (2016)

0 (normal)	<1 cm
1 (small)	1–3 cm
2 (moderate)	3–6 cm
3 (severe)	>6 cm

5 Typical Findings

Traditionally the pelvic floor is divided into the three following compartments: (a) anterior with bladder and urethra, (b) middle with uterus and vagina, and (c) posterior containing the anorectum. However, functionally these are cooperating as units during defecation. Severity of symptom does not correlate well with the clinical grading of POP (Rogers and Fashokun 2016).

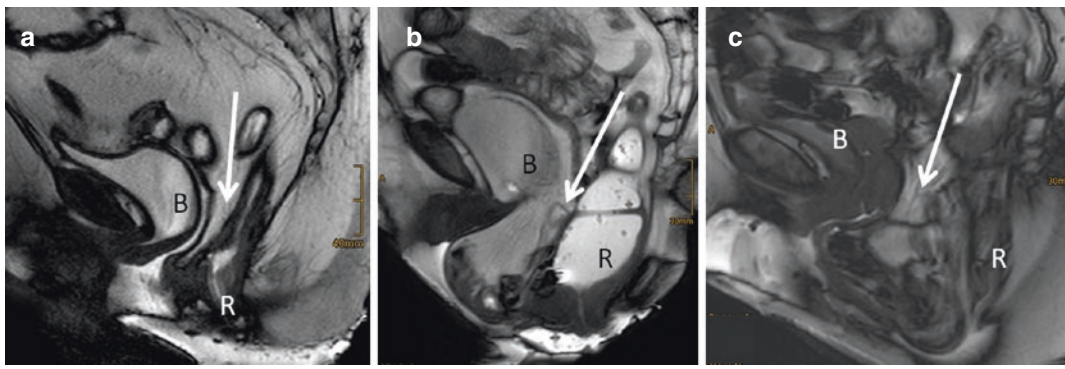

Fig. 7 Spectrum of enteroceles. Enteroceles (*arrow*) containing fat (**a**), small bowel (**b**), and sigmoid colon, small bowel and its mesentery. *R* rectum. In (**b**) a rectocele is displayed, in (**c**) a rectal prolapse

5.1 Anterior Compartment

The bladder as a fluid-filled structure is hyperintense on T2-weighted images. Depending on the degree of filling the shape of the bladder can vary considerably, ranging from a more triangular to a round contour (Fig. 2b vs. Fig. 4a). At rest it is situated superior-posterior to the pubic symphysis (Fig. 2a). On midsagittal images an area of fat-equivalent signal intensity is seen between the pubic bone and the bladder (retropubic space; space of Retzius) which extends to the umbilicus. Abundant fat in the Retzius space is a sign of defect of the urethral suspension ligaments and indicative of level III defects. In females the urethra is normally not well delineated on the midsagittal images, but its typical target-like appearance can be easily visualized on axial images. Surrounding structures like small bowel loops are only partly depicted in the midsagittal plane, but adhesions between the dome of the bladder and bowel loops occur quite often. They can be diagnosed as the bowel loops stay attached to the upper bladder wall and do not glide freely as supposed while the patient is straining.

The pelvic floor, urethra, and bladder are exposed to the increasing intra-abdominal pressure during Valsalva maneuver. Widening of the pelvic floor and descent of up to 2 cm is a physiological finding (Lienemann et al. 2000a). A cystocele is present if the bladder neck or any part of the posterior wall of the bladder moves >1 cm below the PC line (El Sayed et al. 2016) (Fig. 2c). Both the proximal urethra and the bladder neck descend and rotate around the pubic bone, initially moving posterior-inferior.

A nonspecific finding in patients with involuntary loss of urine is funneling of the proximal urethra (Fig. 3b). An additional kinking of the urethra at the urethrovesical junction can occur in large cystoceles. Furthermore, due to the limited space provided by the urogenital hiatus a large cystocele can block the prolapse of other pelvic structures and thus mask a rectocele or enterocele.

Recurrence of a cystocele after retropubic or vaginal surgeries for stress incontinence can be clearly detected by functional MRI. In these patients the proximal urethra and the bladder neck maintain their normal position superior to the symphysis, but the posterior wall of the bladder bulges into the anterior vaginal wall (Fig. 8).

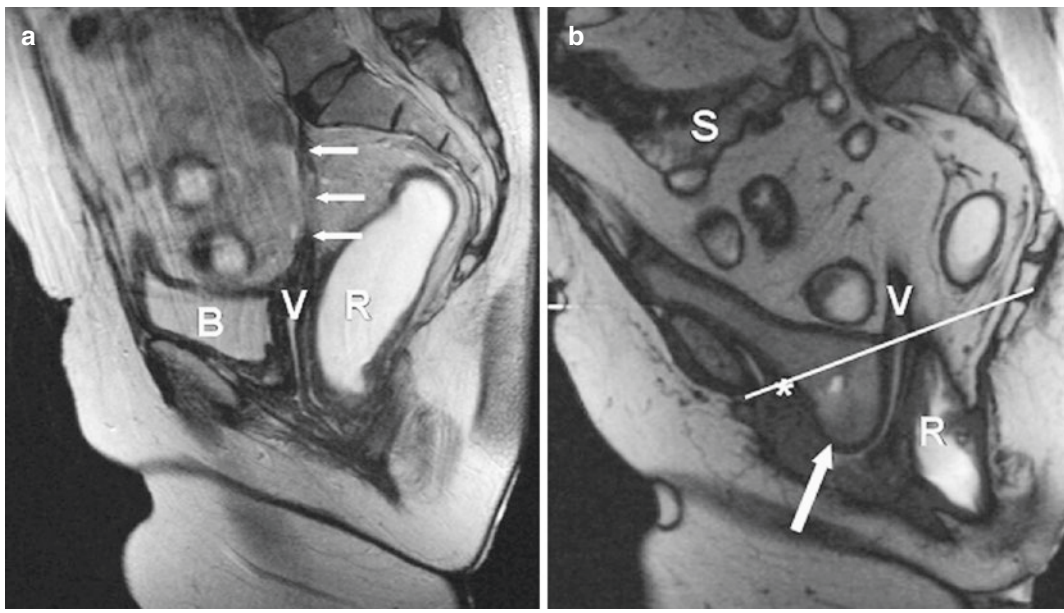

Fig. 8 A 67-year-old female patient after sacrocolpopexy with recurrence of a cystocele. Midsagittal static (**a**) and functional (**b**) T2-weighted MR images at rest (**a**) and during straining (**b**). (**a**) Static MR images demonstrate the synthetic material fixing the vaginal apex (*V*) to the promontory (*arrows*). *B* bladder, *R* rectum. (**b**) Typical findings after sacrocolpopexy are the normal position of the bladder neck (*asterisk*) in contrast to the descent of the posterior wall of the bladder (*arrow*) below the PC line (*white line*). The vagina (*V*) is kept in place by the intact foreign material. *R* rectum, *S* small bowel

Finally in previous procedures for urinary sling material or injections of bulk-enhancing agents such as collagen, all of which are normally hypointense on MR images, should be carefully analyzed (Alt et al. 2014; Carr et al. 1996).

5.2 Middle Compartment

In a normal anatomical setting the vagina, rectum, and posterior components of the levator ani muscle are seen in the same level (Fig. 2a). Therefore, the position of the vagina and uterus depends on the amount of filling of the rectal ampulla. If a vaginal or uterine descent is present, only after the rectum has been emptied both structures move ventrocaudally beyond the PC line (Fig. 2b, c). This is why the PC line itself might underestimate an organ descent in the middle compartment (Kelvin et al. 2000). The landmark to assess uterine prolapse is either the posterior fornix of the vagina or the cervix. In repeated, long-standing prolapse the vagina is often shortened and the vaginal wall may be thickened or even everted. In addition the pouch of Douglas is widened, thus facilitating the development of a peritoneocele or enterocele (Fig. 7). Elongated sacrouterine ligaments may be identified on coronal images. Defects of the endofascial fascia can only be assessed by indirect signs. However typical imaging findings as the drooping moustache sign or the saddleback sign even assist in allocating the level of defect (Bitti et al. 2014).

The pouch of Douglas normally represents the deepest peritoneal reflection within the intraabdominal cavity and predisposes for an internal hernia that have been reported in 18–37% (Rogers and Fashokun 2016). These may contain fat (peritoneocele), small bowel loops (enterocele), or sigmoid colon (sigmoidocele). The criterion to diagnose an enterocele is the descent of small bowel loops below the PC line (Kelvin et al. 2000; Lienemann et al. 2000b). The hernia follows the course of the posterior vagina along the rectovaginal septum and causes posterior vaginal wall bulging. Widening of the rectovaginal space or deepening of the pouch of Douglas below the PC line without bowel loops is defined as a peritoneocele. Occasionally the herniation can be lateral or anterior, in which case coronal images allow a correct assessment. Again a large enterocele can mask either a cystocele or a rectocele (Lienemann et al. 2000b). After sacrocolpopexy or uteropexy dynamic MRI is able to depict the foreign material and to demonstrate its intact function or course (Alt et al. 2014) (Fig. 8).

5.3 Posterior Compartment

The rectum behaves like a flexible and expansible tube. It can fold on itself with a lateral or an anterior displacement and kinking. Most often a bulging of the anterior rectal wall, a rectocele, is noted (Pannu et al. 2000). In MR defecography a rectocele with a depth of 4 cm is considered as a pathological finding (El Sayed et al. 2016; Yoshioka et al. 1991). MR grading of rectoceles is enlisted in Table 4 (El Sayed et al. 2016). Nevertheless it should be emphasized that there is a considerable overlap between healthy volunteers and women with pelvic prolapse (Shorvon et al. 1989). The direction of a rectocele is either anterior (to the distal segment of the posterior vaginal wall) (Fig. 2b), lateral (Fig. 9), or dorsal (Fig. 3a). It is pivotal to include in the report if the rectocele empties completely during defecation or if gel remains trapped within the rectocele. Lateral rectoceles may be missed in the midsagittal images but clearly become apparent in the coronal images (Fig. 9).

Intussusceptions present mucosal or mural rectal wall invaginations which can be located anteriorly or posteriorly or can affect the whole circumference (Kim 2011). They usually begin at 6–8 cm above the anal canal (Kim 2011). In imaging they present as a circumscribed thickening of rectal mucosa and wall (Fig. 3a). Small intususceptions during defecation present a common normal finding seen in nearly 80% of healthy

Table 4 MR grading of rectoceles; modified from El Sayed et al. (2016)

Grade	Width
0 (normal)	No
1 (small)	Outpouching
2 (moderate)	2–4 cm
3 (large)	>4 cm

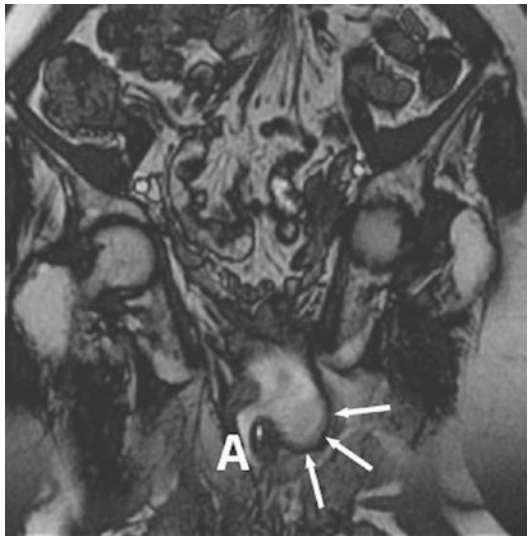

Fig. 9 A 74-year-old female with a history of aggravated and incomplete defecation. Coronal T2-weighted MR image during maximal straining. Large lateral rectocele (*arrows*) to the left side, detectable only in the coronal images, missed in the midsagittal and axial images. *A* anal canal

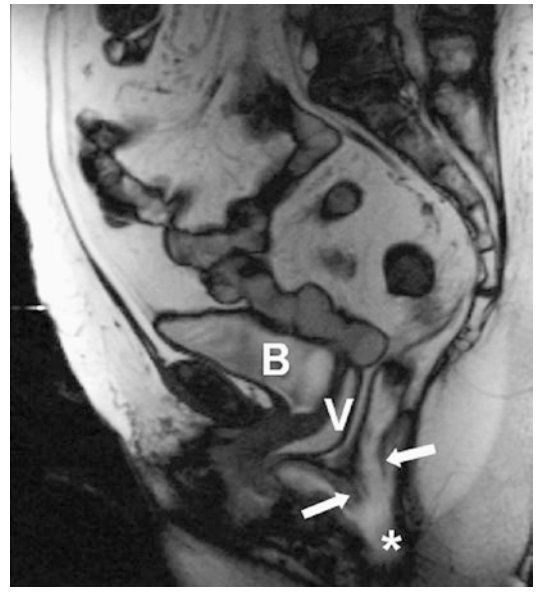

Fig. 10 A 66-year-old female with fecal incontinence. Midsagittal T2-weighted MR images obtained during defecation. The *arrows* mark an internal rectal prolapse with folding of the rectal mucosa and rectal wall in the direction of the opened anal canal (*asterisk*). Moderate descensus of the bladder (*B*) and vagina (*V*)

volunteers (El Sayed et al. 2016; Woodfield et al. 2009). The differentiation between an intussusception and an internal rectal prolapse is not clearly determined and the two terms are often overlapping. A more prominent internal rectal prolapse is often seen as a V-shaped or double rectal wall on the midsagittal image (Fig. 10). Extrarectal intussusception either mucosal or full thickness through the anal canal is defined as rectal prolapse (Mortele 2007). Organ descent of the anterior or middle compartment may lead to compression of the anterior rectal wall. This finding can promote an internal rectal prolapse and might account for a stool entrapment and stool outlet obstruction (Fig. 2c).

The cross point formed by a line along the posterior border of the rectum and the central anal canal is the anorectal junction (Flusberg et al. 2011). It serves as a landmark to define rectal descent. Inferior displacement of the anorectal junction in relation to the PC line is classified grade 1 in 3–5 cm, and grade 2 in displacement of >5 cm below this line (El Sayed et al. 2016; Goh et al. 2000; Halligan et al. 1996).

5.4 Levator Ani Muscle

On the midsagittal images the posterior aspect of the levator ani muscle is demonstrated. A ballooning of the levator muscle on axial images is typically found in patients with weakness of the pelvic floor muscles (Fig. 2d). In contrast, in normal volunteers the genital hiatus and puborectalis sling maintain the typical V-like shape under load (Sprenger et al. 2000). On axial images an asymmetric appearance of the puborectal part of the levator ani muscle can be seen after episiotomy.

During defecation an adequate relaxation of the puborectal sling with a resulting vertical orientation of the posterior levator ani and widening of the anorectal angle is visualized. If the levator ani muscle is still contracting during straining and even during defecation, this paradoxical finding is called dyssynergetic defecation, which can cause incomplete evacuation and stool outlet obstruction symptoms (Bolog and Weishaupt 2005).

Synonymous terms include anismus, dyskinetic puborectalis muscle, spastic pelvic floor syndrome, and pelvic floor synergia (Reiner et al. 2011). Delayed onset of defecation and atypical decrease of the anorectal angle (normal angle 90°–110° at rest) during straining are considered as typical imaging signs indicative of dyssynergetic evacuation. Other findings include impression of the puborectalis muscle or the anal sphincter in the posterior anorectal wall due to paradoxical sphincter contraction and lack of lowering of the pelvic floor during straining and defecation (Reiner et al. 2011). Reiner et al. reported findings of MR defecography in 48 patients suffering from chronic obstipation. Although impaired evacuation was seen in all of the 18 patients with dyssynergetic defecation, it rendered only low sensitivities and PPV. Half of these patients exhibited an abnormal anorectal angle and the majority (16/18 patients) demonstrated paradoxical sphincter contraction (Reiner et al. 2011). Associated findings were pelvic floor relaxation and pelvic organ prolapses. In the control group with obstipation a paradoxical sphincter contraction and abnormal anorectal angle were only rarely seen (Reiner et al. 2011). Prolonged evacuation time of 30 s or longer is typical for this condition and has been reported to yield PPV of 90% (Halligan et al. 2001).

6 MRI of the Pelvic Floor in Asymptomatic Females

Considerable overlap in normal and asymptomatic patients is an evident problem in assessing pelvic floor disorders. Findings often correlate poorly between clinical exam and imaging studies, as well as clinical symptoms of pelvic floor dysfunction (Pannu et al. 2015; Rogers and Fashokun 2016; Pizzoferrato et al. 2014). Particularly stage I prolapses of the anterior and posterior vaginal wall are so common in asymptomatic females that they may be considered within the range of normal findings (Mann 2014). There is still a debate on the definition of a clinically relevant prolapse (Mann 2014). Based on expert panel consensus relevant pelvic organ prolapse as ICS-quantified POP (qPOP) stage II or greater is considered abnormal (Kenton and Mueller 2006). However, larger series showed that approximately half of normal patients even met these criteria. Swift et al. reported almost 50% out of 497 women undergoing routine gynecologic assessment to have POP of at least stage II. This was confirmed in a larger multicenter study of clinically asymptomatic females, where qPOP stages in the following distribution were reported: stage 0 in 24%, stage I in 38%, stage III in 35%, and stage III in 2% (Swift 2000; Swift et al. 2005). Although most studies include asymptomatic volunteers as a control group only few data are published exclusively defining the normal range of findings in asymptomatic individuals (Goh et al. 2000). Goh et al. examined 25 men and 25 women on a 1.0-T system in supine position with the volunteers at rest and during straining. All volunteers had to pass a detailed questionnaire. They measured the descent of the bladder base, cervix, and anorectal junction in relation to the PC line and calculated the pelvic floor hiatus area and perimeter as well as the anorectal angle and the levator plate angle (Goh et al. 2000). Lienemann et al. studied 20 nulliparous females with normal clinical examination and urodynamics (Lienemann et al. 2000a). MRI was performed in the supine position with opacification of vagina and rectum with ultrasound gel. Among the large number (29) of pelvic parameters analyzed, the physiologic position of the bladder base, posterior vaginal fornix, and anorectal junction in relation to the PC line and the normal width of the hiatus were defined. In their study the normal pelvic organs did not descent below the PCL. It is accepted that a rectocele of 2 cm and the descent of bladder base of 1 cm are within the normal range of findings during straining. The normal width of the levator hiatus was 4.7 cm at rest and 5.3 cm under pressure. Schreyer et al. also assessed ten asymptomatic nulliparous females (median 31 years) to define the normal range of organ movement at pelvic floor maneuvers (Schreyer et al. 2012). Using the pubococcygeal line as reference during straining the

anorectal junction moved about 2.5 cm, the bladder base moved 1.5 cm, and the uterovaginal junction showed a relative movement of 3.5 cm (Schreyer et al. 2012). The anorectal angle widened from approximately 93° to 110° with a relative change of 15° (Lienemann et al. 2000a).

7 Value of MRI Versus Conventional Techniques

In the last decade MRI has become an important examination technique to assess complex pelvic floor disorders. Its evident advantage is comprehensive diagnostic information not only in respect of pelvic organ prolapse, but also of muscular floor weakness and associated muscular or fascial defects. It also provides functional information of the pelvic floor in patients suffering from chronic constipation (Pannu et al. 2015; El Sayed et al. 2016; Reiner et al. 2011). Findings assist in treatment stratification in multidisciplinary patient management and may impact on treatment including both urogynecologic and colorectal surgery techniques (El Sayed et al. 2016; Elshazly et al. 2010).

Imaging complements the physical exam that allows diagnosis of POP only by indirect signs and imaging may also reveal findings that are clinical occult but may be relevant for treatment planning (El Sayed et al. 2016; Comiter et al. 1999). Particularly differentiation of high rectoceles from enteroceles, and differentiation of the contents of enteroceles, is clinically important, as it will influence the type of surgery. However, due to the broad overlap of physiological and abnormal findings in patients with pelvic floor dysfunction imaging studies have to be interpreted in the context with the patient's history, the clinical gynecological assessment, and other diagnostic studies, e.g., anorectal manometry, endosonography, or cystomanometry (Pannu et al. 2015; Law and Fielding 2008; Faccioli et al. 2010).

Colpocystoproctography combining voiding cystography, vaginal opacification, and defecography is regarded as the gold standard to assess pelvic organ prolapse. According to the ACR appropriateness criteria both colpocystoproctography and MR defecography with rectal filling are rated with highest appropriateness to assess suspected pelvic organ prolapse (Pannu et al. 2015; Yang et al. 1991c; Faccioli et al. 2010). This X-ray technique is widely available, allows fluoroscopic information but is limited by considerable radiation exposure (Pannu et al. 2015; Goei and Kemerink 1990). In terms of patient comfort a survey in 60 patients undergoing both colpocystoproctography and MRI demonstrated that 90.7% of these women prefer MRI to fluoroscopy, thus yielding a high rate of acceptance (Sprenger et al. 2000).

Several studies compared MRI of the pelvic floor with conventional X-ray techniques. The majority of these studies concluded that functional MRI is at least equal to conventional fluoroscopic methods and can be superior in some aspects. An early study compared defecography and MRI of the pelvic floor in qualitative grading and measurements of anterior rectoceles in 14 patients. They stated that the potential of MRI regarding anterior rectoceles seems absent (Delemarre et al. 1994b). Limitations of this early study were the prone position of the patient and lack of rectal opacification. Lienemann et al. who had already used the recently recommended MRI technique favored dynamic MRI (Lienemann et al. 1997). In 5 asymptomatic volunteers and 44 female patients MRI was either identical (21 cases) or superior (18 cases) to dynamic fluoroscopy. In this study MRI of the pelvic floor was particularly helpful in the depiction of pathologies within the middle compartment and in revealing changes in the dominant type of prolapse (Healy et al. 1997c). They found a significant correlation of standard measurements of the anorectal configuration using MRI and evacuation proctography in women with constipation. In addition, functional MRI was able to show significant changes of muscular parameters in women with otherwise normal proctograms. In comparison to bead-chain cystourethrography/colpocystorectography MRI correctly diagnosed the degree of bladder descent with a coefficient of determination of 0.81 and 0.85 in 32 women

with urinary incontinence or organ prolapse (Gufler et al. 1999b). Cystourethrography alone missed all rectoceles, which were correctly depicted by colpocystorectography and MRI, whereas enteroceles could only be diagnosed by MRI. Comparing colpocystorectography in the upright and supine position with functional MRI no significant difference between MRI and colpocystorectography in either positions was found (Gufler et al. 1999b). Kelvin et al. compared cystocolpoproctography with opacification of all relevant organs to functional MRI in the supine position with opacification of the bladder, vagina, and rectum and added also a post-toilet phase (Kelvin et al. 2000). They conclude that MR imaging and cystocolpoproctography showed similar detection rates for prolapse of pelvic organs but emphasized the strength of MRI as revealing all pelvic organs and pelvic floor musculature. In the ACR recommendations, if available upright MRI is favored over supine position (Pannu et al. 2015). Some studies using a midfield system of 0.5 T with an open magnet configuration are published (Kim 2011; Lone et al. 2016; Lienemann et al. 1997; Sprenger et al. 2000). The latter offers the advantage of evaluating the patient in an upright position, but were limited by a reduced imaging quality due to the surface coil design and limited spatial and temporal resolution. Bertschinger et al. showed that MRI in sitting position was not superior to supine MRI in depiction of clinically relevant bladder prolapse or rectoceles (Bertschinger et al. 2002). Similarly Fielding et al. reported a higher degree of pelvic floor laxity for sitting position that was not superior to supine MRI (Fielding et al. 1998). A recent study compared MRI in supine versus sitting position using a 0.25 T open configuration and 1.5 T MRI unit in 31 (27 females) patients (van Iersel et al. 2017). At rest and defecation no significant difference of the anorectal junction and no significant difference in percentages of cystoceles were found. However, a statistical difference was documented in comparing the grade of descent. These authors conclude that MRI may overestimate the descent due to the more cranial position of the pelvic organs in supine position at rest (van Iersel et al. 2017).

The data on MRI to assess intususceptions are conflicting. Compared with conventional techniques MRI tends to underestimate intussusception which may be due to nonphysiological supine position, but global information of the pelvic floor can be rendered (Pannu et al. 2015; van Iersel et al. 2017). A recent study assessing 41 patients reported superiority of conventional defecography for diagnosing rectoceles and enteroceles, but found MRI more effective for identifying intussusceptions (van Iersel et al. 2017). Advantages of MRI in assessing rectal intussusception include differentiation of mucosal from full-thickness involvement, functional information of pelvic floor movement, and depiction of coexisting pathologies (Mortele 2007). Similarly in suspected dyssynergetic pelvic floor syndrome the value of MRI is rendering comprehensive information. It visualizes the typical features of abnormal defecation and also aids in elucidating other causes of pelvic outlet obstruction (Reiner et al. 2011; Mortele 2007; Bolog and Weishaupt 2005).

References

Alt CD, Brocker KA, Lenz F, Sohn C, Kauczor HU, Hallscheidt P (2014) MRI findings before and after prolapse surgery. Acta Radiol 55:495–504

Bazot M, Gasner A, Ballester M, Daraï E (2011) Value of thin-section oblique axial T2-weighted magnetic resonance images to assess uterosacral ligament endometriosis. Hum Reprod 26:346–5350

Bertschinger KM, Hetzer FH, Roos JE et al (2002) Dynamic MR imaging of the pelvic floor performed with patient sitting in an open-magnet unit versus with patient supine in a closed-magnet unit. Radiology 223:501–508

Bitti GT, Argiolas GM, Ballicu N, Caddeo E et al (2014) Pelvic floor failure: MR imaing evaluation of anatomic and functional abnormalities. Radiographics 34:429–448

Bo K, Lilleas F, Talseth T et al (2001) Dynamic MRI of the pelvic floor muscles in an upright sitting position. NeurourolUrodyn 20:167–174

Bolog N, Weishaupt D (2005) Dynamic MR imaging of putlet obstruction. Clin Imaging 14:293–302

Bump RC, Mattiasson A, Bo K et al (1996) The standardization of terminology of female pelvic organ prolapse and pelvic floor dysfunction. Am J Obstet Gynecol 175:10–17

Carr LK, Herschorn S, Leonhardt C (1996) Magnetic resonance imaging after intraurethral collagen injected for stress urinary incontinence. J Urol 155:1253–1255

Comiter CV, Vasavada SP, Barbaric ZL et al (1999) Grading pelvic prolapse and pelvic floor relaxation using dynamic magnetic resonance imaging. Urology 54:454–454

Delemarre JB, Kruyt RH, Doornbos J et al (1994) Anterior rectocele: assessment with radiographic defecography, dynamic magnetic resonance imaging, and physical examination. Dis Colon Rectum 37:249–259

Dietz HP (2010) Pelvic floor ultrasound: a review. Am J Obstet Gynecol 202:321–334

El Sayed R, MSE FMMM, Azim MSA (2008) Pelvic floor dysfunction: assessment with combined analysis of static and dynamic MR imagin g findings. Radiology 248:518–530

El Sayed RF, Alt CD, Maccioni F et al (2016) Magnetic Resonance Imaging of pelvic floor dysfunction-joint recommendations of the ESUR and ESGAR pelvic floorworkinggroup.EurRadiol.doi:10.1007/s00330-016-4471-

Elshazly WG, Nekady AEE, Hassan H (2010) Role of dynamic MRI in management of obstructed defecation case series. Int J Surg 8:2074–2282

Faccioli N, Comai A, Mainardi P, Perandini S, Farah M, Pozzi-Mucelli R (2010) Defecography: a practical approach. Diagn Interv Radiol 16:209–216

Fielding JR (2002) Practical MR imaging of female pelvic floor weakness. Radiographics 22:295–304

Fielding JR (2003) MR imaging of pelvic floor relaxation. Radiol Clin North Am 41:747–756

Fielding JR, Griffiths DJ, Versi E et al (1998) MR imaging of pelvic floor continence mechanisms in the supine and sitting positions. AJR Am J Roentgenol 171:1607–1610

Flusberg M, Sahni VA, Erturk SM, Mortele KJ (2011) Dynamic MR defecography: assessment of the usefulness of the defecation phase. AJR Am J Roentgenol 196:W394–W399

Goei R, Kemerink G (1990) Radiation dose in defecography. Radiology 176:137–139

Goh V, Halligan S, Kaplan G et al (2000) Dynamic MR imaging of the pelvic floor in asymptomatic subjects. AJR Am J Roentgenol 174:661–666

Goodrich MA, Webb MJ, King BF et al (1993) Magnetic resonance imaging of pelvic floor relaxation: dynamic analysis and evaluation of patients before and after surgical repair. Obstet Gynecol 82:883–891

Gufler H, Laubenberger J, DeGregorio G et al (1999) Pelvic floor descent: dynamic MR imaging using a half-Fourier RARE sequence. J Magn Reson Imaging 9:378–383

Gufler H, Ohde A, Grau G et al (2004) Colpocystoproctography in the upright and supine positions correlated with dynamic MRI of the pelvic floor. Eur J Radiol 51:41–47

Halligan S, Bartram C, Hall C, Wingate J (1996) Enterocele revealed by simultaneous evacuation proctography and peritoneography: does "defecation block" exist? Am J Roentgenol 167:461–466

Halligan S, Malouf A, Batram CI, Marshall M, Hollings N, Kamm MA (2001) Predictive value of impaired evacuation at proctopgraphy in diagnosing anismus. AJR Am J Roentgenol 177:633–636

Handa V, Pannu H, Siddique S et al (2003) Architectural differences in the bony pelvis of women with and without pelvic floor disorders. Obstet Gynecol 102:1283–1290

Healy JC, Halligan S, Reznek RH et al (1997a) Dynamic MR imaging compared with evacuation proctography when evaluating anorectal configuration and pelvic floor movement. AJR Am J Roentgenol 169:775–779

Healy JC, Halligan S, Reznek RH et al (1997b) Magnetic resonance imaging of the pelvic floor in patients with obstructed defaecation. Br J Surg 84:1555–1558

Hjartardottir S, Nilsson J, Petersen C et al (1997) The female pelvic floor: a dome – not a basin. Acta Obstet Gynecol Scand 76:567–571

Hodroff MA, Stolpen AH, Denson MA et al (2002) Dynamic magnetic resonance imaging of the female pelvis: the relationship with the pelvic organ prolapse quantification staging system. J Urol 167:1353–1355

Hoyte L, Ratiu P (2001) Linear measurements in 2-dimensional pelvic floor imaging: the impact of slice tilt angles on measurement reproducibility. Am J Obstet Gynecol 185:537–544

Huddleston HT, Dunnihoo DR, Huddleston PM 3rd et al (1995) Magnetic resonance imaging of defects in DeLancey's vaginal support levels I, II, and III. Am J Obstet Gynecol 172:1778–1782; discussion 1782–1784

van Iersel JJ, Formijne Jonkers HA, Verheijen PM, Broeders IAMJ, Heggelman BG et al (2017) Comparison of dynamic magnetic resonance defaecography with rectal contrast and conventional defaecography for posterior pelvic floor compartment prolapse. Colorectal Dis 19:O46–O53. doi:10.1111/codi.13563

Jundt K, Peschers U, Kentenich H (2015) The investigation and treatment of female pelvic floor dysfunction. Dtsch Arztebl Int 112:564–574

Kelvin FM, Maglinte DD, Hale DS et al (2000) Female pelvic organ prolapse: a comparison of triphasic dynamic MR imaging and triphasic fluoroscopic cystocolpoproctography. AJR Am J Roentgenol 174:81–88

Kenton K, Mueller ER (2006) The global burden of female pelvic flor disorders. BJU Int 98(Suppl 1):1–5

Kim AY (2011) How to interpret a functional or motility test-defecography. J Neurogastroenterol Motil 17:416–420

vKruyt RH, Delemarre JB, Doornbos J et al (1991) Normal anorectum: dynamic MR imaging anatomy. Radiology 179:159–163

Kuhn RJ, Hollyock VE (1982) Observations on the anatomy of the rectovaginal pouch and septum. Obstet Gynecol 59:445–447

Law YM, Fielding JR (2008) MRI of pelvic floor dysfunction: review. AJR Am J Roentgenol 191:S45–S53

Lienemann A (1998) An easy approach to functional magnetic resonance imaging of pelvic floor disorders. Tech Coloproctol 2:131–134

Lienemann A, Anthuber C, Baron A et al (1996) MR colpocystorectography: a new dynamic method for assessing pelvic floor descent and prolapse in women. Acta Radiol 6:182–186

Lienemann A, Anthuber C, Baron A et al (1997) Dynamic MR colpocystorectography assessing pelvic-floor descent. Eur Radiol 7:1309–1317

Lienemann A, Sprenger D, Janssen U et al (2000a) Functional MRI of the pelvic floor. The methods and reference values. Radiologe 40:458–464

Lienemann A, Anthuber C, Baron A et al (2000b) Diagnosing enteroceles using dynamic magnetic resonance imaging. Dis Colon Rectum 43:205–212; discussion 212–213

Lone F, Sultan AH, Stankiewicz A, Thakar R (2016) Interobserver agreement of multicompartment ultrasound in the assessment of pelvic floor anatomy. Br J Radiol. doi:10.1259/bjr.20150704. Epub 2016 Jan 22

Macura KJ, Genadry RR, Bluemeke DA (2006) MR imaging of the female urethra and supporting ligaments in assessment of urinary incontinence: spectrum of abnormalities. Radiographics 26:1135–1149

Maglinte DD, Bartram CI, Hale DA, Park J, Kohli MD, Robb BW, Romano S, Lappas JC (2011) Functional imaging of the pelvic floor. Radiology 258:23–39

Maigne JY, Pigeau I, Roger B (2012) Magnetic resonance imaging findings in the painful adult coccyx. Eur Spine J 21:2097–2104

Mann DKP (2014) What is clinically relevant prolapse? An attempt at defining cutoffs for the assessment of pelvcic organ prolapse. Int Urogynecol 25:451–455

Mortele KJ (2007) Dynamic MR defecography of the posterior compartment: indications, techniques and MR features. Eur J Radiol 61(2007):462–472

Pannu HK, Kaufman HS, Cundiff GW et al (2000) Dynamic MR imaging of pelvic organ prolapse: spectrum of abnormalities. Radiographics 20:1567–1582

Pannu HC, Glanc P, Bhosale PR, Harisinghani MG et al (2015) ACR appropriateness criteris pelvic floor dysfunction. J Am Coll Radiol 12:134–142

Pizzoferrato AC, Nyangoh Timoh K, Fritel X, Zareski E (2014) Dynamic Magnetic Resonance Imaging and pelvic floor disorders: how and when? Eur J Obstet Gynecol Reprod Biol 181:259–266

Reiner CS, Tutuian R, Pohl D, Marincek B, Weishaupt D (2011) MR defecography in patients with dysynergetic defecation:spectrum of imaing findings and diagnstic value. Br J Radiol 84:136–144

Retzky SS, Rogers jr RM, Richardson AC (1996) Anatomy of female pelvic support. In: Brubaker LT, Saclarides TJ (eds) The female pelvic floor disorders of function and support. F.A. Davis Company, Philadelphia, pp 3–21

Rogers RG, Fashokun TB (2016) Pelvic organ prolapse in women: an overview of the epidemiology, risk factors, clinical manifestations, and management. www.uptodate.com

Schreyer CA, Paetzel C, Fürst A et al (2012) Dynamic MR defecography in 10 asymptomatic volunteers. World J Gastroenterol 18:6836–6842

Shorvon PJ, McHugh S, Diamant NE et al (1989) Defecography in normal volunteers: results and implications. Gut 30:1737–1717

Singh K, Reid WM, Berger LA (2001) Assessment and grading of pelvic organ prolapsed by use of dynamic resonance imaging. Am J Obstet Gynecol 185:71–77

Singh K, Reid WM, Berger LA (2002) Magnetic resonance imaging of normal levator ani anatomy and function. Obstet Gynecol 99:433–438

Sprenger D, Lienemann A, Anthuber C et al (2000) Functional MRI of the pelvic floor: its normal anatomy and pathological findings. Radiologe 40:451–457

Swift SE (2000) The distribution of pelvicorgan support in a population of femalesubjects seen for routine gynecologichealth care. Am J Obstet Gynecol 183:277–285

Swift S, Woodman P, O'Boyle A et al (2005) Pelvic Organ Support Study (POSST): the distribution, clinical definition, and epidemiologic condition of pelvic organ support defects. Am J Obstet Gynecol 192:795–806

Tijdink MM, Vierhout ME, Heesakkers JP, Withagen MI (2011) Surgical management of mesh related complications after prior pelvic floor reconstructive surgery with mesh. Int Urogynecol J 22:1395–1404

Vanbeckevoort D, Van Hoe L, Oyen R et al (1999) Pelvic floor descent in females: comparative study of colpocystodefecography and dynamic fast MR imaging. J Magn Reson Imaging 9:373–377

Woodfield CA, Hampton BS, Sung V, Brody JM (2009) Magnetic resonance imaging of pelvic organ prolapse: comparing pubococcygeal and midpubic lines with clinical staging. Int Urogynecol J Pelvic Floor Dysfunct 20:695–701

Woodfield CA, Krisnamoorthy S, Hampton BS, Brody JM (2010) Imaging pelvic floor disorders: trend toward comprehensive MRI. AJR Am J Roentgenol 194:1640–1649

Yang A, Mostwin JL, Rosenshein NB et al (1991) Pelvic floor descent in women: dynamic evaluation with fast MR imaging and cinematic display. Radiology 179:25–33

Yoshioka K, Matsui Y, Yamada O et al (1991) Physiologic and anatomic assessment of patients with rectocele. Dis Colon Rectum 34:704–708

Evaluation of Infertility

Gertraud Heinz-Peer

Contents

G. Heinz-Peer, M.D.
Department of Medical and Interventional Radiology, University Hospital St. Pölten, Propst Führer Strasse 4, St. Pölten 3100, Austria
e-mail: gertraud.heinz@stpoelten.lknoe.at

1 Introduction

Infertility is defined as 1 year of unprotected intercourse that does not result in pregnancy (Hornstein and Schust 1996). Infertility is estimated to affect up to 10% of women of reproductive age (Heinonen et al. 1982). Although uterine pathology accounts for <10% of cases, uterine imaging is important not only for establishing a specific diagnosis, but also for directing corrective therapy (Collins and Woodward 1995; Lev-Toaff 1996). Knowledge of structural abnormalities may indicate potential pregnancy complications including spontaneous abortion, intrauterine growth retardation, preterm delivery, malpresentation, and retained products of conception.

An imaging study to evaluate female infertility and uterine anomalies should necessarily exhibit many characteristics, such as a noninvasive nature, low cost, and high accuracy, among other qualities. Imaging modalities currently used to evaluate infertile women include hysterosalpingography, ultrasound, and magnetic resonance imaging. In this chapter the use of these modalities to assess the various causes of infertility in females is reviewed and specific attention will be drawn to anatomic and physiologic uterine abnormalities.

Med Radiol Diagn Imaging (2017)
DOI 10.1007/174_2017_104, © Springer International Publishing AG
Published Online: 13 July 2017

2 Imaging Techniques

2.1 Hysterosalpingography

Hysterosalpingography (HSG) uses fluoroscopic control to introduce radiographic contrast material into the uterine cavity and fallopian tubes. While today HSG is used primarily to assess tubal patency, this technique also provides indirect evidence for uterine pathology through depiction of abnormal uterine cavity contours.

2.1.1 Cycle Considerations

HSG should not be performed if there is a possibility of a normal intrauterine pregnancy. To avoid irradiating an early pregnancy, the "10-day rule" can be used. That means the procedure should not be performed if the interval of time from the start of the last menses is greater than 10–12 days. If the patient has cycles that are longer than 28 days (menses start usually 14 days after ovulation), the 10-day rule can be stretched to 13–15 days. If the patient has irregular cycles or absent menses, a pregnancy test before performing HSG is recommended.

2.1.2 Technical Considerations

The patient is placed supine with her knees flexed and heels apart. Stirrups on the table to support the feet can be used. The cervix is exposed with a speculum. Visualization of the cervix may be helped by elevating the patient's pelvis, particularly in thin women. The cervix and vagina are copiously swabbed with a cleansing solution such as Betadine and the HSG cannula is placed. A variety of cannulas can be used for HSG (Margolin 1988; Sholkoff 1987; Thurmond et al. 1990). Once correct placement of the cannula is confirmed, the speculum should be removed. Leaving the speculum in is uncomfortable for the patient and a metal speculum obscures findings. Using fluoroscopic guidance, contrast agent at room temperature is slowly injected, usually 5–10 mL over 1 min, and radiographs are obtained. Injection of contrast agent is halted when adequate free spill into the peritoneal cavity is documented, when myometrial or venous intravasation occurs, or when the patient complains of increased cramping, which usually occurs when the tubes are blocked.

2.1.3 Side Effects and Complications

Mild discomfort or pain is commonly experienced by women undergoing HSG (Soules and Spadoni 1982). Routine analgesia is not necessary, although oral Ibuprofen is a reasonable preprocedure medication. Reassurance and rapid and skillful completion of the examination are the best approach. Mild vaginal bleeding is common after HSG. Severe bleeding requiring curettage is unusual and is presumably related to underlying pathology such as endometrial polyps. Other side effects such as vasovagal reactions and hyperventilation may occur and their prevalence may be reduced if the examiner is experienced and calming.

Pelvic infection is a serious complication of HSG, causing tubal damage. In a private practice setting, the overall incidence of post-HSG pelvic infection was 1.4%, occurring predominantly in women with dilated tubes (Pittaway et al. 1983). For this reason, if dilated tubes are noted during the HSG procedure, particularly if there is a dilated tube with free spill, prophylactic administration of antibiotics (e.g., doxycycline—200 mg orally) should be performed before the patient leaves the department and a prescription for 5 days should be given to the patient.

An allergic or idiosyncratic reaction related to the contrast medium can occur after HSG, although the incidence is unknown and is presumably quite low.

Radiation exposure is a side effect not shared by sonohysterosalpingography (SSG). It is a concern, because the women being examined are of reproductive age. The incidence of irradiating an early pregnancy is quite low when HSG is routinely performed in the follicular phase of the cycle. Although cases are few, there is nothing to suggest that inadvertent performance of HSG in early pregnancy is harmful to the fetus (Justesen

et al. 1986). Radiation exposure to the ovaries is minimal and can be further reduced by using good fluoroscopic technique and obtaining only the number of radiographs necessary to make an accurate diagnosis.

2.1.4 Anatomy and Physiology of Fallopian Tubes

The fallopian tubes connect the peritoneal cavity to the "extraperitoneal space." Their function and anatomy are complex, and include conduction of sperm from the uterine end toward the ampulla, conduction of ova in the other direction from the fimbriated end to the ampulla, and support as well as conduction of the early embryo from the ampulla into the uterus for implantation. The normal fallopian tube ranges in length from 7 to 16 cm, with an average length of 12 cm (Fig. 1a). The tube is divided into four regions: (a) the intramural or interstitial portion, which occurs in the wall of the uterine fundus and is 1–2 cm long; (b) the isthmic portion, which is about 2–3 cm long; (c) the ampullary portion, which is 5–8 cm long; and (d) the infundibulum, which is the trumpet-shaped distal end of the tube terminating in the fimbria. Patency of the fallopian tubes is established when contrast medium flows through them and freely around the ovary and loops of bowel at the time of salpingography, using either fluoroscopic or sonographic guidance (Fig. 1b).

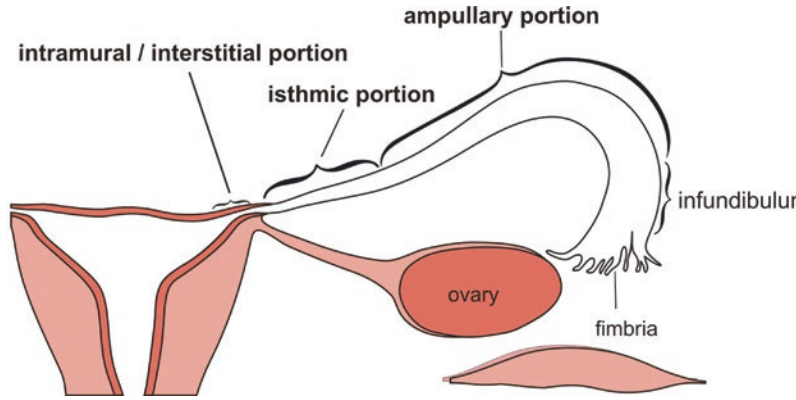

Fig. 1a Scheme of normal fallopian tubes: the normal fallopian tube ranges in length from 7 to 16 cm (average 12 cm). The tube is divided into four regions: (**a**) intramural or interstitial portion (1–2 cm), (**b**) isthmic portion, (2–3 cm), (**c**) ampullary portion (5–8 cm), and (**d**) infundibulum terminating into the fimbria

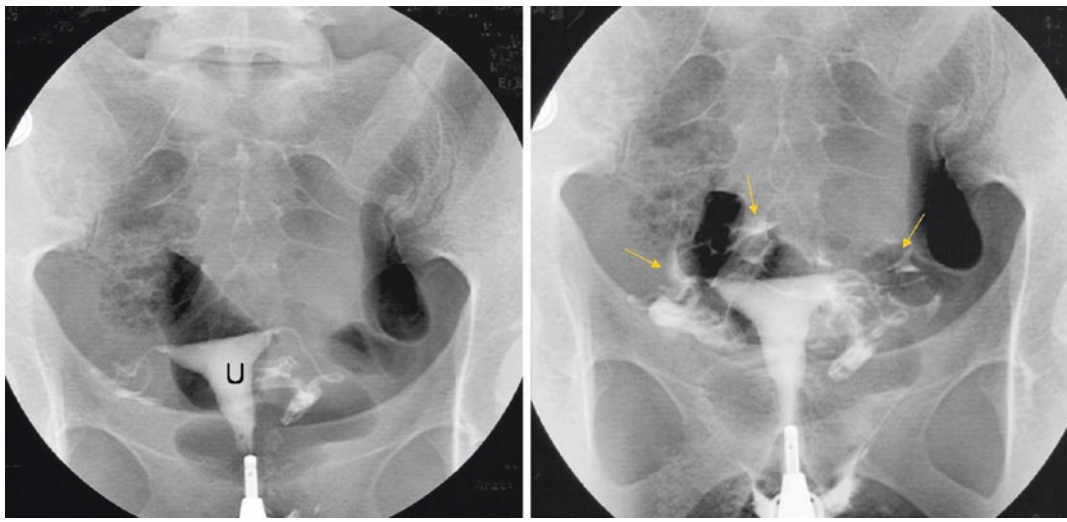

Fig. 1b Normal hysterosalpingogram: the uterus (u) has a normal contour and shape. The fallopian tubes fill bilaterally with evidence of free spill into the pelvic peritoneum (*arrows*)

2.1.5 Pathological Findings

Diverticuli in the isthmic segment of the tube are caused by salpingitis isthmica nodosa (SIN) (Fig. 2). These would be difficult to appreciate by sonography. SIN was described more than 100 years ago as irregular benign extensions of the tubal epithelium into the myosalpinx, associated with reactive myohypertrophy and sometimes inflammation. There is an association between SIN and pelvic inflammatory disease; however, it is not clear whether SIN is caused by pelvic inflammation, or is congenital and predisposes to inflammation.

Obstruction of the tubes can occur anywhere along their length (Fig. 3a–c). Obstruction of the midisthmic portion may be missed by sonography, because of the small caliber of the tube and the absence of dilation when there is obstruction at this level.

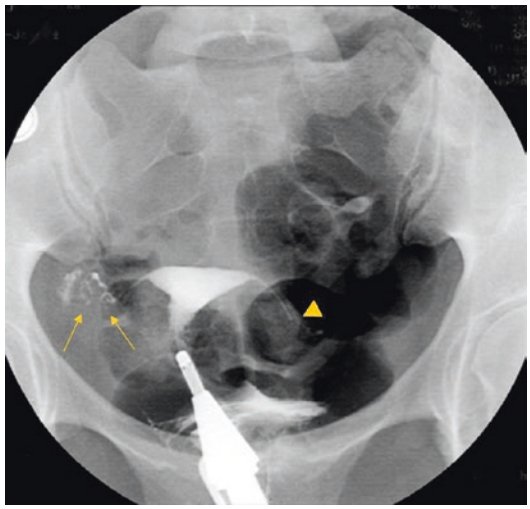

Fig. 2 Salpingitis isthmica nodosa: multiple tiny diverticuli in the right isthmic portion (*arrows*) caused by mucosal proliferation and muscular hypertrophy with mucosal invasion into the muscularis; partial tubectomy on the left side (*arrowhead*)

Polyps are small, smooth filling defects, which can be single or multiple, and do not distort the overall size and shape of the uterine cavity (Fig. 4a, b). Leiomyomas are usually single, larger lobulated masses, which only partially project into the cavity, and often enlarge and distort the cavity.

Synechiae are scars that result from uterine trauma such as complications of pregnancy, curettage, uterine surgery, or uterine infection. Synechiae are generally linear and irregular (Fig. 5a) and extend from one wall to the opposite wall allowing contrast agent to flow around them only in one dimension. For this reason, they are more easily defined than the above-mentioned masses, which in general allow contrast agent to flow around them in two dimensions. Synechiae may also manifest as absence of filling of the entire uterus or part of it, and can be confused with müllerian defect (Fig. 5b).

Asherman syndrome is defined by the combination of infertility, hypomenorrhea or amenorrhea, and a history of uterine curettage. It is estimated to occur in 68% of infertile women who have undergone two or more curettages (Bacelar et al. 1995). The pathophysiology consists of intrauterine adhesions (synechiae) that develop after traumatic endometrial injury, such as postpartum or postabortion uterine curettage (Fig. 6a, b). Less commonly, it results from endometritis (Kurman and Mazur 1987). It is hypothesized that infertility occurs because uterine adhesions and scarring interfere with sperm migration and embryo implantation.

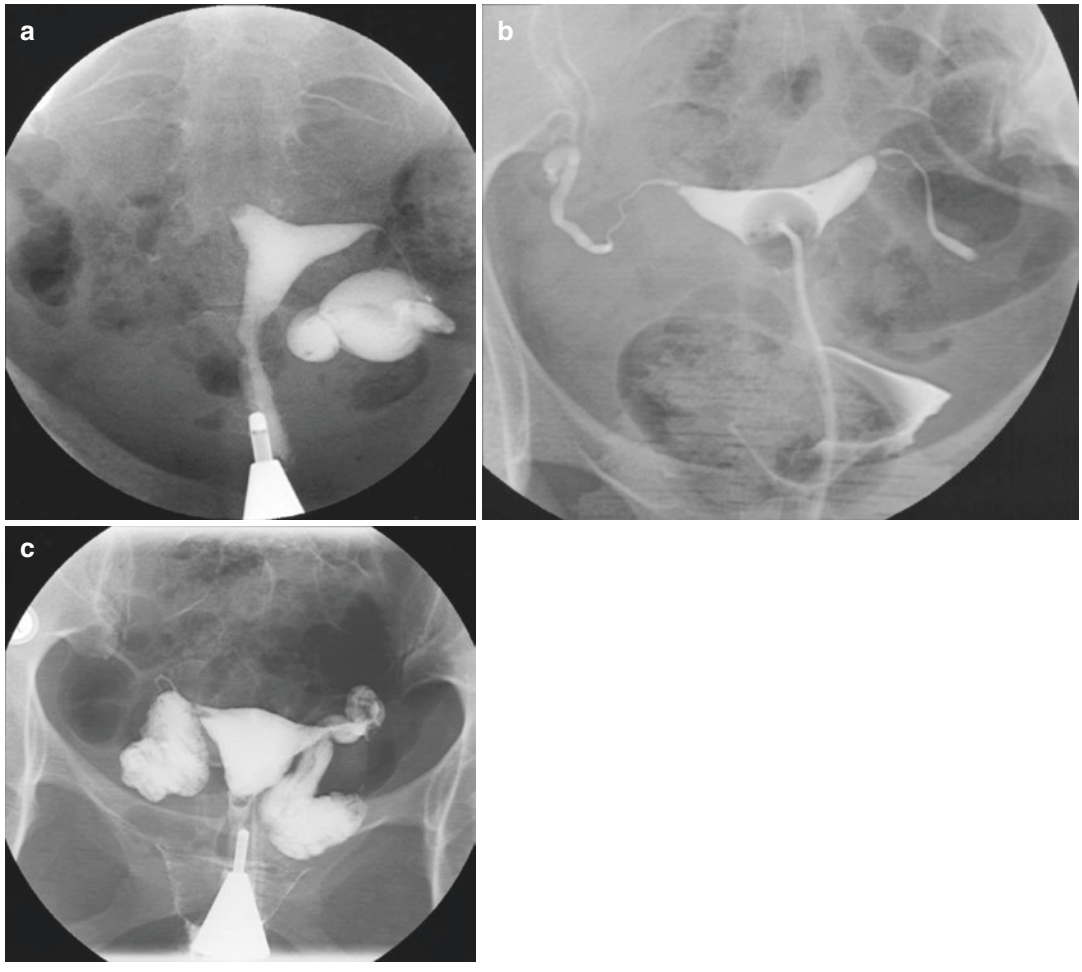

Fig. 3 Bilateral fallopian tube obstruction (three different patients): there is dilated, obstructed tube on the left (hydrosalpinx) and obstruction of the right intramural portion (**a**), nondilated obstruction on both sides at the isthmic/ampullary portion (**b**), and huge bilateral dilatation without spill into the peritoneum—bilateral hydrosalpinx (**c**)

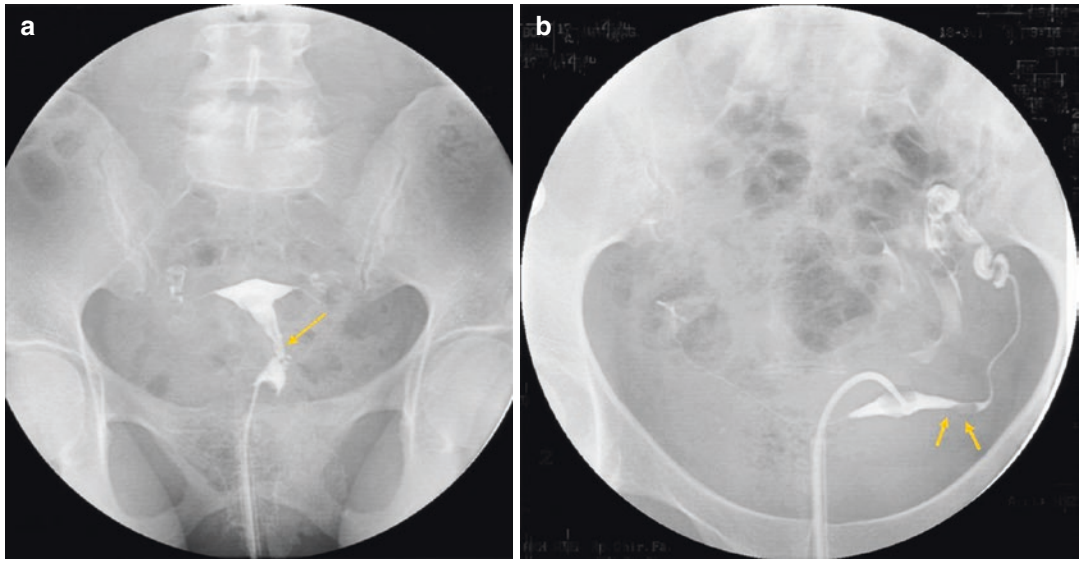

Fig. 4 Endometrial polyps: stalked filling defect within the endometrial cavity probably arising from the cervical canal (*arrow*). Note normal filling of the fallopian tubes and free spill into the peritoneum (**a**). In a different patient the hysterosalpingogram shows a filling defect in the intramural portion of the left tube (*arrows*) causing narrowing but no obstruction; normal filling of the fallopian tubes (**b**)

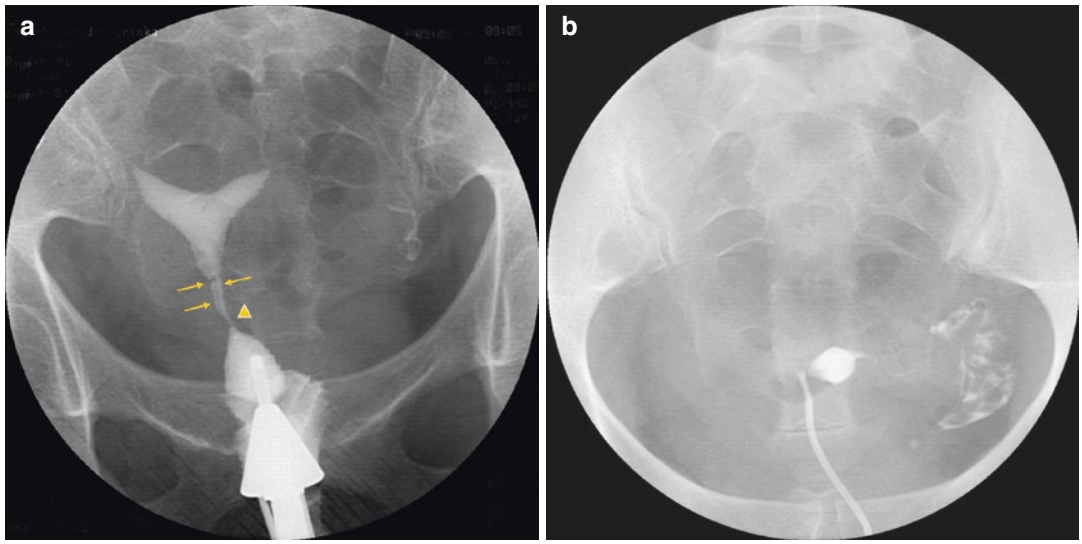

Fig. 5 Synechiae: on hysterosalpingogram irregular borders (*arrows*) and narrowing of the cervical canal (*arrowhead*) are depicted (**a**). In a different patient HSG shows synechiae causing partial obstruction of the endometrial cavity and occlusion of the right fallopian tube (**b**). Note: HSG may not rule out müllerian duct anomaly with certainty in this particular case

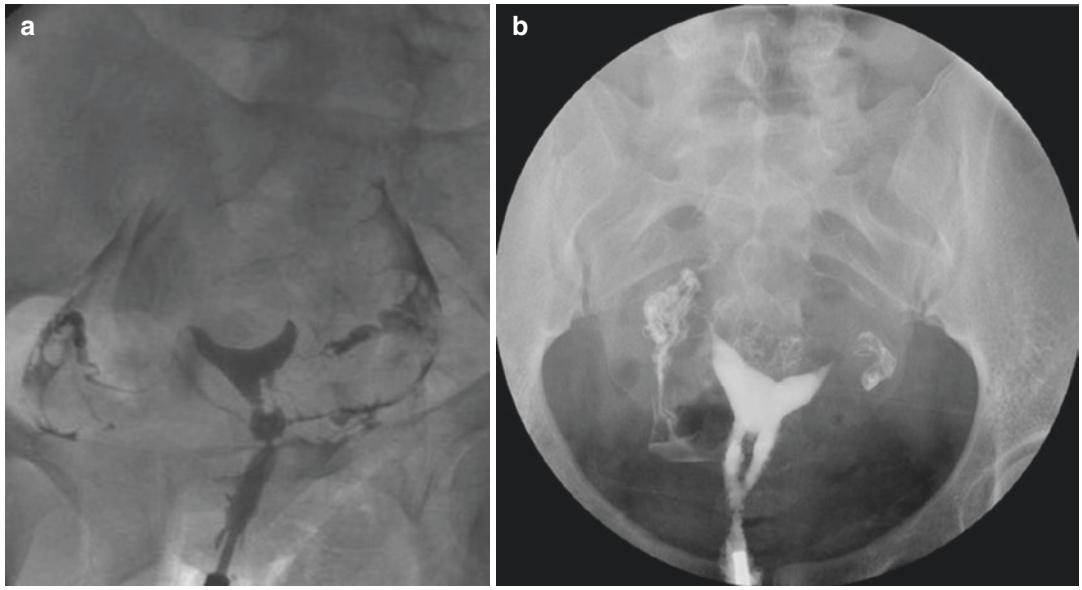

Fig. 6 (**a**, **b**) Asherman syndrome. HSG of two different patients shows intrauterine adhesions which occurred after postabortion uterine curettage

2.1.6 Limitations of HSG

HSG should not be performed when there is active vaginal bleeding. This is to prevent the flushing of clots into the peritoneal cavity. HSG should also not be performed if there is active pelvic infection, because it could exacerbate the infection. The procedure should not be performed within 6 weeks of pregnancy, uterine surgery, tubal surgery, or uterine curettage because the defects in the endometrial or tubal lining predispose to venous intravasation of contrast material.

The major limitations of the procedure are the ability to characterize only patent canals and the inability to evaluate the external uterine contour adequately. HSG also entails exposure to ionizing radiation in these typically young women.

2.2 Sonohysterography and Sonohysterosalpingography

Sonography is frequently used to evaluate uterine pathology because of its excellent diagnostic accuracy, minimal patient discomfort, low cost, and widespread availability. With the addition of transvaginal sonography, color Doppler imaging, and sonohysterography, ultrasound has become a sensitive technique for detecting endometrial and myometrial pathology.

Sonosalpingography (SSG) utilizes transvaginal sonography (TVS) during instillation of either saline or contrast medium into the uterine lumen to evaluate tubal patency and morphology. Tubal patency can be assessed by repeated injections of 3–5 mL of sterile saline in 75% of the patients. Injection of contrast media allows accurate assessment of tubal patency in up to 92% (Lindheim et al. 2006). Preliminary work suggests that three-dimensional and harmonic imaging greatly enhances sonographic depiction of the tube.

Before contrast or saline is introduced, it is recommended that the physician identifies the approximate location of the tube by identifying the ovary and endometrium that invaginates into the uterine cornua.

If there is a pain during injection, this may be a sign of tubal obstruction, either intrinsic or extrinsic from adhesions. Spasm may be present and may cause transitory lack of filling of the proximal portion of the tube (Lindheim et al. 2006).

Hydrosalpinges appear as fusiform cystic structures on TVS. If a hydrosalpinx is seen, patients may be given 200 mg doxycycline initially, and then 100 mg po twice a day for 5 days for prophylaxis of pelvic inflammatory disease (Lindheim et al. 2006).

2.2.1 Cycle Considerations

In premenstrual patients SSG ideally should be scheduled between days 4 and 7 of the menstrual cycle (Lindheim et al. 2006) (Fig. 7a). However, for congenital anomaly evaluation, the timing of the sonography examination is not critical (Fig. 7b). For SSG, cycle considerations of conventional hysterosalpingography should be considered.

In patients with irregular bleeding the examination can be performed without the benefit of optimal scheduling. In such cases, any potentially confusing residual blood within the endometrial cavity can be assessed during SSG using a combination of gentle catheter manipulation and saline flush during real-time sonographic visualization (Lindheim et al. 2006).

2.2.2 Technical Considerations

Imaging should not only focus on conventional sagittal and transverse imaging of the pelvis but also include orthogonal images along the long axis of the uterus to characterize the external uterine contour. Transabdominal ultrasound is usually best performed with a 2–6 MHz transducer. Transvaginal ultrasound should be performed with an 8–5 MHz transducer. Transvaginal sonography has the advantage of improved spatial resolution, although at the expense of a decreased field of view.

SSG utilizes transvaginal sonography during instillation of either saline or contrast medium into the uterine lumen. It is best performed after sonohysterography, since sonohysterography is vital in delineating the endometrial surfaces for the presence of synechiae or intraluminal lesions such as polyps (Fig. 7c) or submucosal fibroids.

The examiner is encouraged to apply gentle pressure with the probe while sonographically assessing the mobility of the uterus, ovary, and tube.

Saline can be used initially for assessment of tubal patency. However, if there is any doubt

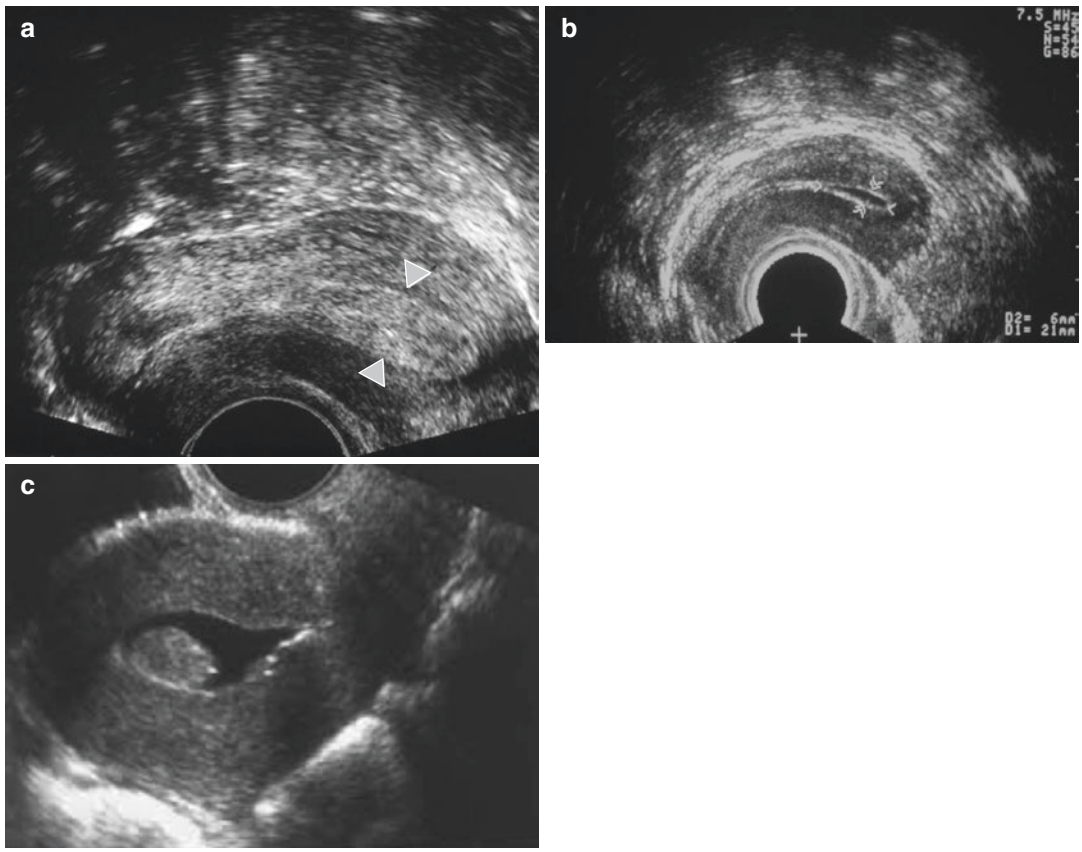

Fig. 7 Normal TVUS: clear demarcation of the relatively thick and hyperechoic endometrium (*arrowheads*) during the secretory phase (**a**), minimal fluid retention during the proliferation phase of the cycle (**b**), small polyp detected during sonohysterography (**c**)

about tubal spill, contrast should be used. It is necessary to have a ballooned catheter to block egress of fluid from the uterine lumen during injection. After sonohysterography has been performed, the saline should be removed prior to instillation of positive contrast.

Some investigators advocate the use of color Doppler sonography with saline instillation in order to best depict tubal patency (Nicolini et al. 1987; Pellerito et al. 1992; Kupesic and Kurjak 2000). This technique can also be used with contrast.

Microbubble contrast agents provide an echogenic contrast to document tubal patency and spillage. The safety of this contrast agent has been established in multiple studies, but its cost makes selected use necessary.

If there is pain during injection, this may be sign of tubal obstruction, either intrinsic or extrinsic from adhesions. Spasm may be present and may cause transitory lack of filling of the proximal portion of the tube.

2.2.2.1 Normal and Abnormal Anatomy

With the use of saline or contrast, the normal tubal lumen is easily identified as thin serpentine adnexal structures.

Hydrosalpinges appear as fusiform cystic structures on TVS. The contrast may dilute or bubbles may come out of suspension, making complete delineation difficult to recognize.

2.2.3 Accuracy

Sonography has a reported accuracy of approximately 90–92% (Nicolini et al. 1987; Pellerito et al. 1992). Sonosalpingography, with infusion of saline into the endometrial canal, provides improved delineation of the endometrium and internal uterine morphology. Three-dimensional ultrasound with surface- and transparent-mode reconstructions of the uterus has reported advantages over conventional two-dimensional scanning. In experienced hands, a sensitivity of 93% and a specificity of 100% have been achieved (Pellerito et al. 1992).

2.2.4 Side Effects and Complications

The side effects and complications of Sono-HSG are for the most part the same as for conventional HSG.

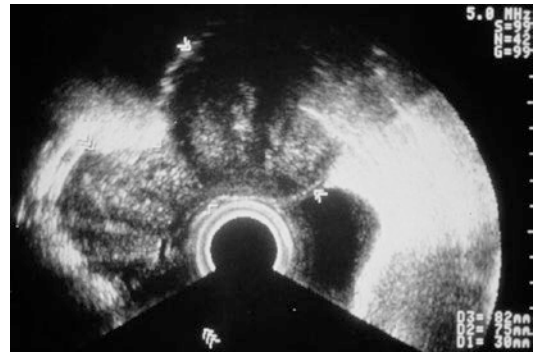

Fig. 8 TVUS: unfavorable ultrasound image caused by a large fibroid

2.2.5 Limitations of Sono-HSG

Sono-HSG shares limitations similar to those of conventional transvaginal ultrasound and can only help evaluate patent endometrial canals (Goldberg et al. 1997).

The major drawback of this modality is its operator dependency. Additional limitations include factors that contribute to an unfavorable ultrasound image, such as a large-body habitus and/or the presence of large fibroids (Fig. 8).

2.3 Magnetic Resonance Imaging

2.3.1 Indications

Magnetic resonance (MR) imaging is suitable for assessing female infertility, as infertility typically results from benign processes in women of reproductive age. The causes of female infertility include ovulatory disorders (i.e., pituitary adenoma and polycystic ovarian syndrome), disorders of the fallopian tubes (i.e., hydrosalpinx, and pelvic inflammatory disease), uterine disorders (i.e., müllerian duct anomaly, adenomyosis, and leiomyoma), and pelvic endometriosis. The applications of MR imaging include evaluation of the functioning uterus and ovaries, visualization of pituitary adenomas, differentiation of müllerian duct anomalies, and accurate noninvasive diagnosis of adenomyosis, leiomyoma, and endometriosis. In addition, MR imaging helps predict the outcome of conservative treatment for adenomyosis, leiomyoma, and endometriosis and may lead to selection of better treatment plans and management.

MR imaging provides clear delineation of internal and external uterine anatomy in multiple imaging planes, although it is not able to assess tubal patency or subtle, peritubular adhesion. The excellent tissue contrast of MR imaging allows specific diagnosis for many gynecological diseases.

As laparoscopic surgery is frequently the modality of choice to treat patients suffering from infertility, an accurate preoperative diagnosis is especially important for planning appropriate surgical intervention.

2.3.2 Technical Considerations

Patients are best imaged with a phased-array MR surface coil. Current standard imaging protocols for infertility evaluation include axial, sagittal, and coronal fast spin echo sequence images of the uterus, which can be supplemented by oblique views to obtain true coronal and axial images of the uterus. Large field-of-view images to look for associated renal anomalies should be obtained. Further imaging of the pelvis with a transverse T1-weighted sequence should be performed. Gd-enhanced MR imaging is important for diagnosis of complex adnexal masses and distinguishing them from malignant processes.

Some authors recommend that an antiperistaltic (1 unit of glucagon or 20 mg of scopolamine butylbromide) should be administered intramuscularly or intravenously before examination.

2.3.3 Limitations

As drawbacks of MRI are its higher cost, limited availability, and longer scanning time than ultrasound, MR imaging is often used as a problem-solving modality when sonography findings are inconclusive (Nicolini et al. 1987; Javitt 1997).

2.3.4 Normal MR Anatomy in Reproductive-Age Women

Uterine zonal anatomy is best demonstrated on T2-weighted images (Fig. 9). The endometrium has high signal intensity. The junctional zone, which corresponds to the innermost myometrium, appears as a band of low signal intensity. The peripheral myometrium has intermediate signal intensity that is higher than that of the striated muscle. The width of the endometrium and the junctional zone varies through the menstrual cycle; they are widest and most clearly visible in the late secretory phase. The uterine corpus is larger than the cervix throughout the reproductive-age period. In general the corpus measures 6–8 cm in length by 5–6 cm in transverse and anteroposterior dimensions (Fleischer and Kepple 1997).

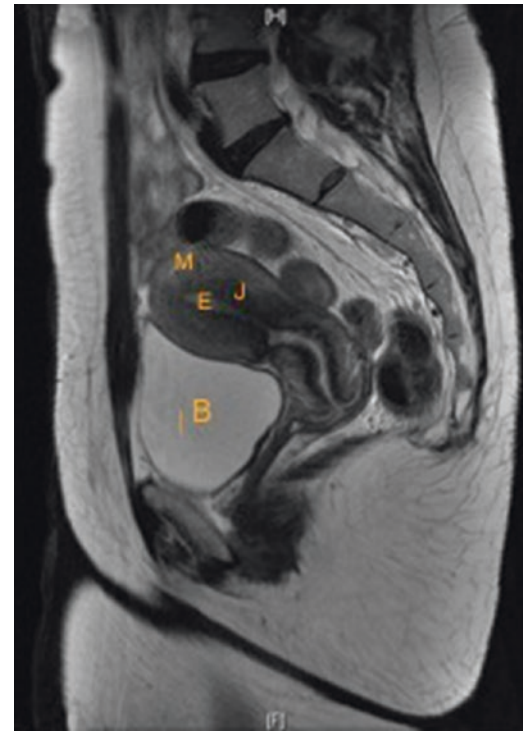

Fig. 9 Normal anatomy in reproductive-age women: sagittal T2W MR image clearly demonstrates uterine zonal anatomy with high signal intensity of the endometrium (E), low signal of junction zone (J), and intermediate signal of the myometrium (M). B (urinary bladder)

The cervix also shows zonal architecture on T2-weighted images. The central area of high signal intensity represents epithelium and mucus, the middle area of low signal intensity represents fibrous stroma, and the outer area of medium signal intensity represents peripheral myometrium. The vaginal wall has low signal intensity on T2-weighted images. The texture of the ovaries is clearly imaged in women of reproductive age with hypointense stroma and hyperintense follicles on T2-weighted images.

Normal fallopian tubes are not routinely imaged because of their small diameter and tortuous course.

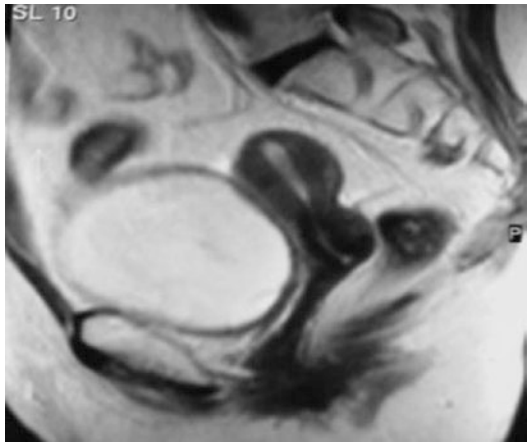

Fig. 10 Normal anatomy in postmenopausal women: sagittal T2W MR images show a smaller uterine corpus with poor delineation of uterine zonal anatomy

2.3.5 Normal MR Anatomy of the Postmenopausal Women

After menopause, the uterine corpus becomes smaller and approximately equal in size to the cervix. The zonal anatomy is indistinct when women are not receiving exogenous hormones (Fig. 10). Although the cervix does not atrophy significantly, the peripheral myometrium is usually unclear. Ovaries may be undetected at MR imaging since they seldom have follicles.

When a woman of reproductive age has a small uterus with indistinct zonal anatomy or undetectable ovaries, as seen in postmenopausal women, the possibility of a disorder related to insufficient hormone secretion should be considered (Imaoka et al. 2003).

3 Ovulatory Dysfunction

Disorders affecting ovulation account for 30–40% of cases of female infertility (Hornstein and Schust 1996). Measures of ovarian function include measurement of basal body temperature, endometrial biopsy, measurement of serum progesterone level, endocrine tests, and monitoring of follicle growth with US. Thus the role of MR imaging is limited to assessment of whether a pituitary adenoma is present (Imaoka et al. 2003).

4 Pituitary Adenoma

Prolactin-producing adenoma (prolactinoma) is the most common functional pituitary adenoma. Its prevalence peaks in women between 20 and 30 years of age. Hyperprolactinemia can be a cause of infertility and is associated with diminished gonadotropin secretion, secondary amenorrhea, and galactorrhea. The patient should first be examined for drug-induced hyperprolactinemia before any infertility workup is initiated. For example, antidepressants, cimetidine, dopamine antagonists, reserpine, sulpiride, verapamil, methyldopa, and estrogen therapy are known to interface with prolactin secretion.

When a patient is suspected to have hyperprolactinemia not associated with drugs, MR imaging is the imaging technique of choice. It can depict a pituitary microadenoma (≤1 cm) (Fig. 11). Most microadenomas have lower signal intensity than the normal pituitary gland on T1-weighted images. A convex outline of the pituitary gland or deviation of the pituitary stalk can also be detected. Dynamic study with intravenous bolus injection of contrast medium is the preferred technique for assessing microadenomas, as it allows excellent delineation between

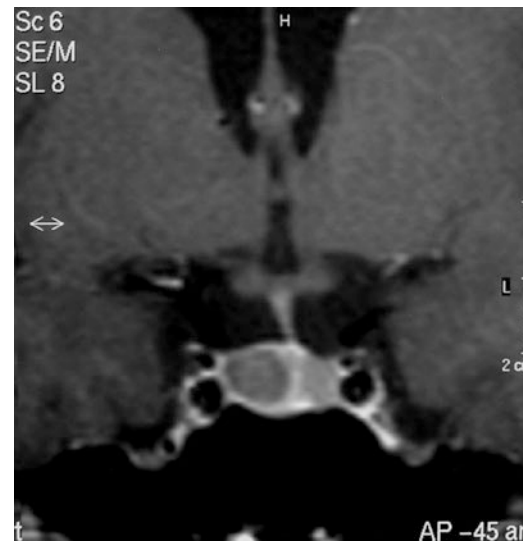

Fig. 11 Pituitary microadenoma: unenhanced T1W MR image shows a right-sided microadenoma leading to hyperprolactinemia

the tumor and the normal pituitary gland. In the dynamic study, the normal pituitary gland and stalk show strong enhancement in the early phase of dynamic imaging, whereas microadenomas show relatively weak enhancement (Miki et al. 1990; Bartynski and Lin 1997).

Macroadenomas (>1 cm) (Fig. 12a–c) occupy the pituitary fossa and may cause visual abnormalities when they put pressure on the optic chiasm. Macroadenomas also tend to invade the cavernous sinus and erode the bony floor. The extent of the tumor can be determined by means of contrast-enhanced MR imaging.

5 Polycystic Ovarian Syndrome

The diagnosis of polycystic ovarian syndrome is based on hormone imbalance and laboratory findings. Patients with this syndrome often

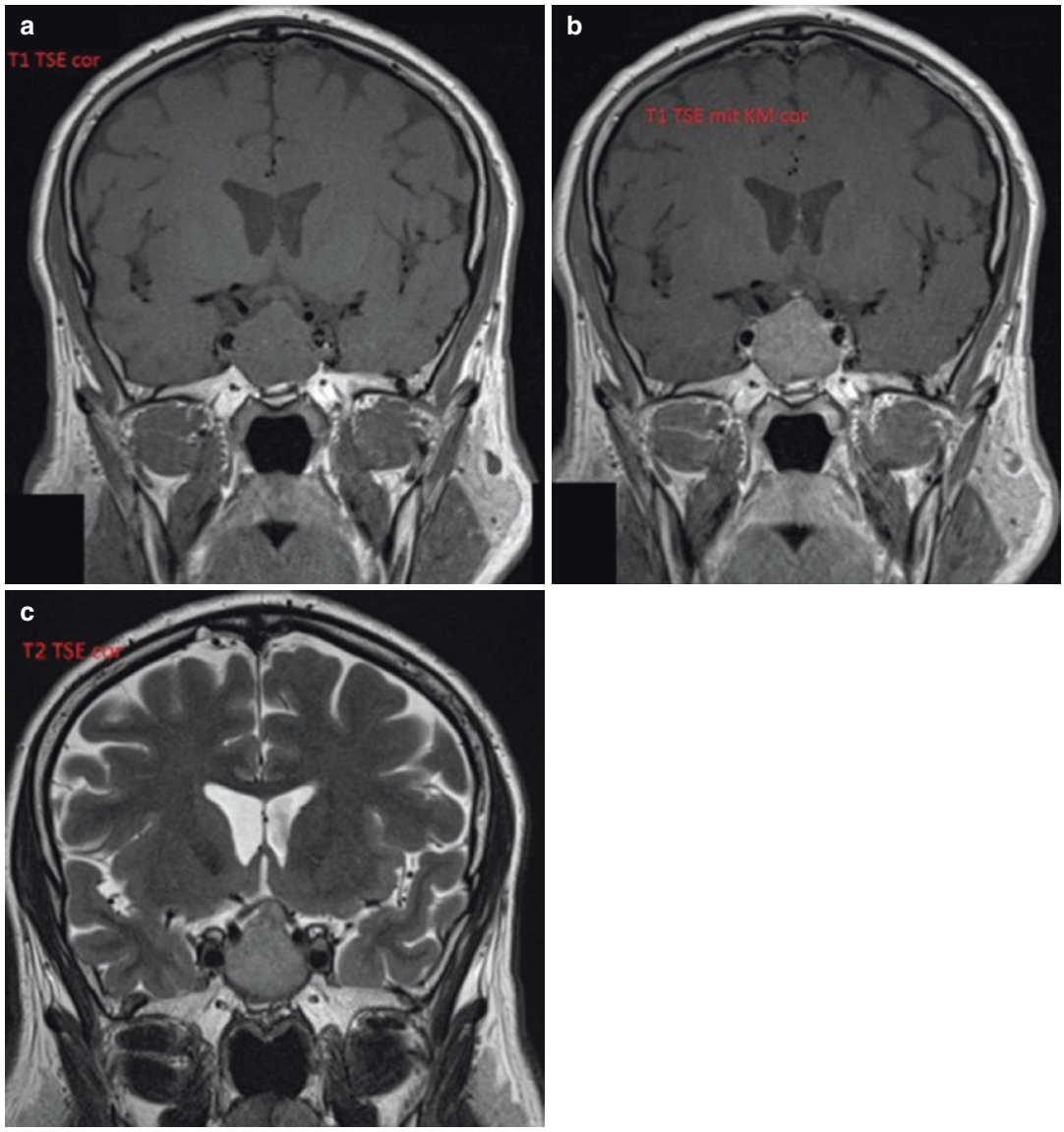

Fig. 12 Pituitary macroadenoma: unenhanced (**a**) and contrast-enhanced (**b**) T1W MR images and (**c**) T2W MR images show a large right-sided pituitary prolactinoma (*arrow*) leading to hyperprolactinemia with consecutive infertility

demonstrate an abnormal ratio of luteinizing hormone to follicle-stimulating hormone. The clinical manifestations include hirsutism, anovulation, and infertility. At gross pathologic analysis, the morphologic findings in the ovaries consist of multiple small follicular cysts surrounded by thickened and luteinized theca. The current recommendations include US as imaging test. Follicle counting is the central diagnostic information, according to recent data with >25 follicles being diagnostic, whereas ovarian size and stromal assessment are less important (Lujan et al. 2013). Monitoring of follicle growth is usually performed with US, and the usefulness of MR imaging is not proved. On T2-weighted images, polycystic ovarian syndrome appears as multiple tiny hyperintense peripheral cysts with hypointense central stroma (Mitchell et al. 1986; Kimura et al. 1996) (Fig. 13a). However, MR imaging findings are nonspecific and serve only as supportive evidence of polycystic ovarian syndrome. Multiple tiny, hyperintense peripheral cysts (Fig. 13b) have been seen in patients with anovulation, medication-stimulated ovulation, or vaginal agenesis (Kimura et al. 1996).

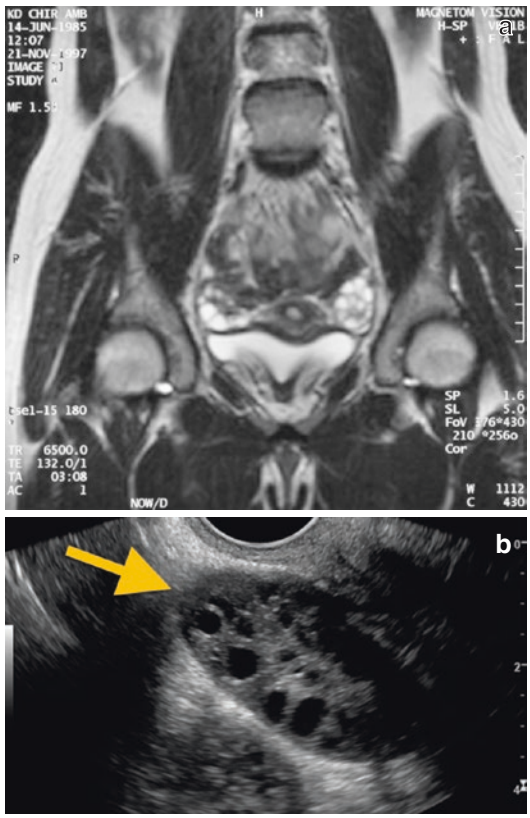

Fig. 13 (**a**, **b**) Polycystic ovarian syndrome: on T2W-coronal MR image both ovaries are studded with multiple small cystic lesions. US image with multiple small cystic ovarian lesions in a patient without PCO

6 Disorders of the Fallopian Tubes

Disorders of the fallopian tubes are a common cause of female infertility, accounting for 30–40% of cases (Hornstein and Schust 1996). Tubal disorders include damage to or obstruction of the fallopian tube and peritubal adhesions. Hysterosalpingography is the mainstay of evaluation of tubal patency, whereas laparoscopy is preferred for assessment of the peritubal environment. MR imaging aids in noninvasive assessment of tubal dilatation and peritubal disease. Fallopian tubes may be assessed by conventional techniques including multiplanar T2-weighted images or by 3D T2WI or alternatively by MR hysterosalpingography (Sadowski et al. 2008). Dilated fallopian tubes manifest as fluid-filled ducts, which appear as retort-, sausage-, C-, or S-shaped cystic masses at MR imaging (Fig. 14a, b). Thin, longitudinally oriented folds along the interior of the tube represent incompletely effaced mucosal or submucosal plicae (Outwater et al. 1998). Pelvic inflammatory disease is one of the most common causes of tubal or peritubal damage. The diagnosis is usually based on clinical or transvaginal US findings. MR imaging can also be helpful in assessment of pelvic inflammatory disease (Fig. 15a, b). Tubo-ovarian abscesses, dilated fluid-filled tubes, and free pelvic fluid can be depicted (Tukeva et al. 1999).

Endometriosis also causes peritubal adhesions. MR imaging is the most sensitive imaging technique for evaluation of endometriosis. Moreover, dilated fallopian tubes with high signal intensity on T1-weighted images, which correspond to hematosalpinx, reportedly correlate with one of the effects of endometriosis (Outwater et al. 1998).

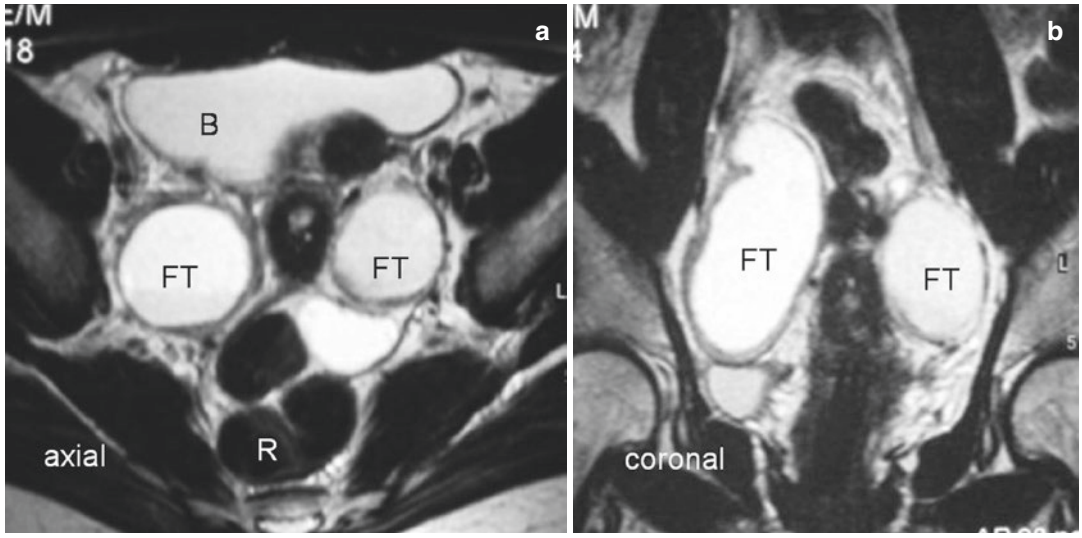

Fig. 14 Bilateral hydrosalpinx: sausage-, C-, or S-shaped cystic masses in the small pelvis as shown by these axial (**a**) and coronal (**b**) T2W MR images are clearly indicative for dilated fallopian tubes

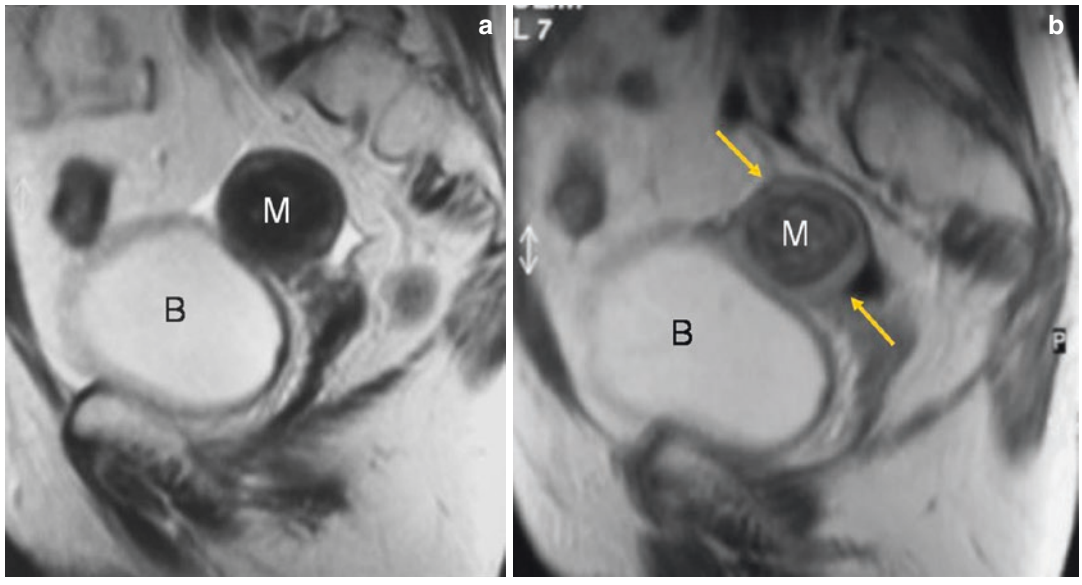

Fig. 15 Tubo-ovarian abscess: unenhanced (**a**) and contrast-enhanced (**b**) T1W MR images show a left-sided adnexal mass (M) with rim-like enhancement (*arrows*) which proved to be an abscess

7 Uterine Disorders

7.1 Müllerian Duct Anomalies

If other causes of infertility are excluded, uterine anomalies may be suggested as a cause of infertility. On the other hand, unknown numbers of uterine anomalies may escape detection since reproductive ability is often unaffected or not noticeably affected (Rock 1997).

Müllerian duct anomalies (MDAs) exhibit a prevalence of approximately 3%. Infertility issues are encountered in 25% of such women. Presenting symptoms vary depending on the

specific anomaly. Amenorrhea is seen with imperforate hymen, vaginal atresia, uterine anomalies, Mayer-Rokitansky-Küster-Hauser syndrome, and Wünderlich syndrome. In the first two conditions, primary amenorrhea presents as cryptomenorrhea, in which menstrual blood cannot be extruded and patients commonly complain of periodic abdominal pain. MR imaging clearly demonstrates the point of obstruction, as well as the presence or absence of hematoceles, which includes hematometra, hematosalpinx, or blood in the rudimentary uterus (Javitt 1997; Togashi et al. 1987). In addition, MR imaging allows evaluation of urinary tract abnormalities which are commonly associated, since embryologically, the müllerian and mesonephric ducts are closely related.

Müllerian duct anomalies may be depicted by HSG; however, the complex situation of the various classes of anomalies seems to be better defined by sonography or MR imaging.

Classification of MDAs according to the system adapted by the American Fertility Society can be readily achieved based on MR findings (Carrington et al. 1990). In one comparative study, MR imaging attained 100% accuracy for diagnosis of uterine anomalies, as compared with 92% for ultrasound and <20% for HSG (Nicolini et al. 1987). In the evaluation of uterine cavity deformation, highly accurate diagnosis of submucosal leiomyomas is easily established on MR imaging, readily differentiating the lesions from adenomyosis and endometrial polyps.

The most basic classification of müllerian duct defects consists of agenesis and hypoplasia, defects of vertical fusion, and defects of lateral fusion. In 1979, Buttram and Gibbons (Buttram and Gibbons 1979) proposed a classification of müllerian duct anomalies that was based on the degree of failure or normal development, and they separated these anomalies into classes that demonstrate similar clinical manifestations, treatment, and prognosis for fetal salvage. Modified in 1988 by the American Society of Reproductive Medicine, the classification remains the most widely accepted schematization and addresses uterovaginal anomalies (Fig. 16, Scheme anomalies).

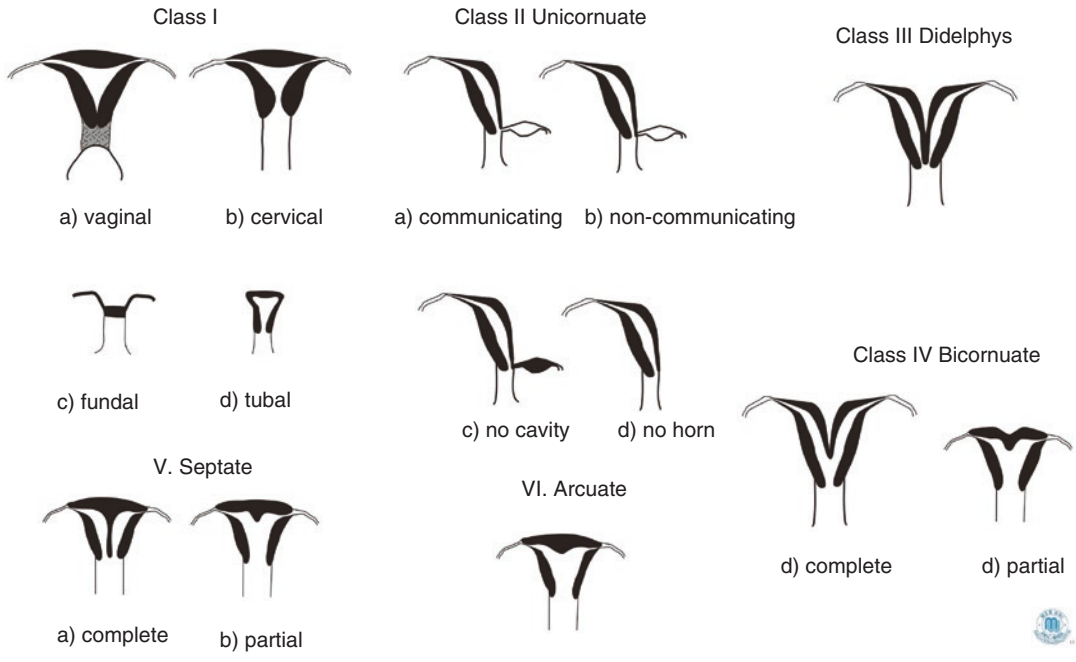

Fig. 16 Schematization of uterovaginal anomalies by the American Society of Reproductive Medicine

7.1.1 Class I: Hypoplasia or Agenesis

Failure of normal development of the müllerian ducts causes uterine agenesis or hypoplasia. Patients present with primary amenorrhea in adolescence. Agenesis or hypoplasia of any part of the genital tract (vagina, cervix, uterus, tubes) may occur either in isolation or more common in combination. This relatively uncommon class of anomalies accounts for approximately 5% of müllerian duct anomalies. Vaginal agenesis is the most common subtype, and is often accompanied by uterine agenesis.

It is necessary to document whether a functioning uterine corpus and cervix are present.

Mayer-Rokitansky-Küster-Hauser syndrome is a malformation of this category. The typical form of this syndrome is characterized by congenital absence of the uterus and upper vagina. The ovaries and fallopian tubes are usually normal. The atypical form of the syndrome includes associated abnormalities of the ovaries and fallopian tubes and renal anomalies (Strübbe et al. 1993) (Fig. 17).

Women with acquired uterine hypoplasia due to drugs, pelvic irradiation, or ovarian failure may have a disproportionately small uterine corpus. In these patients the ratio of the uterine body to the cervix is reduced to less than the normal 2:1, similar to a premenarchal uterus.

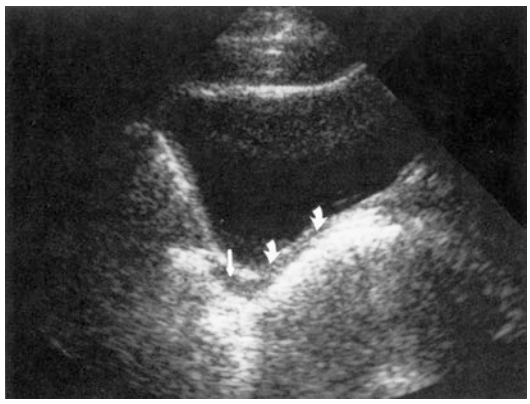

Fig. 17 Class I: uterine agenesis. Sagittal midline sonogram shows normal vagina, small (*curved arrows*) cervix (*straight arrow*), and absent uterus

7.1.2 Class II: Unicornuate

This MDA consists of one normally developed müllerian duct, with the contralateral duct either hypoplastic (subtypes 2a–c) or absent (subtype 2d). Types 2a–c comprise approximately 90% of cases (Heinonen et al. 1982; Rock 1997) (Fig. 18a–c).

Agenesis of a unilateral müllerian duct causes a single banana-shaped uterus with a single fallopian tube. If the rudimentary horn is either noncommunicating or lacks a cavity, it will not be detected by hysterosalpingography. Sonographic findings which are often subtle and easily overlooked include a small uterine cavity, an asymmetric ellipsoid fundal shape, and lateral deviation of the uterus. If the rudimentary horn is present without a cavity, it may be mistaken for a fibroid or the broad ligament.

MRI findings are similar to those seen with ultrasound, but cavity detection in the rudimentary horn can be facilitated by using heavily T2W imaging sequences. Normal zonal anatomy is observed in a small uterus.

If the rudimentary horn is noncommunicating endometrial tissue expelled retrogradely through the fallopian tube during menstruation results in an increased frequency of endometriosis (Brody et al. 1998).

Spontaneous abortion and premature labor may occur in pregnancies with unicornuate uterus, and the poorest fetal survival among all uterine anomalies has been reported (Rock 1997). A potentially lethal complication is uterine rupture which can occur if a pregnancy implants in a rudimentary horn.

7.1.3 Class III: Didelphys

Complete failure of fusion of the two müllerian ducts results in two complete uteri, each with its own cervix (Fig. 19a–c). A longitudinal sagittal vaginal septum is usually, but not always, observed. Among all uterine anomalies, uterus didelphys is associated with the highest successful pregnancy rate, except for arcuate uterus (Rock 1997). Uterus didelphys is the least common of uterine duplication anomalies. HSG will clearly delineate the two separate uterine cavities if each cervix can be cannulated. In a small percentage of cases the vaginal septum may prevent

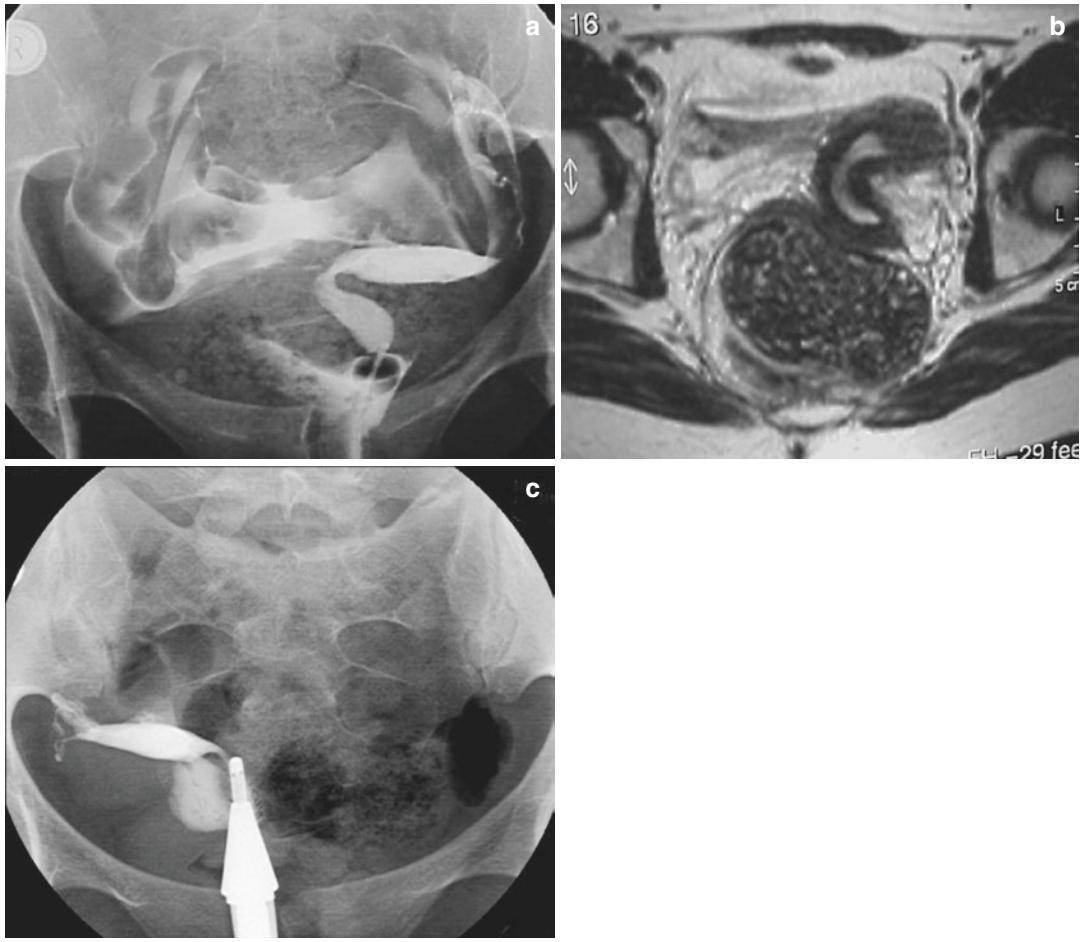

Fig. 18 Class II: left unicornuate uterus: HSG shows uterine cavity deviated toward left side with patent left fallopian tube (**a**). Axial T2W MRI in this patient shows no rudimentary horn on the right side (**b**). In another patient HSG shows right unicornuate uterus with hydrosalpinx (**c**)

cannulation of one cervical canal, leading to the appearance of a unicornuate uterus.

Sonographic images reveal two widely spaced uterine fundi with myometrium and a deep cleft separating the two endometrial cavities. Two separate cervices may not be visible, since endocervical echoes are less prominent than endometrial echoes, but transvaginal imaging can demonstrate these findings better. Sonography is also useful for demonstrating hematocolpos, hematometra, and endometriosis in cases missed by HSG owing to an obstructing vaginal septum. Uterus didelphys with an obstructed hemivagina is termed Wünderlich syndrome (Fig. 19a–c) and is usually associated with ipsilateral renal agenesis. Several series have noted a tendency for the right hemi-uterus to obstruct, in association with right renal agenesis (Imaoka et al. 2003).

MRI is best performed with multiplanar scans. To improve visualization of the fundal contour, coronal images should be obtained in a plane parallel to the tubal ostia and internal os. MR findings are similar to those of sonography, with a deep separating cleft (>3 cm) between the two uterine fundi. The widely spaced uterine horns have an obtuse intercornual angle (>110°), although occasional overlap with a bicornuate anomaly exists. Separate cervices and a vaginal septum (if present) can be demonstrated by caudal axial T2-weighted sections.

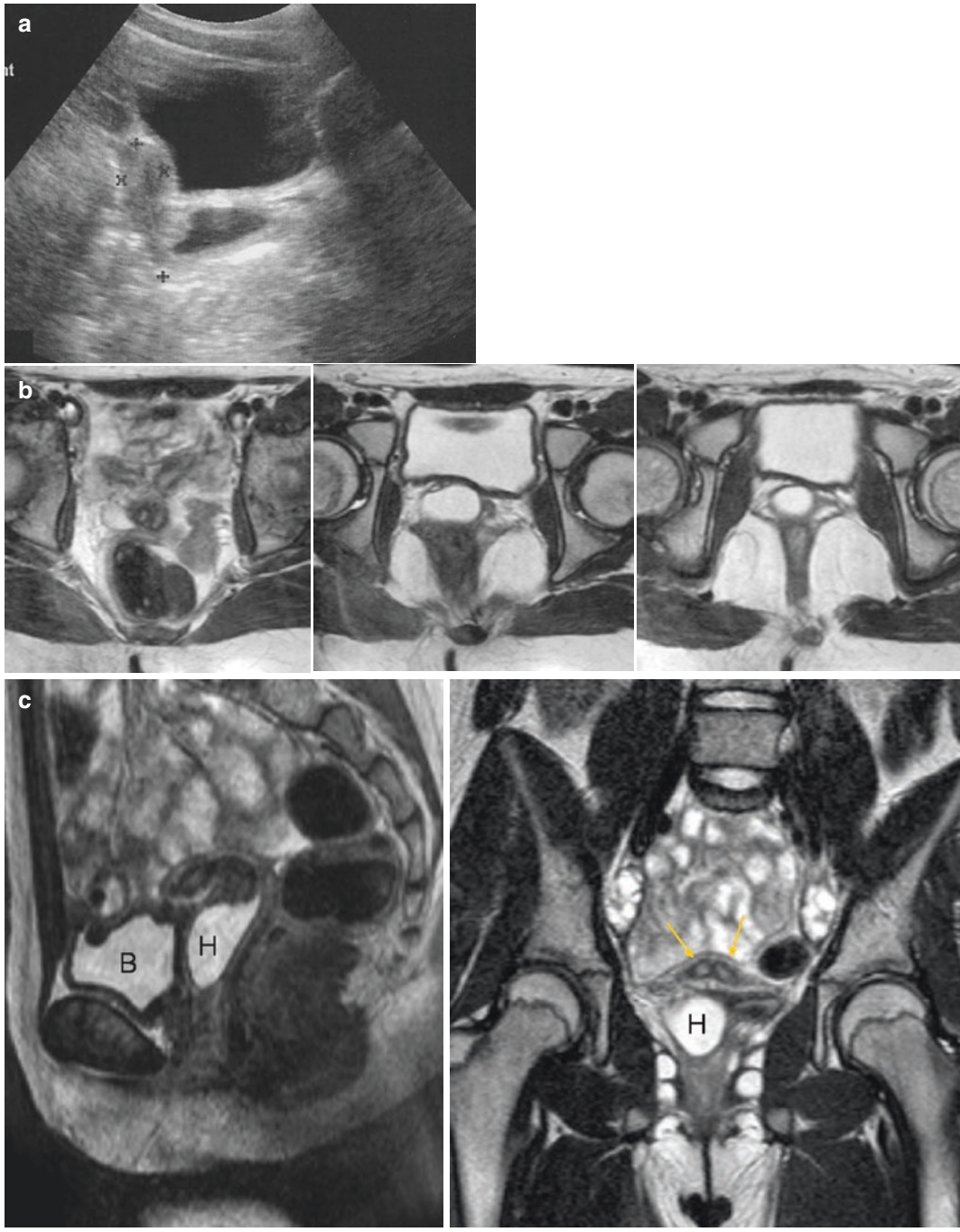

Fig. 19 Class III: Wünderlich syndrome: on ultrasound (**a**) an obstructed hemivagina is seen in an 11-year-old girl presenting with unilateral renal agenesis (not documented). Axial T2W MR images at different levels (**b**) as well as coronal and sagittal images (**c**) show two separate uteri (*arrows*) and two cervices, all of which have normal zonal anatomy indicating an uterus didelphys. In addition, a hematocele (H) due to obstruction of the right hemivagina is depicted. B (urinary bladder)

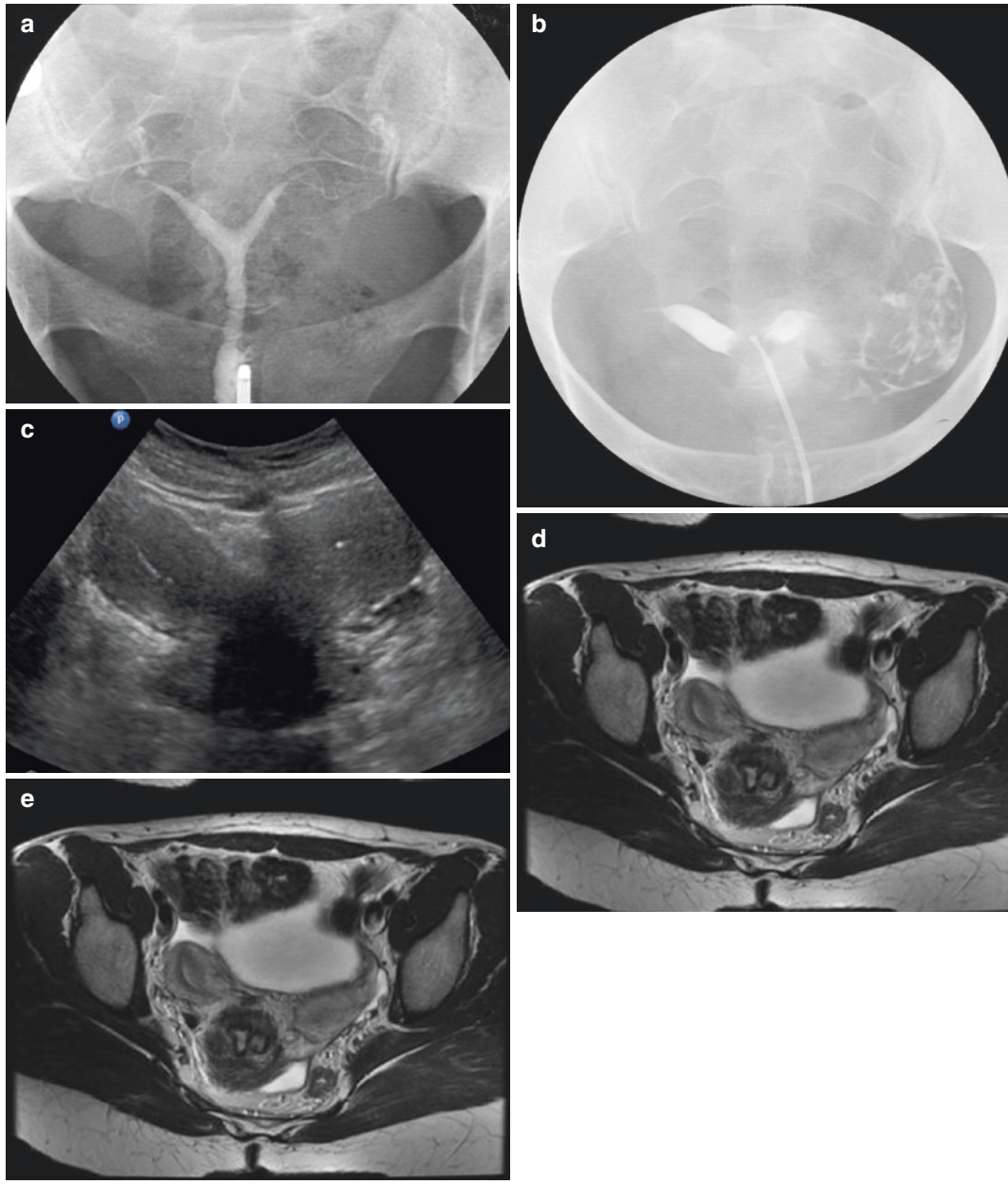

Fig. 20 Class IV: HSG shows widely splayed uterine horns with an intercornual angle >100° and with uterine fundi joined at the lower uterine segment indicating a bicornis unicollis subtype (**a**). HSG (**b**) and hysterosonography (**c**) in a different patient show uterine fundi joined at the level of the cervix suggesting a bicornis bicollis subtype

7.1.4 Class IV: Bicornuate

Partial fusion of two müllerian ducts results in a bicornuate uterus with one cervix. The uterine horns are widely divergent, the uteri fundi joined either at the uterine corpus (bicornis unicollis subtype) (Fig. 20a) or lower uterine segment (bicornis bicollis subtype) (Fig. 20b, c). In most cases there is a single cervix; however there may be two cervical openings, creating an appearance similar to septate uterus. Of all classes of MDAs, it is the bicornuate uterus that has the strongest association with cervical incompetence (Patton 1994). It is crucial to

differentiate between a bicornuate and septate uterus because surgical correction of a bicornuate uterus is not generally warranted, since it is the cervical incompetence and not the cavity malformation that is the cause of the high spontaneous abortion rate with this anomaly. In addition, an abdominal metroplasty must be performed if surgical repair of a bicornuate uterus is undertaken, as opposed to hysteroscopic septoplasty which is performed for a septate uterus (Fielding 1996).

HSG of a bicornuate uterus will demonstrate separate uterine cavities with an intercornual angle that usually exceeds 105°. With this imaging modality, however, the outer uterine contour cannot be evaluated, and overlap with the appearance of a septate uterus can occur.

Sonographic diagnosis of a bicornuate uterus is made by both analysis of the outer fundal contour and visualization of a separate endometrial stripe in each horn. However, sonographic differentiation of a bicornuate uterus from a septate uterus may be difficult.

MRI diagnostic criteria are similar to those described for sonography. Imaging should be performed during the secretory phase to maximize contrast between the T2 signal of endometrium, the junctional zone, and the myometrium. On transaxial images, the intercornual distance exceeds 4 cm, and the tissue dividing the endometrial cavities is isointense with normal myometrium. On coronal images of the fundus, obtained in the plane of the tubal ostia, the serosal concavity exceeds 1 cm (Nicolini et al. 1987).

7.1.5 Class V: Septate

Septate uterus results from failure of resorption of a septum after complete fusion of the müllerian ducts. In the majority of cases the midline septum is partial and extends for a variable distance from the fundus into the corpus or lower uterus segment (subseptate uterus). Less commonly the septum extends to the level of the cervix, forming a complete septate uterus. With a complete septate uterus, there may be two cervical openings, but this is owing to division of one canal, and not two separate cervices as occurs with a uterus didelphys (Fig. 21a–c).

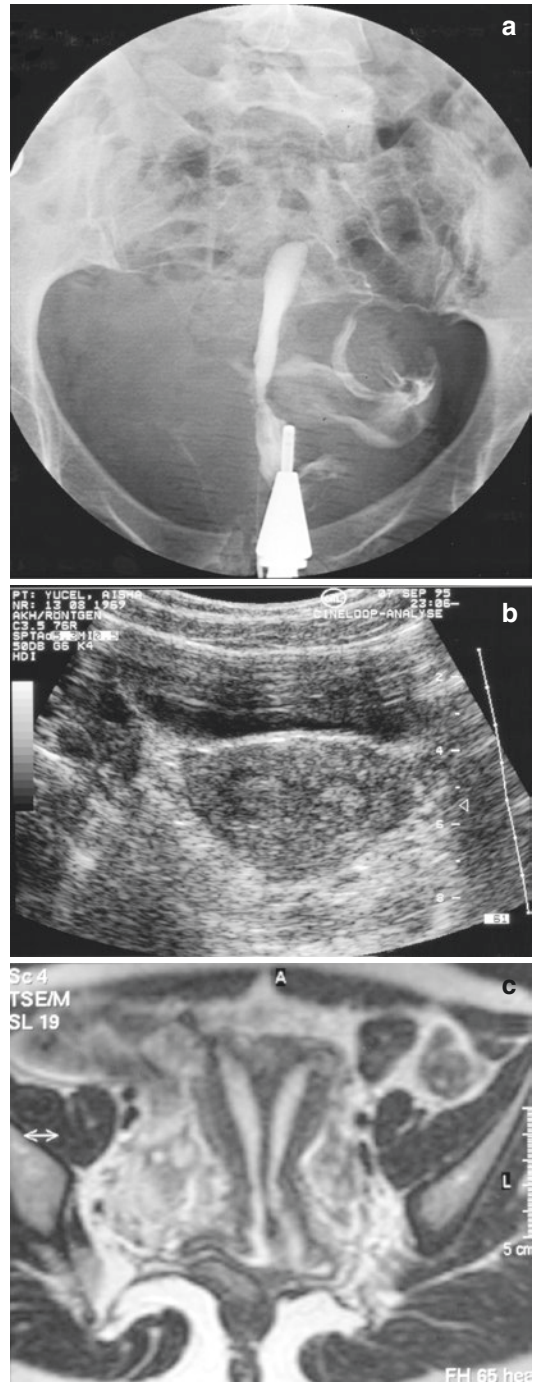

Fig. 21 Class V: complete septate uterus: on HSG one cervical opening was missed; only one uterine cavity was spilled with contrast media; a unicornuate uterus was supposed (**a**). Sonography (**b**) and coronal T2W MRI (**c**) clearly demonstrate the uterine cavity divided by a thick septum extending to the level of the cervix. The angle formed by the medial borders of the two uterine hemi-cavities is <75°

Most patients evaluated for repeated abortions and found to have a uterine anomaly will have a septate uterus (Rock 1997). Avascular fibrous septa can be safely resected hysteroscopically whereas vascularized myometrial tissue within the septum requires metroplasty as a surgical procedure for treatment of this anomaly and may enhance fetal survival, with one report indicating that 95% of patients became pregnant, 73% carried to term, and 77% delivered a live-born baby (Rock and Jones 1977).

HSG of a septate uterus demonstrates two narrowly diverging cavities, yielding a V-shape configuration with relatively straight medial borders. The angle formed by the medial borders of the two uterine hemi-cavities is usually <75°. Diagnosis of a septate uterus is often not possible by HSG because the outer uterine contour cannot be imaged, and angle measurement may be difficult.

Sonography and MRI are each superior to HSG. The external uterine contour is normally convex, flat, or minimally indented by less than 1 cm (Nicolini et al. 1987), in contrast to that of a bicornuate uterus. Coronal MRI allows the characteristic fundal changes of a septate uterus to be identified.

In addition to fundal contour, a second sonographic feature of a septate uterus is splitting of the endometrial echo by a hypoechoic band, most easily seen in the fundus.

7.1.6 Class VI: Arcuate

Formerly this MDA was classified as the mildest form of either a bicornuate or septate uterus. In 1988 the American Fertility Society issued a separate classification of arcuate uterus. Arcuate uterus should be considered a normal variant and it has no effect on fertility.

HSG of the arcuate uterus reveals a broad smooth indentation into the fundal cavity which causes a saddle-shaped appearance (Fig. 22). The indentation is approximately one-fifth the height of the uterus.

Both MRI and sonography reveal a smooth outer contour, associated with a subtle broad-based shallow indentation impressing the endometrial stripe.

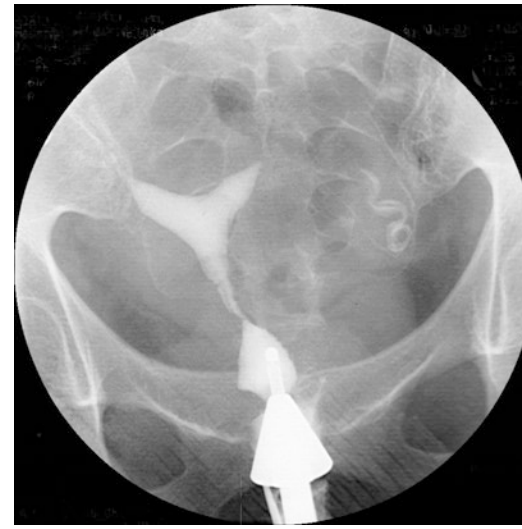

Fig. 22 Class VI: minor indentation of the fundal uterine cavity indicating an arcuate uterus. Note major dextroposition of the uterine cavity with occlusion of the right fallopian tube at the level of the intramural portion

7.1.7 Class VII: Diethylstilbestrol Related

These anomalies comprise sequelae of in utero DES exposure. DES was used to prevent miscarriage in the 1940s–1970s (Fielding 1996). Most likely as a result of DES disrupting vaginal plate development and stromal differentiation, structural anomalies occurred in the fetal vagina, cervix, uterus, and tubes. Because of the variability and overlap of features of associated cervical and vaginal malformations, these changes generally are not incorporated into the basic schematics and are reported as a subset of the primary uterine defect.

Structural anomalies encountered at physical examination are vaginal adenosis and the presence of an anterior cervical ridge or hood. Uterine cavity anomalies associated with DES exposure include hypoplasia, focal constrictions, bulbous dilatation of the lower uterine segment, and a T-shaped uterine configuration. These uterine anomalies are associated with an increased incidence of spontaneous abortion, preterm labor, and ectopic pregnancy (Patton 1994).

HSG is an excellent imaging modality for diagnosing DES-related uterine anomalies. Typical cavity contour changes seen include scalloping and constriction bands, while uterine shape abnor-

malities are hypoplasia, T-configuration, and a bulbous lower uterine segment (Fig. 23).

To date, there has been a paucity of reported ultrasound or MRI studies to detect DES-related uterine changes. Most likely, this reflects relatively subtle findings on these examinations.

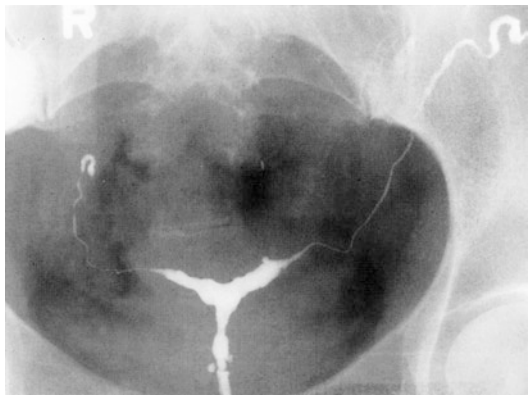

Fig. 23 Class VII. Hypoplastic T-shaped deformity of the uterus with filling of dilated glands in the cervix in a proven DES uterus

7.2 Adenomyosis

Adenomyosis is not a common cause of infertility. The frequency of symptomatic adenomyosis peaks between the ages of 35 and 50 years, and it is most often found in parous women (Braly 1999). However nulligravid women are sometimes affected and experience infertility. The exact reasons for infertility in patients with adenomyosis remain unclear, although an enlarged uterus may be associated with reduced uterine or endometrial receptivity (Fig. 24a, b).

7.3 Leiomyoma

Uterine leiomyoma, especially submucous leiomyoma, may be associated with pregnancy loss rather than infertility. Although leiomyoma is an infrequent cause of infertility, there may be some interference with sperm transport or implantation as a result of distortion, an increased surface area

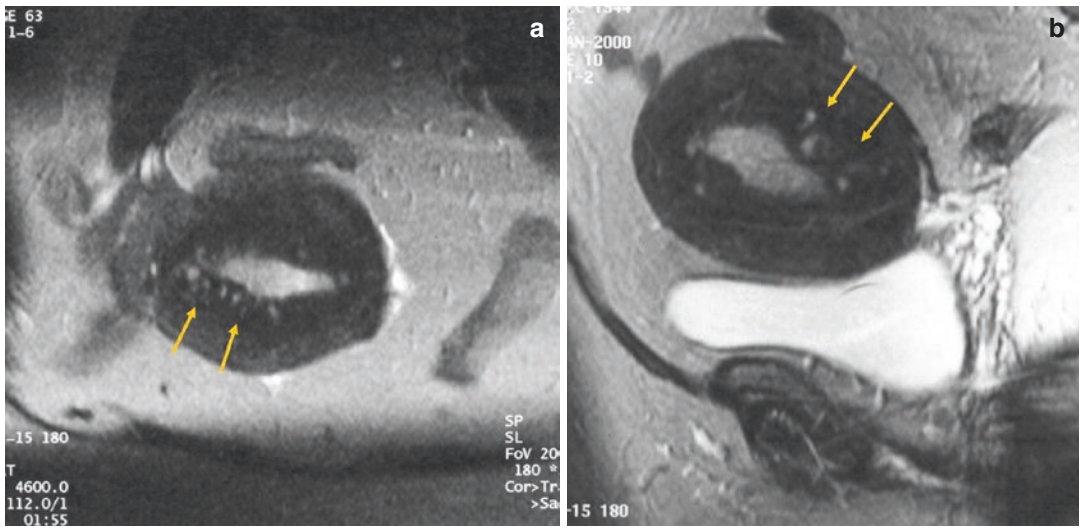

Fig. 24 Adenomyosis: multiple high signal foci predominantly in the posterior aspect of the uterus on these axial (**a**) and sagittal (**b**) T2W MR images indicating a more focal adenomyosis. Poor delineation of the junctional zone

within the uterine cavity, or impingement by the leiomyoma on the endocervical canal or interstitial portion of the fallopian tubes (Thompson and Rock 1997) (Fig. 25a, b).

Both transvaginal ultrasound and MRI are reliable methods for identification of leiomyomas. Sonohysterography can clearly demonstrate the relationship between the endometrium and submucosal leiomyomas and thus serves as an important adjunct to transvaginal US (Becker et al. 2002).

7.4 Endometriosis

Endometriosis is found in 25–50% of infertile women, and 30–50% of women with endometriosis are infertile (Schenken 1999).

Laparoscopy is the mainstay for diagnosis, staging, and treatment of the disease. Transvaginal US is the preferred imaging technique to identify ovarian endometrioma. However, US has limited usefulness in identifying peritoneal implants. MR imaging has also proved to be a useful modality for establishing an accurate diagnosis of endometriosis (Fig. 26a–c).

In conclusion, the various causes of infertility in women need to be carefully evaluated by use of the appropriate imaging techniques. The conventional HSG is still a widely available, rather safe, and rapid as well as easily performable technique to assess tubal patency. HSG is minimally invasive and also entails exposure to low ionizing radiation. Sonohysterography and sonohysterosalpingography allow evaluation of both tubal patency and uterine pathology. MR imaging is a useful modality as an adjunct for routine infertility workups. It is valuable for detection of pituitary adenoma when patients are suspected of having a disorder of the hypothalamic-pituitary-ovarian axis. The role of MR imaging in assessing the pelvic cavity in patients with infertility includes evaluation of the functioning uterus and ovaries, differentiation of müllerian duct anomalies, and accurate noninvasive diagnosis of adenomyosis, leiomyoma, and

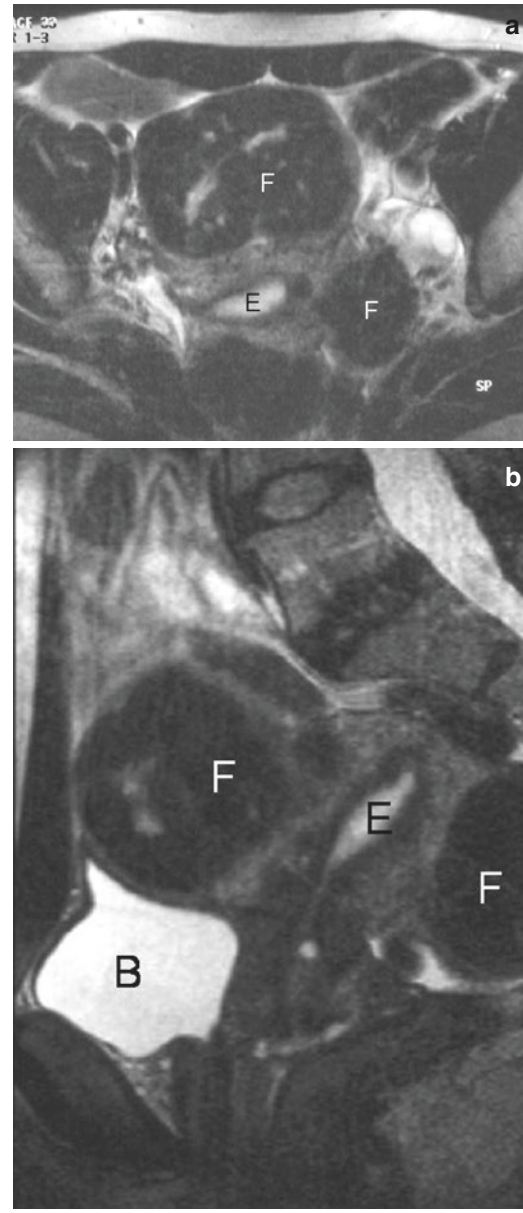

Fig. 25 Leiomyoma: enlarged uterus with large fibroids (F) in the anterior and posterior aspect of the uterus being of typical low signal intensity on this axial (**a**) and sagittal (**b**) T2W MR images. B (urinary bladder), E (endometrium)

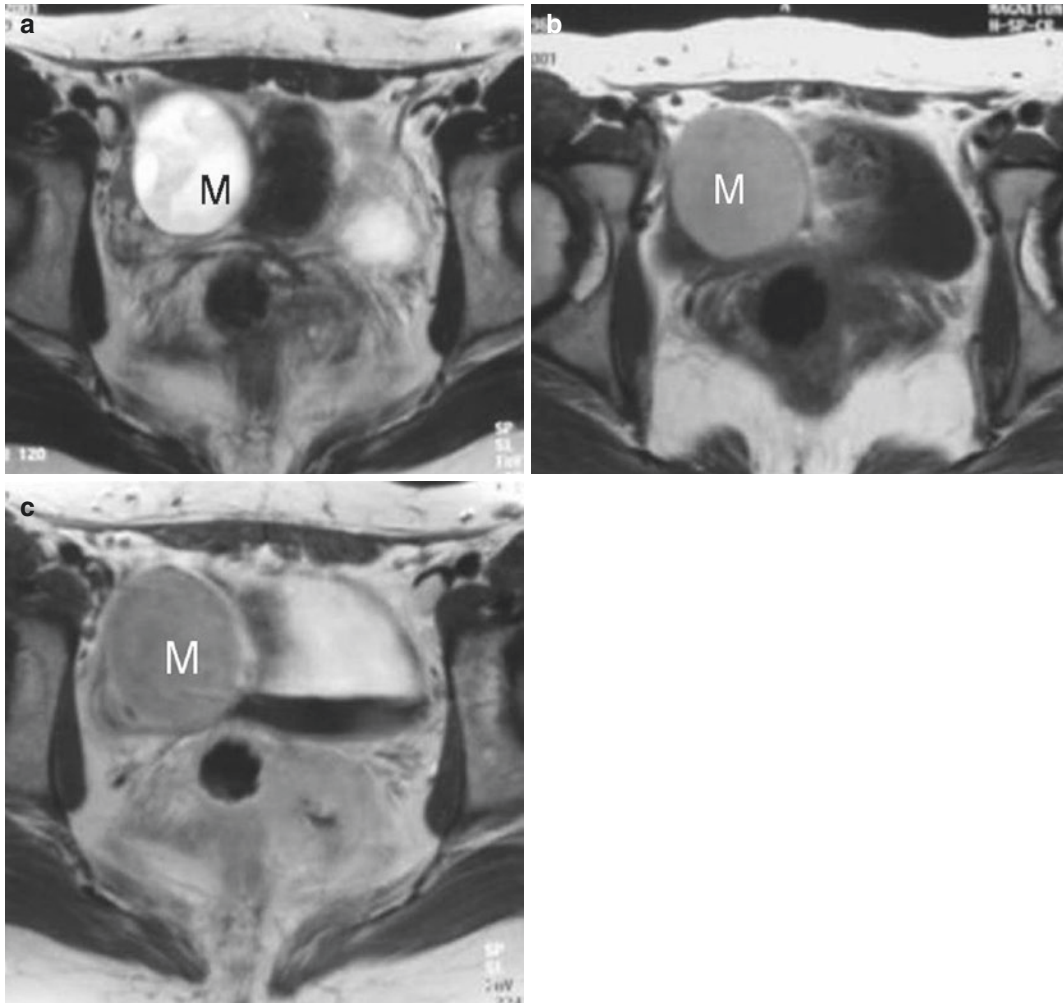

Fig. 26 Endometrioma right ovary: sharply demarcated inhomogeneous cystic mass (M) in the right ovary with predominantly bright signal intensity on axial T2W (**a**), intermediate signal intensity on axial T1W images (**b**), and no contrast uptake after iv application of Gd-DTPA (**c**)

endometriosis. MR imaging also helps to predict the outcome of conservative treatment of adenomyosis, leiomyoma, and endometriosis.

References

Bacelar AC, Wilcock D, Powell M, Worthington BS (1995) The value of MRI in the assessment of traumatic intrauterine adhesions (Asherman syndrome). Clin Radiol 50:80–83

Bartynski WS, Lin L (1997) Dynamic and conventional spin-echo MR of pituitary microlesions. AJNR Am J Neuroradiol 18:965–972

Becker E Jr, Lev-Toaff AS, Kaufman EP, Halpern EJ, Edelweiss MI, Kurtz AB (2002) The additional value of transvaginal sonohysterography over transvaginal sonography alone in women with known or suspected leiomyoma. J Ultrasound Med 21:237–247

Braly PS (1999) Disease of the uterus. In: Scott JR, Di-Saia PJ, Hammond CB, Spellacy WN (eds) Danforth's obstetrics and gynecology, 8th edn. Lippincott Williams & Wilkins, Philadelphia, PA, pp 837–855

Brody JM, Koelliker SL, Fishman GN (1998) Unicornuate uterus: imaging appearance, associated anomalies and clinical implications. AJR Am J Roentgenol 171:1341–1347

Buttram VC, Gibbons WE (1979) Müllerian anomalies: a proposed classification (an analysis of 144 cases). Fertil Steril 32:40–46

Carrington BM, Hricak H, Nuruddin RN, Secaf E, Laros RK Jr, Hill EC (1990) Müllerian duct anomalies: MR imaging evaluation. Radiology 176:715–720

Collins JI, Woodward PJ (1995) Radiological evaluation of infertility. Semin Ultrasound CT MR 16:304–316

Fielding JR (1996) MR imaging of müllerian anomalies: impact on therapy. AJR Am J Roentgenol 167:1491–1495

Fleischer AC, Kepple DM (1997) Normal pelvic anatomy as depicted by various sonographic techniques. In: Fleischer AC, Javitt HC, Jeffrey RB Jr, Jones HW III (eds) Clinical gynaecologic imaging, Philadelphia, PA, Lippincott-Raven, pp 10–22

Goldberg JM, Falcone T, Attaran M (1997) Sonohysterographic evaluation of uterine anomalies noted on hysterosalpingography. Hum Reprod 12:1251–1253

Heinonen PK, Saarikoski S, Pystynen P (1982) Reproductive performance of women with uterine anomalies: an evaluation of 182 cases. Acta Obstet Gynecol Scand 61:157–162

Hornstein MD, Schust D (1996) Infertility. In: Berek JS, Adashi EY, Hillard PA (eds) Novak's gynecology, 12th edn. Lippincott Williams & Wilkins, Baltimore, MD, pp 915–962

Imaoka I, Wada A, Matsuo M, Yoshida M, Kitagaki H, Sugimura K (2003) MR imaging of disorders associated with female infertility: use in diagnosis, treatment, and management. Radiographics 23:1401–1421

Javitt MC (1997) Magnetic resonance imaging in the diagnosis of congenital uterine anomalies. In: Fleischer AC, Javitt MC, Jeffresy RB Jr, Jones HW Jr (eds) Clinical gynaecologic imaging. Lippincott-Raven, Philadelphia, pp 299–310

Justesen P, Rasmussen F, Anderson PE Jr (1986) Inadvertently performed hysterosalpingography during early pregnancy. Acta Radiol Diagn (Stockh) 27:711–713

Kimura I, Togashi K, Kawakami S et al (1996) Polycystic ovaries: implications of diagnosis with MR imaging. Radiology 201:549–552

Kupesic S, Kurjak A (2000) Ultrasound and Doppler assessment of uterine anomalies. In: Kupesic S, de Ziegler D (eds) Ultrasound and infertility Pearl River. Parthenon, New York, NY, pp 147–153

Kurman RJ, Mazur MT (1987) Benign diseases of the endometrium. In: Kurman RJ (ed) Blaustein's pathology of the female genital tract, 3rd edn. Springer, New York, pp 292–321

Lev-Toaff AS (1996) Sonohysterography: evaluation of endometrial and myometrial abnormalities. Semin Roentgenol 31:288–298

Lindheim SR, Sprague C, Winter TC III (2006) Hysterosalpingography and sonohysterography: lessions in technique. AJR Am J Roentgenol 186(1):24–29

Lujan ME, Jarrett BY, Brooks ED, Reines JK, Peppin AK, Muhn N, Haider E, Pierson RA, Chizen DR (2013) Updated ultrasound criteria for polycystic ovary syndrome: reliable thresholds for elevated follicle population and ovarian volume. Hum Reprod 28(5):1361–1368

Margolin FR (1988) A new cannula for hysterosalpingography. AJR 151:729–730

Miki Y, Matsuo M, Nishizawa S et al (1990) Pituitary adenomas and normal pituitary tissue: enhancement patterns on gadopentate-enhanced MR imaging. Radiology 177:35–38

Mitchell DG, Gefter WB, Spritzer CE et al (1986) Polycystic ovaries: MR imaging. Radiology 160:425–429

Nicolini U, Bellotti M, Bonazzi B, Zamberletti D, Candiani GB (1987) Can ultrasound be used to screen uterine malformations? Fertil Steril 47:89–93

Outwater EK, Siegelman ES, Chiowanich P, Kilger AM, Dunton CJ, Talerman A (1998) Dilated fallopian tubes: MR imaging characteristics. Radiology 208:463–469

Patton PE (1994) Anatomic uterine defects. Clin Obstet Gynecol 37:705–721

Pellerito JS, McCarthy SM, Doyle MB et al (1992) Diagnosis of uterine anomalies: relative accuracy of MR imaging, endovaginal sonography, and hysterosalpingography. Radiology 183:795–800

Pittaway DE, Winfield AC, Maxson W, Daniell J, Herbert C, Wentz AC (1983) Prevention of acute pelvic inflammatory disease after hysterosalpingography: efficacy of doxycycline prophylaxis. Am J Obstet Gynecol 147:623–626

Rock JA (1997) Surgery for anomalies of the müllerian ducts. In: Rock JA, Thompson JD (eds) Te Linde's operative gynecology, 8th edn. Lippincott-Raven, Philadelphia, Pa, pp 687–729

Rock JA, Jones HW Jr (1977) The clinical management of the double uterus. Fertil Steril 28:798–806

Sadowski EA, Elizabeth A, Jennifer E, Ochsner JE, Jody M, Riherd JM, Frank R, Korosec FR, Agrawal G, Pritts EA, Klie MA (2008) MR hysterosalpingography with an angiographic time-resolved 3D pulse sequence: assessment of tubal patency. AJR Am J Roentgenol 191:1381–1385

Schenken RS (1999) Endometriosis. In: Scott JR, Di-Saia PJ, Hammond CB, Spellacy WN (eds) Danforth's obstetrics and gynecology, 8th edn. Lippincott Williams & Wilkins, Philadelphia, PA, pp 669–675

Sholkoff SD (1987) Balloon hysterosalpingography catheter. AJR 149:995–996

Soules MR, Spadoni LR (1982) Oil versus aqueous media for hysterosalpingography: a continuing debate based on many options and few facts. Fertil Steril 38:1–11

Strübbe EH, Willemsen WNP, Lemmens JAM, Thijn CJP, Rolland R (1993) Mayer-Rokitansky-Küster-Hauser syndrome: distinction between two forms based on excretory urographic, sonographic, and laparoscopic findings. AJR Am J Roentgenol 160:331–334

The American Fertility Society classifications of adnexal adhesions, distal tubal obstruction, tubal occlusion secondary to tubal ligation, tubal pregnancies, mül-

lerian anomalies and intrauterine adhesions (1988). Fertil Steril 49:944–955

Thompson JD, Rock JA (1997) Leiomyoma uteri and myomectomy. In: Rock JA, Thompson JD (eds) Te Linde's operative gynecology, 8th edn. Lippincott-Raven, Philadelphia, PA, pp 731–770

Thurmond AS, Uchida BT, Rosch J (1990) Device for hysterosalpingography and fallopian tuber catherization. Radiology 174:571–572

Togashi K, Nishimura K, Itoh K, Fujisawa I, Nakano Y, Torizuka K, Ozasa H, Ohshima M (1987) Vaginal agenesis: classification by MR imaging. Radiology 162:675–677

Tukeva TA, Aronen HJ, Karjalainen PT, Molander P, Paavonen T, Paavonen J (1999) MR imaging in pelvic inflammatory disease: comparison with laparoscopy and US. Radiology 210:209–216

MR Pelvimetry

Leonhard Schäffer, Ernst Beinder†,
and Rahel A. Kubik-Huch

Contents

L. Schäffer, MD • E. Beinder MD†
R.A. Kubik-Huch, MD MPH (✉)
Kantonsspital Baden AG, Departments of Obstetrics and Radiology, 5404 Baden, Switzerland
e-mail: rahel.kubik@ksb.ch

Abstract

Arrest of labor with the necessity of performing secondary cesarean section is a major cause of maternal morbidity and mortality. The fetus is likewise affected by prolonged labor. Pelvimetry is performed to identify those women in whom an attempt at vaginal delivery is likely to fail due to a narrow pelvis or pelvic anomaly. Hence, the clinical significance of pelvimetry depends on how the following questions are answered:

- Is primary cesarean section associated with a lower morbidity and mortality of mother and child than secondary cesarean section after arrested labor has been diagnosed?
- Can arrested labor be treated effectively?
- Is there a reproducible method of pelvimetry with few side effects?
- Is there evidence from randomized and controlled studies that pelvimetry improves maternal and/or fetal outcome?

1 Clinical Background

Arrest of labor with the necessity of performing secondary cesarean section is a major cause of maternal morbidity and mortality. The fetus is likewise affected by prolonged labor. Pelvimetry is performed to identify those women in whom an attempt at vaginal delivery is likely to fail due to a narrow pelvis or pelvic anomaly. Hence, the clinical significance of pelvimetry depends on how the following questions are answered:

Med Radiol Diagn Imaging (2017)
DOI 10.1007/174_2017_2, © Springer International Publishing AG
Published Online: 11 February 2017

- Is primary cesarean section associated with a lower morbidity and mortality of mother and child than secondary cesarean section after arrested labor has been diagnosed?
- Can arrested labor be treated effectively?
- Is there a reproducible method of pelvimetry with few side effects?
- Is there evidence from randomized and controlled studies that pelvimetry improves maternal and/or fetal outcome?

1.1 Primary Versus Secondary Cesarean Section

The aim of pelvimetry is to identify maternal pelvic deviations that preclude vaginal delivery or would considerably prolong labor. If the results of pelvimetry suggest that vaginal delivery would be very difficult, primary cesarean section should be suggested. Both the mother and infant can thus be spared secondary cesarean section after protracted labor. The clinical significance of pelvimetry crucially depends on whether primary cesarean section can reduce maternal and fetal morbidity as compared with secondary cesarean section.

Cesarean section is performed as a primary (scheduled) or secondary (nonscheduled, after failure of labor to progress) procedure. The total number of cesarean sections, i.e., the sum of primary and secondary interventions, is 15–30% in Western industrialized countries. The mortality risk associated with vaginal delivery and cesarean section was determined in a study in Bavaria by Welsch (Müttersterblichkeit 2004).

Cesarean section mortality attributable to the intervention is defined as the number of deaths occurring per 1000 cesarean sections during or within 42 days of the intervention and that are due to surgical or anesthesia-related complications in women who were healthy before the operation and had no pregnancy-related risks. In the survey by Welsch, the maternal mortality risk of vaginal delivery versus cesarean section was 1:2.3 for the period from 1995 to 2000. However, the mortality rates no longer differ if only planned cesarean sections are compared with vaginal deliveries and may even be lower (D'Souza et al. 2013).

These figures underline that secondary cesarean sections after protracted labor or arrest of labor account for the excessive mortality of women during delivery.

Prolonged labor or arrest may have further adverse effects on mother and child:

- Perinatal morbidity and mortality: The duration of labor, in particular of the second stage, correlates with a decrease in fetal pH and pO_2 and an increase in pCO_2. Although fetal death during delivery has become rare, asphyxia contributes to perinatal morbidity. Detachment of the placenta due to uterine hyperactivity occurs in 1% of all pregnancies. Protracted labor often ends in vaginal operative delivery with the risk of fetal injury.
- Maternal morbidity: Protracted labor involves numerous complications for the mother. Rupture due to overextension of a uterus not operated on before is nearly always due to excessively prolonged labor. The higher need for vaginal operative delivery in women with protracted labor is associated with a higher rate of maternal injuries, pain, hematomas, urinary retention, and anemia as compared with spontaneous delivery (Angioli et al. 2000). Women with prolonged labor and secondary cesarean section have an increased risk of infection or puerperal fever. Atonic postpartum hemorrhage is a characteristic of long labor and again increases the risk of protracted recovery and infectious complications.
- Birth experience: No adequate systematic data are available on the emotional stress associated with prolonged and traumatic labor with secondary cesarean section. However, many women have problems coping with such an experience and do not become pregnant again.

In summary, prolonged labor and secondary cesarean section bear a considerable risk of maternal morbidity and mortality and also increase fetal morbidity. Modern obstetrical management therefore aims to ensure uncomplicated and speedy spontaneous delivery or, in women where this goal seems unattainable (or is not the mother's preferred option), to plan elective primary cesarean section beforehand. Hence, techniques that can predict the probability of an uncomplicated vaginal delivery before the onset of labor are of the utmost clinical significance.

1.2 Can Arrested Labor Be Treated Effectively?

Normal delivery is based on the complex interaction of maternal factors, fetal properties, and adequate labor. If this interaction of "passages, passenger, and powers" is disturbed, labor is protracted or even arrested. The failure of labor to progress is therefore not a diagnosis but a symptom that is amenable to treatment (e.g., when caused by inadequate uterine contractions) or not (e.g., absolute cephalopelvic disproportion). Isolated evaluation of either of the three factors, passages, passenger, and powers, is of limited value as, for instance, cephalopelvic disproportion can be diagnosed only if one looks at both the maternal pelvis and the fetus ("this pelvis is too small for this fetus").

1.3 Abnormal Length of Labor: Diagnosis and Causes

1.3.1 Diagnosis

The onset of delivery is most commonly defined as the occurrence of regular and painful uterine contractions that result in progressive dilatation and effacement of the cervix.

The course of delivery is determined by the following variables:

- Size and shape of the maternal pelvis
- Flexibility of the maternal soft tissues in the pelvis and adaptation of the ligaments and bony pelvis to the fetus
- Remodeling of the cervix
- Regular birth mechanism of the fetus
- Fetal head molding
- Efficient uterine contractions

The results reported by Friedman in the 1950s as the basis for diagnosing delayed labor have lately been updated (Zhang et al. 2010; Friedman 1955, 1956). Arrest of labor during the first stage (the stage of cervical dilatation) now is the absence of any progression of labor over a period of 4 h despite adequate contractions or 6 h with inadequate contractions diagnosed at cervical dilatation >6 cm and ruptured membranes corresponding to active phase of labor Spong et al. 2012).

The second stage (complete dilatation of the cervix until the onset of expulsive contractions) should not exceed 2 h of pushing in multiparous and 3 h of pushing in primiparous women. However, longer periods may be appropriate as long as progress is being documented and additional factors such as peridural anesthesia or malposition are present.

1.3.2 Inadequate Progression of Labor due to Maternal Factors ("the Passage")

1.3.2.1 Cephalopelvic Disproportion

Failure of adequate progression of labor due to cephalopelvic disproportion with imminent fetal asphyxia is the most common reason to perform secondary cesarean section. Arrest is typically caused by a combination of a large infant, an abnormal birth mechanism, and a narrow maternal pelvis. Detectable abnormal narrowing with an absolute disproportion occurs in 0.5–1% of all deliveries today (Fig. 1). The incidence of

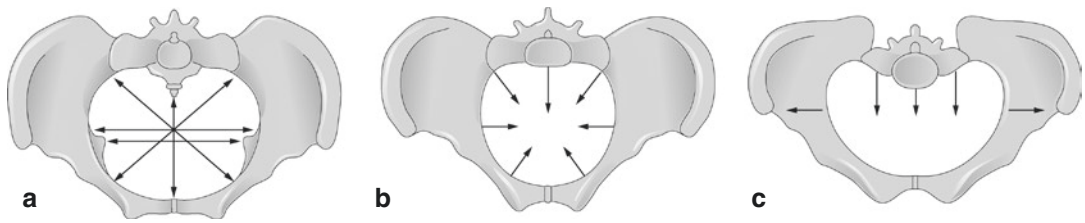

Fig. 1 (**a**–**c**) Pelvic shapes from *left* to *right*: (**a**) normal pelvic shape and width (*cranial view*), (**b**) generally narrow pelvis (all pelvic parameters are shortened), (**c**) platypelloid pelvis with a markedly shorter obstetric conjugate

Table 1 Features of different pelvic shapes in comparison with the gynecoid (normal) pelvis

Pelvic shape	Pelvic inlet	Pelvic outlet	Obstetric conjugate
Android	Normal	Shorter	Normal
Anthropoid	Shorter	Normal	Longer
Platypelloid	Longer	Normal	Shorter

An android pelvis is associated with a higher incidence of deep transverse arrest, an anthropoid pelvis with a higher incidence of dorsoposterior position, and a platypelloid pelvis with high longitudinal position. All three pelvic shapes are characterized by protracted labor

borderline pelvic findings in which the size of the child and the birth mechanism together decide whether spontaneous delivery will be possible is much higher (Table 1).

Other maternal factors that may prolong or arrest labor include cervical leiomyomas or scarring of the cervix after prior surgery (conization, cerclage). Rare causes that prevent fetal descent are pelvic tumors such as large ovarian cysts or a pelvic kidney.

1.3.3 Inadequate Progression of Labor due to Fetal Factors ("the Passenger")

An abnormal birth mechanism (malposition or malpresentation of the fetal head) prevents adequate progression of labor just as often as maternal factors. Other fetal causes are macrosomia or fetal anomalies associated with macrohydrocephalus or an abnormally large circumference of the fetal abdomen or rump (pronounced ascites, sacrococcygeal teratoma).

1.3.4 Inadequate Progression of Labor due to Inefficient Contraction ("the Powers")

Weak uterine contractions as a cause of inadequate progression of labor are most amenable to treatment. Inefficiency may become manifest as hypoactive, hyperactive, or uncoordinated contractions and hypertonic motility. Both hypoactivity and hyperactivity may occur secondary to mechanical obstruction.

1.4 Interventional Management of Inadequate Progression of Labor

Of the three components involved in normal delivery ("passages, passenger, and powers"), only labor ("powers") is easily amenable to treatment.

Assistance in women with hypoactive and uncoordinated contractions is recommended if progression is delayed and cephalopelvic disproportion has been excluded as the cause. Oxytocin is the drug of first choice (Cardozo et al. 1982).

In summary, arrested labor is often a multifactorial process resulting from the complex interaction of maternal pelvic size, size and presentation of the fetus, and labor activity. Effective therapeutic measures are only available for inadequate labor activity while no treatment is available for most other causes of arrested labor.

2 Clinical Methods of Pelvimetry

2.1 External Pelvimetry and Evaluation of Michaelis's Rhomboid

The normal values for the external pelvic measures are 25–26 cm for the interspinous distance, 28–29 cm for the intercrest distance, 31–32 cm for the intertrochanteric distance, and 20 cm for the external conjugate. The internal conjugate is calculated as the external conjugate minus 9 cm.

Michaelis's rhomboid is the rectangular area over the sacral bone formed by the dimple below the spinal processes of L3 to L4 (upper depression), the two posterior spines of the ilia (lateral depressions), and the groove at the distal end of the vertebral column (lower depression). The rhomboid is usually a square, while its height increases considerably relative to its width in women with general narrowing of the pelvis. The lateral dimples are elevated in women with an android pelvis.

External pelvimetry will identify only pronounced deviations from the normal pelvic configuration that are rare in the European population.

2.2 Palpation of the Pelvis

The aim of palpation of the pelvis is to identify prominent bony structures that may obstruct labor. The examiner evaluates the angle of the pubic arch (>90°), the promontory (cannot be reached), the anterior surface of the sacrum (smooth), the coccyx (not prominent and elastic), and the ischial spines (not prominent).

Palpation has the disadvantage that the results cannot be standardized. The examination is extremely uncomfortable for the patient.

3 MR Pelvimetry

Magnetic resonance (MR) pelvimetry was introduced in 1985 by Stark et al. (1985). MRI offers the benefit of accurate measurements of bony pelvic structures without exposure to ionizing radiation. The technique further allows imaging of soft-tissue structures, including the fetus, and has therefore replaced X-ray and computed tomography (CT) pelvimetry to become the modality of choice for obstetric pelvimetry (Stark et al. 1985; Pfammatter et al. 1990; Keller et al. 2003).

3.1 Safety Issues and Contraindications

Whereas prenatal X-ray exposure has been associated with an increased risk of childhood cancer (Stewart and Kneale 1968; Doll and Wakeford 1997), MRI does not use ionizing radiation. However, theoretically, safety issues could be related to possible adverse biologic effect associated with exposure to the static magnetic, gradient magnetic, and RF electromagnetic fields. Numerous studies of MRI in pregnant women have not revealed any experimental or clinical evidence of fetal harm. Thus, to our current knowledge, MRI is considered safe for both the mother and the developing fetus (Kanal et al. 1993; Baker e al. 1994; Masselli et al. 2013; DeWilde et al. 2005; Shellock Frank and Crues John 2003; Ray Joel et al. 2016).

Nevertheless, there is at present still a general consensus that MRI should be performed in the first trimester of pregnancy only if there are clear medical indications, since rapid organogenesis takes place at this time and the fetus is thus most susceptible to any potentially hazardous external influences.

In our institution, MR pelvimetry is typically performed in the last trimester of pregnancy in women whose previous delivery was complicated by protracted labor with strong suspicion for cephalopelvic disproportion who wish to undergo a trial of labor. Alternatively, MR pelvimetry can be performed postpartum in women who plan to become pregnant again.

MR pelvimetry is a short examination, approximately 10 min examination time, without the need of intravenous contrast agents.

Due to the lower energy deposition in tissue, gradient-echo sequences might be preferred to spin-echo sequences for MR pelvimetry in pregnant women (Wright et al. 1992; Wentz et al. 1994; Urhahn et al. 1991; Michel et al. 2002; van Loon et al. 1990; Liselele et al. 2000; Pattinson and Farrell 1997; Van Loon et al. 1997).

On the other hand, T2-weighted spin-echo sequences allow for better assessment of soft tissue structures including the uterus. In our experience, most institutions have therefore now switched to T2-weighted spin-echo imaging.

Pregnant patients should be informed that, to date, there has been no indication that the use of clinical MR imaging during pregnancy has produced deleterious effects, and the MR pelvimetry may be performed with oral and written informed consent (Masselli et al. 2013).

A substantial contraindication to MRI, in general, is claustrophobia; other contraindications such as pacemakers and metallic splinters are comparatively rare in the obstetric population.

It should be kept in mind that many women referred for MR pelvimetry are unfamiliar with MRI and may be intimidated by the sheer bulk of the equipment. Despite current evidence that

MRI has no adverse fetal effects and of which, as discussed above, the women should be informed before MRI, the noise and claustrophobia of an MR exam may well induce fear for the fetus when imaging pregnant women, and they should thus be especially well cared for during the exam by the staff of the MRI suite.

In women with physical effects like vena cava compression syndrome that may occur in late pregnancy, imaging can be performed in the lateral decubitus position.

3.2 MR Imaging Protocol

It has been shown in the literature that there are no significant differences in pelvimetric measurements between spin-echo and gradient-echo sequences (Keller et al. 2003; Wentz et al. 1994; Urhahn et al. 1991).

MR pelvimetry is usually performed in the supine position. Images of the maternal pelvis are acquired with the body coil in axial, sagittal, and oblique (in a plane through the symphysis and sacral promontory) orientation as shown in Fig. 2.

In our institution, MR pelvimetry is always performed on a 1.5-T scanner. We are using T2-weighted turbo spin-echo (TSE) sequences. T1-weighted fast-spoiled gradient-echo sequences (FSPGR) might be used alternatively as discussed above. A large field-of-view (FOV), e.g., 360 mm, is used. Total imaging time is approximately 10 min.

3.3 Image Analysis

After the MR examination, pelvimetric measurements are performed on a workstation using the exterior surface of the appropriate bony cortex as the measuring point (Figs. 2, 3, and 4). The following pelvic distances are measured:

- The obstetric conjugate from the sacral promontory to the top inner cortex of the pubic bone at the symphysis is assessed in the midsagittal plane.

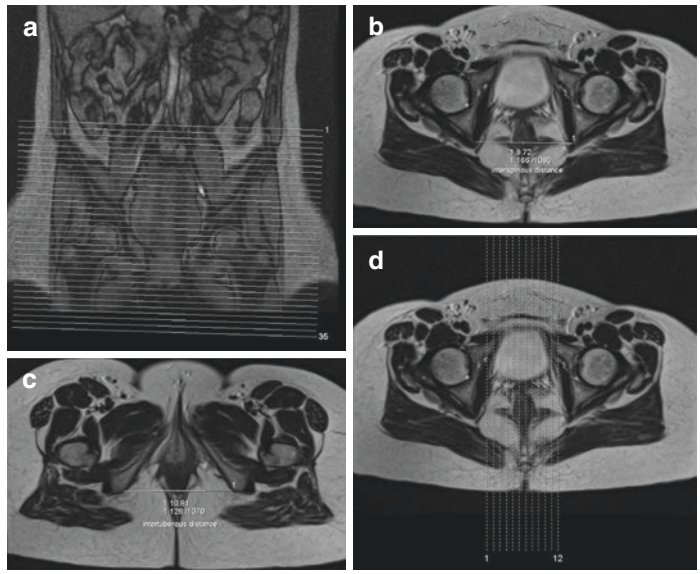

Fig. 2 (**a**–**g**) Imaging protocol for MR pelvimetry in a 34-year-old woman with a history of secondary cesarean section and retroverted uterus. (**a**) Coronal localizing image for the axial plane (TRUFI, TR 6.0 ms, TE 2.53 ms, FOV 400 mm). (**b**) Axial T2-weighted TSE sequence at the level of the interspinous distance (TSE, TR 4500 ms, TE 102 ms, FOV 360 mm). (**c**) Axial T2-weighted TSE sequence at the level of the intertuberous distance (for parameters see (**b**)). (**d**) Localizing image for the midsagittal plane (for parameters see (**b**, **c**)). (**e**) Sagittal T2-weighted TSE sequence (TSE, TR 3200 ms, TE 102 ms, FOV 350 mm): the obstetric conjugate and sagittal outlet are measured in the midsagittal plane. (**f**) Sagittal localizing image for transverse diameter (for parameters see (**e**)). (**g**) Coronal-oblique T2-weighted TSE sequence (TSE, TR 3200 ms, TE 102 ms, FOV 360 mm): the transverse diameter represents the widest transverse distance

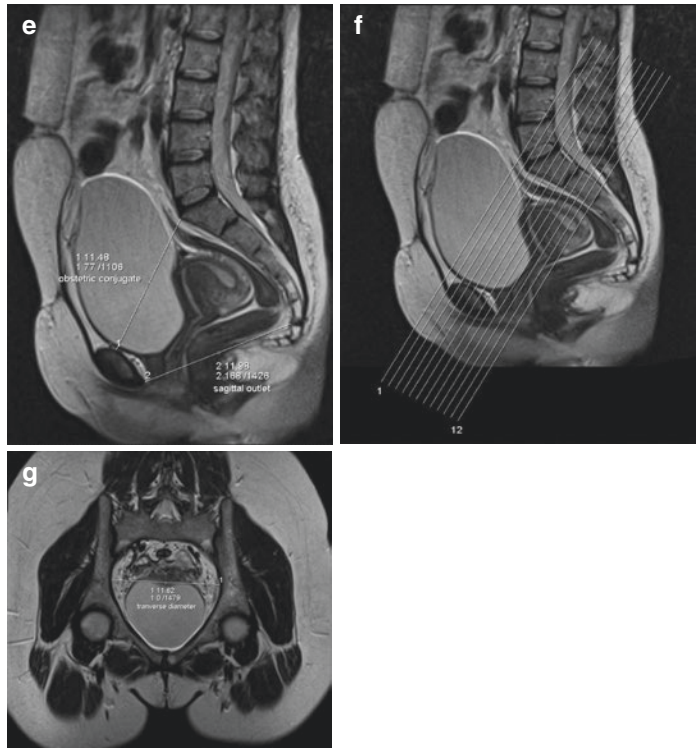

Fig. 2 (continued)

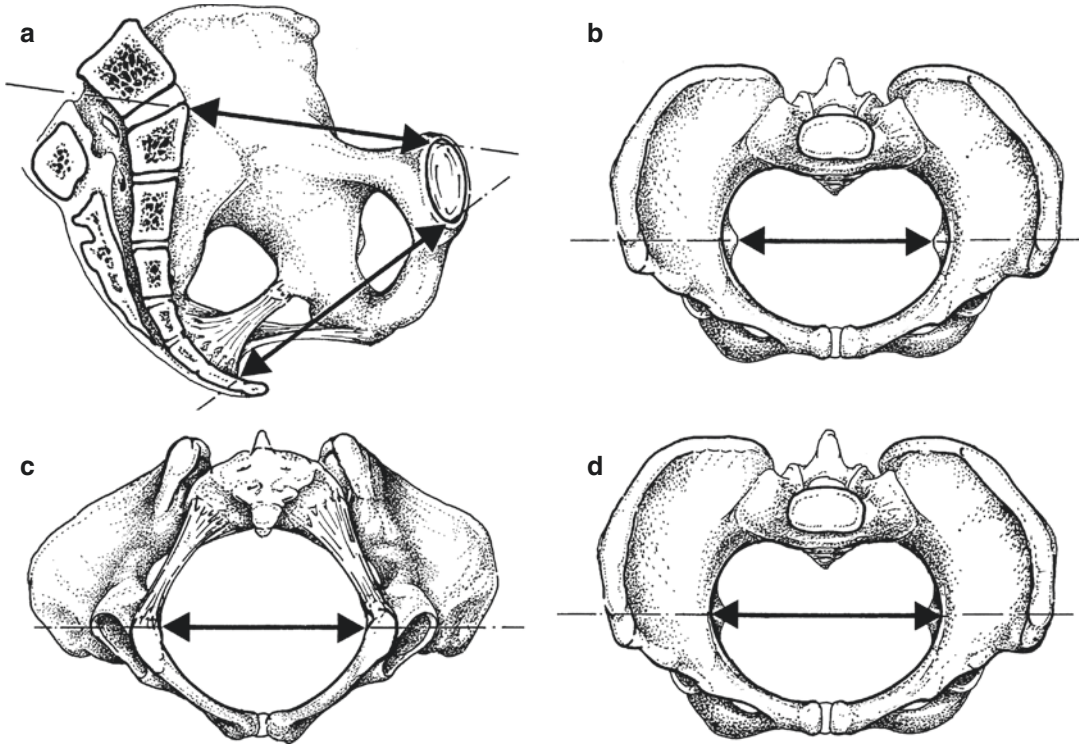

Fig. 3 (**a**–**d**) Pelvimetric diameters (drawings by G. Roth). (**a**) Obstetric conjugate and sagittal outlet. (**b**) Interspinous diameter. (**c**) Intertuberous diameter. (**d**) Transverse diameter (From Michel et al. 2002)

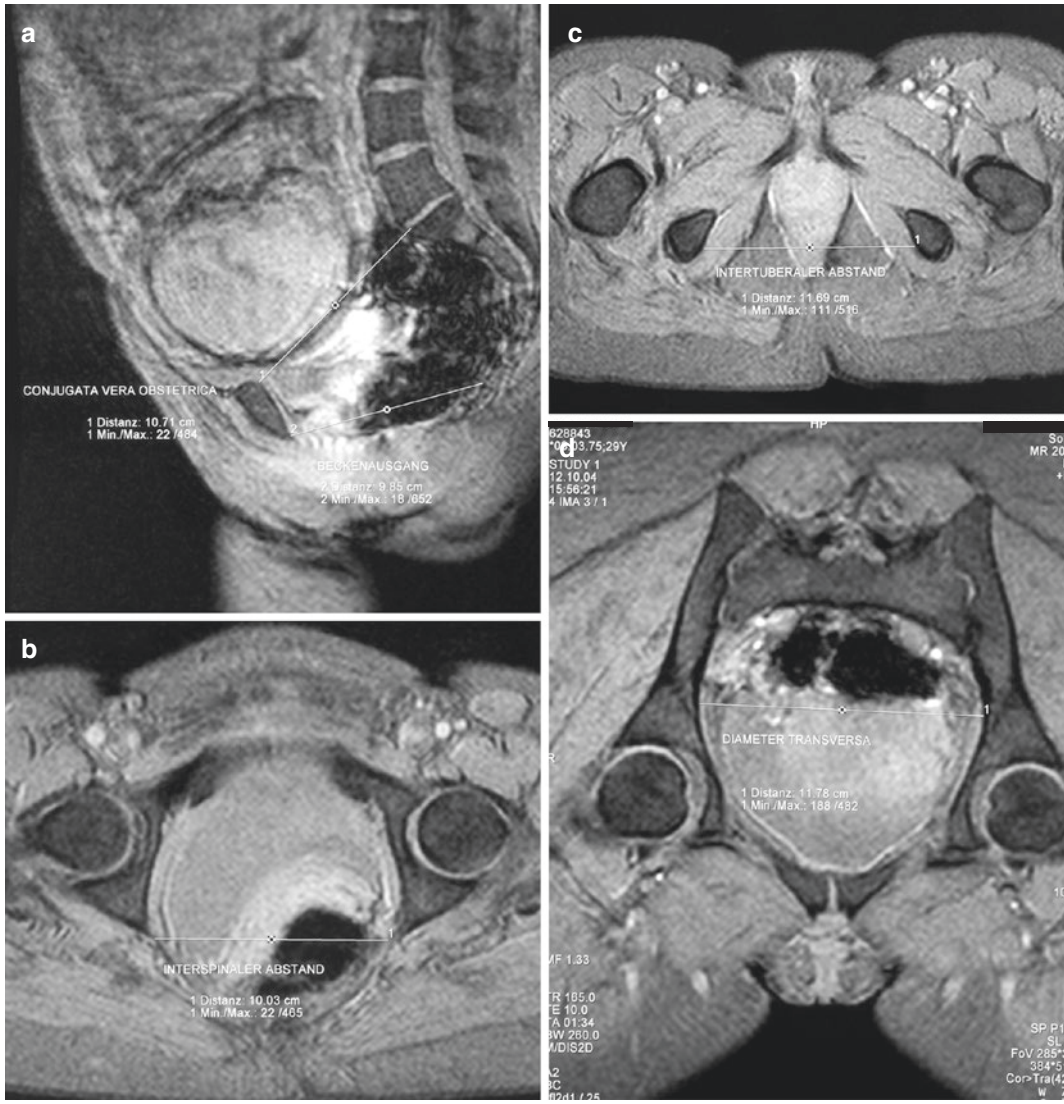

Fig. 4 (**a**–**d**) MR pelvimetry (T1-weighted gradient-echo imaging) in a 29-year-old pregnant woman in the last trimester with small pelvic dimensions. Vaginal delivery was attempted but failed and secondary cesarean section became necessary. The midsagittal section shows (**a**) the obstetric conjugate (10.7 cm) and sagittal outlet (9.8 cm). Axial sections show (**b**) the interspinous distance (10.0 cm), measured at the level of the foveae of the femoral heads, and (**c**) the intertuberous distance (11.7 cm). The oblique section (**d**) shows the transverse diameter (11.8 cm)

- The sagittal outlet, from the end of the sacrum to the bottom of the inner cortex of the symphysis, is also determined in the midsagittal plane.
- The interspinous distance represents the narrowest distance between the ischial spine some millimeters below or in the plane through the fovea capitis. It is measured in the axial plane.
- The intertuberous distance is the widest distance between the ischial tuberosities and is also measured in the axial plane.
- The transverse diameter represents the largest transverse distance (through the promontory and the symphysis) in the oblique axial plane (Keller et al. 2003; Michel et al. 2002).

In our institution, all radiology suite technologists have been trained to select the appropriate images and measure the distances. Measurement is supervised by the radiologist writing the final report.

3.4 Reference Values for MR Pelvimetry

The groundwork in pelvimetry was laid using conventional radiography. Parameters were measured on lateral and anteroposterior views using various techniques to correct the distortion resulting from different distances from the film. These methods have since been superseded by cross-sectional imaging using computed tomography and, in particular, MRI. Nevertheless, values determined by plain radiography were still often used for guidance in the routine clinical setting. Yet studies comparing plain radiography and MR pelvimetry in the same population have described differences in some parameters, e.g., in intertuberous diameter (Wentz et al. 1994; van Loon et al. 1990).

MR pelvimetric reference values in a large study population, stratified by delivery modality, have been established by our own group (Keller et al. 2003). Results are shown in Table 2.

It was demonstrated that the pelvimetric parameters associated with the largest intra- and interobserver error and intraindividual variability are the intertuberous distance and sagittal outlet. Obstetric decision-makers should therefore treat them with caution (Keller et al. 2003).

Table 2 Reference values for MR pelvimetry (Keller et al. 2003) based on 100 women undergoing spontaneous vaginal delivery

Reference values ± SD (cm)	
Obstetric conjugate	12.2 ± 0.9
Sagittal outlet	11.6 ± 1.0
Interspinous diameter	11.2 ± 0.8
Intertuberous diameter	12.1 ± 1.1
Transverse diameter	13.0 ± 0.9

4 Can Pelvimetry Improve Maternal and/or Fetal Outcome?

Only few published studies have investigated the role of external pelvimetry. A prospective cohort study of primiparous African women showed that a combination of maternal height measurement and clinical external pelvimetry can identify a subgroup of patients with a high likelihood of cephalopelvic disproportion (Liselele et al. 2000). Comparable studies that present recent and robust data for Western countries are not available.

A Cochrane review lists four randomized controlled trials (RCT) on pelvimetry for fetal cephalic presentation (Pattinson and Farrell 1997). All of these studies were performed using radiographic pelvimetry. The pelvimetry group had a higher rate of cesarean sections while fetal asphyxia and perinatal mortality tended to be lower, but the difference did not reach significance (OR 0.61, CI 0.34–1.11 and OR 0.51, CI 0.18–1.42, respectively). Due to the small number of patients investigated and the poor quality of the studies quoted, the Cochrane review concludes that the available evidence is not sufficient to prove a significant fetal benefit of radiographic pelvimetry in cephalic presentation.

One RCT has investigated pelvimetry in breech presentation (Van Loon et al. 1997). In this study, Van Loon et al. (1997) demonstrate that pelvimetry significantly reduces the rate of emergency cesarean sections. More recent studies in smaller patient populations show promising results using pelvimetry (mostly performed by MRI) in combination with sonographic weight measurement of the fetus (Spörri et al. 2002; Fox et al. 2004; O'Brien et al. 2002), but these findings must be confirmed by RCTs.

5 Indications for Pelvimetry

5.1 Breech Presentation and Maternal Preference for Spontaneous Delivery

Breech presentation is a common obstetric abnormality occurring in 3–5% of single pregnancies

and 10–15% of multiple pregnancies, but there is no agreement about its most suitable obstetric management. The Canadian Medical Research Council (MRC) initiated an international randomized multicenter trial of planned vaginal birth versus planned cesarean section for breech presentation at term after an uncomplicated pregnancy (Hannah et al. 2000). The results show that planned cesarean section reduces the fetal complication rate while not affecting the maternal complication rate, and the authors conclude that planned cesarean section is the optimal method of delivery for a fetus in breech presentation.

Following publication of these results, the rate of primary cesarean sections for breech presentations increased to up to 80%. Nevertheless, spontaneous delivery in breech presentation may be the preferred option of the mother. In such cases, it is particularly important to exclude cephalopelvic disproportion.

5.2 After Cesarean Section due to Arrest of Labor

The probability of secondary cesarean section after spontaneous onset of labor is about 10% in women without prior cesarean section as opposed to 30–50% in women having had a cesarean section for dystocia before (Abilgaard et al. 2013). In order to reduce the rate of secondary cesarean section, we perform pelvimetry in these patients when high suspicion for cephalopelvic disproportion is present and recommend primary cesarean section for future pregnancies in those women who are found to have a narrow pelvis because they are at high risk of renewed arrest of labor.

5.3 Clinically Conspicuous Abnormalities of Pelvic Shape and Status Post Pelvic Fracture

Only 0.5–1% of all pregnant women have such obvious pelvic anomalies that absolute cephalopelvic disproportion is highly likely. The risk of absolute disproportion is especially high in women after pelvic fracture or with diseases that alter pelvic shape (osteochondroplasia, osteomalacia). In these cases, pelvimetry is mandatory.

References

Abilgaard H et al (2013) Cervical dilation at the time of cesarean section for dystocia – effect on subsequent trial of labor. Acta Obstet Gynecol Scand 92:193–197

Angioli R, Gomez-Marin O, Cantuaria G, O'Sullivan JM (2000) Severe perineal lacerations during vaginal delivery: the University of Miami experience. Am J Obstet Gynecol 182:1083–1085

Baker PN, Johnson IR, Harvey PR, Gowland PA, Mansfield P (1994) A three-year follow-up of children imaged in utero with echo-planar magnetic resonance. Am J Obstet Gynecol 170:32–33

Cardozo LD, Gibb DM, Studd JW et al (1982) Predictive value of cervimetric labour patterns in primigravidae. Br J Obstet Gynaecol 82:33–38

D'Souza R et al (2013) Cesarean section on maternal request for non-medical reasons. Best Practice Res Clini Obstetrics Gynaeco 27(2):165–177

DeWilde JP, Rivers AW, Price DL (2005) A review of the current use of magnetic resonance imaging in pregnancy and safety implications for the fetus. Prog Biophys Mol Biol 87:335–353

Doll R, Wakeford R (1997) Risk of childhood cancer from fetal irradiation. Br J Radiol 70:130–139

Fox LK, Huerta-Enochian GS, Hamlin JA, Katz VL (2004) The magnetic resonance imaging-based fetal-pelvic index: a pilot study in the community hospital. Am J Obstet Gynecol 190:1679–1688

Friedman EA (1955) Primigravid labor. Obstet Gynecol 6:567–589

Friedman EA (1956) Labor in multiparae. Obstet Gynecol 8:691–703

Hannah ME, Hannah WJ, Hewson SA et al (2000) Planned caesarean section versus planned vaginal birth for breech presentation at term: a randomised multicentre trial. Term Breech Trial Collaborative Group. Lancet 356:1375–1483

Kanal E, Gillen J, Evans JA, Savitz DA, Shellock FG (1993) Survey of reproductive health among female MR workers. Radiology 187:395–399

Keller TM, Rake A, Michel SCA, Seifert B, Efe G, Treiber K, Huch R, Marincek B, Kubik-Huch R (2003) Obstetric MR pelvimetry: reference values and evaluation of inter- and intraobserver error and intraindividual variability. Radiology 227:37–43

Liselele HB, Boulvain M, Tshibangu KC, Meuris S (2000) Maternal height and external pelvimetry to predict cephalopelvic disproportion in nulliparous African women: a cohort study. Br J Obstet Gynaecol 107:947–952

Masselli G, Derchi L, McHugo J et al (2013) Acute abdominal and pelvic pain in pregnancy: ESUR recommendations. Eur Radiol 23:3485–3500

Michel SC, Rake A, Treiber K, Seifert B, Chaoui R, Huch R, Marincek M, Kubik-Huch RA (2002) MR obstetric pelvimetry: effect of birthing position on pelvic bony dimensions. AJR Am J Roentgenol 179:1063–1067

Müttersterblichkeit WH (2004) In: Schneider H, Husslein P, Schneider KTM (eds) Die Geburtshilfe, 2nd edn. Berlin/Heidelberg/New York, Verlag

O'Brien K, Rode M, Macones G (2002) Postpartum X-ray pelvimetry. Its use in calculating the fetal-pelvic index and predicting fetal-pelvic disproportion. J Reprod Med 47:845–848

Pattinson RC, Farrell E (1997) Pelvimetry for fetal cephalic presentations at or near term. Cochrane Database Sys Rev (2):CD000161. doi:10.1002/14651858CD00161

Pfammatter T, Marincek B, von Schulthess GK, Dudenhausen JW (1990) MR pelvimetric reference values. Rofo Fortschr Geb Rontgenstr Neuen Bildgeb Verfahr 153:706–710

Ray Joel G, Vermeulen Marian J et al (2016) Association between MRI exposure during pregnancy and fetal and childhood outcomes. JAMA 316:952–961

Shellock Frank G, Crues John V (2003) MR procedures: biologic effects, safety, and patient care. Radiology 232:635–652

Spong CY et al (2012) Preventing the first cesarean delivery: summary of a joint Eunice Kennedy Shriver National Institute of Child Health and Human Development, Society for Maternal-Fetal Medicine, and American College of Obstetricians and Gynecologists Workshop. Obstet Gynecol 120:1181

Spörri S, Thoeny HC, Raio L, Lachat R, Vock P, Schneider H (2002) MR imaging pelvimetry: a useful adjunct in the treatment of women at risk for dystocia. AJR Am J Roentgenol 179:137–144

Stark DD, McCarthy SM, Filly RA, Parer JT, Hricak H, Callen PW (1985) Pelvimetry by magnetic resonance imaging. AJR Am J Roentgenol 144:947–950

Stewart A, Kneale GW (1968) Changes in the cancer risk associated with obstetric radiography. Lancet 1:104–107

Urhahn R, Lehnen H, Drobnitzky M, Klose KC, Gunther RW (1991) Ultrafast pelvimetry using Snapshot-FLASH-MRT – a comparison with the Spinecho and FLASH techniques. Rofo Fortschr Geb Rontgenstr Neuen Bildgeb Verfahr 155:432–435

van Loon AJ, Mantingh A, Thijn CJ, Mooyaart EL (1990) Pelvimetry by magnetic resonance imaging in breech presentation. Am J Obstet Gynecol 163:1256–1260

Van Loon AJ, Mantingh A, Serlier EK, Kroon G, Mooyaart EL, Huisjes HJ (1997) Randomised controlled trial of magnetic-resonance pelvimetry in breech presentation at term. Lancet 350:1799–1804

Wentz KU, Lehmann KJ, Wischnik A et al (1994) Pelvimetry using various magnetic resonance tomography techniques vs. digital image enhancement radiography: accuracy, time requirement and energy exposure. Geburtshilfe Frauenheilkd 54:204–212

Wright AR, English PT, Cameron HM, Wilsdon JB (1992) MR pelvimetry – a practical alternative. Acta Radiol 33:582–587

Zhang J et al (2010) The natural history of the normal stage of labor. Obstet Gynecol 115:705

MR Imaging of the Placenta

Gabriele Masselli

Contents

Abstract

Imaging of the placenta can have a profound impact on patient management, owing to the morbidity and mortality associated with various placental conditions.

1 Introduction

Imaging of the placenta can have a profound impact on patient management, owing to the morbidity and mortality associated with various placental conditions.

Abnormalities of the placenta are important to recognize owing to the potential for maternal and fetal morbidity and mortality.

While ultrasound is still the first imaging method of placental investigation, magnetic resonance imaging (MRI) has many unique properties that make it well suited for imaging of the placenta: its multiplanar capabilities, the improved tissue contrast that can be obtained by using a variety of pulse sequences and parameters, and the lack of ionizing radiation; MRI can be of added diagnostic value when further characterization is required.

Some pathologies are seen more clearly in MRI, such as infarctions and placental invasive disorders. The future development is towards functional placental MRI. Placental MRI has become an important complementary method for evaluation of placental anatomy and pathologies contributing to fetal problems such as intrauterine growth restriction.

G. Masselli, MD, PhD
Umberto I Hospital, Radiology Dea Department, Sapienza University, Viale del Policlinico 155, 00161 Rome, Italy
e-mail: gabriele.masselli@uniroma1.it

Med Radiol Diagn Imaging (2017)
DOI 10.1007/174_2017_8, © Springer International Publishing AG
Published Online: 15 February 2017

In this chapter, we review the appearances and the role of MRI in diagnosis and management of these conditions.

2 Imaging of the Placenta

The placenta is responsible for the nutritive, respiratory, and excretory functions of the fetus (Bernirschke and Kaufmann 2000). The placenta is often overlooked in the routine evaluation of a normal gestation, receiving attention only when an abnormality is detected. Although uncommon, abnormalities of the placenta are important to recognize owing to the potential for maternal and fetal morbidity and mortality (Elsayes et al. 2009). Pathologic conditions of the placenta include placental causes of hemorrhage, gestational trophoblastic disease, retained products of conception, nontrophoblastic placental tumors, and cystic lesions (Linduska et al. 2009).

Ultrasound is widely used as the initial diagnostic imaging technique during pregnancy because of its availability, portability, and lack of ionizing radiation (Elsayes et al. 2009).

Magnetic resonance (MR) imaging provides superior soft tissue contrast resolution, multiplanar imaging capabilities, and image quality independent of the mother's size or fetus' positioning, and it lacks ionizing radiation (Masselli et al. 2011a). MRI can be of added diagnostic value when further characterization is required, particularly in the setting of invasive placental processes such as placenta accreta, placental abruption, and gestational trophoblastic disease (Masselli et al. 2011a, b; Baughman et al. 2008). In particular, MR imaging might well have a pivotal role in the diagnosis of intrauterine bleeding thanks to its high spatial resolution and to the known high sensitivity and specificity in distinguishing blood from other fluid collections (Masselli et al. 2011b).

Moreover, in advanced gestational age, obese women, and posterior placental location, MRI is advantageous due to the larger field of view and its multiplanar capabilities.

Its drawbacks, however, include prolonged imaging time, cost, lack of skilled experience, claustrophobia, and the challenge of remaining supine and still for a prolonged period in advanced gravid state (Bardo and Oto 2008).

3 MRI Protocol

Most patients in the second trimester of pregnancy can tolerate supine positioning within the MR system bore.

For patients in the third trimester, left lateral decubitus positioning may be better tolerated and decrease the risk of impaired venous return from caval compression by the uterus. To maximize signal, a multichannel surface coil is used whenever possible. Ideally, the bladder should be only moderately full, both for patient comfort and to avoid over- or underdistension that could complicate assessment for potential bladder invasion.

All examinations should be performed on a 1.5Tesla (T) system in the supine position with a phased-array body coil. The safety of MR at 3 T has not yet been proven; however, to our knowledge, no published human studies documented any adverse effect on children exposed at higher magnetic fields, such as 3 T (Baughman et al. 2008).

A phased-array coil is preferred to use because it provides a superior signal-to-noise ratio, but in larger patients and towards the end of pregnancy, a body coil may be necessary.

If patients feel uncomfortable lying supine in the scanner (especially in the third trimester), imaging can be obtained with the patient in the lateral decubitus position, decreasing the pressure on the inferior vena cava.

Steady-state free-precession sequences (fast imaging employing steady-state acquisition [FIESTA], true fast imaging with steady-state precession [FISP], balanced fast field echo [FFE]) can provide motion-free images of the abdomen. The protocol includes multiplanar T2-weighted single-shot echo train spin-echo imaging (half-Fourier rapid acquisition with relaxation enhancement [RARE], single-shot turbo spin-echo, or single-shot fast spin-echo), in addition to sagittal T1-weighted gradient-echo imaging with fat suppression (Table 1) (Nagayama et al. 2002).

We recommend that MR examinations performed for placental abnormalities be monitored by a physician who can prescribe additional

Table 1 Summary of MR imaging parameters

Parameter	True FISP[a]		T2-weighted half-Fourier RARE[b]		Sagittal T1-weighted three-dimensional imaging[c]	Sagittal diffusion-weighted imaging[d]
	Transverse	Coronal/ sagittal	Transverse	Coronal/ sagittal		
TR/TE (ms)[e]	4.3/2.2	4.3/2.2	1000/90	1000/90	4.1/1.1	3200/75
Flip angle	50°	50°	150°	150°	10°	10°
Field of view (mm)	320–400	320–400	320–400	320–400	320–400	320–400
Matrix	256 × 224	256 × 224	256 × 224	256 × 224	256 × 224	256 × 192
Parallel imaging factor	2	2	2	2	3	2
Section thickness (mm)	5	5	4	4	2.5	5
Intersection gap (mm)	0	0	0	0	0	0
No. of signals acquired	1	1	1	1	1	6
Receiver bandwidth (kHz)	125	125	200	200	310	1930
Acquisition time (s)	19	21	15–20	15–20	15–18	180

[a]*FISP* fast imaging with steady-state precession
[b]*RARE* rapid acquisition with relaxation enhancement
[c]Imaging was performed with dynamic volumetric interpolated breath-hold examination with fat saturation. Fat saturation was achieved with the chemical shift–selective fat suppression technique
[d]Diffusion-weighted MR images were acquired with *b* values of 50, 400, and 800 s/mm^2
[e]*TR*/*TE* repetition time/echo time

sequences as needed, including fat-suppressed and opposed-phase imaging if a fat containing lesion is suspected, and time-of-flight imaging if further evaluation of a vascular structure is indicated.

Parallel imaging reconstruction algorithms GRAPPA with iPAT factor 2 are used to decrease the MR data acquisition time of the sequences therefore reducing fetal and maternal motion artifacts.

To minimize the deposition of radiofrequency energy in the pregnant patient and optimize temporal resolution, a 256 × 224 matrix is used with a partial-phase field of view of 0.75 in applicable rectangular geometries, such as the axial plane.

An attempt is made to confirm all suspected abnormalities in at least two imaging planes because the normal curvature of the uterus can potentially lead to a false-positive examination in a single imaging plane. When higher-resolution imaging is required to maintain a satisfactory signal-to-noise ratio, additional images can be obtained in the desired plane using a T2-weighted fast spin-echo sequence. This sequence can be performed over a limited area during a breath-hold using some type of flip back pulse to shorten the repetition and acquisition times.

The use of fat suppression in conjunction with T1-weighted sequences improves the conspicuity of blood products.

Some investigators have advocated the use of gadolinium-based contrast agents to improve the specificity of MRI for diagnosis of placenta accreta by better defining the outer placental surface and myometrium and distinguishing placenta accreta from percreta (Palacios Jaraquemada and Bruno 2000; Tanaka et al. 2001).

Therefore, in clinical practices, gadolinium-based contrast agents are not used in pregnancy, except when the potential risks to the patient are outweighed by the potential benefits of contrast-enhanced imaging.

Clinical experience with diffusion-weighted placental imaging is likewise limited (Bonel et al. 2010; Morita et al. 2009), but this sequence has been recently demonstrated to be very useful in the detection of placental hematoma (Masselli et al. 2011b).

4 Normal Appearance

Before interpreting images for pathologic findings, it is necessary to understand the normal anatomy and the normal findings of the placenta at multiplanar MR imaging (Nguyen et al. 2012).

The gravid uterus should be pear shaped, with the fundus and body being wider than the lower uterine segment. The uterine contour is usually smooth, and focal bulging should not be present.

Typically, the placenta is located along the anterior or posterior uterine wall, extending onto the lateral walls.

Placental size is expressed in terms of thickness in the midportion of the organ and should be between 2 and 4 cm. Placental thinning has been described in systemic vascular and hematologic diseases that result in microinfarctions. Thicker placentas (>4 cm) are seen in fetal hydrops, antepartum infections, maternal diabetes, and maternal anemia. Placental thickening can be simulated by myometrial contractions and underlying fibroids (Victoria et al. 2011).

The MR signal of the placenta varies according to the utilized imaging sequence (Leyendecker et al. 2012; Levine and Pedrosa 2005). With the most commonly utilized fetal pulse sequence, HASTE, the placenta demonstrates intermediate signal, hypo- or isointense with respect to the surrounding myometrium. A fine line of separation between the myometrium and the placenta may be visualized, most likely representing the placental-myometrial interface. The placenta is predominantly homogeneous in signal in the early second trimester and has a relatively flat and smooth surface (Fig. 1).

On steady-state free-procession or true FISP images, the placenta is hypo- to isointense with respect to the myometrium and homogeneous in appearance during the second trimester, becoming more heterogeneous as maturation occurs. The placental-myometrial interface may be seen, although it was less distinct than in HASTE images.

On T1 FLASH images, the placenta demonstrates a homogeneous signal, isointense to myometrium.

As the placenta matures, particularly in the third trimester, cotyledons become easier to discern as round, high-signal structures seen in fluid-sensitive sequences, delineated by a subtle peripheral low signal line, likely representing the normal placental septa (Fig. 2). The placenta also becomes more complex appearing, with gentle lobulations seen on its fetal surface and fine vascular channels becoming more distinct as they traverse the placental tissue.

Placental septa and the cotyledons are more often seen when imaging with a 3 T system (Fig. 3).

The normal subplacental vascularity can be seen as numerous flow voids just under the placenta. A few flow voids can also be seen within the placenta and are usually in the region of the insertion point of the umbilical cord.

The myometrium has a variable thickness and thins as the pregnancy progresses.

It can be seen as three distinct layers of signal intensity; the inner and outer layers of the myometrium are seen as thin bands of decreased T2 signal intensity (Fig. 4). The middle layer is thicker, has intermediate T2 signal intensity, and often contains multiple flow voids representing the normal myometrial vascularity.

As the pregnancy progresses, the myometrium can become quite thin and should be visualized as a continuous band of soft tissue low intensity signal surrounding the placenta (Fig. 5).

However, the myometrium may blend into the placenta, and it can be difficult to visualize even at technically adequate examinations in patients with prior cesarean section.

One problem with MR imaging of placenta adhesive disorders is that distinction between the myometrium and the placenta can be difficult on the types of sequences typically used (Kim and Narra 2004; Lax et al. 2007).

If placenta accreta is suspected, additional imaging planes are chosen that best show the placenta-myometrium interface in the region of suspected abnormality or other structures of interest, such as the bladder dome. Such imaging is typically best accomplished in an angled scan plane perpendicular to the placenta-myometrium interface or myometrium-bladder interface (Masselli et al. 2008).

4.1 Placenta Variants

Most placentas are round or discoid in shape, but other shapes should be described when present;

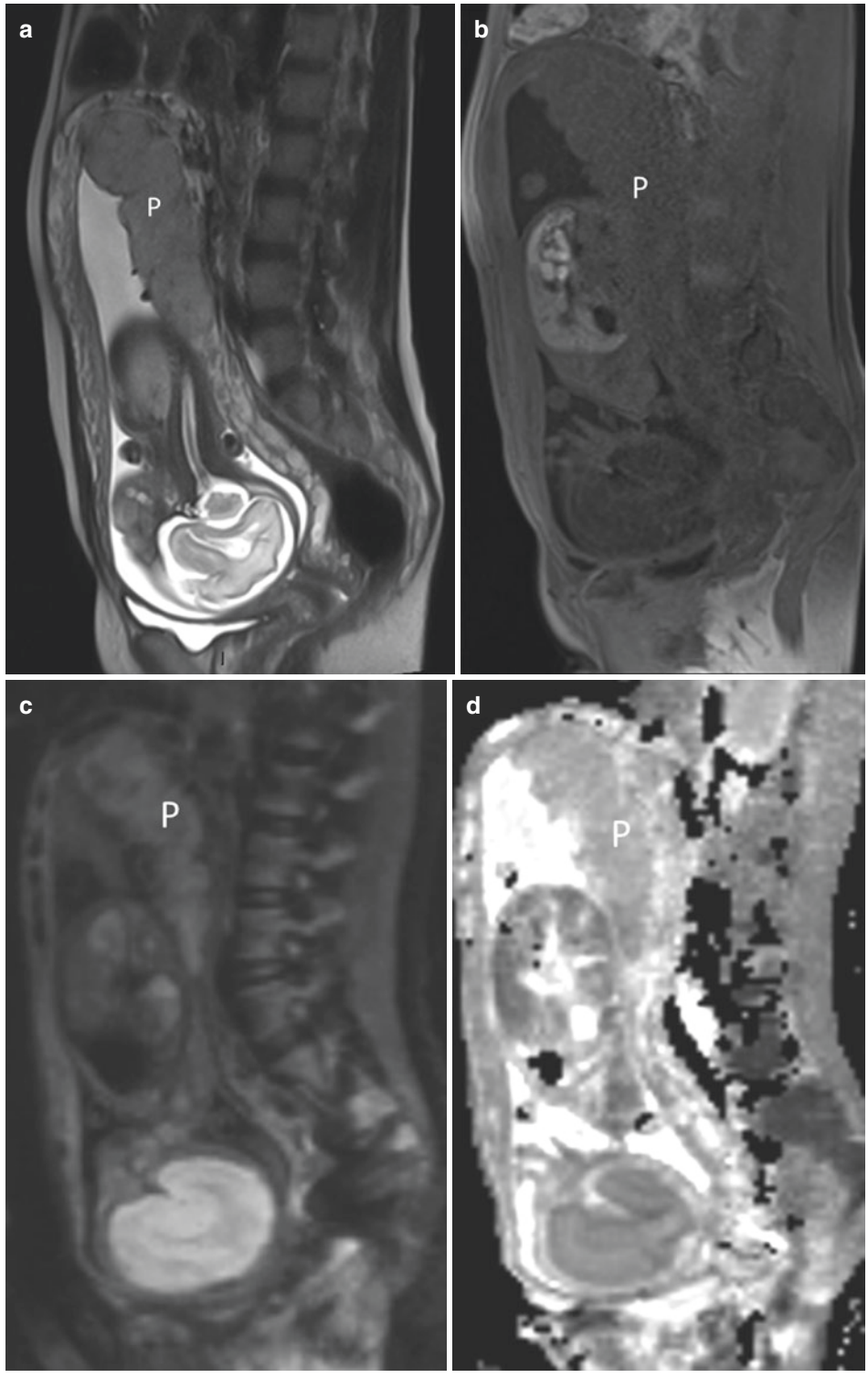

Fig. 1 Normal placenta in this 26-week-old fetus. (**a**) Sagittal T2-weighted half-Fourier RARE T2-weighted MR image shows a placenta (*P*) with intermediate signal intensity. (**b**) Sagittal T1-weighted fat saturation sequence demonstrates a homogeneous placenta, isointense to myometrium. (**c**) Sagittal DWI sequence (B = 800) and ADC map (**d**) demonstrates a homogeneous placenta

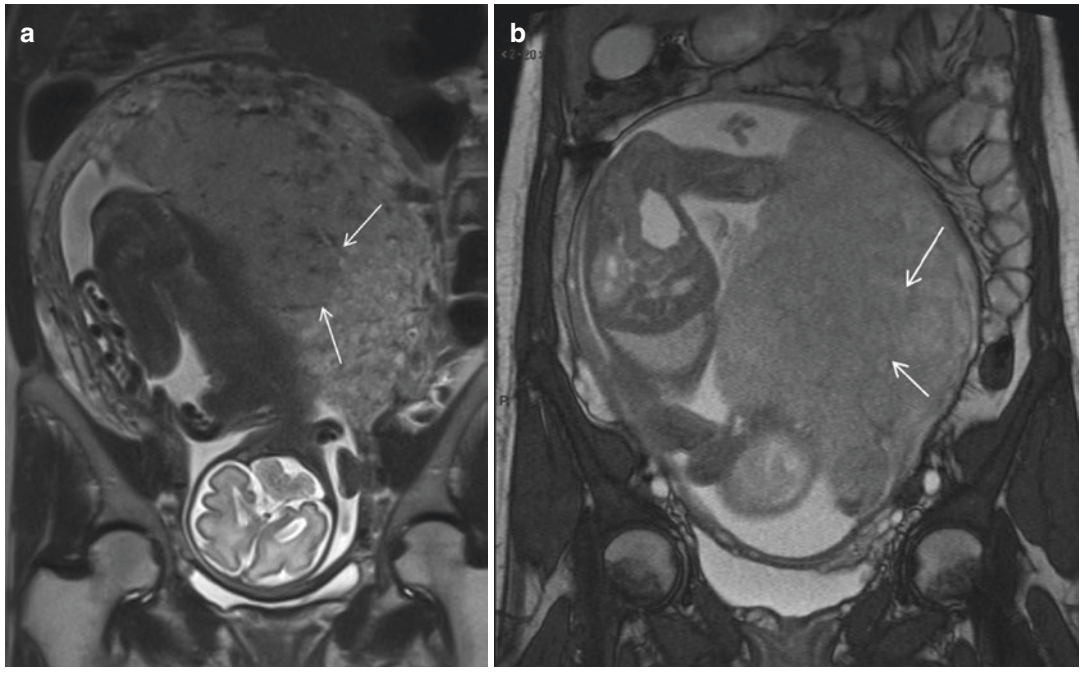

Fig. 2 Coronal T2-weighted half-Fourier RARE (**a**) and true FISP (**b**) MR images show a homogeneous placenta with thin linear areas of decreased signal intensity in a regular pattern (*arrows*) representing normal placental septa

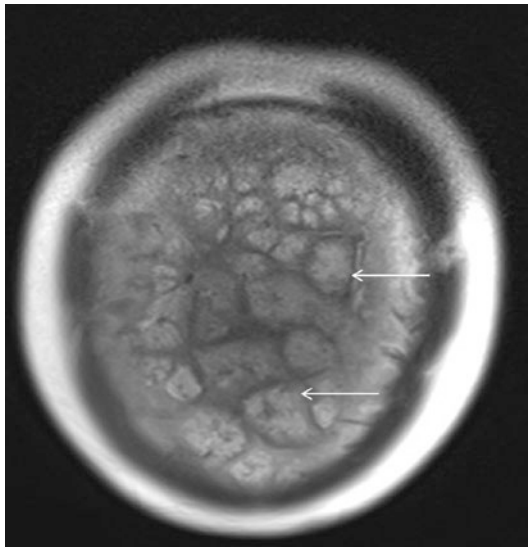

Fig. 3 Coronal T2-weighted half-Fourier RARE at 3 Tesla MR scanner shows the cotyledon structure of the placenta (*arrows*)

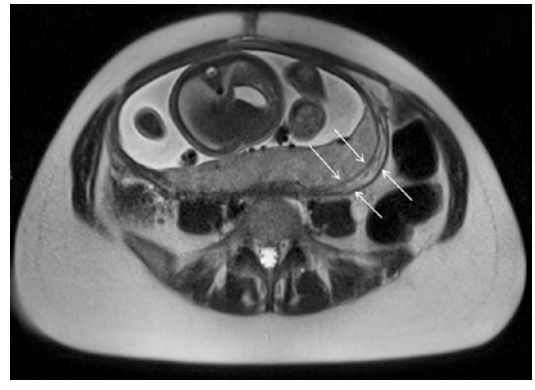

Fig. 4 Axial T2-weighted MR image of healthy second-trimester placenta shows the three layers of the normal myometrium. The hypointense outer (*short arrows*) and inner (*arrows*) layers surround the more hyperintense middle layer, which contains the vasculature

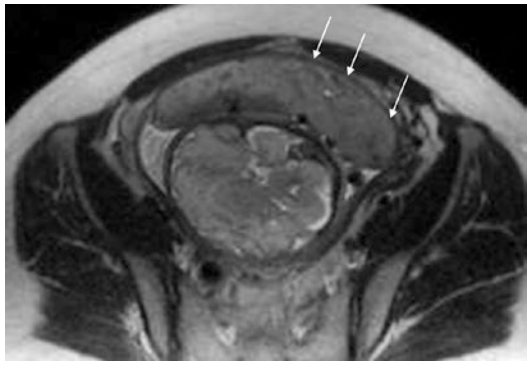

Fig. 5 Axial T2-weighted MR image of healthy third-trimester placenta shows the placenta has homogeneous intermediate signal intensity and the myometrium is visible as a low-signal-intensity line external to the placenta (*arrows*)

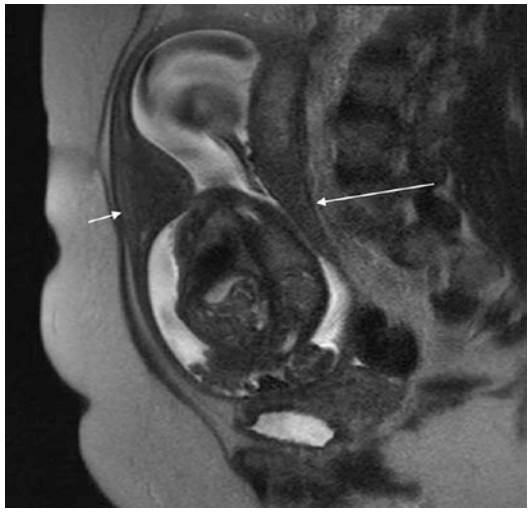

Fig. 6 Sagittal T2-weighted half-Fourier RARE MR image shows a normal placenta with a succenturiate lobe. The main body of the placenta is located along the posterior uterine wall (*arrow*). A second soft tissue structure with similar signal intensity is seen along the anterior uterine wall and represents the succenturiate lobe (*small arrow*)

variant placental shapes include bilobed, succenturiate, circumvallate, and placenta membranacea (Huppertz 2008).

Usually discoid in shape, the placenta can exhibit various morphologies. The placenta can have a separate lobule that is not contiguous with the main placental body, which is called a succenturiate placenta (Fig. 6) (Elsayes et al. 2009).

A small lobule of placenta separate from the main bulk of the placenta is referred to as a succenturiate lobe. This is important to describe when present because of the risk of connecting vessel rupture or retention of the lobe at delivery, both potentially resulting in significant hemorrhage (Bernirschke and Kaufmann 2000).

If there are two lobes of placenta, similar in size, the placenta can be described as bilobed. Circumvallate placenta is best described as having a rolled-up edge. In a retrospective review of 7666 deliveries, the odds ratio of placental abruption in patients with circumvallate placenta was 13.10 (95% confidence limits: 5.65–30.20) (Elsayes et al. 2009). A placenta membranacea or "placenta diffusa" occurs when villous atrophy fails to occur early in gestation. As a result, fetal membranes remain covered with chorionic villi. This rare entity presents with a thinned diffuse placenta covering the uterine cavity, and is associated with placental invasion (Linduska et al. 2009). Annular placenta may be a variant of placenta membranacea, presents with a ring-shaped placenta, and has similar risks of hemorrhage and growth restriction (Derwig et al. 2011).

Lastly, in placenta fenestrata, the placenta may also demonstrate a central defect in which placental tissue is nonexistent, leaving only a membranous sheath.

The normal umbilical cord measures 50–60 cm long, contains two umbilical arteries and one vein, and typically inserts centrally within the placenta (Palacios Jaraquemada and Bruno 2000). A marginal cord insertion, also known as a battledore placenta, occurs within 1–2 cm of the placental edge. With a velamentous cord insertion, the placental vessels insert separate from the placenta and traverse between the amnion and chorion before entering the placenta (Tanaka et al. 2001). Umbilical vessels crossing the internal os of the cervix in the setting of velamentous insertion, a condition known as vasa previa, predispose to catastrophic hemorrhage of the fetal umbilical artery (Palacios Jaraquemada and Bruno 2000). Undiagnosed vasa previa has a fetal mortality rate nearing 60% (Bardo and Oto 2008).

Placenta previa refers to abnormal implantation of the placenta in the lower uterine segment,

overlying or near the internal cervical os (Baergren 2005). Normally, the lower placental edge should be at least 2 cm from the margin of the internal cervical os. The relationship of the placenta to the internal os changes throughout the course of pregnancy as the uterus enlarges. The diagnosis of placenta previa should not be made before 15 weeks' gestation, and low-lying or marginal placental positioning should be revaluated later in gestation to confirm placental position before delivery.

Placenta previa can be subdivided according to the position of the placenta relative to the internal cervical os (To and Leung 1995). Although transvaginal sonography is the imaging standard for making this diagnosis, the position of the placenta is usually demonstrable with transabdominal imaging. In the appropriate clinical setting, the absence of sonographic confirmation of placenta previa does not exclude the diagnosis.

MR imaging allows accurate identification of the position of the placenta; sagittal MR sequence oriented in the plane of the cervix is used to assess the placental margin (Fig. 7).

Given widespread use of endovaginal and translabial ultrasound, this is unlikely to be a common indication for MR examination. However, transvaginal imaging should be undertaken with care in advanced pregnancies, as it can lead to premature rupture of membranes or to infection when the membranes have already ruptured. The placental edge is easily identified with MR Haste and true FISP sequences.

5 Placenta Adhesive Disorders

Abnormal invasive placenta describes a group of conditions that produce the abnormal infiltration of placental tissue into the uterus or also into the surrounding tissues. This condition usually produces severe complications for the mother, such as massive hemorrhage, organ damage, organ failure, and even death (Bernirschke and Kaufmann 2000).

Placenta accreta, placenta increta, and placenta percreta represent a spectrum of placental adhesive disorders (PADs) and occur when a defect of the decidua basalis allows the invasion of chorionic villi into the myometrium (Sebire and Sepulveda 2008; Oyelese and Smulian 2006).

PAD is classified on the basis of the depth of myometrial invasion: placenta accreta is the least severe of the three entities with penetration of the decidua by the chorionic villi. Placenta increta is penetration of the myometrium by the chorionic villi. Placenta percreta is the most severe of the implantation anomalies with invasion of both the myometrium and uterine serosa often with extension into neighboring organs (Bernirschke and Kaufmann 2000).

Prior cesarean section and placenta previa are the two most important risk factors for placenta adhesive disorders; these conditions occur in 5% of patients with placenta previa, in up to 10% of patients after four or more cesarean sections, and in 67% of patients who have both placenta previa and four or more cesarean sections (Oyelese and Smulian 2006).

As abnormal placentation becomes more prevalent, in large part due to the steadily rising rates of cesarean deliveries, there is a need for accurate antenatal diagnosis of this condition to prevent maternal morbidity and mortality because timing and site of delivery, availability of blood products, and recruitment of a skilled anesthesia and surgical team can be arranged in advance.

Diagnostic signs using MRI are similar to those described in US (To and Leung 1995), (Masselli et al. 2011c), (Sebire et al. 2002). Interrupted or myometrial thinning is a common sign but not specific of AIP. Previous cesarean scar is prone to produce some degree of dehiscence when the placenta is located in the lower segment. For this reason, this sign itself is not indicative of PAD, although histologically it could agree with a placenta accreta, increta, or percreta. Presence of lagoons, especially multiple, confluent, and intercommunicated, is probably the most reliable sign of PAD (US and pMRI) (Fig. 8). Tenting of bladder was described as a sign of PAD (Huppertz 2008), but this sign is not specific and surgically represents the bladder adhesion to the previous scar. Although uterine bulging was described as one of the useful signs for diagnosis,

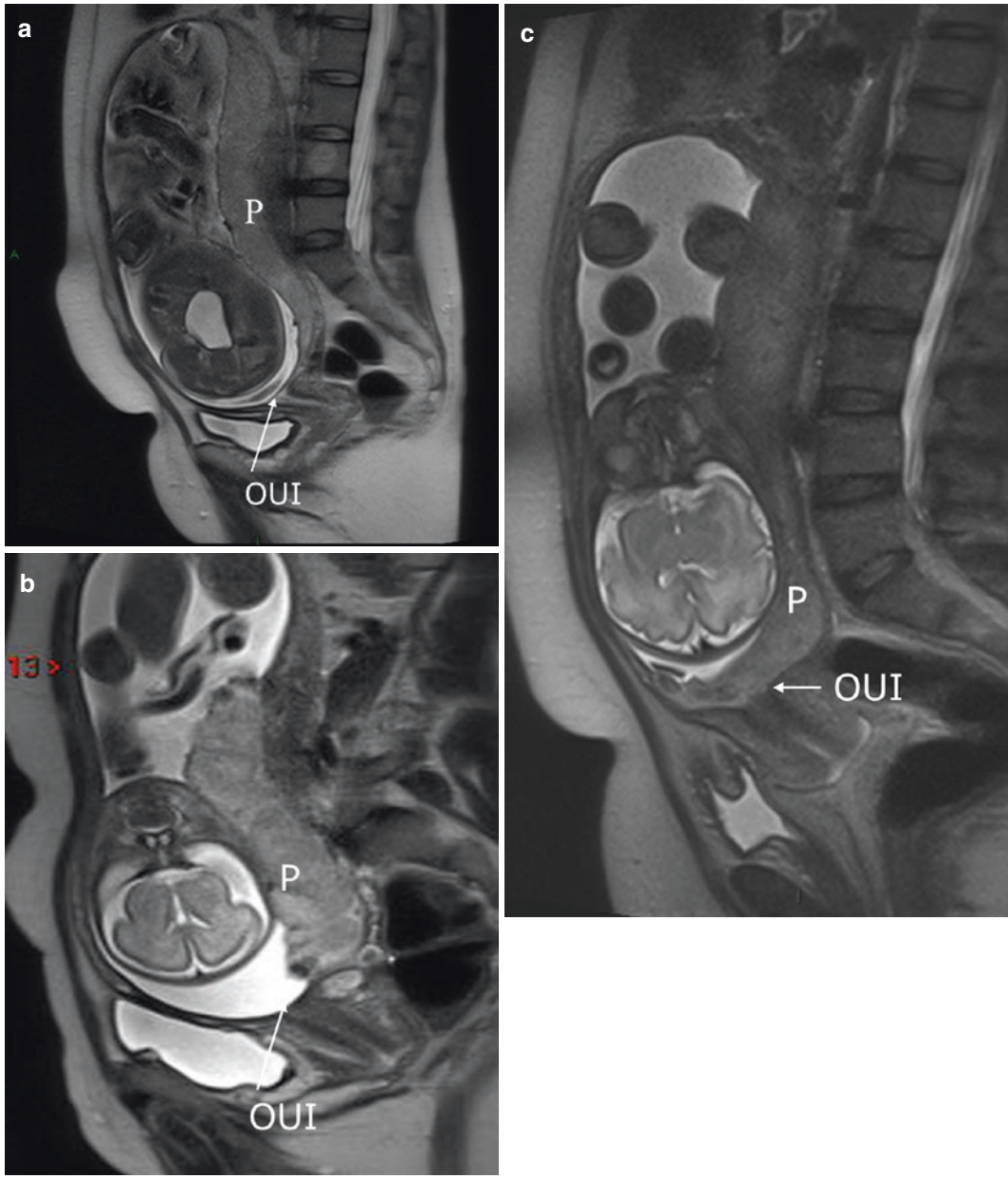

Fig. 7 Spectrum of placenta previa. Sagittal T2-weighted half-Fourier RARE MR images show a low-lying placenta (**a**) where the placental inferior border is within 0.5 cm of the internal uterine os (*OUI*), marginal placenta previa (**b**) where the placental tip is located immediately at the OUI but does not cover it and central placenta previa (**c**), where the placenta entirely covers the OUI

this is not specific at all, as a simple uterine scar dehiscence in a placenta previa can produce it. According to some authors, absence of dark placental bands excludes a diagnosis of PAD, but this asseveration is made based on small series. Presence of lobulations is frequent in PAD (Sebire et al. 2002), although their absence is not an exclusion criteria. For this reason, and as it happens in US analysis, prenatal diagnosis of PAD is based on a group of signs, some of them more predictive of PAD than others. Full area acquisition of MRI allows re-evaluation anytime by

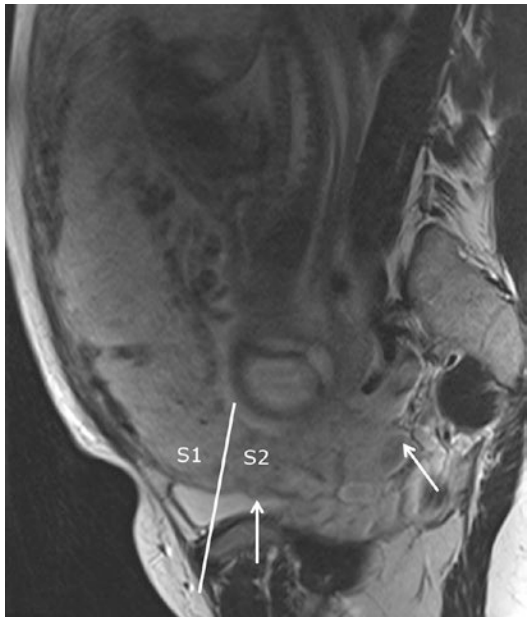

Fig. 8 A 34-year-old woman at 28 weeks' gestation with complete placenta previa and placenta accreta in posterior lower uterine segment (S2). Sagittal T2-weighted half-Fourier RARE MR image shows prominent low-signal-intensity band (*arrow*) on maternal side of placenta and anteriorly irregular placenta-myometrium interface with placental tissue without surrounding myometrium (*small arrow*). Perpendicular plane which divides the posterior bladder wall determines areas S1 and S2

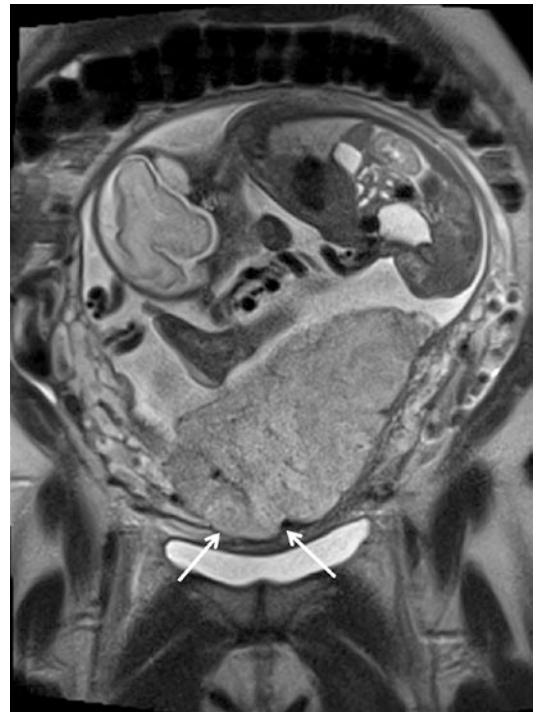

Fig. 9 Placenta percreta in a 33-year-old woman with two prior cesarean deliveries. Sagittal T2-weighted half-Fourier RARE image a shows a broad outward bulge (*arrows*) in posterior placental contour. No underlying myometrium can be seen in this region

different observers, a fact that is not usually possible for US, because image acquisition is dependent on the operator.

MR findings of more severe disease (placenta increta and percreta) include: dark placental bands on T2-weighted images, with loss of normal low signal intensity myometrium, disorganized architecture of the adjacent placenta, focal exophytic mass, and, in case of invasion involving the bladder, thinning of the uterine serosa-bladder interface, focal abnormal signal in the bladder wall, and extension of intermediate signal placental tissue beyond uterine margins with loss of fat planes between uterus and pelvic organs (Fig. 9) (Leyendecker et al. 2012; Masselli et al. 2008; Levine 2006; Warshak et al. 2006; Levine et al. 1997).

However, in some cases it is almost impossible to differentiate between placenta accreta and percreta using MRI, especially if there is no involvement of the adjacent structures. This is because the myometrium becomes extremely thin as pregnancy progresses, and it becomes difficult to visualize.

The most useful findings are uterine bulging, heterogeneous signal intensity within the placenta, and dark intraplacental bands on T2-weighted images.

This appearance is common at locations where the uterus is compressed by the maternal spine, but it can be diffuse. Uterine contractions commonly cause transient focal low-signal intensity thickening of the uterine wall. Unenhanced T1-weighted images do not provide sufficient differentiation between the placenta and myometrium to be useful for assessment of abnormal placental attachment or invasion, as the placenta and the myometrium are both of homogeneous intermediate signal intensity.

Dynamic contrast-enhanced imaging of the placenta shows early intense lobular enhancement of the placental tissue that becomes

confluent with time and precedes enhancement of the myometrium (Tanaka et al. 2001).

Several studies have compared the accuracy and effectiveness of sonography versus MRI in the detection of placenta accreta. Warshak et al. (2006) compared pathologic diagnosis to antenatal ultrasound (including use of an endovaginal transducer) and MRI results. This study retrospectively evaluated 453 women with a diagnosis of placenta previa, low-lying placenta with prior cesarean delivery, or myomectomy, of whom 39 had abnormal placentation.

This study revealed 77% sensitivity, 96% specificity, 65% positive predictive value (PPV), and 98% negative predictive value (NPV) for ultrasound compared to 88% sensitivity, 100% specificity, 100% PPV, and 82% NPV for MRI prediction of abnormal placentation. Another study with fewer patients (n = 13) showed the sensitivities of ultrasound to be 33% and MRI to be 38%, stating that both modalities had a poor predictive value in the diagnosis of abnormal placentation (Lam et al. 2002). A multinstitutional study in 2008 by Dwyer et al. (2008) retrospectively evaluated 32 patients who were clinically at high risk for placenta accreta and had undergone both transabdominal sonography and MRI, of whom 15 had confirmed abnormal placentation at delivery. Sonography had 93% sensitivity, 71% specificity, 74% PPV, and 92% NPV, whereas MRI had 80% sensitivity, 65% specificity, 67% PPV, and 79% NPV. This study did not show a statistically significant difference in sensitivity or specificity between sonography and MRI, concluding that both modalities may be complementary – if findings are inconclusive with one, the other modality may be useful for clarifying the diagnosis.

Some authors have suggested that MR imaging is most clearly indicated when there is a posterior placenta or in patients with previous myomectomy (Levine et al. 1997).

We agree that MRI should be reserved primarily when ultrasound findings are equivocal for abnormal placentation or to assess portions of the uterus inaccessible to sonographic examination in patients with risk factors. Even when ultrasound findings are convincing for a diagnosis of placenta accreta, MRI can be beneficial in planning subsequent management by specifically delineating the extent of an ultrasound diagnosed placenta percreta (Masselli et al. 2008; Palacios Jaraquemada and Bruno 2005).

According to the previous topographic characterization of Palacios et al. (Palacios Jaraquemada and Bruno 2000), these sagittal images obtained through MRI allow the division of anterior placenta invasion into two sectors, delimited by a plane perpendicular to the center of the so-called upper bladder axis. The uterine sectors bordering the upper and lower posterior bladder walls were called S1 and S2, respectively. S1 PADs are generally of easy access and quick hemostasis, whereas S2 PADs – being irrigated by deeply located vessels – often result in a significantly increased surgical complexity and massive hemorrhage.

MRI has another potential benefit compared with US in that it provides a larger field of view, thereby granting an easier evaluation of the topography of placenta invasion and classification of S1 PAD and S2 PAD (Fig. 8).

MRI can detect the presence of new vascularization associated to PAD that indicates a different approach or surgical treatment. Although these differences may be seen by US, it can be difficult to differentiate peripheral placental circulation (lacunae blood flow) from newly formed vessels, especially when the bladder wall is very thin.

This is not a minor issue, because in recent years, many cases of PAD have happened after the first cesarean, so a decision whether or not to perform a hysterectomy must be carefully taken.

6 Placenta Abruption

Antepartum hemorrhage (vaginal bleeding between 20 weeks' gestation and delivery) remains an important cause of maternal and fetal morbidity and mortality. Placenta previa and placental abruption account for more than one-half of cases of antepartum hemorrhage and are increasing in prevalence as the rate of cesarean section increases (Sakornbut et al. 2007; Sinha and Kuruba 2008).

Placental abruption represents premature separation of the placenta from the uterine wall. Although rare (<1% of pregnancies), third-trimester abruption is associated with an increased risk of preterm delivery and fetal death (Oyelese and Ananth 2006).

The diagnosis of placental abruption is clinical and is characterized as the premature detachment of the placenta from its implantation site. The condition may be sudden and painful or clinically silent. It may manifest as a placental hematoma as discussed above, without other symptoms such as pain or vaginal bleeding. Placental abruption affects approximately 1% of births and is the leading cause of vaginal bleeding in the final trimester and may manifest as a placental hematoma (Elsasser et al. 2010).

There are three types of placental hematoma, including retroplacental, subchorionic, and subamniotic. Retroplacental hematomas are defined as being posterior to the placenta, representing 43% of hematomas. Subchorionic hematomas are between the chorion and the endometrium, representing approximately 57% of hematomas. Subamniotic hematomas are rare and are located between the amnion and the chorion (Oyelese and Ananth 2006; Elsasser et al. 2010).

US is frequently performed to confirm the presence of abruption and assess the extent of subchorionic or retroplacental hematoma (Nyberg et al. 1987). The presence of blood in large enough volumes to be visible sonographically indicates retained hemorrhage that may remain symptomatic.

However in up to 50% of cases of abruption US is negative for different reasons (Levine and Pedrosa 2005; Sakornbut et al. 2007; Nyberg et al. 1987): (1) Acute hemorrhage echo texture is very similar to that of the adjacent placenta and is therefore very difficult to detect. (2) The sign of an abnormally thick and heterogeneous placenta is rare, being present only in large acute clots. (3) Many subacute clots result falsely negative since blood dissects out from beneath the placenta and drains trough the cervix.

Diffusion-weighted imaging is an excellent sequence for detecting intrauterine hemorrhagic lesions.

Blood breakdown products cause susceptibility effects and can be accurately demonstrated with the diffusion-weighted sequence (Bonel et al. 2010; Oyelese and Smulian 2006). In our study (Masselli et al. 2008), the diffusion- and T1-weighted sequences were more accurate than the T2-weighted half-Fourier RARE and true FISP sequences in the detection of placental abruption; this finding is in agreement with previously reported evidence (Linduska et al. 2009; Verswijvel et al. 2002). T2-weighted half-Fourier RARE and true FISP sequences have high sensitivity in the detection of acute ischemic lesions and good diagnostic accuracy in the detection of placental hematomas, probably owing to the coexisting condition of acute or subacute bleeding and chronic ischemia in abruption (Linduska et al. 2009). Subchorionic or retroplacental hemorrhage typically demonstrates low T2 and intermediate to high T1 signal. Diffusion-weighted imaging (DWI) has been recently demonstrated to be very useful in the detection of retroplacental hematoma (Fig. 10).

T1- and T2-weighted sequences are complementary, and both are required for complete tissue characterization. By considering the signal intensity changes on T1-, T2-, and diffusion-weighted images, with special reference to the paramagnetic effects of methemoglobin, it is possible to estimate the age of the bleeding and intrauterine hematomas can be accurately classified as follows: hyperacute (first few hours, intracellular

Fig. 10 Subchorionic hemorrhage in a 25-year-old woman at 27 weeks' gestation. Transvaginal gray-scale US scan were suggestive of the presence of placenta previa, whereas MR images correctly depicted the presence of subchorionic hematoma. Sagittal T1-weighted gradient-echo image (**a**) shows the hyperintense subchorionic hematoma located above the internal os. The intrauterine clot shows heterogeneous signal due to the presence of hypo and hyperintense areas to placenta on the axial T2-weighted half-Fourier RARE (**b**) and on coronal true FISP (**c**) images. (**d**) Sagittal diffusion-weighted MR image (*b* value, 800 s/mm^2) and ADC map (**e**) show the hematoma (*arrow*) has hypo- and hyperintense areas. The signal intensity characteristics are suggestive of the presence of hyperacute and subacute bleeding in the hematoma. The placenta (*short arrow*) is not previa and has normal signal intensity

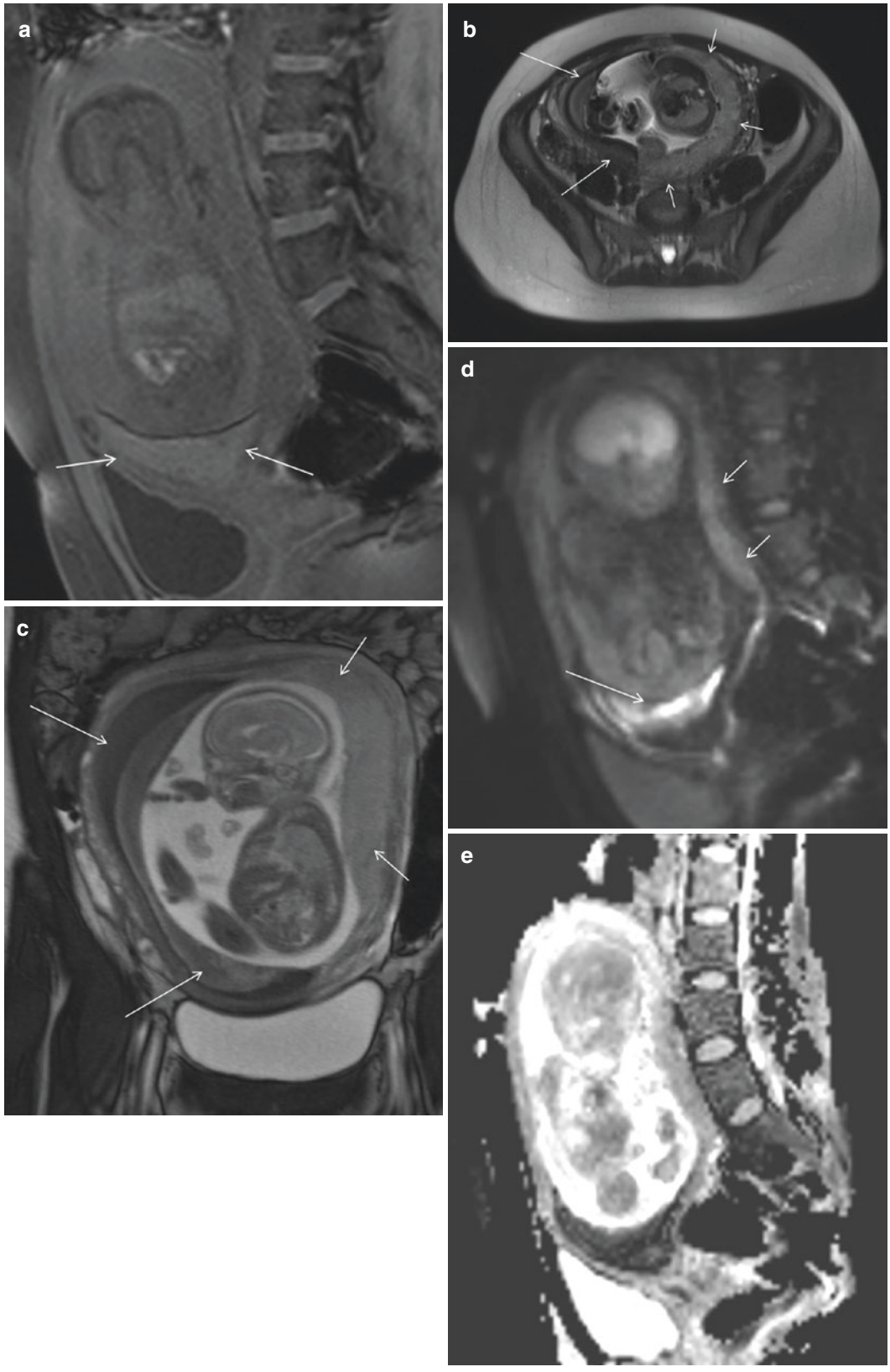
a
b
c
d
e

Table 2 Signal intensities of intrauterine hematoma over time

Stages	T1-weighted MR imaging	T2-weighted MR imaging	Diffusion-weighted MR imaging
Hyperacute	Iso- to hypointense	Hyperintense	Hyper- to hypointense
Acute	Iso- to hypointense	Hypointense	Hypointense
Early subacute	Hyperintense	Hypointense	Hypointense
Late subacute	Hyperintense	Hyperintense	Hyperintense
Chronic	Hypointense	Hypointense	Iso- to hypointense

oxyhemoglobin), acute (1–3 days, intracellular deoxyhemoglobin), early subacute (3–7 days, intracellular methemoglobin), late subacute (≥14 days, extracellular methemoglobin), and chronic (>4 weeks, intracellular hemosiderin and ferritin) (Table 2).

MR signs of acute or recent bleeding within a hematoma can indicate a potentially unstable abruption, whereas hematomas with late subacute bleeding are stable.

Areas of hemorrhage in asymptomatic women are felt to result from venous bleeding of a remote nature, and treatment would typically be expectant management. Evidence of prior hemorrhage is not an uncommon finding in pregnancy, and when identified, it should be described in detail including multidimensional measurements, location, and proximity to the umbilical cord insertion and cervix.

MRI is an extremely accurate exam to identify the origin of second- and third-trimester uterine bleeding with an excellent interobserver agreement. With respect to US, it grants new and additional data that can influence the clinical management of these patients (Masselli et al. 2011c). Obstetricians will use this information to determine proper clinical and sonographic follow-up intervals to assess for fetal growth, anemia, and stress.

7 Solid Placental Masses

Solid placental masses are rare; chorioangiomas are the most common tumor of the placenta and are identified in up to 1% of all placentas evaluated histologically. In up to 1:3500 births, chorioangiomas come to clinical attention (Sakornbut et al. 2007). These masses are typically >5 cm in size and can be associated with polyhydramnios, hydropic changes in the fetus, intrauterine growth restriction, and congestive heart failure of the fetus due to vascularity of the mass. Chorioangiomas are benign tumors that can show intratumoral hemorrhage. Differentiating a placental hematoma from a solid mass, such as a chorioangioma, can be accomplished using color Doppler during sonographic evaluation (Sinha and Kuruba 2008). However, masses that have undergone hemorrhagic infarction or thrombosis can have limited internal flow and remain difficult to diagnose (Zalel et al. 2002a, b). Chorioangiomas can be homogeneous and nearly isointense to placenta on T1- and T2-weighted images (Kawamoto et al. 2000). They are typically round in shape and may protrude from the placental surface. A very subtle thin capsule may be identified on T2-weighted images which does not mimic the regular septae of the placenta (Fig. 11). Peripheral areas of internal hemorrhage, manifesting as T1-shortening, have been described in case reports (Sakornbut et al. 2007; Oyelese and Ananth 2006). Similarly, in those masses with internal infarction or hemorrhage, increased T2-signal and increasing heterogeneity of the signal intensity have been reported. It is important to report the presence of prominent vessels along the fetal surface of the mass given potential for hemodynamic impact on the fetus. If there are early signs concerning for hydrops in the fetus, prompt notification of the ordering provider is indicated.

Similar to teratomas in other tissues, placental teratomas can contain virtually any tissue type including fat, calcification, fluid, and hair. Although teratomas in the placenta are extremely rare, in case reports, pregnancy outcomes are typically good (Elsasser et al. 2010). Although fat and calcification can be readily identified

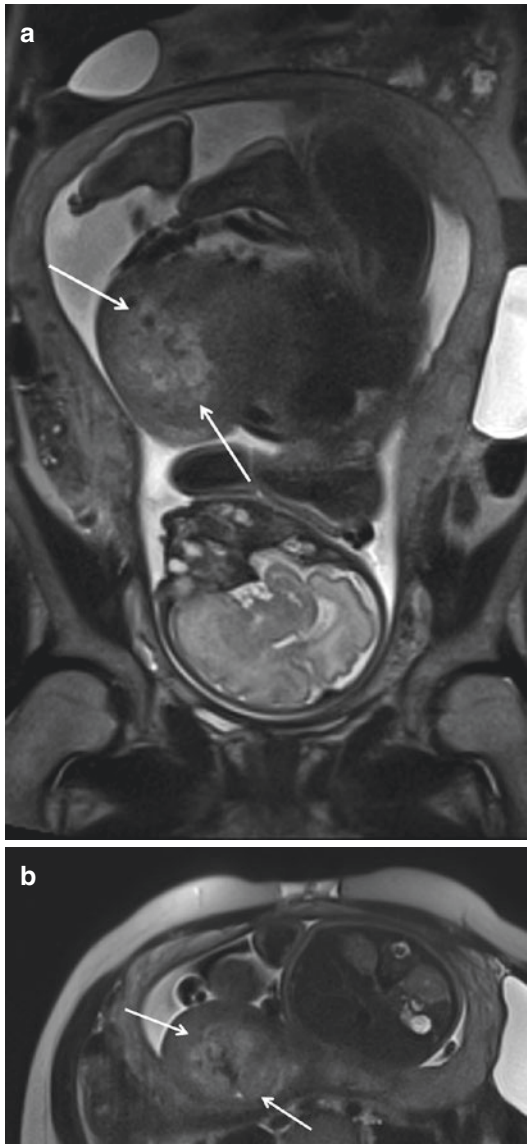

Fig. 11 Coronal (**a**) and axial (**b**) T2-weighted half-Fourier RARE images shows a well-circumscribed mass (*arrows*) arising from the fetal part of the placenta immediately adjacent to the insertion of the umbilical cord. This is the classic location for a chorioangioma

sonographically, differentiation from an anomalous additional gestation or fetus acardius amorphous can be difficult, and MRI may be requested if the diagnosis is uncertain. With a large field of view, the entire contents of the uterus can be readily evaluated in a single acquisition which is helpful in the setting of multiple gestations, excessive fetal movement, or unfavorable maternal habitus. Acquisitions utilizing fat saturation for bulk fat, and opposed phase imaging to identify intravoxel fat, may be helpful in the diagnosis teratoma. Identification of fetal parts would suggest an anomalous additional gestation and may be more readily visible within the mass on T2-weighted and balanced steady-state free-precession imaging. Identification of an umbilical cord (absent in teratoma) can also aid in differentiation (Elsasser et al. 2010).

8 MR Functional Imaging of the Placenta

Despite the fact that MR imaging helps delineate the morphologic alterations of the placenta with appropriate conspicuity during gestation and is of use in the study of placental invasion (as in placenta percreta), few studies have addressed the functional properties of the human placental vasculature.

Magnetic resonance imaging requested for a potentially serious indication provided a unique opportunity to explore the intervillous circulation of placentas from pregnancies complicated by intrauterine growth restriction (IUGR) and to compare them to normal cases. This allowed an innovative characterization of in vivo utero-placental blood flow, correlating a compromised intervillous circulation in IUGR to the deterioration of fetal condition (Moore et al. 2000).

MR images disclosed a homogeneous perfusion overall the placenta in normal cases, while IUGR placentas displayed a low intervillous blood flow, along with many patchy unperfused areas. Intermittent stops worsen the perfusion dynamics of the intervillous mostly in IUGR cases with an elevated ductus venosus pulsatility index. In IUGR placenta maternal placental blood flow is extremely compromised and that superimposed dynamic phenomena concur to worsen the intervillous circulation leading to an end-stage fetal decompensation (Brunelli et al. 2010).

However, MR evaluation of placental perfusion is limited by the inability to administer gadolinium due to concerns for fetal safety, and other forms of evaluation of placental

perfusion, including magnetization transfer, have been described.

This method takes advantage of the ratio of bound protons to total number of protons as a reflection of vascular flow. Owing to the clinical limitations of gadolinium-enhanced perfusion imaging, diffusion-weighted imaging is an alternative technique for studying regional ischemia caused by an insufficient vascular supply.

Among the many causes of diffusion restriction in human pregnancy, hematoma and infarctions are most important because they lead to dysmaturity of the placenta, resulting in smaller diffusive conductance and restricted blood supply owing to tissue degeneration and scarring (Brunelli et al. 2010).

9 Future Directions

Cell-free fetal DNA is now used frequently in the United States as a screening test for aneuploidy. With the growth of this technology, several investigators have looked at using cell-free placental mRNA in maternal plasma to better identify patients with accreta requiring hysterectomy and also as a tool to combine with ultrasound to improve accuracy (Nyberg et al. 1987; Verswijvel et al. 2002). In the patient with risk factors for placental invasion, the combination of a laboratory serum test with ultrasound and/or MRI might yield the most consistent results.

Fusion of ultrasound images on MR volumes has been feasible for fetal antenatal evaluation in a study conducted by Salomon et al. (Masselli et al. 2011c). Utilizing high-resolution ultrasound images with the capability of real-time color Doppler can help determine vascularity of structures, especially as gadolinium-based contrast agents are not routinely used in the setting of pregnancy. This capability may be of particular interest in placental evaluation. Fetal MRI does not currently have a significant role in the evaluation of Twin-to-twin transfusion syndrome (TTTS); however, there are case reports of using MR-guided high-intensity-focused ultrasound (MR-HIFU) for ablation of the abnormal vessels in TTTS (Sebire et al. 2002).

As elsewhere in the body, functional MR techniques are being applied in the placenta in effort to better evaluate normal physiology as well as pathologic states. The use of diffusion-weighted imaging has demonstrated restricted diffusion and reduced ADC values in the placentas of fetuses with growth restriction caused by placental insufficiency (Masselli et al. 2016). Diffusion-weighted imaging has also been proposed for the evaluation of placental invasion. As gadolinium-based contrast agents are not routinely used in pregnancy, noncontrast flow-sensitive methods, such as arterial spin labeling (ASL), have been proposed to assess placental perfusion (Masselli and Gualdi 2013).

In conclusion, MRI is an excellent modality in the evaluation of the placenta, and knowledge of the MR finding of various placental pathologies aids radiologists in the appropriate and timely care of the pregnant patients.

References

Baergren RN (2005) Placental shape aberrations. In: Baergren RN (ed) Manual of Benirschke and Kaufmann's Pathology of the human placenta. Springer, New York, pp 208–221

Bardo D, Oto A (2008) Magnetic resonance imaging for evaluation of the fetus and the placenta. Am J Perinatol 25:591–599

Baughman WC, Corteville JE, Shah RR (2008) Placenta accreta: spectrum of US and MR imaging findings. Radiographics 28(7):1905–1916

Bernirschke K, Kaufmann P (2000) Pathology of the human placenta, 4th edn. Springer, New York

Bonel HM, Stolz B, Diedrichsen L, Frei K, Saar B, Tutschek B, Raio L, Surbek D, Srivastav S, Nelle M, Slotboom J, Wiest R (2010) Diffusion-weighted MR imaging of the placenta in fetuses with placental insufficiency. Radiology 257(3):810–819

Brunelli R, Masselli G, Parasassi T et al (2010) Intervillous circulation in intra-uterine growth restriction. Correlation to fetal well being. Placenta 31: 1051–1056

Derwig IE, Akolekar R, Zelaya FO, Gowland PA, Barker GJ, Nicolaides KH (2011) Association of placental volume measured by MRI and birth weight percentile. J Magn Reson Imaging 34(5):1125–1130

Dwyer BK, Belogolovkin V, Tran L et al (2008) Prenatal diagnosis of placenta accreta: sonography or magnetic resonance imaging? J Ultrasound Med 27: 1275–1281

Elsasser DA, Ananth CV, Prasad V, Vintzileos AM, Vintzileos AM (2010) Diagnosis of placental abruption: relationship between clinical and histopathologi-

cal findings. Eur J Obstet Gynecol Reprod Biol 148: 125–130
Elsayes KM, Trout AT, Friedkin AM, Liu PS, Bude RO, Platt JF, Menias C (2009) Imaging of the placenta: a multimodality pictorial review. Radiographics 29(5):1371–1391
Huppertz B (2008) The anatomy of the normal placenta. J Clin Pathol 61:1296–1302
Kawamoto S, Ogawa F, Tanaka J, Ban S, Heshiki A (2000) Chorioangioma: antenatal diagnosis with fast MR imaging. Magn Reson Imaging 18(7):911–914
Kim JA, Narra VR (2004) Magnetic resonance imaging with true fast imaging with steady-state precession and half-Fourier acquisition single-shot turbo spin-echo sequences in cases of suspected placenta accreta. Acta Radiol 45:692–698
Lam G, Kuller J, McMahon M (2002) Use of magnetic resonance imaging and ultrasound in the antenatal diagnosis of placenta accreta. J Soc Gynecol Investig 9:37–40
Lax A, Prince MR, Mennitt KW, Schwebach JR, Budorick NE (2007) The value of specific MRI features in the evaluation of suspected placental invasion. Magn Reson Imaging 25:87–93
Levine D (2006) Obstetric MRI. J Magn Reson Imaging 24:1–15
Levine D, Pedrosa I (2005) MR imaging of the maternal abdomen and pelvis in pregnancy. In: Levine D (ed) Atlas of fetal MRI. Taylor and Francis Group, Boca Raton, pp 202–210
Levine D, Hulka CA, Ludmir J, Li W, Edelman RR (1997) Placenta accreta: evaluation with color Doppler US, power Doppler US, and MR imaging. Radiology 205:773–776
Leyendecker JR, DuBose M, Hosseinzadeh K, Stone R, Gianini J, Childs DD, Snow AN, Mertz H (2012) MRI of pregnancy-related issues: abnormal placentation. AJR Am J Roentgenol 198(2):311–320
Linduska N, Dekan S, Messerschmidt A, Kasprian G, Brugger PC, Chalubinski K, Weber M, Prayer D (2009) Placental pathologies in fetal MRI with pathohistological correlation. Placenta 30(6):555–559
Masselli G, Gualdi G (2013) MR imaging of the placenta: what a radiologist should know. Abdom Imaging 38(3):573–587
Masselli G, Brunelli R, Casciani E et al (2008) Magnetic resonance imaging in the evaluation of placental adhesive disorders: correlation with color Doppler ultrasound. Eur Radiol 18:1292–1299
Masselli G, Brunelli R, Casciani E, Polettini E, Bertini L, Laghi F, Anceschi M, Gualdi G (2011a) Acute abdominal and pelvic pain in pregnancy: MR imaging as a valuable adjunct to ultrasound? Abdom Imaging 36(5):596–603
Masselli G, Brunelli R, Di Tola M et al (2011b) MR imaging in the evaluation of placental abruption: correlation with sonographic findings. Radiology 259:222–230
Masselli G, Brunelli R, Parasassi T, Perrone G, Gualdi G (2011c) Magnetic resonance imaging of clinically stable late pregnancy bleeding: beyond ultrasound. Eur Radiol 21(9):1841–1849
Masselli G, Perrone G, Kinkel K et al (2016) Are Second Trimester Apparent Diffusion Coefficient Values of the Short Uterine Cervix Associated with Impending Preterm Delivery? Radiology 280(3):897–904
Moore RJ, Strachan BK, Tyler DJ et al (2000) In utero perfusing fraction maps in normal and growth restricted pregnancy measured using IVIM echo-planar MRI. Placenta 21:726–732
Morita S, Ueno E, Fujimura M, Muraoka M, Takagi K, Fujibayashi M (2009) Feasibility of diffusion-weighted MRI for defining placental invasion. J Magn Reson Imaging 30:666–671
Nagayama M, Watanabe Y, Okumura A, Amoh Y, Nakashita S, Dodo Y (2002) Fast MR imaging in obstetrics. Radiographics 22:563–582
Nguyen D, Nguyen C, Yacobozzi M, Bsat F, Rakita D (2012) Imaging of the placenta with pathologic correlation. Semin Ultrasound CT MR 33:65–77
Nyberg DA, Mack LA, Benedetti TJ, Cyr DL, Schuman WP (1987) Placental abruption and placental hemorrhage: correlation of sonographic findings with fetal outcome. Radiology 164:357–361
Oyelese Y, Ananth CV (2006) Placental abruption. Obstet Gynecol 108:1005–1016
Oyelese Y, Smulian JC (2006) Placenta previa, placenta accreta, and vasa previa. Obstet Gynecol 107:927–941
Palacios Jaraquemada JM, Bruno C (2000) Gadolinium enhanced MR imaging in the differential diagnosis of placenta accreta and placenta percreta. Radiology 216:610–611
Palacios Jaraquemada JM, Bruno CH (2005) Magnetic resonance imaging in 300 cases of placenta accreta: surgical correlation of new findings. Acta Obstet Gynecol Scand 84:716–724
Sakornbut E, Leeman L, Fontaine P (2007) Late pregnancy bleeding. Am Fam Physician 75:1199–2006
Sebire NJ, Sepulveda W (2008) Correlation of placental pathology with prenatal ultrasound findings. J Clin Pathol 61:1276–1284
Sebire NJ, Foskett M, Fisher RA, Rees H, Seckl M, Newlands E (2002) Risk of partial and complete hydatidiform molar pregnancy in relation to maternal age. BJOG 109(1):99–102
Sinha P, Kuruba N (2008) Ante-partum haemorrhage: an update. J Obstet Gynaecol 28:377–381
Tanaka YO, Sohda S, Shigemitsu S, Niitsu M, Itai Y (2001) High temporal resolution dynamic contrast MRI in a high risk group for placenta accreta. Magn Reson Imaging 19:635–642
To WW, Leung WC (1995) Placenta previa and previous cesarean section. Int J Gynaecol Obstet 51(1):25–31
Verswijvel G, Grieten M, Gyselaers W, Van Holsbeke C, Vandevenne J, Horvath M, Gelin G, Palmers Y (2002) MRI in the assessment of pregnancy related intrauterine bleeding: a valuable adjunct to ultrasound? JBR-BTR 85:189–192
Victoria T, Johnson AM, Kramer SS, Coleman B, Bebbington M, Epelman M (2011) Extrafetal findings at fetal MR: evaluation of the normal placenta and correlation with ultrasound. Clin Imaging 35:371–377

Warshak CR, Eskander R, Hull AD, Scioscia AL, Mattrey RF, Bernirschke K, Resnik R (2006) Accuracy of ultrasonography and magnetic resonance imaging in the diagnosis of placenta accreta. Obstet Gynecol 108:573–581

Zalel Y, Gamzu R, Weiss Y et al (2002a) Role of color Doppler imaging in diagnosing and managing pregnancies complicated by placental chorioangioma. J Clin Ultrasound 30(5):264–269

Zalel Y, Weisz B, Gamzu R, Schiff E, Shalmon B, Achiron R (2002b) Chorioangiomas of the placenta: sonographic and Doppler flow characteristics. J Ultrasound Med 21(8):909–913

Erratum to: Endometrial Cancer

Mariana Horta and Teresa Margarida Cunha

Erratum to: Med Radiol Diagn Imaging
DOI 10.1007/174_2016_84

The publisher regrets that incorrect affiliation details were included in the published version for authors Mariana Horta and Teresa Margarida Cunha.

The correct affiliation details are provided below.

Mariana Horta (✉)
Serviço de Radiologia,
Instituto Português de Oncologia de Lisboa Francisco Gentil,
Rua Prof. Lima Basto, 1099-023 Lisboa, Portugal
mariana.sf.horta@gmail.com

Teresa Margarida Cunha
Serviço de Radiologia,
Instituto Português de Oncologia de Lisboa Francisco Gentil,
Rua Prof. Lima Basto, 1099-023 Lisboa, Portugal
tmargarida@gmail.com

The updated original online version for this chapter can be found at
DOI 10.1007/174_2016_84

Erratum to: CT and MRI in Ovarian Carcinoma

Rosemarie Forstner

Erratum to: Med Radiol Diagn Imaging
DOI 10.1007/174_2017_17

Inadvertently, the chapter was published online with a co-author - Carolyn M. Zelop, who has not contributed to this chapter. The co-author name has been deleted now from the original version.

The updated online version for this chapter can be found under DOI 10.1007/174_2017_17

R. Forstner (✉)
Salzburger Landeskliniken, Paracelsus Medical University, Müllner Hauptstr. 48, Salzburg 5020, Austria
e-mail: R.Forstner@salk.at

Index

DOI 10.1007/978-3-319-42575-7, © Springer International Publishing AG, part of Springer Nature